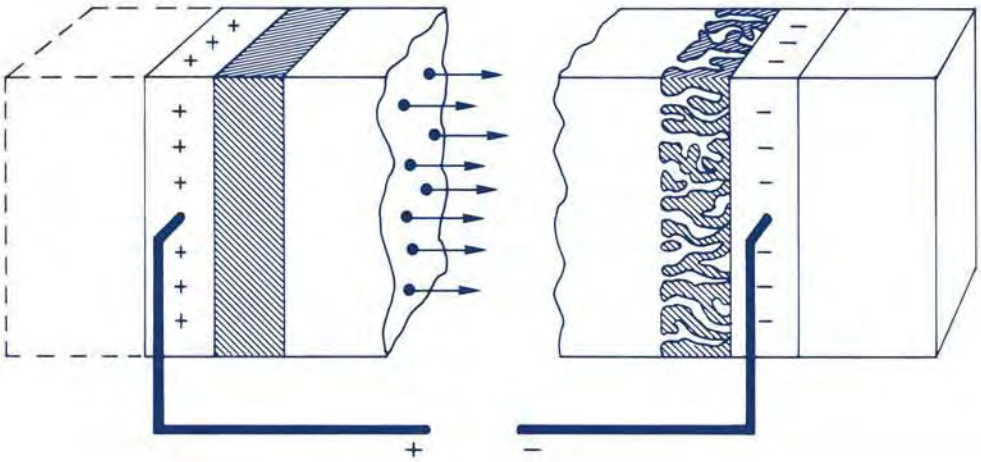

C.G. GRANQVIST

HANDBOOK OF INORGANIC ELECTROCHROMIC MATERIALS

ELSEVIER

HANDBOOK OF INORGANIC ELECTROCHROMIC MATERIALS

This Page Intentionally Left Blank

HANDBOOK OF INORGANIC ELECTROCHROMIC MATERIALS

C.G. GRANQVIST

Department of Technology
School of Engineering
University of Uppsala
Uppsala, Sweden

ELSEVIER
Amsterdam – London – New York – Oxford – Paris – Shannon – Tokyo

ELSEVIER SCIENCE B.V.
Sara Burgerhartstraat 25
P.O. Box 211, 1000 AE Amsterdam, The Netherlands

First edition 1995
Second impression 2002

Library of Congress Cataloging-in-Publication Data

Granqvist, Claes G.
Handbook of inorganic electrochromic materials / C.G. Granqvist.
p. cm.
Includes bibliographical references and index.
ISBN 0-444-89930-8 (acid-free paper)
1. Electrochromic devices--Materials. 2. Metallic oxides--Optical properties. 3. Organic compounds--Optical properties. I. Title.
TA1750.G73 1995
621.381'045--dc20 95-2544
CIP

ISBN: 0-444-89930-8

The paper used in this publication meets the requirements of ANSI/NISO Z39.48-1992 (Permanence of Paper).
Printed in The Netherlands.

To Daniel and Marty

This Page Intentionally Left Blank

Preface

Electrochromic oxides are interesting from the perspectives of basic science and technology, and it seems surprising that no earlier book or detailed treatise is available. I felt that the lack of such a text was becoming more and more of a problem; the research field was expanding rapidly, but no real framework for organizing this wealth of information was at hand. In such a situation, there is always a danger that too much work will be of duplicative nature or will move into dead ends. Although this book certainly leaves many questions unanswered, I hope it improves the conditions for research and development by providing a map of terrain that formerly was only poorly known.

The writing of this book began towards the end of 1990. John Vossen had asked me to prepare a chapter on electrochromism for the series on *Physics of Thin Films* that he was co-editing. I embarked on the writing unaware of the work ahead of me. Very soon the initial plan had to be abandoned, as I realized that nothing but digging to the bottom of the literature on electrochromics would do. The writing grew correspondingly, and soon I was writing a book.

The book covers electrochromism in metal oxides with detailed discussions of materials preparation (mainly by thin film technology), materials characterization, optical properties, device design, and device performance. Extensive references are given to previous work. As regards variable optical properties--i.e., the actual "electrochromism"--the goal is to cover the scientific and technical literature in its entirety. Other aspects such as film preparation and characterization are treated somewhat more selectively. I have tried to include ample references up to mid-1993, with the aim of providing an up-to-date and comprehensive bibliography, even on subject matter slightly outside the core topics of the book. The price of this quest for complete and current coverage is a rather daunting reference list.

The subject matter is organized into 31 chapters; the introductory survey is followed by topical chapters divided into three main parts. Part One, chapters 2-11, covers electrochromic tungsten oxide. This material has been fairly thoroughly investigated, and this segment of the book serves as a case study to introduce relevant techniques and concepts. Part Two, embracing chapters 12-24, discusses films of the other inorganic materials known to exhibit electrochromism. Oxides of molybdenum, iridium, titanium, manganese, vanadium, nickel, cobalt, niobium, etc., are covered in chapters 12-22. The order of presentation might at first seem rather random; however, it allows oxides with different basic microstructures to be discussed in a natural order, and it makes it possible to introduce new concepts in a convenient way. Chapter 23 is of particular importance and treats electrochromism among the oxides from a unified bandstructure perspective. Chapter 24 gives some facts on the electrochromism of non-oxides. Part Three, with chapters 25-31, is devoted to device aspects and shows data on constructions for modulating optical transmittance and reflectance.

Electrochromic devices are of interest in different fields of technology. Among the numerous possible applications one can point to are elements for information display, variable-reflectance mirrors, variable-transmittance windows, and variable-emittance surfaces. In particular, I want to

stress that electrochromism makes it possible to design "smart windows" for variable inlet of light and solar energy into energy-efficient buildings.

Book-writing is often a painful and tiresome job, and this book was no exception. I struggled with the manuscript on and off for more than three years. Of course, the normal tasks of the university professor usually had to be given a higher priority. Therefore the writing normally had to take place during evenings, weekends, and other "spare time". I am grateful to all of you who helped me along! I would like to thank my secretaries Marita Ahlkvist, Anneli Beblein, and Ingrid Riedl at the Physics Department of Chalmers University of Technology and the University of Gothenburg (where I worked until the end of July 1993) and, especially, Lis Timner at the Department of Technology of Uppsala University (where I began working in July 1993). Special thanks to Eva-Britt Sjöqvist, who drew the figures. All of these women were marvelous in transforming scribbling and sketches into neat text and figures. The English was checked by Roberta Aplin Roos. I am also endebted to my wife, Martha Garrett, a researcher and librarian, who carried out the final, computerized literature search. The Swedish Natural Science Research Council is thanked for a special grant to cover some of the costs for preparing the manuscript.

Last but not least, I must thank Martha and my son, Daniel, for their patience and understanding during my absence--both physical and mental.

Uppsala, May 1994 Claes G Granqvist

Contents

Chapter 1

INTRODUCTION

An electrochromic material is able to change its optical properties when a voltage is applied across it. The optical properties should be reversible, i.e., the original state should be recoverable if the polarity of the voltage is changed. These properties make electrochromic materials of considerable interest for optical devices of several different types, such as elements for information display, light shutters, smart windows, variable-reflectance mirrors, and variable-emittance thermal radiators.

Electrochromism is well known in numerous inorganic and organic substances. This book is devoted to the former class. Almost all of the interesting materials are oxides that are employed in the form of thin films. The aim of the book is to present the state-of-the-art for electrochromic oxides with regard to basic materials physics and chemistry, thin film fabrication technology, and device construction.

Electrochromism, as characterized above, can be observed only if the pertinent oxide is incorporated in a system that allows the application of a voltage. The optical modulation in the interesting oxides is connected with differences in their electron density, and hence the electrical contacts needed for the voltage should also allow current injection and extraction. Obviously, one of these contacts must be transparent, or at least arranged in such a way that it does not significantly obscure the optically functional electrochromic material.

This book is the first comprehensive treatise on electrochromic oxides. However, useful surveys of the subject, or at least substantial parts of it, have been given by Lampert *(2002)* and many others *(33-4, 196, 198, 204, 254, 289, 294, 334, 342, 402, 649, 701, 814-5, 840-2, 956a, 1706, 2115, 2612, 3081a, 3333, 3608)*. Faughnan and Crandall *(1046)* and, more recently, Granqvist *(1293)* discussed the properties of electrochromic tungsten oxide in detail. Extensive compilations of papers on electrochromism can be found in proceedings volumes published in 1990 by Carpenter and Corrigan *(612)* and by Lampert and Granqvist *(2006)*.

1.1 Prototype Device Design and Some Key Concepts

One may think of many possible electrochromic device constructions. The most important of these is depicted in Fig. 1.1. The shown arrangement of materials is the preferred one in almost all work aimed at practical utilization of electrochromism, and the set-up is convenient also as a prototype for discussing electrochromic systems in general.

Figure 1.1 shows a number of layers backed by a substrate that in many cases is a glass plate. The glass has a transparent and electrically conducting film and a film of the electrochromic oxide. This oxide has mixed conduction for ions and electrons, and if ions are introduced from an adjacent

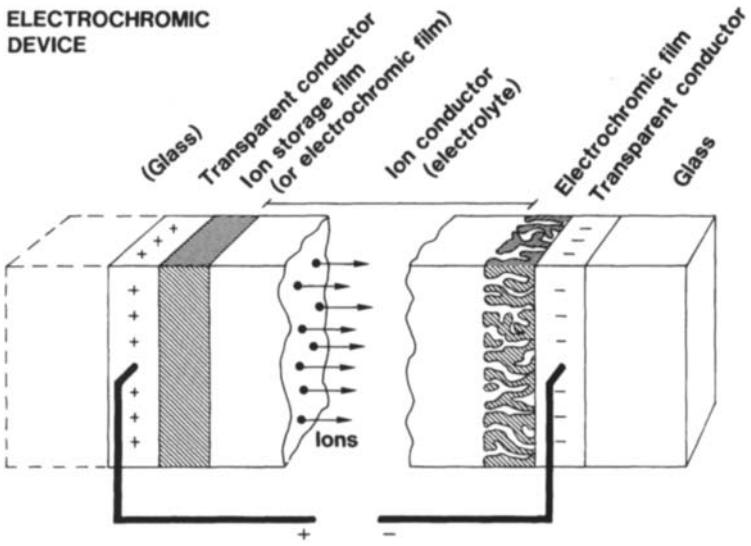

Fig. 1.1 Basic design of an electrochromic device, indicating transport of positive ions under the action of an electric field.

electrolyte or via an adjacent ion conductor there is a corresponding charge-balancing counterflow of electrons from the transparent electron conductor. These electrons will remain in the electrochromic film as long as the ions reside there and, as indicated above, the electrons will then evoke a persistent change of the optical properties. Depending on which electrochromic oxide is used, the electron injection can increase or decrease the transparency. The ion conductor, that comes next in the device, can be a thin film or a bulk-like material; for practical devices one prefers a solid inorganic or organic (polymeric) material, whereas liquid electrolytes are convenient for research and exploratory work. The final components of the device are an ion storage film, with or without electrochromic properties, and another electrical conductor that must be a transparent film if the full device is for modulating light throughput. For some devices at least, it is suitable to have a second glass plate, so that the entire system embodies two substrates--each with a two-layer coating--and an intervening ion conductor that can serve as a lamination material. Each of the films in the device can have a thickness less than one micrometer; such films can be produced by many different techniques.

When a voltage is applied between the (transparent) electrical conductors, as indicated in Fig. 1.1, a distributed electrical field is set up and ions are moved uniformly into and out of the electrochromic film(s). The charge-balancing counterflow of electrons through the external circuit then leads to a variation of the electron density in the electrochromic material(s) and thereby a modulation of their optical properties. If the ion conductor has negligible electronic conductivity, the device will exhibit open circuit memory, so that the optical properties remain stable for long periods of time.

The device design in Fig. 1.1 is appropriate for transmittance modulation, but the set-up can be converted to reflectance modulation, for example by invoking a mirror or a diffuse scatterer behind the electrochromic film. In some cases the electrochromic film itself can turn reflecting, but it is more common that it exhibits absorptance modulation. The voltage applied between the outer films should be of the order of a few volts only. Higher voltages will lead to rapid deterioration of the device.

There are many requirements on the electrochromic film. Obviously, the optical modulation should be large enough for a practically realizable change in the electron density; in other words, the *coloration efficiency* should be large. The conductivity for ions and electrons must be sufficient, so that the optical modulation is not excessively slow. In many cases it is the ion mobility that is the bottleneck, and it is imperative that the electrochromic film has a structure that is permeable enough to permit easy insertion and extraction of ions. The usual terminology here is to speak of ion *intercalation* and *deintercalation*.

The ion storage film has the same demands on electronic and ionic conductivity as the electrochromic one discussed above. If the ion storage film has electrochromic properties, they should be complementary to those of the primary electrochromic film. Thus if the primary electrochromic film darkens upon ion intercalation, the ion storage should darken upon ion deintercalation (and vice versa). Darkening under ion intercalation is referred to as *cathodic coloration*, wheras darkening under ion deintercalation is referred to as *anodic coloration*.

The ion conductor should have sufficient ion conductivity and low enough electron conductivity. The transparent electrical conductor(s) must have low resistivity. The latter property often limits the dynamics of large electrochromic devices. Clearly the entire electrochromic multilayer stack must be durable during the practical service life of the device.

Table 1.1 Summary of key features for the main electrochromic oxides, showing oxide type, whether the coloration is cathodic C or anodic A, whether full transparency can be achieved (yes = Y; no = N), and whether the general structure type embodies a framework F or layers L of MeO_6 octahedra.

Oxide type	Coloration	Full transp.	Structure type
TiO_2	C	Y	F
V_2O_5	C/A	N	L[a]
Cr_2O_3	A	N	F
MnO_2	A	N	F
"FeO_2"	A	N	F
"CoO_2"	A	N	L?
"NiO_2"	A	Y	L
Nb_2O_5	C	Y	F
MoO_3	C	Y	F/L
RhO_2	A	?	F
Ta_2O_5	C	Y	F
WO_3	C	Y	F
IrO_2	A	Y	F

[a] Layer structure with VO_5 units.

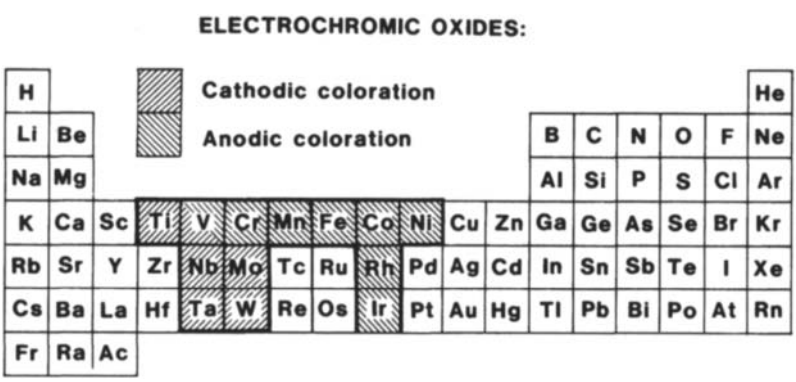

Fig. 1.2 The Periodic Table of the elements, excepting the lanthanides and actinides. The shaded boxes refer to the transition metals whose oxides have well-documented cathodic and anodic electrochromism.

1.2 Survey of Electrochromic Oxide Films

Electrochromism has been well documented for oxides of the elements indicated in the Periodic Table in Fig. 1.2. All of these elements belong to the transition series *(779)*. Different shading is used to denote cathodic and anodic electrochromism. Cathodic coloration is found in oxides of Ti, Nb, Mo, Ta, and W, with tungsten oxide being by far the most extensively studied one. Anodic coloration is found in oxides of Cr, Mn, Fe, Co, Ni, Rh, and Ir, with nickel oxide and iridium oxide being the ones investigated in most detail. Vanadium is exceptional in that the pentoxide (with V^{5+}) exhibits anodic and cathodic eletrochromism within different wavelenth ranges, while the dioxide (with V^{4+}) has anodic electrochromism. Charts that are similar, though not identical, to Fig. 1.2 have been shown by Baba *(196, 204)* and Yu *(3766)*. Only some of the oxides mentioned above can be fully transparent to visible light, notably the oxides based on Ti, Ni, Nb, Mo, Ta, W, and Ir. The other oxides show some residual absorption either across the full visible range or in the blue part of the spectrum. The latter feature is associated with interband absorption in a semiconductor.

It is interesting and important to notice that the electrochromic oxides are based on metallic elements that are located in a well-defined region of the Periodic Table, and, furthermore, that different parts of this region pertain to oxides with cathodic and anodic coloration. Already at this point one may draw the conclusion that the electrochromism is closely related to the electronic structure of the oxides.

Table 1.1 summarizes a number of key properties of the electrochromic oxides. The first column indicates the nominal composition of the oxide. For some of these--notably the oxides based on Fe, Co, and Ni--the situation is complicated by the fact that hydrogen is normally a critical constituent in the material and serves to stabilize a favorable structure. The second and third column in Table 1.1 list the overall optical properties discussed above.

Apart from in the materials discussed so far, electrochromism is known to occur in many binary and ternary mixed oxides and in oxyfluorides. There are also some simple oxides that have been reported as displaying electrochromism, although this phenomenon has not yet been explored in detail; oxides based on Cu, Sr-Ti, Ru, and Pr belong to this latter class. Finally, among the non-oxides pronounced anodic electrochromism is known in transition metal hexacyanometallates.

Essentially all of the electrochromic oxides are constructed from one type of building blocks, viz. MeO_6 octahedra with a central transition metal (Me) atom surrounded by six almost equidistant oxygen atoms. The building blocks are connected either by corner-sharing or by a combination of corner-sharing and edge-sharing, and many different crystal structures are known. It is meaningful to divide these into three-dimensional framework (F) structures and weakly coupled, essentially two-dimensional, layer (L) structures. The pertinent structural group is indicated in the last column of Table 1.1. Detailed discussions of the crystal structures can be found in the standard texts by Wells *(3598)* and by Hyde and Andersson *(1594)*.

It was stressed above that the electrochromic oxide films must be permeable to ions and must show some electrical conductivity. The ions can move and reside in the spaces between the MeO_6 octahedra. However, at least for the framework structures these spaces may not be large enough to yield reasonable intercalation/deintercalation rates and therefore the materials must have a fine-grained character with low-density grain boundaries. Sometimes it is also desirable to have an extended columnar configuration that allows easy transport of ions over the cross-section of the electrochromic film. Such columns were shown schematically in Fig. 1.1. To further open up the

Table 1.2 Major technologies for making thin films of electrochromic oxides.

Category	Method	Variety
Physical	Evaporation	Vacuum
		Reactive (O_2, N_2, H_2O)
		Ion assisted
	Sputtering	Non-reactive (Ar)
		Reactive (Ar + O_2)
		"Chemical" (O_2 + CF_4)
Electrochemical	Electrodeposition	
	Anodization	
Chemical	Vapor deposition	Atmospheric pressure
		Low pressure
		Plasma enhanced
	Sol-gel	Dipping
		Spin-coating
		Spraying
	Spray pyrolysis	
	Decomposition reaction	
	Thermal oxidation	

structure and provide conduits and intercalation sites for the ions, the useful electrochromic films are often *hydrous*, i.e., they are more or less hydrated, hydroxylated, oxy-hydroxylated, etc. These somewhat unspecific materials are referred to as W oxide, Mo oxide, and so forth. Suitably prepared films may have a high capability of ion intercalation with an ion/metal ratio of the order of unity. The mobile ions should be as small as possible with H^+ (protons), Li^+, Na^+, and K^+ being the best. In a water-containing electrolyte or ion conductor, these ions are normally associated with H_2O molecules, i.e., they move together with their so called *coordination spheres*. An overview of the electrochemical reactions of different oxides in aqueous solution can be gained from the detailed treatise by Pourbaix *(2799)*.

Many alternatives are available for making thin films of the electrochromic oxides. Table 1.2 lists the major methods categorized into physical, chemical, and electrochemical ones and further subdivided into varieties. For the various deposition methods, it seems that molecular species, rather than single atoms, are the primary constitutive units. This feature tends to conserve the MeO_6 blocks referred to above, and the films should usually be regarded as *cluster-assembled materials* or *molecular solids* rather than truly amorphous or glassy substances. Reviews specifically for electrochromic films made by chemical vapor deposition and sol-gel technology were given by Donnadieu *(958)* and by Agrawal et al. *(36)*, respectively.

Materials characterization is important and seldom easy. Among the many complicating facts one may note that

(i) transition metal oxides are well known to have numerous different crystal structures even in their bulk state,

(ii) the interesting films are highly disordered, yet not truly amorphous, and show structural inhomogeneities on all scales from the molecular building block up to the film thickness,

(iii) the intercalated ions may not be easy to probe since they normally are very light and since the ionic species can either bond at preferred sites or can be mobile in a host lattice,

(iv) intercalation/deintercalation dynamics depends on ions, sometimes with an unspecified coordination sphere, moving in a material with highly irregular pores and channels,

(v) electrochromism demands a multilayer device configuration, which makes it difficult to analyse any single layer, and

(vi) electrochromism requires understanding of several different subjects such as solid state physics/chemistry, structural chemistry, electrochemistry, thin film science and, sometimes, polymer science as well as device technology.

There is a plethora of techniques for probing these inherently difficult materials. The major ones are summarized in Table 1.3, together with the acronyms that are used in the rest of the book. Acronyms, abbreviations, and symbols are summarized also in the Appendix. Assigning a specific technique to a certain studied property may be ambiguous and, for example, methods for studying the electronic structure also give information on the elemental composition.

So far in the discussion, the attention has been on electrochromic thin films. However, one

Table 1.3 Summary of the major techniques for analyzing electrochromic oxide films.

Studied property	Technique
Crystal structure and elemental composition	Transmission electron microscopy (TEM) Scanning electron microscopy (SEM) X-ray extinction Diffraction (XRD) Scattering Absorption (EXAFS, XANES) X-ray fluorescence (XRF) Vibrational spectroscopy Infrared absorption (IR, FTIR) Raman Secondary ion mass spectroscopy (SIMS) Rutherford backscattering spectroscopy (RBS) Nuclear reaction analysis (NRA)
Ion intercalation and deintercalation	Coulometric titration Chronoamperometry Cyclic voltammetry Impedance spectrometry Beam deflectometry Mirage effect Beam bending Microbalance measurements Nuclear magnetic resonance (NMR)
Electronic structure	Photoelectron spectroscopy X-ray (XPS) Ultraviolet (UPS) Auger (AES) Electron paramagnetic resonance (EPR) Electron energy loss spectroscopy (EELS)
Optical properties	Spectrophotometry Transmittance Reflectance Ellipsometry Attenuated total reflectance (ATR)

should note, mainly for completeness, that some work also has been carried out for electrochromic pigments *(874-5, 1984, 2307, 3733-4)* and bulk glasses. Among the glasses, most work has been reported for the system R_2O-GF-WO_3 (R = Li, Na, K), with the glass former (GF) being B_2O_3 *(473-4, 1558, 2952, 3455)*, P_2O_5 *(1025, 1911, 3266)*, or Nb_2O_5 *(2147)*. In addition, there are results for WO_3-containing glasses prepared by rapid quenching *(3371-2)* and sol-gel technology *(666)*, and for TiO_2- and MoO_3-containing glasses *(1911)*.

1.3 Applications Areas for Electrochromic Devices

There are many uses of materials whose optical properties can be varied reversibly and persistently by a low-voltage signal. These applications have in the past to a large extent served as a motivation for research on electrochromics. Presently the situation seems to be changing somewhat, and there is an increased interest in basic physics and chemistry for the electrochromic materials.

Figure 1.3 illustrates the four main applications of electrochromic devices. Part (a) refers to *information display*. The device embodies an electrochromic film in front of a diffusely scattering pigmented surface. The electrochromic film can be patterned and, for example, be part of a seven-segment numeric display unit of small or large size. It is possible to achieve excellent viewing properties with better contrast--particularly at off-normal angles--than in the conventional liquid-crystal-based displays. One may even think of an "electrochromic writing paper".

Display applications have been discussed ever since the discovery of electrochromism, but so far such displays have not been turned into large-scale consumer items. It is amusing to read in a scientific paper published in 1976 that "a commercial electrochromic wrist-watch display is apparently soon to be marketed in the United States" *(1320)*. That marketing did not happen, and neither did parallel efforts by European and Japanese watch manufacturers lead to products. The reasons why electrochromic displays were not commercialized are not entirely clear, but poor long-term durability is often forwarded as an explanation. Today's electrochromic technology has demonstrated excellent durability in some cases though, and it appears that no major technological obstacles are now holding back electrochromic display systems.

Electrochromic information displays have been surveyed many times in the literature, for example in *(1, 33-4, 266, 338, 342, 499, 649-50, 737-8, 814-5, 1046, 1252-3, 1311, 1318, 1397, 1584, 1885, 2075, 2102, 2225, 2386, 2624, 2842, 3079, 3081, 3333, 3790)*. Much of the work during the 1970s and early 1980s was performed in industrial laboratories, and several of the papers referred to above are based on work in the U.S. by American Cyanamid, RCA Laboratories, IBM, and Bell Laboratories; in The Netherlands by Philips Research Laboratories; in Switzerland by Brown Boveri and Asulab; in the U.K. by Plessey Co; and in Japan by Nippon Kagaku K.K., Sharp Corporation, Toshiba, Hitachi, and Asahi Glass Works. Contrast enhancement can be achieved by optical interference *(2267)* and substrate roughening *(2270)*.

Figure 1.3(b) shows how an electrochromic film can be used to produce a *mirror with variable specular reflectance*. This application seems to be the most mature one, and antidazzling rear-view mirrors built on electrochromic oxide films are currently (1994) available for cars and trucks. Work on variable reflectance mirrors was pioneered at Schott in Germany *(1919)*; subsequent work at this company and at Donnelly Corporation in the U.S. was discussed by Baucke et al. *(282-8, 290-1, 294)*, Lynam et al. *(2120, 2122)*, and others *(1410, 1455)*.

Electrochromic *smart windows*, sketched in Fig. 1.3(c), are considered next. The basic idea

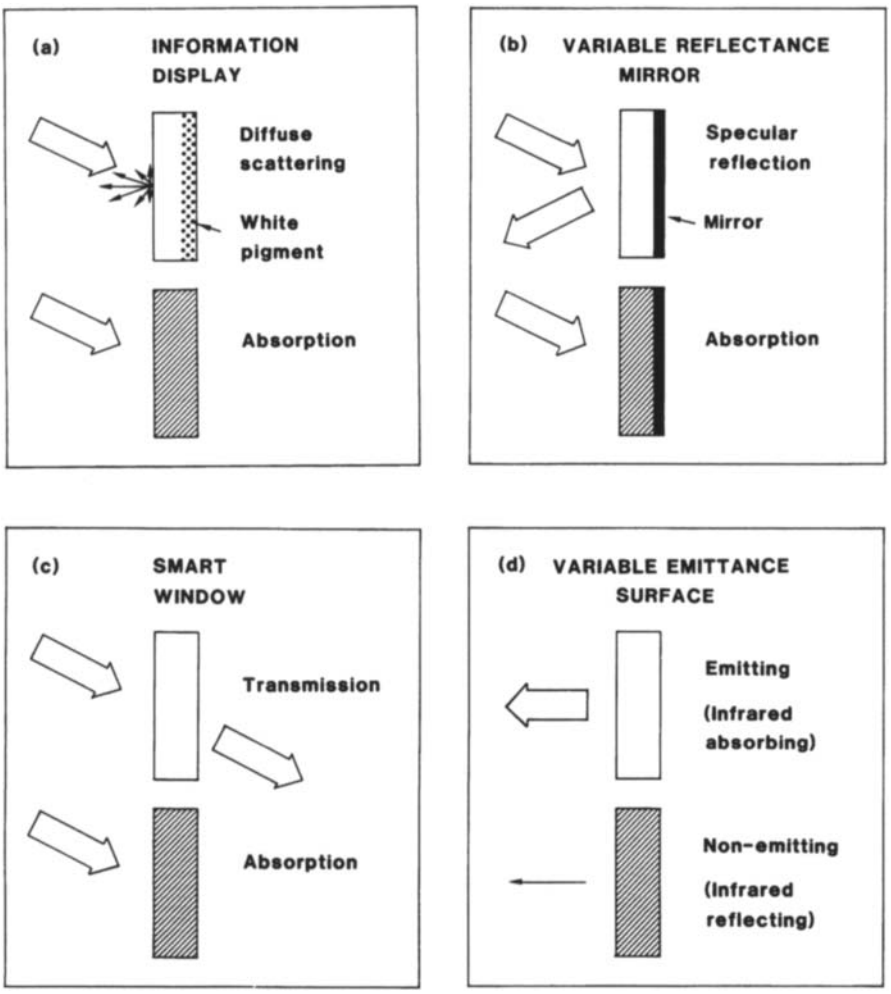

Fig. 1.3 The principles of four different applications of electrochromic devices. Arrows indicate incoming and outgoing electromagnetic radiation; the thickness of the arrow signifies radiation intensity.

is to make an architectural or automotive window with variable transmittance so that a desired amount of visible light and/or solar energy is introduced. Such windows can lead to energy efficiency as well as a comfortable indoor climate. Large research efforts are presently going on both in Industry and in Academia. The term "smart window" was coined in 1984 by Svensson and Granqvist *(3285, 3288)*; it was picked up and used as a generic term by Selkowitz *(3092)*, Truong *(3456)*, and others. Surveys over smart windows research were presented by Granqvist *(1276-88, 1293-4, 1298)*, Lampert *(2002)*, and several others *(347, 515, 891, 1216, 2461, 2713, 2853, 3299)*. Automotive applications were treated by Demiryont *(874-5)*. Thermal and optical analyses of windows were given by Reilly et al. *(2881)* and Sweitzer *(3300)*.

Variable emittance surfaces, outlined in Fig. 1.3(d), are based on a special device design with a crystalline tungsten oxide film at the exposed surface of an electrochromic device. Intercalation/deintercalation of ions makes this surface infrared reflecting/absorbing, i.e., the thermal emittance is low/high. The emitted radiative power is proportional to the emittance. Variable emittance surfaces can be employed for temperature control under conditions when radiative exchange dominates over conduction and convection, such as for space vehicles. This application has not been widely discussed in the open literature, but some basic features were outlined by Braig and Meisel *(471)*.

Electrochromic devices of other types than those already discussed have also been given some consideration in the literature. Thus *electrophotography* was mentioned as early as in the first publication specifically on electrochromism, viz. in Deb's seminal paper of 1969 *(835)*. This application has been discussed more recently by Shizukuishi et al. *(3157)*, Nishimura et al. *(2539)*, and Stikans et al. *(3246-7)*. Among other potential optics-related uses one can note writing boards *(2391)*, thin film retardation plates *(2409-10)*, variable barrier-height semiconductor diodes *(2857)*, and UV photoresists *(2947)*.

For quantitative assessments of device performance, one must know the spectral properties of the light detector (normally the eye), the light source, etc. The visual appearance of an electrochromic film, incorporated in an electrochromic device, is often the technically interesting property, and hence one must specify the luminous efficiency--or relative spectral sensitivity--of the normal human eye. This property is shown in Fig. 1.4. Generally speaking, the spectral curves are confined to the $0.4 < \lambda < 0.7$ μm wavelength range. More precisely, the *photopic* curve--referring to the light-adapted eye--exceeds one percent of the maximum value at $0.43 < \lambda < 0.69$ μm and is peaked at 0.56 μm. Correspondingly, the *scotopic* curve for the darkness-adapted eye lies at $0.40 < \lambda < 0.62$ μm and is peaked at 0.51 μm. Detailed discussions of the retinal spectral sensitivity function and other related items can be found in books by Wyszecki et al. *(1697, 3670-1)* and MacAdam *(2128)*.

The actual visual appearance is not determined only by the eye but also depends of the spectral content of the light within which the object is viewed. The ensuing visual response is then governed by a folding of the spectral curves for the eye sensitivity and for the light source. Standardized light sources (illuminants) are employed in order to derive unique color specifications; the most common ones are shown in Fig. 1.5. The illuminant denoted D_{65} represents normal daylight; an older and less commonly used equivalent is referred to as "illuminant C". Illuminant A represents light from an incandescent tungsten lamp taken to perform as a blackbody radiator at 2856 K.

Illuminant D_{65} and the photopic eye sensitivity are appropriate for judging an electrochromic display device, or the light control of a smart window, during the day. Illuminant A and the scotopic eye sensitivity, on the other hand, are pertinent to electrochromic anti-dazzling rear view mirrors.

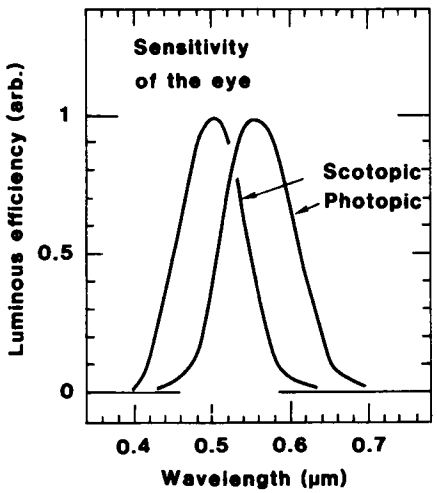

Fig. 1.4 Spectral luminous efficiency for the human eye in its light-adapted (photopic) and darkness-adapted (scotopic) states.

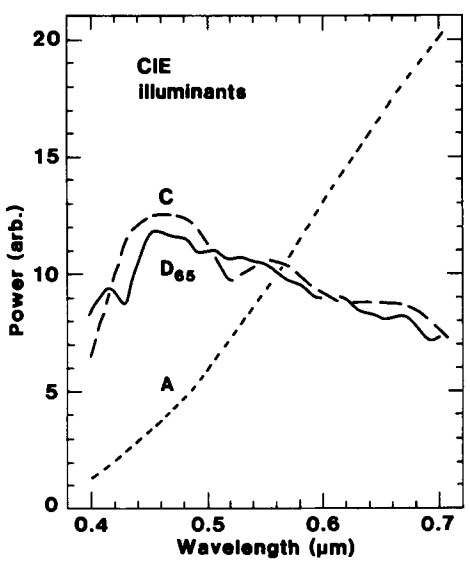

Fig. 1.5 Spectral power distributions for three illuminants specified by CIE (Commission International de l'Eclairage).

Smart windows allow the throughput of radiant energy to be controlled. Figure 1.6 shows two solar irradiance spectra; the one for air mass zero (AM0) corresponds to radiation outside the earth's atmospheric envelope, and the one for 1.5 air mass (AM1.5) corresponds to radiation having passed through the atmosphere from an angle so that the pathlength is 1.5 times the perpendicular depth of the atmosphere. The curves have a skew bell shape and are peaked at wavelengths in the range of the eye sensitivity. The solar irradiance spectra extend well into the infrared; for the AM0 curve, ~6.5 % remains at $\lambda < 2$ μm and for the AM1.5 curve ~5 % remains above this wavelength. Solar irradiance spectra are given in *(170, 389, 1578, 1622, 2661)*.

Finally, variable emittance surfaces operate by modulating the optical properties at long wavelengths. Figure 1.7 shows blackbody exitance spectra for four temperatures between +100 and -50°C. The curves are very broad and extend from ~3 to ~50 μm. It is in this full range that the reflectance must be changed in an electrochromic system designed for thermal radiative control.

1.4 Some Notes on the History of Electrochromism

Optical effects of various kinds have been studied for centuries in transition metal compounds. One example is Prussian Blue, a hexacyanoferrate, that was discovered by Diesbach in 1704 *(1761)*. This material is an excellent dye. It also has electrochromic properties, as discussed later in this book, and it can be changed reversibly between deep blue and transparent states by ion intercalation/deintercalation.

Tungsten trioxide plays a special role in electrochromism. The stoichiometric material is yellowish to greenish in bulk form. It can be chemically reduced to produce a blue compound, and Berzelius *(373-4, 374)* reported as early as in 1815 that the color change took place when hydrogen was passed over gently warmed tungsten trioxide. Color changes obtained by reacting tungsten oxide with sodium were reported in 1824 by Wöhler *(3648)*. The ensuing material had a gold-like appearance. Wöhler was struck by its beauty and wrote:

> *...wenn man ein aus grösseren Kryställchen bestehendes Pulver in Sonnenlichte betrachtet, so ist es von einem Glanze und einer Schönheit, wie man wenige andere Präparate sehen wird.*

We now know that Wöhler had produced a material similar to the one obtainable by ion intercalation into electrochromic crystalline tungsten oxide films. It is commonly referred to as sodium tungsten bronze.

Electrochemical, rather than purely chemical, reduction of tungsten oxide has also been studied extensively for many years. In particular, one could notice work in 1930 by Kobosew and Nekrassow *(1862)*, who found that tungsten oxide powders could be colored blue by electrochemical reduction in acidic solution. It was surmised by them that atomic hydrogen was the cause of the reduction. Reversible color changes during electrochemical treatment of sodium tungsten bronzes were mentioned in 1951 by Brimm et al. *(488)*.

A first step towards an electrochromic device was taken in studies on the coloration associated with electrolytic reduction of artificially produced particulate molybdenum and tungsten oxide layers. Such layers were proposed in 1942 for applications to "electrolytic recording paper" in patent specifications by Talmey *(3356-7)*.

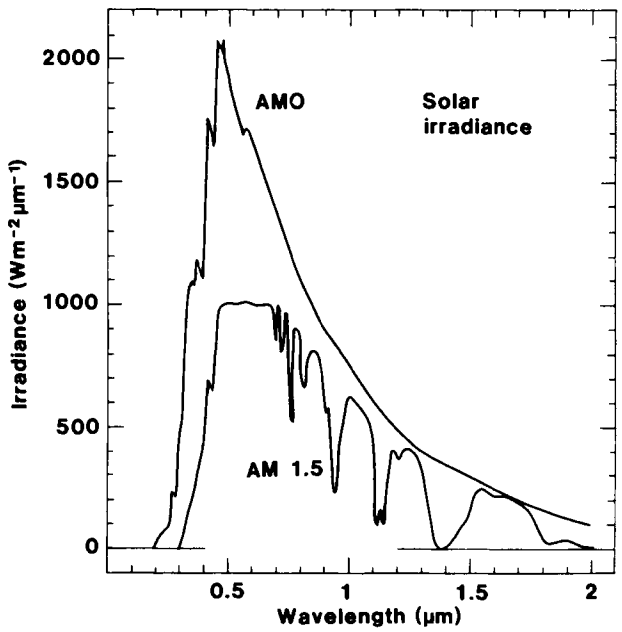

Fig. 1.6 Solar irradiance spectra for two values of the air mass.

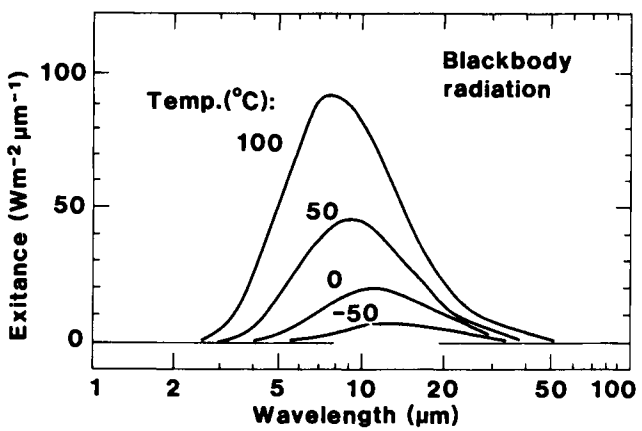

Fig. 1.7 Blackbody exitance spectra at four temperatures.

A very clear description of electrochromism in W oxide films was made in 1953 in an unpublished laboratory report written by Kraus *(1918)*. It reads verbatim:

> *Auf Glasplättchen wurde eine halbdurchlässige Metallschicht (Chrom, Silber), und darauf eine WO_3-Schicht ($\lambda/2$) aufgedampft. Wurde diese Schicht in 0.1 n H_2SO_4 als Kathode geschaltet (-1.5 V), so färbte sie sich in der Durchsicht intensiv blau. Als Anode geschaltet entfärbte sie sich wieder und sperrt im farblose Zustand den Strom. Das Färben und Entfärben der Schicht lässt sich durch Umpolen der Electroden beliebig oft wiederholen. In kathodischer Schaltung tritt hierbei Polarisation auf, deren EMK gegen Cu-Elektroden > 0.6 Volt beträgt.*

The work cited thus far did not lead to widespread interest in electrochromism. In 1969, however, the situation was changed by Deb's publication of a widely known and cited paper *(835)*. It was subsequently followed by a more detailed account of electrochromism in W oxide films *(836)*. Those two papers mark the beginning of the scientific and technical enquiry into electrochromism. The term "electrochromism" was introduced by Platt *(2775)* to represent electric-field-dependent changes in optical absorption spectra of organic dye molecules dissolved in organic solvents, i.e., a situation rather different from the one discussed in this book.

Photoelectrochemistry embodies the study of optical effects in materials during ion intercalation/deintercalation, and much work on optical modifications of passivation layers on metals can be viewed as precursors to studies of electrochromism. Thus Tronstad used ellipsometry to investigate optical changes during electrochemical polarization of nickel and iron surfaces as early as in 1933 *(3454)*. A similar study on nickel oxide was published in 1965 by Reddy et al. *(2870)*. Observations of electrochromism in niobium oxide may date back to 1963, as indicated by Palatnik et al. *(2691)*.

A detailed history of electrochromism remains to be written, and the account here is not based on any in-depth reading of the old literature. Some useful notes on the historical evolution can be found in reviews by Chang *(649)* and by Faugnan and Crandall *(1046)*, as well as in a Ph D Thesis by Giri *(1188)*.

This Page Intentionally Left Blank

Part One

CASE STUDY ON TUNGSTEN OXIDE

This Page Intentionally Left Blank

Chapter 2

BULK CRYSTALLINE TUNGSTEN OXIDE

Tungsten oxide is by far the most extensively studied electrochromic material. Highly disordered films are usually employed in work on electrochromics, and several of the following chapters are devoted to this subject. The present brief chapter on bulk crystalline W oxide provides a baseline for discussing the electrochromic films and also serves to introduce a number of important concepts.

2.1 Crystal Structures of Tungsten Oxide

Tungsten trioxide crystals have perovskite-like atomic configurations based on corner-sharing WO_6 octahedra. Deviations from the ideal cubic perovskite-like structure correspond to antiferroelectric displacements of W atoms and to mutual rotations of oxygen octahedra. The magnitude of the distortion depends on the temperature, which is in agreement with the behavior of most perovskites, and pure WO_3 single crystals go through structural transformations according to the sequence tetragonal→orthorhombic→monoclinic→triclinic→monoclinic as the temperature is lowered from 900 to -189°C *(2010, 2983)*. Tungsten oxide has a tendency to form substoichiometric phases containing edge-sharing octahedra. The overall compositions can be expressed as WO_{3-z} with $z > 0$. Most of the structures can be viewed as Magnéli phases of the series W_mO_{3m-1} and W_mO_{3m-2} (m = 1, 2, ...) *(2158)*. Thus structures of the types $W_{26}O_{77}$ (z = 0.04), $W_{20}O_{58}$ and $W_{40}O_{116}$ (z = 0.1), $W_{12}O_{34}$ ($z \approx 0.17$), $W_{18}O_{49}$ ($z \approx 0.28$) and others are possible. Figure 2.1 illustrates W-centered octahedral "building blocks" arranged with corner-sharing and edge-sharing.

The crystal structure has been studied by high-resolution electron microscopy, and extended defects characterized by crystallographic shear planes, pentagonal bipyramidal columns, and hexagonal tunnels have been identified. Figure 2.2 illustrates arrangements of WO_6 octahedra in two experimental specimens with $z \approx 0.02$ and 0.1. Corner-sharing WO_6 octahedra surround large defects with hexagonal and pentagonal cross-sections. Further details on crystallographic features of WO_{3-z} were given by Sahle et al. *(2965-7)* and others *(448, 568, 1024, 1343, 2346)*, and a summary of the crystal structures can be found in *(2010)*.

Hexagonal WO_3 phases are of particular relevance to electrochromism, as will be seen later. They can be prepared in bulk form by the special techniques of "soft chemistry" (or "chimie douce") *(1069, 1072, 2385)*. The hexagonal structure in WO_3 has been discussed several times by Figlarz et al. *(1068, 1070-1, 1166-7)* and others *(677, 917, 2885-6, 3053, 3189)*. A related hexagonal structure is present also in materials of the type $WO_3 \cdot p(A_2O)$, with $A = Na^+, K^+$, or

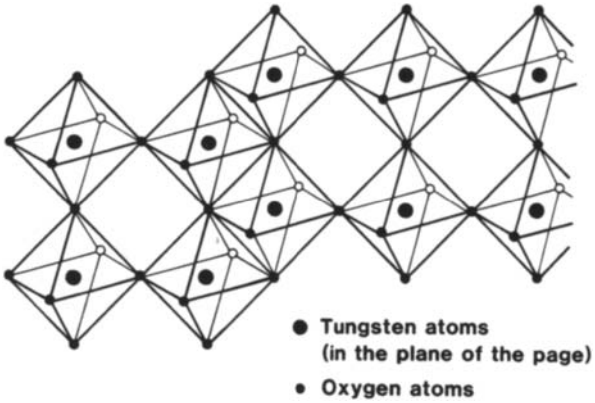

Fig. 2.1 Schematic illustrating a corner-sharing and edge-sharing arrangement of octahedra in a W oxide crystal.

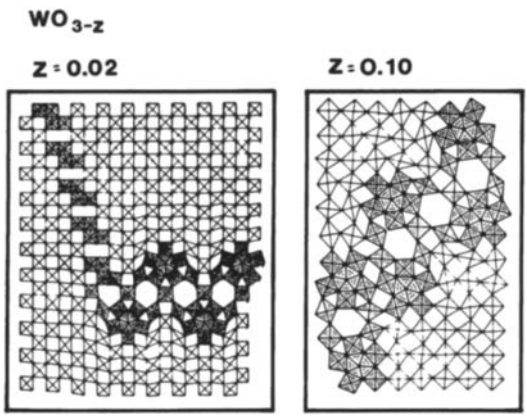

Fig. 2.2 Interpretation of high-resolution transmission electron micrographs for two crystals of WO_{3-z} with different stoichiometry. The WO_6 octahedra are corner-sharing (open box-like symbols) and edge-sharing (shadowed symbols). From Sahle and Sundberg *(2967)*.

NH_4^+ and $0.05 < p < 0.14$, obtainable by heat-treatment of the corresponding tungsten acid C phases *(1958-9)*. Hexagonal phases are characterized by a *one-dimensional tunnel structure* extending through the material.

An even more open pyrochlore structure of WO_3, with a *three-dimensional tunnel structure*, was discovered recently *(775, 1070-2, 2510, 2766, 2886)*. It contains some W and O vacancies as well as H_3O^+ for charge neutrality *(774)*.

2.2 Crystal Structures of Tungsten Bronzes and Ion Intercalated Tungsten Oxide

Tungsten bronzes can be represented as M_xWO_3 with M being an atom from the first column in the Periodic Table. They can be prepared in crystalline bulk form by vapor-phase reactions, solid-state reactions, and electrolytic reduction *(919, 922, 3649)*. Their crystal structure depends on the type and density of the species added to the WO_3 host.

Tungsten bronzes have a venerable history in chemistry, with work by Wöhler *(3648)* going back to the first part of the 19th century, as mentioned in the introduction. They have been the subject of several detailed reviews *(922, 1247, 1249, 1386-7)*. Figure 2.3 summarizes data for M_xWO_3 bronzes with $0 \leq x \leq 1$ and M = Li, Na, K, Rb, and Cs (with ionic radii 0.060, 0.095, 0.133, 0.148, and 0.169 nm, respectively). The phase domains are approximate only. Cubic (perovskite) phases are found within a range that is displaced towards increased x value for increased ionic radii. Such a structure does not exist in pure WO_3, as can be inferred from Fig. 2.3, but it is possible to extrapolate a lattice parameter for a hypothetical material *(3587)*. Tetragonal phases are found at low to intermediate x values for Li_xWO_3 and Na_xWO_3 and at intermediate x values for K_xWO_3. The phase domains are shifted towards smaller x values at elevated temperature *(432, 3621)*. *Hexagonal* phases occur for small incorporation of large ions; K_xWO_3, Cs_xWO_3, and In_xWO_3, that are of considerable interest for electrochromics, were analyzed in 1953 by Magnéli *(2159)*, and results are also available in many more recent publications *(386, 459, 893, 913, 1586-8, 1686, 1944-5, 1989-90, 2807, 2826, 2864, 3298)*. Although is is not indicated in Fig. 2.3, a hexagonal structure has been reported in Li_xWO_3 *(677, 917, 2606, 2886)*. A *pyrochlore* structure can be stabilized in Cs and Rb tungstates *(685, 970, 2605, 2607, 3808)*; it can serve as a host for intercalation of Li^+ and other ions *(971, 1356, 1465, 2886)*.

H_xWO_3 was not discussed above. Here the hydrogens are thought to be statistically attached to the oxygens as hydroxyl groups, so the material may be adequately represented as $WO_{3-x}(OH)_x$ *(3643)*. There are reports about an orthorhombic phase at x = 0.1, tetragonal phases for x = 0.23 and x = 0.33, and a cubic phase for x = 0.5 *(87, 686, 914, 1200, 1510, 1850)*.

Modifications of the crystalline structure during Li^+ intercalation /deintercalation are of particular concern for electrochromic devices and deserve a close look. Figure 2.4, taken from recent work by Zhong et al. *(3810)*, gives a more detailed picture than the earlier one in the left-hand part of Fig. 2.3. The phase diagram was determined from careful X-ray diffraction analysis of WO_3 powder immersed in an electrolyte of 1 M $LiClO_4$ in a 50:50 mixture of propylene carbonate and ethylene carbonate. In order to obtain reliable data, the X-ray diffractograms were subjected to Rietveld profile analysis *(2901-2, 3627)*. It is seen from Fig. 2.4 that Li^+ intercalation makes the sample transform according to monoclinic→tetragonal→cubic with intermediate mixed phases. Deintercalation reverses the sequence of transformations, but the phase changes do not occur at

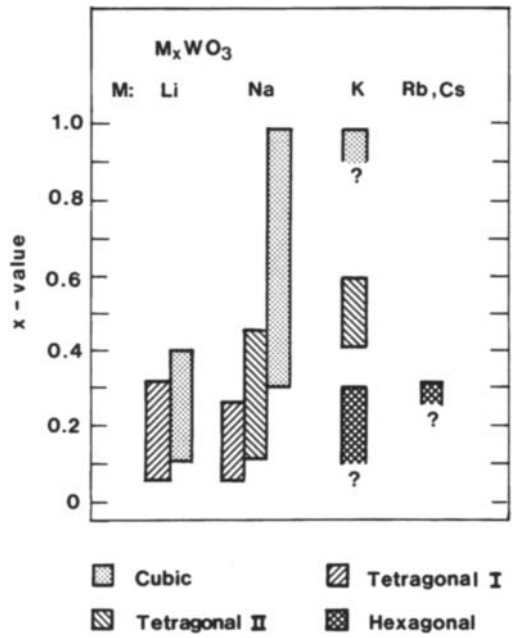

Fig. 2.3 Compositional ranges for the cubic, tetragonal I and II, and hexagonal phases of crystalline M_xWO_3 bronzes. Adapted from Dickens and Whittingham *(922)* by Goodenough *(1246-7, 1249)*.

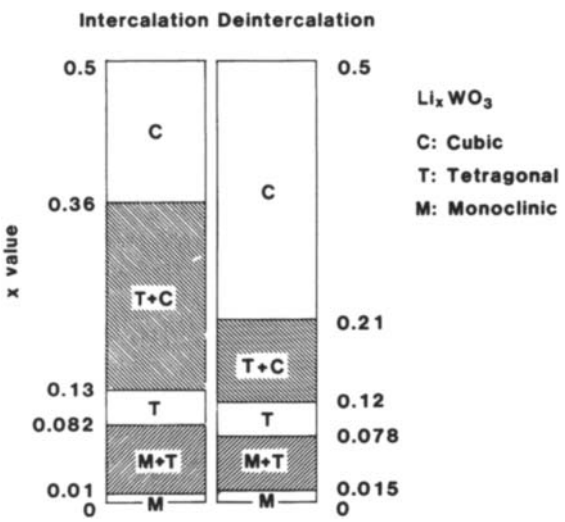

Fig. 2.4 Compositional ranges for the cubic, tetragonal, and monoclinic phases of crystalline Li_xWO_3 bronzes during intercalation and deintercalation. After Zhong et al. *(3810)*.

precisely the same Li contents. The monoclinic structure is stable only for $x < 0.01$, and the tetragonal structure is found at $x \approx 0.1$. A pure cubic phase prevails at $x > 0.36$ for intercalation and at $x > 0.21$ for deintercalation.

Crystal structures of the cubic, tetragonal I, and hexagonal tungsten bronzes are illustrated in Fig. 2.5 *(922, 3621)*. The WO_6 octahedra are shown as well as the sites available for ion intercalation. From an inspection of the structures, it is reasonable to expect that only small ions (H^+, Li^+, Na^+) can be accommodated in the cubic configuration. The tetragonal structure has "tunnels" with sufficient size that K^+ can be incorporated. The hexagonal modification, finally, is characterized by sixfold "tunnels" of sufficient size to include ions as large as K^+, Rb^+, Cs^+, and NH_4^+ *(2159, 2818, 3187)*. Trigonal tunnels in the hexagonal structure can accommodate Li^+ *(3191)*. A particularly clear illustration of ion intercalation in hexagonal WO_3 was shown by Figlarz *(1068)*.

2.3 Optical Properties

WO_3 crystals are birefringent and have an average refractive index for white light of 2.5 *(3029)*. Color changes appear in WO_{3-z} when z is increased, as investigated more than half a century ago by Glemser and Sauer *(1201)*. Intercalation of alkali ions, so that tungsten oxide bronzes are created, also leads to the development of colors (hence the name of these materials). Figure 2.6, after Dickens and Whittingham *(922)* and Goodenough *(1246)*, illustrates the subjective appearances of Na_xWO_3 crystals as a function of x for $0 \le x \le 1$.

The colors are indicative of a strongly wavelength dependent reflectance. Figure 2.7 shows *diffuse* spectral reflectance of Na_xWO_3 in the luminous and near-infrared spectral range, as reproduced from work reported in 1954 by Brown and Banks *(495)* (see also *(1109)*). One immediately observes qualitative differences, with a reflectance maximum at ~0.5 μm for $x < 0.2$ and a reflectance minimum at ~0.5 to ~0.7 μm for $x \ge 0.2$. In the latter samples, there is high reflectance beyond a certain wavelength that shifts towards smaller values as the Na content is increased. At $0.2 < x < 0.5$, the reflectance lies primarlily in the infrared, and the visible appearance is govered by the moderately high reflectance of blue light. At $0.5 < x < 1$, there is high reflectance in the long-wavelength part of the luminous spectrum, and consequently the visible appearance is reddish or yellowish.

Quantitative results on the specular reflectance of small Na_xWO_3 crystals are shown in Fig. 2.8 for $0.5 < \lambda < 2.5$ μm. The data are reproduced from Goldner et al. *(1220)*, whose measurements were performed with a microscope/monochromator system. The reflectance can exceed ~90 % for $\lambda > 1$ μm if the Na content is high enough. Spectral optical data that are analogous to those in Figs. 2.7 and 2.8, but cover less complete compositional ranges, have been reported for H_xWO_3 *(1540)*, Na_xWO_3 *(586, 752, 920, 1110, 2125, 2674, 3076, 3377)*, $K_{0.63}WO_3$ *(2125)*, and WO_{3-z} with $z \ge 0$ *(920, 1110, 2674, 2981-2, 3543)*. For wavelengths larger than those in Fig. 2.7, the reflectance can approach 90% *(2125, 3543)*. Electromodulated optical properties of Na_xWO_3 were reported in *(586, 1191)*.

Theoretical models for the optical properties will be discussed in chapter 10 below.

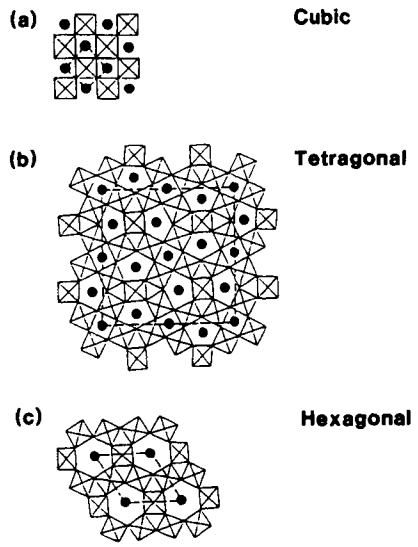

Fig. 2.5 Atomic arrangements for crystalline tungsten bronzes with (a) perovskite, (b) tetragonal I, and (c) hexagonal structure. Dots indicate sites available for ion insertion. Dashed lines mark the boundary of the unit cell. From Dickens and Whittingham *(928, 3621)*.

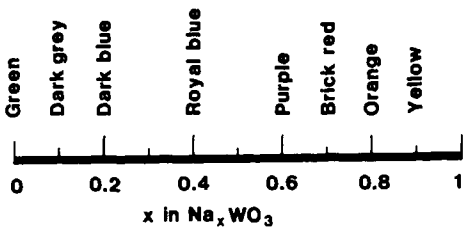

Fig. 2.6 Color vs. ion content, given as x in Na_xWO_3 crystals. After Dickens and Whittingham *(922)* and Goodenough *(1246)*.

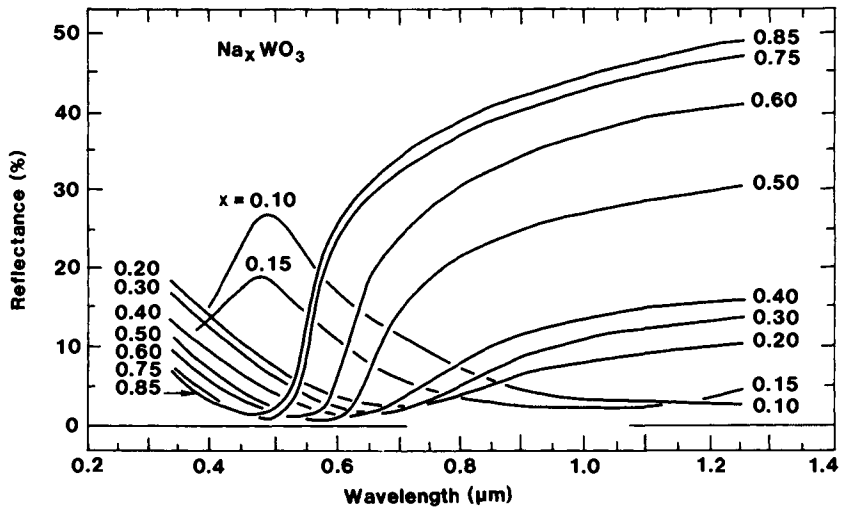

Fig. 2.7 Diffuse reflectance for Na_xWO_3 crystals with several values of x. After Brown and Banks *(495)*.

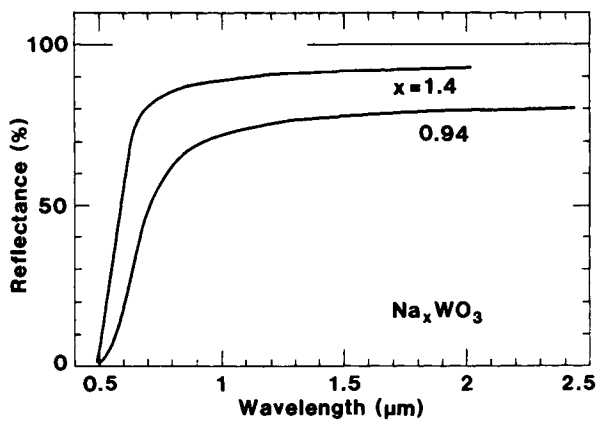

Fig. 2.8 Specular reflectance for Na_xWO_3 crystals with two values of x. From Goldner et al. *(1220)*.

2.4 Electrical Properties

The electrical conduction of W-oxide-based materials poses long-standing problems *(353, 915, 1386-7, 1898a, 3113, 3171-2)*, and defects in the WO_3 lattice play a decisive role for the physical properties. This phenomenon is illustrated in Fig. 2.9, where the temperature dependent electrical conductivity σ is shown for WO_3 and and for WO_{3-z} with $0.006 \leq z \leq 0.278$. The data were reported by Sahle and Nygren *(2966)*. The stoichiometric material has abrupt changes in σ as a result of structure transformations, and oxygen deficiency is able to increase σ by many orders of magnitude. Earlier work on the electrical properties of WO_3 was reported by Berak and Sienko *(353, 3172)* and by Hirose *(1500)*.

The electrical conductivity of M_xWO_3 with M = Li, Na, K is considered next. Data are shown in Fig. 2.10 from a compilation by Webman et al. *(3586)*. Similar sets of results can be found in *(1109, 1188)* and, specifically for Na_xWO_3, in *(2019, 2077-8, 2425)*. The conductivity goes up monotonically with increasing x once a certain critical value around 0.2 is exceeded. There is no apparent dependence on crystal structure or ionic species. At face value the data are in line with predictions from percolation theory *(1109, 2077, 3586-7)* and effective medium theory *(1300)*, which clearly presumes that the tungsten bronzes would have a composite character. However, this view has been criticized in several papers *(784, 1522, 2417-8, 3473)* and now seems untenable.

In his treatise on the onset of metallic conductivity in tungsten bronzes, Mott *(2417)* discussed three possibilities:

(i) Anderson localization *(94)* in the conduction band as a consequence of strong scattering from the intercalated ions,

(ii) formation of an impurity band and localization due to disorder for $x > 0.2$, and

(iii) splitting-off of an impurity band as a consequence of electron correlation and Anderson localization in a pseudogap.

Mott *(2417)* suggested that (i) would be the correct description, but recent high-resolution electron spectroscopic data by Hill and Egdell *(1486)* and Hollinger et al. *(1523)* showed that the metal-nonmetal transition at $x \approx 0.2$ was due to localization in a pseudogap between an impurity band and the WO_3 conduction band, which is in agreement with mechanism (iii). This contention is supported by a recent numerical analysis by Koslowski and von Niessen *(1898a)*. The nature of the pseudogap has been discussed; specifically Hollinger et al. *(1523)* suggested a *Hubbard gap (1564-5)* due to long-range electron interaction, whereas Davies and Franz *(828)* brought attention to the possible manifestations of a *Coulomb gap (829, 999, 2789, 3160)* due to long-range electron interaction. Hill and Egdell *(1486)* argued in favor of *localized small polarons*. It seems more than likely that the last word about the electrical properties of W oxides has not yet been said.

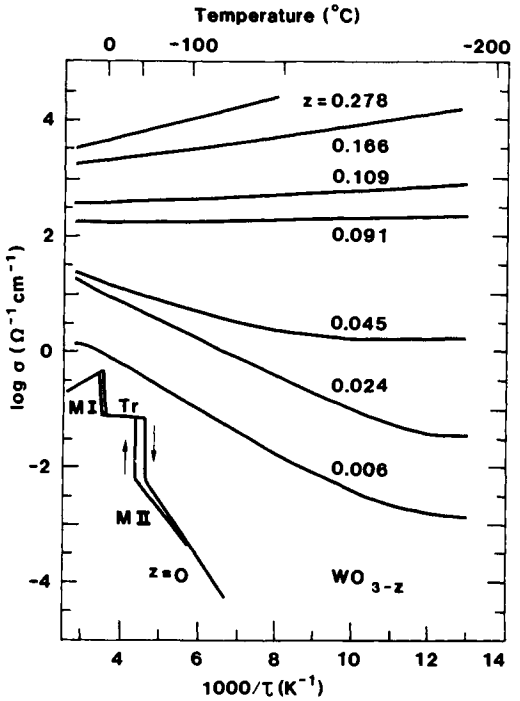

Fig. 2.9 Conductivity σ vs. inverse temperature τ for crystals of WO_{3-z} ($0 \leq z \leq 0.278$). For WO_3, the symbols denote monoclinic phases I and II (M I and M II) and triclinic phase (Tr). Arrows indicate hysteresis. After Sahle and Nygren *(2966)*.

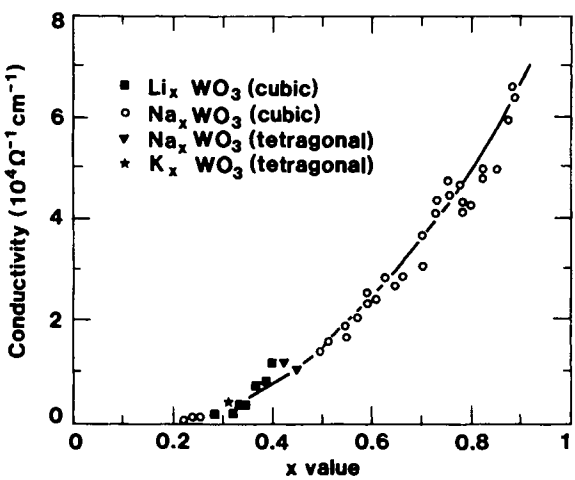

Fig. 2.10 Conductivity vs. ion content for several tungsten bronzes. Symbols show measured results, and the curve indicates the overall variation. After a compilation of data by Webman et al. *(3586)*.

This Page Intentionally Left Blank

Chapter 3

TUNGSTEN OXIDE FILMS: PREPARATION, STRUCTURE, AND COMPOSITION OF EVAPORATED FILMS

Electrochromism has been investigated in considerable detail in evaporated W oxide films. The as-prepared film is considered in this chapter, while effects of ion intercalation/deintercalation are treated later. An introductory section on deposition aspects (3.1) is followed by a detailed account on density as a function of evaporation parameters (3.2). Then follow discussions of elemental composition (3.3) and of microstructure apparent from electron microscopy (3.4) and X-ray extinction (3.5). Vibrational properties are covered with regard to Raman spectroscopy (3.6) and infrared absorption spectroscopy (3.7). This information is used to formulate models for the structure at different levels: local cluster-type models (3.8) as well as descriptions of larger columnar features (3.9). The final section (3.10) is devoted to the crystallization of as-deposited films.

3.1 Deposition Aspects

The standard technique for making W oxide films suitable for laboratory studies uses the condensation of a vapor produced by sublimation from hot WO_3 powder. The heating can be produced by a resistive boat (Ta, Mo, or W), by a refractory crucible, or by an electron beam (*e*-beam). Prebaked (waterfree) powder is sometimes used. The substrate can be unheated or kept at a temperature up to a few hundred degrees, and the evaporation can take place under non-reactive or reactive conditions, i.e., in the absence or presence of a low-pressure reactive gas. This evaporation technique is well known for yielding films with good electrochromism and is widely used *(1046, 1293)*.

A variety of this technique, known as flash evaporation, uses vaporization of continously fed powder under conditions so that each grain is evaporated independently of the other grains. Advantages of the flash technique have been pointed out by Manfredi et al. *(801, 2175-6)* and by Schlotter *(3056-7, 3059)*. Still other varieties of the evaporation technique, with specific advantages, are reactive ion plating (evaporation in the presence of a low-pressure plasma) discussed by Yoshimura *(3742)* and ion-assisted evaporation (involving bombardment of the surface of the growing film by an ion beam) discussed by Arntz et al. *(149)*.

Glass substrates are almost always used, but electrochromic W oxide films can also be evaporated onto flexible polyester substrates *(2948)*.

Deposition rates are stated in many papers, and values up to ~3 nm/s are commonly reported. The highest rates mentioned in the literature are 7 nm/s *(1976, 1980, 2411)*, "up to" 10 nm/s

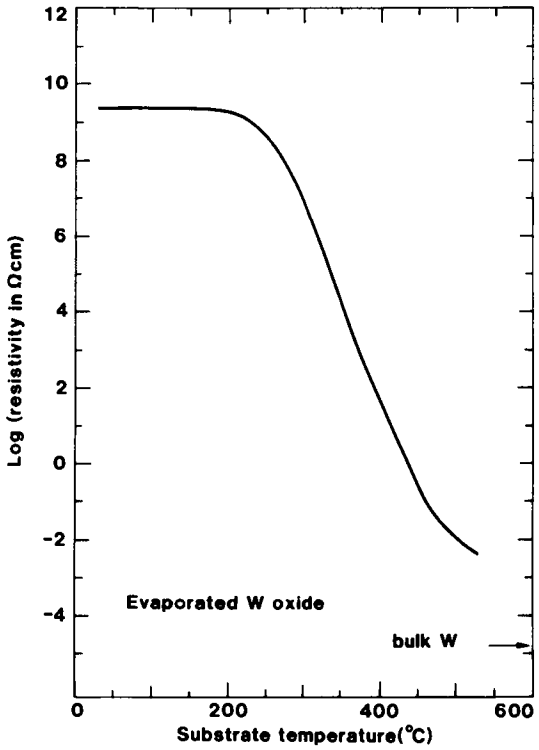

Fig. 3.1 Resistivity of W oxide films evaporated onto substrates at different temperatures. An arrow marks the resistivity of bulk W (at 600°C). After Miyake et al. *(2340)*.

(3073, 3687), 10 nm/s *(1889)*, and 15 nm/s *(1972-4, 1981)*. For thin films made by evaporation one can increase the deposition rate, at the expense of having a smaller surface evenly coated, simply by placing the substrate closer to the vapor source. Detailed evaporation conditions are seldom given; exceptions are in works by Goulding and Thomas *(1271)*, Demiryont and Nietering *(877)*, and Rousselot et al. *(2948)* who investigated vacuum evaporation of WO_3 powder and reactive evaporation of W. Laser evaporation *(683)* gives prospects for very high deposition rates, and some work using this technique to produce WO_{3-z} with $z \approx 0.1$ has been reported by Solodukha et al. *(3207-8)*. It should be noted that congruent evaporation takes place only at the composition $WO_{2.96}$ *(22)*.

The deposition parameters may be critical for the film that is formed. This point is illustrated here with regard to the electrical resistivity (ρ) vs. the substrate temperature (τ_s) during the film deposition. Figure 3.1, reproduced from Miyake et al. *(2340)* who evaporated WO_3 powder from a Mo boat, shows that ρ lies at about 1.5×10^{-9} Ωcm for $\tau_s = 200$°C and drops by many orders of magnitude at larger τ_s. For $\tau_s = 500$°C, the resistivity is only a few orders of magnitude larger than the value for bulk W. The τ_s dependent resistivity most likely depends on oxygen vacancies serving as *n*-type dopants. Hall effect measurements showed that at $\tau_s = 500$°C the electron density was ~2 $\times 10^{18}$ cm^{-3} and the mobility was 75 cm^2/V. A τ_s dependent resistivity drop was found also by Kleperis et al. *(1842)*. When W oxide was reactively evaporated onto unheated substrates, the resistivity increased in proportion with the O_2 partial pressure *(2397)*.

It is important to notice that the vapor produced by heating WO_3 does not consist of individual atoms but is *molecular* in nature. The dominating species is trimeric W_3O_9 molecules, but the details are complicated and dependent on experimental conditions. The occurrence of trimers was found in 1957 through mass spectrometric work by Berkowitz et al. *(361)* and was verified by others *(22, 2165)*. Electron microscopy gave a consistent view *(1434)*. Further, some dimers, tetramers, pentamers, and W_3O_8 species can be found in the vapor. The sublimation energies are ~130, ~151, and 165 to 170 kcal/mole for W_3O_9, W_4O_{12}, and W_5O_{15}, respectively *(361)*. Mass-spectroscopic studies of desorption from tungsten surfaces with chemisorbed oxygen showed the presence of O, WO, WO_2, WO_3, W_2O_6, and W_3O_9 with proportions that depended on temperature and oxygen exposure *(30, 364, 1809-10, 2251, 2812, 3051, 3523)*. Evaporation followed by electron capture negative ionization yielded $(WO_3)_m^-$ clusters, with a dominance for m being 3 and 6 *(2165)*. Hydroxylated molecules represent another possibility for the vapor species *(1202)*. Additional information on the molecular structure has been obtained from infrared absorption and emission of the vapor *(305, 1308, 2517, 3599, 3711)*. Specifically, infrared absorption spectra of the vapor over tungsten trioxide at 1150 to 1300°C showed a narrow band at ~960 cm^{-1} and a broader, more intense, band peaked at ~810 cm^{-1} *(3711)*. Somewhat different bands were found in matrix-insulated samples *(3599)*. Physically, the atomic arrangements are connected with the formation of delocalized molecular orbitals within rings.

3.2 Density

The relative density of evaporated W oxide films varies strongly with the deposition conditions. Figure 3.2 illustrates the influence of the vacuum (or rather the pressure or N_2 of O_2 in the vacuum chamber, denoted p_{N2} and p_{O2}), the substrate temperature during deposition, and the post-deposition annealing temperature (τ_a). The bulk density was taken as 7.16 g/cm^3, corresponding to

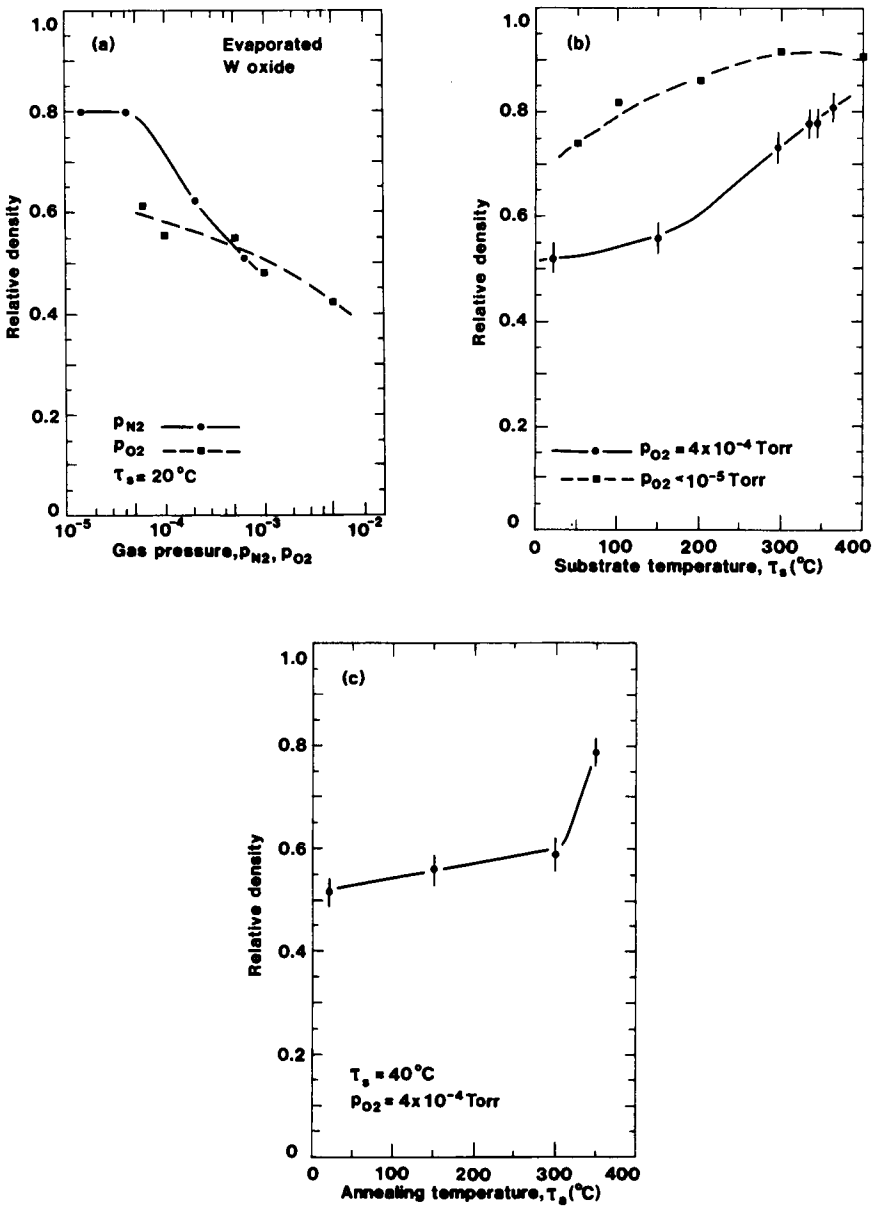

Fig. 3.2 Relative density for W oxide films prepared by evaporation at the shown values of N_2 gas pressure p_{N2}, oxygen gas pressure p_{O2}, substrate temperature τ_s, and post-deposition annealing temperature τ_a. Vertical bars indicate experimental uncertainties. Curves were drawn to guide the eye. After Matsuhiro and Masuda *(2224)*, Morita and Washida *(2397)*, and Shigesato et al. *(3135)*.

monoclinic WO_3. Hexagonal WO_3--which will be discussed in detail below--has a theoretical density of 6.43 g/cm^3 and a measured density of 6.36 g/cm^3 *(1166)*. Films made under good vacuum conditions ($\leq 10^{-5}$ Torr) and with unheated substrates have a relative density of ~0.8.

Figure 3.2(a) refers to films made by *e*-beam evaporation in the presence of some N_2 *(2223-4; see also 333)*, and resistive-boat evaporation in the presence of some O_2 *(2392, 2397)* onto unheated substrates. For the former films, the density was determined from measurements of film thickness and mass; for the latter films, a quartz crystal microbalance was used to record the amount of adsorbable water *(2814)*. This adsorption technique was employed for WO_{3-z} also in an earlier study *(1393)*. In some recent work, for example that of Shigesato et al. *(3132, 3134)*, densities were evaluated by combining data from X-ray fluorescence and thickness determination. The relative density decreases from the initial ~0.8 to values as low as ~0.5 with 10^{-3} Torr of N_2 or O_2 and to ~0.4 with 5 x 10^{-3} Torr of O_2. Densities similar to those for deposition in O_2 were found also with deposition in Ar and Ar + 10 % O_2 *(2397)*, and densities similar to those for evaporation in N_2 were reported also in *(1607, 1726, 2459, 2467)*. Densities of films evaporated in the presence of some H_2O were reported by Schlotter and Pickelmann *(3058)* and by Shigesato et al. *(3134)*. They found a gradual density decrease when the H_2O pressure was increased up to ~10^{-4} Torr; beyond ~5 x 10^{-4} Torr, the deposit was powdery.

Figure 3.2(b) shows relative density versus substrate temperature for non-reactive deposition (vacuum better than 10^{-5} Torr) as reported by Miyake et al. *(2340)*, and for weakly reactive deposition (p_{O2} = 4 x 10^{-4} Torr) as reported by Shigesato et al. *(3132, 3135)*. The relative density goes up gradually with increasing τ_s and can approach 0.9 at τ_s = 440°C. At even higher temperature, the density may drop somewhat, and the film surface develops roughness, at least for evaporation in good vacuum *(2340)*. Figure 3.2(c) gives data for post-deposition annealing of films made at τ_s = 40°C and p_{O2} = 4 x 10^{-4} Torr *(3132, 3135)*. The relative density increases slowly with increasing annealing temperature up to $\tau_a \approx$ 300°C. Then there is a rapid densification at $300 < \tau_a < 350$°C, and at τ_a = 350°C the relative density is ~0.8. It is evident that direct deposition with a certain substrate temperature does not lead to the same structure as post-deposition annealing of the film at that same temperature. Data in agreement with those in Figs. 3.2(b) and (c) were reported by Nanba and Yasui *(2494)*.

3.3 Elemental Composition: Oxygen Deficiency and Hydrogen Content

The films cannot be considered as comprised of stoichiometric tungsten trioxide. Instead they can be characterized with regard to the nonstoichiometry in their tungsten-oxygen framework--i.e. the magnitude of z in WO_{3-z}--and their hydrogen content. Furthermore, one can distinguish between hydrogen in hydroxyl groups and in water molecules.

The *oxygen content* can be determined by several different techniques. Rutherford Backscattering Spectroscopy (RBS), applied to films made by evaporation from a resistive source *(884-5, 1013, 1168-9, 1519)*, showed that the structure could be represented by WO_{3-z} with z = 0.24 ± 0.05, and very similar results were obtained by X-ray fluorescence (XRF) *(3050)*, X-ray Photoelectron Spectroscopy (XPS) *(162)*, and Auger Electron Spectroscopy (AES) *(256)*. Somewhat different values of z were reported in *(270, 1271)*. As-deposited *e*-beam-produced films had z ≈ 0.3 as determined by AES, XRF, and atomic absorption measurements *(1726, 2463-5, 2467)*, or z ≈ 0.2 as determined by XPS *(2494)*. Deposition onto substrates heated to

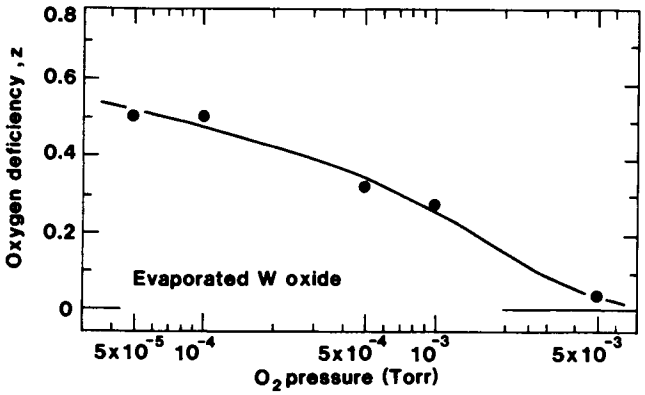

Fig. 3.3 Oxygen deficiency vs. O_2 pressure for reactively evaporated W oxide films. From Morita and Washida *(2397)*.

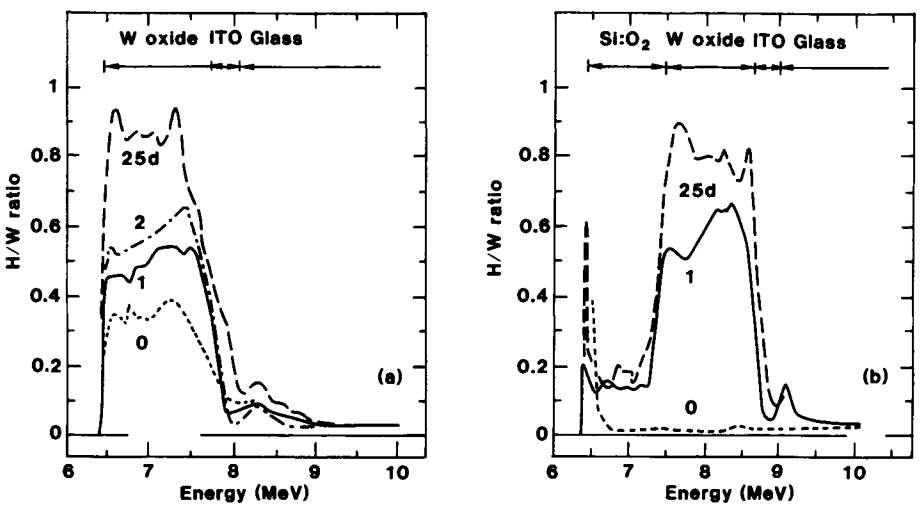

Fig. 3.4 Depth profiles for H/W atom ratios as determined by NRA. Data are shown for the two indicated multilayer stacks, incorporating evaporated W oxide films, exposed to air with 80 % relative humidity for the shown number of days (d). From Wagner et al. *(3560)*.

150 and 300°C gave $z \approx 0.1$ and $z \approx -0.1$, respectively, as seen from XPS. One concludes that an approximate composition corresponding to $WO_{2.7}$ is valid for the tungsten-oxygen framework in films made by vacuum evaporation onto unheated substrates, and that more stoichiometric films are obtained at elevated substrate temperature.

The oxygen deficiency depends on the evaporation conditions, and reactive deposition in the presence of some O_2 makes it possible to produce films with a stoichiometry that approaches WO_3. This fact is illustrated in Fig. 3.3, which shows z as a function of O_2 pressure from work by Morita and Washida *(2397)*. Consistent results were reported by Bange et al. *(255)*. The magnitudes of z were obtained from AES and, judging from the RBS and XPS data referred to above, are overestimated by roughly a factor two. Deneuville et al. *(885)* and Sun and Holloway *(3273-4)* found that z was ~0.1 for reactive evaporation in ~10^{-3} Torr of O_2. Morita *(2392)* reported effects on z of storing films in air.

The *hydrogen content* can be accurately determined by Nuclear Reaction Analysis (NRA). A particularly useful technique is based on the $^1H(^{15}N, \alpha\gamma)^{12}C$ nuclear reaction, for which a narrow (width 1.8 keV) resonance occurs at 6.4 MeV with a cross-section of 1650 mb; γ quanta, emitted at 4.43 MeV, can be counted on a NaI detector and yield direct information on the hydrogen depth profile. Hydrogen can be incorporated into the growing film, depending on evaporation conditions, and it can also be taken up later due to exposure of the film to water vapor in ambient air.

Figure 3.4, reproduced from Wagner et al. *(3560)*, shows H/W profiles for reactively evaporated W oxide films with relative densities of ~0.7 exposed to air with a relative humidity (RH) of 80 % at room temperature. The sample pertinent to part (a) is a W oxide film backed by a glass substrate coated with a layer of In_2O_3:Sn (known as Indium Tin Oxide, or ITO), or a similar tandem film with a top layer of evaporated SiO_2 (part b). The hydrogen content grows with time and reaches a H/W ratio of ~0.9 after 25 days. Even larger H/W ratios--up to ~1.6--could be achieved during the course of days or months depending on the storage conditions, temperature, and RH *(3564)*. The hydrogen profiles in Fig. 3.4 are rather even over the full cross-sections of the films. A SiO_2 top layer is able to prevent the initial hydrogen incorporation, but already after one day the H/W ratio is the same as in the absence of a top layer. Analogous NRA data have been reported for W oxide films at RH = 60 % *(3561)*, as well as for W oxide films overcoated with SiO_2 (studied at 95°C) *(3563)* and overcoated with Ta_2O_5 (studied at room temperature) *(2852)*; data are given also in *(2445)*. The H/W profiles in Fig. 3.4 seem to broaden upon prolonged exposure to humid air. This can be understood as an effect of oxygen incorporation and is consistent with an uptake of water molecules rather than hydrogen in the form of ions, atoms, or molecules *(3560)*.

In recent work by Wagner et al. *(3564)*, a combination of NRA to detect hydrogen and RBS to detect oxygen was used to distinguish between hydration and hydroxylation. The films were prepared by reactive evaporation at relatively high p_{O2}. The data were interpreted on the premise that the excess oxygen was bound in water molecules, which led to the derived stoichiometry

$$H_{0.3}WO_{3.0} \cdot pH_2O \qquad (0 < p < 0.8)\,, \tag{3.1}$$

with the second term signifying the time- and environment-dependent hydration.

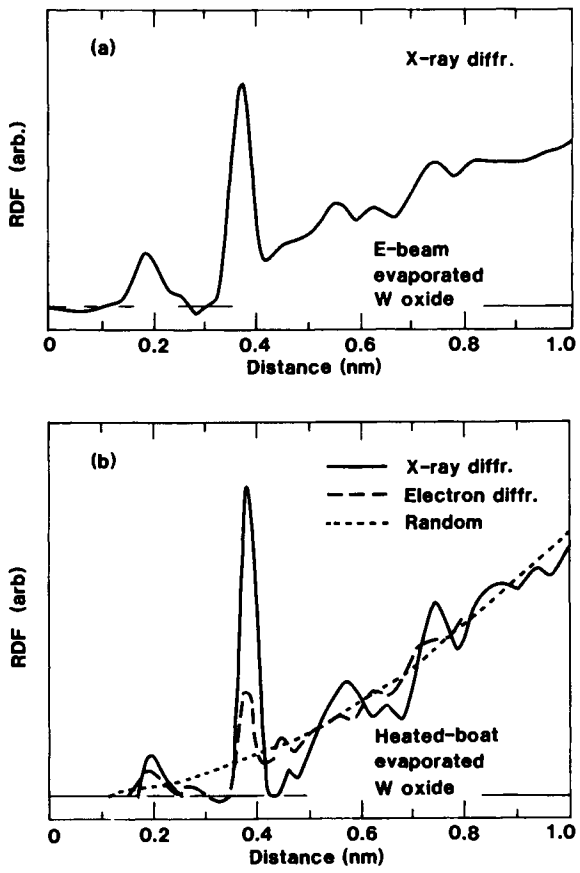

Fig. 3.5 Radial distribution function RDF for W oxide films made by *e*-beam evaporation (part a) and evaporation from a heated resistive boat (part b) onto unheated substrates. Solid curves were obtained by X-ray diffraction and dashed curve by electron diffraction. Dotted curve in part (b) corresponds to an RDF in the absence of any long-range order. After Nanba and Yasui *(2494)*, Ramans et al. *(2831)*, and Zeller and Beyeler *(3791)*.

3.4 Microstructure Studied by Electron Microscopy

The microstructure can be probed by several techniques. The most direct is high-resolution transmission electron microscopy, which, in principle, is capable of giving direct information on the arrangement of W atoms. The technique implies that the sample is placed in vacuum, so losses of loosely bound water may cause some minor structural changes of the as-deposited film prior to or during the analysis.

It is somewhat surprising that no work has been reported so far with electron microscopy having atomic resolution, i.e., analogous to the microscopy underlying Fig. 2.2. However, careful high-resolution microscopy by Shiojiri et al. *(3149-50)* indicated the presence of microcrystallites (clusters) with a diameter of ~1 nm, or, more precisely, with a distribution between 0.8 and 1.2 nm *(1719)*. Grains smaller than 2 nm were detected by Bohnke *(421-2)* and Green *(1306)*. Other work mentions grains with diameters of 1.5 to 8 nm for films made on unheated substrates *(346, 1322-3)* and grains with diameters of ~10 nm for τ_s = 185°C *(1436)*.

3.5 Microstructure Studied by X-ray Extinction

The term X-ray extinction is used to denote techniques involving the scattering and absorption of X-rays. Hence "extinction" is employed here in the same way as in optics. Specifically, microstructural information on evaporated W oxide films can be inferred from small-angle X-ray scattering, extended X-ray absorption finestructure spectroscopy (EXAFS), and X-ray absorption near-edge spectroscopy (XANES), whereas standard X-ray diffraction (XRD) seldom gives useful information. Also electron diffraction measurements are possible, though somewhat less ideal since they are performed in vacuum and hence susceptible to effects due to losses of loosely bound water.

Nanba and Yasui *(2494)* carried out a particularly elaborate study by applying X-ray scattering to W oxide films made by *e*-beam evaporation at a pressure of 4 x 10^{-4} Torr onto substrates kept at room temperature, 150°C, and 300°C. They also investigated films deposited at room temperature and subsequently annealed at 300°C. Figure 3.5(a) shows a radial distribution function (RDF), derived by Fourier transforming the scattering data, for a film made on an unheated substrate. The RDF contains all obtainable structural information *(1849, 1937, 2086)*; in principle it gives information only on the general density correlation, but since the scattering power of the tungsten atoms is much larger than that of the oxygen atoms, the computed RDF approximates the radial distribution around a W atom. The curve in Fig. 3.5(a) shows a large and narrow peak at ~0.4 nm, a smaller and broader peak at ~0.2 nm, and numerous small peaks at distances larger than 0.5 nm. The peaks became more pronounced at increased τ_s and τ_a, as discussed later.

The RDF in Fig. 3.5(a) is not specific to *e*-beam evaporation, but similar results have been obtained for W oxide films made by evaporation from resistively heated boats onto substrates at τ_s < 90°C. Such data, based on X-ray scattering, have been reported by Zeller and Beyeler *(3791)*, Aleshina et al. *(67)*, and Olevskii et al. *(2630)*. Data from Zeller and Beyeler *(3791)* are reproduced by the solid curve in Fig. 3.5(b). There is an almost perfect agreement with the peak structure in the curve in Fig. 3.5(a). This observation is important, since it indicates that the atomic arrangement in the evaporated film does not depend critically on the details of the deposition

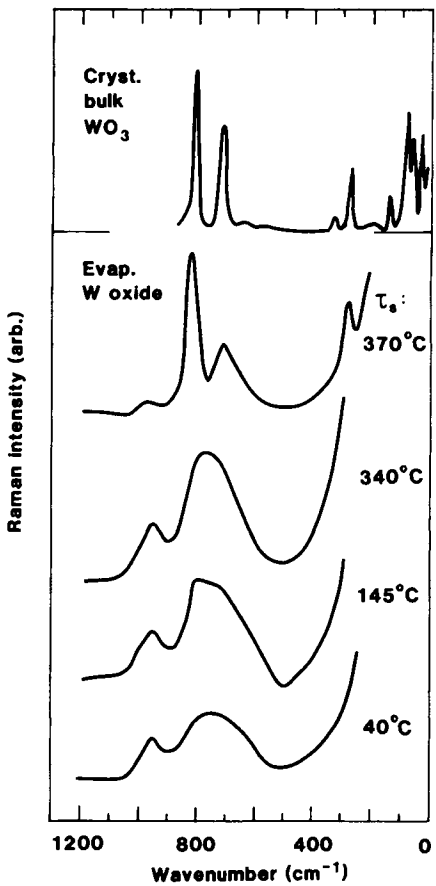

Fig. 3.6 Raman spectra for crystalline bulk WO_3 (upper curve) and W oxide films made by evaporation onto substrates at the shown temperatures (lower four curves). After Salje *(2977)* and Shigesato et al. *(3135-6)*.

method. An analogous RDF for distances up to 0.6 nm was found in laser evaporated W oxide films *(3208)*. Electron diffraction measurements were used to derive RDFs in work by Ramans et al. *(2831)* and Kukuyev et al. *(1952)*. Data from the former of these studies are included in Fig. 3.5(b), where they are represented by the dashed curve. One can note a good qualitative agreement with the X-ray data. The RDF was influenced by exposure of the film to water vapor *(1952)*.

EXAFS for the L_{III} edge of tungsten was applied to evaporated W oxide films in some recent work using high-intensity synchrotron radiation *(244, 246, 380, 528, 1987, 3433)*. From theoretical modelling (multishell simulation) of EXAFS spectra, and with consideration of phase shifts, it was possible to extract detailed information on atomic separations. The first tungsten-oxygen coordination shell could be decomposed into three subshells with separations assigned to W=O terminal oxygens (a_1), W-O-W bridging oxygens (a_2), and next-nonbridging oxygens presumably associated with water molecules (a_3). The values of a_1, a_2, and a_3 were found to depend on the evaporation conditions. For fast evaporation, leading to chemically unstable films, it was reported that $0.167 < a_1 < 0.175$ nm, $0.18 < a_2 < 0.20$ nm, and $0.21 < a_3 < 0.23$ nm *(246)*, whereas slow evaporation onto substrates at $\tau_s \approx 200$°C, that yielded chemically stable films, gave $a_1 \approx 0.1743$ nm, $a_2 \approx 0.1866$ nm, and $a_3 \approx 0.2132$ nm *(244)*. The values of a_2 can be appreciated by comparing them with separations of the W-O-W bridging oxygens in WO_{3-z} crystals *(245, 380, 955)*. In these crystals a_2 increases monotonically for increasing z, and the separation for the stable disordered film is consistent with $z \approx 0.1$. The magnitudes of a_1 and a_3 give measures of the inherent asymmetry of the polyhedral building blocks of the W oxide film structure. Data that are analogous to those for W oxide films have been reported for K_2O-P_2O_5-WO_{3-z} glasses *(3266)*. EXAFS was used to analyze W-W separations in recent work on nanocrystalline tungsten *(1443)*.

XANES spectra for the L_I and L_{III} edges of tungsten were reported recently by Balerna et al. *(245)*. Local distortions in the structure of W oxide and of the tungsten valence state could be correlated with a pre-edge peak in the L_I spectrum and with the "white line" in the L_{III} spectrum. Some analogy was found with XANES studies of the WO_3-alumina and WO_3-titania supported oxide systems *(1485, 1550)*.

3.6 Molecular Bonding Studied by Raman Spectroscopy

Vibrational spectroscopy is of much interest for elucidating structural and compositional features. This section considers Raman spectroscopy, which gives information on the tungsten-oxygen bonding. Figure 3.6, mainly from Shigesato et al. *(3135-6)*, shows spectra for W oxide films made by *e*-beam evaporation at $p_{O2} = 4 \times 10^{-4}$ Torr onto substrates kept at the shown values of τ_s. At $\tau_s = 40$°C, the spectrum is characterized by a broad peak centered at ~750 cm^{-1} and a narrow peak around ~950 cm^{-1}. Deposition onto heated substrates does not significantly change these characteristic features until $\tau_s > 340$°C. At $\tau_s = 370$°C, however, the feature around ~750 cm^{-1} is split into two peaks, and a new peak appears at ~280 cm^{-1}; the peak at ~950 cm^{-1} is still present, but its height is decreased. Analogous Raman spectra have been given several times for evaporated films *(1126, 1843, 2298, 2492-3, 2831, 3153)*.

The Raman data for thin films can be compared with spectra for bulk-like crystalline WO_3 *(304, 807, 1917, 2231, 2252, 2923, 2977, 3340, 3411-2)*; such a spectrum is shown in the upper part of Fig. 3.6. Clearly, the three major peaks in the spectrum for the film made at $\tau_s = 370$°C are

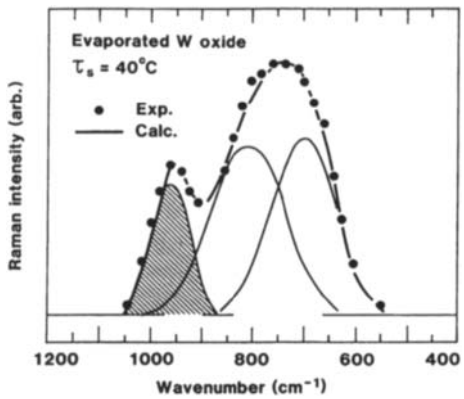

Fig. 3.7 Raman spectrum as measured for a W oxide film made by evaporation onto a substrate at temperature τ_S (dots) and as computed for a sum of three Gaussians (solid curve). The left-hand Gaussian (shaded) represents W=O stretching vibrations. The solid curve corresponds to a part of the lowest curve in Fig. 3.6. From Shigesato et al. *(3135-6)*.

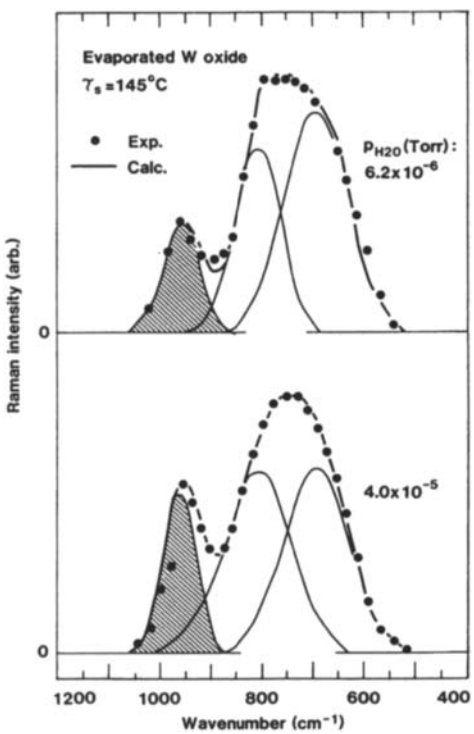

Fig. 3.8 Raman spectra for W oxide films made by evaporation at a substrate temperature τ_s and water vapor partial pressures p_{H2O} (dots), and as computed for a sum of three Gaussians (solid curves). The left-hand Gaussian (shaded) represents W=O stretching vibrations. From Shigesato et al. *(3134)*.

manifestations of the crystalline structure, and the broad feature around ~750 cm^{-1} for films made with $\tau_s < 340°C$ represents a mixture of two of the strong peaks of the crystalline state. The peaks around ~750 cm^{-1} are due to W-O stretching modes. The peak at ~950 cm^{-1}, which is not found in ordinary bulk WO_3 samples, is of particular relevance for the microstructure of disordered films and deserves special consideration. This Raman structure has been observed in hydrated W oxides of the types $WO_3 \cdot pH_2O$ (p = 1/3, 1, 1.72, 2) and $Na_2WO_4 \cdot 2H_2O$ *(807, 860, 1126, 2583, 2747, 2832)*. The structure was noted in some hexagonal WO_3 samples *(824, 860-1, 2298, 2746-7)*, although it was very weak; in dehydrated hexagonal material, studied by Daniel et al. *(807)*, it was absent.

Absorption at ~960 cm^{-1} has been ascribed to asymmetric stretching vibration modes of terminal W=O bonds *(641, 807, 1406, 2986, 3236)*, and the same assignment has been made for absorption at 930 to 990 cm^{-1} in tungsten polyanions *(1946, 2492-3, 2924)*. Under conditions when longitudinal optical phonons can be excited, such modes due to W-O bonds will show up at ~970 cm^{-1} *(806)*. A useful compilation of wavenumbers for characteristic Raman peaks was given by Falaras et al. *(1030)*.

With the purpose of shedding further light on the presumed W=O stretching modes, Shigesato et al. *(3134-6)* deconvoluted their Raman spectra in the range 550 to 1050 cm^{-1} into sums of Gaussian components. Figure 3.7 shows results for $\tau_s = 40°C$ and $p_{O2} = 4 \times 10^{-4}$ Torr, and Fig. 3.8 shows corresponding data for $\tau_s = 145°C$ and a H_2O partial pressure, denoted p_{H2O}, of 6.2×10^{-6} and 4.0×10^{-5} Torr. The Raman spectra can be accurately represented by three partly overlapping Gaussians. The one centered at ~900 cm^{-1} has about the same width irrespective of deposition conditions, whereas the one at ~807 cm^{-1} is wide at low τ_s and high p_{H2O} and seems to give a measure of the crystallite size. The most interesting Gaussian is the one at ~960 cm^{-1}, whose intensity is large at low τ_s and high p_{H2O}, while its width does not depend noticeably on the deposition parameters. The latter data give strong evidence in favor of W=O modes being located at internal surfaces rather than inside dense clusters. A similar interpretation was discussed earlier by Gabrusenoks et al. *(1126)*.

When films were stored in an aqueous H_2SO_4 electrolyte, their Raman spectra showed pronounced changes; they were interpreted by Shiyanovskaya et al. *(3153)* as signs of hydrate formation. The evaporation rate had a significant influence on the hydrate structure.

3.7 Molecular Bonding Studied by Infrared Absorption Spectroscopy

This technique for vibrational spectroscopy gives information that is complementary to the one from Raman spectra; the fundamental reason is that infrared-active modes are related to dipole moments, whereas Raman-active modes are related to the polarisability tensor. The infrared (IR) data can provide particularly clear evidence on the hydrogen-oxygen system, but changes in the tungsten-oxygen framework can be followed as well. Figure 3.9, taken mainly from Yoshiike and Kondo *(3738)*, shows Fourier Transform Infrared (FTIR) spectra for a W oxide film made by *e*-beam evaporation in as-deposited state and after storing at 25°C and 50 % relative humidity for two different periods of time. The main feature is a broad absorption around ~800 cm^{-1}. Comparison with data for WO_3 bulk crystals *(1796, 1822, 2231, 2592, 2923, 2977)*, for example the spectrum in the upper part of Fig. 3.9, makes it evident that this absorption is associated with the lattice dynamics of the tungsten-oxide framework. Different spectra pertain to the cubic, tetragonal,

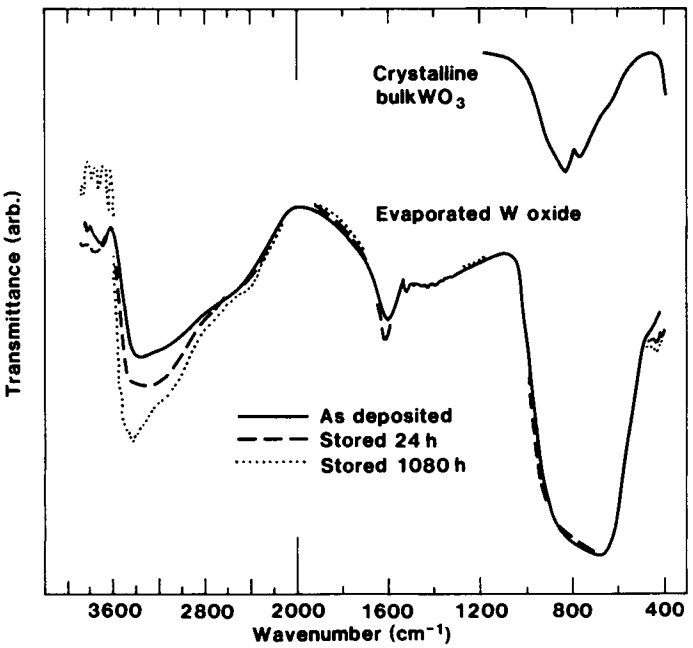

Fig. 3.9 Infrared absorption spectra for crystalline bulk WO_3 (upper curve) and for an evaporated W oxide film (lower curves). The partially overlapping curves were obtained for an as-deposited film and after storing it at 25°C and 50 % relative humidity for the shown periods of time. Note the scale change at 2000 cm^{-1}. After Salje *(2977)* and Yoshiike and Kondo *(3738)*.

orthorhombic, monoclinic, and triclinic crystal modifications *(1822)*, but the differences are not large. The clear absorption features around ~1600 cm^{-1} and ~3400 cm^{-1} are not found in bulk WO_3; they are caused by H-O-H deformation and O-H stretching vibrations, respectively. One concludes from Fig. 3.9 that the as-deposited film is hydrous, and that the degree of hydroxylation and hydration can be enhanced by storing it at room temperature in a moderately humid atmosphere.

Yoshiike and Kondo *(3738)* argued that the amount of physisorbed water increased with time but came to equilibrium within 24 h, and that the amount of chemisorbed OH groups continued to increase with time for at least several weeks. Supporting evidence was found by ^1H Nuclear Magnetic Resonance. The reaction scheme can involve hydroxylation according to

$$-O-W=O + H_2O \rightarrow -O-W\begin{matrix}\diagup OH \\ \diagdown OH\end{matrix} \tag{3.2}$$

or hydrolysis according to

$$-O-W-O-W-O + H_2O \rightarrow -O-W-OH + HO-W-O, \tag{3.3}$$

as postulated by Yoshiike and Kondo *(3738)*.

The decrease of the hydroxylation and hydration upon annealing was recently studied by Shigesato et al. *(3134)*, using the FTIR technique. Expectedly, the absorption at ~3400 cm^{-1} decreased during treatment at τ_a = 150°C, but for samples made at $p_{H2O} = 4 \times 10^{-5}$ Torr there remained some weak absorption features at ~3050, ~3200, and ~3530 cm^{-1}. Such an absorption may indicate well defined incorporation of "structural" water in films made by evaporation in the presence of water vapor.

IR spectra in good agreement with the data in Fig. 3.9 can be found in many papers *(219, 877, 1142-3, 1790, 1841, 2024, 2392, 2875, 3058, 3135-6, 3208, 3737, 3744)*. In principle, IR spectroscopy can discriminate between hydrogen at pore surfaces and in the interior of the W oxide *(3558)*.

It is possible to use IR absorption spectroscopy (as well as thermogravimetry, which will be discussed later) to quantitatively estimate the degree of hydroxylation and hydration. Specifically, molar absorptivity data pertinent to the O-H stretching vibrations at the ~3400 cm^{-1} band *(3669)* can be used for this purpose. The sensitivity of the IR absorption spectroscopy, and hence of the water detection ability, can be enhanced by attenuated total reflectance (ATR). The ATR technique was employed by Badilescu et al. *(219)*, who studied samples comprising IR transparent crystals (such as KRS-5 or ZnSe) with evaporated W oxide films on both sides. The incorporated water density was found to drop with increasing film thickness and was consistent with the presence of a 15 nm thick H_2O layer irrespective of film thickness up to 0.3 μm. Treatment at RH = 66 % increased the water content uniformly in the films. The hydration decreased approximately linearly with increasing substrate temperature during deposition and was close to zero at $\tau_s \approx 300$°C. After hydration at RH = 66 %, films prepared at $\tau_s \approx 300$°C contained about half the amount of water that films made on unheated substrates contained. In recent work on *e*-beam evaporated films *(2494, 3135-6)*, it was found that there were 1.0, 0.7, and 0.5 hydrate-oxygens per W for films deposited with substrates at room temperature, 150°C, and 300°C, respectively.

The sensitivity of the ATR technique can be enhanced still further by using a thin metal coating

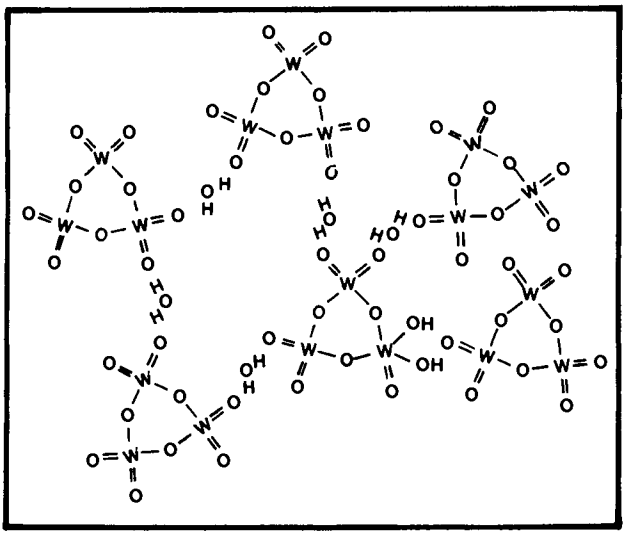

Fig. 3.10 Simple structural model of evaporated W oxide films built from W_3O_9 trimeric molecules. From Arnoldussen *(147)*.

as an overlayer or underlayer for the film being studied, with the overlayer being the superior option *(220, 1432, 1441-2, 2485)*. This approach was used by Badilescu et al. *(219)*, with Ag as metal coating, to resolve weak IR absorption bands in W oxide.The Ag is known to exhibit catalytic properties--particularly in granular form as in a very thin inhomogeneous coating--and the presence of water can lead to the formation of silver tungstates and polytungstates *(710)*. Furthermore, small Ag particles can give spectrally selective absorption *(11)*. It follows that Ag enhanced ATR data should be interpreted with caution, but the technique is inherently very powerful.

3.8 Cluster-type Microstructures

The data characterizing the W oxide film can be used to formulate models for its microstructure. Several such models have been put forward, as discussed below.

It is instructive to begin with a simple model proposed in 1981 by Arnoldussen *(147)*. It starts with W_3O_9 molecules--being the dominant species in the vapor as stressed in Sec. 3.1--that are interconnected through hydrogen bonds, water bridges, and van der Waal's attraction. Hence this model is an example of a cluster-assembled material, or nanophase composite *(2409)*. Figure 3.10 gives a schematic representation of such a solid. High proton mobility can take place along chains of water molecules by sequential H_3O^+ rotations accompanied by proton transfer to adjacent H_2O.

The most detailed and trustworthy structural model presented so far is that by Nanba and Yasui *(2494)* who computed RDFs from several crystalline tungsten oxides and their hydrates and compared with observed data (cf. Fig. 3.5a). Eight different crystals were used as starting points, specifically monoclinic WO_3 (space group $P2_1/a$) and tetragonal WO_3 (P4/nmm) which are polymorphic forms of the ReO_3-type structure *(3668)*, $W_{18}O_{49}$ (P2/m) and $W_{20}O_{58}$ (P2/m) which are substoichiometric oxides with edge-sharing octahedra *(3668)*, layered $WO_3 \cdot 2H_2O$ ($P2_1/n$; modelled from $MoO_3 \cdot 2H_2O$) and $WO_3 \cdot H_2O$ (Pnmb) *(1920, 3312)*, and, finally, hexagonal WO_3 (P6/mmm) and $WO_3 \cdot (1/3)\ H_2O$ (Fmm2) which can be viewed as dehydrated tungsten oxyhydrates with three-, four-, and six-membered rings formed by WO_6 octahedra *(677, 1070, 1166-7, 3053, 3190)*. All of the computed RDFs yielded peaks at ~0.2 nm due to W-O nearest neighbors and at 0.37 to 0.40 nm due to W-W nearest neighbors and, to a smaller extent, W-O next-nearest neighbors. These features stem from the basic octahedral WO_6 building blocks. The peaks at radii larger than 0.5 nm are of more decisive importance for the structural models, and in particular the characteristic peak at ~0.73 nm--which shows up in experimental RDFs for films made by *e*-beam evaporation as well as evaporation from resistive boats--could be observed *only* for hexagonal WO_3 and $WO_3 \cdot (1/3)\ H_2O$. This particular structure could account also for the other peaks in the RDFs, and hence it is natural to proceed to formulate models based on the hexagonal atomic arrangements. Clusters based on $WO_3 \cdot (1/3)\ H_2O$ required too large a size to satisfy the observed coordination of nearest-neighbor W-W. The *hexagonal-type structure* is consistent also with the infrared and Raman spectra reported above.

Figure 3.11 (upper left-hand panel) shows a structural model based on hexagonal WO_3, in which the three- and six-membered rings are displayed in the projected X-Y plane and four-membered rings are parallel to the vertical Z direction. This cluster size is in line with electron microscopic observations. The three-member rings can be ascribed to the trimeric W_3O_9 molecules produced during evaporation, and such molecules can be tied together to also form the six-member rings; hence there is some analogy to the older structural model due to Arnoldussen *(147)*. Finally,

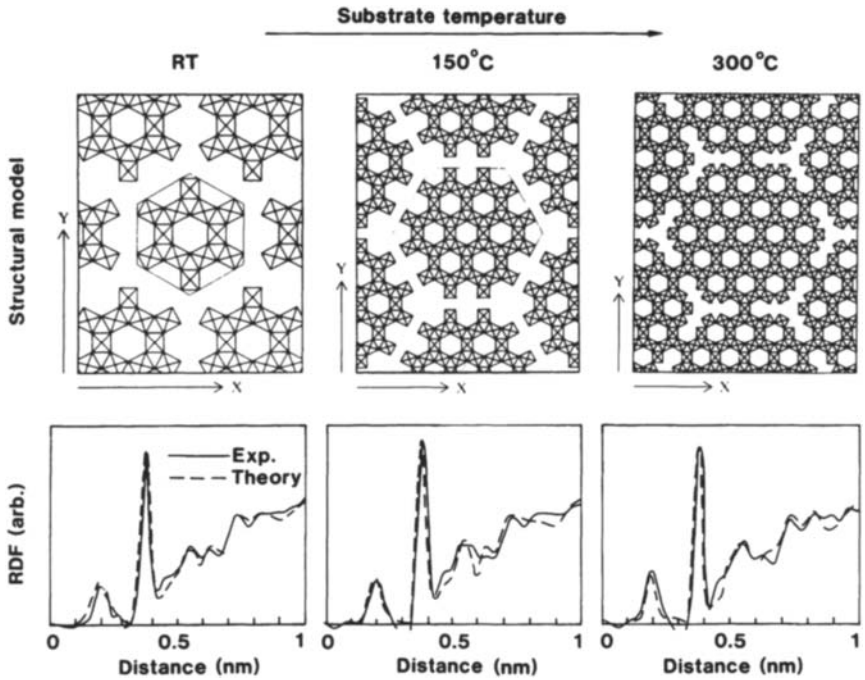

Fig. 3.11 Upper parts show structural models, based on connected WO_6 octahedra, for W oxide films made by evaporation onto substrates at room temperature (RT) and at two elevated temperatures. The arrows in the X- and Y-directions denote 2 nm. Lower parts show corresponding radial distribution functions (RDFs) as determined from X-ray scattering (solid curves) and as computed from the shown structural models (dashed curves). The solid curve in the lower left-hand panel was shown also in Fig. 3.5(a). From Nanba and Yasui *(2494)*.

the clusters were arranged in space with consideration of their hexagonal plate configuration so that they constituted a "film". The separation between the clusters was chosen to account for the observed overall density (cf. Fig. 3.2). It is believed that the clusters are linked by hydrogen bonds through water molecules. RDFs were computed for the cluster-based model. As seen from the lower left-hand panel of Fig. 3.11, there is excellent agreement between theory and experiment, which gives strong credibility to the structural model constructed from hexagonal WO_3. Also the terminal W=O bonds can be accounted for in this model.

The modelling was extended also to W oxide films prepared by evaporation onto substrates with τ_s above room temperature. It can be inferred from the middle panels of Fig. 3.11 that the same basic structure as for the unheated film prevails at τ_s = 150°C, although the cluster size has grown to ~3 nm. At τ_s = 300°C, represented by the right-hand panels in Fig. 3.11, one has to invoke further cluster growth as well as WO_6 octahedra shared between neighboring clusters. Hence there seems to be a qualitative change from isolated to percolating clusters at a sufficiently high substrate temperature.

Structural models have been put forward in several other studies, as surveyed next. A chemical approach to the structure of disordered W oxide films was applied by Schlotter and Pickelmann *(3058)*. They regarded the film as a "xerogel", specifically a fine-grained hydrated tungsten oxy-hydroxide with reduced stoichiometry. The internal surfaces of the porous oxide matrix were taken to be covered with acidic hydroxyl groups generated during the sublimation process. These so called Bronsted sites can be responsible for ion exchange and chemisorption reactions. According to Schlotter and Pickelmann *(3058)*, the evaporated W oxide films can be regarded as solid acids.

Another study, based on several physical measurements *(244, 1126, 1842, 2832)*, resulted in a structural model embracing clusters of three to eight WO_6 octahedra, each sharing corners and edges. The model also included terminal W=O bonds as well as W-O-W bridges. The similarity to the model by Nanba and Yasui is apparent.

Structural models were used to compute X-ray scattering also in *(67, 1952, 2630)*. Thus Aleshina et al. *(67)* argued that the orthorhombic (space group Pnmb) configuration of WO_3 *(1763)*--that was not included in the study by Nanba and Yasui *(2494)*--could lead to acceptable agreement between theory and experiment, including the 0.73 nm peak. However, this modelling had to assume that the orthorhombic units were arranged in crystallites shaped as parallelepipeds which, apparently, is not supported by electron microscopy Kukuyev et al. *(1952)* favored a structure comprising "ordered chains" of WO_6 octahedra, whereas Olevskii et al. *(2630)* considered linear arrangements of three corner-sharing WO_6 octahedra as the basic building blocks.

The cluster-type structural models discussed above have pointed to the importance of the octahedral coordination of the W atoms, i.e., the fact that WO_6 units are the essential building blocks of the disordered or "amorphous" structure. Before leaving this subject one could widen the perspective and stress that "amorphicity" in principle can be modelled in different ways as discussed by Finney *(1079-80)* and Zallen *(3786)*. Thus the amorphous structure can be thought of as constructed from microcrystals. A second model is based on random close packing --sometimes referred to as the Bernal model *(366-8)*--which envisages the structural units as hard or soft spheres in a container that does not induce crystallization. Thirdly, the continuous random network model comprises structural units with certain local bonding requirements met while allowing for the formation of rings with a variety of members by bond bending. Still other models consider random coils or are based on Monte Carlo or molecular dynamics concepts. Clearly the microstructure of the evaporated W oxide films have features of microcrystalline as well as

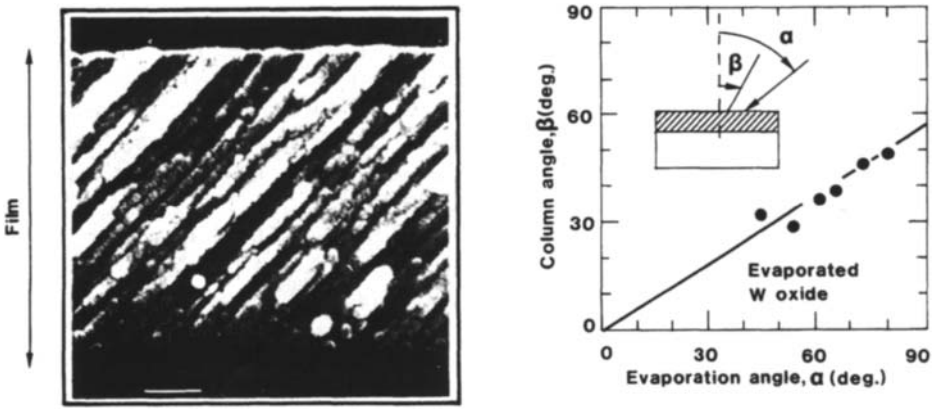

Fig. 3.12 Left-hand part depicts a section scanning electron micrograph of a W oxide film made by evaporation at an angle 72° to the substrate normal. The white scale bar at the bottom has a length of 329 nm. Right-hand part shows column angle vs. evaporation angle, with angles defined in the inset. The line represents the relation $\beta = 0.64\,\alpha$. From Motohiro and Taga *(2410-1, 3320)*.

continuous random network character. One notes in this context that FeF_3, with a local atomic arrangement similar to that of WO_3, has been represented by use of models based on random close packing *(2084-5)* and a continous random network *(722, 1328-9)*. An approximate rescaling of the data for FeF_3 to the case of WO_3 was done by Green *(1306)*.

3.9 Columnar Microstructures

Inhomogeneities on scales larger than the one discussed above are possible irrespective of the structure being of cluster-type or crystalline. In fact, microstructural features occur at sizes from atomic or molecular dimensions up to dimensions of the order of the film thickness, as elaborated by Messier et al. *(2301-3)*. Columnar features with cross sections of the order of a few nm can be understood from models based on ballistic aggregation of structural elements and ensuing reaccomodation of these *(477-9, 943, 2021, 2278, 2450, 2452, 3173, 3322-4)*, as well as on growth instabilities in continuum theories *(1750, 2074, 2242, 3229, 3360)*. Columns with linear sizes exceeding 100 nm can be represented by a stuctural zone diagram for evaporated films that was first put forward by Movchan and Demchishin *(2422)*. For films prepared by normal evaporation--with the vapor flux having perpendicular incidence towards the substrate--the columns are oriented normal to the substrate. The intercolumnar regions hence allow easy mass transport across the film, which is of obvious importance for ion intercalation/deintercalation. Clear evidence for a columnar microstructure was found by scanning electron microscopy of fractured edges of W oxide films *(38, 290)*.

It is possible to increase the columnar character, and decrease the density, by depositing W oxide at oblique incidence angle *(32, 35, 2352, 2410-1)*. The left-hand part of Fig. 3.12 gives a clear illustration of extended columns in a film prepared by *e*-beam evaporation with the vapor flux having an angle α of 72° from the substrate normal. The column inclination angle β is ~45°. A "tangent rule" *(943, 2021, 2526)*,

$$\tan \beta = (1/2) \tan \alpha, \tag{3.4}$$

is often put forward to account for column tilts. This rule predicts that β should be 57°. The general validity of the "tangent rule" is questionable, though, as seen both in experimental studies *(1119, 2243-4, 2488, 3324)* and at least some theoretical modelling *(1930-1, 2278-80)*, and the discrepancy between experiment and "rule" for W oxide is not surprising. On the other hand, there is also some recent theoretical work that tends to support the validity of the "tangent rule" *(2686)*. The right-hand part of Fig. 3.12, taken from Motohiro and Taga *(2410, 3320)*, shows that the relation between column tilt and vapor incidence can be approximated by $\beta \approx 0.64\,\alpha$ at least for $\alpha > 45°$. Recently, it has been shown that oblique columnar structures can be produced by codeposition with the two fluxes coming from different directions *(3282)*.

Tungsten oxide with very large porosity, having a density as small as ~1%, can be produced by the gas evaporation technique *(1297)*, i.e., by heating of W in the presence of an oxygen-containing gas with a pressure of several Torr *(130, 1449, 1718)*.

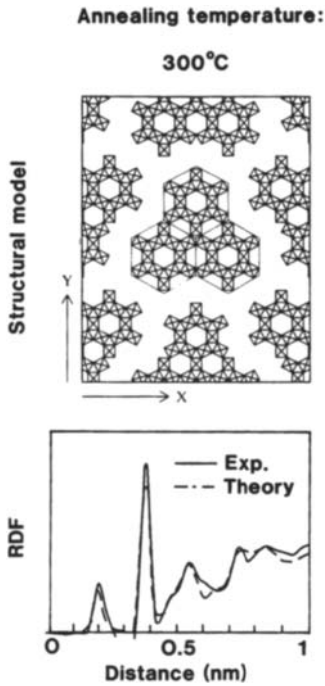

Fig. 3.13 Upper part shows a structural model, based on connected WO_6 octahedra, for W oxide films made by evaporation followed by annealing post-treatment. The arrows denote 2 nm. Lower part shows radial distribution functions (RDFs) as determined by X-ray scattering (solid curve) and as computed from the shown structural model (dashed curve). From Nanba and Yasui *(2494)*.

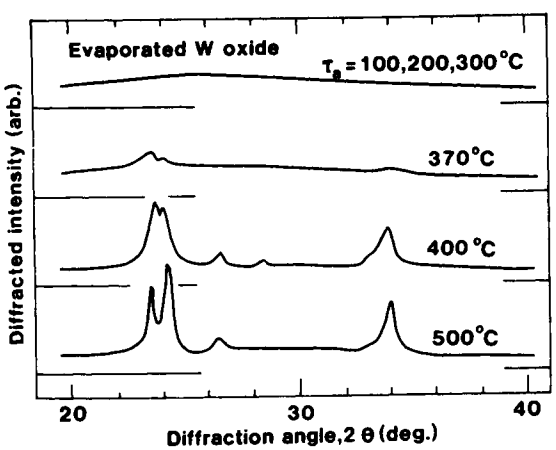

Fig. 3.14 X-ray diffractograms for evaporated W oxide films treated at the shown values of annealing temperature τ_a. From Matsuhiro and Masuda *(2224-5)*.

3.10 Crystallization of As-deposited Films

Annealing at an elevated temperature can be used to improve the lattice order of WO_{3-z} films made at different substrate temperatures. It is possible to use RDFs of annealed films to derive structural models as illustrated before in Fig. 3.11 *(1952, 2494)*. Figure 3.13 shows data for a W oxide films evaporated onto an unheated substrate and subsequently treated at τ_a = 300°C so that it has 0.2 hydrate-oxygens per tungsten atom. The structural model needed to reproduce the experimental RDF has aggregates of three of the clusters comprising the as-deposited film *(2494)*. It is evident that deposition followed by annealing at a certain temperature leads to a less dense and less crystalline structure than direct deposition onto a substrate at the same temperature.

At high enough annealing temperatures it is possible to follow the crystallization of as-deposited films by conventional XRD measurements. Figure 3.14, reproduced by Matsuhiro and Masuda *(2224-5)*, shows data for ~0.5 μm thick films *e*-beam evaporated in the presence of 8 x 10^{-4} Torr of N_2 onto unheated substrates and subsequently annelated at successively increased temperatures up to 500°C. Up to 300°C the films are "X-ray amorphous", i.e., featureless. Structure indicating long-range atomic order develops gradually above 300°C; the changes are particularly large between 370 and 400°C. Analogous data have been reported several times *(418, 927, 2840, 3050, 3135)*. Crystallization was studied through electron diffraction as early as in the pioneering work by Deb *(836)*, and this technique was used also by Sharon et al. *(3116)*. The annealed films can show clear texture, and Gavrilyuk et al. *(1150)* found that films made at τ_s < 400°C predominantly had (100) planes oriented parallel to the substrate, and that films made at τ_s > 400°C had (001) planes with this orientation.

Detailed information on annealing-dependent effects can be gained from Differential Scanning Calorimetry (DSC) and Thermal Gravimetric Analysis (TGA). The solid curve in Fig. 3.15(a), taken from Zeller and Beyeler *(3791)*, shows a DSC spectrum for a W oxide film during heating by 10°C/minute. Analogous results were reported in *(38, 2840, 3150)*. A broad endothermic peak is seen around 170°C, and a narrower endothermic peak lies at ~300°C. These two dominant features almost conceal the exothermic peak(s) associated with crystallization. In order to display the effect of crystallization, a sample was dehydrated by heating at 150°C for 16h. The ensuing DSC spectrum, shown by the dashed curve in Fig. 3.15(a), indicates an exothermic peak centered at 345°C. During rerun (cooling) the DSC spectrum is featureless, as given by the dotted line in this figure. Analogous data have been recorded for bulk specimens *(443, 1154)*.

Complementary results can be gained from the TGA data in Fig. 3.15(b), taken by Agrawal and Habibi *(38)* during heating with 10°C/minute. Similar results were reported by Randin *(2840)*. The sample used to obtain the shown data was prepared by evaporating W oxide onto glass and scraping off the deposit until 30 to 50 mg was collected. The mass was decreased by ~8 % during heating from 50 to 450°C. The change took place in two broad ranges, in qualitative agreement with the DSC spectrum. The volatiles evolved during the annealing were investigated by studying the outgoing purge gas (N_2) from the TGA cell by FTIR spectrometry. The mass decrease was due to loss of water. Powder samples showed TGA curves *(1155)* similar to the one in Fig. 3.15(b).

The loss of water during heating can also be followed by vibrational spectroscopy. Figure 3.16, taken from Schlotter and Pickelmann *(3058)*, depicts IR absorption spectra for a film in as-deposited state and after treatment in vacuum at τ_a = 180°C for 2h. The absorption features at ~1600 cm^{-1} and ~3400 cm^{-1}, which are a measure of hydroxylation and hydration as discussed before, are

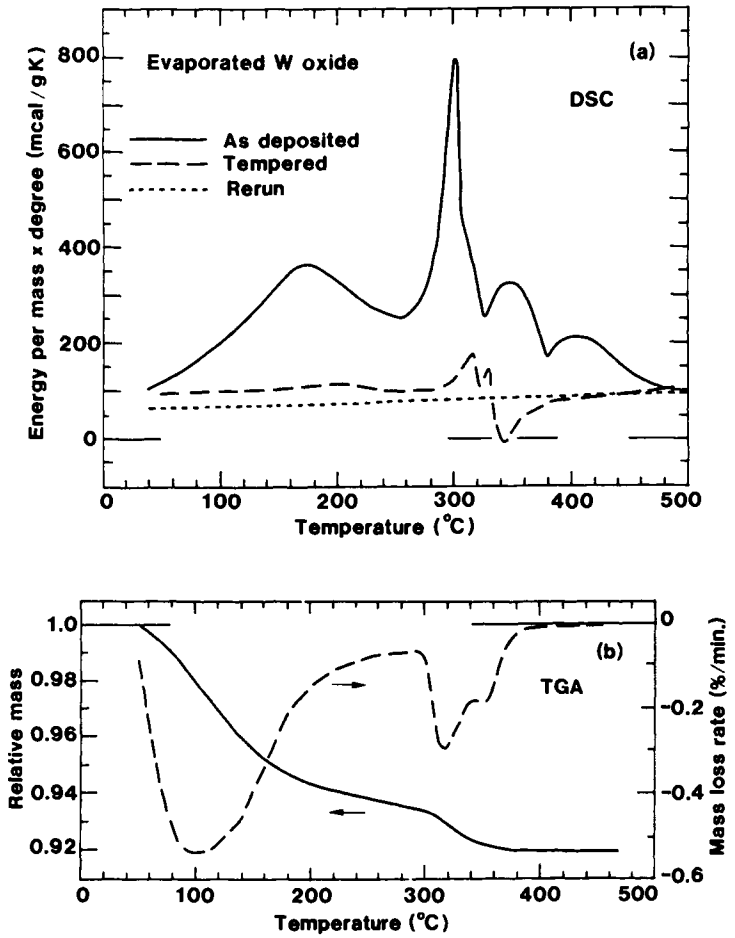

Fig. 3.15 Differential Scanning Calorimetry (DSC; part a) and Thermal Gravimetric Analysis (TGA; part b) spectra for evaporated W oxide films. DSC data were taken during heating of as-deposited and tempered films, and also during a rerun, as shown for the different curves. TGA data were taken during heating and refer to the relative mass (solid curve; left-hand scale) and to the first derivative of this function (dashed curve; right-hand scale). After Agrawal and Habibi *(38)* and Zeller and Beyeler *(3791)*.

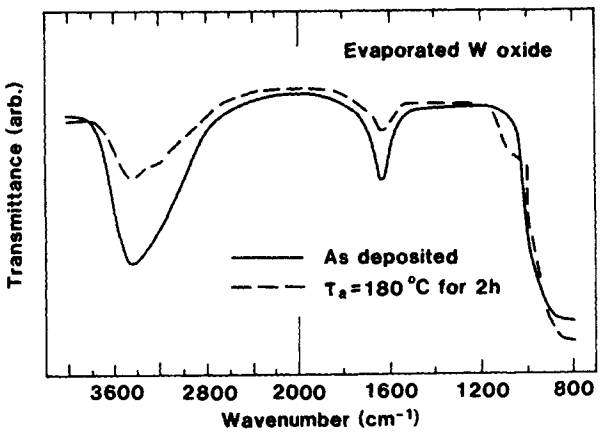

Fig. 3.16 Infrared absorption spectra for an evaporated W oxide film in as-deposited state (solid curve) and after annealing in vacuum at the shown temperature and duration (dashed curve). Note the scale change at 2000 cm^{-1}. After Schlotter and Pickelmann *(3058)*.

less pronounced in the annealed film. This is consistent with the TGA data in Fig. 3.15(b). Similar annealing-dependent changes in IR absorption spectra have been reported elsewhere *(2392, 3135-6, 3208, 3704)*.

The oxygen deficiency can be influenced by annealing *(884, 2494)*. Vacuum treatment up to τ_a = 550°C did not affect z, as seen from RBS, whereas annealing in the presence of oxygen made z approach zero at τ_a = 200°C. Stoichiometric changes during annealing have also been inferred from XPS spectra *(1511)*.

Crystallization can be induced not only by annealing at a high temperature but also by treating evaporated films at a moderately elevated temperature (> 25°C) at a high relative humidity (> 50 %), as studied by Yoshiike and Kondo *(3739)*. From a combination of electron diffraction and XRD measurements, it was inferred that the crystallization starts at the air interface and progresses so that it extends across a ~1 μm thick layer after ~1 day. It was argued that the crystallization was connected with the dissociation of W-O-W bonds and the formation of $WO_3 \cdot H_2O$ or $H_2WO_4 \cdot H_2O$ with a dense glassy structure. It is possible that these processes are akin to those in the common "sealing" of anodic alumina *(3605)*.

This Page Intentionally Left Blank

Chapter 4

TUNGSTEN OXIDE FILMS: PREPARATION, STRUCTURE, AND COMPOSITION OF SPUTTER-DEPOSITED FILMS

Sputter-deposition is a well established technique for industrial thin film preparation, and the technique is convenient also for laboratory-type work. This chapter follows the format of the previous one, although it is shorter since sputtering has not been investigated as widely as evaporation. Separate sections cover deposition aspects (4.1), characterization of as-deposited films by several techniques (4.2), cluster-type microstructures (4.3), columnar microstructures (4.4), and crystallization of as-prepared films (4.5).

4.1 Deposition Aspects

Sputter-deposited W oxide films cannot a priori be expected to exhibit the same composition and microstructure as in films made by evaporation of WO_3 and discussed above. One reason for this is that the deposition process *(660, 1031)* involves dislodging of species from a target by ion impact at energies large enough for breaking up molecular (W_3O_9) bonds when sputtering is carried out from an oxide target or from an oxidized metal target. By the same argument it is unlikely that W_3O_9 molecules can form in the sputter plasma. Indeed sputtering of oxidized W(100) by ~500 eV Ar^+ ions, studied by Benninghoven et al. *(344)*, produced W_2^+, W_2O^+, O^+, WO_3^-, W^+, O^-, and WO^+ in order of increasing yield, while other ionic species such as WO_2^+ and O_2^+ were less abundant. Azens et al. *(187-8)* found for sputtering from tungsten oxide surfaces that the ionic abundancies depended on the stoichiometry. Studies of the sputter yield from tungsten surfaces bombarded with oxygen, carbon and other ions were reported in *(189, 992-3, 1452)*.

Sputter rates for the deposition of WO_{3-z} in Ar + O_2 plasmas are given in Fig. 4.1 for different sputter parameters and modes. The data for dc and rf sputtering are from Kaneko et al. *(1739)* and Akram et al. *(50)*, respectively. The latter data were given also by Kitao et al. *(1829)*. Beyond a certain O_2 content, the rate goes down and approaches a constant value of ≤ 0.1 nm/s. This decrease is due to oxidation of the sputter target. Discussions of large-area reactive sputtering under different conditions, with a view to W oxide, were given by Howson et al. *(392-3, 1555)*. An analysis of the sputter discharge parameters for W oxide preparation can be found in *(1306)*. Higher sputter rates can be accomplished by increasing the power density on the target. The highest rate in the literature is 3.4 nm/s, which was reported by Hichwa et al. *(1483)* for reactive dc magnetron sputtering at different O_2 contents for a power density of 34 W/cm^2 ; electrochromism was not reported for these latter films, though. Reactive rf sputtering of W in O_2 gave 1 nm/s at 13

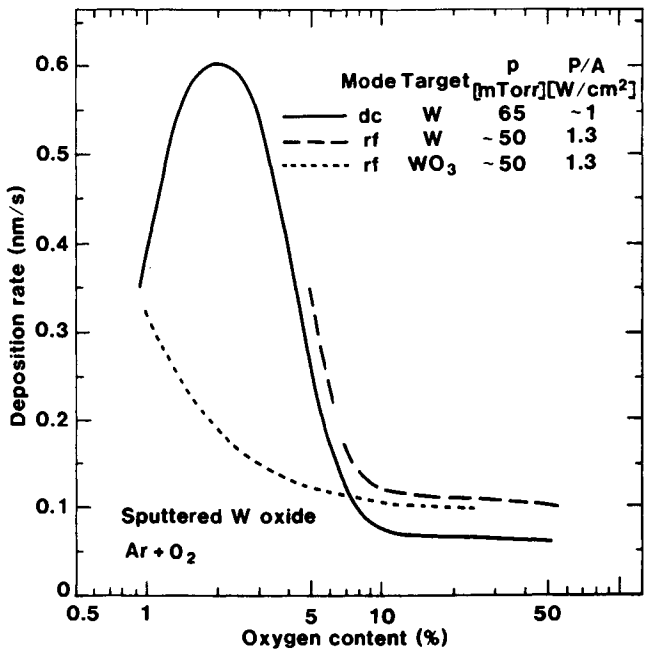

Fig. 4.1 Deposition rate vs. oxygen content for sputtering from the shown target materials in Ar + O_2. The curves refer to different sputter modes and different value of gas pressure p and power density P/A. After Akram et al. *(50)* and Kaneko et al. *(1739)*.

W/cm^2 *(3742)*. By selecting appropriate sputter parameters, one can avoid stress buildup in the deposited films *(1733)*. Increased porosity can be achieved by oblique angle sputtering *(3091)*.

It is possible to enhance the sputter rate at a given power density by additions to the sputter gas, and Giri *(1188)* showed that the rate could increase by a factor of about two for sputtering in Ar + 6 % O_2 when a H_2 addition went from 0 to ~3 %. This effect is likely to be due to hydrogen ions bombarding the target surface, thereby decreasing its oxide coverage *(2182)*. Even more dramatic rate enhancements were found by Harding *(1426)*, who carried out dc magnetron sputtering of W in O_2 + CF_4. We return to the properties of such W oxyfluoride films in chapter 13.

Just as for evaporated films, it is instructive to show the large role of the deposition parameters by considering their effect on the electrical resistivity. Figure 4.2, reproduced from Kaneko et al. *(1739)*, refers to dc sputtering of metallic tungsten in Ar + O_2 at 65 mTorr total pressure, an average power density on the target of ~1 W/cm^2, and 100 V substrate bias. When the O_2 content is low, the resistivity approaches the value for bulk tungsten, and it is obvious that the deposited film has metallic properties. At ~2.5 % O_2 there is an abrupt increase of the resistivity by some ten orders of magnitude, and above 3 % O_2 the deposited film has dielectric properties. At the highest oxygen contents, the resistivity is not far from the value for films made by evaporation of WO_3 powder onto substrates at $\tau_s < 200°C$ (cf. Fig. 3.1). Electrical data similar to those in Fig. 4.2 have been reported in a series of papers by Kaneko, Miyake et al. *(1737-8, 1740, 2341-2)*. Hall effect and carrier concentration as a function of O_2 content were given in *(2342)*. Results of the type shown in Fig. 4.2 are characteristic for reactive vacuum deposition of metals that form non-conducting oxides *(9, 10)*. Films made with oxygen contents between ~3 and 6 %, which gave deposits with a nominal composition WO_{3-z}, showed pronounced electrochromism *(1739)*. Relations between deposition parameters and the occurrence of electrochromism were also reported in *(884)*.

4.2 Characterization of As-deposited Films by Several Techniques

As discussed in chapter 3 above, vibrational spectroscopy and X-ray scattering are techniques of choice for assessing the microstructure of heavily disordered W oxide films. Results based on such measurements are presented in the following sections, in addition to some XPS data.

Oxygen/tungsten ratios have been determined by RBS. The experiments showed $z \sim 0.1$ *(1168)* or $z \sim -0.1$ *(806)*, and it is clear that the deviation from stoichiometry was small. Hydrogen uptake during storage in air has been studied by NRA *(2445)*; this effect was considerably less pronounced than for similarly exposed evaporated films, which speaks in favor of the sputtered films being denser than the evaporated ones.

Raman spectroscopy was applied to films made by rf sputtering of W in Ar + O_2 and O_2 plasmas in work by Pham Thi and Velasco *(2744, 2746-7)* and by Daniel et al. *(806)*. Films, deposited onto glass showed a broad spectral feature around ~800 cm^{-1} and a narrower and smaller feature around ~940 cm^{-1}. Annealing made the ~800 cm^{-1} band split into two and the ~940 cm^{-1} band vanish. These results are in excellent agreement with observations on evaporated films (cf. Fig. 3.6), which points to the significance of terminal W=O modes also in sputter-deposited samples. Surface enhanced Raman scattering was observed in thin W oxide films backed by silver *(2743, 2747)*. This latter technique yields data that are somewhat akin to those obtained by

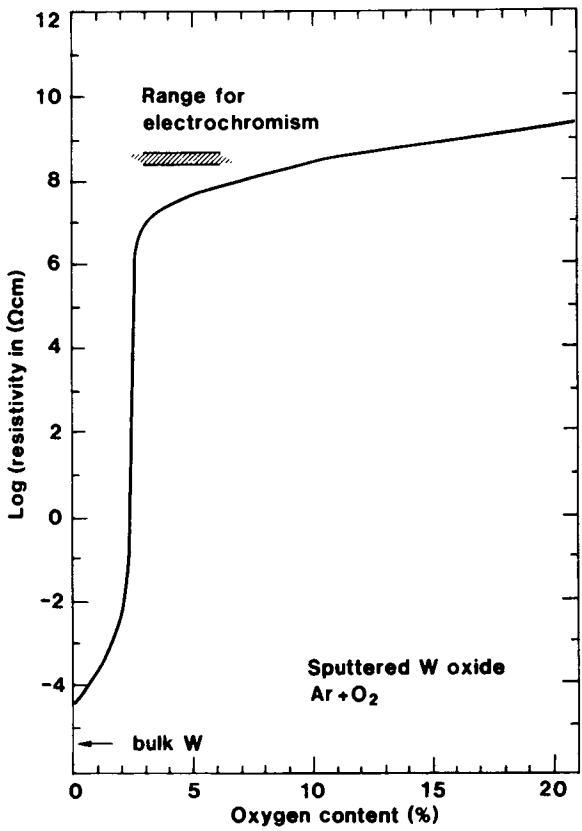

Fig. 4.2 Resistivity vs. oxygen content for sputtering of W in Ar + O_2. An arrow marks the resistivity of bulk W (at room temperature). The oxygen contents that led to films with pronounced electrochromism are indicated by the shaded band. After Kaneko et al. *(1739)*.

enhanced infrared ATR.

Infrared absorption spectroscopy on thin W oxide films made by sputtering of WO_3 in O_2 and Ar + O_2 was reported by Akram et al. *(50)*, Daniel et al. *(806)*, and Pham Thi and Velasco *(2747)*. Absorption due to H-O-H deformation was found at ~1600 cm^{-1} and due to O-H stretching at ~3400 cm^{-1}. This is in full analogy with data on evaporated films (cf. Fig. 3.9), and one concludes that these sputter-deposited films were hydrous. Ageing in air, studied by Daniel et al. *(806)*, led to a noticeable increase in the water absorption bands at ~1600 cm^{-1} and ~3400 cm^{-1} after a few hours, whereas the main absorption band due to W-O remained unchanged. After several days, a new absorption appeared at 1425 cm^{-1} due to W-O-H deformation, and the O-H stretching band split into three components centered at 3440, 3220, and 3050 cm^{-1}. Such a two-stage ageing is similar to the one for evaporated films discussed in Sec. 3.7 *(3738)*. The first step involves physisorption of water in pores and at the surface, and the second step can be due to hydroxylation and/or hydrolysis, the second mechanism being the preferred one.

Gérard et al. *(884, 1169)* probed stoichiometry deviations by XPS. They studied films deposited under different oxygen pressures, so that they consisted of WO_{3-z} with $0 \leq z \leq 0.5$ (according to RBS). Figure 4.3 shows the number of electrons collected from the $W4f_{5/2}$ and $W4f_{7/2}$ levels vs. energy measured from the Fermi level. The relative locations of the overlapping peaks represent chemical shifts due to tungsten atoms in different oxidation states (W^{6+}, W^{5+}, and W^{4+}), and the areas under the peaks correspond to the relative proportions of atoms in these states. It is evident that substoichiometry is connected with the occurrence of tungsten atoms in oxidation states below 6+. For $z \approx 0.5$, the amounts of W^{5+} and W^{4+} were as large as 33 and 23 %, respectively. XPS was used to study sputter-deposited films also by Tada *(3313)*. Section 7.7 will give a more detailed discussion on the interpretation of XPS data for W oxide.

4.3 Cluster-type Microstructures

Radial distribution functions have been derived for disordered W oxide films made by sputtering in Ar + O_2 *(3791)*, Ar + O_2 + H_2 *(1306)*, and under unspecified conditions *(2630)*. Figure 4.4 illustrates an RDF from the work by Zeller and Beyeler *(3791)* in the same manner as in Fig. 3.5(b). The RDF is very similar to the corresponding data for evaporated films (cf. Figs. 3.5 and 3.11) and, in particular, the conspicuous peak at ~0.73 nm shows up distinctly. Following arguments given earlier, this speaks in favor of the sputtered films being built from structural elements (clusters) with hexagonal configuration, just as for the evaporated films. However, it is probably not meaningful to try to establish the cluster size, or the space arrangement of the individual clusters, solely from this RDF. The analysis by Green *(1306)* was consistent with a W-W separation of 0.377 nm, and arguments were given to support a microstructure composed of ring structures with WO_6 octahedra sharing corners. Oleevskii et al. *(2630)*, on the other hand, argued for a structure built from units comprising three disordered WO_6 octahedra, two being joined by an edge and the third being linked by a corner. Even if these models have some differences, their unifying features are more important and, in particular, the role of the WO_6 octahedra is unanimous. X-ray amorphous films have been made through sputtering in several studies apart from those mentioned above *(432, 806, 1270, 2076, 3440)*.

An earlier study by Green et al. *(817, 1320)* on W oxide films made by rf sputtering of WO_3 in Ar + O_2 reported that the as-deposited material appeared tetragonal crystalline when studied by

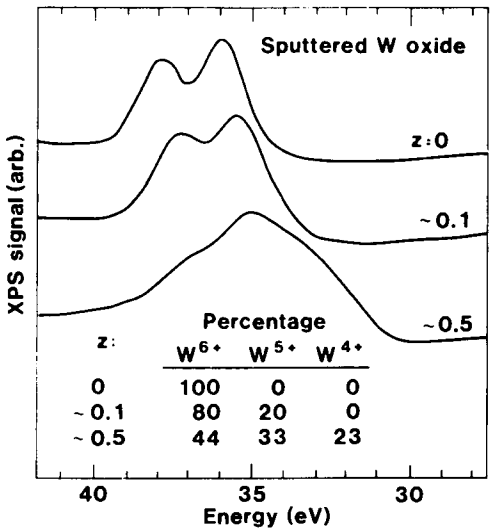

Fig. 4.3 XPS spectra for reactively sputter-deposited W oxide films with different degrees of oxygen deficiency z. Based on integrated peak intensities, the relative proportions of W atoms in different oxidation states were as shown in the inset table. After Gérard et al. *(1169)*.

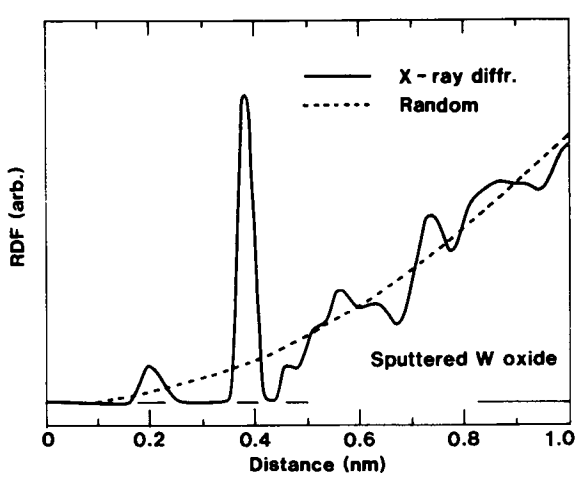

Fig. 4.4 Radial distribution function (RDF) for a W oxide film made by sputtering in Ar + O_2, as obtained from X-ray scattering. Dotted curve corresponds to an RDF in the absense of any long-range order. From Zeller and Beyeler *(3791)*.

electron diffraction. Considering that crystallization is easily induced by electron irradiation--as discussed shortly--it is not impossible that the as-deposited film was heavily disordered, and that crystallization took place in the electron microscope. Films deposited under unspecified conditions by Hitchman *(1502-3)* also appeared crystalline in as-deposited state.

Films that definitely are crystalline in as-deposited state can be obtained by sputtering onto a substrate at high enough temperature, and work by Goldner et al. *(1228, 1231)* showed clear X-ray diffraction peaks for materials made by rf sputtering in Ar + O_2 onto a substrate at τ_s = 325°C. Reactive sputtering in Ar + O_2 onto substrates kept at τ_s < 430°C led to crystalline orthorhombic films, and traces of a $W_{20}O_{58}$ phase was found if the O_2 content was not too large *(2189-91)*. Effects on RFDs upon crystallization were reported in *(1306)*.

4.4 Columnar Microstructures

Sputter-deposited W oxide films were studied by electron microscopy in work by Giri and Messier *(1188-9)*. Scanning electron microscopy was applied to surfaces and fracture edges of ~10 μm thick films, and transmission electron microscopy was applied to films thinnner than 0.1 μm. It was found that these disordered films had a highly anisotropic structure with columns and voids depending on preparation conditions and film thickness. In ~1-μm-thick films, which are of interest for electrochromic devices, at least three different and distinct void sizes were recognized:

(i) large voids (5 to 10 nm) around 300 to 500-nm-size columns,

(ii) medium voids (3 to 5 nm) around ~100-nm-size columns, and

(iii) small voids (1 to 3 nm) around 10 to 30-nm-size columns.

It was also surmised that microvoids around 1 to 3-nm-size columns would be present; these latter features might represent the "canonical" clusters discussed above, but this remains conjectural. The general features of the columnar microstructure can be understood from ballistic aggregation and adatom mobility and are captured in the structural zone diagram of Thornton *(3413, 3617)*--being an extension of work by Movchan and Demchishin *(2422)*--and its elaborations to include evolutionary effects *(2301, 2303)*.

Nodular film growth was reported by Giri *(1188)* in films made by sputtering at high gas pressure. The nodules are caused by rapid growth of extrinsic nucleation centers *(480, 2451, 3218)* and look like cones with their apices at the substrate and their bases at the film surface. A region around the nodules is expected to be under compressive stress, while a more detached surrounding film is generally under tensile stress. This stress situation may cause microcracks with ensuing film degradation.

4.5 Crystallization of As-deposited Films

Annealing can lead to crystallization signified by distinct peaks in X-ray diffractograms. Different values of the crystallization temperature are found in the literature. Two studies *(2190, 2831)*

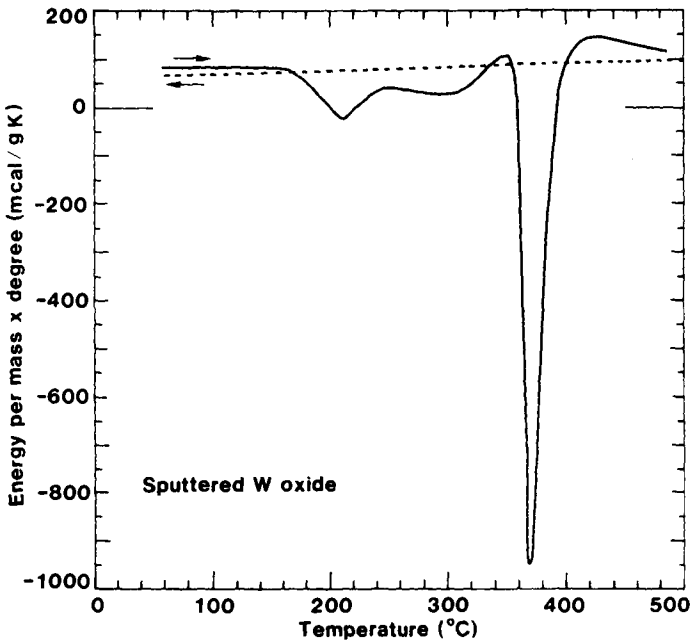

Fig. 4.5 Differential scanning calorimetry spectrum for a W oxide film made by sputtering in Ar + O_2. Data are given for increasing and decreasing temperature, as indicated by the arrows. From Zeller and Beyeler *(3791)*.

showed that crystallization took place at 100 to 130°C, whereas a third study *(2747)* indicated that crystallization occurred after 1/2 h at τ_a = 360°C. The latter films became orthorhombic when prepared by sputtering in Ar + 20 % O_2 and tetragonal when prepared by sputtering in pure O_2. Orthorhombic structures were reported also in some other work *(432, 1829, 1837)* on films annealed in air or vacuum at τ_a = 400 °C for several hours. Infrared absorption spectra and Raman spectra indicated that a heavily disordered structure was present after heating to 220°C, and that crystallization took place during heating up to 420°C *(806)*. Obviously the properties during film preparation and post-treatment are of great significance for the crystallization and for the resulting structure.

DSC has been used to provide more detailed information on the annealing process and Fig. 4.5, reproduced from Zeller and Beyeler *(3791)*, shows a spectrum plotted in the same way as in Fig. 3.15(a). The solid curve was recorded during heating by 10°C/minute. A sharp exothermic peak, indicating crystallization, is found at ~370°C. This is slightly above the crystallization temperature for the evaporated film of Fig. 3.15(a) and in surprising disagreement with the crystallization temperature inferred from X-ray diffraction on sputter-deposited films. The absence of endothermic peaks is significant and proves that this film was not strongly hydrated, which is in marked contrast with the case of evaporated films. The fact that IR absorption spectroscopy showed signs of water in other sputter-deposited W oxide films *(51, 806)*, as mentioned above, casts doubt on the general validity of the dehydrated character evinced in Fig. 4.5.

Thermomanometry, i.e., measurements of pressure rises during monotonic heating runs in vacuum, is a useful technique for studying gas evolution from thin films and powders *(1995)*. Green *(1306)* used this method to investigate dc sputtered W oxide films and found evidence for water desorption at ~100°C and possible indications of O_2 evolution in conjunction with crystallization at ~400°C.

Crystallization under *e*-beam irradiation was studied by Giri *(1189)* and was mentioned also by Green *(1306)*. Crystallization took place at high current density (~160 mA/cm^2) in films deposited at high gas pressure. The crystallized film showed electron diffractograms in good agreement with the tetragonal phase, or with "resemblance to the hexagonal phase", depending on deposition conditions. It is possible that this dichotomy reflects differences in the cluster-type microstructure of the as-deposited films.

This Page Intentionally Left Blank

Chapter 5

TUNGSTEN OXIDE FILMS: PREPARATION, STRUCTURE, AND COMPOSITION OF ELECTROCHEMICALLY AND CHEMICALLY PREPARED FILMS

There are numerous electrochemical and chemical techniques that are suitable for making W oxide films. Many of these have not been studied in depth, but a fair amount of information is available. This chapter is divided according to film preparation technique and surveys electrodeposition (5.1), anodization (5.2), chemical vapor deposition and spray pyrolysis (5.3), and sol-gel-based techniques (5.4). Some other techniques are touched upon in a final section (5.5). Discussing electrochemical techniques before purely chemical ones turns out to be convenient for some of the electrochromic oxides treated in subsequent chapters, and this order is used here as well in order to maintain the same format.

5.1 Electrodeposition

Electrodeposition from aqueous peroxotungstic acid solutions has been explored by Yamanaka *(3704)* and others *(760, 810, 2283, 2313, 2384, 2730)* as a technique for making electrochromic films with properties similar to those obtainable with evaporated layers. According to Shen and Tseung *(3125)*, it is advantageous to have an alcohol addition to the solution. Annealing post-treatment was needed, and ~180°C for 1 h gave optimized electrochromic properties. As-deposited films were blue; they changed into a colorless state after treatment at $\tau_a > 140$°C for 1 h. Such an annealing decreased the thickness to ~60 % of its initial value. XPS was used to investigate the oxygen deficiency; the z value was ~0.38 at $\tau_a = 180$°C and about zero at $\tau_a = 400$°C. Annealing at temperatures below 400°C gave films that were X-ray amorphous, whereas Reflection High-Energy Electron Diffraction (RHEED) patterns gave evidence for extremely fine crystallites. FTIR spectra indicated strong hydration of as-deposited films as well as strong absorption due to W=O vibrations at $\tau_a \geq 180$°C. It is possible to electrodeposit W oxide incorporating Ni, Co, or polyaniline, as demonstrated by Shen et al. *(3123-4)*.

In a different process, hydrated W oxide films were produced through electrodeposition by potential cycling in colloidal solutions of $Na_2WO_4 \cdot 2H_2O$ in 2 M H_2SO_4 *(1954, 2929)*.

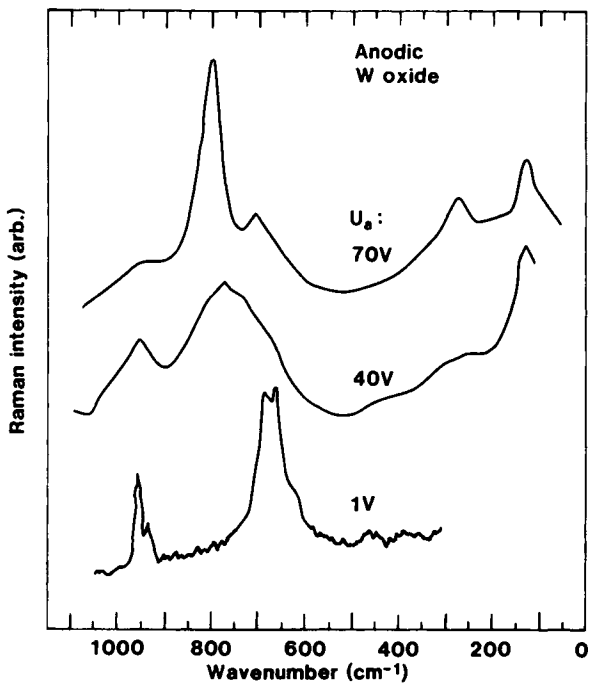

Fig. 5.1 Raman spectra for W oxide films made by anodization at the shown voltages U_a. After Delichere et al. *(860)* and Ohtsuka et al. *(2584-5)*.

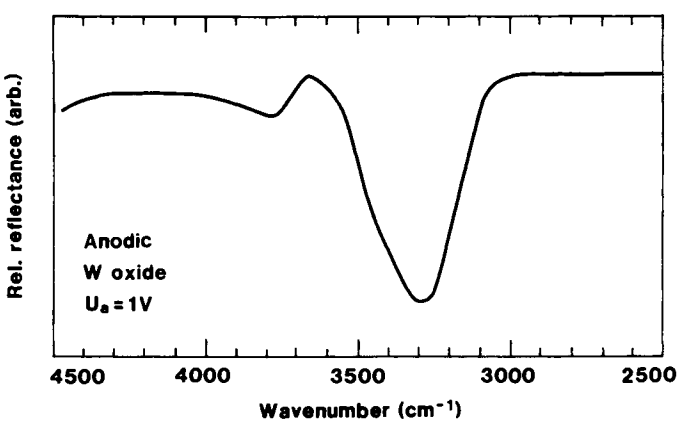

Fig. 5.2 Infrared reflectance of p-polarized light for an anodic W oxide film. The data refer to $[R(d) - R(0)]/R(0)$, where $R(d)$ is the reflectance for a tungsten surface with a 142-nm-thick film, and $R(0)$ is the reflectance of the bare tungsten surface. After Ohtsuka et al. *(2485)*.

5.2 Anodization

Anodization is another electrochemical technique that is able to produce W oxide films on metallic tungsten in sheet, rod, or thin film form. Films can be grown in an acid medium by applying an anodizing voltage U_a. Anodization has been conducted under potentiostatic, potentiodynamic, and galvanostatic conditions with $U_a < 120$ V. In most cases, the processing took place at room temperature.

Falaras et al. *(860, 1029)* carried out a detailed study of samples made by potentiostatic anodization of W plates in 1 N H_2SO_4. When different magnitudes of U_a were applied for 2 minutes each, the oxide thickness (in nm) was obtained from 3.1 U_a (with U_a in volts); the relative density was 0.85 irrespective of U_a. The films showed enhanced crystallinity at increased anodizing voltage; at $U_a = 30$ V, the films appeared featureless by TEM and transmission electron diffraction, but at 40 and 60 V the diffraction patterns were sufficiently distinct to allow an identification with the hexagonal structure. RHEED data gave supporting structural information. High resolution TEM for films made at 40 and 60 V gave direct evidence for six-sided "tunnels" in the films, which is a characteristic feature of the hexagonal WO_3 modification. Furthermore, it was found that these films were comprised of crystallites looking like hexagonal plates with linear extents between 5 and 25 nm. Raman spectra for films made at two voltages are shown as the upper and middle curves of Fig. 5.1. At $U_a = 40$ V, the spectrum indicates a heavily disordered structure, and the resemblance to spectra for W oxide films made by evaporation onto unheated substrates (cf. Fig. 3.6) is very good. One observes again the peak at ~950 cm^{-1} signalling W=O terminal stretching modes. At $U_a = 70$ V, the Raman spectrum indicates a crystalline structure with resolved peaks due to the W-O stretching modes. Potentiostatic anodization at voltages from 20 to 75 V have also been discussed by Kelly *(1996)* and others *(2503-5, 2875-6)*.

Ohtzuka et al. *(2584-5)* investigated anodization at voltages much lower than those mentioned above. The ensuing films then appeared to be different from the earlier ones. Specifically, W sheet was anodized at $U_a = 1.0$ V (relative to a reference hydrogen electrode, RHE) in 0.1 M of H_2SO_4 or $HClO_4$ for long times. The film grew linearly with time, and the thickness was 100 nm after ~4 h. The lower part of Fig. 5.1 shows a Raman spectrum of such a film made in $HClO_4$. The peak at ~960 cm^{-1} is due to W=O and the peak at ~930 cm^{-1} to ClO_4^- contamination. Anodization in H_2SO_4 gave an analogous contamination peak at ~990 cm^{-1} due to SO_4^{2-}. The strong peak at ~670 cm^{-1} is peculiar to anodic W oxide made at low U_a, and a corresponding feature has been found so far only in amorphous films prepared by sol-gel technique. Ohtsuka et al. *(2584)* demonstrated that a similar Raman peak (at ~640 cm^{-1}) could be seen in precipitates formed from a mixture of Na_2WO_4 and HCl according to a standard procedure *(1780)*. Since this Raman peak increased, schematically, according to

$$WO_4^{2-} < \text{polyanion} < \text{precipitate},$$

it appears to be an indicator of the degree of polymerization. One may note that a Raman peak at ~640 cm^{-1} was observed in similarly prepared gels in work by Chemseddine et al. *(667-8)*. They assigned this feature to W-O-W bridges formed during the polycondensation process *(1365, 2924)*.

Ohtsuka et al. *(2585)* also studied IR absorption via reflectance of p-polarized light for films with thicknesses up to 142 nm. Figure 5.2 shows two absorption bands: a strong and broad feature

around ~3280 cm^{-1} due to O-H stretching in H_2O, and a narrow band at ~3780 cm^{-1} tentatively assigned to stretching vibrations of O-H bonded to W atoms. The analogy with data for evaporated films (Fig. 3.9) is good.

Anodization of W plates and of 200-nm-thick W films made by non-reactive sputtering was conducted at $1 < U_a < 2$ V in 0.5 M H_2SO_4 by Machida and Enyo *(2144)*. XRD indicated an orthorhombic $WO_3 \cdot 2H_2O$ structure. The film growth rate is very low for potentiostatic anodization at U_a being of the order of a few volts, as obvious from the data above, but it is possible to enhance the rate by potentiodynamic cycling even at $|U_a| < 1$V *(560, 564, 1991, 2895, 3778)*. Such films are crystalline *(2895)*.

Anodization has been reported for galvanostatic conditions, specifically for W sheet and rod material in 0.01 to 1 N H_3PO_4, H_2SO_4, HNO_3, and $HClO_4$ *(928-32, 934, 1256, 2655, 2694, 3278, 3296, 3518)*. Detailed studies were conducted for anodization at 8 mA/cm^2 in 1 N HNO_3 at 25°C and in 1 N H_2SO_4 at 50 and 70°C. The anodic charging depended on temperature, and at 25 and 50°C the electrode potential reached ~80 V after a few minutes and subsequently remained at that level; at 70°C the potential went through a peak after ~1 minute and then dropped gradually to ~20 V after 10 minutes. In any case, the film thickness increased monotonically with time. The anodizing temperature was of crucial importance for the film structure (as seen from XRD) and for the film morphology (as seen from SEM). At 25 and 50°C the films were mainly of WO_3, and at 70°C they were mainly of $WO_3 \cdot H_2O$. Some admixture of $WO_3 \cdot 2H_2O$ was found irrespective of temperature. Treatment of films, made by galvanostatic anodization, at $\tau_a \approx 350$°C in Ar led to the evolution of a highly heterogeneous structure apparently based on a monoclinic atomic arrangement *(3296)*. Crystallization by *e*-beam irradiation was reported by Aladjem et al. *(52)*. Electrical and mechanical breakdown phenomena have been studied in galvanostatically produced films *(937-8)*. Anodization in acetic acid was discussed by Arora and Kelly *(153-4)*.

The anodization reported above used acid electrolytes. However, it is possible to anodize potentiostatically also in nitrate melts, and work by Sabbatini et al. *(2961)* and Yurkinskii et al. *(3773-7)* showed good results for anodization of W sheet and thin films in $NaNO_3$, KNO_3, $NaNO_3 + KNO_3$, $LiNO_3 + NaNO_3 + KNO_3$, and $NaNO_3 + KNO_3 + Cd(NO_3)_2$ at 5 to 30 V and 150 to 350°C for 10 to 30 minutes. The films made in $LiNO_3 + NaNO_3 + KNO_3$ showed largest porosity. Anodization in alkaline NaOH solutions was discussed by Ortiz et al. *(2659-60)*.

5.3 Chemical Vapor Deposition and Spray Deposition

Chemical Vapor Deposition (CVD), including plasma enhanced CVD and spray deposition, have many attractive features for practical thin film manufacturing. Pyrolysis of $W(CO)_6$ on substrates at ~400°C is considered first. This technique was used extensively by Donnadieu et al. *(426, 820-1, 823-5, 959-61, 3759)*, who made depositions at atmospheric pressure and then post-treated the deposits at 500 to 600°C in oxidizing or reducing atmosphere. The film thickness increased by a factor between 1.3 and 3.4 as a result of the annealing. This CVD-based technique led to electrochromic W oxide films with different compositions. Their relative density lay in the range 0.7 to 0.8. XPS, RBS, and RHEED showed *(824, 3759)* that the oxygen nonstoichiometry and the proportion of tungsten atoms in different oxidation states depended on the preparation. Films with $z < 0$ as well as $z > 0$ could be obtained, and there was evidence for some carbon incorporation. The films made in an oxidizing environment were monoclinic crystalline, and showed some

preferred orientation with (001) planes parallel to the substrate, as seen from XRD *(820)*. Films were analyzed by Raman spectroscopy *(824)*; no peak could be detected at ~950 cm^{-1}, which is at variance with the observations for evaporated and sputter-deposited W oxide films, and hence it appears that the films made by CVD did not show clear evidence for terminal W=O bonds.

Highly disordered W oxide films, made by pyrolysis of $W(CO)_6$, were reported on by Olevskii et al. *(2630)*. Their study embraced analyses of RDFs, and a distorted WO_6 octahedron linked to two distorted WO_5 units was put forward as the most probable structural element.

Plasma enhanced chemical vapor deposition (PECVD) is a modern technique capable of yielding very high rates for deposition onto substrates that can be kept at a low temperature. This technique was developed by Benson et al. *(345, 349, 3283, 3435)* and by Rothschild and Forte *(2947)* to make tungsten-oxide-based films. The process used a decomposition of WF_6 or $W(CO)_6$ vapor together with oxygen in an electrodeless capacitive rf discharge at a pressure lower than 1 Torr. The substrates could remain below 100°C during the film formation. The deposition rate was found to depend on the preparation conditions such as gas flow, gas pressure, gas mixing ratio, and rf power. Figure 5.3 shows deposition rate as a function of rf power at otherwise constant parameters for decomposition of WF_6. The rate increases linearly with increasing power and levels off at the highest power. This levelling corresponds to full WF_6 consumption, and running the PECVD process at diminished WF_6 flow gave levelling at a proportionally lowered rate. The maximum rate is ~40 nm/s, which is about an order of magnitude larger than the highest rate reported so far for sputter deposition and also much larger than the maximum rate for evaporation. The film density decreased with increasing WF_6 flow and increasing rf power and reached a maximum at an intermediate pressure. The films made by Rothschild and Forte *(2947)* had an approximate composition $WO_{2.9}F_{0.2}$, as determined by XPS. This analysis technique revealed some carbon contamination even in films made from nominally pure WF_6. As-deposited films were heavily disordered; they crystallized upon heating in air at $\tau_a > 300$°C.

Spray deposition onto heated surfaces can often be viewed as a variety of CVD, since the spray droplets may evaporate before striking the surface. Hence it is difficult to draw a clear demarcation line between CVD and spray deposition *(396, 398, 3084, 3533)*. Spraying of aqueous solutions of metatungstic acid ($H_6W_{12}O_{39}$) was reported by Hurditch *(1583)* and by Zeller and Beyeler *(3791)*. Films with good electrochromism were obtained for $150 < \tau_s < 200$°C, whereas no electrochromism was found at $\tau_s > 320$°C. This difference was connected with a loss of water, as seen from IR spectroscopy *(1583)*. A DSC measurement was reported for a film made at $\tau_s =$ 200°C *(3791)*; the spectrum was rather complex in the range between 200 and 500°C with clear evidence for both endothermic and exothermic peaks. An exothermic feature between 320 and 400°C indicated that crystallization took place around 350°C. Figure 5.4 illustrates an RDF determined by use of X-ray scattering from a film made at $\tau_s = 200$°C; it forms a counterpart to Figs. 3.5(a) and 4.4 for evaporated and sputter-deposited W oxide films, respectively. The peaks at ~0.2 and ~0.4 nm are consistent with the earlier data, but the peaks at distances larger than 0.5 nm look very different, and in particular a strong peak at 0.61 nm is apparent only in the spray-deposited film. Clearly the spray-deposited film is composed of WO_6 octahedra with an arrangement that is very different than the one in evaporated and sputtered films, but the actural structural elements behind the RDF in Fig. 5.4 are not known.

Spray deposition, using solutions of WCl_6 dissolved in ethanol or N,N-dimethylformamide, was studied by Craigen et al. *(781)* and others *(1802, 3793, 3795, 3812)*. Spraying took place in air onto substrates heated to $200 < \tau_s < 500$°C. The W oxide films thus formed showed

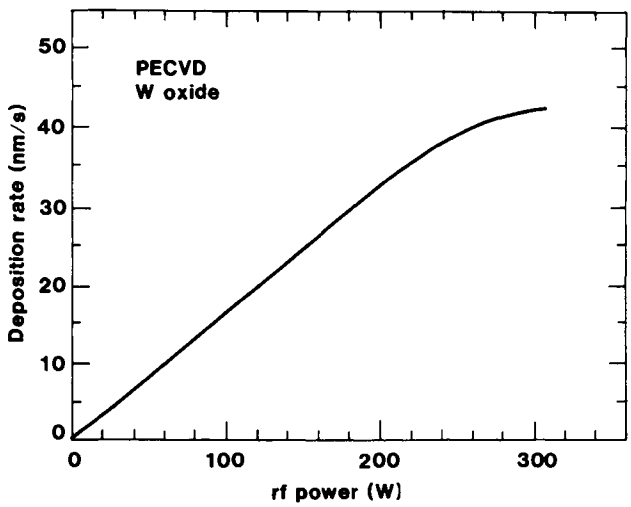

Fig. 5.3 Film deposition rate vs. rf power for PECVD with $WF_6 + O_2$. The curve indicates a trend based on about ten individual data points. From Benson and Svensson *(345)*.

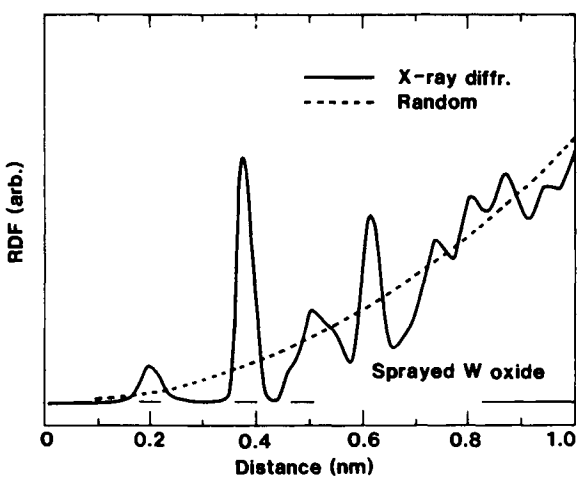

Fig. 5.4 Radial distribution function (RDF) for a W oxide film, made by spray deposition, as obtained from X-ray scattering. Dotted curve corresponds to an RDF in the absence of any long-range order. From Zeller and Beyeler *(3791)*.

electrochromism. XPS data gave evidence for some Cl contamination. XRD showed that films deposited at $\tau_s \geq 300°C$ were crystalline. The crystallite size had a maximum of ~60 nm for $\tau_s \approx$ 420°C and was slightly influenced by the film thickness. The electrical resistivity varied monotonically from ~10^5 Ω cm at $\tau_s = 200°C$ to ~1 Ω cm at $\tau_s = 400°C$.

5.4 Sol-gel-based Techniques

Sol-gel-derived films can be made from colloidal solutions by dipping, spin-coating, or spraying. The colloidal oxide can be obtained through a polycondensation process either by acidification of an aqueous salt or by hydrolysis of an organometallic compound. The sol-gel technique has been surveyed several times *(490-3, 1413, 2097)*. In the most widely studied technique, used by Chemseddine et al. *(666-70)* and others *(1370, 1372, 1699, 1700, 2332, 2492)*, acidification was accomplished by passing a solution based on Na_2WO_4 or K_2WO_4 through a proton exchange resin. The ensuing solution, which underwent spontaneous polymerization, was applied to glass plates either directly as drops, by spin coating, or by spraying. After drying by heating it was possible to obtain hard coatings with good electrochromism and some optical anisotropy. Raman and EPR data were given for the solution. A detailed study of solutions for sol-gel deposition with tungsten chloroalkoxide precursors was given recently by Judeinstein et al. *(1698, 1701-2, 1704)*.

Heat treatment forms part of the film production by the sol-gel route, and it is natural to consider first thermal data obtained by DSC and TGA. Such results, taken from work by Nanba et al. *(2492)*, are plotted in Fig. 5.5 in a way that allows direct comparison with analogous results for evaporated films (cf. Fig. 3.15). The DSC spectrum for the as-deposited film displays a broad endothermic peak at ~100°C and a narrow exothermic peak at ~430°C. Consistent data were reported by Judeinstein and Livage *(1701)*. After annealing in air at 190°C for 2 h, the endothermic peak has vanished, and the exothermic feature is split into two peaks at ~350 and ~410°C. The TGA spectrum for the as-deposited film shows a ~10 % mass decrease at $\tau_a < 200°C$, whereas no corresponding effect is apparent for the annealed film. The endothermic DSC peak and the mass decrease seen in TGA indicate dehydration from an initial composition with ~1.5 H_2O molecules per W atom. The exothermic DSC peaks, and corresponding data for films annealed in vacuum for different periods of time, are consistent with transformations to hexagonal and monoclinic phases of W oxide. The dehydration and crystallization are accompanied by a densification from an initial relative density of ~0.57 to ~0.92 after 2 h at 400°C in 2 x 10^{-2} Torr.

Raman spectra have been reported by Nanba et al. *(2494)* and by Nonaka et al. *(2551)*. Figure 5.6, from the former of these studies, shows that the as-deposited film has a strong peak at ~960 cm^{-1}, which is assigned to stretching vibrations of terminal W=O bonds, and a broad peak centered at ~660 cm^{-1}. The spectrum is similar to the one for anodic oxide films prepared at a low voltage (cf. Fig. 5.1), and the peaks at ~660 cm^{-1} can be explained analogously for the two types of samples. It remains as a possibility that the sol-gel material should be regarded as composed of isopolytungstate species *(3480)*. After treatment at $\tau_a = 190°C$ for 2 h in air, the peak at ~960 cm^{-1} decreased in strength and a strong feature developed around ~700 cm^{-1}. It is interesting that the overall spectrum strongly resembles the one for W oxide films evaporated onto substrates that are not too hot (cf. Fig. 3.6). After treatment at $\tau_a = 400°C$ for 2 h in air, the Raman data indicate a crystalline structure (cf. upper curve in Fig. 3.6).

Infrared absorption spectra were also reported by Nanba et al. *(2492)*. Figure 5.7 shows data that correspond to those in Fig. 5.6. One observes absorption due to the tungsten-oxygen

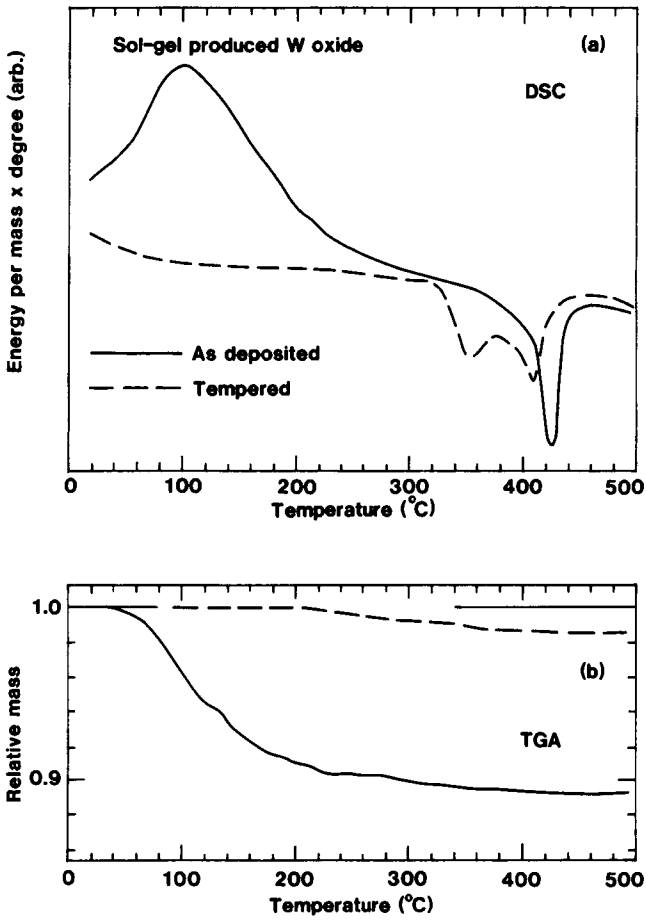

Fig. 5.5 Differential Scanning Calorimetry (DSC; part a) and Thermal Gravimetric Analysis (TGA; part b) spectra for W oxide films produced by sol-gel technology. Data were taken for as-deposited and tempered films. After Nanba et al. *(2492)*.

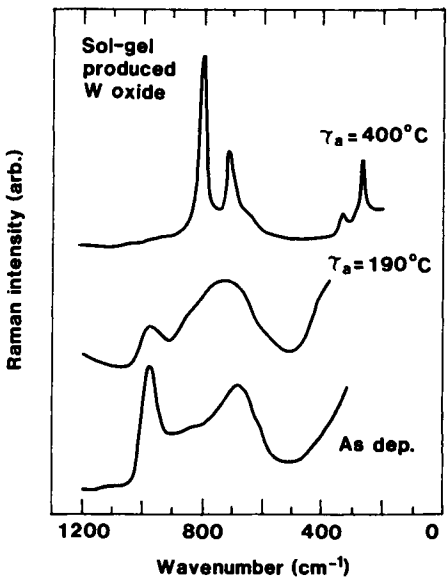

Fig. 5.6 Raman spectra for W oxide films produced by sol-gel technology. Data are shown for an as-deposited film and after annealing at the shown temperature τ_a. From Nanba et al. *(2492)*.

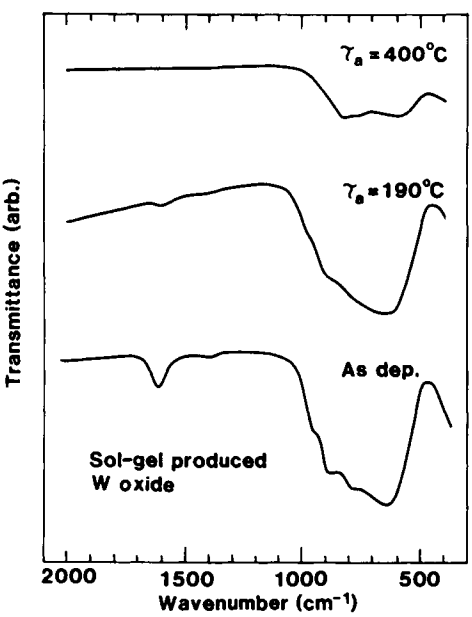

Fig. 5.7 Infrared transmittance spectra for W oxide films produced by sol-gel technology. Data are shown for an as-deposited film and after annealing at the shown temperature τ_a. From Nanba et al. *(2492)*.

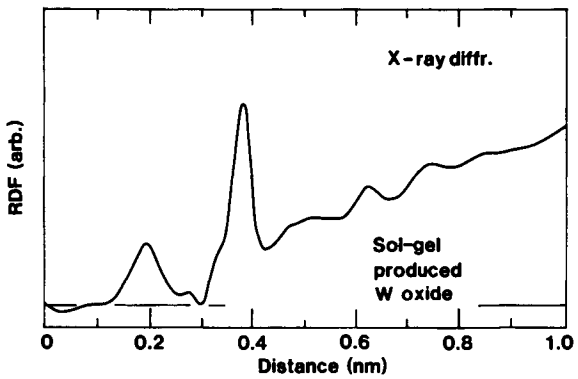

Fig. 5.8 Radial distribution function (RDF) for a W oxide film produced by sol-gel technology. From Nanba et al. *(2492)*.

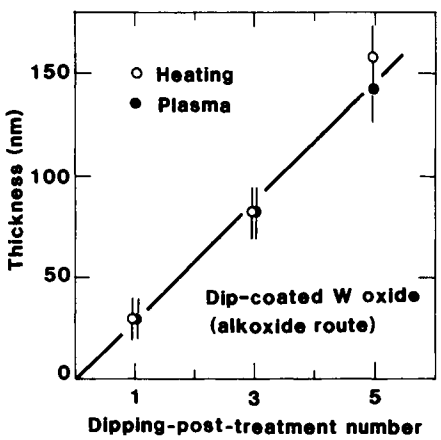

Fig. 5.9 Film thickness vs. number of dipping/post-treatment cycles for W oxide films made by dip coating. Open and filled symbols denote post-treatment by heating and by oxygen rf plasma, respectively. From Unuma et al. *(3490)*.

framework at 600 to 900 cm^{-1} (cf. upper curve in Fig. 3.9) and a pronounced peak at ~1600 cm^{-1}. The latter feature is strongly diminished at τ_a = 190°C and is not detectable at τ_a = 400°C. The IR absorption can be understood on the premise that the sol-gel-produced samples are hydrated rather than hydroxylated. Effects of "interlayered" and "coordinated" water molecules were seen in dielectric spectroscopy by Gacoin et al. *(1127)*.

X-ray scattering yielded structural information that was displayed as RDFs. Figure 5.8, again from Nanba et al. *(2492)*, shows data plotted in full analogy with those for an *e*-beam evaporated film in Fig. 3.5(a). The two sets of data are strikingly similar, and hence the basic structural features discussed for evaporated films seem to be applicable also to the sol-gel-produced W oxide. RDFs were also obtained for annealed films.

The results of the different structural characterization techniques lead to a model for initial film evolution in which polymerization takes place through a polycondensation process. Heat-treatment leads to dehydration, cluster growth, and atomic rearrangements such as the increase of bridging oxygens, transformations of the network from edge-sharing into corner-sharing octahedra, and growth of three-dimensional networks. The ensuing crystals can be of a hexagonal, monoclinic, or orthorhombic character.

Dip coating, using a solution of tungsten hexaethoxide [$W(OC_2H_5)_6$] or tungsten oxo-tetra butoxide, has been applied successfully by Unuma et al. *(3490)* and Bell et al. *(319, 1307)*, respectively. In the former technique, the W compound was dissolved in a mixture of butanol and acetylacetonate at elevated temperature. A substrate was dipped into this solution and, after a meniscus had settled, the substrate was withdrawn at a constant rate of the order of ~10 mm s^{-1}. The layer was then dried at room temperature for 1 h to vaporize the solvent. The tungsten hexaethoxide thus formed was decomposed either by heating at 350°C for 1 h or by oxygen rf plasma treatment at ~200°C for 1 h. The film thickness was ~30 nm after one dipping. In general, the thickness d' per withdrawal obeys *(490, 3077)*

$$d' \propto (v_s \eta_s)^r, \tag{5.1}$$

where v_s is the withdrawal speed and η_s is the solution viscosity. The exponent r is 2/3 for low speed and viscosity, which are the usual conditions for thin film deposition, whereas r is 1/2 for high speed and viscosity. A somewhat different relation for d' was given in *(3732)*. As illustrated in Fig. 5.9, thicker layers could be built up by repeated dipping/post-treatment cycles in which case each dipping added ~30 nm. The as-deposited films were amorphous, as judged from XRD. Heating to 350°C for 6 h, or to a higher temperature for a shorter time, led to crystallization. A corresponding densification by a factor as large as ~1.7 was reported in similar work by Lynam et al. *(2124)*.

Spin coating, using one of several starting solutions and followed by heat treatment, can give electrochromic W oxide films. One possibility is to use a solution of hexaphenoxy-tungsten, i.e., $W(OC_6H_5)_6$, in toluene and heating to more than 150°C *(3699)*. Treatment at a temperature of above 400°C led to crystallization. The films made by this route had a somewhat brownish color due to organic residues *(3707)*. Alkoxide technology--using $W(OC_2H_5)_6$, $WO(OC_2H_5)_4$, or $WO_2(OC_2H_5)_2$ in ethanol, or suspensions of the polymer $[WO_2(OC_2H_5)_2]_\infty$ as the starting solution--has been studied recently by several groups *(1939-40, 1952, 2566, 2582, 3340, 3692, 3715)*. By spinning at 2000 to 4000 rpm one could get a 20 to 30-nm-thick film with a relative density of ~0.72. Thicker layers could be made by repeating this deposition sequence. Figure 5.10

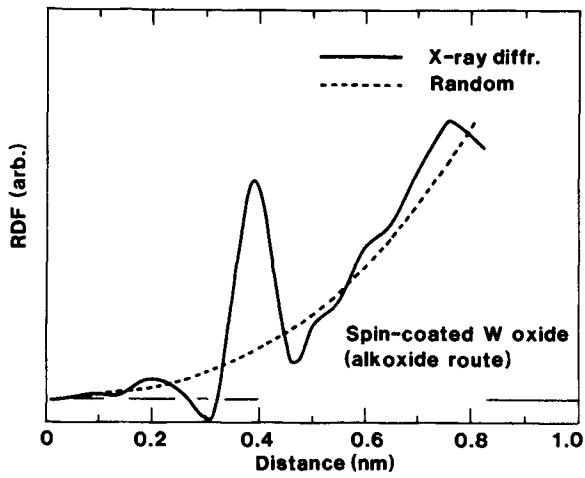

Fig. 5.10 Radial distribution function (RDF) for a W oxide film, made by spin-coating via the alkoxide route, as obtained from X-ray scattering. Dotted curve corresponds to an RDF in the absence of any long-range order. From Kukuyev et al. *(1952)*.

shows a RDF determined by Kukuyev et al. *(1952)*. From a comparison with RDFs for films made by evaporation (Fig. 3.5), sputter-deposition (Fig. 4.4), and spray-deposition (Fig. 5.4), it appears that the alkoxide route leads to films with larger variation in W-W and W-O bond lengths than any of the other techniques. Tungsten oxide films made by sol-gel techniques can contain as much as 10 % carbon *(319, 787)*, which is clearly of importance for the structure.

Several other starting solutions have been used successfully for sol-gel deposition of W oxide films. Thus Kudo et al. *(1942, 1946-7, 2622)* and Itoh et al. *(1645a)* used polytungstic acids, whose atomic arrangement is reminiscent of hexagonal or pyrochlore W oxide *(1816, 1948, 2605, 3467)*. Habib et al. *(1370, 1372-3, 1377)* found that WCl_6 in 2-propanol is convenient for making coatings on glass. Such films can be employed without further processing. However, a complicating fact is that WCl_6 must be handled under a controlled atmosphere. Still another option, discussed by Mance et al. *(2170)*, is based on xylene/2-propanol solutions of $[n\text{-}(C_8H_{17})_2NH_2]_2[W_4O_{13}]$. Spin-coating was followed by heat treatment at 500 to 600°C.

5.5 Miscellaneous Techniques

Thermal decomposition of oxalatotungstate compounds, specifically $K_6[W_4O_8(C_2O_4)_5] \cdot 4H_2O$, could give non-stoichiometric W-oxide-based films as discussed by Baba, Tada et al. *(199, 200, 204-5, 1117, 1204, 3313, 3317, 3748)*. The starting chemical was synthesized by electrolytic reduction of a tungstate solution in the presence of oxalate, followed by precipitation. As-deposited films were X-ray amorphous and crystallized upon heating at $\tau_a > 300$°C. The initial density was 3.3 g/cm^3. Some carbon and potassium were incorporated in the films, particularly before annealing had taken place. Infrared absorption spectra showed clear evidence for C=O stretching vibrations of the oxalato groups that seemed to be coordinated to the W atoms in the films. XPS data verified that the films contained a mixture of W^{5+} and W^{6+}. Schematic representations of the film structure were given in *(1117, 3313, 3317)*.

Thermal oxidation of tungsten has been studied in considerable detail with regard to isothermal oxidation *(1875)* and laser-induced oxidation *(1301)*. Oxidation offers a simple way to make electrochromic coatings backed by metal *(2876)*. Heating in air at ~750°C for 1/2 h gave ~25-μm-thick WO_3 layers with triclinic crystalline structure. Infrared absorption spectroscopy showed that these layers were essentially anhydrous. Their electrochromic properties were reported to be similar to those for films made by anodization or evaporation. Tungsten oxide surfaces oxidized in air or oxygen were also studied in *(2046, 2760-3, 2962, 3223, 3295, 3606)*.

Plasma spraying is a technique capable of extremely high deposition rates. In work by Ladouceur et al. *(1993)*, WO_3 powder with sizes up to 125 μm was injected into an Ar + He plasma and sprayed onto metal foils. Most of the particles melted during the spraying and formed a sponge-like deposit. TGA showed that different oxygen deficiencies with $z \leq 0.03$ were obtained depending on spraying conditions.

Zeolite-encapsulation of W oxide is a new technique explored by Ozin et al. *(2683)*. Essentially, a volatile hexacarbonyltungsten compound was used as a precursor in the synthesis of a highly organized assembly of W oxide encapsulated in the 1.3-nm-supercages found in zeolite Y.

This Page Intentionally Left Blank

Chapter 6

TUNGSTEN OXIDE FILMS: ION INTERCALATION/DEINTERCALATION STUDIED BY ELECTROCHEMICAL TECHNIQUES

There is a wealth of information concerning electrochemical characterization of W oxide films. An introductory section (6.1) covers reactions for ion intercalation/deintercalation and states some basic facts for electrochemical measurement technology. Diffusion constants for mobile ions in the W oxide framework are discussed next (6.2). Then follow a series of sections wherein the essential electrochemical features are presented from the perspective of the experimental technique, specifically, electromotive force measurements (6.3), chronoamperometry for the kinetics of ion intercalation/deintercalation (6.4), cyclic voltammetry (6.5), impedance spectroscopy (6.6), beam deflectometry (6.7), and microbalance measurements (6.8).

6.1 Ion Intercalation Reactions and Electrochemical Analysis: Some Introductory Remarks

Intercalation compounds can be formed through the uptake or exchange of guest molecules, atoms, or ions by host lattices having suitable structures. These processes are well known examples of solid state reactions that can occur at low temperatures. The books edited by Mandelcorn *(2172)* and by Whittingham and Jacobson *(3622a)* may serve as standard texts for intercalation phenomena. The hosts can be of different types, including framework lattices and layer structures. The guest species can also show a large variety, but the types of interest for electrochromism are almost exclusively H^+ (protons) and the alkali ions Li^+, Na^+, K^+, ... These mobile ions can be coordinated to water molecules. Among the possible reaction mechanisms, the pertinent ones for electrochromism are related to host lattices with some electronic conductivity, for which an effective lattice charge can be accomplished by the intercalation. Thus the intercalation proceeds under synchronous uptake of ions and electrons into the solid. From a chemical point of view, the intercalation process can be considered as a topotactic redox reaction by electron and ion transfer *(1366, 3061)*. The reaction is reversible, and the host lattice retains its basic structural integrity during the course of forward and backward reaction. Anion intercalation is unfavorable under most conditions, which can be understood from steric and energetic arguments *(3061)*. Some aspects of the ion intercalation compounds are similar to those of the chlathrates *(2171)* A brief overview over intercalation chemistry, with a view to electrochromism and WO_3, has been given by Haas and Goldner *(1369)*. For stoichiometric tungsten oxide, the intercalation process described above can

be written

$$WO_3 + xM^+ + xe^- \leftrightarrow M_xWO_3, \tag{6.1}$$

with $M^+ = H^+, Li^+, Na^+, K^+, \ldots$ and e^- denoting electrons.

In an electrochromic thin film device, the ions are inserted from an ion containing medium usually in liquid or solid form (i.e., from an electrolyte or via an ion conductor). The normal technique uses an applied electric field to intercalate and deintercalate the ions. It is immediately clear that reaction 6.1 above cannot give a fully correct picture of the relevant processes. Indeed, the W oxide films--as discussed earlier--usually contain hydroxyl groups and incorporated water molecules and are substoichiometric with regard to the tungsten-oxygen framework. Furthermore, the intercalated ions can be associated with water molecules. The pertinent reaction for proton intercalation/deintercalation can then be written

$$WO_{3-z-q}(OH)_q \cdot pH_2O + xH^+ \cdot rH_2O + xe^- \leftrightarrow WO_{3-z-q-x}(OH)_{q+x} \cdot (p + xr)H_2O, \tag{6.2}$$

where it is presumed that the added protons are bound in hydroxyl groups. This representation is impractical in many cases, and, neglecting non-stoichiometry and hydration,

$$WO_{3-q}(OH)_q + xH^+ + xe^- \leftrightarrow WO_{3-q-x}(OH)_{q+x} \tag{6.3}$$

is obtained. The pertinent magnitude of q is in principle measurable by XPS. Such determinations have been made for some electrochromic oxides but, it seems, not yet for W oxide.

Intercalation/deintercalation of Li^+ is expected to proceed in analogy with reactions 6.2 and 6.3, but again a detailed description cannot be given. Since the virgin film is normally hydrous, exchange reactions between H^+ and Li^+ are of importance. A simplistic representation, however, can be stated as

$$WO_3 + xLi^+ + xe^- \leftrightarrow Li_xWO_3\,. \tag{6.4}$$

Reactions analogous to those in 6.3 and 6.4 will be discussed for several electrochromic oxides in Part Two of this book.

With all the uncertainties and unspecificity veiling the intercalation/deintercalation reactions, one may wonder whether it is vain to look for a reasonably certain and specific model for the electrochromism. In fact, such a model *is* possible, and this is so because the optical properties are governed largely by the insertion/extraction of electrons, i.e., it is the xe^- term in the reactions that is most important. The ion transport, with all its complexity, serves for charge balancing only. However, one should not be misled into believing that the ionic transport is unimportant; indeed, it usually determines the speed by which the optical properties can be modulated, and interactions between the mobile ions and the immobile oxide framework or layer are important for cycling durability, etc.

Several methods are available for intercalating (but not deintercalating) ions, apart from the electrochemical alternative mentioned above. Thus one can use photoinjection of H^+, that is possible up to high ion densities. The detailed mechanism seems to be that organic molecules, absorbed on the W oxide surface, are injected under the action of ultraviolet irradiation as discussed by

Gavrilyuk et al. *(1147)*. Data on photoinjection of H^+ are available for films exposed to methanol vapor *(1146-7, 1150, 1152)*, ethanol solution *(2476)*, and formic acid solution *(927)*. Furthermore, H^+ can be included by reactive sputtering in the presence of hydrogen gas *(884, 1306)* and by exposure to atomic hydrogen (from a HCl + Zn reaction) *(3645)* or molecular hydrogen (in connection with catalytic decomposition) *(1168, 1640, 1845-6, 3194)*. For Li^+, Na^+, etc., it is possible to employ vacuum codeposition or sequential deposition to prepare ion intercalated films. Thus coevaporation of Na and WO_3 from separate sources has been reported *(1322-3)* as well as rf sputtering from a $WO_3 + Li_2CO_3$ or $WO_3 + Li_2O$ composite target in Ar or in Ar + O_2 *(1499, 1824, 2147-8)*. Still another possibility is to deposit a Li_3N film on top of the W oxide; the Li_3N is dissociated and Li enters to a final approximate composition of $Li_{0.4}WO_3$ *(2608)*. Such "dry lithiation" is possible also by overcoating a W oxide film with Li atoms released by heating $LiNbO_3$ in vacuum *(162, 165-6)*. Ion implantation of Cu and Ag was reported in *(2949)*. Charge insertion without an external source of electrons is possible by the "RCA technique" wherein the W oxide is covered with H_2SO_4 and then brought in metallic contact with a wire or foil of indium or tin *(782)*. A supplementary and more specific discussion of the various ways to incorporate ions and electrons in W oxide will be given in Sec. 9.3 below.

Electrochemical analysis is highly convenient for intercalation compounds, especially when intercalation and deintercalation are accomplished by contact with an adjacent electrolyte. Such characterization techniques are very well established and have an immediate link to electrochromic device performance. Electrochemical technology is introduced in several books *(268, 1130, 1304, 2138)*. In most cases of present interest, the sample under study is a W oxide film with an electrically conducting backing; in studies of electrochromism it is normal to use a layer of doped SnO_2 or In_2O_3 on glass as a substrate for the film (cf. Ch. 25 for a detailed discussion). This sample is in contact with a--most often liquid--electrolyte, with 1 M $H_2SO_4 + H_2O$ or 1 M $LiClO_4$ + PC (denoting propylene carbonate by PC) as typical examples. Voltages are applied in ac or dc mode, between the sample--called the "*working electrode*"--and a *counter electrode* such a piece of Pt foil also immersed in the electrolyte. Reliable voltage measurements can be done by using an auxiliary, ideally nonpolarising, *reference electrode*. It is customary to have for this purpose electrodes based on Hg/Hg_2Cl_2 (saturated Calomel electrode, denoted SCE), Hg/Hg_2SO_4 (saturated sulfate electrode, denoted SSE), Ag/AgCl, $Ag/AgClO_4$, or Li metal. The potentials are normalized, through the Electrochemical Series, to the reference hydrogen electrode, RHE.

It will be shown later that for disordered W oxide, ion intercalation is associated with optical coloration whereas deintercalation is associated with bleaching. Hence one may make the replacements intercalation → coloration and deintercalation → bleaching throughout the following chapters on W oxide.

6.2 Diffusion Constants

It is convenient to begin with a discussion of diffusion constants for ions and electrons, since their magnitudes give important clues to the subsequent electrochemical characterization. Chemical diffusion constants can be extracted by many different techniques--most commonly from electrochemical ones such as chronoamperometry, chronocoulometry, chronopotentiometry, cyclic voltammetry, and ac impedance measurements *(1532-3)*. A useful discussion of different methods for measuring diffusion constants for electrochromic layers was given by Goldner *(1217)*. Three

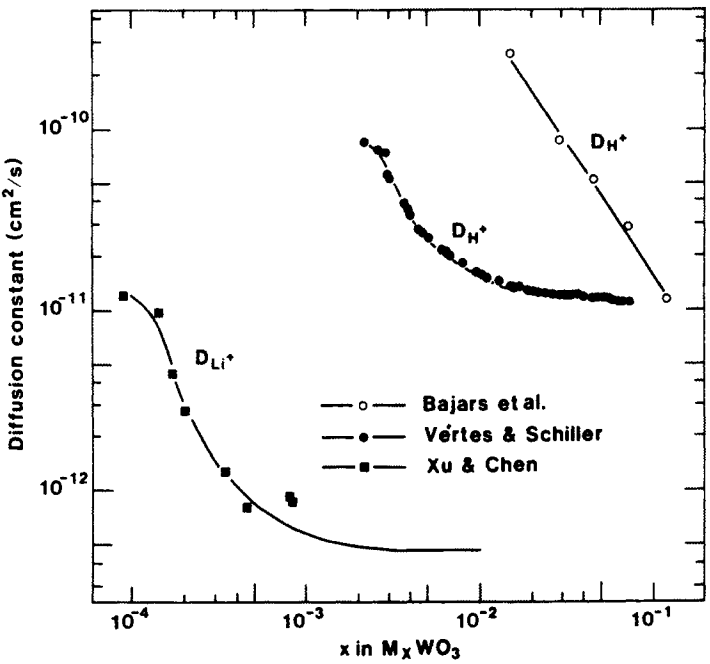

Fig. 6.1 Chemical diffusion constants D_{M+} ($M^+ = H^+, Li^+$) vs. the amount of ion intercalation, represented as x in M_xWO_3. After Bajars et al. *(239)*, Vértes and Schiller *(3530)*, and Xu and Chen *(3674)*.

of the techniques mentioned above will be described here (with the exclusion of chronocoulometry and chronopotentiometry). The usual configuration for determining a diffusion constant D_{M+} includes a W oxide film with a conducting electrode, in contact with a liquid electrolyte. Data normally are taken at room temperature. The magnitude of D_{M+} depends critically on the diffusing ionic species M^+, the character of the film (crystallinity, porosity, hydration, ...), and of the electrolyte. No detailed and systematic study redarding the dependence of D_{M+} on film structure etc. appears to have been made, and therefore the present discussion relies mainly on trends and orders of magnitude. A recent discussion of D_{M+} in the context of electrochromism was given by Whittingham *(3621)*.

Figure 6.1 shows D_{M+}, with $M^+ = H^+$ and Li^+, as obtained from three different sources. For convenience, the ion intercalated material is denoted M_xWO_3 with $10^{-4} < x < 10^{-1}$. The data by Vértes and Schiller *(3530)* refer to evaporated films in contact with 0.1 N H_2SO_4; the diffusion-controlled lateral spread of an optically absorbing region was directly measured by microdensitometry. Results by Bajars et al. *(239)* were obtained by ac impedance measurements on a system similar to the previous one. The diffusion constants reported by Xu and Chen *(3674)* were taken on sol-gel-derived films in contact with 0.5 M $LiClO_4$ + PC by use of chronopotentiometry. Two significant features illustrated in Fig. 6.1 are that D_{H+} is larger than D_{Li+} by roughly an order of magnitude, and that the diffusion constants depend on the ion intercalation with a rapid order-of-magnitude drop of D_{M+} at low x followed by a more stable level for D_{M+} at larger x. A drop of D_{Li+} with increasing ion intercalation was also noted by Zhang and Goto *(3799)*. The fact that D_{H+} is much larger than D_{Li+} can be seen as a natural consequence of the difference in ionic diameter, although complications due to hydration spheres should not be forgotten. The decrease of D_{M+} at large ion contents has been described in terms of blocking of channels for easy ion transport at large x. A detailed fit of the experimental D_{H+}s was accomplished by Vértes and Schiller *(3530)*, who used an effective-medium theory applied to a system with channels for "fast" and "slow" diffusion. Similar notions were forwarded by Galyamov and Roginskaya *(1134)*, who associated the "fast" and "slow" steps with diffusion at the boundaries and in the interiors of grains, respectively. The possibility of employing modern concepts such as diffusion on fractal systems *(1447)* should be noted.

The dependence of the diffusion constant--specifically D_{Li+}--on temperature, thin film deposition conditions, and electrolyte composition is illustrated in Fig. 6.2, which is reproduced from work by Nagai et al. *(1725, 2464-5, 2467)*. The films were produced by *e*-beam evaporation, with some gas present in the chamber, and tested in an electrolyte of 1 M $LiClO_4$ in γ-butyrolactone or PC. A certain amount of water was added to the electrolyte. The gas composition was not stated, but the film density was consistent with the presence of N_2 (cf. Fig. 3.2a). Figure 6.2(a) refers to 1000 ppm of water and $2 \times 10^{-5} < p_{N2} < 5 \times 10^{-4}$ Torr. An increased pressure, with ensuing enhanced porosity, is seen to increase D_{Li+} by as much as two orders of magnitude. The addition of water to the electrolyte, so that H^+ diffusion is possible together with Li^+ diffusion, also increases the diffusion constant, as apparent from Fig. 6.2(b) pertaining to films made at 5×10^{-5} Torr. The temperature dependence of D_{Li+} is elucidated in Fig. 6.2; the diffusion is thermally activated, and Arrhenius plots gave an activation energy of ~0.5 eV, except for the most porous film which had an activation energy of ~0.2 eV. It is clear that an addition of water to the electrolyte merely enhances the diffusion constant, whereas porosity also has an effect on the diffusion mechanism. The temperature dependence of D_{H+} was studied by Randin and Viennet *(2845)*. The diffusion was themally activated with an activation energy that increased from ~0.25 eV for a

Table 6.1 Diffusion constant of ionic species M^+ for W oxide films prepared by several different techniques.

Technique	Ion (M^+)	D_{M+} (cm^2/s)	Reference
Evaporation	H^+	10^{-10} - 2.5×10^{-7}	*431, 1046, 1048, 1418, 1503, 1544, 1912, 2368, 2845, 2875, 2879*
	Li^+	1.5×10^{-12} - 5×10^{-9}	*295-6, 419, 1214, 1504, 1726, 2148 2368, 2393, 2463-5, 3313*
	Na^+	6×10^{-20} - 1.8×10^{-16}	*1310, 1316, 3674*
Sputtering	Li^+	~10^{-11}	*813, 3313, 3799*
Anodization	H^+	5×10^{-8}	*431, 2879*
PECVD	Li^+	~10^{-11}	*349*
Sol-gel	Li^+	5×10^{-12} - 3×10^{-11}	*1370, 1372, 1943*
Therm. decomp.[a]	Li^+	3×10^{-10}	*3312*

[a] Thermal decomposition of oxalatotungstate compound.

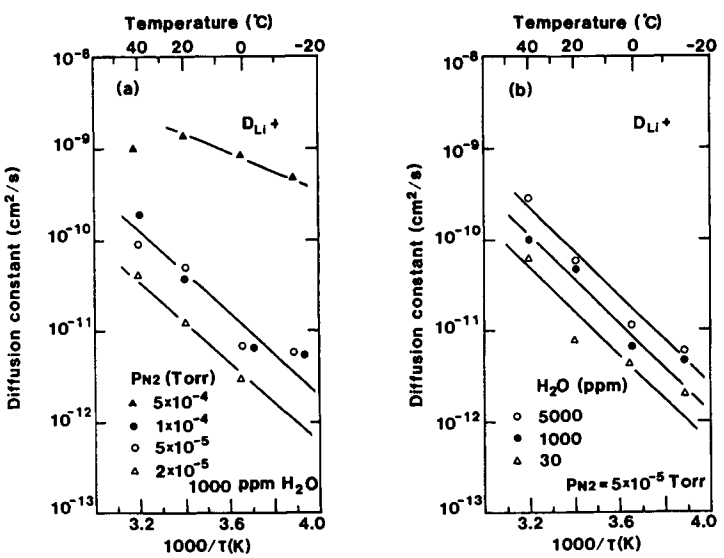

Fig. 6.2 Chemical diffusion constants vs. inverse temperature τ for (predominantly) lithium diffusion in W oxide films. Data are given for the shown values of nitrogen pressure p_{N2} and H_2O content. From Nagai et al. *(1725, 2464-5, 2467)*.

heavily disordered as-evaporated film to ~0.47 eV for a crystalline film treated at τ_a = 400°C for 1 n. Data on D_{Li+} for an aprotic polymer electrolyte was reported by Baudry et al. *(296)* for the temperature range 25 to 100°C.

Additional data on diffusion constants, as obtained from different electrochemical measurements, have been reported in several places. Sometimes the pertinent x values were not stated, which makes it impossible to perform anything other than coarse order-of-magnitude comparisons. Table 6.1 lists D_{M+} for various film preparation techniques and ionic species. Even if the brackets for the diffusion constants are very wide, one may safely conclude that

$$D_{H+} >> D_{Li+} >> D_{Na+}.$$

There are several investigations on the role of film preparation parameters for the magnitude of the diffusion constant. Thus it was found by Zhang and Goto *(3799)* that an increased oxygen deficiency led to enhanced D_{Li+}. Crystallization of evaporated films was studied by Randin and Viennet *(2845)*, who reported that D_{H+} went from an initial ~5 x 10^{-10} cm²/s to ~2 x 10^{-11} cm²/s after annealing at 350°C for 1 h and to ~10^{-11} cm²/s after annealing at 400°C for 1 h. A similar change of D_{H+} was seen by Bohnke and Bohnke *(418)* in heat-treated films. Crystallization induced by storing an evaporated film for 1 year in air made D_{H+} shrink from 1.8 x 10^{-10} cm²/s to 2 x 10^{-11} cm²/s *(1503)*. Rf sputtered films, that were crystalline in as-deposited state, had $D_{H+} \approx 10^{-11}$ cm²/s *(1503)* and $D_{Li+} \approx 2 \times 10^{-12}$ *(1320)*. The role of crystallization was studied also in some recent work by Judeinstein and Livage *(1702)*. In the case of crystalline orthorhombic W oxide they found $D_{Li+} \approx 10^{-12}$ cm²/s at x = 0.1 and $D_{Li+} \approx 3 \times 10^{-12}$ cm²/s at x = 0.3. A disordered hydrous film with the nominal composition $WO_3 \cdot 2H_2O$ yielded $D_{Li+} \approx 9 \times 10^{-11}$ cm²/s at x = 0.08. Field-dependent diffusion constants were discussed in *(1316)*. One observes a general tendency that crystallization causes a drop of the diffusion constant by roughly an order of magnitude. The diffusion constants given above are much larger than their counterparts for crystalline bulk materials *(2538, 3621)*.

It is possible to increase the diffusion constant over that of pure crystalline W oxide by adding an alloying element that stabilizes an open hexagonal structure characterized by hexagonal tunnels (cf. Fig. 2.5). Work along these lines was reported for K_xWO_3 by Joo et al. *(1684-7)* and others *(728-9, 732, 1464, 3709-10)* and for Cs_xWO_3 by Zhong and Colbow *(3807)*. Most of the films were made by single-source evaporation followed by annealing at ~400°C. This post-treatment gave transparent films, presumably as a result of oxygen uptake *(1254-5)*. It was discovered that D_{H+} and D_{Li+} could be enhanced by one to three orders of magnitude as a consequence of the hexagonal configuration and the orientation of the tunnels. Zhong and Colbow *(3808)* prepared pyrochlore-type films by evaporating a starting material that could be represented as $(CsO)_{0.44}W_2O_6$. D_{H+} was ~7 x 10^{-9} cm²/s irrespective of hydrogen incorporation. These crystalline films exhibit diffusion constants comparable with those in typical W oxide films with very disordered structures.

Another interesting material, capable of easy Li^+ diffusion, is LiW_3O_9F which is built up by a peculiar packing of hexagonal tungsten bronze layers *(654-5, 871, 2421)*. Crystalline films of $W_9Nb_8O_{47}$, having pentagonal tunnels *(1603-4)*, were studied by Lemons et al. *(2042)* in an attempt to obtain a large D_{H+}. Films of BaO + WO_3, in principle capable of having pentagonal tunnels, were checked for electrochromism by Molnar et al. *(2382)*; the Ba additions were found to inhibit the electrochromism, though.

As pointed out before, ion intercalation is accompanied by electron insertion, and it is of

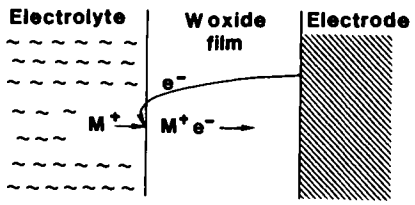

Fig. 6.3 Schematic model for transport of ions M^+ and electrons e^- in a W oxide film between an electrolyte and a conducting electrode.

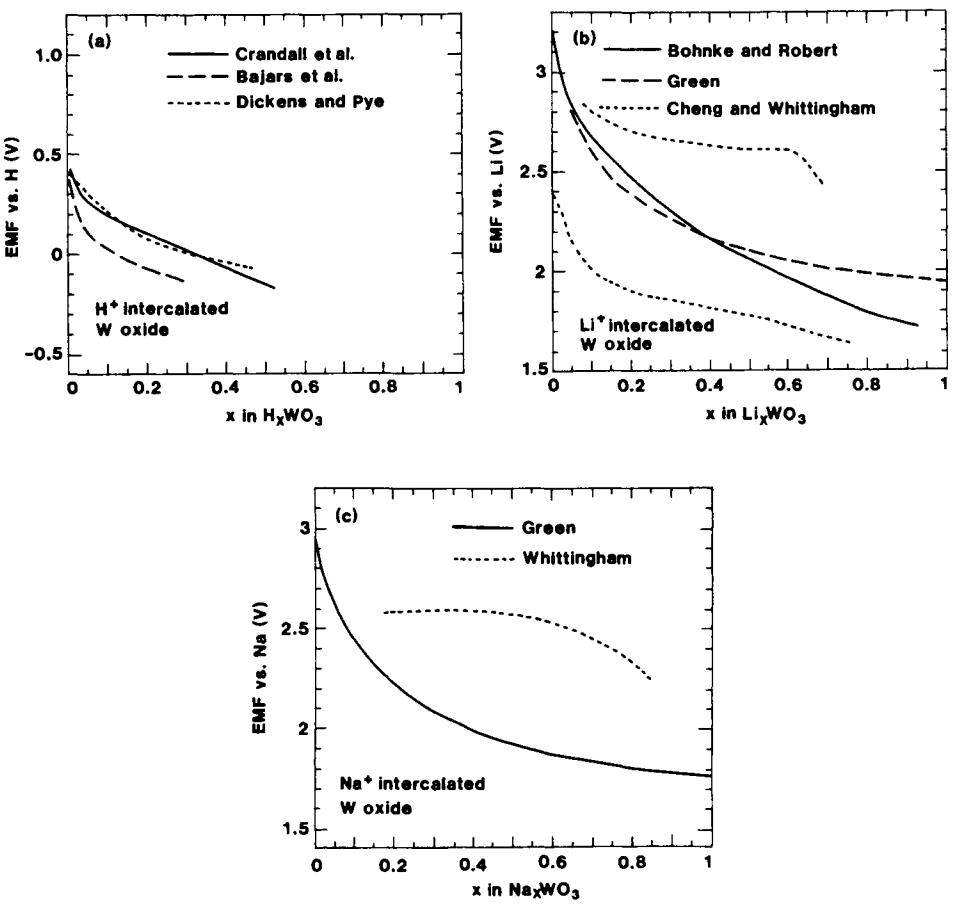

Fig. 6.4 Normalized EMF vs. amount of ion intercalation, represented as x in M_xWO_3, for hydrogen (a), lithium (b), and sodium (c) in W oxide films (solid and dashed curves) and bulk samples (dotted curves). After Bajars et al. *(239)*, Bohnke and Robert *(432)*, Cheng and Whittingham *(678)*, Crandall et al. *(786)*, Dickens and Pye *(919)*, Green *(1309)*, and Whittingham *(3620)*.

interest to determine the diffusion coefficient D_{e^-} pertinent to the electrons. Such determinations were made by Crandall and Faughnan *(782)* and others *(2738, 3687)*, who analyzed the dynamics of electrochromic coloration under electron injection from a metallic point contact. It was found that $2.5 \times 10^{-3} < D_{e^-} < 7.5 \times 10^{-3}$ cm²/s, and that the D_{e^-}s were rather insensitive to temperature changes. Thus one concludes that

$$D_{e^-} >> D_{M^+}$$

irrespective of ionic species.

The great difference between D_{e^-} and D_{M^+} leads to the simple model for charge transport illustrated in Fig. 6.3. Transfer of M^+ ions takes place at the electrolyte/oxide interface. Electrons are then attracted from the electrode. Inside the film, the diffusion of M^+ ions manifests itself as a spreading of a plasma region from the electrolyte interface towards the electrode interface. The spreading may be even or uneven depending on the importance of large-scale pores, grain boundaries, and other extended defects. In a few studies *(2879, 3313)* it was proposed that the ions were neutralized at the electrolyte interface, and that further diffusion was by atoms, but this view has not been accepted elsewhere. In contrast with the model in Fig. 6.3, some work on ellipsometrically measured optical properties, was interpreted on the premise that the ion density changed uniformly over the film cross-section upon intercalation and deintercalation *(307, 2639, 2650)*.

6.3 Electromotive Force

When a W-oxide-based film is immersed in an electrolyte, an electromotive force (EMF) can be measured with respect to a secondary electrode. The EMF depends on the degree of ion intercalation and is conveniently given with regard to the ionic element, i.e., the voltage is measured as a function of x between electrodes of M^+ intercalated W oxide and M. The relationship is often referred to as a coulometric titration curve. EMF data were summarized by Whittingham *(3621)*. They allow, for example, a calculation of the free enthalpy of formation for M_xWO_3 compounds.

Figure 6.4 shows EMFs for $M^+ = H^+$, Li^+, Na^+ and $0 \leq x \leq 1$. Solid and dashed curves pertain to films and dotted curves to bulk samples. Part (a) shows results for heavily disordered H^+ intercalated W oxide, specifically for disordered films made by evaporation *(239, 786)* and for a bulk sample *(919)*. EMFs for bulk crystalline H_xWO_3 were given also in *(130, 913, 1660)*. The three sets of data in Fig. 6.4(a) are in good agreement and show that the EMF decreases monotonically from ~0.5 V at x = 0 to ~-0.1 V at $x \approx 0.5$. Similar results were reported for $x < 0.15$ in other work *(430-1, 1502, 2845, 2857, 2896)*. Figure 6.4(b) refers to Li^+ intercalated W oxide, which is the most extensively studied system. The solid curve is reproduced from Bohnke and Robert *(432)*, specifically their results for a thin evaporated film ion intercalated at a low voltage, and the dashed curve is taken from Green *(1309)* who studied microcrystalline sputter-deposited films. The EMF varies monotonically from ≥ 3 V at x = 0 to ≤ 2 V at x = 1. Analogous data were reported by others *(295-6, 349, 591, 1504, 1725, 1947, 2370, 2391, 2463, 2465, 2467)* for films made by evaporation, sputtering, anodization, PECVD, and sol-gel coating. The dotted curves in Fig. 6.4(b) apply to crystalline (upper curve) and heavily disordered (lower curve) bulk samples *(678)*. Results for crystalline materials were also given in *(408, 921, 2732, 3809-*

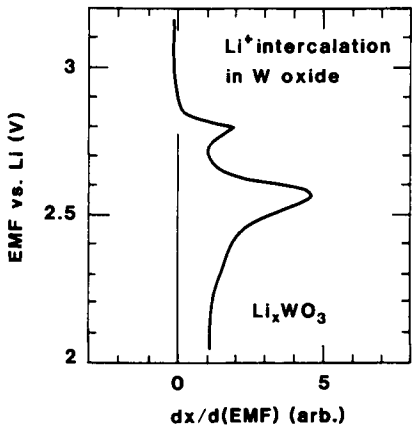

Fig. 6.5 Normalized EMF vs. dx/d(EMF) for Li^+ intercalation into W oxide (having a composition Li_xWO_3). After Zhong et al. *(3810)*.

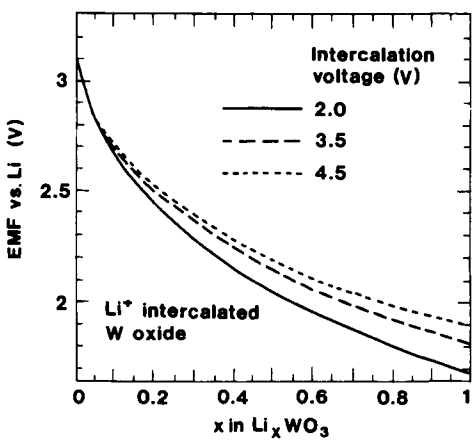

Fig. 6.6 Normalized EMF vs. lithium content, represented as x in Li_xWO_3, for a W oxide film made by evaporation. Ion intercalation was carried out at the shown voltages. Solid curve corresponds to the solid curve in Fig. 6.4(b). From Bohnke and Robert *(432)*.

10). These data lie on either side of the values for thin films.

The EMF vs. x curve of a crystalline material is rather flat for mixed phases and exhibits slopes at phase transitions. These features can be easily seen by plotting dx/d(EMF) rather than x on the abscissa. Figure 6.5, referring to Li^+ intercalation, shows that dx/d(EMF) is peaked at ~2.8 and 2.57 V; the data were taken by Zhong et al. *(3809-10)*. Comparing with Fig. 2.4 makes it clear that the peaks correspond to the monoclinic → tetragonal and tetragonal → cubic transitions, respectively. Deintercalation gave peaks at somewhat different EMFs; they can be interpreted analogously.

Figure 6.4(c) shows results for microcrystalline Na^+ intercalated W oxide films made by evaporation and sputtering *(1309-10, 1315, 1317)* as well as for crystalline Na_xWO_3 samples *(3620)*. The EMFs for the film vary from ~3 V at x = 0 to ~1.76 V at x = 1; the EMFs for the bulk Na_xWO_3 crystals are similar to those for bulk Li_xWO_3 crystals and very different from results for the films. EMF data are available also for Li^+ intercalated hexagonal films of K_xWO_3 *(1685, 1687)* and for H^+ and Li^+ intercalated hexagonal films of Cs_xWO_3 *(3807-8)*.

The monotonic variation of the EMF for M^+ intercalated W oxide as a function of x, which is apparent for the thin films reported on in Fig. 6.4, indicates that the intercalation/deintercalation reaction proceeds topotactically, i.e., without major changes in the crystal structure. The only reported exception is the EMF data for lithiated W oxide given by Mohapatra and Wagner *(2370)*. They found that the EMF was independent of x for $x > 0.4$ and interpreted this as an effect of the formation of an intermediate phase. Their findings have not been corroborated by more recent work, though. We note in this context that Cheng and Whittingham *(678)* reported that a bulk $Li_{0.67}WO_3$ compound decomposed on heating into Li_2WO_4 and a low-lithium-content phase, and it is reasonable to expect a similar disproportionation of Li_xWO_3 films with high x values upon sufficient heating.

The influence on the coulometric titration curves of various parameters has been explored, and data have been given for effects of different film thickness *(432, 2370)*, grain size *(1317)*, thin film fabrication technique *(432, 2391, 2467)*, post-deposition storage in humid air *(3737)* or electrolyte *(3516)*, electrolyte concentration *(1725, 2463, 2896)*, and voltage applied during the ion intercalation. Among these parameters, the applied voltage has been found to play a major role. Figure 6.6, reproduced from Bohnke and Robert *(432)*, shows EMF vs. x for a Li^+ intercalated disordered W oxide film made by evaporation. The curves refer to intercalation under the application of three different voltages relative to an Ag/Ag^+ reference electrode. The EMF is enhanced at high voltages, which was interpreted as an irreversible effect due to metallic Li precipitation at the electrode interface of the W oxide film. It is obvious that such a metallic film will deteriorate the electrochromism seen in transmission. Irreversible Na^+ incorporation was inferred from electrochemical measurements by Kodintsev et al. *(1864)*.

A theoretical expression for the x-dependent EMF was first derived from statistical thermodynamics by Crandall et al. *(786)*. They found that

$$\mathrm{EMF} = a + bx - \nu \frac{R_g \tau}{F_c} \ln\left(\frac{x}{1-x}\right), \tag{6.5}$$

where a, b, and ν are constants, R_g is the gas constant, and F_c is Faraday's constant. The second term in the expression is due to structural changes and the third term to system entropy. Specifically, the value of b can be related to the nearest neighbor interactions among the inserted species *(173, 430, 2896)*. An essentially identical formula was subsequently derived from a

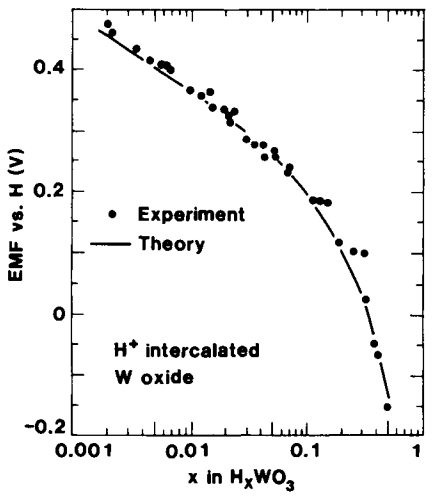

Fig. 6.7 Normalized EMF vs. hydrogen content, represented as x in H_xWO_3, for disordered W oxide films. Experimental data correspond to several samples, and the theoretical curve was obtained from Eq. 6.5 with a = 0.16 eV, b = -0.53 eV, and v = 2. From Crandall et al. *(786)*.

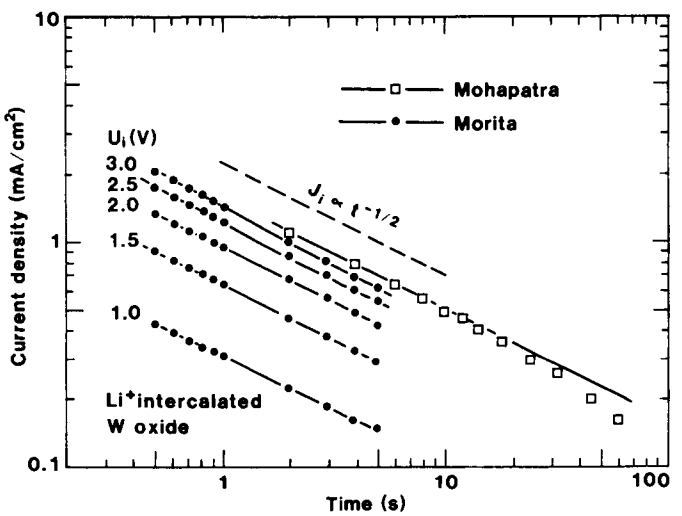

Fig. 6.8 Current density vs. time for Li^+ intercalation into evaporated W oxide films. Symbols denote experimental data for different voltages U_i, and solid lines are fits to these data. Dashed line indicates the time dependence inherent in Eq. 6.6. After Mohapatra *(2368)* and Morita *(2393)*.

somewhat more general analysis based on classical thermodynamics *(1502)*, and a similar relation can be founded on considerations of electrochemical kinetics *(2877)*. An $x^{2/3}$-dependence of the second term has been stated in some work *(1316-7)*. Figure 6.7 shows a comparison between Eq. 6.5 and experimental EMF data for an evaporated W oxide film in contact with 7.2 N H_2SO_4 *(786)*. A very good fit was obtained with a = 0.16 eV, b = -0.53 eV, and ν = 2. Analogous comparisons between theory and experiment were given in several other analyses *(430-2, 1045, 1725, 2114, 2463, 2896)*. According to Faughnan and Crandall *(1045)*, a negative value of b is a strong argument in favor of the H^+ intercalated W oxide film being homogeneous rather than of composite nature.

6.4 Chronoamperometry: Kinetics for Ion Intercalation and Deintercalation

Ion intercalation and deintercalation are not symmetric phenomena; intercalation is largely governed by the properties at the boundary between the electrolyte and the W oxide film, whereas deintercalation is mainly influenced by ion transport in the film. These two phenomena are discussed below with emphasis on the time evolution of the charge transport currents. Small samples in contact with liquid electrolytes are considered in most cases. Extensions to other experimental situations will be treated later in connection with device properties. Comprehensive discussions, mainly of proton intercalation/deintercalation, were given by Faughnan and Crandall *(1046)*, Krasnov et al. *(1913-6)*, and Vasko et al. *(3522)*. There is some recent work stressing the advantages of chronocoulometry over chronoamperometry *(780)*.

Intercalation kinetics in principle is rather complicated, and several mechanisms can limit the current. One may think of transport of ions and electrons through the bulk of the W oxide film, a barrier at the electron-injecting interface, a barrier at the ion-injecting interface, a barrier at the counter electrode in a device configuration, and charge transport in the electrolyte. In many cases it seems that the most significant factor is the barrier at the ion-injecting interface--i.e., at the boundary between the electrolyte and the W oxide film--as first discussed by Crandall and Faughnan *(783)*. The barrier can be viewed as a Helmholtz double layer *(410)*. The intercalation current J_i can be derived from the Butler-Volmer relation with due consideration of the x-dependent EMF (cf. Eq. 6.5), which has the effect of decreasing the intercalation rate. In general the time dependence $J_i(t)$ must be obtained numerically, but in an intermediate time range, and for a symmetric barrier, one obtains *(783)*

$$J_i(t) \propto t^{-1/2} \exp(U_i/R_g\tau), \tag{6.6}$$

where U_i is the voltage applied during the intercalation process. At small enough times, this formula may be replaced by a $t^{-1/4}$ dependence *(1046)*. Equation 6.6 represents the same time dependence as the one expected from a diffusion-limited process.

Figure 6.8, replotted from Mohapatra *(2368)* and Morita *(2393)*, shows the time evolution of J_i for evaporated W oxide films in contact with 1 M $LiClO_4$ + PC. The dependencies on t and U_i are in agreement with Eq. 6.6. For $t > 10$ s the data drop below the straight line fitted at $t < 10$ s; according to Mohapatra *(2368)*, this may be a real effect. One may notice that Bohnke et al. *(431, 434)* recently questioned the validity of the U_i-dependence inherent in the Crandall-Faughnan

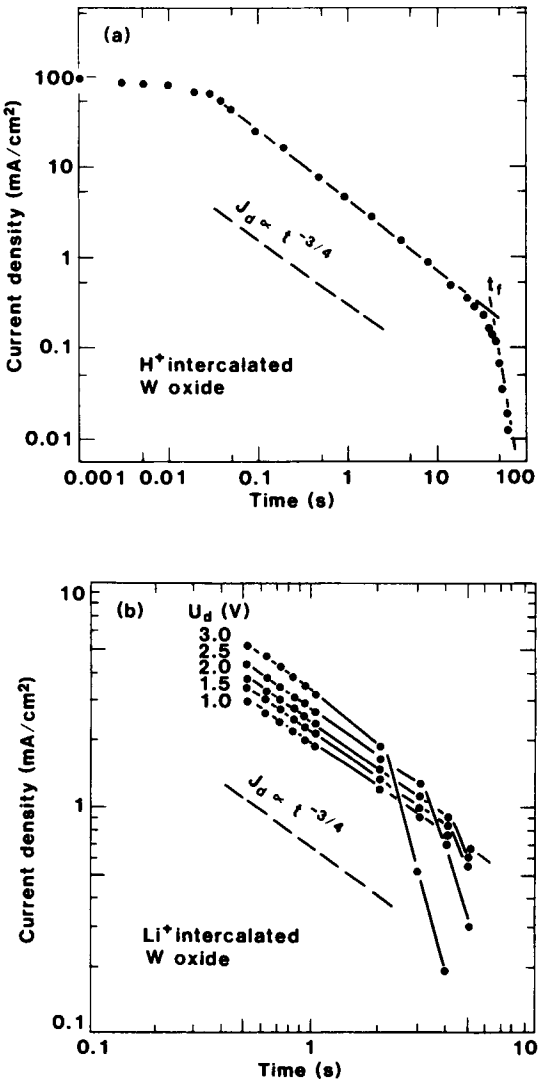

Fig. 6.9 Current density vs. time for deintercalation of H^+ (part a) and Li^+ (part b) from evaporated W oxide films. Filled circles denote experimental data (for different voltages U_d in part b), and solid curves are fits to these data. Dashed lines indicate the time dependence inherent in Eq. 6.7. Part (a) shows the construction for obtaining the time t_f. Note that the ranges for current density and time are different in parts (a) and (b). From Faughnan et al. *(1048)* and Morita *(2393)*.

theory and instead focused on the importance of ionic diffusion for species intercalated in the W oxide film.

Deintercalation kinetics is simpler to treat than intercalation kinetics because no barrier needs to be included in the analysis which, basically, is an effect of the x-dependent EMF acting in the direction of the applied voltage U_d. Since $D_{e^-} >> D_{M+}$, the deintercalation current J_d will be dominated by field-driven space-charge-limited ion flow in a region which initially lies at the interface towards the electrolyte and whose thickness increases as deintercalation progresses until a time t_f when no more (mobile) ions reside in the film. As shown by Faughnan et al. *(1048)*,

$$J_d(t) \propto D_{M+}^{1/4} U_d^{1/2} t^{-3/4} \tag{6.7}$$

is valid in an intermediate time range up to

$$t_f \propto D_{M+}^{-1} U_d^{-2} . \tag{6.8}$$

An extension of the theory to treat small times was given by Gupta and Ferreira *(1357)*. It is evident that measurements of t_f constitute a convenient way to determine D_{M+}.

Figure 6.9, taken from Faughnan, Crandall et al. *(1048)* and Morita *(2393)*, reports J_d for evaporated W oxide films in contact with H_2SO_4 and 1 M $LiClO_4$ + PC. The dependencies on t --over ~3 orders of magnitude for H^+ intercalation and ~1 order of magnitude for Li^+ intercalation-- and U_d are those expected from Eq. 6.7. In Fig. 6.9(a) the time t_f is defined as the intercept between two straight lines. Figure 6.10, reporting data for evaporated W oxide films in contact with 1 M $LiClO_4$ + PC, shows that t_f scales with U_d in the manner predicted by Eq. 6.8.

Time dependent current densities during intercalation/deintercalation, in good agreement with the data shown above, have also been found for protons and Li^+ ions in other work on evaporated films *(427, 2368, 3740)*, as well as for films prepared by anodization *(431, 2895)* and CVD *(426, 431)*. Furthermore, such data have been recorded for W oxide films containing Li_2O + Nb_2O_5 *(2148)*. Reichman and Bard *(2875)* observed faster kinetics in films made by anodization than in films made by evaporation. Deviations from the theoretical expressions for J_i and J_d were noted by Nagai and Kamimori *(2463)*; they speculated that the reason might be non-ideal measurement configurations, but it should be remarked that their films were produced by evaporation at $p_{N2} = 5 \times 10^{-5}$ Torr and hence very porous. It is not obvious that the analyses by Faughnan et al. *(783, 1048)* are fully applicable under these circumstances. Deviations were noted also in some studies of devices that incorporated a solid electrolyte *(3154, 3156)*, and it was argued that the coloration was connected with a charge build-up at the contact between the W oxide film and the electrolyte. In work on crystalline $WO_3 \cdot H_2O$ films made by anodization *(3278)*, it was reasoned that the main rate-controlling mechanism during intercalation was the diffusion of oxygen vacancies from the interface between the film and a 1 N H_2SO_4 electrolyte into the bulk of the film.

Haranahalli et al. *(1417-8)* studied evaporated W oxide films with and without porous semi-transparent overlayers of Au. The overlayer was either biased or electrically floating. Figure 6.11 shows some results for a 0.6-μm-thick W oxide film; it is seen that the deintercalation is faster when an Au layer is present *(1418)*. Similarly, the intercalation could be made faster by an Au layer. These effects could be understood as a result of electron transfer at both sides of the W oxide film. Haranahalli and Holloway *(1418)* also studied effects of changing the film thicknesses and

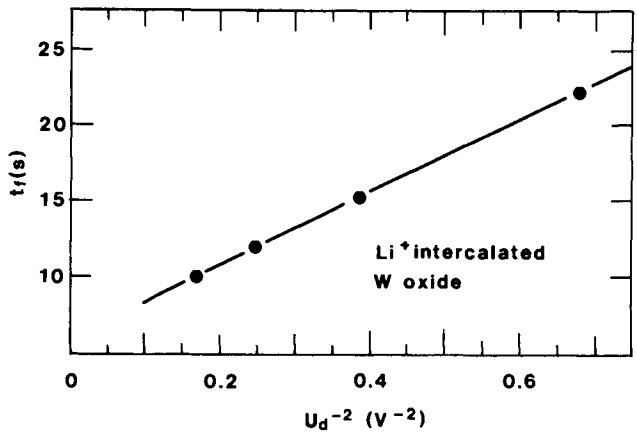

Fig. 6.10 Time t_f, corresponding to complete Li deintercalation from an evaporated W oxide film, vs. inverse voltage squared, U_d^{-2}. Filled circles denote experimental data, and the straight line is a fit to them. From Mohapatra *(2368)*.

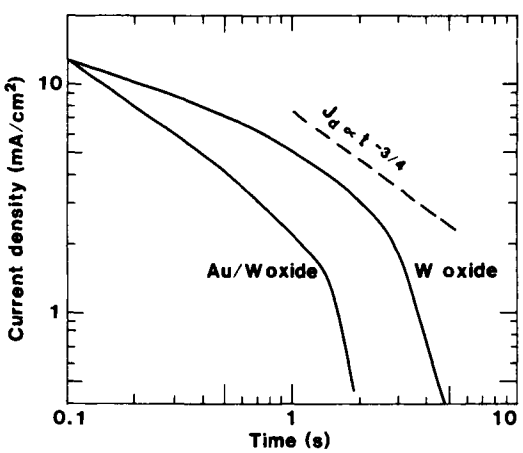

Fig. 6.11 Current density vs. time for deintercalation of ions from evaporated W oxide films with and without a porous Au top layer. The same voltage was applied to obtain the two curves. Dashed line indicates the time dependence inherent in Eq. 6.7. From Haranahalli and Holloway *(1418)*.

found pronounced deviations from the power laws for t in Eqs. 6.6 and 6.7 when the W oxide film was thin (< 0.4 μm). Further details on this work will be given in Sec. 31.2.

6.5 Cyclic Voltammetry

In cyclic voltammetry, a voltage is applied between the W oxide film and a counter electrode. The voltage is swept back and forth between two setpoints, usually in a triangular manner; alternatively, the voltage is pulsed between two levels *(2663)*. The current flowing into and out of the film in conjunction with the ion intercalation/deintercalation is measured. Cyclic voltammetry can be used non-quantitatively to give a "fingerprint" of the electrochemical processes, to trace reversible and irreversible effects, and to ascertain voltage levels that yield stable operation. Voltages outside the stability range can lead to gas evolution, metal electroplating, etc. Quantitative cyclic voltammetry is also possible *(2446)*, for example for measurements of charge densities associated with intercalation/deintercalation processes. Commercial potentiostats can be used for cyclic voltammetry; an alternative low-cost system particularly suitable for electrochromics was described recently by Kirkup et al. *(1814)*.

Figure 6.12 illustrates a number of characteristic features of voltammograms taken on highly disordered W oxide films in contact with liquid electrolytes. The data are from Reichman and Bard *(2875)*, who studied evaporated films in 1 M H_2SO_4; the shown voltage range is between 0 and 1.7 V vs. RHE. One first observes that the curves are smooth, which indicates that no well-defined phase changes occur. With the voltage increasing, the current goes from a negative value, passes a broad maximum, and approaches zero at the highest voltages; this curve branch corresponds to ion deintercalation (bleaching). With the voltage decreasing, the current remains close to zero until the voltage drops below ~0.5 V vs. RHE at which point the current gets progressively negative; this branch corresponds to ion intercalation (coloring). The upper curves in Fig. 6.12 show the effect of changing the voltage scan rate from 1 to 200 mV/s. Clearly the current related to ion intercalation/deintercalation gets larger the higher the scan rate. The curves in the middle and lower parts of Fig. 6.12 are voltammograms taken at different times from the beginning of a continuous cyclic scanning process at 100 mV/s. These curves were obtained for a film prepared so that it initially contained only a small amount of water, as inferred from IR transmission spectra. Continued cycling leads to progressive changes in the voltammograms, the most salient one being the increase in the current. It was verified that the changes in the voltammograms were connected with water incorporation in the films, which illustrates that the film *composition* can be altered during the voltammetric cycling. The lower set of curves in Fig. 6.12 was measured for a film prepared so that it initially contained some water. Now the time-dependent changes in the voltammograms are different from those for the anhydrous film and show a progressive decrease in the current. This effect is caused by dissolution of the W oxide film in the electrolyte and hence illustrates that film *degradation* can take place during voltammetric cycling.

Voltammograms corresponding to proton intercalation/deintercalation, similar to those above, have been reported many times *(256, 417-8, 627, 651, 728, 1607, 1841, 2445, 2622, 2840, 2898)*. The influence of the electrolyte pH was studied by Shimizu et al. *(3144)*. Berezin and Malinenko *(356)* investigated crystalline films prepared by evaporation at $\tau_s > 380°C$, or by annealing at a similar temperature, and found that the current displayed well defined peaks at two different voltages. This was interpreted as a consequence of there being two pathways for proton

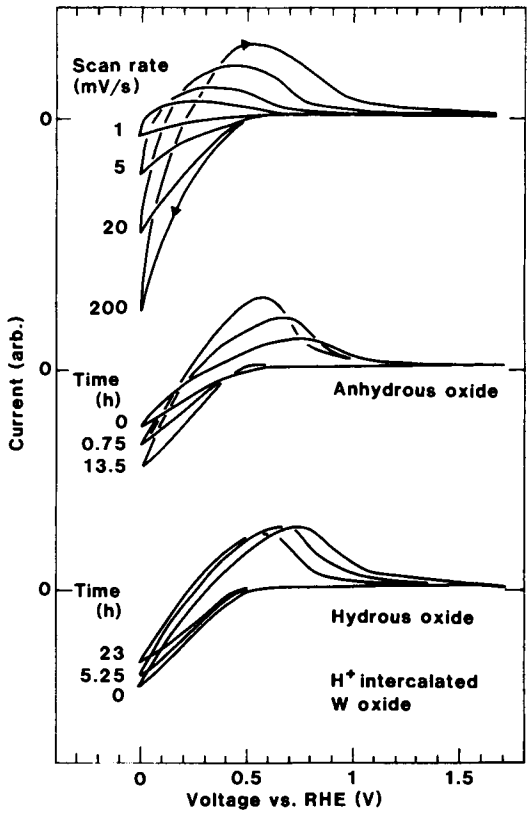

Fig. 6.12 Cyclic voltammograms for H^+ intercalation/deintercalation in evaporated W oxide films in 1 M H_2SO_4. Upper set of curves pertains to different voltage scan rates. Arrows denote scan direction. Middle and bottom sets of curves illustrate time evolutions during continuous cyclings of anhydrous and hydrous films, respectively. After Reichman and Bard *(2875)*.

diffusion, which is consistent with the conclusions by Vértes and Schiller *(3530)* and by Galyamov and Roginskaya *(1134)* discussed in Sec. 6.2 above.

The electrolyte composition can have a large influence on the voltammogram as evidenced in Fig. 6.13, showing results from Bohnke et al. *(427)*. The electrolyte was anhydrous 1 M $LiClO_4$ + PC mixed with controlled amounts of water. The currents can be much enhanced by adding water, and it is likely that mixed intercalation/deintercalation of H^+ and Li^+ takes place. Voltammograms for films in 2.5 M $LiClO_4$ + PC, containing up to 10 % water, were given in *(428)*.

Pure Li^+ intercalation in disordered W oxide films has been studied in several works. Figure 6.14 shows results for an as-deposited film in 0.3 M $LiClO_4$ + PC, as reproduced from Yoshiike et al. *(3741)*. The film was prepared by evaporation in 4 to 5 x 10^{-4} Torr of N_2 and is hence porous. The voltammogram is rather similar to the ones corresponding to proton intercalation shown in Fig. 6.12. Other studies have explored the roles of water additions *(1350)*, voltage scan speed *(2463)*, number of cycles *(2396, 2467, 3058, 3301)*, film thickness *(2463)*, annealing treatment *(3132)*, and porosity caused by the addition of O_2 *(2397)* as well as N_2 and H_2O *(2465, 3738)* during the evaporation. Data were given for conventionally evaporated films also in *(432, 2257, 2716, 3699)* and for flash evaporated films in *(3059)*. Analogous results were plotted on a linear time scale in *(96-9)* and for galvanostatic switching in *(725)*.

As-deposited films can permanently incorporate Li^+ so that the voltammograms are altered. This important effect is documented in the two left-hand cyclic curves in Fig. 6.14, which were obtained after storing the evaporated film (0.3 μm thick; 0.3 cm^2 in area) in a small quantity (3 ml) of 0.3 M $LiClO_4$ + PC at 70°C for the given periods of time. The results were reported by Yoshiike et al. *(3741)*. By extending the voltage ranges to progressively more negative values it appears that, essentially, the entire cyclic voltammograms are shifted towards more negative voltages. A fast initial shift is followed by a slow change for time periods as long as 500 h. A convenient measure of the shift is provided by the starting potential for the cathodic reaction, defined by U_c in Fig. 6.14. The as-deposited film has $U_c \approx 0.4$ V vs. SCE, whereas $U_c \approx -0.15$ V is found after 500 h. The shift is enlarged when the amount of electrolyte is increased, and U_c can drop to ~-0.35 V after 500 h. This indicates that the amount of incorporated Li^+ is the decisive factor. As discussed later, it seems that Li^+ replaces H^+ in the W oxide film. By adding a "supporting electrolyte" of $LiBF_4$, which serves as an acidity compound, it is possible to prevent the exchange between Li^+ and H^+ without deteriorating the PC and hence to practically eliminate the voltage shift; this can be a considerable advantage for applications.

Ageing in a humid atmosphere can significantly change the W oxide films, as pointed out in Sec. 3.7 in connection with IR absorption data. A detailed study of these ageing effects has been performed by Yoshiike et al. *(3737-9, 3741)*. Figure 6.15 summarizes voltammograms taken on differently modified films in 0.3 M $LiClO_4$ + 0.03 M $LiBF_4$ + PC, as reproduced from *(3737)*. The post-treatment took place at selected temperature and relative humidity for different times. Specifically, the voltammograms in Fig. 6.15 refer to an as-deposited film containing only a small amount of H_2O, a film treated at 25°C and 50 % RH for 16 h so that it contained a large quantity of physisorbed H_2O, a film treated under the same conditions for 168 h so that it was hydroxylated and contained many O-H groups, and treated at 40°C and 95 % RH so that the film was hydrated and could be represented as $WO_3 \cdot H_2O$ or $H_2WO_4 \cdot H_2O$. It is seen that physisorbed water can give a marginal enhancement of the current, whereas hydroxylation and--in particular--hydration significantly decrease the current.

Deposition technologies other than evaporation are considered next. Data on microcrystalline

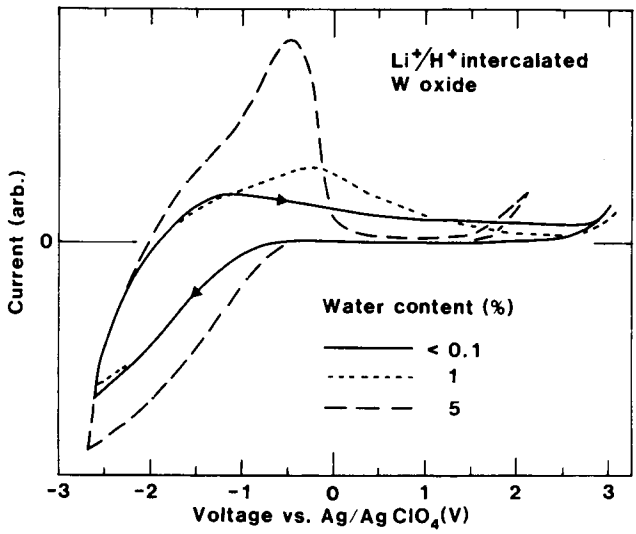

Fig. 6.13 Cyclic voltammograms for mixed H^+ and Li^+ intercalation/deintercalation in evaporated W oxide films in 1 M $LiClO_4$ + PC with the shown amounts of water. The voltage scan rate was 50 mV/s. Arrows denote scan direction. From Bohnke et al. *(427)*.

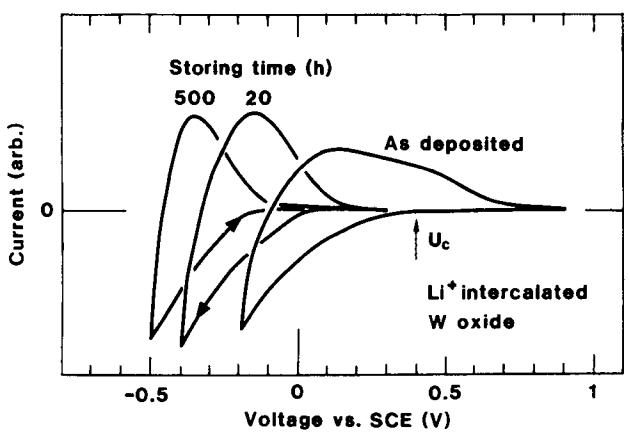

Fig. 6.14 Cyclic voltammograms for Li^+ intercalation/deintercalation in evaporated W oxide films in 0.3 M $LiClO_4$ + PC. Data are given for the as-deposited film and after storing it in a small quantity of a heated electrolyte for the shown times. The voltage scan rate was 200 mV/s. Arrows mark the voltage U_c for the onset of a cathodic reaction, as well as scan direction. From Yoshiike et al. *(3741)*.

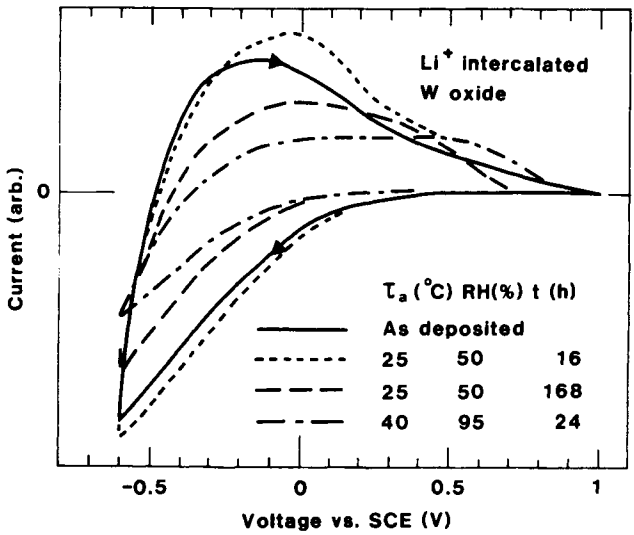

Fig. 6.15 Cyclic voltammograms for Li^+ intercalation/deintercalation in evaporated W oxide films in 0.3 M $LiClO_4$ + 0.03 M $LiBF_4$ + PC. Data are given for the as-deposited film and after treating it at the shown temperature τ_a and relative humidity RH for the shown time t_a. The voltage scan rate was 200 mV/s. Arrows denote scan direction. From Yoshiike et al. *(3737)*.

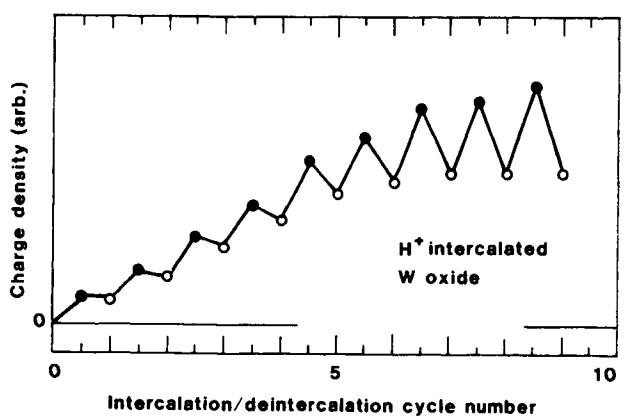

Fig. 6.16 Charge density vs. number of intercalation/deintercalation cycles for a sputter-deposited W oxide film in 1 N H_2SO_4. Filled (open) circles refer to intercalated and dark (deintercalated and bleached) samples. Adjacent data points are joined by straight lines. From Kitao et al. *(51, 1829)*.

films made by dc *sputtering* of W in O_2 and tested in H_2SO_4 or HCl have been reported several times *(627, 2445, 3516)*. Some weak structure, that was presumably associated with the crystalline nature of the films, could be seen in the voltammograms. Results for films made by rf sputtering of WO_3 in O_2 or Ar + 10 % O_2 were reported in *(627, 732, 2499, 2500, 2715, 2854)*. Current-voltage curves connected with Li^+ intercalation/deintercalation in sputter-deposited films were given in *(96-9)*.

Charge densities related to continued ion intercalation/deintercalation are easily extracted from cyclic voltammograms. The data shown in Fig. 6.16, from Kitao et al. *(51, 1827, 1829)*, refer to a W oxide film made by reactive rf sputtering of WO_3 in Ar + O_2 and subsequently treated in 1 N H_2SO_4. The inserted charge goes up monotonically with the number of intercalation/deintercalation cycles and seems to level off when the cycle number is ~10. A similar conclusion can be drawn from Fig. 6.12 for evaporated W oxide films. Only part of the inserted charge is removed during the deintercalation half-cycle; this is a significant result which will be further discussed below in connection with physical depth profiling of intercalated species. Data that are almost identical to those in Fig. 6.16 were given in *(3688)*.

Electrodeposited W oxide films were prepared from aqueous peroxotungstic acid solutions by Yamanaka *(3704)* and others *(810, 2313)*. Figure 6.17 shows voltammetric data *(3704)* referring to ion intercalation/deintercalation in 1 M $LiClO_4$ + PC + 2% H_2O. It is reasonable to expect that both H^+ and Li^+ are effective (cf. Fig. 6.13). As-deposited films gave currents that decreased rapidly with the increasing number of voltage scans, which signifies film dissolution (cf. lower set of curves in Fig. 6.12). Films treated at $\tau_a > 100°C$ for 1 h were stable, though, and had voltammograms of the kind illustrated by the solid curve in Fig. 6.17. Consistent data were shown elsewhere too *(810, 2730)*. According to Miles et al. *(2313)*, addition of a small amount of $HClO_4$ to the electrolyte was conducive to durability. Annealing at $\tau_a > 200°C$ led to irreversible changes of the film structure and a decreased capacity for ion intercalation/deintercalation, as evident from the dashed and dotted curves in Fig. 6.17. The voltammograms for the electro-deposited films are indicative of a highly disordered structure.

Anodized W surfaces have been studied several times by voltammetry; the films have been made potentiostatically at high *(2875-6)* and low voltage *(2144,2584)*, potentiodynamically *(564, 2895)*, galvanostatically *(929)*, or under unspecified conditions *(2265)*. Measurements in H_2SO_4 have shown several times that structure appears in the voltammograms; this is evidence for crystallinity. Although the data are not fully consistent--which is hardly surprising since the anodization parameters can have a strong influence on the crystal structure--it appears that two more or less well defined peaks occur during the cathodic scan, which speaks in favor of two separate pathways for H^+ incorporation.

Regarding *CVD*, Bohnke et al. *(426)* studied films made by pyrolysis of $W(CO)_6$ and subsequent annealing. Data for such films, treated in 1 N H_2SO_4, are given in Fig. 6.18. Voltammograms for the films, whose crystal structure was monoclinic, showed clear peaks both in the cathodic and anodic sweep directions, which indicates that different electrochemical processes dominate in specific voltage ranges. It was conjectured *(426)* that the features seen during the cathodic sweep are due to H^+ originating from two sources: adsorbed on the oxide surface or enclosed in its pores, and in the bulk of the electrolyte.

Sol-gel-derived W oxide films have been investigated in some detail by Livage et al. *(667, 669, 1698-9, 1700, 1702, 1704)* and others *(319, 787, 1372, 2170)*. Figure 6.19 reproduces results from Judeinstein and Livage *(1699, 2094)* that illustrate well how voltammograms can be

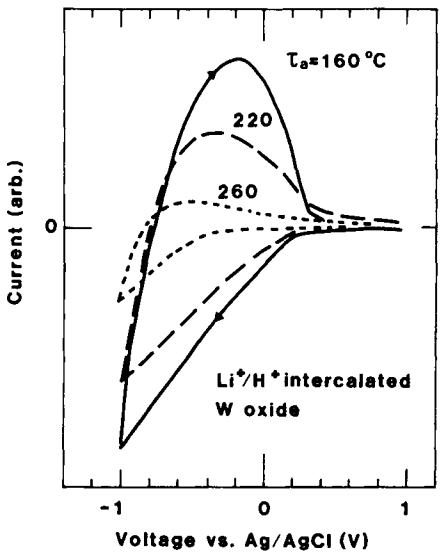

Fig. 6.17 Cyclic voltammograms for mixed Li^+ and H^+ intercalation/deintercalation in electrodeposited W oxide films in 1 M $LiClO_4$ + PC + 2 % H_2O. Data are given for films annealed for 1 h at the shown temperature τ_a. The voltage scan rate was 100 mV/s. Arrows denote scan direction. From Yamanaka *(3704)*.

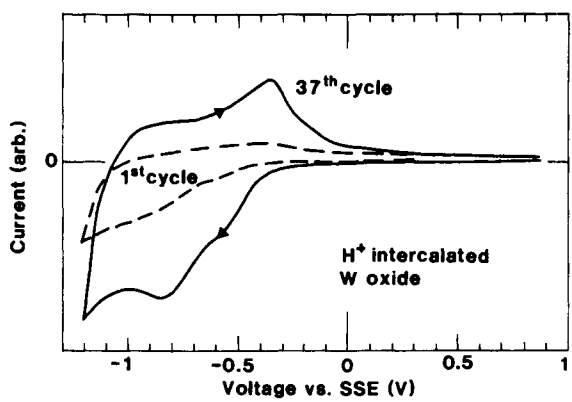

Fig. 6.18 Cyclic voltammograms for H^+ intercalation/deintercalation in a monoclinic crystalline CVD-produced W oxide film in 1 N H_2SO_4. Data are shown for the initial cycle and the 37th cycle. The voltage scan rate was 100 mV/s. Arrows denote scan direction. From Bohnke et al. *(426)*.

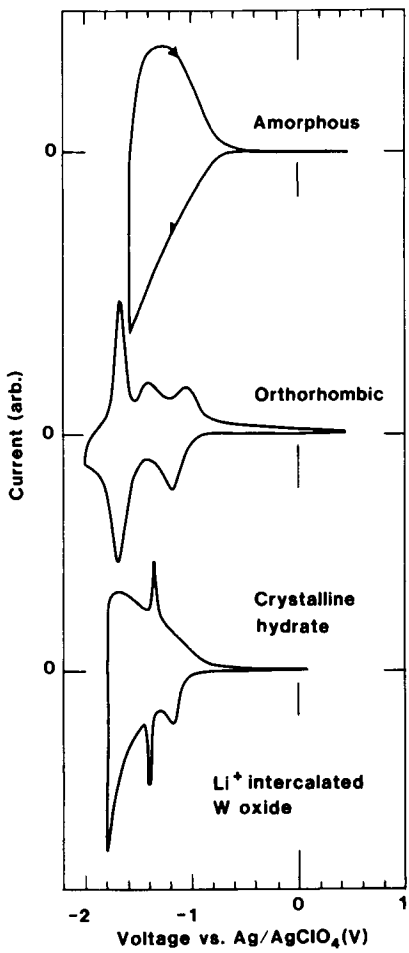

Fig. 6.19 Cyclic voltammograms for Li^+ intercalation/deintercalation in sol-gel-derived W oxide films in 1 M $LiClO_4$ + PC. Data are given for different crystallinity and composition; the bottom curve has been slightly smoothed. The voltage scan rate was 10 mV/s. Arrows denote scan direction. From Judeinstein and Livage *(1699)*.

influenced by different crystallinity and composition. The voltammograms were taken after ~500 cycles in 1 M $LiClO_4$ + PC in order to eliminate irreversible effects and at a slow voltage scan rate. The upper curve, taken for a highly disordered polymer-like film, is similar to voltammograms for films evaporated onto unheated substrates (cf. Fig. 6.12). The middle curve, pertaining to an annealed orthorhombic crystalline film, is distinctly different and shows two peaks during the cathodic sweep and three peaks during the anodic sweep. The bottom curve, for a hydrated crystalline film of $WO_3 \cdot 2H_2O$, looks like a superposition of the other two curves. Cyclic voltammograms for sol-gel-type deposits have been reported elsewhere as well, specifically for films made by spin-coating from solutions based on hexaphenoxy-tungsten *(3699)*, alkoxides *(1133)* and WCl_6 + 2-propanol *(1370, 1372)*, and for films made by dip coating *(3490)*. Featureless appearances of the voltammograms indicated highly disordered structures. A similar conclusion can be drawn for films made by thermal oxidation *(1190, 2876)*.

Films prepared by decomposition of oxalatotungstate compounds showed voltammograms characteristic of two redox couples, as reported by Tada et al. *(1117, 3313)*; a somewhat different behavior was reported earlier for such films, though *(1204)*. The existence of two redox couples indicates different sites for cation insertion, with can be reconciled which models for the specific film structure.

6.6 Impedance Spectrometry

Impedance spectrometry is a well-established technology *(2136, 2138, 2185, 2823-4)*. In practice, one applies a small ac voltage, often superimposed on a much larger dc bias, to a W oxide film with a conducting electrode on one side and an electrolyte on the other side. Measurements are performed of the in-phase and out-of-phase current (or of the amplitude and phase of the current) in a range of frequency ω preferrably encompassing several decades. It is convenient to plot the impedance Z in the complex plane (Nyquist plot), and the relation Re(Z) vs. -Im(Z) contains a wealth of information that allows conclusions to be drawn regarding charge transport both at interfaces and inside the material. This old technique is now in a stage of rapid development, and it seems likely that its full potential has not yet been explored as regards electrochromic W oxide films. In chronoamperometric intercalation/deintercalation studies the dynamic voltage range is normally much larger than in impedance spectroscopy, and hence results from these two techniques are not necessarily comparable. The latter point was underscored in some work on Ir oxide films *(1192, 1264)*, and it applies just as well to W oxide and any other material.

Figure 6.20 illustrates several characteristic features for the complex impedance of W-oxide-based films. The data were obtained by Yoshiike et al. *(3737)*, who studied evaporated films backed by SnO_2-coated glass and in contact with an electrolyte of 0.3 M $LiClO_4$ + 0.03 M $LiBF_4$ + PC. The frequency range was 10^{-1} to 10^5 Hz. A low ω consistently gave large values of Re(Z) and -Im(Z), and a high ω gave small values of these quantities. At the largest potentials, corresponding to very small ion intercalation, the curves in Fig. 6.20 are monotonic. At lower potential, a well defined semicircle appears in the complex plane, a steep increase of -Im(Z) is seen at low ω, and traces of a second circle appear at high ω. When the potential is lower--and eventually negative-- the main semicircle shrinks. The ion content x goes up in proportion with the drop of potential and is ~0.06 at U = -100mV vs. SCE.

The complex impedance data reported in different studies are not fully consistent, which no

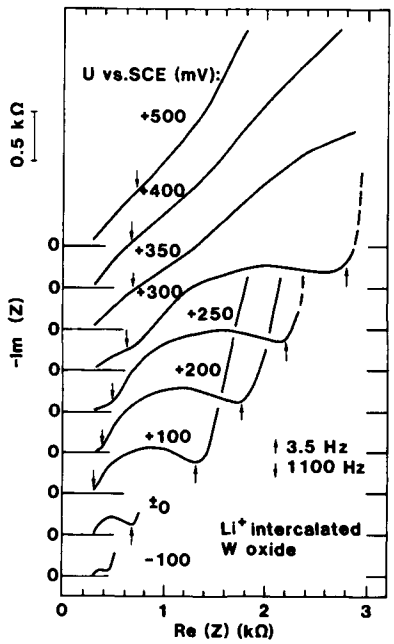

Fig. 6.20 Complex impedance Z vs. frequency in the 10^{-1} to 10^{5} Hz range for evaporated W oxide films with Li^{+} intercalated at the shown voltages U. The curves are vertically displaced. Arrows locate points corresponding to two fixed frequencies. Dashed curves signify that the individual data points showed large scattering. From Yoshiike et al. *(3737)*.

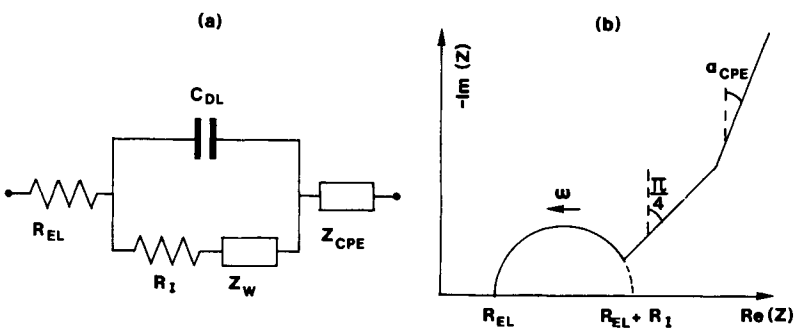

Fig. 6.21 Modified Randles circuit (part a) and its rendering in the complex impedance plane as a function of frequency ω (part b). The symbols are discussed in the main text. Dashed lines are used to define angles with respect to the imaginary axis.

doubt is a reflection of different film structures and measurement configurations. However, a linear relationship between Re(Z) and -Im(Z) at low frequencies followed by a semicircle at higher frequencies has been reported by Bohnke et al. *(418-9, 422, 431)*, who used electrolytes with $LiClO_4 + H_2O$ as well as H_2SO_4 and found steep linear parts, and by Bajars et al. *(239)*, who studied symmetric devices with two electrodes and an intervening H_2SO_4 electrolyte and found a linear part with a slope of ~45°. Impedance spectroscopy has also been used to study the roles of different thin film preparation techniques *(417-8, 422, 3737)*, substrate conditions *(418-9, 422)*, temperature *(296, 2845)*, and number of intercalation/deintercalation cycles *(430)*. Devices with solid electrolytes were investigated in *(239, 295-6, 977, 1544, 1758)*. Additional data can be found in *(1256, 1504, 1545, 1702, 2463-4)*. The interface between W oxide and Ta oxide was analyzed in *(1136)*.

The strength of impedance spectroscopy as an analytic technique rests on circuit models that are able to adequately represent the experimental data. The *Randles circuit (2847)* forms a suitable starting point and framework for elaboration. It comprises four elements arranged as shown in Fig. 6.21(a): a resistance R_{EL} mainly representing the electrolyte, another resistance R_I for charge transfer at the interface between electrolyte and intercalation host, a capacitance C_{DL} representing the Helmholtz double layer, and a circuit component Z_W--known as the Warburg element *(3576)*--that describes diffusion effects. For normal diffusion one can write

$$Z_W \propto (1 - i)\,(D_{M+}\,\omega)^{-1/2}\,. \tag{6.9}$$

The classical Randles circuit is valid for semi-infinite diffusion, and it has to be modified to account for the low frequency properties of a thin film, as first discussed by Ho et al. *(1504)* (see also *(273)*). To this end one may add a *constant phase element* to the circuit, following work by Bohnke and Bohnke *(419)*. Specifically, if ion diffusion inside pores is the rate limiting process, the impedance can be written

$$Z_{CPE} = A_{CPE}\,(i\,\omega)^{-\eta}, \tag{6.10}$$

with $0 < \eta < 1$. For $\eta = 1$, A_{CPE} is a true capacitance and one recovers the circuit model in *(1258)*. The exponent η is related to the porosity of the film, and expressions involving fractal dimensions are known as reviewed by Le Mehaute *(2039)*.

Figure 6.21(b) is a schematic representation of a generalized Randles circuit in the complex plane. Going from high to low frequency, there is a semicircle centered on the real axis and cutting this axis at R_{EL} and $R_{EL} + R_I$; then there is a transition to a linear part with 45° slope as governed by the Warburg element; and finally there is a bend to another linear part--dominated by the constant phase element--defined by an angle α_{CPE} to the imaginary axis. The exponent in Eq. 6.10 is related to this angle by

$$\eta = 1 - 2\alpha_{CPE}/\pi. \tag{6.11}$$

The curve shape depends on the values of the constitutive parameters, and it may be that one or more of its characteristic features are not manifest. It is obvious that the Nyquist plots permit determination of diffusion constants (cf. Eq. 6.9), frequency ranges within which diffusion or interface charge transfer dominate the properties, etc., and that such plots also have a bearing on the

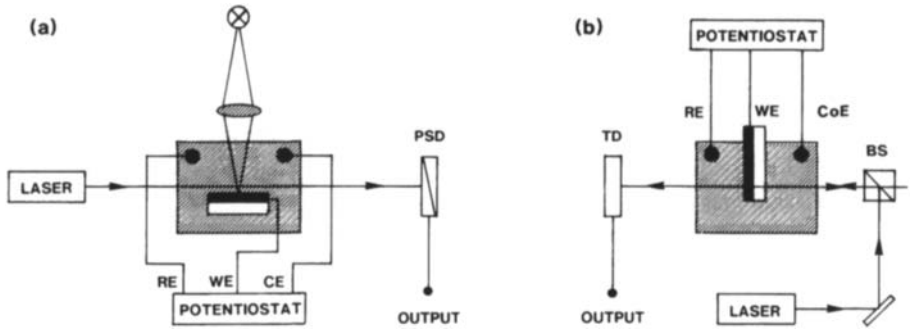

Fig. 6.22 Schematic representation of experimental systems for beam deflectometry. Part (a) shows an arrangement for recording density changes in the electrolyte via the "mirage effect" in conjuction with photothermal beam deflectometry. Part (b) illustrates a system for combined measurements of mechanical and optical data under ion intercalation/deintercalation. PSD is position sensitive detector, TD is transmittance detector, BS is beam splitter, RE is reference electrode, WE is working electrode, and CoE is counter electrode.

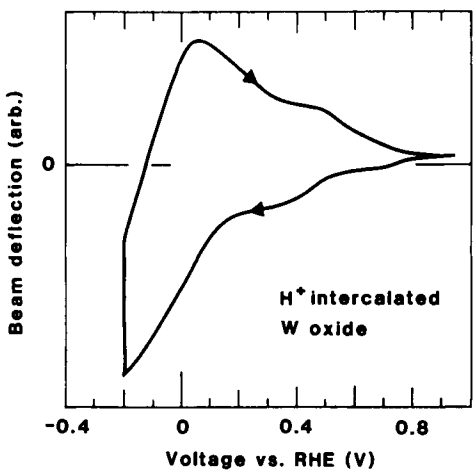

Fig. 6.23 Cyclic deflectogram in a mirage-effect configuration for H^+ intercalation/deintercalation in an anodic W oxide film in 1 M H_2SO_4. The voltage scan rate was 50 mV/s. Arrows denote scan direction. After Kötz et al. *(1901)*.

structural properties.

There is an overall agreement between theory and the experimental data in Fig. 6.20. The rapid increase in the curves observed at the lowest frequencies does not give evidence for any diffusion-limited behavior represented in a Warburg element, but one may note that an approximate 45° slope was indeed observed in the work by Bajars et al. *(239)*. Extensions of the classical Randles circuit, other than those already discussed, have been proposed in some work; for example, a second *RC* loop has been incorporated to account for high frequency properties possibly caused by electron injection at the electrode interface *(3737)*. Other extensions have been discussed in *(1097-9, 1544-5)*.

The centers of the semicircles shown in Fig. 6.20 lie below the real axis, rather than on the axis as given by the simple theory. This seems to be a general feature for W oxide films, and it can be inferred also from *(239, 296, 418-9, 422)*. Displaced semicircle centers can be related to non-classical diffusion in porous media *(2039, 2426)*, but it seems that these aspects have not yet been elaborated for electrochromic W oxide.

From the discussion above it should be clear that impedance spectroscopy of ion intercalation compounds with rough or porous structure--preferrably characterized by fractal or multifractal measures--stands out as a fertile area for future studies. A detailed coverage of the relevant literature is not meaningful here, but a good grasp of the field can be obtained from *(250, 276-7, 403, 451, 661, 703, 945, 1157, 1235, 1487, 1716, 1765, 1863, 2204, 2281, 2427, 2564, 2689-90, 2825, 3002, 3571)*.

6.7 Beam Deflectometry

The earlier discussed electrochemical techniques represent standard practice. There are also some new and emerging technologies for electrochemical characterization that should be mentioned, although their application to electrochromic W oxide is still in its infancy. The techniques of present concern are referred to as beam deflectometry. Some of the possible experimental arrangements are illustrated in Fig. 6.22.

Figure 6.22(a) shows a set-up with a laser beam passing parallel to the surface of a film immersed in an electrolyte. The electrolyte density is varied by ion intercalation/deintercalation, which is conveniently accomplished by use of a potentiostat. This leads to a refractive index profile for the path of the laser beam, which hence is deflected. The phenomenon is aptly called a *mirage effect (2937)*. Quantitative data can be recorded on a position-sensitive detector. Figure 6.23 shows results for an anodic W oxide film in H_2SO_4, as reported by Kötz et al. *(1901)*. The cyclic deflectogram displays structure that can be associated with the crystalline nature of the film; it is in excellent agreement with cyclic voltammograms for the same film. The data give unambiguous evidence for proton intercalation/deintercalation. The mirage effect has been used to distinguish between H^+ and Li^+ intercalation into W oxide films immersed in electrolytes containing both of these ionic species *(2779)*.

The refractive index gradient underlying the mirage effect can also be created by a temperature difference between the film and the electrolyte. The heating can be done by pulsed monochromatic light. It is straight-forward to combine this *photothermal deflection spectroscopy* with measurements of concentration gradients obtained by ion intercalation/ deintercalation, as shown in Fig.6.22(a).

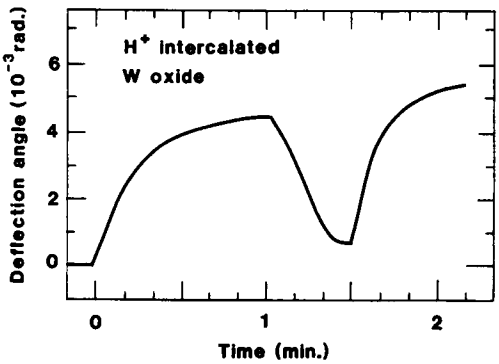

Fig. 6.24 Deflection angle vs. time for galvanostatic H^+ intercalation/deintercalation in an electrodeposited W oxide film in 1 M H_2SO_4. After Córdoba-Torresi et al. *(760)*.

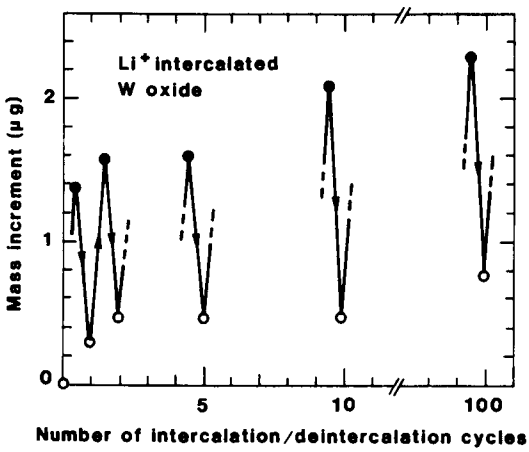

Fig. 6.25 Mass increment as a function of the number of intercalation/deintercalation cycles of a 0.3 μm x 1.8 cm^2 W oxide film made by evaporation and treated in $LiClO_4$ + PC. Filled (open) circles refer to the mass after intercalation (deintercalation). Solid lines with arrows indicate the time evolution of the mass increment. From Yoshiike and Kondo *(3740)*.

Another beam deflection method is based on the *mechanical properties* of a film being changed through ion intercalation/deintercalation. The stress can be recorded easily provided that the film is backed by a flexible substrate such as a very thin glass plate. Figure 6.22(b) shows a suitable set-up in which the coated substrate is fixed at its upper end and extends freely into the electrolyte. A laser beam is sent via a beam splitter onto the substrate. Ion intercalation/deintercalation manifest themselves in a bending of the substrate; this effect is readily detected on a position-sensitive detector. The deflection angle $\Delta\theta$ of the laser probe beam is related to the stress σ_s by *(848)*

$$\sigma_s = \frac{Y}{6(1-\nu)} \frac{d_g^2}{d} \frac{\Delta\theta}{s} , \qquad (6.12)$$

where Y is Young's modulus for the glass substrate, ν is Poisson's ratio, d_g is the thickness of the substrate, and s is the sample length. It is suitable to combine such measurements with transmittance detection. The technique has been described by Decker et al. *(848, 2968, 3035)*.

Figure 6.24, taken from work by Córdoba-Torresi et al. *(760)*, shows experimental data for an electrodeposited W oxide film in a H_2SO_4 electrolyte. Cyclic proton intercalation/deintercalation gives rise to a periodic increase and decrease of the deflection angle. Combined with optical measurements, these results give clear proof that coloring is assocated with H^+ intercalation and that bleaching is associated with H^+ deintercalation. Similar data were obtained for evaporated W oxide films in $LiClO_4$ + PC by Decker et al. *(848)*.

6.8 Microbalance Measurements

In a vibrating quartz microbalance, changes in the resonance frequency are directly proportional to mass changes of the oscillating system. The microbalance is well known as a monitor of vacuum deposited matter *(991)*, and it can also operate very well in a liquid electrolyte. The latter application was employed for example in *(369, 757, 760, 1488-9, 1967, 2550, 2705, 3694)*. The technique has been reviewed by Buttry *(578-80)*. Microbalance measurements hence allow unambiguous determinations of the mass of the intercalated/deintercalated species for a film backed by a suitably cut single crystalline quartz wafer. When the measurements are carried out as a function of a periodic voltage scan, one speaks of a *voltamassogram*. The measurements can be done *in situ* (i.e., in the electrolyte) or *ex situ* (i.e., after withdrawal from the electrolyte and rinsing).

Yoshiike and Kondo *(3740)* used the vibrating quarz technique for ex situ studies of evaporated W oxide films immersed in $LiClO_4$ + PC. Figure 6.25 displays the mass difference as a function of the number of intercalation/deintercalation cycles for a 0.3-μm-thick film with an area of 1.8 cm^2. The first cycle shows an increase of the mass by 1.4 μg, followed by a drop of the mass by 1.1 μg. It is noteworthy that deintercalation leaves some mass permanently inserted in the film. Further cycling leads to an increase of the intercalated mass as well as to an increase of the mass that is not deintercalated. After extended cycling, more than 30 % of the totally intercalated mass resides permanently in the film.

In situ measurements on W oxide films in aqueous H_2SO_4 electrolytes were reported by Masuda and Baba *(2209)* and Córdoba-Torresi et al. *(760)*. A modulation of the resonance frequency was seen, and the voltamassogram was consistent with intercalation of protons

accompanied by some water molecules. Effects of film dissolution and of mechanical stress transfer to the substrate were noted as well. Similar studies of films in a $LiClO_4$ + PC electrolyte showed reversible Li^+ intercalation/deintercalation *(1611)*. Babinec *(207)* studied W oxide films, made by evaporation and sputtering, in different electrolytes. The data indicated a highly complex pattern of --sometimes competing--intercalation of variously solvated protons and lithium ions.

Chapter 7

TUNGSTEN OXIDE FILMS: ION INTERCALATION/DEINTERCALATION STUDIED BY PHYSICAL TECHNIQUES

Physical characterization can elucidate a number of aspects on ion intercalation/deintercalation that the electrochemical techniques are unable to provide. This chapter discusses depth profiling of the intercalated species by several different techniques (7.1), structure determination by X-ray extinction and electron diffraction (7.2), Raman spectroscopy (7.3), infrared absorption spectroscopy (7.4), electron paramagnetic resonance (7.5), nuclear magnetic resonance (7.6), and electron spectroscopies applied to core levels (7.7) and to valence- and conduction bands (7.8). The "physical" techniques of interest here are not restricted to pure physics research but are equally applicable to solid-state chemistry and materials research.

7.1 Depth Profiling of Intercalated Species

Elemental depth profiles can be recorded by several experimental methods such as Nuclear Reaction Analysis (NRA), Rutherford Backscattering Spectroscopy (RBS), Secondary Ion Mass Spectroscopy (SIMS), and Auger Electron Spectroscopy (AES). There are many varieties of these techniques; for examples, a range of nuclear reactions can be used for NRA *(1789)*. Results from all of the techniques are useful, among other things, for cross checks on alternative methods such as the electrochemical ones.

Proton intercalation into W oxide films is considered first; data have been recorded by NRA and SIMS. One should note already at the outset that most films are strongly hydrous, so the relative shift of the hydrogen content upon H^+ intercalation/deintercalation may not be so large (cf. reaction 6.2). The initial NRA studies by Gérard et al. *(1168-9)*, using the $^1H(^{11}B, \alpha)^8Be$ reaction, were not able to resolve any changes in the hydrogen level for evaporated and sputter-deposited films irrespective of their color, which led to the contention that electrochromism was not directly associated with proton intercalation/deintercalation. This conclusion was also drawn by Bange et al. *(255, 258, 2852, 3562)*, who used NRA based on the $^1H(^{15}N, \alpha\gamma)^{15}C$ reaction to study evaporated films; these data are discussed in more detail in Sec. 29.4 below. However, other NRA work by McIntyre et al. *(2265)*, employing the $^2H(^3He, p)^4He$ reaction to anodic deuterated hydrous films, was fully consistent with proton intercalation/ deintercalation. An early SIMS study of hydrogen in evaporated W oxide, reported by Muramatsu et al. *(2432)*, also did not show any measurable change of the ion content upon cycling in H_2SO_4. Later work by Zhong et al. *(3811)*

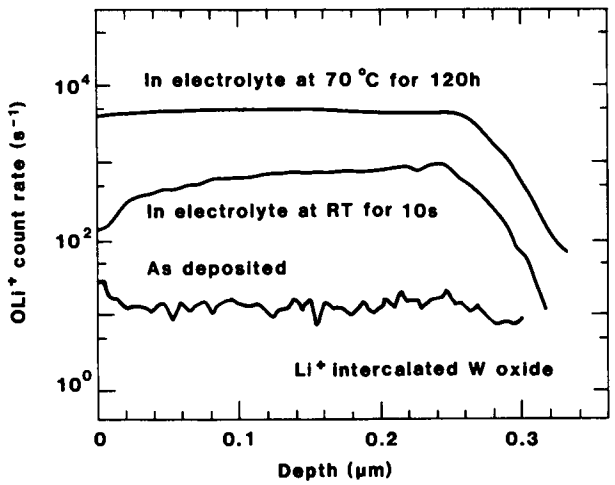

Fig. 7.1 Depth profiles for OLi^+ ions as determined by SIMS. Data are shown for an as-evaporated W oxide film and after treatment of this film in an electrolyte of 0.3 M $LiClO_4$ + 0.01 M H_2O + PC at room temperature (RT) and elevated temperature for the shown times. After Yoshiike et al. *(3741)*.

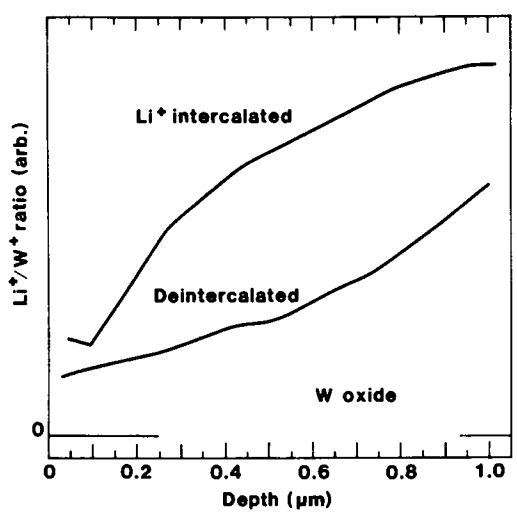

Fig. 7.2 Depth profiles for Li^+/W^+ ion ratios as determined by SIMS. Data are shown for an evaporated W oxide film in Li^+ intercalated/deintercalated state. After Zhong et al. *(3811)*.

gave different results, though, and the H concentration was indeed modulated under intercalation/deintercalation, although as much as ~90 % appeared to reside in the film even in its deintercalated state.

Li^+ intercalation has been investigated by SIMS and AES. Yoshiike et al. *(3741)* studied evaporated W oxide films immersed in an electrolyte of 0.3 M $LiClO_4$ + 0.01 M H_2O + PC. They reported SIMS data for molecular OLi^+ ions, with readings normalized to the signal for W^+ ions. In Fig. 7.1, the bottom curve gives a background rate of ~10 counts/s for an as-deposited film. Immersing a ~0.25-μm-thick film in the electrolyte for 10 s led to an increase of the OLi^+ signal by some two orders of magnitude, and treatment at 70°C for 120 h gave a further enhancement of this signal by a factor ~5. It is noteworthy that even a short exposure to a Li^+ containing electrolyte gave a substantial accumulation of lithium over the full cross-section of the film. This is a clear indication that its structure is highly porous. It was verified that ClO_4^- ions were unable to penetrate into the films, and that an addition of $LiBF_4$ to the electrolyte diminished the rate by which Li^+ was incorporated. Spontaneous Li^+ intercalation in sol-gel-produced hydrated amorphous films was found by Judeinstein et al. *(1704)*.

There are several studies of elemental depth profiles after intercalation/deintercalation cycling of evaporated W oxide films in contact with $LiClO_4$ + PC *(1437-9, 1762, 2227, 2396, 3702, 3811)* or Li^+ conducting polymers *(295-6)*. Figure 7.2, after Zhong et al. *(3811)*, shows normalized count rate for Li^+/W^+ as obtained by SIMS for a 0.96-μm-thick sample. The Li^+ content was modulated by a factor ~2 through the intercalation/deintercalation, and the lithiation content was substantial even in the deintercalated state. Supporting evidence on the composition was gathered for similar materials by use of an inductively coupled plasma mass spectrometer *(3811)*. Under extended cycling, the amount of incorporated Li^+ might be gradually enhanced, at least for the intercalated state *(1439, 2227)*. The lithium density has been determined for similarly prepared specimens also by AES *(2393, 2396)*; these data indicated an accumulation of lithium in the inner parts of the film, but this was probably an artefact ("knock-on effect") of the Ar^+ ions used for sputtering during the depth profiling. AES data on Na profiles for films cycled in $NaClO_4$ + PC electrolytes were given in *(106, 1762)*. Some SIMS data are available also for sol-gel-derived films *(1699, 1700)*.

The tungsten/oxygen ratio was determined through RBS by Gérard et al. *(1169)* and McIntyre et al. *(2265)* for different degrees of ion intercalation. No clear evidence was found for any change of this ratio, which shows that oxygen atoms do not play a major role in the intercalation/deintercalation.

7.2 Structure Determination by X-ray Extinction and Electron Diffraction

EXAFS is a powerful technique capable of giving information on structural changes during ion intercalation/deintercalation in heavily disordered materials. It was applied by Kuzmin and Purans *(1987)* to the WL_{III} edge in W oxide films evaporated onto polyimide substrates at $\tau_s \approx 100°C$. Protonation was accomplished in an aqueous H_2SO_4 electrolyte. The associated electron insertion then yields tungsten ions not only in the 6+ state--pertaining to a WO_3 structure--but also in a 5+ state. These effects will be discussed at length in Secs 7.5 and 7.7 below. EXAFS spectra showed unambiguous differences between the intercalated and deintercalated states, and elaborate multishell analysis allowed the RDF to be reconstructed around W^{6+} and W^{5+} sites. Such data are shown in

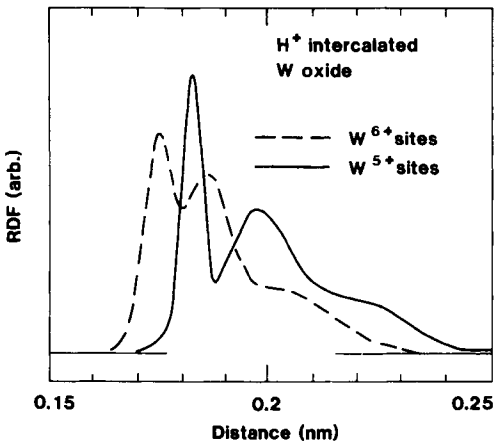

Fig. 7.3 Radial distribution functions (RDFs) obtained by EXAFS from evaporated W oxide films with different levels of H^+ intercalation. The data pertain to the first coordination shell around W^{6+} and W^{5+} sites. After Kuzmin and Purans *(1987)*.

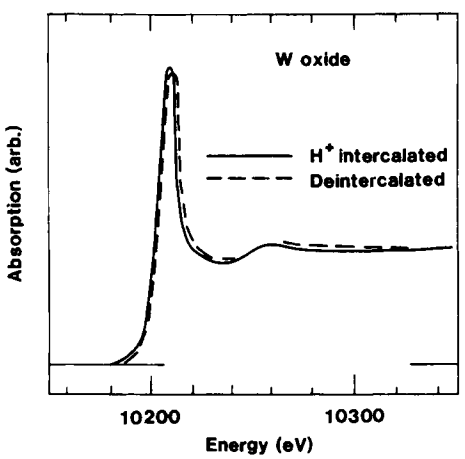

Fig. 7.4 XANES spectrum of the WL_{III} edge for an evaporated W oxide film in H^+ intercalated and deintercalated states. From Kuzmin and Purans *(1987)*.

Fig. 7.3 with regard to the first coordination shell, signifying tungsten-oxygen separations. One finds three more or less well-defined peaks in both cases, just as for crystalline WO_3. The atomic separations are different, and the average distance was 0.1881 nm for the 6+ state and 0.1992 nm for the 5+ state. Hence the tungsten-oxygen distance is increased by ~6% when the tungsten ion charge is decreased by the localization of one extra electron.

Intercalation-dependent effects can be traced also in XANES spectra. Figure 7.4, again after Kuzmin and Purans *(1987)*, shows a pronounced resonance near the WL_{III} absorption edge. This so called "white line" is attributed to $2p \rightarrow 5d$ transitions with the final state of the photoelectron in the continuum with *5d* atomic character, and with the core hole at the *2p* level screened by other electrons. Ion intercalation was found to cause a downwards shift of the "white line" by 1.5 to 1.8 eV and to lower its amplitude somewhat. A quantitative explanation of these effects is not yet available.

Electron diffraction cannot give as detailed information as EXAFS but is nevertheless useful. This technique was used by Kukuyev et al. *(1952)* to study structural modifications upon ion intercalation in highly disordered evaporated W oxide films, and RDFs were evaluated in the manner mentioned in Sec. 3.5. The dashed curve in Fig. 7.5 shows an RDF for an as-deposited film prepared with the substrate at 80 to 90°C. The structural features are similar to those in Fig. 3.5. Hydrogen insertion was accomplished by exposing such films to the products of a chemical reaction between Zn and HCl. The corresponding RDF, shown by the solid curve in Fig. 7.5, indicates that the basic octahedral configuration remains, but that some interatomic distances are enlarged, and also that high-order correlations can be qualitatively altered. It was conjectured that the ion intercalation is associated with structural transformations from a state with non-linear arrangements of corner-sharing octahedra to a state with a planar arrangement of such octahedra, but the details of this transformation were not discussed. A less detailed study, using electron diffraction and TEM, did not reveal any structural changes upon Li^+ intercalation *(1436)*.

In *crystalline* W oxide, XRD can give direct information the atomic structure and its modifications upon ion intercalation/deintercalation. A detailed study was carried out by Gavrilyuk et al. *(1150)*, who prepared films by evaporation onto substrates at $100 < \tau_s < 500$°C, followed by annealing in air at $400 < \tau_a < 450$°C for 1 to 2 h. The samples were then treated in 0.1 N H_2SO_4 + C_2H_5OH. The films displayed pronounced texture, which tended to somewhat obscure the intercalation-dependent structural modifications. Figure 7.6 shows typical data; an initial structure, reported to be triclinic, was found to go over into tetragonal phases of $H_{0.23}WO_3$ and $H_{0.33}WO_3$ upon increased proton insertion. In addition, the texture was changed along with the crystal structure. Samples treated by ultraviolet irradiation according to a procedure in *(1152)* showed lattice order transformations in full analogy with those in the ion intercalated ones. In a study similar to that reported on in Fig. 7.6, Zhong et al. *(3811)* prepared porous W oxide films by evaporation onto unheated substrates, followed by treatment in air at $\tau_a = 350$°C for 2 to 3 h. The ensuing films were monoclinic. Proton intercalation/deintercalation was carried out in aqueous H_2SO_4 solutions or from a solid electrolyte. These films showed diffraction peaks indicating the presence of tetragonal $H_{0.33}WO_3$. Deintercalation yielded samples with a structure closely resembling that of the as-deposited films. Results similar to those just described were also found by Aleshina et al. *(66)* and Miyake et al. *(2340)*. Donnadieu et al. *(963)* reported reversible changes between cubic intercalated and monclinic deintercalted states. The observed structural transformations were in rather good agreement with bulk data for Li_xWO_3, shown in Fig. 2.4.

Li^+ intercalation into crystalline W oxide was studied by Schuster et al. *(3073)*, who prepared

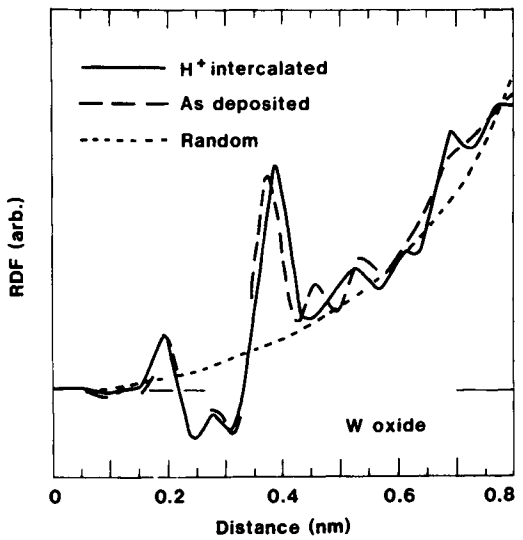

Fig. 7.5 Radial distribution function (RDF) obtained by electron diffraction from an evaporated W oxide film in as-deposited state and after H^+ intercalation. Dotted curve refers to an RDF in the absence of any long-range order. After Kukuyev et al. *(1952)*.

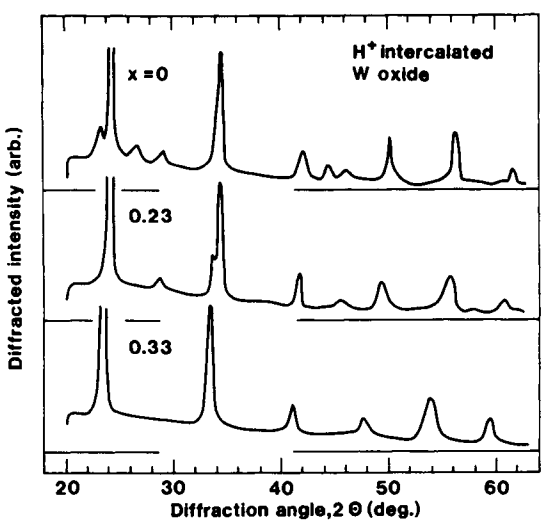

Fig. 7.6 X-ray diffractograms for crystalline W oxide films with different amounts of H^+ intercalation, represented as x in H_xWO_3. The upper curve is in good overall agreement with diffractograms in Fig. 3.14. After Gavrilyuk et al. *(1150)*.

films by evaporation at $100 < \tau_s < 300°C$ and $10^{-6} < p_{O2} < 8 \times 10^{-5}$ Torr, followed by annealing in air at $\tau_a = 400°C$ for 2 h. As-deposited films were monoclinic with a small addition of a hexagonal phase. After repeated intercalation/deintercalation cycles in $LiClO_4$ + PC, the intercalated phase was tentatively described as being $Li_2W_4O_{13}$, whereas the deintercalated phase was $Li_2W_4O_{13}$ plus a monoclinic structure. Diffraction lines due to lithiated W oxide were also reported in *(3811)*. Experiments to elucidate the structures that can form upon large Li^+ intercalation were carried out by Hashimoto et al. *(1439)*. Their films were made by *e*-beam evaporation onto substrates at τ_s = 187°C. Lithiation was performed in 1 M $LiClO_4$ + PC by application of a voltage as large as 3.5 V vs. a Pt electrode. XRD showed lines that were identified as stemming from $7Li_2WO_3 \cdot 4H_2O$ overlayed on broad features characteristic of "amorphous" W oxide.

Proton insertion into W oxide films made by reactive rf sputtering was studied by Pham Thi and Velasco *(2747)*. Different crystal structures were found depending on sputter gas composition and annealing temperature. The films were treated in H_2SO_4 or H_3PO_4, and the intercalated state could be represented as $H_{0.3}WO_3$. XRD showed that an initially orthorhombic film transformed into a tetragonal structure upon H^+ intercalation, whereas an initially tetragonal film remained in this state. Deintercalation was accompanied by a gradual restoration of the initial phase. Intercalation in an X-ray amorphous film led to irreversible formation of a tetragonal structure. This transformation was impeded when a solid electrolyte was used. A conclusion of this investigation is that, irrespective of the initial state of crystallinity, there is a tendency that ion intercalation favors the development of a tetragonal structure. Additional data on H^+ intercalation into rf-sputtered W oxide were given in Kaneko et al. *(1740)*.

Tungsten oxide films produced by chemical techniques are considered next; they have been studied with regard to proton intercalation by use of diffraction techniques. Kukuyev et al. *(1952)* employed alkoxide technology together with spin coating and reported RDFs based on electron diffraction for films in as-deposited state (cf. Fig. 5.10) and after proton insertion. The two sets of data did not show major differences. Spray pyrolysis with a WCl_6 solution was used by Zhang et al. *(3795)* to make films. Proton intercalation into strongly disordered films gave no evidence for the evolution of any crystalline structure, as seen from XRD, whereas intercalation into crystalline films showed diffraction features typical of tetragonal $H_{0.23}WO_3$.

7.3 Raman Spectroscopy

Raman spectroscopy gives structural information primarily on the vibrational properties of the tungsten-oxygen framework. In particular, a feature at ~950 cm^{-1}--associated with W=O terminal bonds--is of interest in the Raman spectra, as discussed in Sec. 3.6. No Raman spectroscopic study has yet been published for evaporated W oxide films, but detailed results are available for films prepared by sputtering and anodization as elaborated below.

Rf sputtering of W in Ar + O_2 was used by Daniel et al. *(806)* to prepare W oxide films. Ion intercalation/deintercalation was accomplished in 1 N H_2SO_4. Raman spectroscopy showed features up to 1200 cm^{-1} in wavenumber. As-prepared and deintercalated samples displayed spectra similar to the bottom curves in Fig. 3.6. Proton intercalation led to an increase of the Raman intensity at ~950 cm^{-1}. No quantitative assessment of this effect was given, but it is evident that the inserted protons lead to local structures with W=O terminal groups. One may note that the films could degrade under prolonged exposure to the probing laser beam. Raman spectra for similarly

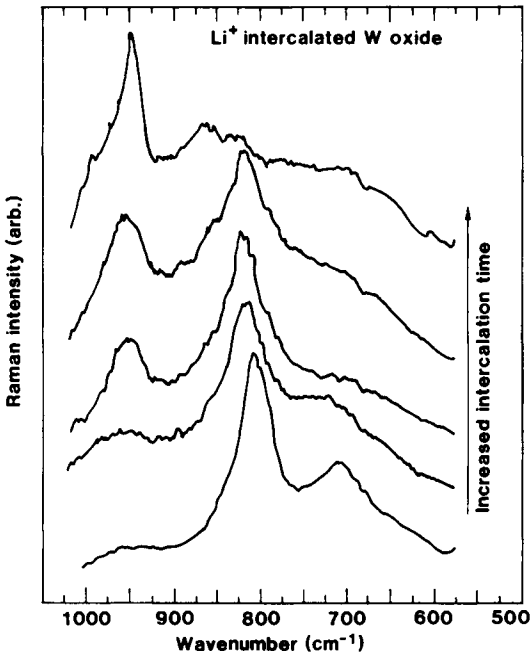

Fig. 7.7 Raman spectra for a hexagonal crystalline W oxide film made by anodization and intercalated with different amounts of Li^+ (subjected to intercalation for different times). From Delichere et al. *(860)*.

prepared films were given also by Pham Thi and Velasco *(2747)*. However, this latter work only reported data for the 550 to 950 cm^{-1} interval, which does not allow definitive conclusions as to the W=O bond.

Anodic W oxide films were analyzed by Raman spectroscopy by Delichere et al. *(860-1, 1030)*. The samples were prepared by anodization in H_2SO_4 at various voltages (U_a), which led to different crystallinity as discussed in Sec. 5.2. Ion intercalation/deintercalation was performed in aqueous electrolytes with H_2SO_4 as well as in hydro-organic electrolytes with 1 M $LiClO_4$ + 1 % H_2O and with $NaClO_4$. Figure 7.7 refers to a film produced at $U_a = 70$ V, which gave a hexagonal structure, and subsequently treated with a Li^+ electrolyte. The bottom curve, obtained after the shortest intercalation time, is almost identical with the spectrum for an as-prepared film in Fig. 5.1. An increase of the intercalation time gave spectra characterized by a gradual increase of the peak at ~950 cm^{-1} due to W=O terminal vibrations and a concomitant blurring of the peaks at < 900 cm^{-1} caused by vibrations of the tungsten-oxygen framework. Neither the H_2O addition nor the intercalated ionic species affected this general behavior. Less crystalline films, made at lower U_a, had a significant peak at ~950 cm^{-1} already in as-prepared state, and the peak enhancement upon ion intercalation was not as dramatic as for the well-crystallized films. After extended intercalation/deintercalation cycling, the Raman spectra indicated a gradual increase of the hexagonal-type crystallinity and also an enhancement of the hydration. Delichere et al. *(861-2, 1030)* also put forward a schematic model for the ion intercalation and its relationship to the W=O terminal bonds. This model departs from the hexagonal structure with large voids including the ions (cf. Fig. 2.5). It is assumed that the ions bond to one oxygen atom, so that one W-O bond is broken and a W=O bond is established instead. The model is highly speculative at the moment, but it seems feasible to test certain aspects of it; for example the intensity of the ~950 cm^{-1} bond would be expected to scale with the amount of intercalated species in a characteristic manner, and bonds due to Li-O vibrations might appear at low wavenumbers in Raman spectra *(1433)* as well as in IR absorption spectra *(1964, 2765, 3368-9, 3741)*.

Raman spectroscopy has been applied by Ohtsuka et al. *(2584-5)* to films made through anodization at a low voltage followed by ion intercalation in H_2SO_4. These films are qualitatively different from those discussed immediately above and show a high degree of disorder (polymer-like structure). The bottom curve in Fig. 7.8 illustrates a Raman spectrum for a sample treated at a voltage 1.0 V vs. RHE, in which case the proton content is expected to be very near zero. The spectrum is in excellent agreement with that for an as-prepared film, shown in Fig. 5.1; the strong peak at ~670 cm^{-1} is a signature of the degree of polymerization as pointed out in Sec. 5.2, and the peak at ~950 cm^{-1} signals W=O terminal bonds. The application of a voltage of 0.3 V produced a proton content that can be given as $x \approx 0.024$ in H_xWO_3. The Raman spectrum for such a film showed strongly diminished peaks, as apparent from the middle curve in Fig. 7.8. At a voltage yielding $x \approx 0.14$ the Raman features are gone, presumably as a result of absorption in the film. They could be regained by proton deintercalation.

Some Raman data for sol-gel-derived W oxide films were given by Falaras et al. *(1030)*. Figure 7.9, taken from their work, shows that ion insertion into monoclinic films leads to the evolution of Raman spectra in a way that is fully analogous with the one for samples made at high-voltage anodization (cf. Fig. 7.7).

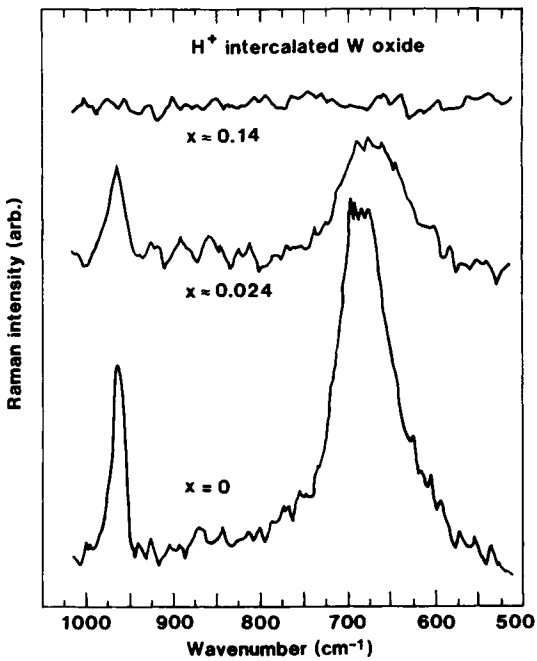

Fig. 7.8 Raman spectra for a very disordered W oxide film made by anodization and intercalated with different amounts of H^+ (represented as x in H_xWO_3). From Ohtsuka et al. *(2584-5)*.

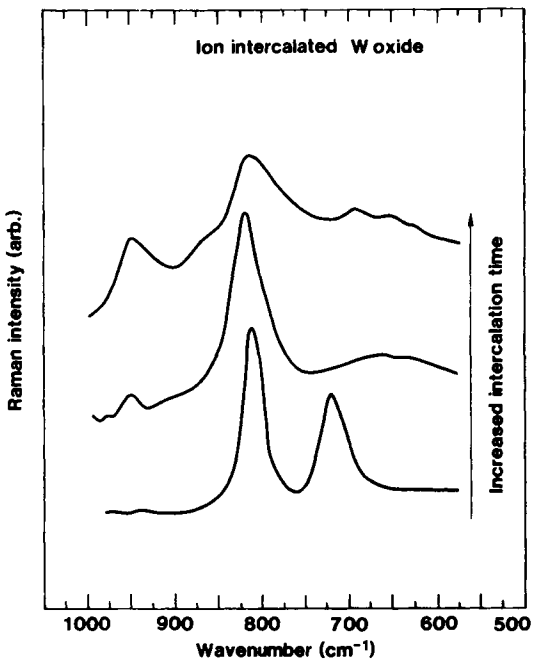

Fig. 7.9 Raman spectra for a monoclinic crystalline W oxide film made by sol-gel deposition and intercalated with different amounts of ions (subjected to intercalation for different times). From Falaras et al. *(1030)*.

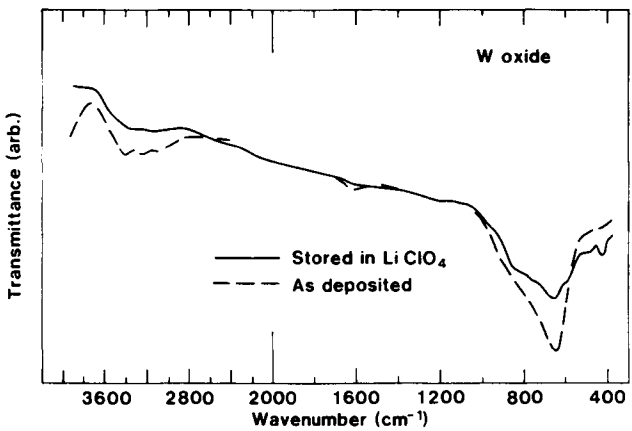

Fig. 7.10 Infrared absorption spectra for an evaporated W oxide film in as-deposited state (dashed curve) and after immersion in 0.3 M $LiClO_4$ + PC at 70°C for 500 h (solid curve). Analogous data for films stored in humid air were reported in Fig. 3.9. Note the scale change at 2000 cm^{-1}. After Yoshiike et al. *(3741)*.

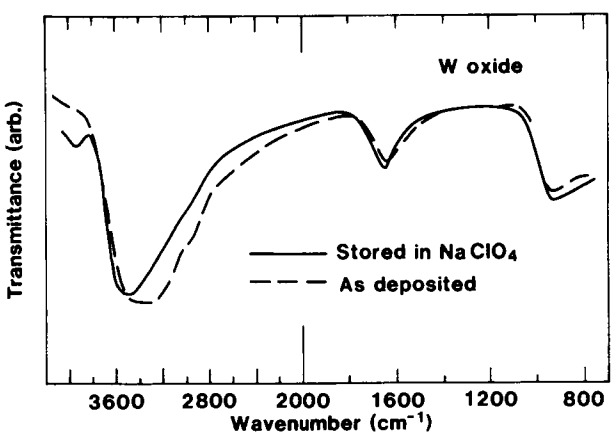

Fig. 7.11 Infrared absorption spectra for an evaporated W oxide film in as-deposited state (dashed curve) and after immersion in 1 M $NaClO_4$ + PC at room temperature for 1/2 h (solid curve). Analogous data for an annealed film were reported in Fig. 3.16. Note the scale change at 2000 cm^{-1}. After Schlotter and Pickelmann *(3058)*.

7.4 Infrared Absorption Spectroscopy

IR absorption spectroscopy is a powerful technique particularly for elucidating changes in hydration and hydroxylation that occur upon ion intercalation/deintercalation. Despite the obvious merits of this technique, and the general availability of IR spectrophotometers, is has been employed in a rather limited number of studies, and the data obtained are so far not very consistent. This feature is almost certainly due to different compositions of the films, specifically different values of p and q in $WO_{3-z-q}(OH)_q \cdot pH_2O$ (cf. reaction 6.2). It is surprising that electromodulated IR absorption in conjunction with lock-in techniques has not been used in more than one investigation until now, despite its obvious bearing on electrochromic modulation of optical properties. Below is a discussion of IR absorption related to ion exchange reactions upon *immersion* of evaporated W oxide films in different electrolytes, followed by results for *intercalation/deintercalation* of different ions in films made by several techniques. An important conclusion will be that alkali ions can replace protons in hydroxyl groups inside the films.

Yoshiike et al. *(3741)* studied evaporated W oxide films immersed in $LiClO_4$. In Fig. 7.10 the dashed curve refers to a FTIR spectrum of an as-deposited film; it shows absorption due to the tungsten-oxide framework in a broad range around ~800 cm^{-1}, absorption due to various O-H stretching modes at ~3400 cm^{-1}, and weak absorption due to H-O-H deformation modes in molecular water at ~1600 cm^{-1} (cf. Fig. 3.9). Storing the film in 0.3 M $LiClO_4$ + PC at 70°C for 500 h within a closed container yielded the spectrum represented by the solid curve in Fig. 7.10. The O-H streching modes are less intense, and changes in the low-frequency modes may indicate some modifications in the tungsten-oxygen framework. In order to interpret the FTIR data, Yoshiike et al. *(3741)* carried out measurements on powders of WO_3, H_2WO_4 and Li_2WO_4. The spectra for films stored in $LiClO_4$ resembled those expected for a mixture of H_2WO_4 and Li_2WO_4, which was taken as an indication for Li^+ replacing H^+ on inner surfaces of the film.

Schlotter and Pickelmann *(3058)* reported unambiguous evidence for alkali ions replacing protons on pore surfaces of evaporated W oxide films. Virgin W oxide films were immersed in 1 M $NaClO_4$ + PC solutions. Microprobe analysis showed that the Na^+ concentration increased monotonically with time; after 1 h it lay at ~90 % of its ultimate value, and after ~24 h it reached saturation. This maximum value corresponded to ~0.2 Na^+ per W atom. Similar experiments on films treated at τ_a = 180°C for 2 h (cf. Fig. 3.16) indicated a somewhat slower rise in the Na^+ density, but the saturation value was unchanged. Analogous results were found for immersion in K^+-containing electrolytes. Figure 7.11 shows IR spectra for a film in as-deposited state and after storage in 1 M $NaClO_4$ + PC for 1/2 h. The O-H vibrations become less pronounced upon treatment in $NaClO_4$, whereas the H-O-H modes stemming from molecular water are not significantly changed. Alkali insertion was completely reversible, and the original IR spectrum could be regained by keeping the Na^+-containing film in H_2SO_4. The Na^+ ions could be further exchanged reversibly by K^+ at a rate that was ~100 times faster than the one for H^+-Li^+ exchange. This rate difference is probably connected with a partially covalent H^+ bonding, which contrasts with the ionic bonding for the alkali ions. From chemisorption experiments with Bronsted bases such as ammonia and pyridine *(3058)*, it was proved that the interior surfaces of evaporated porous W oxide films were covered with acidic Bronsted sites (proton donors). These Bronsted sites are identical with the sites for exchange between protons and alkali ions. This picture of alkali incorporation agrees with that for ion exchange in zeolite-like compounds such as many clays. Tungsten oxide films in contact with Li^+-containing electrolytes are of special interest in

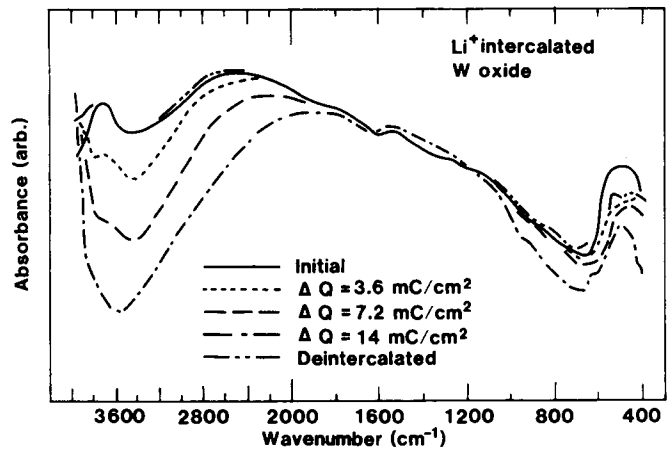

Fig. 7.12 Infrared absorption spectra for an evaporated W oxide film subjected to Li^+ intercalation/deintercalation. Data are shown for the film in initial state, after intercalation to the shown charge densities ΔQ, and after deintercalation. Note the scale change at 2000 cm^{-1}. After Yoshiike et al. *(3740)*.

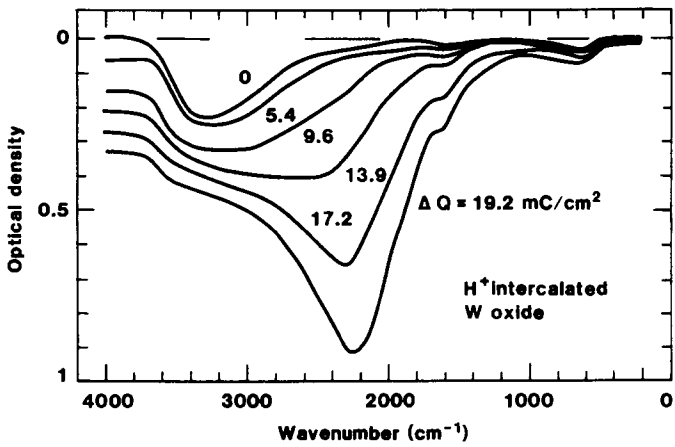

Fig. 7.13 Infrared optical density spectra for a W oxide film made by sputtering in Ar + O_2 and subjected to H^+ intercalation/deintercalation. Data are shown for the film in intial state (uppermost curve) and after ion intercalation corresponding to the shown charge densities ΔQ. After Kitao et al. *(1829)* and Yamada et al. *(3688)*.

electrochromic device technology. The ion exchange for this particular case can be written, schematically, as

$$W\text{-}O\text{-}H + Li^+ \leftrightarrow W\text{-}O\text{-}Li^+ + H^+ \tag{7.1}$$

This reaction is also in agreement with experimental data of Kawakami et al. *(1962)*.

The rest of this section deals with IR absorption spectroscopy for probing intercalation/deintercalation reactions. Proton intercalation/deintercalation of *evaporated* W oxide films in contact with H_2SO_4 was studied by Pickelmann and Schlotter *(2751)*. The IR spectrum was rather unaffected by this process, and in particular the absorption at ~3400 cm^{-1} did not change much, which was taken as evidence that the intercalated protons do not bind to the Bronsted sites at the pore surfaces; another possibility is that the initial material was so hydrous that the changes caused by H^+ intercalation were not detected. One can note that IR studies of compressed W oxide powder indeed showed an increase of the ~3400 cm^{-1} absorption under proton insertion *(1153)*. In work by LeBihan and Grandet *(2024)*, some minor displacements of IR absorption bands at ~2680 cm^{-1} and ~2400 cm^{-1}--ascribed to hydroxyl groups incorporated in the WO_3 matrix--were detected upon proton intercalation. Badilescu et al. *(219)*, employing IR ATR technology, showed that intercalation with H^+ from H_2SO_4 was associated with the development of a broad absorption band around ~1170 cm^{-1}, a narrow band at ~1030 cm^{-1}, and "shoulders" at ~930 and ~870 cm^{-1}. Treating evaporated films in D_2O led to an absorption feature at ~2350 cm^{-1} which was taken as evidence for O-D stretching vibrations *(2541)*.

Yoshiike and Kondo *(3740)* reported FTIR spectra for evaporated W oxide films which were intercalated/deintercalated in 0.3 M $LiClO_4$ + PC, as well as in electrolytes containing Na^+ and K^+ ions. Figure 7.12 shows data for a 0.3-μm-thick film in initial state, after intercalation corresponding to three different charge densities, and after final deintercalation. The plot, given in absorbance units, is drawn so that it allows easy comparison with the IR transmittance data reported previously. The most salient feature is the increase of the O-H stretching mode intensity at ~3400 cm^{-1} which occurs in direct correspondence with the quantity of inserted charge. This correlation was verified both by comparing heights of the absorption peaks and areas under such peaks. The amount of molecular water, on the other hand, was found to be low irrespective of the charge insertion. Deintercalation brought back the initial FTIR spectrum. In order to explain the data, Yoshiike and Kondo *(3740)* formulated a phenomenological model involving alkali ions replacing protons on the pore surfaces, insertion of the liberated protons in interstitial positions in the WO_3 lattice, and adsorption of a H_2O molecule next to a W=O bond.

Infrared absorption in *sputter-deposited* W oxide films is considered next. Recent results were reported by Yamada et al. *(51, 1829, 3688)* for films made by rf sputtering of WO_3 or W in Ar + O_2 followed by intercalation/deintercalation in 1 N H_2SO_4. Figure 7.13 shows optical density (i.e., the logarithm of the transmittance) vs. wavelength for samples run through a sufficient number of cycles that reversible properties had been established. Without inserted charge (except the one during non-reversible initial cycling), the same absorption features appear as in the earlier shown IR spectra. Charge insertion leads to the evolution of an intense broad absorption band. A detailed analysis showed an increase of a band centered at ~2400 cm^{-1} in proportion with the charge, and a simultaneous smaller decrease of a band at ~3400 cm^{-1}. The ~2400 cm^{-1} band was also seen in the study by LeBihan and Grandet *(2024)* referred to above, where it was assigned to hydroxyl groups in a WO_3 matrix. Similar films, made by rf sputtering of W in Ar + O_2 and ion intercalation

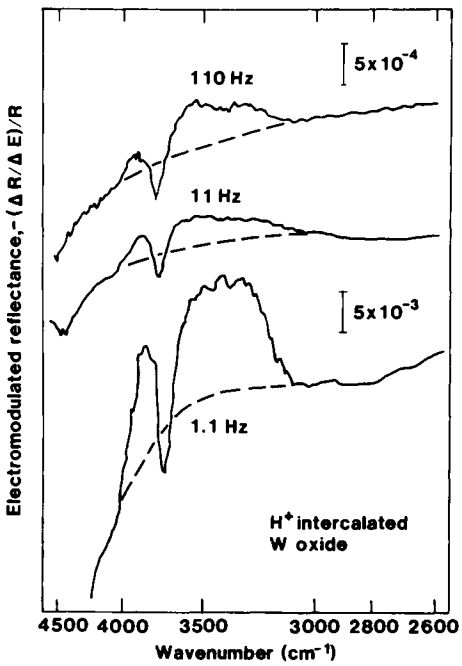

Fig. 7.14 Normalized electromodulated IR reflectance spectra for an anodic W oxide film measured at three frequencies. The vertical scales for the topmost curve and for the other two curves are indicated by the vertical bars. Dashed curves represent somewhat arbitrary baselines. Note that the wavenumber axis in non-linear. From Ohtsuka et al. *(2585)*.

in 1 N H_2SO_4, were analyzed by Daniel et al. *(806)*. In spite of the similar sample fabrication, the IR absorption spectra looked rather different from those shown in Fig. 7.13. Daniel et al. *(806)* analyzed the 1800 to 1000 cm^{-1} wavenumber range in detail and found that proton intercalation was associated with the growth of an absorption band at ~1620 cm^{-1} and the occurrence of a narrow absorption band at ~950 cm^{-1}. The former band was assigned to water--presumably in protonated form--and the latter band to vibrations of W=O terminal groups. Intercalation being associated with an increased number of W=O modes is in agreement with Raman data referred to in Sec. 7.3.

Ohtsuka et al. *(2585)* reported infrared spectra of W oxide films prepared by low-voltage *anodization* in 0.1 M H_2SO_4. Fabrication aspects and IR data for as-prepared films were given in Sec. 5.2. Relative reflectivity was measured for the 4500 to 2600 cm^{-1} range in in the manner used to get the results shown in Fig. 5.2, and difference spectra for intercalated and deintercalated samples were obtained from data recorded after application of voltages +1.0 and -0.1 V vs. RHE, respectively. From such difference spectra it was concluded that proton intercalation manifested itself as a shift towards lower wavenumbers of the hydroxyl stretching absorption. A more detailed image of the intercalation-dependent spectral features was gained by electromodulated infrared reflectance. In this powerful, well suited and little used technique, the voltage is changed between two levels at a certain frequency, and a properly normalized reflectance change is detected at the same frequency by lock-in technique. It is then possible to obtain low-noise spectra. Ohtsuka et al. *(2585)* switched the voltage between +1.0 and -0.1 V vs. RHE and recorded the quantity $\{[R(-0.1) - R(+1.0)]/\Delta E\}/R(+1.0)$. Here $R(U)$ denotes the reflectance for applied voltage U, and ΔE is the span in the voltage modulation. Figure 7.14 shows electromodulated reflectance spectra at three frequencies for a 47-nm-thick film. A frequency-dependent splitting of an absorption band centered at ~3780 cm^{-1}, ascribed to hydroxyl groups bonded to tungsten, can be seen, whereas an absorption band at ~3280 cm^{-1}, associated with molecular water, was not electromodulated. Elements of a general theory for electromodulated infrared vibrational spectroscopy have been given recently *(665, 2678)*.

Spin coated W oxide films, produced from a solution of WCl_6 in 2-propanol, were investigated by Habib and Maheswari *(1373)*. They used subtractively normalized interfacial FTIR spectroscopy, which is a useful technique for detecting small potential-dependent signals from thin surface layers on electrodes *(1371)*. The sample--which was investigated *in situ*--consisted of a W oxide film, backed by a polished gold plate, in contact with a 1 to 2-μm-thick electrolyte of aqueous 0.5 M H_2SO_4. The electrolyte was confined by an IR transparent window. Figure 7.15 shows spectral absorbance for a 0.2-μm-thick film with different levels of ion intercalation. An increase of the signals in the ~3400 and ~1600 cm^{-1} bands is consistent with intercalation of H^+ and/or H_3O^+. Detailed studies of the IR absorbance in the 1500 to 500-cm^{-1}-range indicated changes in signals due to W=O and W-O bonds. The experimental evidence was in favor of rapid H^+ insertion followed by slower H_3O^+ insertion. The reactions may be written, very schematically, as

$$W{=}O + xH^+ + xe^- \leftrightarrow W\text{-}O\text{-}H_x \tag{7.2}$$

or

$$W{=}O + xH_3O^+ + xe^- \leftrightarrow W\text{-}O\text{-}H_x + xH_2O. \tag{7.3}$$

Infrared absorption data on sol-gel-produced W oxide films, determined by Miura et al. *(2333)*, indicated changes in the W-O bond length upon Li^+ intercalation. Judeinstein et al. *(1704)* found evidence for permanent solvent incorporation in hydrated films immersed in $LiClO_4$ + PC.

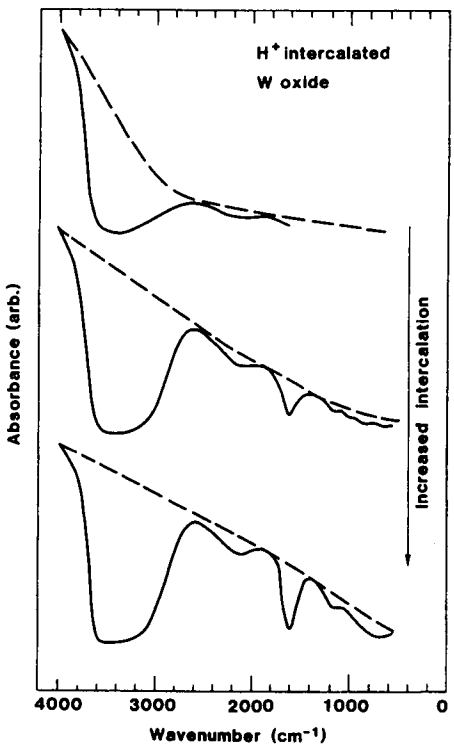

Fig. 7.15 Infrared absorbance spectra for a W oxide film made by spin coating and subjected to H^+ intercalation/deintercalation. Solid curves indicate measured data assembled during repeated scans, and dashed curves represent background signals. After Habib and Maheswari *(1373)*.

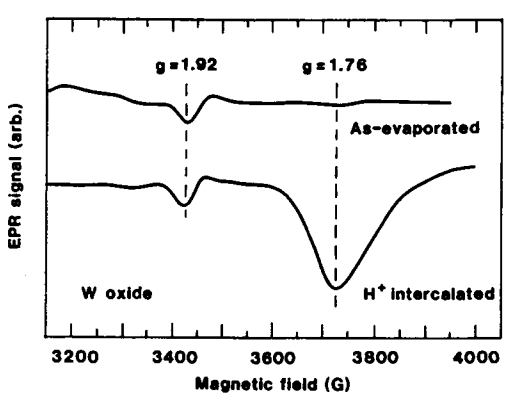

Fig. 7.16 EPR spectra for an evaporated W film in as-deposited state and after intercalation with H^+. Vertical dashed lines indicate two g-values. From Gérard et al. *(1168)*.

7.5 Electron Paramagnetic Resonance

Electron Paramagnetic Resonance (EPR) has been used to study W oxide films. The technique, reviewed in *(1566)*, is of great value for assessing the valence state of the tungsten ion since W^{5+} ($5d^1$ configuration) gives a signal due to its unpaired electron whereas W^{6+} ($5d^0$ configuration) does not give any signal. Observations of EPR signals are hampered by their broadness (caused by the distorted surrounding of the W^{5+} ions), background effects (because the films are electrically conducting), and saturation at large rf power. In order to obtain easily measurable effects, a sufficient amount of sample material is needed, which may require deposition onto flexible spin-free foils that are subsequently formed into a roll and inserted in the cavity of an EPR spectrometer, or material that has been scraped off from extended substrate areas.

Evaporated W oxide films were analyzed by Deb *(839)*, Gérard et al. *(1168)*, and others *(1126, 1842, 2758)*, and rather--though not fully--consistent data were reported. Figure 7.16, from Gérard et al. *(1168)*, shows EPR spectra at 77 K. Two signals are apparent, corresponding to the g-values 1.76 and 1.92. The former, which is most pertinent for understanding electrochromism, is extremely weak in as-deposited films, but it can be clearly observed after H^+ intercalation in an electrolyte, as well as after heating in vacuum or hydrogen gas, or after UV irradiation. The EPR signal is somewhat non-symmetric and has a half-width of ~450 G. It can be roughly described by the spin Hamiltonian for a d^1 ion in an axially symmetric ligand field, viz.

$$H = g_{\|}\beta H_z S_z + g_{\perp}\beta(H_x S_x + H_y S_y), \tag{7.4}$$

with S = 1/2 and ß denoting the Bohr magneton. The spectrum reported by Lusis et al. *(1126, 1842)* corresponded to the Landé factors $g_{\|} = 1.56 \pm 0.02$ and $g_{\perp} = 1.75 \pm 0.02$. The observed g-values are consistent with those of W^{5+} in glassy silicate and phosphate matrices *(2478, 3679)*, some crystals *(2180)*, and in poly-phosphotungstate anions *(3259)*, whereas most crystalline matrices give lower g-values *(2381)*. In WO_3 single crystals, isolated W^{5+} centers are stable only under UV irradiation *(1156, 3048-9)*. Gérard et al. *(1168)* identified deposition parameters that did not yield films with the expected EPR signature and speculated that W^{5+} - W^{5+} interaction and bipolaron formation might take place. This view has been contested by others, though *(1126, 1842)*. One EPR study of evaporated and sputter-deposited W oxide films *(2758)* did not indicate any clear signal due to W^{5+}.

The EPR signal at $g = 1.92$ is independent of the ion intercalation. As first pointed out by Deb *(839)*, the effect undoubtedly is due to Mo^{5+}, whose g-value has been found to lie at this value in various crystalline matrices and in non-stoichiometric MoO_3 thin films, as discussed further in Sec. 12.7. It should be noted that Mo is a common impurity in W, and that Mo can be reduced in preference to W in crystals *(186, 839)* and thin films *(1045)*. The use of Mo boats as evaporation sources led to a strong enhancement of the signal at $g = 1.92$ *(1126, 1842)*. Gérard et al. *(1168)* also reported an EPR signal at $g = 2.004$, which is in analogy with observations for some crystalline W-oxide-based powders *(76, 2208)*. This is a surface signal, which is possibly associated with adsorbed O_2^- *(1554)*.

Livage et al. *(669, 2098)* reported EPR spectra for some sol-gel-derived films. The data are principally similar to those in Fig. 7.16, with signals due to W^{5+} and Mo^{5+} ions being apparent. The W^{5+} feature was analyzed in terms of the spin Hamiltonian of Eq. 7.4, and the Landé factors were found to be $g_{\|} = 1.72$ and $g_{\perp} = 1.79$, indicating a more symmetric surrounding for the W^{5+}

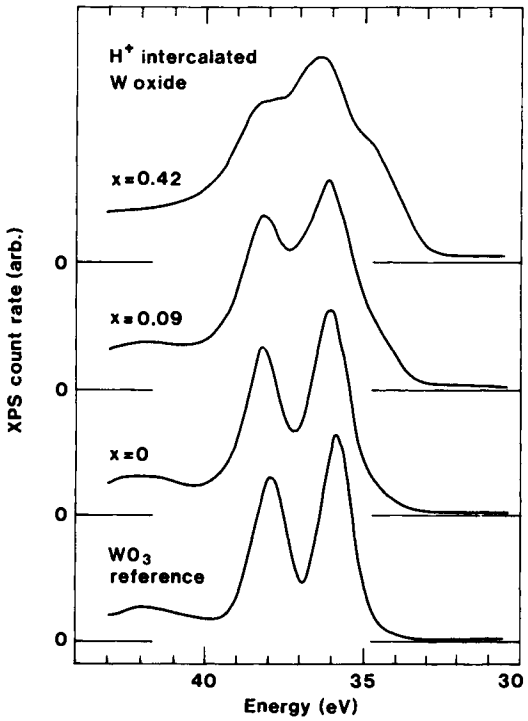

Fig. 7.17 XPS count rate vs. binding energy for *W4f* electrons in evaporated W oxide films with different amounts of inserted charge (represented as x in H_xWO_3). The bottom curve was measured on a WO_3 reference sample. From Bange et al. *(93, 254, 2669-70, 3382-3).*

ion than in the evaporated films discussed by Lusis et al. *(1126, 1842)*.

7.6 Nuclear Magnetic Resonance

Nuclear Magnetic Resonance (NMR) is a useful technique since, among other things, it allows the local surroundings of an intercalated ionic species to be probed via motional narrowing effects. Conventionally, the requirements on sufficient sample volume are similar to those for EPR, but NMR can be extended to the study of surface phenomena *(112)*. Molinié and Paoli *(2380)* used ^1H NMR to study evaporated W oxide films in H^+ intercalated and deintercalated states. The NMR signals had about the same amplitudes irrespective of intercalation, but the width was enlarged by roughly a factor two by the H^+ intercalation. The observed line shape led to the surmise that the protons observed in the H^+ intercalated state were bound to water molecules thus forming H_3O^+ ions. In principle, ^1H Magic-Angle Spinning NMR is capable of giving detailed information on the binding of water molecules to different sites on internal surfaces of porous materials *(1579)*.

Judinstein and Livage *(1699)* reported ^7Li NMR of sol-gel-derived W oxide films treated in $LiClO_4$ + PC. The spectrum of a $Li_{0.3}WO_3$ film consisted of a single peak. Its shift, relative to a LiCl + H_2O reference, was as small as approximately 1 ppm, which indicates that the intercalated lithium is fully ionized in the W oxide framework. The NMR linewidth became smaller upon hydration, which was attributed to motional narrowing due to increased mobility of the Li^+ ions in the water-containing material.

7.7 Electron Spectroscopies Applied to Core Levels

When ions are intercalated into W oxide films, the electronic structure undergoes characteristic changes as regards the core levels for the tungsten oxygen framework and for the intercalated species. Changes also occur in the valence- and conduction bands as discussed in Sec. 7.8 below. XPS is a suitable technique for analyzing the core level modification, and a fair amount of consistent data have been gathered, particularly for evaporated films.

Bange et al. *(93, 254, 2669-70, 3382-3)* have carried out detailed XPS measurements on evaporated W oxide films. The bottom curve in Fig. 7.17 shows their data in the 44 to 31-eV-range for films annealed in air so that they are expected to be fully oxidized WO_3. Two pronounced peaks appear: they are the spin orbit split doublet due to $W4f_{7/2}$ at 35.85 eV and $W4f_{5/2}$ at 38.0 eV. The structure is shifted by ~5 eV toward higher energy relative to the metal. The energies of the *W4f* peaks, and the magnitude of the chemical shift, are consistent with a large body of earlier work on bulk W and WO_3 *(206, 271, 343, 379, 388, 745-7, 832, 972, 1085, 1159, 1378, 1520, 1523, 1525, 2258, 2512, 2514, 2522, 2737, 2961, 2979, 3004, 3556-7)*. It is thus clear that the main peaks in the shown XPS spectrum represent the W^{6+} state. The minor peak at ~42 eV is probably due to $W5p_{3/2}$ electrons *(664)*. The other curves in Fig. 7.17 were obtained on a film in as-deposited state and for films treated in 2 M HCl so that the shown intercalation levels--given as x in H_xWO_3--were reached. It is assumed throughout this section that the densities of electrons and protons are equal. The XPS spectrum for the as-deposited film (x = 0) is very similar to the one for the WO_3 reference, whereas an enhancement of x leads to a blurring of the doublet and to the appearance of a low-energy shoulder. Data that are qualitatively similar to those in Fig. 7.17 have

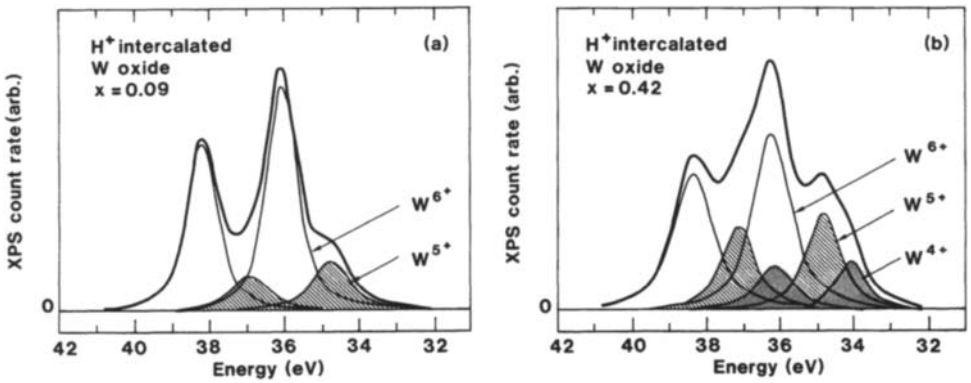

Fig. 7.18 Deconvoluted XPS spectra for evaporated W oxide films with different amounts of inserted charge (represented as x in H_xWO_3). The pairs of bell-shaped curves represent $W4f_{7/2}$ - $W4f_{7/2}$ doublets due to tungsten ions in the valence states 6+ (open), 5+ (lightly shaded), and 4+ (heavily shaded). The upper curve is an envelope. From Bange et al. *(93, 2670, 3382-3).*

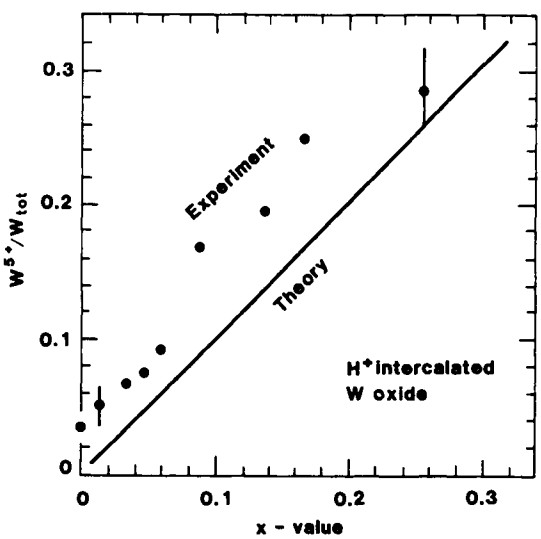

Fig. 7.19 Relative number of tungsten atoms in 5+ state (W^{5+}/W_{tot}) vs. degree of charge insertion (represented as x in H_xWO_3) for evaporated W oxide films. Dots indicate experimental data with error bars typical for small and large intercalation. The line represents a theoretical case in which each inserted electron contributes one W^{5+} ion. From Bange et al. *(2669-70, 3382-3).*

also been reported in other work on films intercalated with H^+, Li^+, Na^+, K^+, Cs^+, and Mg^{2+} *(745-6, 886, 3606)*, in UV-irradiated films *(1519)* and powders *(1085)*, and in bulk samples of WO_3 containing Li, Na, or oxygen vacancies *(664, 1521, 2979, 3606)*. Yoshiike et al. *(3741)* reported an apparent displacement of the *W4f* spectrum for films immersed in hot $LiClO_4$ for many hours.

Deconvolution of XPS spectra for $x > 0$ makes it possible to obtain quantitative information on the relative number of W atoms in valence states different from +6. A suitable procedure, described recently in *(92-3, 2670, 3225, 3382-3)*, involves smoothing of the initial data by an appropriate filter, subtraction of a "Shirley background" *(3152)*, and computer fitting of two or three doublets (mixed Gaussians and Lorentzians) having different intensities. As an alternative to the "Shirley background", a (modified) procedure due to Tougaard *(3432)* has been favored in some recent work *(2891, 3418)*. The XPS doublets are constrained by the $W4f_{7/2}$ - $W4f_{5/2}$ spin-orbit separation being 2.15 eV and the areal ratio of the two peaks being 0.75, which is in accordance with data for the WO_3 reference sample in Fig. 7.17 and with theory for splitting of *4f* levels. Figure 7.18 shows deconvoluted XPS spectra for two magnitudes of the proton density. The secondary doublet (shaded), with the $W4f_{7/2}$ peak at ~34.7 eV, is assigned to W^{5+}. At $x < 0.25$ it was sufficient to include two doublets in the analysis, and from areal ratios of the doublets one can then derive the relative number of W atoms in 5+ state, denoted W^{5+}/W_{tot}. At large x values, a third doublet had to be invoked, as illustrated for $x = 0.42$ in Fig. 7.18(b). This latter doublet has its $W4f_{7/2}$ peak at ~34 eV; it is assigned to W^{4+}. The energy displacement relative to W^{6+} is reasonably consistent with XPS data on bulk WO_2 samples *(747, 1085, 2522, 3004)*. Similar, though less quantitative, deconvolutions have been reported for UV-irradiated films *(1519)*, for non-stoichiometric W oxide films *(1169)* (cf. Fig.4.3) and bulk samples *(1159, 1378)*, and for $Na_{0.62}WO_3$ *(832-3)*. The XPS spectra are not consistent with the presence of WOOH, since this compound is expected to give a shift of the $W4f_{7/2}$ peak towards a somewhat higher energy than in WO_3 *(271)*.

Bange et al. *(2669-70, 3382-3)* compared magnitudes of W^{5+}/W_{tot}, derived from XPS, with x values obtained from electrical measurements of inserted charge. Figure 7.19 shows that the two sets of data correlate very well. Complete agreement according to the solid line would indicate that each electron gives rise to one tungsten ion in 5+ state; clearly the actual case is not far from this. The fact that the x values seem to be larger than the W^{5+}/W_{tot}-values by a small and constant amount can be reconciled with the evaporated W oxide films being non-stoichiometric and characterized by $z \approx 0.15$.

Core levels due to intercalated ions have been reported for *Li1s*, *Na1s*, *K2p*, and *Cs3d* electrons *(745-6, 1437, 1439)*. The XPS peaks due to *Li1s*, *Na1s*, and *K2p* increased and decreased as expected in an intercalation/deintercalation experiment. The *Li1s* electrons have a very small photo-ionization cross-section, and their signal is not easy to observe by XPS.

AES has been used to study the tungsten/oxygen ratio at different ion intercalation levels *(2024, 2380)*. The ratio was found to remain constant.

7.8 Electron Spectroscopies Applied to Valence- and Conduction Bands

This section regards electron spectroscopy for the 15 to -2 eV range relative to the Fermi energy (E_F), which is the interval for valence- and conduction bands in W oxide. The basic features of this

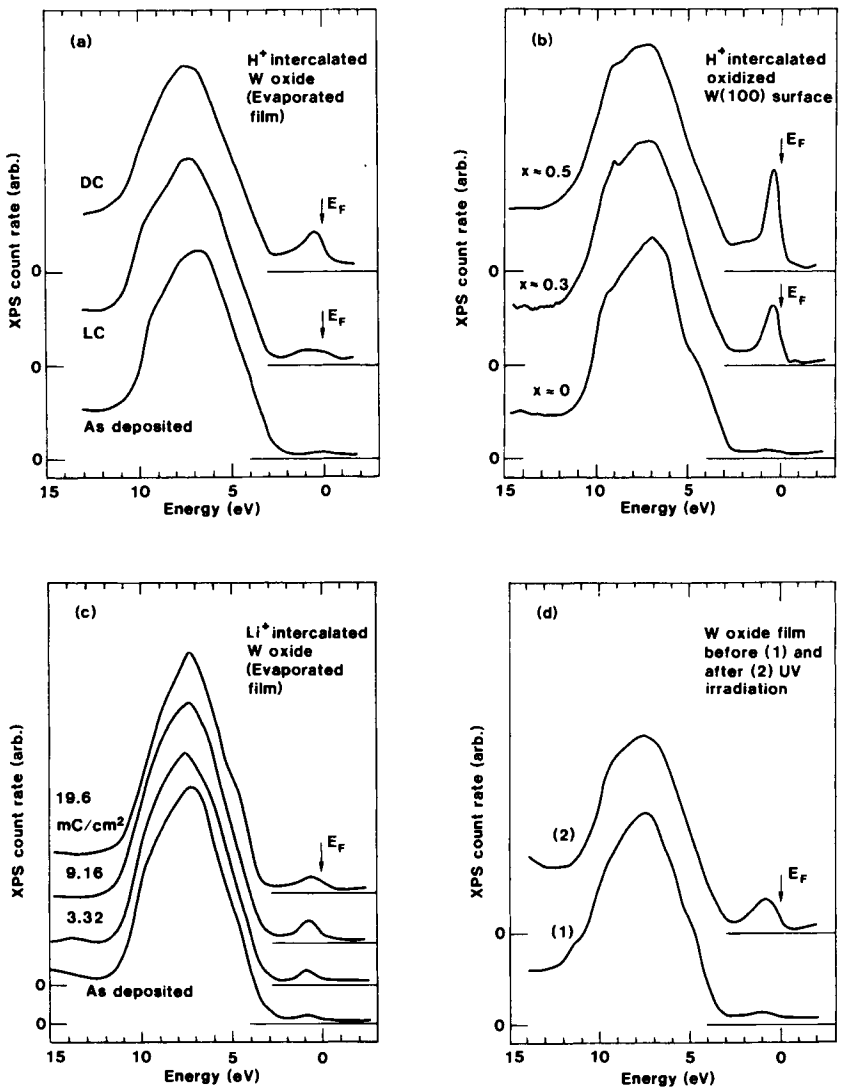

Fig. 7.20 XPS count rate vs. binding energy for valence- and conduction electrons in W-oxide-based films. Part (a) refers to H^+ intercalated evaporated films in as-deposited, lightly colored LC, and deeply colored DC states; part (b) refers to oxidized W(100) surfaces with different amounts of inserted charge (represented as x in H_xWO_3); part (c) refers to Li^+ intercalated evaporated films having the shown charge densities; and part (d) refers to an evaporated film before and after UV irradiation. Some of the data have been slightly smoothed. Arrows denote the Fermi energy E_F. From Colton et al. *(745-6)*, Hashimoto and Matsuoka *(1436-7)*, Hollinger et al. *(1519)*, and Wertheim et al. *(3606)*.

band structure are well known, and work using phenomenological models *(1065, 1244-6)*, the augmented plane wave method *(2232-3, 2236)*, and linear combinations of atomic orbitals *(1535, 3652-5)* showed that an *O2p* valence band was well separated from conduction bands derived from *W5d* orbitals. The conduction bands are split into two groups with--using common notation *(1246)*--three bands arising from π-antibonding combinations of $W5dt_{2g}$ and *O2p* orbitals and, at higher energy, two bands arising from σ-antibonding $W5de_g$ and *O2p* orbitals. In stoichiometric WO_3, the *O2p* bands are filled and the conduction bands are empty. These notions have been corroborated and elaborated in subsequent bandstructure computations using a non-self-consistent Korringa-Kohn-Rostocker method applied to (hypothetical) cubic WO_3, a self-consistent non-relativistic atomic-orbital-based method applied to monoclinic and orthorhombic WO_3 *(520-1)*, and a self-consistent semi-relativistic linear muffin-tin method applied to cubic WO_3 *(699)*. The basic t_{2g} character of the conduction electrons has been clearly documented from two-dimensional angular correlated positron annihilation data taken on $Na_{0.64}WO_3$ *(46)*. In a strongly disordered material the energy band model is expected to remain valid as long as the molecular bonds are not severely disrupted *(2412)*. Now follows a review of experimental data for valence- and conduction bands in W-oxide-based films--as derived from XPS, ultraviolet photoelectron spectroscopy (UPS), X-ray fluorescence (XRF), and electron energy loss spectroscopy (EELS)--as well as a discussion of the current theoretical understanding of these data.

XPS spectra are considered first; they give information primarily on the occupied electron states. Figure 7.20 summarizes several sets of measurements, obtained by use of AlKα radiation with a half-width of less than 0.5 eV. Part (a), reproduced from Colton et al. *(745-6)*, refers to evaporated W oxide films in as-prepared state and after H^+ intercalation by use of H_2SO_4. The amount of intercalated species was not given, but the middle curve was taken on a lightly colored film with a moderate H^+ content, and the upper curve was taken on a deeply colored film with a high H^+ content. Figure 7.20(b) shows data due to Wertheim et al. *(3606)* for a W oxide layer prepared by oxidation of a single crystal (100) slice of tungsten followed by ion intercalation from aqueous NaOH or H_2SO_4 solutions. The three curves represent samples with H^+ contents --expressed as x in H_xWO_3--estimated to be ~0, ~0.3, and ~0.5. Figure 7.20(c) refers to evaporated films in as-deposited state and after Li^+ intercalation from 1 M $LiClO_4$ + PC to the shown charge densities; these data were reproduced from work by Hashimoto and Matsuoka *(1436-7)*. Finally, Fig. 7.20(d) was obtained by Hollinger et al. *(1519)* for an evaporated W oxide film in as-deposited condition and after UV irradiation. The four sets of data show a consistent pattern: A broad band lies between ~11 and ~3 eV, and a narrow peak--whose intensity increases in proportion with the amount of ion intercalation or the UV flux--occurs slightly below E_F. The latter peak is very weak in as-prepared unirradiated films. XPS spectra in qualitative agreement with those in Fig. 7.20 have also been reported in other work on H^+-intercalated evaporated films *(1470, 1952, 3590)* as well as in such films intercalated with Li^+, Na^+, K^+, Cs^+, and Mg^{2+} *(745-6, 1439, 1470, 3590)*. UPS applied to evaporated films indicated some minor changes in the valence electron spectrum depending on H^+ intercalation *(2432)*. Similar peaks have been found around E_F in XPS spectra for bulk $WO_{2.9}$, $WO_{2.72}$ *(1159)*, $H_{0.5}WO_3$ *(745-6)*, $Li_{0.34}WO_3$ *(3606)*, and Na_xWO_3 *(587, 664, 1513, 3606)*, as well as in UPS spectra for bulk Na_xWO_3 *(325-6, 1000, 1486, 1512, 1520, 1523)*, electron- or ion-irradiated (presumably non-stoichiometric) WO_3 *(489, 1085, 1087)*, and in as-deposited W oxide films *(1511)*. It is generally agreed that the main XPS feature at 11 to 3 eV is the *O2p*-dominated valence band, and that the reason for the peak closely below E_F is that *electrons--introduced in conjuction with the ion*

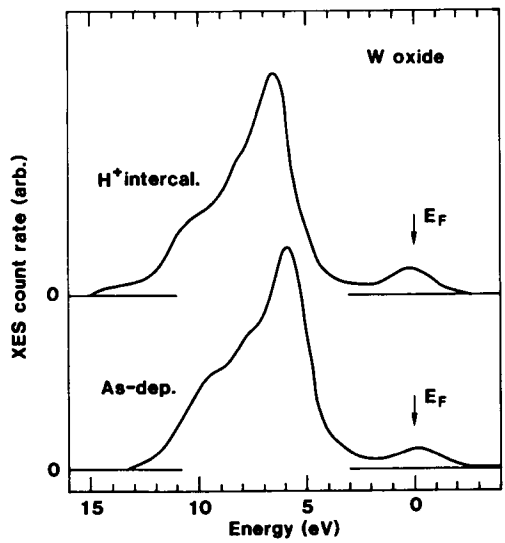

Fig. 7.21 XPS count rate vs. binding energy for valence- and conduction electrons in an evaporated W oxide film in as-deposited state and after H^+ intercalation. Arrows denote the Fermi energy E_F. From Kukuyev et al. *(1952)*.

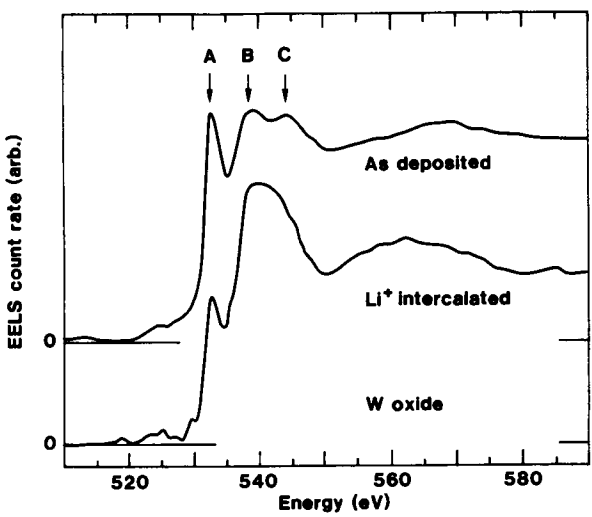

Fig. 7.22 EELS count rate vs. energy loss for evaporated W oxide films in as-deposited and Li^+ intercalated states. The data have been somewhat smoothed. Three features above the *O1s* edge are denoted by letters. From Hashimoto and Matsuoka *(1436-7)*.

intercalation or by some other means--occupy the otherwise empty lower part of the conduction band derived from *W5d* orbitals.

Hashimoto and Matsuoka *(1436-7)*, whose XPS data for Li^+ intercalated films were given in Fig. 7.20(c), measured the shift of the Fermi energy with regard to the *O2s* line (22.53 eV) for annealed WO_3 films. They noted a minor increase of E_F in proportion with the amount of Li^+ intercalation; at the highest charge density (19.6 mC/cm^2) the E_F shift was ~0.3 eV. The energy gap between the top of the valence band and the bottom of the small band at ~E_F seemed to remain constant during this shift.

Kukuyev et al. *(1952)* reported XRF spectra for evaporated W oxide films in as-deposited state and after H^+ intercalation by exposure to atomic hydrogen from a reaction between Zn and HCl. Figure 7.21, taken from this work, shows band features in overall agreement with those of the XPS spectra in Fig. 7.20. However, the XRF technique seems to lead to more resolvable structure on the high-energy flank of the *O2p* valence band and to show differences depending on the amount of H^+ intercalation. These effects were discussed in the light of recent bandstructure calculations *(520, 699)* and of features of model clusters having octahedral coordination *(505)*. It was argued that the H^+ intercalation leads to a decrease of the $W5d_\sigma$ - $O2p_\sigma$ interaction and an increase of the $W5d_\pi$ - $O2p_\pi$ interaction, but in the absence of corroborating evidence this conclusion should be regarded as preliminary.

Whereas the XPS and XRF techniques primarily mirror occupied states, the EELS technique can also give information on unoccupied states. EELS spectra were reported recently by Hashimoto and Matsuoka *(1436-7)* for evaporated oxide films in virgin state and after treatment in 1 M $LiClO_4$ + PC + 0.3 % H_2O. The zero-loss spectra of films in the two states were very similar and yielded structures due to core levels and plasmons. These assignments were made by comparison with earlier EELS data for 300 keV electrons transmitted through W oxide films *(2912)*, ≤ 0.5 keV electrons backscattered from films grown on single crystal W(100) surfaces *(923, 2011)*, and for ≤ 50 eV electrons backscattered from polycrystalline Na_xWO_3 samples *(1001, 1486)*. The *O1s* EELS spectra are more illuminating, though, and show clear differences for virgin and Li^+ intercalated films, as apparent from Fig. 7.21. The peaks denoted A, B, and C, that are clearly resolved for the as-deposited film, can be ascribed to losses due to transitions from the *O1s* level to empty states in the *W5d* conduction band. Peak A is strongly depressed in the Li^+ intercalated sample, which is consistent with a partial filling of the states slightly below E_F (cf. Fig. 7.20). Li^+ intercalation also leads to an apparent merging of the B and C peaks, which may indicate conduction band modifications of presently unknown character.

This Page Intentionally Left Blank

Chapter 8

TUNGSTEN OXIDE FILMS: ULTRAVIOLET ABSORPTION AND SEMICONDUCTOR BANDGAP

This chapter is the first one discussing optical properties of electrochromic films. It is convenient to introduce here the experimentally recorded quantities and the characteristics that are conveniently extracted from these.

The measureable optical properties are the transmittance T, reflectance R, absorptance A, and emittance E. Instead of giving the transmittance though a sample, it is common practice to state the *optical density* (OD) or *absorption coefficient (a)*. The latter two measures are related to the transmitted spectral intensity $I(\lambda)$ by

$$I(\lambda)/I_0 \approx e^{-a(\lambda)d} = e^{-OD(\lambda)}, \tag{8.1}$$

where I_0 is the intensity in the absence of any sample and d is the sample thickness. Equation 4.1 does not include reflection from the sample surfaces and thus is not fully quantitative. In chemical literature, optical density is sometimes referred to as "absorbance".

The materials of interest are characterized in terms of their complex refractive index $N = n + ik$, where n and k are known as the optical constants, or, alternatively, by the complex dielectric function $\varepsilon = \varepsilon_1 + i\varepsilon_2 = N^2$. The relation between a and k reads

$$a = (4\pi/\lambda)\, k. \tag{8.2}$$

Specifically, the present chapter covers the semiconductor bandgap in as-prepared films (8.1), explanations for the bandgap widening that occurs in very disordered films (8.2), logarithmic bandedges (so called Urbach tails) (8.3), and bandgap widening upon ion intercalation (8.4).

8.1 Semiconductor Bandgap in As-prepared Films

Data for evaporated W oxide films are considered first. Figure 8.1, taken from Deb's pioneering work *(836)*, shows optical density vs. wavelength in the $0.22 < \lambda < 0.4$ μm range at two thicknesses and three temperatures. The substrates (quartz) were kept at ~75°C during the film deposition. Generally speaking, the transmittance is lower the smaller the wavelength. The onset of low transmittance shifts towards a longer wavelength as the temperature goes up. In the thin film (d = 0.05 μm), some weak peaks in the OD appear at ~0.236 and 0.282 μm; they are most

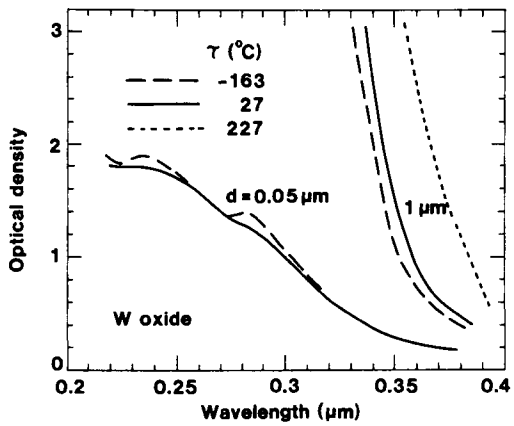

Fig. 8.1 Spectral optical density for evaporated W oxide films with two thicknesses d, as measured at three temperatures τ. From Deb *(836)*.

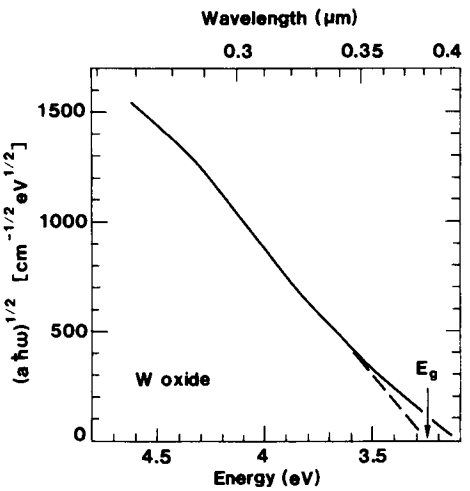

Fig. 8.2 $(\alpha\hbar\omega)^{1/2}$ vs. energy for an evaporated W oxide film. Dashed line indicates an extrapolation for determining the bandgap E_g. From Deb *(836)*.

prominent at low temperature.

The optical density data in Fig. 8.1 are indicative of absorption at the semiconductor bandgap E_g in W oxide. Quantitative values of E_g can be derived by applying a relation of the type

$$\hbar\omega a \propto (\hbar\omega - E_g)^{\eta} \tag{8.3}$$

in the spectral range where the absorption is strong. In Eq. 8.3, ω is angular frequency, $\hbar$ is Planck's constant divided by 2π, the exponent η depends on the kind of optical transitions that prevail, and thermal broadening is neglected. For crystalline semiconductors, η is 1/2, 3/2, 2, and 3 when the transitions are direct allowed, direct forbidden, indirect allowed, and indirect forbidden, respectively *(3203, 3658)*. In the case of an amorphous semiconductor, η should be 2 as a result of the non-conservation of wavevectors; under the latter condition one speaks of a "Tauc gap" *(3374-5, 3657)*.

Figure 8.2 shows a plot of a vs. $\hbar\omega$ from room-temperature data of the type shown in Fig. 8.1. It is seen that Eq. 8.3 is well obeyed in the $4.5 > \hbar\omega > 3.5$ eV interval when $\eta = 2$. A linear extrapolation according to the dashed line gives $E_g = 3.25$ eV.

There are several studies wherein bandgaps have been evaluated by plotting room-temperature data for $(\hbar\omega)^{1/2}$ as a function of $(\hbar\omega - E_g)$ and extrapolating towards zero absorption. For heavily disordered evaporated films one has found $3.2 < E_g < 3.4$ eV *(836, 877, 1312-3, 1322, 1737, 2340, 2480-1, 3116, 3206, 3683, 3744)*. E_g is temperature dependent and shrinks when the temperature is increased and rises when the temperature is lowered *(836, 2480-1)*, which is apparent from Fig. 8.1.

The bandgap depends on the materials preparation conditions and is diminished in films evaporated onto substrates at elevated temperature. Figure 8.3, plotted from data by Miyake et al. *(2340)*, shows a monotonic drop of E_g with increasing τ_s from the initial 3.25 eV to 2.7 eV at τ_s = 500°C. The decrease is strongest at $\tau_s > 300$°C, which indicates that crystallization is causing the bandgap narrowing. Data supporting those in Fig. 8.3 have been found in several investigations *(836, 1047, 1322, 1847, 2480-1, 3206)*. The background pressure during the evaporation appears to be another significant parameter, with reactive deposition leading to an enhancement of E_g *(1126)*; no detailed study of this phenomenon seems to be available, though.

For sputter deposition, most studies have reported $3.0 < E_g < 3.4$ eV, with a tendency that a high pressure of the sputter gas and a high O_2 admixture in reactive sputtering give a low E_g *(51, 1737, 1739-40, 1829, 2341-2)*; bandgaps up to 3.55 eV have been stated in some work, though *(1305-6, 2188)*. Crystallized films made by sputtering had $E_g = 2.9$ eV *(50, 1829)*. Films made by CVD showed a bandgap that decreased monotonically from 3.2 eV at $d \approx 0.1$ μm to ~2.5 eV at $d \approx 1$ μm *(825, 960-1)*, which was believed to follow from a thickness-dependent change in the crystallinity. For W oxide films made by anodizing, differing results have been reported with E_gs as widely apart as 3.05 and 3.73 eV being stated *(861-2, 933, 935, 941)*. Films with high E_gs had a hexagonal-like structure. Crystalline anodic films with monoclinic, triclinic, and orthorhombic structure and different degrees of hydration had $2.55 < E_g < 2.79$ eV as seen from photoelectrochemical measurements *(933, 3296)*.

The bandgaps for crystallized films are consistent with data for bulk samples, and a detailed study by Koffyberg et al. *(1872)*, based on photo-electrochemical measurements, gave $E_g = 2.62 \pm 0.04$ eV for indirect transitions and E_gs equal to 3.53 ± 0.02 eV and 3.74 ± 0.03 eV for direct transitions. These bandgaps are in general agreement with results of other work using photo-

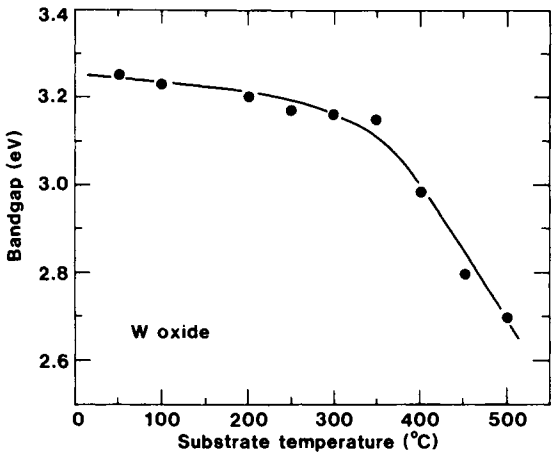

Fig. 8.3 Bandgap for W oxide films evaporated onto heated substrates. After Miyake et al. *(2340)*.

electrochemical technology *(573-5, 1190, 2505, 2970)*, diffuse optical reflectance *(748, 1110, 1407, 2794)*, photoacoustic measurements *(2038, 2167)*, and transmittance through single crystalline platelets *(353, 1542, 1648, 2976, 3070)*. Detailed bandstructure calculations for the monoclinic structure gave $E_g = 2.4$ eV *(520)*.

8.2 Bandgap Widening in Disordered Films: Possible Explanations

It is an interesting empirical fact that the bandgap can be larger in the strongly disordered state than in the (monoclinic) crystalline state. The enhancement can be as much as 0.5 to 0.6 eV. Possible reasons for this effect are discussed here.

Structural transformations may conseivably be at the root of the bandgap widening, and such transformations could account for an increase of E_g by 0.2 to 0.3 eV when WO_3 crystals were cooled to temperatures below -50°C *(1542, 1648)*. A somewhat smaller increase was found in *(2978)*. Vapor deposited W oxide films are composed of clusters with hexagonal-like lattice order, as discussed in Sec. 3.8, and it is possible that the bandgap of this hexagonal material is larger than that of the monoclinic structure to a sufficient extent to account for at least a good part of the bandgap widening in the disordered films. Some wide bandgaps stated for hexagonal-like anodic films *(861-2)* are consistent with this view. Unfortunately, there do not seem to be any measurement of E_g for hexagonal bulk crystals, which could have verified or refuted this suggestion.

Quantum confinement in semiconductor clusters offers an alternative, and more fundamental, explanation for the bandgap widening in the disordered state. This effect has been discussed extensively in recent literature *(1458, 1927-8, 3574, 3594-5)*. The net effect on E_g is a widening due to the particle-in-a-box quantum localization energy *(998, 1002)*, which is partly balanced by Coulomb repulsion *(501)* and electron correlation *(1714)*. Experimental studies on clusters of PbI_2, PbS, CdS, ZnS, and ZnO, and of porous Si, have shown a widening of E_g by as much as 1 eV when going from the bulk to ~3 nm particle size *(1723, 2562, 2964, 3358-9, 3573, 3575, 3596, 3801, 3813)*; this is in reasonable agreement with theoretical predictions. Quantum confinement can also lead to multiple absorption peaks at energies higher than E_g *(1002, 1262, 1448, 1956, 3359, 3362, 3512, 3574, 3593)*. It is noteworthy that such peaks were indeed observed by Deb *(836)*, as illustrated in Fig. 8.1. They cannot be ascribed to direct optical transitions, since the peak energies are not the ones expected *(1872)*. Any assignment of the absorption peaks to quantum confinement is highly speculative, though, since the experimental data is very scanty. The possibility that quantum confinement contributes to the widening of E_g at small grain sizes was pointed out by Green and Hussain *(1313)*.

A different approach to bandgap widening is based on a well known semi-empirical relation between refractive index and bandgap, stating that

$$n^4 E_g \approx \text{constant} \ , \tag{8.4}$$

where the constant is ~95 eV. This is commonly referred to as the "Moss rule" *(2403-7)*. According to this "rule", a lowering of n--for example by enhanced porosity in the disordered state--tends to increase E_g. This tendency is clearly consistent with experimental evidence. A relation with clear resemblance to Moss's rule was put forward by Ravindra et al. *(1361, 2858)*.

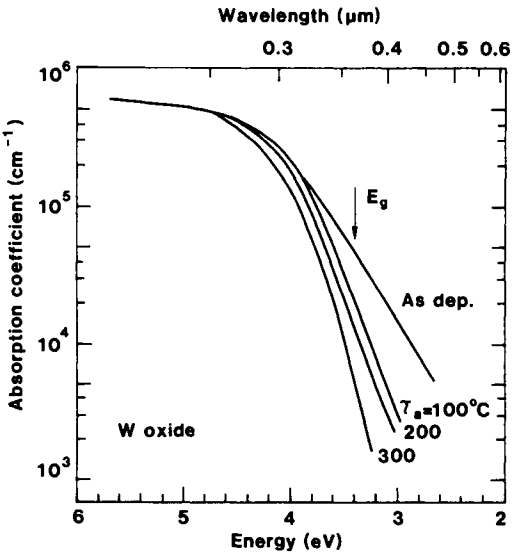

Fig. 8.4 Absorption coefficient vs. energy for W oxide films in as-deposited state and after annealing to the shown temperatures τ_a. The bandgap E_g of the as-deposited film is indicated by the arrow. After Nakamura et al. *(2480-1)*.

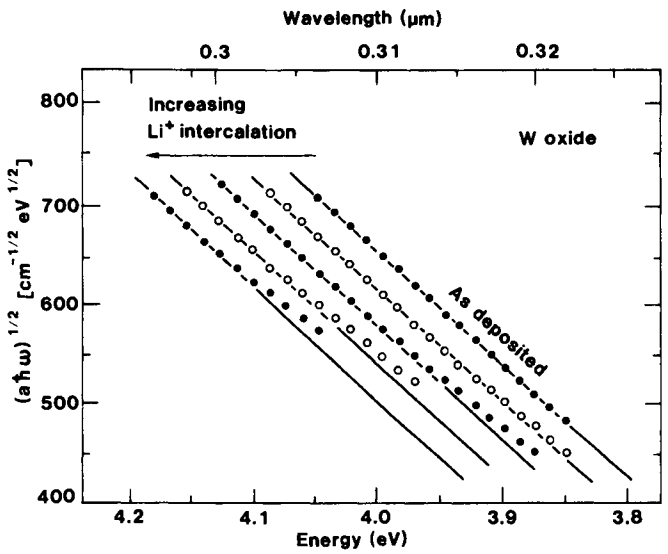

Fig. 8.5 $(a\hbar\omega)^{1/2}$ vs. energy for an evaporated W oxide film with different amounts of Li^+ intercalation. Filled and open circles represent measured values and lines are fits to determine E_g from Eq. 8.3 with $\eta = 2$. After Nakamura et al. *(2480-1)*.

Equation 8.4 can be justified from an electron band model, as elaborated by Finkenrath *(1075-8)*.

8.3 Urbach Tails

Equation 8.3 is not obeyed around the semiconductor bandgap, but instead the absorption can be represented by a logarithmic dependence according to

$$a \propto \exp\left[\Gamma(\hbar\omega - \hbar\omega_0)\right] , \tag{8.5}$$

where Γ and ω_0 are constants. This effect is not caused by thermal broadening but is a fundamental property, known as the Urbach effect *(967, 1538, 1963, 3491)*. Figure 8.4, from Nakamura et al. *(2480-1)*, shows that Eq. 8.5 describes the bandgap tail quite accurately for $a < 10^4$ cm^{-1}, and that Γ depends on the annealing temperature to some extent. Curves similar to those in Fig. 8.4 have been given elsewhere too *(836, 1047, 1313)*. The Urbach tailing effect has been reported for many semiconductors and glasses, and several explanations have been put forward *(981, 1678, 1848, 3519)*. Among these explanations one may note work by Redfield *(968, 2872-3)* who considered the role of electric microfields caused by ionized lattice defects and ensuing excitonic effects, work by Skettrup *(3185)* who regarded bandgaps within "cells" whose size is governed by the phonon coherence length and for which the number of phonons is given by Bose-Einstein statistics, and work by Sumi and Toyosawa et al. *(3064, 3272)* who focused on excitons. Recently a general approach to the Urbach effect--based on the density of electron states in a random three-dimensional potential--was forwarded by John et al. *(1678)*. This latter work was subsequently extended towards detailed computations for self-trapped small polaron states *(1327, 1687)*. The change in Γ inherent in Fig. 8.4 may thus be connected with a change in the disorder and of small-polaron localization, but no definitive conclusions can be drawn on this matter. Measurements of logarithmic band edges in W oxide films kept at different temperatures did not indicate any noticeable change in Γ, which seems difficult to reconcile with available theories.

8.4 Bandgap Widening upon Ion Intercalation

Only a few investigations have been reported concerning the effect of ion intercalation on E_g. This is regrettable since bandgap shifts, at least in principle, carry information that is very relevant to theoretical interpretations of electrochromism. Nakamura et al. *(2480-1)* studied evaporated films in H_2SO_4 and $LiClO_4$ + PC electrolytes and found that E_g was widened in proportion with the amount of ion intercalation. Figure 8.5 illustrates the energy dependence of $(a\hbar\omega)^{1/2}$ in the same way as in Fig. 8.2 and shows that E_g can be increased by as much as ~0.15 eV. An analogous study of H^+ intercalation gave a bandgap widening of up to ~0.05 eV. The quantity of intercalated ionic species was estimated from the electrochromic absorption band in the near infrared, which will be discussed shortly. This can give only a semiquantitative measure of the ionic content. No clear bandgap widening was observed upon H^+ intercalation in some CVD-produced films *(3536)*. Green et al. *(1312, 1322)* prepared films with different degrees of crystallinity by coevaporation of WO_3 and Na from separate sources. Representing the material as Na_xWO_3, it was seen that E_g increased monotonically from 3.25 to ~3.42 eV when x went from zero to 0.05, and that E_g appeared erratic for $x > 0.05$. Evaporated H_xWO_3 films yielded $3.06 < E_g < 3.32$ eV for $0 < x <$

0.14 *(1313)*. Delichere et al. *(861-2, 1030)* studied Li^+ intercalation into anodic W oxide films with hexagonal structure. $Li_{0.13}WO_3$ showed an increase of E_g by ~0.1 eV relative to the unintercalated material, and E_g was enhanced by ~0.25 eV at "maximum" Li^+ content. In contrast with the data mentioned above, recent results by Berera et al. *(355)* on lithiated crystalline W oxide prepared by rf sputtering indicated some bandgap narrowing as a consequence of the Li incorporation.

The E_g enhancement upon insertion of ions and electrons, found in most experiments, has been interpreted in terms of a partial filling of the conduction band so that the lowest electron states are blocked *(1322, 2481)*. Nakamura and Yamada *(2481)* assigned the bandgap widening to the Burstein-Moss effect *(569, 2405)*, which presupposes a parabolic and rigid conduction band. This cannot be the full story behind the widened E_g, though, since the Burstein-Moss shift is at least partly balanced by many-body effects due to electron-ion and electron-electron scattering *(18, 358, 692, 1401, 3099a)*, and also structural changes accompanying the ion intercalation/deintercalation can have a significant effect on E_g. A detailed analysis of E_g shifts associated with ion insertion in W oxide films remains a topic for future study.

Chapter 9

TUNGSTEN OXIDE FILMS: OPTICAL PROPERTIES IN THE LUMINOUS AND NEAR-INFRARED RANGE

This is a key chapter of the present book. Optical properties are discussed with regard to the $0.4 < \lambda < 2$ μm interval; this lies in between the spectral range where the absorptance is strong due to excitations across the semiconductor bandgap, and the range where molecular vibrations cause absorption. The interval includes the spectral sensitivity of the eye (cf. Fig. 1.4) as well as most of the solar spectrum (cf. Fig. 1.6) and is therefore of central importance for almost all applications of electrochromic materials. Bearing this in mind, it is natural that there is a vast amount of published data on spectral transmittance, reflectance, and absorptance. As-prepared films are treated first with discussions of spectral absorptance (9.1) and refractive index (9.2). The films can be colored by ion intercalation and accompanying electron insertion, as well as by several other techniques, as surveyed in (9.3). The coloring corresponds to a near-infrared absorption peak, whose location depends on the crystallinity (9.4). Transmittance and reflectance of ion intercalated films are discussed in (9.5), followed by an exposition of the optical constants of such films (9.6). Coloration efficiency--being the property of primary relevance for most applications--is discussed in detail in the final section (9.7).

9.1 Spectral Absorptance of As-prepared Films

The spectral absorptance depends critically on the film preparation, and both non-absorbing and strongly absorbing states can be obtained. The absorption can be ascribed to non-stoichiometry and is associated with built-in charge, as discussed below. Irrespective of their initial properties, the films may be useful in electrochromic devices.

Evaporated films are considered first. Figure 9.1, reproduced from Gabrusenoks et al. *(1126)*, shows spectral optical density pertinent to two different preparation conditions. Solid and dashed curves refer to evaporation under low (~0.8 mTorr) and high vacuum, respectively. Low-vacuum evaporation gives a film that is essentially non-absorbing at $3 > \hbar\omega > 0.5$ eV, whereas high-vacuum evaporation--or evaporation at high rate--leads to a broad and distinct absorption band centered at ~1.2 eV. Absorption bands of this general type are responsible for the electrochromism, as discussed at length below. The figure also shows strong absorption for energies above ~3 eV due to excitations across the semiconductor bandgap. Measurements analogous to those in Fig. 9.1 have been reported several times; in some work a small absorptance peak was reported at 1.4 to 1.2 eV *(817, 884, 1152, 1894, 3783)*, whereas no such peak could be discerned in other work *(745,*

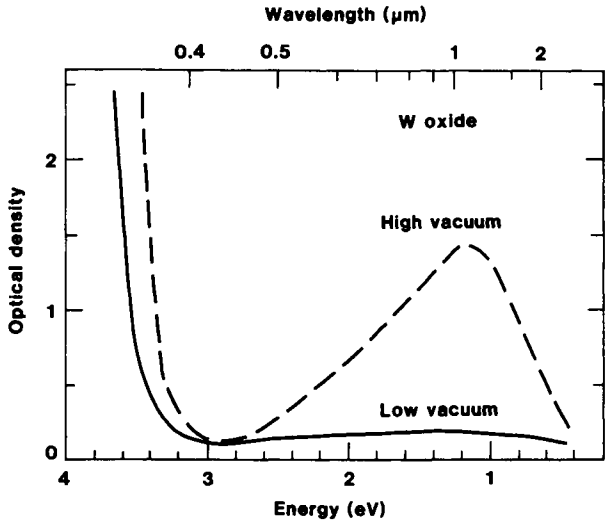

Fig. 9.1 Spectral optical density for W oxide films evaporated under two different vacuum conditions. After Gabrusenoks et al. *(1126)*.

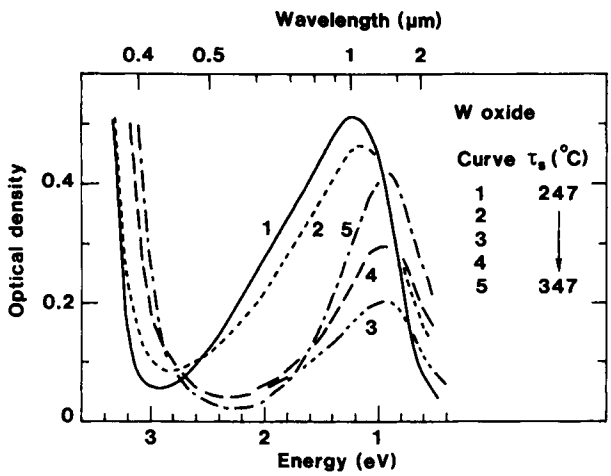

Fig. 9.2 Spectral optical density for W oxide films prepared by evaporation onto substrates at different temperatures τ_s. The variously designated curves 1 through 5 refer to increasing temperatures in the range from 247 to 347°C. From Cikmach et al. *(708)*.

836, 1150, 1728, 1842, 1953, 2393, 2476). Even if the deposition conditions were incompletely characterized in many cases, there is a clear tendency that evaporation at a pressure above 10^{-5} Torr and at $\tau_s < 300°C$ does not lead to any absorption peak. The role of the residual gas pressure was studied by Morita and Washida *(2397)*, who measured optical absorption in the $3.1 > \hbar\omega > 1.4$ eV range. Pundur et al. *(2816)* made a connection between absorption peaks in the near-infrared and built-in charge. This connection will be clarified below. Resonant absorption in discontinuous W oxide films backed by silver was studied in *(158)*.

The substrate temperature is an important parameter for the near-infrared absorption band, and it is interesting to follow the evolution of this band as τ_s is increased monotonically through the range where crystallization occurs, i.e., around 300°C (cf. Fig. 3.15). Figure 9.2, taken from Cikmach et al. *(708)*, reports data for a film evaporated onto an extended substrate across which a temperature gradient was maintained. At $\tau_s \approx 247°C$ one observes an absorption peak at ~1.2 eV, similar to the dashed curve in Fig. 9.1. For higher substrate temperatures there is an initial decrease of the absorption peak followed by an increase, and the peak location displays a concomitant change to ~0.9 eV. Clearly the energy shift of the absorption peak, which takes place at the same time as E_g is diminished, indicates that crystallization occurs. Post-deposition annealing can give a strong absorption peak at ~0.9 eV, as will be discussed below.

As-sputtered films can show different optical properties depending on the deposition conditions, which is clearly illustrated in Fig. 9.3 with regard to the spectral absorption coefficient. The data are replotted from Deneuville and Gérard *(884)* who prepared films by rf sputtering from W as well as WO_3 targets in Ar + O_2 mixtures and determined the oxygen non-stoichiometry through RBS. The absorption is rather weak across the full $2 > \hbar\omega > 0.5$ eV range when $z = 0.40$. For larger non-stoichiometry, the absorption goes up and displays a broad peak centered at ~1.2 eV at least as long as the non-stoichiometry is not too large. Approximately the same peak position was found earlier for heavily disordered evaporated films. An absorption band whose intensity depends on the deposition conditions can be inferred also from transmittance spectra reported by Kaneko et al. *(1737-8, 1740, 2341-2)* for films made by rf sputtering of W in Ar + O_2 gas mixtures having various compositions and pressures. A near-infrared absorption band was found in *(3170)*, whereas no such feature could be seen in *(806, 817)*.

There are some scattered optical data for W oxide films produced by electrochemical and chemical techniques. Thus anodic layers, characterized by a hexagonal structure and a wide bandgap, showed a weak and broad absorption feature around ~1.5 eV *(861-2)*. Films made by decomposition of oxalatotungstate compounds had an absorption peak at ~1.4 eV; this feature disappeared gradually during annealing and could not be detected in films treated at $\tau_a \approx 280°C$ *(1117, 3313)*. No such absorption was apparent in some films made by CVD *(824)*, sol-gel deposition *(669)*, and alkoxide technology in conjunction with spin coating *(3715)*.

9.2 Refractive Index of As-prepared Films

This section moves from qualitative to quantitative optical properties and considers the refractive index n, which has been determined primarily for films made under conditions that do not lead to strong absorption in the near infrared. The refractive index can be computed from measured transmittance and reflectance by use of Fresnel's relations, and many evaluation schemes are available *(450, 1451, 2692, 3577)*.

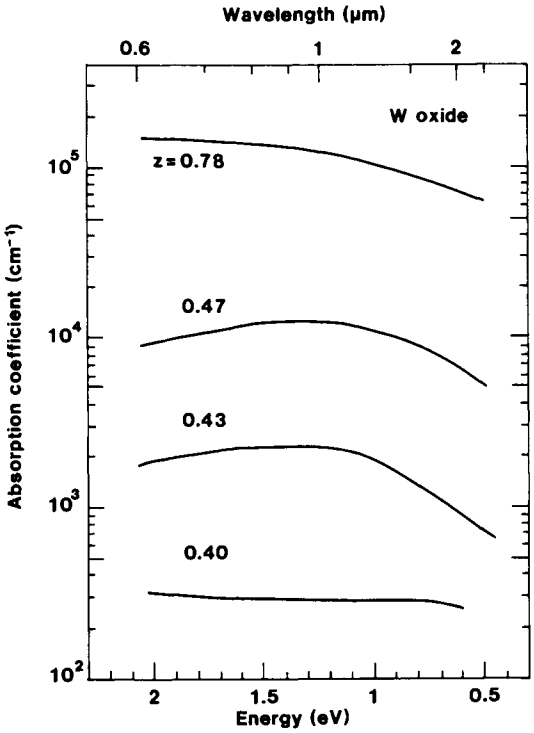

Fig. 9.3 Spectral absorption coefficient for non-stoichiometric W oxide films, denoted WO_{3-z}, prepared by reactive sputtering. From Deneuville and Gérard *(884)*.

Evaporated films are considered in Fig. 9.4(a), showing data reported by Deb *(836)*, Faughnan et al. *(1047)*, and Ottermann et al. *(2670)*. It is seen that n displays pronounced dispersion with a magnitude that is larger the shorter the wavelength. For the mid-luminous range, n lies around 2 to 3. Spectral data in general agreement with those in Fig. 9.4(a) can be found in several places *(627, 877, 1313, 1322, 2245, 3744)*. The role of τ_s on the refractive index was studied by Miyake et al. *(2340)* who found, surprisingly, a drop of n at the highest substrate temperatures.

The spread in the reported refractive indices is large for evaporated W oxide films, as evinced by Fig. 9.4(a). Increased porosity has the effect of lowering n, and hence different evaporation parameters can explain some of the variation. Nevertheless, the spread in n is considerably larger than one might have expected, and it is not impossible that some of the evaluated data are wrong. It may be of relevance to observe that early work on evaporated Mo oxide films *(834, 843)*, reporting high refractive indices and strong optical dispersion, was subsequently criticized *(3470)*, and it was argued that the original evaluation had been done incorrectly. Mo oxide films will be discussed in Sec. 12.9 below.

Green *(1305-6)* reported n for films made by reactive dc magnetron sputtering; his data are reproduced in Fig. 9.4(b). The refractive index is about 2, with a tendency that an increase in τ_s lowers n. Other work on reactive dc sputtering gave films with similar refractive indices *(627, 878, 2037, 2188-91, 2245)*. Marszalek et al.*(2188-91)* used a special theoretical technique *(3303)* to separate the refractive indices pertinent to the outer and inner film surface; for strongly disordered films the two indices were very similar, but for crystalline films the outer surface could have a refractive index of ~2.6, while the inner surface had a refractive index of ~2.3. The relation between n and O_2 gas flow in large-area dc magnetron sputtering was assessed by Howson et al. *(392-3, 1555)*. Films made by reactive rf sputtering had refractive indices between 2.1 and 2.5 depending on deposition parameters and wavelength *(51, 627, 1228, 1230-1, 1737, 1739-40, 1829, 2291, 2342)*. Specifically, ellipsometric measurements by Goldner et al. *(1228, 1230-1, 2291)* yielded $n \approx 2.5$ at $\lambda = 0.564$ μm, and $n \approx 2.25$ at $\lambda = 0.633$ μm.

Anodic films showed widely different refractive indices depending on the preparation conditions. Thus galvanostatically produced films had $n \approx 2.18$ at $\lambda = 0.633$ μm as found from ellipsometry *(307, 2637, 2639, 2642, 2653)*, high-voltage potentiostatic anodization--leading to hexagonal-type crystalline films--had $n \approx 2$ *(861-2, 1030)*, and low-voltage potentiostatic anodization leading to extremely porous surface layers had $n \approx 1.64$ *(2584)*. Anodic films can show optical anisotropy *(2649)*.

CVD-produced W oxide films were studied in some detail by Donnadieu et al. *(820, 960, 3536)*. The refractive index showed strong dispersion and was dependent on the preparation conditions and the film thickness. Figure 9.4(c) shows a typical spectral refractive index (for a 0.319-μm-thick film annealed in O_2 at 500°C). There is an apparent similarity to the results for evaporated films. The data by Davazoglou and Donnadieu *(820)* were further analyzed by Toyoda *(3434)* and by Donnadieu et al. *(822, 2874)* who parameterized the spectral dependence of the refractive index in terms of a single-oscillator energy and a dispersion energy, following Wemple and Di Domenico *(3600-1)*.

Sol-gel-produced films had refractive indices similar to those for evaporated ones *(627)*. Films made by decomposition of an oxalatotungstate compound were very porous and had $n \approx 1.55$ at $\lambda = 0.633$ μm *(1117)*. Thermally oxidized tungsten surfaces showed thickness dependent refractive indices *(2962)*; such surfaces have also been assessed with regard to the thermal infrared

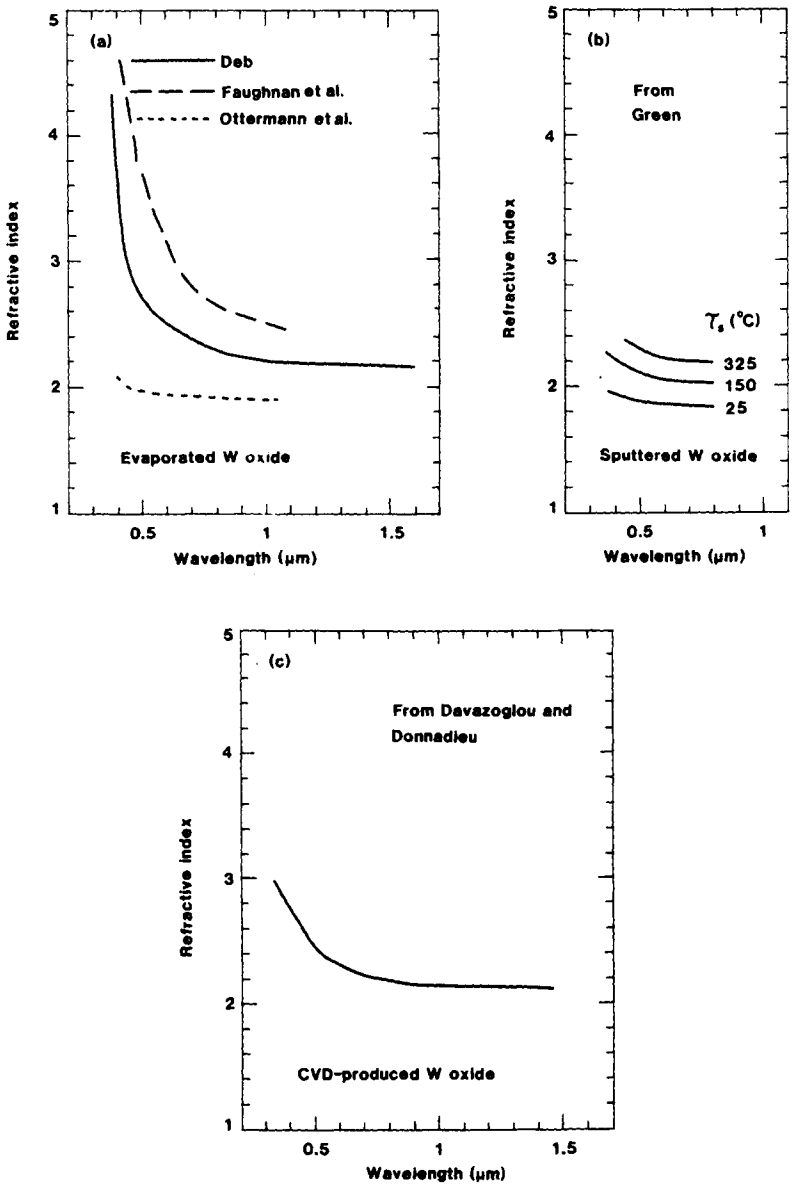

Fig. 9.4 Spectral refractive index for W oxide films made by (a) evaporation, (b) sputtering onto substrates at the shown tempratures τ_s, and (c) CVD followed by annealing post-treatment. After Davazoglou and Donnadieu *(820)*, Deb *(836)*, Faughnan et al. *(1047)*, Green *(1306)*, and Ottermann et al. *(2670)*.

range *(2760-4)*.

Obliquely evaporated W oxide films, briefly discussed in Sec. 3.9, have an inclined columnar structure that depends on the deposition angle α. It is hence reasonable to expect a relation between n and α. According to Motohiro and Taga *(2410)*, n goes down when the α goes up, the effect being of the order of 0.2 when α increases from 50 to 75°. The obliquely evaporated films are birefringent *(946, 1515, 2245, 2520, 3199, 3200)*, i.e., they have different refractive indices with regard to the propagation of the ordinary and extraordinary rays. The difference between the refractive indices, denoted Δn, depends on α *(2410, 3320)*. As seen from Fig. 9.5, an increasing angle α leads to an increase of Δn, a peak value on the order of 0.05 for $\alpha \approx 70°$, and a drop of Δn at very large angles. The magnitude of Δn depends to some extent on the substrate temperature during the evaporation, and a decrease of Δn by ~0.01 was noted when τ_s went from ~50 to ~400°C *(2409-10)*.

9.3 Coloration Techniques for Disordered Films: The Eightfold Way

Electrochromism takes place upon simultaneous insertion of ions and electrons in a film having contact with an electrolyte in liquid or solid form. This coloration technique is of great technological interest, and it has been presumed in most of the earlier treatment. However, there are several other coloration techniques, and it is advisable to survey all of them jointly since they then shed light on much of the basic physics and chemistry that underlies the optical properties and hence pave the way towards subsequent theoretical analyses. Figure 9.6(a)-(h), which much of this section will revolve around, illustrates eight different ways to color disordered W oxide, as well as examples of the ensuing optical properties. The data pertain to evaporated films, except those in Fig. 9.6(e) that were measured for sputter-deposited films. The plots give either the absorption coefficient or the optical density; the latter can be viewed as an uncalibrated absorption coefficient. Already at the outset one can observe that all of the coloration techniques lead to broad and intense absorption bands peaked at an energy E_p between 1.5 and 0.9 eV. Still other ways to produce color in W oxide are by choosing an appropriate deposition rate, vacuum during the deposition, and substrate temperature; these latter parameters were discussed in Sec. 9.1 above. The absorption is stronger for red light than for blue light, and hence the colored W oxide films have a bluish appearance. Crystalline W oxide films are capable of modulated reflectance, as discussed later.

Figure 9.6(a), reproduced from Yamada et al. *(3685-6)*, shows the evolution of the spectral absorption coefficient when a charge density ΔQ is introduced into a W oxide film backed by ITO-coated glass through *ion intercalation from an electrolyte* of 1 M H_2SO_4. An absorption band centered at ~1.3 eV increases monotonically upon increased ΔQ and reaches a maximum of ~10^5 cm^{-1}. Quantitative assessments of a vs. ΔQ will be dealt with later, and at the moment only the general shapes of the absorption bands are of interest. Data in good agreement with those in Fig. 9.6(a)--showing E_p in the range 1 to 1.5 eV--have been found in numerous studies on evaporated films, specifically for H^+ intercalation *(116, 292, 651-2, 745, 1313, 1501, 1826-9, 2480-1, 3050, 3286, 3645, 3808)*, Li^+ intercalation *(1437, 1439, 1607, 1728, 1827, 1865, 2393, 2480-1, 3057, 3744)*, combined $H^+ + Li^+$ intercalation *(3704, 3707)*, Na^+ intercalation *(1858)*, and for Na incorporation by coevaporation with W oxide *(1322)*.

Analogous results have been reported for H^+, Li^+, and Na^+ intercalation in sputter-deposited films *(51, 806, 817, 1320, 1743, 3170)*, for H^+ intercalation in CVD-produced films *(960-2)*,

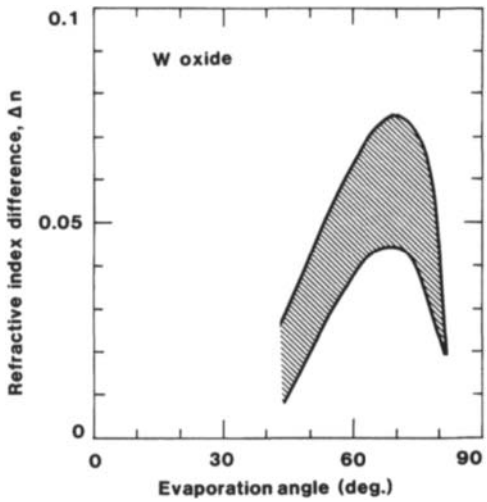

Fig. 9.5 Refractive index difference Δn vs. evaporation angle for birefringent W oxide films prepared by oblique angle evaporation. The shaded band represents numerous scattered data points. After Motohiro and Taga *(2410, 3320)*.

and for Li^+ intercalation in sol-gel-derived films *(669)*. Some Li^+ intercalated films made by PECVD had an E_p as high as ~1.7 eV *(3283)*. At very large Li^+ contents, the absorption may decrease upon further lithiation *(159, 1439, 1728, 2368)*.

Figure 9.6(b) shows another way of coloring W oxide by an electric current. This technique, here termed *electrocoloration*, was first used by Deb *(835-6, 838)* who applied an electric field of ~10^4 V/cm along a ~1-μm-thick evaporated film through the use of gold electrodes. The technique was also studied by Thomas and Lloyd *(3405)*. Coloring originated at the cathode and propagated during the course of hours towards the anode. Moisture and elevated temperature led to more rapid dynamics. On field reversal, the colored region migrated toward the anode and, seemingly, disappeared into it. The coloration and bleaching could be repeated many times. Figure 9.6(b) shows that the coloration is associated with an absorption band around 1.3 eV.

Coloration under *UV irradiation* is illustrated in Fig. 9.6(c). This again is a technique that was first applied to W oxide by Deb *(836, 838)*. Coloration occurs with radiation having photon energies exceeding E_g and is most efficient for highly disordered films exposed to photons whose energy is ~4 eV *(836)*. High-pressure Hg and Xe lamps are suitable for the irradiation. Data from work by Gavrilyuk et al. *(1150, 1152)* are shown in Fig.9.6(c); they refer to 1.8-μm-thick evaporated films in the presence of ordinary air or methanol vapor. Irradiation in air gave a rather weak absorption feature peaked at ~1.3 eV; its magnitude was comparable with the one reached by electrocoloration *(836)*. When vapor of methanol (or ethanol, formic acid, etc.) was present, the absorption could be strongly enhanced, but it was not as strong as that obtainable by proton intercalation from an electrolyte *(1150)*. The absorption was particularly strong when the films were highly porous *(2459)*. For crystalline W oxide films, it appears that texture influences the ease by which UV coloration can take place *(1150)*. The coloration is the result of photocatalytic decomposition of the vapor accompanied by proton insertion. The latter point was verified by NRA *(1145)*. Optical data in good agreement with those shown in Fig. 9.6(c) have been reported for evaporated films *(708, 836, 838, 844, 884, 1146, 1802, 2476-7, 2539, 2766a)*, sputter-deposited Ta-doped films *(884)*, and for films made by sol-gel techniques *(2098, 3715)*. The relation between the UV induced coloration and the gas composition was studied by Yao et al. *(3717, 3719)*. According to Cikmach et al. *(708)*, the weak coloration accomplished by evaporation onto a heated substrate (cf. Fig. 9.2) could be strongly enhanced by UV irradiation in the presence of a hydrogen-containing vapor. Ohtani et al. *(2582)* reported UV coloration of W oxide films overcoated with Ti oxide and in contact with an aqueous formic acid solution. Hybrid films composed of W oxide and polyethylene glycol were capable of enhanced UV coloration *(1938)*. Structural data for UV colored films were reported in Fig. 7.6. Bleaching of UV irradiated films can be performed by exposure to a strongly oxidizing agent such as ozone *(836)*. UV radiation can also be used for rejuvenating W oxide films that have undergone many intercalation/deintercalation cycles in an electrolyte *(1851)*.

Figure 9.6(d) refers to coloring upon annealing in vacuum, here called *thermocoloration*. The shown data stem from Kukuev et al. *(1953)* who studied films annealed in vacuum for 15 minutes at 300°C. The thermochromism is associated with a strong peak in the absorption coefficient at ~1.2 eV. Similar absorption features were reported elsewhere too *(884, 1126)*. The coloration is accompanied by built-in negative charge *(1953)*. It is obvious that thermocoloration has a strong resemblance to the coloration upon deposition onto heated substrates discussed above (cf. Fig. 9.2).

Coloring can be produced by *exposure to atomic hydrogen* (H^o) obtained, for example, by

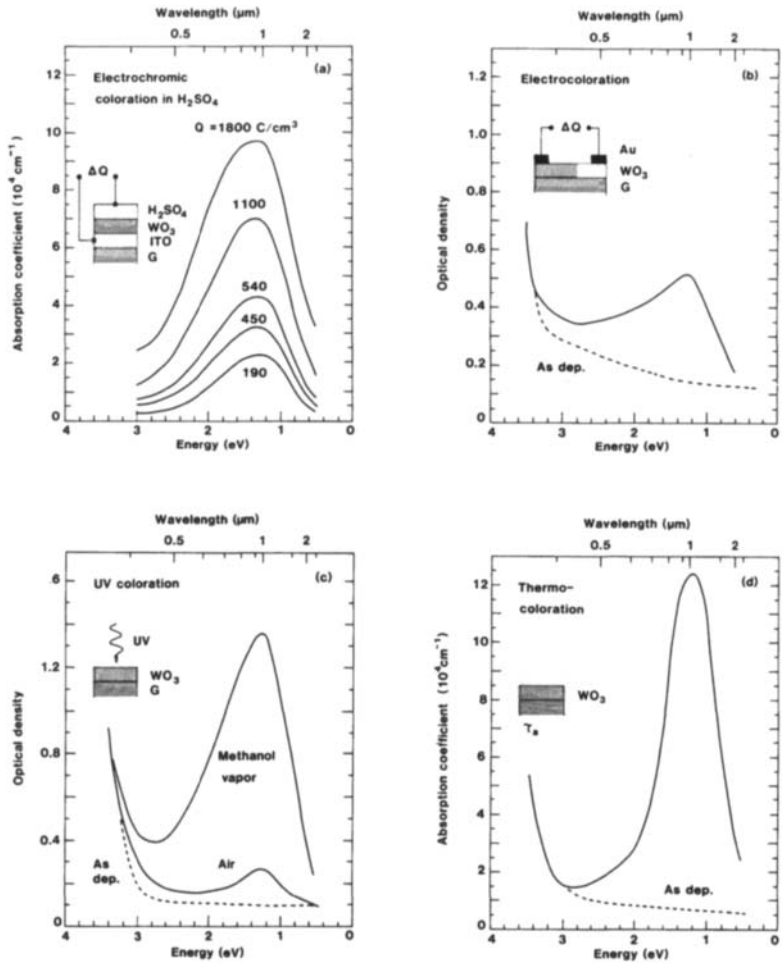

Fig. 9.6 (a-d) Spectral absorption coefficient, or spectral optical density, for W oxide films colored (a) *electrochemically* by insertion of different charge densities ΔQ in a configuration with a film backed by glass G coated with In_2O_3:Sn (i.e., ITO) and immersed in H_2SO_4; (b) by *electrocoloration* with charge insertion between gold electrodes; (c) by *UV irradiation* in the presence of different gases; (d) by *thermocoloration* after annealing at a high temperature τ_a; (e) by *introduction of atomic hydrogen* H° evolved from a HCl + Zn mixture so that films with a schematic composition H_xWO_3 were produced;

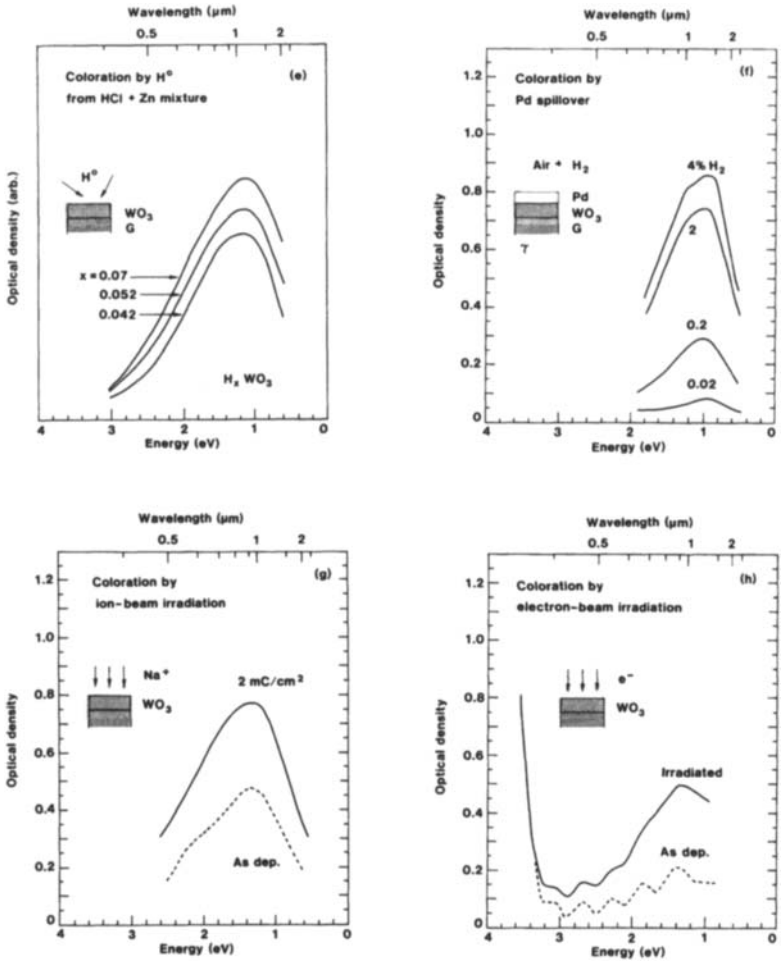

Fig. 9.6 (f-h) (f) by "*spillover*" in Pd-covered films exposed to air with different H_2 contents and kept at elevated temperature τ; (g) by *ion-beam irradiation* to the shown dose; and (h) by *e-beam irradiation*. The films were prepared by evaporation, except those in part (e) which were made by sputtering. Data for colored (as-deposited) films are indicated by solid (dashed) curves. The various coloration techniques are indicated in the insets. References are given in the main text.

mixing HCl and Zn. In fact, W oxide can serve as an indicator for atomic hydrogen at $\tau < 400°C$ *(2287-90, 3376)*. Figure 9.6(e), obtained from Wittwer et al. *(3645)*, shows optical density for sputter-deposited films whose proton content is given, roughly, by a value x in H_xWO_3. The peak in OD lies at $E_p \approx 1.2$ eV. A similar result was reported for evaporated films by Faughnan and Crandall *(1046)*. As an alternative to the HCl + Zn technique, H^o can be produced in a microwave discharge *(1313, 1360)*.

In a somewhat related coloration technique, H_2 gas is brought in contact with a thin Pd layer on top of a W oxide film. The Pd serves to catalytically decompose the H_2, and proton insertion takes place *(350, 460, 1510)*. One may speak of coloration by *Pd spillover* or, alternatively, of "hydrochromism". Figure 9.6(f), taken from work by Ito and Kubo *(1640)*, shows optical density for an evaporated W oxide film with a thickness of a few μm coated with a semi-transparent Pd layer. The W oxide film was evaporated onto a substrate at 250 to 300°C and was subsequently annealed in O_2. When the Pd/WO_3 tandem layer was in contact with air and H_2, a near-infrared absorption band developed; its strength went up monotonically for increasing H_2 content. The peak lies at ~0.95 eV--i.e., at a lower energy than for the earlier studied samples--which is due to the crystalline character of the films. The data in Fig. 9.6(f) were recorded at 71°C, and the coloration was less intense at lower temperatures *(1640)*. Faster coloration dynamics upon hydrogen exposure was accomplished recently in devices incorporating Pd- or Pt-covered microcrystalline hydrated W oxide films prepared by high-voltage anodization *(1641)*. Coloration by Pd spillover into W oxide films has also been reported in other work *(1168, 1845-6, 3194)*. Spillover from the hydrogen storage material $LaNi_5$, though a metal or oxide layer, into a W oxide film was used to assess hydrogen permeability of the metal or oxide layer by visual inspection *(23-4, 3151)*. Spontaneous bleaching of H^+ intercalated W oxide films can be accomplished by coating them with Pd *(1313)*; this effect may be termed "Pd spillout". One could observe in this context that porous Pd layers with very high optical transmittance can be prepared by slow photo-electrodeposition *(850)*, and that transparent films of the catalytically active metals Pt, Re, and Rh can be produced analogously *(850, 1456, 2793)*. Very thin discontinuous or semi-continuous Pd films were studied in *(1950)*.

Ion beam irradiation offers a direct way of introducing ions in W oxide films. Figure 9.6(g) shows results from Koshida and Tomita *(1894)* for a 0.32-μm-thick film, evaporated under conditions that led to a moderately strong absorption band at $E_p \approx 1.3$ eV, irradiated with a beam of ~10 kV Na^+ ions to a dose of 2 mC/cm^2. No sputtering was apparent as a result of this irradiation. The near-infrared absorption band was enhanced roughly by a factor two as a consequence of the ion implantation. Additional data on ion irradiated samples has been obtained in several studies *(117, 148, 1893, 1895-6, 2394, 2852, 3370, 3564, 3566)*. Oxygen loss during ion-beam irradiation has been discussed for WO_3 *(1996)*, but this effect did not seem to be of significance for Na^+ irradiation in the present case *(1895)*. Ion bombardment can lead to amorphization of initially crystalline films *(1996)*.

The final coloration technique considered here is based on direct *electron-beam irradiation*. Figure 9.6(h), taken from Baba and Ikeda *(193)*, shows that an absorption band with $E_p \approx 1.3$ eV is induced in an evaporated film by the impinging electrons. Some additional results were given by Morita et al. *(2394)*. The coloration may be associated with electron stimulated oxygen desorption *(2835)*, which is a well known effect for WO_3 single crystals *(2525)* and powders *(2082)*, as well as for W oxide surface layers *(2082)*. The maximum penetration range (in nm) for the electrons has been given as $18.5\ E_o^{1.3}$ with E_o being the electron energy (in keV) *(1084)*.

9.4 Energy for the Absorption Peak

The data in Fig. 9.6 give a rather consistent picture with an absorption peak centered at ~1.3 eV in most cases. However, the annealed film reported on in Fig. 9.6(f) showed a lower E_p. This indicates that E_p depends on τ_a, as has been pointed out several times in work on films made by evaporation *(884, 1046, 1126, 1146, 1842)* and sputtering *(3170)*. Deneuville and Gérard *(884)* reported a detailed study regarding the effect of τ_a on evaporated films in transparent state and after UV coloration. Figure 9.7, based on their work, indicates that E_p shifts abruptly from ~1.4 to ~0.7 eV upon annealing in the range $350 < \tau_a < 400$°C. The data refer to a UV-colored film treated under vacuum with annealing periods of 2 h at increasing temperature. Vacuum annealing of a transparent film gave a somewhat more progressive shift of E_p from ~1.4 to ~0.7 eV over the $300 < \tau_a < 500$°C interval. Films annealed in oxygen showed $E_p \approx 1.4$ eV for $\tau_a < 200$°C, $E_p \approx 0.7$ eV for $\tau_a > 350$°C, and ill-defined absorption peaks at intermediate annealing temperatures. Single crystals of WO_3 colored with H° from a HCl + Zn mixture showed $E_p \approx 0.9$ eV at room temperature *(918)*. A low-temperature modification of H^+ intercalated WO_3 single crystals had $E_p \approx 1.3$ eV *(2978)*.

There is a weak dependence of E_p on the amount of intercalated species. Figure 9.8 displays results for evaporated W oxide films intercalated with H^+ from 1 M H_2SO_4 electrolytes. The data were taken from work by Yamada et al. *(1501, 1827-8, 3685-6)*; some spectral curves underlying the E_p data were given in Fig. 9.6(a). It appears that E_p is displaced towards higher energy by less than 0.1 eV as a result of the inserted charge density. A similar tendency has also been seen in other work on H^+ intercalation *(51, 2481, 3050, 3645)*, Li^+ intercalation *(2481, 3057)*, and Na incorporation *(1322, 1743, 1858)*. A more unambiguous shift of E_p upon ion intercalation will be discussed for Mo oxide in Sec. 12.9.

9.5 Transmittance and Reflectance of Ion Intercalated Films

Spectral absorptance was discussed in Secs. 9.3 and 9.4 above. This quantity is of great significance for elucidating the physical absorption mechanism and for certain applications, but spectral transmittance and reflectance are of more immediate value when daylighting, solar energy utilization, and energy efficiency are of prime concern. Data of this latter type have been given at many places in the literature, but more often than not the spectra are confined to undesirably narrow ranges or are limited in other ways. Figure 9.9 shows transmittance data from Miyake et al. *(2340)* for 0.4-μm-thick W oxide films prepared by evaporation onto substrates of ITO-coated glass at τ_s = 50°C so that a heavily disordered structure prevailed (part a) and at τ_s = 400°C so that the structure was crystalline (part b). H^+ was intercalated to different charge densities from a 1 N H_2SO_4 electrolyte. The disordered film is transparent in the unintercalated state and exhibits a very wide minimum, around 1 μm in wavelength, that becomes progressively deeper with increasing ion intercalation. The overall behavior is the same for the crystalline film , but the infrared transmittance is lower irrespective of the degree of intercalation. The drop in transmittance at $\lambda < 0.4$ μm is influenced by absorption in the glass substrate, and the oscillations in the curves are due to optical interference. Other spectral transmittance data on evaporated films are available for H^+ intercalation *(161, 255, 627, 2669-70, 3013, 3382)* and Li^+ intercalation *(96-9, 149, 159, 161, 163, 927, 2223-5, 2466, 2468, 3015, 3073, 3286-8)*. Similar results have also been recorded with "dry

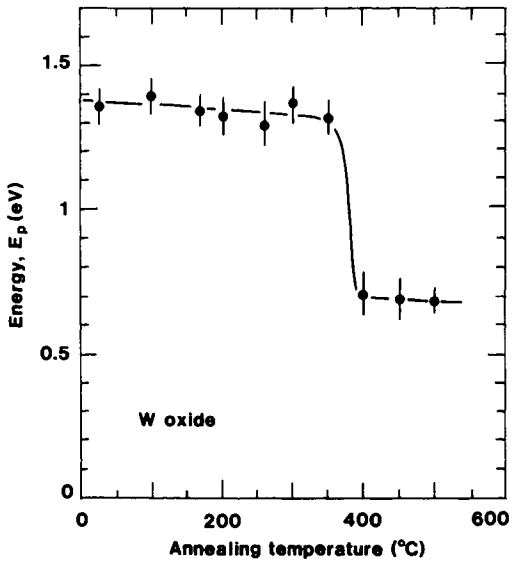

Fig. 9.7 Energy for the peak of the near-infrared absorption band E_p vs. annealing temperature for UV-colored evaporated W oxide films treated in vacuum. The values of E_p were extracted from published spectral absorption coefficients, and the precise energies were sometimes hard to locate; this explains the uncertainties indicated by the vertical bars. The curve was drawn for convenience. After Deneuville and Gérard *(884)*.

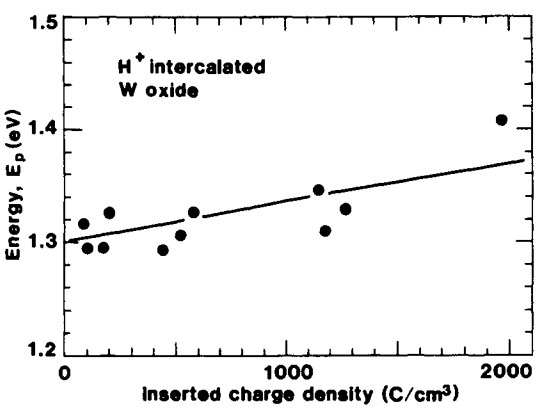

Fig. 9.8 Energy for the peak of the near-infrared absorption band E_p vs. the amount of inserted charge density for H^+ intercalated W oxide films made by evaporation. The line was drawn for convenience. From Hiruta et al. *(1501)*.

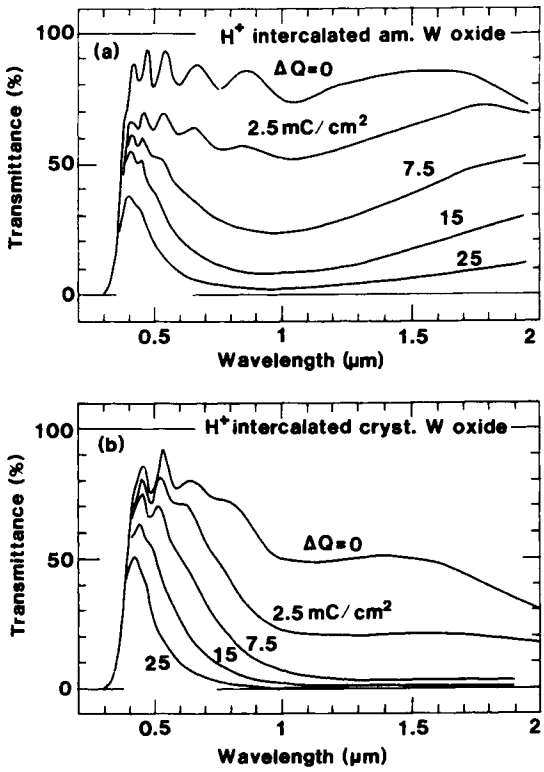

Fig. 9.9 Spectral transmittance for "amorphous" (part a) and crystalline (part b) evaporated W oxide films in unintercalated state and after H^+ intercalation to the shown charge densities ΔQ. From Miyake et al. *(2340)*.

lithiation" by depositing Li atoms on top of a W oxide film *(162, 166)*.

Spectral transmittance of sputter-deposited films is shown in Fig. 9.10 in a way that allows direct comparison with results for evaporated films. The data are redrawn from Kaneko et al. *(1740)* who prepared films by rf sputtering from a WO_3 target in Ar + O_2 onto substrates at τ_s = 200°C and obtained disordered or crystalline structures depending on the Ar/O_2 ratio. H^+ was inserted from 1 N H_2SO_4 into 0.48 to 0.53-μm-thick films. The transmittance modulation upon ion intercalation is comparable to the one in evaporated samples and is larger for disordered films than for crystalline films. Analogous data on sputter-deposited films have been given for H^+ intercalation *(627, 1738-9, 2341)* and Li^+ intercalation *(96-9, 165, 1233-4)*. There are also reports on H^+ + Li^+ intercalation into CVD-produced films *(823-4, 958, 962, 3283, 3435, 3536)* as well as on H^+ and Li^+ intercalation into sol-gel-produced layers *(319, 627, 787, 2124, 2170)*. Films made by decomposition of oxalatotungstate compounds and cycled in 0.25 M KCF_3SO_3 were discussed in *(1117)*. Delichere et al. *(861-3)* described the use of optical multichannel detection to record optical spectra and applied this technique to films made by anodization and intercalation with H^+ + Li^+.

The spectral reflectance of strongly disordered W oxide films is 10 to 20 % irrespective of intercalation level and fabrication technique, as seen in numerous studies *(730-1, 958, 962, 1227, 1313, 1322, 2466, 2468, 3050, 3283, 3536, 3793)*. However, a much larger infrared reflectance can be obtained at high intercalation levels in crystalline films, as illustrated in Fig. 9.11. In part (a), referring to H^+ intercalation, the solid curve represents data for a 0.14-μm-thick film made by rf sputtering and treated in a H_2SO_4 electrolyte, according to work reported by Goldner et al. *(1223-4, 1229)*. The reflectance increases monotonically with increasing wavelength and reaches ~60 % at 2.5 μm. Additional data for H^+ intercalated sputtered films were shown in other publications by Goldner et al. *(1221-2, 1228, 1230-1)*. More recent work by Rubin *(2949)* showed data similar to those given by the solid curve in Fig. 9.11(a) for films made by ion-assisted sputtering--using an unbalanced magnetron--in the presence of O_2 and H_2 onto substrates kept at room temperature. H^+ intercalation into films made by evaporation followed by annealing in air or N_2 at 340 to 400°C yielded films with a reflectance of ~35 % at λ = 2.5 μm *(3050)*. Zhang and Colbow *(3793)* reported data for a 0.45-μm-thick film made by spray pyrolysis at $\tau_s \approx$ 400°C followed by H^+ intercalation from a solid electrolyte. The dashed curve in Fig. 9.11(a) stems from their work; the reflectance reaches ~ 42 % at λ = 2.5 μm.

Figure 9.11(b) pertains to Li^+ intercalation. The solid curves, obtained from Cogan et al. *(730-1)*, show reflectance spectra for a 0.12-μm-thick film prepared by rf sputtering from WO_3 in Ar + 10 % O_2 onto a substrate at τ_s = 466°C. Li^+ intercalation from a 1 N $LiClO_4$ + PC electrolyte gives a progressive increase of the infrared reflectance up to ~58 % at λ = 2.5 μm for $Li_{0.5}WO_3$. Similar data for Li^+ intercalated sputtered films have been given in *(725, 1837, 2856)*. Surprisingly, an increased crystallinity did not always give enhanced IR reflectance, as found by Klein and Yen *(1837)*. Very high reflectance, up to a remarkable ~81 % at λ = 2.5 μm, was reported for sputter-deposited films in work by Goldner et al. *(1220)*; the dashed curve in Fig. 9.11(b) stems from this latter study. Similar data were obtained by Rubin *(2949)* for Ag_xWO_3 films made by ion-assisted sputtering onto substrates at τ_s = 450°C; this film did not show electrochromism. Bulk data for WO_3-based bronzes were reported in Fig. 2.8.

Figure 9.12 elaborates the role of substrate temperature for the optical properties of Li_xWO_3 films. An increased τ_s gives a higher reflectance, which unquestionably follows from an improved crystallinity.

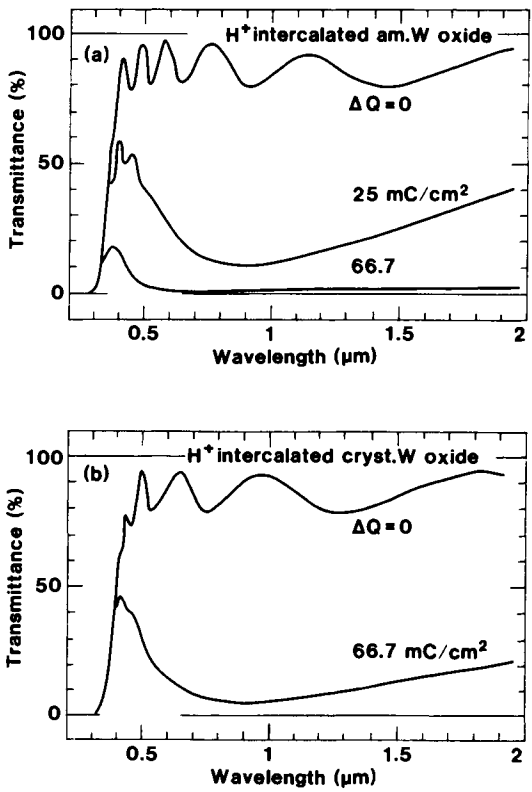

Fig. 9.10 Spectral transmittance for "amorphous" (part a) and crystalline (part b) sputter-deposited W oxide films in unintercalated state and after H^+ intercalation to the shown charge densities ΔQ. From Kaneko et al. *(1740)*.

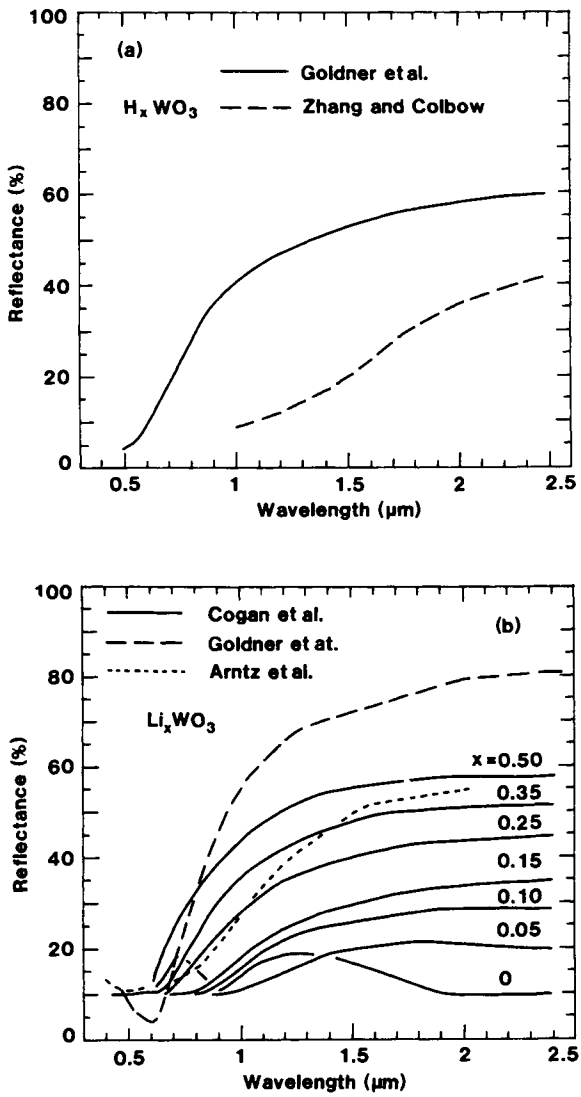

Fig. 9.11 Spectral reflectance for crystalline W oxide films intercalated with H^+ (part a) and Li^+ (part b). The data were replotted from the following works and are based on the stated techniques: Goldner et al. *(1220, 1223-4, 1229)*, sputtering; Zhang and Colbow *(3793)*, spray pyrolysis; Cogan et al. *(730-1)*, sputtering; Arntz et al. *(148-9)*, ion-assisted evaporation.

The dotted curve in Fig. 9.11(b), reproduced from Arntz et al. *(148-9)*, shows spectral reflectance for an evaporated film prepared at $\tau_s \approx 90°C$ and bombarded during growth with 400 eV oxygen ions so that a crystalline structure was obtained. After Li^+ intercalation, the reflectance reached ~55 % at $\lambda = 2$ μm. The possibility of employing ion-assisted evaporation for preparing crystalline films without excessive substrate heating is noteworthy and important. Further general information on the influence of ion-assistance on the evolution of the structure and optical properties of films can be gained from several reviews *(2192-3, 2239, 3028)*. One may note, finally, that Na containing films showed enhanced IR reflectance when the grain size was increased *(1322)*. When assessing W oxide films backed by transparent conducting layers, it is important to be aware that the latter can lead to infrared reflectance; cf., for example *(1726, 2466-7)*. Transparent electrodes are discussed in Ch. 25 below.

9.6 Optical Constants of Ion Intercalated Films

Spectral optical constants, $n(\lambda)$ and $k(\lambda)$, for electrochromic W oxide films have been given in several places in the literature. Usually the studied wavelength range is too small and the film composition is insufficiently characterized to allow more than qualitative conclusions. Figure 9.13 gives some data on n and k subject to these qualifications. Part (a) refers to work by Ottermann et al. *(2670)* on evaporated films intercalated with H^+ from a 1 M HCl electrolyte. The expected near-infrared peak in k develops at increased proton content, and at the same time n decreases by as much as ~0.3 at $\lambda = 0.55$ μm upon going from WO_3 to $H_{0.38}WO_3$. Figure 9.13(b) shows analogous data for a CVD-produced film in deintercalated (bleached) state and after H^+ intercalation (coloring) from 1 N H_2SO_4 *(3536)*.

A tendency that ion intercalation decreases n and increases k in the luminous range can be noted also in Fig. 9.14, showing data from Ohtsuka et al. *(2583)*. The measurements were taken at $\lambda = 0.633$ μm for highly porous W oxide films made by low-voltage potentiostatic anodization followed by H^+ intercalation from a 0.1 M H_2SO_4 electrolyte. It is found that k increases monotonically and n decreases monotonically when x goes from zero to 0.14 in H_xWO_3. Consistent results for n and k have been reported for Li^+ intercalated films made by evaporation *(2459)* (see Fig. 10.11 below), H^+ intercalated crystalline films made by sputtering *(1228, 1230-1, 2291)*, Li^+ intercalated hexagonal crystalline films made by high-voltage potentiostatic anodization *(861-2)*, and in *(293)*. Data for $k(\lambda)$ of $H_{0.17}WO_3$ were given in *(284-5)*.

9.7 Coloration Efficiency

Coloration efficiency (CE) is defined as the change in optical density per unit of inserted charge, i.e.

$$CE = \Delta(OD)/\Delta Q \ . \tag{9.1}$$

A high CE gives a large optical modulation at small charge insertion/extraction. The coloration efficiency is a very important parameter for electrochromic devices, and a detailed exposition is given below. By definition, CE is taken to be *positive* when the absorption goes up under ion

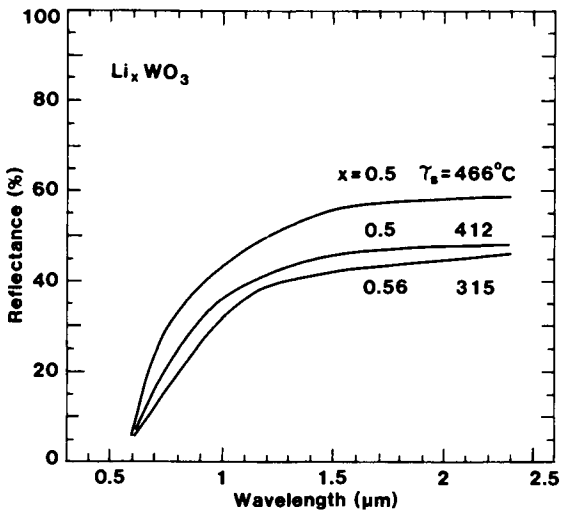

Fig. 9.12 Spectral reflectance for crystalline Li^+ intercalated W oxide films, having the shown lithium contents, prepared by sputtering onto substrates at the indicated temperatures τ_s. From Cogan et al. *(730)*.

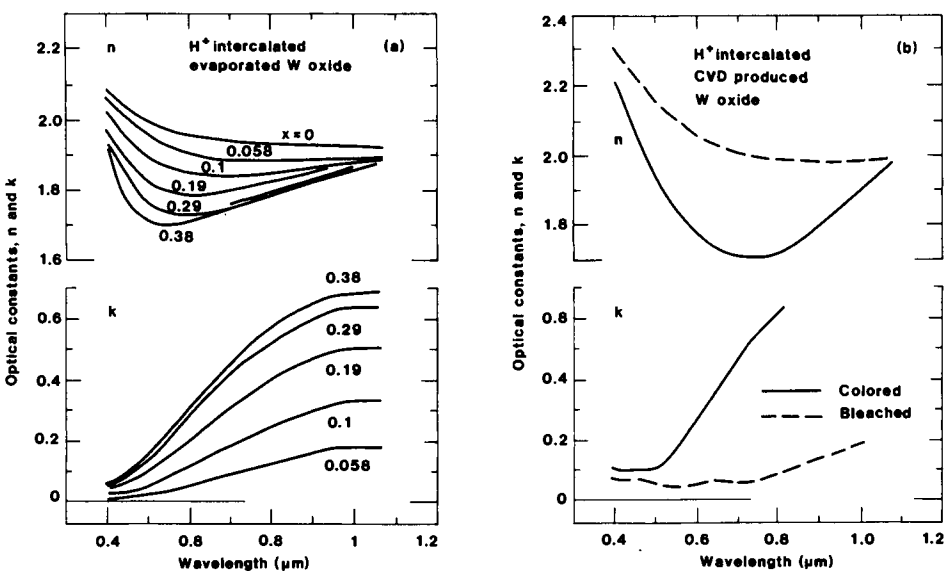

Fig. 9.13 Spectral optical constants for W oxide films. Part (a) refers to an evaporated film intercalated with H^+ to the shown magnitudes (given as x in H_xWO_3); the curve for x = 0 was earlier shown in Fig. 9.4(a). Part (b) gives results for a CVD-produced film in bleached and colored states. After Ottermann et al. *(2670)* and Villachon-Renard et al. *(3536)*.

intercalation (cathodic electrochromism) and *negative* when the absorption goes down under ion intercalation (anodic electrochromism). The CE is positive for W oxide.

Figure 9.15, from Bohnke et al. *(427)*, serves to illustrate a number of salient features of the relation between Δ(OD) and ΔQ for disordered evaporated films. The data pertain to $\lambda = 0.633$ μm for films of two thicknesses intercalated with H^+ and Li^+. The relation remains approximately linear--i.e., the CE is constant--up to a certain OD that depends on the film thickness. For $d = 0.24$ μm, Fig. 9.15(a) a shows that this "critical" OD is ~0.45 and corresponds to an inserted charge density of ~15 mC/cm^2. At $d = 0.66$ μm, the CE is constant up to OD > 1, as seen from Fig. 9.15(b). The intercalated species plays a subordinate role, and the dependence on the H_2O addition to the $LiClO_4$ + PC electrolyte (denoted δ in Fig. 9.15) may not be significant. Quantitatively, the CE lies between 37 and 49 cm^2/C at $\lambda = 0.633$ μm. Bohnke et al. *(427)* also studied films in a H_2SO_4 electrolyte and found CEs that were fully consistent with those in Fig. 9.15.

The coloration efficiency is spectrally dependent, which is readily understood from data in the previous sections of this chapter. Figure 9.16(a) shows results for H^+ intercalated films deposited onto unheated substrates, after Ottermann et al. *(2445, 2668-70)* and Yoshimura *(3742)*. The curves are peaked at 1.3 to 1.4 eV, as expected for strongly disordered films. At $\lambda = 0.633$ μm, the curves correspond to CEs of 50 to 55 cm^{2}C^{-1}, which is in acceptable agreement with the data in Fig. 9.15. Consistent CEs, determined at discrete wavelengths between 0.5 and 0.9 μm, have been reported many times in the literature *(160, 255, 422, 426, 428-9, 494, 627, 652, 728, 1184-5, 1439, 1726, 1736, 1826-7, 1858, 2016, 2224-5, 2340, 2358, 2466, 2468, 2895, 3088, 3274)*. One may note a few studies stating non-linear Δ(OD) vs. ΔQ relations *(292, 3073)*, and work wherein differences among coloration and bleaching cycles were stressed *(1889, 3811)*.

The CE remains constant only up to a certain magnitude of inserted charge density, as apparent from Fig. 9.15(a). The corresponding maximum ion content has been given approximately as $H_{0.36}WO_3$ *(1736)* and $Li_{0.4}WO_3$ *(2368)*. Analogous results were inferred for sputter-deposited *(1375)* and sol-gel-produced *(1704)* films.

The CE is influenced by the evaporation conditions; this important effect is first considered with regard to reactive evaporation at a specified magnitude of p_{O2}. The oxygen leads to a decrease of the CE, which can be seen from Fig. 9.17 based on data by Sun and Holloway *(3274)*. At $p_{O2} < 10^{-5}$ Torr and $\lambda = 0.7$ μm, the CE is marginally smaller than the values in Fig. 9.16. Increasing p_{O2} by two orders of magnitude makes CE drop to about half the initial value. RBS verified that the decrease in CE was associated with a lowering in the oxygen non-stoichiometry (cf. Fig. 3.3). This result is in line with the fact that W oxide films have increased CE if made from a WO_2 powder evaporant (rather than from the conventional WO_3 material), as found by Yoshimura et al. *(3744)*.

The coloration efficiency can be changed by annealing, which is illustrated in Fig. 9.16(a) where two of the curves reproduced from Yoshimura *(3742)* refer to evaporated films treated for 2 h in air at 200 and 400°C. Annealing at $\tau_a = 200$°C yielded a decrease of the CE across the full $0.4 < \lambda < 1.5$ μm range, whereas annealing at $\tau_a = 400$°C yielded a decrease of the CE in the luminous range and an increase of the CE in the infrared. The coloration efficiency of the latter film was strongly peaked at ~0.7 eV, which signals that crystallization had taken place (cf. Fig. 9.7). Matsuhiro and Masuda *(2224-5)* found that the CE at $\lambda = 0.5$ μm was decreased by crystallization, but this result was not supported in some other work *(2340)*. Bombardment with energetic electrons can decrease the CE *(1887)*.

In reactive ion plating, evaporation takes place through an oxygen plasma. Figure 9.16(b)

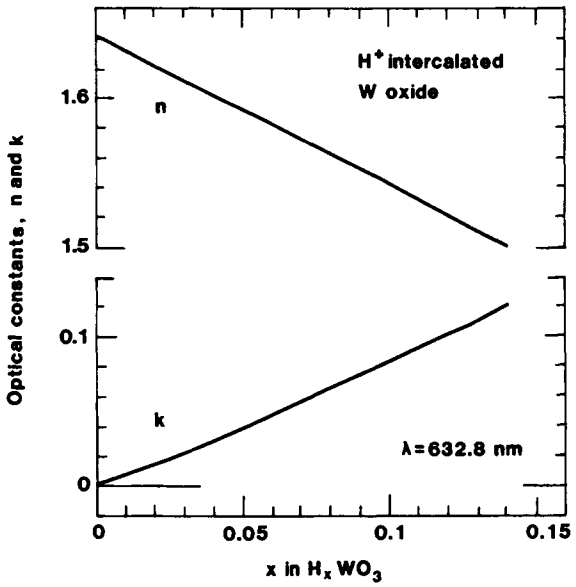

Fig. 9.14 Optical constants at $\lambda = 0.633$ μm for an anodic W oxide film intercalated with H^+ to the magnitudes given as x in H_xWO_3. The curves were constructed from published data on $x(U)$, $n(U)$, and $k(U)$, where U is the potential relative to RHE. U may be somewhat uncertain as regards details. After Ohtsuka et al. *(2583)*.

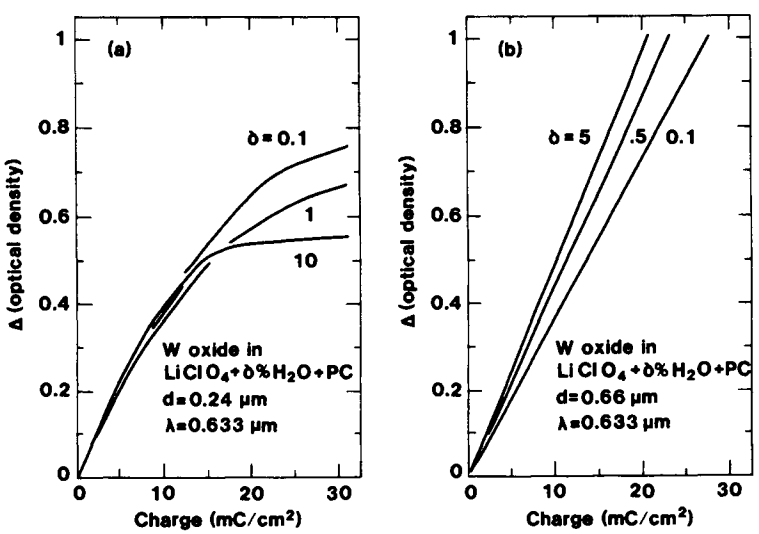

Fig. 9.15 Change in optical density vs. inserted charge density for evaporated W oxide films of two thicknesses d. The films were treated in $LiClO_4 + H_2O$ + PC electrolytes, whose water content is denoted δ. Optical measurements took place at the wavelength 0.633 μm. From Bohnke et al. *(427)*.

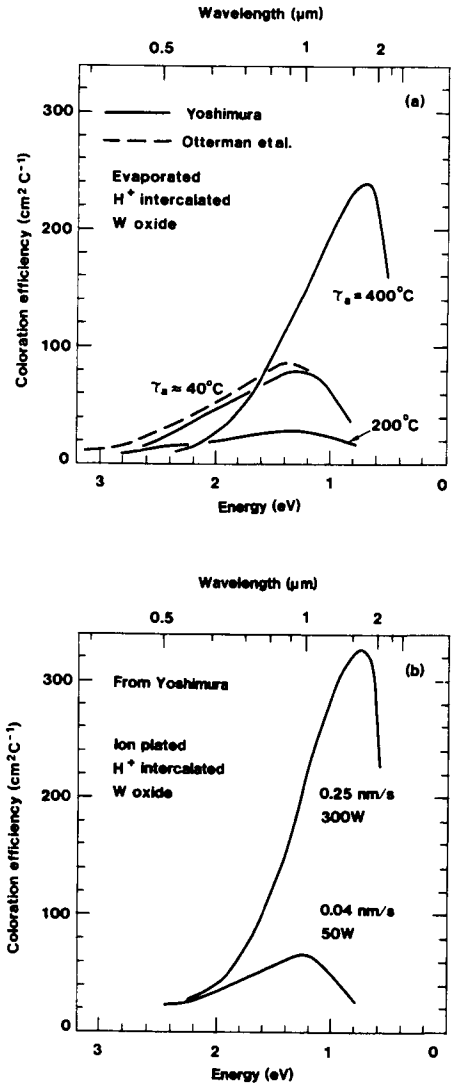

Fig. 9.16 Spectral coloration efficiences for H^+ intercalated W oxide films made by evaporation and annealed at the shown temperatures τ_a (part a), and made by reactive ion plating at the shown rates and rf power densities (part b). After Ottennann et al. *(2445, 2668-70)* and Yoshimura *(3742)*.

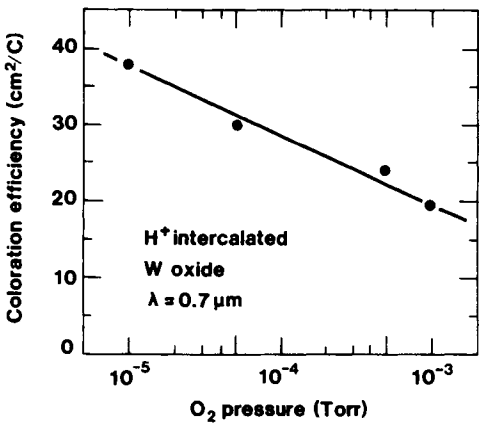

Fig. 9.17 Coloration efficiency at $\lambda = 0.7$ μm vs. oxygen pressure for H^+ intercalated W oxide films made by reactive evaporation. After Sun and Holloway *(3274)*.

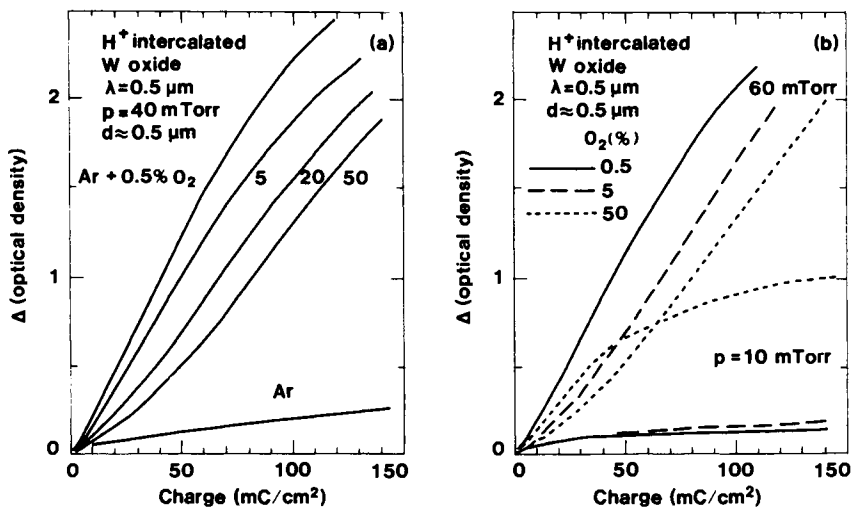

Fig. 9.18 Change in optical density vs. inserted charge density for H^+ intercalated W oxide films made by rf sputtering at different gas pressures p and gas compositons, as indicated in parts (a) and (b). Film thickness d and wavelength λ were as stated. From Kaneko et al. *(1740)*.

shows CEs from Yoshimura *(3742)* for samples made with the shown deposition rates and rf powers and at $\tau_a = 200°C$. The film made at high rate shows a strong peak in the CE at ~0.8 eV and it appears that crystallization has occurred, whereas the film made at low rate shows a small peak at ~1.3 eV and seems to have a strongly disordered structure.

For the case of sputter-deposited films, the preparation parameters play an important role for the CE. Figure 9.18, from Kaneko et al. *(1740)*, illustrates the relation between $\Delta(OD)$ and ΔQ in a way that is analogous to Fig. 9.15. The films were made by reactive rf sputtering from a WO_3 target onto substrates at $\tau_s \approx 200°C$ in Ar + O_2 with different mixing ratios and at different gas pressures p. Films with thicknesses of $0.48 < d < 0.53$ μm were H^+ intercalated from a H_2SO_4 electrolyte. Optical data were measured at $\lambda = 0.5$ μm. Sputtering in pure Ar gave a low CE, as apparent from the bottom curve in Fig. 9.18(a); this film was crystalline. Adding O_2 led to disordered films with a rather linear $\Delta(OD)$ vs. ΔQ relation up to an inserted charge density of ~100 mC/cm^2. The CE was largest for a small O_2 admixture and for a not too low total gas pressure, as seen from Figs. 9.18(a) and (b). Analogous results have also been found in other work based on the technique outlined above *(50-1, 1737-8, 2341)*, in studies using rf sputtering from W in $O_2 + H_2$ *(627, 1188-9)*, and for dc bias sputtering of W in Ar + O_2 *(627, 1739)*.

From Fig. 9.18 one extracts a maximum CE of ~30 cm^{2}C^{-1} at $\lambda = 0.5$ μm. Elsewhere, in evaluations of CE at discrete wavelengths, it was reported for sputter-deposited films that CE lay between 20 and 40 cm^{2}C^{-1} at $\lambda = 0.5$ μm *(51, 1188-9, 1737-9)*, between 50 and 60 cm^{2}C^{-1} at $\lambda \approx 0.6$ μm *(50, 1829, 3056-7)*, and around 95 cm^{2}C^{-1} at $\lambda = 0.8$ μm *(51)*. Somewhat lower CEs were reported in *(1375)*.

Spectral data for CE are reported in Fig. 9.19, after Yoshimura *(3742)* and Cogan et al. *(725, 2854)*. The dashed curves in part (a) refer to films made by rf sputtering from W in Ar + 10 % O_2 onto substrates at two temperatures and subsequently intercalated with Li^+ *(725)*. For the heavily disordered film made at $\tau_s \approx 40°C$, the CE is peaked at ~1.5 eV and has a value of ~50 cm^{2}C^{-1} at $\lambda = 0.5$ μm. Similar data were given in *(162)*. The crystalline film prepared at $\tau_s \approx$ 310°C has a CE that is lower than in the disordered film for energies below 1 eV; its CE is peaked at ~0.9 eV. These data are consistent with results for evaporated films, cf. Fig. 9.16(a). The solid curves in Fig. 9.19(a) were obtained for films made by rf sputtering from a W target at a rf power of 600 W and different oxygen pressures *(3742)*. These films were colored by H^+ intercalation. At $p_{O2} \approx 0.8$ mTorr, the spectral CE was in good agreement with the one for $\tau_s \approx 310°C$. Enhancing p_{O2} up to 30 mTorr yielded a dramatic increase of the CE in the infrared, with a maximum value as high as ~490 cm^{2}C^{-1}. Figure 9.19(b) elaborates the effect of P_{rf} for films made at $p_{O2} \approx 30$ mTorr. Going from 100 to 1000 W, the CE is increased and shows peak values from ~150 to ~700 cm^{2}C^{-1}; at the same time the energy where the peak is located goes from ~1.1 to ~0.85 eV, indicating P_{rf} dependent crystallization. Unfortunately, Yoshimura *(3742)* did not report any structural analysis.

Regarding CVD-prepared films, it has been found that CEs at $\lambda = 0.633$ μm lay in the range 32 to 44 cm^{2}C^{-1} for H^+ intercalation, with the specific value being dependent on the deposition parameters *(422, 426, 821, 823, 825)*. Similar films intercalated with Li^+ were reported to have a somewhat smaller CE *(422, 426)*.

Anodic W oxide films seem to display widely different CEs at $\lambda = 0.633$ μm depending on anodizing parameters and details of the ion intercalation for coloration *(422, 863, 2895)*. Bohnke and Bohnke *(422)* reported that the CE was 120 cm^{2}C^{-1} for $U_a = 40$ V but only 33 cm^{2}C^{-1} for $U_a = 70$ V. No doubt this difference can be associated with structural effects, and it was pointed

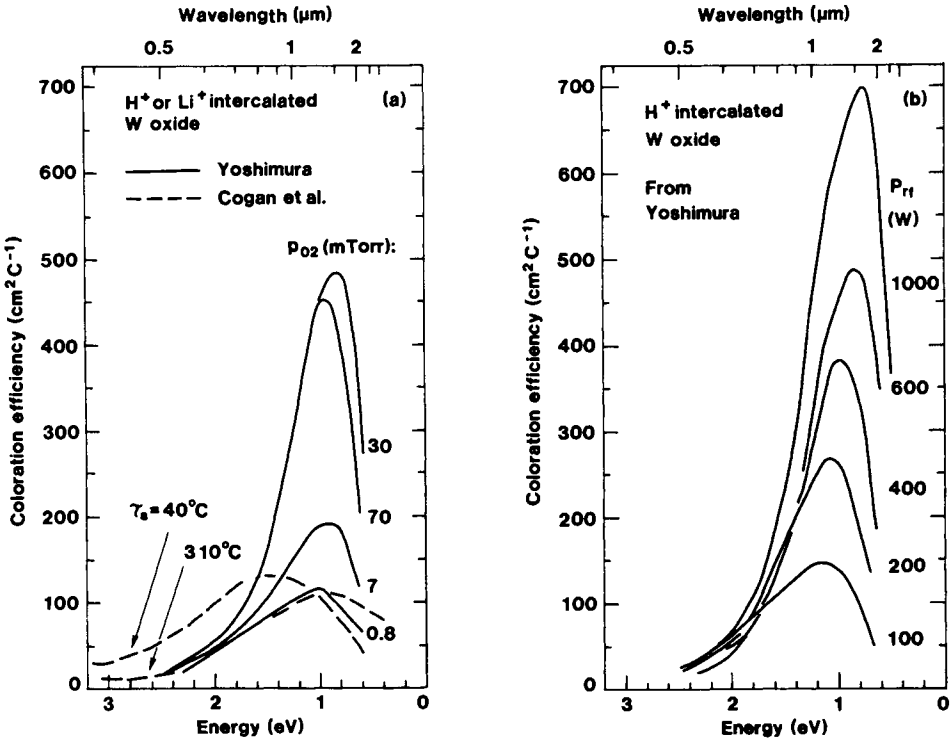

Fig. 9.19 Spectral coloration efficiencies for W oxide films made by rf sputtering at different powers P_{rf} and gas pressures p_{O2} (solid curves; H^+ intercalation), and at different substrate temperatures τ_s (dashed curves; Li^+ intercalation). After Cogan et al. *(725)* and Yoshimura *(3742)*.

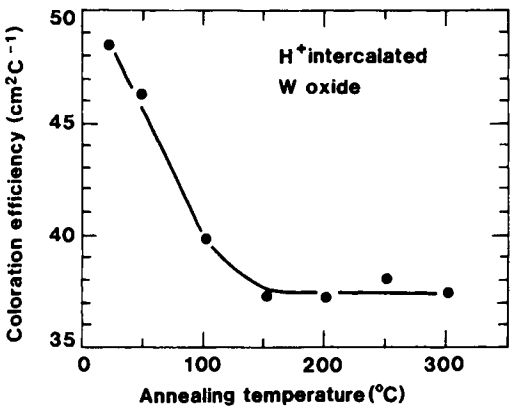

Fig. 9.20 Coloration efficiency at $\lambda = 0.55$ μm vs. annealing temperature for H^+ intercalated W oxide films made by dip coating. The curve was drawn for convenience. From Lynam et al. *(2124)*.

out before that films made at low U_as are much more disordered than films made at high U_as (cf. Raman spectra in Fig. 5.1). The highest CEs reported so far (for a transmittance configuration) is a remarkable 260 cm^2C^{-1} stated by Delichere et al. *(863)* for films made by anodization at 40 V followed by intercalation through a two-step process in an electrolyte of 1 M $LiClO_4$ + 1 % H_2O + PC. The potential applied during the coloration was -2.5 V vs. Ag for a short time, followed by a longer step at -1.5 V.

Tungsten oxide films made by dip coating followed by annealing post-treatment were studied by Lynam et al. *(2124)*. Figure 9.20 reports CEs at $\lambda = 0.55$ μm and shows a drop from an initial value of ~48 cm^2C^{-1} to ~37 cm^2C^{-1} for $\tau_a > 150$°C. Somewhat lower CEs were given by Caskey et al. *(627)*. The decrease of the CE is accompanied by a significant densification. For films made by decomposition of oxalatotungstate compounds, the CE was ~77 cm^2C^{-1} at $\lambda = 0.633$ μm *(1117)*. Some data are also available for electrodeposited films *(760)*.

From the compilation of CE data, one concludes that the magnitude of this technologically important parameter can be strongly influenced by the thin film fabrication method and the ensuing microstructure of the W oxide.

This Page Intentionally Left Blank

Chapter 10

TUNGSTEN OXIDE FILMS: THEORETICAL MODELS FOR THE OPTICAL PROPERTIES

Several theoretical models have been put forward in order to explain the electrochromism in W oxide with different microstructure. For *disordered* films prepared by evaporation, there was initially a suggestion by Deb *(836)* that F-like color centers--embracing oxygen vacancies each with one trapped electron--could be responsible for the electrochromism. Oxygen extraction was proposed as an alternative cause by Chang et al. *(651)*, and similar notions were put forward for anodic films in work by Sunseri et al. *(3278)*. The color center concept is discussed in (10.1) below. When the connection between optical modulation and a double insertion/extraction of ions and electrons became accepted--primarily through work by Faughnan et al. *(1047)*--the theoretical modelling became focused on polaron absorption (10.2) and on a closely related mechanism based on intervalency charge transfer (10.3). Similar ideas were put forward independently as early as in 1974 by Lusis et al. *(2116)*. In *crystalline* films, the interest has been centered on free-electron effects ever since the work in 1977 by Schirmer et al. *(3050)*. The crystalline material can be viewed as a tungsten bronze with a variable electron density and with electrons undergoing scattering predominantly against the intercalated ions. The optical properties can be understood schematically by the Drude theory (9.4) and in more detail by Gerlach's theory *(1170-1)* applied to ionized impurity scattering (9.5). Inhomogeneities, that are known to be present in any real W oxide film, may be modeled by Effective Medium Theory (9.6).

Among the other ideas that have been put forward to explain the electrochromism in W oxide, one may note those by Donnadieu et al. *(821, 962)*. They considered a "Hubbard splitting" *(2416-7)* of the π-antibonding combination of $W5dt_{2g}$ and $O2p$ orbitals. The origin of this splitting was supposed to lie in the Coulomb repulsion among electrons in localized states, and absorption is then due to electronic transitions between the two bands. This model appears to predict that the electrochromic absorption occurs at an energy that depends on the electron density, i.e., on the amount of ion intercalation, which is not consistent with experimental evidence. Consequently, this model has not gained general acceptance.

10.1 Absorption in Disordered Films: Color Centers

Ion intercalated disordered tungsten oxide films contain W atoms in 6+ as well as in 5+ states. The existence of W^{5+} was clearly documented in XPS spectra for spin-orbit-split $W4f$ core levels, as discussed in Sec. 7.7. In particular, Fig. 7.19 showed that the W^{5+} content was proportional to x in films represented as H_xWO_3. An even more direct manifestation that the W^{5+} proportion governs

the electrochromism can be gained from EPR measurements of the type illustrated in Fig. 7.16. It was shown by Kleperis et al. *(1126, 1842)*, who investigated evaporated films treated in H_2SO_4, that the EPR signal at $g \approx 1.7$ increased at the same time as the optical absorption peak at $E_p \approx 1.3$ eV became stronger. Figure 10.1 proves that the relation between these two quantities is accurately linear. The emerging picture then is that the inserted electrons are localized on tungsten sites, where they take part in processes responsible for the electrochromism.

The *color center* concept, i.e., absorption due to localized states, makes it meaningful to represent the characteristic absorption feature in electrochromic films by the use of Smakula's equation *(904, 1047, 3198)*. It can be written

$$N_s f_s \approx 0.87 \times 10^7 \frac{n}{(n^2+2)^2} a_p d\, \Omega_{1/2} , \tag{10.1}$$

where N_s is the number of color centers per cm^2, f_s is an oscillator strength, n is the refractive index of the uncolored material, a_p is the absorption coefficient (in cm^{-1}) at E_p, d is the film thickness, and $\Omega_{1/2}$ is the full width at half maximum (in eV) of a Gaussian-type absorption band. An analysis of experimental data on electrochromic evaporated tungsten oxide films yielded that f_s was approximately 0.1 *(1047)*. To put this value in perspective, one should note that F center absorption in alkali halides typically has $f_s \sim 0.6$ *(904)*, whereas excited state transitions within transition metal impurities normally have $10^{-4} < f_s < 10^{-2}$. It was stressed by Dexter *(904)* that there are many approximations and uncertainties underlying Smakula's equation, and one should not put too much credence on quantitative values for f_s. Equation 10.1 has been used several times to analyze the absorption in electrochromic W oxide films *(2393, 3274, 3744)*.

10.2 Absorption in Disordered Films: Small Polarons

Specific models for the optical absorption are considered next with a focus on *small polaron* effects. Small polarons are formed when excess electrons polarize their surrounding lattice so that localization of the wave function takes place essentially to one lattice site, as discussed by Mott *(181, 2418-9)*, Emin *(1011)*, and others *(128, 1526, 3162)*. A small overlap between wave functions corresponding to adjacent sites, as well as strong disorder, are conducive to polaron formation. These conditions are not uncommon in solids, and physical phenomena related to polarons have been discussed in rare-gas solids, molecular crystals, various glasses, alkali halides, and--being most pertinent to the present case--transition metal oxides *(1010, 3258)*. The absorption is connected with polaron transfer by hopping between neighboring W sites, denoted i and j, schematically according to

$$W_i^{5+} + W_j^{6+} + \text{photon} \rightarrow W_i^{6+} + W_j^{5+} . \tag{10.2}$$

The excess energy during the photon-assisted hopping is given off as phonons. The EXAFS data shown in Fig. 7.3 provided a direct indication of lattice polarization in disordered W oxide being associated with electron localization. This experimental evidence gives strong support to polaron formation.

Optical absorption due to small polarons is conveniently discussed with regard to the potential

energy of the electron-lattice system along a one-dimensional lattice configuration coordinate. Such a diagram is shown in Fig. 10.2, where the parabola represent energy along a coordinate q passing through the sites i and j. Here U_p is the energy gained by polarizing the lattice, and v represents an energy spread caused by inequivalence among the lattice sites. Optical transitions appear vertical on such a diagram (Franck-Condon principle); they correspond to an energy $4U_p$, indicated by the heavy arrow. The absorption spectrum for such a two-well system has been discussed extensively *(415, 458, 1081, 1941, 2880, 3045, 3047, 3049)*. The theory accounts for transitions to a set of quantum levels separated by a phonon energy. The relative intensities of these transitions are governed by the Poisson distribution which, for strong electron-phonon interaction, can be approximated by a Gaussian; the physical reasoning was clearly exposed by Schirmer *(3046)*. The polaron absorption spectrum is given by

$$a_{pol}(\omega) \propto \omega^{-1} \exp\left[\frac{(\hbar\omega - v - 4U_p)^2}{8U_p\hbar\omega_0}\right] , \tag{10.3}$$

with $\hbar\omega_0$ being a typical phonon energy.

Figure 10.3, after Schirmer et al. *(3050)*, shows a least-square fit between absorptance as computed from small polaron theory and as measured for an evaporated W oxide film colored in H_2SO_4. The theoretical curve was obtained from $\omega^2 a_{pol}(\omega)$ with $U_p = 0.275$ eV, $\hbar\omega_0 = 0.098$ eV, and $v = 0$. This value of the polaron binding energy is similar to, or somewhat higher than, that of other *d*-electron systems *(567, 1941)*, and the phonon energy is close to that of LO phonons in WO_3 (cf. Secs. 3.6 and 3.7). An inclusion of $v > 0$ in the analysis would yield a lowering of U_p and $\hbar\omega_0$ *(3050)*. The fact that $\omega^2 a_{pol}$, rather than a_{pol}, was used followed from a neglect of the frequency dependence of electronic transition dipole moments in the derivation of an early version of Eq. 10.3 *(3046)*; this ω^2 factor is of little significance for the present analysis. The main conclusion from Fig. 10.3 is that the measured absorption is well represented by small polaron theory at energies lower than E_p. At higher energies, between E_p and E_g, the observed absorption is higher than the one predicted from the above theory of small polaron absorption. Such a discrepancy can be inferred also from absorption spectra shown in the previous chapter (cf. Figs. 9.1, 9.2, and 9.6), and corroborating evidence can be gained from bulk materials *(567, 1941)*. An enhanced high-energy absorption is not necessarily inconsistent with the small polaron concept, though, but may be ascribed to optical transitions to energy states higher than those indicated in Fig. 10.2.

Small polaron absorption has also been discussed in some more recent studies. Thus Yamada et al. *(1828, 3685-6)* analyzed films produced in the same way as those above, and Svensson et al. *(345, 3283)* studied films made by PECVD followed by treatment with n-butyl lithium in n-hexane. The results were in good qualitative agreement with those obtained by Schirmer et al. *(3050)*.

Thermomodulated absorptance spectra offer a possibility to test the theories for small polaron absorption in some detail. Data of this kind have been given several times *(345, 1828, 1869, 3283, 3685-6)*. Figure 10.4, from Kitao et al. *(1828)*, shows a spectrum for thermal modulation at 1.3 Hz around room temperature for a H^+ intercalated evaporated W oxide film. The data lie on a characteristic wave-shaped curve. They are compared with a calculation of $a_{pol}[\Delta(a_{pol})/\Delta\tau]$, with a_{pol} obtained from an early version of Schirmer's theory for small polaron absorption *(3047, 3050)*. It thus appears that the ω^2 factor, referred to above, was not included. The derivation of the

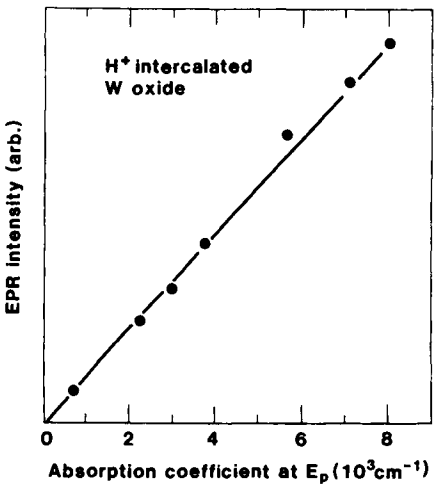

Fig. 10.1 EPR signal corresponding to W^{5+} vs. absorption coefficient at the peak of the optical absorption band associated with electrochromism in H^+ intercalated disordered W oxide films. The line was drawn for convenience. From Kleperis et al. *(1126, 1842).*

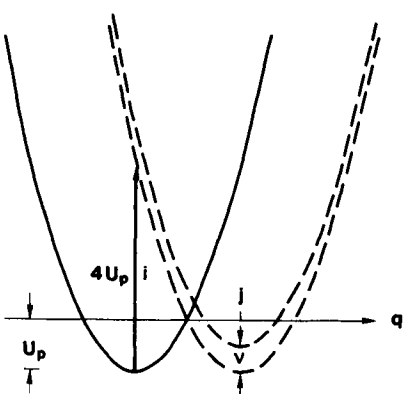

Fig. 10.2 Energy vs. lattice configuration coordinate q, passing through the sites i and j. The polaron binding energy is U_p, and the energy spread among non-equivalent sites is v. The heavy arrow indicates optical transitions. After Schirmer et al. *(3050).*

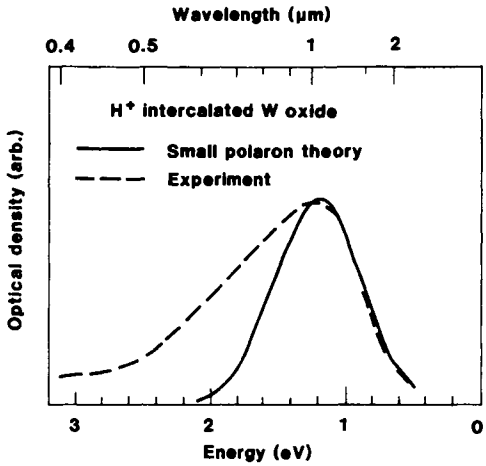

Fig. 10.3 Spectral optical density for a H^+ intercalated evaporated W oxide film as computed from Eq. 10.3 with $U_p = 0.275$ eV, $\hbar\omega_0 = 0.098$ eV, and $\nu = 0$, and as determined from experiments. After Schirmer et al. *(3050)*.

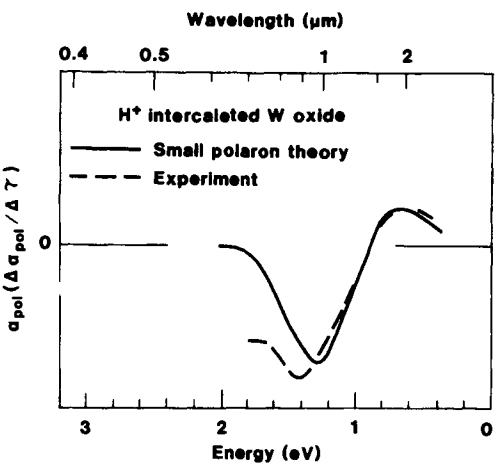

Fig. 10.4 Spectral thermomodulated absorptance for a H^+ intercalated evaporated W oxide film as computed from small polaron theory and as determined from experiments. a_{pol} is polaron absorptance and τ is temperature. After Kitao et al. *(1828)*.

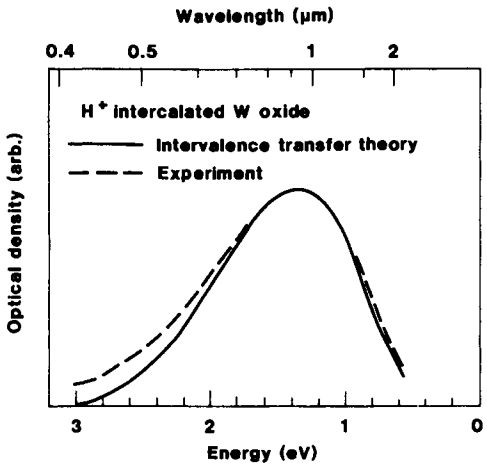

Fig. 10.5 Spectral optical density for a H^+ intercalated evaporated W oxide film as computed from a theory for intervalence charge transfer and as determined from experiments. After Gabrusenoks et al. *(1126)*.

theoretical curve has not been discussed in detail, but, nevertheless, the agreement between the two sets of data in Fig. 10.4 gives clear evidence that small polaron theory can explain the experimental results at photon energies less than E_p. Temperature dependent absorptance spectra in qualitative correspondence with those in Fig. 10.4 have also been recorded for PECVD-produced films intercalated with Li^+ *(345, 3283)*.

One could note, for completeness, that polaron effects have been used to explain physical phenomena also in tungsten-oxide-based bulk crystals in work by Salje et al. *(1158, 2978, 2981-2, 3048-9)* and others *(353, 1600)*. The physics is fairly complex, with different extents of the polaron wavefunction, as well as polaron pairing (bipolarons) *(3055)*, occurring at different temperatures and crystal compositions.

10.3 Absorption in Disordered Films: Intervalence Charge Transfer

An alternative model for the absorption in electrochromic W oxide is connected with *intervalence charge transfer* theory, as discussed by Faughnan et al. *(1047)*. The physical content is similar to that of small polaron theory, although the cause of the absorption is less specific. Intervalence transfer is responsible for the optical absorption in many transition metal compounds *(74)*. The theory for intervalence charge transfer absorption has been reviewed by Hush *(1585)*. Gabrusenoks et al. *(1126)* correlated the optical absorption in their H^+ intercalated evaporated W oxide films with this latter model. Specifically, they employed the Bryksin *(503)* theory of intraband absorption in disordered systems with strong electron-phonon interaction. By using reasonable values of the activation energy for thermal hopping, the width of the $W5dt_{2g}$ states band, and the location of the Fermi energy, they were able to produce a theoretical curve in excellent agreement with the measured data, as seen from Fig. 10.5. However, the fit involves several parameters, and it seems not yet possible to discriminate in a meaningful way between the prediction from small polaron theory (Fig. 10.3) and intervalence charge transfer theory (Fig. 10.5).

10.4 Transmittance and Reflectance of Crystalline Films: Drude Theory

Ion intercalation into crystalline W oxide films can lead to high reflectance in the infrared, as seen in Figs. 9.11 and 9.12. This phenomenon is caused by electrons entering extended states, rather than localized states as in strongly disordered W oxide. Below a certain frequency--known as the plasma frequency ω_{pl}--the electrons can follow the oscillating electromagnetic field so that screening takes place and hence reflectance appears. This section outlines theories for semiconductors containing a large density of free electrons and applies these theories to calculate the optical properties of crystalline W oxide films.

The simplest model for the influence of the free electrons is the classical *Drude theory (3658)*. It accounts for free electrons undergoing scattering, of unspecified nature, characterized by a constant relaxation frequency γ or, alternatively, a constant mean free path. The complex dielectric function can be written

$$\varepsilon_1^{Drude}(\omega) = \varepsilon_\infty - \left[\omega_N^2 / \left(\omega^2 + \gamma^2\right)\right] , \qquad (10.4)$$

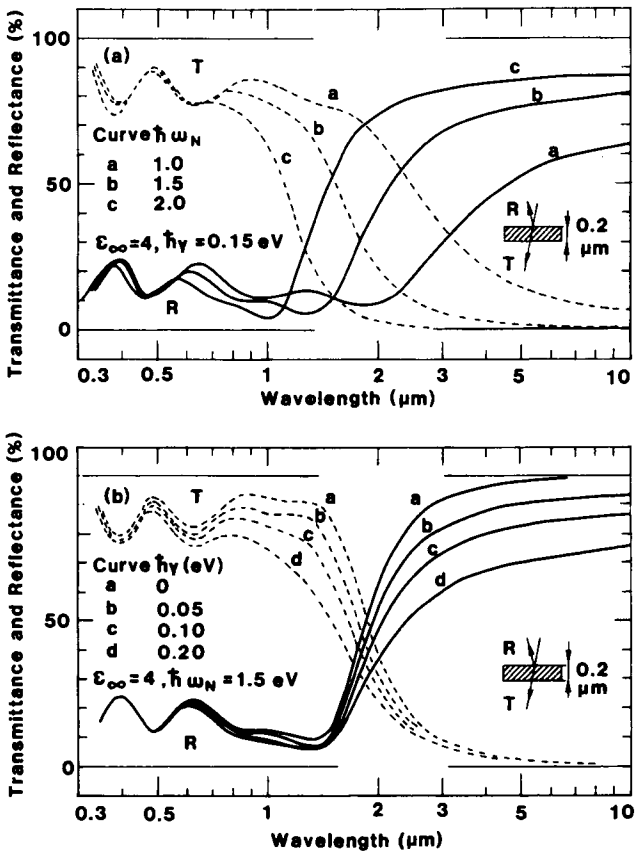

Fig. 10.6 Computed spectral normal transmittance T (dashed curves) and reflectance R (solid curves) for a 0.2-μm-thick slab of a material characterized by the Drude theory (Eqs. 10.4 and 10.5) specified by the shown values of high-frequency dielectric constant ε_∞, unscreened plasma energy $\hbar\omega_N$, and relaxation energy $\hbar\gamma$. After Yoshida *(3735)*.

$$\varepsilon_2^{\text{Drude}}(\omega) = (\gamma/\omega)\left|\omega_N^2/\left(\omega^2+\gamma^2\right)\right| , \tag{10.5}$$

where ε_∞ is the dielectric constant extrapolated towards high energy. The parameter ω_N, sometimes referred to as the unscreened plasma frequency, is related to the free-electron density n_e and the effective conduction-band mass m_c^* through

$$\omega_N^2 = n_e e^2/\varepsilon_0 m_c^* . \tag{10.6}$$

where e is the electronic charge and $\varepsilon_0 = 8.854 \times 10^{-12}$ As/Vm is the permittivity of free space. The frequency at which $\varepsilon^{\text{Drude}} = 0$ yields ω_{pl}, which is connected with ω_N by the approximate relation

$$\omega_{pl}^2 = \left(\omega_N^2/\varepsilon_\infty\right) - \gamma^2 , \tag{10.7}$$

Figure 10.6 illustrates spectral transmittance and reflectance for a 0.2-μm-thick slab of a hypothetical material whose optical properties are described by the Drude theory with the shown values of ε_∞, $\hbar\omega_N$, and $\hbar\gamma$. The infrared reflectance is high and principally similar to experimental results for ion intercalated crystalline W oxide films. The onset of the reflectance is shifted towards shorter wavelengths when $\hbar\omega_N$ is increased, and the change between low and high reflectance becomes sharper when $\hbar\gamma$ is decreased.

Measured spectral reflectance curves have several times been compared with predictions from the Drude theory. With regard to bulk crystals, it was found by Goldner et al. *(1220)* that the data in Fig. 2.8 could be accurately reproduced by taking $\varepsilon_\infty = 4$ and suitable values for $\hbar\omega_N$ and $\hbar\gamma$; specifically the curves for x = 0.94 and x = 1.4 corresponded to $\hbar\omega_N = 4.19$ eV and $\hbar\gamma = 0.41$ eV, and to $\hbar\omega_N = 4.51$ eV and $\hbar\gamma = 0.15$ eV, respectively. These relaxation energies are consistent with results for Na_xWO_3 crystals *(2674)*. With regard to thin films, there are results for samples produced by evaporation followed by annealing *(3050)*, ion assisted evaporation *(148)*, rf sputtering onto heated substrates *(1220, 1223-4, 1228-9, 1234)*, and CVD *(3793)*. Generally, it was found that $\varepsilon_\infty \approx 4$ and $\hbar\omega_N < 4$ eV could lead to an acceptable fit between experiment and theory; the value of $\hbar\gamma$, which gives a measure of the density of scattering centers, was ~2 eV in the early work of Schirmer et al. *(1228, 3050)*, and ~1 eV in subsequent work by Goldner et al. *(1223-4, 1228-9, 1234)* and by Arntz et al. *(148)*. Recently Goldner et al. *(1220)* presented detailed data on $\hbar\omega_N$ and $\hbar\gamma$, shown in Fig. 10.7, indicating that the two quantities are correlated. It appears that $\hbar\gamma$ falls off with increasing $\hbar\omega_N$ and can reach a value as low as ~0.4 eV. Further, it is seen that relaxation energies are smaller for bulk crystals than for corresponding films, thus indicating that the latter might attain an increased degree of electrochromic reflectance modulation if produced under more ideal conditions.

10.5 Transmittance and Reflectance of Crystalline Films: Theory for Heavily Doped Semiconductors with Ionized Impurity Scattering

The Drude theory is simple and suitable for parameterizations of experimental data. However, it does not provide any real insight into the basic scattering mechanisms for the free electrons. In order to proceed towards a more quantitative description of the optical properties, a *dynamical resistivity* $\rho = \rho_1 + i\rho_2$ is introduced. The dielectric function can then be written

Table 10.1 Exponent s in the real part of the dynamic resistivity for different scattering mechanisms and scattering models.

Scattering mechanism	Scattering model	s
Ionized impurities	Coulomb potential	-3/2
Dislocations	Charged monopole line	-2
	Charged dipole line	-1
Neutral defects (short ranged)	δ potential	1/2
Acoustic phonons	Deformation potential coupling	1/2
	Piezoelectric coupling	-1/2
Optical phonons	Polar coupling	-1/2

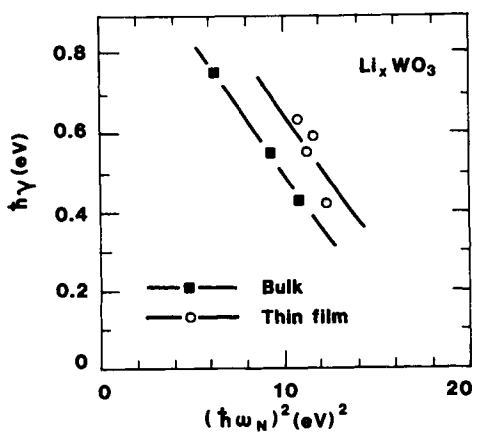

Fig. 10.7 Unscreened plasma energy squared $(\hbar\omega_N)^2$ vs. relaxation energy $\hbar\gamma$ obtained from Drude analyses of reflectance spectra for Li_xWO_3 crystals in bulk and thin-film form. Lines were drawn for convenience. After Goldner et al. *(1220)*.

$$\varepsilon = \varepsilon(WO_3) + i/(\varepsilon_0 \omega \rho), \tag{10.8}$$

where $\varepsilon(WO_3)$ refers to the W oxide host lattice, which does not contain intercalated ions and inserted electrons. The Drude theory can be restated as

$$\rho_1^{Drude} = \gamma/(\varepsilon_0 \omega_N^2), \tag{10.9}$$

$$\rho_2^{Drude} = -\omega/(\varepsilon_0 \omega_N^2), \tag{10.10}$$

from which it is seen that ρ_1^{Drude} contains the whole effect of the scattering, whereas ρ_2^{Drude} is independent of the scattering and can be understood as a result of the inertia of the free electrons.

There are many scattering mechanisms for the free electrons that may influence the optical properties, at least in principle. Thus one can separate between electron-defect scattering (against grain boundaries and external surfaces, neutral and ionized point defects, dislocations, precipitations, and clusters), electron-lattice scattering (against local deformation potentials, etc.), and electron-electron scattering. A general approach to electron scattering can be founded on solutions of the Boltzmann transport equation, and thorough discussions have been given by Nag *(2458)* and by Chattopadhyay and Queisser *(662)*. The expressions given for the frequency-dependent case are usually not accurate enough for quantitative analyses, though. However, a somewhat different approach leads to practically useful results; it rests on the equivalence of Joule heat and energy loss *(585)* and was discussed in reviews by Gerlach *(1170-1)*. This theory is employed below.

Formally, one can go beyond the Drude theory by substituting

$$\gamma \rightarrow \gamma_1(\omega) + i\gamma_2(\omega) \tag{10.11}$$

in Eq. 10.9. ρ_1 still is directly connected with the electron scattering, and a comparison of experimental and theoretical data for this quantity yields a crucial test of the validity of the models used. The comparison is straight-forward in the energy range

$$\hbar\omega_{pl} < \hbar\omega < E_g \tag{10.12}$$

since ρ_1 obeys a power law

$$\rho_1 \propto \omega^s \tag{10.13}$$

where s takes different values depending on the scattering mechanism. Correspondingly one has

$$\varepsilon_2 \propto \omega^{s-3}. \tag{10.14}$$

Table 10.1, based on work by Gerlach *(1170-1)*, summarizes the exponents applicable to different scattering mechanisms, each represented by a certain scattering model.

Whereas many of the scattering mechanisms in Table 10.1 are of little importance for a well crystallized W oxide films, one cannot neglect the role of the ions that are intercalated together with the electrons. These ionized impurities are predicted to yield s = -3/2. By considering the role of the

ions only, one expects to obtain the limiting performance of crystalline electrochromic W oxide. Following Gerlach *(1170-1)*, the dynamic resistivity due to *ionized impurity scattering* can be written

$$\rho(\omega) = i\,\frac{Z^2 n_i}{6\pi^2 \varepsilon_0 n_e^2 \omega}\int_0^\infty k^2\,dk\left(\frac{1}{\varepsilon^{eg}(\mathbf{k},\omega)} - \frac{1}{\varepsilon^{eg}(\mathbf{k},0)}\right) - i\,\frac{\omega}{\varepsilon_0 \omega_{pl}^2}\,, \tag{10.15}$$

where Z is the charge of the ions, n_i is their density, and ε^{eg} is the dielectric function of the free electrons and accounts for the screening of the ions. For the intercalation of H^+, Li^+, etc., one should put $Z = 1$. Further, at least as a first approximation, it is adequate to set the densities of ions and electrons equal, i.e.,

$$n_i = n_e. \tag{10.16}$$

The remaining part of the theory regards ε^{eg}, for which one can use the Random Phase Approximation, RPA *(2083, 2161)*. For the case of electron scattering processes, it is the longitudinal part of the dielectric function that is relevant, and in the limit of small damping one has for the denerate electron gas *(2083)*

$$\varepsilon^{eg}(k,\omega) = \varepsilon_\infty + \left(3\omega_N^2/k^2 v_F^2\right)(F_1 + iF_2)\,, \tag{10.17}$$

$$F_1 = \frac{1}{2} + \frac{1}{8z}\left[1 - (z-u)^2\right] ln\left|\frac{z-u+1}{z-u-1}\right| + \frac{1}{8z}\left[1 - (z+u)^2\right] ln\left|\frac{z+u+1}{z+u-1}\right|\,, \tag{10.18}$$

$$F_2 = (\pi/2)u\,, \qquad z+u<1, \tag{10.19}$$

$$F_2 = (\pi/8z)\left[1-(z-u)^2\right], \quad |z-u|<1<z+u\,, \tag{10.20}$$

$$F_2 = 0\,, \qquad |z-u|>1, \tag{10.21}$$

$$z = k/2k_F\,, \tag{10.22}$$

$$u = |\omega|/kv_F\,, \tag{10.23}$$

$$v_F = \hbar k_F/m_c^*\,, \tag{10.24}$$

$$k_F = \left(3\pi^2 n_e\right)^{1/3}\,. \tag{10.25}$$

It is known *(2161)* that the RPA in principle can give a very good description of a heavily doped semiconductor, such as ion intercalated crystalline W oxide. However, the theory is not entirely correct since it leaves out the influence of exchange and correlation in the electron gas. These effects can be included rather easily in refined theories *(1563, 3179)*, but the lack of a detailed characterization of crystalline W oxides does not justify such an elaboration at present.

The equations given above allow a calculation of the limiting optical properties of crystalline electrochromic W oxide, provided that $\varepsilon(WO_3)$ and m_c^* are specified. Judging from the refractive index data in Fig. 9.4, one can put $\varepsilon(WO_3) \approx 4.8$. The situation is less clear regarding m_c^*, but

analyses by Dickens et al. *(920)* and Owen et al. *(2674)* of the optical properties of Na_xWO_3 with $x < 0.5$ give credence to $m_c^* = 0.5m$, with m being the free-electron mass. Figure 10.8, reproduced from Svensson and Granqvist *(3284)*, shows spectral reflectance with n_e as parameter. The results pertain to a 0.2-μm-thick slab backed by a "glass" substrate specified by the refractive index 1.53. When n_e is increased from 10^{21} to 10^{22} cm^{-3}, the onset of strong reflectance is shifted towards a shorter wavelength and the transition appears progressively sharper. The basic similarity with the data based on Drude theory in Fig. 10.6 should be appreciated, but it is important to remember that whereas the Drude theory represents electron scattering only with a free parameter, the present calculation *quantitatively* accounts for scattering from the ions that are unavoidable in an electrochromic material.

It is straight forward to evaluate integrated solar (sol) and luminous (lum) properties from the spectral optical data. The pertinent quantities are obtained by weighting the optical data with the appropriate solar spectrum (Fig. 1.6) and the luminous efficiency for photopic vision (Fig. 1.4), respectively. Figure 10.9 shows R_{sol}, R_{lum}, T_{sol}, and T_{lum} for WO_3 films with $0.05 \leq d \leq 0.5$ μm and $10^{20} \leq n_e \leq 10^{22}$ cm^{-3}. At $n_e < 10^{21}$ cm^{-3}, the optical properties are governed almost entirely by reflectance at the film boundaries. The reflectance is as large as ~20 %, which is a consequence of the high refractive index of undoped WO_3. At $n_e > 10^{21}$ cm^{-3}, R_{sol} goes up and T_{sol} goes down monotonically in a manner consistent with the shifted plasma frequency and the film thickness. The results for T_{lum} and R_{lum} show a qualitatively similar behavior. However, R_{lum} can reach a value as low as ~5 % for $n_e \approx 6 \times 10^{21}$ cm^{-3}, and T_{lum} can display a concomitant weak maximum, which occurs because of destructive interference at $0.4 < \lambda < 0.7$ μm. For $n_e > 10^{21}$ cm^{-3} it is found that $R + T$ is less than unity, signifying that plasma absorption is of importance.

Figure 10.9 contains a wealth of information. To take one example, one can consider a 0.2-μm-thick W-oxide-based film whose electron density is varied from a low value up to 5×10^{21} cm^{-3}. The ensuing optical performance (solid curves) goes from a state with ~82 % transmittance of solar energy to another state with ~35 % transmittance of solar energy. The latter state implies ~63 % luminous transmittance and ~5 % luminous reflectance. These properties point to the highly variable energy throughput one can hope to achieve in a smart window employing optimized electrochromic layers.

Experimental reflectance data on crystalline W oxide films were discussed with a view to different scattering mechanisms by Schirmer et al. *(3050)* already in 1977. Subsequently, Goldner et al. *(1221-2)* evaluated the dynamic resistivity of some H_xWO_3 films and found that an approximate relation $\rho_1 \propto \omega^{-2}$ was obeyed for $\hbar\omega < E_g$; consequently (cf. Table 10.1) they argued that dislocations were the dominant scattering centers. This assignment is debatable, though, and if one considers the influence of exchange and screening in the electron gas, as well as experimental uncertainties, it may well be that ionized impurity scattering gives a description that is equally good--and indeed preferrable on physical grounds. The latter points were made by Hamberg and Granqvist *(1399)*.

10.6 Optical Properties of Granular Films: Effective Medium Theories

Tungsten oxide films are not homogeneous. Thus strongly disordered films in general are cluster-assembled materials, which can also exhibit a column structure on a scale that is larger than that of

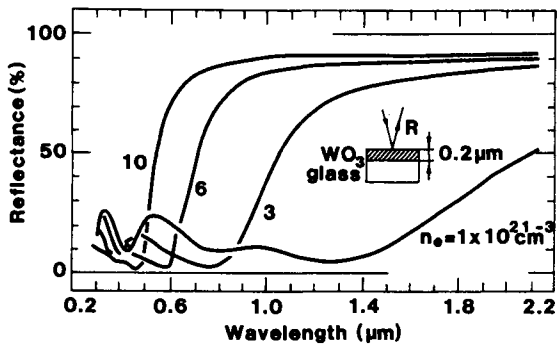

Fig. 10.8 Computed spectral normal reflectance R for a 0.2-μm-thick slab of a material, characterized by the theory for a semiconductor with ionized impurity scattering, on glass. The curves pertain to different values of the free-electron density n_e. After Svensson and Granqvist *(3284)*.

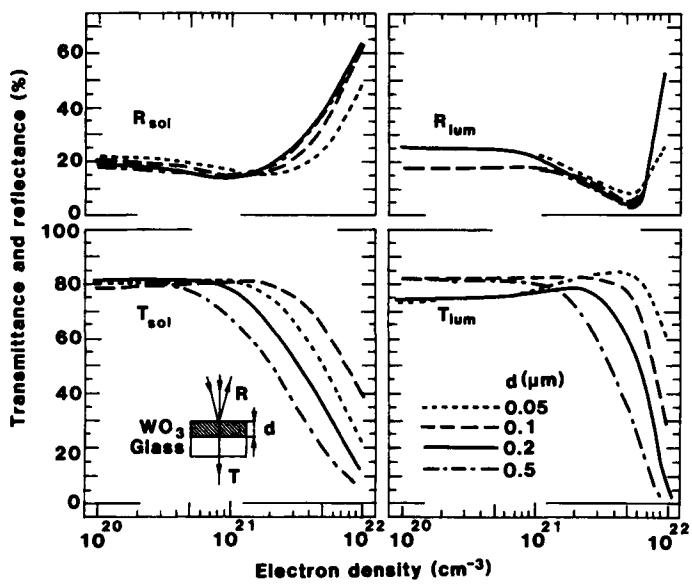

Fig. 10.9 Solar (sol) and luminous (lum) transmittance T and reflectance R computed from a model for the optical properties of crystalline W oxide. Results are given for several film thicknesses d. From Svensson and Granqvist *(3284)*.

the clusters. In crystalline films one cannot disregard grain boundaries, shear planes, and other defects. These issues were discussed at length in chapters 2 and 3. The influence of the granular nature of W oxide films on their optical properties has been considered only rarely. However, one may note one study by Nagai *(2459)* who regarded electrochromic Li^+ intercalated films as mixtures of insulating WO_3 and metallic Li_xWO_3, and another study by Demiryont and Schulz *(878)* who took an as-deposited film to be composed of $WO_{2.5}$ and WO_3. Tungsten-molybdenum oxide films, and films of many other mixed oxides and metal-particle-containing oxides, can show electrochromism, as will be discussed in Ch. 13; these materials can also be regarded as "granular".

The optical properties of granular materials can be modeled by use of Effective Medium Theory (EMT). It applies when the inhomogeneities are large enough to be assigned unique dielectric functions and small enough that the quasi-static limit applies. The analysis below considers a two-phase material with components A and B; their dielectric functions are ε_A and ε_B, and the corresponding volume fractions are f_A and f_B (= 1 - f_A). The dielectric function of the granular, "effective", material is denoted $\bar{\varepsilon}$. It should be stressed at the outset that a complete EMT can be formulated only when a full structural characterization of the granular material is at hand, which is never the case in a real sample, and hence all EMTs are approximate. They can be expected to be accurate only if based on a model that represents the actual microstructure of the material under analysis. A detailed discussion of EMTs for two-component materials was given recently by Niklasson *(2531)*.

Assuming that ε_A, ε_B, f_A, and f_B are known, and that the granular material is isotropic, one can write rigorous limits--known as Bergman-Milton bounds--for the effective dielectric function according to *(169, 359, 2316-7)*

$$\bar{\varepsilon} = \frac{\varepsilon_A\varepsilon_B + 2\varepsilon_h(f_A\varepsilon_A + f_B\varepsilon_B)}{2\varepsilon_h + f_A\varepsilon_B + f_B\varepsilon_A} \quad . \tag{10.26}$$

The bounds are obtained with

$$\varepsilon_h = \zeta\varepsilon_A + (1 - \zeta)\varepsilon_B \quad , \tag{10.27}$$

$$\varepsilon_h^{-1} = \zeta\varepsilon_A^{-1} + (1 - \zeta)\varepsilon_B^{-1} \quad , \tag{10.28}$$

when ζ is varied between zero and unity. The bounds form two circular arcs in the complex plane, and the area surrounded by these represent the permissible values for $\bar{\varepsilon}$. The structural parameter ζ is related to the pair and three-point correlation functions for the granular material *(1058-9, 1992)* and can be specified if the microtopology is well-defined, such as in a fractal structure *(2528)*. By incorporating more detailed structural information, i.e., higher order correlation functions, one can derive a hierarchy of narrower bounds on $\bar{\varepsilon}$ *(2277, 2316-7)*.

The scheme to obtain $\bar{\varepsilon}$, sketched above, is theoretically sound but often of limited practical value owing to the lack of precision in materials characterization. An alternative way to obtain $\bar{\varepsilon}$ is to specify explicit microstructures and carry out calculations of $\bar{\varepsilon}$ for these. Even if strictly valid only for the considered microstructures, the corresponding EMTs are often good approximations to granular thin films.

One may start by representing the pertinent microstructures by Random Unit Cell (RUC) models that are simple enough to permit a theoretical treatment and yet do not leave out the essential

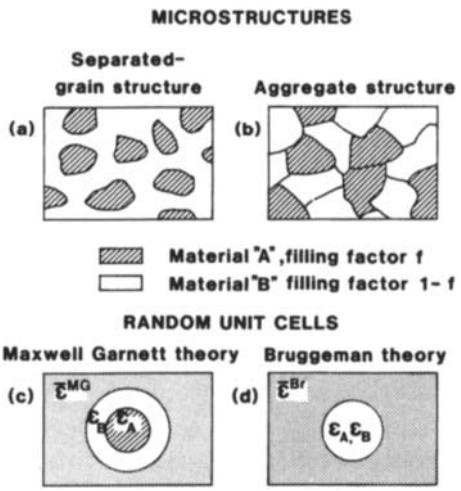

Fig. 10.10 Microstructures and Random Unit Cells for two types of granular materials. From Niklasson and Granqvist *(2533)*.

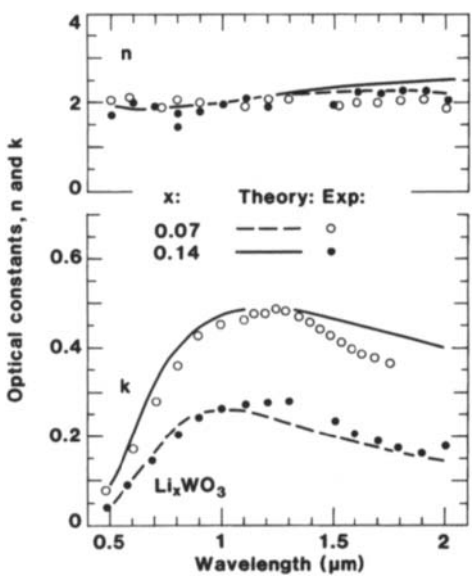

Fig. 10.11 Spectral optical constants, n and k, for evaporated W oxide films with two values of the charge insertion (represented as x in Li_xWO_3). Circles refer to experimental quantities and curves to data computed fromthe Bruggeman effective medium theory applied to a composite of WO_3 and Drude-like $LiWO_3$. FromNagai *(2459)*.

physics *(2533)*. Figure 10.10 shows two cases that are regarded as typical. The separated-grain structure is modelled by a RUC which is a core of "A" surrounded by a shell of "B", so that the ratio of core volume to shell volume equals $f\,(=f_A)$. The aggregate structure is modeled by a sphere having a probability f of being "A" and $1-f$ of being "B". The RUCs are embedded in the effective medium, whose properties are to be determined.

A basic definition of an effective medium is that the embedded RUC should not be detected in an experiment using radiation confined to a specific wavelength range. Thus the extinction of the RUC should be the same as if it were replaced by a sphere whose dielectric function is $\bar{\varepsilon}$. This criterion makes it fruitful to use an optical theorem for absorbing media stating that

$$C_{ext} = 4\pi \,\mathrm{Re}\,[S(0)/k^2]\,, \tag{10.29}$$

$$k = 2\pi\,\bar{\varepsilon}^{1/2}/\lambda\,. \tag{10.30}$$

Here C_{ext} is the extinction of the RUC compared with that of the surrounding material, and $S(0)$ is the scattering amplitude in the forward direction. Requiring that $C_{ext} = 0$ yields

$$S(0) = 0\,, \tag{10.31}$$

which expresses the fundamental property of an effective medium. The same condition has been given elsewhere in somewhat different contexts *(1006, 3264)*.

The strength of the classical scattering approach to $\bar{\varepsilon}$ lies in the fact that $S(0)$ is known for (stratified) spheres by the Lorenz-Mie theory *(1784, 3509)*. The expressions for $S(0)$ can be written as power series in a size parameter, and setting the leading term to zero gives explicit formulas for $\bar{\varepsilon}$. For the coated sphere RUC, applicable to the separated-grain structure, one then obtains (with $\bar{\varepsilon} = \bar{\varepsilon}^{MG}$)

$$\frac{\bar{\varepsilon}^{MG} - \varepsilon_B}{\bar{\varepsilon}^{MG} + 2\varepsilon_B} = f\,\frac{\varepsilon_A - \varepsilon_B}{\varepsilon_A + 2\varepsilon_B}\,. \tag{10.32}$$

This is the well known formula for the *Maxwell Garnett* EMT *(1137-8)*. One can show that Eq. 10.32, and an analogous expression for the inverted structure with A↔B, correspond to the Bergman-Milton bounds in Eqs. 10.26 to 10.28 with $\zeta = 0$ and $\zeta = 1$, respectively. For the spherical RUC, applicable to the aggregate structure, one obtains (with $\bar{\varepsilon} = \bar{\varepsilon}^{Br}$)

$$f\,\frac{\varepsilon_A - \bar{\varepsilon}^{Br}}{\varepsilon_A + 2\bar{\varepsilon}^{Br}} + (1-f)\,\frac{\varepsilon_B - \bar{\varepsilon}^{Br}}{\varepsilon_B + 2\bar{\varepsilon}^{Br}} = 0\,. \tag{10.33}$$

This is the constitutive equation for the *Bruggeman* EMT *(498)*. It is unchanged under A↔B exchange. RUC arguments can also be forwarded *(2533)* to derive some other EMTs *(1408, 3127)*; the corresponding values of $\bar{\varepsilon}$ fall inside the Bergman-Milton bounds.

The Bruggeman EMT was used by Nagai *(2459)* in an attempt to explain the optical properties of ion intercalated W oxide on the premise that the material was a granular composite of metallic $LiWO_3$ and insulating WO_3. The filled and open circles in Fig. 10.11 indicate experimentally determined optical constants for two samples produced by evaporation of W oxide in the presence

of some N_2 and lithiation in an electrolyte of γ-butyrolactone with 1 M $LiClO_4$ and ~1 % H_2O. The ensuing material was represented as Li_xWO_3, with x obtained from the inserted charge density. It is seen that n is approximately 2 and that k is peaked at ~1.3 μm; this is in agreement with the results in Fig. 9.13 and elsewhere. Theoretical data were obtained from Eq. 10.33 with ε_A given by a Drude expression and $\varepsilon_B = 4$. Specifically, with the notation in Eqs. 10.4 and 10.5, the parameter values $\varepsilon_\infty = 4.14$, $\hbar\omega_N = 5$ eV, and $\hbar\gamma = 1$ eV were used to derive the solid and dashed curves in Fig. 10.11. The agreement between theory and experiment is rather good. The implications of this fit are not obvious, though, and it is not clear that the granular model underlying the EMT is of much physical significance.

Recently, Davazoglou and Donnadieu *(822)* used the Bruggeman EMT in order to account for the dispersion parameters of W oxide films prepared by CVD onto substrates at 400°C followed by annealing post-treatment at 500 and 600°C. The model assumed that three components were present in the film: a crystalline phase, an "amorphous" phase, and voids. Theory and experiment could be reconciled, but the complexity of the model may leave one in a quandry about the uniqueness of the theoretical fit.

Chapter 11

TUNGSTEN OXIDE FILMS: ELECTRICAL PROPERTIES

Optical and electrical effects are closely related. This chapter aims at elucidating features that are of importance for the electrochromism of tungsten-oxide-based films from considerations of their electrical dc conductivity (11.1), electrical ac conductivity (11.2), thermoelectric effect (11.3), and photoelectric effects (11.4).

11.1 Electrical dc Conductivity

There are many studies of electrical conductivity σ in the literature, and its dependence on the amount of ion intercalation x, temperature τ, applied electric field F, frequency ω, and various deposition and post-treatment parameters has been reported. Figure 11.1 forms a suitable starting point for the discussion. It shows σ vs. x for two types of films and can be viewed as the counterpart to Fig. 2.10 that showed results for bulk crystals. One of the films reported on in Fig. 11.1 was prepared by evaporation followed by H^+ intercalation from H_2SO_4 *(785)*, and the other was made by sputtering and post-treatment with atomic hydrogen evolved from a mixture of HCl and Zn *(3645)*. The thicknesses were 0.5 and 0.7 μm, respectively. For the evaporated film, the conductivity rises abruptly at a certain "critical" ion content x_c. At a low temperature one finds that the conductivity obeys a relation

$$\sigma \propto (x - x_c)^{\Gamma} \tag{11.1}$$

with $x_c \approx 0.31$ and $\Gamma \approx 1.6$. An increase of the temperature displaces x_c towards a smaller value. Relation 11.1 is strikingly similar to predictions from bond percolation theory *(83)*, but, as already discussed in Sec. 2.4, the agreement is almost certainly fortuitous. Data for a H^+ intercalated evaporated film at $\tau \approx 123$ K yielded $x_c \approx 0.22$, which is in good agreement with the results in Fig. 11.1 *(3645)*.

The conductivity onset, and the shape of the σ vs. x relation, are dependent on thin film fabrication technique. This is apparent from Fig. 11.2, which gives data for ~0.5-μm-thick W oxide films evaporated in controlled amounts of oxygen, treated in electrolytes of γ-butyrolactone with 1 M $LiClO_4$ and ~1 % H_2O, and measured at room temperature *(2459)*. At low p_{O2}, the σ vs. x relation is very similar to the one in Fig. 11.1. However, an increase of p_{O2} causes a drop in σ, which indeed is the expected result since the oxygen leads to a stoichiometry closer to WO_3 as well as a larger porosity (cf. Fig. 3.2a). One also observes that a sputter-deposited film at

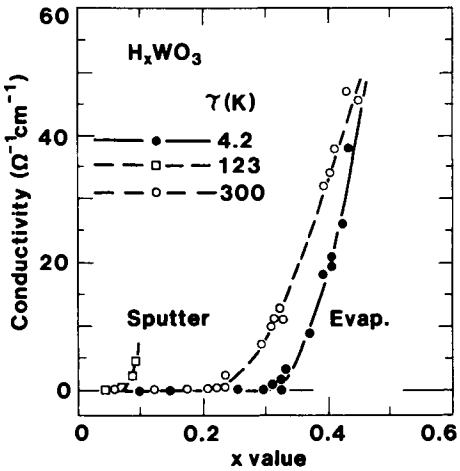

Fig. 11.1 Electrical conductivity vs. H^+ content, given as x in H_xWO_3, for films prepared by the shown techniques and studied at the shown temperatures τ. Symbols denote measured data. The solid curve represents Eq. 11.1 and the dashed curves were drawn for convenience. After Crandall and Faughnan *(785)* and Wittwer et al. *(3645)*.

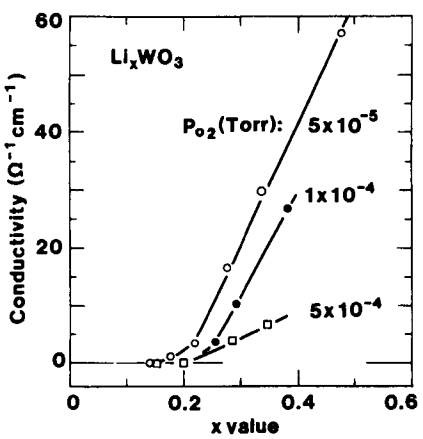

Fig. 11.2 Electrical conductivity vs. Li^+ content, given as x in Li_xWO_3, for films evaporated at the shown pressures of O_2. Symbols denote measured data and curves were drawn for convenience. From Nagai *(2459)*.

$\tau \approx 123$ K--reported on in Fig. 11.1--has x_c as small as ~0.05, which underscores the critical influence of the deposition method.

The dependence of σ on x and τ, that can be inferred from the data on evaporated films in Fig. 11.1, is analyzed in more detail in Fig. 11.3, where particular emphasis is on $x < x_c$. At $\tau = 300$ K one finds that σ is a function of x even at low H^+ intercalation; thus σ increases by about six orders of magnitude when x goes from 0 to 0.2. Qualitatively similar behavior has been found for W oxide films subjected to several of the coloration schemes outlined in Fig. 9.6, viz. electrochemical H^+ intercalation *(1334-5, 3645, 3795)*, electrocoloration *(835-6)*, ultraviolet irradiation in air *(1168, 1272, 3404)* and in C_2H_5OH *(2477)*, thermocoloration *(884, 1272, 3404)*, exposure to atomic hydrogen *(3645)*, Pd "spillover" in films exposed to H_2 *(2156, 3117)*, ion bombardment *(117)*, and electron bombardment *(1887)*.

Figure 11.3 shows that the temperature dependence of σ is fully consistent with a relation

$$\sigma \propto \exp\left[-(\tau_0/\tau)^{1/4}\right], \tag{11.2}$$

where τ_0 is a constant, as long as $x < x_c$. Close to x_c, the conductivity is only weakly dependent on temperature. Analogous $\tau^{-1/4}$-dependencies have been reported several times *(116, 3404, 3645)*; one may also note that a $\tau^{-1/7}$-dependency was claimed in some work *(327, 801)*.

Equation 11.2 is Mott's famous "$\tau^{-1/4}$ law" *(1621, 2413-5, 3128)* accounting for variable-range hopping of charge carriers between randomly distributed localized electronic states. The parameter τ_0 is a measure of the extent of the wavefunction for the charge carriers. This theory has been derived from percolation-theoretic arguments by Ambegaokar et al. *(84)*, Pollak *(2788)*, and others *(1891, 2673, 3159)*. These derivations neglect lattice polarisation, though, and therefore their applicability to polaron transport is in doubt. More recently Triberis et al. *(3442-51)* have studied electrical properties due to small-polaron hopping in disordered systems. They found that a $\tau^{-1/4}$ relation normally was valid, although other exponents could occur depending on temperature, whether the polaron hopping was correlated or not, and whether strong density-of-states effects were at hand. A summary of the results for the electrical conductivity was given in *(3451)*. At $\tau^{-1/2}$ relation can occur because of interpolation between low-temperature hopping and high-temperature activated conduction *(3814)*.

In sufficiently restricted temperature intervals, it is possible to illustrate the conductivity by use of a simple Arrhenius law, i.e.,

$$\sigma \propto \exp\left(-E_a/k_B\tau\right), \tag{11.3}$$

where E_a is activation energy and k_B is Bolzmann's constant. This approach has been taken in several studies, and the effects on E_a of different deposition and post-treatment parameters have been reported. Fig. 11.4 shows E_as, based on measurements at $115 < \tau < 300$ K, for evaporated W oxide films in virgin transparent state and after coloration by ultraviolet irradiation *(884)*. The data refer to annealing in vacuum (part a) and oxygen (part b). Prior to the heat treatment, the activation energies lay between 0.22 and 0.36 eV. Annealing in air produced a monotonic decrease of E_a, whereas annealing in O_2 yielded an initial rise to ~0.5 eV at ~200°C followed by a sharp decrease at ~400°C. Other work showed that below 300 K one has $0.3 < E_a < 0.4$ eV for as-evaporated films *(327, 801, 1334, 2186)* and for UV colored sputter-deposited films *(1168)*. At higher temperatures there is evidence that E_a shifts to a larger value *(836, 1271, 2186)*.

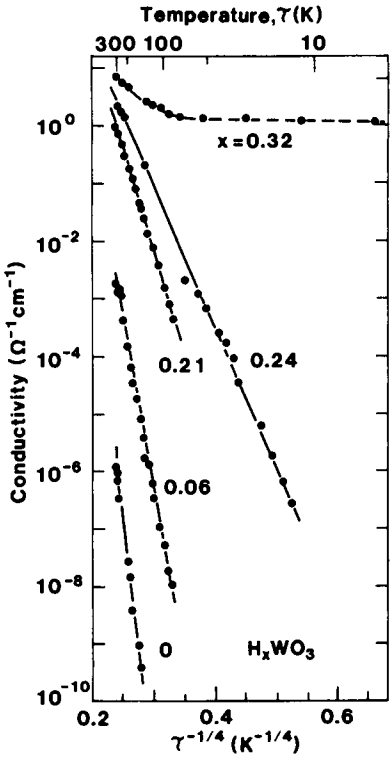

Fig. 11.3 The logarithm of the electrical conductivity plotted vs. $\tau^{-1/4}$, where τ is temperature, for films with different H^+ content, given as x in H_xWO_3. The film thickness was 1 μm, except for the film with x = 0.32 that was 0.5 μm thick. Solid lines represent Eq. 11.2, and the dashed curve was drawn for convenience. After Crandall and Faughnan *(785)*.

If the conductivity is dominated by polaron hopping, one may make use of the simple configurational coordinate diagram in Fig. 10.2 and identify E_a with U_p. A relation

$$E_a = E_p/4 \tag{11.4}$$

is then obtained. With $E_p \approx 1.4$ eV, one predicts that $E_a \approx 0.35$ eV, which is in very good agreement with data for unannealed W oxide films. This simple relation no longer holds for annealed films, though, as can be inferred by comparing Figs. 9.7 and 11.4, and the implications of an agreement with Eq. 11.4 remain uncertain. A temperature-dependent increase of E_a has been treated theoretically by considering thermally activated tunneling between overlapping potentials of deep centers *(1334-5)*. For the sake of completeness, one could note that E_a has been studied in relation to deposition parameters for films made by evaporation *(3094)*, rf sputtering *(1168, 1737, 2341-2)*, and CVD *(957, 962, 2874)*.

Voltage-dependent electrical conduction has been studied several times *(327, 801, 836, 1271, 2392, 3404)*. Detailed results were reported by Thomas and Goulding *(3404)*, who showed that evaporated W oxide films in virgin state were ohmic at $\tau > 200$ K and electric fields $F < 4 \times 10^3$ V/cm. For films exposed to air, σ dropped for $F > 10^3$ V/cm at room temperature; this is probably associated with the same processes as those responsible for electrocoloration. Theoretically, small polaron hopping in disordered materials gives at low temperature *(3446)*

$$\sigma \propto \exp\left[-(\tau_o/\tau)^{1/4}\left(1 - F^2/g(\tau)\right)\right] , \tag{11.5}$$

where g is a function, and an analogous relation holds at high temperature *(3445)*. A F^2-dependence can also be inferred from some earlier work *(129, 3158)*.

The conductivity of W oxide films can change significantly upon exposure to different gases, and hence electrical measurements can be used for gas sensing applications. This has been discussed in detail for propane *(3440)* and H_2S *(3678)*. Tungsten oxide surfaces are able to catalyze a variety of chemical reactions, and work on different types of catalysts gives reasons to believe that gas sensing is possible for a whole range of hydrocarbons (such as olefins) and N_2O *(235, 892, 1799, 3039-40)*. Gas sensing with WO_3 ceramics was studied in *(445-7)*. Surface Acoustic Wave devices represent another possibility to use W oxide films for gas detection. By using a dual delay line arrangement, with a W-oxide-based film in one delay path, it was possible to detect H_2S down to less than 10 ppb *(502, 3531)*. Optical detection of H and H_2 was mentioned in Sec. 9.3 above.

The variable resistance of ion intercalated W oxide has potential applications in electronic hardware implementations of neural networks *(3399)*, where this material can serve as a synaptic element with a wide dynamic range *(2833, 3399)*.

11.2 Electrical ac Conductivity

Frequency-dependent conduction has been reported by Mansingh et al. *(2186)*, Marszalek *(2188)*, and Solodukha and Zhukov *(3205)*. It was found *(2186, 3205)* that a relation

$$\mathrm{Re}\,\sigma \propto \omega^h \tag{11.6}$$

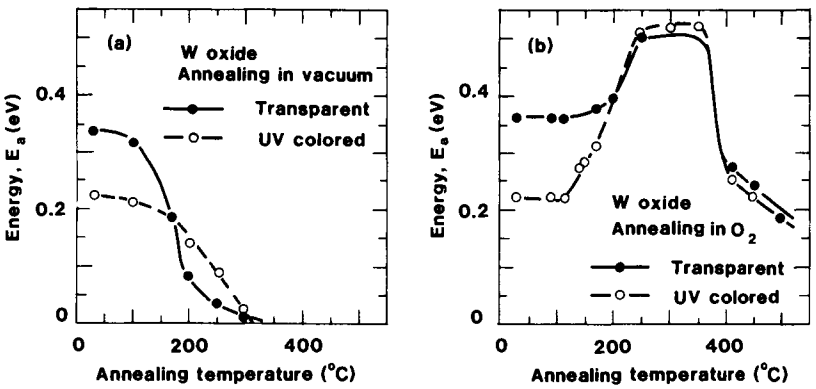

Fig. 11.4 Activation energy E_a as a function of annealing temperature for evaporated W oxide films in transparent and UV colored states. Parts (a) and (b) refer to heat-treatment in vacuum and oxygen, respectively. Circles indicate measured data, and curves were drawn for convenience. After Deneuville and Gérard *(884)*.

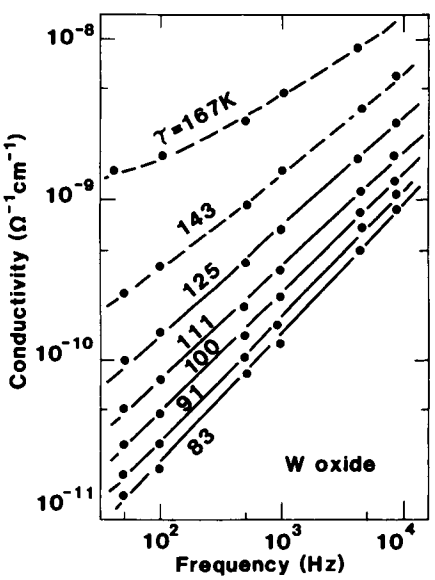

Fig. 11.5 Electrical ac conductivity, studied at several temperatures τ, for an evaporated W oxide film. Filled circles denote measured data. Solid lines represent Eq. 11.6, and dashed curves were drawn for convenience. From Mansingh et al. *(2186)*.

was obeyed over at least two orders of magnitude in frequency, provided that the temperature was low enough. This is illustrated in Fig. 11.5, showing results from Mansingh et al. *(2186)*. At $\tau <$ 125 K the data lie on a straight line corresponding to $0.64 < h < 0.77$; above this temperature Eq. 11.6 is followed only roughly.

Figure 11.6 illustrates the temperature dependence of the exponent h in Eq. 11.6. The circles, corresponding to the lines in Fig. 11.5, indicate that the data by Mansingh et al. *(2186)* can be expressed as

$$h = 1 - D_f = 1 - \tau/\tau^* , \tag{11.7}$$

where D_f and τ^* are parameters. The data by Solodukha and Zhukov *(3205)*, represented by the filled squares in Fig. 11.6, also indicate that h has a negative contribution proportional to τ. The latter data were given as loss tangents; they have been analyzed by Niklasson *(2530)*.

In order to shed some light on the results in Fig. 11.6, one can note that power laws are ubiquitous in the dielectric response of almost all materials *(1683)*. Interpretations of this "universal response" in terms of fractal geometric structures and fractal time processes have recently been put forward by Niklasson *(2529-30)* and others *(945, 3161)*, and under certain conditions one can identify D_f in Eq. 11.7 with a dimension for a fractal time process. Simple examples of such processes are the hopping of charge carriers in an exponential distribution of activation energies, or, equivalently, multiple trapping in an exponential band tail. In this case, τ^* in Eq. 11.7 is a parameter characterizing the steepness of the distribution.

11.3 Thermoelectric Effect

Thermoelectric power S of W oxide films has been studied by Goulding et al. *(1271-2, 3404)* and others *(1323, 2037)*. Figure 11.7 shows data for two films evaporated under slightly different conditions. It appears that significant discrepancies exist among different samples. However, the S vs. τ relation is reversible and rather linear at $\tau < 300$ K, whereas the thermoelectric power displays a pronounced and irreversible peak at $\tau > 350$ K. The latter feature is connected with thermocoloration. Fairly linear S vs. τ relations have also been recorded at $\tau < 350$ K for Na_xWO_3 films made by coevaporation *(1323)* and for reactively dc sputtered films intercalated with H^+ *(2037)*.

The temperature dependence of the thermoelectric power can be analyzed in different ways. It was shown by Thomas and Goulding *(3404)* that their measurements were consistent with a relation

$$S \propto \tau^{1/2}. \tag{11.8}$$

The accuracy of the fit is illustrated in Fig. 11.8, showing data for evaporated films colored to different extents by UV irradiation.

The $\tau^{1/2}$-dependence in Eq. 11.8 is in agreement with several theoretical predicitons based on variable range hopping of charge carriers, i.e., the same mechanism as the one underlying the $\tau^{-1/4}$ variation of the electrical conductivity in Eq. 11.2 *(1891, 2673, 3822-3)*. However, the observed $\tau^{1/2}$ function does not agree with results of some recent calculations of the thermoelectric power due to small polaron hopping in amorphous materials *(3442-4)*. This discrepancy among the theoretical

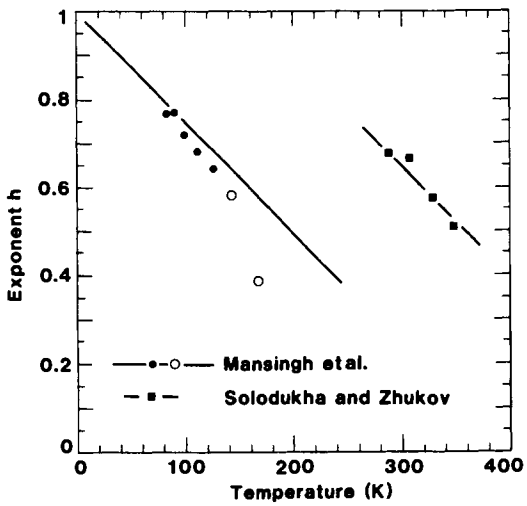

Fig. 11.6 Exponent h in the electrical ac conductivity vs. temperature. Symbols denote experimental data, with open circles indicating uncertain values. Solid curve represents Eq. 11.7, and dashed curve was drawn for convenience. After Mansingh et al. *(2186)* and Solodukha and Zhukov *(3205)*.

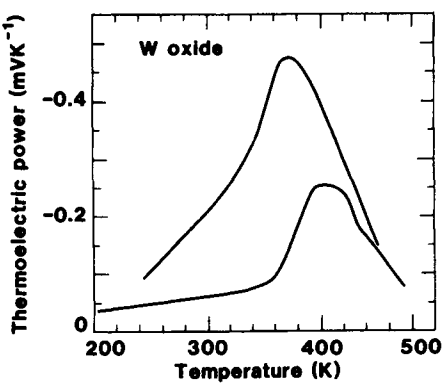

Fig. 11.7 Thermoelectric power vs. temperature for two evaporated W oxide films made under somewhat different conditions. The curves were drawn through a large number of individual data points. After Goulding and Thomas *(1271)*.

expressions is not understood at present.

It is evident from Fig. 11.8 that the thermoelectric power at any given temperature decreases with increasing coloration. The results pertaining to 300 K are shown in Fig. 11.9 as well. This figure includes data for films colored by heating them up to $\tau_a \approx 440$ K. For these latter samples it appears that S(300 K) is peaked at ~50 % coloration. Results for films colored by UV irradiation and by heating were reported in *(1272)* as well.

Films colored through coevaporation of Na and WO_3 were investigated by Green and Travlos *(1323)*. Figure 11.10, taken from their work, shows that S(303 K) drops monotonically when the Na content is increased. The data refer to films with grain sizes of ~5 nm or ~12 nm.

11.4 Photoelectric Effects

When W oxide films are irradiated with short wavelength light, they can show photoconductivity. This effect was studied for evaporated films by Deb *(836)* as early as in his initial work on electrochromism. Figure 11.11 shows spectral photocurrent between two gold electrodes on the surface of a W oxide film upon its exposure to monochromatic radiation. The as-deposited strongly disordered film has an onset of photoconductivity at ~0.35 μm. This wavelength is somewhat shorter than that for the optically detected bandgap (cf. Fig. 8.1) which--according to Deb *(836)*--may be intepreted as a consequence of a mobility gap in the disordered state. The photocurrent peaks at ~0.26 and ~0.3 μm seem to agree with peaks in the optical absorption, as apparent from Fig. 8.1, and it is conceivable that these features are associated with size quantization in W-oxide-based clusters (cf. Sec. 8.2). The peaks in the photocurrent remain after coloring by broad-band ultraviolet exposure.

Figure 11.11 also shows photocurrent for a W oxide film crystallized by annealing in air. The spectrum is red-shifted, which is in qualitative agreement with the change of E_g. Three peaks are clearly resolved in the photocurrent. The onset of photocurrent may be associated with impurity conduction *(836)*.

Spectrally dependent photocurrent has been studied several times for W oxide films made by different techniques. Thus flash evaporated samples were irradiated with UV light or X-rays while kept at ~90 K, and a spectral photocurrent similar to the one in Fig. 11.11 was recorded *(2175)*. Optical excitation of such films using light with $\lambda = 0.85$ μm, on the other hand, did not produce any noticeable photocurrent *(801)*; this is consistent with the absorption at that wavelength being associated with small polarons, as argued by Dallacasa et al. *(802)*. Films made by sputtering showed an onset of photoconductivity at ~0.4 μm *(1190)*. For films made by high-voltage anodization, the onset was also at ~0.4 μm and the photocurrent was peaked at ~0.3 μm *(933, 935)*, and the same was true for films made by sol-gel-technique *(1698)*. Oxidized tungsten surfaces showed a photocurrent onset at ~0.5 μm *(1190, 1425, 1514, 3223)*. When one contemplates the different degrees of crystallinity associated with the various experimental techniques, it seems that all of the results for the photoconductivity are consistent with those in Fig. 11.11. Spectral sensitization of W oxide with photoactive dyes (several different phthalocyanines) is possible in order to optimize surfaces for photo-electrochemical applications *(1187)*.

The final data discussed here were obtained by Manfredi et al. *(2175)* who studied flash evaporated W oxide films. Transparent films were irradiated with UV light at $0.25 < \lambda < 0.27$ μm, and with X-rays, while kept at ~90 K. The films were then heated at a constant rate up to ~400 K

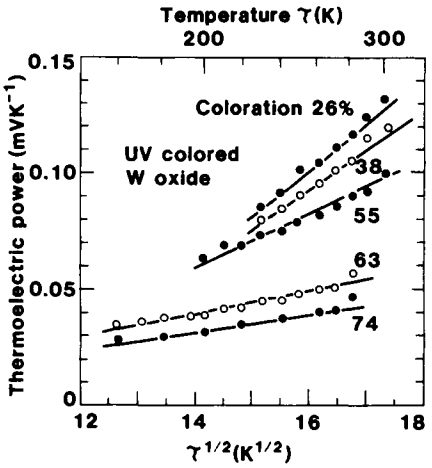

Fig. 11.8 Thermoelectric power vs. square root of temperature τ for an evaporated W oxide film colored by UV irradiation to the shown fractions of the full range (measured at $\lambda \approx 1$ μm). Open and filled circles denote measured data, and lines were drawn to illustrate Eq. 11.8. After Thomas and Goulding *(3404)*.

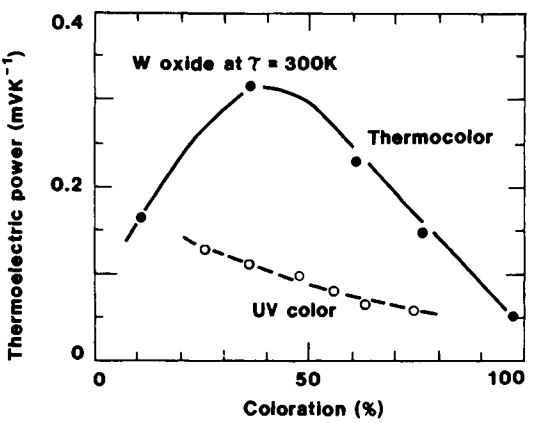

Fig. 11.9 Thermoelectric power vs. fraction of full coloration (measured at $\lambda \approx 1$ μm) for evaporated W oxide films subjected to UV irradiation and heating. Open and filled circles denote measured data, and curves were drawn for convenience. From Thomas and Goulding *(3404)*.

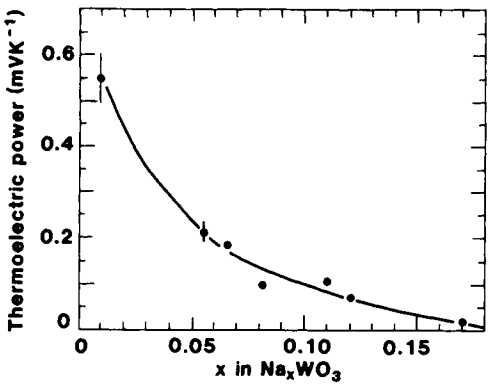

Fig. 11.10 Thermoelectric power vs. Na content, given as x in Na_xWO_3, for films made by coevaporation of Na and WO_3. Dots indicate measured data (with uncertainties represented by bars), and the curve was drawn for convenience. After Green and Travlos *(1323)*.

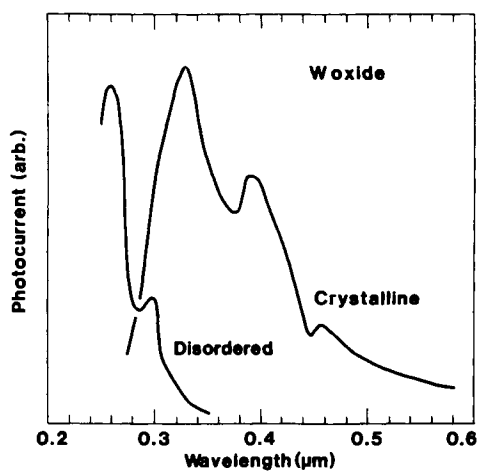

Fig. 11.11 Spectrally dependent photocurrent for an evaporated W oxide film in disordered as-deposited state and after crystallization by heating to ~380°C for 4 h in air. The curves were drawn through sets of individual data points. The vertical scales are different for the two curves. From Deb *(836)*.

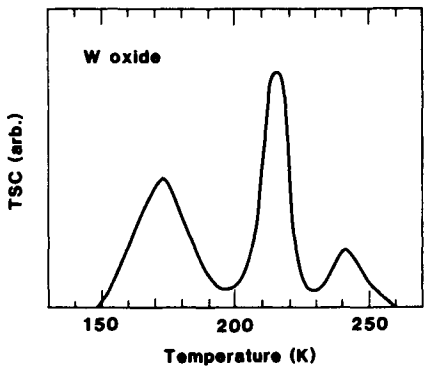

Fig. 11.12 Thermally stimulated conductivity TSC vs. temperature during heating of a transparent UV-irradiated evaporated W oxide film. After Manfredi et al. *(2175)*.

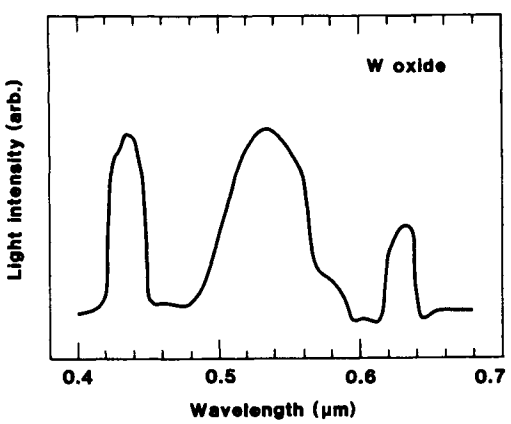

Fig. 11.13 Phosphorescence spectrum of a transparent UV-irradiated evaporated W oxide film at liquid nitrogen temperature. After Manfredi et al. *(2175)*.

with an applied bias of 300 to 2000 V, and the thermally stimulated conductivity (TSC) was recorded. Figure 11.12 shows a TSC spectrum with distinct peaks at 173, 216, and 240 K, corresponding *(676)* to the activation energies 0.93, 0.89, and 0.23 eV, respectively. Light emission (phosphorescence) was observed after UV excitation of cold films. Figure 11.13 displays an emission spectrum, again showing three distinct peaks at the photon energies 2.8, 2.3, and 2.0 eV. The data in Figs. 11.12 and 11.13 are consistent with an energy level diagram with trap levels located below the conduction band, and with a band of hopping levels (responsible for the electrical conduction) about 0.2 to 0.6 eV above the valence band *(2175)*.

This Page Intentionally Left Blank

Part Two

ELECTROCHROMISM AMONG THE OXIDES (EXCEPT TUNGSTEN OXIDE)

This Page Intentionally Left Blank

Chapter 12

MOLYBDENUM OXIDE FILMS

Molybdenum oxide films show pronounced electrochromism and have many, though not all, properties in common with W oxide. The discussion below covers the crystal structure of bulk-like Mo oxide (12.1) and the characterization of films made by evaporation (12.2), sputtering (12.3), and by electrochemical and chemical techniques (12.4). Subsequent sections deal with the ion intercalation/deintercalation reactions and diffusion constants (12.5), analyses of the intercalation/deintercalation by electrochemical (12.6) and physical (12.7) methods, ultraviolet absorption and semiconductor bandgap (12.8), optical properties in the luminous and near-infrared range (12.9), and coloration efficiency (12.10). It will be seen that coloration efficiency and other optical data are similar for films of Mo oxide and W oxide.

12.1 Crystal Structure of Bulk-like Molybdenum Oxide

For Mo oxide, just as for W oxide, the basic structural element is an octadedron with a metal atom at the center and oxygen atoms at the corners. An orthorhomic structure is thermodynamically favored at room temperature. It may be visualized as consisting of corner-sharing chains of MoO_6 octahedra, which share edges with two similar chains to form layers of MoO_3 stoichiometry; the layers, which are stacked in a staggered arrangement, are only held together by weak van der Waal's forces *(100, 911, 919, 1070-2, 1801)*. In each MoO_6 octahedron of this unique structure, one oxygen is unshared, two oxygens are common to two octahedra, and three oxygens are in part-shared edges and common to three octahedra. This layer structure is usually referred to as the α phase. An orthorhombic Mo oxide hydrate is known too *(1421)*. Furthermore, there is a monoclinic Mo oxide (ß phase) *(602, 1070-2, 1421-2, 2252-3)* that can be regarded as a metastable analogue of WO_3, illustrated in the right-hand part of Fig. 2.1. It is important to observe that *both a layer structure and a framework structure* can be accomplished in Mo oxide. The open crystal structures of Mo oxide and its hydrates make these materials excellent as intercalation hosts for H^+, Li^+, and other ions *(375-6, 788, 907, 919, 1480, 1962)*. This property renders them interesting for application in electrochromic devices.

One could remark that a large literature exists for low-temperature measurements on $K_{0.3}MoO_3$, $Rb_{0.3}MoO_3$, and $Tl_{0.3}MoO_3$ (known in physics jargon as "blue bronzes"), which are convenient materials for investigating charge density waves and their pinning/depinning. The "blue bronzes" are characterized by quasi-one-dimensional conductivity. A review of this subject was given by Grüner *(1344)*, and recent studies of MoO_3-based materials can be found in *(132, 740,*

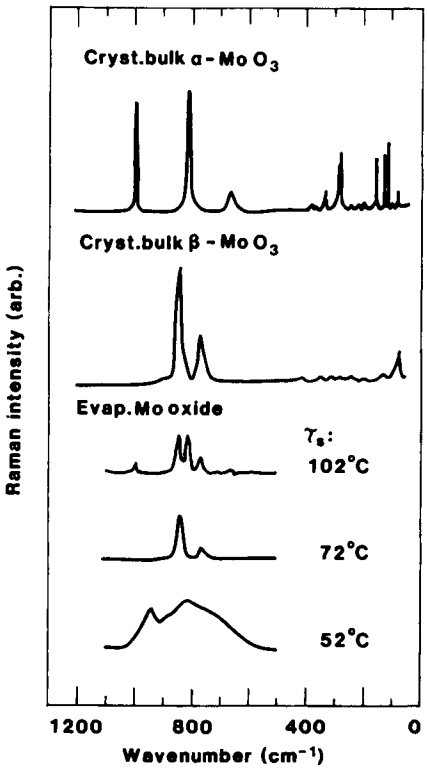

Fig. 12.1 Raman spectra for crystalline MoO_3 with α and ß structures (upper two curves) and for Mo oxide films made by deposition onto substrates at the shown temperature τ_s (lower three curves). Corresponding data for W oxide were reported in Fig. 3.6. After McCarron *(2252)* and Ramans et al. *(2831)*.

851-4, 858, 980, 1446, 1459, 1498, 1659, 1674, 2420, 2482, 2797, 3568, 3794). $K_{0.3}MoO_3$ can serve as a host for cyclic Li intercalation/deintercalation *(3095).*

It is possible to prepare Li_xMoO_2 and Na_xMoO_2 with x up to ~1 *(744, 3364, 3366).* These materials can serve as intercalation hosts and are of interest in battery technology. The structure embraces MoO_2 layers with alkali atoms in van der Waal's gaps *(2250);* the layers consist of MoO_6 octahedra with off-center Mo atoms, leading to the formation of double chains.

12.2 Films Made by Evaporation: Preparation and Characterization

There are many techniques for making Mo oxide films. The most widely used is thermal evaporation from a resistive source. In full analogy with the case of W oxide, the evaporated species are molecules; the dominating one is Mo_3O_9, and evidence has also been found for Mo_4O_{12} and Mo_5O_{15} *(363, 2165, 2517).* It follows from this analogy that one expects vacuum deposited films of Mo oxide and of W oxide films to show many similarities. This is indeed the case, as will become clear from the discussion below. A thermodynamic study on the evaporation of Mo oxide was reported recently *(2987).*

Evaporated Mo oxide films have been studied in numerous works. Conventional vacuum evaporation is the standard technique, although evaporation under slightly reactive conditions *(843, 1655, 2831, 3717)* as well as flash evaporation *(1709-10)* have been used. Deposition rates of 3 to 4 nm/s have been reported several times *(1501, 1655, 1710),* with maximum values up to 10 nm/s *(3789)* and 17 nm/s *(843).* Densities, relative to the one for orthorhombic crystalline MoO_3, were given as 0.74 *(432),* 0.79 *(2972),* and 0.87 *(1501).* The density deficit was independent of film thickness. High-resolution TEM showed that as-evaporated "amorphous" films comprised microstructural elements with a linear extent of about 1.5 nm *(2972, 3150).* Atomic force microscopy indicated that the surface structure of ~1-μm-thick films, evaporated in the presence of some N,N-dimethylformamide, consisted of ~25-nm-diameter clusters aggregated into irregular grains with sizes ranging from 100 to 190 nm *(706).* Films of $K_{0.3}MoO_3$ were produced by coevaporation of MoO_3 and K_2MoO_4 *(3768).*

Raman spectroscopy is able to provide important structural information, as discussed for W oxide in Sec. 3.6. Figure 12.1, based mainly on work by Ramans et al. *(2831),* shows spectra for films deposited onto substrates kept at different temperatures. Evaporation onto a low-temperature substrate yielded a broad spectral feature centered at ~800 cm^{-1} and a second peak around ~960 cm^{-1}. Evaporation onto heated substrates made the former peak split up into several ones, whereas the latter peak vanished. The thin film data can be compared with spectra for bulk samples reported by McCarron *(2252)* and others *(994-5, 2482, 2509)* and shown in the upper part of Fig. 12.1. It then appears that the features at ~800 cm^{-1} are due to phonons in a disordered Mo-O framework and that the partly crystallized material consists of a mixture of the α and ß phases. The peak at ~960 cm^{-1} is of considerable interest; it can be assigned to Mo=O stretching vibrations, which lie in the 900 to 1000 cm^{-1} range for numerous polymolybdates *(69, 184, 741, 894, 1107, 1423, 1748, 2119, 2230, 2924, 3637-8).* For α-MoO_3 crystals, the sharp Raman peak at ~1000 cm^{-1} is associated with the unique molybdenyl bond characterizing the layered structure.

Infrared absorption spectra for evaporated Mo oxide films have been reported in *(120, 124-6, 1707-8, 2298),* and corresponding data for bulk samples were given in *(994).* Julien et al. *(1708)* studied the annealing of films prepared at $\tau_s = 30°C$ and found a progressive growth of an

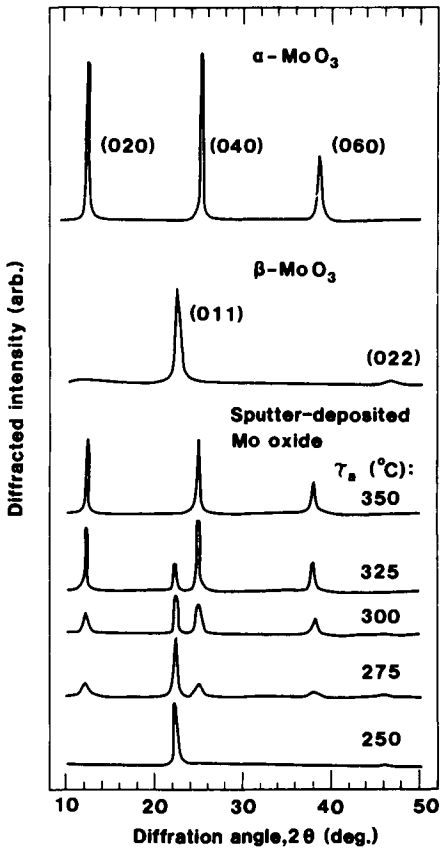

Fig. 12.2 X-ray diffractograms for sputter-deposited Mo oxide films. The upper two curves were obtained from films with clear α and β structures. The lower five curves were measured for a β phase film that was annealed at successively higher temperature τ_a so that a gradual transformation into the α phase took place. The peaks are designated by *(hkl)* indices. From Carcia and McCarron *(602)*.

absorption peak at ~985 cm^{-1} due to the molybdenyl bond in the α phase.

Further structural information on evaporated Mo oxide films has been obtained by electron diffraction and X-ray extinction. Julien et al. *(1708)* used XRD to verify that films deposited at τ_ss being 120 and 240°C contained a mixture of the α and β phases. Ramans et al. *(2831)* evaluated RDFs from electron diffraction and found them to be in good agreement with data on similarly prepared and analyzed W oxide films. Burattini el al. *(244, 528)* used the EXAFS technique to study Mo oxide films evaporated onto poly-imide substrates at $\tau_s \approx 150$°C. Mo-O distances, derived from elaborate multishell simulation, again underscored the strong structural kinship between oxides of Mo and W. EXAFS data for crystalline samples of α-MoO_3 were given in *(1986)*.

Crystallization takes place when as-evaporated Mo oxide films are heated, as may be inferred from Fig. 12.1. Specifically, a transformation to a well-defined orthorhombic structure occurred around 250 to 350°C *(1708, 3470)*.

12.3 Films Made by Sputter-deposition: Preparation and Characterization

Molybdenum oxide films have been prepared by rf sputtering in Ar + O_2 from targets of Mo or MoO_3 *(602, 2347, 2575, 2856)* and by dc sputtering in Ar + O_2 from Mo targets *(1657-8)*. Deposition rates were lower than 0.2 nm/s. The most detailed work is by Carcia and McCarron *(602)*, who employed rf sputtering onto water cooled substrates and obtained films that were amorphous as judged from XRD. Annealing at ~250°C led to a crystalline structure being a mixture of the α and β phases; the α phase was dominating for $\tau_a > 400$°C. Sputtering onto substrates kept at 150 to 250°C gave polycrystalline films whose structure depended on p_{O2}. Deposition at 0.08 nm/s in 50 % O_2 gave α-MoO_3 films with a pronounced tendency for the molecular MoO_6-based chains to be parallel to the substrate. Deposition at 1.4 nm/s in 5 to 10 % O_2, on the other hand, yielded β-MoO_3 films. Corresponding X-ray diffractograms are shown by the upper two curves in Fig. 12.2. Mixed α + β phases were found at intermediate oxygen admixtures. Annealing of films that were intially of β-type led to a change into the α structure. This transformation took place gradually between 250 and 350°C, as apparent from the lower curves in Fig. 12.2. The power in the sputtering plasma, and the application of substrate bias, also influenced the ratio between the α and β phases in the films.

12.4 Films Made by Electrochemical and Chemical Techniques: Preparation and Characterization

Electrodeposition from various solutions has been employed to prepare Mo oxide films; work has been reported for solutions based on $Li_6Mo_7O_{24}$ *(197)* and $(NH_4)_6Mo_7O_{24}$ *(3718)*, aqueous Li_2MoO_4 solutions *(2543-4, 3419)*, and Mo dissolved in H_2O_2 *(810, 1349)*.

Anodization has been used extensively with acetic acid electrolytes containing sodium borate and water *(151, 153-4, 803, 897-9)* and with H_2SO_4 electrolytes *(2144)*.

Chemical vapor deposition has been investigated especially by Donnadieu et al. *(5, 960)*. Initially, $Mo(CO)_6$ was decomposed at ~300°C in order to make Mo-rich films *(614-5, 637-8, 3105)*; they were subsequently annealed under oxidizing conditions at 500 to 600°C. The ensuing deposits were composed of α-MoO_3 with preferred orientation. As an alternative to the Mo

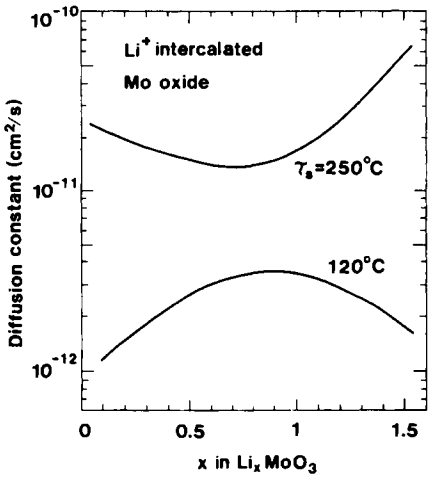

Fig. 12.3 Chemical diffusion constant for Li^+ in Mo oxide films flash evaporated onto substrates at two temperatures τ_s. The amount of ion intercalation is represented as x in Li_xMoO_3. The curves were drawn through sets of individual data points with a certain scattering. After Julien et al. *(1709)*.

carbonyl, it is possible to use MoO_2Cl_2 *(1174-5, 3105)*. PECVD was employed by Benson et al. *(349, 3283, 3435)*, whose depositions took place in a plasma containing $Mo(CO)_6 + O_2$. There was no need for post-treatment. The deposition rate was 2.9 nm/s under the conditions used. Tölgyesi and Novak *(3419)* prepared Mo oxide films by spraying acidic Li_2MoO_4 solutions onto Cu-covered glass plates with ITO layers. Direct sublimation from ammonium molybdate solutions also can produce Mo oxide films *(987, 2184)*.

Among the *sol-gel*-related techniques, one can note spin coating from a peroxo-polymolybdate solution, followed by annealing *(1490)*. RFDs were analyzed, and the evidence for corner-sharing and edge-sharing MoO_6 structural units was discussed. Sol-gel technology via the alkoxide route is another viable option *(2292, 3715)*; IR absorption measurements on the latter films gave clear evidence for Mo=O bonds.

Thermal oxidation of molybdenum sulfide films can yield Mo oxide *(3321)*. One technique based on this approach is to prepare MoS_3 by electrodeposition from an aqueous solution of $(NH_4)_2MoS_4$ *(315, 317, 384, 2012)* and to subsequently oxidize these films between 400 and 550°C *(316, 1346)*. The process takes place in two steps with a rapid transformation from MoS_3 to MoO_2, followed by a slower oxidation to MoO_3. Another technique *(948-9, 1676)*, involving several steps, employs (i) preparation of a suspension of MoS_2 single layers in water through an exfoliation technique, (ii) mixing with a water-immiscible organic solvent such as benzene and spontaneous collection of the layers at the boundaries between the two phases, (iii) spontaneous spreading of the MoO_2 on substrates dipped into the solution, (iv) desorption of the organic solvent, and (v) oxidation at ~470°C for 1 h. For both of the sulfide-based techniques, the ensuing films were polycrystalline α-MoO_3 with preferred orientation.

12.5 Ion Intercalation/deintercalation Reactions and Diffusion Constants

Ion intercalation/deintercalation is responsible for the electrochromism in Mo oxide films, just as for W oxide. An overall reaction, subject to the same limitations as for W oxide, can be written in analogy with reaction 6.1 as

$$MoO_3 + xM^+ + xe^- \leftrightarrow M_xMoO_3 \qquad (12.1)$$

with $M^+ = H^+, Li^+, \ldots$.

Diffusion constants for ion intercalation/deintercalation have been extracted through different techniques. Julien et al. *(1709-10)* studied Li^+ intercalation into thin films made by flash evaporation onto substrates at 120 and 250°C. Their results are illustrated in Fig. 12.3. For τ_s = 120°C, when an $\alpha + \beta$ phase is present, D_{Li+} lies between 10^{-12} and 5×10^{-12} cm^2/s with the largest values for $x \sim 1$ in Li_xMoO_3. Interestingly enough, much higher D_{Li+}s were found at τ_s = 250°C, when a layered α phase was formed. The shown data underscore that there can be an advantage in having a layered structure rather than a disordered framework structure. Furthermore, it is of significance that intercalation levels up to $Li_{1.5}MoO_3$ can be accomplished.

A spin-coated Mo oxide film had $D_{Li+} \approx 7 \times 10^{-13}$ cm^2/s *(1490)*, and PECVD-produced films had even lower D_{Li+}s with values between 3×10^{-14} and 10^{-13} cm^2/s being reported *(349)*. For the PECVD films, it was conjectured that a sizeable fluorine incorporation in the Mo-based film would be responsible for the low D_{Li+}, but no conclusive evidence was put forward for this.

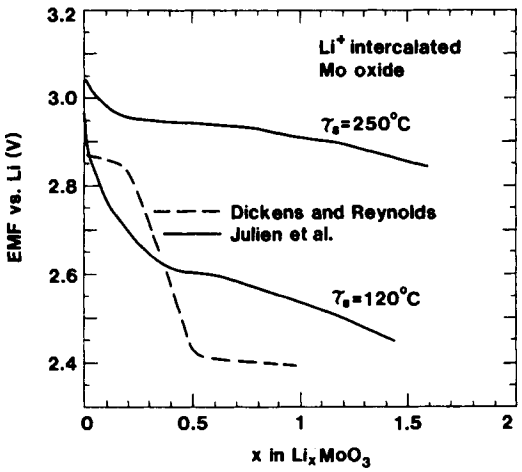

Fig. 12.4 Normalized EMF vs. amount of Li^+ intercalation, represented as x in Li_xMoO_3, in Mo oxide films flash evaporated onto substrates at the shown temperatures τ_s (solid curves) and in a bulk sample (dotted curve). After Dickens and Reynolds *(921)* and Julien et al. *(1709)*.

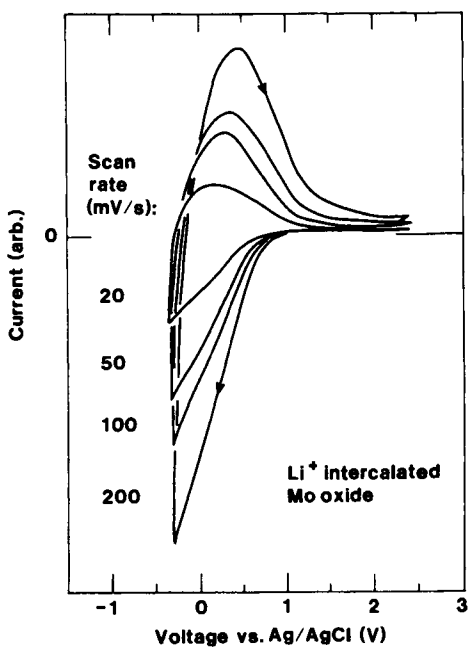

Fig. 12.5 Cyclic voltammograms for Li^+ intercalation/deintercalation in an electrodeposited Mo oxide film in $LiClO_4$ + PC. The curves pertain to different voltage scan rates. Arrows denote scan direction. From Dao et al. *(810, 1349)*.

Crystalline α-MoO_3 bulk samples have diffusion constants that are strongly orientation-dependent, which is expected from layered crystal structure. Thus D_{H+} lay between 10^{-8} and 10^{-6} cm^2/s along the MoO_6-based chains and was ~10^{-15} cm^2/s perpendicular to them *(26, 2913, 3188)*. D_{Li+}s for bulk α-MoO_3 fell between 10^{-11} and 10^{-10} cm^2/s *(376)*, while lithiated samples showed $3 \times 10^{-10} < D_{Li+} < 10^{-8}$ cm^2/s *(921)*. The layered structure is open enough to be able to include molecules as large as those in polyaniline *(394)*.

Electron diffusion in evaporated Mo oxide films has been studied by Zelaya-Angel et al. *(3789)* who found $D_{e^-} \approx 8 \times 10^{-4}$ cm^2/s. Thus $D_{e^-} >> D_{M+}$ as for W oxide.

12.6 Ion Intercalation/deintercalation Studied by Electrochemical Techniques

Electromotive force has been measured during Li^+ intercalation. Figure 12.4 shows data from Julien et al. *(1709)* for films flash evaporated onto substrates at two different temperatures. The α-type film prepared at τ_s = 250°C had an EMF that lay remarkably constant in the range between 3.0 and 2.9 V. The α + β-type film made at τ_s = 120°C, on the other hand, showed an EMF that dropped more in the manner of W oxide (cf. Fig. 6.4b). Similar intercalation-dependent decreases were noted in Mo oxide films made by conventional evaporation *(432)* and PECVD *(349)*. Results for a bulk sample of MoO_3 is also given in Fig. 12.4 *(921)*. The EMF is fairly independent of the Li content for $x < 0.2$ and $x > 0.5$. Similar data were given in *(26, 2370)*.

Cyclic voltammetry has been used to study ion intercalation/deintercalation for films made by evaporation *(3720)*, electrodeposition *(316, 810, 1349)*, anodization *(2144)*, spray deposition *(3419)*, spin coating *(1490)*, and thermal oxidation of MoS_3 *(315, 1346)*. Figure 12.5 reports data on films prepared by electrodeposition in a hydrogen-peroxide-based solution, followed by heat treatment at 130°C *(810, 1349)*. Voltammograms were taken at different voltage scan rates with the film immersed in a $LiClO_4$ + PC electrolyte. Voltammograms obtained with films prepared by other techniques were similar. One may observe a basic similarity with voltammograms taken on W oxide films (Figs. 6.12-6.15).

12.7 Ion Intercalation/deintercalation Studied by Physical Techniques

Physical characterization of ion intercalated, or otherwise post-treated, Mo oxide films has been performed by X-ray extinction, infrared absorption spectroscopy, EPR, and XPS. Machida and Enyo *(2144)* applied XRD to films made by anodization in a H_2SO_4 electrolyte and argued that proton insertion led to an increase of the distances between the layers of linked MoO_6 octahedra. It was inferred that the protons were accommodated in hydroxyl groups, i.e., the ion intercalated material could be represented as $MoO_{3-x}(OH)_x$. This result agrees with neutron scattering data on a bulk sample with $x = 0.34$ *(908)*. Films made by oxidation of MoS_3 and subsequently intercalated with H^+ or Li^+ were studied by Guay et al. *(1346)* who used EXAFS and XANES. The ions led to an expansion of the interlayer distances in the α-phase oxide, the effect being most pronounced for Li^+. Extended intercalation/deintercalation cycling was found to disintegrate the material. Infrared absorption data were reported in *(221)*.

EPR data have been recorded for Mo oxide films made by evaporation *(123, 834, 843)*, sputtering *(3559)*, and thermal decomposition of ammonium molybdate *(2184)*. No EPR results

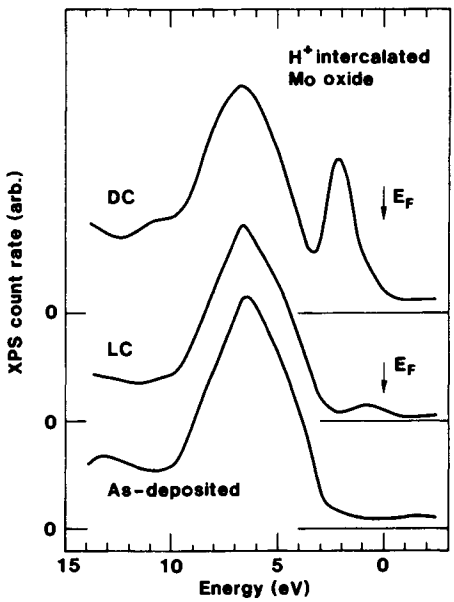

Fig. 12.6 XPS count rate vs. binding energy for valence- and conduction electrons in evaporated Mo oxide films. The curves refer to a film in as-deposited state and after H^+ intercalation to lightly colored LC and deeply colored DC states. Arrows denote the Fermi energy E_F. Corresponding curves for W oxide were shown in Fig. 7.20(a). From Colton et al. *(745-6)*.

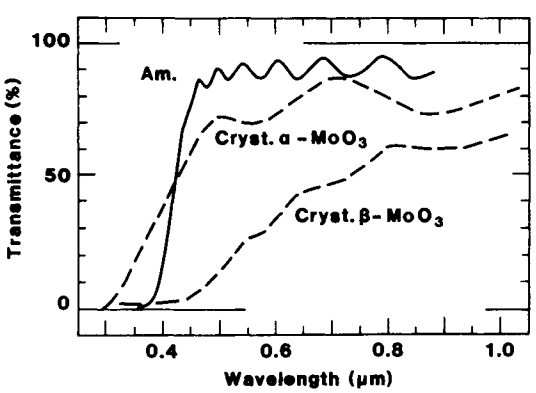

Fig. 12.7 Spectral transmittance for Mo oxide films prepared by reactive sputtering in different Ar + O_2 mixtures onto substrates at different temperatures. Solid curve refers to an "amorphous" film, and dashed curves refer to crystalline films with α and β structure. After Carcia and McCarron *(602)*.

seem to be available for ion-intercalated samples, but data have been published for films that--from the analogy with W oxide--are expected to exhibit properties closely related to those of such samples. As-evaporated films showed a signal at $g = 1.92$, whose strength increased under UV irradiation *(843)* or annealing up to $\tau_a \approx 200°C$ *(123)*. This signal vanished upon annealing at $\tau_a \approx 250°C$ for 2 h. Sputter-deposited films did not produce any EPR lines in as-deposited state, but a signal at $g = 1.92$ developed upon UV irradiation *(3559)*. Wagner et al. *(3559)* noted a direct correspondence between the optical absorption and this EPR signal. Films made from ammonium molybdate were analyzed in terms of a spin Hamiltonian (Eq. 7.4) and the Landé factors were given as $g_{\parallel} = 1.925$ and $g_{\perp} = 1.943$ *(2184)*. Furthermore, an EPR signal was detected at $g = 2.00$ *(123, 834, 2184)*.

The EPR signal at $g = 1.92$ is due to Mo^{5+}. This assignment can be made unambiguously from work on molybdenum ions in various crystalline matrices *(350, 1554, 1620, 2208, 2577, 2759, 3099, 3103, 3221)*. It follows--from admittedly somewhat scanty data--that the optical absorption in the Mo oxide films scales with the Mo^{5+} density, which is in full analogy with the case for W oxide (cf. Fig. 10.1). The signal at $g = 2.00$ has been ascribed to free electrons *(834)* and to Mo^{3+} *(123, 2184)*, although O_2^- adsorbed on surfaces seems to be more likely, just as for W oxide (cf. Sec. 7.5). It should be pointed out that Mo^{4+} would not easily be detected by EPR.

XPS data have been recorded for evaporated Mo oxide films in the energy ranges pertinent to core levels and to valence- and conduction bands. Molybdenum oxide is characterized by a spin-orbit-split doublet due to $Mo3d_{5/2}$ at 232.65 eV and $Mo3d_{3/2}$ at ~236 eV *(385, 972, 1085, 3557)*. This structure has been clearly seen in evaporated films *(121-2, 745-6)*. H^+ intercalation from H_2SO_4 *(745-6)*, as well as heating in vacuum to more than 100°C *(121-2, 3222)*, yielded an apparent smearing and displacement of this structure. Analogous data have been found in UV irradated powder pellets *(1085)*. The XPS core level spectra are consistent with a partial transformation from Mo^{6+} to Mo^{5+}, but no quantitative analysis seems to be available for films.

Valence- and conduction band XPS spectra are shown in Fig. 12.6. The data, obtained from Colton et al. *(745-6)*, were measured for an evaporated Mo oxide film in as-deposited state and after H^+ intercalation from H_2SO_4 to light-colored and dark-colored states. The most striking feature is the peak located 1 to 2 eV below the Fermi energy, whose intensity increased under ion intercalation. A similar effect was observed in Mo oxide films colored in an electric field *(2819)* and in UV-irradiated powder pellets *(1085)*. The peak is assigned to inserted electrons occupying the otherwise empty *4d* and *5s* orbitals. The pronounced peak lying ~6.5 eV below the Fermi energy in Fig. 12.6 is due to *O2p* electrons.

12.8 Ultraviolet Absorption and Semiconductor Bandgap

Figure 12.7, after Carcia and McCarron *(602)*, is a suitable starting point for the discussion; the dashed curves show transmittance in the $0.3 < \lambda < 1$ μm interval for crystalline films made by reactive sputtering under conditions so that either a pure othorhomic α phase or a pure WO_3-type β phase was present. The bandgaps were found to be different with $E_g \approx 3.1$ eV for the α phase and $E_g \approx 2.9$ eV for the β phase. Diffusely reflecting powder specimens had similar bandgaps *(602, 2750)*. Films made so that they comprised a mixture of the two phases showed intermediate bandgaps. Single crystals of α-MoO_3 had $E_g \approx 3.1$ eV for light polarized with the E-vector perpendicular to the crystallographic *c* axis and $E_g \approx 3.2$ eV with polarization parallel to this axis

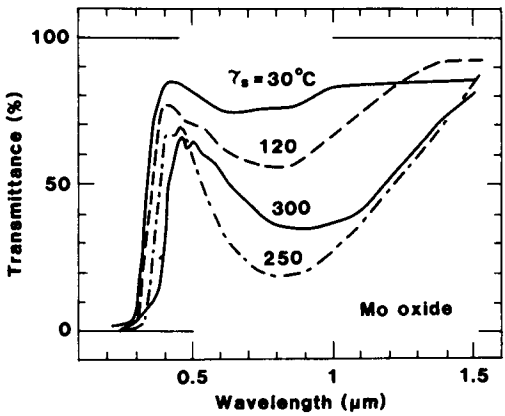

Fig. 12.8 Spectral transmittance of Mo oxide films evaporated onto substrates at different temperatures τ_s. From Julien et al. *(1710)*.

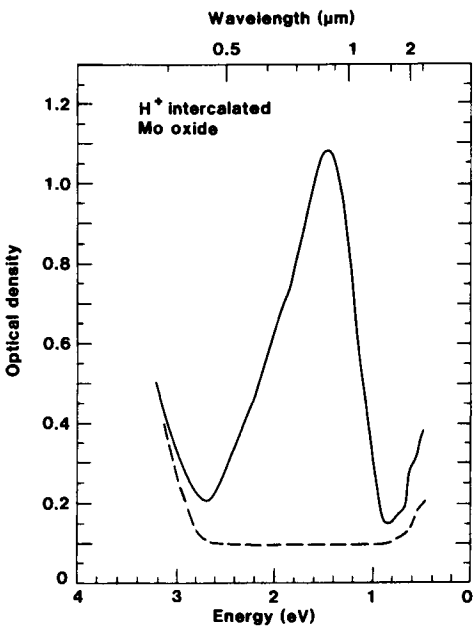

Fig. 12.9 Spectral optical density for an evaporated Mo oxide film colored by H^+ intercalation. Dashed curve refers to the uncolored film. Corresponding data for W oxide were shown in Fig. 9.6(a). After Zelaya-Angel et al. *(3789)*.

(834). The E_gs increased if the temperature was lowered. Clear evidence of an Urbach tail was found at low absorption *(834)*.

Bandgaps of "amorphous" and fine-grained crystalline Mo oxide films have been evaluated several times. The solid curve in Fig. 12.7 shows that the transmittance of an "amorphous" film increases sharply at ~0.4 μm, i.e., the bandgap lies in between the values for the α and β phases. It was found that $2.7 < E_g < 3.2$ eV pertained to films made by evaporation *(602, 745, 834, 1501, 1710, 3470-1)*, sputtering *(2347)*, and CVD *(5, 960)*. In most studies, the E_gs were evaluated from Eq. 8.3 with $\eta = 2$ *(5, 118-9, 1312, 2347)*.

The relation between E_g and the degree of crystallinity--changed by deposition onto substrates kept at different temperatures--was considered in some work. Thus Julien et al. *(1710)* found $E_g \approx 3.15$ eV for flash evaporation onto an unheated substrate and $E_g \approx 2.85$ at $\tau_s = 300$°C. Their results are apparent from the transmittance data in the left-hand part of Fig. 12.8. It was also found by Anwar and Hogarth *(118)* that E_g went down when τ_s was increased, but the reported E_gs were at variance with crystal data. The relation between E_g and τ_s is in qualitative agreement with results on W oxide films in Fig. 8.3, but the fact that Mo oxide can have crystalline phases with different E_gs complicates the interpretation in the latter case.

It was claimed in some work *(118-9)* that E_g would be thickness dependent for evaporated films. However, this effect was no longer evident when the absorption was evaluated with full consideration of boundary reflectance and interference effects *(3805)*.

Bandgap widening upon ion intercalation has been noted but not studied in detail *(745, 1312)*. Green et al. *(1312)* reported that E_g increased when H^+ or Li^+ was intercalated up to a level given by $x \approx 0.05$ in M_xMoO_3; above this ionic content, E_g appeared to drop.

12.9 Optical Properties in the Luminous and Near-infrared Range

The optical properties of as-deposited Mo oxide films depend on experimental parameters. An example is provided by Fig. 12.8, from Julien et al. *(1710)*, referring to flash evaporation onto heated substrates at pressures lower than 5×10^{-6} Torr. An increase of τ_s led to the development of a transmittance minimum in the near-infrared; its strength increased progressively for τ_s being 30, 120, and 250°C, and decreased for still higher τ_ss. Oxygen deficiency is a likely cause of the absorption responsible for the transmittance minimum.

Refractive indices have been evaluated for films prepared so that their near-infrared absorption was weak. Tubbs *(3470)* showed that n decreased from ~2.3 at 0.4 μm to ~2.1 at 0.7 μm and remained at ~2 in the near-infrared. These results are in excellent agreement with measurements on some other films made by evaporation *(602, 3767)*, sputtering *(2347)*, and anodization *(897-8)*. They are also consistent with single-crystal data *(834)*. One may note that the early work by Deb *(834, 843)* reported much higher refractive indices and a stronger dispersion; the evaluations underlying these results have been criticized, though *(3470)*. High refractive indices were claimed also for some CVD-produced films *(5, 2874)*. A somewhat anisotropic refractive index was observed in films made by oblique angle evaporation *(2410)* and by anodization *(898)*.

Ion intercalation into Mo oxide films leads to the evolution of an absorption band in much the same way as for W oxide. Figure 12.9, redrawn from Zelaya-Angel et al. *(3789)*, shows that the spectral optical density exhibits a pronounced peak at energies between 1.5 and 1.6 eV, i.e., at a slightly higher energy than for W oxide (cf. Fig. 9.6a). Analogous data have been shown in other

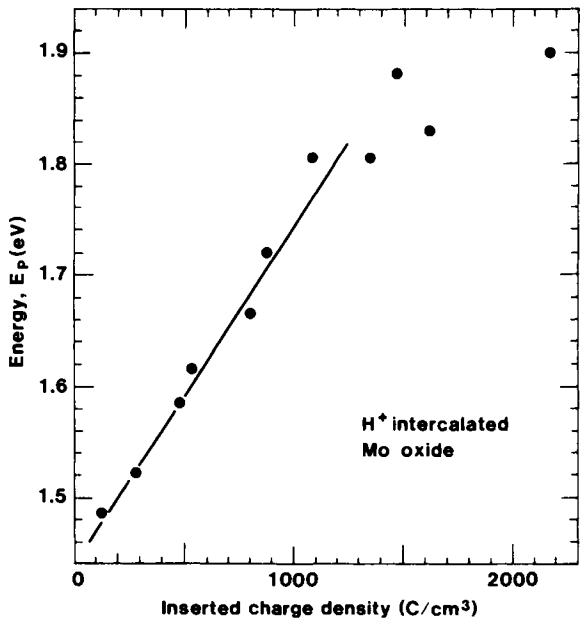

Fig. 12.10 Energy for the peak of the near-infrared absorption band E_p vs. amount of inserted charge density for H^+ intercalated Mo oxide films made by evaporation. The line was drawn for convenience. Corresponding data for W oxide were shown in Fig. 9.8. From Hiruta et al. *(1501)*.

work on spectral absorption for evaporated films intercalated with H^+ *(745, 1501, 1827, 3685-6)* or Li^+ *(3716-7, 3720)*, and for Li^+ intercalated films made by electrodeposition *(2543, 3419)*, spray coating *(3419)*, and spin coating *(1490)*. Sputter deposited films treated in a $LiClO_4$ + PC electrolyte had $E_p \approx 1.4$ eV *(2856)*, and PECVD-produced films treated in a $LiBF_4$ + PC electrolyte had $E_p \approx 2$ eV *(349, 3435)*. The latter films, whose absorption peak lay within the visible spectrum, were deposited in the presence of CF_4 and contained a significant amount of fluorine (Mo/F ratio of ~2). The occurrence of an absorption peak in the near-infrared can be inferred also from some spectral transmittance data on films made by evaporation *(1710, 3015)* and electrodeposition *(315-6, 810)*.

The location of E_p depends on the amount of ion intercalation. The clearest evidence is in work by Yamada et al. *(1501, 1827-8, 3685-6)*, whose results for evaporated films are reproduced in Fig. 12.10. It is seen that E_p goes up rather linearly from ~1.5 to ~1.8 eV when the inserted charge density was increased from zero to ~1000 C/cm^3. At still larger charge insertion, E_p seems to level off. A tendency that charge insertion shifts E_p towards higher energies can also be inferred from *(745, 2543)*. E_p is shifted upon ion intercalation in W oxide films as well (cf. Fig. 9.8), but the effect seems to be significantly larger in Mo oxide.

In analogy with the case of W oxide, near infrared absorption bands can be induced in Mo oxide by several techniques other than ion intercalation from an electrolyte. One such method--deposition in vacuum onto a heated substrate--was apparent from Fig. 12.8. All of the techniques used so far have yielded absorption bands peaked between 1.4 and 1.6 eV. Most work has been reported for UV irradiation of evaporated films *(834, 838, 843, 1655, 2766a, 3470-1, 3717)*, but some similar results are also available for films made by electrodeposition *(3718)* and sol-gel technology *(3715)*. Enhanced UV coloration has been reported for irradiation in the presence of organic vapors *(1145, 1147, 3717)*, especially C_2H_5OH, and water vapor *(146)*. Deb and Chopoorian *(843)* mentioned that the UV coloration was enhanced when the Mo oxide film was backed by a TiO_2 layer. Recent work by Yao et al. *(3716-8, 3720)* showed that electrolytic coloration and coloration by UV irradiation can be mutually supportive of each other. In other investigations, Mo oxide films have been colored by X-ray and γ-ray irradiation *(1149, 1655)*, application of a strong electric field (electrocoloration) *(146, 838)*, thermocoloration *(843, 1655)*, ion-beam irradiation *(117, 1892, 2479)*, and neutron bombardment *(987)*. Pichat et al. *(2750)* found that proton insertion could take place as a result of UV irradiation of MoO_3 powder; this effect was particularly strong in the presence of TiO_2. Changes in electrochemical properties upon ion-beam irradiation were studied in *(1897)*.

Regarding theoretical analyses of the optical data, spectral absorption as well as thermomodulated absorption have been analyzed in terms of polaron theory in precisely the same way as for W oxide (cf. Sec. 10.2) *(1827-8, 3283, 3685-6)*. It seems that the studies of Mo oxide have so far given no insights in addition to those reached for W oxide.

12.10 Coloration Efficiency

Coloration efficiencies have been evaluated for films prepared by several different techniques. Data are summarized in Fig. 12.11 for samples made by evaporation and H^+ intercalation *(1827, 3686)*, reactive rf sputtering in Ar + O_2 and Li^+ intercalation *(725, 2347)*, CVD and H^+ intercalation *(960)* as well as electrodeposition and Li^+ intercalation *(197, 2543)*. The films studied by Cogan

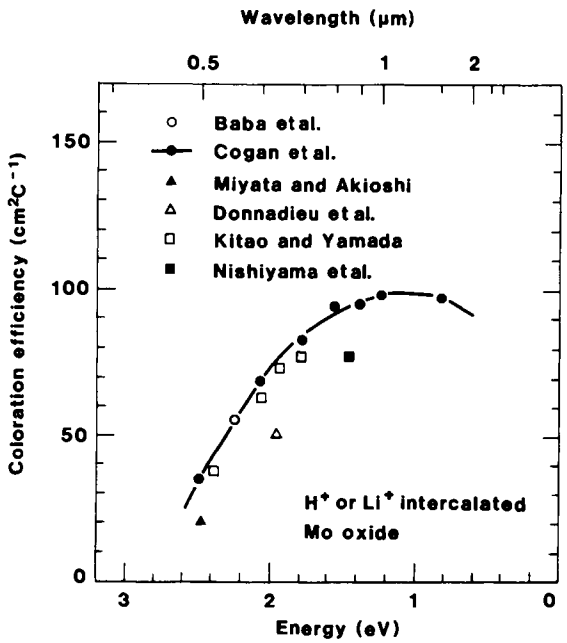

Fig. 12.11 Spectral coloration efficiencies for H^+ or Li^+ intercalated Mo oxide films prepared by several techniques. Symbols indicate evaluated data, and the curve was drawn for convenience. After Baba et al. *(197)*, Cogan et al. *(725)*, Miyata and Akioshi *(2347)*, Donnadieu et al. *(960)*, Kitao and Yamada *(1827)*, and Nishiyama et al. *(2543)*.

et al. *(725)* were sputter-deposited onto substrates kept at 351°C, so that they ought to be crystalline, whereas the other films were made under conditions expected to yield disordered films. With this in mind, and contemplating the structural differences likely to take place among films made by different techniques even if the substrate is not heated, the consistency of the coloration efficiency data in Fig. 12.11 is surprising. For completeness one may note that some earlier data on sputter-deposited films *(2856)* indicated low CEs, but apparently these results were superseded by more recent work by the same authors *(725)*. Some fluorinated Mo oxide films made by PECVD appeared to have low CEs *(349)*. Figure 12.11 shows that Mo oxide has a coloration efficiency that is ~40 cm^2C^{-1} at $\lambda = 0.5$ μm and that the CE increases towards longer wavelengths. These values are similar to those of W oxide films made by several different techniques as discussed in Sec. 9.7.

Chapter 13

MISCELLANEOUS TUNGSTEN- AND MOLYBDENUM-OXIDE-CONTAINING FILMS

Several complex tungsten-oxide-containing and molybdenum-oxide-containing films have been studied with regard to their electrochromism. It is expected that such films will be of growing importance in the future since improved durability as well as a desirable, usually neutral, color can be accomplished in multicomponent films. This chapter covers films of binary oxides (especially W-Mo oxide) (13.1), ternary oxides (especially W-Mo-V oxide) (13.2), W oxyfluoride (13.3), and composites of W oxide and metal (13.4).

13.1 Binary Oxides, Especially Tungsten-Molybdenum Oxide

Mixed W-Mo oxides have been studied in considerable detail, and warrant an elaborate discussion. Bulk crystals of $W_{1-y}Mo_yO_3$ have hexagonal, orthorhombic, or monoclinic structures within compositional ranges that depend on whether classical techniques for chemical synthesis or "chimie douce" are applied *(1070-2, 1162, 1480-1, 2792, 2980)*. Using classical routes, WO_3-like structures prevails for $y < 0.96$, whereas layered MoO_3-like structures are found for $0.96 < y < 1$. The crystal chemistry is very complicated with twelve different phases having been identified *(2980)*. Hexagonal structures are well documented, confirming earlier observations *(1275, 1419-20)*. H^+ intercalation into hexagonal $W_{1-y}Mo_yO_3$ crystals was investigated in *(1162)*.

Thin films with a nominal $W_{1-y}Mo_yO_3$ composition have been studied several times, particularly as regards the optical properties after ion intercalation from acidic electrolytes. The ensuing films can be represented, schematically, as $H_xW_{1-y}Mo_yO_3$. The absorption band responsible for the electrochromism depends on x and y in a characteristic and interesting manner. Figure 13.1, from work on evaporated films by Faughnan and Crandall *(1045)*, shows E_p vs. y for $x \ll 1$ and for $x \approx 0.5$. When x is small, E_p varies linearly with increasing y from $E_p \approx 2.1$ eV at $y \approx 0$ to $E_p = 1.54$ eV at $y = 1$ (i.e., for Mo oxide). For $x \approx 0.5$, on the other hand, E_p varies linearly from $E_p \approx 1.4$ eV for $y = 0$ (i.e., for W oxide) to $E_p \approx 2.1$ eV for $y = x = 0.5$ and then, following another line, back to the value for Mo oxide. Some samples with $y = 0.5$ showed even larger shifts of E_p.

The data on $E_p(x, y)$ can be understood as a result of small polaron (or intervalency charge transfer) absorption (cf. Secs. 10.2 and 10.3) and, in fact, give good support to models based on localized electrons. In the mixed oxide, electron transitions can take place according to $Mo^{5+} \rightarrow Mo^{6+}$, $Mo^{5+} \rightarrow W^{6+}$, and $W^{5+} \rightarrow W^{6+}$. It is assumed that the Mo levels are lower in energy than

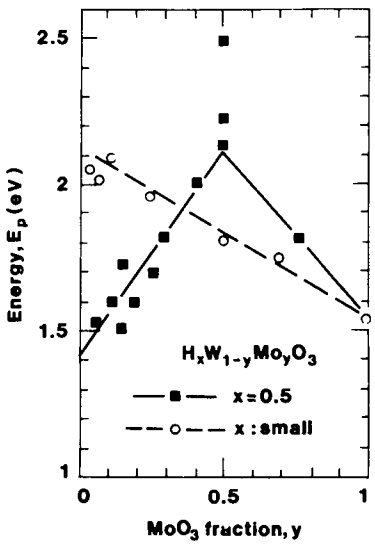

Fig. 13.1 Energy for the peak of the electrochromic absorption band E_p vs. MoO_3 fraction in mixed W-Mo oxide films intercalated with H^+ to two different levels. Symbols denote experimental data, and lines were obtained from Eqs. 13.1 and 13.2 with the parameter values given in the text. From Faughnan and Crandall *(1045)*.

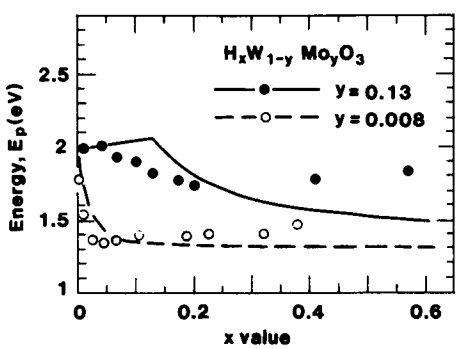

Fig. 13.2 Energy for the peak of the electrochromic absorption band E_p vs. the amount of H^+ intercalation in mixed W-Mo oxide films with two different compositions. Symbols denote experimental data, and curves were obtained from Eqs. 13.1 and 13.2 with the parameter values given in the text. From Kitao and Yamada *(1827, 3686)*.

the corresponding W levels. When x < y, the inserted electrons are trapped at the Mo sites, and the transitions $Mo^{5+} \rightarrow Mo^{6+}$ and $Mo^{5+} \rightarrow W^{6+}$ are possible, whereas when x > y the Mo^{6+} sites are saturated and the transitions $Mo^{5+} \rightarrow W^{6+}$ and $W^{5+} \rightarrow W^{6+}$ can take place. The absorption peak in the mixed oxide hence has two contributions that are different depending on whether x < y or x > y. Taking E_p to be a weighted mean of the peak energies corresponding to the pertinent transitions, one can write, with obvious notation,

$$E_p = \left[(1 - y)E_p^{MoW} + (y - x)E_p^{MoMo}\right] / (1 - x), \text{ for } x < y \ , \tag{13.1}$$

$$E_p = \left[yE_p^{MoW} + (x - y)E_p^{WW}\right] / x, \text{ for } x > y \ . \tag{13.2}$$

These formulas were first given by Faughnan and Crandall *(1045)*, and they have also been used to analyze results for other W-Mo oxides *(1827, 3686)*. The lines in Fig. 13.1 were obtained by using $E_p^{WW} \equiv E_p(WO_3) = 1.4$ eV, $E_p^{MoMo} \equiv E_p(MoO_3) = 1.54$ eV, and $E_p^{MoW} = 2.13$ eV. The former two quantities are in excellent agreement with earlier data (cf. Figs. 9.7 and 12.10).

A shift of E_p towards higher energies when Mo oxide is incorporated in W oxide has also been observed in other work on films made by evaporation *(1501, 1827, 3013, 3050, 3460-1, 3685-6)*, CVD *(960)*, and sol-gel technology *(3754)*. Figure 13.2, from Yamada et al. *(1501, 1827, 3685-6)*, shows results for E_p vs. x at two y values; these data are complementary to those in Fig. 13.1. The energies for the absorption peaks change in a characteristic way under ion intercalation. The variation can be reconciled with predictions from Eqs. 13.1 and 13.2, represented by the curves in Fig. 13.2, by setting $E_p(WO_3) = 1.3$ eV, $E_p(MoO_3) = 1.45$ eV, and $E_p^{MoW} = 2.03$ eV. One should note the similarity between the parameter values used to generate the theoretical data in Figs. 13.1 and 13.2. Less quantitative optical data are available elsewhere for electrochromic W-Mo oxide films made by evaporation *(3015)*, sputtering *(732)*, electrodeposition *(810, 812, 952, 2729)*, PECVD *(349)*, and sol-gel technology *(1490, 2124)*. Studies of the photochromic response under UV irradiation in the presence of C_2H_5OH indicated a maximum effect at $y \approx 0.08$ *(3719)*.

For luminous and solar modulation, it is of interest to consider the absorption not only at E_p but in an extended spectral range. Data of the latter kind are illustrated in Fig. 13.3, after Yamada and Kitao *(3686)*. The spectral absorption coefficient for the W-Mo oxide is broader than for W oxide or Mo oxide alone and, in particular, the luminous absorptance is significantly enhanced in the mixed oxide film. The latter film shows a low-energy shoulder on the absorptance curve; this can be taken to signify that two separate absorption mechanisms are at play, as assumed in the small-polaron-based theory outlined above.

Figure 13.4 reports coloration efficiencies for H^+ intercalated W-Mo mixed oxide films and, for comparison, also for the pure oxides *(1827, 3686)*. The ability to produce a higher luminous CE in the mixed films than for the individual constituents is interesting and of considerable interest for applications.

Many binary oxide systems are of potential interest for electrochromism. Among the W-oxide-containing alternatives, one can note WO_3-V_2O_5, WO_3-Nb_2O_5, WO_3-Ta_2O_5, and WO_3-TiO_2. Bulk crystals of the WO_3-V_2O_5 system can be though of as constructed from regular blocks of corner-sharing octahedra, with the blocks separated from each other by edge-sharing octahedra *(629, 1473-4, 1624)*. Various block sizes are possible, with 4 x 4 being a typical case. A similar atomic

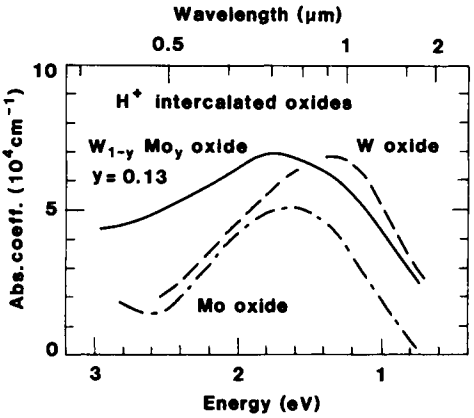

Fig. 13.3 Spectral absorption coefficients for H^+ intercalated W- and Mo-containing oxide films. After Yamada and Kitao *(3686)*.

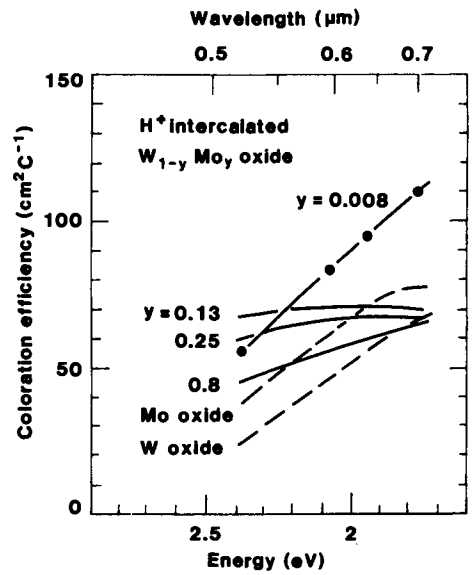

Fig. 13.4 Spectral coloration efficiency for H^+ intercalated evaporated films based on W-Mo oxide with four compositions (solid curves) and on the pure constituents (dashed curves). The curves were drawn to represent data at four discrete wavelengths (indicated by the filled circles on the curve for $W_{1-y}Mo_y$ oxide with y = 0.008). After Kitao and Yamada *(1827, 3686)*.

arrangement prevails for the WO_3-Nb_2O_5 system *(1471, 2299, 2945)*. The WO_3-Ta_2O_5 system was reported on in *(3060)*. With regard to *films* of electrochromic binary mixed oxides, detailed work has been reported for the systems WO_3-V_2O_5 *(1559, 1813, 3015)*, WO_3-Nb_2O_5 *(2148)*, WO_3-TiO_2 *(1270, 1437, 2227, 3715)*, WO_3-CuO_x *(1559)*, WO_3-SnO_x *(161)*, and MoO_3-V_2O_5 *(1312, 3015)*. It was found by Huang et al. *(1559)*, who studied WO_3-V_2O_5 and WO_3-Cu_xO films formed by coevaporation of powders, that charge insertion made the valence shifts underlying the electrochromic absorption take place sequentially with the ions of smallest atomic number changing their valency first. Films of W-Ti oxide are able to achieve superior durablility, as discussed in some detail in Sec. 31.8 below.

13.2 Ternary Oxides, Especially Tungsten-Molybdenum-Vanadium Oxide

One of the reasons why mixed oxides are of interest for electrochromics-based technology is that favorable--usually neutral--colors can be achieved. Thus very broad spectral absorption features have been observed for several mixed oxides *(1559, 2147, 2730, 3015)*. Figure 13.5, from work by Sato and Seino *(3015)*, illustrates this point for a 0.6-μm-thick film based on WO_3 (54 %), MoO_3 (10 %), and V_2O_5 (36 %) at different levels of ion intercalation from a $LiClO_4$ + PC electrolyte. The film can shift from a yellowish transparent state to a dark brown state. The spectral transmittance is fairly constant in the main part of the luminous spectrum, and the near-infrared transmittance minimum, characteristic of pure W oxide, does not appear. It is evident from Fig. 13.5 that the *color of the film can be changed significantly when oxides are mixed to different proportions.*

The quantification of the color properties is considered next; this discussion is a necessary prerequisite for an analysis of the spectral data that follows toward the end of this section. Color can be specified in several ways; the subject is well known and treated in several books *(1342, 1428, 1697, 2128, 3670-1)*. The CIE Colorimetric System is adopted here; it is able to produce color specifications in terms of *tristimulus values* (or chromaticity coordinates). For this purpose, one identifies three independent spectral functions with an ideal observer's color-matching functions $\bar{x}$, $\bar{y}$, and $\bar{z}$; they represent red, green, and blue primaries. Any color then can be described as an additive mixture of these primaries. The $\bar{y}$ curve is chosen to be identical with the photopic luminous efficiency curve of the ideal observer (cf. Fig. 1.4). The CIE tristimulus values (X, Y, Z) corresponding to a certain color stimulus $\phi(\lambda)$ are obtained from

$$X = K \int d\lambda \, \phi(\lambda) \, \bar{x}(\lambda) \,, \tag{13.3}$$

and analogously for Y and Z. For transmitted and reflected light the color stimuli are $T(\lambda)\Sigma(\lambda)$ and $R(\lambda)\Sigma(\lambda)$, where $\Sigma(\lambda)$ is the relative spectral irradiance function of the illuminant irradiating the object. Figure 1.5 showed three specific functions for $\Sigma(\lambda)$. The normalization constant K is given by

$$K = \left[\int d\lambda S\,(\lambda) \, \bar{y}\,(\lambda) \right]^{-1}, \tag{13.4}$$

so that Y becomes the luminous transmittance or the luminous reflectance. The chromaticity coordinates, following standard notation, are given by

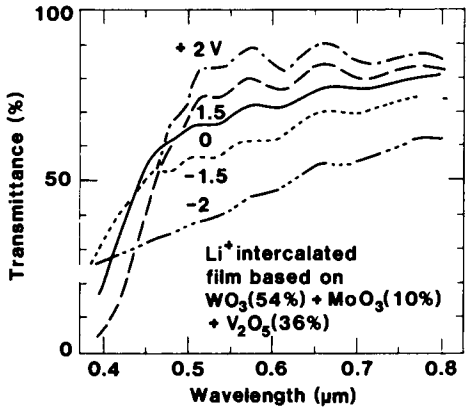

Fig. 13.5 Spectral transmittance for an electrochomic film based on $WO_3 + MoO_3 + V_2O_5$ intercalated with Li^+ by application of the shown voltages. From Sato and Seino *(3015)*.

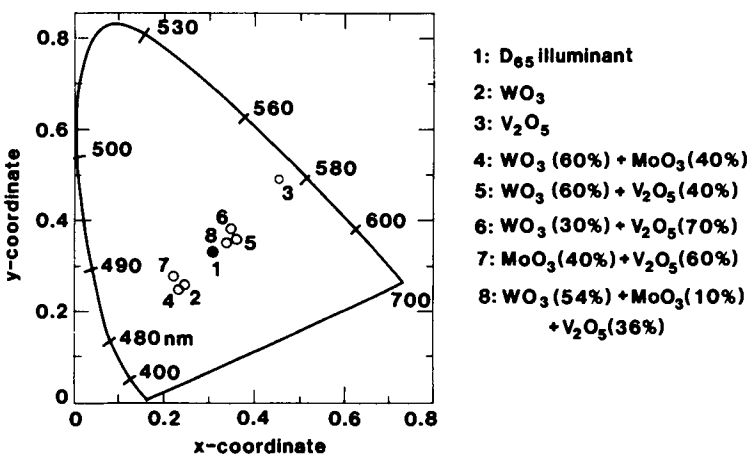

Fig. 13.6 CIE 1931 chromaticity diagram and (x, y) coordinates for transmission through electrochromic films based on the shown materials. From Sato and Seino *(3015)*.

$$x = X(X + Y + Z)^{-1}, \tag{13.5}$$

and correspondingly for y and z. Since

$$x + y + z = 1 \tag{13.6}$$

it is sufficient to state the magnitudes of x and y.

The above relations lead directly to the CIE 1931 chromaticity diagram given in the main part of Fig. 13.6, showing the spectrum locus (i.e., the chromaticity coordinates of monochromatic stimuli in the $0.38 < \lambda < 0.78$ μm range) and the purple line (connecting the ends of the spectrum locus). The chromaticity coordinates of any real color lie inside this boundary. For daylighting applications, one can use the D_{65} illuminant with a correlated color temperature of 6504 K (cf. Fig. 1.5). The chromaticity coordinate for this illuminant is marked in Fig. 13.6.

Additive color mixture makes it possible to obtain any color as a combination of a specified achromatic color--defined by illuminant D_{65} in the present case--and a certain monochromatic color known as the dominant color. It is also convenient to introduce a complementary color, being a monochromatic color with the property that when mixed in a suitable proportion with the color considered it yields a match with the achromatic color. Another useful concept is excitation purity, defined as the ratio of two lengths in the chromaticity diagram; the first length is the distance between the chromaticity point of the achromatic color and that of the color considered, and the second length is the distance along the same direction and in the same sense from first point to the boundary of real colors in the chromaticity diagram. It is then clear that is is possible to represent a pair of chromaticity coordinates with two alternative entities: a dominant (or complementary) color and an excitation purity.

The discussion above provides a sufficient background for appreciating experimental data plotted in a chromaticity diagram. The various data points in Fig. 13.6 were obtained from experimental transmittance curves reported by Sato and Seino *(3015)* for films based on WO_3, V_2O_5, WO_3-MoO_3, WO_3-V_2O_5, MoO_3-V_2O_5, and WO_3-MoO_3-V_2O_5. Spectral data for the latter sample were given in Fig. 13.5. It is found that films of WO_3, $WO_3 + MoO_3$ and $MoO_3 + V_2O_5$ have blue as their dominant color, whereas the other samples are red. The V_2O_5-based film has a high excitation purity. The most interesting data are for the ternary $WO_3 + MoO_3 + V_2O_5$ film, whose excitation purity is very small. This chromaticity analysis hence indicates that *by mixing several electrochromic oxides one can produce a film with an almost neutral color appearance* when illuminated with daylight.

There are only a few available chromaticity studies on electrochromic systems *(1123, 3147)*. This lack of data is surprising, since such analyses tell a lot about practical device performance.

Obviously, many ternary oxides are capable of showing electrochromism. Some bulk materials of interest can be found among the systems V_2O_5-WO_3-VO_2 *(630)* and $(V_{1-y}Mo_y)_2O_5$ *(3615)*; they are known to serve as excellent hosts for Li^+ intercalation. Electrochromic oxide films include WO_3-Nb_2O_5-Li_2O *(2147-8)* and (Ti,Nb)-doped WO_3 *(1184-5)*.

13.3 Tungsten Oxyfluoride

Tungsten oxyfluoride is of interest both because the physical and chemical properties are different

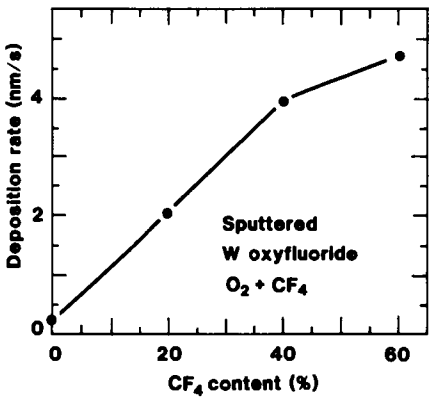

Fig. 13.7 Deposition rate vs. CF_4 content for sputtering of W in $O_2 + CF_4$. After Harding *(1426)*.

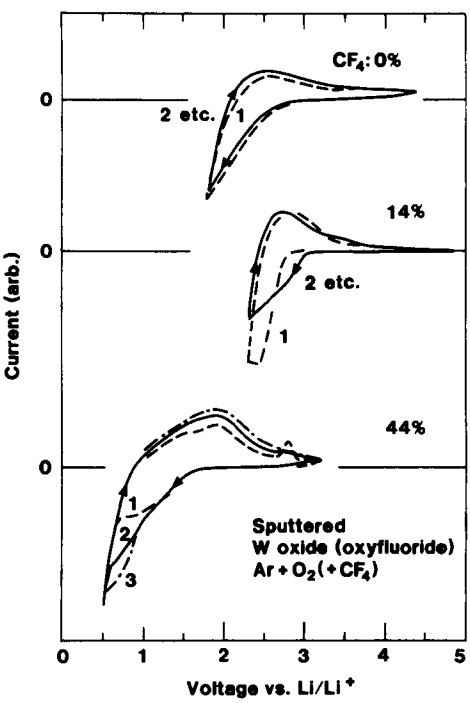

Fig. 13.8 Cyclic voltammograms for Li^+ intercalation/deintercalation in W oxide and oxyfluoride films prepared by sputtering in $Ar + O_2$ (+ CF_4) with the shown CF_4 contents. The number of voltammetric cycles is indicated. The voltage scan rate was 20 mV/s. Arrows denote scan direction. From Azens et al. *(190)*.

from those in the oxide and because films can be prepared at high deposition rates. Specifically, by sputtering W in a plasma comprised of (Ar) + O_2 + CF_4 it was possible to obtain a higher deposition rate than in the absence of CF_4. Rate enhancements in the presence of CF_4 were first reported by Harding *(1426)*, and later studies of sputtering in CF_4-containing plasmas have been reported by Ross *(2938)* and Azens et al. *(190)*. Figure 13.7 gives quantitative information on the sputter rate, as determined by Harding *(1426)*; the rate rose by a factor as large as 20 when the CF_4 content went from 0 to 60 %.

In order to understand the origin of the enhanced deposition rate, one should observe that "chemical" sputtering can take place in a fluorine-containing plasma. The details are not known, but from studies of plasma etching in the presence of CF_4 it has been concluded that highly reactive atomic F can be produced by the reaction

$$CF_4 + e^- \rightarrow CF_3^* + F + e^- \rightarrow CF_2 + 2F + e^- . \qquad (13.7)$$

CF can also be formed in the discharge *(751)*. When O_2 is present, additional F can be liberated through the oxidation of CF_x radicals. The pertinent reactions were discussed in *(1412, 1429, 2367, 2783, 2955, 3237)*. It is likely that atomic F reacts with the target surface and dislodges species at a rate that is governed by the F density. The analogy with reactive ion etching of tungsten is obvious; this process has been discussed several times *(25, 379, 529, 1096, 2724-5, 2749, 2838, 3280)*. The importance of WOF_4 as an etch product has been stressed *(379, 2724)*. Thermodynamic data for gaseous W oxyfluoride molecules were surveyed in *(947)*.

Azens et al. *(190)* tested W oxyfluoride films by use of cyclic voltammetry in a 1 M $LiClO_4$ + PC electrolyte. Figure 13.8 shows data for films deposited in the presence of different amounts of CF_4. Without CF_4, the usual voltammogram for disordered W oxide was obtained (cf. Fig. 6.12). At low fluorination (14 % CF_4), the voltammograms were markedly different and showed evidence for evolution during the first voltammetric cycle. Thereafter the conditions remained stable and, in fact, it seemed that the reversibility under Li^+ intercalation/deintercalation was better than for "pure" W oxide. At high fluorination, the voltammograms changed significantly during the first four cycles, and the reversibility was incomplete. It is hence found that fluorination can lead to W-oxide-based films that serve as good intercalation hosts for Li^+. The film composition is not known, but one may speculate that a composition similar to LiW_3O_9F is formed. The latter material is capable of easy Li^+ diffusion, as mentioned in Sec. 6.2. Furthermore, some cubic and tetragonal W oxyfluorides have been mentioned in the literature *(2894, 3197)*.

Figure 13.9 shows optical properties of a ~0.4-μm-thick W oxyfluoride film in as-deposited, bleached, and colored states. The colored film has a rather constant transmittance in the luminous and near-infrared spectral range, which is very different from the behavior of a "pure" W oxide film. In order to gain more quantitative electro-optical data, the coloration efficiency was calculated for films with different degrees of fluorination. Figure 13.10 shows that at zero fluorination the CE is peaked at $\lambda \approx 0.9$ μm where the magnitude is ~85 cm^2/C. This is in agreement with earlier results; cf. Sec. 9.7. An increase of the CF_4 fraction gives a lowering of the CE, particularly in the infrared, and a displacement of the wavelength for the maximum CE towards a shorter value. It is then clear that the fluorine incorporation improves the color neutrality by degrading the coloration efficiency except at the blue end of the spectrum.

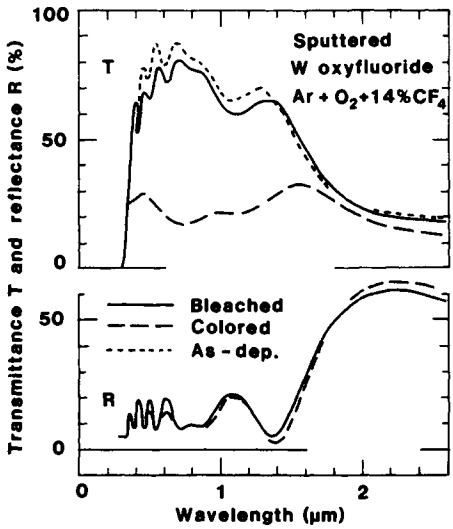

Fig. 13.9 Spectral transmittance of a W oxyfluoride film prepared by sputtering in a plasma of the shown composition. Data are given for as-deposited, colored (Li^+ intercalated), and bleached states. From Azens et al. *(190)*.

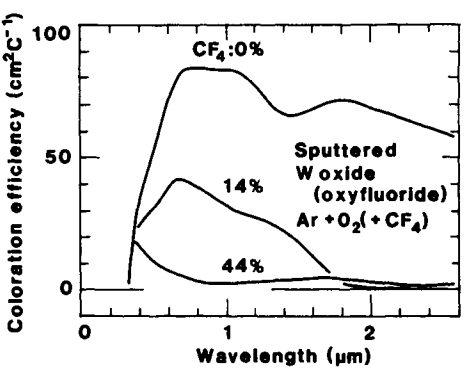

Fig. 13.10 Spectral coloration efficiencies for W oxide and oxyfluoride films made by sputtering in Ar + O_2 (+CF_4) with the shown CF_4 contents. From Azens et al. *(190)*.

13.4 Composites of Tungsten Oxide and Metal

Tungsten oxide films containing dispersed metal particles have been studied for the systems WO_3-Au *(160, 163, 3168-70)*, WO_3-Pt *(3169)*, and WO_3-Ag *(160, 163)*. Much of the work has been motivated by the desire to develop multiple-color electrochromic films for display applications. Recently, some work has been reported on WO_3-Au powders for detection of minute quantities of ammonia in air *(2157)*.

Films of WO_3-Au were produced by Sichel et al. *(3168-70)*, who employed reactive rf sputtering from a compressed mixed-particle target in the presence of $Ar + O_2$. Figure 13.11 shows spectral optical density of a 0.14-μm-thick film with 8.7 at. % Au in as-deposited state and after H^+ intercalation from a H_2SO_4 electrolyte. As-deposited films were blue in transmission as a result of the absorption maximum at $\lambda \approx 0.6$ μm. Coloration by H^+ intercalation made the absorption peak grow in intensity and gradually shift in wavelength so that the film appeared pink or red. Bleaching by a sufficient voltage could produce films with good transparency. Similar properties were observed in WO_3-Au films made by alternate evaporation of the two constitutents onto substrates at $\tau_s \approx 250$°C followed by Li^+ intercalation/deintercalation in a $LiClO_4$ + PC electrolyte *(160, 163)*.

At least in the sputter-deposited films, the granular structure--with Au particles being 2 to 12 nm in linear size--prevailed only in an intermediate range of metal concentration. Up to 2.8 at. % Au, the film properties were similar to those for "pure" W oxide. It then appears that some Au became incorporated in the oxide lattice and was not occluded as particles. Similar observations of "lost" metal have been made for other codeposited oxide-metal composites *(2527, 2533)*. Above 11 at. % Au, the composite films behaved as granular metals.

The optical properties of the WO_3-Au films could be understood, at least in principle, from the Maxwell Garnett EMT (Eq. 10.32). The W-oxide-based matrix was modified by the presence of some dispersed metal atoms and, more importantly, the Au particles had properties governed by particle-size-induced boundary scattering. Judging from earlier work on Au particles in discontinuous films *(2559)* and gas evaporated layers *(1299)*, it is reasonable to set the mean free path equal to the particle radius. When ions were intercalated into the composite, it was not correct to assume that they were evenly distributed. Instead, at least for H^+, there was evidence that the ions accumulated at the boundaries of the Au particles. The EMT should then embrace "dressed" particles with surface layers different from the embedding matrix. The significance of ion accumulation can be understood from electrical measurements *(3168-9)* which showed, surprisingly, that the conductivity was diminished when Au was added.

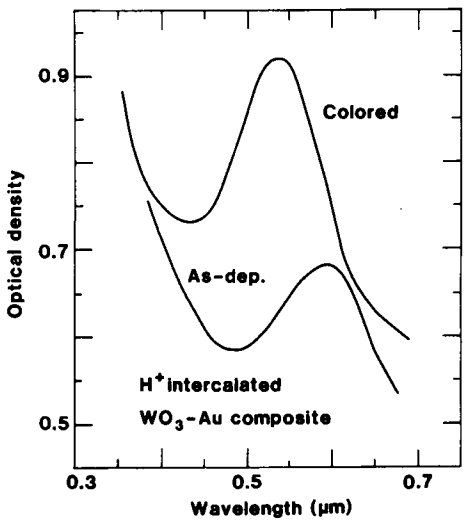

Fig 13.11 Spectral optical density of an electrochromic film based on WO_3 + Au in as-deposited and H^+ intercalated states. From Sichel and Gittleman *(3168-9)*.

Chapter 14

IRIDIUM OXIDE FILMS

The earlier chapters have dealt with electrochromic thin films based on oxides comprising octahedral MeO_6 units with predominant corner-sharing, so that the overall stoichiometry tends towards MeO_3. This chapter, and several following ones, is devoted to *rutile-like* materials with MeO_6 octahedra having both corner-sharing and edge-sharing; the stoichiometry then tends towards MeO_2. Specifically, the present chapter considers Ir oxide. This material has been investigated in detail, so that certain aspects are better known than they are for W oxide. Iridium oxide shows *anodic* electrochromism, i.e., the optical modulation is opposite to that in oxides of W and Mo. Some comments on bulk-like IrO_2-based materials are given first (14.1).

Electrochromic thin films of Ir oxide films have been produced by several different techniques, and the ensuing films have been designated by acronyms such as AIROF, SIROF, TOIROF, AEIROF, CEIROF, and PRIROF. Here IROF stands for "iridium oxide film" and A, S, TO, AE, CE, and PR denote "anodic" *(339)*, "sputtered" *(3041)*, "thermally oxidized" *(3023)*, "anodically electrodeposited" *(3705)*, "cathodically electrodeposited" *(3705)*, and electrodeposited by a "periodic reverse" voltage *(3749)*. The references are to the papers in which these acronyms were introduced. These terms are not used below, but the films are referred to simply as "Ir oxide".

This chapter basically follows the same format as Ch. 12 dealing with Mo oxide. The various sections cover the preparation and characterization of films made by evaporation and sputter-deposition (14.2) and by electrochemical and chemical techniques (14.3), ion intercalation/deintercalation reactions and diffusion constants (14.4), ion intercalation/deintercalation studied by electrochemical (14.5) and physical (14.6) techniques, optical properties (14.7), and coloration efficiency (14.8).

14.1 Crystal Structure of Bulk-like Iridium Oxide

The electrochromically active Ir oxide is akin to, but not idential with, IrO_2. The latter material has been studied in detail by Murphy et al. *(2441)* and Rogers et al. *(2926)*; the structure is of rutile type and can be thought of as constructed from almost octahedral building blocks. More specificlly, the ideal rutile structure may be described as an hexagonal closepacked oxygen lattice with octahedrally coordinated metal ions forming edge-shared infinite chains. The chains are crosslinked so that they form an equal number of identical vacant channels. These channels may allow intercalation/deintercalation of ionic species. The channels contain two tetrahedral and one octahedral site per Ir ion, where ion accommodation seems likely. $Li_{1.5}IrO_2$ with (pseudo)tetragonal structure is known. The channel diameter in IrO_2 is as small as ~0.13 nm, so it is not obvious how

Li^+ or larger ions are transported. Possibly the fact that IrO_2 is electrically conducting *(576, 2926, 2956-7)* contributes to the intercalation, as noted in *(2441)*. The electrochromic material is hydrous and appears not to have been investigated as regards structure *(543)*.

14.2 Films Made by Evaporation and Sputter-deposition: Preparation and Characterization

Evaporation, either of Ir oxide or of metallic Ir in the presence of oxygen, can undoubtedly be used for preparing films. According to available data on mass evaporation rates *(1955)*, a source temperature larger than ~2000°C would be necessary. This rules out resistively heated vapor sources, whereas *e*-beam sources could be used. No work has been reported on as-evaporated electrochromic Ir oxide films, whereas evaporated metallic films have been converted to Ir oxide by an oxidizing post-treatment through electrochemical cycling in a H_2SO_4 electrolyte *(3120)*, or by exposure to an oxygen-containing atmosphere *(3017-9, 3023, 3025)*. These latter films will be discussed below.

Sputter-deposition has been studied extensively as a technique for making electrochromic films. Numerous reports refer to a material made by reactive rf or dc sputtering in the presence of O_2 or $O_2 + H_2O$ onto substrates at or closely above room temperature *(337, 819, 1120, 1379-84, 1730, 1758, 1760, 1764, 2017, 2511, 2999-3001, 3041-2, 3121, 3544, 3741a, 3772)*. The deposition rate was of the order of 1 nm/minute, which is rather dismal for applications, and the build-up of an electrochromic film took more than one hour. Figure 14.1, reproduced from Kanai et al. *(1730)*, indicates that the rate increased from ~0.5 to ~3 nm/minute when the power density at the substrate went from 0.3 to 0.9 W/cm^2, and the rate was also somewhat dependent on p_{O2}. The films were visibly clear or "non-clear" as indicated by the different symbols, and it appears that excessive O_2 pressures and power densities led to nontransparent films. The density of this kind of films was ~10 g/cm^2 *(1381, 1383)*. The relative density--compared to 11.68 g/cm^2 for bulk IrO_2--was 0.86, so that the films must be regarded as compact. The density can be diminished by electrochemical cycling, as discussed later. Sputtering in the presence of H_2 can yield films with enhanced proton conductivity *(2016)*.

An alternative procedure involves dc sputtering in Ar + 20 % O_2 onto substrates kept at -35±3°C by liquid nitrogen cooling *(454, 1744)*. The sputter gas was humidified by bubbling through water, and it is obvious that water vapor condensed on the substrate during thin film deposition. The relative density was found to be ~0.34 *(1744)*, i.e., these films were highly porous. The deposition rate was ~20 nm/minute. More recently, electrochromic Ir oxide films were made by rf magnetron sputtering in Ar + O_2 *(1921)* or $O_2 + H_2O$ *(1835-6)*; in these cases the sputter rate was 10 to 20 nm/minute. *(1921)*. Sputter-deposited films have also been discussed in *(244-5, 728-9, 2854, 2856)*.

Water incorporation is of large significance for the properties of sputter-deposited Ir oxide films. Some hydration and hydroxylation comes naturally, since it is not possible to totally exclude the influence of water vapor either during deposition or during a subsequent exposure to ambient air. The hydrous nature has been varied consciously by mixing water vapor in the sputter gas *(454, 1744, 3041)*, by cooling the substrate to a low temperature *(454, 1744)*, or by a more or less complete evacuation of the vacuum system prior to sputter deposition *(3000)*. Still another possibility of keeping the Ir oxide film hydrous is to mix in a second oxide during the deposition,

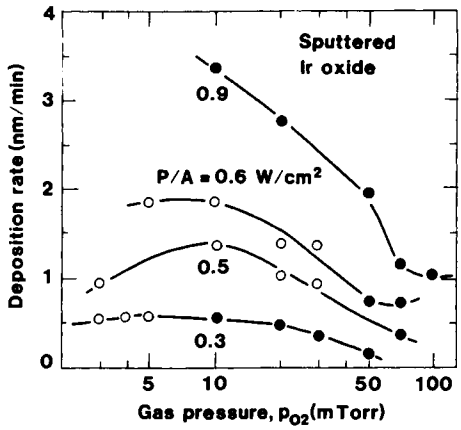

Fig. 14.1 Deposition rate vs. oxygen pressure for sputtering from an Ir target at the shown values of power density *P/A*. Open circles refer to clear films and filled circles to films being "unclear" or with "medium" clarity. Curves were drawn for convenience. From Kanai et al. *(1730)*.

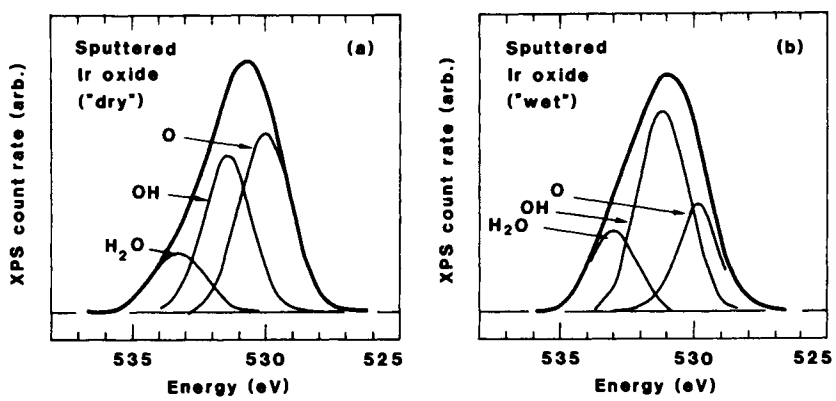

Fig. 14.2 Deconvoluted XPS spectra for Ir oxide films sputter-deposited in the presence of a small (part a) and large (part b) amount of water vapor. The three lower bell-shaped curves represent *O1s* electrons bound as oxide, in hydroxyl groups, and in water molecules. The upper curve is the envelope. From Sanjinés et al. *(3000)*.

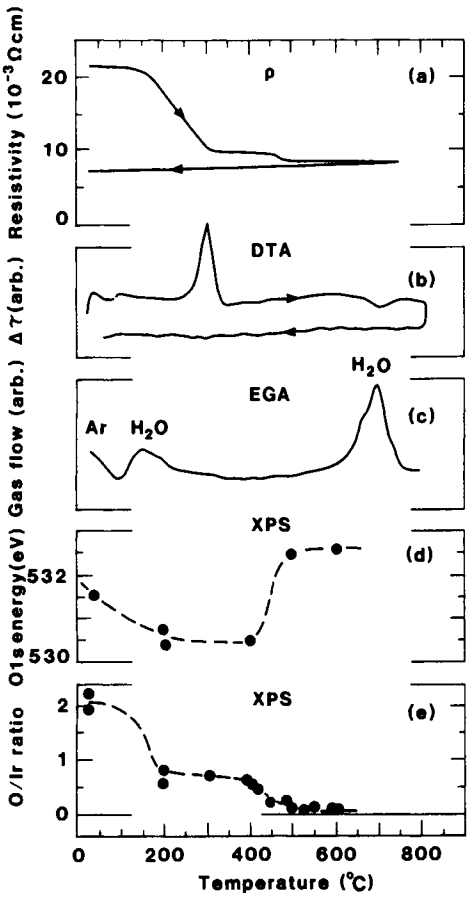

Fig. 14.3 Changes of physical properties during annealing of sputter-deposited Ir oxide films. Data are given for (a) electrical resistivity, (b) differential thermal analysis DTA measuring the temperature difference $\Delta\tau$ between the sample and a reference, (c) evolved gas analysis EGA measuring the flow rate and gaseous species, (d) location of the *O1s* peak in XPS spectra, and (e) O/Ir atomic ratio determined from peak intensities in XPS spectra. Solid lines and filled circles indicate experimental data, and dashed curves were drawn for convenience. Arrows denote direction of the temperature scan. After Hackwood et al. *(1381, 1383)* and Sanjinés et al. *(3000)*.

and it was shown *(2545)* that Ir-Sn oxide films had favorable properties. It is not known why a SnO_2 admixture is beneficial.

Electron microscopy has been use to analyze the microstructure of the films. SEM studies of films slowly rf sputtered onto flat substrates indicated smooth surfaces with no features having sizes above 50 nm *(1381, 1383, 2999)*. Sputtering onto thin wires, on the other hand, gave films with a characteristic morphology comprised of well defined platelets whose orientation depended on the amount of H_2O admixture *(1836)* and on the presence of a low-voltage substrate bias *(1835)*. TEM investigations showed some fine grains with a diameter of ~2.5 nm *(2999)*, which was consistent with XRD line broadening *(1921)*.

EXAFS and XANES have been employed to probe the microstructure of Ir oxide films prepared by sputtering in Ar + O_2 onto unheated poly-imide substrates *(244-5)*. Multishell simulation indicated that the Ir-O nearest-neighbor and next-nearest-neighbor distances, as well as the coordination numbers, were similar to those expected for IrO_2.

XPS studies of as-deposited films have given valuable insights into the role of hydration. Figure 14.2, taken from Sanjinés et al. *(3000)*, refers to two samples rf sputtered at ~1.2 nm/minute and $\tau_s \approx 22^oC$ with different amounts of residual water vapor in the system; for simplicity the corresponding films are denoted "dry" and "wet". The *O1s* signal centered around 531 eV binding energy is rather broad and can be deconvoluted into three individual bell-shaped peaks pertaining to oxide (530±0.5 eV), hydroxide (531±0.5 eV), and water (533±1eV). These assignments can be made unambiguously since the three separate binding energies are characteristic for many hydrous transition metal oxides *(177, 1082, 1804, 2739-41, 2917, 3644)*. Significant amounts of hydration and hydroxylation are apparent, and, in particular, the influence of OH groups is very strong in films made by sputtering in the presence of some water vapor. RBS data showed that the O/Ir ratio was 1.8 to 2.2 in "dry" films (i.e., consistent with IrO_2) and 2.4 to 2.7 in "wet" films *(2999, 3000)*. XPS analyses of *O1s* signals will be discussed several times below.

Heat treatment of sputter deposited films, together with continuous monitoring of property changes, give important information on the composition and stability of the films. Measurements on films made under nominally "dry" conditions have been reported by Hackwood et al. *(1381, 1383)* and Sanjinés et al. *(3000)*. Figure 14.3 shows the evolution of several properties upon heating to ~700°C. Part (a) refers to the resistivity of a ~0.3-μm-thick film heated in air *(1383)*. The resistivity drops in two steps at ~200 and ~460°C. The changes were irreversible, and the resistivity varied smoothly when the film was cooled. Resistivity steps signal changes in crystallinity and/or stoichiometry. It was found by Sanjinés et al. *(3000)* that the temperature-dependent resistivity curve was somewhat different if the heating took place in Ar or in vacuum, or whether the film was hydrous. Figure 14.3(b) shows results from Differential Thermal Analysis (DTA) of a similar film heated and subsequently cooled at 10°C/minute in flowing Ar *(1381, 1383)*. The vertical scale indicates the difference between sample temperature and reference temperature. These data are closely related to differential calorimetry scans, such as the one for W oxide shown in Fig. 3.15(a). The strong exothermic peak at ~300°C corresponds to an enthalpy change of ~1.1 eV. Such large changes indicate pronounced modifications in the bonding, and XRD measurements *(1383)* verified that the structure went from amorphous to crystalline. Specifically, the grain size was ~15 nm at $\tau_a \approx 590^oC$ and ~25nm at $\tau_a \approx 790^oC$. A small and broad endothermic feature is seen in the DTA spectrum at ~700°C. Evolved Gas Analysis (EGA) is reported on in Fig. 14.3(c), where the vertical axis indicates the gas flow *(1381, 1383)*. Some gas that came off at low temperature was identified as Ar; this gas must have been trapped during the

sputtering. At ~120°C there was evidence for H_2, O_2, and H_2O leaving the sample, and a major loss of the same gases took place at ~700°C.

XPS data taken in ultrahigh vacuum can provide an interesting complement to the results obtained from resistivity, DTA, and EGA. Figure 14.2(d) shows the binding energy for the *O1s* peak (cf. Fig. 14.2) *(3000)*. Heating up to ~400°C led to a shift towards a lower binding energy, which is clearly consistent with a loss of OH groups and H_2O. The O/Ir atomic ratio can be estimated from the heights of the peaks due to $Ir4f_{7/2}$ and *O1s* in XPS spectra *(3000)*. Figure 14.3(e) shows that the initial stoichiometry was close to IrO_2. Annealing led to a drop of the O/Ir ratio in two steps, and very little oxygen remained at ~600°C. The various sets of data in Fig 14.3 were taken under somewhat different conditions. Nevertheless, the pattern of stoichiometry/ crystallinity transformations is reassuringly consistent.

14.3 Films Made by Electrochemical and Chemical Techniques: Preparation and Characterization

Electrodeposition has been used successfully as a technique for making electrochromic Ir oxide films in work by Baba et al. *(201, 3749, 3752, 3755)* and Yamanaka *(3705-6)*. The first attempts involved dc electrolysis of an aqueous $Ir(SO_4)_2$ solution followed by annealing at 350°C *(201, 3755)*. These films showed some undesirable optical absorption. However, fully transparent films could be produced with ac electrolysis at 1/12 Hz of an aqueous sulfatoiridate(III, IV)complex solution *(3749)*; the deposition took place in the cathodic half-cycle, and the films were post-treated by anodic oxidation in the same electrolyte in order to remove any remaining metallic Ir. Successful results have also been reported for dc electrolysis of a strongly alkaline $IrCl_4 \cdot H_2O$ solution at ~15°C *(3705-6)*. Films could be formed both under anodic and cathodic conditions, with the anodic ones having superior stability. Heat-treatment at 100°C for 1 h led to harder films. Electron microscopic studies *(3705)* indicated smooth films comprised of crystallites with diameters around ~1.5 nm. XPS measurements were consistent with Ir in 4+ state. Photo-electrochemical deposition from an electrolyte containing $Ir_2(SO_4)_3$ was reported in *(2214)*.

Anodization is the most widely used technique for making Ir oxide films of interest for electrochromics as well as for other applications such as electrocatalysis, electroanalysis (pH meters), neural stimulation electrodes, etc. The preparation and properties were reviewed by Burke and Lyons *(534)*. Thick films can be conveniently made by potential cycling in acidic electrolytes, whereas the application of a constant potential is ineffective. A typical procedure is to employ linear voltage ramps between -0.25 and +1.25 V vs. SCE in 0.5 M H_2SO_4. The build-up of the film can be followed by voltammetry, indicating that the Coulombic charge associated with each half-cycle increases. Figure 14.4, reproduced from recent work by Hitchman and Ramanathan *(1503a)*, traces the evolution of the voltammogram up to 10^4 cycles. Similar results, albeit for a smaller number of cycles, have been given many times in the literature *(391, 544, 553, 555, 565, 596, 1089, 1265-6, 1269, 1394, 1680, 2061, 2265, 2268, 2329, 2665, 2757, 2836-7, 2963, 3017, 3118, 3260, 3792)*. It appears that neither the voltage scan rate nor the voltage ramp profile are of major importance, and thick Ir oxide films could be grown by one-second pulses between the potential limits stated above *(1265, 1905, 2634, 2753, 2757)*. Growth is possible in many aqueous electrolytes, such as NaOH *(546, 554)* and $LiClO_4$ at pH = 9 *(2756-7)*. Most work has been reported for anodized bulk iridium, but films made by evaporation *(3119-20)* or sputter-

deposition *(390, 1581, 1901, 1904-5)* have been anodized too. Voltammetry applied to (100) surfaces of single crystal IrO_2 was reported in *(1462)*.

The voltammograms in Fig. 14.4 show a number of characteristic features. The main peak at ~0.7 V vs. SCE in Fig. 14.4(a) is associated with an $Ir^{4+} \leftrightarrow Ir^{3+}$ transition which--as discussed later--is responsible for the electrochromism. After some thousand cycles, this peak starts to shift towards a higher voltage, as seen from Fig. 14.4(b). The structure between -0.25 and -0.05 V vs. SCE is due to hydrogen adsorption/desorption; it may not be observed in anodized films made by evaporation *(3120)*. The "prepeak", or shoulder, at ~0.4 V vs. SCE is associated with the resistivity of the film; this feature has been modelled in recent work *(1267)*. The rapid current increases at the endpoints of the displayed voltage range are due to gas evolution.

The electrochemistry of Ir oxide films has been studied many times. In most cases, cyclic voltammetry has been used for different anodic and cathodic sweep limits, voltage ramp shapes, scan rates, electrolyte type, pH, etc. Data are given, apart from in the work cited above, in *(117, 178, 311, 335, 340-1, 506-9, 554, 753, 793, 1192, 1268, 1384, 1546, 1744, 2260, 2423-4, 2740, 2754-5, 2898, 2915, 3544, 3552-3, 3555, 3772)*. A detailed discussion of this wealth of information is not meaningful in the present context, but one should note the study by Pickup and Birss *(2753)* on the mechanism for thin film growth. According to them, an initial compact IrO_2 layer is formed. At a voltage larger than 1 V vs. SCE, the outer monolayer of this dense oxide becomes hydrated, and it then inhibits further modification of the underlying oxide. Potential cycling yields a reduction of the compact oxide to Ir metal followed by reformation so that an accumulation of hydrous oxide takes place. A duplex film structure was also surmised in some earlier work *(551)*.

Anodic Ir oxide seems to be non-homogeneous on different length scales. Thus SEM images indicated a characteristic "mud crack" pattern, at least for films on bulk Ir, on the scale of 1 to 10 μm *(177, 391, 753, 2423, 2756-7)*. The flaky appearance signified that internal stresses had led to a break-up at the film/substrate interface. This tendency was less pronounced for films grown in $LiClO_4$ than in H_2SO_4 *(2756-7)*. SEM imaging at higher resolution, as well as TEM analyzes, indicated pores and voids on the scale 50 to 100 nm, in addition to microvoids with ~2.5-nm-diameter *(2268, 2329)*. The relative density of the material was found to be as low as ~0.17 *(2268)*, which is much smaller than for sputter-deposited films. According to Burke and Whelan *(563, 565)*, the anodic Ir oxide can be described as a hydrated hydroxide comprising aggregates of primary octahedral species which form a mixture of linear and branched chains as well as ring structures. Such a "gel-type" or "polymeric" structure may be akin to that formed in some W oxide films produced by low-voltage anodization or sol-gel deposition (cf. the discussion around Figs. 5.1 and 5.6).

Very little is known about the crystalline structure of the anodic films. According to Mitchell et al. *(2329, 2837)*, electron diffractograms were consistent with a hexagonal structure in fine grains. The elemental composition of the films will be discussed later in connection with ion intercalation/deintercalation.

Among the purely *chemical techniques* for making Ir oxide films, one should note pyrolysis of $IrCl_3 \cdot 3H_2O$ in isopropanol solution *(134, 177, 1866, 2100-1, 2916, 3544)* or in aqueous solution *(671)*. Samples have been prepared by manually painting suitable supports with the solutions. Spray pyrolysis might give thin films of optical quality, but no work along those lines seems to have been reported. A similar technique would be useful for making Ir-based mixed oxide films *(281, 846, 2928)*. A CVD-based technique for Ir has been proven recently *(736)*; the

ensuing films might be oxidized by a suitable post-treatment.

14.4 Ion Intercalation/deintercalation Reactions and Diffusion Constants

Iridium oxide films display pronounced electrochromism and bleach/color when ions are intercalated/deintercalated. The mechanism responsible for the electrochromism has been subject to considerable controversy over the years, but it is now generally accepted that the optical effects are connected with ion intercalation/deintercalation just as for W oxide and Mo oxide. Some early claims *(339-40, 3120)* that the electrochromism in Ir oxide would be of purely electronic nature have been convincingly disproved.

The ionic species involved in the intercalation/deintercalation reaction has been debated at length, and it is convenient to give a brief overview over the situation here, before the most pertinent data are discussed in detail. In essence, two mechanisms have been put forward to account for the electrochromism of (mainly anodic) films in aqueous electrolytes, viz. a cation (proton) process according to

$$IrO_x(OH)_{3-x} + xH^+ + xe^- \leftrightarrow Ir(OH)_3 \qquad (14.1)$$

and an anion (hydroxyl ion) process according to

$$Ir(OH)_{3+x} - xOH^- + xe^- \leftrightarrow Ir(OH)_3 \ . \qquad (14.2)$$

$Ir(OH)_3$ represents the transparent state. This composition can be expressed, alternatively, as $HIrO_2 \cdot H_2O$ or $IrOOH \cdot H_2O$. The magnitude of the ion intercalation/deintercalation can be large, and a maximum x value of unity has been observed for highly porous films made by anodic oxidation *(2268)*. It is imperative that some degree of hydration is present in order to have a substantial ion intercalation/deintercalation *(1462)*. For comparison, one could note that the largest x value for reversible electrochromism in W oxide is ~0.3. At x = 1, the colored Ir-oxide-based material may be written as $IrO_2 \cdot H_2O$ for the cation process and as $IrO_2 \cdot 2H_2O$ for the anion process, and, with this similarity in mind, it is hardly surprising that it has been difficult to distinguish clearly between the two alternative processes.

Bleaching by H^+ intercalation and coloration by H^+ deintercalation has been favored in several studies *(1265-6, 1268, 1905, 2265, 2268)*. However, objections to cation transport, and support for anion transport, have been voiced to explain (i) the absence of electrochromism in some (nominally) water-free proton conducting electrolytes *(335, 2898)*, (ii) voltammograms interpreted so as to indicate that more than one ionic species would be responsible for the electrochromism *(335, 341, 3119)*, and (iii) dimensional changes during coloration and bleaching *(1382, 2262)*. It appears that none of these objections is fully impeccable, though. More complicated processes, involving simultaneous cation and anion transport and pertinent to a porous gel-type structure, have been put forward in other work *(390, 553-5, 563, 565, 2754)*. Recently much of the previous data have been reconciled, and several controversial features removed, through work by Kötz et al. *(1901)* who showed that H^+ exchange was dominant in electrolytes with pH < 4, whereas OH^- exchange dominated at pH > 4; these data are discussed in Sec. 14.5 below.

Intercalation/deintercalation is possible for small alkali ions *(2265, 2754-7, 3018, 3706)*.

Schematically, this can be described by

$$IrO_2 + xM^+ + xe^- \leftrightarrow M_xIrO_2 \qquad (14.3)$$

with M = Li, Na. Intercalation/deintercalation of F^- has been proposed *(2899)* but was not documented in detailed studies *(2265)*.

Thickness changes during treatment of compact sputter-deposited Ir oxide films in 0.5 M H_2SO_4 have been studied by Hackwood et al. *(1382)* through direct mechanical stylus measurements. Figure 14.5 refers to the thickness evolution upon immersion in the electrolyte. The as-deposited film was rather unaffected by this treatment, whereas when the film had undergone two intercalation/deintercalation cycles its thickness increased from ~78 to ~95 nm during 3 minutes of immersion. This was thought to be caused by hydration. The thickness increment led to a drop of the relative density from an initial ~0.86 to ~0.63. The thickness evolution during cyclic ion intercalation/deintercalation is illustrated in Fig. 14.6. Electrochromic bleaching was associated with a thickness decrement during the initial cycling. This was originally taken as evidence for coloring by OH^- insertion, but recent analyses *(1901)* did not lend credence to such processes in acid electrolytes.

Diffusion constants have been evaluated for Ir oxide films by use of different techniques. For films made by potential cycling in an acid, it was found that D_{H+} lay between 10^{-7} and 10^{-10} cm^2/s *(554-5, 565, 2755)*, which is in the same range as for most W oxide films (cf. Table 6.1). The magnitude of D_{H+} had an apparent dependence on potential scan direction, which indicates that the *electrical conductivity* of the Ir oxide is of decisive importance for the ion intercalation/deintercalation. Thus the (absorbing) IrO_2 is metallic, wheras the (transparent) $HIrO_2$ is a good insulator. Sputter deposited films have D_{H+}s similar to those for anodic layers. Li^+ diffusion has been studied in one work *(2755)*; it appeared that the electronic conductivity did not have any noticeable effect on the ionic diffusion, which may be expected if $D_{Li+} << D_{H+}$.

14.5 Ion Intercalation/deintercalation Studied by Electrochemical Techniques

EMF measurements under ion intercalation have not been reported. One may note, however, that an analysis by Beni and Shay *(340-1, 3119)* indicated that the formula first given by Crandall et al. *(786)*--i.e., Eq. 6.5--is valid provided that one uses a very small value for the parameter b signifying the strength of the interaction between the intercalated ions.

Cyclic voltammograms have been reported many times for Ir oxide films prepared by several different techniques. Figure 14.7 contains an overview of voltammograms taken in 0.5 M H_2SO_4 at a voltage scan rate of 10 mV/s. Specifically, data are given for evaporated Ir-C films oxidized by thermal treatment *(3023)* or plasma treatment *(3016)* (part a), Ir oxide films made by rf sputtering onto substrates under conditions such that porous or compact films were formed *(819, 1744, 3042)* (part b), an evaporated Ir film anodized by potential cycling in H_2SO_4 *(1744)* (part c), and Ir oxide films made by electrodeposition using ac electrolysis *(3749, 3752)* or dc electrolysis *(201)* in sulfatoiridate solutions (part d). Analogous data were also given in *(1267, 1764, 3016, 3544)*. The results in Fig. 14.7(c) are consistent with the many voltammograms taken on anodized bulk iridium (cf. Fig. 14.4); references to this latter work were given in Sec. 14.3 above. It should be noted that ion intercalation/deintercalation in anodic films can take place without noticeable

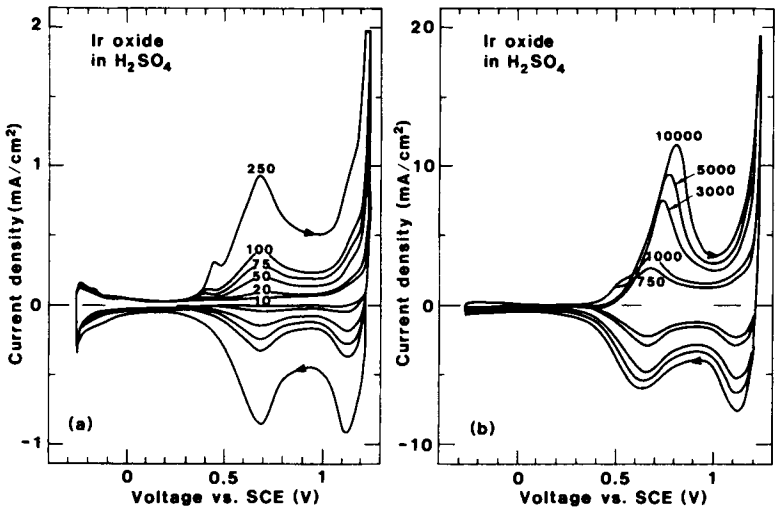

Fig. 14.4 Cyclic voltammograms for an Ir oxide film growing by potential cycling in 0.5 M H_2SO_4. The data pertain to the shown number of cycles; note that the vertical scale differs by a factor of ten between parts (a) and (b). The voltage scan rate was 3 V/s during cycling and 30 mV/s during recording. Arrows denote scan direction. From Hitchman and Ramanathan *(1503a)*.

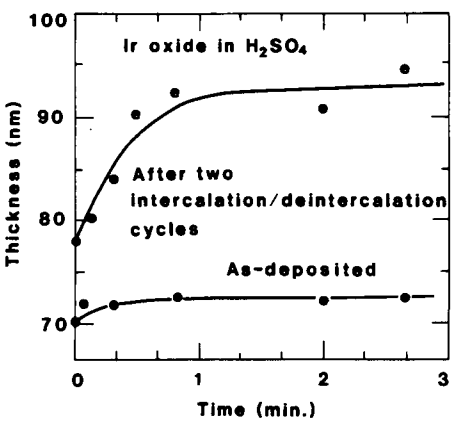

Fig. 14.5 Thickness evolution during immersion of sputter-deposited Ir oxide films in 0.5 M H_2SO_4. Data refer to an as-deposited film and the same film after it had undergone two ion intercalation/deintercalation cycles. Dots indicate measured data, and curves were drawn for convenience. From Hackwood et al. *(1382)*.

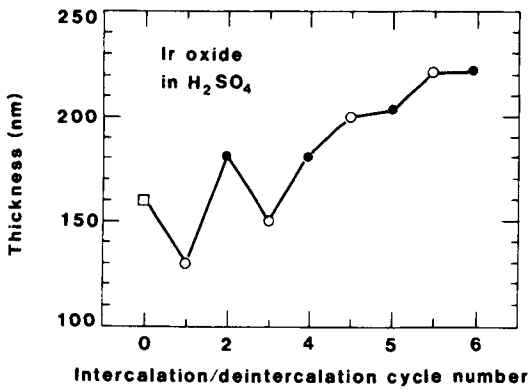

Fig. 14.6 Thickness evolution of a sputter-deposited Ir oxide film during cyclic ion intercalation/deintercalation in 0.5 M H_2SO_4. The initial thickness is denoted by an open square, and colored (bleached) samples are indicated by filled (open) circles. Adjacent data points are joined by straight lines. After Hackwood et al. *(1382)*.

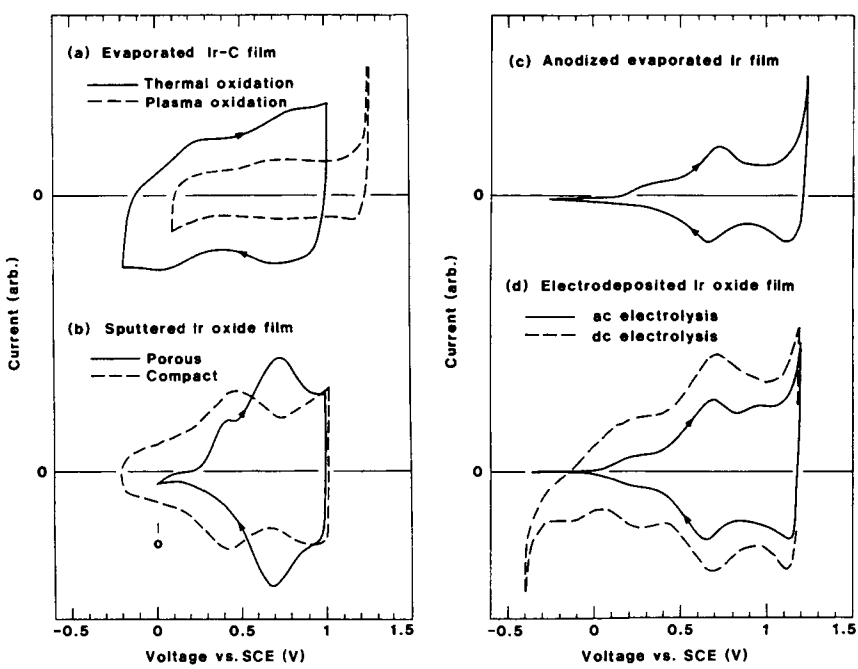

Fig. 14.7 Cyclic voltammograms for ion intercalation/deintercalation of Ir oxide films in 0.5 M H_2SO_4. The films were prepared by various techniques, and the data were compiled from several sources, viz. (a) oxidation of evaporated Ir-C, Sato et al. *(3016, 3023)*; (b) sputter-deposition, Kang and Shay *(1744)*, (c) anodization of an evaporated film, Kang and Shay *(1744)*; and (d) electrodeposition, Baba et al. *(201, 3749, 3752)*. The voltage scan rate was 10 mV/s. Arrows denote scan direction.

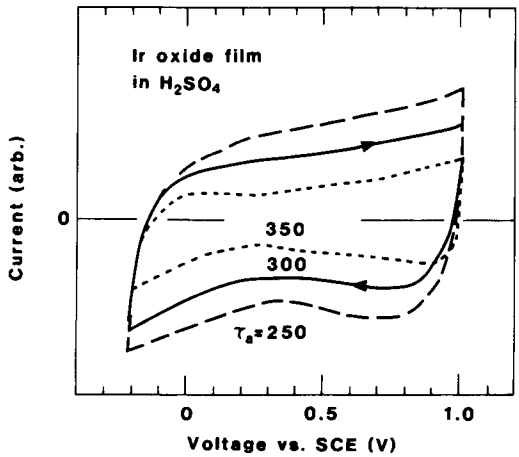

Fig. 14.8 Cyclic voltammograms for Ir oxide films, made by thermal oxidation of an evaporated Ir-C layer, in 0.5 M H_2SO_4. The films were annealed at the shown temperature τ_a. The voltage scan rate was 10 mV/s. Arrows denote scan direction. From Sato et al. *(3023)*.

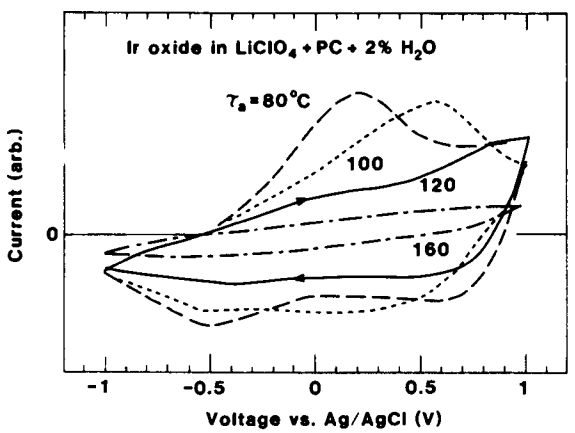

Fig. 14.9 Cyclic voltammograms for Ir oxide films, made by anodic electrodeposition, in an electrolyte of 1 M $LiClO_4$ + PC + 2% H_2O. The films were annealed for 1 h at each of the shown temperatures τ_a. The voltage scan rate was 100 mV/s. Arrows denote scan direction. From Yamanaka *(3706)*.

thickness increments if the voltage scan is limited to about zero to 1.0 V vs. SCE *(1266)*.

Most of the voltammograms in Fig. 14.7 show a consistent pattern, its most salient features being the waves at ~0.7 V vs. SCE both in the cathodic and the anodic scan directions. An interpretation of the features in the voltammograms was provided before in connection with the discussion around the data in Fig. 14.4. With regard to Fig. 14.7, one should notice the "prepeak" at 0.3 to 0.4 V vs. SCE, which is clearly seen in most of the samples; exceptions are for the sputter-deposited compact film and, perhaps, the plasma oxidized Ir-C film. The "prepeak" is believed *(1267)* to be associated with the electrical conductivity, and its occurrence is tied in with the existence of a large range of electrochromic modulation of the optical properties.

Thermally oxidized Ir-C films have been investigated with regard to the evolution of voltammograms under extended potential cycling, for different voltage scan rates and electrolytes, and for differently post-treated films *(3017-9, 3023)*. Figure 14.8, from Sato et al. *(3023)*, shows the effect of annealing a film so that its hydration is diminished and its density is increased. The dashed curve pertaining to $\tau_a = 250°C$ indicates a large intercalation/deintercalation current. These specimens showed pronounced electrochromism. An increase of τ_a diminished the intercalation/deintercalation capability, and electrochromism was gradually lost.

Some work has been reported for Ir-oxide-based films treated in $LiClO_4$ + PC electrolytes containing some water. Evaporated and thermally oxidized films *(3018)* as well as anodically electrodeposited films *(3706)* have been studied. Figure 14.9 shows that heat treatment for 1 h at $\tau_a = 160°C$ almost eliminated the ion intercalation/deintercalation ability. In a separate experiment *(3706)* it was shown that the water addition had a large importance for maintaining the intercalation/deintercalation capability over an extended number of cycles.

Impedance spectroscopy was applied to anodic Ir oxide films by Glarum and Marshall *(1192)*, whose results were further discussed in *(1264)*. The data were consistent with a model embodying a highly porous film with essentially all oxide sites accessible to the electrolyte. The ac conductance per unit area went from less than $10^{-2}\ \Omega^{-1}\ cm^{-2}$ at voltages below 0.4 V vs. SCE up to ~100 $\Omega^{-1}\ cm^{-2}$ at 1 V vs. SCE. A subsequent analysis of similarly prepared samples by Aurian-Blajeni et al. *(178)* was carried out by use of an equivalent circuit somewhat similar to the modified Randles circuit in Fig. 6.21(a) and incorporating a constant phase element. It was concluded that the electron conductivity controlled the charge transfer at low potentials, whereas the charge transfer was presumably due to ion (proton) diffusion at large potentials. Similar inferrences were made by Katsube et al. *(1758)* who applied impedance spectroscopy to sputter-deposited films and interpreted the data in terms of a Randles circuit.

Beam deflectometry, employing the mirage effect, was used recently by Kötz et al. *(1261, 1901)* to study ion intercalation/deintercalation in anodic Ir oxide films immersed in different electrolytes with pH ranging from strongly acidic (pH = 0, using $HClO_4$) to strongly alkaline (pH = 14, using NaOH). The deflectometry was carried out together with cyclic voltammetry. Figure 14.10 shows that the peak structure in the deflectograms and the voltammograms are matching, as was pointed out for W oxide in Sec. 6.7. The slight differences in peak positions can be ascribed to the response time for the deflectometric recording. The cyclic voltammogram for the film in $HClO_4$ is in good agreement with the data in Fig. 14.7(c). The deflectogram indicates a negative beam deflection signal during anodic oxidation (and coloration), which proves that H^+ is exchanged by the film and is expelled during the positive scan thereby increasing the electrolyte concentration at the film surface. A less dominant influence of ClO_4^- exchange can not be excluded. The Ir oxide film shows an entirely different behavior in NaOH. Now anodic oxidation is accompanied by a

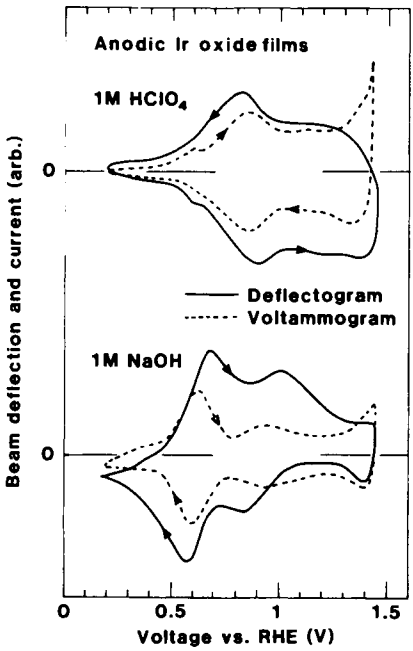

Fig. 14.10 Cyclic deflectograms and voltammograms for ion intercalation/deintercalation in anodic Ir oxide films immersed in the shown electrolytes. The voltage scan rate was 50 mV/s. Arrows denote scan direction. After Kötz et al. *(1901)*.

positive beam deflection, indicating that the electrolyte concentration is decreasing at the film surface as a consequence of hydroxyl ion consumption. Some weaker effect of Na^+ intercalation cannot be ruled out, though. Beam deflection studies with variously buffered electrolytes showed that the shift in the sense of the deflection took place at pH ≈ 4.

Thus the beam deflection experiment essentially resolves the long-standing controversy about the ionic species involved in the intercalation/deintercalation process in a Solomonic way: Both the cation and the anion processes are found to be valid, with H^+ exchange (reaction 14.1) dominating at pH < 4 and OH^- exchange (reaction 14.2) dominating at pH > 4.

Microbalance measurements on anodic Ir oxide films, reported by Masuda et al. *(2213)* and more recently by Birss et al. *(390)*, form a nice complement to the beam deflection data. Thus the microbalance can detect small counterfluxes of heavy ions (and molecules) that go undetected by beam deflection. Birss et al. *(390)* found for a H_2SO_4 electrolyte that the oxidation process in reaction 14.1 could involve an expulsion of 1.5 H^+ and 0.25 SO_4^{2-} and a concurrent incorporation of one water molecule. An exchange of H_3O^+, which is possible as well, may change the results of this analysis; this latter mechanism was favored by Masuda et al. *(2213)*. For a KOH electrolyte, the oxidation process in reaction 14.2 could involve the insertion of OH^- along with some K^+ and an expulsion of one water molecule.

14.6 Ion Intercalation/deintercalation Studied by Physical Techniques

RBS and *NRA* were used by McIntyre et al. *(2264-5)* to obtain depth profiles for ionic species intercalated into Ir oxide films. Figure 14.11 shows results for an anodic film cycled in deuterated 0.5 M D_2SO_4 and subsequently reduced (bleached) at 0.0 and oxidized (colored) at 1.0 V vs. SCE. The bell-shaped NRA spectra in the right-hand part of Fig. 14.11 were distinctly different for the two states; the ratio of the areas for the peaks pertaining to reduced and oxidized conditions was 1.51 ± 0.10. This is in agreement with the cation process in reaction 14.1.

RBS spectra are shown in the left-hand part of Fig. 14.11. The sloping curves corresponding to channels in the range ~185 to ~203 indicate that a continuous gradient in O and D exists over the cross-section of the film, with the outer surface being most deuterated. The RBS data suggest that, in an aqueous electrolyte, H_3O^+ exchange can take place at the film surface, whereas H^+ exchange dominates well below the film surface. The data in Fig. 14.11, taken in an acidic electrolyte, do not lend any support to OH^- exchange, which is the expected result.

McIntyre et al. *(2264-5)* also carried out NRA analyses of films that had undergone potential cycling in aprotic non-aqueous electrolytes such as 1 M $LiAsF_6$ + 2-methyltetrahydrofuran and 0.1 M $NaAsF_6$ + PC. The data showed unambiguously that Li^+ and Na^+ were exchanged in basic agreement with reaction 14.3. Evidence was found for Li^+ replacing H^+ in the films, which appears to be analogous to the ion-exchange processes known to occur in W oxide, discussed in Sec. 7.4. Experiments with elecytrolytes containing K^+ and F^- did not indicate any intercalation of these species.

X-ray extinction, specifically X-ray absorption and EXAFS at the L_I and L_{II} edges of Ir, were used by Hüppauff and Lengeler *(1581)* for *in situ* analyses of anodic Ir oxide films subjected to ion intercalation/deintercalation in a 1 N H_2SO_4 electrolyte. The valence state of Ir could be evaluated by this technique, provided that it was properly calibrated through studies of well-characterized reference samples. The valence changed from an initial value of 3+, consistent

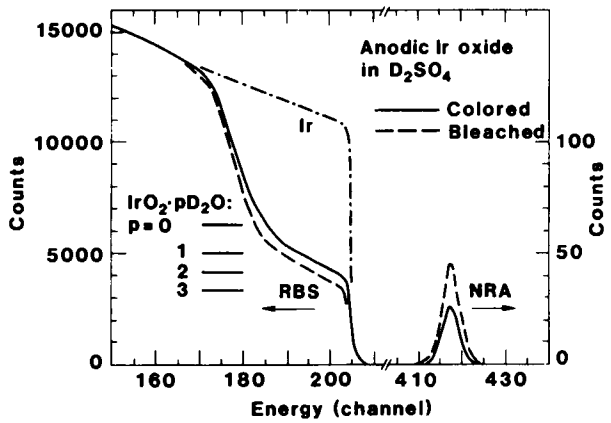

Fig. 14.11 RBS spectra (channels below 210) and NRA spectra (channels above 400) for an anodic Ir oxide film in a $D_2SO_4 + D_2O$ electrolyte. Solid and dashed curves refer to the film being fully oxidized (colored) and reduced (bleached), respectively. The dash-dotted curve indicates a RBS spectrum for an Ir metal surface. The horizontal lines in the left-hand part signify the expected levels in RBS spectra for the shown compositions. The curves were drawn as fits to a large number of individual data points, given in the original publication. Note that different vertical scales are valid for RBS and NRA. After McIntyre et al. *(2264-5)*.

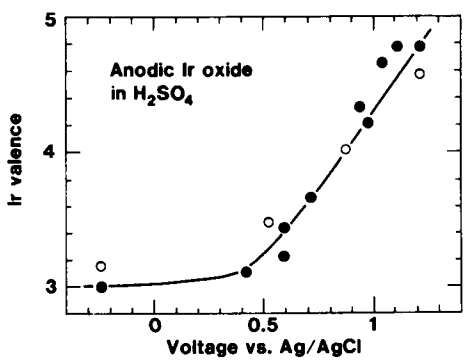

Fig. 14.12 Ir valence vs. voltage for an anodic Ir oxide film in H_2SO_4. Filled (open) circles were obtained from X-ray absorption at the L_{III} (L_I) edges. The curve was drawn for convenience. After Hüppauff and Lengeler *(1581)*

with $Ir(OH)_3$, to a final value of 4.8+ at the oxygen evolution potential. Figure 14.12 illustrates the relation between valence state and applied potential. The valence increase was accompanied by a spread in interatomic distances.

Vibrational spectroscopy, surprisingly, has not been used extensively to probe ion intercalation/deintercalation in Ir oxide films. Only one study appears to be available, by Lezna et al. *(2061)*, wherein electromodulated infrared reflectance was measured for films grown by potential cycling in 0.5 M H_2SO_4. The reflectance difference $\Delta R = R(1.3) - R(0.45)$ was recorded at 11 Hz, where $R(U)$ is the p-polarized reflectance at 45° incidence angle recorded at a voltage U vs. RHE. Figure 14.13 illustrates a deconvoluted spectrum of $\Delta R/R$; it shows an increased absorption in the O-H stretching region for the reduced (bleached) state. Specifically, this absorption comprises a main band at ~3440 cm^{-1}, with a halfwidth of ~320 cm^{-1}, and a less prominent superimposed band at ~3280 cm^{-1}. Only a tentative interpretation of these data is possible. One should note, however, that the formation of hydroxyl groups upon bleaching is consistent with reaction 14.1.

Several *XPS studies of the core level electrons* for anodic Ir oxide films in H_2SO_4 were reported during a short course of time *(177, 1394, 1902, 1905, 2739-40)*. Figure 14.14, from Kötz et al. *(1905)*, shows spectra for *O1s* electrons and for the spin-orbit-split doublet due to $Ir4f_{7/2}$ and $Ir4f_{5/2}$. The data were obtained with the films treated in the electrolyte at three different potentials: 0.0, 0.9, and 1.25 V vs. SCE. The *O1s* peak shifted markedly when the sample went from the bleached state at 0 V vs. SCE to the colored state at 1.25 V vs. SCE. The *Ir4f* electron peaks, on the other hand, were not shifted to a comparable extent. When the relative scattering cross sections for *Ir4f* and *O1s* electrons *(603)* were used to account for the peak heights in the XPS spectra, it became clear that the O/Ir ratio lay constant at 3.0 ± 0.2.

The *O1s* spectra were deconvoluted into contributions due to oxide, hydroxide, and water in the same manner as in Fig. 14.2. It appears from Fig. 14.15, again from Kötz et al. *(1905)*, that the OH contribution is totally dominating in the bleached state, whereas the "pure oxide" contribution dominates in the colored state. Some molecular water was found to reside in the film irrespective of the applied voltage. The XPS data in Figs. 14.14 and 14.15 are clearly fully consistent with the cation mechanism for ion intercalation/deintercalation in reaction 14.1.

It should be remembered that XPS spectra are taken in high vacuum, so that some loosely bound water might have been lost prior to the analyses. Furthermore, the technique is surface sensitive and does not provide information on the chemical constitution well below the film surface. In fact, there is some evidence from work by Augustynski et al. *(177)* that the chemical binding is different for the first oxide monolayers, where the composition may be $Ir(OH)_4$. The same work also indicated that sulphur was present in the films, presumably due to SO_4^{2-} incorporation.

Some core level XPS spectra have also been reported for films made by thermal oxidation of evaporated Ir-C *(3019)*, by dipping a substrate in $IrCl_3$ and then heat-treating it *(177)*, and by direct oxidation of single-crystalline Ir in flowing oxygen at 900 K *(2739)*.

UPS is the most successful method for investigating the band structure at the solid-vacuum interface and is able to give significant information regarding the mechanism for the electrochromism in Ir oxide. The technique has to be used *ex situ* with emersed films. Kötz and Neff *(1904)* carried out a careful and detailed study on Ir films prepared by sputter deposition and subsequent anodization by potential cycling between -0.25 and +1.3 V vs. SCE at 1 Hz in 0.1 M $HClO_4$. Figure 14.16 shows UPS spectra from this work *(1904)*. The upper curve refers to a clean Ir surface. The distinct drop of intensity indicates the location of the Fermi energy. The other

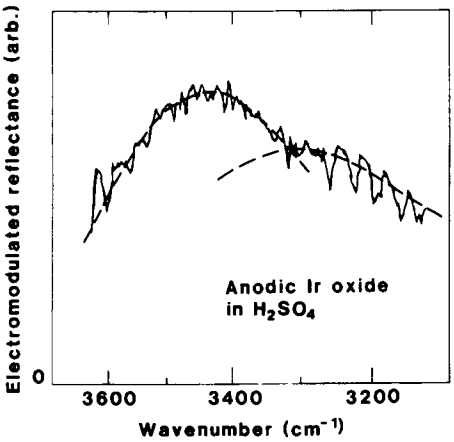

Fig. 14.13 Electromodulated infrared reflectance spectrum for an anodic Ir oxide film in H_2SO_4. The dashed curves represent an approximate deconvolution into two peaks. From Lezna et al. *(2061)*.

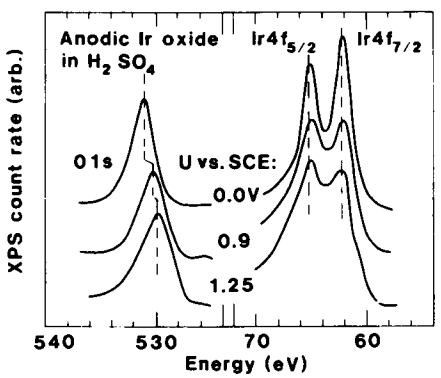

Fig. 14.14 XPS spectra for anodic Ir oxide films exposed to a H_2SO_4 electrolyte at the shown potentials U. The curves were drawn through large sets of individual data points. The vertical dashed lines indicate the positions of the peaks in the spectra. After Kötz et al. *(1905)*.

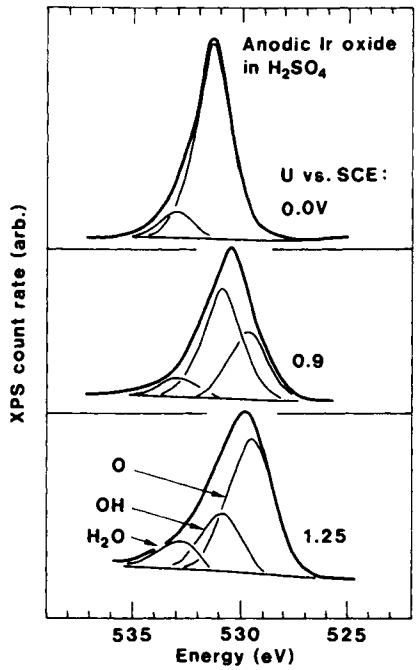

Fig. 14.15 Deconvoluted XPS spectra for anodic Ir oxide films exposed to a H_2SO_4 electrolyte at the shown potentials U. The upper (thick) bell-shaped curves were drawn through large sets of individual data points. The triplets of (thin) bell-shaped curves represent *O1s* electrons bound as oxide, in hydroxyl groups, and in water molecules. Near-horizontal lines indicate backgrounds for the spectra. After Kötz et al. *(1905)*.

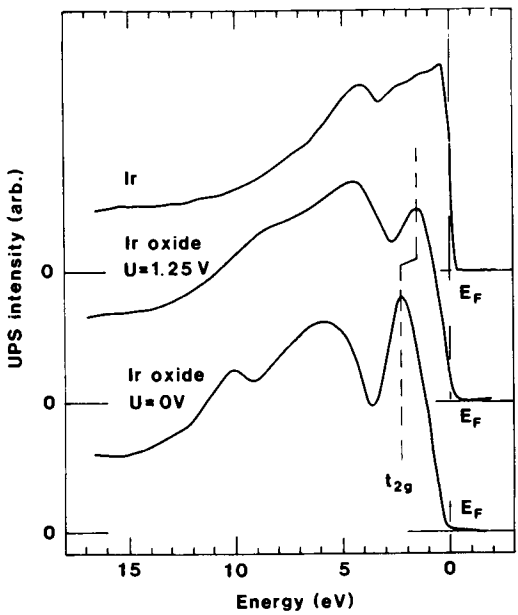

Fig. 14.16 UPS spectra for a pure Ir film and after its oxidation by potential cycling, in a $HClO_4$ electrolyte, stopped at a voltage U vs. SCE. The emersed oxide films were rinsed in pure water before the analysis in order to remove traces of electrolyte which otherwise would influence the spectra. The locations of the Fermi energy E_F and the t_{2g} band of electron states are indicated. After Kötz and Neff *(1904)*.

two curves were measured for oxidized films with the potential stopped at 1.25 V vs. SCE (colored film) and at 0.0 V vs. SCE (bleached film). The UPS signature is seen to be changed by the oxidation, and the density of states at E_F is strongly diminished. Furthermore, a pronounced peak stands out at ~2 eV. This can be assigned to the t_{2g} band of IrO_2 *(808, 2237, 2905, 3607)*, and the broad features from 3 to 12 eV most probably emanate from emission from *O2p* states. Spectra similar to those in Fig. 14.16, though less detailed, were also recorded by XPS *(1905)*.

The lower part of Fig. 14.17 gives an interpretation of the UPS spectra in terms of bandstructure. The solid curve represents the measured density of states (at 0 V vs. SCE) and the histogram represents a computed density of states, specifically obtained from a linear-combination-of-atomic-orbitals interpolation applied to fit results of a nonrelativistic augmented-plane-wave calculation *(2237)*. There is a convincing correlation between the two sets of data. The upper part of Fig. 14.17 shows the locations of the peaks assigned to *O2p* and t_{2g} electrons, as well as of E_F, as a function of voltage. The most salient feature is the shift of the Fermi level: At low voltages (bleached film) E_F lies in the gap between the t_{2g} and the e_g states and the material is insulating, and at high voltages E_F lies well into the tail of the electron density of states so that the material is conducting. It thus appears that bandstructure models can be used to explain the properties of anodic Ir oxide films, as originally suggested by Gottesfeld *(1264)* and by Mozota and Conway *(2424)*. The data are in agreement with with reaction 14.1 with the mobile electrons entering the t_{2g} band.

14.7 Optical Properties

A first observation is that, despite a widespread interest in the optical properties of Ir oxide films, a surprisingly meagre stock of data is available except at a few discrete wavelengths (notably 0.633 μm). For example, no measurement seems to be available for the optical bandgap.

Evaporated Pt-C films, subjected to post-deposition oxidation, have been studied by Sato et al. *(3016-9, 3023, 3029)*. The initial technique used plasma oxidation; the ensuing films had a refractive index of ~1.5 as determined by ellipsometry *(3016)*. Subsequent work employed thermal oxidation. Figure 14.18, from Sato et al. *(3023)*, shows the transmittance at $\lambda = 0.633$ μm for a 0.135-μm-thick film on ITO-coated glass. The voltage was swept between -0.2 and +1.0 V vs. SCE at 10 mV/s with the film immersed in 0.5 M H_2SO_4. The transmittance, relative to the value for an uncoated glass substrate, was found to vary monotonically between a rather transparent state at -0.2 V vs. SCE and a rather non-transparent state at +1.0 V vs. SCE. The electrochromism became less pronounced when the films were annealed for 20 minutes at temperatures above the ideal value of 250°C. Cyclic voltammograms corresponding to the optical data in Fig. 14.18 were shown earlier in Fig. 14.8.

The transmittance in the fully colored and bleached states is further elaborated in Fig. 14.19. A thickness increase yields a significant drop of both of these states, which indicates that some residual absorption remained in the most transparent state. This absorption could be diminished if the films were voltage cycled within a sufficiently wide voltage range so as to promote anodic oxidation. Thus Sato *(3017, 3019)* used triangular sweeps between -0.25 and +1.25 V vs. SCE and found that the transmittance of a bleached 0.09-μm-thick film could be enhanced from ~70% to ~85%, relative to the uncoated glass, after 70 cycles. It was speculated *(3017)* that this effect was due to increased hydration. Some electrochromism has been found also for Ir oxide films in a

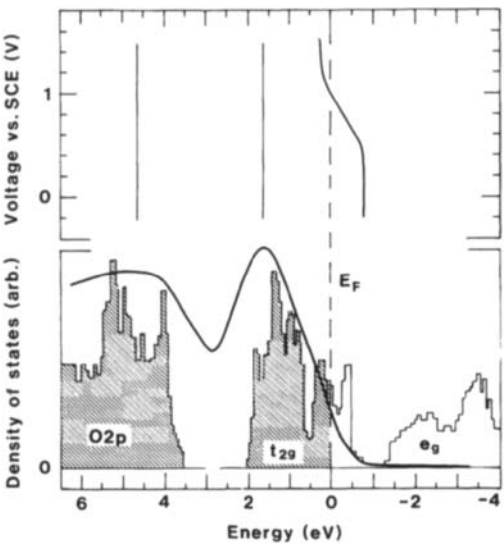

Fig. 14.17 Lower part shows electron density of states as measured (solid curve) by UPS applied to a bleached Ir oxide sample and as computed (histogram) with the various bands assigned to electrons of different character. Filled states, below the Fermi energy E_F, are indicated by shaded areas. Upper part indicates voltage-dependent locations of the peaks in the UPS spectra due to *O2p* and t_{2g} electrons, as well as of E_F. After Kötz and Neff *(1904)*.

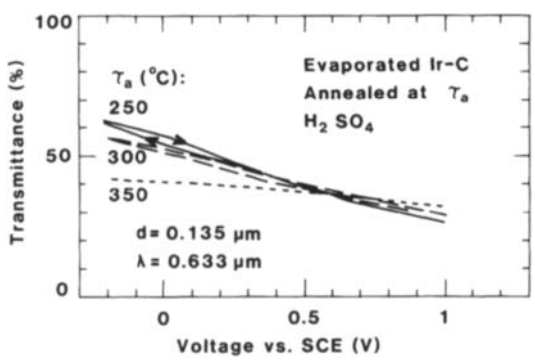

Fig. 14.18 Transmittance vs. voltage for evaporated Ir oxide films treated in H_2SO_4. The samples had been annealed at the shown temperatures τ_a. At the applied voltage sweep rate, 10 mV/s, there was some hysteresis in the transmittance, as indicated by the arrows. From Sato et al. *(3023)*.

$LiClO_4$ + PC electrolyte *(3018)*.

Recently Sato et al. *(3025)* tried to model the spectral reflectance of their films by the Bruggeman effective medium theory, i.e., Eq. 10.33. The composite material was taken to comprise Ir and air. This approach is unjustified, though, and there is ample evidence--as discussed above--that one of the phases is akin to IrO_2 rather than Ir.

Sputter-deposition under different conditions has been used to make Ir oxide films with varying porosity and hydration. Figure 14.20, from Dautremont-Smith et al. *(819, 3042)*, shows the voltage dependent transmittance at $\lambda = 0.633$ μm for a rf sputtered compact ~0.09-μm-thick film cycled in 0.5 M H_2SO_4 at 10 mV/s. The data are directly comparable with those for the evaporated films in Fig. 14.18. At -0.2 V vs. SCE, the sputter-deposited film has practically the same transmittance as the bare ITO-coated substrate, and thus the absorptance was close to zero. At +1.0 V vs. SCE, on the other hand, the transmittance was as low as ~33%. The sputter parameters leading to films with these properties were referred to as "improved", and some absorptance could remain in the bleached state under other conditions. Data similar to those in Fig. 14.20 were reported also by Kanai et al. *(1730)*. A large optical modulation of the transmittance at $\lambda = 0.633$ μm has been shown in *(3041, 3121)* for compact sputter-deposited films.

Dc sputtering onto cooled substrates can give very porous films, as pointed out before. The spectral optical density of a colored porous film is reproduced from Kang and Shay *(1744)* in Fig. 14.21. An absorption band centered at $\lambda \approx 0.6$ μm produced a blue color. In the bleached state, the film was almost non-absorbing at $\lambda > 0.5$ μm. The figure also shows an optical density spectrum for a compact film made by rf sputtering onto a non-cooled substrate and colored to the same charge density as for the porous film. The compact film has an almost spectrally independent absorptance. The latter feature was also found in other work *(1764, 2856, 3741a)*. It can be inferred from Fig. 14.21 that a change in the hydration produces optical modifications. This effect was studied by Hackwood et al. *(1379)*, who found that the transmittance at $\lambda = 0.633$ μm dropped when a film was heated to above 100°C. It was pointed out that this phenomenon might be used for optical writing by use of a laser beam *(454, 1379)*.

Kang and Shay *(1744)* attempted to explain the absorption band at $\lambda \approx 0.6$ μm by considering the porous film to be a composite of IrO_2 and water and using the Maxwell Garnett effective medium theory, i.e., Eq. 10.32. Taking IrO_2 to be a Drude metal, they were able to derive the correct position of the absorption maximum. Nevertheless, the theoretical approach is unsatisfactory because the optical properties of IrO_2 *(1206)* are not Drude-like but have pronounced structure in ε_2 due to both intraband and interband transitions; these features can be understood from the bandstructure *(2237)* sketched in the lower part of Fig. 14.17.

Optical properties of films made by *electrodeposition* have been reported a few times; the samples were made from Ir-sulfate-based *(201, 3706)* or Ir chloride *(3749)* solutions. Figure 14.22 shows spectral optical density for a film made by the latter technique. Coloration and bleaching were performed in 0.5 M H_2SO_4. The conspicuous peak at $\lambda \approx 0.6$ μm, seen earlier in some sputter-deposited samples, is observed once again.

Electrochromism of Ir oxide was discovered in *anodic* films by Buckley and Burke *(506)* who reported in 1975 that reversible transitions took place between a whitish metallic appearance at low potentials and a blue-black color at high potentials if the voltage was cycled slowly. A similar effect was stated somewhat later by Rand et al. *(2837)*. In fact, variable optical data for Ir oxide films were reported in 1974 by Otten and Visscher *(2665-6)* who, however, interpreted their findings as being a consequence of pit formation rather than reversible coloration.

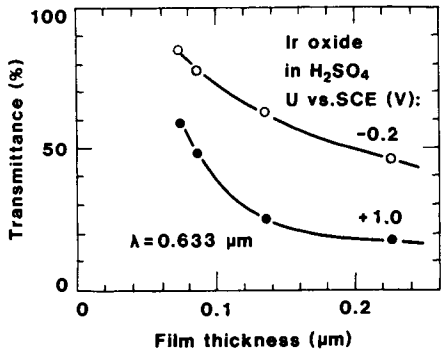

Fig. 14.19 Transmittance vs. film thickness for evaporated Ir oxide films treated in H_2SO_4 at the shown voltages *U*. Circles refer to measured data, and curves were drawn for convenience. After Sato et al. *(3023)*.

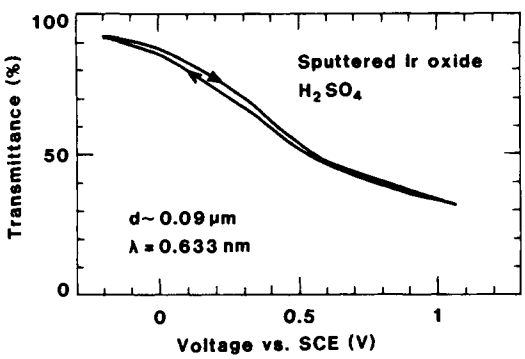

Fig. 14.20 Transmittance vs. voltage for a sputter-deposited Ir oxide film treated in H_2SO_4. At the applied voltage sweep rate, 10 mV/s, there was some hysteresis in the transmittance, as indicated by the arrows. From Dautremont-Smith et al. *(819, 3042)*.

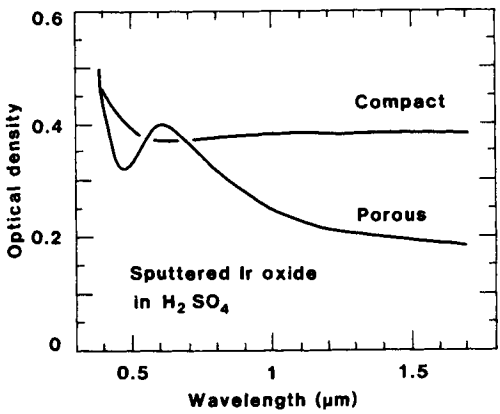

Fig. 14.21 Spectral optical density of porous and compact sputter-deposited Ir oxide films colored in H_2SO_4 to the same charge density. After Kang and Shay *(1744)*.

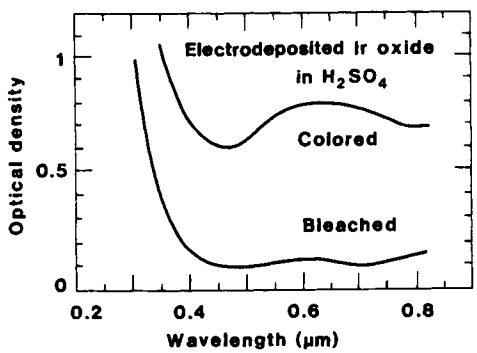

Fig. 14.22 Spectral optical density of an electrodeposited Ir oxide film in H_2SO_4. From Yoshino et al. *(3749)*.

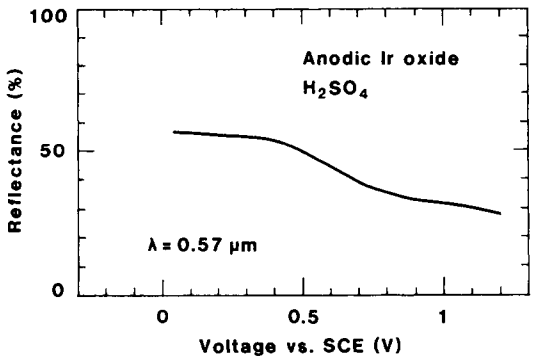

Fig. 14.23 Reflectance of p-polarised light incident at 45° vs. voltage for an anodic Ir oxide surface treated in H_2SO_4. After Kolb *(1884)*.

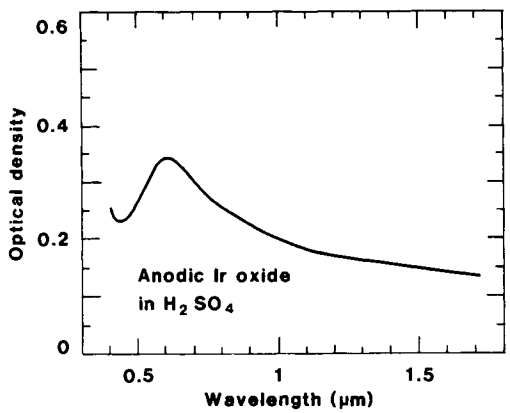

Fig. 14.24 Spectral optical density of an anodic Ir oxide film in H_2SO_4. After Kang and Shay *(1744)*.

Most of the work on anodic Ir oxide has been performed on oxidized bulk samples, so that only reflectance measurements were possible. Reflectance changes during potential sweeps have been studied by Gottesfeld et al. *(1266, 1268)* and Kolb *(1884)*. Figure 14.23, taken from the latter work, shows the reflectance modulation at $\lambda = 0.57$ μm when a voltage is applied to a film in 0.5 M H_2SO_4. The reflectance went from ~58% at 0 V vs. SCE to ~27% at 1.2 V vs. SCE. Transmittance changes during anodization of a 0.04-μm-thick evaporated Ir film were reported in *(3118-9)*.

Spectral optical density was reported by Kang and Shay *(1744)* for an Ir oxide film made by anodization in 0.5 M H_2SO_4. Figure 14.24 gives data for a film colored to the same charge density as for the films reported on in Fig 14.21. The optical properties of the anodic layer are very similar to those for the porous sputter-deposited film, which speaks strongly in favor of a structural kinship among these two types of samples. Kolb *(1884)* reported the presence of a second absorption peak at $\lambda \approx 0.3$ μm.

Optical constants have been measured by Ord *(2836)*, who used ellipsometry at $\lambda = 0.633$ μm and found that n was ~1.46, while k was ~0 or ~0.12 depending on whether the sample was bleached or colored, respectively. Similar values were determined at $\lambda = 0.546$ μm *(1268)*.

Burke and Scannell *(555)* demonstrated that the electrochromism was lost upon UV irradiation. One may speculate that this phenomenon is associated with a decomposition of surface-adsorbed species along with electron insertion, so that *UV bleaching* in the Ir oxide is the counterpart of UV coloration in oxides of W and Mo, which was discussed in some detail before.

14.8 Coloration Efficiency

Coloration efficiency has been determined for Ir oxide films produced by several different techniques. The most detailed work was carried out for sputter-deposited films made under conditions so that a compact structure was to be expected. Kanai et al. *(1730)* investigated coloration efficiency as a function of sputtering parameters. Figure 14.25, reproduced from this work, illustrates CE vs. p_{O2} for a power density of 0.5 W/cm^2 on the target. Corresponding data for the deposition rate were given in Fig. 14.1. It is seen that the CE goes from ~-20 to ~-13 cm^2/C when p_{O2} was increased from 3 to 70 mTorr. Rather similar results were found for other power densities. Analogous, or somewhat less negative, CEs were reported for other sputter-deposited films *(728-9, 732, 819, 1380, 2016, 2854, 3042)*. As pointed out in Sec. 9.7, the CE is taken to be negative to account for the fact that Ir oxide colors anodically. The spectral dependence of the CE is weak *(732, 2854)*, which is consistent with the optical density data for the compact sputter-deposited film reported on in Fig. 14.21.

Anodic Ir oxide films had a CE of ~ −17 cm^2/C at $\lambda = 0.633$ μm *(816, 818-9)*, and a similar value was stated for thermally oxidized Ir-C films *(3017, 3023)* and for some electrodeposited films *(201, 3749)*. One should note, however, that Yamanaka *(3705-6)*, who studied films made by anodic electrodeposition from an $IrCl_4 \cdot H_2O$ solution, reported CEs as being ~ -11, ~ -17, and ~ -33 cm^2/C for the wavelengths 0.4, 0.5, and 0.6 μm, respectively.

The electrochromism of sputter-deposited Ir-Sn oxide has attracted some interest, and CEs for such films were reported by Niwa et al. *(2545)*. Figure 14.26 shows that the relative magnitude of |CE| decreases when the Ir/(Ir+Sn) ratio is diminished. However, the |CE| remains close to the value for Ir oxide as long as the Sn content is lower than ~50%. This indicates that the amount of Ir can

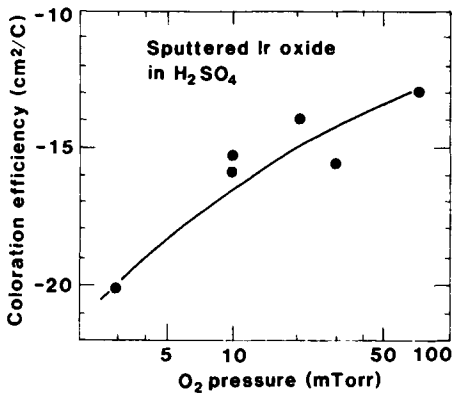

Fig. 14.25 Coloration efficiency as a function of oxygen pressure for Ir oxide films made by reactive rf sputtering. Coloration was performed in H_2SO_4. Dots indicate experimental data, and the curve was drawn for convenience. After Kanai et al. *(1730)*.

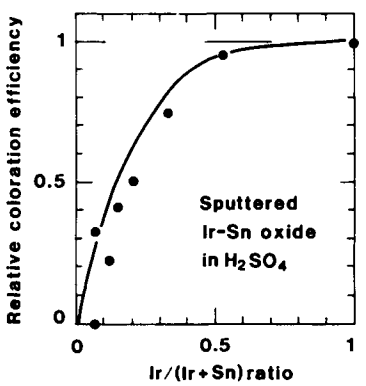

Fig. 14.26 Relative coloration efficiency for films made by reactive rf sputtering from a sintered IrO_2-SnO_2 target. Dots indicate experimental data. The curve was obtained from a theoretical model outlined in the text. From Niwa et al. *(2545)*.

be replaced to a significant amount by a cheaper material without strongly affecting the electrochromism. The curve in Fig. 14.26, which fits the data quite well, was obtained from a model assuming that the absorption can be associated with the number of Ir-Ir pairs having the atoms in nearest-neighbor and next-nearest-neighbor positions. It should be noted that IrO_2 and SnO_2 are structurally very similar, and hence it is likely that the composite oxide is of rutile-type with Ir and Sn atoms randomly positioned on the metal sites in the lattice.

Chapter 15

TITANIUM OXIDE FILMS

The previous chapter on Ir oxide was the first one in a series devoted to rutile-like electrochromic oxides. The present chapter treats Ti oxide. This oxide has *cathodic* electrochromism--just as the oxides of W and Mo--which distinguishes it from Ir oxide with anodic electrochromism. Chapter 23 below will explain this dichotomy from a model founded on electronic bands for the rutile structure. The discussion that follows next covers the same topics as in Ch. 14, viz. the crystal structure of bulk-like Ti oxide (15.1), preparation and characterization of films made by evaporation and sputter-deposition (15.2) and by electrochemical and chemical techniques (15.3), ion intercalation/deintercalation reactions and diffusion constants (15.4), ion intercalation/deintercalation studied by electrochemical (15.5) and physical (15.6) techniques, optical properties (15.7), and coloration efficiency (15.8).

15.1 Crystal Structure of Bulk-like Titanium Oxide

Bulk TiO_2 can have different crystal structures at normal pressure--viz., rutile, anatase, and brookite--and a structure denoted TiO_2(II) can be stable at high pressure *(711)*. Still other polymorphs are known to exist *(252, 1057)*. Whatever the crystal structure, the Ti^{4+} ions are surrounded by six O^{2-} so that the basic building blocks are slightly distorted TiO_6 octahedra.

Electrochromism has been reported for the *anatase* phase. This structure has tetragonal symmetry, and the structure comprises TiO_6 octahedra sharing two adjacent edges with two other octahedra so that infinite planar double chains are formed. These chains share corners with identical chains. Empty sites in the structure also form double chains that can be described similarly to the chains of TiO_6 units. A clear representation of the structure can be found in *(2443)*. The zig-zag rows of vacant sites are large enough to accommodate H^+ and Li^+, whereas other ions may be too large to fit into the crystal lattice *(2600)*. The *rutile* structure was discussed in Sec. 14.1 in connection with Ir oxide. If anatase-type TiO_2 is heated to ~900°C it transforms into the more stable rutile phase. Just before the transformation one can observe an amorphous structure *(3475-6)*.

The Ti oxides may form substoichiometric Magnéli phases of the type Ti_mO_{2m-1} with $4 \leq m \leq 9$ *(104)*. A detailed discussion has been given by Le Page and Strobel *(2047-9)*. Schematically, the Magnéli phases can be represented as rutile-like structures with every m^{th} octahedron at a shear plane. The shear is associated with extended "tunnels" as for W oxide (cf. Sec. 2.1).

Among the many Ti-oxide-based compounds of possible interest, one may note $H_xTi_{2-x/4}O_4 \cdot H_2O$ with layer structure *(3005)*, and $TiOF_2$ with perovskite structure *(1034, 3727-8)*.

15.2 Films Made by Evaporation and Sputter-deposition: Preparation and Characterization

Titanium oxide films have been made by a variety of techniques. Most of these are related to applications of the films as hard coatings or as high-index optical coatings, but some results of relevance to electrochromism are known too. *Evaporation* from resistive sources is possible *(2815, 3150)*, as well as reactive *e*-beam evaporation *(172, 257, 964, 1208, 2667, 3088)*, rf biased ion plating *(1556)*, and evaporation in conjunction with exposure to an oxygen ion beam *(1926, 2343-4)*. *E*-beam evaporation of Ti in $p_{O2} \approx 2.8 \times 10^{-4}$ Torr gave a deposition rate of ~0.3 nm/s (3088). Deposition with $\tau_s < 300°C$ yielded films that were amorphous as probed by XRD or electron diffraction *(1208, 3088)*; TEM images indicated that the grain size was ~1 nm *(3150)*. Annealing of films at $\tau_a > 400°C$ *(1208, 3150)*, or deposition at $\tau_s \approx 400°C$ *(257, 2667)*, led to films with the anatase structure and a grain size of 10 to 30 nm. As-evaporated films can contain a large density of hydrogen, with values of H/Ti in excess of 0.4 found by NRA *(257, 2667)*; the hydrogen content decreased rapidly at $\tau_a > 100°C$.

Sputtering has been used to make Ti-oxide-based films in many studies. Representative work includes rf sputtering of Ti in Ar + O_2 *(370, 725, 1731, 2721-2, 2820, 3584, 3667)*, dc plasmatron or magnetron sputtering of Ti in Ar + O_2 *(2294-7, 2820, 3043-4, 3269, 3623)* or in the same gas with the addition of a chemically reactive component *(2495)*, ion-beam sputtering of Ti in Ar + O_2 *(879)*, and sputtering followed by electron cyclotron resonance plasma oxidation *(8)*. A theoretical model for the formation of Ti oxide films by reactive sputtering was put forward in *(1808)*.

The sputter rate is normally low for Ti oxide films, and the possibility of obtaining high-rate deposition by adding a reactive component to the plasma deserves attention. Figure 15.1, replotted from Nandra *(2495)*, shows that the rate went from ~0.05 nm/s in a sputter plasma of Ar + O_2 to a magnitude that was an order of magnitude larger when Cl_2 or CCl_3F was mixed into the plasma. Substantial rate increases were obtained also for dc sputtering in Ar + O_2 + CCl_4 and for rf sputtering from a TiO_2 target in Ar + O_2 + Cl_2 or Ar + O_2 + CCl_4. The films have an unknown content of Cl and F. One could note that even larger rates were obtained by sputtering of W in O_2 + CF_4 (cf. Fig. 13.7). The anatase phase prevailed for Ti oxide films sputtered in Ar + O_2 at τ_s or τ_a above 350°C, whereas a rutile phase was obtained at higher temperatures *(3269)*. The ranges where the anatase and rutile phases can be found depend also on p_{O2} and on the presence of magnetic fields at the substrate, and possibilities of obtaining rutile structures at low substrate temperatures have been mentioned in some work *(2721, 3044, 3130, 3623, 3667)*. Inclined columnar microstructures were observed in films made by oblique angle sputtering *(3323)*.

15.3 Films Made by Electrochemical and Chemical Techniques: Preparation and Characterization

Anodization is considered first. This technique has been used to produce Ti oxide films under potentiostatic and potentiodynamic conditions in a variety of electrolytes such as H_2SO_4 *(155-6, 228, 900, 940, 1910, 2036, 2216, 2311, 2447, 2586-7, 2651, 3102, 3131)*, HCl *(2587)*, Na_2SO_4 *(183, 888, 3427, 3684)*, NaOH *(228, 2447, 3788)*, KOH *(155-6)*, HNO_3 *(155)*, Na_2CO_3 + $NaHCO_3$ *(985-6, 2651)*, Na_2SO_4 + H_2SO_4 *(2015)*, H_3PO_4 + Na_3PO_4 *(2586-7)*, and

$Na_2HPO_4 + NaH_2PO_4$ *(2588)*. The film thickness increased fairly linearly with applied voltage; the constant of proportionality lay between 2.4 and 2.8 nmV^{-1} for 0.1 M H_2SO_4, 0.1 M HCl, and 0.1 M H_3PO_4 + 0.1 M Na_3PO_4 *(2586-7, 3102)*.

Arsov et al. *(155-6)* carried out a detailed study on the crystallinity of anodic Ti oxide films prepared under a variety of conditions. Up to a certain voltage--for example 80 V in 0.5 M H_2SO_4 --the films were heavily disordered. The anatase phase was found above this voltage, and the rutile phase began to appear above 135 V. Beyond 180 V, the structure was entirely rutile-like. Figure 15.2 shows Raman spectra for three films prepared under different conditions *(156)*. The spectra are very dissimilar and can be assigned to rutile, anatase, and presumably a mixture of rutile + anatase + brookite. Raman spectra for single crystals of rutile *(2795)*, single crystals of anatase *(2581)*, natural brookite *(135)*, and sol-gel-derived bulk titania glass *(2103)* are available in the literature.

Titanium oxide films have been prepared also by other electrochemical and chemical techniques. Among the numerous possibilities one may note CVD using alkoxides *(1968)*, notably $Ti(OC_3H_7)_4$ *(643-8, 1093, 1125)*; atomic layer epitaxy using $TiCl_4$ and water as reactants *(2909-10)*; spray pyrolysis *(1785)*, notably with Ti acetylacetonate *(3678)* or $TiCl_4$ *(3475, 3477, 3800)*; sol-gel deposition using $Ti(OC_4H_9)_4$ *(964, 2453, 2475)*, $Ti(OC_3H_7)_4$ *(1878, 2210, 2679-80, 2682)*, or $Ti(OC_2H_5)_4$ *(1807)*; plasma spraying *(2578)*; and thermal oxidation *(183, 695, 826, 2985, 3174)*. Excepting the latter two, these film preparation techniques are capable of giving anatase-type structures; sol-gel deposition with titanium tetrabutoxide gave disordered films that could then be transformed into the anatase phase by treatment at $\tau_s = 400^oC$ for 2 h *(954)*. CVD using $Ti(OC_3H_7)_4$ was able to yield rutile, anatase, or TiO_2(II) phases depending on the deposition conditions *(643, 648)*.

Porous Ti oxide films were recently produced by Masuda et al. *(2210)*, who employed a two-step replication technique. Anodic porous alumina was employed as a template, and the surface structure was replicated with methyl methacrylate injected into the micropores. After polymerization and dissolution of the alumina, a poly-(methyl methacrylate) negatype was created. A Ti oxide film was then obtained by dipping the negatype in a solution containing Ti isopropoxide and withdrawing the negatype at a constant rate. The polymer was removed in acetone and a highly porous Ti oxide film remained. An analogous procedure was used for other metals as well *(2211-2)*.

15.4 Ion Intercalation/deintercalation Reactions and Diffusion Constants

Titanium oxide can serve as an intercalation host for H^+ and Li^+. The reactions describing the intercalation/deintercalation of ionic species can be represented, schematically, as *(2588)*

$$TiO_2 + xH^+ + xe^- \leftrightarrow TiO_{2-x}(OH)_x \tag{15.1}$$

and

$$TiO_2 + xLi^+ + xe^- \leftrightarrow Li_xTiO_2, \tag{15.2}$$

where TiO_2 is transparent and the hydroxylated or lithiated material is absorbing. There are

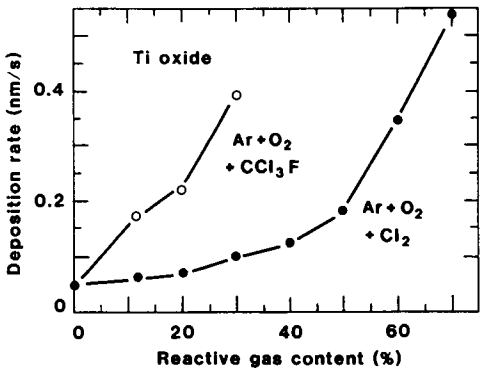

Fig. 15.1 Deposition rate vs. reactive gas content for sputtering of Ti in Ar + O_2 + CCl_3F and Ar + O_2 + Cl_2. After Nandra *(2495)*.

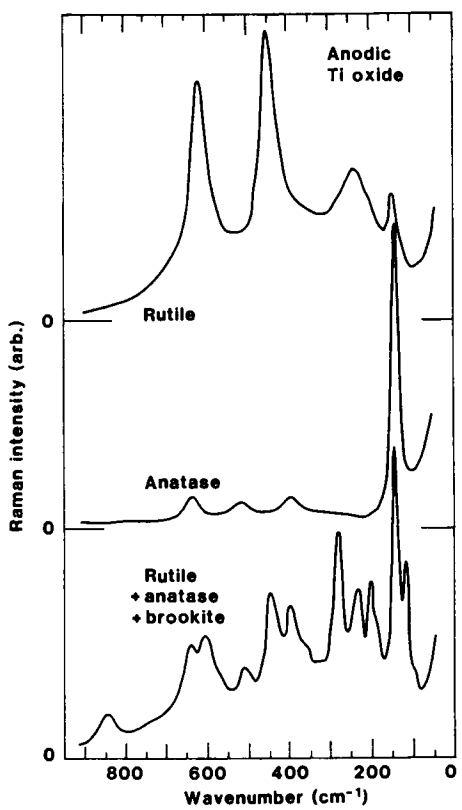

Fig. 15.2 Raman spectra for anodic Ti oxide films. Titanium was oxidized in 0.5 M KOH at 120 V for 300 s to obtain the rutile spectrum, in 0.5 M H_2SO_4 at 120 V for 30 s to obtain the anatase spectrum, and in 1 M KOH at 80 V for 10 s to obtain the rutile + anatase + brookite spectrum. After Arsov et al. *(156)*.

indications *(985, 2588)* that the full $0 < x < 1$ range can be covered, at least for protons.

Lithiation of bulk TiO_2 has been studied several times, but it appears that a consensus has not yet been reached concerning the results. Regarding the anatase phase, reversible Li^+ intercalation/deintercalation has been reported for bulk specimens *(2443, 3622)* and for powders *(441, 2593, 2600, 2602, 2664)*. The intercalation/deintercalation reaction remained stable for at least 88 000 cycles, as found by Ottaviani et al. *(2664)*. The rutile phase, on the other hand, was found to be able to incorporate only 1 to 2 % Li *(2438)*. Quite different results were stated recently by Macklin and Neat *(2150)*, who reported that anatase TiO_2 had poor cycling durability whereas the rutile phase could be converted electrochemically into hexagonal $LiTiO_2$ which then served as a good intercalation/deintercalation host at 120°C; the Li content could be varied in the $0.5 < x < 1.0$ range for Li_xTiO_2.

Kanamura et al. *(1731)* measured the diffusion constant for Li^+ in sputter-deposited Ti oxide films; the anatase phase had $D_{Li+} \approx 4 \times 10^{-13}$ cm²/s, and the rutile phase had $D_{Li+} \approx 1.4 \times 10^{-13}$ cm²/s. For anodic films, Dyer and Leach *(985)* found $D_{H+} \approx 10^{-13}$ cm²/s. These values are much lower than those reported by Ottaviani et al. *(2664)* who stated that anatase powder with a mean grain size of ~40 μm had $D_{Li+} \approx 10^{-10}$ cm²/s. Again there is an obvious lack of consistency.

15.5 Ion Intercalation/deintercalation Studied by Electrochemical Techniques

Cyclic voltammograms have been reported for Ti oxide samples prepared by several different techniques. Figure 15.3 shows results from Ottaviani et al. *(2664)* for anatase powder layers in a $LiClO_4$ + PC electrolyte. The voltammograms have different shapes depending on the voltage sweep rate, which is a manifestation of the limited diffusion constant for Li^+. Curves similar to those for 40 and 1 mV/s have been measured at comparable rates for sol-gel films produced from $Ti(OC_4H_9)_4$ *(954, 2475)*. Voltammograms have also been reported for films made by reactive *e*-beam evaporation *(3088)*, sputtering *(3584)*, anodization *(888)*, and thermal oxidation *(695)*. Beam deflection measurements for films in a H_2SO_4 electrolyte were reported in *(2968)*.

15.6 Ion Intercalation/deintercalation Studied by Physical Techniques

EPR is a powerful technique for distinguishing between metal ions with different valence states. It was employed by Doeuff and Sanchez *(954)* to analyze sol-gel-produced films in electrolytes of $LiClO_4$ + PC. Li^+ intercalation was accompanied with the occurrence of an EPR signal at $g \approx 1.93$. This signal is consistent with Ti^{3+} ions in a field with a distorted octahedral symmetry, i.e., with electron localization on metal ions just as in W oxide. Noda et al. *(2546)* studied anatase Ti oxide powder and found an EPR signal with $g \approx 1.98$ under irradiation with light. To put the above *g*-values in perspective, one can note that 1.96, 1.97, and 1.98 have been reported for, respectively, reduced rutile *(1651)*, anatase *(1650)*, and porous titania glass *(1176)*.

XPS was recently applied by Özer *(2679)* to films prepared by sol-gel technology using Ti isopropoxide solutions. Photoelectron spectra due to *Ti2p* electrons were recorded in the 457 to 462 eV range. Li^+ intercalated and deintercalated films had XPS spectra peaked at 495.5 and 460.2 eV, respectively. XPS data for oxygen-depleted TiO_2 were reported in *(3006)*.

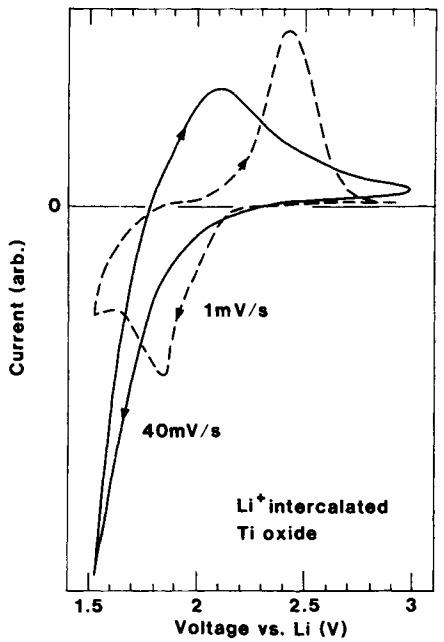

Fig. 15.3 Cyclic voltammograms for Li^+ intercalation/deintercalation in anatase Ti oxide powder in $LiClO_4$ + PC. Data are given for two different voltage scan rates. Arrows denote scan direction. After Ottaviani et al. *(2664)*.

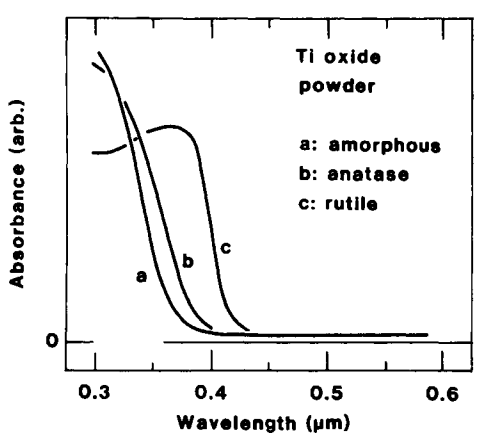

Fig. 15.4 Spectral absorbance of Ti oxide powders with different crystal structures. From Noda et al. *(2546)*.

15.7 Optical Properties

Optical properties around the semiconductor bandgap are considered first. Figure 15.4, from Noda et al. *(2546)*, shows spectral absorbance for TiO_2 powder with "amorphous", anatase, and rutile structure. The "amorphous" structure has a bandgap that is slightly wider than that of the anatase phase, whereas the rutile structure has a significantly narrower bandgap. The data in Fig. 15.4 may indicate that the "amorphous" Ti oxide can be viewed as a fine-grained anatase phase. The bandgap is basically consistent with results from recent bandstructure calculations *(1195-6, 1395, 2709, 2798)*.

The bandgap can be evaluated from Eq. 8.3 with $\eta = 2$ as for W oxide. Figure 15.5, pertaining to an *e*-beam evaporated film, shows an evaluation by Gofuku et al. *(1208)*. The energy dependence of $(a\hbar\omega)^{1/2}$ is linear except at the lowest energies, and a bandgap of 3.4 eV is readily extrapolated. Similar E_gs were found for other films made by ion assisted evaporation *(1926)*, sputter-deposition *(2820, 3130)*, anodization *(1910, 2036, 2311)*, CVD *(1125, 3676)*, and sol-gel technology *(2679)*.

Films made under sufficiently oxidizing conditions are almost non-absorbing. Figure 15.6 shows the spectral refractive index for films prepared by Bange et al. *(257)* through the use of three different techniques. The refractive indices are different, but the films have a comparable dispersion.

The refractive index can be varied by annealing post-treatment. Figure 15.7, from Suhail et al. *(3269)*, shows that the refractive index for reactively dc magnetron sputtered films was increased substantially as the films were kept for 1/2 h at successively higher temperatures up to 400°C. At the highest temperatures, the extinction coefficient began to increase, which may be caused by oxygen desorption *(2820)*.

The differences in refractive indices, observed for films made by various techniques, can be rationalized in terms of different hydrogen contents. Thus Ottermann et al. *(2667)* used NRA to study the relation between n at 0.55 μm and the H/Ti atom ratio. Figure 15.8, taken from this work, shows that n is strongly correlated with the hydrogen content, and the refractive index of bulk anatase TiO_2 is obtained in the limit of a small amount of hydrogen. Data roughly consistent with those in Fig. 15.8 were reported elsewhere for films made by reactive evaporation *(172)*, ion-beam sputtering *(879)*, anodization *(2311)*, CVD *(1125, 3676)*, and sol-gel technology *(2679)*.

Ion intercalation into Ti oxide produces coloration, i.e., the material is electrochromic. This effect was observed for bulk anatase TiO_2 in contact with butyl lithium *(3622)*. A significant amount of work has been done on anatase powder layers. The initial study, reported in 1974, was by Inoue et al. *(1614)* who investigated Ti oxide powders in a resin binder interfaced between two glass substrates with transparent conducting layers. By applying a dc voltage larger than 20 V, it was possible to switch the samples between a white and a dark blue or black state. Anatase powders in a $LiClO_4$ + PC electrolyte were studied more recently by Ohtsuku et al. *(2593, 2600)* and Ottaviani et al. *(2664)*. Li^+ intercalation caused strong absorption. Coloration under UV irradiation of rutile TiO_2 particles was reported by Highfield and Grätzel *(1484)* who made their measurements with a photoacoustic technique.

Effects of proton insertion--or possibly hydroxyl ion extraction--have been studied for Ti oxide films produced by anodization in various electrolytes. Figure 15.9, from Ohtsuka et al. *(2588)*, refers to samples in a 0.1 M H_2SO_4 electrolyte buffered by Na_2HPO_4 + NaH_2PO_4 to pH ≈ 7. Optical constants were measured by ellipsometry at $\lambda = 0.546$ μm. Applying a voltage, so

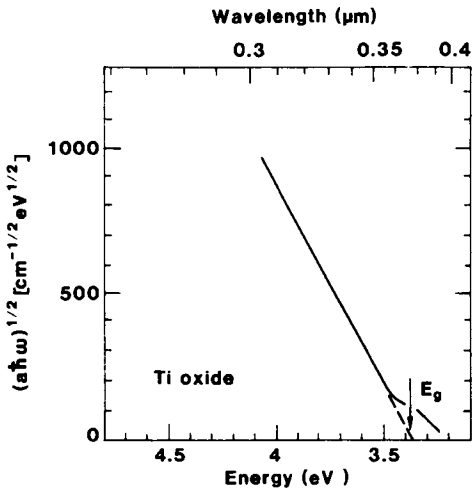

Fig. 15.5 $(\alpha\hbar\omega)^{1/2}$ vs. energy for an evaporated Ti oxide film. Dashed line indicates an extrapolation for determining the bandgap E_g. A similar plot was given in Fig. 8.2 for W oxide. After Gofuku et al. *(1208).*

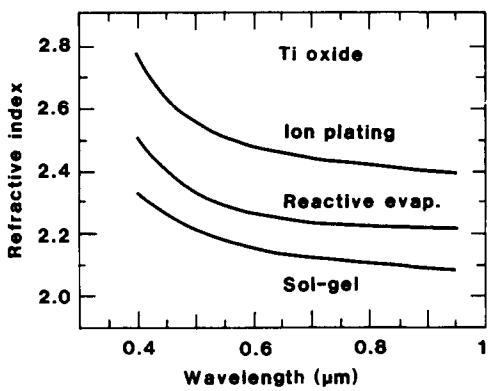

Fig. 15.6 Spectral refractive index for Ti oxide films made by three techniques. From Bange et al. *(257).*

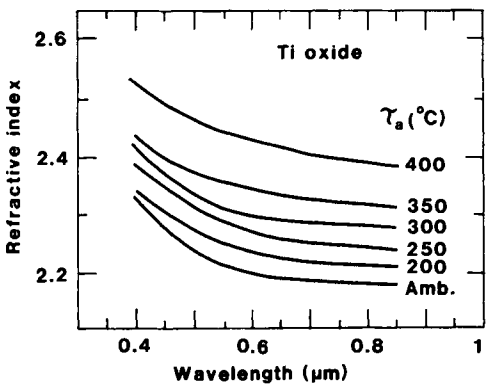

Fig. 15.7 Spectral refractive index for Ti oxide films made by sputtering onto substrates kept at ambient temperature and after annealing post-treatment for 1/2 h at each of the temperatures τ_a. After Suhail et al. *(3269)*.

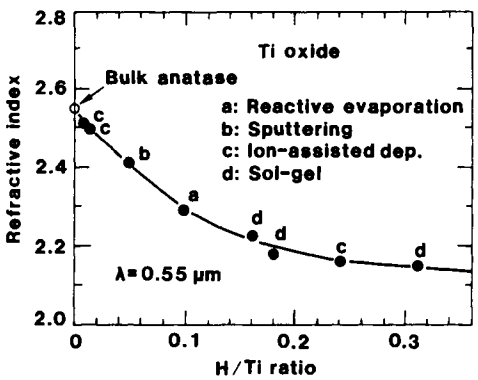

Fig. 15.8 Refractive index at $\lambda = 0.55$ μm versus H/Ti atom ratio for Ti oxide films made by various techniques. Different deposition parameters were used for some of the techniques in order to prepare films with different porosities and hydrogen contents. Circles denote experimental data, and the curve was drawn for convenience. After Ottermann et al. *(2667)*.

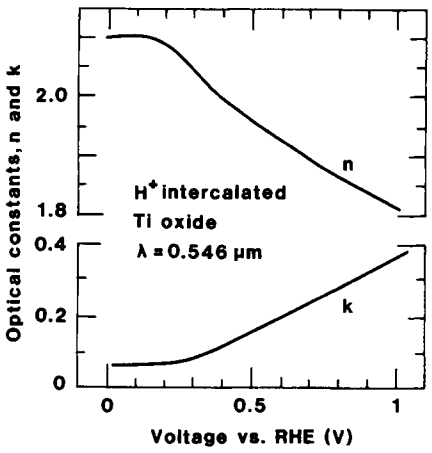

Fig. 15.9 Optical constants at $\lambda = 0.546$ μm for anodic Ti oxide films intercalated with H^+ by the application of a voltage. The curves were drawn through a number of individual data points pertaining to two different film thicknesses. After Ohtsuka et al. *(2588)*.

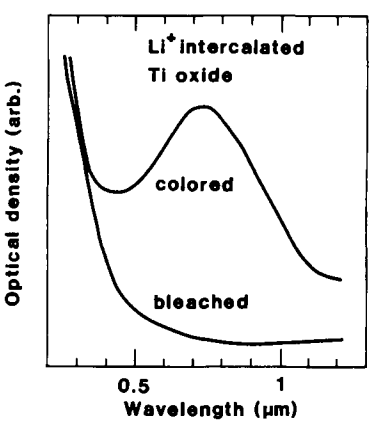

Fig. 15.10 Spectral optical density for a sol-gel-produced Ti oxide film in bleached state and after coloration by Li^+ intercalation. From Doeuff and Sanchez *(954)*.

that H^+ was inserted, made k increase from a low value and n decrease from an initial magnitude of ~2.1. At a voltage of ~1 V vs. RHE, corresponding to the film being close to TiOOH, one finds $k \approx 0.35$ and $n \approx 1.8$. The maximum value of the extinction coefficient is remarkably high and, apparently, exceeds that of W oxide at a comparable wavelength. Other ellipsometric measurements on anodic films in different electrolytes yielded extinction coefficients up to ~0.1 for ion intercalated specimens *(888, 985, 2015, 2216, 2651)*. Coloring under H^+ insertion has been observed for bulk titania glasses prepared by the sol-gel route *(1176, 2388)*.

Electrochromic coloring under Li^+ intercalation has been studied for films made by reactive *e*-beam evaporation *(3088)* and by sol-gel deposition *(954, 2679, 2682)*. Figure 15.10 shows results from Doeuff and Sanchez *(954)* for a film made by the latter technique; the film was colored in a 1 M $LiClO_4$ + PC electrolyte. The coloration, reportedly to a gray state, is associated with an absorption band centered at $\lambda \approx 0.75$ μm. The color properties could be changed by the addition of some Cr^{3+} or Al^{3+} from suitable sol-gel solutions *(953)*. Sol-gel films tended to loose their electrochromism after heat treatment at 300°C *(2679)*.

The peak in optical density seen in Fig. 15.10 points at polarons being the cause of the absorption. This assignment is in line with work by Bogolomov et al. *(415)* and Rüscher et al. *(2960)* who studied the crystalline Magnéli phases Ti_mO_{2m-1}, with m being 4 and 6, and analyzed absorption bands centered at ~1 eV. UV colored TiO_2 particles showed a broad absorption maximum at ~1 eV; it was tentatively ascribed to polarons *(1484)*.

15.8 Coloration Efficiency

Coloration efficiencies have been stated for some films made by reactive evaporation of Ti *(3088)* and reactive sputtering of Ti *(725)*. Their magnitudes were reported to be lower than 5 cm^2/C. This appears to be inconsistent with the strong electrochromic absorption for anodic and sol-gel-prepared films, as reported above, and it is likely that if the vapor-deposited films had been made under other conditions, their CEs would have been much larger. The latter contention is strongly corroborated by results by Gillet et al. *(1184-5)*, who found that when films were made by evaporation of $H_2Ti_3O_7$ the CE at $\lambda = 0.633$ μm was as large as 33 cm^2/C upon coloration in H_2SO_4 and 14 cm^2/C upon coloration in $LiClO_4$ + PC. Furthermore, recent work by Gutarra et al. *(1361a)* showed that Ti oxyfluoride films had large CEs.

This Page Intentionally Left Blank

Chapter 16

MANGANESE OXIDE FILMS

Manganese oxide is another rutile-type material and is in this respect akin to the Ir oxide of Ch. 14 and Ti oxide of Ch. 15. Managnese oxide has been used for a long time in electrical battery technology *(3072)*, but many questions remain unanswered despite a very large amount of work. One reason for this state of affairs is to be found in the crystal chemistry of Mn oxide, which shows a bewildering complexity. Structural aspects of bulk-like materials are discussed below (16.1). Then follow brief discussions of the preparation and characterization of thin films (16.2), ion intercalation/deintercalation reactions and diffusion constants (16.3), ion intercalation/deintercalation studied by electrochemical and physical techniques (16.4), and optical properties (16.5).

16.1 Crystal Structure of Bulk-like Manganese Oxide

Manganese oxide can have many different crystal structures. For example, there are about twenty oxides containing Mn^{4+} among the natural minerals. Many of these have been prepared synthetically as well. Following common practice, the minerals are referred to by name and the synthetic crystals by Greek letters.

The basic building blocks of most Mn oxides are MnO_6 octahedra that are linked by edges to form single or double chains. These chains in turn share corners with other chains, so that tunnels are formed. The sizes of these tunnels, given by the number of Mn-O chains on each side, are 1x1 in pyrolusite with rutile structure (also known as β-MnO_2), 2x1 in ramsdellite, and 1x1 as well as 2x2 in hollandite (α-MnO_2). An intergrowth structure between the pyrolusite and ramsdellite phases, known as nsutite or γ-MnO_2 *(1205, 3378)*, has attracted much interest for rechargeable Li batteries. Spinel-type oxide, denoted λ-MnO_2, can be obtained by complete delithiation of $LiMn_2O_4$ *(1580, 1746-7)*. A layered hydrate is referred to as δ-MnO_2.

Among the hydrated and hydroxylated oxides, which are of interest for electrochromism, one notes birnessite ($MnO_{1.84} \cdot 0.6H_2O$) with a layer structure *(214, 229, 3263)*, manganite and groutite (MnOOH), and brucite ($Mn(OH)_2$). The manganite and groutite phases are structurally closely related to pyrolusite and ramsdellite, respectively *(2907)*.

Lithiated Mn oxide is of much interest in contemporary battery technology *(3397)*, and considerable work has been carried out for spinel-type $LiMn_2O_4$ *(265, 1062, 1364, 2064-5, 2106, 2151, 2173, 2383, 2635, 3126, 3164-5, 3365, 3367, 3396, 3675)*. Other recently studied materials are α-MnO_2 *(2943)*, Li_2MnO_3 with NaCl-type structure *(2906)*, Li_xMnO_2 with ramsdellite-type structure *(2942, 3398)*, $LiCr_yMn_{2-y}O_{4.35}$ with spinel structure *(2774)*, and composites of MnO_2 and Li_2MnO_3 *(2548)*.

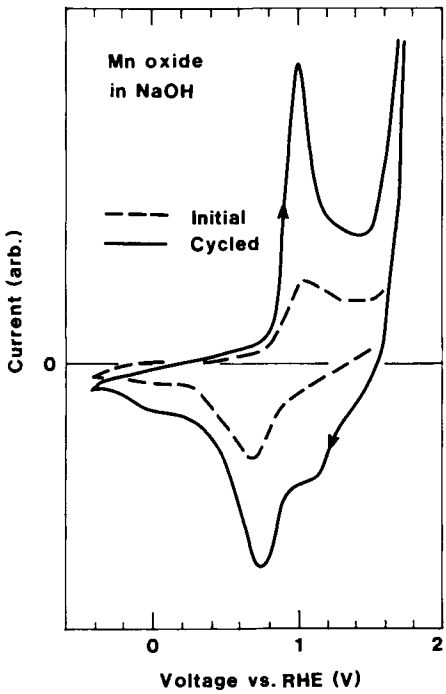

Fig. 16.1 Cyclic voltammograms for a Mn surface in initial state and after 500 voltage cycles in 1 M NaOH at 43 mV/s. Arrows denote scan direction. After Burke and Murphy *(540)*.

16.2 Preparation and Characterization of Thin Films

Thin films of Mn oxide have been made by numerous methods. A well known standard technique is *electrodeposition* from an aqueous solution of ~0.5 M $MnSO_4$ and 0.5 M H_2SO_4 at 2 mA/cm^2 and ~90°C *(2524)*; it was used in several studies related to ion intercalation and electrochromism *(758-9, 881-2, 1970, 2026, 2654, 3195, 3384, 3753)*. The relative density of the films can be as low as ~0.3 *(3226)*. Electrodeposition from other solutions has been used as well to make films of Mn oxide *(1004, 1139)* and Mn-Ni oxide *(2127)*. XPS demonstrated that electrodeposited films contain hydrogen *(1139)*.

Potential cycling in an electrolyte of 1 M NaOH was used by Burke and Murphy *(540)* to build up oxide layers. The thickness increased with the number of cycles up to more than 10^4 cycles. The film growth was followed by voltammetry, and Fig. 16.1 shows the performance during the initial sweep between -0.4 and +1.75 V vs. RHE and after 500 cycles between the same limits. Pronounced peaks were observed at ~1 V vs. RHE during the anodic sweep and at ~0.7 V vs. RHE during the cathodic sweep.

Among the many other possible film preparation techniques, one could note evaporation *(759)*, sputter-deposition *(2583, 3502)*, chemical precipitation by alternate immersions in $MnSO_4$ and in NaOH or KOH *(756)*, sol-gel technology used to prepare birnessite Mn oxide *(212, 214-5, 2731)* and spinel-type $LiMn_2O_4$ *(265)*, and *e*-beam evaporation used to prepare $LiMn_2O_4$ *(3164-5)*.

16.3 Ion Intercalation/deintercalation Reactions and Diffusion Constants

The propensity for Mn oxide to form large tunnels makes it a suitable host for ion intercalation/deintercalation. The reactions for H^+ and Li^+ may be written

$$MnO_2 + xH^+ + xe^- \leftrightarrow MnO_{2-x}(OH)_x \tag{16.1}$$

and

$$MnO_2 + xLi^+ + xe^- \leftrightarrow Li_xMnO_2. \tag{16.2}$$

MnO_2 shows strong optical absorption whereas the hydroxylated material is considerably less absorbing, i.e., the material is electrochromic.

Li^+ intercalation/deintercalation in Mn oxide has been studied intensely for battery applications *(215, 1062, 1364, 1800, 2064-5, 2596-9, 2944, 3196, 3365, 3367)*. It is hence clear that there is a large body of knowledge on lithiated Mn oxide that is ready to be exploited in the field of optics.

Electrochemical characterization of Mn-oxide-based films has been carried out by numerous techniques, in most cases with battery applications in mind. Sol-gel-prepared birnessite films were studied by Bach et al. *(214)*, who found that D_{Li+} varied from ~2×10^{-9} cm^2/s when the Li content was a few percent to ~2×10^{-11} cm^2/s at ~50 % Li. Composition-dependent diffusion constants are shown in Fig. 16.2. Consistent data were given by Pereira-Ramos et al. *(2731)*. Bulk-type birnessite has a diffusion constant that is much lower than the one for the thin film. A bulk Li_xMnO_2 material made by synthesis of MnO_2 and $LiNO_3$ had D_{Li+}s between 10^{-8} and 2×10^{-9}

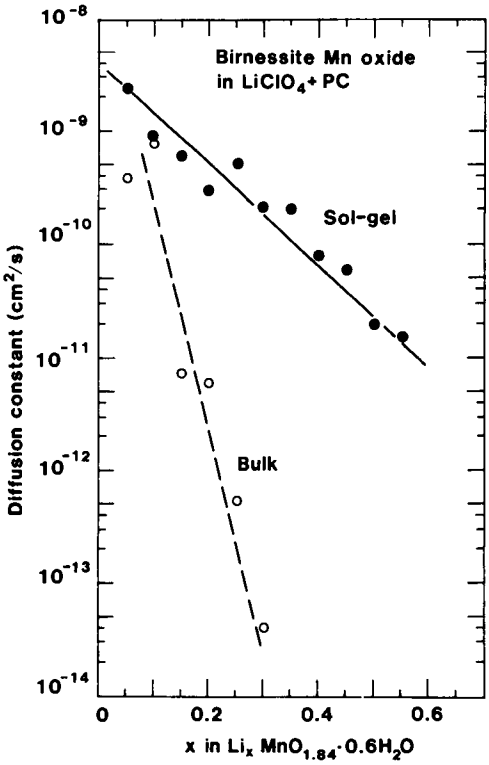

Fig. 16.2 Diffusion constant for Li^+ in layered birnessite Mn oxide as a sol-gel-prepared film and as a bulk material. The lithium content is given as x in $Li_xMnO_{1.84} \cdot 0.6H_2O$. After Bach et al. *(214)*.

cm^2/s *(2065)*. For sodium insertion, a value of $D_{Na+} \approx 5x10^{-14}$ cm^2/s was given *(3550)*. Thin films with a nominal MnO composition had D_{Li+}s in the range of 10^{-14} to 10^{-15} cm^2/s *(673)*.

16.4 Ion Intercalation/deintercalation Studied by Electrochemical and Physical Techniques

Cyclic voltammograms were reported by Cordoba-Torresi and Gorenstein *(758-9)* and De Mishima et al. *(881-2)* for evaporated and electrodeposited films in aqueous 0.1 M $Na_2B_2O_7$ electrolytes at pH = 9.2. Curves similar to those in Fig. 16.1 were reported. Cyclic voltammograms have also been given for evaporated films in $LiClO_4$ + γ-butyrolactone *(3088)*, electrodeposited films in NaOH *(1139, 3753)*, chemically deposited films in NaOH *(756)*, and sol-gel-prepared films in $LiClO_4$ + PC *(214)*.

De Mishima et al. *(881-2)* reported on the physical characterization of ion intercalated Mn oxide films. Raman spectra indicated reversible changes under H^+ (or OH^-) intercalation/deintercalation in an aqueous borate electrolyte, but the data were not interpreted in terms of specific vibration modes *(882)*. IR spectra were given in *(2594)*. Core level XPS data on similar samples gave clear evidence for changes in both the $Mn2p_{3/2}$ and *O1s* peaks under ion insertion. The latter feature was most readily interpreted, and Fig. 16.3, replotted from De Mishima et al. *(881)*, shows that a decomposition can be made into contributions due to O, OH, and H_2O; this is in good agreement with the results for Ir oxide in Figs. 14.2 and 14.15. Similar data were obtained for Mn oxide catalysts *(3782)*. It seems that the Mn oxide can be changed between a state in which the material is dominated by "pure oxygen" bonding and another state in which the "pure oxygen" and hydroxyl ion signals are of comparable magnitude. This is consistent with reaction 16.1 for proton intercalation/deintercalation. One could note, however, that some IR absorption spectra for hydrogen-containing Mn oxide did not show evidence for hydroxyl groups *(1722)*. EPR appears to be a useful technique for investigating Mn oxide; it was applied recently to battery materials *(88)*.

16.5 Optical Properties

Optical bandgaps can be inferred from measurements by Lee et al. *(2026)* on electrodeposited films. It appears that E_g is at ~0.4 and ~0.6 μm for the β and γ phases, respectively. Thus only the β–MnO_2 structure is capable of high luminous transmittance.

Electrochromism, specifically a loss of absorptance under charge insertion, was first observed by Lee et al. *(2026)* who studied Mn oxide films in both acidic and alkaline electrolytes. Subsequently this effect was also found in other work on reactively evaporated *(759, 3088)* and electrodeposited films *(758-9, 881-2, 3753)*, in anodized layers *(540)*, and in some layers made by an unspecified method *(675)*. Figure 16.4, from Cordoba-Torresi and Gorenstein *(758-9)*, shows spectral optical density of an electrodeposited film in an aqueous 0.1 M $Na_2B_2O_7$ electrolyte with pH = 9.2. By varying the voltage between 0 and 0.8 V vs. SCE, the absorption was altered by roughly a factor two irrespective of wavelength between 0.35 and 0.8 μm. Yoshino et al. *(3753)* scanned the voltage between -0.8 and +0.8 V vs. SCE and were able to achieve bleaching to an almost colorless state. They reported a cycling durability up to 10^4 times at potential sweeps

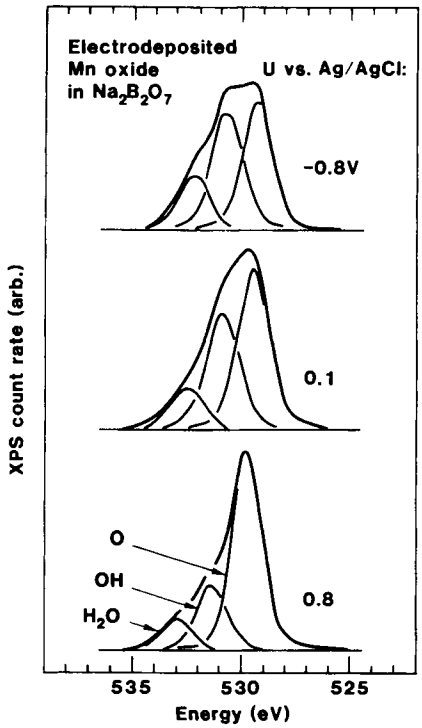

Fig. 16.3 Deconvoluted XPS spectra for electrodeposited Mn oxide films treated in an aqueous $Na_2B_2O_7$ electrolyte at the shown potentials U. The upper (thick) curves are envelopes, and the triplets of (thin) bell-shaped curves represent *O1s* electrons bound as oxide, in hydroxyl groups, and in water molecules. After De Mishima et al. *(881)*.

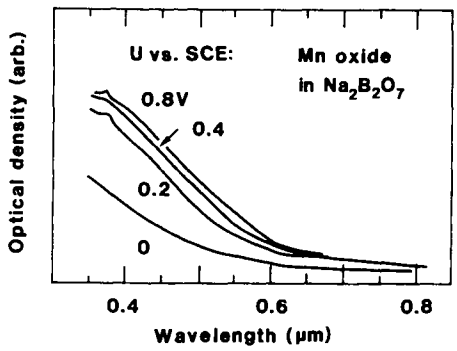

Fig. 16.4 Spectral optical density for an electrodeposited Mn film treated in an aqueous $Na_2B_2O_7$ electrolyte at the shown potentials *U*. From Cordoba-Torresi and Gorenstein *(758-9)*.

between -0.5 and +0.5 V vs. SCE. In contrast with the observations mentioned above, some other electrodeposited films were reported not to display significant electrochromism *(1139)*.

The coloration efficiency was found to be about -7 cm^2/C at $\lambda = 0.633$ μm for reactively evaporated films in $LiClO_4$ + γ-butyrolactone *(3088)*. This is in rough agreement with observations on electrodeposited films in borate electrolytes within the voltage range covered in Fig. 16.4 *(758-9)*.

The physical basis for the absorption has not been investigated. One could note, however, that the absorption in manganosite (MnO_{1+z} with $z < 0.001$) has been ascribed to small polarons *(306)*.

This Page Intentionally Left Blank

Chapter 17

VANADIUM DIOXIDE FILMS

Vanadium oxides can be classified in the five homologous series V_mO, V_mO_{m-1}, V_mO_{m+1}, V_mO_{2m-1}, and V_mO_{2m+1} with m = 1, 2, 3, ... *(3524)*. The present chapter treats matrials related to the dioxide, VO_2, whereas Ch. 18 below will give an in-depth discussion of the most oxygen-rich oxide, V_2O_5.

Vanadium dioxide has attracted a lot of interest because of its unique capability of going from a semiconducting monoclinic phase to a (semi)metallic tetragonal rutile phase at a temperature in the vicinity of room temperature, specifically at 68°C. The atomic displacements are very small in the structural transformation, which motivates that the V-dioxide-based films are discussed here together with the other rutile-type electrochromic oxides. The properties of V dioxide have been reviewed by Bugayev et al. *(516)*, Chudnovskii *(705)*, and Goodenough et al. *(1246)*. This chapter covers crystal structures and electrical properties of bulk-like V dioxide (17.1), preparation and characterization of thin films (17.2), ion intercalation/deintercalation reactions and ensuing changes in electrical conductivity (17.3), and optical properties (17.4).

17.1 Crystal Structures and Electrical Properties of Bulk-like Vanadium Dioxide

The high-temperature rutile structure of V dioxide is characterized by equidistant V atoms along the tetragonal *c* axis, whereas the low-temperature monoclinic structure has V-V distances alternating between a larger and a smaller value and has V-V pairs tilted off the monoclinic *a* axis. The atomic displacements are small for the monoclinic ↔ tetragonal transformation, and both structures can be thought of as built up from somewhat distorted VO_6 octahedra with the chain configuration characteristic for rutiles.

The structural transformation is manifested in a large change of many physical properties. Figure 17.1, based on data by MacChesney and Guggenheim *(2135)* and Morin *(2387)*, illustrates this fact for the case of the electrical conductivity, which is found to increase by several orders of magnitude when the phase change temperature is surpassed. The magnitude of the conductivity change, as well as its hysteresis, depends on sample preparation, as one can infer from the shown data. Several theoretical models have been put forward to explain the change in the electrical, and other, properties. Most of these theories are based on a Mott-Hubbard-like transition caused, essentially, by the off-axis displacement of the V atoms *(2418, 3824)* or electron trapping in homopolar bonds *(1246-7)*.

Apart from the phases mentioned above, V dioxide has a number of metastable structures

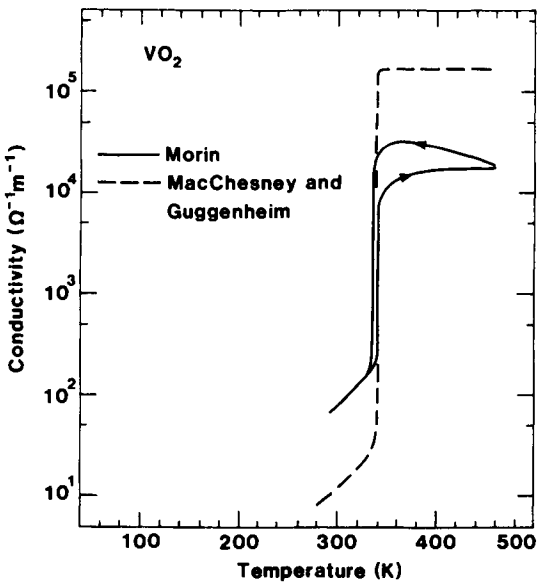

Fig. 17.1 Electrical conductivity vs. temperature for two VO_2 crystals. Arrows denote directions of the temperature sweeps. After MacChesney and Guggenheim *(2135)* and Morin *(2387)*.

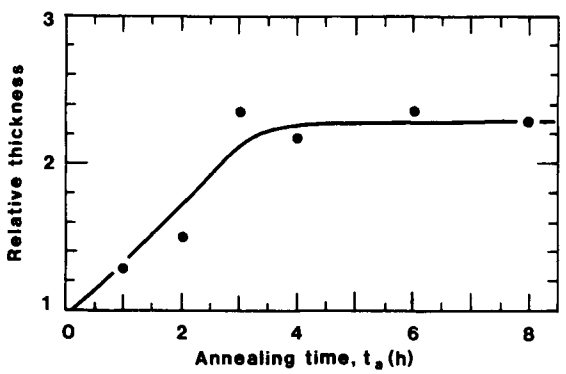

Fig. 17.2 Relative thickness vs. annealing time t_a for a vanadium-based film treated at 400°C in the presence of air. Dots indicate measured data and the curve was drawn for convenience. From Jiang et al. *(1672-3)*.

derived from various arrangements of VO_6 octahedra; one may notice the materials conventionally denoted VO_2(A), VO_2(B), and paramontroseite VO_2 *(2618-20, 3401-2)*. The VO_2(A) and VO_2(B) phases comprise layers with basic building blocks, being two edge-sharing octahedra, arranged in different corner- and edge-sharing configurations. Four different V dioxide hydrates were reported in a comprehensive study by Théobald *(3401)*.

The stability range for the rutile phase can be changed by substitutions in the VO_2 lattice. Thus $M_yV_{1-y}O_2$ with M = Nb, Mo, W, Ru, and Re showed a decrease of the phase change temperature in proportion with the magnitude of y *(1547-8, 2135, 2830, 2893, 2911, 3027, 3361)*, whereas M = Ti, Sn had the opposite effect *(242, 3392)*. The phase change temperature was depressed also in $VO_{2-y}F_y$ crystals *(301-2, 640)*.

The VO_2 structure is open enough so as to allow intercalation/deintercalation of small ions such as H^+ *(694)* and Li^+ *(889, 2377, 2441-2, 3781)*. The hydrogenated material can be represented as $VO_{2-x}(OH)_x$ for $0.16 < x < 0.37$. Furthermore, Li^+ insertion has been studied in $Li_{1-y}V_2O_4$ ($0.7 < y < 0.9$) with a defect rocksalt structure *(890)*. $LiVO_2$ has a structural phase change--principally similar to the one in VO_2--that correlates with a "critical" V-V separation *(1248)*.

17.2 Preparation and Characterization of Thin Films

Vanadium dioxide films have been prepared by many techniques. A detailed coverage of the literature is not meaningful--considering the few studies on their electrochromism thus far reported--and only work regarded to be of particular interest is cited below. Evaporation was reported in *(211, 618-20, 623-5, 1121, 1536, 2563, 3097)*; some of the films were prepared by ion-assisted deposition or were converted into a dioxide by annealing post-treatment. One should observe in this context that when solid VO_2 is heated, the liberated species are predominantly VO_2 molecules *(1028)*. Different varieties of sputtering were used to make V dioxide films in *(210-1, 635-6, 883, 1036, 1969, 2861, 2927, 3392, 3528)*. Anodization was employed in *(68, 2166)*. X-ray analysis was used to show that the crystallite size was smaller than ~1 nm and that the local microstructure deviated significantly from that in crystalline VO_2. CVD with V oxychloride *(1036, 3346)*, V acetylacetonate *(208, 1325, 3098)*, or V triisobutoxide *(3334)*, as well as thermal decomposition of V naphthenate *(1782-3)*, are other useful techniques. Sol-gel-deposition from V isopropoxides was reported in *(2105, 2711, 3219)*. Finally, simple thermal oxidation of metallic vanadium is a viable technique for making V dioxide films *(243, 313, 621-2, 1672-3, 2402, 3297)*.

Thermal oxidation of metallic vanadium films was recently studied by Jiang et al. *(1672-3)*, who found that V dioxide films of a surprisingly high quality could be prepared by this comparatively simple technique. Figure 17.2 shows the relative thickness increase when an initially 0.12-μm-thick film was annealed at ~400°C in the presence of air for a time t_a up to 8 h. The film became thicker as a result of the oxidation, with a relative thickness increase by a factor as large as ~2.3 for $t_a > 3$ h. This increase is the one expected when bulk-like pure V is converted into bulk-like VO_2.

The electrical properties evolve with the progess of the oxidation, and Fig. 17.3 illustrates data on the temperature dependent conductivity $\sigma(\tau)$ of films annealed for different times. As-depositied films had $\sigma \sim 4 \times 10^5\ \Omega^{-1}m^{-1}$. After annealing for $t_a = 1$ h, the conductivity dropped and varied

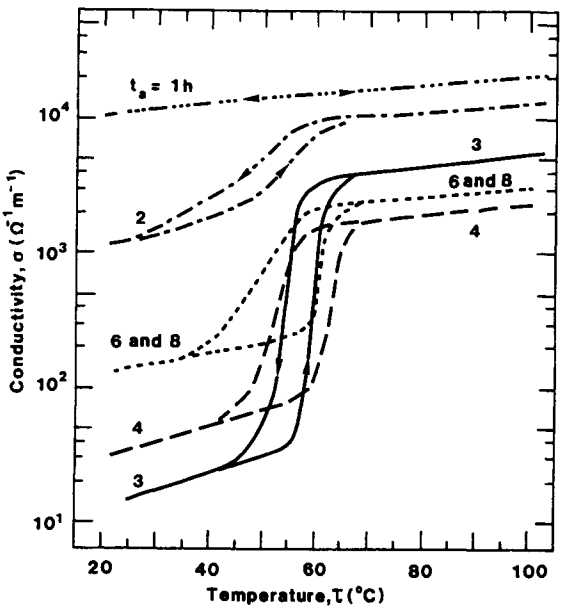

Fig. 17.3 Electrical conductivity vs. temperature $\sigma(\tau)$ for an initially 0.12-μm-thick vanadium-based film annealed for the shown time t_a at 400°C in the presence of air. From Jiang et al. *(1672-3)*.

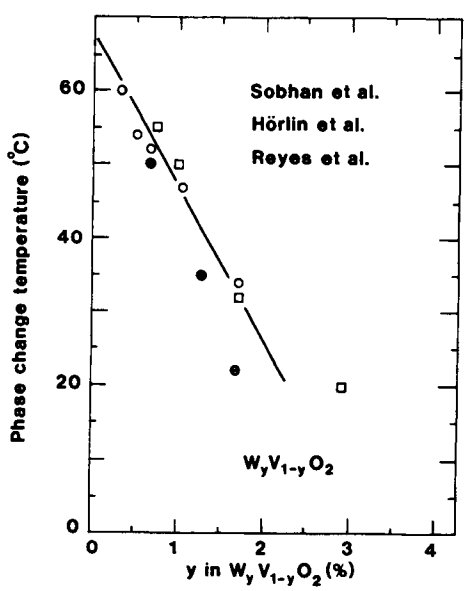

Fig. 17.4 Phase change temperature, inferred from electrical measurements, for $W_yV_{1-y}O_2$ films (solid dots) and bulk crystals (open squares and circles). After Hörlin et al. *(1547)*, Reyes et al. *(2893)*, and Sobhan et al. *(3204)*.

approximately linearly between ~10^4 $\Omega^{-1}m^{-1}$ at 20°C and ~2 x 10^4 $\Omega^{-1}m^{-1}$ at 100°C. At t_a = 2 h, the low-temperature conductivity decreased by about one order of magnitude, while the high-temperature conductivity went down by a much smaller extent. A poorly defined hysteretic conductivity transition is seen. At t_a = 3 h, the $\sigma(\tau)$ characteristic became significantly different, and the conductivity changed abruptly from ~40 to ~$3x10^3$ $\Omega^{-1}m^{-1}$--i.e., by about two orders of magnitude--at ~57°C. The conductivity transition is in keeping with data for VO_2 crystals, shown in Fig. 17.1, thus proving that the heat treated film has a stoichiometry close to VO_2. At t_a > 3 h, Fig. 17.3 shows that the conductivity transition became progressively less well defined, which is most likely associated with the formation of VO_z with z > 2.

The phase change temperature in thin films is usually somewhat lower than in bulk crystals, which can be inferred from a comparison of the conductivity data in Figs. 17.1 and 17.3. A further lowering can be induced by substituting some of the vanadium by tungsten, i.e., by making films with an approximate composition $W_yV_{1-y}O_2$ *(3204, 3485)*, and by fluorination of dioxide films *(1793-4)*. Figure 17.4, from Sobhan et al. *(3204)*, shows data for $W_yV_{1-y}O_2$ films prepared by reactive cosputtering of W and V in Ar + O_2. An addition of 2 to 3 at. % of W stabilizes the rutile phase down to room temperature. The film data are consistent with results for bulk crystals *(1547, 2893)*. One may note, in passing, that some earlier attempts to make $W_yV_{1-y}O_2$ films by ion beam sputtering *(1688-9)* were unsuccessful in lowering the phase change temperature at the rate indicated in Fig. 17.4, which may have been caused by an uneven distribution of the W atoms.

17.3 Ion Intercalation/deintercalation Reactions and Changes in Electrical Conductivity

Ion intercalation/deintercalation in V dioxide films has not been studied in detail, and few facts are known with certainty. However, one can note work by Kuwabara et al. *(1974)*, who prepared electrochromic samples with films of evaporated VO_2 operating in conjunction with proton conducting tin phosphate ($Sn(HPO_4)_2 \cdot H_2O$) solid electrolytes and evaporated W oxide films. Experimental data, primarily based on FTIR and XPS, were taken as evidence for reversible changes between V^{4+} and V^{5+}. This may indicate that the initial film was oxygen-rich--i.e., that its composition was VO_z with z > 2--but no definitive conclusion can be drawn on the basis of the published data.

More conclusive evidence for proton intercalation can be inferred from Chippindale et al. *(694)* who studied bulk samples with hydrogen inserted chemically, electrochemically, and by Pt spillover. For small hydrogen contents, the material was monoclinic H_xVO_2, i.e., the intercalation proceeded in a truly topotactic manner. At higher hydrogen density, specifically at 0.16 < x < 0.37, the structure changed to an orthorhombic rutile-related modification. Inelastic neutron scattering showed that this latter material contained hydroxyl groups, so that it could be identified with a $VO_{2-x}(OH)_x$ material produced earlier by high-pressure high-temperature processing *(2848)*.

The results by Chippindale et al. *(694)* indicate that a reaction

$$VO_2 + xH^+ + xe^- \leftrightarrow VO_{2-x}(OH)_x \qquad (17.1)$$

would be valid for proton intercalation/deintercalation in V dioxide films, but only further experimental work can show the correctness of this surmise. For Li^+ intercalation into films, the

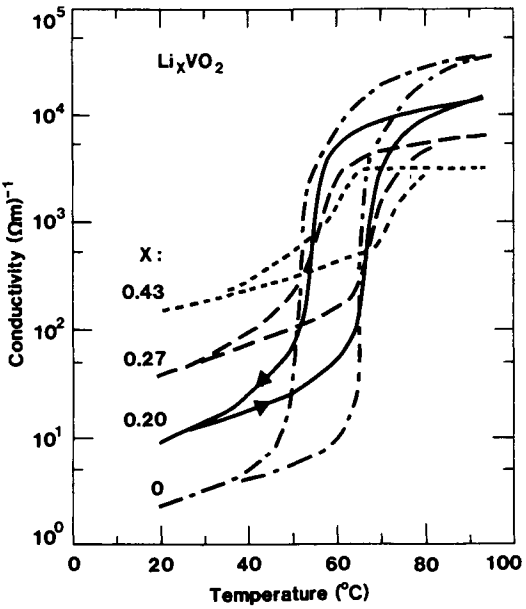

Fig. 17.5 Electrical conductivity vs. temperature for a 0.17-μm-thick V dioxide film, made by sputter-deposition and annealing post-treatment, in unintercalated state and after Li^+ intercalation to the shown magnitudes, given as x in Li_xVO_2. From Khan et al. *(1795)*.

reaction

$$VO_2 + xLi^+ + xe^- \leftrightarrow Li_xVO_2 \qquad (17.2)$$

was been suggested by Khan et al. *(1795)*, following work on bulk VO_2 *(2441-2)*.

Ion intercalaion changes the relation between electrical conductivity and temperature. Detailed results have been reported by Khan et al. *(1795)* for lithiated films made by reactive rf sputtering followed by annealing post-treatment and immersion in an electrolyte of 0.1 M $LiClO_4$ + PC. Figure 17.5, taken from that work, shows data for films with different Li^+ contents. The unlithiated film showed a hysteretic conductivity transition by about three orders of magnitude within a ~15°C wide interval centered at ~60°C. This is in overall agreement with data shown before in Figs. 17.1 and 17.3. Li^+ intercalation made the low-temperature conductivity increase and the high-temperature conductivity decrease; thus the conductivity transition became less pronounced and was smaller than one order of magnitude for the material denoted Li_xVO_2. A similar tendency has been observed for Li_xVO_2 bulk materials *(2377)*. A smearing of the conductivity step is in agreement with the general tendency for impurities and structural imperfections in the VO_2 lattice to deteriorate the structural phase transition; such an effect has been seen for stoichiometry deviations *(1332)*, W substitution *(1688-9, 3204, 3485)*, fluorination *(1793)*, and ion implantation *(3484)*.

17.4 Optical Properties

Films made by thermal oxidation of vanadium are first considered. Figure 17.6, from Jiang et al. *(1672-3)*, shows results for films in virgin state and after annealing post-treatment in the presence of air for two different durations. The transmittance of the oxidized films was measured at 20 and 100°C, being below and above the phase change temperature. The annealing produced films with well developed thermochromism, i.e., with a transmittance that was significantly different at different temperatures.

Figure 17.7, from Khan et al. *(1795)*, reports transmittance data for a V dioxide film made by reactive sputtering and annealing post-treatment. The as-deposited film has a spectral transmittance at room temperature that is in good agreement with that for the oxidized metallic film reported on in Fig. 17.6. Li^+ intercalation from an electrolyte of 0.1 M $LiClO_4$ + PC increased the transmittance in proportion with the lithium density over the full $0.4 < \lambda < 2.5$ μm interval. Hence V dioxide is electrochromic and shows increased transmittance in the ion intercalated state. The material has some optical absorption at least up to a lithium density corresponding to $Li_{0.43}VO_2$.

Transmittance data for the as-deposited film and the $Li_{0.43}VO_2$ film were also taken at 80°C, i.e., above the phase change temperature. As seen in Fig. 17.8, some thermochromism also exists in the lithiated material, although the relative modulation of the optical properties is not as large as for the unintercalated state. Therefore Fig. 17.8 proves that V dioxide films have a property that may be termed *thermo-electrochromism*.

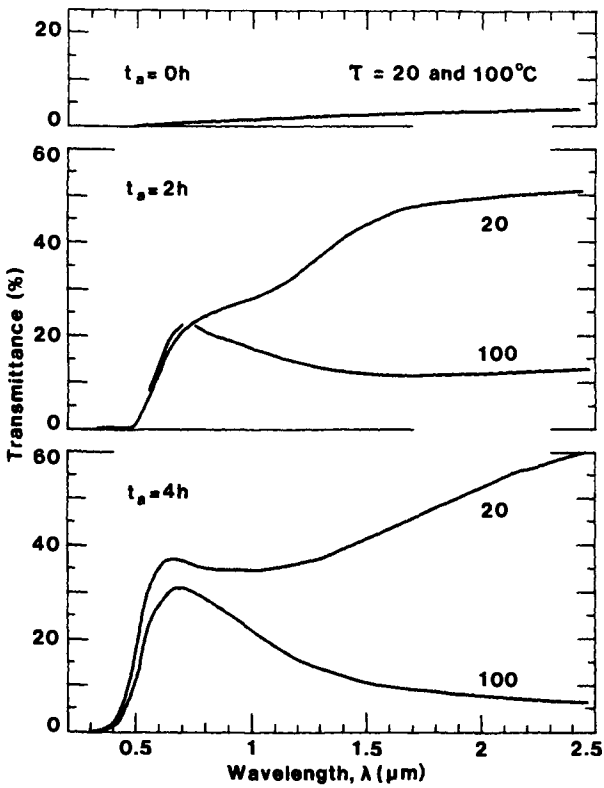

Fig. 17.6 Spectral normal transmittance for an initially 0.12-μm-thick V-oxide-based film in unoxidized state and after annealing for the shown time t_a at 400°C in the presence of air. Data were taken at two temperature τ. Electrical conductivity for these films was reported in Fig. 17.3. From Jiang et al. *(1672-3)*.

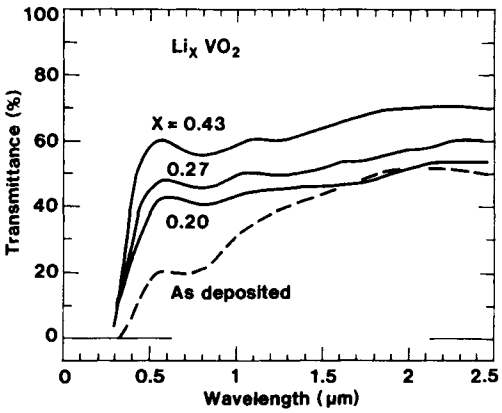

Fig. 17.7 Spectral transmittance at room temperature for a 0.17-μm-thick V dioxide film, made by sputter-deposition and annealing post-treatment, in unintercalated state and after Li^+ intercalation to the shown magnitudes, given as x in Li_xVO_2. Electrical conductivity for these films was reported in Fig. 17.5. From Khan et al. *(1795)*.

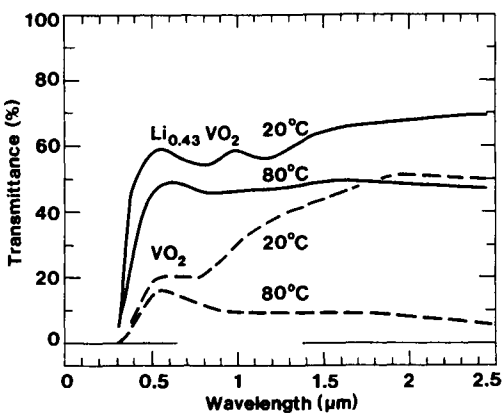

Fig. 17.8 Spectral transmittance at two temperatures for a 0.17-μm-thick V dioxide film in unlithiated and lithiated states. Upper solid and dashed curves are identical with curves in Fig. 17.7. From Khan et al. *(1795)*.

This Page Intentionally Left Blank

Chapter 18

VANADIUM PENTOXIDE FILMS

The electrochromic oxides considered until now have been of framework type and related to the defect perovskites and rutiles. This chapter is the first one among three in which oxides with a *layer structure* are discussed. A detailed treatise is given here for materials related to V_2O_5, referred to as V pentoxide, with special attention to the crystal structure of bulk-like V pentoxide (18.1), and to the preparation and characterization of films made by evaporation (18.2), sputter-deposition (18.3), and electrochemical and chemical (especially sol-gel) techniques (18.4). Then follow discussions of ion intercalation/deintercalation, ion exchange, and diffusion constants (18.5), and of the ion intercalation/deintercalation studied by electrochemical (18.6) and physical (18.7) methods. The optical properties of V-pentoxide-based materials are different from those of the oxides discussed so far in that bandstructure effects constitute an integral part of the electrochromism. The optical properties are reviewed in detail with regard to data for as-prepared films (18.8), data for ion intercalated films (18.9), and theoretical models (18.10). The final section gives results for V pentoxide films containing some fluorine and carbon (18.11).

18.1 Crystal Structure of Bulk-like Vanadium Pentoxide

Vanadium pentoxide--i.e., V_2O_5 or $VO_{2.5}$--can be thought of as being built from VO_6 octahedra arranged in a way that is similar to that in α-MoO_3 and anatase, and there is also a strong kinship to R-Nb_2O_5 (to be discussed in Sec. 21.1) *(1594)*. However, the octahedra are irregular in V_2O_5 with five V-O distances between 0.159 and 0.202 nm and a sixth distance as large as 0.279 nm *(216)*. The structure is orthorhombic with the large V-O separation along the crystallographic c direction. The unit cell parameters are a = 1.151 nm, b = 0.356 nm, and c = 0.437 nm. It is expedient to think of the structure as comprising *layers of square pyramids of VO_5*, with five oxygen atoms surrounding the vanadium atom; the layers are ~0.44 nm apart. A representation in terms of VO_5 units allows one to give a consistent description of many different V_2O_5-based materials *(966, 1015, 1132)*.

The layer structure of V_2O_5 makes it very well suited as an intercalation host, and a wealth of information is available on H^+ and Li^+ containing materials. Proton intercalation into crystalline bulk-like materials, up to a maximum of $H_{1.9}VO_{2.5}$, has been accomplished by hydrogen spillover with a Pt catalyst *(440, 910, 1479, 1495, 3415-6)*, by an electrochemical technique *(909)*, by exposure to atomic hydrogen generated in a microwave discharge *(3104)*, and by heating in hydrogen *(3228)*. The latter technique was reported to yield $H_{1.5}VO_{2.5}$, presumably having a

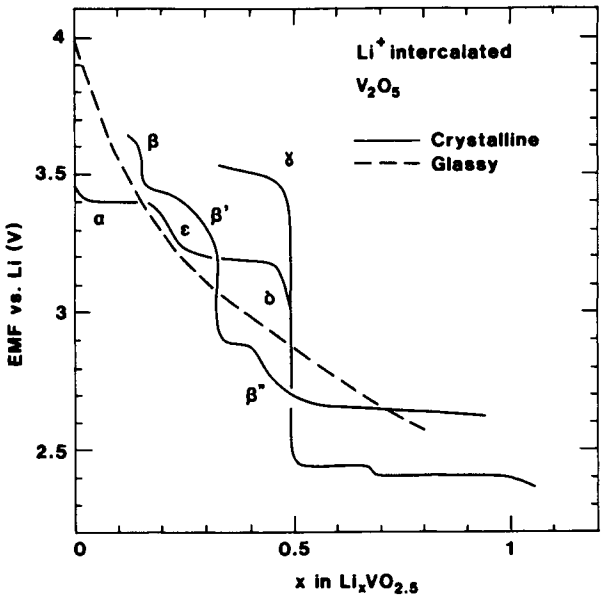

Fig. 18.1 Normalized EMF vs. amount of intercalated Li^+, represented as x in $Li_xVO_{2.5}$, in V pentoxide crystals (solid curves) and glass (dashed curve). Greek letters designate different crystalline phases. After Liaw et al. *(2073)* and Machida et al. *(2145)*.

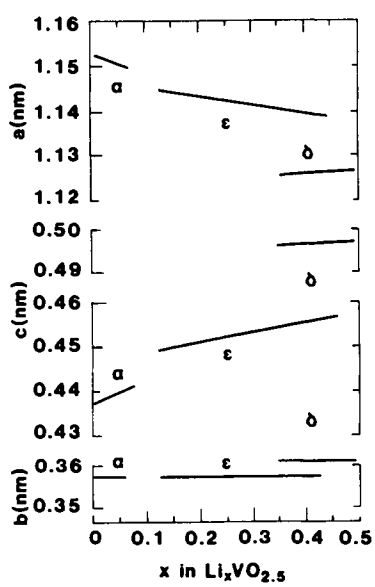

Fig. 18.2 Unit cell parameters *a*, *b*, and *c* of lithiated V pentoxide. The various lines pertain to the α, ε, and δ phases. The lines were drawn through numerous data points representing individual measurements. From Cocciantelli et al. *(718)*.

hydrogen bonded layer structure built from VO_6 octahedra *(1023)*. Hydrogen insertion into V_3O_7 and V_6O_{13} was studied in *(693, 910)*.

Vanadium pentoxide, and a number of related materials, have attracted much interest for applications in lithium batteries *(3567)*. Regarding V_2O_5, several crystal structures are useful as intercalation hosts. Since battery applications have been in focus, EMFs have been measured in many studies, which makes it convenient to illustrate the structural evolution as a result of lithiation in a diagram of EMF as a function of Li content. Figure 18.1, based on data provided by Liaw et al. *(2073)* and Machida et al. *(2145)*, shows EMFs for several well-defined crystal structures and for heavily disordered V pentoxide. The α, γ, δ, and ε phases have two-dimensional layer structures characterized by different degrees of "puckering" of the VO_5 units, whereas the β and β' phases have three-dimensional tunnel structures *(632, 718-9, 1132, 1427, 2440, 2790)*. Supporting EMF data have been reported many times for crystalline V_2O_5-based materials *(613, 718, 908, 912, 921, 1040, 1043, 1273, 1561, 1960, 2072, 2145, 2434, 2733-4, 3612-3, 3615, 3625, 3780)*. New phases may appear at large Li contents; they have been referred to as γ', ζ, and ω *(719-21, 870)*.

Concerning crystalline oxides with less oxygen, extensive work has been carried out on Li, and to some extent Na, intercalation into V_6O_{13} *(17, 639, 1537, 1707, 2001, 2152, 2429-31, 2434, 2439, 2773, 3227, 3609, 3614, 3625)*. Its structure is more regular than for V_2O_5, and a representation in terms of VO_6 octahedra is suitable; the V-O separations lie between 0.164 and 0.228 nm *(3634)*. EMFs have also been reported for V_3O_7, V_4O_9, V_8O_{15}, V_3O_5, and V_2O_3 *(1403, 2434, 2439, 3438, 3625)*. Li intercalation into crystalline LiV_3O_8 has attracted considerable attention for battery applications *(442, 2066, 2699, 2705, 2769-71, 2773, 2822, 3078, 3082, 3614)*. The structure contains both VO_6 and VO_5 units. LiV_3O_8 has been plagued by poor cycling capability in Li^+ conducting electrolytes, but it appears that heavily disordered LiV_3O_8 behaves better in this respect *(2772)*. Another material with potential battery-related applications is KV_5O_{13} *(2174)*. Finally, one should note work on Li intercalation into V oxides containing some Mo *(2433, 2925, 3437)*, W *(2433)*, Na *(2712, 2822, 3610)*, or Ag *(360, 2035, 3349-51)*. $Ag_xV_2O_5$ also can serve as an intercalation host for silver ions *(3325)*.

Heavily disordered V pentoxide is of interest in connection with electrochromic films, and EMFs for bulk materials of this type are considered next. Rapid quenching of molten material between twin rollers (sometimes referred to as "splat cooling") has been used to make glassy V_2O_5 in numerous investigations *(263, 925, 1177, 1460, 1717, 2095, 2145-6, 2408, 2455, 2457, 2903-4, 2914, 2993-4)*, and the same technique has been applied also to V_2O_5-MoO_3 *(3468)*. The dashed curve in Fig. 18.1, taken from work on glassy V_2O_5 by Machida et al. *(2145)*, shows that the EMF drops smoothly from a value as large as ~4 V vs. Li when the lithium content is increased. No evidence can be found for crystalline phases. A similar monotonic EMF variation, although appearing to be somewhat displaced downwards in voltage, was reported for a similarly prepared material by Nabavi et al. *(2457)* and for a material based on electrolytic deposits by Sato et al. *(3021-2)*.

The structure of glassy V_2O_5 represents a long-standing problem *(3659)* with partly conflicting data; however, a recent assessment by Nabavi et al. *(2455)* showed clear evidence for structural units of both VO_5 and VO_4. A glassy state can be stabilized in V pentoxide also by the addition of a small amount of a glass former such as P_2O_5 *(157, 2974-5)*.

It is of interest to consider changes of the lattice parameters when lithium is intercalated into V_2O_5 powder. Figure 18.2, from Cocciantelli et al. *(718)*, shows schematically the variations of

a, *b*, and *c* when x in $Li_xVO_{2.5}$ lies in the range from zero to 0.5. The different branches can be associated with the phases α, ε, and δ intoduced in Fig. 18.1. Data consistent with those in Fig. 18.2 were also given in *(1561, 2433, 2440, 3436)*.

18.2 Film Made by Evaporation: Preparation and Characterization

Evaporation is a viable technique for making V pentoxide films. Mass spectrometry studies of the molecules effusing from a source containing V_2O_5 showed that the predominant species were V_4O_{10}, V_6O_{14}, and V_6O_{12}, with some evidence also for V_4O_8 and V_2O_4 *(362)*. Hence evaporation leads naturally to the formation of a more or less substoichiometric oxide, which is analogous with the case of evaporated W oxide and Mo oxide.

Thermal evaporation of V_2O_5 powder from different types of sources has been reported in several studies. Quartz crucibles are convenient since contamination is minimized. Suitable source temperatures lie in the 800 to 900°C range *(176)*. The maximum film deposition rates given in the literature is ~2.5 nm/s, referring to 25 cm between source and substrate *(745-6)*, and up to 5 nm/s for 10 cm *(2305)*. As-deposited films form rather loosely packed structures, and it was reported that a 0.5-μm-thick V pentoxide layer had a density of 2.42 g/cm^3 *(75)*, corresponding to 0.72 of the density of bulk orthorhombic V_2O_5.

As-evaporated films appeared X-ray amorphous at $\tau_s < 180$°C and crystalline at $\tau_s > 180$°C, as inferred from several investigations *(176, 745-6, 1118, 1144, 1151, 1859, 2305-6, 2991)*. The crystallized films tended to have a layer structure with the crystallographic *c* axis perpendicular to the substrate *(1859)*. Audiere et al. *(175-6, 2991)* made detailed studies by DTA of the crystallization upon heating of "amorphous" films. Crystallization was indicated by an exothermic peak lying at ~340°C irrespective of τ_s; another weaker signal at ~300°C was tentatively assigned to a glass transition. The crystallization enthalpy was highest when τ_s was lowest. Bulk samples made by splat cooling, on the other hand, had already crystallized at 210 to 240°C *(1177, 2914)*. The DTA data indicate that the "amorphous" V pentoxide films do not have a unique structure, but their disorder is enhanced for increased quench rate. Vacuum annealing of pentoxide films above 350°C led to a slow transition to VO_2 *(3097)*.

The structural properties of as-evaporated and annealed V pentoxide films have not been studied in great detail. However, some data are available, especially from EXAFS and vibrational spectroscopy. EXAFS was applied to evaporated V pentoxide films by Burattini et al. *(528)*. The data were interpreted in terms of a structural model involving distorted octahedra joined by corners and edges to form a random network.

Raman spectroscopy was employed to study as-evaporated and annealed V pentoxide films by Lewis et al. *(2059)*, whose data are shown by the upper two curves in Fig. 18.3. The "amorphous" as-evaporated film produced a number of broad peaks, whereas the crystalline film--annealed in air at 500°C for several hours--gave distinct peaks. One can compare with results for a splat-cooled sample *(2993)*, whose Raman spectrum appeared to have peaks with widths intermediate between those of the film data in Fig. 18.3. The bottom curve in the figure refers to a sample comprised of crystalline V_2O_5 powder. The Raman spectrum is in good agreement with that of the crystallized film. Consistent Raman spectra can be found in the literature for polycrystalline samples *(1424, 2993)* and single crystals *(12, 1186, 2892)*. The peaks in the Raman intensity can be interpreted in terms of specific lattice modes; for example the Raman peak at ~1000 cm^{-1} pertains

to V=O stretching vibrations.

Figure 18.4 shows IR absorption data. The upper part, after Sanchez et al. *(2991)*, refers to a V pentoxide film evaporated onto a substrate at room temperature. A number of broad absorption features cover the full range between 1100 and 300 cm^{-1}. Rather similar absorption spectra were obtained for "amorphous" V pentoxide made by splat cooling *(2095, 2455, 2914, 2993, 3468)* and for vanadium bulk glasses containing a glass former such as P_2O_5 *(925, 2975)*. However, the data are not entirely identical, and a comparison of the upper three curves in Fig. 18.4 shows that only the film has an absorption centered at ~880 cm^{-1}. The bottom curve in Fig. 18.4 displays IR absorption for a typical polycrystalline specimen. The curve was taken from Rivoalen et al. *(2914)*, and similar spectra have been reported elsewhere in the literature *(12, 272, 715, 910, 1105, 1153, 1186, 1479, 1495, 1781, 2434, 2834, 3415)*. Analogous spectral features have been studied also for bulk and surface phonons in single crystals (with different orientations between the polarization vector and the crystallographic orientation) *(6, 7, 449, 712, 715, 1478, 1821, 2784-5, 2892)*. The most complete work on bulk crystals is that of Abello et al. *(12)* who carried out a factor analysis and assigned the various absorption features to well-defined lattice vibrations. The strong absorption at ~1000 cm^{-1} is caused by the vanadyl bond, specifically by V=O terminal stretching vibrations, whereas the modes at lower wavenumbers are due to various types of in-plane and out-of-plane vibrations of the V-O-V network. One can conclude from Fig. 18.4 that the characteristic absorption features of crystalline V pentoxide still remain in the "amorphous" material, although the absorption minima are broadened by a factor ~3. Hence the basic structure, containing VO_5 units, is expected to prevail in evaporated films.

EPR is a convenient experimental method for elucidating effects of V^{4+} ions, i.e., non-stoichiometry effects in V pentoxide. This technique was used by Sanchez et al. *(2991)* to study evaporated films. The EPR spectrum was interpreted as a ~200 G broad signal centered around g = 1.96 and a superimposed spectrum corresponding to a spin Hamiltonian for an axially symmetric field (Eq. 7.4 with $g_{\parallel}$ =1.913, $g_{\perp}$ = 1.980, and additional terms representing hyperfine structure). Only the broad signal was caused by ions in the interior of the film, and the hyperfine spectrum vanished when the film was scraped off the substrate. The broad spectrum may be interpreted on the premise that the V^{4+} ions have a non-statistical distribution in a disordered matrix. A more detailed discussion of EPR specra will be given in Sec. 18.4 in connection with films prepared by sol-gel technology.

The mechanical and chemical properties are of central importance for practical applications of evaporated V pentoxide films. These aspects were investigated by Sanchez et al. *(2991)*, who found that heavily disordered films made by condensation onto substrates at $\tau_s < 120°C$ were readily scraped off glass substrates by a razor blade, whereas crystalline films made at $\tau_s > 185°C$ were tenaciously adherent. Films made at $\tau_s < 20°C$ reacted easily with atmospheric humidity and were dissolved if immersed in water for a few seconds. Crystalline films made at $\tau_s > 250°C$, on the other hand, appeared practically insoluble. EPR spectra for hydrated films showed evidence for solvated vanadyl ions, i.e., $VO(H_2O)_5^{2+}$. An analogous high reactivity with water was also found for "amorphous" vanadium pentoxide made by splat cooling *(2308, 2455, 2904, 2914)*. One concludes that as-evaporated V pentoxide films have properties that make them unsuited for applications in electrochromic devices as well as for most other practical uses. However, it should be remarked that the possibility of dissolving the oxide in water can be turned into an advantage, and it is straight-forward to make gels that can serve as precursors for films produced by sol-gel technology, as discussed in Sec. 18.4 below.

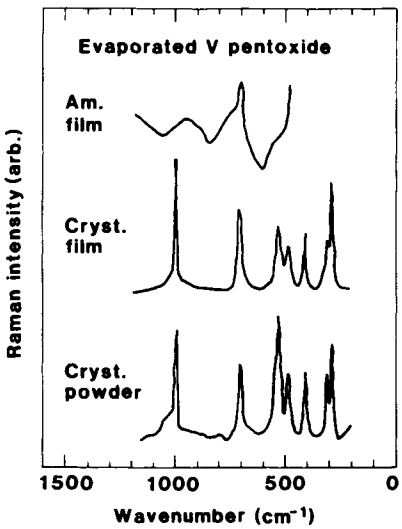

Fig. 18.3 Raman spectra for "amorphous" and crystalline V pentoxide samples. The curves were drawn through data showing a certain amount of scattering. After Lewis et al. *(2059)*.

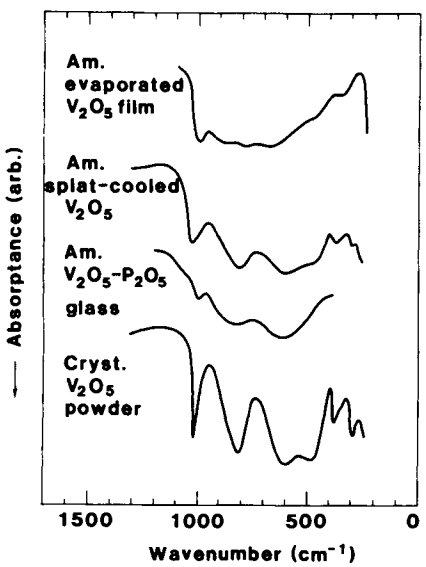

Fig. 18.4 Infrared absorption spectra for "amorphous" and crystalline V-pentoxide-related materials prepared in different ways. The data refer to an evaporated V pentoxide film condensed onto a substrate at τ_s = 20°C, a splat-cooled V pentoxide platelet, a bulk glass of 95% V_2O_5 and 5% P_2O_5, and a sample of crystalline V_2O_5 powder. After Livage and Collongues *(2095)*, Rivoalen et al. *(2914)*, Sakurai and Yamaki *(2975)*, and Sanchez et al. *(2991)*.

Except in the works already referred to, evaporated V pentoxide films were studied in *(295-6, 1709, 1777, 1791-2, 2701, 3231)*. Thus far the discussion has considered only films made by conventional evaporation. One could note, for completeness, that V pentoxide films have also been prepared by flash evaporation *(2436-7)*, by laser evaporation with a pulsed Nd:YAG laser *(1797)*, and by oxidation of an evaporated metallic V film through thermal treatment *(750, 2985)* or exposure to an Ar^+ laser beam in air *(3309-10)*. Flash evaporation was able to give films with good homogeneity, and this technique was also employed for depositing $Li_xV_2O_5$ *(2436)*. Evaporated V_2O_5-P_2O_5 films were studied in *(1693)*.

18.3 Films Made by Sputter-deposition: Preparation and Characterization

Sputtering has been used extensively for making V pentoxide films, and detailed studies have been carried out for films made by rf sputtering in Ar + O_2 *(41-4, 165-6, 723, 726, 734-5, 1411, 1868, 2110, 3612, 3616)*, dc magnetron sputtering in Ar + O_2 *(279, 3036, 3352-5, 3664)*, and ion-beam sputtering in Ar + O_2 *(636, 636a)*. Some data are also available for sputtering in a H_2-containing plasma *(1813)* and in Ne + O_2 *(20)*. Rf sputtering has been used for making films from targets of V_2O_5-ZnO-B_2O_3 *(1867, 1873)* and VO_2-SiO_2 *(1868)*.

The highest deposition rate reported so far is ~1 nm/s, which was found by Wruck et al. *(3664)* who employed dc magnetron sputtering from an oxidized target. In most other works, the deposition rate was between 0.03 and 0.2 nm/s.

Aita et al. studied reactive rf diode sputtering of V_2O_5 in considerable detail and were able to trace "phase maps" for the parameters that gave crystalline films by deposition in Ar + O_2 *(43)* and Ne + O_2 *(20)*. Crystalline films could be prepared even onto unheated substrates; they had a tendency to grow with their crystallographic *c* axis perpendicular to the substrate, i.e., with layers parallel to the substrate. The interlayer separation (the *c* parameter) depended on the sputter conditions. Thus Fig. 18.5(a), obtained from Aita et al. *(42)* for films sputtered at 10^{-2} Torr of Ar + O_2 and $\tau_s < 100$°C, shows that *c* varies continuously from ~0.436 nm with 2 % O_2 to ~0.442 nm with pure oxygen. A value as large as 0.445 nm was found with some other sputter parameters *(43)*. Figure 18.5(b), plotted from data by Aita and Kao *(41)*, indicates that for a film made in an oxygen-deficient plasma *c* can be increased by annealing at 280°C for several hours. Bulk V_2O_5 has an interlayer spacing of 0.437 nm *(216)*, and it is evident that films with both smaller and larger separations can be obtained depending on the preparation and post-treatment conditions. This expansion/contraction effect may be associated with vacancies or interstitials in the layer of vanadyl oxygen *(1067, 2000)*. Surface roughness on a scale much smaller than 1 μm has been seen by SEM *(279, 636, 636a, 723, 734)*; the roughness could be modified by the application of substrate bias.

Figure18.6 shows a Raman spectrum, after Bates et al. *(279)*, for a V pentoxide film made by reactive dc magnetron sputtering onto a substrate kept at room temperature. A number of peaks are seen; they are in reasonable agreement with the bulk data in Fig. 18.3. The strong peak at ~145 cm^{-1} is associated with the layered structure, which is well developed despite the fact that the film was not deliberately heated.

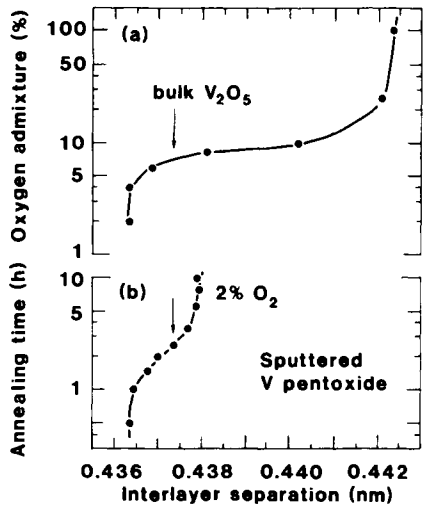

Fig. 18.5 Interlayer separation (crystallographic *c* parameter) for sputter-deposited V pentoxide films. Part (a) refers to different oxygen contents in the Ar + O_2 plasma, and part (b) to the annealing of a film made with Ar + 2 % O_2. Dots indicate measured values, and curves were drawn for convenience. Arrows denote the interlayer separation for bulk V_2O_5. After Aita et al. *(41-2)*.

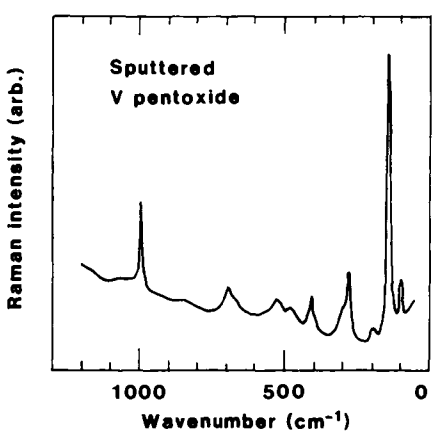

Fig. 18.6 Raman spectrum for a sputter-deposited V pentoxide film. From Bates et al. *(279)*.

18.4 Films Made by Electrochemical and Chemical Techniques (Especially Sol-gel Deposition): Preparation and Characterization

Following the common format of the various chapters, *electrodeposition* is considered first. Films can be made from different electrolytes, and some data have been reported for anodic deposition from a $VOSO_4$ solution at pH = 4 *(549)* and from a saturated NH_4VO_3 solution *(108-9, 2810-1)*. Heat treatment of the latter films at ~300°C converted them to crystalline orthorhombic V_2O_5 *(109)*. It is also possible to produce films by electrodeposition from V_2O_5 sols made by protonation of a vanadate solution passing an ion-exchange resin *(3750-1)*.

Anodization is possible though associated with some problems since V pentoxide is rapidly dissolved in aqueous electrolytes. Nevertheless, it is feasible to use an acetic acid electrolyte containing a very small amount of water and saturated with sodium borate *(152-4, 716, 1007, 1767-9, 2060, 2149, 2641, 2726)*. The initial work by Keil and Salomon *(1768-9)* was interpreted on the premise that a dioxide was formed, but a more recent study by Mackintosh and Plattner *(2149)* identified the anodic layer with a pentoxide. The film density was 0.9 of that for bulk V_2O_5 *(2641)*.

Regarding *CVD*, one can use a simple technique involving the decomposition of $VOCl_3$ vapor with humidity *(248, 2305, 3306, 3346-7)*. As-deposited films were highly disordered and were readily dissolved in water. Crystallization took place by heating to ~240°C. Infrared absorption spectra showed absorption bands at ~1610 cm^{-1} and ~3500 cm^{-1}, proving that losely bound water was present *(2305, 3306)*. Presumably the films were structurally similar to the hydrated zerogels produced by sol-gel technique, to be discussed shortly. Thermal decomposition of $VO(OC_2H_5)_3$ represents another CVD route for the production of V pentoxide films *(1616-9)*. It is likely that these films contain less water than those made by hydrothermal processing.

Sol-gel deposition is capable of producing V pentoxide films with particularly interesting properties; the remainder of the present section is devoted to this technique. The sol-gel films are normally hydrated and have water molecules in between the pentoxide layers so that the composition can be expressed as $V_2O_5 \cdot pH_2O$. One can note already here that this structure is especially well suited for ion insertion in that the interfoliar water can serve as a conduit for mobile ions.

Precursors for thin film fabrication--i.e., V pentoxide gels--have been studied for more than a century, and the pertinent literature is vast. The subject was reviewed in detail by Livage *(2092)*, and useful summaries may also be found in other papers by the same author *(2089-91, 2094, 2097-8)*. Three techniques for gel fabrication have been widely used during recent years, viz.

(i) dissolution in water of "amorphous" V_2O_5 produced by rapid quenching from the liquid or gaseous state *(247, 523-5, 1177, 1727, 1823, 1831, 1908, 2308, 2991, 3307-8, 3796-7)*,

(ii) protonation of vanadates in aqueous solution, most conveniently by passing a metavanadate solution through a proton exchange resin and subsequently letting the polymerization progress spontaneously *(108, 1179, 1609, 1830, 2040-1, 2338, 2989, 3611-2, 3724)*, and

(iii) hydrolysis of V alkoxides *(2323, 2454, 2456, 2992)*.

The alkoxide technique has also been used to prepare mixed V_2O_5-TiO_2 films and MVO_5 with M =

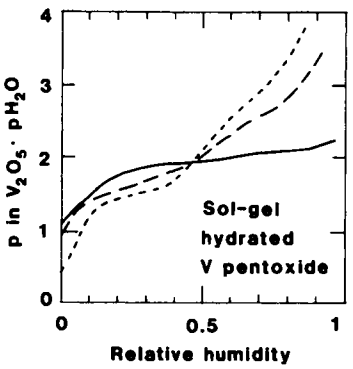

Fig. 18.7 Water adsorption isotherms for hydrated V pentoxide films made from gels prepared under somewhat different conditions. After Barboux et al. *(264)* (dotted curve) and Kittaka et al. *(1834)* (solid and dashed curves).

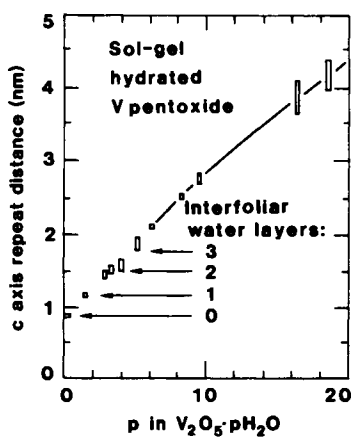

Fig. 18.8 Repeat distance in the *c* direction for sol-gel-produced V pentoxide films with different degrees of hydration. Discrete interfoliar water layers are found at low to moderate hydration, whereas a continuous swelling takes place at high hydration (indicated by the curve). From Aldebert et al. *(62)*.

Nb, Ta, and Nb_yTa_{1-y} *(79-81, 1491-3, 2324)*. Aerogels of V pentoxide, with a relative density as low as ~0.03, were made by supercritical drying of gels in bulk form or as dip-coated layers *(1494, 3267)*.

The gels have a fibrous character, and TEM studies showed the presence of ribbon-like structures about 10 nm wide and more that 1 μm long *(262, 525, 1179, 1492, 1907, 2034, 2096, 2323)*. Recent work demonstrated that tiny threads, ~3 nm wide and ~100 nm long, form first; these threads then grow lengthwise, and edge-to-edge self-assembly yields the ribbons that can be observed in the gels *(236-7)*. Interaction among the ribbons can lead to spindle-like nematic tactoids whose orientation is preserved, or even enhanced, in thin films formed from the gels.

XRD patterns have been reported several times for sol-gel-produced films, for example in *(60, 1830, 3724)*. Two sets of patterns can be observed; an *00l* series corresponding to a one-dimensional stacking of the ribbons perpendicular to the substrate, and an *hk0* series corresponding to the two-dimensional configuration of the ribbons. The *00l* series represents the *repeat distance* between the layers, which in its turn depends on the amount p of interfoliar water in the $V_2O_5 \cdot pH_2O$ gel. The *hk0* series, on the other hand, is independent of p, and electron diffraction from a single ribbon *(2033-4)* showed that an indexation was possible with $a = 2.7$ nm and $b = 0.36$ nm. This indicates that the basic structure of the *ab* plane in orthorhombic V_2O_5 is preserved, albeit with a larger repeat distance in the *a* direction. It was stated *(2033)* that the latter feature was associated with hydroxyl bonding in the V_2O_5 lattice giving rise to a corrugation in the ribbon structure. More recent work by Kittaka et al. *(1834)* did not show any evidence for corrugation, though. According to Yao et al. *(3724)*, who carried out a very careful X-ray analysis of the *00l* series by use of Rietveld refinement and Patterson maps, the ribbons comprise two uncorrugated V_2O_5 sheets facing each other at a distance of 0.28 nm. This structure appears to be identical to the one for hydrated V pentoxide prepared by hydrothermal synthesis *(2616, 2618, 3722-3)* and to the structure of δ-$Ag_yV_2O_5$ *(102)*.

Reversible water adsorption at the oxide-air interface determines the degree of hydration. Figure 18.7, from Barboux et al. *(264)* and Kittaka et al. *(1834)*, shows water adsorption isotherms, i.e., the magnitude of p in $V_2O_5 \cdot pH_2O$, as a function of the relative humidity. Adsorption isotherms were also given in *(1830)*. The data were inferred from weighings of bulk samples. It is seen that $1.4 < p < 1.9$ is valid in a wide range around RH = 0.3. Such films are often referred to as "xerogels". In the absence of water vapor, one finds $p \approx 0.5$. The shape of the water adsorption isotherm can be interpreted on the premise that multilayer adsorption prevails *(264)*.

The incorporation of water into V pentoxide can be ascribed to an intercalation process, and a one-dimensional expansion in the crystallographic *c* direction can be inferred from the *00l* XRD-series *(62, 1830, 3724)*. Figure 18.8, from Aldebert et al. *(62)*, shows that the repeat distance in the *c* direction increases in steps of 0.28 nm up to $p = 6$, suggesting the formation of as much as three well-defined layers of water molecules. A continuous swelling then takes place for $p > 6$. The smallest repeat distance, being ~0.88 nm, corresponds to $p \sim 0.5$. The water uptake can be somewhat influenced by preintercalation of metal ions *(1833)*.

Vanadium pentoxide films dehydrate in fairly discrete steps under heat treatment *(13, 15, 60, 108, 1834, 1907, 2092, 2096)*. A transition from $p \approx 1.8$ to $p \approx 0.5$ occurs at ~120°C, and a fully dehydrated and heavily disordered state is reached at ~250°C. Crystallization into orthorhombic V_2O_5 takes place at ~350°C. Cooling of materials with $p > 5$ leads to water expulsion *(15, 63)*, suggesting that no more than two unfrozen water molecule layers can remain. Reduced xerogels,

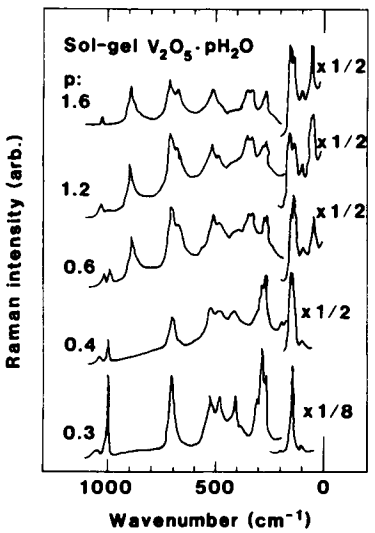

Fig. 18.9 Raman spectra for sol-gel-produced V pentoxide films with different degrees of hydration, given by the magnitude of p. The intensities are demagnified at low wavenumbers by the shown factors. From Abello et al. *(13)*.

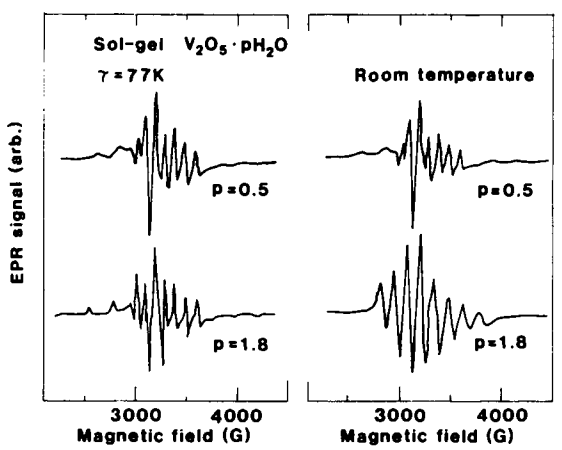

Fig. 18.10 EPR spectra at two temperatures τ for sol-gel-produced V pentoxide films with two degrees of hydration, given by the magnitude of p. From Barboux et al. *(263)* and Gharbi et al. *(1178)*.

with an appreciable amount of V^{4+} ions, have $p \approx 2.5$ at RH = 0.3, i.e., an enhanced degree of hydration *(209)*.

XRD data for V pentoxide gels were discussed above. X-ray absorption, apparent in EXAFS as well as XANES spectra for the vanadium *K*-edge, has been used to probe the local structure *(2456, 2995, 3249-51)*.

Vibrational spectroscopy has been used to elucidate the position, orientation, and bonding of water molecules in $V_2O_5 \cdot pH_2O$ *(13-4, 1831-2, 2890, 2993, 3510)*. Some additional information has been gained from dielectric relaxation measurements *(225)*. Figure 18.9 shows Raman spectra for samples with five magnitudes of p; the data are reproduced from Abello et al. *(13)* and Repelin et al. *(2890)*. The spectrum for $p \approx 0.3$ is similar to the one for a crystalline V_2O_5 film, illustrated before in Fig. 18.3. When p is increased, a new strong mode appears at ~890 cm^{-1}, and a mode at ~1030 cm^{-1} replaces the V=O vibration at ~1000 cm^{-1} in pure V_2O_5. The spectra can be interpreted as follows: at $p \approx 0.3$ the V_2O_5 layers are connected as in bulk crystals, and the water molecules are most likely trapped in cavities in the structure; at $p \approx 0.6$ the V_2O_5 units are no longer connected as in the bulk but the V atoms are linked to water molecules through $V\text{-}OH_2$ bonds; and at $0.6 < p < 1.6$ it seems that water with three different types of bonding is present. The role of water was further discussed in *(218)*.

The hydrated vanadium pentoxide gels always contain some V^{4+} ions that are easily detected by EPR. Figure 18.10, from Barboux et al. *(263)* and Gharbi et al. *(1178)*, shows spectra measured at 77 K (left-hand part) and at room temperature (right-hand part) for a xerogel layer with $p \approx 0.5$ (upper part) and $p \approx 1.8$ (lower part). The spectra can be reconciled with the spin Hamiltonian for an ion in an axially distorted ligand field *(2096, 2453, 2456, 2989)*, viz.

$$H = g_{\parallel}\beta H_z S_z + g_{\perp}\beta(H_x S_x + H_y S_y) + A_{\parallel} S_z I_z + A_{\perp}(S_x I_x + S_y I_y) \,. \tag{18.1}$$

This is Eq. 7.4 with additional terms representing hyperfine interaction. V^{4+} has S = 1/2 and I = 7/2. At low temperatures, the *g* tensor for the material with $p \approx 0.5$ is similar to that for crystalline V_2O_5 *(2990)*, whereas the hyperfine lines become sharper when $p \approx 1.8$, and the spectrum is then more akin to that of solvated $VO(H_2O)_5^{2+}$ ions *(251)*. Looking at the room temperature data, the spectrum for $p \approx 0.5$ is almost identical to the one recorded at 77K. The spectrum for $p \approx 1.8$, on the other hand, is now rather isotropic. This is due to a Brownian motion of paramagnetic species at the surface of the oxide. This kind of "molecular tumbling" becomes possible when there is enough water to allow the vanadyl ions to move in the interfoliar space *(1178)*.

It is of interest to look also at EPR spectra for reduced xerogels, i.e., materials containing a substantial fraction of the vanadium as V^{4+}. Such data are shown in Fig. 18.11, after Babonneau et al. *(209)*. At $V^{4+}/V \approx 0.01$, one recovers the curves for $p \approx 1.8$ in Fig. 18.10. However, the spectra are modified substantially when the V^{4+}/V ratio is increased up to 0.16 and, in particular, a broad signal centered at $g = 1.97$ is superimposed on the hyperfine spectrum as a consequence of the V^{4+} ions.

Spin-coating of an organic solution containing V_2O_5, benzyl alcohol, and isobutanol can be employed for making V pentoxide films *(2474, 3145-6)*. The appropriate solutions were transparent, which apparently makes them different from the precursors used in the sol-gel deposition discussed at length above. Crystallization of the spin-coated layers took place at ~300°C, as inferred from XRD. The spin coating technique has been extended to the fabrication of V_2O_5-TiO_2 films *(2475)*.

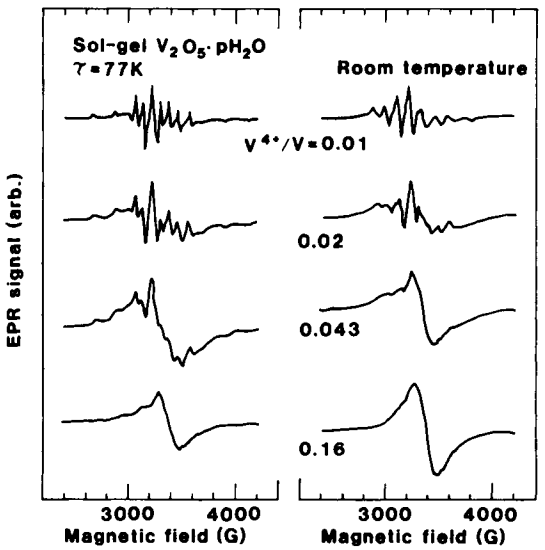

Fig. 18.11 EPR spectra at two temperatures τ for sol-gel-produced hydrated V pentoxide films. Data are shown for four magnitudes of the V^{4+}/V ratio. The degree of hydration (p value) increased from ~1.8 at low reduction to ~2.5 at high reduction. From Babonneau et al. *(209)*.

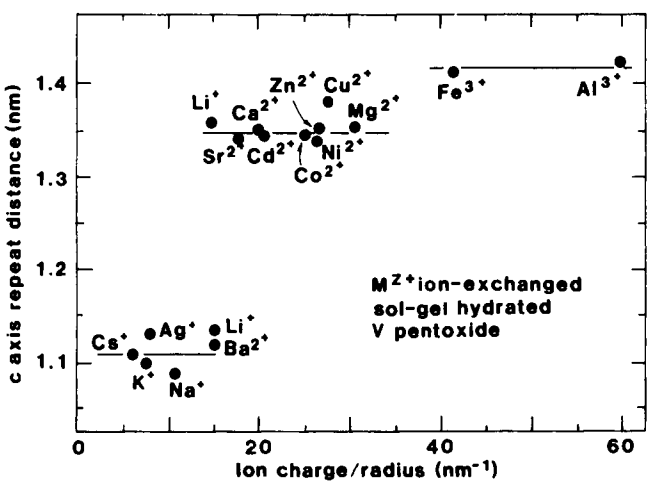

Fig. 18.12 Repeat distance in the *c* direction vs. ion charge/radius for sol-gel-produced ion-exchanged V pentoxide films. From Baffier et al. *(230)*.

Finally, one might note that V_2O_5-like surface layers can be produced on bulk V by thermal conversion. Specifically, an exposure to CO_2 laser beams in the presence of air allowed controlled oxidation *(527, 3492)*.

18.5 Ion Intercalation/deintercalation Reactions, Ion Exchange, and Diffusion Constants

The layered structure of V pentoxide films makes them well suited as hosts for ion intercalation/deintercalation even when they have good crystallinity. The mobile ions have been Li^+ in almost all cases for which electrochromism has been investigated. The pertinent ion intercalation/deintercalation reaction is then, as usual disregarding hydration,

$$VO_{2.5} + xLi^+ + xe^- \leftrightarrow Li_xVO_{2.5} . \tag{18.2}$$

Hydrated V pentoxide is readily modified via *ion exchange*, which makes it possible to alter the host material for ion intercalation/deintercalation in a suitable way. Ion exchange properties have been investigated in considerable detail for sol-gel-produced films, and it has been found that the one-dimensional layer stacking is preserved after the ion exchange, but that the *c* axis repeat distance can be changed in a characteristic way *(2093)*. A wide range of species can be intercalated, which makes hydrated V pentoxide in some respects similar to a smectic clay.

Metal ion insertion is considered first. The process is simple and involves immersion of a hydrated V pentoxide film in a suitable solution for a few minutes. Results have been presented for Li^+, Na^+, K^+, Rb^+, Cs^+, Ag^+, Mg^{2+}, Ca^{2+}, Sr^{2+}, Ba^{2+}, Mn^{2+}, Fe^{2+}, Co^{2+}, Ni^{2+}, Cu^{2+}, Zn^{2+}, Al^{3+}, and Fe^{3+} supplied from chlorides, bromides, iodides, sulfates, nitrates, and perchlorates *(213, 222-4, 226, 229-31, 462, 2617, 2731, 2735, 3820-1)*. The *c* axis repeat distance depends on the ionic species and is governed by a competition between the energy to separate the V_2O_5 layers and the solvation energy of the ion. It was argued by Baffier et al. *(230)* that the ratio between ionic charge and ionic radius would be a suitable parameter for illustrating the data, and Figure 18.12--taken from their work--shows that the *c* axis repeat distance is ~1.1 or ~1.35 nm depending on the ionic species. These separations correspond to a single or a double layer of interfoliar water molecules. Li^+ ions represent a limiting case, and either of the two separations is possible in hydrated films. Heating of the ion exchanged films to more than 350°C removes the water, and the ensuing films can be represented as $Na_{0.33}V_2O_5$, $K_{0.36}V_2O_5$, $Cs_{0.28}V_2O_5$, $Ag_{0.36}V_2O_5$ etc. *(229, 3820-1)*. Lithium intercalation/deintercalation is then possible for example according to

$$Na_{0.17}VO_{2.5} + xLi^+ + xe^- \leftrightarrow Li_xNa_{0.17}VO_{2.5} . \tag{18.3}$$

Organic solvents can be intercalated by replacing the interfoliar water. Many solvents, polar as well as non-polar, have been studied *(61, 131, 2043, 2339)*. Propylene carbonate has been investigated in detail, and it was shown *(61, 2043)* that the *c* axis repeat distance was 2.15 nm, corresponding to a double-layer intercalant. A large range of other molecular species have been inserted and one could note, for completeness, work on metalocenium ions *(64, 2627-8)*, alkylammonium and alkylamines *(461-2)*, ferrocenylalkylammonium halides *(2627-8)*,

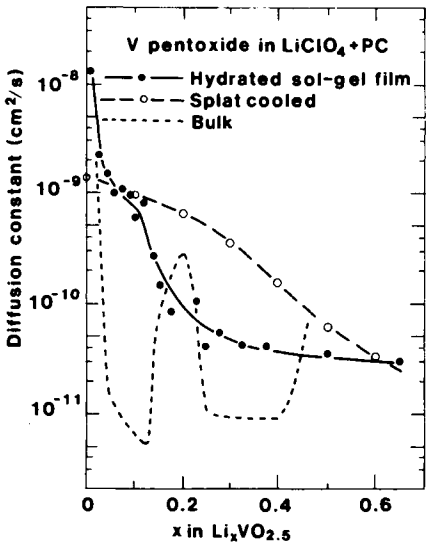

Fig. 18.13 Chemical diffusion constant for lithium ions in V-pentoxide-based materials immersed in 1 M $LiClO_4$ + PC. Data are given for a sol-gel-produced film composed of $V_2O_5 \cdot 1.6\ H_2O$, a splat-cooled glassy sample, and a V_2O_5 crystal. From Baddour et al. *(218)*, Farcy et al. *(1040)*, and Machida et al. *(2145-6)*.

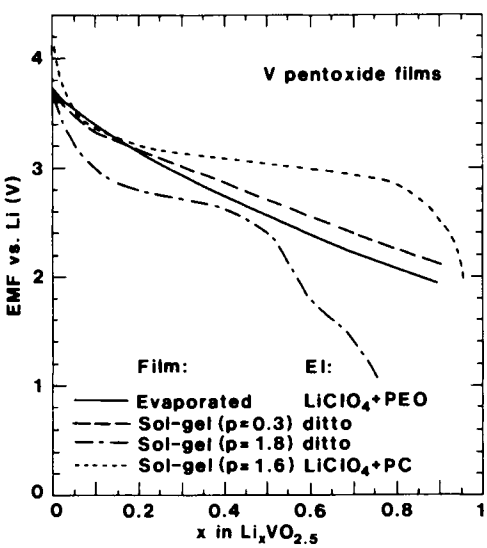

Fig. 18.14 Normalized EMF vs. lithium content, represented as x in $Li_xVO_{2.5}$, for V pentoxide films made by two techniques and immersed in two electrolytes (El.). The sol-gel-produced film has a nominal composition $V_2O_5 \cdot pH_2O$. After Baddour et al. *(217-8)*, Baudry et al. *(295-6)*, and Livage *(2092)*.

tetrathiafulvalene *(1019, 3508)*, benzidine *(1019, 2205)*, pyridine and pyrazine *(616, 2953)*, poly-aniline *(1732, 2088, 2337)*, poly-pyrrole *(3666)*, viologens *(1756, 2487)*, poly-thiophene *(1732a)*, poly-vinylpyrrolidone *(2087)*, poly-propyleneglycol *(2087)*, and tris-bipyridyl metal complexes *(2486)*. Glucose oxidase has been incorporated for biosensor applications *(1203)*. Pyridine can intercalate also powdered V_2O_5 *(3026)*.

Chemical diffusion constants for Li^+ intercalation have been evaluated with regard to films made by different techniques. For evaporated films, Julien et al. *(1707)* reported that D_{Li+} lay between 2 and 3 x 10^{-9} cm/s depending on the amount of ion intercalation. Figure 18.13 was obtained from work by Baddour et al. *(218)* who studied hydrated V pentoxide xerogel films, with a nominal composition $V_2O_5 \cdot 1.6\ H_2O$, immersed in an electrolyte of 1 M $LiClO_4$ + PC. D_{Li+} is ~10^{-8} cm^2/s at low intercalation. The diffusion constant drops with increasing intercalation and is less than 5 x 10^{-11} cm^2/s when x in $Li_xVO_{2.5}$ exceeds 0.3. Data for similar sol-gel-produced films were reported in *(217, 2338)*.

Dehydrated ion-exchanged sol-gel films of $Na_{0.33}V_2O_5$ were studied by Bach et al. *(213)*. D_{Li+} was similar to that for the hydrated disordered film when x was small; at larger Li^+ contents, D_{Li+} decreased rapidly and a value as low as ~10^{-13} cm^2/s was reported for x = 0.4. This difference between disordered sol-gel films and crystalline materials is similar to the one for birnessite Mn oxide films reported on in Fig. 16.2.

Concerning films made by other techniques, evaporated layers of V pentoxide had $D_{Li+} \approx 2$ x 10^{-12} cm^2/s at room temperature and showed a thermally activated behavior similar to the one for W oxide films *(295-6)*. A sputter-deposited film had $D_{Li+} \approx 10^{-13}$ cm^2/s *(1813)*, and $10^{-11} < D_{Li+} < 10^{-10}$ cm^2/s was reported for electrodeposited films *(2810)*. Films made by evaporation of a mixture of V_2O_5 and P_2O_2 had $D_{Ag+} \approx 10^{-15}$ cm^2/s *(1693)*.

There are several studies on lithium diffusion in bulk-like materials based on V pentoxide. Figure 18.13 shows data from Machida et al. *(2145-6)* on splat-cooled glassy samples. Their D_{Li+}s are similar to those for the hydrated sol-gel-produced film, to within an order of magnitude. Splat-cooled V_2O_5-P_2O_5 had $10^{-9} < D_{Li+} < 10^{-8}$ cm^2/s *(2974)*. Data for crystalline V_2O_5, reproduced from Farcy et al. *(1040)*, are given by the dotted curve in Fig. 18.13. D_{Li+} varies between a value larger than 10^{-9} cm^2/s and ~5 x 10^{-12} cm^2/s depending on the composition. Other data for Li diffusion in crystalline V_2O_5 were given in *(3441, 3780)*. V_6O_{13} had $10^{-9} < D_{Li+} < 10^{-8}$ cm^2/s *(3227, 3609)*, and similar or somewhat larger diffusion constants were reported for $Li_{1+y}V_3O_8$ and $Na_{1+y}V_3O_8$ *(2712, 2769-70, 3431)*. Measurements at 95°C gave $10^{-8} < D_{Na+} < 10^{-7}$ cm^2/s for V_6O_{13} *(2430-1)*.

18.6 Ion Intercalation/deintercalation Studied by Electrochemical Techniques

Vanadium pentoxide films have been studied in considerable detail by use of electrochemical techniques. This section presents data from EMF measurements, chronoamperometry, cyclic voltammetry, and beam deflectometry.

EMF data for Li^+ intercalation have been reported several times. Rather different data have been given depending on the nature of the film and the electrolyte. Figure 18.14 illustrates results for evaporated and sol-gel-produced films in electrolytes with $LiClO_4$ in poly-ethylene oxide (PEO) or in PC. The solid curve represents data by Baudry et al. *(295-6)* for an evaporated film in contact with an amorphous $LiClO_4$ + PEO electrolyte at 80°C. The EMF falls off for increasing

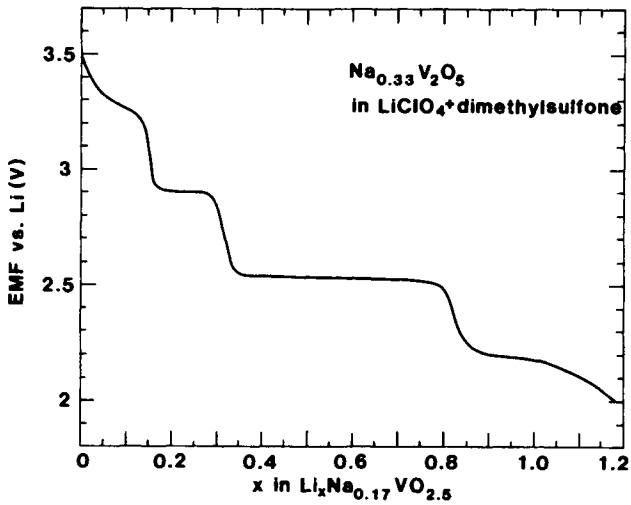

Fig. 18.15 Normalized EMF vs. lithium content for a sodium-exchanged V pentoxide film made by sol-gel technology. From Bach et al. *(213)* and Pereira-Ramos et al. *(2735)*.

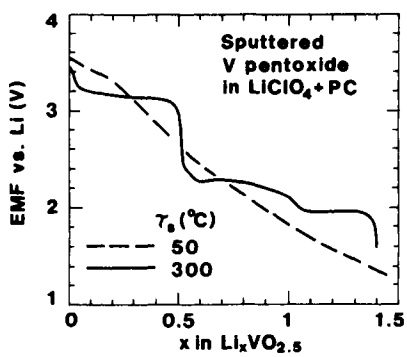

Fig. 18.16 Normalized EMF vs. lithium content, represented as x in $Li_xVO_{2.5}$, for V pentoxide films made by reactive sputtering onto substrates at two temperatures τ_s. After Talledo *(3352)*.

intercalation in much the same way as for a glassy material made by splat cooling (cf. Fig. 18.1).

For hydrated sol-gel-produced films, the EMF depends on the amount of hydration, i.e., on the value of p in $V_2O_5 \cdot pH_2O$. Data for films with $p \approx 0.3$ and $p \approx 1.8$ immersed in a $LiClO_4$ + PEO electrolyte are given in Fig. 18.14, from Livage *(2092)*. At low hydration, the EMF function is similar to the one for the evaporated film, which is the expected result. However, at $p \approx 1.8$ the EMF decreases in steps during the intercalation, which is indicative of a somewhat crystalline state (cf. Fig. 18.1). Sol-gel-produced films in electrolytes capable of ion insertion by replacing interfoliar water have somewhat modified EMFs. This is shown by the dotted curve in Fig. 18.14, obtained from work by Baddour et al. *(217-8)* and Pereira-Ramos et al. *(2731)* who used an electrolyte of $LiClO_4$ + PC. The EMF is enhanced and lies above 2.5 V vs. Li up to a Li/V ratio of 0.9. Additional results are available elsewhere for the EMF during Li^+ intercalation/deintercalation in sol-gel-produced and electrodeposited films *(108-9, 131, 2323-4, 2331, 2334, 2336, 2338-9, 2456)*.

It was mentioned before that sol-gel-produced films could be ion exchanged in a NaCl solution and then dehydrated by heating, so that a film of $Na_{0.33}V_2O_5$ was obtained. Figure 18.15 shows EMF during Li^+ intercalation into such a film, after Bach et al. *(213)* and Pereira-Ramos et al. *(2735)*. The EMF drops in a series of steps.

Sputter-deposited V pentoxide films were studied recently *(3352, 3612, 3616)*. Talledo *(3352)* used dc magnetron sputtering of V in Ar + 12 % O_2 onto substrates at ~50°C and 300°C. The rate was below 0.1 nm/s. Figure 18.16 shows the EMF during Li^+ intercalation from a $LiClO_4$ + PC electrolyte into ~0.1-μm-thick films. At $\tau_s \approx 50$°C, the EMF drops monotonically in about the same way as for evaporated films and for "dry" sol-gel-produced films (cf. Fig. 18.14). Clearly these films are heavily disordered. At $\tau_s = 300$°C, the EMF goes down sharply at the compositions LiV_2O_5 and $Li_2V_2O_5$. A large change at a Li/V ratio of ~0.5 was found for bulk samples with different crystalline phases (cf. Fig. 18.1).

Vanadium oxide films were also made by West et al. *(3612, 3616)*, who used reactive rf sputtering from a V_2O_5 powder target in Ar + O_2. The rate was between 0.1 and 1 nm/s depending on the O_2 content. Figure 18.17 shows the EMF when Li^+ was intercalated from a $LiCF_3SO_3$ + PEO electrolyte into films that were several micrometer in thickness. These films had an average grain size of 3 to 5 nm. The EMF was found to depend on the amount of O_2 in the sputter plasma. When pure O_2 was used, the data are indicative of near-stoichiometric V_2O_5, whereas the lowered EMFs when less O_2 was present probably are associated with oxygen deficiency in the films.

Chronoamperometry was used by Kobayashi et al. *(1858)* to study ion intercalation/deintercalation in evaporated V pentoxide films. Figure 18.18 shows the current density as a function of applied voltage and time during Na^+ intercalation from a $NaClO_4$ electrolyte. The current density follows approximately a relation $J_i \propto t^{-1/2}$, which is the time evolution expected for interface-controlled ion intercalation (cf. Eq. 6.6). During deintercalation, Fig. 18.19 shows that the current density obeys approximately $J_d \propto t^{-3/4}$ up to a certain limiting time. This is typical for space charge limited ion flow (cf. Eq. 6.7). There is a noteworthy similarity among the chronoamperometry data for V pentoxide and W oxide.

Cyclic voltammetry is considered next. The information gained from this technique is, to a large extent, similar to the one obtained from EMF measurements and discussed in detail above. Therefore the treatment of cyclic voltammetry is rather brief here.

Talledo *(3352)* recorded cyclic voltammograms for sputter-deposited pentoxide films. Figure 18.20 illustrates data for a 0.1-μm-thick film made by deposition at $\tau_s = 50$°C. The first

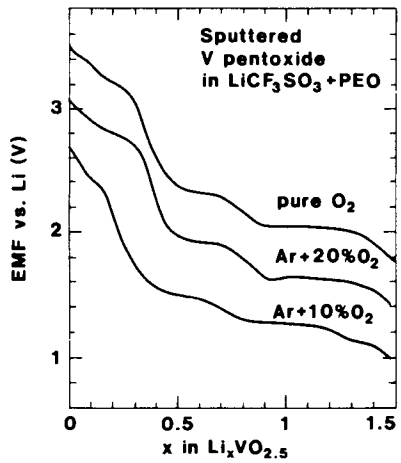

Fig. 18.17 Normalized EMF vs. lithium content, represented as x in $Li_xVO_{2.5}$, for V pentoxide films made by reactive sputtering in different mixtures of Ar and O_2. From West et al. *(3612, 3616)*.

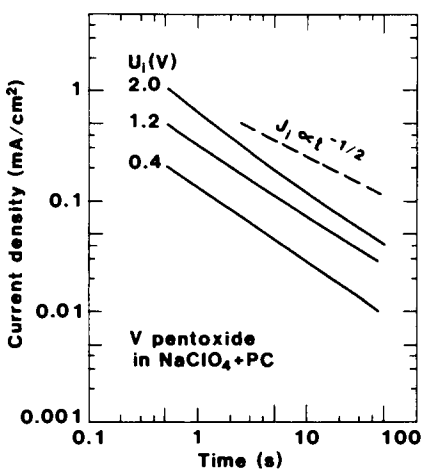

Fig. 18.18 Current density vs. time for Na^+ intercalation into evaporated V pentoxide films. Data are shown for different intercalation voltages U_i. Dashed line indicates the time dependence inherent in Eq. 6.6. From Kobayashi et al. *(1858)*.

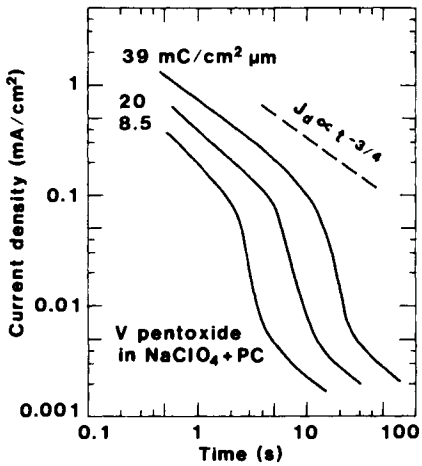

Fig. 18.19 Current density vs. time for Na^+ deintercalation from evaporated V pentoxide films initially containing the shown charge densities. Dashed line indicates the time dependence inherent in Eq. 6.7. From Kobayashi et al. *(1858)*.

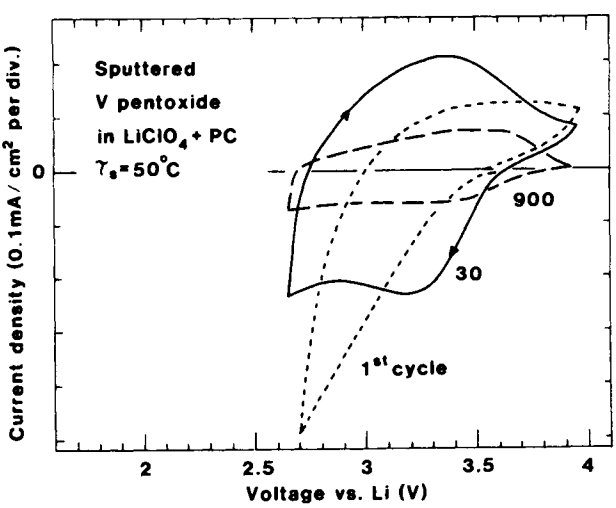

Fig. 18.20 Cyclic voltammograms for Li^+ intercalation/deintercalation in a V pentoxide film in 1 M $LiClO_4$ + PC. The film was sputter-deposited onto a substrate at τ_s. Data are given for different numbers of voltammetric cycles. The voltage scan rate was 20 mV/s. Arrows denote scan direction. After Talledo *(3352)*.

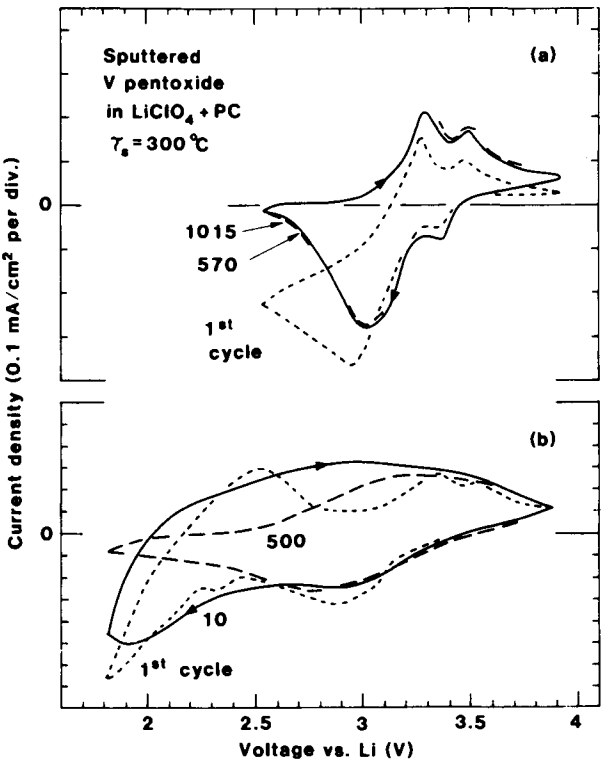

Fig. 18.21 Cyclic voltammograms for Li^+ intercalation/deintercalation in V pentoxide films in 1 M $LiClO_4$ + PC. The films were sputter-deposited onto substrates at τ_s. Data in parts (a) and (b) refer to different voltage ranges and different numbers of voltammetric cycles. The voltage scan rate was 20 mV/s. Arrows denote scan direction. After Talledo *(3352)*.

voltammetric cycle shows current insertion/extraction similar to that of strongly disordered W oxide (cf. Figs. 6.12 to 6.15). The voltammograms evolved during continued sweeps, as apparent from the solid and dashed curves in Fig. 18.20. After 300 cycles, the voltammogram was very similar to the one after 30 cycles, but after 900 cycles the current density had dropped significantly, showing that degradation took place during prolonged intercalation/ deintercalation cycling.

Figure 18.21 shows corresponding data for a more crystalline 0.1-μm-thick film made at τ_s = 300°C. Part (a) refers to voltage sweeps between ~2.6 and 3.9 V vs. Li, which is the same range as for the more disordered film made at τ_s = 50°C. Again the voltammograms evolved during the initial cycling, but no long-term degradation was noted at least up to ~1000 cycles, as apparent from the similarity between the solid and dashed curves in Fig. 18.21(a). Cyclic voltammograms were also recorded for the same voltage range in work by Cogan et al. *(723, 726-7, 2854)*; their voltammograms were almost identical to those shown in Fig. 18.21(a), and durability was verified for up to 7500 cycles. Cyclic voltammograms for sputter-deposited films can also be found in *(96-9, 3353, 3664)*.

Long term durability prevails only if the voltage sweep is confined to a "safe" range. This point is illustrated in Fig. 18.21(b), showing voltammograms for 1.8 to 3.9 V vs. Li. The voltammogram was significantly changed after 500 cycles and became similar to that of the disordered material reported on in Fig. 18.20. It is interesting to note that a voltammogram measured for a sol-gel-produced hydrated V pentoxide film looked almost identical to the dashed curve in Fig. 18.21(b) *(2731)*.

Figure 18.22 shows cyclic voltammograms for V pentoxide films made by spin coating with a solution prepared from V_2O_5, benzyl alcohol, and isobutanol; the data were reproduced from work by Shimizu et al. *(2474, 3145-6)*. A film annealed at τ_a = 400°C served as a good host for Li^+ intercalation/deintercalation, and the voltammogram is similar to the solid and dashed curves for a sputter-deposited film in Fig. 18.21(a). Annealing at 250°C, on the other hand, was apparently too low for establishing a structure suitable for Li^+ intercalation.

Apart from in the work referred to so far, voltammograms are available for other V pentoxide films produced by evaporation *(295-6, 734)*, electrodeposition *(549, 3750)*, and sol-gel technology *(1907, 2331, 2453, 2456)*. Voltammograms for $Na_{0.33}V_2O_5$ were given in *(213, 2735)* and for V_2O_5-TiO_2 in *(2475)*.

Regarding *beam deflectometry*, Scarminio et al. *(3036)* studied the mechanical stress that evolved upon Li^+ intercalation into sputter-deposited V pentoxide films. The stress level showed a one-to-one correspondence to variations of the lattice parameter *c* and to changes in the EMF.

18.7 Ion Intercalation/deintercalation Studied by Physical Techniques

SIMS measurements were used to unambiguously document ion intercalation in evaporated V pentoxide films that had undergone treatment in $LiClO_4$ + PC *(295-6, 1118)*. Figure 18.23, from Fujita et al. *(1118)*, shows that Li^+ could be intercalated and deintercalated. These films displayed electrochromism. Some lithium remained in the deintercalated state, which is consistent with data for W oxide films (cf. Fig. 7.2). Analogous results were recorded by Kobayashi et al. *(1858)* for Na^+ intercalation/deintercalation.

XRD was employed to determine the crystallographic *c* parameter--i.e., the interlayer separation--during Li^+ intercalation in sputter-deposited V pentoxide films. Data from Talledo

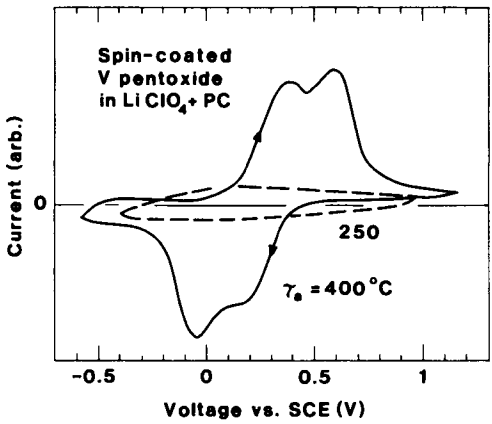

Fig. 18.22 Cyclic voltammograms for Li^+ intercalation/deintercalation in spin-coated V pentoxide in 1 M $LiClO_4$ + PC. The films were annealed at two different temperatures τ_a. The voltage scan rate was 50 mV/s. Arrows denote scan direction. From Shimizu et al. *(3145-6)*.

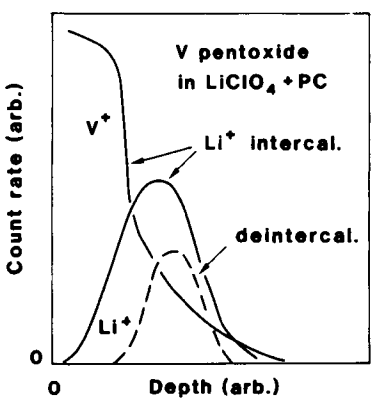

Fig. 18.23 Depth profiles for Li^+ and V^+ determined by SIMS. Data are shown for an evaporated V pentoxide film in Li^+ intercalated and deintercalated states. After Fujita et al. *(1118)*.

(3352) are shown in Fig. 18.24; they were recorded for ~0.6-μm-thick films deposited at $\tau_s \approx$ 300°C. Results for unintercalated films were consistent with those shown before in Fig. 18.5. The interlayer separation grows approximately linearly with the amount of Li^+ intercalation for $x < 0.5$ in $Li_xVO_{2.5}$. At higher Li^+ densities, it seems that another linear variation takes place up to $x \approx 1$. The crystallographic *a* parameter varied in a non-monotonic manner and shrank for $x < 0.5$ *(3352)*.

Electrodeposited films were similarly analyzed under Li^+ intercalation by Andrukaitis et al. *(109)* and Ptitsyn et al. *(2810-1)*. Fig. 18.24 shows that the *c* axis lattice expansion is very similar to that of sputter-deposited films, at least for $x < 0.5$. Consistent data were found for electrodeposited films with Li^+ inserted chemically, rather than electrochemically *(2810-1)*.

It is interesting to compare the thin film data in Fig. 18.24 with similar results for powder samples having well specified crystalline phases (cf. Fig. 18.2). Bulk-like specimens showed abrupt changes in the interlayer distance for $0 < x < 0.5$ depending on whether the α, ε, or δ phase was present. The films, on the other hand, showed a smooth variation. A reasonable explanation is that the films are disordered with crystallites being predominantly--but in no way exclusively--of α, ε, and δ type when the Li^+ intercalation is increased.

For sol-gel-produced films, the behavior under ion intercalation is different from that of the earlier discussed films as a consequence of the presence of interfoliar water molecules. Sol-gel films were studied in $LiClO_4$ + PC electrolytes by Araki et al. *(131)*, Baddour et al. *(218)*, and Miura et al. *(2331, 2336)*. The propylene carbonate intercalates first and forms a double layer so that the *c* axis repeat distance is 2.15 nm, as discussed in Sec. 18.5 above. XRD spectra for such films display a well-defined *00l* series. When Li^+ is intercalated electrochemically, the XRD signature is changed, and a competing *00l′* series appears at $x \approx 0.1$ *(131, 218)*. This feature is illustrated in Fig. 18.25, after Baddour et al. *(218)*. The *00l′* series dominates entirely at $x > 0.1$. These XRD spectra are consistent with a precipitous shrinkage of the *c* axis repeat distance even at fairly low levels of Li^+ intercalation, and the broad peaks at $x = 0.75$ indicate disorder in the material. Figure 18.26, based on an evaluation of XRD data taken by Araki et al. *(131)*, shows that the *c* axis repeat distance is less than 1.05 nm at $x > 0.2$. Sol-gel-produced films immersed in $LiClO_4$ + PC were also studied by Miura et al. *(2331, 2336)*, who found different behavior with a *c* axis repeat distance less than 1.2 nm irrespective of the Li^+ content. Sol-gel-produced films that were chemically lithiated by immersion in a solution of LiI and acetonitrile had a maximum *c* axis repeat distance of ~1.4 nm at $x \approx 0.1$ and showed a decrease of this distance at higher intercalation levels *(2335)*.

EPR was used by Nabavi et al. *(2453)* to characterize hydrated V pentoxide films made through sol-gel technology. Figure 18.27 refers to a film in as-prepared state and after electrochemical Li^+ intercalation from a $LiClO_4$ + PC electrolyte. In the initial state, the EPR spectrum was analogous to the one shown before in Figs. 18.10 and 18.11. Li^+ intercalation yielded a new EPR signal superimposed on the original one. The new signal corresponded to a single line, about 300 G in width and centered at $g = 1.96$, which grew in intensity upon Li^+ intercalation. This feature is typical for localized V^{4+} ions with exchange magnetic interaction between paramagnetic neighbors *(2453)*. Thus the electrons that are expected to be introduced along with the Li^+ ions are localized on vanadium sites and change their valency from 5+ to 4+.

Core level XPS spectra have been measured for Li^+ intercalated V pentoxide films prepared by evaporation *(745-6, 1118)* and electrodeposition *(109)*. Figure 18.28 shows results for the latter type of samples, as reported by Andrukaitis et al. *(109)*. The unintercalated film displayed a

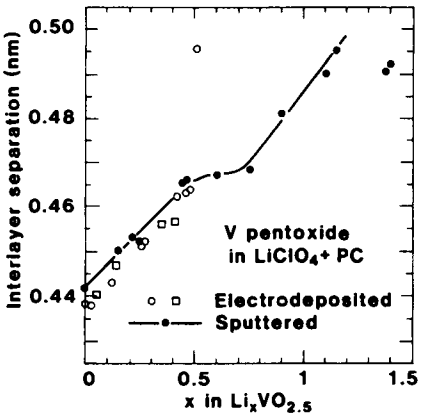

Fig. 18.24 Interlayer separation (crystallographic *c* parameter) for V-pentoxide-based films prepared by sputter-deposition and electrodeposition. Lithium was intercalated from $LiClO_4$ + PC electrolytes. Symbols denote experimental data, and the curve was drawn for convenience in order to represent the results for the sputter-deposited films. From Andrukaitis et al. *(109)* (open circles), Ptitsyn et al. *(2811)* (open squares), and Talledo *(3352)* (filled circles).

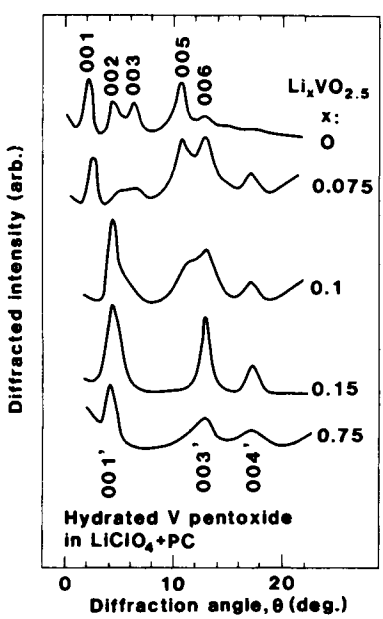

Fig. 18.25 X-ray diffractograms for sol-gel-produced hydrated V-pentoxide-based films in 1 M $LiClO_4$ + PC. The lithium content is given as x in $Li_xVO_{2.5}$. The diffraction peaks belong to two series, denoted *00l* and *00l'*. After Baddour et al. *(218)*.

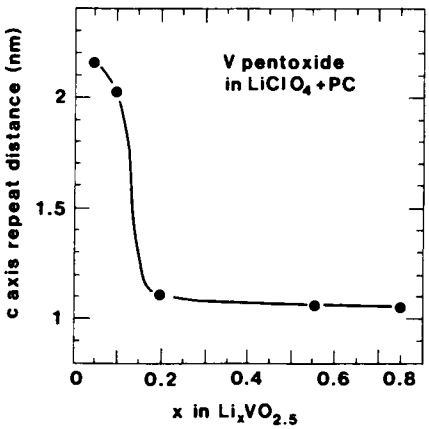

Fig. 18.26 *c* axis repeat distance for sol-gel-produced V pentoxide films electrochemically treated in a 1 M $LiClO_4$ + PC electrolyte so that the lithium content was x in $Li_xVO_{2.5}$. Filled circles represent data by Araki et al. *(131)*, and the curve was drawn for convenience. After an evaluation by Miura et al. *(2336)*.

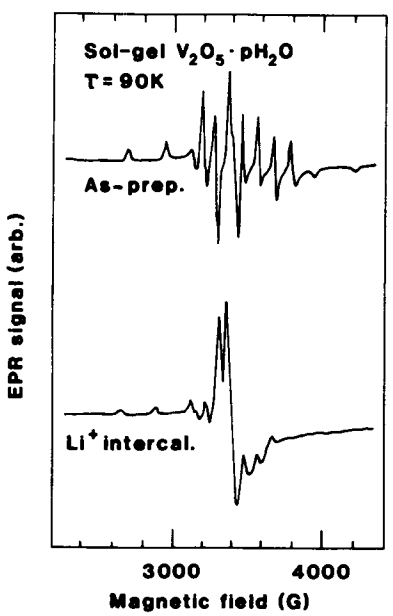

Fig. 18.27 EPR spectrum measured at 90 K for a sol-gel-produced hydrated V pentoxide film in as-prepared state and after lithium intercalation from a 1 M $LiClO_4$ + PC electrolyte. From Nabavi et al. *(2453)*.

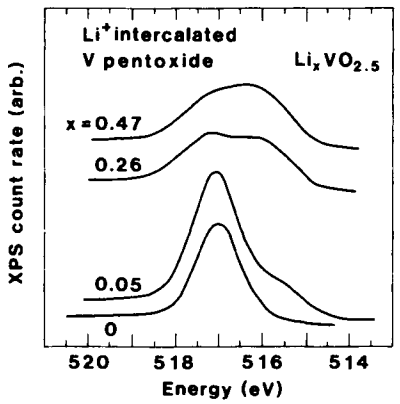

Fig. 18.28 XPS count rate vs. binding energy for $V2p_{3/2}$ electrons in electrodeposited V pentoxide films lithium intercalated from a 1 M $LiClO_4$ + PC electrolyte to the levels represented as x in $Li_xVO_{2.5}$. From Andrukaitis et al. *(109)*.

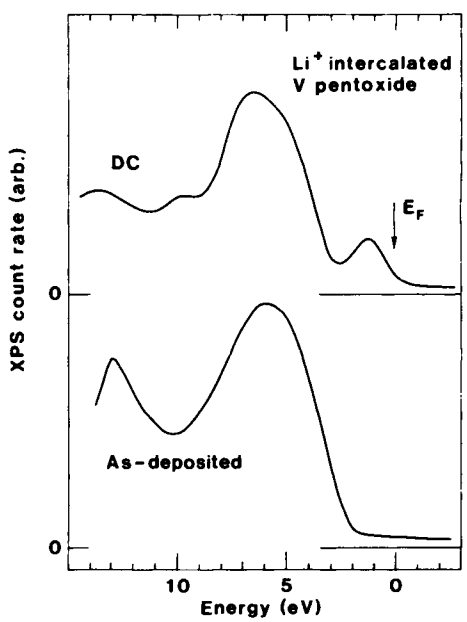

Fig. 18.29 XPS count rate vs. binding energy for valence and conduction electrons in a V pentoxide film in as-deposited state and after lithium intercalation from a LiCl-containing electrolyte until a dark colored DC state was present. The data were smoothed. Arrow denotes the Fermi energy E_F. From Colton et al. *(745-6)*.

peak centered at ~517 eV which is due to $V2p_{3/2}$. When Li^+ was intercalated from a $LiClO_4$ + PC electrolyte, the curve shape changed and a second peak at about ~516 eV grew in proportion with the amount of lithium. When x in $Li_xVO_{2.5}$ was ~0.3, the two peaks were of similar magnitude. It is known from the literature that the binding energy for $V2p_{3/2}$ electrons is 516.6 to 517.5 eV in crystalline V_2O_5, whereas the corresponding energy is 515.7 to 516.0 eV for VO_2 *(4, 745-6, 1118, 1337, 2014, 2282, 2512-3, 3032, 3557)*. Hence the data in Fig. 18.28 can be interpreted on the premise that the Li^+ intercalation is accompanied by a transformation from V^{5+} to V^{4+}, i.e., one finds the same result as the one reached above from EPR.

XPS spectra for valence and conduction bands were reported by Colton et al. *(745-6)*, who studied evaporated V pentoxide films in an electrolyte of LiCl and methanol. Data are shown in Fig. 18.29 for a film in as-deposited state and after Li^+ intercalation to a dark colored state. The as-deposited film showed a peak at a binding energy of 6 eV, which is mainly due to *O2p* electrons. Li^+ intercalation gave rise to a peak about 1.5 eV below the Fermi level. This feature is ascribed to electrons populating the lower part of the conduction band derived mainly from *V3d* orbitals. The peaks at higher energies in Fig. 18.29 are probably due to contamination. The main features of the XPS data are consistent with electron insertion in a material whose electronic structure corresponds to that of V_2O_5, as obtained from cluster calculations *(1647, 2020)*, a tight-binding scheme *(1067, 1997-2000)*, and combinations of atomic orbitals *(519, 2708)*. XPS applied to valence and conduction bands gives results that are analogous to those for W oxide (Fig. 7.20) and Mo oxide (Fig.12.6).

18.8 Optical Properties of As-prepared Films

The optical properties of V-pentoxide-based films are qualitatively different from those of the oxides considered thus far in that bandstructure effects play an important role in the luminous range, where they offer possibilities such as multicolor electrochromism. Therefore it is not meaningful to treat absorption around the optical bandgap separately from the luminous properties, as done in the earlier chapters. Instead a comprehensive discussion of the optical properties of as-prepared films will be given first; it is then followed by a corresponding exposition of the properties of ion intercalated films.

Figure 18.30 gives an overview of the optical absorption in the $0.5 < \hbar\omega < 5$ eV range for V pentoxide films made by three different techniques. Specifically, the data pertain to an evaporated vanadium film converted to oxide by heating in O_2 at $\tau_a \approx 300°C$ *(750)*, a film made by reactive rf sputtering of vanadium in Ar + 25% O_2 *(1411)*, and a sol-gel-produced hydrated film *(522)*. The spectra show a fair degree of consistency and the following three features will be discussed below:

(i) an absorption for blue light and in the ultraviolet, showing a peak at ~3 eV,

(ii) a strong variation of the absorption in the $2 < \hbar\omega < 3$ eV range, signifying the optical bandgap, and

(iii) an absorption peak at energies below 1 eV, whose magnitude depends on the density of V^{4+} ions.

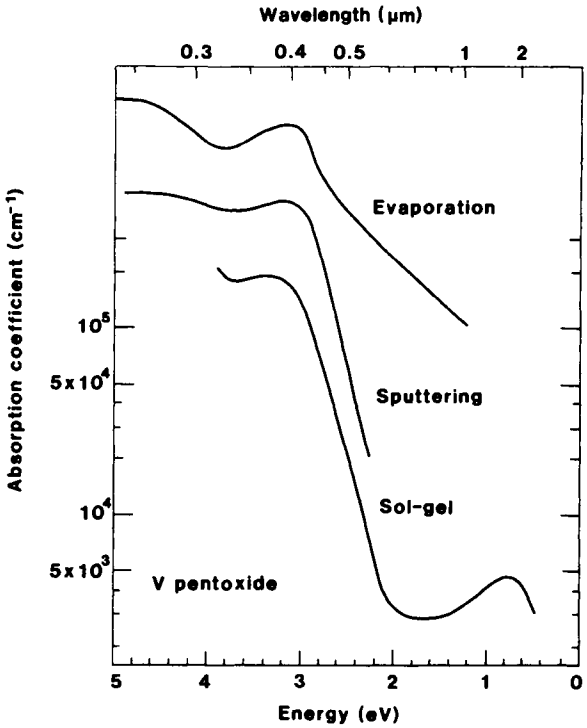

Fig. 18.30 Spectral absorption coefficient for V pentoxide films made by three different techniques. The vertical scale pertains to the sol-gel-produced film. The other two curves show the relative absorption coefficient. From Bullot et al. *(522)*, Conlon and Doyle *(750)*, and Hansen and Aita *(1411)*.

The absorption peak at ~3 eV and the onset of absorption above 4 eV are related to the bandstructure of V_2O_5. As stressed by Parker et al. *(2708)*, the material is basically a wide-bandgap semiconductor with a direct bandgap of ~3.3 eV, but within this gap there is a split-off localized band lying ~0.6 eV below the (main) conduction band. Indirect transitions are possible across a band of about 2 eV. The split-off band was found also by Bullett *(519)* and Lambrecht et al. *(1999)*, and it was argued that its origin was to be found in subtle effects concerning V-V interaction mediated by an oxygen atom.

The optical bandgap should be derivable from Eq. 8.3 with $\eta = 2$. This value of η is expected both from the fact that the V pentoxide films are disordered, so that non-conservation of wavevectors can prevail, and because the bandgap is of indirect-allowed character. Figure 18.31 is a plot of $(a\hbar\omega)^{1/2}$ vs. $\hbar\omega$ for a sol-gel-produced film analogous to the one reported on in Fig. 18.30 *(522)*. The linear graph in Fig. 18.31 shows that, indeed, one finds $\eta = 2$. An extrapolation towards zero absorption gives $E_g = 2.25 \pm 0.02$ eV. The curve was obtained for a sample with $V^{4+}/V = 0.097$, but it was found that E_g was not influenced by the degree of reduction. The middle curve in Fig. 18.30 indicates that a similar bandgap was found for a sputter-deposited film; specifically, it was reported that such films had $E_g \approx 2.2$ eV *(41, 44, 723, 726-7, 734, 1411, 2854)*. The same bandgap was stated for an evaporated film *(1151)*. A sputter-deposited film annealed at 280°C, which is too low to cause crystallization, had $E_g = 2.34$ eV *(2110)*. Optical bandgaps similar to those reported above can also be estimated from spectral transmittance and absorptance curves for other films made by evaporation *(745-6, 1118, 1148, 1858-9, 2748)*, sputtering *(165, 3352-4, 3664)*, electrodeposition *(3750-1)*, and sol-gel technology *(1907)*. One thus concludes that an optical bandgap of ~2.2 eV is obtained quite generally, irrespectively of the technique for thin film manufacturing. Data for bulk crystals of V_2O_5 are not directly comparable since they showed bandgaps that depended critically on the orientation of the sample and on the polarization state for the light *(1477, 1778, 2372, 2708)*.

Figure 18.32 explores the absorption in the $2 < \hbar\omega < 2.5$ eV range for a hydrated V pentoxide film made by sol-gel technology. The data, from Bullot et al. *(522)*, are consistent with a logarithmic bandedge (i.e., an Urbach tail) according to Eq. 8.5. The slope of the curve depends on the V^{4+}/V ratio. The results were found to agree with predictions from a theory by Miller and Abrahams *(2314)* based on potential disorder arising from non-stoichiometry.

Figure 18.33 illustrates absorption in the range well below E_g for hydrated V pentoxide films with $0.023 < V^{4+}/V < 0.097$ and thicknesses between 3.9 and 5.5 μm *(522)*. A broad peak is seen in the infrared wavelength range; similar data were also reported in *(209)*. One could note that absorption features have been seen at $\hbar\omega < E_g$ in single crystals of V_2O_5; this absorption was ascribed to oxygen vacancies, dopants, and bandstructure effects *(713-4, 2373, 3486)*.

It is apparent from Fig. 18.33 that the intensity of the absorptance band, peaked at E_p, goes up when the V^{4+} fraction is increased. Figure 18.34 shows that the absorption coefficient at E_p is proportional to the V^{4+}/V ratio. This correlation is in principle in agreement with the EPR data for W-oxide-based films in Fig. 10.1.

The refractive index of evaporated V pentoxide films was studied by Michailovits et al. *(2306)* who found a smooth variation from ~2.1 at $\lambda = 0.6$ μm to 1.87 at $\lambda = 2.4$ μm. An anodic, and presumably denser, film had $n \approx 2.3$ at $\lambda = 0.633$ μm *(2640-1)*. Aerogel layers expectedly have a low refractive index *(1494)*.

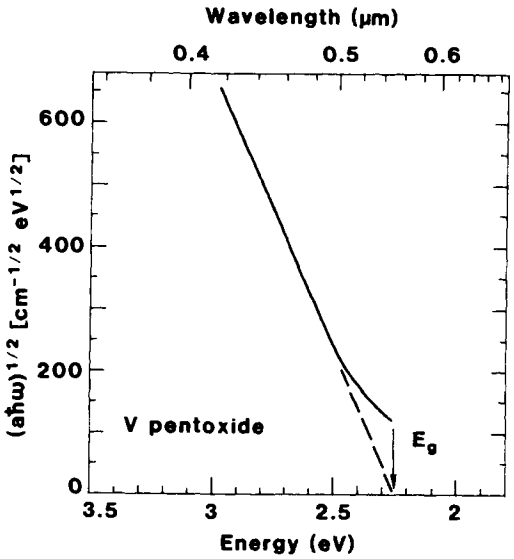

Fig. 18.31 $(\alpha\hbar\omega)^{1/2}$ vs. energy for a hydrated V pentoxide film produced by sol-gel technology. Dashed line indicates an extrapolation for determining the bandgap E_g. After Bullot et al. *(522)*.

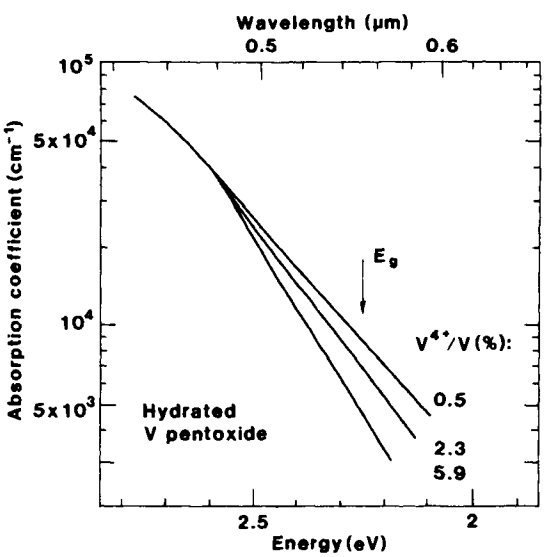

Fig. 18.32 Absorption coefficient vs. energy for hydrated V pentoxide films produced by sol-gel technology so that different values of the V^{4+}/V ratio were obtained. The bandgap E_g is indicated by the arrow. After Bullot et al. *(522)*.

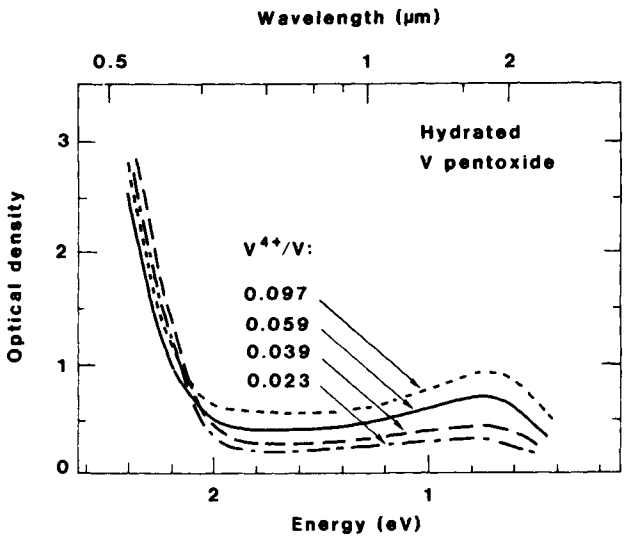

Fig. 18.33 Spectral optical density for hydrated V pentoxide films produced by sol-gel technology so that different values of the V^{4+}/V ratio were obtained. The data were not corrected for reflectance from the film. After Bullot et al. *(522)*.

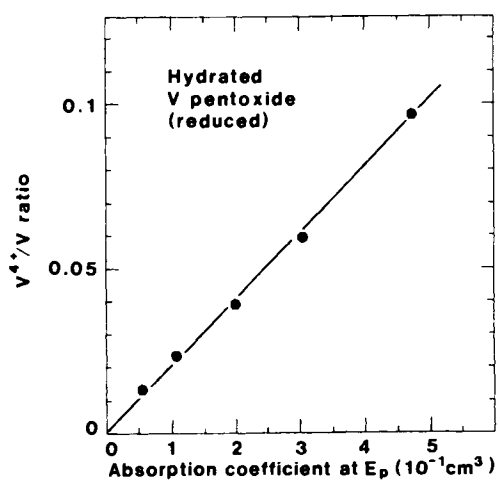

Fig. 18.34 V^{4+}/V ratio vs. absorption coefficient at the peak of the optical absorption band for hydrated V pentoxide films produced by sol-gel technology so that different levels of reduction were obtained. Dots indicate measured data, and the line was drawn for convenience. After Bullot et al. *(522)*.

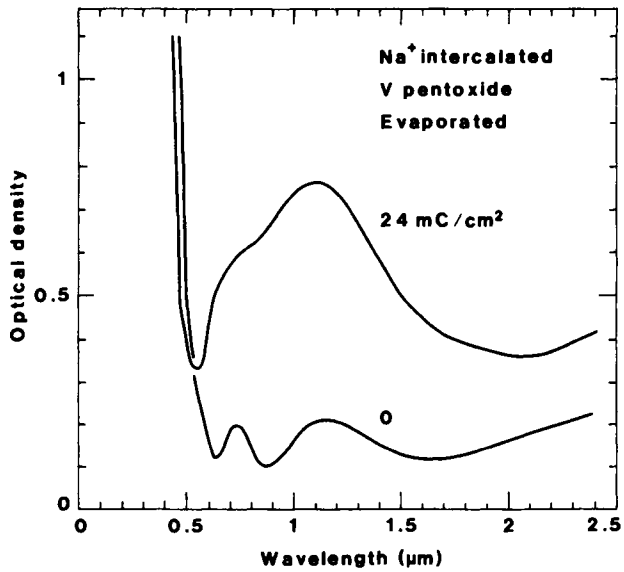

Fig. 18.35 Spectral optical density for an evaporated V pentoxide film in an electrolyte of $NaClO_4$ + PC. The curves refer to two different densities of inserted charge. From Kobayashi et al. *(1858)*.

18.9 Optical Properties of Ion Intercalated Films, and Coloration Efficiency

Ion intercalation into V pentoxide films causes electrochromism. The first reports were by Gavrilyuk and Chudnovskii *(1144)* who investigated films made by evaporation onto substates at 150 to 200°C, and by Witzke and Deb *(3646)* who studied sputter-deposited films. The former films were immersed in distilled water or in aqueous solutions of Li salts. When a voltage was applied to the film, its color changed from yellow, via green and blue, to black, This coloration was reversible. The possibility of obtaining states of different color is a feature specific to V pentoxide; it may be an advantage or disadvantage depending on the intended applications. The perceived color is dominated by absorption in the V pentoxide, but the film thickness can cause color changes due to optical interference.

Electrochromism has been discussed several times for evaporated V pentoxide films. The intercalated ions have been H^+ *(1144)*, Li^+ *(734, 745-6, 1118, 1144, 3014-5)*, and Na^+ *(1858-9)*. Figure 18.35, from Kobayashi et al. *(1858)*, shows spectral optical density for a film in an electrolyte of 1 M $NaClO_4$ + PC. Ion intercalation produces several effects, viz.

(i) an apparent bandgap widening, i.e., the absorptance is decreased in the blue end of the spectrum,

(ii) growth of an absorption peak (or peaks) in the near-infrared, and

(iii) an enhancement of the overall absorptance level at $\lambda > 0.5$ μm.

The thin film deposition parameters determine the degrees to which (i) to (iii) show up in different samples. Thus the near-infrared absorption band was much more apparent at $\tau_s = 200$°C than at $\tau_s = 140$°C *(1859)*. It took 1 to 2 minutes to color and bleach a 0.13-μm-thick film in $LiClO_4$ + PC, and the open circuit memory exceeded one day *(1118)*.

Sputter-deposited films, treated in electrolytes of $LiClO_4$ + PC, are considered next *(96-9, 165-6, 723, 726-7, 734, 2854, 3352-5, 3664)*. Figure 18.36, from the comprehensive work by Talledo *(3352)*, shows spectral absorptance for 0.1-μm-thick films deposited by reactive dc magnetron sputtering onto substrates at ~50°C so that a heavily disordered (or nanocrystalline) structure was found, and onto substrates at ~300°C so that a polycrystalline state occured. The lithium content, i.e., the magnitude of x in $Li_xVO_{2.5}$, was increased by ion intercalation from a $LiClO_4$ + PC electrolyte. The data in Fig. 18.36(a) show that the main effect in the disordered film was a bandgap widening from $E_g \approx 2.25$ eV at x = 0 to $E_g \approx 3.1$ eV at x = 0.75. The shift of the bandgap was proportional to x. For polycrystalline films, the behavior upon increased x was more complicated. The bandgap went from $E_g \approx 2.38$ eV at x = 0 to $E_g \approx 2.75$ at x =1.1. This shift was not proportional to x, though, but took place predominantly at x ≈ 0.5. The absorption at $\lambda > 0.5$ μm increased when x went from 0 to 0.5 and then decreased when x went from 0.5 to a value larger than unity. It is interesting to note that the bandgap shifts in nanocrystalline and polycrystalline films occurred in a manner similar to the EMF vs. x function (cf. Fig. 18.16). Data for sputter-deposited films in contact with Li^+ conducting polymers were reported in *(733)*.

Electrochromism has also been investigated in V pentoxide films made by other techniques and subsequently lithiated in $LiClO_4$ + PC electrolytes. Electrodeposited films showed different colors when Li^+ was intercalated *(108, 549, 3750-1)*, and this was found also for sol-gel-produced films

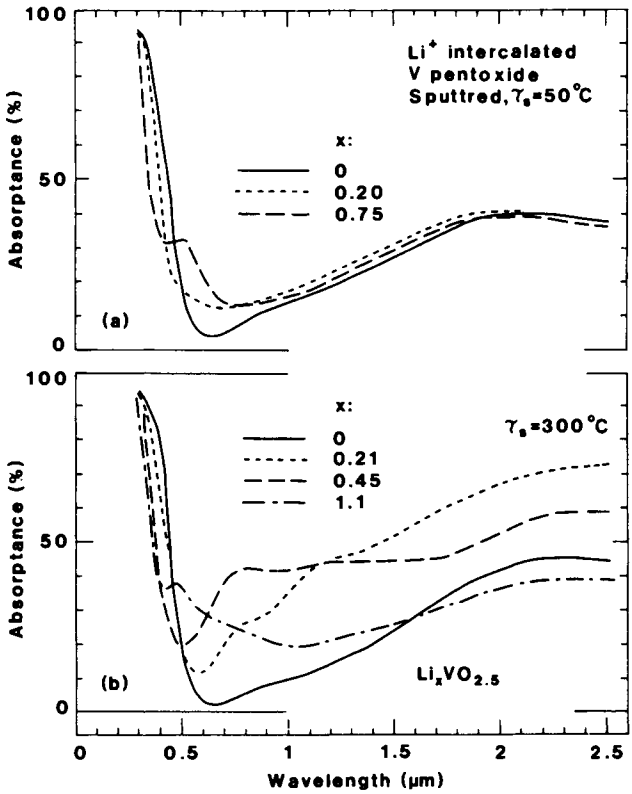

Fig. 18.36 Spectral absorptance for V pentoxide films sputter-deposited onto substrates at two temperatures τ_s. The films were Li^+ intercalated to the magnitudes given as x in $Li_xVO_{2.5}$. From Talledo *(3352)*.

(108, 1907, 2453, 2456) and films made by spin coating a chemical solution based on V_2O_5 dissolved in benzyl alcohol and isobutanol *(2474-5, 3145-6)*. Figure 18.37 shows characteristic data for films made by these three techniques; specifically, the data were reproduced from Kouda et al. *(1907)* (part a), Yoshino et al. *(3750)* (part b), and Nagase et al. *(2474)* (part c). The three sets of data are similar and resemble results for evaporated films (cf. Fig. 18.35). The absorption band has two peaks centered approximately at the wavelengths 0.8 and 1.2 μm. Electrochromism has been noted, but not studied in detail, also for anodized layers *(2641)*.

The optical properties of V pentoxide films can be changed by means other than ion intercalation from an electrolyte. Thus, in analogy with results for W oxide, electrocoloration was observed when electrons were injected via a contact on a single crystal of V_2O_5 *(1155)*. UV coloration of evaporated V pentoxide films incorporating organic molecules was seen to give a widening of E_g and absorption at $\hbar\omega < E_g$ *(1145, 1148, 1151)*. Thermocoloration was found when V pentoxide was heated to $\tau_a > 100°C$ *(1151, 2718)*, and presumably the same effect was responsible for coloration under intense irradiation from a Nd:YAG laser *(1797)*. Coloration under ion bombardment was reported in *(2479)*.

The coloration efficiency was determined by Kobayashi et al. *(1858-9)* for evaporated V pentoxide films in $NaClO_4$ + PC. Figure 18.38 shows results for films deposited onto substrates at two temperatures. At $\tau_s = 140°C$ the CE is peaked at ~1.6 eV, and at $\tau_s = 200°C$ the peak lies at ~1.2 eV. One should note that a principally similar displacement of the peak towards lower energies was also observed upon increased crystallinity for W oxide films (cf. Figs. 9.16 and 9.19). Coloration efficiencies for evaporated V pentoxide films seem to depend strongly on the conditions for thin film fabrication *(1859)*.

Cogan et al. *(723, 727, 732-3)* studied the coloration efficiency for sputter-deposited films. At $\hbar\omega < 2.5$ eV, the CE was positive with values up to 35 cm^2/C at low densities of inserted charge. The coloration seemed to be a non-linear function of the inserted charge density, and at large charge densities the CE was no larger than ~10 cm^2/C. At $\hbar\omega > E_g$, the bandgap shift manifested itself as a strongly negative peak in the CE at $\hbar\omega \approx 3.1$ eV.

Sol-gel-prepared films in $LiClO_4$ + PC had a CE of about 19 cm^2/C at $\lambda = 0.8$ μm *(1907)*. A film made by spin-coating from an organic solution had CE ≈ 14 cm^2/C at the same wavelength.

18.10 Theoretical Models for the Optical Properties

This section considers the present theoretical understanding for the optical properties of V pentoxide films under ion intercalation/deintercalation. It will be argued that the electrochromism can be reconciled, at least qualitatively, with bandstructure effects and with polaron absorption.

The bandstructure of V_2O_5 has been studied several times *(519, 1067, 1773, 1997-2000, 2708)*. Figure 18.39 illustrates the density of states as calculated by Bullett *(519)* from an *ab initio* atomic orbital framework (similar to the well known linear-combination-of-atomic-orbitals method). The *O2p* and *V3d* states are shown. The complicated layer structure of V_2O_5 leads to many bands; generally, they have low dispersion which explains, at least partly, the spikey nature of the bands. The most bonding part of the *d* band is split off from the rest of the *d* band, as pointed out by Bullett *(519)* and others *(1999, 2708)*. The Fermi level in stoichiometric V_2O_5 lies in the gap between the *O2p* and *V3d* bands; it is marked in Fig. 18.39 and was taken as the zero-level for the energy scale.

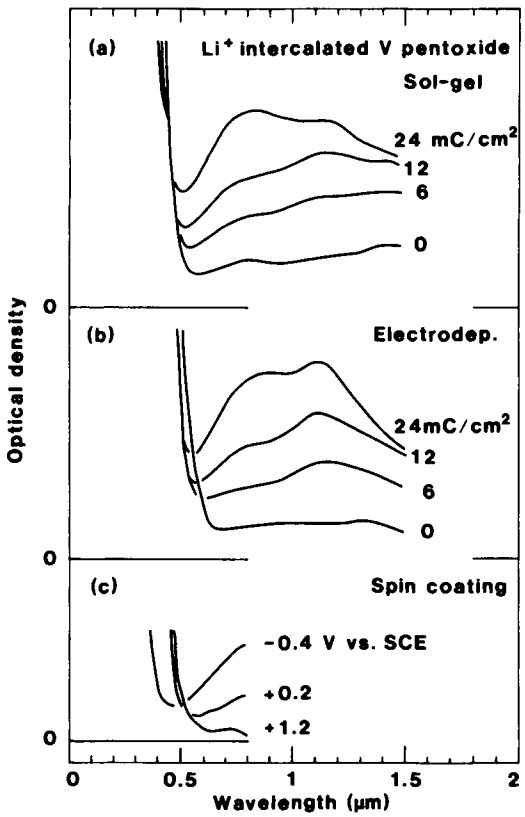

Fig. 18.37 Spectral optical density for V pentoxide films made by three different techniques and Li^+ intercalated in $LiClO_4$ + PC. The curves refer to the shown densities of inserted charge (parts a and b) or treated at the shown voltages (part c). After Kouda et al. *(1907)*, Nagase et al. *(2474)*, and Yoshino et al. *(3750)*.

The optical bandgap for near-stoichiometric V pentoxide corresponds to the energy between the top of the *O2p* band and the bottom of the split-off part of the *V3d* band. Insertion of some ions and electrons, in a rigid-band scheme, makes E_F lie in the split-off band, and further ion intercalation leads to a filling of the split-off band. Transitions between the two parts of the *d* band are parity-forbidden, so that the optical bandgap then corresponds to the energy between the top of the *O2p* band and the bottom of the main part of the *V3d* band. This can account for the abrupt bandgap widening, and the drop of the EMF, when x in $Li_xVO_{2.5}$ exceeds ~0.5. Hence the bandstructure explains directly why ion intercalation leads to electrochromism associated with the disappearance of an absorption of blue light. Some optical transitions between a partially filled split-off band and the main part of the *V3d* band may possibly explain the background level of the optical absorption at $\hbar\omega < E_g$. In Cr-containing V pentoxide, it appeared that E_g was considerably larger than in pure V pentoxide *(733)*. This is consistent with the bandstructure scheme since when Cr^{6+} replaces V^{5+} there should be excess electrons entering the split-off band.

The near-infrared absorption band, shown clearly in Figs. 18.35 and 18.37, is probably due to small polaron absorption. The anisotropic character of V pentoxide may lead to two different potentials for electron localization, which then accounts for the double-peak character of the absorption.

Near-infrared absorption bands were observed in several earlier studies with polarized light incident along different crystallographic axes in V_2O_5 single crystals *(713, 1478, 1778, 2373)*. Work involving optical measurements *(713)*, surface characterization *(743)*, and EPR *(3517)* led to the conclusion that this absorption was caused by oxygen vacancies in the V_2O_5 lattice. Empty *3d* orbitals of V atoms adjacent to such vacancies are able to localize excess electrons, which produces pairs of V^{4+} in the vicinity of the vacancy. Charge transfer to neighboring orbitals was suggested *(713)* as an explanation for the absorption in single crystalline V_2O_5. Clearly this explanation is intimately related to polaron absorption.

An interpretation of the near-infrared absorption in terms of small polaron effects is supported by numerous studies of the electrical conductivity in splat cooled samples *(2455, 2457, 2994)* as well as in thin films made by evaporation *(1792, 2436)*, sputtering *(1868)*, and sol-gel depositon *(523-4, 526, 2989, 2991)*. In particular, one should note that the theory of Triberis and Friedman, discussed in Sec. 11.1 in connection with small polaron effects in W oxide, is applicable also to V pentoxide films *(2437, 3447)*.

18.11 CF-doped Vanadium Pentoxide Films

Metal oxyfluoride films can be prepared by reactive sputtering in the presence of $O_2 + CF_4$, as discussed in Sec. 13.3. This technique was recently used by Talledo et al. *(190, 3352)* to study the electrochromism in V-pentoxide-based films incorporating some carbon and fluorine.

Films were made by reactive magnetron sputtering in $Ar + O_2 + CF_4$. RBS was used to determine the composition; typically the films contained ~2 at.% F and ~6 at.% C, and hence they can be termed CF-doped V pentoxide. XRD patterns were consistent with V_2O_5. Figure 18.40 shows the evolution of the EMF when Li^+ was intercalated into the CF-doped material. Comparing with Fig. 18.16 pertaining to an undoped oxide, one finds that the first major drop of the EMF takes place at a lower Li content--specifically at $x \approx 0.32$ rather than at $x \approx 0.5$ as in the undoped material.

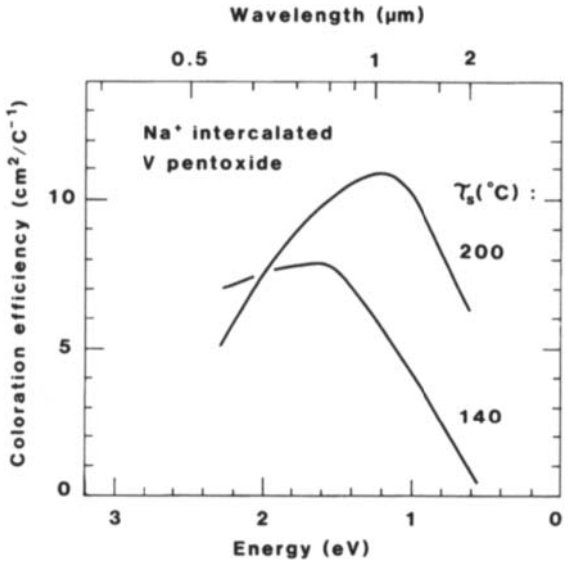

Fig. 18.38 Spectral coloration efficiency for V pentoxide films evaporated onto substrates at two temperatures τ_s and Na^+ intercalated in $NaClO_4$ + PC. After Kobayashi et al. *(1859)*.

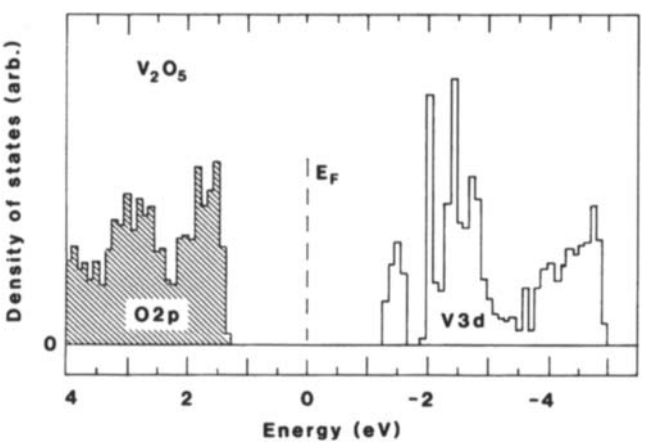

Fig. 18.39 Spectral density of states for V_2O_5, showing filled *O2p* states and empty *V3d* states. The Fermi energy is denoted E_F. After Bullett *(519)*.

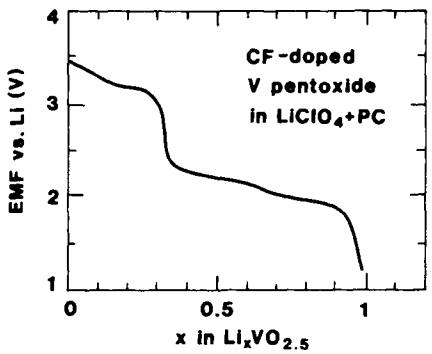

Fig. 18.40 Normalized EMF vs. lithium content, represented as x in $Li_xVO_{2.5}$, for CF-doped V pentoxide films made by reactive sputtering. After Talledo *(3352)*.

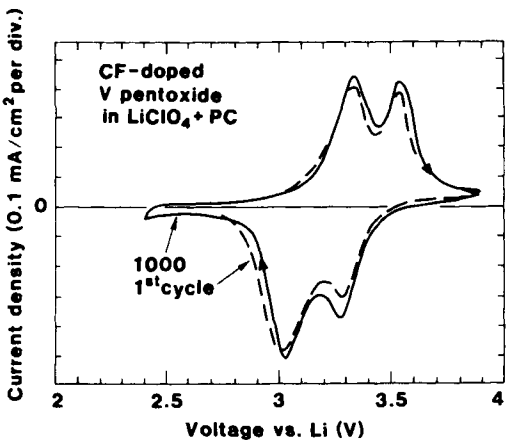

Fig. 18.41 Cyclic voltammograms for Li^+ intercalation/deintercalation in a CF-doped sputter-deposited V pentoxide film in $LiClO_4$ + PC. Data are shown for the first and thousandth voltammetric cycle. The voltage scan rate was 20 mV/s. Arrows denote scan direction. After Talledo *(3352)*.

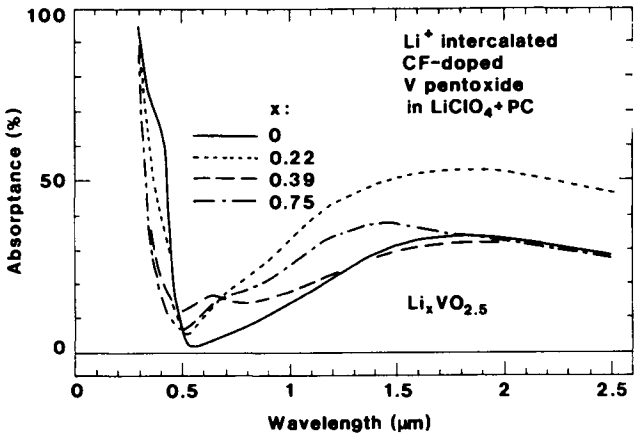

Fig. 18.42 Spectral absorptance for a CF-doped V pentoxide film intercalated with Li^+ to the magnitudes given as x in $Li_xVO_{2.5}$. From Talledo *(3352)*.

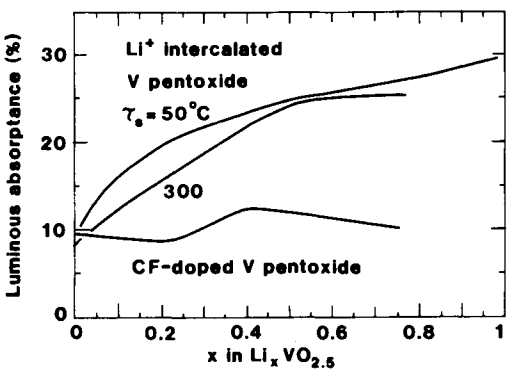

Fig. 18.43 Luminous absorptance for V-pentoxide-based films vs. the magnitude of Li^+, given as x in $Li_xVO_{2.5}$, intercalated from an electrolyte of $LiClO_4$ + PC. From Talledo *(3352)*.

Figure 18.41 shows cyclic voltammograms for a 0.1-μm-thick CF-doped V pentoxide film. The overall curve shape is the same as for the undoped oxide (cf. Fig. 18.21), and a double-peak structure is well developed both for the anodic and cathodic sweep. It is noteworthy that the intercalation and deintercalation curves remained very stable at least for 1000 voltammetric cycles between 2.4 and 3.9 V vs. Li. Thus it appears that the cycling durability is at least as good as for V pentoxide deposited at $\tau_s \approx 300°C$.

Spectral absorptance for a 0.08-μm-thick film of CF-doped V pentoxide is shown in Fig. 18.42. The absorptance can be directly compared with data in Fig. 18.36(b). The luminous absorptance of Li^+ intercalated samples was lower in the case of CF doping. To some extent this was due to the fact that a significant bandgap widening took place at lower intercalation levels when CF-doping was present.

Figure 18.43 elaborates the integrated luminous absorptance of 0.1-μm-thick films of V pentoxide deposited onto substrates at 50 and 300°C and of a 0.08-μm-thick film of CF-doped V pentoxide annealed at 300°C. For the undoped material, the luminous absorptance increases monotonically with increasing lithium content and exceeds 20% when x in $Li_xVO_{2.5}$ is larger than ~0.5; for the CF-doped material, on the other hand, the luminous absorptance remains at about 10%. The low luminous absorptance in CF-doped V pentoxide is of considerable interest for electrochromic devices designed for regulating transmitted light.

The drop in the EMF and the abrupt bandgap widening seem to occur at a diminished lithium content when CF doping is present. These results fit nicely with the bandstructure scheme outlined in Sec. 18.10 for V pentoxide. Specifically, the fluorine atoms are expected to serve as n-type dopants and provide electrons that enter the split-off part of the *V3d* band. It then only takes a small quantity of Li^+ with accompanying electrons to fill the split-off band and hence to cause a change to a material characterized by electron insertion into the main *V3d* band.

This Page Intentionally Left Blank

Chapter 19

NICKEL OXIDE FILMS

Hydrous nickel oxide can have a layer structure and resembles in this respect the V pentoxide of the previous chapter. The material of present interest can be represented as NiO_xH_y, but it is usually referred to, for simplicity, as Ni oxide. Its electrochromism is anodic. This chapter covers crystal structures for bulk-like Ni oxide (19.1), and preparation and characterization of films made by evaporation (19.2), sputter-deposition (19.3), and by electrochemical and chemical methods (19.4). Then follow discussions of ion intercalation/deintercalation reactions and diffusion constants (19.5), analyses of the intercalation/deintercalation by electrochemical (19.6) and physical (19.7) techniques, and data on ultraviolet absorption and the semiconductor bandgap (19.8). Optical properties in the luminous and near-infrared wavelength range are described in three sections--specifically, for films made by evaporation (19.9), sputter-deposition (19.10), and by electrochemical and chemical techniques (19.11). An organization according to preparation technique is suitable in this chapter since the as-prepared films can be fairly different, and hence the electrochromism evolves along separate paths. The chapter is ended by discussions of coloration efficiency (19.12) and some notes on theoretical models for the electrochromism (19.13).

19.1 Crystal Structure of Bulk-like Nickel Oxide, Especially Materials Used as Battery Electrodes

Battery electrodes based on Ni oxide have been used and studied for a century, and an almost impenetrable literature exists on this topic. Present applications concern batteries of the types Ni-Cd, Ni-Fe, Ni-Zn, and Ni-H. At least to some degree, this battery-related work can be used as a basis for understanding the electrochromism, but one is left with an impression that much of the early literature on Ni oxide electrodes is characterized by a repetition of dubious statements rather than by clarity. The subject has been reviewed at length *(267, 275, 482, 773, 1032-3, 1355, 1396, 1509, 2246, 2315, 2631)*.

The crystal structures of the electrochemically interesting Ni oxides have been subject to much interest over the years. Representative work is reported in *(274, 412-3, 556-7, 856-7, 867, 887, 1026, 1050-1, 1071, 1074, 1161, 1199, 1302-3, 1345, 1679, 1722, 1860-1, 1988, 2025, 2246-8, 2256, 2284, 2631, 2698, 3474)*. It is appropriate to start from β-$Ni(OH_2)$, having a brucite structure with weakly bound layers of edge-sharing NiO_6 octahedra stacked along the unique *c* axis. Between these layers there are empty octahedral sites and H-containing tetrahedral sites. The OH bond is thought to be parallel to the *c* axis. The brucite structure is common to several metal hydroxides as well as to some halogenides, and $Co(OH)_2$ and $Fe(OH)_2$ will be discussed later in

Secs. 20.1 and 22.4, respectively. β-$Ni(OH)_2$ can intercalate water, thus forming what is commonly known as α-$Ni(OH)_2$. An idealized formula $3Ni(OH)_2 \cdot 2H_2O$ was proposed by Bode et al. *(412)*, but subsequent work by Le Bihan et al. *(2022-3, 2025)* and McEwen *(2256)* has rejected this well-organized atomic arrangement in favor of a turbostatic structure--analogous to the one in some layered minerals and in carbon black--with equidistant $Ni(OH)_2$ layers similar to those in β-$Ni(OH)_2$ separated by water molecules bound to the OH groups via hydrogen bonds. A related but more ordered α* phase can be obtaiend via "chimie douce" from sodium nickelate *(467, 868)*. There are structures also combining features of both the α and β phases *(1724)*.

Ni oxyhydroxides with higher oxidation states have been studied intensely but are still incompletely understood. One basic type is β-NiOOH, which can be described simply as β-$Ni(OH)_2$ with one proton and one electron removed per formula unit. Removal of the proton leads to an expansion of the *c* axis parameter from 0.4605 to 0.485 nm. A hydrated variety is known as γ-NiOOH; its composition depends on the manufacturing route, and alkali ions can be incorporated, as discussed later. Sometimes one makes a distinction between γ_1 and γ_2 structures with different crystallinity *(413)*.

The NiO_6 building blocks, common to all of the hydroxides and oxyhydroxides mentioned above, are also found in $Ni_3O_2(OH)_4$.

The majority of the work on Ni oxide electrodes is strongly geared towards proton (and/or hydroxyl ion) intercalation/deintercalation. However, there are related materials that can serve as intercalation hosts for Li^+. Such intercalation has been documented for $LiNiO_2$ *(799, 800, 1251, 2067, 2603-4, 2883, 3410)*, $LiNi_{1-y}Co_yO_2$ *(873, 2604)*, and $LiNi_{1-y}Mn_yO_2$ *(2939)*. One could also note a newly discovered Li_2NiO_2 phase with the $Ni(OH)_2$ structure *(800)*. Intercalation of Na^+ into $NaNiO_2$ was discussed in *(2378)*.

19.2 Films Made by Evaporation: Preparation and Characterization

Reactive evaporation is a widely used and studied technique for making Ni oxide films *(37, 253, 2005, 2112, 2123, 2462, 2518, 2941, 3088, 3390)*. Reactive evaporation of NiO powder in the presence of O_2 can be viewed as the standard method; it yielded deposition rates up to ~1 nm/s *(253)*. Agrawal et al. *(37)* and Bange et al. *(253)* evaluated the relative density of the films from thickness measurements and RBS. Figure 19.1 illustrates the dependence on p_{O2} in a manner that allows direct comparison with results for W oxide, for example (cf. Fig. 3.2a). The relative density falls off for $p_{O2} > 10^{-4}$ Torr and is as low as ~0.5 at $p_{O2} \approx 5 \times 10^{-4}$ Torr.

The microstructure of evaporated Ni oxide films was studied by Agrawal et al. *(37)*, who found that the grain size was ~4 nm at $p_{O2} \approx 5 \times 10^{-4}$ Torr; these grains formed clusters with an extent of 60 to 100 nm. At $p_{O2} \approx 10^{-4}$ Torr, the grain size was 5.4 nm, and the films had a columnar microstructure. Electron diffractograms were consistent with a cubic NiO structure *(37, 2005, 3088)*, whereas XRD was unable to discriminate between a cubic and a hexagonal structure *(37)*. IR spectroscopy gave evidence for OH groups, but the intensity of the spectral absorption bands was too weak to be in agreement with $Ni(OH)_2$ *(37)*. XPS and RBS data indicated that the O/Ni ratio was considerable larger than one *(37, 253, 2123)*. The ensuing model is that the evaporated films consist of ~5-nm-diameter overstoichiometric clusters with hydroxyl groups on their surfaces and possibly with some hydration *(37)*. The material may be represented, roughly, as $NiO(OH)_z$ with $z \approx 0.25$ in the bulk and $z \approx 0.5$ at the surface *(2518)*.

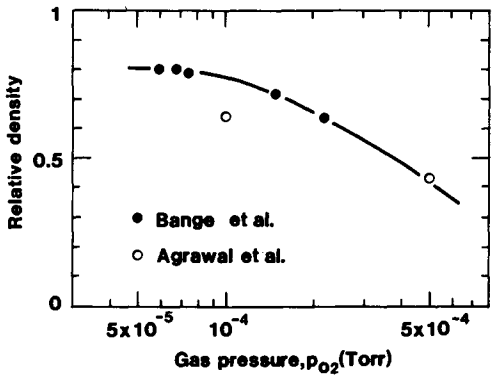

Fig. 19.1 Relative density for Ni oxide films made by reactive evaporation at different values of the oxygen gas pressure p_{O2}. Data were obtained from Agrawal et al. *(37)* and from Bange et al. *(253)*.

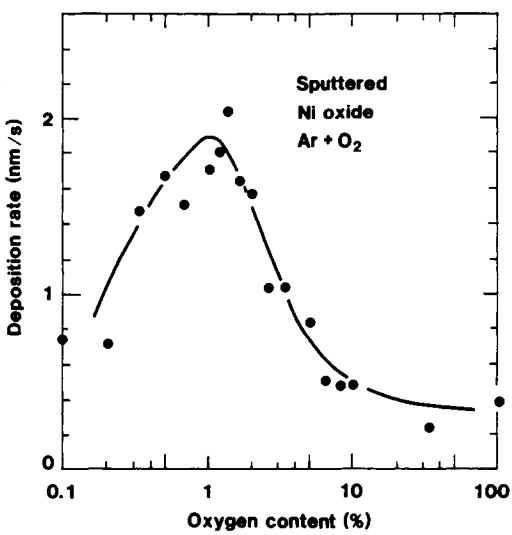

Fig. 19.2 Deposition rate vs. oxygen content for sputtering from Ni in Ar + O_2. Dots indicate measured data and the curve was drawn for convenience. From Wruck et al. *(3663)*.

19.3 Films Made by Sputter-deposition: Preparation and Characterization

Sputter-deposition has been employed several times as a technique for making thin Ni oxide films. Magnetron as well as diode sputtering have been used with dc and rf excitation in reactive and non-reactive processes. The magnetic properties of Ni targets are of practical importance for magnetron sputtering.

Figure 19.2, reproduced from Wruck et al. *(3663)*, shows deposition rate as a function of oxygen content for dc planar magnetron sputtering from a metallic target in Ar + O_2. The rate was peaked at ~2 nm/s for ~1% of O_2 in the sputter plasma, and the rate dropped sharply at larger oxygen contents. The relation between rate and p_{O2} is in principle agreement with data for dc sputtered W oxide films (cf. Fig. 4.1). According to Estrada et al. *(1021)*, too high sputter rates could lead to films that were incapable of extended color/bleach cycling in electrochromic devices. The relative density of Ni oxide films made by slow diode sputtering was approximately 0.8 to 0.9 *(238, 749)*.

It is illuminating to show the electrical resistivity of films prepared from Ni targets in the presence of oxygen. Such data are plotted in Fig. 19.3, again after Wruck et al. *(3663)*. At low O_2 content, the film was metal-rich and conducting. The maximum resistivity was reached at an O_2 content of ~1%, and the presence of more oxygen made the resistivity gradually fall off. The latter feature differs qualitatively from the behavior of W oxide (cf. Fig. 4.2).

Transmission electron microscopy has been used to investigate film microstructures, and grains with average sizes of 1.5 to 10 nm have been reported several times *(211, 1021, 2867, 3294)*. EXAFS measurements yielded RDFs that could be interpreted on the premise of a fine-grained crystallinity *(381)*.

Electron diffraction has given information on the crystal structure, and a dominating fcc NiO-like phase was reported in *(1021, 2867, 3665)*. More detailed structural information was recorded by XRD; some studies indicated a NiO-like material *(95, 2076, 2310, 3663)*, whereas other work showed the presence of a disordered Ni_2O_3 phase *(1827, 3689-90)*. It is probably of significance that the latter films were deposited at very low rates and in the presence of oxygen. The lattice parameter of NiO-like films was 0.422 nm for samples annealed at 120°C, and this parameter decreased to 0.417 nm--the bulk value--after annealing at 400°C *(95)*. Annealing of N_2O_3-like films to temperatures above 300°C yielded a transformation to NiO *(3690)*.

Film stoichiometries have been investigated by electron spectroscopy. Thus XPS applied to films made by dc and rf sputtering in Ar + O_2 gave evidence for a minority phase of Ni_3O_4 (or NiO · Ni_2O_3) *(95, 2310, 2867)*. Slow diode sputtering, on the other hand, led to XPS spectra indicating Ni_2O_3 *(749)*. Oxygen deficient films, i.e., NiO_z with $z < 1$, were seen in AES studies of some films made by dc sputtering *(133)*.

Hydrogen-containing Ni oxide films have been prepared by sputtering in H_2 + O_2 *(590, 1120, 3293)*. The H_2 admixture led to an increase of the deposition rate *(1120)*. IR absorption spectroscopy showed the presence of OH groups. Films prepared by Fujiwara et al. *(1120)* and Svensson and Granqvist *(3293)* were transparent, which speaks in favor of $Ni(OH)_2$, whereas Campet et al. *(590)* argued for a film composition with some 30% of NiOOH.

The experimental evidence accumulated so far for reactively sputter-deposited Ni oxide indicates that different compositions can be obtained depending on the preparation conditions. An adequate representation for as-deposited films is H_xNiO_y with $0 < x < 2$ and $1 < y < 2$.

In addition to the already cited work, sputtering for producing Ni oxide films was discussed in

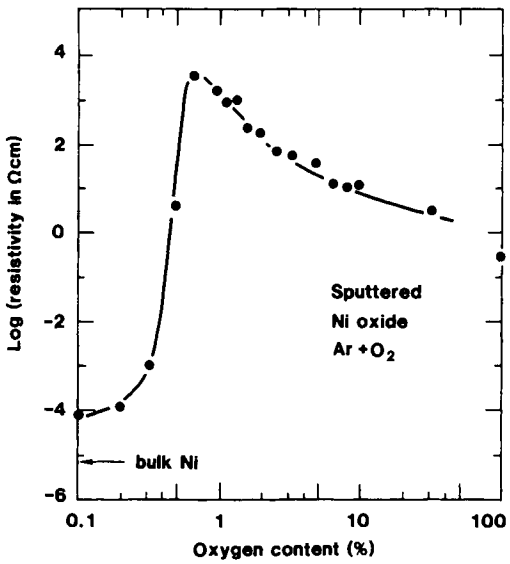

Fig. 19.3 Resistivity vs. oxygen content for sputtering of Ni in Ar + O_2. An arrow marks the resistivity of bulk Ni (at room temperature). Dots indicate measured data and the curve was drawn for convenience. From Wruck et al. *(3663)*.

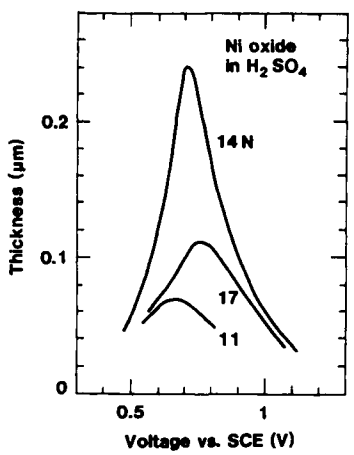

Fig. 19.4 Limiting film thickness for anodization of Ni in H_2SO_4 with the shown concentrations at 15°C. After Blondeau et al. *(400)*.

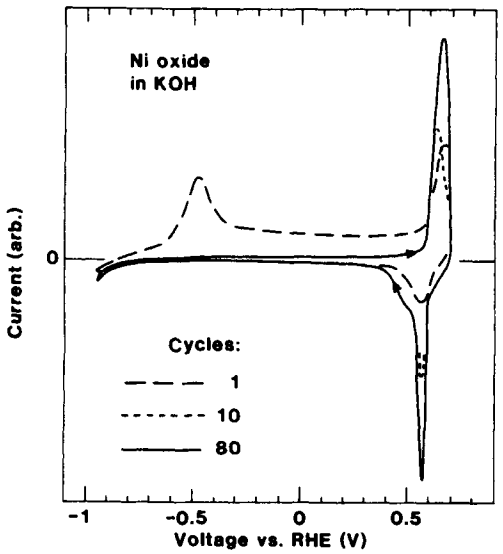

Fig. 19.5 Cyclic voltammograms for a Ni oxide film grown by potential cycling in 1 N KOH. The data pertain to the shown number of cycles. The voltage scan rate was 0.1 V/s. Arrows denote scan direction. From Schreibler Guzmán et al. *(3068)*.

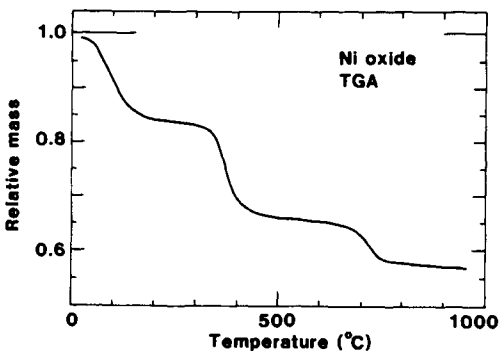

Fig. 19.6 Thermal Gravimetric Analysis TGA spectrum of a Ni oxide film made by alternate dipping in 0.01 M $NiSO_4$ and 0.01 M KOH. Data were taken at a heating rate of 10°C/minute. From Fantini et al. *(1037)*.

(96, 604, 849, 1039, 1557, 1591, 2005, 2220, 2535, 3129, 3270, 3290-2).

19.4 Films made by Electrochemical and Chemical Techniques: Preparation and Characterization

There are many electrochemical and chemical techniques for making thin films of Ni oxide. Most of the work has been geared towards porous battery electrodes or passivating layers (i.e., very thin films for corrosion resistance) and is not of immediate relevance to studies of electrochromism, which require films with thicknesses exceeding ~0.1 μm. Nevertheless, some interesting electrochemical and chemical methods are available, as discussed below.

Electrodeposition from Ni-containing electrolytes has been used extensively. Two techniques are popular; they are referred to here as the *nitrate route* and the *sulfate route*. The nitrate route, involving galvanostatic cathodic electrodeposition from a 0.01 to 1 M $Ni(NO_3)_2$ solution, originated in battery technology but has also been exploited for electrochromic films *(485, 487, 594, 895-6, 1027, 1066, 1721, 2130-1, 2499, 2636, 2698, 3541)*. A proposed reaction scheme is *(1033)*

$$NO_3^- + 7\,H_2O + 8e^- \rightarrow NH_4^+ + 10\,OH^- \tag{19.1}$$

$$10\,OH^- + 5\,Ni^{2+} \rightarrow 5\,Ni(OH)_2\,. \tag{19.2}$$

The current efficiency for film deposition was reported to be 86% *(757)*. There are indications that the relative film density is ~0.5, and that the film surface is very rough *(609)*. The initially produced film is α-$Ni(OH)_2$, as inferred from various characterization techniques including Raman scattering *(895-6)* and EXAFS *(2698)*. The latter technique showed that the Ni coordination sphere was 0.005 nm smaller in the α-phase than in the β-phase, which can be ascribed to differences in the hydrogen bonding. Thermogravitometry indicated a small mass decrease at ~100°C and a larger mass decrease at 300 to 400°C *(1066)*; a similar behavior will be discussed in connection with Fig. 19.6 below. Electrodeposition from mixed nitrate solutions has been used to produce Ni oxide films containing Ag, Co, Ce, Cr, Co, Cu, Fe, La, Pb, Mg, Mn, Y, Zn, or Co + La (*329, 768-71, 1623, 2752, 3211*). Superimposed layers of $Mn(OH)_2$ and $Ni(OH)_2$ were studied in *(316)*.

A common sulfate route electrodeposits Ni oxide films through potential cycling in 0.1 M $NiSO_4 \cdot 6\,H_2O$ + 0.1 M NH_4OH by triangular sweeps between -0.5 and +1.5 V vs. SCE at 20 mV/s *(1590, 2004, 2007-8, 2508, 2657, 2727, 3762-5)*. Improved film properties were obtained when a non-ionic detergent, specifically poly-oxy ethylene sorbitan monolaureate, was added to the electrolyte *(1590)*. Angle-resolved IR spectrophotometry gave credence to the as-deposited film being of α-$Ni(OH)_2$ *(2508)*. An analogous mixed sulfate solution was used for preparing Co-containing Ni oxide films *(2127)*. Films have also been made by potential cycling in 0.1 M $NiSO_4$ + 0.1 M NaAC + 0.005 M KOH *(1038, 2155)* known as "Brigg's solution" *(484, 486, 1682)*, potentiostatic deposition in $NiClO_4$ + $(NH_4)_2SO_4$ *(691)*, galvanostatic deposition in 0.5 M $NiSO_4$ + 0.2 M KNO_3 + 0.1 M KOH *(1193)*, and galvanostatic deposition in 0.005 M $NiSO_4$ + 0.0015 M $(NH_4)_2SO_4$ followed by heat treatment at 250°C *(674, 2389)*. The latter films were studied by TGA; these data indicated that the virgin films could be represented as $NiOOH \cdot 1.3\,H_2O$ *(2389)*. Nickel hexaferrocyanate films, made by potential cycling *(1690)*, can be transformed into Ni oxide

by immersion in KOH or LiOH *(1692)*.

Anodization in concentrated H_2SO_4 under well controlled conditions can produce films with thicknesses as large as ~0.25 μm, as discovered by Blondeau et al. *(400)*. According to Fig. 19.4, a concentration of 14 N and a voltage of ~0.7 V vs. SCE are favorable, and other conditions gave smaller thicknesses. A temperature of ~15°C was preferable, and higher and lower temperatures led to thinner films. Subsequent studies by Blondeau et al. *(399)* showed electron diffractograms consistent with a sulphur-containing NiO structure; the films had a relative density of 0.4 to 0.63 and contained pores with sizes 2 to 5 nm. The presence of a NiO-like film was in agreement with some optical *(2684)* and Raman measurements *(864)*, whereas other experiments indicated a composition akin to $NiSO_4 \cdot H_2O$ *(2285)*.

Thick Ni oxide films can also be produced by anodization in the oxygen evolution range in buffered neutral borate solutions *(1539, 2140-1, 2629, 2643)*. According to MacDougall et al. *(2140-1)*, the films have a duplex character with an inner 1 to 2-nm-thick NiO-like passivation layer and a much thicker spongy outer structure. This porous layer is built up at a current efficiency of less than 1%. A duplex structure was also argued for by Okuyama and Haruyama *(2629)*, who studied thin passive films.

Immersion of Ni in concentrated KOH is able to produce oxide films at a slow rate; a 5 N solution gave a 60-nm-thick homogeneous layer after ~30 h *(1646)*. This is too slow for applications in electrochromic devices. However, potential cycling in 0.1 to 1 N KOH or NaOH, typically by triangular voltage sweeps at ~0.1 V/s, can give a continuous evolution of a film much in the same way as for potential cycling of Ir in H_2SO_4 (cf. Fig. 14.4). Cyclic voltammetry is a convenient technique for following the build-up, and Figure 19.5--from Schreibler Gusmán et al. *(3068)*--shows results for cycling from -0.95 to +0.7 V vs. RHE in 1 N KOH. During the initial sweep, there is a characteristic peak at ~-0.5 V vs. RHE. Such a feature has been observed several times in other work *(558, 1140, 3065-7, 3650-1)*. It can be ascribed to simultaneous nickel dissolution and oxide formation with some possible influence from the oxidation of hydrogen accumulated on the electrode. At 0.55 to 0.65 V vs. RHE there are distinct current peaks representing charge insertion and extraction (and, as discussed later, accompanying changes in the optical absorption). These peaks became larger as the potential cycling progressed, which signifies that film growth took place. Evidence for an increased capacity for charge insertion and extraction was found also by Burke and Whelan *(562)*, who reported that film growth was noticeable even after 250 cycles in NaOH. According to Visscher and Barendrecht *(3540)*, there is an initial oxidation of Ni to α-$Ni(OH)_2$, followed by a conversion to β-$Ni(OH)_2$. Thus the films are expected to have a non-homogeneous layered structure, which is consistent with some optical results *(3661)*. Additional studies of film growth under repetitive voltage sweeps in KOH were reported in *(556-8, 1239, 2007-8, 3069, 3167)*. Film growth is also possible under pulsed voltage (square wave) conditions in KOH, NaOH, KCl, $NiCl_2$, and KBr *(983, 1193, 3539)*. Chialvo et al. *(1163, 3539)* used pulses in the kHz range and documented by scanning electron microscopy that the as-prepared films had a scaly appearance. Thick films grown by potential cycling of amorphous Ni-Co-based alloys were discussed in *(2068-9)*.

As pointed out above, there is a very large literature on the properties of very thin Ni oxide films in which issues relevant to the passivation of metals (corrosion resistance) are elaborated in detail. Some of these studies discuss--or at least touch on--film structures and may also be of relevance for thicker films with pronounced electrochromism. Thus anodic films have been investigated in electrolytes based on KOH *(3, 2104, 2266, 3591-2)*, NaOH *(1389-90, 1416,*

2688), H_2SO_4 *(455, 1416, 2591, 2862, 3787)*, $H_2SO_4 + K_2SO_4$ *(411, 1745, 2868-70)*, $H_2SO_4 + Na_2SO_4$ *(1475)*, Na_2SO_4 *(1416)*, K_2CO_3 *(3, 416)*, borates *(3008)*, and several different phosphates *(657-9)*. For strong acids there was evidence from EXAFS and RHEED that a NiO-like structure was present *(455)*. However, films produced in neutral or alkaline electrolytes may well have different compositions, as emphasized by Hara and Sugimoto *(1416)*.

There are miscellaneous purely chemical techniques for making Ni oxide films. *CVD* is one of these. Tolstikhina et al. *(3420-1)* decomposed $Ni(CO)_4$ vapors in an oxidizing atmosphere at 85 to 180°C and obtained fine-grained oxide films with carbon contamination. Other CVD processes used precursor gases of $NiBr_2$ *(634)*, $NiCl_2$ *(634)*, and $Ni(C_5H_7O_2)_2$ *(2201, 2710)*. The latter process required $\tau_s > 250$°C. Spray pyrolysis of $Ni(NO_3)_2 \cdot 6\ H_2O$ onto glass plates was reported in *(2326)*.

Colloidal precipitation has been studied in detail, using alternate immersions in $NiSO_4$ and in either KOH, NaOH, or LiOH *(597-601, 1037, 1089, 1259, 2129, 3525-6)*. Up to 100 dippings were used in some of the work. The structure and composition of these films were recently studied by Fantini et al. *(1037)*, whose TGA data, measured during heating in N_2 or O_2, are reproduced in Fig. 19.6. The mass decrease around 100°C was undoubtedly due to water loss, and the mass decrease at 350 to 400°C can be interpreted as a transition from a hydroxylated material into an oxide of the type Ni_2O_3. The ultimate NiO structure was reached at 700 to 750°C. These compositional changes are in accordance with measurements by DSC and XRD *(1037)*. TGA spectra for powder specimens indicated, apart from an initial water loss, a major transformation between 200 and 300°C, i.e., at lower temperatures than for the films made by alternate dippings *(260, 583, 887)*. The alternate dipping technique is applicable also to the production of Ni oxide films with additions of Co, Cd, Fe, Mn, and Zn *(756, 3488-9)*. To this end, the dippings can be either in a mixed sulfate solution or sequentially into different sulfate solutions.

Several other dipping and immersion techniques have been reported. One of these employs the immersion of substrates in 1 M Ni sulfate, 0.25 M potassium persulfate, and ammonia *(2803)*. A 0.275-μm-thick film accumulated in 1 h. Judging from the published data, this film is of NiOOH character. Dipping in $Ni(NO_3)_2$ followed by heat treatment at 300°C has been reported *(3037)*, as well as an unspecified sol-gel technique *(2005)*. Still other methods involving homogeneous chemical precipitation were discussed in *(1590, 3428)*.

NiO films can be produced simply by *thermal oxidation* of nickel in the presence of oxygen at a temperature above 300°C *(761, 969, 1124, 1358, 1577, 2364, 3305, 3311, 3462)*. According to Hugot-Le Goff et al. *(761, 1577)*, such films do not display electrochromism, most likely as a result of too dense a structure. Films of this type will not be discussed further.

19.5 Ion Intercalation/deintercalation Reactions and Diffusion Constants

Ion intercalation/deintercalation has been discussed extensively for Ni oxide. Many claims have been made in the literature, but it may be fair to say that little consensus has been reached. The discussion here starts with the Bode reaction scheme, which was introduced to account for charging/discharging phenomena of Ni electrodes in KOH electrolytes *(412-3, 1575, 2631)*. Its essentials are captured by

$$\begin{array}{ccc} \alpha\text{-}Ni(OH)_2 - H^+ - e^- & \leftrightarrow & \gamma\text{-}NiOOH \\ \uparrow\downarrow & & \uparrow\downarrow \\ \beta\text{-}Ni(OH)_2 - H^+ - e^- & \leftrightarrow & \beta\text{-}NiOOH \end{array} \quad (19.3)\ (19.4)$$

Some characteristic features of the α, β, and γ oxides were discussed in Sec. 19.1. The $\alpha \leftrightarrow \gamma$ and $\beta \leftrightarrow \beta$ pathways, involving transitions of the type $Ni^{2+} \leftrightarrow Ni^{3+}$, are of interest for electrochromism and for charging/discharging of batteries. The $\alpha \rightarrow \beta$ reaction corresponds to dehydration and occurs under extended potential cycling for example in KOH. The $\beta \rightarrow \gamma$ reaction takes place at excessive charge insertion.

The Bode reaction scheme must be applied with sufficient flexibility, as underscored by Oliva et al. *(2631)* and others. In particular, three aspects of the scheme may need elaboration:

(i) The reactions are written as involving only proton exchange. This is not the only possibility, though, and analogous formulas can be given in terms of OH^- exchange. In fact, there has been much debate as to the dominance of H^+ or OH^-, as further discussed below. For several years a corresponding confusion existed for Ir oxide, as mentioned in Sec. 14.4. With regard to Ni oxide, one should observe the work in 1969 by Feuillade and Jacoud *(1066)*, who studied electrodeposited films by isotopic exchange (^{16}O - ^{18}O and ^1H - ^3H) and concluded that several different ionic species could be transferred at the interface between the oxide and an electrolyte.

(ii) The Bode scheme does not account for intermediate reaction steps or non-equilibrium effects. Such features can occur, however, as argued by Arvia et al. *(3066, 3068-9, 3534-5)* on the basis of extensive cyclic voltammetry studies.

(iii) The relevance of the γ-phase, as it is expressed above, is questionable. In particular, it has been observed that the formal Ni oxidation state can be considerably larger than +3 *(413, 2104, 2631)*. Recent work based on electrochemical measurements *(772)*, Raman scattering *(896)*, and EXAFS *(594)* showed that for films in contact with KOH it was adequate to express the γ-phase as $K(NiO_2)_3$, in which case the formal Ni oxidation state is +3.67.

A simplified reaction scheme is of interest for representing the gradual optical changes that take place under ion intercalation/deintercalation in electrochromic Ni oxide films. Following Ezhov et al. *(1027)*, one may write

$$Ni(OH)_2 - xH^+ - xe^- \leftrightarrow NiO_x(OH)_{2-x} . \quad (19.5)$$

It is assumed that the $\beta \leftrightarrow \beta$ pathway in reaction 19.4 is dominating (just as, normally, in batteries). Here $Ni(OH)_2$ is transparent whereas (for x = 1) NiOOH is strongly absorbing.

Lithium intercalated Ni oxide has only recently begun to attract interest. Its relevance to electrochromic device design is obvious, and a Li^+ conducting electrolyte between a W oxide film and a Ni oxide film can be expected to show excellent electrochromic properties. Lithium intercalation/deintercalation has been accomplished by cycling potentiodynamically electrodeposited Ni oxide films in saturated LiOH solutions *(2727)* and by treating anodic *(761, 1577)* and sputter-

deposited *(133, 590, 847, 2714-6)* films in $LiClO_4$ + PC. The lithiated material can be transparent; it may consist of LiNiOOH or Li_2NiO_2. The corresponding colored material may be NiOOH or $LiNiO_2$, respectively.

Diffusion constants have been evaluated under the assumption that H^+ intercalation/deintercalation is dominating in electrochemically prepared Ni oxide films *(483, 1027, 2109, 2130-1, 2728, 3193, 3478-9)*. The data on D_{H+} lie in an exceedingly wide range--between 7×10^{-14} and 2×10^{-9} cm^2/s at room temperature. The only conclusion one can draw is that the investigated materials must have had radically different microstructures. Bulk nickelates have D_{H+}s around 10^{-8} cm^2/s *(3546-7)*. Regarding D_{Li+}, the only available result is a "tentative" one, being 10^{-11} cm^2/s for a sputter-deposited film *(847)*.

19.6 Ion Intercalation/deintercalation Studied by Electrochemical Techniques

Films have been investigated in detail by use of cyclic voltammetry, impedance spectrometry, beam deflectometry, and microbalance measurements. These data are reviewed below.

Cyclic voltammetry has been applied to Ni oxide films prepared by all of the major techniques surveyed in Secs. 19.2 to 19.4. Evaporated films are considered first. Figure 19.7, from Lampert and Caron-Popowich *(2005)*, shows data for an *e*-beam evaporated Ni oxide film in 1 M KOH. Voltammograms are reported for the initial cycle and after ~200 slow intercalation/deintercalation cycles. The voltammograms evolved upon continued cycling, and the current densities during ion intercalation/deintercalation went up. It was pointed out in Sec. 19.2 that the as-evaporated film could be represented approximately as $NiO(OH)_{0.25}$. It is then reasonable to assume that extended cycling in KOH leads to increased hydroxylation so that the stabilized electrochemical reaction takes place according to the $\beta \leftrightarrow \beta$ pathway in the Bode scheme, i.e., by reaction 19.4. Evolving cyclic voltammograms, principally similar to the ones in Fig. 19.7, were also reported in *(37, 253, 2123)*.

Cyclic voltammograms for sputter-deposited films are given in Fig. 19.8; the data were reproduced from Gorenstein et al. *(1258)* and Campet et al. *(590)* for films in electrolytes of KOH and NaOH, respectively. The overall curve shapes are similar, though not identical, and well defined peaks pertain to ion intercalation/deintercalation. There is a noteworthy similarity to the voltammograms for the evaporated films (Fig. 19.7). The voltammograms for the sputter-deposited films evolved under continued cycling, and large charge densities could be inserted and extracted after a sufficient number of cycles *(95, 590, 749, 1039, 1259, 2005, 3033, 3662, 3665)*. According to an analysis by Conell et al. *(749)*, the $\beta \leftrightarrow \beta$ pathway is gradually approached during the potentiodynamic treatment.

Lithium intercalation into Ni oxide films is of particular interest for electrochromic devices, as mentioned above. Figure 19.9 shows data from Decker et al. *(847)*, who studied sputter-deposited films in $LiClO_4$ + PC electrolytes. Initially the voltage was scanned between 1.1 and 3.7 V vs. Li. The corresponding voltammograms displayed an evolution towards progressively larger charge densities associated with the Li^+ intercalation/deintercalation. After the 20^{th} voltammetric cycle, the scan range was narrowed to be 1.0 to 2.5 V vs. Li, and it was verified that reversible electrochemical conditions prevailed. The data indicate that the pristine Ni oxide film undergoes an "activation" involving permanent lithium incorporation, and that the ensuing material serves as excellent host for further Li^+ intercalation/deintercalation. The nature of the "activated" state is not

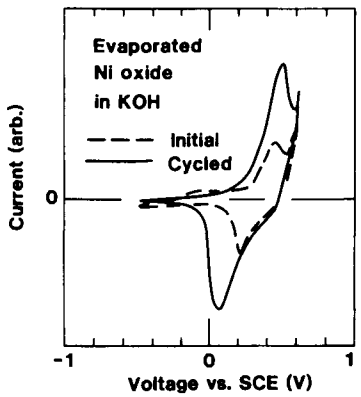

Fig. 19.7 Cyclic voltammograms for an evaporated Ni oxide film in KOH. Data are shown for the initial cycle and after ~200 cycles. The voltage scan rate was 6 mV/s. Arrows denote scan direction. From Lampert and Caron-Popowich *(2005)*.

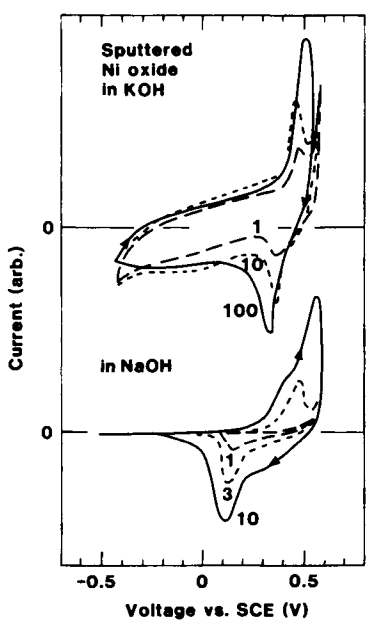

Fig. 19.8 Cyclic voltammograms for sputter-deposited Ni oxide films in KOH (upper part) and NaOH (lower part). Data correspond to the shown number of cycles. The voltage scan rates were 10 mV/s (upper curves) and 5 mV/s (lower curves). Arrows denote voltage scan direction. After Gorenstein et al. *(1258)* and Campet et al. *(590)*.

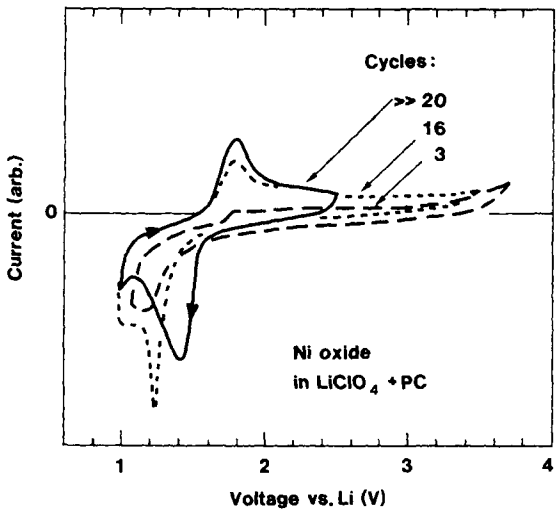

Fig. 19.9 Cyclic voltammograms for sputter-deposited Ni oxide films in $LiClO_4$ + PC. Data correspond to the shown number of cycles. The voltage scan rate was 10 mV/s. Arrows denote voltage scan direction. After Decker et al. *(847)*.

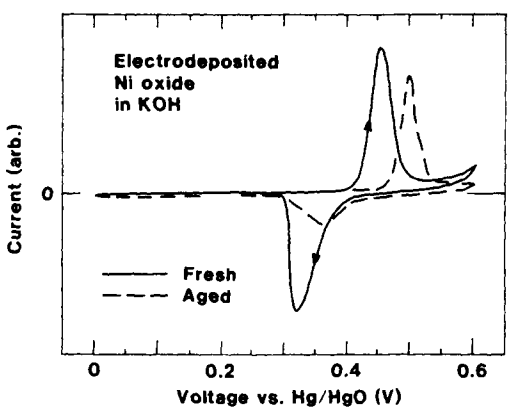

Fig. 19.10 Cyclic voltammograms for Ni oxide films electrodeposited from a nitrate solution and studied in KOH. Data are given for the film in "fresh" and "aged" states. The voltage scan rate was 2 mV/s. Arrows denote voltage scan direction. From Carpenter et al. *(609)*.

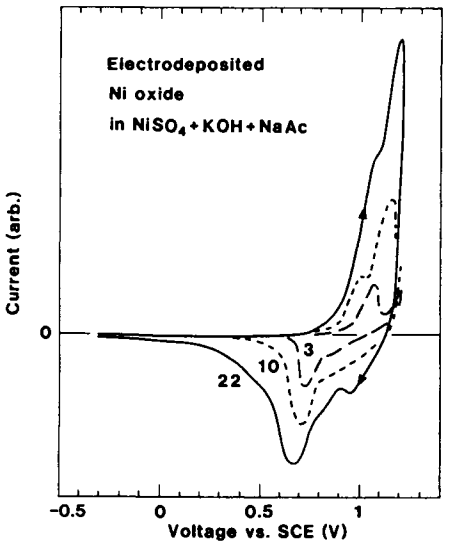

Fig. 19.11 Cyclic voltammograms for Ni oxide films electrodeposited from a "Briggs solution". Data refer to the shown number of cycles. The voltage scan rate was 10 mV/s. Arrows denote voltage scan direction. From Fantini and Gorenstein *(1038)*.

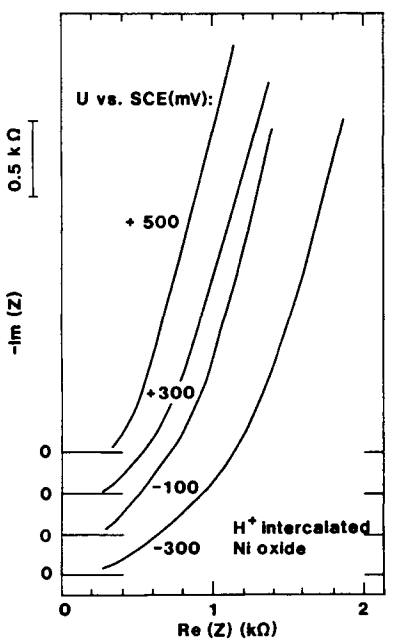

Fig. 19.12 Complex impedance Z vs. frequency for a sputter-deposited Ni oxide film with H^+ intercalated at the shown voltages U. Data were taken for decreasing U. The curves are vertically displaced. After Gorenstein et al. *(1258)*.

known at present. Voltammograms for lithiated Ni oxide films were also reported in *(2715-6)*.

There is a vast number of papers reporting cyclic voltammograms for electrochemically and chemically prepared films, and it is not meaningful to try to cover the entire literature here. With regard to electrodeposition, it was pointed out above that there are two main technologies, referred to as the nitrate and sulfate routes. Figure 19.10, from Carpenter et al. *(609)*, shows cyclic voltammograms for a film electrodeposited from a $Ni(NO_3)_2$ solution and investigated in 1 M KOH. The data pertain to films in as-deposited state and after ageing in the electrolyte. Ageing caused a shift of the current peaks towards higher voltages, which was interpreted as an effect of a transition from an initial $\alpha \leftrightarrow \gamma$ pathway to an ultimate $\beta \leftrightarrow \beta$ pathway. Similar voltage shifts during an $\alpha \leftrightarrow \beta$ transformation were discussed in detail by Visscher and Barendrecht *(3541)* for electrodeposited films, by Glarum and Marshall *(1193)* for films made by pulse anodization, and by Oliva et al. *(2631)* for sintered battery electrodes. Depending on the deposition conditions, it is possible to make films with double-peak features during voltammetric scans *(3541)*; such structures are associated with inhomogeneous films having a mixed or layered α/β configuration.

Figure 19.11, after Fantini and Gorenstein *(1038)*, reports data for Ni oxide films electrodeposited via the sulfate route (specifically from a "Briggs solution"). Film growth yielded increasing charge densities connected with ion intercalation/deintercalation. The voltammograms may give evidence for the presence of both α and β phases. Data similar to those in Fig. 19.11 were reported elsewhere as well for films deposited from sulfate solutions *(3384)*.

The growth of anodic films under potential cycling is conveniently studied by voltammetry. Data of this type were earlier reported in Fig. 19.5.

Impedance spectrometry is a powerful method for studying thin films. It was employed by Gorenstein et al. *(1258)* for a detailed analysis of ion intercalation/deintercalation in sputter-deposited Ni oxide films in a KOH electrolyte. Figure 19.12 depicts Nyquist diagrams, plotted in analogy with Fig. 6.20, for the complex impedance Z in the 6.5×10^{-3} to 6.5×10^{4} Hz frequency range as different voltages U were applied to a film. A presumed H^+ intercalation is found to change the curve shapes. At U = -400 mV and at the highest frequencies, the impedance curves showed evidence for a semicircle in the complex plane. The data can be interpreted in terms of the modified Randles circuit shown in Fig. 6.21, and it is possible to extract U-dependent values of the pertinent circuit elements, viz. the interfacial resistance R_I, the double-layer capacitance C_{DL}, the Warburg element Z_W, and the constant phase element Z_{CPE} (taken to be a pure capacitor C_L in the work by Gorenstein et al. *(1258)*). Specifically going from -0.5 to +0.6 V vs. SCE, it was found that R_I decreased by about four orders of magnitude whereas Z_W and C_L increased strongly.

Figure 19.13 gives an even clearer demostration of the applicability of a modified Randles circuit; it shows Nyquist diagrams for a sputter-deposited Ni oxide film in as-deposited state and after Li^+ intercalation from a $LiClO_4$ + PC electrolyte *(847)*. Going from high to low frequency, there is a well-defined semicircle (from which R_I and the electrolyte resistance can be evaluated), a linear part with 45° slope (governed by Z_W), and another linear part (determined by Z_{CPE}). The analysis allows, among other things, an estimate of D_{Li+} (cf. Sec. 19.5).

Impedance spectrometry has been applied also to Ni oxide films made by anodization in concentrated H_2SO_4 *(762)* or H_2SO_4 + Na_2SO_4 *(1766)*, by pulse anodization *(1193)*, and by electrodeposition from a "Briggs solution" *(2155)*. Glarum and Marshall *(1193)* interpreted their data on the premise that a phase boundary movement took place in individual grains as H^+ was intercalated/deintercalated; the dynamics of this movement was determined by the electrical

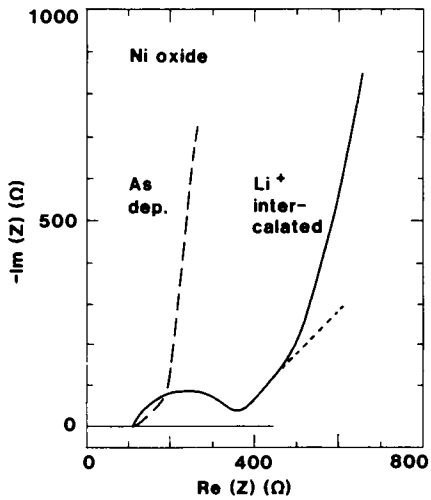

Fig. 19.13 Complex impedance Z vs. frequency for a sputter-deposited Ni oxide film under as-deposited conditions and after Li^+ intercalation from $LiClO_4$ + PC. The dotted line represents a 45° slope. After Decker et al. *(847)*.

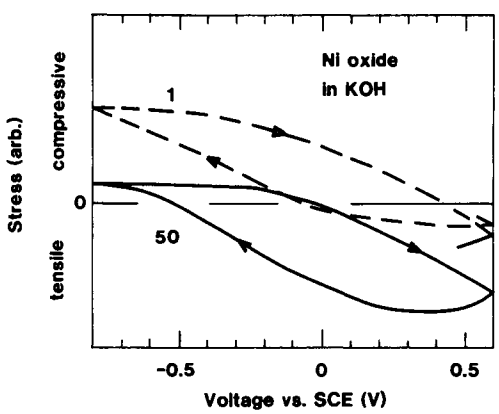

Fig. 19.14 Mechanical stress vs. voltage during potentiodynamic treatment of a sputter-deposited Ni oxide film in KOH. Dashed and solid curves were measured during the first and 50^{th} voltage sweep, respectively. Arrows denote scan direction. From Andersson et al. *(95)* and Scarminio et al. *(3033)*.

conductivity. Impedance spectrometry was used to study Ni oxide battery electrodes in *(383, 2044, 2137, 3819)*).

Beam deflectometry can be employed to elucidate changes in mechanical properties under ion intercalation/deintercalation, as pointed out in Sec. 6.7. This technique has been used *(95, 849, 1020, 3033)* to investigate sputter-deposited Ni oxide films in a KOH electrolyte. The stress level in the film--conveniently determined from the bending of a thin glass substrate--changed upon the application of a voltage to the film, as illustrated in 19.14. The overall stress varied during the initial voltage sweeps, which may be associated with permanent ion incorporation or irreversible structural modifications. The data give clear evidence for ion intercalation/deintercalation in principle agreement with the Bode reaction scheme. Similar results were found for Ni oxide films overcoated with 0.1-μm-thick Pd layers serving as "proton filters" *(95, 3033)*. The latter data show convincingly that proton exchange dominated the intercalation/deintercalation under the given conditions. Beam deflectometry has been applied also to electrodeposited films in KOH *(1259, 2936)* and to sputter-deposited films in $LiClO_4$ + PC *(847-8, 2714, 3034)*. The stresses were higher under Li^+ intercalation than under H^+ intercalation, which is to be expected from the difference in ionic radius. There was evidence that cations from the electrolyte participated in the electrochemical reaction.

Detailed *microbalance studies* of Ni oxide films have been carried out in order to shed further light on the intricacies of the ion intercalation/deintercalation processes. The upper part of Fig. 9.15, from Nemetz et al. *(2518)*, shows a voltamassogram and a corresponding voltammogram for a 0.62-μm-thick evaporated film after ten voltage cycles in 1 M NaOD. This electrolyte was used, rather than the chemically equivalent NaOH, in order to augment the mass effects. The voltammogram is similar to the dashed curve in Fig. 19.7, which may indicate that stable electrochemical conditions had not yet been attained. At voltages below 0.2 V vs. SCE, there is a weak mass change whose magnitude is proportional to the voltage. It is possible to assign this effect to H^+ exchange (in a corresponding NaOH electrolyte), specifically to H^+ ejection during electrochromic coloration. At voltages above 0.2 V vs. SCE, the mass changes sharply in conjunction with the occurrence of peaks in the voltammogram, indicating ion intercalation/deintercalation. The mass difference is ascribed to OH^- exchange, specifically to OH^- incorporation during coloration. According to the analysis by Nemetz et al. *(2518)*, the inclusion of one OH^- ion takes place at the same time as two H^+ ions are expelled. This model for the ion intercalation/deintercalation may seem fairly *ad hoc*, but it is nevertheless able to reconcile several experimental facts. Voltamassograms for evaporated Ni oxide films were discussed also in *(757, 2462)*. Principally similar data, again pointing at the presence of cation intercalation, were discussed by de Faria et al. *(849)*.

The lower part of Fig. 9.15 refers to data for a Ni oxide film, made by electrodeposition from $Ni(NO_3)_2$, in 1 M KOH. The results are from Cordoba-Torresi et al. *(757)*. Once again the major changes in the voltamassogram occur when the voltammogram displays distinct peaks. In order to account for the quantitative mass changes, it was surmised that intercalation/deintercalation took place with OH^- as well as hydrated alkali ions. A study by Bernard et al. *(369)* of similarly prepared films in 5 M solutions of LiOH, NaOH, KOH, RbOH, and CsOH showed that the alkali ions were associated with different numbers of water molecules (3 for Li^+; 2 for Na^+; 1 for K^+, Rb^+, and Cs^+). In addition to a fast exchange of these hydrated units, there was evidence for slower H^+ intercalation/deintercalation. Results for anodically prepared Ni oxide films were included in *(757)*.

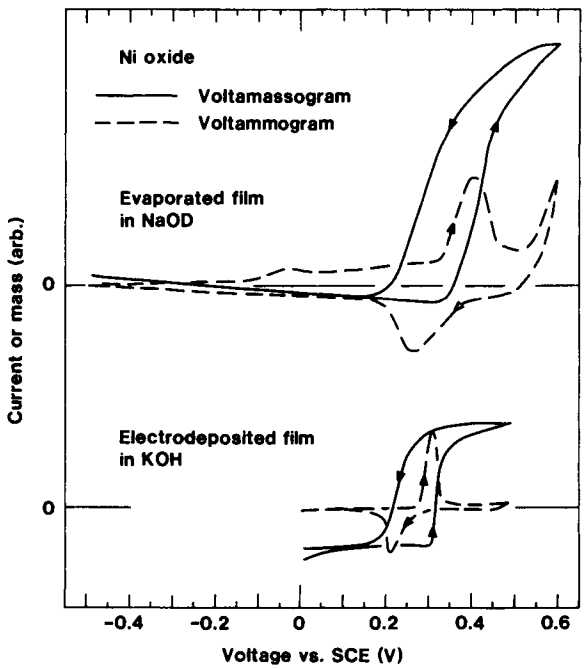

Fig. 19.15 Cyclic voltamassograms and voltammograms for Ni oxide films made by the shown techniques and studied in the shown electrolytes. The voltage scan rate was 10 mV/s. Arrows denote scan direction. After Cordoba-Torresi et al. *(757)* and Nemetz et al. *(2518)*.

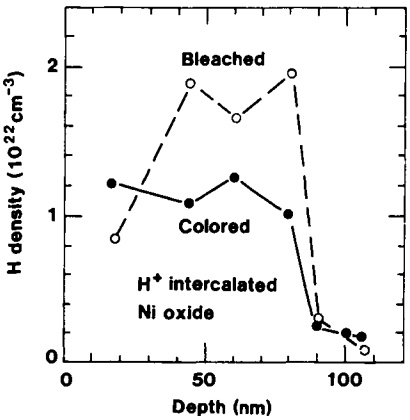

Fig. 19.16 Depth profiles for the H density as determined by NRA. The data refer to a ~0.2-μm-thick sputter-deposited Ni oxide film in bleached and colored states. Adjacent data points were joined by straight lines. After Svensson and Granqvist *(3290-2, 3294)*.

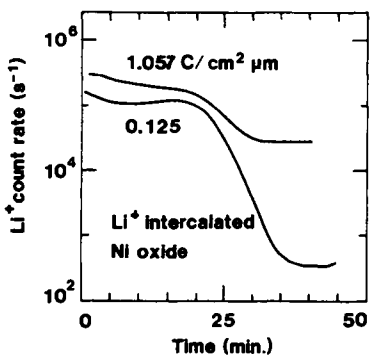

Fig. 19.17 Depth profiles for Li^+ ions as determined by SIMS. Data are shown for a sputter-deposited Ni oxide film with two densities of inserted charge. After Decker et al. *(847)*.

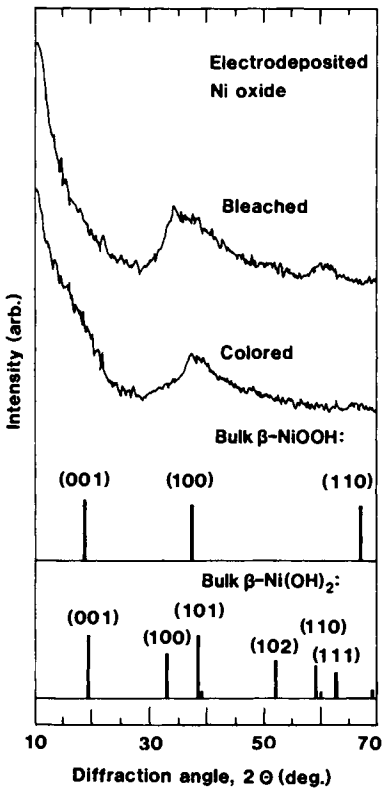

Fig. 19.18 X-ray diffractograms for an electrodeposited Ni oxide film in bleached and colored states. The vertical bars in the lower part indicate diffracted intensities for bulk samples of β-NiOOH and β-$Ni(OH)_2$. From Chigane and Ishikawa *(691)*.

The microbalance studies show that the ion intercalation/deintercalation processes may be very complicated and dependent upon the nature of the film--which in its turn is a function of the deposition parameters--and on the electrolyte. Apparently a competition of H^+, OH^- and (hydrated) alkali ions can take place at least for films in direct contact with aqueous electrolytes.

19.7 Ion Intercalation/deintercalation Studied by Physical Techniques

Depth profiling of intercalated species has been accomplished by NRA and SIMS. The former analytical tool, specifically the ^{15}N technique, has been used to investigate the hydrogen content in Ni oxide films at different levels of charge insertion. Figure 19.16, from Svensson and Granqvist *(3290-2, 3294)*, refers to films made by rf magnetron sputtering of Ni in O_2, followed by electrochemical cycling in 1 M KOH. The hydrogen density was higher in the bleached state than in the colored state. The data are consistent with the bleached state being $Ni(OH)_2$ and the colored state being NiOOH, but the error bars on the H density were so large that one should not draw too far-reaching conclusions. Results analogous to those in Fig. 19.16 have also been obtained for anodic films in KOH *(761)* and for evaporated films in multilayer devices with Ta_2O_5 and W oxide *(253, 256, 3562)*; the latter data will be further discussed in Sec. 29.4.

Lithium intercalated sputter-deposited films have been studied by SIMS *(590, 847)*. Data for a dc sputtered Ni oxide film in $LiClO_4$ + PC are shown in Fig. 19.17, after Decker et al. *(847)*. The Li^+ count rate is given as a function of depth, represented by a sputtering time. A high charge insertion yields a high count rate, proving that Li^+ enters the Ni oxide. Accompanying changes in the H^+ content, with an inwards movement of hydrogen upon lithium incorporation, were documented by Campet et al. *(590)*.

Structure determination during ion intercalation/deintercalation can be accomplished by XRD. The inherent problem with thin films giving too weak diffraction peaks can be alleviated through a low angle (LA) of incidence for the X-rays; the analysis technique is then referred to as LAXRD. Measurements have been reported by Chigane and Ishikawa *(691)*, who studied Ni oxide films --electrodeposited from a solution of $NiCl_2$ and $(NH_4)_2SO_4$--in a borate buffer electrolyte. The X-rays were incident at a near-glancing angle of 0.3°. Figure 19.18 shows diffracted intensity vs. angle for a 0.4-μm-thick film in bleached and colored states. The broad peaks can be identified, at least tentatively, with the bulk data for β-NiOOH and β-$Ni(OH)_2$ given in the lower part of the figure. Both of these phases are hexagonal. The colored film has a structure of β-NiOOH type, and the bleached film has a structure of β-$Ni(OH)_2$ type. Hence the electrochromism is associated with the $\beta \leftrightarrow \beta$ path in the Bode scheme (reaction 19.4). The absence of clear diffraction from the *(001)* planes in β-NiOOH and β-$Ni(OH)_2$ is consistent with the crystallographic *c* axis being parallel to the substrate. Reactions according to the $\alpha \leftrightarrow \gamma$ path can be ruled out since the pertinent phases are rhombohedral, and γ-NiOOH would give diffraction peaks at the angles 12.8° and 26°.

Raman spectroscopy is an alternative and complement to (LA)XRD for elucidating structural changes during ion intercalation/deintercalation. Its usefulness rests on having access to well-defined absorption spectra for the relevant Ni oxide phases; such data can serve as "fingerprints" for the reactions taking place in thin films. Following Johnston and Graves *(1679)*, who studied bulk-like samples prepared by established methods, β-$Ni(OH)_2$ has three distinct absorption bands at 318, 450, and 3580 cm^{-1}. These bands are present also in α-$Ni(OH)_2$, although with altered intensities, and in addition there are absorption peaks at several other wave numbers. The higher

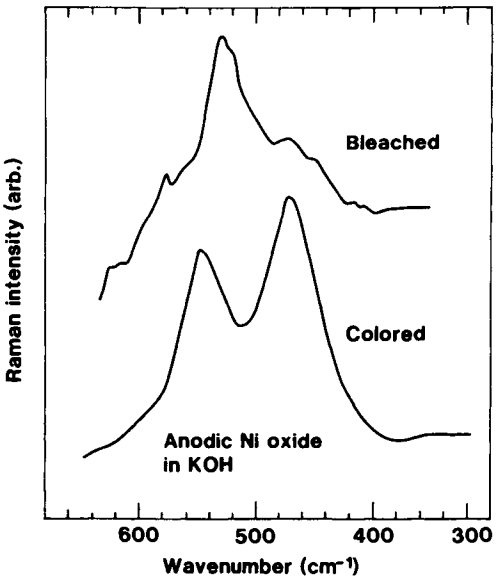

Fig. 19.19 Raman spectra for an anodic Ni oxide film in KOH. The film was potentiostatically colored and bleached at +0.5 and -0.5 V vs. SCE, respectively. After Cordoba-Torresi et al. *(761)*.

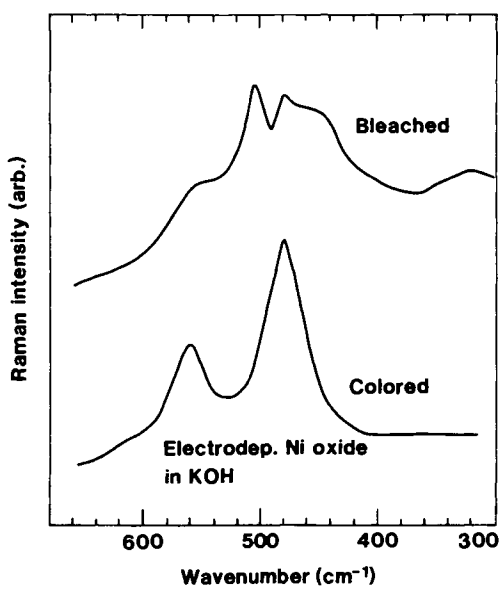

Fig. 19.20 Raman spectra for an electrodeposited Ni oxide film in KOH. The film was potentiostatically colored and bleached at +0.5 and -0.5 V vs. SCE, respectively. The curves have been smoothed. After Cordoba-Torresi et al. *(761)*.

oxides--β-NiOOH, γ-NiOOH, and $Ni_3O_2(OH)_4$--all have absorption bands at 469 to 478 cm^{-1}, and the γ-phase has additional bands at 548 and 3585 cm^{-1}. The similarity of the Raman features for a whole range of higher Ni oxides was emphasized by Melendres et al. *(2284)*. Supplementing Raman data for bulk-like speciments and Ni oxide electrodes can be found in *(763-5, 864, 866, 896, 1030, 1653)*. Bulk NiO has a broad absorption feature at 525 cm^{-1} due to multiphonon processes *(864, 866, 924, 1030)*.

Evaporated Ni oxide films were discussed in *(761, 865-6)*. The bleached material showed a broad and complicated Raman peak centered at ~520 cm^{-1}. Coloring induced a shoulder on this peak within the 450 to 500 cm^{-1} range. These data are consistent with a NiO-dominated material colored through hydroxylation.

Anodization in concentrated H_2SO_4 leads to films of sulfur-containing NiO, as pointed out in Sec. 19.4. Figure 19.19, after Cordoba-Torresi et al. *(761-2, 1577)*, shows Raman spectra for such films after potentiodynamic cycling in 1 M KOH. The bleached state displays a dominating peak at ~525 cm^{-1} indicating NiO and, perhaps, a secondary peak around 450 cm^{-1} due to $Ni(OH)_2$. The colored state has two clear peaks at ~470 and ~545 cm^{-1}. According to Johnston and Graves *(1679)*, this may indicate γ-NiOOH. Additional Raman data for anodized films were given in *(864-6, 1030)*. Melendres and Tani *(2285)* also studied films made by anodization in concentrated H_2SO_4; according to them the Raman spectrum indicated the presence of $NiSO_4 \cdot H_2O$. Thin films made potentiostatically in 0.05 M NaOH were discussed in *(2286)*.

Films prepared by electrodeposition from a $Ni(NO_3)_2$ solution have been analyzed by Cordoba-Torresi et al. *(761)* whose data are shown in Fig. 19.20. The colored film shows a double-peak structure similar to the one for the anodic film in Fig. 19.19. The bleached film had a complicated spectrum that could be decomposed into three additive components due to NiO, NiOOH, and $Ni(OH)_2$. Additional Raman data for electrodeposited films were given in *(762, 1027, 1577)*. Spectra from surface enhanced Raman spectroscopy, with a Ni oxide film deposited onto a rough gold surface, were analyzed by Desilvestro et al. *(895-6)*.

Infrared absorption spectroscopy is considered next. One should again note that β-$Ni(OH)_2$ comprises stacked layers of NiO_6 octahedra with hydroxyl groups parallel to the *c* axis and lying alternately above and below the *(0001)* plane. The hydroxyl groups are "free"--i.e., hydrogen bonding is absent--and therefore the vibrational modes of the OH groups do not couple to the lattice modes. This leads to a characteristic infrared absorption signature with a well defined spike at a wavenumber ~3650 cm^{-1}, corresponding to an antisymmetric stretching fundamental. In contrast with this, β-NiOOH is a hydrogen-bonded material whose IR absorption signature is a broad absorption peak centered at ~3450 cm^{-1}. These absorption features have been amply documented for bulk-like specimens *(260, 583, 1074, 1541, 1551, 1653, 1679, 1722, 1860-1, 2022, 2123, 2325, 2508, 2631, 2828, 3469)*. One could note, for completeness, that IR absorption spectra are also available for NiO bulk crystals *(180, 1180, 2363, 2365)*. It is obvious that IR spectra, particularly in the 3000 to 4000 cm^{-1} range, are able to identify the nature of the Ni oxide films.

Estrada et al. *(1022)* studied films made by dc magnetron sputtering of Ni in O_2 and immersed in 1 M KOH. The films were backed by infrared-reflecting In_2O_3:Sn layers, which made it convenient to apply IR reflectance spectroscopy *(310, 2263)*. In this technique, minima in the reflectance of obliquely incident p-polarized light correspond directly to maxima in the absorptance. This reflectance spectroscopy is inherently more sensitive than transmittance spectroscopy.

Figure 19.21, from Estrada et al. *(1022)*, shows IR reflectance spectra for a 0.15-μm-thick Ni oxide film in bleached state. After one voltage sweep from +0.6 to -0.8 V vs. SCE, the

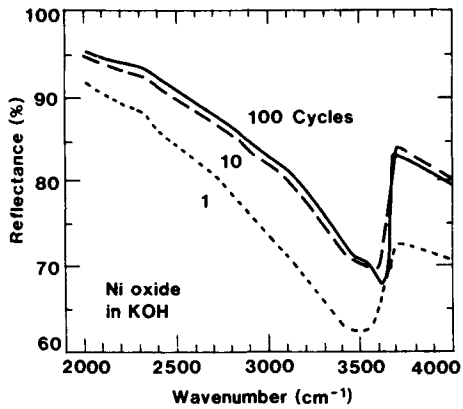

Fig. 19.21 Spectral infrared reflectance, measured at 60° angle-of-incidence and p-polarized light, for a sputter-deposited Ni oxide film in KOH. The film was cycled between +0.6 and -0.8 V vs. SCE for the shown number of times, and measurements were conducted in the bleached state. From Estrada et al. *(1022)*.

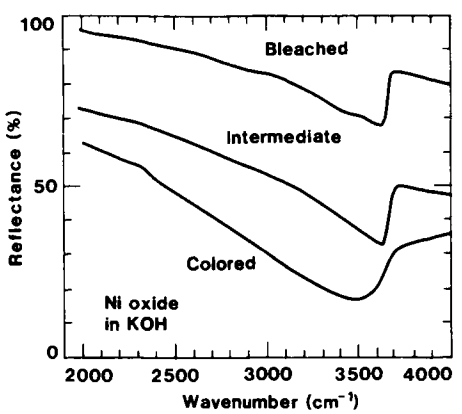

Fig. 19.22 Spectral infrared reflectance, measured at 60° angle-of-incidence and p-polarized light, for a sputter-deposited Ni oxide film in KOH. Data are shown for three states of coloration. From Estrada et al. *(1022)*.

spectrum displays a broad absorption feature at ~3500 cm^{-1}, proving that hydrogen bonding is present. After 100 voltammetric cycles, the reflectance level is increased, and a distinct absorption appears at ~3620 cm^{-1}, signaling "free" hydroxyl groups in β-$Ni(OH)_2$. After 10 cycles the properties are intermediate, though rather close to those for the long-term-cycled and electrochemically stable material. The hydrogen in the film after the initial cycle is likely to stem from the KOH electrolyte, and no absorption feature at ~3500 cm^{-1} was apparent in as-deposited films.

Figure 19.22 shows IR spectra for the same electrochemically stable film at three states of charge insertion. The colored film has a reflectance between ~60 and ~20 % and a broad absorption at ~3500 cm^{-1}, indicating a β-NiOOH-like structure. The bleached film has a reflectance between ~95 and ~70 % and a distinct absorptance spike at ~3620 cm^{-1}, showing that the material is β-$Ni(OH)_2$-like to a large extent. A tiny shoulder at ~3450 cm^{-1} may indicate that some hydrogen bonding remains, but this cannot be stated with certainty. At intermediate coloration, the IR reflectance spectrum lies in between the other two curves. Absorptance features were also noticed at ~580 cm^{-1} and 380 cm^{-1} *(95, 3665)*. The major conclusion of the infrared spectroscopy is that, after a sufficient number of intercalation/deintercalation cycles, the sputtered films follow the $\beta \leftrightarrow \beta$ reaction path.

Infrared analysis has also been applied to Ni oxide films made by other techniques than sputter deposition. Thus evaporated films were studied with FTIR by Lynam and Habibi *(2123)*. The as-deposited film was hydroxylated by cycling in KOH, and the ensuing bleached material showed a strong absorption peak at ~3640 cm^{-1}, clearly associated with OH in β-$Ni(OH)_2$. Somewhat different results were claimed by Nemetz et al. *(2518)*, whose IR spectra showed a broad absorption band at ~3400 cm^{-1} irrespective of the film being colored or bleached; the absorption intensity was increased under coloration. Data in good agreement with those in Fig. 19.22 have been shown for films made by electrodeposition *(1590, 2657)* and chemical precipitation *(3428)*.

Nickel oxide films made by potential cycling in NaOH have been studied several times *(309, 1390, 3539)*. Visintin et al. *(3539)* presented evidence for films being β-$Ni(OH)_2$ and β-NiOOH. Films made by electrodeposition from nickel sulfate solutions showed complicated FTIR spectra with clear evidence for H_2O *(2004, 2508, 3112, 3762-5)*. These films have a duplex structure with an inner α-$Ni(OH)_2$ phase and an outer β-$Ni(OH)_2$ phase in the bleached state. Reactions can take place according to $\alpha/\beta \leftrightarrow \gamma/\beta$ *(2508)*. Films made by the nitrate route were studied in *(1027)*.

XPS has been used to investigate the valence state of nickel and oxygen when ions were intercalated into Ni oxide films made by sputtering *(95, 1557, 3270)* and electrodeposition *(691)*. Spectra for $Ni2p_{3/2}$ are characterized by a doublet in the 850 to 865 eV range; at higher energies one finds another doublet due to $Ni2p_{1/2}$. When ions are intercalated, the $Ni2p_{3/2}$ feature broadens somewhat, and deconvolution can reveal contributions due to Ni^{2+} and Ni^{3+}. Figure 19.23, replotted from Suiyang et al. *(3270)*, shows data for a Ni oxide films made by rf magnetron sputtering in $O_2 + H_2$ followed by coloring in a 1 M KOH electrolyte. Two doublets, due to Ni^{2+} and Ni^{3+}, can be resolved. An as-deposited transparent film, on the other hand, only showed evidence for Ni^{2+}. Clearly these results are consistent with the view that a transparent film of $Ni(OH)_2$ is made absorbing through electron extraction so that at least part of the films is transformed into NiOOH.

The *O1s* spectrum is of particular interest since it carries information on whether the oxygen is in "pure oxide", hydroxyl groups, or water molecules (cf. the discussions around Figs. 14.2,

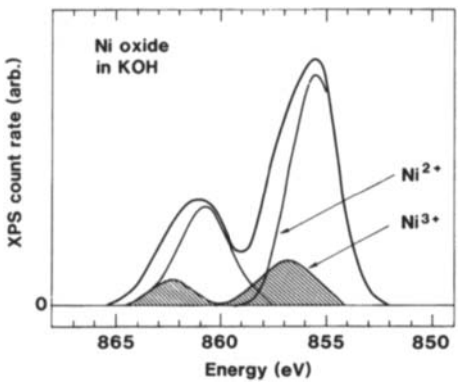

Fig. 19.23 Deconvoluted XPS spectrum for a sputter-deposited Ni oxide film colored in KOH. The pairs of doublets represent $Ni2p_{3/2}$ electrons in the valence states 2+ and 3+ (shaded). The upper curve is an envelope, which is in good agreement with measured data. After Suiyang et al. *(3270)*.

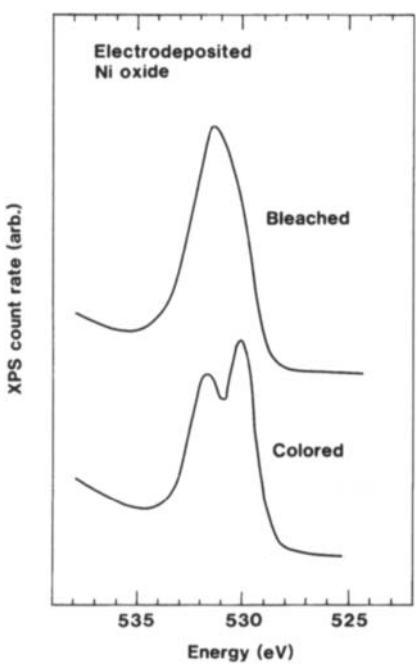

Fig. 19.24 XPS spectra representing *O1s* electrons for an electrodeposited Ni oxide film in bleached and colored states. From Chigane and Ishikawa *(691)*.

14.15 and 16.3). Figure 19.24 shows data from Chigane and Ishikawa *(691)* for Ni oxide films electrodeposited from an ammine complex solution and subsequently colored and bleached in a borate buffer solution. The bleached film is characterized by a single peak centered at ~531 eV, whose origin undoubtedly is in OH groups. A similar peak is seen in the colored state, but this film also displays a second peak at ~530 eV due to oxide. No trace of H_2O was found, which would have yielded an XPS signal around 533 eV. The *O1s* data give strong credence to the prevailing idea that, indeed, the bleached state is β-$Ni(OH)_2$ and the fully colored film is β-NiOOH. XPS data for dc magnetron sputtered films also showed one *O1s* peak for the bleached state and two peaks for the colored state *(95)*.

XPS spectra for nickel oxide, in good agreement with data in Figs. 19.23 and 19.24, have also been measured for films made by sputtering *(2219, 2221, 2867, 3662, 3665)* and electrodeposition *(2007-8)*.

There is an extensive literature on bulk-like Ni oxides, mostly related to surfaces of single crystals *(227, 233, 385, 500, 605, 1017, 1086, 1122, 1243, 1454, 1804-6, 1812, 1815, 1929, 2027, 2215, 2271, 2273, 2398, 2625-6, 2918-9, 3213, 3422-3, 3481, 3487, 3513, 3557)*. This XPS work is motivated by the important applications of Ni oxide in catalysis, and it is only partly relevant to electrochromism in thin films. In the case of clean NiO-like surfaces, the high-energy satellites for the *Ni2p* and *O1s* electrons--indicated also in Figs. 19.23 and 19.24--have been associated with multielectron final states induced by defect sites *(3422)*.

19.8 Ultraviolet Absorption and Semiconductor Bandgap

Ultraviolet absorption has been studied for films made by reactive evaporation *(2941)*, electrodeposition from $Ni(NO_3)_2$ *(611)*, anodization in concentrated H_2SO_4 *(399)*, spray pyrolysis *(2326)*, and thermal oxidation of metallic Ni *(969, 2941)*. The absorption increased sharply at energies above an optical bandgap of 3.6 to 4.0 eV. This was also true for thin passivating layers on Ni *(2684-5)*. Photocurrent spectra yielded E_gs that were marginally smaller *(611, 3628)*. Absorbing films, containing NiOOH, had an effective bandgap of 1.7 to 1.8 eV *(611, 2803)*.

The E_gs measured for transparent Ni oxide films agree well with bulk data based on absorptance *(754, 2521)*, reflectance *(679, 1572, 2800)*, photocurrent *(1870)*, and electroreflectance *(2275)*. A detailed study was carried out by Newman and Chrenko *(2521)*, who found a series of absorption lines at $1 < \hbar\omega < 3.5$ eV--due to internal transitions of the Ni atoms--and a steep increase of the absorptance at $\hbar\omega > 3.5$ eV. The absorption coefficient was larger than 10^6 cm^{-1} at 4 eV and beyond. Absorption lines have been found by electroreflectance in thin Ni oxide films *(1039)*.

The bandstructure of NiO, and the nature of its optical bandgap, have been debated intensely for many years, and it is worthwhile at least mentioning this issue here. A long held contention is that NiO is a "Mott insulator" *(2418)*--indeed it is often regarded as the prototype Mott insulator *(472)*. Whereas this view has been favored in some recent work *(2272)*, the prevailing view now is that NiO is an ordinary band insulator, and that the optical bandgap is due to *d-d* transitions with an electron removed from the valence band and placed into the conduction band *(1113-5, 1567-72, 2027, 3030-1, 3386-7)*; specifically, the bandgap transitions correspond to $3d^8 \rightarrow 3d^9L$, where L denotes a hole on a O^{2-} ligand. Additional bandstructure data for NiO can be found in *(27-8,*

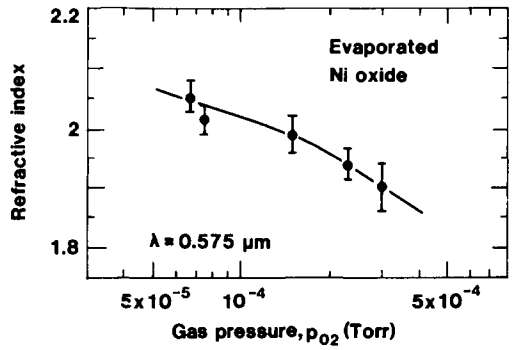

Fig. 19.25 Refractive index for Ni oxide films made by reactive evaporation at different values of the oxygen gas pressure p_{O2}. The data are presented in a way that allows direct comparison with Fig. 19.1. After Bange et al. *(253)*.

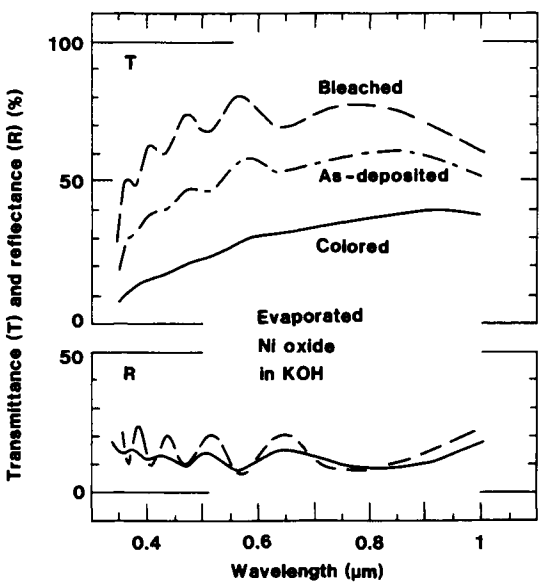

Fig. 19.26 Spectral transmittance for an evaporated Ni oxide film in as-deposited state and after coloration and bleaching in KOH. After Ottermann et al. *(2670)*.

113, 2234-5, 2558, 3779). Bandstructures are not known in any detail for the more relevant Ni hydroxides, but some salient features were discussed by Kuklin *(1951).* Electronic structures of the structurally related $Mg(OH)_2$ *(796)* and CdI_2 *(3232)* have been considered recently.

19.9 Optical Properties in the Luminous and Near-infrared Range: Evaporated Films

The optical properties depend on the evaporation conditions. An example is given in Fig. 19.25, showing the refractive index at $\lambda = 0.575$ μm as a function of oxygen gas pressure during reactive *e*-beam evaporation; the data were replotted from Bange et al. *(253).* The refractive index is ~2.05 at a low p_{O2}, and it drops to ~1.9 at $p_{O2} = 3 \times 10^{-4}$ Torr. This effect is caused by a diminished film density, as apparent from Fig. 19.1. The optical absorption increased with increasing deposition rate.

Electrochemical treatment of evaporated films can alter their optical absorption in proportion with the exchanged charge *(256, 2005, 2445, 2462, 2518).* Figure 19.26, from Ottermann et al. *(2670),* shows transmittance and reflectance for a reactively *e*-beam evaporated Ni oxide film in as-deposited state and after coloration and bleaching in 1 M KOH. The absorptance was strongly modulated, particularly at short wavelengths in the luminous range. An analogous modulation of the spectral transmittance was reported in *(37, 253, 2123, 3088).* Supporting data, recorded by optical multichannel analysis, were given in *(762, 865-6, 1030, 1577).* Figure 19.26 also shows that the as-deposited film has some absorption in the full $0.35 < \lambda < 1$ μm range.

Optical constants for evaporated Ni oxide films treated in an 1 M KOH electrolyte are given in Fig. 19.27, after Ottermann et al. *(2245, 2669-70).* The real part n showed dispersion and went monotonically from ~2.1 at $\lambda = 0.4$ μm to ~1.83 at $\lambda = 1$ μm. The magnitude of the imaginary part k varied strongly with the amount of charge exchange and lay at 0.12 ± 0.02 in the $0.4 < \lambda < 1$ μm range for 10.6 mC/cm^2. Pure crystalline NiO has $k << 0.01$ *(2521).*

19.10 Optical Properties in the Luminous and Near-infrared Range: Sputter-deposited Films

Sputter-deposited Ni oxide films have optical properties that are fairly similar to those of evaporated films. The as-prepared films have an absorption that depends on the sputtering ambient. According to Miedzinska et al. *(2310),* films deposited in Ar + O_2 onto room-temperature substrates at a pressure of 40 mTorr had $k \sim 0.03$ in the mid-luminous range for a certain O_2 content, and $k \sim 0.3$ when this content was increased by about seven times. This effect was ascribed to the presence of Ni^{3+}, specifically to the amount of Ni_3O_4 (or $Ni_2O_3 \cdot NiO$). Sputtering in $O_2 + H_2$, on the other hand, gave transparent films with low k *(3293).*

Electrochemical treatment is capable of changing the transmittance as studied for films sputter-deposited in different gas ambients and treated in KOH *(238, 1020, 1258-9, 2005, 2535, 3033-4, 3037)* or $LiClO_4$ + PC *(133, 590, 847, 1039, 2714, 3034).* The observed optical effect was smaller for Li^+ intercalation than for polarization in KOH *(3034).* Effective lithiation requires an electrochemical "activation", which in itself leads to some transmittance increase *(847, 2715).* Bleaching of initially colored films can take place by Li^+ implantation *(1557).*

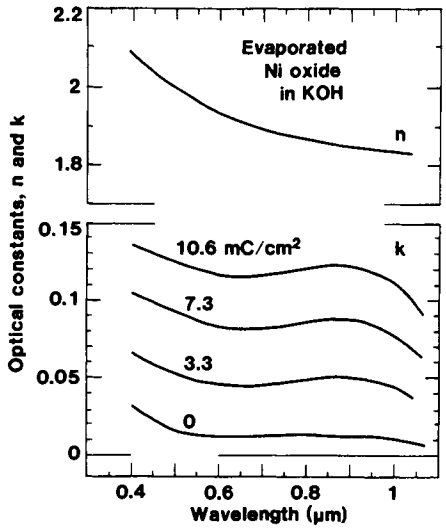

Fig. 19.27 Spectral optical constants, $n + ik$, for evaporated Ni oxide films in KOH. The data for k depend on the extracted charge density. After Ottermann et al. *(2245, 2669-70).*

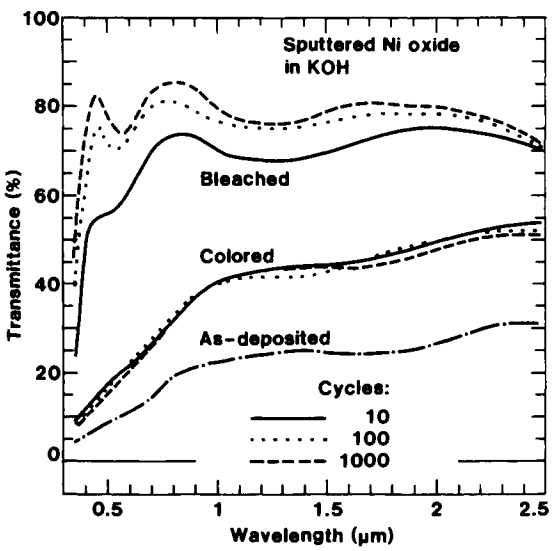

Fig. 19.28 Spectral transmittance for a sputter-deposited Ni oxide film in virgin state and after coloration and bleaching in KOH for the shown number of cycles. After Estrada et al. *(1021).*

Spectral optical properties have been studied for films sputter-deposited in O_2 *(95-6, 749, 1021, 2535, 3290-2, 3294)*, Ar + O_2 *(1591, 1827, 3662-3, 3665)*, and O_2 + H_2 *(3270, 3293-4)*. Figure 19.28, after Estrada et al. *(1021)*, shows transmittance for a 0.11-μm-thick film made by dc magnetron sputtering in O_2 followed by cycling in 1 M KOH. The as-deposited film has a transmittance below 30 % in the full $0.4 < \lambda < 2.5$ μm range due to absorption. Cycling in the electrolyte led to a gradual evolution of electrochromism. Of the order of 100 intercalation/deintercalation cycles were needed to establish a state with maximum transmittance, whereas the colored state was reached after less than 10 cycles. One should note again that the optical modulation is strongest at short wavelengths, though it is still significant at $\lambda = 2.5$ μm. The reflectance remained low irrespective of the intercalation level.

Conell et al. *(749)* studied the evolution of electrochromism in Ni oxide films made by slow rf diode sputtering in O_2. It took well over 1000 cycles to approach the limits of the optical modulation; the sluggishness is presumably connected with a high film density. The colored state seemed to establish itself at a slower pace than the bleached state, which contrasts with the results shown in Fig. 19.28.

The discussion above shows clearly that the deposition parameters are important for the ensuing optical properties. This effect is further elucidated in Fig. 19.29, showing data from Andersson et al. *(95)* on the transmittance in fully colored and bleached states for 0.1-μm-thick films deposited onto substrates at two different temperatures. For an unheated substrate, the optical modulation is large and consistent with the results in Fig. 19.28. At $\tau_s = 250$°C, the modulation is much smaller and, in particular, it is not possible to reach a deeply colored state. Data taken at $\tau_s = 120$°C were intermediate between those shown in Fig. 19.29. A film annealed at 400°C for 40 h did not display any electrochromism whatsoever after 100 voltammetric cycles, although there was evidence for some charge insertion and extraction. It is likely that the τ_s-dependence of the electrochromism is associated with hydrogen loss and accompanying densification.

It is evident that Ni oxide films can undergo a large number of electrochromic color/bleach cycles without noticeable degradation; some samples were tested successfully for up to 2×10^4 cycles *(3290-2, 3294)*. Furthermore the open circuit memory is good, and the films maintain their optical properties for extended periods of time in air. In one experiment *(1021)*, a film remained fully transparent for at least 9 h while the colored state was bleached by ~1 % during 1 h and by ~3.5 % during 9 h. These properties, as well as the wide spectral range for transmittance changes, indicate that electrochromic Ni oxide films are suitable for modulating wavelength-integrated luminous and solar transmittance. Their magnitudes are shown in Fig. 19.30 as a function of the charge per unit area extracted from transparent films *(1021, 3293)*. T_{lum} could go from ~80 % to about 20 % for films made by sputtering in O_2 and to less than 10 % for films made by sputtering in O_2 + H_2, whereas T_{sol} could go from ~75 % to about 30 % for films made by sputtering in O_2 and to less than 20 % for films made by sputtering in O_2 + H_2. The film thickness was not of critical importance for the transmittance modulation *(3293)*.

Palladium spillover offers an alternative technique for affecting the optical properties of Ni oxide films. Specifically, Scarminio et al. *(3033)* exposed as-sputtered dark Ni oxide films with a Pd top layer to a hydrogen-rich gas and found that the samples bleached significantly.

Regarding quantitative optical properties, the spectral dependence of the refractive index was reported by Mücke et al. *(2445)*; the dispersion was similar to that for evaporated films (cf. Fig. 19.25), but the entire curve was higher by approximately 0.25. This may be a manifestation of the larger density in the sputter-deposited films.

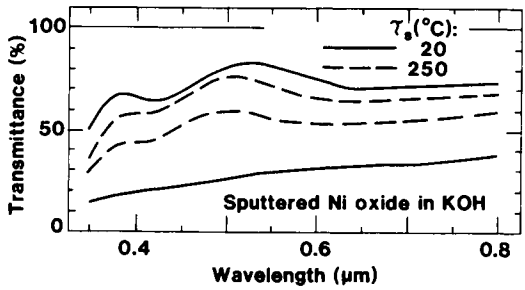

Fig. 19.29 Spectral transmittance for Ni oxide films sputter-deposited onto substrates at a temperature τ_s. Coloration and bleaching were carried out in KOH. After Andersson et al. *(95)*.

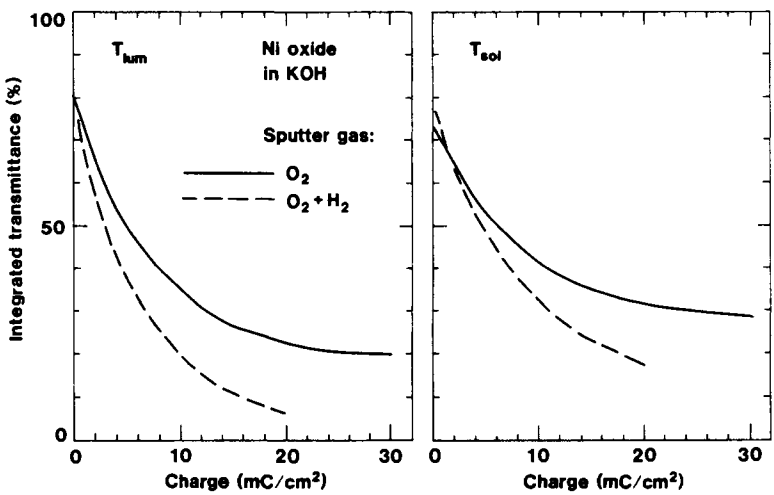

Fig. 19.30 Wavelength-integrated luminous (lum) and solar (sol) transmittance for sputter-deposited Ni oxide films subjected to charge extraction in KOH. The films were produced with two sputter gases. After Granqvist et al. *(1021, 3293)*.

Figure 19.31 reports the spectral absorption coefficient for films made by sputtering and coloration in KOH; the data were reproduced from Nilsson and Niklasson *(2535)* (see also *3293-4)*. There is a general drop in the absorption at increasing wavelength. It is interesting to observe two shoulders on the curves: one at 0.5 to 0.6 μm and the other at 0.7 to 0.85 μm. The difference between the spectra indicates a dominating peak around 0.53 μm. These results are fairly consistent with results by Miedzinska et al. *(2310)*, who found that sputter-deposited oxygen-rich films had peaks at 0.57 and ~1 μm. The peaks are likely to be associated with Ni^{3+} ions. This contention is supported by optical data for bulk samples of Li-doped NiO, which showed absorption peaks at 0.55, 0.88, and 1.56 μm *(73)*. It should be noticed that crystal field absorption due to Ni^{2+} is well known--it has been studied both in NiO *(2521)* and $Ni(OH)_2$ *(2107)*--but this effect gives an absorption that is too weak by at least an order of magnitude to explain the data in Fig. 19.31. A trustworthy explanation for the absorption peaks associated with Ni^{3+} is yet to be found.

19.11 Optical Properties in the Luminous and Near-infrared Range: Films Made by Electrochemical and Chemical Techniques

The electrochromism of electrodeposited Ni oxide films has been studied in detail. Figure 19.32 shows spectral transmittance in the luminous range for a film made from a $Ni(NO_3)_2$ solution, after Carpenter et al. *(609)* (see also *749, 769)*. The optical modulation is strong, particularly at short wavelengths. Coloration and bleaching in 1 M KOH took less than 1 s for small samples. Larger sizes, or thicker films, led to slower optical changes. The spectral absorption is shown in more detail in Fig. 19.33, after Corrigan and Knight *(772)* (see also *611)*. The absorbance was recorded *in situ*, relative to its value in the bleached state, during charge extraction from a 20-nm-thick film on a gold surface. The absorption is peaked at $\lambda \approx 0.45$ μm and shows a shoulder at $\lambda \approx 0.3$ μm.

Whereas the optical modulation was excellent during the intitial intercalation/ deintercalation cycling, prolonged operation led to severe deterioration. This is clear from the dashed curves in Fig. 19.32, showing that the transparency is lost and the modulation range diminished after 500 cycles. Significant degradation was, in fact, noticed already after 180 cycles *(771)*. Corrigan et al. *(329, 769-71)* reported on an extensive program to improve the properties of films electrodeposited via the nitrate route. Initial tests of Ni oxide in 0.01 M, 0.1 M, and 1 M KOH indicated a slight improvement of the durablility in the least concentrated electrolyte. Replacing the KOH with 0.1 M of LiOH, NaOH, CsOH, or $Ba(OH)_2$ led to small but unambiguous differences in the durability, with LiOH being best and $Ba(OH)_2$ worst. The addition of trace amounts (3×10^{-4} M) of $K_3Fe(CN)_6$ to 1 M KOH had a larger effect, and films could remain reasonably stable up to 3500 cycles. Codeposition from 90/10 % electrolytes of $Ni(NO_3)_2$ with added nitrates of Cd, Ce, Cr, Co, Cu, Fe, La, Pb, Mg, Mn, Ag, Y, or Zn could give an improvement of the durability, with Ce and La being the best. Still better properties, with durability reported up to 2000 cycles, were seen in ternary oxides with 5 % Co and 5 % La. It is worth noting that nickel battery electrodes can be improved by adding Li to the electrolyte and Co to the oxide *(143, 145, 626, 756, 1033, 1052-3, 2662)*. One may speculate that the degradation, both in electrochromic films and in battery electrodes, is caused by mechanical deformations *(3818)*, and that these are impeded by the additions to the electrolyte and/or oxide. It must be stressed, finally, that despite all of these efforts to improve the durability of films deposited from $Ni(NO_3)_2$, sputter-deposited Ni oxide can have much superior durability.

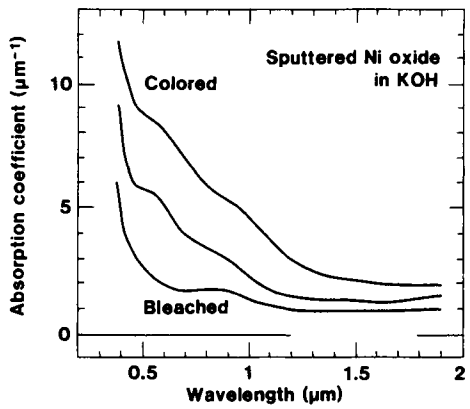

Fig. 19.31 Spectral absorption coefficient for sputter-deposited Ni oxide films subjected to charge extraction in KOH. Data are shown for colored, intermediate, and bleached states. From Nilsson and Niklasson *(2535)*.

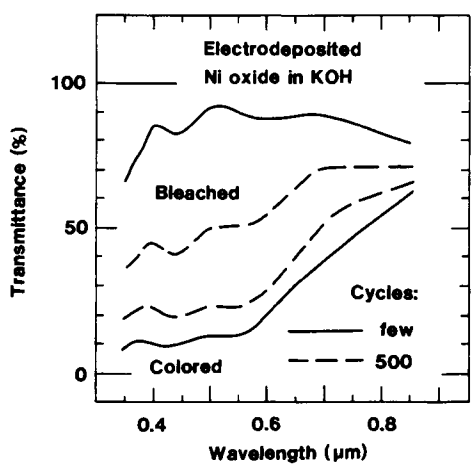

Fig. 19.32 Spectral transmittance for Ni oxide films electrodepostied from a $Ni(NO_3)_2$ solution. The films were colored and bleached in KOH for a variable number of cycles. After Carpenter et al. *(609)*.

Transmittance data for films deposited via the nitrate route were also given in *(762, 1259)*. Films electrodeposited by variations of the sulfate route, or by other means, were discussed in *(647, 691, 1038, 1590, 2007-8, 2127, 2389, 3384, 3764-5)*. It seems that the optical properties were consistent with those shown in Figs. 19.32 and 19.33. Regarding durability, Morisaki et al. *(2389)* indicated a rapid deterioration of films made from $NiSO_4 + (NH_4)_2SO_4$, whereas Chen et al. *(674)* claimed that similarly prepared films could withstand as much as 10^5 color/bleach cycles. Clearly durability needs to be studied in more detail.

Optical constants have been measured by ellipsometry at wavelengths in the luminous range for films made by electrodeposition from $Ni(NO_3)_2$. According to Ord *(539, 2648)* and Visscher and Barendrecht *(3541)*, the different hydrous Ni oxide phases have refractive indices of 1.4 to 1.5. Both α-$Ni(OH)_2$ and β-$Ni(OH)_2$ are characterized by $k \approx 0$, whereas β-NiOOH has $k \approx 0.17$ and γ-NiOOH has $0.3 < k < 0.4$.

There are many studies of optical changes during electrochemical treatment of anodized nickel surfaces. The first published report, it seems, was in 1933 by Tronstad *(3454)*, who used ellipsometry to follow optical changes during anodization of Ni in $H_2SO_4 + Na_2SO_4$. This investigation was also referred to in the historic outline in Sec. 1.4. Subsequent work has shown that the luminous reflectance can be modulated typically between light yellow and brownish black for Ni anodized in concentrated H_2SO_4 *(762, 865-6, 1030, 1577)* or in the oxygen evolution range in buffered neutral borate solutions *(2140)*. A similar modulation could also be obtained by extended potential cycling of Ni in KOH *(2007-8, 2269)* or NaOH *(562)*. According to McIntyre et al. *(2261, 2269)*, it is possible to have very rapid switchings between colored and bleached states; the coloring time was reported to be 50 ms and the bleaching time to be 19 ms.

Anodized Ni surfaces have also been studied in numerous other works; typically, the samples were prepared by potential cycling in KOH, LiOH, or NaOH, or by passivation in alkaline, neutral, or acidic eletrolytes *(411, 657-9, 681-2, 1389-90, 1416, 1475-6, 1646, 1745, 1949, 2068, 2104, 2266, 2591, 2684, 2688, 2868-70, 3008, 3540, 3542, 3661)*. The optical constants, often determined by ellipsometry, are highly inconsistent, which almost certainly is a consequence of different structures and compositions of the films. Notwithstanding this somewhat dismal state of affairs, it is interesting to note that k values as high as ~0.5 have been reported several times for wavelengths within the luminous range *(681, 1745, 2591, 2688)*. Hence it appears that the inherent luminous absorptance can be larger in anodic Ni oxide than, for example, in W oxide.

Optical modulation data are available for some films made by purely chemical techniques. Thus films prepared by dipping in $Ni(NO_3)_2 \cdot 6\ H_2O$ followed by heat-treatment were studied by Scarminio et al. *(3037)*, who made spectral measurements and verified that electrochromism could be observed. Electrochromism was documented at a fixed wavelength also for films made by alternate dippings in $NiSO_4$ and KOH *(1037, 1259)*, by sol-gel technique *(2005)*, and by homogeneous chemical precipitation *(3428)*.

Tolstikhina et al. *(3420-1)* studied the optical properties of Ni oxide films made by CVD using $Ni(CO)_4$. Figure 19.34 shows the refractive index at $\lambda = 0.633$ μm for films deposited onto substrates with temperatures between 85 and 180°C; n goes from ~1.8 at $\tau_s = 100$°C to ~2.1 at $\tau_s = 180$°C, indicating that the film density is strongly affected by τ_s. Heating the films to $\tau_a > 300$°C in the presence of O_2 led to a precipitous increase of the absorptance across the luminous range. This proves that Ni oxide films are capable of thermocoloration. Films made by CVD from Ni acetyl acetonate were studied by Maruyama and Arai *(2200)*, who found excellent electrochromism.

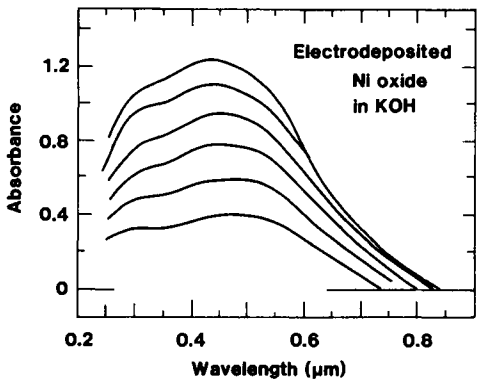

Fig. 19.33 Spectral relative absorbance for a Ni oxide film electrodeposited from a $Ni(NO_3)_2$ solution and colored in KOH by successively increased charge extration. After Corrigan and Knight *(772)*.

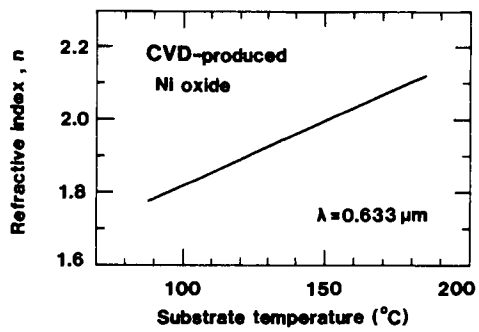

Fig. 19.34 Refractive index for Ni oxide films made by CVD onto substrates at different temperatures. The curve was drawn through a series of data points. After Tolstikhina et al. *(3420)*.

19.12 Coloration Efficiency

The change in optical density is linearly dependent on the charge insertion/extraction up to a certain limiting charge per volume unit. This behavior is illustrated in Fig. 19.35 for Ni oxide films made by reactive rf sputtering from a NiO target in Ar + O_2 and subsequent coloration and bleaching in NaOH. The data are from Yamada et al. *(3686, 3689-90)* who studied the optical properties at λ = 0.64 μm. Analogous results were shown in Fig. 9.15 for W oxide.

A coloration efficiency of -36 cm^2C^{-1} is consistent with Fig. 19.35. The CE was weakly dependent on the sputtering conditions. This is seen in Fig. 19.36, where the data pertain to sputtering at different total gas pressures with the O_2/Ar ratio kept at 0.1.

Spectral coloration efficiencies have been evaluated for evaporated Ni oxide films treated in KOH. Results are shown in Fig. 19.37, after Otterman et al. *(2445, 2668-70)*. In accordance with earlier shown results, the CE is strongly negative at short wavelengths, with a value as large as ~-60 cm^2C^{-1} at λ = 0.4 μm. The CE falls off towards longer wavelengths but is still substantial at λ = 1 μm. CEs have been evaluated at discrete wavelengths for other films made by evaporation *(37, 253, 2005, 2123, 3088)*, sputtering *(238, 749, 2005, 3033-4, 3663)*, electrodeposition via the nitrate *(609)* and sulfate *(674, 2389)* routes, CVD *(2200)*, and deposition from chemical solutions *(1037, 2005, 3037)*. All of these data are in fair agreement with the CEs in Fig. 19.37, albeit usually somewhat less negative.

19.13 Towards a Theoretical Model for the Optical Properties

The physical mechanism for the optical absorption in Ni-oxide-based films is not known. One could note that small polaron effects have been put forward to account for IR absorption *(180-1)* and electrical properties *(1598-9)* of Li-doped NiO crystals. A model involving small polarons has been seriously questioned by others, though *(28, 457)*. With the purpose of elucidating the absorption mechanism in Ni oxide films, Nilsson and Niklasson *(2535)* carried out ac electrical measurements and evaluated the complex dielectric permittivity in the 10^{-3} to 10^7 Hz frequency range for sputter-deposited films with different states of coloration. The activation energy for the conduction process was derived from data taken at different temperatures. Polaron absorption requires a relation between this activation energy and structure in the optical absorption (cf. Fig. 19.31). No such relation was found, which disproves the polaron mechanism.

Bandstructure effects, analogous to those in V pentoxide, might explain the electrochromism in Ni oxide, but this remains conjectural since bandstructures are virtually unknown among the brucites. Absorption at intermediate coloration may be reconciled with effective medium theory.

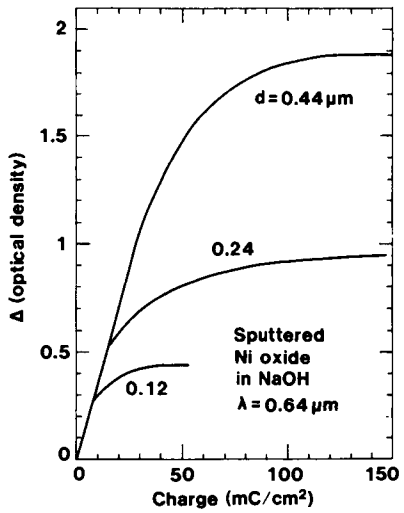

Fig. 19.35 Change in optical density vs. extracted charge density for Ni oxide films made by sputtering in Ar + 10% O_2 with a total gas pressure of 0.04 Torr. Ion intercalation/deintercalation was carried out in a NaOH electrolyte. Data are shown for three film thicknesses *d*. From Yamada et al. *(3689-90)*.

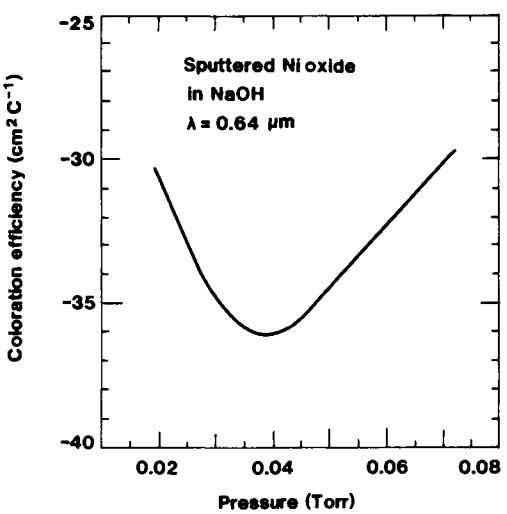

Fig. 19.36 Coloration efficiency for Ni oxide films sputter-deposited in Ar + 10 % O_2 with different total gas pressures. Ion intercalation/deintercalation was carried out in a NaOH electrolyte. The curve was drawn to represent five separate data points. After Yamada et al. *(3689-90)*.

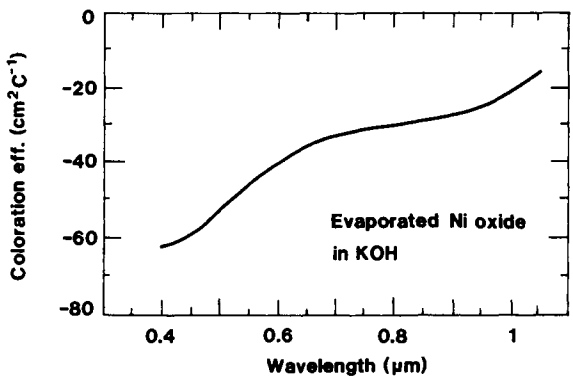

Fig. 19.37 Spectral coloration efficiency for an evaporated Ni oxide film in KOH. After Ottermann et al. *(2445, 2668-70).*

This Page Intentionally Left Blank

Chapter 20

COBALT OXIDE FILMS

Cobalt oxide has many properties that are similar to those of Ni oxide, discussed in the previous chapter. The electrochromism is anodic. However, and in contrast with Ni oxide, it seems that Co oxide can not produce a state that is fully transparent to visible light.

This chapter covers the crystal structure of bulk-like Co oxide (20.1), preparation and characterization of films made by evaporation and sputter-deposition (20.2) and by electrochemical and chemical techniques (20.3), ion intercalation/deintercalation reactions and diffusion constants (20.4), ion intercalation/deintercalation studied by electrochemical (20.5) and physical techniques (20.6), experimental optical properties (20.7), and some notions concerning the theoretical interpretation of the optical data (20.8).

20.1 Crystal Structure of Bulk-like Cobalt Oxide

Several Co-oxide-based materials have layer structures that are analogous to their counterparts among the Ni oxides. With regard to electrochromism, the most interesting crystalline oxides are $HCoO_2$ and $LiCoO_2$ and their anion-deficient varieties. There are also $Co(OH)_2$ and CoOOH with structures similar to $Ni(OH)_2$ and NiOOH *(1073, 1722)*.

The structure of $LiCoO_2$ was determined in detail by Jonston et al. *(1681)* and by Orman and Wiseman *(2658)*. It can be described as a layered rock-salt with alternate planes of Co and Li atoms. Both of these species are surrounded by six oxygens in octahedral coordination; the CoO_6 octrahedra are compressed and the LiO_6 octahedra are elongated. The correctness of this structure was verified by EPR data on Ni^{3+}-doped $LiCoO_2$ *(111)*. The lithium-deficient oxide, denoted $Li_{1-x}CoO_2$, can have different structural modifications depending on x *(869, 1251, 2293, 2361, 2882)*. These phases are known as O3, P3, O2, O2*, and P2, where O and P indicate whether the Li is in an octahedral or prismatic surrounding and the number indicates how many O-Co-O sheets are contained in the elementary crystallographic cell. A different, more spinel-like, structure can be stabilized by low-temperature synthesis *(1352-4, 2884, 2940)*. Configurations with various types of layer stackings can be obtained also in $Na_{1-x}CoO_2$ *(468, 3257)*. Finally, well-characterized spinel structures have been observed for Co_3O_4 and $Li_xCo_3O_4$ *(1003, 2806, 3261, 3395, 3803-4)*.

Crystals of $HCoO_2$ can be obtained by ion exchange of O3-type $LiCoO_2$ using mechanical treatment in the presence of water *(1064)* or by low-temperature hydrothermal processing *(1063)*. Another route uses oxidation of β-$Co(OH)_2$ brucite *(859)*. The structure of $HCoO_2$, determined by Delaplane et al. *(859)*, is closely related to that of $LiCoO_2$ with layers of Co atoms in between

layers of O. Each Co atom is surrounded equidistantly by six O forming a flattened octahedron, and each octahedron shares edges with six neighboring octahedra so that nearly close-packed layers of O atoms are formed. The O-Co-O sheets are joined by strong hydrogen bonds parallel to the crystallographic *c* axis. Recent EPR data supported this structure assignment *(111)*.

Battery-related work has recently been reported for $LiCoO_2$-type electrodes *(174, 298, 572, 2781-2, 3089, 3756)*.

20.2 Films Made by Evaporation and Sputter-deposition: Preparation and Characterization

Thin Co oxide films have been prepared by several techniques. Reactive evaporation in the presence of O_2 was used in *(3088, 3390)*. Seike and Nagai *(3088)* deposited films at 0.26 nm/s and verified by XRD that CoO with cubic structure was present. Metallic films can be oxidized to CoO by heating to ~300°C in water vapor *(969)*.

Reactive sputtering of Co in Ar + O_2 has been used for making Co oxide films; their composition depended on the gas mixture *(604, 755, 1453, 1457)*. Lithiated Co oxide films can also be made by sputtering, as demonstrated by Goldner et al. *(1218-9, 3588-9)*. The desired composition is $LiCoO_2$; it is expected to yield interesting electrochromic properties, as discussed later. The films were prepared by rf sputtering in Ar + O_2 from a $LiCoO_2$ powder target onto substrates at ~300°C. The deposition rate was as low as ~0.025 nm/s. XRD indicated that a rhombohedral structure, characteristic of $LiCoO_2$, was present. Electron microscopy showed that the films were polycrystalline, columnar, and densely packed; the mean grain size was 7 nm. Chemical analysis gave that the Li/Co ratio was ~0.4, i.e., much lower than desired. One could note, in passing, that Li-depleted surface layers have been observed on $LiCoO_2$ bulk specimens *(1771-2)*. The sputter-deposited films contained defects *(3589)*, and the layers that in the ideal structure should be occupied solely by Li contained a mixture of Li and Co. A similar defect model was previously described for $Na_{0.7}CoO_2$ crystals *(3257)*. Reactively sputtered CoO films were discussed in *(604)*.

Stoichiometry control, particularly maintaining the required Li content, is notoriously difficult in vacuum deposited films. However, recent work by Antaya et al. *(114-5)* showed that laser ablation from a sintered $LiCoO_2$ target could produce films with the same composition as in the starting material. The target was irradiated with the 0.308 μm output from a XeCl laser. The films consisted of a mixture of the "normal" layered $LiCoO_2$ phase, discussed above, and the newly discovered spinel-like low-temperature modification.

20.3 Films Made by Electrochemical and Chemical Techniques: Preparation and Characterization

Electrochemical techniques have been used to prepare Co oxide films. The work is fairly extensive but in no way as daunting as for Ni oxide, the reason being that Co oxide is not a standard component in battery technology (except as an admixture to improve the durability of Ni oxide batteries).

Electrodeposition is a convenient technique for making films, and electrolytes containing

$Co(NO_3)_2$ *(351-2, 539, 797, 1257, 1721, 3176)* or $CoSO_4$ *(1592, 1933, 3201, 3384)* have been used. TGA was applied by Gorenstein et al. *(1257)* to films made by the nitrate route; their data are shown in Fig. 20.1. The mass falls off in steps, and the curve can be interpreted as showing that an intial film of $Co(OH)_3$ (or $CoOOH \cdot H_2O$) was dehydrated at ~80°C and then reduced to Co_3O_4 in the range from 130 to 300°C. The latter reaction is consistent with some earlier results *(185)*. The mass loss at 400 to 450°C may indicate a final reduction to CoO.

Anodization has been carried out in KOH *(314, 1240-1, 2561, 3635-6)*, NaOH *(536, 540, 778, 1009, 1665, 2286, 3177)*, KOH + K_2SO_4 *(1240-1)*, NaOH + NaH_2PO_4 *(536)*, $HClO_4$ *(1209-10)*, borate electrolytes *(570, 827, 1415, 2589-90, 2687, 3012, 3175)*, and carbonate-bicarbonate mixtures *(570, 827, 1172-3)*. Potential cycling in a neutral electrolyte was able to build up thick layers with electrochromic properties. Figure 20.2, from Burke et al. *(536)*, shows that the film became thicker upon extended cycling so that it was able to accommodate larger and larger charge densities. Similar behavior was demonstrated earlier for oxides of Ir (Fig. 14.4), Mn (Fig. 16.1), and Ni (Fig. 19.5). The Co oxide films can have a duplex structure with a passivation layer of compact CoO closest to the metal base *(2589-90, 3012)*. The rest of the film may be porous and/or hydrous.

Anodization at high frequencies is a suitable technique for preparing thick films of Co oxide. Specifically, films grown by repetitive voltage switchings between two levels for samples immersed in NaOH, KOH, or KOH + H_2SO_4 were studied in *(1164, 1786-7)*. The frequency range was, typically, 50 Hz to 4 kHz. SEM showed a spongy rough surface, whose detailed appearance depended on the preparation conditions. TGA and DTA indicated dehydration at temperatures up to 150°C and dehydroxylation around 220°C.

Infrared absorption spectra, reported by Kessler et al. *(1787)*, shed further light on the relation between preparation parameters and ensuing film structure. Such data are shown in Fig. 20.3 for anodization in 1 M NaOH with the voltage switched at 1 kHz between a lower value of -1.8 V vs. RHE and an upper value U_u of 0.1, 0.3, or 0.5 V vs. RHE. As-deposited films made with $U_u = 0.1$ or 0.3 V vs. RHE had IR spectra characterized by one prominent absorption at 590 cm^{-1}, while films made at $U_u = 0.5$ V vs. RHE had peaks also at 670 and 320 cm^{-1} and an additional shoulder at ~560 cm^{-1}. Films annealed at 480°C for 4 h showed main absorption maxima at 670, 570, and 390 cm^{-1}.

The IR spectra can be interpreted by comparison with bulk data. Thus Co_3O_4 spinel has absorption bands at 570 and 670 cm^{-1} *(680, 1003, 2255, 2806)* due to vibrations of the CoO_6 and CoO_4 polyhedra, respectively. Clearly, anodization at a high U_u, or annealing at a sufficient temperature, led to a spinel-like structure. Anodizing at $U_u < 0.5$ V vs. RHE yielded an IR spectrum akin to that of $HCoO_2$ *(859)* or CoOOH *(1722)*, and it is expected that CoO_6 octahedra in either of those structures give rise to the measured IR spectrum. $Co(OH)_2$ has absorption maxima at ~540 and ~440 cm^{-1}; this structure cannot be reconciled with the IR data in Fig. 20.3.

Among the purely *chemical techniques* for making Co oxide films one can note thermal decomposition of $Co(NO_3)_2$ at 200 to 500°C, leading to Co_3O_4 *(414, 3110-1, 3527)* or CoO *(1592)*. $Co(OH)_2$ films were made by alternate dippings in $CoSO_4$ and KOH or NaOH *(756)*. CoO was prepared by CVD of $CoBr_2$ in the presence of water vapor *(634)*, and an alternative CVD technique--using cobalt(II)acetate and substrate temperatures between 300 and 500°C--yielded Co_3O_4 + CoO *(2203)*. Sol-gel technique was used in *(628)* and spray pyrolys in *(689)*.

An interesting technique for making $LiCoO_2$ films was reported by Plichta et al. *(2780)*; it involves spraying a lithium-cobalt-containing solution onto a surface at 400°C, followed by annealing in air at 525°C for 12 h.

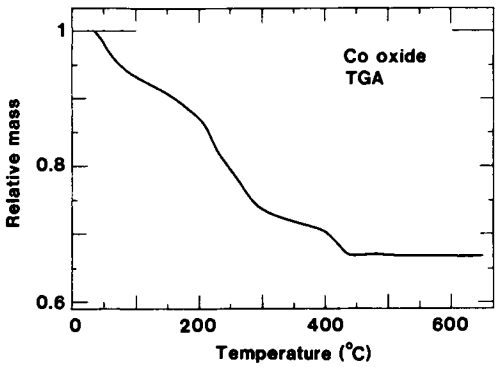

Fig. 20.1 Thermal Gravimetric Analysis TGA spectrum of a Co oxide film made by electrodeposition. Data were taken at a heating rate of 10°C/minute. From Gorenstein et al. *(1257)*.

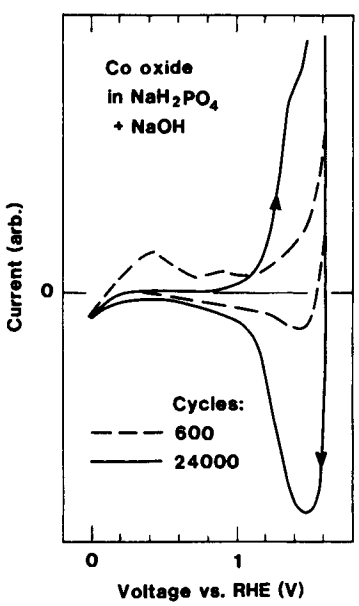

Fig. 20.2 Cyclic voltammograms for a Co surface in a neutral NaOH + NaH_2PO_4 electrolyte. Cycling was carried out at 3.3 V/s, and the analytic scans were taken at 33 mV/s. Arrows denote scan direction. After Burke et al. *(536)*.

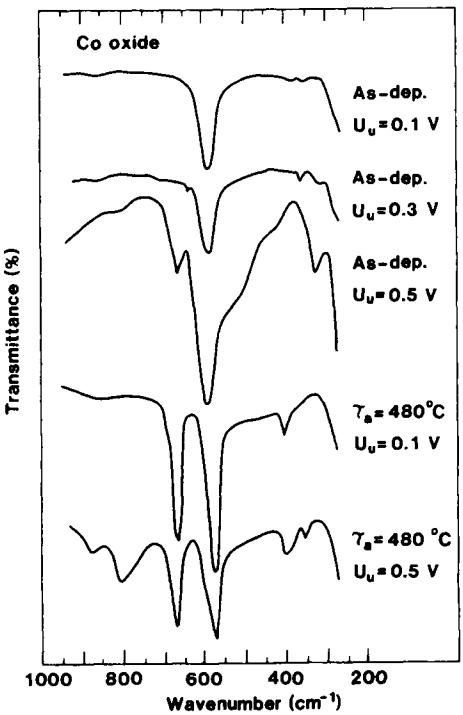

Fig. 20.3 Infrared transmission spectra for Co oxide films made by anodization in NaOH with a repetitive square-wave potential. Switching took place at 1 kHz between -1.8 V vs. RHE and U_u. Films were studied in as-deposited state and after annealing at τ_a for 4 h. From Kessler et al. *(1787)*.

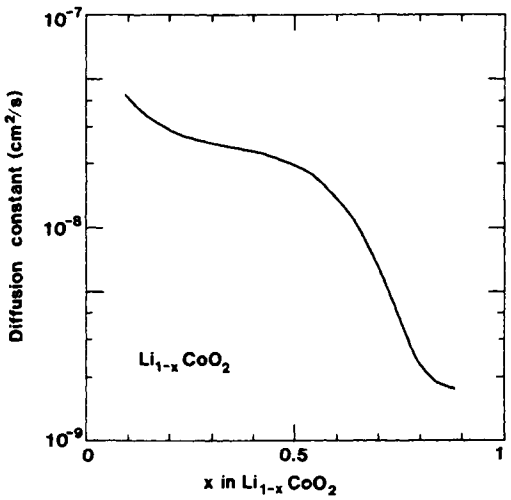

Fig. 20.4 Chemical diffusion constant for lithium in $Li_{1-x}CoO_2$ bulk samples. After Honders et al. *(1533)*.

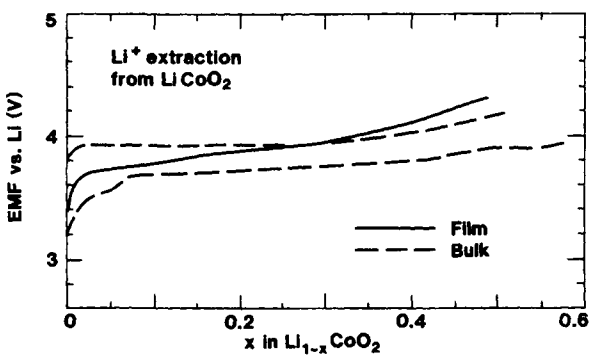

Fig. 20.5 Normalized EMF vs. the amount of Li^+ extracted from initially stoichiometric $LiCoO_2$ films made by laser ablation. Results are also shown for bulk-like samples processed in two different ways, as discussed in the main text. After Antaya et al. *(115)*.

20.4 Ion Intercalation/deintercalation Reactions and Diffusion Constants

Cobalt oxides can serve as excellent hosts for ion intercalation/deintercalation. The electrochemistry is very complicated, and a summary states 14 different redox reactions in aqueous solution; they concern different oxidation states for Co and lie at voltages between 0.11 and 1.49 V vs. RHE *(1786)*. With regard to electrochromism, the most interesting reaction involves reactions between Co^{3+} and Co^{4+} *(540)* (and not 2+ and 3+ states as for Ni oxide). The pertinent intercalation/deintercalation reaction may be written

$$HCoO_2 - xH^+ - xe^- \leftrightarrow H_{1-x}CoO_2 , \tag{20.1}$$

which emphasizes that $HCoO_2$ can serve as an ion extraction material. Alternatively to $HCoO_2$ one may write β-CoOOH, i.e., focusing on the closely related brucite structure *(536, 3176, 3636)*. In analogy with the case for many other oxides, one can write the reactions in terms of OH^- transport rather than H^+ transport. The counterpart to reaction 20.1 for $LiCoO_2$ is

$$LiCoO_2 - xLi^+ - xe^- \leftrightarrow Li_{1-x}CoO_2 . \tag{20.2}$$

For both of the reactions above, x can not be increased to unity since some protons or Li^+ are needed to maintain the otherwise unstable "CoO_2" structure. Electrochromism results from the fact that ion extraction increases the optical absorption.

Data on diffusion constants seem to be available mainly for Li^+ in bulk-type samples *(1533, 2361-2, 3408-9)*. Figure 20.4, replotted from Honders et al. *(1533)*, shows that D_{Li+} is ~6 x 10^{-8} cm^2/s at x = 0.1 and ~2 x 10^{-9} cm^2/s at x = 0.8. These values are impressively high and underscore the great potential of Co oxide for various ionic devices. Other measurements of D_{Li+} were in good agreement *(3408-9)*. $Na_{1-x}CoO_2$ had $D_{Na+} \approx 10^{-8}$ cm^2/s for x = 0.3 *(3257)*.

20.5 Ion Intercalation/deintercalation Studied by Electrochemical Techniques

The EMF varies with the amount of lithium extraction. Data for $LiCoO_2$ films made by laser ablation were reported by Antaya et al. *(115)*. Figure 20.5, from that work, shows that the EMF increases from ~3.7 V vs. Li at low extraction levels to ~4.1 V vs. Li at $x \approx 0.4$. The data are intermediate between those for bulk-like samples with layer structure obtained by high-temperature processing (upper dashed curve in Fig. 20.5) and with spinel-type structure obtained by low-temperature processing (lower dashed curve in Fig. 20.5). This provides evidence in favor of the film being a mixture of the two phases. The results in Fig. 20.5 pertain to the first extraction cycle, and reinsertion back to x = 0 is not possible; this feature was indicated by a precipitous drop of the EMF at $x \approx 0.12$ during Li^+ intercalation in the films. Bulk data in basic agreement with those shown in Fig. 20.5 were found in several studies *(1251, 1533, 2361-2, 2782, 2882, 3408, 3756)*.

EMF data for $Na_{1-x}CoO_{2-y}$ with $0 < x < 0.4$ and $0 < y < 0.073$ were reported in *(468, 1251,*

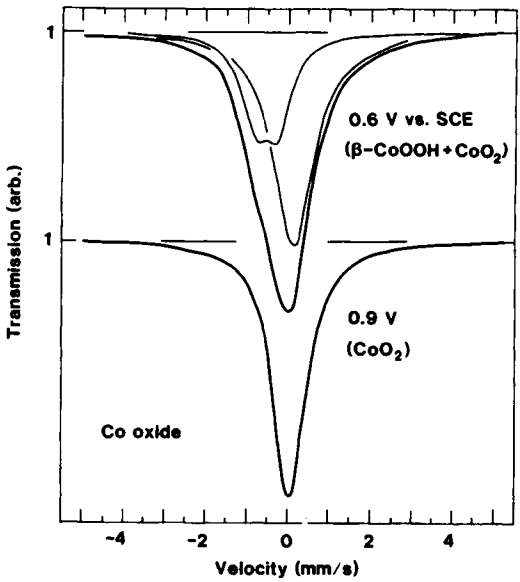

Fig. 20.6 Mössbauer emission spectra taken with an emitter being a ^{57}Co-containing electrodeposited Co oxide film and an absorber of ^{57}Fe-enriched $K_4Fe(CN)_6 \cdot 3H_2O$. Data are shown after electrochemical treatment at two voltages. The spectrum taken at 0.6 V vs. SCE was deconvoluted into two contributions. After Simmons et al. *(3176)*.

2351, 2374-6). When the Na content was varied, the EMF changed in a step-like manner somewhat similar to the behavior of $LiVO_{2.5}$ (cf. Fig. 18.1). This may be explained by electronic and/or structural effects.

Cyclic voltammetry is a standard technique that has been applied to films made by almost all of the procedures mentioned above. Generally speaking, the voltammograms were complicated, and both the anodic and cathodic sweeps could show multiple peaks due to several different electrochemical reactions. It is not meaningful to discuss these data here. Impedance spectrometry was applied to bulk-like samples in *(3407)*.

20.6 Ion Intercalation/deintercalation Studied by Physical Techniques

Only a little work has been done concerning the physical characterization of Co oxide films. However, *Mössbauer data* taken by Simmons et al. *(3175-6)* are original and deserve attention. The films to be analyzed here were prepared by electrodeposition from a $Co(NO_3)_2$ solution containing some ^{57}Co, followed by electrochemical treatment at 0.6 and 0.9 V vs. SCE in a buffered borate electrolyte *(3176)*. Figure 20.6 shows Mössbauer emission spectra. At 0.6 V vs. SCE, the spectrum could be decomposed into two components: a doublet whose isomer shift and quadrupole splitting are consistent with β-CoOOH, and a singlet with an isomer shift consistent with CoO_2. At 0.9 V vs. SCE, the Mössbauer spectrum indicated nothing but CoO_2. It is clear that treatment at a high enough voltage led to a conversion of Co^{3+} to Co^{4+}. Storage of a CoO_2 film in air for 3 months yielded a decomposition and ensuing formation of Co_3O_4.

20.7 Optical Properties

It has been known for a long time that Co oxides can have different colors, and hence electrochemical reactions can be accompanied by electrochromism. Indeed, the observed color changes have sometimes been used in attempts to identify the pertinent electrochemical reaction. According to the literature, the first observation of electrochromism was in electrodeposited films, and it is convenient to consider this experimental technique first. As early as in 1964, Benson et al. *(351-2)* prepared Co oxide films from a $Co(NO_3)_2$ solution; the as-deposited $Co(OH)_2$ films were blue, and they could be turned black by oxidation to β-CoOOH. Air oxidation yielded a brown product indentified with $HCoO_2$. A subsequent study by Burke and Murphy *(539)* found a reversible transition between an orange and a dark brown state under potential cycling.

Recently, Gorenstein et al. *(797, 1257)* carried out a more detailed investigation of the electrochromism of Co oxide made from $Co(NO_3)_2$. Optical transmittance in the $0.3 < \lambda < 1.1$ μm range is shown in Fig. 20.7 for films treated in KOH; the data refer to the as-deposited state and to films with two levels of charge insertion. One should observe that the films have anodic electrochromism and increase their transmittance under charge insertion. A tentative explanation is that the intial absorbing films comprises hydrogen-deficient $HCoO_2$, and that proton intercalation leads to a more stoichiometric and transparent state. It is also evident that the films were absorbing at $\lambda < 0.5$ μm; this indicates that bandstructure effects are important, as discussed in Sec. 20.8.

Anodized layers can show color variations upon electrochemical treatment similar to those for the electrodeposited films *(314, 536, 540, 1787)*. Optical modulation of anodic films has also been documented by ellipsometry *(2589-90, 2687)* and by modulated reflectance spectroscopy *(1415)*.

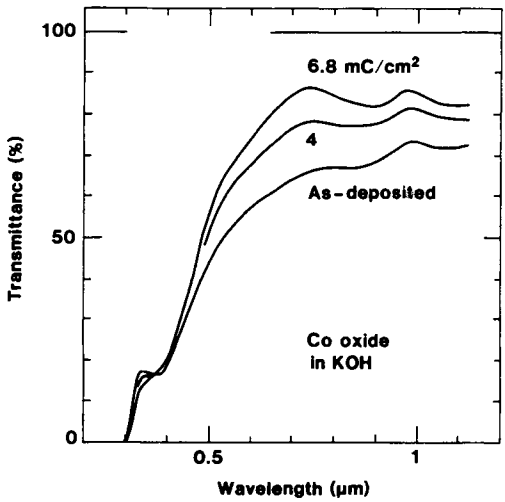

Fig. 20.7 Spectral transmittance for an electrodeposited Co oxide film in as-deposited state and after charge insertion in KOH to the shown densities. After Gorenstein et al. *(797, 1257).*

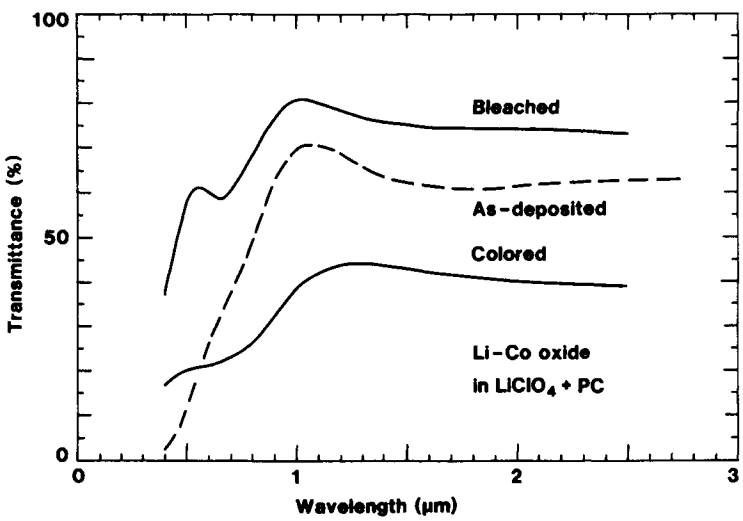

Fig. 20.8 Spectral transmittance for a sputter-deposited Li-Co oxide film in as-deposited state and after coloration and bleaching in $LiClO_4$ + PC. After Wei et al. *(3588-9).*

Seike and Nagai *(3088)* reported electrochromism in evaporated Co oxide films. The electrolyte was 1 M $LiClO_4$ in γ-butyrolactone. Spectral transmittance curves were in basic agreement with those in Fig. 20.7.

Coloration efficiencies have been evaluated a few times. Gorenstein et al. *(797, 1257)* reported CE = -25 cm^2/C at $\lambda = 0.633$ μm for electrodeposited films, and Seike and Nagai *(3088)* stated CE = -11 cm^2/C at the same wavelength for evaporated films.

Lithium-cobalt oxide films made by rf sputtering were studied by Wei et al. *(3588-9)* with regard to optical properties. The dashed curve in Fig. 20.7 shows spectral transmittance for a 0.2-μm-thick film. The transmittance lay between 60 and 70 % at $\lambda > 1$ μm. At shorter wavelengths, the transmittance dropped sharply and was only ~12 % at $\lambda = 0.5$ μm. The spectral absorptance, evaluated from transmittance and reflectance data, was consistent with direct allowed transitions across a bandgap of 2.2 eV *(3589)*. The solid curves in Fig. 20.8 refer to the bleached and colored states of a film cycled in 1 M $LiClO_4$ + PC. Roughly speaking, the transmittance was twice as high in the bleached state as in the colored state. The cycling durability appeared dubious, and the amplitude of the optical modulation decreased to about half of the initial value as early as after 15 cycles corresponding to a charge insertion/extraction of 7.5 mC/cm^2 (or 0.2 Li per formula unit).

20.8 Towards a Theoretical Model for the Optical Properties

Several of the characteristic optical properties of Co oxide and lithiated Co oxide films can be reconciled with bandstructure arguments, and it is appropriate to discuss these matters in a unified way.

The bandstructure of $LiCoO_2$ has been elaborated in recent work *(795, 1771, 3514)*. The stoichiometric material is an insulator with a narrow filled t_{2g} band separated from a narrow e_g band by 2.7±0.3 eV. Neither of the bands is "pure"; they contain *Co3d* states as well as *O2p* states. One should note that the lithium-deficient material studied by Wei et al. *(3589)* had a bandgap of 2.2 eV, in acceptable agreement with the expected separation between the two parts of the *Co3d* band. Extraction of Li from $LiCoO_2$, in this bandstructure picture, leads to a partial emptying of the top of the t_{2g} band.

No bandstructure calculation seems to be available for $HCoO_2$, but it is reasonable to expect that this material is optically analogous to $LiCoO_2$. In fact, it is not too far fetched to carry the analogy one step further and also consider CoO, having a rock-salt structure. The analogy is meaningful since one regains CoO by a simple replacement of all Li in $LiCoO_2$ by Co. The optical absorption of CoO has been studied several times *(179, 680, 754, 969, 2800, 2804, 3514)*. The main energy gap lies at 2.5±0.3 eV (i.e., at a wavelength of ~0.5 μm), which is consistent with the spectra in Figs. 20.7 and 20.8. Some optical data for bulk materials show clear evidence for a second gap at higher energies *(179, 2804)*, which again agrees with results for the Co oxide film. Bandstructure calculations for CoO were reported in *(27, 472, 2027, 2234-5, 2558, 3386-7, 3514)*.

The bandstructure model discussed above implies that absorption in the colored electrochromic film is associated with empty states at the top of the t_{2g} band, just as for Ir oxide (cf. Fig. 14.17). This is consistent with electrical conductivity data and the fact that thermopower measurements showed p-type conduction *(3588-9)*. Polaron absorption in lithium-doped CoO was claimed by Austin et al. *(179-80)*, but this view was strongly criticized by Bosman et al. *(456-7)* and now seems untenable.

This Page Intentionally Left Blank

Chapter 21

NIOBIUM OXIDE FILMS

Niobium oxide shows both similarities and differences when compared with the defect perovskites and rutile-type oxides discussed in earlier chapters, and the composition of present interest--related to Nb_2O_5--may be categorized as being of block-type. The electrochromism is cathodic. The pertinent material is referred to here simply as "Nb oxide".

Crystal structures for bulk-like specimens are addressed first (21.1). Then follow discussions of preparation and characterization of films made by evaporation and sputter-deposition (21.2) and by electrochemical and chemical techniques (21.3), ion intercalation/deintercalation reactions and diffusion constants (21.4), studies of intercalation/deintercalation by electrochemical (21.5) and physical (21.6) techniques, optical properties (21.7), and coloration efficiency (21.8).

21.1 Crystal Structure of Bulk-like Niobium Oxide

Niobium pentoxide crystals are built, essentially, from NbO_6 octrahedra arranged so that the overall stoichiometry is $NbO_{2.5}$ (or Nb_2O_5). Most of the structures consist of blocks of corner-sharing octahedra with a well defined cross section in one plane and, in principle, infinite extent in the perpendicular direction, being the crystallographic *c* axis. The blocks are connected by edge-sharing octahedra, yielding two sets of columns with different bases. The simplest structure, referred to as R-Nb_2O_5, comprises blocks with cross sections being 2x2 octahedra *(1339)*. When the cross sections are 4x4 octahedra, one speaks of M-Nb_2O_5 and N-Nb_2O_5 *(103, 1471, 2299)*. Another, more complicated, structure exists in H-Nb_2O_5 (also called α-Nb_2O_5), with blocks having cross sections of 3x4 and 3x5 octahedra as well as tetragonally coordinated Nb atoms (one of totally 28 per unit cell) *(1141)*. A high-density oxide, known as B-Nb_2O_5, can be thought of as built from corner-sharing rutile blocks *(2018)*. M-Nb_2O_3 is tetragonal, whereas the other varieties are monoclinic. Lithium insertion into N-Nb_2O_5 and H-Nb_2O_5 was studied in *(630-1)*.

There are numerous substoichiometric phases with block-type structure; they can be represented as $NbO_{2.5-z}$ with $0 < z < 0.083$. Specifically, one may note $Nb_{12}O_{29}$, $Nb_{22}O_{54}$, $Nb_{47}O_{116}$, $Nb_{25}O_{62}$, $Nb_{53}O_{132}$, and $Nb_{28}O_{70}$ *(1141, 1340-1, 1589, 2538, 2553-7, 2958-60)*. The blocks include units of the types 3x4, 3x3 + 3x4, as well as 3x4 + 3x5; excepting $Nb_{12}O_{29}$, there are some Nb atoms with tetrahedral coordination. The block-type materials are often referred to as Wadsley-Roth phases *(2945)*.

Among the lower oxides, NbO_2 shows a semiconductor-metal transition along the crystallographic *c* axis. It is similar to the transition for VO_2, discussed in Sec. 17.1, and occurs at ~800°C. The structure is of rutile-type, although with Nb-Nb pairing present for the

semiconducting phase *(2160, 3388)*. A defect perovskite structure exists in NbO_2F *(1034, 2442)*.

21.2 Films Made by Evaporation and Sputter-deposition: Preparation and Characterization

Al-Ismail et al. *(70)* prepared Nb oxide films by evaporation at a rate up to 1 nm/s. Electron diffraction did not show any signs of crystallinity. Reactive evaporation in the presence of oxygen has been used to make NbO-like films *(926)* and non-stoichiometric Nb oxide films *(1260, 3515)*; they were subsequently transformed to pentoxide by annealing post-treatment. Evaporated films were also reported on in *(3721)*. Ion plating has been used to make highly compact Nb_2O_5 films at rates up to ~0.7 nm/s *(996)*, and filtered-arc evaporation *(2195)* was able to produce Nb oxide films at ~3 nm/s *(328)*.

Sputter deposition has been used to make Nb oxide films in several studies; they have embraced direct rf sputtering *(2200, 3760-1)*, reactive sputtering in $Ar + O_2$, $Ne + O_2$, or $Kr + O_2$ *(2, 40, 162, 725, 2030-1, 2973)*, and sputtering of metallic Nb followed by thermal oxidation in air *(1749, 3093)* or via a glow discharge *(1749)*. A detailed investigation was carried out by Lee and Aita *(40, 2030-1)*, who described "phase maps" indicating the parameter space yielding different types of Nb oxide when the discharge voltage and oxygen content were altered. They reported a maximum film deposition rate of ~0.5 nm/s. A different fabrication route was reported by Cabanel et al. *(581-2)*, who used magnetron sputtering in the presence of N_2 to make highly porous NbN_x films that were subsequently converted to whitish--probably powdery--pentoxide by air oxidation for 1 h at a temperature as low as 300°C. X-ray diffraction from these films did not show signs of crystallinity. Heat treatment of NbN_x in air at 550°C, on the other hand, led to crystalline samples of H-Nb_2O_5 *(582)*. One may note, for completeness, that rf sputtering from a NbO_2 target in $Ar + H_2$ gave rutile-type niobium dioxide films *(1131)*, and that a metastable dioxide phase could be stabilized under special high-pressure sputtering conditions *(2565)*.

21.3 Films Made by Electrochemical and Chemical Techniques: Preparation and Characterization

Anodization is a standard technique for making Nb oxide, and films have been grown in electrolytes containing H_2SO_4 *(154, 717, 936, 939, 942, 1450, 1695, 2238, 2653, 2655, 2968, 3729, 3758)*, NH_4HSO_4 *(1549)*, H_3PO_4 *(439, 504, 1705, 2169)*, NaOH *(984, 1694)*, tetraborates *(804, 985, 2984)*, and in the molten salt KNO_3 *(323)*. The thickness was ~0.8 nm/V for anodization in H_2SO_4 *(2653, 3758)* and 2.2 nm/V for anodization in H_3PO_4 *(1705)*. As-prepared films appeared amorphous, and heating to ~500°C, or anodizing at ~430°C, led to films of H-Nb_2O_5 type *(323, 1450)*.

Few niobium compounds have sufficient volatility and are stable enough to serve as precursor gases in CVD processes. However, $Nb(OC_2H_5)_5$ has been used *(978)* and, more recently, (methyl)cyclopentadienyl-tetracarbonyl-niobium was employed for PECVD deposition of Nb oxide *(903)*.

Sol-gel technology, specifically hydrolysis of Nb-containing alkoxides, has been reported several times *(436, 1330, 1965, 2028)*. Boiko et al. *(436)* prepared films by spin coating

followed by heating at 200 to 250°C for 15 minutes. The ensuing structure was described as B-Nb_2O_5. Lee and Crayston *(2028)* also found B-Nb_2O_5 films, which were transformed to H-Nb_2O_5 by heating at ~900°C. FTIR studies of as-deposited layers showed evidence for Nb-O vibrations, associated with a framework of NbO_6 octahedra, at 600 to 700 cm^{-1} *(2258)*. Additional absorption at ~900 cm^{-1} was tentatively ascribed to Nb=O terminal bonds, which is in analogy with the properties of W oxide, etc. Furthermore, Lee and Crayston *(2028)* studied composites of Nb oxide and silicone, made by overcoating oxide films with a silicone gel. The silicon addition yielded improved electrochemical stability. Sol-gel coatings based on peroxo-polyniobic acid were described by Kishimoto et al. *(1817)*. Radial distribution functions of these latter films were consistent with a structural model built from polyhedra.

Thermal oxidation of Nb, to make dielectric oxide films, has been used extensively for example in the preparation of quantum tunneling devices (utilizing quasiparticle tunneling as well as the Josephson effect). Thermal oxidation in air, in the range 500 to 600°C, was employed by Reichman and Bard *(2877-8)*, and Gomes et al. *(1236-7)* to make whitish and probably powdery layers with thicknesses up to 20 μm. Thermal oxidation of Nb was also studied in *(1960, 2058)*. Possibilities of obtaining well-controlled oxidation in an oxygen glow discharge have been explored *(1274)*. Niobium oxide aerogels were described in *(2240)*.

21.4 Ion Intercalation/deintercalation Reactions and Diffusion Constants

Ion intercalation/deintercalation has been studied several times for Nb oxide, but the pertinent reactions have not been ascertained. One might assume, following experience from other electrochromic oxides as well as the scanty evidence presently available, that proton and lithium ion intercalation/deintercalation can be represented by

$$NbO_{2.5} + xH^+ + xe^- \leftrightarrow NbO_{2.5-x}(OH)_x \tag{21.1}$$

and

$$NbO_{2.5} + xLi^+ + xe^- \leftrightarrow Li_xNbO_{2.5}, \tag{21.2}$$

respectively. The pure oxide is transparent, whereas the ion intercalated oxide is absorbing.

Diffusion constants for H^+ intercalation were reported by Gomes and Bulhoes *(1236)* who investigated thick layers, made by thermal oxidation, immersed in H_2SO_4. It was found that D_{H+} lay between ~$5x10^{-9}$ and ~$5x10^{-7}$ cm^2/s, with the tendency that a large film thickness and a low intercalation level gave maximum diffusion constant. A consistent value of D_{H+} was stated for films made by oxidation of sputter-deposited NbN_x films *(581-2)*. For D_{Li+}, the available data do not show consistency. Thus sol-gel-produced films in a $LiClO_4$-containing electrolyte had $D_{Li+} \approx 6 \times 10^{-8}$ cm^2/s *(2028)*, whereas sputter-deposited films in a similar electrolyte had $D_{Li+} \approx 1.4 \times 10^{-12}$ cm^2/s. It is conceivable that different levels of hydration account for this discrepancy.

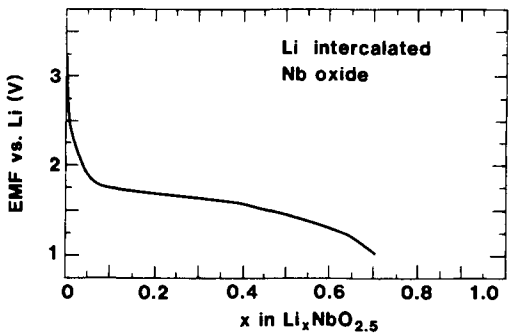

Fig. 21.1 Normalized EMF vs. the amount of Li^+ intercalation, represented as x in $Li_xNbO_{2.5}$, in a thermally oxidized Nb oxide film. From Kumagai et al. *(1960)*.

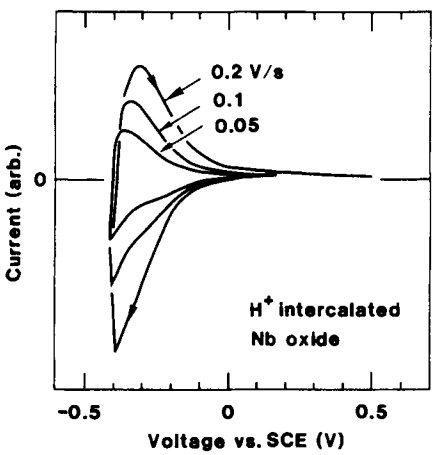

Fig. 21.2 Cyclic voltammograms for Li^+ intercalation/deintercalation in disordered Nb oxide films in 0.5 M H_2SO_4. Data are given for different voltage sweep rates. Arrows denote scan direction. After Cabanel et al. *(582)*.

21.5 Ion Intercalation/deintercalation Studied by Electrochemical Techniques

EMF was measured in electrolytes of $LiClO_4$ + PC for Nb oxide films made by sputtering *(3760)* and thermal oxidation *(1960, 2878)*. Data from Kumagai et al. *(1960)*, reproduced in Fig. 21.1, show that the EMF falls off upon increasing Li^+ intercalation in approximately the same way as for W oxide (cf. Fig. 6.4b).

Chronoamperometry was used to study the kinetics of ion intercalation into films made by sputtering followed by oxidation post-treatment *(582)* and by sol-gel deposition *(2028)*. The intercalation current varied with time as $t^{-1/2}$, which is consistent with a diffusion process (cf. Eq. 6.6). The deintercalation current was measured for sol-gel-prepared films *(2028)*; the initial time evolution appeared to lie in between $t^{-1/2}$ and $t^{-3/4}$, where the former dependence accounts for diffusion and the latter is consistent with field-driven space-charge-limited ion flow (cf. Eq. 6.7).

Cabanel et al. *(582)* reported cyclic voltammograms for films obtained by reactive sputtering in the presence of N_2 followed by oxidation post-treatment. Figure 21.2 shows data taken at different voltage sweep rates. The voltammograms are rather featureless and in this respect resemble corresponding data for heavily disordered electrochromic W oxide films. Analogous voltammograms have been reported for H^+ intercalation into films made by sputter-deposition *(3760-1)*, anodization *(1450)*, and thermal oxidation *(1236-7, 2877)*, and for Li^+ intercalation into films made by sputtering *(3760-1)*, sol-gel technology *(2028)*, and thermal oxidation *(2877)*. Impedance spectra have been reported for sputter-deposited films *(582)* and anodized layers *(939, 942, 984, 1450)*.

21.6 Ion Intercalation/deintercalation Studied by Physical Techniques

Hayashi et al. *(1450)* used several different techniques to analyze anodic Nb oxide films treated in H_2SO_4 and D_2SO_4. Deuterium profiles were measured with SIMS, and clear evidence was found for ion intercalation across the entire film with a density that was larger at a more negative intercalation potential. XRD applied to similar films *(1450)* showed peaks corresponding to a number of specific lattice planes. Figure 21.3 illustrates the lattice spacing corresponding to the *(004)* reflections in Nb oxide; the ion intercalation led to a clearly noticeable lattice expansion. XRD from thermally oxidized films was reported in *(1236, 1960, 2878)*, and characteristic changes were found to follow upon ion intercalation/deintercalation. For films in a Li^+ conducting electrolyte, conflicting evidence has been reported as to reversible intercalation/deintercalation *(1960)* or permanent Li incorporation *(2878)*.

XPS applied to the *O1s* electrons, at 525 to 536 eV binding energy, is able to provide important information on the composition of proton intercalated oxides. Figure 21.4, from Gomes et al. *(1237)*, shows data for thermally oxidized Nb in as-prepared state and after ion intercalation in H_2SO_4 so that the H/Nb ratio was ~0.1. The "pure" oxide had an almost symmetric peak centered at 531.4 eV, whereas the protonated material exhibited a shoulder at high energies. Following the discussion around the corresponding XPS data for oxides of Ir and other metals (cf. Figs. 14.2 and 14.15, for example), the present data can be interpreted on the premise that proton intercalation is associated with hydroxyl ion formation. This lends support to the mechamism for proton intercalation/deintercalation shown in reaction 18.1 above. Kumagai et al. *(1960)* reported analogous XPS data for films in $LiClO_4$ + PC electrolytes. An analysis of the doublet due to

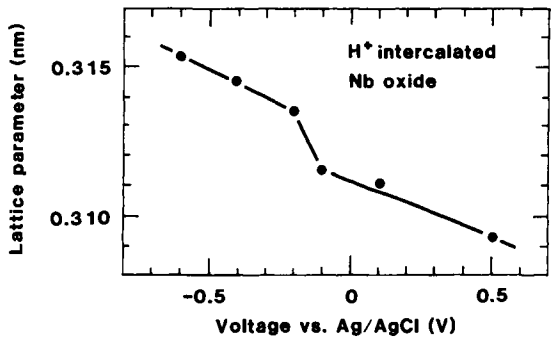

Fig. 21.3 Lattice parameter, corresponding to the *(004)* reflection, for anodic Nb oxide films in a H_2SO_4 electrolyte. Dots represent data from XRD, and the curve was drawn for convenience. After Hayashi et al. *(1450)*.

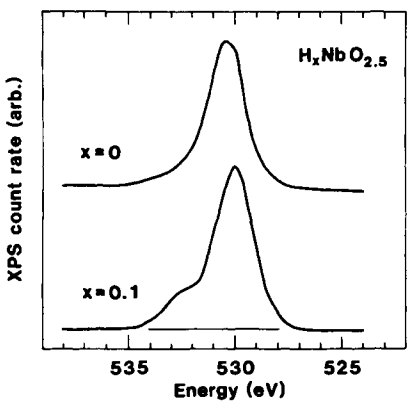

Fig. 21.4 XPS spectra for a thermally oxidized Nb film in as-prepared state and after H^+ intercalation to the shown level (given as x in $H_xNb_{2.5}$). From Gomes et al. *(1237)*.

$Nb3d_{3/2}$ and $Nb3d_{5/2}$, between 204 and 212 eV, indicated a slight shift towards lower energy as a result of ion intercalation *(1237, 1960)*. This was taken to signify a $Nb^{5+} \leftrightarrow Nb^{4+}$ transformation, i.e., electrons localized at Nb sites.

21.7 Optical Properties

The semiconductor bandgap is considered first. Spectrophotometric measurements on anodic films yielded $E_g \approx 3.2$ eV *(323, 985)* whereas photoconductivity data on similar films indicated $E_g \approx 3.4$ eV *(717, 936)*. Some CVD-produced samples had $E_g \approx 3.5$ eV *(978)*. Films that presumably were more disordered than the previous ones--made by reactive sputtering and low-temperature oxidation--were studied by Cabanel et al. *(582)* and Maruyama and Arai *(2200)*, who found that E_g was as large as 3.8 to 3.9 eV. Hence it seems that lattice disorder leads to bandgap widening just as, for example, in the case of W oxide (cf. Fig. 8.3). According to Belozerov et al. *(323)* bandgap widening followed upon ion intercalation, at least for small ion densities.

The refractive index of as-prepared Nb oxide films depends on the fabrication technique. The highest values, with $n \approx 2.4$ at $\lambda = 0.633$ μm, were reported for ion plating *(996)*. Refractive indices in the range 2.1 to 2.3 were stated for films made by evaporation followed by oxidation *(3515)*, sputtering *(2, 2722, 2973)*, anodization *(2207, 2238, 2653, 3729, 3758)*, and CVD *(978)*. Films made by reactive sputtering in N_2 followed by low-temperature oxidation *(582)* again showed anomalous--and particularly interesting--results with $n \approx 1.7$ and $k \approx 2 \times 10^{-3}$ at $\lambda = 0.53$ μm.

Electrochromism has been observed in several studies of Nb oxide. The first scientific paper seems to have appeared in 1974 when Palatnik et al. *(2961)* reported that sintered tablets of Nb_2O_5 were colored when brought in contact with hydrogen-loaded graphite rods under a H_2SO_4 electrolyte. They also found that coloration and bleaching of anodically formed Nb oxide layers took place under cyclic electrochemical treatment in H_2SO_4. Palatnik's paper *(2961)* quotes patent specifications and "USSR Authors' Certificates" dating back to 1963, which makes it likely that an electrochromic effect had been documented in Nb oxide well before the seminal and widely known work by Deb *(835-6)* on the electrochromism of W oxide. Electrochromism in Nb was mentioned in 1977 by Witzke and Deb *(3646)*.

Not much is known about the spectral optical properties of Nb oxide. Figure 21.5, reproduced from Yu *(3760)*, shows transmittance through a 0.3-μm-thick film sputter-deposited onto an ITO-coated glass substrate and subsequently lithiated to the shown levels in an electrolyte of 1 M $LiClO_4$ + PC. Li^+ intercalation lowered the transmittance rather evenly over the $0.35 < \lambda < 0.9$ μm range. Some data for Li^+ intercalation from a 0.1 M LiOH electrolyte were given in *(3761)*. Dry lithiation, by the deposition of Li onto a Nb oxide film, was studied by Ashrit et al. *(162, 166)*, whose results were qualitatively similar to those in Fig. 21.5.

In an original study, Malyuk *(2168)* considered electrochromic coloring and bleaching of Nb_2O_5 in contact with molten salts such as KNO_3, $NaNO_3$, and $K_2Cr_2O_7$. Under these conditions, it is possible that the observed electrochromic effect was associated with oxygen exchange.

Evolution of optical absorption upon H^+ or Li^+ intercalation has also been reported for films made by sputter-deposition in N_2 followed by oxidation *(582)*, anodization *(985, 1450, 2169)*, sol-gel deposition *(2028)*, and thermal oxidation *(1236-7, 2877)*. Some of these studies showed an absorption that was gradually enhanced at increasing wavelength, at least into the near infrared

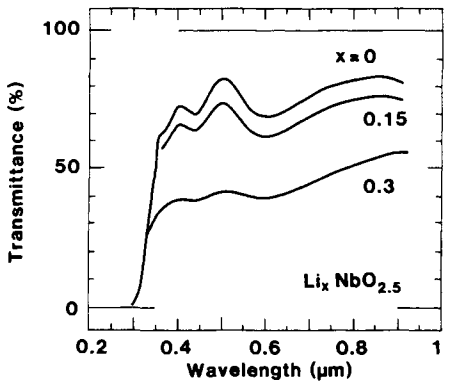

Fig. 21.5 Spectral transmittance for a sputter-deposited Nb oxide film Li^+ intercalated to the shown levels (given as x in $Li_xNbO_{2.5}$). From Yu *(3760)*.

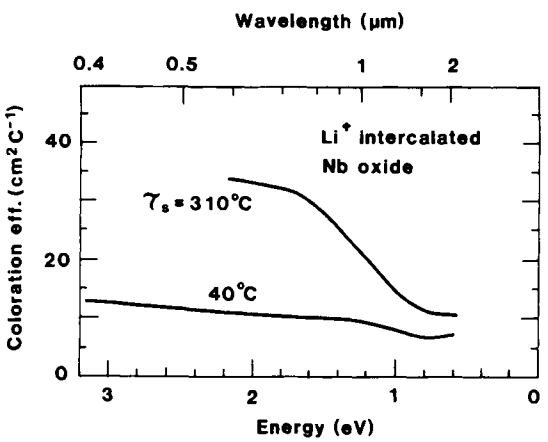

Fig. 21.6 Spectral coloration efficiency for Li^+ intercalated Nb oxide films made by reactive sputtering. Data are shown for two values of the substrate temperature τ_s during deposition. After Cogan et al. *(725)*.

(1450, 2028). This result is consistent with recent observations of coloration of evaporated Nb oxide films under UV irradiation in the presence of C_2H_5OH vapor *(3721)*. In contrast with these data, the presumably much more porous films studied by Cabanel et al. *(582)* were reported to exhibit a broad absorption maximum at a wavelength of 0.5 to 0.6 μm, i.e., in the middle of the luminous spectrum, and similar results were also observed for sputter-deposited films immersed in 0.1 M Na_2CO_3 + 0.1 M $NaHCO_3$ *(2200)*.

Polaron absorption is a likely cause for the electrochromism. In order to support this view, one could note that recent measurements by Bryksin et al. *(504)* on nonlinear current-voltage characteristics for anodic Nb oxide films were interpreted in terms of small polaron hopping, and that the same mechanism was invoked by Jouve *(1694)* to explain the temperature-dependent electrical conductivity of similarly prepared films, at least above ~90°C. In sub-stoichiometric bulk oxides--specifically the Wadsley-Roth phases mentioned in Sec. 21.1--Rüscher et al. *(2958, 2960)* observed a broad absorption peak centered at $\lambda \approx 0.7$ μm and interpreted this phenomenon as an effect of polarons.

21.8 Coloration Efficiency

Cogan et al. *(725)* reported spectral coloration efficiencies for Nb oxide films made by reactive rf sputtering in Ar + O_2 followed by lithium intercalation. Figure 21.6 shows data from their measurements on films deposited onto substrates at two temperatures. Somewhat surprisingly, the CEs were largest when the substrate was warmest and reached ~34 cm^2C^{-1} at $\lambda = 0.6$ μm for τ_s = 310°C. For τ_s = 40°C, on the other hand, the CE was 10±3 cm^2C^{-1} irrespective of wavelength. The latter result is similar to data reported by Ashrit et al. *(162)*. Porous Nb oxide films made by sputtering in N_2 followed by oxidation had a CE of 25 to 30 cm^2C^{-1} at $\lambda = 0.62$ μm *(582)*, whereas a sol-gel-produced film had ~6 cm^2C^{-1} at $\lambda = 0.8$ μm *(2028)*. Clearly, further work is needed to establish the spectral CE as a function of film preparation technology and, in particular, to demonstrate under what conditions one can reach high CEs.

This Page Intentionally Left Blank

Chapter 22

MISCELLANEOUS OXIDE FILMS

Electrochromism has been noted, though not studied in detail, in several oxides. They are discussed briefly below. The emphasis is on optical properties, and other aspects are given cursory presentations. It should be pointed out that some oxides, whose optical properties appear not to be significantly changed under ion intercalation/deintercalation, are discussed under ion storage materials in Ch. 27. The demarcation between electrochromic films and ion storage films is not sharp, though. This chapter covers oxides of rhenium (22.1), rhodium (22.2), ruthenium (22.3), iron (22.4), chromium (22.5), tantalum (22.6), copper (22.7), and praseodymium (22.8). Doped strontium titanate is discussed in (22.9).

22.1 Rhenium Oxide

Rhenium oxide is a defect perovskite, i.e., it has the same crystal structure as electrochromic W oxide and β-type Mo oxide. ReO_3 is not known as an electrochromic material, and it is not expected to have this property to any large degree. Nevertheless it is of interest to pay some attention to Re oxide here since it provides clues to the mechanism underlying the electrochromism in oxides of W, Mo, etc.; these aspects are discussed in Ch. 23.

Crystalline ReO_3 can serve as an intercalation host for H^+ and Li^+ *(633, 2442)*. A number of crystallographic modifications take place as the ionic content is increased, which is in analogy with the case of WO_3 (cf. Fig. 2.3).

Optical data have been obtained from reflectance measurements on single crystals *(1956)* and from calorimetric measurements on polycrystalline samples *(3583)*. The luminous absorption was strong, with broad peaks at photon energies being ~0.4 and ~1.0 eV. These results are in good agreement with bandstructure calculations *(2232-3)*.

22.2 Rhodium Oxide

Rutile-like structures exist among several noble-metal-based oxides. Thus Ir oxide--discussed in Ch. 14--has this structure, and the same is true for bulk crystals of RhO_2, RuO_2, OsO_2, and PtO_2. The interatomic distances are very similar for all of them *(576, 2009, 2428, 2441)*. The bandstructures are analogous as well--at least for RuO_2, OsO_2, and IrO_2--although the Fermi levels lie at different positions in the t_{2g} band *(808, 2237, 2905)*; cf. Fig. 14.17. Burke and O'Sullivan *(547, 552)* discovered the electrochromism of Rh oxide in 1978, and more detailed studies were

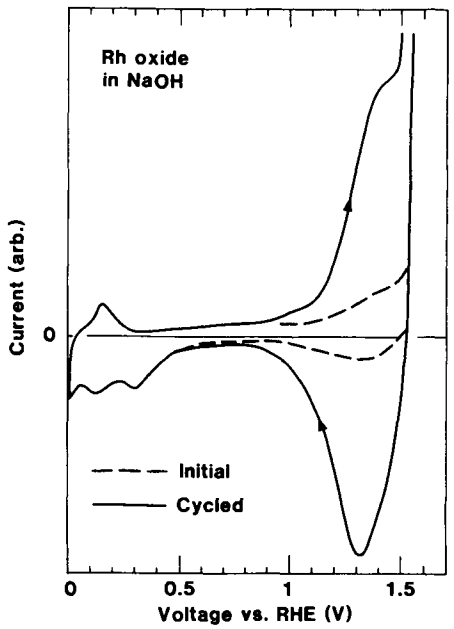

Fig. 22.1 Cyclic voltammograms for a Rh surface in virgin state and after potential cycling in the shown range for 40 s at 5 Hz in 1 M NaOH. The voltage scan rate during recording was 30.8 mV/s. Arrows denote scan direction. From Burke and O'Sullivan *(547)*.

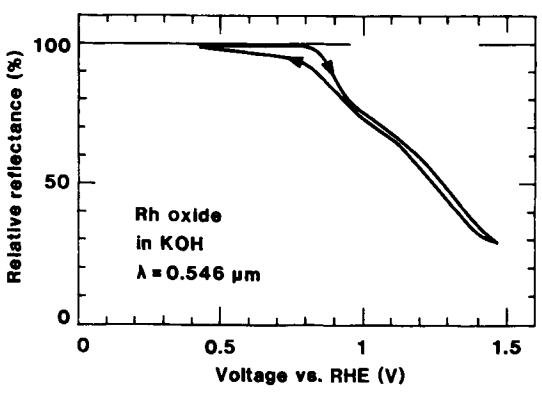

Fig. 22.2 Relative reflectance for light incident at 45° vs. voltage for an anodized Rh surface treated in 5 M KOH. The voltage scan rate was 0.15 V/s. After Gottesfeld *(1263)*.

carried out by Gottesfeld *(1263)*. Some electrochromism was also found in Ru oxide *(2908)*, as discussed in Sec. 22.3, whereas no results appear to be available for Os oxide and Pt oxide.

Rhodium oxide films can be grown to large thicknesses by voltage cycling or voltage pulses applied to Rh immersed in strongly alkaline electrolytes, for example NaOH or KOH with pH > 11 *(537, 547-8, 552, 1263)*. The thickness increased fairly linearly with the number of cycles, at least up to 7000 cycles. The behavior is similar to that of Ir oxide, except that voltage cycling is normally performed in acidic electrolytes for Ir.

Figure 22.1 shows cyclic voltammograms for Rh oxide films in 1 M NaOH within the 0.01 to 1.55 V vs. RHE range, as reproduced from Burke and O'Sullivan *(547)*. The data are somewhat similar to those in Fig. 14.4. The shoulder at ~1.4 V is associated with the electrochromism and can be assigned to transitions between Rh^{3+} and Rh^{4+}; the reaction takes place close to the voltage giving O_2 gas evolution in aqueous electrolytes. Cyclic voltammograms were also shown and discussed in *(530, 537, 544-5, 550, 552, 1263, 3554)*. Some data showed evidence for a "prepeak" that may be caused by resistive effects *(1267)*.

Burke and O'Sullivan *(547)* reported that anodized Rh was pale yellow at low voltages and dark green to almost black at high voltages. Hence it follows that Rh oxide has pronounced electrochromism but appears unable to attain a fully bleached state. Judging from the colors, the film composition shifted from hydrated Rh_2O_3 to hydrated RhO_2 upon voltage increase. Exchange of H^+ or OH^- were suggested to account for this reaction *(547, 1263)*. Figure 22.2, from Gottesfeld *(1263)*, illustrates the relative change of the reflectance at $\lambda = 0.546$ μm for an anodic Rh oxide film. In the reflecting state, the properties were close to those for metallic Rh, whereas the relative reflectance was only ~30% at 1.48 V vs. RHE. Similar reflectance changes were recorded at other wavelengths throughout the luminous spectrum. The coloration efficiency, as well as the response times upon voltage changes, where similar to those for anodic Ir oxide *(1263)*. Almost no changes in the reflectance modulation were found upon cycling between 0.42 and 1.47 V vs. RHE for up to 105 times at 0.5 Hz in 1 or 5 M KOH *(1263)*.

22.3 Ruthenium Oxide

This oxide is similar to the Rh oxide discussed above. Thin films of Ru oxide have been investigated primarily because of their applications as oxygen-evolving and chlorine-evolving anodes. Anodization is a useful manufacturing technique, just as for Ir oxide and Rh oxide, and cyclic voltammograms were similar to those in Figs. 14.4 and 14.7 *(382, 391, 530, 532, 538-9, 543, 546, 561, 596, 1385, 1546, 2837, 3439)*. Ruthenium oxide films have also been made by evaporation *(2706)*, sputter-deposition *(318, 1882-3, 1788, 1906, 1934-6)*, electrodeposition *(3555)*, CVD *(1324, 3769)*, chemical deposition from $Ru(NH_3)_6Cl_2$ *(202)*, and thermal decomposition of $RuCl_3 \cdot 3H_2O$ *(140, 543, 1866, 1903, 3549, 3603)*. The latter type of film was tested by XPS, and it was verified that the ion intercalation/deintercalation could be represented by a reaction analogous to 14.1.This similarity further attests to the kinship between the oxides of Ru and Ir. Films made via the chloride route sometimes had poor substrate adherence.

Rishpon and Gottesfeld *(2908)* investigated films prepared from $RuCl_3$ in 0.5 M H_2SO_4. The diffusion contant for H^+ lay between 10^{-12} and 10^{-11} cm^2/s. D_{Li+} had a similar value at 80°C *(140)*. The optical properties were somewhat modulated by potential cycling, but the films did not exhibit any transparent state. In a bandstructure picture it appears that, qualitatively, the

displacement of the Fermi energy upon electron insertion/extraction is not large enough to place it in the gap between the t_{2g} and e_g bands. The optical properties of "pure" Ru oxide films made by reactive dc magnetron sputtering were reported by Belkind et al. *(318)*.

22.4 Iron Oxide

Iron oxides can have many different crystalline forms. According to a useful listing by Larramona and Gutiérrez *(2013)*, there are FeO (wustite), $Fe(OH)_2$ (brucite-type), α-Fe_2O_3 (hematite), α-FeOOH (goethite), γ-FeOOH (lepidocrocite), β-FeOOH (akaganéite), ε-FeOOH, and $5Fe_2O_3 \cdot 9H_2O$ (ferrihydrite). All of these materials contain iron ions with octahedral coordination. In addition there are Fe_3O_4 (magnetite), γ-Fe_2O_3 (maghemite), and δ-FeOOH with iron ions having both octahedral and tetrahedral coordination *(1198)*. Several of these oxides--notably the hydrous ones--have all the features of good intercalation hosts.

Thin iron oxide films can be made by a variety of techniques. Reactive sputtering in Ar + O_2 *(2080)* or Ar + H_2O *(3815)* was able to produce α-Fe_2O_3, γ-Fe_2O_3, or Fe_3O_4 depending on deposition and/or post-treatment conditions.

Among the electrochemical techniques, one may note film formation under potential cycling in 0.04 to 1 M NaOH or KOH *(55, 535, 541, 1362-3, 1445, 1560, 2013, 3003)* and under a constant potential in various borate, sulfate, phosphate, perchlorate, carbonate-bicarbonate, and hydroxide electrolytes *(191-2, 269, 409, 476, 739, 1102, 1207, 1261, 1435, 1505, 1696, 1932, 2139, 2226, 2330, 2444, 2541, 2547, 2645, 2647-8, 3009-11, 3071, 3086, 3304, 3495, 3628, 3784-5)*. It appears that different types of films can be produced, with FeOOH and $Fe(OH)_2$ being typical examples. The films have a duplex character with a relatively dense inner part and a loosely packed outer part. Electrodeposition can be carried out from a sulfate solution *(3384)*.

The sol-gel technique was used recently by Campet et al. *(591)*. An alkoxide solution was applied by spin coating, and the ensuing film was heat treated at 350 or 550°C so that Fe_2O_3 was formed. CVD of iron acetylacetonate was used to make films of α-Fe_2O_3 *(2710)*. Film preparation by alternate dippings in $FeSO_4$ and in KOH or NaOH was reported in *(756)*.

The electrochemical reaction underlying the electrochromism can only be guessed at. According to Burke and Murphy *(541)* one may write

$$Fe(OH)_2 - H^+ - e^- \leftrightarrow FeOOH\,, \tag{22.1}$$

which is analogous to reaction 19.5 for Ni oxide. With regard to lithiation of Fe_2O_3, Campet et al. *(591)* suggested

$$Fe_2O_3 + xLi^+ + xe^- \leftrightarrow Li_xFe_2O_3\,. \tag{22.2}$$

Cyclic voltammetry has been reported mainly for films made by electrochemical methods. The voltammograms were complicated, but it seemed that only a peak at 0.3 V vs. RHE (in the anodic sweep) was associated with electrochromism *(541)*. A sol-gel-produced Fe_2O_3 film showed an almost featureless voltammogram *(591)*.

The optical bandgap depends on the crystal structure. According to Gutiérrez and Beden *(1362)*, α-, β-, γ-, and δ-FeOOH have E_gs between 2.95 and 3.26 eV. These materials can be

regarded as transparent to visible light. On the other hand γ-Fe_2O_3 has $E_g \approx 2.5$ eV, FeO has $E_g \approx 2.4$ eV *(466)*, and α-Fe_2O_3 has $E_g \approx 2.2$ eV *(2710, 3148, 3417)*; these materials therefore show luminous absorption associated with the bandgap.

Optical changes during electrochemical treatment were, it seems, first noted in 1967 by Kruger and Calvert *(1932)*, who used ellipsometry at $\lambda = 0.546$ μm to study passivation layers in a neutral borate electrolyte. Similar, but more extensive, investigations were reported later by several groups *(409, 672, 1505, 1560, 1696, 2648, 3304)*. Figure 22.3, from Jovancicevic et al. *(1696)*, shows that the spectral optical constants depend critically on the potential. Specifically, k could go from a low value at $\lambda > 0.45$ μm for 0.2 V vs. RHE to a value as large as 0.4 to 0.6 for -0.2 V vs. RHE. A clear difference in k upon potential changes was also seen by Szklarska-Smialowska and Kozlowski *(3304)*. This variation shows that the Fe oxide layer displays electrochromism. Electromodulated reflectance of films undergoing potential cycling in a 0.1 M NaOH electrolyte was discussed in *(1362-3, 2013, 2684-5)*, and a similar study with an 1 M Na_2SO_4 electrolyte was described in *(1414, 3269)*.

Burke and Murphy *(541)* performed a less quantitative study that was more directly geared towards electrochromism. They made visual inspections of iron that was electrochemically cycled in NaOH and found that thin surface layers could change between a transparent state ($Fe(OH)_2$-type) and a yellow-green state (FeOOH-type). Thicker layers tended to have a permanent brown color, and hence the usefulness of Fe oxide in practical applications to electrochromics remains to be demonstrated.

Sol-gel-prepared Fe_2O_3 films in contact with an electrolyte of $LiCF_3SO_3$ + PC had different behavior, as discussed by Campet et al. *(591)*. The optical properties were almost independent of the Li^+ intercalation level, and the films showed strong absorption at $\lambda < 0.5$ μm as expected from the known magnitude of E_g.

The experimental basis is too small to allow a meaningful discussion of the mechanism for the electrochromism. One could note, however, that the optical and electrical properties of Fe_3O_4 can be explained in terms of small polarons *(855)*.

22.5 Chromium Oxide

There are many bulk Cr oxides with different structures, viz. Cr_2O_3 (corundum), CrO_2 (rutile), Cr_5O_{12} (three-dimensional framework), Cr_2O_5 (presently unknown), "Cr_3O_8" (or, more correctly, Cr_8O_{21} with pairs of CrO_6 octahedra bound together by CrO_4 tetrahedra), and CrO_3 (unconnected strings of corner-sharing CrO_4 tetrahedra) *(1880, 2552, 3238, 3633)*. Among the ternary phases, one can note MCr_3O_8 with M = Li, Na, K, Rb, Tl, and Cs *(3629-32)*. The $LiCr_3O_8$ structure comprises somewhat staggered strings of $(Li,Cr)O_6$ octahedra connected by edge-sharing in the c direction; the Li and Cr atoms are randomly distributed. The strings are mutually linked through CrO_4 tetrahedra by sharing corners to form a three-dimensional framework structure.

Several of these oxides have been studied with regard to their applicability in rechargeable lithium batteries. This work has embraced Li^+ intercalation/deintercalation in Cr_2O_3, CrO_2, Cr_5O_{12}, Cr_2O_5, Cr_6O_{15}, "Cr_3O_8", and a Cr_3O_8 + Cr_2O_5 + graphite mixture (known as Seloxcette) *(375-8, 1880, 3344-5)*. According to Takeda et al. *(3344-5)*, large intercalation levels could be obtained in Cr_2O_5, Cr_6O_{15}, and "Cr_3O_8", with the latter being the best. A heavily disordered oxide, denoted a-Cr_3O_8, was studied in *(3343-4, 3695)*. CrO_3, which at first sight might seem an ideal

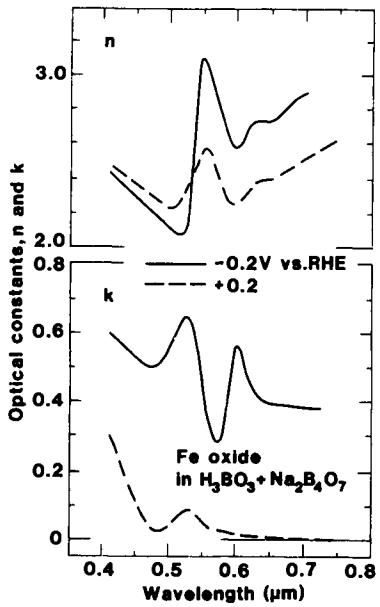

Fig. 22.3 Spectral optical constants at two applied voltages for an electrochemically prepared Fe oxide film in a borate electrolyte. After Jovancicevic et al. *(1696)*.

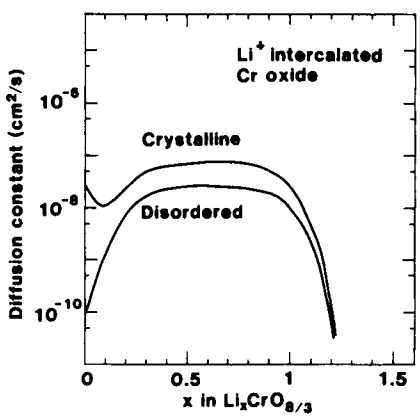

Fig. 22.4 Chemical diffusion constant for Li^+ in "Cr_3O_8"-type materials with crystalline and heavily disordered structures. The curves were drawn to represent sets of somewhat scattered data. After Yamamoto et al. *(3695)*.

intercalation host, is surprisingly resistent to intercalation *(377)*; furthermore, it dissolves in organic electrolytes and therefore appears useless for most applications. Li^+ intercalation/deintercalation in MCr_3O_8 with M = Li, Na, and K was reported in *(1879-81)*.

Evaporation is a convenient technique for making Cr oxide films. When Cr_2O_3 is vaporized under inert conditions, the principal gaseous species are Cr, CrO, CrO_2, O, and O_2, whereas under oxidizing condition one finds CrO_3 as well *(595, 1333)*. Moisture promotes the volatilization *(595)*. The films have a dominating Cr_2O_3 stoichiometry. Seike and Nagai *(3088)* discussed Cr oxide films made by *e*-beam evaporation of Cr in 8 x 10^{-4} Torr of O_2. The deposition rate was 0.24 nm/s.

Electrochemical techniques are applicable for growing thin oxide layers on bulk Cr. Anodization has been carried out in H_2SO_4 *(465, 1444, 3085, 3271)*, $Na_2SO_4 + H_2SO_4$ *(1414)*, and in phosphate *(3096)* and borate *(3096)* electrolytes. A consistent picture has emerged with a Cr_2O_3 film whose outer part is hydrous. Thermal oxidation also yields Cr_2O_3 *(1876, 2079, 2304, 2985)*.

The mechanism for ion intercalation/deintercalation is not known in detail, but it is reasonable to assume that the reaction

$$Cr_2O_3 + xLi^+ + xe^- \leftrightarrow Li_xCr_2O_3 \qquad (22.3)$$

captures the essentials for the only film material that so far has been tested with regard to electrochromism *(3088)*.

No study seems to be available on diffusion constants for thin Cr oxide films. However, Yamamoto et al. *(3695)* investigated "Cr_3O_8"-type battery electrodes in an electrolyte of 1 M $LiClO_4$ in a mixture of equal weights of PC and 1,2-dimethoxyethane and inferred the values of D_{Li+} given in Fig. 22.4. Data are shown both for a crystalline sample and for a heavily disordered material (a-Cr_3O_8) made by heat treating "Cr_3O_8" with water and $(NH_4)_2SO_4$. The diffusion constants could be very high; they lay between 10^{-8} and 10^{-7} cm^2/s within a wide compositional range. Considerably lower values were reported for a Seloxcette material *(376)* and for $NaCr_3O_8$ and KCr_3O_8 *(1879)*.

Regarding optical properties, the bandgap has been evaluated from photocurrent spectra measured on anodic films; E_g lay between 2 and 2.6 eV *(3085, 3279)*. Reported bulk data on E_g are highly inconsistent for Cr_2O_3 and range from 2.4 to 7 eV. One study asserted that the gap should exceed 3.6 eV *(3757)*.

The only study reported thus far on the electrochromism of Cr oxide films was carried out by Seike and Nagai *(3088)*, who investigated reactively evaporated films immersed in electrolytes of 1 M $LiClO_4$ in γ-butyrolactone. The films could be modulated between a pale brown and a dark brown state. The coloration was anodic. Figure 22.5 shows spectral transmittance in colored and bleached states. Weak electrochromism is apparent, but the films remained rather absorbing for visible light irrespective of the level of ion intercalation. The coloration efficiency was -4 cm^2/C at $\lambda = 0.633$ μm. The films could be run through 10^5 color/bleach cycles. The amount of charge that was inserted and extracted per cycle dropped to about half its initial value during this test.

22.6 Tantalum Oxide

Tantalum oxide, Ta_2O_5, normally exists in either of two modifications: a high-temperature structure known as H-Ta_2O_5 (or α-phase), or a low-temperture structure known as L-Ta_2O_5 (or β-phase). Orthorhombic L-Ta_2O_5 is of most interest for applications to electrochromics. Its crystal structure is very complicated and comprises metal atoms arranged in sheets and oxygen atoms with either distorted octahedral (TaO_6) or pentagonal bipyramid (TaO_7) coordination *(3243)*. There are similarities to some of the Nb_2O_5 phases discussed in Sec. 21.1. Defect structures in L-Ta_2O_5 have attracted much interest *(240-1, 475, 1874, 3265)*, and it has been discovered that stoichiometry deviations can be accommodated in fully ordered monophase structures with varying unit cells. This capability has led to the notion of an "infinitely adaptive structure" *(90-1)*. L-Ta_2O_5 is the only pure metal oxide known to have such a property *(2945)*.

Crystal structures other than those mentioned above have been stabilized by crystallization of Ta_2O_5 in hydrochloric acid *(1652)*, by oxidation of Ta or TaC *(3062, 3389)*, and by explosive compression *(481, 3202)*; the latter techniques were capable of yielding rutile-type TaO_2. The binary system Ta_2O_5-WO_3 exhibits structures principally similar to those for L-Ta_2O_5 *(3239-3242)*.

Tantalum oxide films are of interest for many applications, and numerous preparation techniques are known. Electron-beam evaporation is possible *(71, 1469, 2813)* but is prone to give inhomogeneous films. Denser and more stoichiometric films can be made by ion-assisted evaporation *(71, 2274)* and reactive ion plating *(2813)*. Different varieties of sputter-deposition have been used, including reactive dc sputtering from Ta in Ar + O_2 *(71, 1483, 1798, 2076, 2542, 2950-1, 3618)*, rf sputtering *(725, 1825-6, 2621, 2720, 2889, 3391)*, and ion-beam sputtering *(880)*. Using the dc magnetron technique, Hichwa et al. *(1483)* demonstrated deposition rates up to 2.5 nm/s. Thermal oxidation of sputtered Ta films was studied in *(1461)*.

Anodization is a viable technique for making Ta oxide films. Sulphuric acid has been used in most work *(154, 766, 2207, 2217, 2644, 2646, 2653, 2656, 3758)*, but orthophosphoric acid *(439, 502)*, citric acid *(3626)*, and NH_4HSO_4 *(1549)* are alternatives. Film growth under potential cycling in H_2SO_4 was reported in *(336)*.

CVD is possible from precursors such as $TaCl_5$, $Ta(OCH_3)_5$, and $Ta(OC_2H_5)_5$; the latter is convenient since it is a liquid at room temperature. CVD from $Ta(OC_2H_5)_5$ was used by Kajiwara et al. *(1720)* and Tominaga et al. *(3424)*. Post-treatment at 625 to 750°C gave polycrystalline films with L-Ta_2O_5 structure. The same precursor was used for PECVD at a deposition rate of 0.065 nm/s *(2435)*. CVD together with UV irradiation has been employed for growing well-characterized films from $Ta(OCH_3)_5$ *(3691)* and from $TaCl_3$ with O_2 + O_3 *(3363)*.

Different varieties of the sol-gel technique have been used successfully for the preparation of Ta oxide films. Kishimoto et al. *(1817-20)* applied spin coating from $Ta(OC_2H_5)_5$ added to a C_2H_5OH + H_2O_2 solution. An "amorphous" film of $Ta_2O_5 \cdot pH_2O$ with $p \approx 6.5$ was formed upon drying. TGA and DTA indicated a loss of hydration at 80 to 120°C, a release of structural water at ~430°C, and crystallization at ~650°C. X-ray analysis and RDFs showed that the films consisted of a columnar arrangement of structural elements that could be viewed as fragments of the L-Ta_2O_5 unit cell *(1819)*. Somewhat related drop-coating and dip-coating methods, also based on a $Ta(OC_2H_5)_5$ solution, were described in *(1112, 3425)*.

Proton intercalation/deintercalation has been discussed for electrochemically prepared films *(336, 2217)*. It was suggested by Beni and Schiavone *(336)* that the inserted ions would be

accommodated in hydroxyl groups. The ion conductivity was studied by Kishimoto et al. *(1817)* for sol-gel-produced samples; the room-temperature value was ~3 x 10^{-6} S/cm for films annealed at 80°C and ~10^{-8} S/cm for films annealed above 240°C. The electrical conductivity appears not to be known but is likely to be low. Thus $Ta_2O_5 \cdot pH_2O$ films have been used as pure ion conductors in electrochromic devices; this application requires a very low electrical conductivity for proper device operation.

Tantalum oxide films are of considerable interest in optical and optoelectronic technology, and expectedly there are many studies of their optical properties. Sputter-deposited films have bandgaps between 4.1 and 4.5 eV *(880, 1798, 2950)*. The depostion conditions are of critical importance for E_g, which is true both for sputtering and CVD *(2621)*. Films made by PECVD could show E_gs as large as 5.3 eV *(2435)*. One should observe that even if a considerable spread is found for the reported E_gs, all of the films are transparent for visible light. The refractive index also depends on the preparation parameters. The densest films, made by reactive ion plating, had $n > 2.5$ at $\lambda = 0.55$ μm *(2813)*.

Ion intercalation/deintercalation causes electrochromism. The phenomenon does not seem to have been studied in detail, but a few results are known. Thus Cogan et al. *(725)* prepared films by reactive rf sputtering and found weak cathodic electrochromism with a spectral coloration efficiency of the same magnitude as for their Ti oxide films, viz. less than 5 cm^2/C. Matsuda and Sugimoto *(2217)* investigated sulfuric-acid-anodized Ta surfaces and reported that the extinction coefficient at $\lambda = 0.541$ μm could be modulated between zero and about 0.15. The latter value is lower than for some films of W oxide (cf. Fig. 9.13) and Ti oxide (cf. Fig. 15.9) but still large enough to warrant an interest for applications in electrochromics. Polaron transport governs the electrical properties of Ta oxide films, as discussed by Bryksin et al. *(504)*, and it is reasonable to expect that polaron absorption is also responsible for the optical modulation.

As indicated above, Ta oxide films are of importance not only as optically functional electrochromic layers but also as ion conductors, and they are used in the latter capacity in a number of devices for regulating optical transmittance and reflectance. These aspects are elaborated in Secs. 26.2 and 29.4.

22.7 Copper Oxide

Copper oxide, specifically Cu_2O (cuprous oxide), can show electrochromism *(2681)*. The oxide has a structure that is qualitatively different from that of the earlier discussed materials and is constructed from building blocks being Cu_4 *tetrahedra* with oxygen atoms at their centers. The tetrahedra are connected into two arrays by corner-sharing. Among the other copper oxides, one may note CuO (cupric oxide) with Cu atoms at the centers of O_4 rectangles.

Cu_2O layers have attracted considerable interest since they can be employed in photovoltaic cells *(1091-2, 1095, 1116, 1463, 1649, 2567, 2633, 2829, 3083)* and in spectrally selective solar absorbers *(182, 2796, 2934-5, 3038)*. This oxide is also noteworthy as a prototypical exciton system *(31, 299, 470)*. CuO has been studied as an intercalation material for lithium batteries *(1405, 1605-6, 2560)*.

Films with a nominal Cu_2O composition have been produced by many techniques. Evaporation was recently studied by Özer and Tepehan *(2681)* who found from XPS measurements that the Cu/O ratio was about 1.8. Reactive sputtering of Cu in an Ar + O_2 plasma

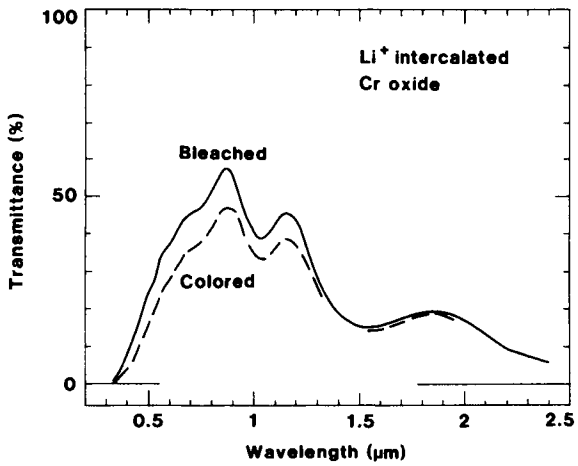

Fig. 22.5 Spectral transmittance for a reactively evaporated Cr oxide film after coloration and bleaching in $LiClO_4$ + γ-butyrolactone. From Seike and Nagai *(3088)*.

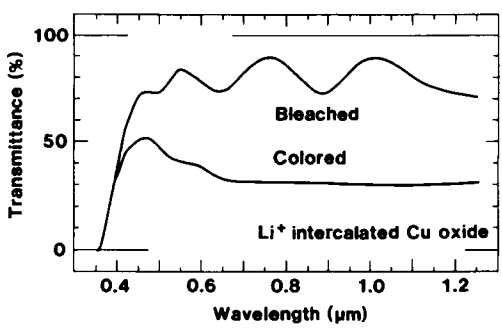

Fig. 22.6 Spectral transmittance of a reactively evaporated Cu oxide film after coloration and bleaching in $LiClO_4$ + PC. From Özer and Tepehan *(2681)*.

can give Cu, Cu_2O, Cu_2O + CuO, or CuO as the oxygen content is increased *(312, 973, 1116, 2817)*.

Electrochemical techniques can be used for making Cu oxide films, although it must be borne in mind that the electrochemistry of copper is extremely complex and various oxides with Cu^+, Cu^{2+}, and Cu^{3+} can appear, as well as hydroxides and other hydrous oxides. Anodizing, usually in alkaline or neutral electrolytes, has been carried out under potentiostatic *(1091, 2796, 3083, 3163)* and potentiodynamic *(19, 85-6, 531, 533, 974, 1088, 1165, 1402, 2187, 2652, 3106, 3262, 3464)* conditions. Thermal and chemical oxidation of Cu are other standard techniques for making Cu_2O *(182, 965, 1092, 1463, 1649, 2633, 2934-5, 3038, 3083)*.

The semiconductor bandgaps of Cu oxides have been studied several times. It is well documented that Cu_2O has a direct forbidden gap at 2.0 to 2.2 eV, whereas CuO has a gap at 1.35 to 1.7 eV *(31, 182, 798, 973, 1092, 1116, 1425, 1871, 2681, 2934-5, 2998)*. This implies that Cu_2O is absorbing in the short-wavelength half of the luminous spectrum, whereas CuO absorbs in the full luminous spectrum.

Figure 22.6 illustrates the electrochromism that can be obtained in a 0.09-μm-thick reactively evaporated cuprous oxide film in 1 M $LiClO_4$ + PC. The data were reproduced from recent work by Özer and Tepehan *(2681)*. Bleaching and coloring were accomplished at about ±2.5 V. The transmittance was changed rather uniformly at wavelengths between 0.5 and 1.2 μm. The coloration and bleaching were slow, and it took ~3 minutes to fully modulate the optical properties. This sluggishness is not unexpected since Cu_2O is known to have a low electrical conductivity. Nothing seems to be known about the cycling durability of these Cu oxide films.

Some results have also been published for electrodeposited Cu oxides (with a possible CuO character). Again it was impossible to accomplish a fully bleached state *(203)*.

22.8 Praseodymium Oxide

Non-stoichiometric Pr oxide films were produced by Thomas and Owen *(3406)* by use of organometallic CVD. Ion intercalation was accomplished in a $LiCF_3SO_3$ + PC electrolyte. At least 500 intercalation/deintercalation cycles could be accepted without apparent degradation. Optical measurements showed absorption irrespective of the ionic content. The absorption decreased upon Li^+ intercalation, and hence Pr oxide films exhibit somewhat anodic electrochromism.

22.9 Doped Strontium Titanate

Strontium titanate, $SrTiO_3$, is a perovskite capable of electrocoloration at elevated temperature when doped with transition metal ions. The Sr atoms occupy central positions in TiO_6 octahedra. Doping is necessary for obtaining sufficient electrical conductivity. The studies of strontium titanate are of interest mainly since they shed light on the early work on electrochromism in the defect perovskites WO_3 and MoO_3.

Optical effects in $SrTiO_3$ doped with Mo, Ni, and Al were studied in detail by Blanc and Staebler *(395)* and by Faughnan *(1044)*, and an analysis of $SrTiO_3$ doped solely with Ni was reported somewhat later by Mohapatra and Wagner *(2371)*. The dopant atoms substitute Ti in the perovskite lattice. Figure 22.7 shows data from Blanc and Staebler *(395)*. When a

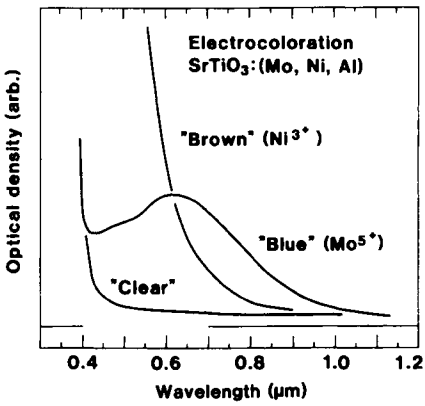

Fig. 22.7 Spectral optical density for $SrTiO_3$ bulk samples doped with Mo, Ni, and Al. Data refer to electrocolored parts and to a clear piece. Their color, and the ions responsible for the absorption, are stated. From Blanc and Staebler *(395)*.

voltage--probably of the order of a few hundred volt--was applied across the sample, color fronts spread from the contacts into the originally clear material. Spectral data are shown for these colored parts of the specimen. Specifically, the blue appearance was due to Mo^{5+} and the brown appearance was due to Ni^{3+}. The clear sample contained Mo^{6+} and Ni^{2+}. The dynamics of the coloration was governed by the diffusion of oxygen vacancies.

There are striking analogies to the electrochromism in Mo oxide and Ni oxide. The absorption band for the "blue" material in Fig. 22.7 is similar to that observed in molybdenum oxide (Fig. 12.9) where it is associated with Mo in 5+ state, and the short wavelength absorption for the "brown" material in Fig. 22.7 is similar to the optical performance of colored nickel oxide with Ni in 3+ state.

One may note that doped $SrTiO_3$ is capable of photochromism *(1016, 1044, 1049, 2448-9)*, and that the related $BaTiO_3$ can show electrocoloration *(1899)*.

Thin films of $SrTiO_3$ and $BaTiO_3$ have been prepared by reactive evaporation *(1601-2)*. For $SrTiO_3$, it was also possible to use reactive rf sputtering *(589-90, 592, 3275)*. Semiconductor bandgaps were found at ~3.2 eV, which is about the same energy as for well-crystallized bulk materials *(588)*.

Chapter 23

SYSTEMATICS FOR THE ELECTROCHROMISM IN TRANSITION METAL OXIDES

Chapters 2 through 22 have discussed various aspects of a number of transition metal oxides capable of showing electrochromism. The present chapter aims at a systematization of the optical data in order to elucidate why certain transparent oxides become absorbing or reflecting under ion intercalation, why other oxides can become transparent under ion intercalation, and why still others--though capable of ion intercalation/deintercalation--are unable to attain transparency. Structural properties are addressed first (23.1), and the ubiquity of the MeO_6 building blocks is reiterated. The octahedral coordination of the Me has important consequences for the electronic bands and, specifically, the *d* band is split into two parts conventionally denoted the t_{2g} and e_g bands (23.2). This feature of the electronic bands then forms a cornerstone in a conceptual framework of the electrochromism, elaborated in the last section (23.3). Few references are given below, and the reader is referred to the topical chapters for details. The systematic discussion in this chapter is based on earlier work by Granqvist *(1289, 1291-2, 1295-6).*

23.1 The Ubiquitous MeO_6 Octahedron

The electrochromic oxides can be categorized in different ways, for example as framework structures and layer structures (cf. Sec. 1.2). For the present exposition, it is appropriate to make a more detailed distinction into structures with perovskite-like, rutile-like, layer-type, and block-type configuration. Almost all of them can be constructed from *one kind of building block--the ubiquitous MeO_6 octahedron.*

Figure 23.1 serves as a convenient starting point for the discussion. It illustrates the cubic primitive unit cell for the *perovskite structure* with the general composition $CMeO_3$. As drawn, the Me ions occupy the corners of the cube, and the O ions bisect the unit cell edges. The central atom, denoted C, can be neglected here since it is absent in the electrochromic oxides of interest. The corresponding (defect) perovskite MeO_3 configuration is often referred to as "the rhenium oxide structure". Clearly, this structure can be visualized as an infinite framework of corner-sharing octahedra each with a metal ion surrounded by six equidistant oxygen ions. In between these octahedra there are extended tunnels that can serve as conduits and intercalation sites for mobile ions. The structure was shown in Fig. 2.1 for the particular case of W oxide. Other oxides with this structure are β-MoO_3 and, obviously, ReO_3.

Rutile-like structures are characterized by almost octahedral MeO_6 units forming a framework with infinite edge-shared chains and an equal number of vacant tunnels. Among the rutile-like

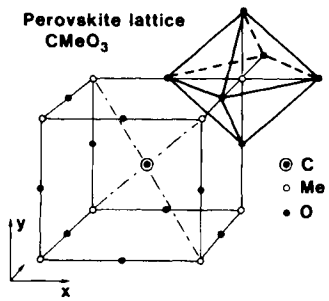

Fig. 23.1 Unit cell for the perovskite lattice. Octahedral symmetries are emphasized.

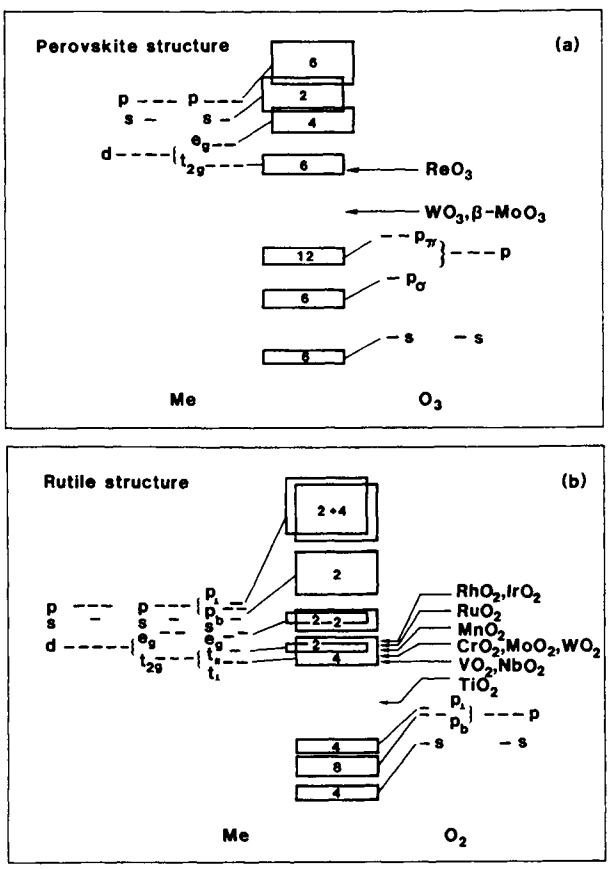

Fig. 23.2 Schematic bandstructures for the MeO_3 defect perovskite structure (part a) and for the MeO_2 rutile structure (part b). The incipient atomic and molecular levels are shown, using standard notation. The numbers in the different bands denote electron capacities. Arrows indicate Fermi energies. After Honig *(1534)*.

materials of interest for electrochromics, one notes TiO_2, MnO_2, VO_2, RuO_2, IrO_2, and RhO_2.

The *layer and block structures* are less easy to characterize uniquely. Most phases of Nb_2O_5 comprise MeO_6 octahedra in a defect perovskite arrangement. Ta_2O_5 has many properties in common with Nb_2O_5. Among the Co oxides, $LiCoO_2$ contains octahedral CoO_6 and LiO_6 units, and $HCoO_2$ is similar. NiOOH and $Ni(OH)_2$ comprise layers of edge-sharing NiO_6 octahedra. V_2O_5 also can be represented by distorted VO_6 octahedra, although the deviations from the ideal octahedral positions are so large that it is more adequate to describe the material in terms of layers of VO_5 units. For electrochromic Fe oxide, the microstructure is not known, but one could observe that most of the iron oxides have FeO_6 units; layer structures are likely to occur.

Among the remaining electrochromic oxides, Cr_2O_3 has a corundum structure characterized by face-shared distorted CrO_6 octahedra.

The only real exception, being an electrochromic material not constructed from MeO_6-like units, is Cu_2O which comprises OCu_4 tetrahedra. However, this material seems to have a rather poor electrochromic performance, and it is neglected for the present discussion.

One concludes that bulk crystals of almost all of the electrochromic oxides are built from highly regular arrangements of edge-sharing and corner-sharing MoO_6 octahedra. Electrochromic thin films of these materials rarely exhibit long-range order, though. The only electrochromic oxide for which film structures have been accurately characterized is W oxide and, as stressed in Sec. 3.8, there is no doubt that the WO_6 units prevail in the films. It is natural to assume that similar, though not identical, conditions exist for the other oxides of interest. Thus these films must be described as microcrystalline rather than as truly amorphous.

23.2 Canonical Bandstructure

The discussion above lends credence to the view that the electronic bandstructures of the electrochromic oxides can be discussed by reference to the crystal-field-effects existing in corner-shared and edge-shared MeO_6 octahedra. Such bandstructures were elaborated in considerable detail by Goodenough *(1246)*, and an easily readable description of the key features was given by Honig *(1534)*. These bandstructures are introduced next for the defect perovskite and rutile configurations.

The perovskite structure was shown in Fig. 23.1. A corresponding energy level diagram for the defect perovskite--here denoted MeO_3--is illustrated in Fig. 23.2(a). The atomic s, p, and d levels of Me are indicated, as well as the $2s$ and $2p$ levels of O. For WO_3 and ReO_3, the pertinent Me levels are $6s$, $6p$, and $5d$. The positions of these levels on the vertical energy scale are governed by their values for the isolated atoms as well as by the Madelung energies of the atoms when located in the perovskite lattice. Each Me ion is octahedrally surrounded by six oxygen ions, and each oxygen is linearly flanked by two Me ions. As a consequence of this arrangement, the d level is split into e_g and t_{2g} levels (using the conventional notation) as shown in the left-hand part of Fig. 23.2(a). The splitting arises because the e_g orbitals point directly at the electronegative O whereas the t_{2g} orbitals point away from the nearest neighbors into empty space and hence are lower in energy. Similarly, the $O2p$ orbitals are split as indicated in the right-hand part of Fig.23.2(a); the $2p_\sigma$ orbitals point directly at the nearest electropositive Me ions whereas the $2p_\pi$ orbitals point into empty space. In the perovskite lattice, the incipient molecular energy levels broaden into bands, whose relative widths and repulsion can be obtained from general arguments

(1534).

The number of states available for electron occupancy is fixed for each band. For example, counted per MeO_3 formula unit, the t_{2g} band has a capacity for six electrons (allowing for spin degeneracy), and the p_π band has a capacity for twelve electrons (allowing for spin and electron degeneracy). The pertinent electron capacities are indicated by the numbers in the various bands in Fig. 23.2(a). WO_3 and the iso-structural β-MoO_3 have 24 electrons in the shown bands, so that the Fermi energy lies in the gap between the t_{2g} and p_π band. The bandgap is wide enough to render the material transparent. ReO_3, on the other hand, has 25 electrons so that the lower part of the t_{2g} band is occupied and the material is non-transparent.

When ions and electrons are intercalated, the Fermi level is moved upwards in the presumed rigid-band scheme. The validity of such a model, in general terms, has been discussed by Julien and Balkanski *(1708)*. In the case of WO_3 and β-MoO_3, the excess electrons must enter the t_{2g} band and the material, in principle, transforms from a transparent to an absorbing or from a transparent to a reflecting state depending on whether the electrons occupy localized or extended states. When the ions and the accompanying electrons are extracted, the material returns to its original transparent state. In ReO_3, the Fermi energy also moves upwards upon ion insertion, but it remains well within the t_{2g} band irrespective of the content of mobile ions. Consequently the optical properties are not expected to be changed qualitatively, although quantitative changes in the absorptance may result from density-of-states effects that are outside the realms of the schematic bandstructure. Clearly, the discussion above explains why W oxide and Mo oxide are cathodic electrochromic materials, whereas Re oxide is not known, or expected, to be electrochromic.

Rutile and rutile-like structures are found among many MeO_2 oxides. Several of them are electrochromic--either cathodic or anodic--any may or may not attain a transparent state. The electrochromism can be understood from the basic bandstructure in Fig. 23.2(b). It deviates from its counterpart for the perovskites because the MeO_6 building blocks are edge-sharing and distorted. One can depart from the atomic s, p, and d levels for the Me ions and the s and p levels for the oxygen ions. Every Me ion is almost octahedrally surrounded by oxygen ions, and every oxygen ion is roughly trigonally surounded by Me ions. Hence the d levels are first split into e_g and t_{2g} levels, and the oxygen p levels are split into levels with orbitals p_b in the basal plane of the triangular array (wherein the oxygen ion is surrounded by three Me ions) and with orbitals $p_\perp$ perpendicular to that array. A further splitting occurs because the ideal octahedral symmetry is absent, and the ensuing Me levels--whose origin is not discussed here--are designated $t_{||}$, $t_\perp$, p_b, and $p_\perp$. In addition, the degeneracy of the e_g level is lifted. When the ions are arranged in the rutile lattice, one expects overlap among the $t_{||}$ and $t_\perp$ bands as well as among the two e_g bands. Hence the final schematic bandstructure, in fact, is quite similar to that of the perovskites. Depending on the parameters of the rutile unit cell, the $t_{||}$ band may collapse into an atomic-like sharp level. Electron band capacities can be deduced as for the perovskites and are indicated by the numbers in the bands.

The arrows in the left-hand part of Fig. 23.2(b) indicate the Fermi levels for several rutile-like oxides. For TiO_2, the Fermi level lies in the gap between the $Ti3t_{2g}$ and the $O2p_\perp$ bands, and ion intercalation is expected to lead to a transformation from a transparent to an absorbing state in much the same way as for WO_3 and β-MoO_3. This is consistent with experimental results on Ti oxide films. For VO_2, MnO_2, and RuO_2, the initial absorbing state cannot be eliminated by ion insertion. Again this is as expected from the bandstructure. RhO_2 and IrO_2 are especially interesting, since their Fermi levels lie close to the gap between the t_{2g} and e_g bands. Indeed, if

ions are inserted up to about one per formula unit in an Ir oxide film, it is transformed from an absorbing to a transparent state. In the bandstructure picture, the transparency is associated with the bandgap referred to above. One should note that transitions between pure t_{2g} and e_g states are parity-forbidden. Rhodium oxide films are similar to Ir oxide films, but their optical properties have not been studied in detail.

Figure 23.2(b) lists a number of rutile-type oxides other than those mentioned above, specifically NbO_2, CrO_2, MoO_2, and WO_2. Whereas these materials undoubtedly can be prepared as thin films, the fabrication is fairly awkward since the rutiles are not the highest oxides. More specifically, the oxygen partial pressure would have to be very accurately controlled in a reactive process. It is much easier to make Nb_2O_5, which is an electrochromic block-type material, than NbO_2. And rather than MoO_2 and WO_2 with (almost) rutile structure, one can make excellent electrochromic films of perovskite-type Mo oxide and W oxide.

The *layer structures* are not amenable to a simple theoretical treatment analogous to the one for the perovskites and rutiles. One should note, however, that the highest occupied states in $LiCoO_2$ are of t_{2g} character, and that V_2O_5 has an interesting bandstructure with a filled *O2p* band separated from a *V3d* band with a split-off lower portion. Band splittings are characteristic features of layer structures, as discussed by Yoffe et al. *(1106, 3639)*. No detailed bandstructure data seem to be available for Nb oxide or hydrous Ni oxide.

A common feature for the majority of the electrochromic oxides is that electron transport takes place in the t_{2g} band. Figure 23.3 illustrates the relative dispositions of the pertinent atomic orbitals along an edge in the primitive unit cell of the perovskite lattice. The t_{2g} orbital lobes, in the chosen representation, point at an angle of 45° away from this edge. The $O2p_\pi$ orbital lobes, on the other hand, point along the side of the unit cell. Ion transport, as stressed many times, occurs in tunnels between the rows of MeO_6 octahedra.

23.3 A Conceptual Framework for Electrochromism Among the Transition Metal Oxides

The schematic bandstructures in Fig. 23.2 indicate the fate of the electrons that enter the electrochromic films, and the next issue is the likely physical mechanisms by which these electrons cause a modulation of the optical properties.

Figure 23.4 again surveys the bandstructures of the electrochromic oxides capable of attaining a fully transparent state. For WO_3, β-MoO_3, TiO_2 and, possibly, also for Nb_2O_5, the Fermi energy lies between the *O2p* and the t_{2g} bands. Insertion of electrons makes the lower part of the latter band populated. If the oxide is heavily disordered, the excess electrons and their lattice polarisation can hop from one ion site to another by absorbing a photon so that the materials exhibit polaron absorption. The peak absorption lies in the near infrared, which renders the oxides bluish. For a sufficiently well-ordered material it is possible to have metallic-like properties, i.e., high reflection at wavelengths larger than the plasma wavelength. Crystalline WO_3 has this property. Well-ordered MoO_3 transforms into the layered α phase, and well-ordered TiO_2 is too dense for easy ion insertion.

The t_{2g} band is almost full in IrO_2, RhO_2, delithiated $LiCoO_2$ and, possibly, deprotonated $Ni(OH)_2$. These oxides are strongly absorbing. Polaron absorption is not observed, and intraband absorption in a composite material characterized by parts having various electron densities

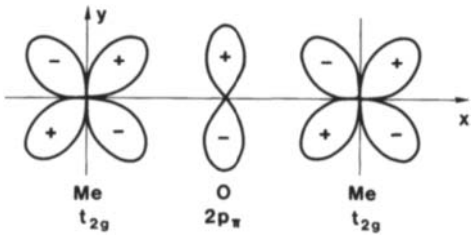

Fig. 23.3 Atomic orbitals along an edge in the primitive unit cell of the MeO_3 defect perovskite lattice. The t_{2g} lobes point at an angle of 45° away from the x axis. The x and y axes were defined in Fig. 23.1. After Honig *(1534)*.

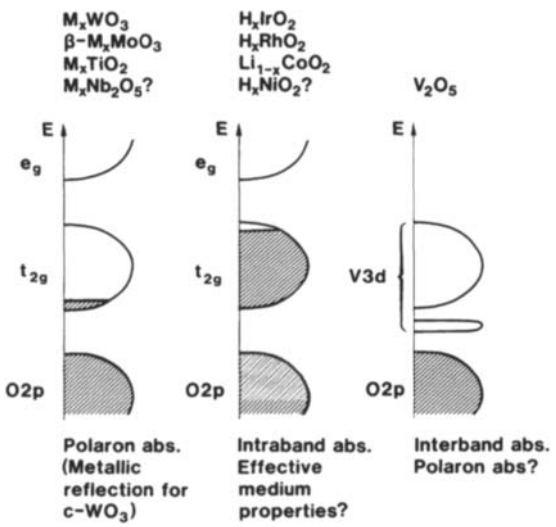

Fig. 23.4 Schematic bandstructures and suggested absorption mechanisms for several electrochromic oxides. From Granqvist *(1295-6)*.

(conductivities) and shapes is a more likely cause for the optical behavior. In principle, effective medium theory could account for the optical properties, but in the absence of substantial evidence for a composite structure the proposed absorption mechanism must be regarded as conjectural. Electron insertion associated with a filling of the t_{2g} band leads to optical transparency, as noted above.

V_2O_5 shows some absorption of blue light. This is readily explained as a result of transitions between the top of the *O2p* band and the split-off lower portion of the *V3d* band. Insertion of electrons can fill this split-off band. Since transitions between the two components of the *d* band are parity-forbidden, the net effect will be an apparent widening of the optically observed bandgap, which is then determined by transitions between the top of the *O2p* band and the lower part of the main *d* band. Hence interband transitions govern the short-wavelength electrochromism in V_2O_5. At a larger density of electron insertion, it is reasonable to expect that polaron absorption could lead to long-wavelength absorption.

This Page Intentionally Left Blank

Chapter 24

INORGANIC NON-OXIDE ELECTROCHROMIC MATERIALS

It is of interest to consider some inorganic non-oxide electrochromic materials. There are at least three reasons for this:

(i) A few of the materials, such as W sulfide (24.1) and heteropolyacids (notably polytungstic acid) (24.2), have an obvious kinship to electrochromic W oxide.

(ii) New mechanisms for electrochromic modulation of the optical properties are conceivable among materials such as some metal nitrides (24.3).

(iii) There are materials that show electrochromism yet their main application may be as counterelectrodes in metal-oxide-based electrochromic devices; graphite (24.4), β-zirconium nitride chloride (24.5), and Prussian Blue (PB) belong to this category.

In fact, there are many transition metal hexacyanometallates, and PB is only one--but the most well known and widely studied--member of a group of materials. With regard to PB, separate discussions are given for the structure and its capability for oxidation/reduction (24.6), the preparation and characterization of thin films (24.7), and the optical properties of films (24.8). Finally, there are some remarks on alternative hexacyanometallates (24.9). It should be stressed that organic electrochromic materials are taken to lie outside the scope of this book.

24.1 Tungsten Sulfide

Budkevich et al. *(510-2)* studied evaporated W sulfide films, expected to have an approximate WS_3 composition. Figure 24.1 displays spectral data indicating that the colored state has a pronounced absorptance maximum at $\lambda \approx 1$ μm. This is in good agreement with corresponding data for W oxide (cf. Sec. 9.4). The W sulfide films were susceptible to UV coloration.

24.2 Heteropolyacids, Especially Phosphotungstic Acid

Phosphotungstic acid (PWA) has been studied by Tell et al. *(3379-81)* for applications in electrochromic devices. The material is a hydrate with a representative formula $H_3PO_4(WO_3)_{12} \cdot pH_2O$ *(469)*; it is commonplace to put p = 29, but lower hydration levels are easily reached by

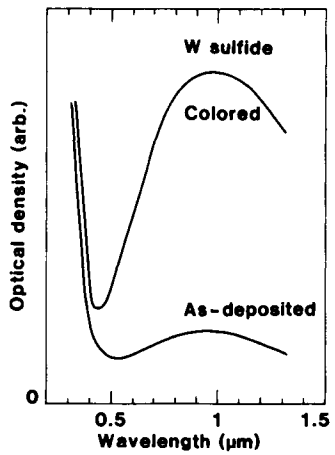

Fig. 24.1 Spectral optical density for a W sulfide film in bleached and colored states. From Budkevich et al. *(512)*.

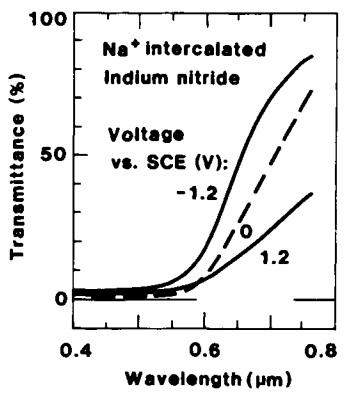

Fig. 24.2 Spectral transmittance of a InN_x film treated in Na_2SO_4 at the shown voltages. From Takai *(3336-7)*.

drying the acid.

Tell's studies *(3379-81)* dealt with pressed layers of PWA powder. The coloration efficiency (corresponding to a transmittance configuration), was ~60 cm^2/C at $\lambda = 0.7$ μm *(3379)*, which is comparable to CEs for W oxide films (cf. Sec. 9.7). Data were also reported *(3381)* for pressed layers of polymolybdic acid and of mixtures of this material with PWA and vanadium. A TiO_2 addition was used in some experiments *(3381)*.

Electrochromism has been observed in PWA solutions *(651-2, 2162-3)*. According to Maheswari and Habib *(2162-3)*, the CE was lower than in Tell's work *(3379)*, presumably as a result of undesired chemical dissolution.

It may be worthwhile to note that there are numerous heteropolyacids *(3259)*, and that phosphate tungsten bronzes have recently attracted much interest *(1326a)*. It seems likely that several new classes of precursors for electrochromic films could be developed by starting from such materials.

24.3 Indium Nitride and Tin Nitride

Takai *(3336-8)* reported optical data on films of InN_x and SnN_x prepared by reactive ion plating. Electrochromism was tested in Na_2SO_4 and $LiClO_4$ + PC electrolytes, and optical changes were observed between different shades of brown and gray. Figure 24.2 shows data for a 0.5-μm-thick InN_x film treated in 1 M Na_2SO_4.

24.4 Graphite

Graphite is a well known host for intercalation of alkali metals and other substances. Its potential for electrochromic device technology was studied by Pfluger et al. *(2742)*. Pyrolytic graphite was in contact with a water-free Li^+ electrolyte. By applying a voltage of 3 to 5 V, it was possible to change the appearance of the graphite from black to gold. The latter color is characteristic for LiC_6 *(2595)*. The change was reversible and occurred with a time constant of ~0.2 s. Solid electrolytes, such as Li_3N, can be used in conjunction with graphite.

More recently, Klein et al. *(1838)* studied electrochromism in C_{60} (buckminsterfullerene). Lithiation by use of $LiClO_4$ + γ-butyrolactone yielded increased absorption at $\lambda > 0.8$ μm, which was associated with the formation of C_{60}^-.

24.5 β-zirconium Nitride Chloride

Powders of β-ZrNCl were shown by Yamanaka et al. *(3708)* to exhibit electrochromism. This material has a layer structure, and Li^+ can be intercalated in vacant octahedral sites between close-packed chloride layers. Films were made from suspensions of fine-grained particles and were studied in electrolytes of $LiClO_4$ in tetrahydrofuran. The films could change reversibly between a pale yellow-green state and black when Li^+ was intercalated/deintercalated.

24.6 Prussian Blue: Bulk Structure and Oxidation/reduction Capability

Transition metal hexacyanometallates form an important class of insoluble mixed valence compounds. They have the general formula $M_k[M'(CN)_6]_l$, where M and M' are transition metal ions with different valencies. The compounds may be hydrous and contain ions different than metals. Iron hexacyanoferrate, often referred to as Prussian Blue, is most widely studied and may serve as a prototype for a whole class of compounds. PB is very well known in the dyeing trade as a pigment for paints, laquers, printing inks, etc. Its properties have been reviewed by Robin and Day *(2921)*, Itaya et al. *(1633)*, and others.

The chemical formula for Prussian Blue is $Fe_4^{3+}[Fe^{2+}(CN)_6]_3$. There is also another, soluble, PB with the fomula $KFe^{3+}Fe^{2+}(CN)_6$. Chemical reduction leads to $K_4Fe_4^{2+}[Fe^{2+}(CN)_6]_3$ or $K_2Fe^{2+}Fe^{2+}(CN)_6$, which is colorless and known as Everitt's salt (or Prussian White). Chemical oxidation produces $Fe_4^{3+}[Fe^{3+}(CN)_6A^-]_3$ or $Fe^{3+}Fe^{3+}(CN)_6$, with A^- being the anion of the electrolyte. Partial oxidation leads to a substance known as Berlin Green (or Prussian Green), whereas complete oxidation yields a yellowish product called Prussian Yellow. The reactions can be illustrated, highly schematically by only looking at the valence states of the iron ions, as

$$\underset{\text{clear}}{(2+,\,2+)} \leftrightarrow \underset{\text{blue}}{(3+,\,2+)} \leftrightarrow \underset{\text{green}}{[(1-\delta)(3+,\,2+) + \delta(3+,\,3+)]} \leftrightarrow \underset{\text{yellow}}{(3+,\,3+)}\,. \qquad (24.1)$$

It has been known since 1724 that iron is the cause of the color *(496)*. The "solubility", referred to above, strictly means the ease of peptization.

PB has a cubic unit cell with a lattice parameter of 1.02 nm. Fe^{2+} and Fe^{3+} are located alternately on a face centered lattice in such a way that Fe^{3+} ions are surrounded octahedrally by N atoms and Fe^{2+} ions are surrounded octahedrally by C atoms. According to detailed studies on PB and related materials *(571, 831, 1467, 2108)*, the structure is disordered with one fourth of the ferrocyanide sites unoccupied. In contrast with some earlier claims, no Fe^{3+} was found in interstitial positions.

Electrochemical studies, that were pioneered by Neff as late as in 1978 *(1008, 2515)*, show that PB has many properties in common with the intercalation oxides discussed extensively elsewhere in this book, and the possibility of going reversibly between colored PB and colorless Everitt's salt leads to anodic electrochromism. The intercalation is highly selective *(127, 790-1, 1608)*, and the feasibility of ion incorporation can be expressed, schematically, by $Li^+ << Na^+ < K^+ < Rb^+ < Cs^+$.

24.7 Prussian Blue: Preparation and Characterization of Thin Films

Thin films of PB can be made by a couple of different techniques. Electrochemical deposition is a standard method that has been studied intensely by Itaya et al. *(1626-31, 1634-9)* and many others *(690, 776, 1012, 1061, 1404, 1430-1, 1742, 1886, 2062, 2249, 2401, 2601, 2776, 3429, 3673)*. The compositions of the films are not known in full detail, but it appears well founded that insoluble PB is the main constituent. A transformation to the soluble form may be possible by electrochemical cycling in the presence of potassium ions *(1012, 1060, 1242, 1770, 2111, 2399, 2400)*, although the evidence underlying this contention may be given an alternative explanation

(1632). Some recent results based on the mirage effect did not support an insoluble → soluble transformation *(2777-9)*.

Among the other possible methods for making PB films one may note immersion of suitable substrates in solutions of $FeCl_3$ and $K_3Fe(CN)_6$ in excess KCl, as first demonstrated by Neff *(2515)*. An alternative involves PB solutions containing H_3PO_2 *(3714)*. Both of these techniques are presumably autocatalytic in nature. Casting of PB films from a solution with an organic solvent containing surfactants was reported in *(2081, 3430)*. Photodeposition is able to make PB coverages on TiO_2 particles *(3318)*.

Cyclic voltammetry has been used extensively to study ion intercalation/deintercalation, especially for K^+ ions. The literature data are fairly consistent with Fig. 24.3, from Itaya et al. *(1633)*, being a typical example. Specifically, the voltammogram pertains to an electrodeposited PB film, backed by a conducting SnO_2-based layer, in 1 N K_2SO_4. The current maxima at ~0.2 V vs. SCE refer to K^+ intercalation/deintercalation with concomitant changes between transparent and blue states. Further electrochemical reactions are evident at higher voltages.

The charge density involved in the intercalation/deintercalation reaction has been studied during extended cycling with the purpose of illustrating the durability. Figure 24.4, again from Itaya et al. *(1634, 1637)*, shows data for electrodeposited films subjected to voltage switching between 0.6 and -0.2 V vs. SCE at 5 Hz in KCl solutions of different pH. At pH ≈ 4, one notes a remarkable durability up to ~10^7 cycles. Degradation proceeded rapidly for both lower and higher pH, as apparent from the data taken at pH = 1.4 and pH = 6.3. Miles et al. *(2312-3, 3248)* reported that more than 10^5 cycles could be accepted with KCl at pH values between 2 and 3, and consistent results were given in *(171)*. Excellent durability in non-aqueous electrolytes was shown by Leventis and Chung *(2054)*.

24.8 Prussian Blue: Optical Properties

Optical properties in colored and bleached states have been reported for PB films made by electrodeposition *(1626-7, 1629, 1632, 1637, 1741-2, 1751-2, 2054, 2312-3, 2601, 3248, 3429)*, autocatalytic deposition *(2515, 3714)*, and casting *(2081, 3430)*. The data were reassuringly consistent. Figure 24.5 reports spectral absorbance from a detailed study of electrodeposited films by Itaya et al. *(1629)*. At 0.6 V vs. SCE, the film displayed a strong absorption centered at $\lambda \approx 0.7$ μm; this film consisted of Prussian Blue. At -0.2 V vs. SCE, the film was reduced and had the colorless appearance characteristic of Everitt's salt. At 1.1 and 1.4 V vs. SCE, finally, the film showed some absorption and attained the properties of Berlin Green and Prussian Yellow, respectively. One should particularly note the ability of going between an intensely blue and an almost colorless state by switching the voltage between 0.6 and -0.2 V vs. SCE. It should also be pointed out that the oxidized PB film had an overall absorptance that was much weaker than for the unoxidized state.

The coloration efficiency of PB was evaluated by Itaya et al. *(1629)* and Tada et al. *(3314)* who found it to be -81.5±0.5 cm^2/C at $\lambda = 0.7$ μm and -68 cm^2/C at $\lambda = 0.633$ μm, respectively.

Electrochromic devices can utilize PB films in at least four different ways. The most direct is to simply use PB in contact with a K^+ conducting electrolyte. This approach was taken by Itaya et al. *(1626)*, who studied electrodeposited films in 1 M KCl electrolytes (pH = 4) containing a diffusely scattering TiO_2 pigment. By applying voltage pulses so that the charge density was varied

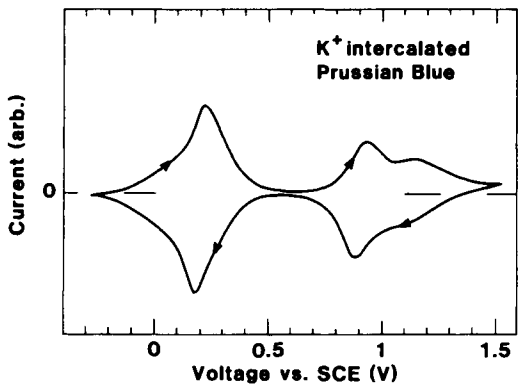

Fig. 24.3 Cyclic voltammogram for K^+ intercalation/deintercalation in an electrodeposited PB film in 1 N K_2SO_4. The voltage scan rate was 5 mV/s. Arrows denote scan direction. After Itaya et al. *(1633)*.

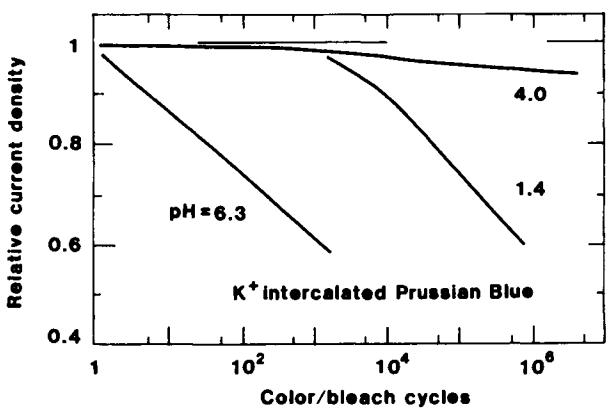

Fig. 24.4 Relative inserted charge density during long-term ion intercalation/deintercalation in electrodeposited PB films in KCl. Data refer to different pH values of the electrolyte. Curves were drawn to indicate a number of data points. After Itaya et al. *(1634, 1637)*.

by ~5 m C/cm^2, it was possible to switch the device between white and blue states with a time constant less than 0.1 s and a durability exceeding 10^5 cycles.

The second approach is to use a complementary device with an anodically coloring PB film and a cathodically coloring electrochromic film such as W oxide. Devices of this type have been studied in considerable detail, particularly in arrangements with an intervening polymer electrolyte. Results are given in Ch. 30 below. PB films operating in concert with polyaniline *(976)* or plasma polymerized Yb-diphthalocyanine *(1753)* have recently been discussed.

Thirdly, PB pigments in polymer matrices have been investigated for uses in display elements. The polymers studied so far embrace poly-perfluoro sulfonic acid ("Nafion") *(1530-1)*, poly-(vinyl-amine hydrochloride) *(1909)*, poly-aniline (2053), poly-pyrrole *(2055)*, and poly-(3-methylthiophene) *(2056)*.

The final PB-related approach to electrochromic devices is founded on the unique capability of this material to be strongly absorbing in an intermediate mixed valence state but transparent, or at least only weakly absorbing, both under reduced and oxidized conditions. This opens possibilities to develop single-layer (or "electrolyte-free") devices with one PB layer between electrically conducting surfaces. When a voltage is applied, part of the PB layer is reduced, another part is oxidized, while the central region with untransformed PB shrinks and eventually vanishes. Devices of this type were conceived of and developed by Carpenter and Conell *(606-8)*. Figure 24.6, reproduced from their work, shows that the absorption peak around $\lambda \approx 0.7$ μm went down to about half the original intensity when 8 V was applied across the film. The times for coloration and bleaching were ~1 and ~3 s, respectively. Even in the bleached state, there remained a significant absorption of blue light, indicating that not all of the PB had been transformed.

Photochromism has been observed in PB *(3816-7)*, which is in analogy with the properties of other electrochromic materials. PB-based electrical batteries, with obvious structural similarities to electrochromic devices, were discussed in *(1528-9, 1741, 1975, 2516)*.

24.9 Alternative Hexacyanometallates

There are numerous alternative hexacyanometallates of at least potential interest for electrochromic devices. One may get an idea of the richness of options by contemplating that among the rare earth hexacyanoferrate (HCF) compounds, here represented as $M_k[Fe(CN)_6]_l$, there are data for (k, l) being (1, 1) and (4, 3) and M being Ce, Pr, Nd, Sm, Eu, Gd, Tb, Dy, Ho, Er, Tm, Yb, and Lu *(2900)*. With regard to other hexacyanoferrates (HCFs), results have been given for VHCF *(610, 3114-5)*, CoHCF *(1671, 1691)*, NiHCF *(1690)*, CuHCF *(3180-3)*, MoHCF *(956)*, and PdHCF *(1670)*. Excepting NiHCF and MoHCF, these are all known to exhibit electrochromism. Figure 24.7 illustrates data for electrodeposited films of VHCF in 0.1 M K_2SO_4 + 3.6 M H_2SO_4 from Carpenter et al. *(610)*, and for CuHCF in 0.5 M K_2SO_4 from Siperko and Kuwana *(3180)*. Electrochromism is apparent; the optical changes lie in the mid-luminous range for CuHCF and mainly in the ultraviolet for VHCF.

Widening the scope to the full range of hexacyanometallates, one may note that $M_k[M'(CN)_6]_l$ compounds with (M, M') being (Fe, Ru), (Fe, Os), (Cu, Ru), (Cu, Os), (Fe, Cr), and (Cr, Fe) have absorption peaks at wavelengths between 0.37 and 0.60 μm *(2108)*. Films of the (Fe, Ru) compound--i.e., $Fe_4^{3+}[Ru^{2+}(CN)_6]_3$ known as Ruthenium Purple--were studied by Itaya et al. *(1628)* and others *(171, 2827)*. Figure 24.8, from the former work, shows striking

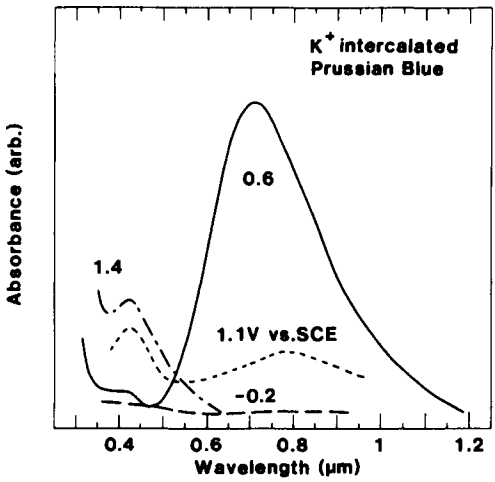

Fig. 24.5 Spectral absorbance for an electrodeposited PB film in KCl at pH = 4.0. Data pertain to four applied voltages. From Itaya et al. *(1629)*.

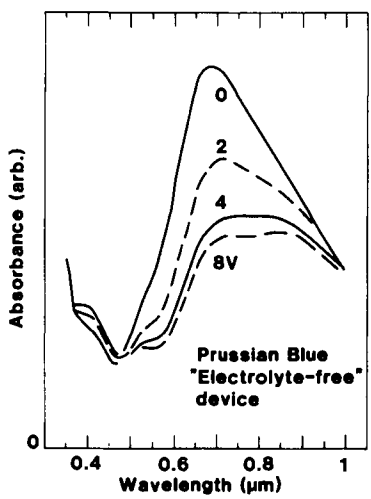

Fig. 24.6 Spectral absorbance for an "electrolyte-free" electrochromic device with a single electrodeposited PB film between two electrically conducting surfaces. Data refer to four values of the voltage across the PB film. From Carpenter and Conell *(607-8)*.

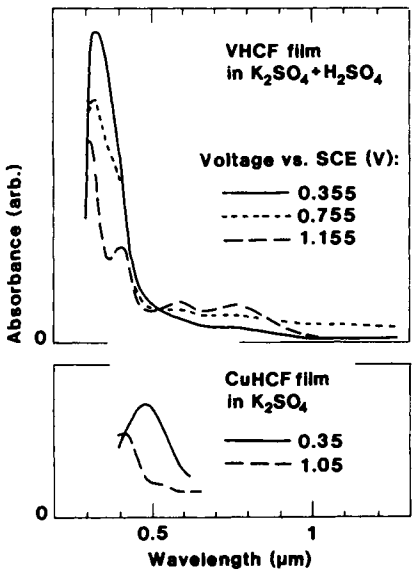

Fig. 24.7 Spectral absorbance for electrodeposited vanadium- and copper hexacyanoferrate films in the shown electrolytes. Data are given for different applied voltages. After Carpenter et al. *(610)* and Siperko and Kuwana *(3180)*.

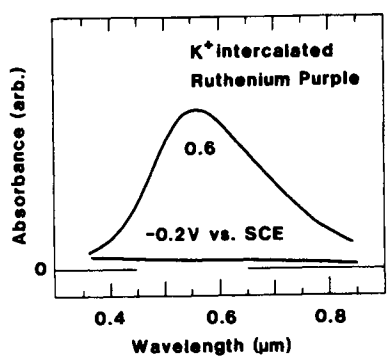

Fig. 24.8 Spectral absorbance for an electrodeposited film of Ruthenium Purple at two different applied voltages. From Itaya et al. *(1628)*.

electrochromism for an electrodeposited film in 1 M KCl (pH = 4). At 0.6 V vs. SCE there was a strong absorption peak whose shape almost matched the luminous efficiency of the human eye (cf. Fig. 1.4), and at -0.2 V vs. SCE the absorption was almost nil.

Part Three

ELECTROCHROMIC DEVICES

This Page Intentionally Left Blank

Chapter 25

TRANSPARENT ELECTRICAL CONDUCTORS

Chapters 2-24 treated electrochromic materials in great detail and hence lay a solid foundation for discussions of *electrochromic devices*. The remainder of the book is devoted to this latter subject. It was pointed out as early as in Sec. 1.1, that an electrochromic device embraces several layered materials, and that at least one of them must serve as a transparent electrical conductor. This material is discussed in the present chapter.

Two groups of materials are of particular interest for use as transparent electrical conductors. The first group contains a number of *heavily doped oxide semiconductors* with typical film thicknesses of a few times 0.1 μm. Their fabrication requires precise stoichiometry control and the deposition rate is slow. Properly made they are hard, compact, strongly adherent to glass, and chemically inert. The electrical resistivity is rather independent of film thickness. The luminous and near-infrared absorptance can be very small, but the films are prone to show some iridescence due to thickness variations over extended surface areas. These films are discussed in (25.1). The second group of transparent electrical conductors embraces *coinage metal films* with typical film thicknesses of a few times 0.01 μm. Such films can be made without stoichiometry control and at high deposition rate; they are soft, porous, sometimes poorly adherent to substrates, catalytically active, and chemically reactive depending on the external conditions. The electrical resistivity is strongly thickness dependent, and the optical properties are characterized by absorption but not iridescence. Further details are given in (25.2) below. The properties of transparent electrical conductors have been reviewed from a general viewpoint in *(371, 697, 1281-3, 1285-6, 1368, 1399, 1661-4, 1900, 2179, 3551)* and from the viewpoint of electrochromics in *(1290, 2121, 2328)*. One should note that, whereas ρ is the fundamental property, device performance is often governed by the "resistance per square" R_{sq}, defined by $R_{sq} = \rho d$, which typically should lie in the range 1 to 100 Ω.

A third option for the transparent electrical conductor is a *metal grid or mesh*. It is of interest mainly in connection with devices for regulating general lighting levels or for out-of-focus viewing. For a large grid or mesh size, the "transmittance" is governed by the unobscured geometric area fraction, whereas for a very fine grid or mesh the optical properties can be obtained from electrodynamics *(1877, 2276, 2802)*.

25.1 Doped Oxide Semiconductor Films

Transparent electrical conductors based on doped oxide semiconductors comprise a wide-bandgap host material--normally of In_2O_3, SnO_2, or ZnO--which is doped either by substitution of some of

the atoms or by oxygen vacancies. The most viable alternatives are In_2O_3:Sn (often referred to as ITO), SnO_2:F, SnO_2:Sb, and ZnO:Al. A consistent and fairly detailed theoretical model has emerged from recent work *(322, 1005, 1391, 1399, 1675, 3100-1, 3133)*. The optical and electrical properties can be described by use of an effective mass model for n-doped semiconductors well above the Mott critical density. At the high doping levels that are of practical interest, the impurities are singly ionized and the associated electrons occupy the bottom of the conduction band in the form of an electron gas. A straight-forward generalization to doping by doubly ionized oxygen vacancies in SnO_x is discussed in *(3252-5)*. At least for InO_x, new high-precision electron probe microanalysis indicated that the doping efficiency can be considerably less than unity *(320)*. The ionized impurities behave approximately as point scatterers, which, at least for In_2O_3:Sn, is consistent with pseudopotential arguments. Screening of the ions can be described through the Random Phase Approximation *(2083)*, which works well as a consequence of the small effective electron radii *(2161)*. Exchange and correlation in the electron gas can be included by the Hubbard and Singwi-Sjölander schemes *(1562-3, 3179, 3520)*. The free-electron properties govern the electrical resistivity and the optical properties at least in the luminous and near-infrared spectral ranges; they are most conveniently discussed in terms of a complex dynamic resistivity, which is directly related to the dielectric function *(585, 1170-1, 1338)*. From such an analysis it is clear that the ionized impurities are the dominant scattering centers, although grain boundary scattering can play some role in the mid-luminous spectral range. It should be apparent that there is a strong similarity between the theories for the doped oxide semiconductor electrodes and for the crystalline electrochromic W oxide films discussed in Sec. 10.5.

The dc resistivity of the semiconductor-based transparent electrical conductors is of decisive influence for the dynamics of large-area devices, as discussed below, and a minimum value is desirable. The magnitude of ρ is governed by the ability to introduce dopant atoms, in most cases substitutionally, without the creation of dopant-based absorbing aggregates. The electrical and optical properties of the films are dependent on the detailed thin film deposition conditions, as discussed in the vast topical literature. The intention is not to cover this literature in detail here but merely to point at some key results and give selected references to representative work. For ITO, that is most commonly used in electrochromic devices, films with $\rho < 2 \times 10^{-4}$ Ωcm have been obtained by several different techniques such as reactive evaporation *(792, 1398-1400, 1656, 2353, 2672, 2676a, 3139-40)*, reactive sputtering *(1103, 1160, 2181, 2199, 2322, 2497, 2859-60, 3137-40, 3181, 3697)*, as well as CVD and spray pyrolysis *(1101, 2202, 2954)*. The very lowest resistivities, $\rho \leq 1 \times 10^{-4}$ Ωcm, were obtained with activated reactive evaporation and ion plating *(2501-2, 3339)* and with reactive rf magnetron sputtering *(2859)*. Among the many methods that have been suggested for depressing ρ, one may note preconditioning of the deposition material *(2359)*, Ge additives *(3602, 3677)*, and post-deposition laser irradiation *(990)*. Resistivities below 2×10^{-4} Ωcm have been reported also for ZnO:Al made by reactive and nonreactive sputtering *(1595-7, 2319, 2321, 3007, 3341)*, SnO_2:Sb made by activated reactive evaporation *(2839)*, SnO_2:F made by spray pyrolysis *(29)*, ZnO_x made by reactive evaporation *(2318-20, 2498)*, InO_x made by coevaporation of In and In_2O_3 *(321, 2695-7)*, and $Cd_xSn_yO_2$ made by reactive sputtering *(1367-8, 2348)*.

Optical data for optimized transparent electrical conductors based on heavily doped semiconductors can be computed quantitatively from a theory that embraces the ideas outlined above *(1399)*. Specifically, the theory includes three additive contributions: (i) free electron effects represented by n_e electrons per volume unit that undergo ionized impurity scattering against an

equal density of positive charges according to the theory by Gerlach *(1170)*, (ii) valence electron effects represented by a parameterization of the n_e-dependent bandgap widening, and (iii) phonon effects described by a set of Lorentzian oscillators in basic agreement with bulk data *(3619)*. Structural rearrangements due to dopant incorporation--that were verified in recent EXAFS data on ITO *(2703-4)*--are not explicitely included. The only essential free parameter in the theory is n_e, which is related to the experimental value of ρ. Further details on the application of this model to In_2O_3:Sn and ZnO:Al are given in *(1399, 1675)*. Many of the relevant formulas were shown in Sec. 10.5. Figure 25.1 illustrates computed transmittance and reflectance in the $0.3 < \lambda < 50$ μm range and five n_es for a 0.2-μm-thick film described by parameters pertinent to In_2O_3:Sn. The film is backed by a substrate with a refractive index equal to 1.5. The film is transparent at short wavelengths and reflecting at long wavelengths; the cross-over between those two regimes depends on n_e and occurs at a smaller wavelength the larger the electron density. The general agreement with Fig. 10.8 should be observed. The semiconductor bandgap shifts towards the ultraviolet as n_e goes up, and at the same time the phonon-induced structure at $20 < \lambda < 30$ μm is washed out. At $n_e = 1 \times 10^{21}$ cm^{-3}, which is realized experimentally in In_2O_3:Sn films with very low resistivity, the onset of high reflectance lies at ~1 μm. At $n_e = 3 \times 10^{21}$ cm^{-3}, theory predicts an onset of high reflectance at ~0.7 μm, but those high n_es cannot be reached in real samples because of the limitations on achievable doping levels.

Figure 25.1 shows that an increase in n_e, yielding a decrease in ρ, has the effect of diminishing the transmittance particularly in the infrared. In a practical electrochromic device --especially one for modulating solar energy throughput--there is a tradeoff situation, and an optimum n_e can be given. Figure 25.2 shows computed solar and luminous transmittance and reflectance as a function of electron density for In_2O_3:Sn films with four thicknesses. T_{sol} drops sharply at high n_es and is as small as ~54 % for a 0.5-μm-thick film with $n_e = 10^{21}$ cm^{-3}. The transmittance limitation is caused mainly by absorption around the plasma wavelength, and the increase of R_{sol} is not as pronounced as the decrease of T_{sol}. For T_{lum}, the drop takes place only at $n_e > 10^{21}$ cm^{-3}, which is understandable since the integration to obtain the luminous properties is performed at shorter wavelengths than for the solar properties. The general resemblance between Figs. 10.9 and 25.2 should be noted.

25.2 Coinage Metal Films

Electrical and optical properties of transparent electrical conductors based on coinage metal films are considered next. Very thin films are needed in order to have a sizeable transmittance. The growth of thin metal films can be characterized in terms of a series of rather well defined stages, at least for films prepared by vapor depositon onto amorphous substrates such as glass *(696, 3202)*. The initial deposition leads to the formation of metallic nuclei on the substrate surface. Continued deposition makes these nuclei grow via surface diffusion and direct impingement. The metal islands thus formed are mobile and undergo coalescence growth *(2057)* so that larger and more irregular islands are created. The growing film then passes through large-scale coalescence, so that an extended metallic network is developed. Subsequently the voids between the metallic paths become smaller and more regular, and a uniform metallic layer finally may be formed. It is obvious that metallic conduction is possible only for thicknesses exceeding the one where large scale coalescence takes place. The absolute thickness scale for the growth sequence depends on many parameters

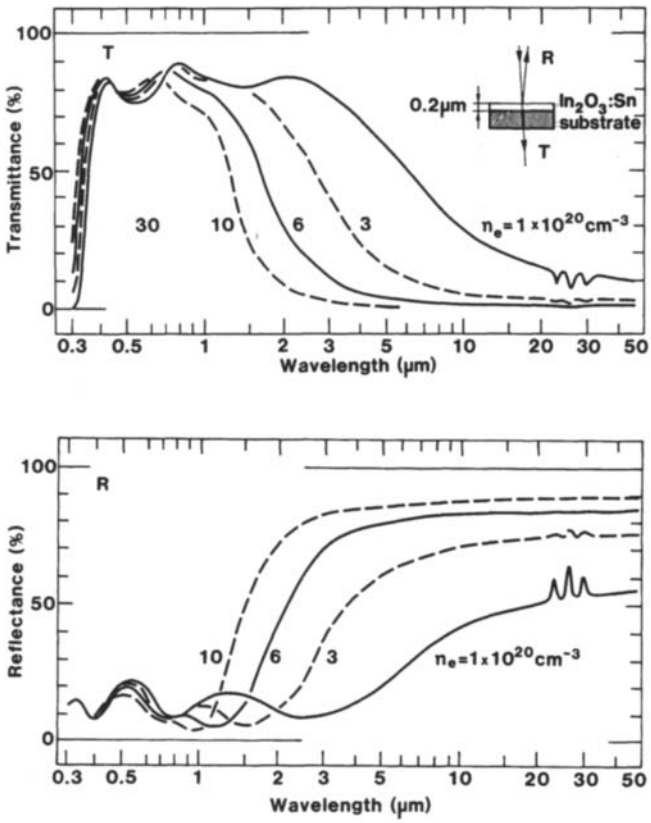

Fig. 25.1 Spectral normal transmittance T and reflectance R computed from a model for the optical properties of In_2O_3:Sn. The shown values of electron density n_e and film thickness were used. From Hamberg and Granqvist *(1399)*.

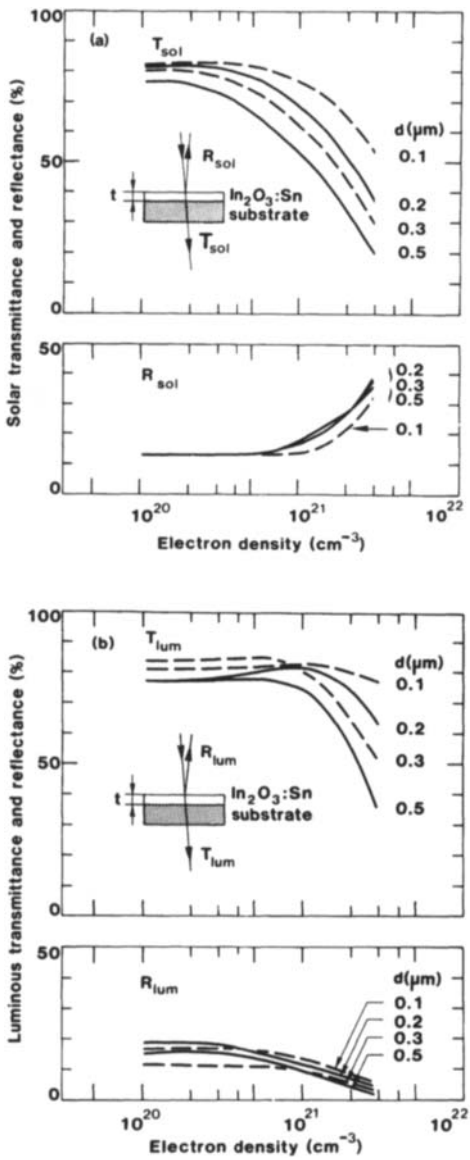

Fig. 25.2 Solar (part a) and luminous (part b) transmittance T and reflectance R vs. electron density computed from a model for the optical properties of In_2O_3:Sn. Results are given for four film thicknesses d. From Hamberg and Granqvist *(1399)*.

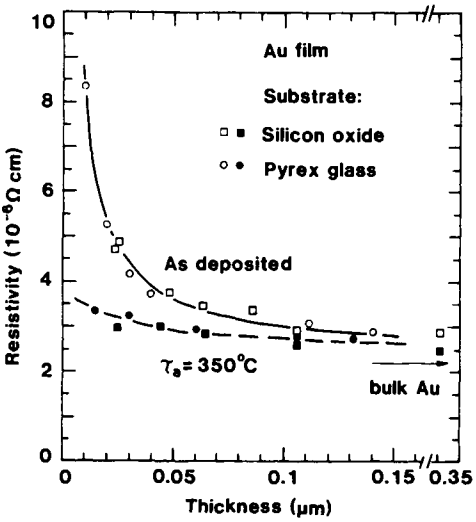

Fig. 25.3 Thickness-dependent electrical resistivity of Au films, evaporated onto two different substrates, in as-deposited state and after annealing at the shown temperature τ_a. The curves were drawn for convenience. An arrow indicates the resistivity of bulk Au. From van Attekum et al. *(3503)*.

such as deposited species, availability of (artificially added) nucleation centers, substrate temperature, vacuum conditions, presence of electric fields, etc.

Figure 25.3 shows resistivity data for evaporated gold films, reproduced from van Attekum et al. *(3503)*, which serve as a convenient starting point for the discussion. For the as-deposited film, ρ falls off sharply with increasing thickness and reaches an ultimate value of ~3 x 10^{-6} Ω cm at large thickness irrespective of the substrate being silicon oxide or Pyrex glass. This resistivity is more than 25 times smaller than the lowest resistivity for the doped oxide semiconductors. After treatment of the gold films at τ_a = 350°C for 15 to 30 minutes, ρ became significantly lower, especially at small thickness, and approached the bulk value. Representative data, that are in principle agreement with those in Fig. 25.3, have been given in *(1516-7, 2988, 3505-6)* and elsewhere. It has been demonstrated through extensive work that it is possible to lower ρ at small thicknesses by deposition at a low substrate temperature *(3054)*, in the presence of a small amount of gas *(1104, 2719)*, with an electric field along the substrate *(105)*, by the application of inorganic or organic nucleation centers *(72, 663, 3551)*, and by bombarding the growing film by ions supplied either by an external source *(2192-3, 2197, 2496, 3028)*, inherently during sputtering *(3498)*, or by bias evaporation in conjunction with a partially ionized beam of impinging metal atoms *(234)*. An interesting technique, capable of giving patterned low-resistivity gold films, is focused ion-beam irradiation of a substrate in contact with gold-bearing gases such as $C_7H_7F_6O_2Au$ *(397)* or others *(2300)*. Patterned films can also be made by direct focused ion-beam deposition *(2472)*. Thin coinage metal films may show preferred crystallographic orientation *(950, 1925)*.

A great amount of work has gone into theoretical modelling of the thickness-dependent metallic resistivity, but despite these efforts the situation is not yet fully clear. The major reasons for the resistivity increase in the thin-film limit are scattering against the external film boundaries and against its internal grain boundaries. For external boundary scattering, the theories are based on the semiclassical Boltzmann formalism *(1108, 3210)* or on quantum mechanical treatments using first-order perturbation schemes *(584, 700, 1083, 3393-4, 3453)*. The results can be summarized by

$$\rho = \rho_\infty [1 + G(d^{-1}, cl_\infty)] \ , \tag{25.1}$$

where ρ_∞ is the resistivity in the limit of infinite thickness and G is a function of inverse thickness and intrinsic scattering mean free path l_∞ times a constant c. In the semiclassical Fuchs-Sondheimer theory *(1108, 3210)*, c is 1 - p_s with p_s being a "specularity parameter", and in the quantum mechanical theory (in the limit of a continuous density of state for the metal) c can be identified with h^2 with h being the rms value of the microscopic roughness of the surface potential *(3393-4)*. In practice, the applicability of the theory is often limited by the existence of larger (mesoscopic) fluctuations of the local film thickness, although atomically flat gold films can be prepared on heated glass substrates *(1593)*. After averaging the corresponding local resistivity over the entire film *(1654, 2489, 2887, 3453)*, it is possible to obtain an acceptable fit to experimental data *(3504, 3507)*. Internal grain boundaries can also be of significance for the resistivity of thin metal films. Detailed investigations have shown *(1516-7, 3505-6)* that this effect can be represented by an exponential dependence on l_∞/D, with D being the average grain diameter. This dependence has been corroborated by quantum mechanical calculations *(2888)*. In many other works on the conductivity of granular metals, the analysis has been performed in terms of a semiclassical theory by Mayadas and Shatzkes *(2241)*.

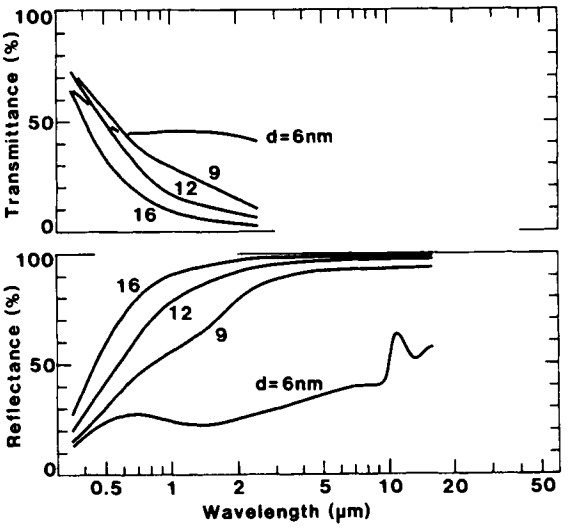

Fig. 25.4 Spectral transmittance and reflectance for Ag films on glass substrates. Data are shown for four thicknesses d. After Valkonen et al. *(3497)*.

Regarding optical transmittance through thin coinage metal films, silver is the superior material on account of its low luminous and solar absorptance *(1035, 3496-7)*. Gold and copper show absorption at $\lambda < 0.5$ μm. TiN, which is noble-metal-like as regards its electronic properties, is similar to Au in its optical behavior *(709, 2897, 3184, 3220, 3499)*. Typical transmittance and reflectance data for very thin evaporated silver films are shown in Fig. 25.4, where results from Valkonen et al. *(3497)* are replotted for the $0.35 < \lambda < 16$ μm range. At $d = 6$ nm, the reflectance was low, indicating that the film consisted of discrete islands. At $d \geq 9$ nm, however, the reflectance showed a metallic behavior. The transmittance was below 55 % at $\lambda = 0.5$ μm for these films. Figure 25.4 shows that the transmittance is severely limited due to the details of thin film growth. If a metallic-like electrical conductivity is required, one is confined to $T_{lum} < 50$ % and $T_{sol} < 40$ % for films prepared by conventional evaporation *(3497)*. However, optimized ion-assisted evaporation or special sputter technology can yield T_{lum} and T_{sol} up to 60 % *(3202, 3498)*. If an even higher transmittance is required, it is possible to use a multilayer coating including one or several dielectric layers, but such layers may in certain electrochromic devices have the undesired effect of preventing ion permeation. The durability of Ag-based films can be significantly enhanced through the application of an additional metal layer (for example of Cu) *(688)*. A similar beneficial effect of Al has been noted for TiN-based films *(101)*.

Theoretical models for the optical properties of very thin films must account for their non-homogeneous character. Such models are available for thicknesses well below large-scale coalescence *(308, 404-7, 2029, 2366, 2532, 2559, 3234-5, 3545, 3640-2)*, well above large-scale coalescence *(3202)*, and at the crossover *(830, 1128-9, 3680-2)*. Except at crossover, effective-medium-type theories (cf. Sec. 10.6) are appropriate for (semi)quantitative descriptions of the optical properties.

Chapter 26

ELECTROLYTES AND ION CONDUCTORS

Electrochromic devices incorporate a material that serves to transport ions to and from the electrochromic thin film. For the prototype five-layer design in Fig. 1.1, this electrolyte or ion conductor takes the middle position and allows ions to be shuttled between an electrochromic film and an ion storage film (also called "counter electrode"). One sometimes speaks of a "rocking-chair" operation. Electrolytes and ion conductors were reviewed from a general viewpoint in *(136, 642, 1388, 1744, 2133-4, 2850, 3327-8, 3660)* and from the perspective of electrochromics in *(2469-70, 3457)*.

In order to achieve acceptable dynamics of an electrochromic device, the ion conductivity should be larger than a certain limiting value that can be put between 10^{-4} and 10^{-7} S/cm depending on the intended application. The electrical conductivity should be very low, preferrably below 10^{-12} S/cm. Intense research on highly ion-conducting electrolytes has been going on for many years in the context of battery development. A lot of information is available that greatly facilitates practical electrochromic device construction, but it should be kept in mind that in electrochromics one has the special requirement that the electrolytes be stable under irradiation, in addition to the usual requirements of electrochemical and thermal stability. This chapter covers liquid electrolytes (26.1), inorganic solid electrolytes with separate discussions of proton conductors (26.2) and (mainly) alkali ion conductors (26.3), and polymer electrolytes with separate discussions of proton conductors (26.4) and (mainly) lithium ion conductors (26.5).

26.1 Liquid Electrolytes

Liquid electrolytes comprise a solute in a solvent. The electrolyte layer can be thin, and ~50 μm is sufficient for achieving optical modulation in an electrochromic device with a W film in contact with a liquid containing 1 M per liter of a lithium salt *(2469)*. The limiting performance is set by the variation in electrolyte conductivity upon ion intercalation/deintercalation).

The solvation of the solute ("supporting electrolyte") can be described in terms of Born's equation for the electrostatic energy of solvation E_{el}, viz.

$$E_{el} = (N_A Z^2 e^2 / 2r_i)(1 - \varepsilon_s^{-1}) , \qquad (26.1)$$

where Z is the charge of the ions, r_i is their radius, N_A is Avogadro's number, and ε_s is the dielectric constant of the solvent. In principle, there are many contributions to the solvation energy *(2707)*, but Born-type solvation according to Eq. 26.1 typically accounts for more than 80 %

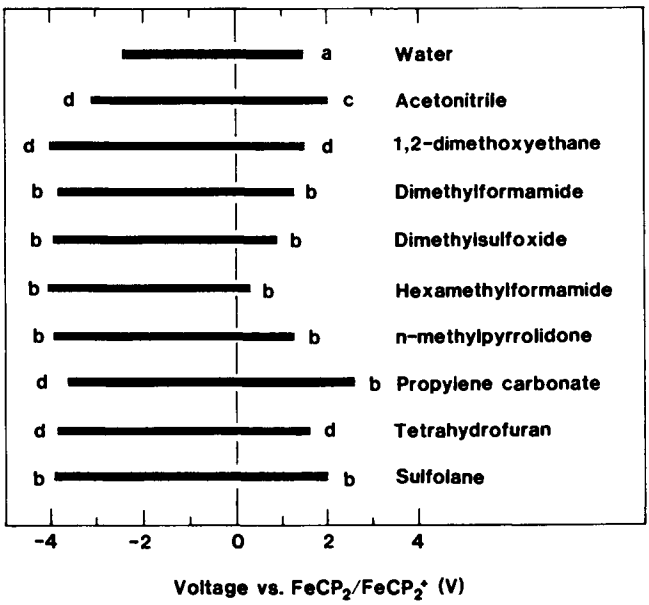

Fig. 26.1 Usable potential windows for ten different solvents. Pt was used as working electrode, and the letters indicate that the supporting electrolytes were (a) $HClO_4$, (b) $LiClO_4$, (c) Et_4NClO_4, and (d) Bu_4NClO_4. Voltages are given with reference to a Ferrocene/Ferrocinium electrode at a potential +0.39 V (+0.3 V) vs. RHE in aqueous (non-aqueous) electrolytes. From Nagai et al. *(2469)*.

when ε_s exceeds 25. Water has $\varepsilon_s \approx 78$ and therefore serves as a good solvent.

The ion conductivity--denoted σ and here referring to 25°C--varies by orders of magnitude between different electrolytes. With regard to 1 M aqueous solutions, H_2SO_4 gives the highest value with $\sigma \approx 0.39$ S/cm, followed by HCl and HNO_3 with $\sigma \approx 0.34$ and 0.33 S/cm, respectively. Corresponding data for other supporting electrolytes with Li^+, Na^+, and K^+ typically have conductivities between 0.07 and 0.21 S/cm *(2469)*.

Non-aqueous solvents can be more effective than water, particularly for organic and organometallic solutes. In some cases, compounds that are electroactive in water can be inert in non-aqueous solvents, and furthermore some non-aqueous media allow safe operation over a wider voltage span than aqueous ones. Among the non-aqueous solvents, one notices methanol, ethanol, n-butanol, tetrahydrofuran (THF), 1,2-dimethoxyethane (DME), acetone, acetonitrile (AN), dimethylformamide (DMF), propylene carbonate (PC), and others *(2469)*. Their ε_ss range from 65 (PC) to 7.2 (DME). The boiling points lie between 242°C (PC) and 65°C (methanol), and the freezing points lie between -44°C (AN) and -114°C (ethanol). One should observe the toxicity of many of the non-aqueous solvents, with some of them being strongly poisonous or cancer suspect reagents. Properties of many aqueous solvents were reviewed in *(1625, 2183)*. The solubilities of numerous supporting electrolytes are good in several of the solvents mentioned above, with limits up to 2 or 3 M in a number of cases *(2469)*. Typical conductivities for several different supporting electrolytes are 0.02 to 0.04 S/cm in AN, 0.01 to 0.02 S/cm in DMF, while lower conductivities are observed in DME and THF. Electrolytes incorporating $LiClO_4$ are widely used; their conductivities are ~3, ~6, and ~23 mS/cm for PC, DME, and DMF, respectively. The high conductivity in DMF cannot be directly understood from Born-type solvation, but the viscosity of the solvent is of importance. The $LiClO_4$-containing media are thermodynamically unstable, and, for example, 2 M $LiClO_4$ in DMF has an explosive force that is ~50 % of that of TNT. The viscosity of $LiClO_4$-based electrolytes can be increased by additions of poly-methyl methacrylate *(433)*.

The electrolytes can be used without appreciable degradation only in limited ranges of electrical potential. These "potential windows" must be wide enough in practical applications. The upper and lower potential limits are determined by many factors, such as the solute and solvent combination, reactions at the surface between the (transparent) electrical conductor and the electrolyte, and impurities in the electrolyte. Figure 26.1 shows practical potential windows for several solvents. The non-aqueous electrolytes are stable in larger ranges than for water, and, in particular, PC can be used to larger positive and negative voltages than H_2O. The basic cathodic potential limit is given by H_2 evolution in protic electrolytes and by cation reduction--in many cases alkali metal deposition--in aprotic electrolytes. For the commonly used PC, the stability is good when applied in conjunction with lithium, although it might be noted that decomposition into propylene gas and carbonate ions can take place on graphite electrodes *(906)*; the carbonate ions then can react with Li to form insoluble Li_2CO_3. Decomposition of the (transparent) electrical conductors can also give a limitation of the cathodic potential; the pertinent reduction potentials in aqueous media can be obtained from Pourbaix diagrams *(2799)*. Still another reason for a limitation of the cathodic potential is to be found in impurities--particularly O_2 and H_2O--that are difficult to remove to the ppm level. Reduction of O_2 can give O_2^{2+} that then reacts with and degrades organic compounds *(497)*. Reduction of H_2O can take place beyond 1.4 V vs. Li in PC *(566, 905)*. The anodic potential limit is given either by oxidation of the solvent (for protophilic media) or of the anion (for protophobic media). An example of the latter type is oxidation of ClO_4^- in PC *(566, 905)*. Further

issues related to the stability of liquid electrolytes were discussed in *(2469)*.

26.2 Inorganic Solid Electrolytes and Ion Conductors: Introductory Remarks and Data for Proton Conductors

The first discovered inorganic materials with a high ion conductivity were in the group of β-aluminas *(1041, 1573, 1961, 3725)*. They continue to be of much interest *(997)*. However, many alternatives have been found through later research. Most of the work on inorganic solid electrolytes and ion conductors has been geared towards devices such as solid state batteries, fuel cells, chemical sensors, etc., and, generally speaking, optical properties have seldom been investigated in detail. The mobile species are normally cations such as H^+, Li^+, Na^+, K^+, Ag^+ and Cu^+; among the possible anions it seems that only F^- would be of concern for electrochromics. The solid electrolytes show thermally activated conduction unless phase transitions are involved. The discussion to follow outlines the properties of a number of inorganic materials essentially along the exposition in a review by Truong et al. *(3457)*.

Proton conduction is a somewhat controversial subject that was reviewed recently by Kreuer *(1922)*. It was stressed that--more than for other species--the transport of protons is assisted by the dynamics of their surroundings, such as molecular movements (rotations or translations) and phonons. It is customary to speak of a *Grotthuss mechanism* to denote transport by proton transfer and subsequent molecular reorientation, and a *vehicular mechanism* to denote transport by cooperative motion of charged molecule-proton complexes and neutral molecules.

Proton conduction is well known in phosphotungstic acid [$H_3PO_4(WO_3)_{12} \cdot 29\ H_2O$, denoted PWA], molybdotungstic acid [$H_3PO_4(MoO_3)_{12} \cdot 29\ H_2O$], and hydrated zirconium phosphate [$ZrO(H_2PO_4)_2 \cdot 7\ H_2O$, denoted ZP]. Their conductivity can exceed 0.1 S/cm at room temperature *(2369, 2622)*. There are known techniques for spin-coating these materials *(1942, 1946, 2622)*. However, despite their excellent conductivity neither PWA nor ZP have been considered promising for electrochromic devices, due to their instability *(2369)*.

A more stable alternative may be hydrogen uranyl phosphate ($HUO_2PO_4 \cdot 4H_2O$, denoted HUP). It exists in different phases depending on the temperature; a tetragonal structure is stable at room temperature *(2745, 3143)*. Its conductivity is ~5 x 10^{-3} S/cm *(1468, 1553, 2045, 2744, 3141)*. Somewhat higher conductivities were obtained by replacing the (PO_4) groups by (IO_6) *(3142)*, whereas somewhat lower conductivities were found in the related $HUO_2AsO_4 \cdot 4H_2O$ *(1923-4)*. Regarding the mobile species, arguments have been given in favor of H_3O^+ *(2744)*, cooperative motion of H_3O^+ and H_2O *(1923)*, and $(H_2O)_4H^+$ *(742)*. The fabrication of thin stable and uniform HUP layers was described in *(56, 1552)*.

A somewhat related ion conductor containing phosphate groups is $Sn(HPO_4)_2 \cdot H_2O$ (denoted SP) with a conductivity between 10^{-5} and 10^{-6} S/cm *(1972, 1981)*. The analogous $Zr(HPO_4)_2 \cdot H_2O$ can have a conductivity up to ~8 x 10^{-3} S/cm *(57-8, 89)*; the precise value may depend on the water content *(617)*. The material can be produced by sol-gel synthesis *(330)*. A proton conductor with $\sigma \approx 5 \times 10^{-3}$ S/cm can be prepared by ion exchanging Na-ß"-Al_2O_3 ceramic so that "hydronium"-ß-Al_2O_3 is formed.

Another class of protonic conductors is found among the *hydrated oxides*, whose conductivity depends both on the amount of incorporated water and on the porosity *(262, 264, 698, 988, 1014, 3186, 3529, 3696)*. Particularly high conductivity exists in pyrochlore-type

$Sb_2O_5 \cdot pH_2O$ with $p > 4$, which can have $\sigma > 10^{-3}$ S/cm *(988, 1840, 2787, 3493-4, 3696)*, $Ta_2O_5 \cdot 3.92H_2O$ which can have $\sigma \approx 4 \times 10^{-4}$ S/cm *(3186)*, and $SnO_2 \cdot 2H_2O$ which can have a similar conductivity *(593)*. Ion conductors based on Sb_2O_5 can be prepared by screen printing *(2218)*, which is an attractive technique for device fabrication. Ta_2O_5-based films made by several different techniques had conductivities between 1.5×10^{-5} and 3×10^{-6} S/cm *(979, 1817, 2971)*, and evaporated films of $SbHP_2O_8 \cdot 3H_2O$ had $\sigma \approx 10^{-6}$ S/cm *(1983)*.

Protonation of oxide and fluoride films, in conjunction with decomposition of atmospheric water, is important for certain electrochromic devices as discussed later in Sec. 29.3. Some basic information about adsorption and decomposition of water on clean oxide surfaces can be found in *(3403)*. It should be noted, though, that the decomposition may be very different for a surface with many defects than for a single crystalline one, so work carried out in the spirit of "pure" surface science--using ultrahigh vacuum conditions, for example--may only give an incomplete picture of what goes on in the hydrated oxides of technical interest.

26.3 Inorganic Solid Electrolytes and Ion Conductors: Mainly Alkali Ion Conductors

Lithium ion conduction is possible in a rather wide range of materials. Generally speaking, their conductivity is not as large as for the proton conductors, but many of the Li^+ conductors can be prepared in thin film form, show good durability, and allow humidity-independent device operation. The highest conductivities are found among the β-alumina ceramics, with Li-Na-β-Al_2O_3 having $\sigma \approx 5 \times 10^{-3}$ S/cm *(1042, 2946)* and Li-β-Al_2O_3 having $\sigma \approx 1.3 \times 10^{-4}$ S/cm *(1775)*. Lithium-exchanged HUP yielded $\sigma \approx 3 \times 10^{-6}$ S/cm *(1468)*.

Li_3N is an interesting material, whose conductivity depends critically on stoichiometry and crystallographic orientation *(1574, 3548)*. Pure Li_3N showed $\sigma \approx 4 \times 10^{-8}$ S/cm *(1574)*, whereas Li-rich bulk samples can have $\sigma \approx 2 \times 10^{-4}$ S/cm. LiN_x films made by evaporation of Li_3N in the presence of N_2 can yield $\sigma \approx 10^{-3}$ S/cm *(2345, 2608)*. Evaporation of Li_3N at $\tau > 1000°C$ leads to decomposition into Li and N_2. If the Li is deposited onto a MgF_2 film, the Li atoms can diffuse into the film which then serves as a solid Li^+ conductor of interest for electrochromic devices *(3746)*. A similar decomposition and release of Li atom takes place when $LiNbO_3$ is heated *(162, 165)*.

Among other Li^+ conductors with $\sigma > 10^{-7}$ S/cm, one can note "amorphous" $mLiF \cdot nAlF_3$ films with $1 < m/n < 5/3$; they are capable of giving $\sigma \approx 10^{-4}$ S/cm *(2613-5)*. This material can be viewed as a fluorine substitute of the more hygroscopic $LiAlCl_4$ with $\sigma \approx 10^{-6}$ S/cm in the bulk *(1574, 3604)*. Conductivities of $\sim 10^{-4}$ S/cm have been found in LiF + 20% NiF_2 *(805, 2609)*, and high conductivities were reported for the systems LiF-CuF_2, LiF-TiF_3, LiF-ScF_3, LiF-VF_3, and LiF-CrF_3 as well *(2609, 2611)*. Conductivities up to 7×10^{-7} S/cm were obtained in thin films of the systems LiF-MgF_2-AlF_3 and LiF-FeF_2-ScF_3 *(2610)*. In LiI + 40% Al_2O_3, the conductivity was 1.2×10^{-5} S/cm *(2070)*, and in LiI-CaF_2 and LiI-CaI_2 it lay between 10^{-5} and 10^{-6} S/cm *(3052)*. $LiBO_2$ films had a conductivity of 10^{-8} to 10^{-7} S/cm *(162, 165)* and $Li_3Sc_2(PO_4)_3$ had $\sigma \approx 3 \times 10^{-6}$ S/cm *(82)*. A sizeable Li^+ conductivity was also found in Li_2WO_4 *(3745)*.

Bulk glasses with high Li^+ conductivity are known in numerous systems containing Li_2O, Li_2S, LiCl, LiBr, and LiI *(577, 656, 1711-2, 2050-1, 2198, 2671, 2821, 3212, 3373, 3458, 3472, 3569-70)*. Bulk glasses of $LiTaO_3$ and $LiNbO_3$ can have conductivities up to $\sim 10^{-5}$ S/cm *(1194)*, whereas thin films of these latter materials and of $3Li_2O \cdot B_2O_3$ showed $\sigma \approx 10^{-7}$ S/cm

(1232, 1644, 3107). A recent study of rf sputtered $LiNbO_3$ films gave Li^+ conductivities between 4×10^{-9} and 3×10^{-8} S/cm depending on preparation conditions *(324)*. Additional work on glassy multi-component Li^+ conducting films prepared by evaporation, sputtering, and sol-gel technology was reported in *(249, 278-80, 437, 702, 975, 989, 2052, 2350, 2920)*. Properties of the corresponding bulk glasses were reviewed in *(2801)*.

Among the Na^+ conductors, Na-β-alumina is of particular interest; it can have $\sigma \approx 1.4 \times 10^{-2}$ S/cm *(1961, 3725)*. This class of materials has compositions ranging from $Na_2O \cdot 11Al_2O_3$ (β-alumina) to $Na_2O \cdot 5Al_2O_3$ (β"-alumina) *(3245)*. Thin film fabrication is notoriously difficult *(1774)*, although advances in sol-gel technology may lead to useful materials *(3385, 3693, 3730-1)*. The analogous gallate Na-β-Ga_2O_3 also shows very high Na^+ conductivity *(1094)* and can be prepared in thin film form by sputtering followed by high-temperature heat treatment *(2349)*. Aluminogallates are known too *(45)*. Other useful Na^+ conductors are $Na_{1+x}Zr_2Si_xP_{3-x}O_{12}$ (known as NASICON) *(300, 438, 517-8, 3414)* with $\sigma \approx 7 \times 10^{-4}$ S/cm and $Na_{0.5}In_{0.5}Zr_{0.5}S_2$ *(3452)*. A lower, but still practically interesting, Na^+ conductivity can be found in $NaAlCl_4$, $NaSbO_3$, $NaTaWO_6$, $NaTa_2O_5F$, $2NaO \cdot 3Nb_2O_5$, and $Na_{0.72}In_{0.72}Sn_{0.28}O_2$ *(872, 1574, 3178)*. One could note that NASICONs may be produced by a sol-gel route *(2736)*, and such layers can be transformed into proton conductors by ion exchange with hydronium or ammonium ions *(3192)*.

Conductors of some other ions may also be of interest for electrochromic devices. Thus K^+ conduction with $\sigma > 10^{-7}$ S/cm is possible in $2K_2O \cdot 3Nb_2O_5$, $K_{0.72}In_{0.72}Sn_{0.28}O_2$, $K_{0.72}In_{0.72}Hf_{0.28}O_2$, and $K_{0.72}In_{0.72}Zr_{0.28}O_2$ *(872, 3178)*. Ag^+ conductivity of ~0.3 S/cm is possible in bulk $RbAg_4I_5$ *(2675-6)*; this seems to be the highest value at room temperature for any solid ion conductor. Thin film fabrication is difficult due to possible decomposition and hydration, but films with conductivities between 0.25 and 0.04 S/cm have been reported *(452-3, 901, 1319, 1776, 2534, 3332)*. Analogous properties have been found in KAg_4I_5 *(2675)* and $CsAg_4Br_{2.5}I_{2.5}$ *(902)*. Among the silver pyrophosphate iodides, high Ag^+ conductivity is possible with $Ag_{19}I_{15}P_2O_7$ having $\sigma \approx 0.09$ S/cm at room temperature *(3326, 3329)*. Again thin film manufacturing is problematic with conductivities up to ~0.03 S/cm being stated for optimized evaporation conditions *(150)*. $Ag_6I_4WO_4$ has $\sigma \approx 0.05$ S/cm *(1985, 3108, 3330)*. Regarding F^- ion conductors, recent reviews contain a wealth of information *(2614, 2865)*. Thin film of evaporated PbF_2 and $PbSnF_4$ were studied in *(2899)*; F^- conductivities were 10^{-6} S/cm and 3×10^{-4} S/cm, respectively, which is in reasonable agreement with bulk data *(2863, 2866)*.

An interesting possibility of increasing the ionic conductivity is by adding fine particles of a dielectric material such as Al_2O_3 or SiO_2 *(2071, 3109)*. The size of the particles is critical and, for example, for AgI + 30% Al_2O_3 one can enhance the conductivity by a factor of 40 when the diameter is ~0.6 μm but only by a factor of 2 when the diameter is ~1 μm. Similar results have been obtained for CuCl + Al_2O_3 and LiBr + Al_2O_3 *(653, 2483)*. The enhancement effect can be interpreted by the use of models built on continuum percolation, effective medium theories, and fractal concepts *(2164, 2490-1, 2930-1)*.

26.4 Polymer Electrolytes: Introductory Remarks and Data for Proton Conductors

Polymer electrolytes are of great and increasing interest for electrochromic devices and allow

convenient designs incorporating resilient and adhesive layers. In contrast with the liquid electrolytes, there are no obvious problems with leakage and fluid-mechanics-induced distortions, and in contrast with the solid inorganic electrolytes and ion conductors, one can avoid the complexities of stoichiometry- and crystallinity control in thin layers of multielement materials and instead benefit from the strengths of organic synthesis. Polymer electrolytes can be non-inflammable, but the risks of toxic fumes upon overheating should be remembered. The electrolytes can be strongly adherent to W oxide *(96-7, 3314, 3316)* and other materials *(387)*. On the negative side, one can note that the ion conductivity may not be as high as in the other types of electrolytes and ion conductors, and that some polymers are prone to degrade upon ultraviolet irradiation and heating. The interesting polymers are generally transparent or translucent; they can be given a diffuse white appearance by incorporation of a suitable pigment such as TiO_2. It is possible to achieve electrochromism in polymers with pigments of WO_3 and IrO_2 *(2307)*.

Proton conduction with conductivities of 0.01 to 0.1 S/cm at room temperature can be accomplished in polymers containing sulfonic acids. Among the most prominent materials one notes poly-vinyl sulfonic acid (poly-VSA), poly-styrene sulfonic acid (poly-SSA), poly-ethylene sulfonic acid (poly-ESA), poly-2-acrylamido-2-methyl-propane sulfonic acid (poly-AMPS), poly-perfluoro sulfonic acid (usually referred to under the trade name "Nafion"), poly-toluene sulfonic acid (poly-TSA), as well as certain copolymers such as poly-(VSA, AMPS), poly-(HEM, AMPS) with HEM denoting 2-hydroxy ethyl methacrylate, poly-(BPEI, AMPS) with BPEI denoting branched poly-ethylene imine, and poly-(SSA, DVB) with DVB denoting divinyl benzene *(48, 1183, 1713, 2843)*. The proton conduction is governed by the equivalent weight (EW) of the polymer--defined as the molecular weight of the monomer unit divided by the number of acid groups--and by the water content *(789)*. EW ranges from 108 for poly-VSA to ~1200 for Nafion, and the conductivity shows a consistent variation with poly-VSA being the most conducting polymer. The water molecules are bound to the $-SO_3H$ groups and provide H^+ conduction by creating hydrogen bridges between the sulfonic acid groups. The conductivity goes up with increasing values of the H_2O/SO_3 ratio until it reaches ~6, and the conductivity then remains at a constant level for even larger water contents. Excessive water may lead to degradation of W oxide films, as discussed in Sec. 31.7. TiO_2 pigmentation yields only a marginal drop of the conductivity.

Another class of proton conductors is based on the addition of H_2SO_4 or H_3PO_4 to poly-vinyl alcohol (PVA) *(2786)*, poly-ethylene imine (PEI) *(47, 49)*, BPEI *(3063)*, or poly-vinyl pyrrolidone (PVP) *(141)*. A review was given in *(2809)*. Drying of appropiate stock solutions, sometimes followed by heating to a moderate temperature, could produce films suitable for electrochromic devices. Hydroxylated polymeric quaternary ammonium chloride is another proton conductor; its conduction mechanism is somewhat unclear *(2727)*. Still another possibility is offered by anion-grafted ormosils synthesized by sol-gel technology *(365)*.

The PVP-H_3PO_4 polymer, as well as many others, has a strongly temperature dependent ion conductivity. This feature can be used to advantage in thermo-electrochromic devices, as discussed later in Sec. 30.1. The upper curve in Fig. 26.2, based on compilations by Bohnke and Bohnke *(423)* and by Deroo *(891)*, shows that the conductivity varies smoothly from ~10^{-8} S/cm at 10°C to ~10^{-3} S/cm at 80°C for "amorphous" $(PVP)_{0.5}$-H_3PO_4.

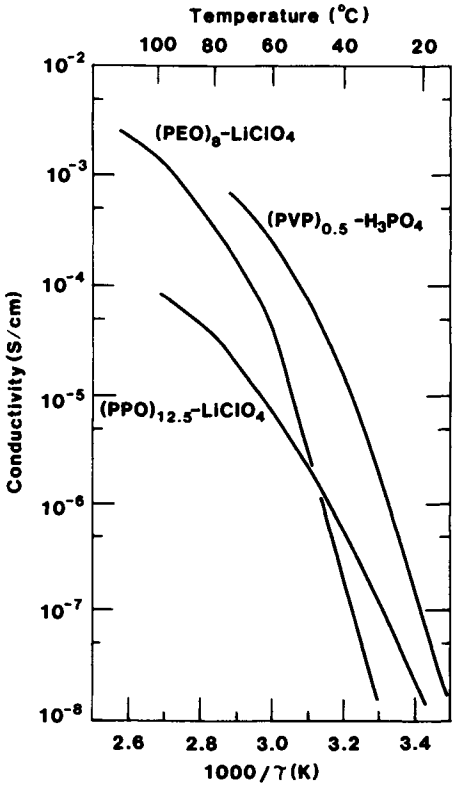

Fig. 26.2 Conductivity vs. inverse temperature τ for the shown polymer electrolytes. From a compilation of data by Bohnke and Bohnke *(423)* and Deroo *(891)*.

26.5 Polymer Electrolytes: Mainly Lithium Ion Conductors

Among the polymer-based alkali ion conductors, one can obtain a substantial conductivity through direct interaction between an appropriate salt and a macromolecule. In the case of Li^+ conduction, which has been most widely investigated, complexes with $LiClO_4$, LiI, LiBr, $LiAsF_6$, $LiCF_3SO_3$, etc., have been studied for many polymers. Table 26.1 lists a number of the most important ones and gives selected references to original work. There are numerous ways to improve the properties of the polymers; one example concerns PMEO for which plasticizers of ethylene carbonate and propylene carbonate can be used *(1582)*. Polymer electrolytes based on poly-vinyl butyral deserve attention since this material is well established for lamination of glass *(2682)*. High K^+ conduction has been accomplished in PEO, PMEO *(1857)*, and poly-(etyhene oxide, urethane) (PEOU) *(3314, 3316, 3319)*. Substantial Na^+ conductivity was found in poly-aziridine *(687)*. It seems likely that high ion conduction can be achieved in many other polymers and copolymers as well. Ion conduction in PEO and PPO-based systems is most thoroughly investigated, and in particular PEO can form many different types of complexes and serve as a conductor not only for Li^+ but also for Na^+, K^+, Rb^+, Cs^+, and NH_4^+; the properties of these polymers have been reviewed several times *(137-8, 3537, 3579)*.

Ion motion in polymers is possible only in the elastomeric phase *(372)*, whose extent can be obtained from phase diagrams. Such data are available for PEO-$LiClO_4$ and PEO-$LiCF_3SO_3$ as well as for other binary systems *(1054, 2922)*. The conductivity normally obeys a phenomenological relation, known as the Vogel-Tamman-Fulcher (VTF) equation, stating that

$$\sigma \propto \tau^{1/2} \exp\left[-E_a/k_B(\tau - \tau_g)\right] \tag{26.2}$$

where E_a is a pseudo-activation energy and τ_g is an ideal glass transition temperature (47°C for PEO). The relation is expected to be obeyed at least when the polymer and salt form a single phase and τ is above the melting point of the polymer (~60°C for PEO). Below the melting point, where $\sigma = 0$ might at first be expected, polymer chain entanglement leads to a "constrained" ion conducting phase representing some 10 to 25 % of the volume. Theoretical aspects of the ionic conductivity were reviewed in *(2849)*.

Specific data on Li^+ conductivity at room temperature are listed in Table 26.1 for several polymers. It is seen that PPG-PMMA as well as some poly-siloxanes have conductivities in the 10^{-4}-S/cm-range, and that $\sigma > 10^{-7}$ S/cm is found in several polymer systems. The latter range is valid also for crosslinked PEO and PPO. Poly-(ethylene oxide, acrylate) with carbonate plasticizers can have a conductivity up to 10^{-3} S/cm. PEOU has shown conductivities up to 8×10^{-5} S/cm. Data for some other Li^+ conducting polymers were summarized in *(891, 2470)*.

The Li^+ containing PPG-PMMA electrolyte listed in Table 26.1 is of particular interest for electrochromic devices. Low-molecular-weight PPG is a natural starting point for constructing an electrolyte, since it can give a high conductivity when complexed with alkali metal salts. However the PPG-salt system is hydrophilic and has poor mechanical stability and adhesiveness. These problems can be overcome by polymerizing methyl methacrylate in PPG complexed with $LiClO_4$ or $LiCF_3SO_3$, using azobisisobutyronitrile as initiator *(2178)*. It is interesting that the salt makes the two otherwise incompatible polymers compatible. Ionic conductivities up to 7×10^{-4} S/cm have been obtained *(190)*. The temperature dependence of the conductivity followed the VTF relation for $-20 < \tau < 110$°C. The transparency of this electrolyte is excellent *(3647)*. Highly conducting

Table 26.1 Li^+ conducting polymer systems and their conductivity at room temperature.

Polymer	Conductivity (S/cm)	Reference
Poly-ethylene oxide (PEO) (no crosslinking)		*139, 444, 463, 1803, 2132*
Poly-propylene oxide (PPO) (no crosslinking)		*139, 3579*
Poly-(ethylene oxide, siloxane) (PEOS)	$\sim 10^{-4}$	*1527, 2473*
Poly-(ethylene glycol, siloxane)		*464, 3224, 3244*
Poly-(propylene oxide, siloxane)	$\sim 10^{-4}$	*59, 2473*
Poly-(ethylene oxide, methyl methacrylate)(PEO-PMMA)	4×10^{-6}	*2099*
Poly-(ethylene oxide, acrylic acid) (PEO-PAA)	4×10^{-6}	*2677, 3463*
Poly-(propylene glycol, methyl methacrylate)(PPG-PMMA)	7×10^{-4}	*190, 2177-8, 3647*
Poly-ethylene succinate		*982, 3580*
Poly-ethylene adipate	$\sim 10^{-7}$	*144*
Poly-ethylene imine (PEI)		*47*
Poly-(ethylene oxide, 2-vinylpyridine)	4×10^{-6}	*2063*
Poly-*oligo*-oxyethylene methacrylate (PMEO)	$\sim 10^{-5}$	*259, 1856-7, 2580, 3672*
Poly-*bis*-methoxy-ethoxy-ethoxy phosphazene	6×10^{-5}	*401*
Poly-*N*-methyl aziridine		*136*
Poly-propiol actone		*3581*
Poly-(1,3 dioxolane)		*54*
Poly-urethane elastomer	$\sim 10^{-7}$	*3090*
Poly-tetra-hydro furan	$\sim 10^{-6}$	*54*
Complex poly-siloxanes		*3465-6*

PEO with $LiN(SO_2CF_3)_2$ as the dissolved salt was discussed in *(142)*.

Very high Li^+ conductivities are possible in solid polymer systems that incorporate solvents *(777)*. Thus PEOS "swollen" in PC so that the weight increased by 160 % yielded $\sigma \approx 6 \times 10^{-4}$ S/cm; the PC did not significantly degrade the mechanical properties, whereas other solvents had such an effect *(1527)*. A conductivity as high as $\sim 4 \times 10^{-3}$ S/cm has been reported for dimensionally stable free-standing foils with $LiClO_4$ or $LiCF_3SO_3$ in organic solvents immobilized in a polymer network of PVP, poly-acrylo nitrile, poly-tetra ethylene glycol diacrylate, or poly-vinyl chloride *(16, 53)*, and similar conductivities have been obtained in rubbery solids of crosslinked plasticized gels comprising poly-(*N,N*-dimethyl acryl amide) complexed with lithium salts *(951)*. $LiClO_4$ + PC has been stiffened by additions of PMMA; these electrolytes had a conductivity of $\sim 2 \times 10^{-3}$ S/cm *(433, 1100)*. It may be possible to increase the conductivity of a given polymer by oxide particle additives *(2549, 2808, 3624)*.

Thin polymer-based Li^+ conducting *films* can be prepared by vacuum deposition. Thus coevaporation of PEO + $LiCF_3SO_3$ and of PEO + LiI could yield a remarkable $\sigma \approx 3 \times 10^{-2}$ S/cm *(1642-3, 1645)*. Glow discharge polymerization of methyl benzene sulfonate and octamethyl cyclo tetra siloxane (OMCTS) followed by treatment in LiI + PC and hybridization with PEO gave purely Li^+ conducting ~1-μm-thick films with $\sigma > 10^{-7}$ S/cm *(2570)*, and similar properties were obtained by glow discharge polymerization of OMCTS followed by treatment in $LiClO_4$ and PPO *(2571, 2573)*. Other Li^+ conducting films produced by glow discharge polymerization were reported in *(2568-9, 2572, 3482-3)*.

Most applications of electrochromism are expected to take place at ambient temperature, and hence the conductivities mentioned above are of interest. In some cases, however, the temperature dependence of the polymer conductivity is essential. Figure 26.2 showed experimental data on the conductivity of PEO-$LiClO_4$ and PPO-$LiClO_4$ *(423, 891, 2922)*. The strong temperature dependence should be noted. For PEO-$LiClO_4$, a change in the slope at ~60°C signals melting of the crystalline polymer. "Amorphous" PPO-$LiClO_4$, on the other hand, displays a smooth variation of conductivity.

This Page Intentionally Left Blank

Chapter 27

ION STORAGE MATERIALS: BRIEF OVERVIEW

Most electrochromic devices include an ion storage material that operates in concert with an electrochromic oxide film and enables ions to be moved repeatedly back and forth in order to evoke a reversible optical modulation. The ion storage is sometimes referred to as the "counter electrode" of the device. The requirements on this material are different depending on whether the device is designed for reflectance modulation or transmittance modulation. The *reflecting device* can include a mirror-like or scattering layer that obscures the ion storage layer, and only its electrochemical properties are of interest. In a *transmitting device*, on the other hand, both the electrochemical and optical properties of the ion storage of are crucial importance. Under all conditions, the ion intercalation/deintercalation should take place via a fully reversible electrochemical reaction.

This chapter gives a brief overview of ion storage materials suitable for reflecting display-type devices (27.1) and for transparent devices (27.2). There are also some comments on the feasibility of combining the layers for ion storage and for transparent electrical conduction (27.3).

27.1 Materials for Reflecting Display-type Devices

The most widely studied ion storage material for display-type devices comprises carbon (graphite) with transition metal oxide particles and, if needed for structural integrity, an organic binder. Ion intercalation into graphite and other disordered carbons has been investigated in several works *(232, 1090, 1347-8, 1466, 3166, 3348, 3712)*. The active area of the carbon can be large enough that the EMF of the ion storage material does not change appreciably during ion intercalation/deintercalation, and the transition metal oxide allows the EMF to be tuned to a suitable level. These properties make it possible to use simple drive circuitry even for multi-segmented electrochromic devices. Figure 27.1, from Ando et al. *(106)*, illustrates how the EMF can be adjusted by having different mixing ratios for two transition metal oxides; by proper selection one can obtain electrochromic devices that bleach during short-circuiting and color rapidly under the application of a constant voltage pulse. Other experiments embracing ion storage layers of carbon, with or without transition metal oxides, have been reported numerous times *(1181-2, 1885, 1972, 1980, 3342, 3698, 3700, 3703, 3741)*. In particular, one could note work by Giglia and Haacke *(1182)* on ion storage layers prepared by standard paper making techniques utilizing acrylic fibers loaded with carbon and MnO_2, and work by Yamanaka *(3700)* on carbon layers incorporating $Fe_2(WO_4)_3$ or $KFeFe(CN)_6$ (i.e., Prussian Blue).

Pure transition metal oxide layers are also useful for ion storage and can be used in several different ways. Devices built around opaque electrolytes or ion conductors can have an

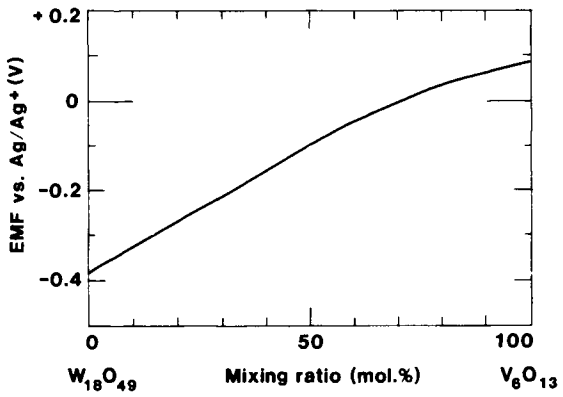

Fig. 27.1 EMF vs. composition for $W_{18}O_{49}$ + V_6O_{13} mixtures. From Ando et al. *(106)*.

electrochromic oxide film analogous to the one for modulating the optical properties. This type of ion storage film--specifically using W oxide--was employed in several investigations *(270, 1314, 1552, 1979, 1994, 2390, 2397)*. One could observe, in particular, a study by Morita *(2391)* on sputter-deposited W oxide films incorporating 5 to 20 vol.% of Cr, Au, Ta, or Pt. The EMF could be rather independent of the degree of Li^+ intercalation; it varied by less than 0.1 V when the Li/W ratio went from 0.1 to 0.4 provided that Au or Ta was present in the film. Other transition metal oxide films studied for ion storage purposes include oxides of Cr, Mo, Ni, V, and Ir *(1979, 1994, 3578)*. Recently, Kuwabara et al. *(1979)* compared several oxides and found that W and Mo oxides were the best, followed by Cr oxide and V dioxide. Supplementary studies have been made of numerous 10 to 20-μm-thick oxide layers prepared by spraying suspensions of particles *(1973)*.

Metallic counter electrodes, whose ability to store ions is doubtful and certainly depends on whether an oxide layer was present or not, have been discussed a few times in connection with electrochromic devices, and results have been given for Al, Ti, Fe, Ni, Cu, Zn, Zr, Pd, Ag, Sn, Pt, Au, and Pb *(1972, 2352, 3154, 3745)*. The threshold voltage for coloration depended on the metal that was used.

27.2 Materials for Transparent Devices

The choice of ion storage material is more critical for transparent devices than for reflecting devices. One possibility for the former is to use a substance, where redox reactions take place, dispersed in a liquid-like electrolyte. Work along these lines has been reported by Kamimori et al. *(1726)*, but the approach has not gained widespread popularity. A possible redox couple is Ferrocene dissolved in a polymer electrolyte *(2471)*. Most studies aimed at transparent electrochromic devices has been focused on *thin solid films* of ion storage materials. Three types of films have been investigated in detail, viz.

(i) electrochromic films that color and bleach in a manner that is complementary to the function of the primary electrochromic film (for example an anodically coloring film operating in concert with a W oxide film),

(ii) electrochromic films with low coloration efficiency, whose influence on the overall optical properties of the device is small, and

(iii) transparent films with optical properties that remain practically unchanged under ion intercalation/deintercalation.

Electrochromic films have been discussed in several previous chapters of this book, and hence there is no need to dwell here on the materials required for option (i). With regard to (ii), it is possible to use crystalline W oxide as an ion storage layer with a luminous coloration efficiency being much smaller than the one for heavily disordered W oxide (cf. Figs. 9.16a and 9.19a). Transparent devices that combine disordered and crystalline W oxide films have been discussed a few times in the literature *(725, 2224-5, 2856)*.

The rest of this section is devoted to option (iii) and covers transparent films of Sn oxide and Ce oxide. Porous Sn oxide films, made by sol-gel-related techniques, can serve as hosts for Li^+

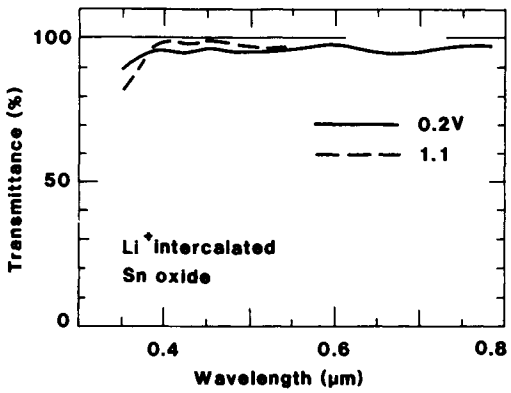

Fig. 27.2 Spectral transmittance of a sol-gel-deposited Sn oxide film in $LiClO_4$ + acetonitrile. Data are shown for two applied voltages. The 100%-line, presumably, corresponds to the transmittance of an ITO-coated glass substrate. After Olivi et al. *(2632)*.

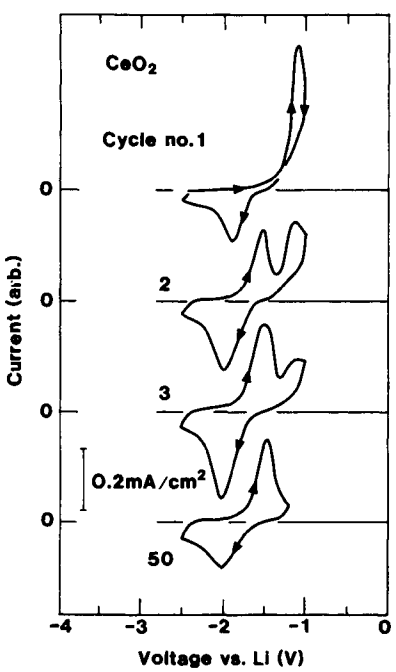

Fig. 27.3 Cyclic voltammograms for Li^+ intercalation/deintercalation in a sputter-deposited Ce oxide film. Data are shown after different numbers of voltammetric cycles. The voltage scan rate was 20 mV/s. Arrows denote scan direction. From Zheng et al. *(3806)*.

intercalation/deintercalation as found recently by Olivi et al. *(2632)*. Figure 27.2 illustrates the transmittance through a ~1-μm-thick layer backed by ITO-coated glass and immersed in 0.1 M $LiClO_4$ + AN. The film remained transparent irrespective of the applied voltage being 0.2 or 1.1 V. Cyclic voltammetry verified that ions were intercalated/deintercalated. Impedance measurements gave $D_{Li+} \approx 6 \times 10^{-9}$ cm²/s. Sol-gel techniques pertinent to Sn oxide have been discussed in *(944, 1351, 1496-7, 2154, 2805)*. Porous Sn oxide can also be made by other techniques--even with those normally suited for preparing dense layers such as ion plating *(3770-1)*. Porous Sn oxide can be employed in gas sensors, as reviewed in *(3582)*.

Cerium dioxide is another interesting transparent material for reversible Li^+ intercalation/deintercalation. Recent work was reported in *(297, 1238, 2143, 3230, 3426, 3500-1, 3806)*. An addition of Ti oxide may be favorable for achieving rapid reaction kinetics *(297, 3230)*. Films of CeO_2 have been prepared by evaporation *(65, 77-8, 110, 172, 1440, 1518, 1615, 2519, 3276)*, sputter-deposition *(1213, 1524, 1715, 2327, 3074-5, 3277, 3565, 3806)*, sol-gel technology *(297, 2969, 3230, 3501)*, and laser ablation *(2997)*. Figure 27.3, from Zheng et at. *(3806)*, shows voltammograms for a sputter-deposited Ce oxide film in 1 M $LiClO_4$ + PC. Film evolution took place during the initial voltage cycling until electrochemically stable conditions were reached.

A characteristic feature of CeO_2 is its extremely rapid onset of optical absorption at a bandgap wavelength of 0.39 μm *(65, 1518, 2969, 3276, 3806)*. This is an important property, since Ce dioxide films can be fully transparent and still provide protection from UV irradiation of whatever is behind the film (for example an organic polymer layer).

Transparent materials capable of Li^+ intercalation/deintercalation are also found among the polymers. Recent work on poly-organo disulfide has demonstrated this property *(952, 3538)*.

27.3 Comments on Ion Storage in Transparent Electrical Conductors

The possibility of combining the layers for ion storage and for transparent electrical conduction has attracted some attention, and films based on In_2O_3 and SnO_2 have been studied in $LiClO_4$ + PC *(724, 767, 1214-5, 1225, 2948, 3233, 3289, 3760-1)*. It seems--although the evidence is hardly conclusive--that the technique for making the film is of great importance for its ability to incorporate ions. Thus cyclic voltammetry and optical measurements indicated Li^+ intercalation/deintercalation and weak electrochromism in some films *(724, 1214-5, 1225, 3760-1)*, whereas no such effects were found in ITO films prepared by *e*-beam evaporation under conditions that led to optimized electrical conductivity *(3289)*. In a recent work, where the efficiency of various ion storage layers was assessed, ITO films were found to be poor *(1979)*. One could note in this connection the somewhat perplexing NRA results by Wagner et al. *(3562)*, who found that the hydrogen content in ITO increased during electrochromic coloration while it decreased in an adjacent W oxide film. These data will be further analyzed below (cf. Fig. 29.11).

Rf sputtered ITO films with a grain size of 30 to 40 nm had diffusion constants for Li^+ between 6×10^{-13} and 5×10^{-17} cm²/s *(1214)*, whereas a similarly prepared In_2O_3 film had a corresponding diffusion constant of ~10^{-11} cm²/s *(3760-1)* at least at small intercalation levels. Some data on oxygen diffusion in ITO were given in *(357)*.

This Page Intentionally Left Blank

Chapter 28

DEVICES WITH LIQUID ELECTROLYTES

Electrochromic devices can be divided into distinct groups according to several different principles. This book considers the nature of the electrolyte or ion conductor in order to obtain a convenient and meaningful categorization. Thus devices incorporating liquid, solid inorganic, and solid organic electrolytes are treated separately in this and the following two chapters. For each of these three classes one can have, at least in principle, devices that are transparent or reflecting. The reflectance can be diffuse white, as required in an element for information display, or specular as required for a variable-reflectance mirror.

This chapter treats display-type devices with proton conducting (28.1) and lithium ion conducting (28.2) electrolytes, as well as transparent devices with dispersed redox agents (28.3) and with charge balanced configurations (28.4). Special emphasis is given the limits on the optical modulation, area-related effects, and durability issues. The final section considers exploratory work on devices for variable thermal emittance (28.5).

28.1 Display-type Devices with Proton Conducting Electrolytes

It is hardly surprising that the first prototype devices using electrochromism-based technology drew extensively on standard electrochemical practise for ion intercalation/deintercalation in aqueous acidic electrolytes. Obviously, such arrangements require reliable sealing. The initial development was strongly geared towards small display devices, such as those used in wrist watches. Excellent viewing properties, with high optical contrast even at large angles of incidence, were distinctive assets that spurred further development.

Aqueous H_2SO_4 electrolytes were natural choices for the initial studies, and device-oriented work was reported as early as in 1975 by Chang et al. *(651)*, Faughnan et al. *(1047)*, and Giglia *(1181)*. The inset of Fig. 28.1 shows a typical design. A glass plate, coated with a transparent electrical conductor and a W oxide film, is separated from a substrate with a layer of a counter electrode by a pigmented electrolyte. A suitable spacer and seal confine the electrolyte. The transparent conductor can be doped In_2O_3 or SnO_2, the electrolyte can contain an alcohol diluent in order to lower the acid reactivity of the H_2SO_4, the pigment can be TiO_2, the counter electrode can be a carbon + binder material that may also incorporate some transition metal oxide, and the substrate can be steel. The composite counter electrode has ion storage capability. The TiO_2 addition may cause photochromism *(3701)*.

Figure 28.1, from Faughnan et al. *(1046-7)*, illustrates the change in the reflectance at λ = 0.633 μm during a color/bleach cycle for a device with an active area of 0.33 cm^2. The reflectance

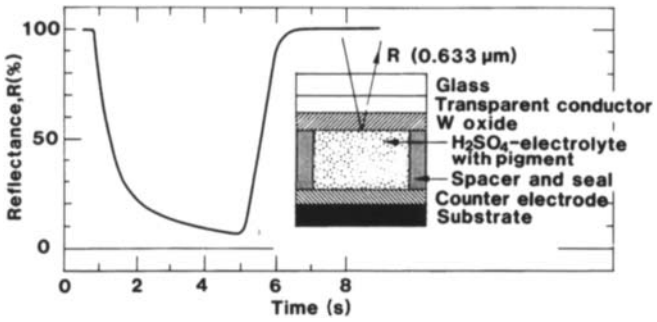

Fig. 28.1 Reflectance R vs. time for an electrochromic device of the type shown in the inset. The reflectance in the bleached state was set to 100 %. After Faughnan et al. *(1046-7)*.

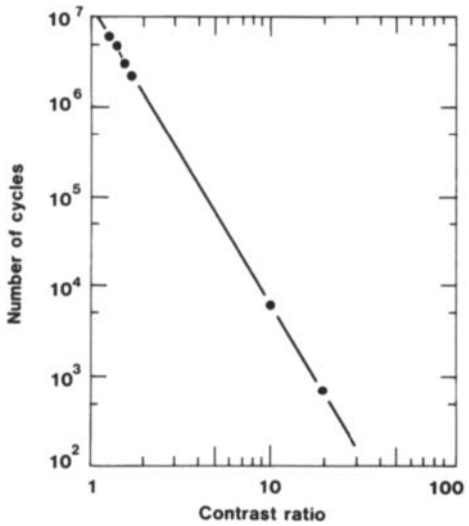

Fig. 28.2 Number of color/bleach cycles vs. contrast ratio for electrochromic devices of the type shown in the inset of Fig. 28.1. Dots indicate experimental data, and the line was drawn for convenience. After Faughnan and Crandall *(1046)*.

decreased to less than 10 % of its initial value during the course of ~2 s and returned to the initial magnitude in ~1 s. The dynamics followed the expressions in Sec. 6.4.

Durability under extended color/bleach cycling was studied in *(1046, 1181)*. This important property depends on the applied voltage and the ensuing change in the optical response. It is convenient to introduce a contrast ratio (CR), defined simply as the reflectance in bleached state divided by the reflectance in colored state, and to measure the number of cycles a device can take as a function of the CR. Figure 28.2 summarizes results for evaporated W oxide films from work by Faughnan and Crandall *(1046)* who studied devices of the type shown in Fig. 28.1. The log-log plot indicates a linear dependence; at CR = 2 the device could be run through ~10^6 cycles, whereas only ~6000 cycles were possible at CR = 10. The durability could be improved if the film deposition was "optimized" *(1046)* but nevertheless long-time operation was problematic for these devices. The degradation mechanisms are discussed in more detail in Secs. 31.7-31.9 below. Device-related work has also been reported for electrochromic La_2O_3-WO_3 films in contact with H_2SO_4 *(3798)* and for symmetric arrangements with two W oxide films of different areas and intervening H_2SO_4 *(1734)*.

28.2 Display-type Devices with Lithium Ion Conducting Electrolytes

Durability problems associated with aqueous acid electrolytes have led to a considerable amount of device-oriented work with $LiClO_4$ + PC as the electrolyte. Display-type devices, with a design essentially like the one in Fig. 28.1, are considered next. Initial work was described by McGee et al. *(2257)*, and detailed studies have since been reported by Ando et al. *(106)*, Matsuhiro et al. *(2222)*, and Yamanaka *(3703)*. Some experiments have been reported also in *(1607, 2386, 3342, 3698, 3700, 3710, 3741)*. In the work by Ando et al. *(106)*, the pigment and counter electrode were integrated in a 0.4-mm-thick layer comprising TiO_2, carbon powder, $W_{18}O_{49}$, V_6O_{13}, and organic binder, and the substrate was ITO-coated glass. The $W_{18}O_{49}/V_6O_{13}$ ratio was chosen to obtain an EMF that allowed bleaching at zero applied voltage, which was an advantage for the intended display applications. The electrochemical properties of this counter electrode were discussed elsewhere (cf. Fig. 27.1). Extended color/bleach cycling was performed by applying a square wave (1.5 V, 1 Hz), leading to a periodic charge insertion/extraction of 6 mC/cm^2. Figure 28.3 shows that this level of the charge insertion had decreased only by ~10 % after ~3 x 10^7 cycles, which proves that the devices have a cycling durability for at least one year. In Yamanaka's work *(3703)*, a porous TiO_2-pigmented PTFE sheet was used as reflector, the counter electrode was carbon powder with added iron tungstate (mainly $Fe_2(WO_4)_3$) and organic binder, and the substrate was ITO-coated glass. Color/bleach cycling was accomplished with a square wave (1.35 V, 1 Hz) yielding a charge insertion/extraction of 5 mC/cm^2. It is apparent from Fig. 28.3 that no decay of the charging capability had occurred after more than 10^7 cycles, which again points at the good durability that can be accomplished. Several details of the device design were critical for achieving a cycling durability on this order of magnitude. A device with electrochromic $K_{0.33}WO_3$, an electrolyte of $LiClO_4$ + PC permeating Al_2O_3 powder, and a graphite counter electrode was mentioned in *(3710)*.

A straight-forward approach to counter electrodes in reflecting devices is to make them identical to the displayed electrochromic films. Excellent reversibility of the optical response may be expected from this "charge balanced" arrangement. Morita et al. *(2390, 2392, 2395-7)* has

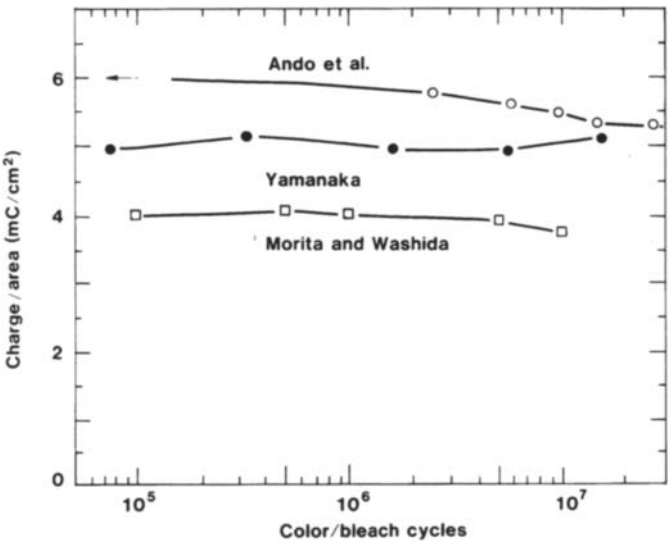

Fig. 28.3 Inserted charge per unit area and cycle during long-term color/bleach cycling of three types of electrochromic display-type devices. Dots indicate measured data, and lines were drawn for convenience. Arrow indicates an initial value of the charge/area. After Ando et al. *(106)*, Morita and Washida *(2396)*, and Yamanaka *(3703)*.

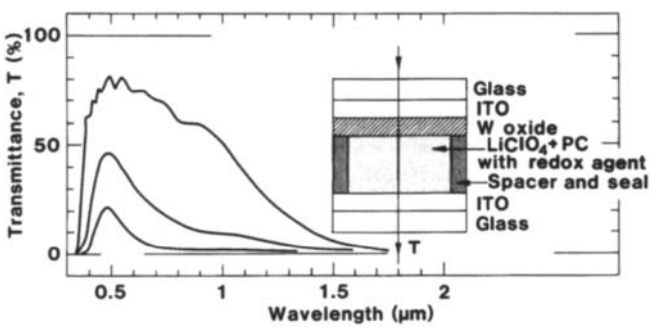

Fig. 28.4 Spectral transmittance T at three states of coloration for an electrochromic device of the type shown in the inset. After Kamimori et al. *(1726)*.

described work on such symmetric designs, specifically including two W oxide films separated by a porous ceramic reflector and a $LiClO_4$ + PC electrolyte. It was not necessary to insert charge into any one of the W oxide films prior to device assembly, but both films could initially remain in their uncolored state. By running the device through a "training period" of ~100 intercalation/deintercalation cycles, it was possible to establish a reversibly moving charge density with ensuing coloration and bleaching. Figure 28.3 indicates the cycling durability of optimized symmetric devices subjected to (2.5 V, 1 Hz), which gave a reversible charge insertion of 4 mC/cm^2 *(2396)*. Degradation, though noticeable, was not severe up to 10^7 color/bleach cycles.

The color/bleach response times can be decreased by evaporating the W oxide film at oblique incidence, which promotes the porosity. Miyoshi and Iwasa *(2352)* studied this effect using, essentially, the design by Yamanaka *(3703)* except that the counter electrode was a gold film. The coloring time went down monotonically, though not very much, when the deposition angle α (cf. Fig. 3.12) increased up to 70°. The bleaching time was influenced to a larger extent; it was ~1 s at $\alpha = 0$ and as small as ~0.3 s at $\alpha \approx 50°$. Beyond this angle, the bleaching time increased again. Detailed data will be given later (cf. Fig. 31.1)

Designs with two spin-coated V pentoxide films and an intervening electrolyte of 1 M $LiClO_4$ + PC with TiO_2 pigment was recently used in multi-color electrochromic devices *(2474, 3146)*.

28.3 Transparent Devices with Dispersed Redox Agents, Including Area-related Effects and Durability Issues

Transparent electrochromic devices are especially of interest for smart windows. The simplest arrangements comprise two glass sheets with transparent electrically conducting layers, a W oxide film, and an intervening electrolyte. Prototype devices of this general kind were described by Steele and Golden *(3233)*. The durability under extended color/bleach cycling was questionable, though.

An alternative design, with proven long-term durability, has been discussed in detail by Kamimori et al. *(1726)* and in other papers from the Asahi Glass Works in Japan *(2358, 2460, 2466, 2468-70)*. The inset of Fig. 28.4 shows the device arrangement; two glass plates have transparent electrically conducting layers on their facing sides, and one of these substrates carries a ~0.6-μm-thick evaporated W oxide film. The electrolyte forms an intervening 50 to 100-μm-thick layer and is based on $LiClO_4$ + PC; it contains dispersed redox agents and has a "semisolid" consistency. The transparent conductors are ITO films with $R_{sq} \approx 10\ \Omega$. Figure 28.4 illustrates the transmittance of the device in fully colored and bleached states and at intermediate coloration. At $\lambda = 0.55$ μm, for example, the transmittance could be varied between ~75 and 13 %. The general decrease of the transmittance at $\lambda \approx 1$ μm is caused by reflectance from the ITO layers (cf. Fig. 25.1).

The transmitting devices are normally much larger than the reflecting display-type devices, and for the former the size itself, and the electrical properties of the transparent electrical conductors, become of critical importance for the response dynamics. Figure 28.5 shows the change of the luminous transmittance during one color/bleach cycle in which a voltage step of ±1 V was applied between the ITO layers. The smallest device with 4 x 4 cm^2 area had a response time of less than 30 s. The largest device with 30 x 40 cm^2 area required several minutes to attain full coloration, whereas bleaching took ~1 minute. Large devices do not change their optical properties uniformly when voltage steps are applied but differences may be noticeable between the central and peripheral

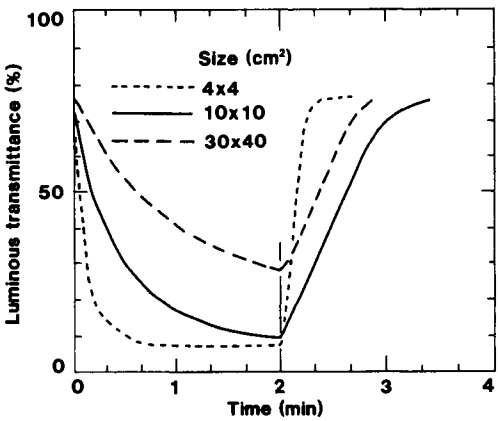

Fig. 28.5 Luminous transmittance vs. time for coloring and bleaching of electrochromic devices of the type shown in the inset of Fig 28.4. The devices have different sizes. From Kamimori et al. *(1726)*.

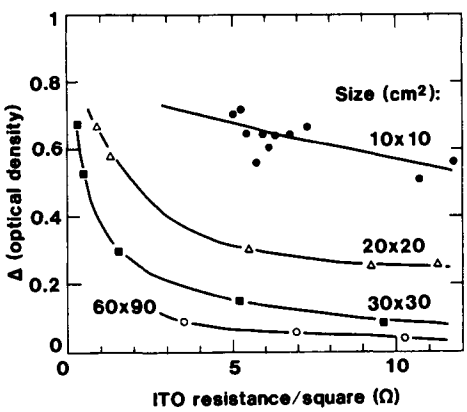

Fig. 28.6 Change of optical density vs. resistance of ITO layers in electrochromic devices of the type shown in the inset of Fig. 28.4. Data are given for four device sizes. Symbols denote measured data, and curves were drawn for convenience. From Kamimori et al. *(1726)*.

zones. Figure 28.6 elaborates the role of the resistance for the transparent electrical conductors and shows the change of the optical density when a voltage of 1 V was applied during 30 s to devices of different areas. The response was strongly influenced by the resistance per square, at least for areas larger than 20 x 20 cm^2, and R_{sq} should preferably be of the order of 1 Ω for devices approaching the m^2-scale. This is just about possible with 1-μm-thick ITO films, as discussed in Sec. 25.1. A further discussion of response dynamics will be given in Sec. 31.4 below.

Durability problems may be harder to overcome for transmitting devices than for reflecting display-type devices, since the former are normally exposed to a harsher environment and have to comply with larger charge insertion per unit area. On the other hand, the requirements on cycling durability in general are less severe for transmitting devices. Figure 28.7 shows the inserted charge/area for a transmitting 10 x 10 cm^2 device subjected to voltage cycling at (1 V, 1/120 Hz) for up to 2 x 10^5 cycles (~1 year). Data are given both for indoor and outdoor exposure. Ultraviolet irradiation caused some coloration in the latter case. The initial charge insertion was about three times larger than for the display-type devices reported on in Fig. 28.3. A significant drop of the charge/area took place beyond 10^4 cycles, particularly for outdoor exposure. However, the coloration efficiency did not show any corresponding drop, and hence one may keep up the optical modulation by current drive rather than voltage drive. Expectedly, the degradation became more pronounced when the inserted charge density was increased. The major cause of the drop of the charge/area indicated in Fig. 28.7 is thought to be an irreversible accumulation of lithium in the W oxide film, which shifts its EMF in the cathodic direction (cf. Sec. 31.2).

Figure 28.8 illustrates durability against heating. An increase of the temperature, which will take place in a practical window installation exposed to solar irradiation, produced a lowered value of the charge/area during the course of a few days, whereas no further changes were apparent for longer time spans. This degradation may be caused by a temperature dependence of the ion exchange reaction at the Bronsted sites, according to the mechanism by Schlotter and Pickelmann *(3058)* discussed in Sec. 7.4. Weathering tests indicated some changes in the charge/area primarily during the first 1000 h.

One should note that the transparent devices can be converted to specularly reflecting ones simply by deposition of a metallic film, such as Al or Cr, onto the rearmost surface. Properties suitable for automotive rear-view mirrors with antidazzling capability could be achieved by inserting/extracting 7 mC/cm^2 *(1726)*.

The device properties depend on the technique for preparing the W oxide films. Schlotter *(3057)* studied films made by flash evaporation as well as by reactive dc sputtering onto ITO-coated glass kept at $\tau_s \approx 150°C$. The films were dense and considerably more durable than conventionally evaporated films when operated in $LiClO_4$ + PC or $LiClO_4$ + H_2O + PC electrolytes. Despite their density, the films were able to show rapid dynamics with a response time of 0.05 s at $\lambda = 0.633$ μm for CR = 2. Another notable result was that a 1.6-μm-thick sputter-deposited film could produce a transmittance that was as low as ~10^{-3} of the initial value after 5 s; the initial transmittance could be restored after another 5 s. Judging from the published data, an even lower transmittance could have been reached if a longer coloration time had been used.

28.4 Transparent Charge-balanced Devices

Transparent electrochromic devices can incorporate a thin film that serves as an ion storage and

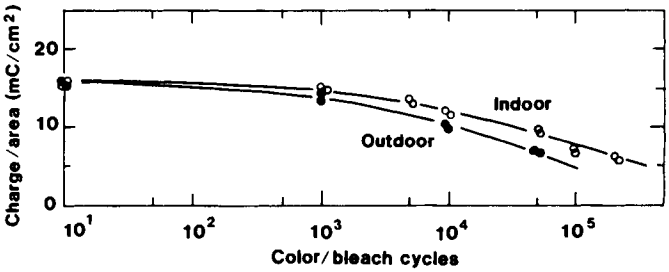

Fig. 28.7 Inserted charge per unit area and cycle during long-term color/ bleach cycling of electrochromic devices of the type shown in the inset of Fig. 28.4. Data are given for indoor and outdoor exposure. Symbols denote measured data, and curves were drawn for convenience. From Kamimori et al. *(1726)*.

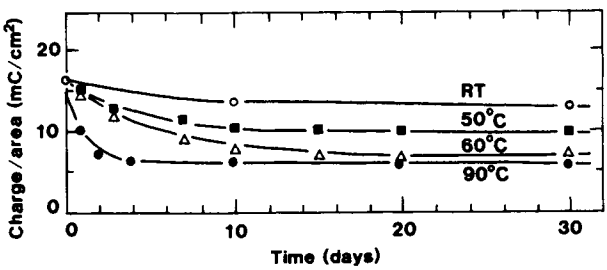

Fig. 28.8 Inserted charge per unit area and cycle during color/bleach cycling of electrochromic devices of the type shown in the inset of Fig. 28.4. Data are given for the device kept at room temperature RT and at three elevated temperatures. Symbols denote measured data, and curves were drawn for convenience. From Kamimori et al. *(1726)*.

where redox reactions take place. One then obtains the prototype design first shown in Fig. 1.1. Charge is moved back and forth to produce the optical modulation, and the operation is termed *"charge balanced"* (or "rocking-chair" type). It is obvious that the ion storage film must be transparent at least when the (primary) electrochromic oxide film is in its bleached state, so the carbon-containing layers used successfully in the earlier discussed display-type devices now are useless.

A simple approach is to use *two* W oxide films with different crystallinities. These films have different coloration efficiencies (cf. Figs. 9.16a and 9.19a), and when charge is shuttled from a heavily disordered film into a crystalline film the combined coloration efficiency is lowered in the luminous wavelength range (but increased in the infrared), and the optical effect is reversed when the charge is moved back into the disordered film. The CE of the device simply is the difference of the CEs of the individual W oxide films. Devices incorporating disordered as well as crystalline W oxide films have been discussed by Matsuhiro and Masuda *(2224-5)* and Rauh et al. *(2856)*. A simulation based on empirical ODs *(2856)* indicated that, for example, 10 mC/cm^2 displacement of charge density could alter the transmittance at $\lambda = 0.55$ μm between 61 and 31 %. At $\lambda > 0.9$ μm, on the other hand, the device was most transparent when the charge was in the disordered film.

A variety on the theme mentioned above was suggested recently by Demiryont *(876)*. She considered a non-stoichiometric W oxide (WO_x) film working in concert with a more stoichiometric (WO_3-like) film. The desired stoichiometries were obtained by judiciously chosen sputtering parameters *(877-8)*. Li^+ insertion, from an unspecified electrolyte, into the WO_x film was found to decrease the overall transmittance to a larger extent than a corresponding Li^+ insertion into the WO_3 film. The optical function was not fully expounded, though. Theoretical assessments indicated that the transmittance could be modulated by ~20 %--for example from ~25 to ~5 %.

The possibility of having devices with a layer that combines ion storage and electrical conduction was explored by Golden and Steele *(1214, 3233)*. Their design incorporated one glass substrate with a rf sputtered ITO film, another glass substrate with an ITO film coated with evaporated W oxide, and an intervening 1 M $LiClO_4$ + PC electrolyte. Strong optical modulation was observed with the transmittance at $\lambda = 0.55$ μm changing between ~70 and ~15 %. No degradation was noted for up to 100 color/bleach cycles.

A principally superior option is to combine a disordered W oxide film with an anodically coloring ion storage layer. Work along these lines, with Prussian Blue as the ion storage (or complementary electrochromic film), has been reported by Kase et al. *(1751-2)*. Some data were also given in *(1527)*. The inset of Fig. 28.9 shows the device design, comprising two glass sheets with SnO_2:Sb transparent conducting layers and either an evaporated W oxide film or an electrodeposited PB film. The coated glasses are in contact with a $LiClO_4$ + PC electrolyte. An auxiliary electrode, based on poly-(4,4',4"-triphenyl amine), was inserted in the electrolyte and was activated when needed to compensate for charge imbalance between W oxide and PB films due to residual impurities in the electrolyte. The main part of Fig. 28.9 illustrates the spectral transmittance in the bleached state and after insertion of a charge density of 15.7 mC/cm^2. Figure 28.10 shows typical changes in the luminous transmittance during a color/bleach cycle for samples of two sizes. The range and rate of the optical modulation were comparable to those of the device reported on in Fig. 28.5, although the optical modulation was somewhat faster for the presently analyzed sample. Thermal durability was reported for 60°C during 1000 h, as well as weatherability for an equal time span. The device depicted in Fig. 28.9 has been applied to curved glass for automotive applications *(1751)*. The color/bleach dynamics is discussed in Sec. 31.4 below.

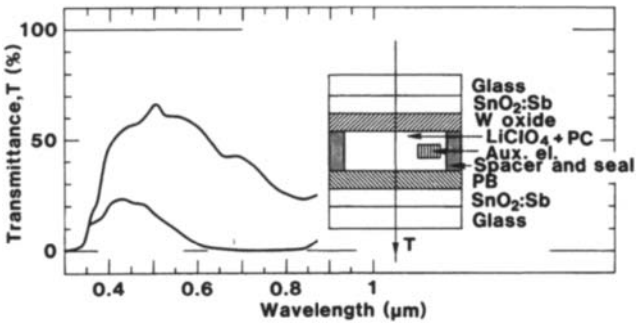

Fig. 28.9 Spectral transmittance T at two states of coloration for an electrochromic device of the type shown in the inset. An auxiliary electrode was placed in the electrolyte for "refreshing" the electrochromic films. After Kase et al. *(1751-2)*.

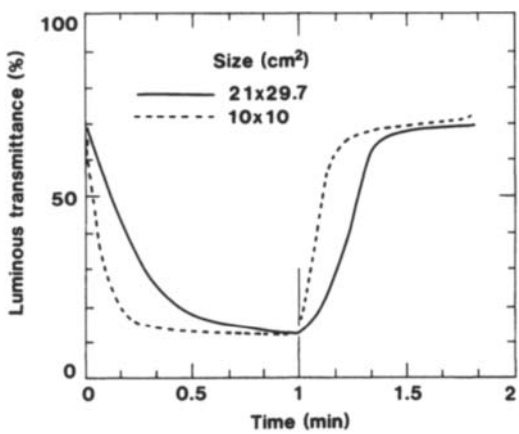

Fig. 28.10 Luminous transmittance vs. time for coloring and bleaching of electrochromic devices of the type shown in the inset of Fig. 28.9. Data are given for devices of different sizes. From Kase et al. *(1752)*.

Yamanaka *(3706)* discussed a variety of the earlier device design. As shown in the inset of Fig. 28.11, there are two glass sheets with ITO layers ($R_{sq} \approx 10\ \Omega$), an evaporated W oxide film with thickness between 0.3 and 0.83 μm, a 0.06-μm-thick electrodeposited Ir oxide film, and an electrolyte of 1 M $LiClO_4$ + PC + 2 % H_2O. The water addition was necessary for having charge insertion into the Ir oxide. Figure 28.11 illustrates the spectral transmittance in the bleached state and after insertion of 17.5 mC/cm^2. The overall coloration efficiency was 22 cm^2/C at $\lambda = 0.4$ μm, 38 cm^2/C at $\lambda = 0.5$ μm, and 65.5 cm^2/C at 0.6 μm; these values may be somewhat higher than for a single W oxide film. Cycling durability was tested under the application of a square wave (1.5 V, 0.05 Hz); the device could withstand ~10^5 cycles, particularly when the W oxide film was thick. Another similar device design, showing good modulation of the luminous transmittance, embodied evaporated films of W oxide and Ni oxide and an intervening liquid electrolyte of PEO + $LiClO_4$ *(2462)*.

Cogan et al. *(731)* investigated a liquid-electrolyte-based device specially designed to demonstrate transmittance modulation in the infrared. It comprised two pieces of glass coated with ITO having $R_{sq} = 180\ \Omega$, a crystalline electrochromic W oxide film, a Nb oxide counter electrode, and a $LiClO_4$ + PC electrolyte. As stressed before, crystalline W oxide has a CE that is peaked well into the infrared, and Nb oxide can have a low CE irrespective of wavelength. The ensuing optical modulation took place primarily in the infrared, and the transmittance at $\lambda = 1.4$ μm could be varied between 25 and 50 % while the transmittance at $\lambda = 0.6$ μm remained at a fixed value above 80 % to within less than 1 %.

Many organic substances show electrochromism and can serve as ion storage layers in devices based on W oxide films *(1612, 3713)*. Such a device was reported by Yoshida et al. *(3736)*; specifically, it incorporated sputter-deposited W oxide, electropolymerized polyaniline, and an electrolyte of $LiClO_4$ + PC. Transmittance changes between ~80 and ~4 % could be obtained with time constants of ~10 s. The cycling durability was ~5 x 10^5 times.

The majority of the device constructions use electrochromic W oxide. An exception was investigated by Chen et al. *(674)*, whose construction embodied a ~0.1-μm-thick Ni oxide film and a doped sodium silicate electrolyte in "semi-solid" form. Figure 28.12 illustrates the design and shows that the transmittance modulation was substantial. The open circuit memory was longer than 24 h, and the durability was reported to exceed 10^5 color/bleach cycles. This durability is remarkably good, particularly if one considers the fact that no counter electrode was used in the shown device arrangement.

28.5 Comment on Devices for Variable Thermal Emittance

In principle, one can use electrochromism for achieving surfaces with variable thermal emittance. Such devices have not been widely discussed in the past. A major reason for this apparent lack of interest is that the forward transparent conductor--either of a metal or of a heavily doped oxide semiconductor--tends to reflect strongly beyond a plasma wavelength that is directly related to the electrical conductivity. The plasma wavelength normally lies on the luminous or near-infrared spectral range (cf. Figs. 25.1 and 25.4).

However, there may be ways to evade the influence of the transparent electrical conductor, and Fig. 28.13 shows a conceptual design in which a crystalline electrochromic W oxide film is placed between an IR transparent substrate and an ion-permeable electrical conductor that does not reflect

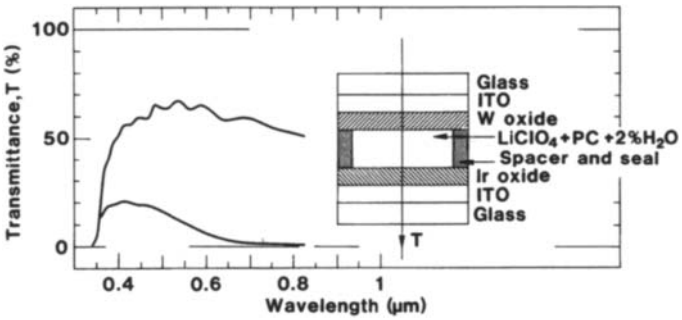

Fig. 28.11 Spectral transmittance T at two states of coloration for an electrochromic device of the type shown in the inset. After Yamanaka *(3706)*.

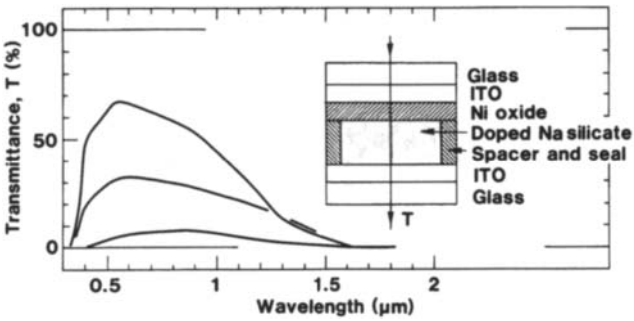

Fig. 28.12 Spectral transmittance T at three states of coloration for an electrochromic device of the type shown in the inset. After Chen et al. *(674)*.

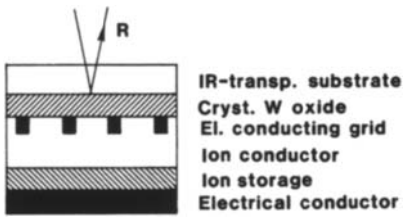

Fig. 28.13 Principle design of a "diffusion-controlled" electrochromic device for emittance modulation via a changed infrared reflectance R.

strongly (for example a metallic grid). The shown device also includes an ion conductor and ion storage, and an electrical conductor on the rear side. The ion conductor and/or ion storage should be of a bulk-like high-emittance material. Various modifications on this design principle are possible. When a voltage is applied between the electrical conductors, ions will diffuse into or out of the crystalline W oxide, whose reflectance is thereby changed. "Diffusion-controlled" electrochromic devices of this general type (albeit with a glass substrate) have been sketched several times in work by Baucke *(282-8, 290, 293)*, but no device results have been reported.

Another design of an emittance-modulating device was proposed by Cogan et al. *(735)*. They considered a high-emittance substrate with, in order, a metal grid, an ion storage film, an ion conductor, a crystalline W oxide film, and an outer metal grid. Measurements demonstrated a capability to vary the hemispherical emittance in the 8-14 μm "atmospheric window" between ~75 and 30%.

This Page Intentionally Left Blank

Chapter 29

DEVICES WITH SOLID INORGANIC ELECTROLYTES AND ION CONDUCTORS

The first part of this chapter covers reflecting devices with *bulk-type* proton (29.1) and sodium ion (29.2) conductors. The remaining sections deal with *thin film* arrangements. With regard to proton conductors, there are separate discussions on devices relying on ambient humidity (Deb devices) (29.3) and devices with charge-balanced operation (29.4). It is not always possible to distinguish between these two modes of operation, though. Devices with thin film alkali ion or silver ion conductors are described in (29.5). The final section discusses a photo-electrochromic multilayer stack (29.6).

29.1 Reflecting Devices with Bulk-type Proton Conductors

This section regards electrochromic devices built around several of the proton conductors discussed in Sec. 26.2, such as phosphotungstic acid (PWA), zirconium phosphate (ZP), hydrogen uranyl phosphate (HUP), and Sb oxides. Rather long term durability was reported for some of these devices.

Mohapatra et al. *(2369)* discussed prototype devices with pressed PWA pellets of unknown porosity separating two W oxide films. Electrochromism was observed, but the PWA underwent reduction accompanied by irreversible coloration during the course of several days. This unwanted coloration was due to the formation of W^{5+} and appeared to be an inherent property of the PWA/W oxide interface.

Similar symmetric devices with ZP as proton conductor were also studied by Mohapatra et al. *(2369)*. Specifically, the investigated material was $ZrO(H_2PO_4)_2 \cdot 7\ H_2O$. The electrochromic W oxide film was dissolved at a rate similar to the one for such films in contact with water, which may have been caused by the existence of some free water in this strongly hydrated ZP. An analogous device design, although with a carbon counter electrode, was tried by Kuwabara et al. *(1976, 1980, 1982)*, who reported durability up to ~10^3 color/bleach cycles with a proton conductor of $Zr(HPO_4)_2 \cdot H_2O$.

Kuwabara et al. *(1976)* extended their studies of solid proton conductors in electrochromic devices to encompass $M'(HPO_4)_2 \cdot H_2O$ with M' = Ti, Sn, Ce and $M''(NaH)(PO_4)_2 \cdot pH_2O$ with M'' = Ti, Zr. It was found that M' = Sn, i.e., the material earlier designated SP, was the best in terms of coloration efficiency, operating voltage, and memory capability. Devices incorporating white SP have been further analyzed in later work by Kuwabara et al. *(1972-4, 1979, 1981)*. The SP layers were made by different techniques. Initially, 1.7-μm-size SP particles were dispersed in

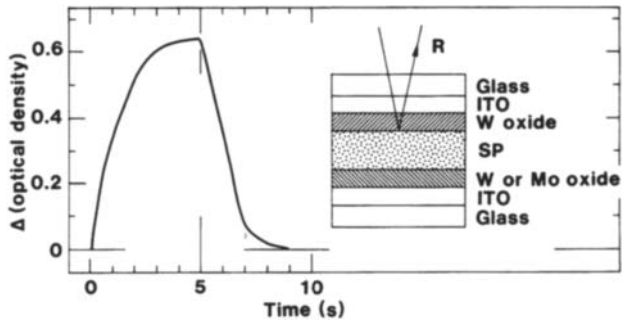

Fig. 29.1 Change in optical density vs. time for an electrochromic device of the type shown in the inset. SP denotes $Sn(HPO_4)_2 \cdot H_2O$. The data are based on measured reflectance R. After Kuwabara et al. *(1979)*.

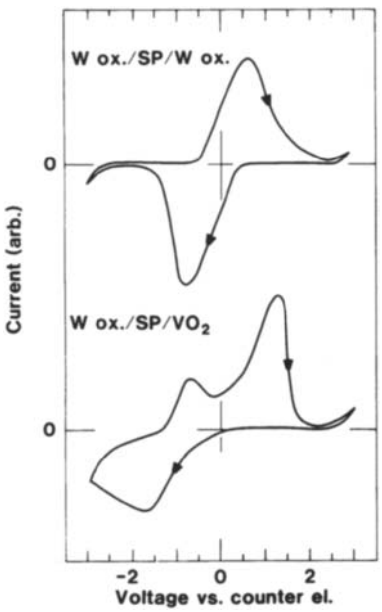

Fig. 29.2 Cyclic voltammograms for H^+ intercalation/deintercalation in a symmetric W oxide/SP/W oxide device and an unsymmetric W oxide/SP/VO_2 device. SP denotes $Sn(HPO_4)_2 \cdot H_2O$. The voltage scan rate was 100 mV/s. Arrows indicate scan direction. From Kuwabara et al. *(1974)*.

acetone and sprayed onto substrates with or without counter electrodes until a thickness of 40 to 60 μm was obtained *(1973)*. An alternative method was developed later, in which electrophoresis was applied to SP particles dispersed in acetone with addition of NH_4OH *(1981)*. By using 300 V for 1 minute, it was possible to prepare ~30-μm-thick layers on glass substrates precoated with ITO and W oxide. Depositions could be made both onto anodes and cathodes, with anodic deposition being preferrable for electrochromic devices. Numerous counter electrodes were investigated in conjunction with the SP layers. Metal plates of Ag, Al, Au, Cu, Fe, Ni, Pt, Sn, Ti, Zn, and Zr, as well as Pt black and graphite, were studied, with Au, graphite, Pt, and Ag being the superior ones for reasons that were not explained *(1972)*. Further studies were made of the oxides CoO, NiO, SnO, Fe_3O_4, Co_3O_4, Ir_2O_3, VO_2, and MnO_2 spray deposited to form 10 to 20-μm-thick layers backed by graphite *(1973)*; among these VO_2, Ir_2O_3, and MnO_2 gave the best electrochromic performance.

Studies by Kuwabara et al. have also been carried out for counter electrodes of vacuum evaporated W oxide, Mo oxide, Cr_2O_3, NiO, VO_2, and V_2O_5 *(1974, 1979)*. The inset of Fig. 29.1 shows a typical device design from this work, with two evaporated W oxide films (or one W and one Mo oxide film) separated by a SP layer made by electrophoresis. The main part of this figure illustrates the change in optical density, obtained by measuring the reflectance of light from an incandescent source, under the application of (±2.5 V, 0.1 Hz). Coloration corresponding to $\Delta(OD) = 0.6$ took 3 s, and bleaching from this state to $\Delta(OD) < 0.1$ took 2 s. The dynamics was slower with counter electrodes of Cr_2O_3 and VO_2, and the device performance was even worse with NiO and V_2O_5. With ITO only, the change in optical density was as small as 0.03.

It is interesting to look at cyclic voltammograms for the latter device designs. They are qualitatively different for symmetric (such as W oxide/SP/W oxide) and unsymmetric (such as W oxide/SP/VO_2) devices. Figure 29.2 illustrates data obtained with a simple two-electrode arrangement for linear voltage sweeps between +3 and -3 V vs. the counter electrode. The voltammogram of the symmetric device appears symmetric and is composed of two half-cycles of the type shown in several figures in Sec. 6.5, whereas the voltammogram of the unsymmetric device is unsymmetric and indicates that several different ion intercalation/deintercalation processes take place. Durability exceeding 10^6 cycles was reported for the symmetric device *(1974)*.

Howe et al. *(1552)* reported data for devices with layers of HUP as solid electrolyte. A typical arrangement comprised two glass plates with ITO layers, each having a ~1-μm-thick evaporated W oxide film. HUP was incorporated by gently pressing a precipitating HUP solution so that a ~100-μm-thick pale yellowish to transparent layer was formed. Such devices were tested with charge insertion/extraction of 5 to 10 mC/cm^2, and optical modulation times down to 0.3 s were noted. The durability could be up to 5 x 10^5 cycles. Some experiments were also conducted with devices whose upper layer was prepared from a slurry of colored W oxide particles (obtained by mixing uncolored WO_3 powder with Zn in an acidic solution). The addition of a small amount of Pd improved the optical response dynamics.

Devices with HUP were also reported by Takahashi et al. *(3331)*. They used flexible 1 to 3-mm-thick tablets of HUP, pressed together with Teflon powder, between an evaporated W oxide film and an Ag counter electrode. Up to 16 mC/cm^2 was inserted, and the durability was seen to be as high as 2 x 10^6 cycles at (~3 V, 1 Hz). Further work on the use of HUP in conjunction with electrochromic W oxide films was discussed briefly in *(239, 2747)*. Ion transfer at the interface between W oxide and HUP was investigated in *(2126)*.

Antimony oxides have been used successfully in some electrochromic prototype devices. Thus

Lagzdons et al. *(1994)* employed $HSbO_3 \cdot 2\ H_2O$ interfaced between two W oxide films, or between one film of W oxide and another film of Ni oxide. Coloration and bleaching were observed, as well as symmetric and unsymmetric cyclic voltammograms. Matsudaira et al. *(2218)* studied display-type devices incorporating a white mixture of $Sb_2O_5 \cdot pH_2O$ and Sb_2O_3. Except for an evaporated W oxide film on ITO-coated glass, the entire unit was manufactured by screen printing. These devices withstood cycling at ±1.3V for more than 10^6 times. Kuwabara et al. *(1971, 1977-8)* prepared devices with an evaporated W oxide film, a proton conductor of $Sb_2O_5 \cdot 2H_2O$, and a graphite counter electrode. The antimony oxide was spray deposited or applied by electrophoresis onto both W oxide and graphite prior to device assembly. A recent work by Vaivars et al. *(3494)* used a layer of of $Sb_2O_5 \cdot pH_2O$ paste as proton conductor in between films of W oxide and Ir oxide. The performance was not discussed in detail, but it appears that the cycling durability was remarkably good with some devices surviving 10^7 color/bleach cycles.

Fehlner et al. *(1055)* carried out work on electrochromic devices based on unsupported 2 to 10-μm-thick slabs of transparent porous lithium fluorhectorite prepared by electrophoretic deposition of suspended mica. One side of this slab had an evaporated W oxide film and an ITO layer; the other side had a rf sputtered Ir oxide film and an ITO layer. The transmittance could be varied between ~50 and ~15%. The mica-based layer is supposed to be a proton conductor with interlayer Li replaced by H; it required equilibration in the presence of humid air.

29.2 Reflecting Devices with Bulk-type Sodium Ion Conductors

Efforts have been made to develop electrochromic devices operating with mobile Na^+ ions, specifically employing β-alumina and NASICON. Green and Kang *(1314, 1316-7)* investigated prototype devices centered on β-alumina. The ion conductor was a 0.7-mm-thick polished plate with more than 99 % density and white appearance, which served as a substrate for thin films deposited onto both sides. The films were based on anhydrous W oxide, prepared by evaporation or sputter-deposition, overcoated with dc or rf sputtered ITO and rf sputtered protective 0.2-μm-thick SiO_2. Insertion of 6 mC/cm^2 gave a dark blue color. Coloring typically took 10 s, and bleaching was slower; operation at 10 Hz required heating to a temperature higher than 70°C.

Barna *(270)* studied devices based on a 2-mm-thick polished white plate of NASICON. One of its surfaces was coated with a W oxide film and a transparent electrical conductor, and the other surface had an ion storage layer made by sputtering from a $Na_{0.3}WO_3$ target, and a metallic conductor. Several problems of such devices were identified; one of them was an interaction between the W oxide film and the transparent conducting top layer; it prevailed irrespective of the latter being Au, In_2O_3, SnO_2, or Cd_2SnO_4 and led to a persistent brown or gray coloration. This problem is not of a universal nature, though, and it did not appear in the principally similar devices studied by Green and Kang *(1314, 1316-7)*.

29.3 Devices with Thin Film Proton Conductors Relying on Incorporated Water (Deb Devices)

Numerous thin films have been used as electrolytes and ion conductors in electrochromic prototype devices. It is convenient to start with thin dielectric films incorporating some water, since they can

be used in devices that are structurally simple. The inset of Fig. 29.3 illustrates a design with a glass substrate coated with four superimposed layers: a transparent electrical conductor such as ITO, electrochromic W oxide, hydrated dielectric material, and a semitransparent top layer of Au. Initial work on such arrangements was reported in 1974-6 by Deb *(837, 844-5)* and others *(1576, 3405)* (see also *840-2*); they have subsequently become known as *"Deb devices"*.

The most critical part of a Deb device is its hydrated layer. It must be porous, in which case water adsorption takes place spontaneously upon exposure to a humid ambience, as is well known from many investigations *(707, 1811, 2153, 2574, 2576, 2814)*. Porosity and columnar microstructures are normally found in vapor deposited films as mentioned in Sec. 3.9, and the capacity of such films to adsorb humidity is often a nuisance for optical design. Here, on the contrary, the water is necessary for achieving electrochromism. The presence of water in MgF_2 and Na_3AlF_6 (cryolite) films was clearly seen in recent IR ATR spectra *(164)*, and water incorporation can be inferred also from NRA depth profiles such as those shown for SiO_2 and Ta_2O_5 in Fig. 3.4 and in *(2852, 3560-3)*. The porosity of these materials is strongly dependent on the thin film deposition technique *(2194, 2196)*. Detailed experimental studies have been reported for Deb devices incorporating porous dielectric films of MgF_2 *(348, 844, 885, 3256, 3285, 3288, 3435, 3743, 3747)*, SiO_x *(494, 844, 1841, 1844, 2117-8, 3460)*, LiF *(167-8, 3256)*, Cr_2O_3 *(1613, 3020, 3024, 3144, 3155-7)*, Ta_2O_5 *(1826)*, and $HSbP_2O_8 \cdot 3H_2O$. Some results are also available for CaF_2, ZrO_2, and Na_3AlF_6 *(844, 1392-3)*.

The top layer has been a 0.01 to 0.02-μm-thick Au film in almost all Deb devices. Hydrogen can permeate this film by undergoing dissociative chemisorption, and a recent analysis of gas sorption phenomena showed *(107)* that an old theory due to Wang *(3572)* was essentially correct. The Au film limits the overall luminous transmittance of the device to less than 50 %, as earlier shown in Fig. 25.4. Small atoms, such as hydrogen, are mobile in Au down to temperatures as low as 18 K *(3209)*.

Figure 29.3 shows spectral transmittance through a Deb device with 0.15 μm of evaporated W oxide, about 0.1 μm of MgF_2 evaporated in the presence of 5×10^{-4} Torr of air, and ~0.015 μm of Au; the data were taken from Svensson and Granqvist *(3285, 3288)*. In fully bleached state, the transmittance had a peak value of ~50 % at $\lambda \approx 0.52$ μm, while T_{sol} was ~25 %. The fully colored state had $T_{sol} \approx 3$ %. These values are in excellent agreement with those found for a similar device in work by Benson et al. *(348)*. Efforts to increase the transmittance by having an ITO top electrode were reported in *(348)*. The coloration of the Deb device is small at low applied voltages, but it increases rapidly when a "critical" voltage of ~1.3 V is exceeded. This effect is related to the decomposition of water into $H^+ + OH^-$ and ensuing proton insertion into the W oxide film. There is a simultaneous electrochemical oxidation at the Au electrode which according to Lusis et al. *(1841, 2117-8)* can be summarized by the reaction

$$Au + 3OH^- \rightarrow Au(OH)_3 + 3e^- \ . \qquad (29.1)$$

This reaction is consistent with extensive work on the electrochemistry of gold surfaces *(1018, 1211-2, 3215-7)*. Oxygen gas is evolved at voltages above 1.8 V, and hydrogen gas is evolved at a reverse bias above 0.9 V. Gas formation can lead to morphological changes as well as to film delamination *(1393, 3743)* and should be avoided in practical devices.

The importance of a large film porosity is evidenced by Fig. 29.4, which shows data by Deneuville et al. *(885)* on the dynamics of coloration and bleaching of a Deb device with 0.3 μm of

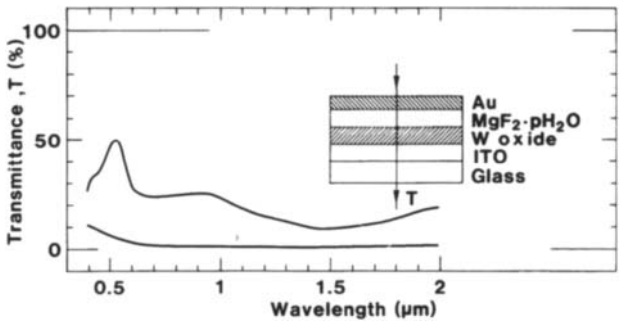

Fig. 29.3 Spectral transmittance T at two states of coloration for a Deb-type electrochromic device of the type shown in the inset. After Svensson and Granqvist *(3285, 3288)*.

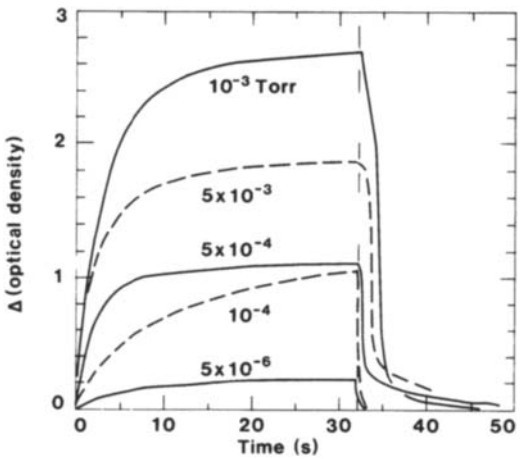

Fig. 29.4 Change in optical density during coloration and bleaching of a Deb device of the type shown in Fig. 29.3. The W oxide and MgF_2 films were evaporated at the shown pressures. The electric field was reversed after 32 s. From Deneuville et al. *(885)*.

W oxide, 0.05 μm of MgF_2, and 0.015 μm of Au. The films of W oxide and MgF_2 were evaporated at the shown pressures of ambient air, and the device was operated at (±3 V, 0.015 Hz). The coloration increased gradually with a time constant of ~10 s and reached a limiting value that was enlarged in proportion to the gas pressure. Bleaching was faster and was completed during the course of a few seconds. Ashrit et al. *(167)* put forward a model for the dynamics, accounting for a continuous exchange of water in the films and in the ambience. The decisive factor for the ultimate coloration was the amount of incorporated water rather than the porosity as such. This point is proved in Fig. 29.5 which shows that the absorption in the fully colored state scales with the H/MgF_2 ratio (obtained from NRA measurements). Exposure of the interface between the W oxide and MgF_2 films to humid air is efficient for creating a large coloration *(3747)*. Deb devices incorporating MgF_2, SiO_x, and LiF have withstood ~10^4 color/bleach cycles *(167, 844, 1841)*. The shelf-life is much longer, though, with durations exceeding 10 years having been mentioned *(840-1)*.

The relative humidity of the ambience plays a large role for Deb devices operated in air, and designs incorporating MgF_2, SiO_x, and LiF become nonfunctional if the water is desorbed, as under vacuum. Such a strong dependence on the ambient conditions is not a necessary limitation for Deb-type devices, though, but designs with Cr_2O_3 are able to maintain their incorporated water at least to a pressure lower than 10^{-6} Torr. This remarkable effect is illustrated in Fig. 29.6, from Inoue et al. *(1613)*. An evaporated 0.2-μm-thick Cr_2O_3 film and a SiO_x film were exposed to humid air, so that their weight increased, and were then subjected to vacuum. For SiO_x the ensuing weight change corresponded to full water desorption, but for Cr_2O_3 a substantial amount of water remained to the lowest pressure. Arrangements with Cr_2O_3 could operate at CR = 2 and 1 Hz for more than 5 x 10^6 color/bleach cycles *(3144)*. In the absence of an applied voltage, the devices showed rapid spontaneous bleaching. However, an open-circuit memory of ~10 minutes and low power dissipation during coloring and bleaching could be accomplished if the Cr_2O_3 was mixed with 50 weight % of V_2O_5, whereas several other oxide additives (MgO, TiO_2, CeO_2, MnO_2, NiO, Al_2O_3, B_2O_3, SiO, GeO_2) were less favorable *(3155)*. Double-layer dielectrics of Cr_2O_3 together with Cr_2O_3-V_2O_5 were studied in *(3156-7)*. Improved device performance could also be obtained with a three-layer dielectric, specifically consisting of SiO_2, Cr_2O_3, and a third layer--in proximity with the W oxide--of either SiO_2, Nb_2O_5, or Cr_2O_3-V_2O_5 *(3020)*.

A reflecting Deb-type device was discussed by Pilipovich et al. *(2768)*. Instead of having a W oxide film, the base was a $Na_{0.8}WO_3$ single crystal onto which a hydrated SiO_x film and a semitransparent Au film had been deposited. By applying voltages and intercalating/deintercalating protons in the $Na_{0.8}WO_3$, it was possible to modulate the reflectance with a time constant of the order of 1 s. Somewhat similar, though less controlled, results were reported elsewhere *(2032)*. The surface region of the bronze is sodium depleted and serves as a semiconducting base into which the protons are intercalated *(2259, 2846)*.

29.4 Charge-balanced Devices with Thin Film Proton Conductors

The reliance of most Deb devices on ambient water is problematic and presumably is the reason why their durability is often limited to ~10^4 color/bleach cycles. Charge balanced devices are technically superior; they incorporate a counter electrode that operates in concert with the electrochromic oxide (usually W oxide) film and allow reversible movements of protons--and,

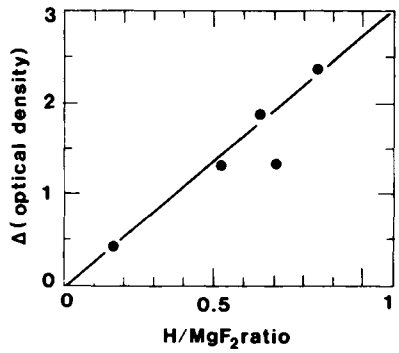

Fig. 29.5 Change in optical density between fully colored and bleached states as a function of H/MgF_2 ratio for Deb devices of the type shown in Fig. 29.3. The MgF_2 layers were evaporated at different pressures and contained different amounts of water. Dots represent data, and the line was drawn for convenience. From Deneuville et al. *(885)*.

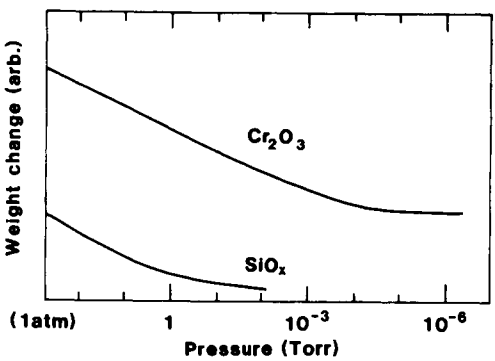

Fig. 29.6 Weight change when hydrated films were evacuated to successively lower pressures. From Inoue et al. *(1613)*.

perhaps, hydroxyl groups--between two thin films. The inset of Fig. 29.7 shows a reflecting device, studied by Watanabe et al. *(3578)*, with an anodically coloring Ir oxide film on ITO-coated glass. This counter electrode was prepared by deposition of ~3 nm Ir oxide by reactive rf sputtering followed by deposition of ~12 nm of Ir metal by nonreactive rf sputtering, and then ac anodizing the tandem layer with a 0.5 Hz square wave in an aqueous H_2SO_4 solution. The initial oxide layer was required for assuring adhesion to the ITO for more than ~200 color/bleach cycles, and ac anodization at a suitable frequency was needed for uniformity of the oxide evolution. The Ir oxide film was then coated with ~0.2 μm of Ta_2O_5 and ~0.3 μm of W oxide; both layers were made by *e*-beam evaporation. Then followed a ~0.25-μm-thick dense ITO layer prepared by ion plating, and finally a ~0.1-μm-thick Au film that served as electrical conductor and optical reflector.

Figure 29.7 illustrates the change in optical density at $\lambda = 0.633$ μm upon application of +1.4/-1.0 V during two separate color/bleach events. The rapid dynamics are noteworthy, with $\Delta(OD) = 0.5$ being reached after as little as ~0.08 s during coloring, and bleaching from $\Delta(OD) = 0.8$ to $\Delta(OD) = 0.04$ taking only ~0.13 s. The reported coloration efficiency--converted to the value corresponding to a transmittance measurement--was reported to be ~180 cm^2/C, which is remarkably high; it was determined for less than 3 mC/cm^2 of charge insertion. Durability tests with a reversible optical change of $\Delta(OD) \approx 0.47$ at 2 Hz showed no degradation up to 10^6 color/ bleach cycles.

Analogous transmitting devices with films of W oxide, hydrated Ta_2O_5, and Ir oxide were reported by Niwa et al. *(2360, 2545, 2971, 3335)*; some results were summarized in *(1827)*. A CE of ~70 cm^2/C was given for transmission at $\lambda = 0.633$ μm, which is consistent with earlier reported CEs for separate films of W oxide and Ir oxide and casts doubt on the CE stated by Watanabe et al. *(3578)*. Niwa's devices were integrated in prototype sunglasses capable of varying the transmittance between 70 and 10 % with a response time of a few seconds and a cycling durability of more than 10^6 times *(2360)*. Some results are available for analogous devices with ZrO_2 or SiO_x replacing the Ta_2O_5 *(1120, 1844)*.

Several charge-balanced devices with moderate to low humidity dependence have been studied, primarily for applications on automotive rear view mirrors. Work by Bange et al. *(253, 258, 2445, 2669-70, 3560, 3562-3)* was mainly concerned with the symmetric and asymmetric designs shown in the insets of Figs. 29.8 and 29.9, respectively. Similar structures, with an ion conducting SiO_x films, were discussed by Kleperis et al. *(1844)*. The symmetric device incorporates two W oxide films made by reactive resistive evaporation, two proton conducting SiO_2-based films, a reflecting Rh film interposed between the SiO_2-based layers, and a metallic back conductor which is also a Rh film. All of the latter films were made by *e*-beam evaporation. The intermediate Rh film is almost completely permeable to protons and plays practically no role for the dynamics of the electrochromic system. It is advantageous to use Rh, rather than for example Pd, as reflector since the former metal does not take up as much hydrogen and hence remains dimensionally stable. The symmetric device showed some dependence on relative humidity; the dynamics were best at a relative humidity of 30 %, and the device became non-functional at zero humidity. Analogous data for devices that differed in that Pt replaced Rh and/or Ta_2O_5 replaced SiO_2 were reported in *(255-6, 2668)*. The asymmetric device in Fig. 29.9 is somewhat simpler and includes one film of each of electrochromic W oxide, proton conducting Ta_2O_5, anodically coloring Ni oxide, and Al back reflector. Again the W oxide was made by resistive evaporation and the other layers by *e*-beam evaporation. A similar electrochromic device was studied in *(1825)*.

The main parts of Figs. 29.8 and 29.9 illustrate spectral reflectance in fully colored and fully

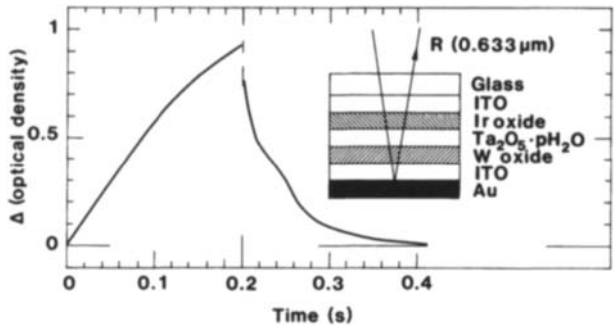

Fig. 29.7 Change in optical density vs. time for an electrochromic device of the type shown in the inset. Coloring and bleaching were recorded in separate experiments. The data are based on measured reflectance R. From Watanabe et al. *(3578)*.

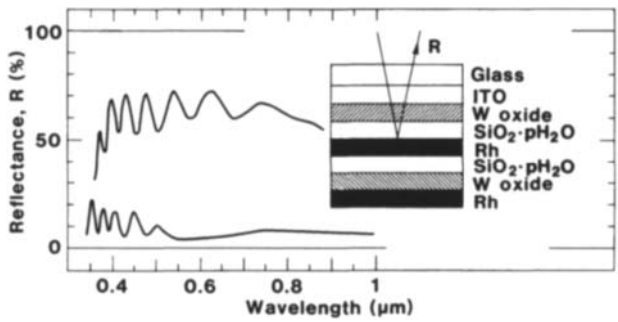

Fig. 29.8 Spectral reflectance R at two states of coloration for a symmetric electrochromic device of the type shown in the inset. After Bange et al. *(258)*.

bleached states for the two device types. The asymmetric design is capable of a maximum reflectance around 80 %, whereas the symmetric design has a limiting reflectance of ~72 %. Coloration efficiencies were evaluated at $\lambda = 0.55$ μm *(256, 2669-70)*; the symmetric device had CE = 38 ± 1 cm^2/C, and the asymmetric device had CE = 86 ± 5 cm^2/C. The latter value indicates that the strong anodic coloration in Ni oxide enhances the optical modulation. For the asymmetric device, the CE was found to be enlarged in thin layers and the maximum value was 105 cm^2/C. Thus it appears that there is some interfacial enhancement of the CE, which might be akin to the effects discussed by Yoshimura et al. *(3747)*.

Figure 29.10 shows cyclic voltammograms for the two device types. The symmetric configuration had a symmetric voltammogram that was consistent with the upper graph in Fig. 29.2. The voltammogram for the asymmetric configuration was more interesting and indicated that no current was drawn between -0.5 and +0.2 V. The reflectance at $\lambda = 0.55$ μm showed "bistable" behavior in this voltage range and was ~75 % for the anodic sweep direction and lower, with a magnitude depending on the Ta_2O_5 thickness, for the cathodic sweep direction *(256)*.

The devices were subjected to detailed NRA analyses, and hydrogen depth profiles were extracted *(258, 2851-2, 3562-3)*. The symmetric device showed large numbers of H atoms in the W oxide and the SiO_2-based layers. The number increased upon prolonged exposure to air and could reach ~1.5 H/W and ~0.8 H/Si. Color/bleach cycling did not produce noticeable differences in the hydrogen densities. Such changes should have been observed if a proton charge of a magnitude comparable to the electronic charge was involved in the electrochromism.

Figure 29.11 shows detailed hydrogen profiles for an asymmetric device at different levels of coloration. At zero applied voltage, corresponding to an uncolored sample, one can observe distinct levels of H in the Ni oxide and W oxide films. At +1.8 V, the sample was dark blue. The H content in the Ni oxide film was now lowered to about half the initial value, and, very surprisingly, the H content was altered around the W oxide/ITO interface so that it decreased in the W oxide and increased in the ITO. The integral amount of H remained almost unchanged. Returning to zero voltage, the initial hydrogen profile was recovered. Applying ~1.5 V, which is a larger voltage than needed to bleach the sample, produced drastic changes in the hydrogen profile. The content increased in the Ni oxide, decreased in the $Ta_2O_5 \cdot pH_2O$, and decreased very sharply in the W oxide. The integral amount of H was strongly diminished, implying a loss to the ambience. Assuming transport of one proton per electron, the H/W ratio ought to have been shifted by ~0.3 during the color/bleach cycle. This was clearly not the case, and one is left in a quandry regarding the interpretation of these data.

Several of the devices mentioned above used Ta_2O_5-based films as elements in multilayer designs. One could observe, in passing, that deposition of Ta_2O_5 directly onto ITO can produce optical absorption *(704)*. This effect is presumably due to interface reactions leading to the reduction of ITO *(2228-9)*; it can be avoided if the Ta_2O_5-based film is deposited under oxygen-rich conditions. Analogous results have been observed for Y_2O_3 films in contact with ITO *(2229, 2700)*.

Rice and Bridenbaugh *(2899)* discussed devices with Au as top layer, an ion conducting fluoride layer, Ir oxide, and SnO_2-coated glass. The fluoride was either evaporated PbF_2 or $PbSnF_4$, and the Ir oxide was prepared by potential cycling of a metal film in 0.5 M H_2SO_4. It was first believed *(2899)* that the device operated by intercalation/deintercalation of F^- in the Ir oxide. However, this appears untenable in the light of subsequent analyses *(2265)*, and it is most likely that the mobile species were protons.

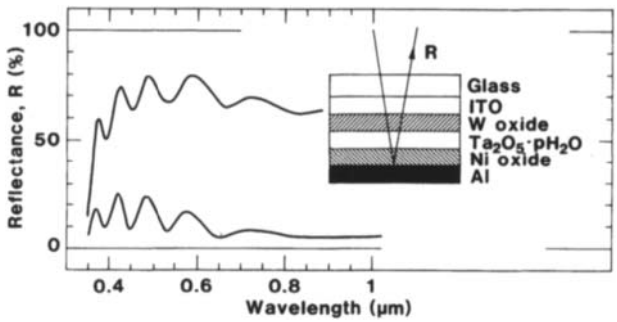

Fig. 29.9 Spectral reflectance R at two states of coloration for an asymmetric electrochromic device of the type shown in the inset. After Bange et al. *(258)*.

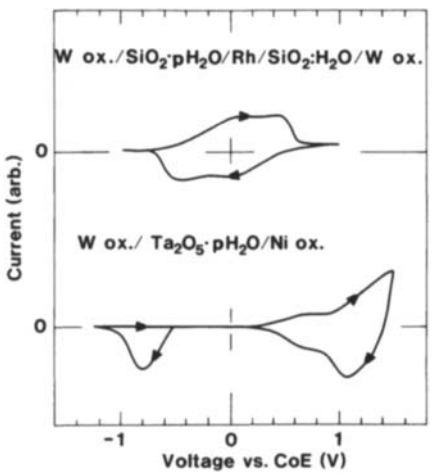

Fig. 29.10 Cyclic voltammograms for H^+ intercalation/deintercalation in a symmetric W oxide/$SiO_2 \cdot pH_2O$/Rh/$SiO_2 \cdot pH_2O$/W oxide device and an asymmetric W oxide/$Ta_2O_5 \cdot pH_2O$/Ni oxide device. The voltage scan rate was 30 mV/s. Arrows denote scan direction. After Bange et al. *(258)*.

29.5 Devices with Thin Film Alkali Ion Conductors and Silver Ion Conductors

Devices with Li^+ conducting films were first investigated by Miyamura et al. *(2345)*, Oi et al. *(2615)*, and Yoshimura et al. *(3746)*. Miyamura et al. *(2345)* evaporated a five-layer stack (0.3 μm W oxide, 0.03 μm LiF, 0.2 μm Li_3N, 0.5 μm LiF, and Ni) onto In_2O_3-coated glass. The device was cycled ~10^5 times at 1 Hz. The LiF layers were needed in order to achieve reversible coloration and bleaching. Oi et al. *(2615)* studied three-layer structures (0.3 μm W oxide, 0.8 μm $LiAlF_4$, and 0.6 μm LiIn) on ITO-coated glass. The $LiAlF_4$ film was made by evaporation of LiF and AlF_3 at a 1:1 molecular ratio. Coloring took 5 to 70 s and bleaching took 15 to 80 s. Yoshimura et al. *(3746)* prepared four-layer stacks (0.5 μm W oxide, 0.1 μm Li-doped MgF_2, Pd, and 0.3 μm MgF_2) on ITO-coated glass. Li doping was accomplished by first evaporating the MgF_2 film and then depositing some Li by heating of Li_3N; it was argued that the Li would diffuse into the MgF_2. The device dynamics were fast, but severe degradation occurred after ~10^2 color/bleach cycles. Some work has also been reported with LiI films *(1729)*.

The above mentioned studies on Li^+ containing thin film devices were of a somewhat preliminary character. However, renewed efforts with Li^+ conducting electrochromic thin film systems were reported recently by Chu et al. *(702)*. The studied configuration had superimposed layers of W oxide, Li_3AlF_6, and an ion storage material including WO_3, Li_2O, and MO (M being Fe, Mn, V, Ce, Sb, or Nb). The transmittance could be modulated between ~80 and ~10%.

Yoshimura et al. *(3745)* also studied prototype devices with ITO-coated glass covered with 0.4 μm W oxide, 0.25 μm Li_2WO_4, a metal (Au, Pd, or Al), and 0.3 μm MgF_2 for protection. The best performance was obtained when the W oxide was evaporated with 0.5 nm/s onto substrates at $\tau_s \approx 160°C$ in good vacuum (10^{-6} Torr). The dynamics were fast and coloring corresponding to $\Delta(OD) = 0.3$ took 0.05 s while bleaching took 0.2 s. No significant difference occurred in the optical modulation when the devices were operated in vacuum (10^{-2} Torr), which strongly indicates that Li^+ are indeed the mobile ions. The devices were run through 10^4 color/bleach cycles. Evaporation of W oxide onto unheated substrates in a poorer vacuum (10^{-4} Torr) led to water incorporation; these samples had inferior open circuit memory and also some absorption in the bleached state.

Goldner et al. *(1216, 1218-9, 1226, 1232)* have reported extensive work on transparent electrochromic devices with Li^+ conducting films. The inset of Fig. 29.12 shows a design with a glass substrate coated with, in order, ITO and crystalline electrochromic W oxide deposited by rf sputtering with $\tau_s \approx 450°C$, $LiNbO_3$ sputtered onto an unheated substrate, evaporated V_2O_5, and In_2O_3 deposited by sputtering with $\tau_s \approx 200°C$. It is not obvious that the $LiNbO_3$ was water free, and hence it may be that proton conduction played some role for the device. Figure 29.12 shows the transmittance modulation under the application of ±3 V; the modulation was achieved by altering the *reflectance*, rather then the absorptance, of the W oxide. It took ~1 minute to change a 1-cm^2-area device between its extrema in transmittance. The relatively slow dynamics was probably related to a modest electrical conductivity of the top In_2O_3 layer, which was deposited at a temperature that was lower than the optimum one. It was found that $LiTaO_3$ could serve as a replacement for lithium niobate. Some data are also available for a device comprising glass, ITO, crystalline W oxide, $LiNbO_3$, In_2O_3, and ITO *(1216)*; the In_2O_3 layer served as a transparent ion storage in this case. The latter device could be cycled more than 3 x 10^3 times at ±3 V. Recently, Goldner et al. *(1218-9, 1226)* found that $LiCoO_2$ films could serve as superior ion storage layers, thus replacing the In_2O_3. NRA analyses applied to such devices were able to prove that lithium was transported back

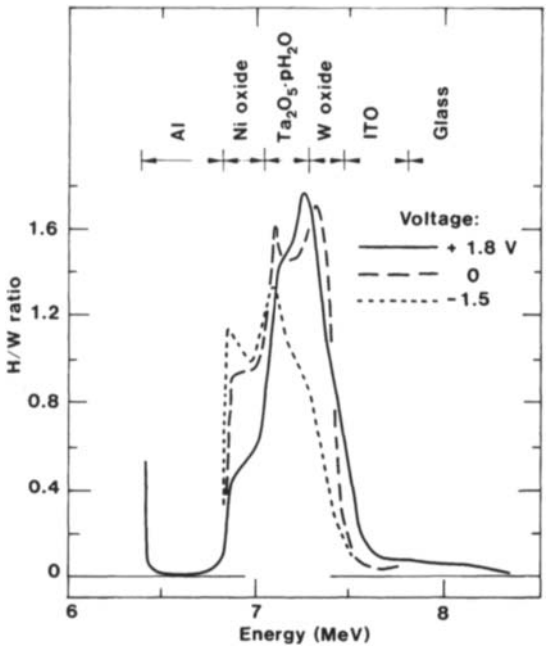

Fig. 29.11 Depth profiles for H/W atom ratio as determined by NRA. Data are shown for the indicated multilayer stack with three voltages applied between the electrodes. After Wagner et al. *(3562)*.

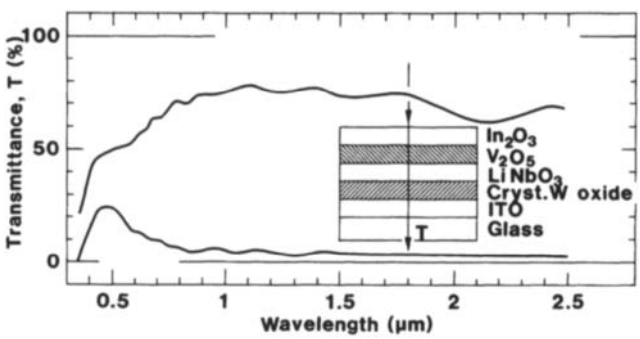

Fig. 29.12 Spectral transmittance T at two states of coloration for an electrochromic device of the type shown in the inset. After Goldner et al. *(1216, 1232)*.

and forth between the W oxide and the $LiCoO_2$ in conjunction with the optical modulation. Another recently reported device embodies an electrochromic W oxide film, a V pentoxide or Nb oxide counter electrode film, and an intervening $LiBO_2$ layer *(162, 166)*.

Devices using mobile Na^+ have not been widely studied, but one may observe a brief report by Kuriyama et al. *(1966)*.

Finally, one could note some work from 1974-5 on thin film devices including Ag^+ conductors. Deb and Witzke *(844)* and Green et al. *(1319-20)* studied multilayers comprising a transparent conductor, $RbAg_4I_5$, and evaporated W oxide. The ion conductor was prepared by evaporation and was believed to be somewhat overstoichiometric in AgI. The device was transparent, with some optical scattering caused by the $RbAg_4I_5$. It was unstable due to moisture attack and electrochemical reactions.

29.6 A Photo-electrochromic Thin Film Device

Hirochi et al. *(1499, 1824)* proposed a structurally simple device showing *"photoelectrochromism"*, i.e., a combination of photochromic and electrochromic properties. The design is illustrated in the inset of Fig. 29.13; it embraces an ITO-coated substrate, two superimposed layers made by rf sputtering from a WO_3-Li_2CO_3 sintered powder target (1:1 molecular ratio), and an opaque outer Au electrode. The substrate remained below 100°C during the depositions. The first W-oxide-containing layer was made by nonreactive sputtering in Ar and was heavily disordered and absorbing; the second layer of this material was made by reactive sputtering in Ar + O_2 and was crystalline (as verified by RHEED) and almost nonabsorbing. During deposition of the second layer, the first one became nonabsorbing while remaining disordered. The optical properties could be modulated when a voltage was applied between the ITO and Au electrodes. It was stated that Li^+ were the mobile ions, but the role of incorporated water probably cannot be disregarded. One could note the principle similarity between the present device design and that of Matsuhiro and Masuda *(2224-5)* and Rauh et al. *(2856)* who studied disordered W oxide films operating in concert with crystalline W oxide ion storage layers. In the present case, the lack of a well-defined purely ion conducting layer may preclude long-term open circuit memory.

In the absence of UV irradiation, devices of the kind shown in Fig. 29.13 required voltages of the order of 10 V to produce sizeable changes in the OD during reasonable times. Such voltages are prone to give degradation. Nevertheless the devices are of considerable interest since they can produce voltage-controlled photochromism. At zero voltage, almost no coloration was obtained by UV irradiation from a Hg lamp. However, photochromism was observed when 2 V was applied, and the OD varied with time and irradiation intensity. Figure 29.13 shows that Δ(OD), determined from reflected light at $\lambda = 0.633$ μm, could be ~0.4 after 3 s. Bleaching in the absence of UV light took a few seconds.

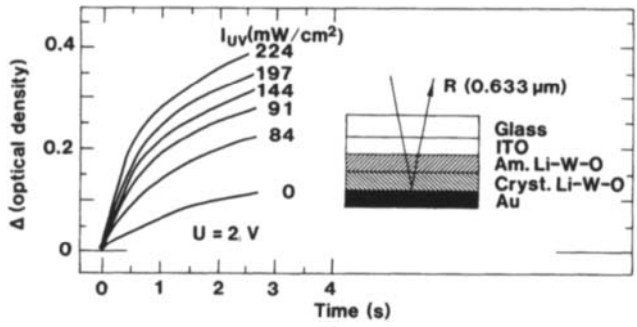

Fig. 29.13 Change in optical density vs. time for a device of the type shown in the inset. The curves refer to the shown UV irradiation intensities I_{UV} and were recorded with a voltage U between the ITO and Au electrodes. The data are based on measured reflectance R. After Hirochi et al. *(1499)*.

Chapter 30

DEVICES WITH POLYMER ELECTROLYTES

The rapid advances in polymer electrolytes during recent years are paralleled by an upsurge of interest in electrochromic devices including such materials. This chapter covers constructions in which the mobile species are protons (30.1), lithium ions (30.2), and sodium or potassium ions (30.3).

30.1 Proton Conducting Polymers

Work on electrochromic devices with polymer electrolytes was pioneered in 1981-2 by Giglia and Haacke *(1182-3)*, Randin *(2843-5)*, and Shizukuishi et al. *(3154)*. The studies were focused on poly-sulfonic acids, and it was found that poly-AMPS were superior to poly-SSA, poly-ESA, and Nafion. Detailed information was given for a display-type device with poly-AMPS *(1182-3)*. The basis was SnO_2-coated glass upon which a film of W oxide was deposited by evaporation. The electrolyte comprised a 1 to 10-μm-thick layer of poly-(HEM, AMPS) and a ~0.5-mm-thick layer of poly-AMPS/TiO_2 pigment/PEO mixed to 8:1:1 by weight. The poly-(HEM, AMPS) was included to separate the W oxide from the poly-AMPS; this was necessary for obtaining long-term durability. An admixture of PEO improved the dimensional stability of the polymer. The counter electrode was prepared by following standard paper making techniques utilizing acrylic fibers loaded with carbon powder and a MnO_2 additive. The latter component raised the EMF to a sufficient level that bleaching of the device could be accomplished by short-circuiting. A protective metal encasement completed the design. An assembly sequence suitable for industrial manufacturing was given. Displays of this kind had a color/bleach switching time of 0.9 s, could be cycled more than 10^7 times, showed open circuit memory for up to 2 days, and had a shelf life exceeding 3 years. It appears that a device of practical interest was ready. However, it was never marketed.

Another polymer-based design suitable for information display was studied by Dautremont-Smith et al. *(816, 818-9)*. It embodied opacified Nafion in a symmetric configuration between anodic or sputter-deposited Ir oxide films backed by SnO_2-coated glass. The Nafion was boiled first in an aqueous solution of a barium salt ($Ba(NO_3)_2$, $BaBr_2$, or $Ba(ClO_4)_2$) and subsequently in H_2SO_4 so that a white precipitate of $BaSO_4$ was occluded in the polymer. The devices had a color/bleach switching time of the order of a second and an open circuit memory of a few days. The moderately low coloration efficiency of the Ir oxide, as well as the cost, limit the practical usefulness of these devices. Their excellent durability is an advantage, though.

Several groups have studied transparent electrochromic devices built around poly-AMPS.

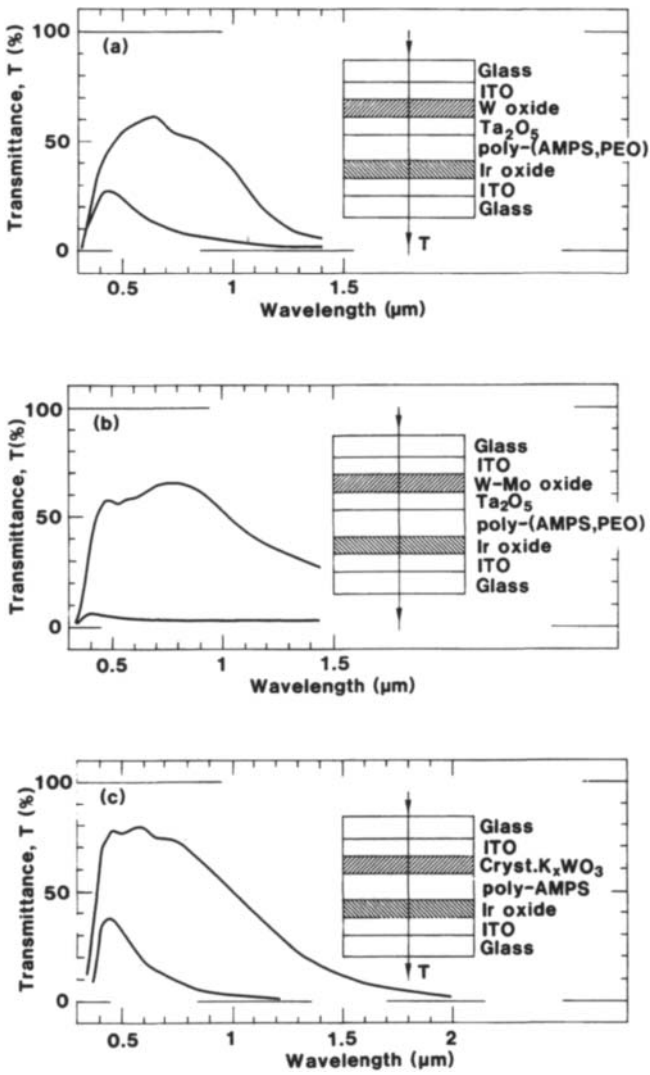

Fig. 30.1 Spectral transmittance T at two states of coloration for electrochromic devices of the three types shown in the insets. After Cogan and Rauh *(732)*.

Work by Cogan et al. is considered first *(728-9, 732, 2854-5)*. The insets of Fig. 30.1 illustrate three related designs that have been investigated. They incorporate films of disordered W oxide, disordered W-Mo oxide, or hexagonal crystalline K_xWO_3, together with Ir oxide films serving as ion storage and for augmenting the coloration efficiency, and Ta_2O_5 films for protecting the W oxide from degradation and for providing extended open-circuit memory. All films were made by reactive rf sputtering. The electrolyte was with or without 8 weight % PEO. Prior to lamination, the W-oxide-based films were protonated in a H_2SO_4 electrolyte to a value compatible with the maximum safe charge insertion into the Ir oxide film. The three devices all showed rather high transmittance in the bleached state and low transmittance in the colored state. Regarding designs with disordered W oxide or disordered W-Mo oxide, Figs. 30.1 (a) and (b) show that the transmittance could be ~60 % in the luminous and near-infrared spectral range. The design with crystalline K_xWO_3, on the other hand, had a transmittance up to ~80 %, as apparent from Fig. 30.1 (c). The device with W-Mo oxide was capable of yielding an exceptionally low transmittance in the colored state. The device in Fig. 30.1 (a) has been cycled successfully for 2 x 10^5 times under the application of -1.2 and +0.2 V for 35 s each. Devices with poly-SSA or BPEI-H_3PO_4 between films of W oxide and Ir oxide were analyzed by Katsube et al. *(1757-9)* and Lassègues and Rodriguez *(2016)*, respectively.

Metal grid electrodes can provide the low resistance needed for optical modulation with acceptable dynamics even in large-area devices. This approach was taken by Ho et al. *(1506-8)*, whose design is illustrated in the inset of Fig. 30.2. The grid electrode was made of Ni or Cu; the open areas were ~0.76 mm across and covered ~20 % of the glass. The electrolyte was poly-AMPS containing some water and *N,N*-dimethyl formamide. The device was completed by a glass plate covered with SnO_2:F and evaporated W oxide. Figure 30.2 shows the change of transmittance at $\lambda = 0.55$ μm during galvanostatic cycling with ±0.15 mA/cm^2; the voltage did not exceed 1 V. The transmittance could change between ~68 % and a value lower than 20 %. Durability was observed for up to 10^4 cycles.

Numerous organic substances show electrochromism and may be used as counter electrodes in devices with W oxide films *(1612, 3713)*. The inset of Fig. 30.3 shows a design by Dao and Nguyen *(812-3, 2523)*; it includes an electrolyte of poly-AMPS and a counter electrode of poly-(*N*-benzyl aniline) (denoted poly-BAn). The W oxide film was made by electrodeposition from a peroxotungstic solution onto SnO_2-coated glass according to a procedure in *(810, 3704)*, and the anodically coloring poly-BAn layer was prepared on SnO_2-coated glass as described in *(684, 809, 811)*. The main part of Fig. 30.3 illustrates the range of optical modulation, from a yellow "transparent" state to a deep blue colored state. Devices of this type were durable for more than 10^5 color/bleach cycles.

Principally similar devices were studied in work by Akhtar and Weakliem *(48)* and Jelle et al. *(1666, 1666a, 1668-9)* who worked with constructions embodying evaporated W oxide, poly-(BPEI, AMPS) electrolyte, and polyaniline counter electrode. These devices could switch between a fairly transparent and a colored state. Figure 30.4 illustrates the achievable range of optical properties *(1666)*; the modulation extended out to a wavelength of at least 3 μm *(1669)*. A related device, though also involving a layer of Prussian Blue, was described in *(1667)*.

Work has also been reported for proton conducting polymers other than poly-AMPS and derivatives thereof *(47, 141, 423-4, 1755, 2723)*. Pedone et al. *(2723)* studied electrochromism in devices with PEO-H_3PO_4, and Armand et al. *(141)* and Bohnke and Bohnke *(423-4)* investigated devices with PVP-H_3PO_4. The inset of Fig. 30.5 illustrates a specific design *(423-4)*.

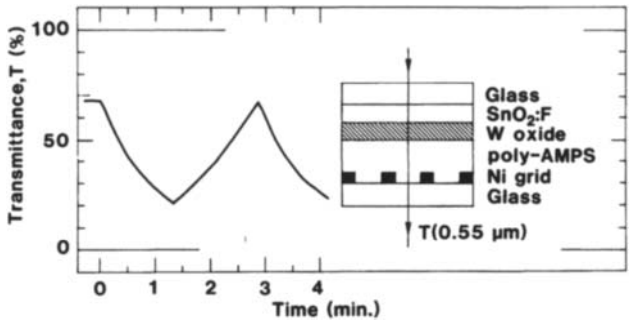

Fig. 30.2 Change in transmittance T vs. time during galvanostatic cycling of an electrochromic device of the type shown in the inset. After Ho et al. *(1507-8)*.

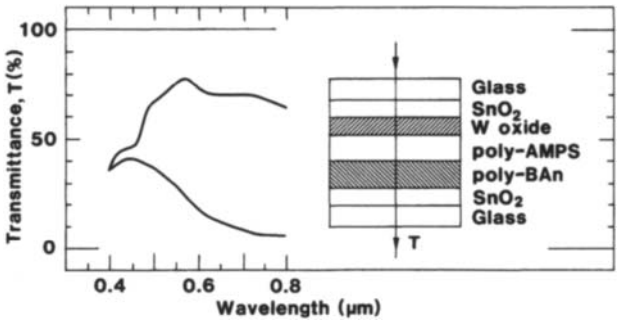

Fig. 30.3 Spectral transmittance T at two states of coloration for an inorganic-organic hybrid electrochromic device of the type shown in the inset. After Dao and Nguyen *(812, 2523)*.

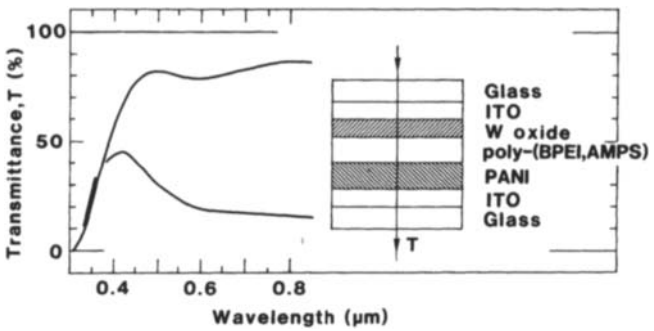

Fig. 30.4 Spectral transmittance T at two states of coloration for an inorganic-organic hybrid electrochromic device of the type shown in the inset. PANI denotes poly-aniline. From Jelle et al. *(1666)*.

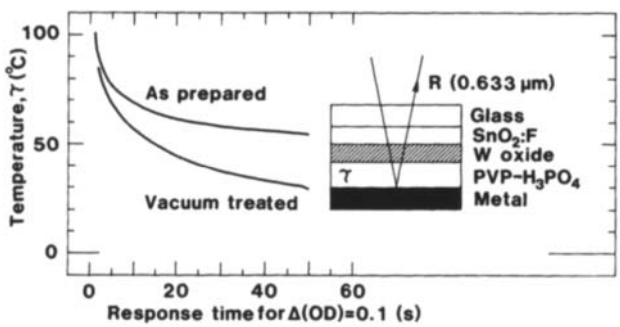

Fig. 30.5 Response time corresponding to $\Delta(OD) = 0.1$ vs. temperature τ for a thermo-electrochromic device of the type shown in the inset. Data are based on reflectance R and are given for the polymer electrolyte in as-prepared and vacuum treated state. After Armand et al. *(141)*.

Application of a voltage makes the optical properties change at a rate that is strongly dependent on the temperature, and hence the device shows "*thermo-electrochromism*". The basis for this property lies in the temperature dependent conductivity of the polymer, illustrated in Fig. 26.2. Figure 30.5 shows the response time corresponding to $\Delta(OD) = 0.1$ as a function of temperature when a constant voltage was maintained *(141)*. The as-prepared electrolyte yielded a very strong variation of the response time in the $60 < \tau < 70°C$ range. Vacuum treatment of the polymer at $\tau < 60°C$ decreased its water content, which led to a decrease of the response time at low temperatures. Devices of the type discussed here can be thermally addressed, for example through localized heating by a laser beam. They can show open circuit memory for months.

Akhtar et al. *(47)* reported data for devices with PEI-H_2SO_4 and PEI-H_3PO_4 electrolytes. Optical switching between transparent and blue states could be accomplished by applying ±3 V. The time constant was less than 1 s and the cycling durability larger than 6×10^4 times.

Electrochromic Ni oxide films were used by Pennisi and Lampert *(2727)* in a device incorporating polymeric quaternary ammonium hydroxide. The Ni oxide was made by electrodeposition according to the sulphate route, and the electrolyte was prepared by ion exchange from a polymeric quaternary ammonium chloride. Electrochromism was observed. The durability of these devices was hampered by a gradual dissolution of the film and by outgassing from the electrolyte.

30.2 Lithium Ion Conducting Polymers

Among the lithium ion conductors, most work has been reported for $(PEO)_8$-$LiClO_4$. It has eight heteroatoms per lithium ion and is characterized by high ion conductivity and high value of E_a (cf. Fig. 26.2 and Eq. 26.2). The fabrication of this polymer electrolyte was described in *(442)*. Scrosati et al. *(2702, 3079-81)* and Bohnke et al. *(423-5)* studied thermo-electrochromism in devices of the type illustrated in Figs. 30.5 and 30.6 and found that the electrochemical and optical properties were strongly temperature dependent. Figure 30.6, from Bohnke and Bohnke *(423-4)*, shows the change in OD upon the application of 3.0 or 3.5 V during 0.5 s. The optical density was very small at $\tau < 50°C$, which is consistent with the low ion conductivity of the polymer. At $\tau \approx 50°C$ there was an abrupt increase of $\Delta(OD)$, signalling the conductivity increase at melting, and at above 50°C there was a monotonic increase of $\Delta(OD)$ particularly at 3.5 V. At $\tau \approx 80°C$, the response time for coloring by $\Delta(OD) = 0.3$ was ~0.25 s, and the corresponding response time for bleaching was ~0.17 s. A more developed device design, incorporating an ion storage layer of lithiated Ni oxide, was discussed by Passerini et al. *(2716-7)*. Results have also been reported for some transparent devices with ion storage layers of Mn oxide *(675)*, poly-BAn *(812)*, and polyaniline *(2283)*. These latter devices were capable of operating at room temperature. The construction with polyaniline was prepared on flexible polymer substrates.

The low Li^+ conductivity of PEO-$LiClO_4$ at room temperature limits its applicability in several electrochromic devices. However, there are superior options with higher ion conductivities, such as PEO-$LiSO_3CF_3$ and PEO-$LiN(SO_2CF_3)_2$ *(142)*. The former material was used by Visco et al. *(3538)*, who explored the electrochromism in devices with W-Mo oxide films and transparent poly-organodisulfide counter electrodes. A similar polymeric material, although with an addition also of a metal silicate, was reported on by Ma et al. *(2127)*, who employed Co-containing Ni oxide as one member in a charge-balanced electrochromic device and either mixed Mn-Ni oxide or

Nb oxide as the other member.

PEO-$LiN(SO_2CF_3)_2$ was used by Baudry et al. *(295-6)*, who studied transparent devices of the kind shown in the inset of Fig. 30.7. The ion storage layer is an evaporated film of V pentoxide. Figure 30.7 shows the transmittance at $\lambda = 0.63$ μm during cycling with ±1.7 V at room temperature. Coloration to a transmittance of 13 % took place during ~10 s, whereas bleaching to a transmittance of 41 % required ~2 s. The cycling durability was more than 10^4 times. It was possible to improve the properties somewhat by replacing the pentoxide with sol-gel-prepared CeO_2-TiO_2 or CeO_2-ZrO_2 films *(2142, 3426, 3500-1)*. Electrolytes of PEO-$LiN(SO_2CF_3)_2$ were also used in investigations of devices with electropolymerized electrochromic layers and counter electrodes of CeO_2-TiO_2 *(1238, 2143)*.

Andersson et al. *(96-9)* have made detailed studies of electrochromic devices with films of W oxide and V pentoxide, and an intervening layer of a PPG-PMMA-$LiClO_4$ electrolyte. This electrolyte served as an excellent lamination material. Figure 30.8 illustrates the device construction as well as the spectral transmittance in fully bleached and colored states when the W oxide film is 0.76 μm, the PPG-PMMA-$LiClO_4$ layer is 12.5 μm, and the V pentoxide film is 0.2 μm. At $\lambda =$ 0.633 μm, for example, the transmittance could be modulated between ~20 and ~72 %, which is a much larger range than for the device in Fig. 30.7. When the W oxide film was ~0.2 μm thick and the V pentoxide film was ~0.1 μm thick, the corresponding modulation range lay between ~39 and ~90 %. Some results have also been reported with lithiated Ni oxide films as counter electrode *(590, 2715, 2717)*.

A variety of the above device was discussed recently by Cogan et al. *(733)*. As shown in the inset of Fig. 30.9, they used a polymer electrolyte of poly-vinyl pyrrolidone plasticized with γ-butyrolactone and poly-ethylene glycol and doped with lithium triflate (denoted PVP-γBL-PEG-$LiCF_3SO_3$); this polymer joins a W oxide film and a Cr-containing V pentoxide counter electrode with a composition $Cr_{0.5}V_{1.5}O_{5.3}$. The optical modulation upon ±2V, corresponding to a reversible charge insertion of 23 mC/cm^2, was similar to that of the device in Fig. 30.8.

Several other Li^+ conducting polymers have been tried for electrochromic device applications. Stevens et al. *(3244)* studied poly-(ethylene glycol, siloxane) containing $LiSO_3CF_3$ between one glass with ITO and a W oxide film and another glass with only ITO. Spectral data were reported; at $\lambda = 0.633$ μm the transmittance could be modulated between ~21 and 76 %. Electrolytes of PEI-$LiClO_4$ and PEI-$LiSO_3CF_3$ were used in *(47, 812-3)*. Devices with PEO-PAA-$LiSO_3CF_3$ (including PEOs with two different molecular weights) or PMEO-LiSCN between layers of W oxide and PB were described by Kobayashi et al. *(1852-5, 2537)* and Oyama et al. *(2677)*. Similar devices, with a Li^+-doped oxymethylene poly-oxyethylene electrolyte, were described by Habib and Maheswari *(1374, 1376)*, and Li^+ conducting copolymers based on methacrylates were exploited by Ohno and Yamazaki *(2579-80)*. Thermo-electrochromism was observed in a device with PPO-$LiClO_4$ but otherwise analogous with the one in Fig. 30.6 *(423)*. In this latter work, Δ(OD) was measured under the application of a voltage pulse, and Δ(OD) was seen to increase monotonically with increasing temperature. The variation was smooth, which is consistent with the temperature dependence of the polymer conductivity in Fig. 26.2.

Devices with gel-type electrolytes were studied in *(1527, 1703)*. Judeinstein et al. *(1703)* produced organically modified TiO_2 gels that were proton conducting in as-deposited state and whose conductivity could be enhanced by dissolving $LiClO_4$. They were integrated in devices with W oxide films prepared by sol-gel technology *(668-9)*. Symmetric devices could be cycled more than 4 x 10^4 times under the application of ±2.5 V; the response time was 50 s and the open circuit

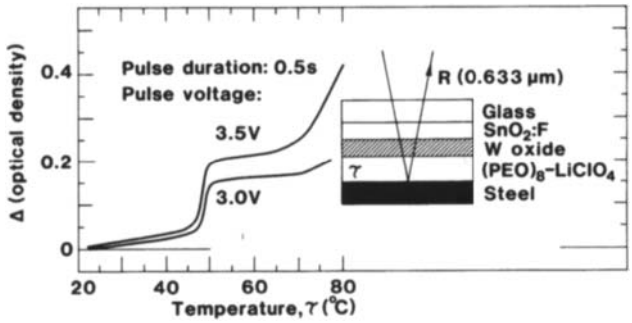

Fig. 30.6 Change in optical density vs. temperature τ when 0.5 s pulses, with the shown voltages, were applied to a device of the type shown in the inset. The optical data are based on measured reflectance R. After Bohnke and Bohnke *(423)*.

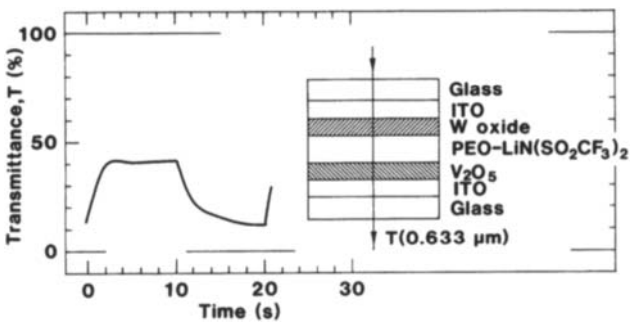

Fig. 30.7 Change in transmittance T vs. time during potentiostatic cycling of a device of the type shown in the inset. After Baudry et al. *(295-6)*.

memory longer than half a year. Honda et al. *(1527)* prepared PEOS-$LiClO_4$ swollen in PC and used these electrolytes in devices with films of W oxide and PB. The time constants for coloration and bleaching were ~5 s.

30.3 Sodium and Potassium Conducting Polymers

Devices with Na^+ conducting electrolytes have not attracted much attention, but one could note a design with PMEO-NaSCN between films of W oxide and PB *(1852-5, 2537)*. A similar device, with a copolymer of PMEO and a methacrylic sodium salt, was reported in *(2580)*.

K^+ conducting polymers have been considered for operation in conjunction with films of W oxide and PB. The first work was by Tada et al. *(3314)*, whose device design is shown in the inset of Fig. 30.10. It embodies two ITO coated glass plates; one of them has a 0.93-μm-thick W-oxide-based film prepared by decomposition of an oxalatotungstate compound, and the other plate has a 0.23-μm-thick electrodeposited PB film. The intervening electrolyte was of poly-(ethylene oxide, urethane) containing KCF_3SO_3; it was solidified by heating to 60°C. The thickness ratio of the PB to W oxide film was 0.25 for optimum performance. Optical changes during the application of 1.5 V for 10 s to 3 x 3 cm^2 devices scaled with the polymer conductivity, which shows that the dynamics is governed by K^+ transport in the electrolyte. Figure 30.10 illustrates spectral transmittance for the bleached state and for two amounts of charge transport. Going from $\Delta Q = 0$ to $\Delta Q \approx 7$ mC/cm^2 gives a large variation in the transmittance, corresponding to T_{sol} changing from 56 to 14 %. The coloration efficiency was 143 cm^2C^{-1} at $\lambda = 0.633$ μm, which is consistent with both the W-oxide-based film and the PB film contributing to the coloration. The open circuit memory was better than 2 weeks.

Kobayashi et al. *(1852-5, 2537)* and Ohno and Yamazaki *(2580)* studied a device design similar to the one in Fig. 30.10, although with vapor deposited W oxide and an electrolyte of PMEO-KSCN or PMEO-MAA-K^+. They observed that the optical modulation corresponded to $\Delta(OD) \approx 1$ at $\lambda = 0.8$ μm. The time constants for coloration and bleaching were ~10 s. Somewhat less favorable properties were observed with electrolytes containing LiSCN and NaSCN. It appeared that K^+ could intercalate PB, and hence provide coloration, whereas this was probably not the case for Li^+ and Na^+. Device data with a K^+ conducting electrolyte were also given by Béraud and Deroo *(354)*.

Habib et al. *(1377)* investigated a device that again can be represented by Fig. 30.10, but with a W oxide film made by spin coating from a WCl_6-containing solution and an electrolyte of PVA-H_3PO_4-KH_2PO_4. This electrolyte is expected to be a conductor for both H^+ and K^+, where the H^+ should assure rapid dynamics in the coloration of W oxide and K^+ is suited for insertion into PB, as remarked above. Initial experiments showed optical modulation with CEs consistent with the one obtained by Tada et al. *(3314)*. The durability was poor, which was suspected to be a result of water in the electrolyte.

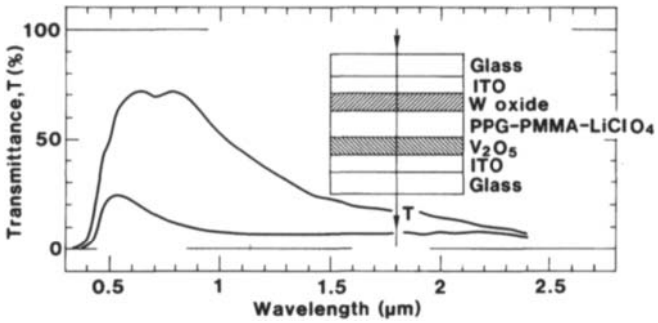

Fig. 30.8 Spectral transmittance T at two states of coloration for an electrochromic device of the type shown in the inset. After Andersson et al. *(96-9)*.

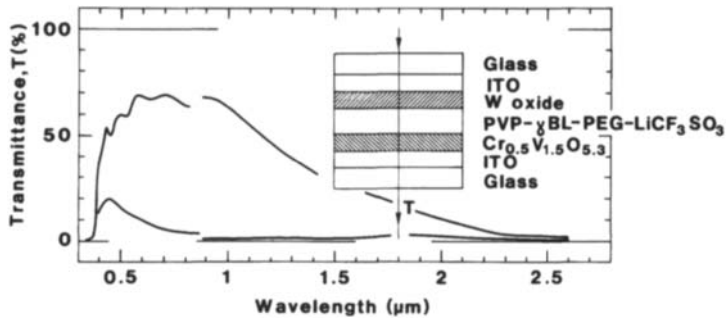

Fig. 30.9 Spectral transmittance T at two states of coloration for an electrochromic device of the type shown in the inset. After Cogan et al. *(733)*.

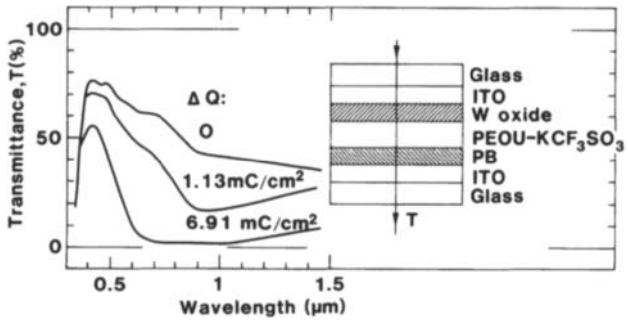

Fig. 30.10 Spectral transmittance T at three amounts of charge transport ΔQ for an electrochromic device of the type shown in the inset. After Tada et al. *(3314)*.

Chapter 31

TIME-DEPENDENT DEVICE PERFORMANCE: A UNIFIED TREATMENT

Chapters 28-30 treated the properties of several types of electrochromic devices. It is convenient to discuss some of these properties in a unified way, and this final chapter covers results on time-dependent effects with particular attention to color/bleach response time, variations of the optical properties under open circuit conditions (i.e., the non-volatility of the optical "memory"), and durability. Most of the discussion is focused on W oxide and W-oxide-based devices, but some data are also given for Ir oxide.

The color/bleach response times are influenced by many parameters. Separate discussions are given for the effects of film porosity (31.1), applied voltage and electrolyte hydration (31.2), temperature (31.3), and the geometric area of the device (31.4). The non-volatility of the optical memory is treated with respect to open circuit performance (31.5) and effect of drive circuitry (31.6).

Durability is of the utmost importance for practical devices. There are many possible degradation mechanisms. Most of them involve non-reversible interaction between adjacent layers, such as dissolution, permanent ion incorporation, electromigration, etc. The underlying cause of the degradation may be found in fundamental physical and chemical mechanisms as well as in operation at excessive voltage or current density. The previous three chapters illustrated the durability of several *specific* electrochromic devices, and the main purpose of the following discussion is to elucidate a few *general* degradation modes with particular attention to W oxide films. Specifically, the exposition covers etching in acid electrolytes (31.7), non-reversible ion incorporation from the electrolyte and cycling-induced crystallization (31.8), and ion incorporation from the substrate (31.9). Comments on the durability of Ir oxide films are given in (31.10). Recent surveys of durability issues have been given by Czanderna and Lampert *(794, 2003)*.

31.1 Color/bleach Response Time: Effects of Film Porosity

The discussion is begun by considering a small W oxide film backed by a material with high electrical conductivity and in contact with an electrolyte having high ionic conductivity and an ample supply of mobile species. The diffusion constant for the pertinent ions in the W oxide is then of decisive influence, and the data in Sec. 6.2 in principle give the color/bleach dynamics. It is obvious that a high porosity of the W oxide film leads to short response times, and oblique angle evaporation, deposition in the presence of a gas, etc., are capable of giving rapid dynamics.

Figure 31.1 illustrates the color/bleach times as a function of the evaporation angle (cf. Fig. 3.12) from work by Agnihotry et al. *(32, 35)* and Miyoshi and Iwasa *(2352)*. Device designs and

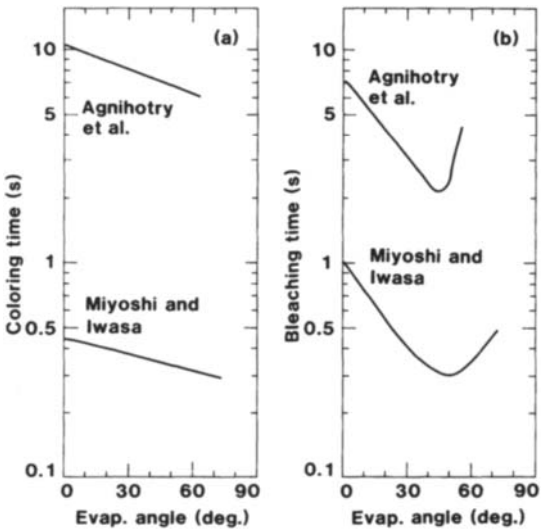

Fig. 31.1 Times for coloring (part a) and bleaching (part b) of small electrochromic W oxide films prepared by oblique angle evaporation. The evaporation angle was measured from the substrate normal. The data were fairly scattered, and the curves indicate approximate mean values. After Agnihotry et al. *(32, 35)* and Miyoshi and Iwasa *(2352)*.

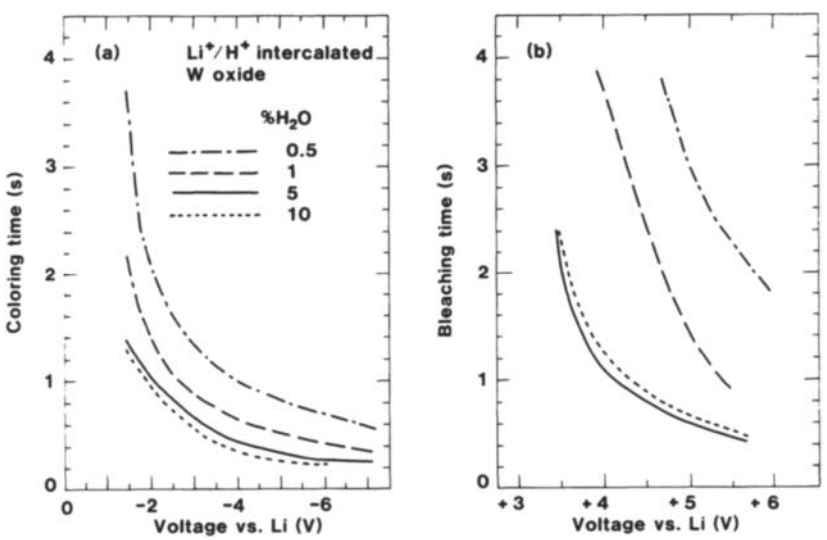

Fig. 31.2 Times for coloring (part a) and bleaching (part b) of small 0.4-μm-thick electrochromic W oxide films in electrolytes of $LiClO_4$ + dioxolane + water. Effects of different applied voltages and water admixtures are illustrated. From Bohnke et al. *(428)*.

measurement configurations were not identical in the two sets of experiments, and quantitative comparisons of data are not meaningful. However, it is clear that an increase of the evaporation angle from 0 to 70° led to a monotonic decrease of the coloration time by ~30 %. The effect of oblique angle evaporation was even more pronounced for the bleaching time, which could be reduced by as much as a factor of three when the evaporation angle went from zero to ~50°. Beyond this angle, the bleaching time increased. The latter effect remains unexplained.

Sun and Holloway *(3274)* studied films made by reactive evaporation of tungsten in the presence of different amounts of O_2. An enhancement of the O_2 content increased the coloration time and decreased the bleaching time. The oxygen alters the porosity (cf. Fig. 3.2a) as well as the film stoichiometry, and the ensuing effect is not easily predicted.

31.2 Color/bleach Response Time: Effects of Applied Voltage and Electrolyte Hydration

The role of the applied voltage has been studied several times for small W oxide films in contact with liquid electrolytes. The most detailed work is by Bohnke et al. *(428)*, who investigated evaporated films of different thicknesses in contact with solutions of 2.5 M $LiClO_4$ in dioxolane with various water admixtures. The possible usefulness of this electrolyte was inferred from previous studies of rechargeable Li-TiS_2 batteries *(1839)*. Color/bleach times were defined so that they corresponded to $\Delta(OD) = 0.3$ at $\lambda = 0.633$ μm. Figure 31.2 shows data as a function of voltage for 0.4-μm-thick films. Expectedly, both the coloring and bleaching times decreased upon increased voltage levels. Addition of water up to 5 weight % decreased the response times, but the effects of a further addition up to 10 weight % were smaller and may be different for coloring and bleaching. Quantitatively, the coloration times were several seconds for low voltages and low hydration, whereas times shorter than 0.5 s easily were reached at sufficient voltage and hydration.

Figure 31.3 gives a complementary view on the relation between color/bleach dynamics and applied voltage. The results, reported by Bohnke et al. *(426)*, were obtained for films prepared by pyrolysis of $W(CO)_6$ followed by annealing and electrochemical treatment in 1 N H_2SO_4. The dashed curves indicate voltammograms for the initial intercalation/deintercalation cycle and after 37 cycles, and the solid curves denote the change in optical density at $\lambda = 0.633$ μm per time increment as the voltage was swept. The strong correlation between the two sets of data should be noted and, expectedly, the optical dynamics was high when the current density was large.

The influence of the water content is further elaborated in Fig. 31.4, which shows coloration at -3 V and bleaching at +5.5 V (at $\lambda = 0.633$ μm) for films with different thicknesses. A 0.24-μm-thick film had unambiguous minima in the response times for electrolytes containing a few percent water. At $d = 0.4$ μm, minima may exist around ~5 % water but their existence was less certain. Finally, at $d = 0.5$ μm the response times decreased monotonically at increased hydration. Rather few water admixtures were checked, and hence it is not possible to state precise locations of the minima. Effects similar to those in Figs. 31.2 and 31.4 were also seen with electrolytes of $LiClO_4$ + PC + H_2O *(427, 429)*. It appears that intercalation of H^+ as well as Li^+ is of importance, which is in agreement with electrochemical data in Fig. 6.13, but a detailed interpretation of the results is not yet possible. Voltage-dependent response times, defined as mentioned above, have been reported also for H^+ and Li^+ intercalation in W oxide films prepared by CVD *(823, 825)* and anodization *(863, 2895)*, and a comparison of data for films made by several different techniques

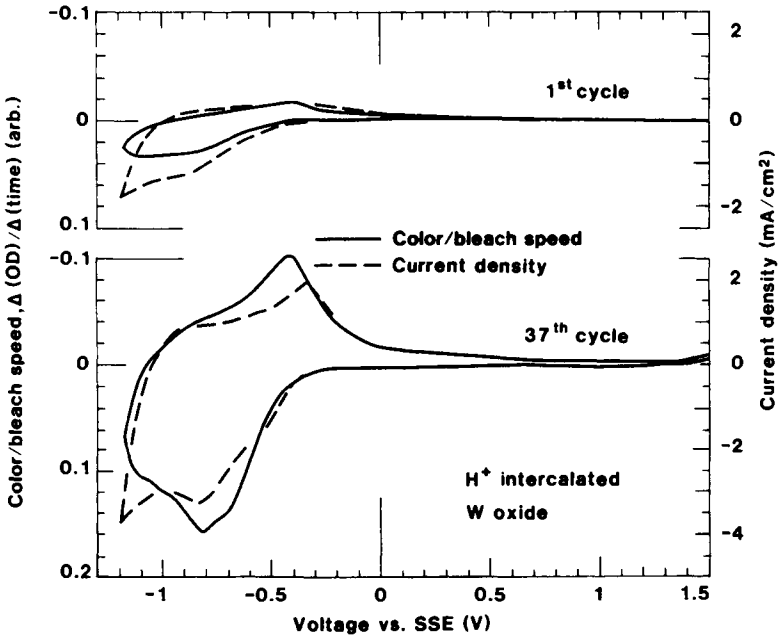

Fig. 31.3 Cyclic voltammograms (dashed curves) and color/bleach speed (solid curves) for H^+ intercalation/deintercalation in a monoclinic crystalline CVD-produced W oxide film in 1 N H_2SO_4. Data are given for the initial and 37^{th} cycle. The voltage scan rate was 100 mV/s. Arrows denote scan direction. The voltammograms were also depicted in Fig. 6.18. After Bohnke et al. *(426)*.

has been reported *(422)*. Some further results on response times can be found in *(106, 1889)*.

In the standard electrochromic device, a voltage is applied to an electrical conductor below the electrochromic oxide film. It is possible, however, to change the dynamics also by applying a voltage to a thin metal (Au) layer on top of the electrochromic (W) oxide, as investigated by Haranahalli et al. *(1417-8)*. The metal layer limits the achievable optical modulation (cf. Fig. 25.4), but its influence on the reponse dynamics can be beneficial. Figure 31.5 illustrates the relative change in transmittance at $\lambda = 0.7$ μm for a three-layer coating of electically conducting Sn oxide, electrochromic W oxide, and semitransparent Au in 1 N H_2SO_4. Coloring and bleaching were obtained by application of a positive or negative voltage to the tin oxide. The curves in Fig. 31.5 refer to the Au layer being electrically floating or having $U_{Au} = \pm 0.5$ V (with regard to the tin oxide). U_{Au} has a strong effect on the response dynamics, and the color/bleach times were as small as ~0.05 s under appropriate bias. These times are much shorter than under unbiased conditions.

31.3 Color/bleach Response Time: Effects of Temperature

Diffusion constants show thermally activated behavior (cf. Fig. 6.2) and, typically, they are changed by one order of magnitude when the temperature is altered by ~30°C. It is therefore natural that color/bleach response times are strongly temperature dependent. Figure 31.6(a) shows data from Ando et al. *(106)* for display-type devices with $LiClO_4$ + PC electrolytes and TiO_2 pigmented counter electrodes comprised of $W_{18}O_{49}$-V_6O_{13} (cf. Fig. 27.1). The coloring time was taken to be the period for inserting 6 mC/cm^2 at -1.5 V with regard to the counter electrode, and the bleaching time was the period for removing 90 % of the inserted charge in a short-circuited device. The response times increased monotonically when the temperature was lowered. At 20°C, say, the response time was ~0.1 s, whereas it was ~1 s at -35°C. Most practical uses of electrochromic devices will be at temperatures that do not deviate too much from normal room temperature, and hence the slow low-temperature dynamics would normally not be a severe problem. Temperature dependent response times were also discussed in *(423, 1726, 2468, 2841-2)*.

Some results are available for color/bleach response times of Ir oxide films. Their temperature dependence has been studied, and it is appropriate to present the data here. Figure 31.6(b), after Hackwood et al. *(1380)*, illustrates the response time corresponding to $\Delta(OD) = 0.6$ as a function of temperature. Almost indistinguishable results were obtained for 0.2-μm-thick films on different substrates (Ta or SnO_2-coated glass) and immersed in different electrolytes (4 M H_2SO_4 or 5 M NaOH). At 20°C the time was as small as ~0.04 s, and at -40°C it was ~5 s. Similar data were given in *(1382, 3041)*. The functional dependence in Fig. 31.6(b) is indicative of temperature-activated processes. The color/bleach time was size-dependent and increased from values such as those in Fig. 31.6(b) for linear sizes less than 0.6 cm by about an order of magnitude for sizes of ~7.5 cm *(818-9)*. Anodic Ir oxide films had response times similar to those for sputter-deposited films *(339-40, 1265-6, 3118-9)*. The times of the anodic films could be diminished if they were heated in H_2SO_4. The smallest color/bleach times reported so far were ~0.01 s for bleaching and 0.02 s for coloring *(339)*.

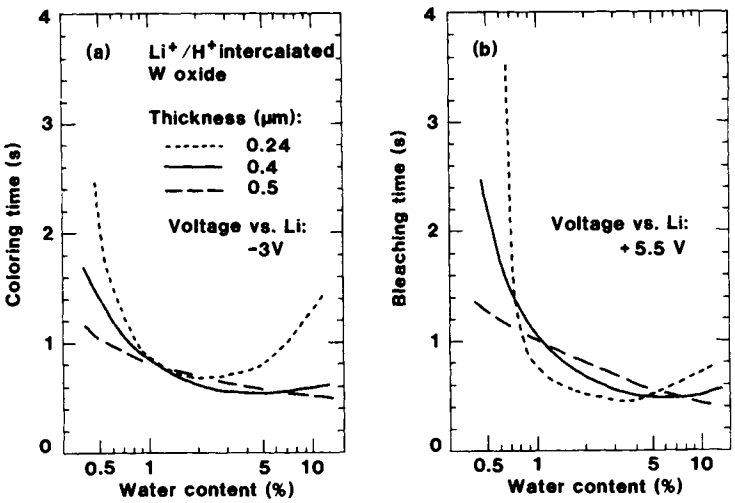

Fig. 31.4 Times for coloring (part a) and bleaching (part b) of small electrochromic W oxide films under potentiostatic conditions in electrolytes of $LiClO_4$ + dioxolane + water. Effects of different film thicknesses and water admixtures are illustrated. From Bohnke et al. *(428)*.

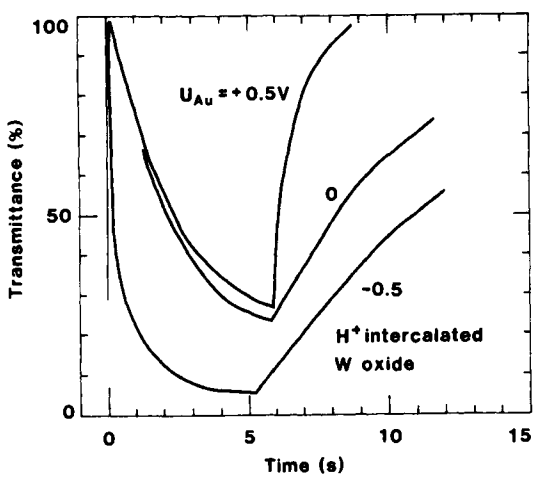

Fig. 31.5 Relative transmittance vs. time during coloring and bleaching of a three-layer coating of Sn oxide, electrochromic W oxide, and Au. Data refer to three different voltages U_{Au} applied to the gold film. From Haranahalli and Holloway *(1418)*.

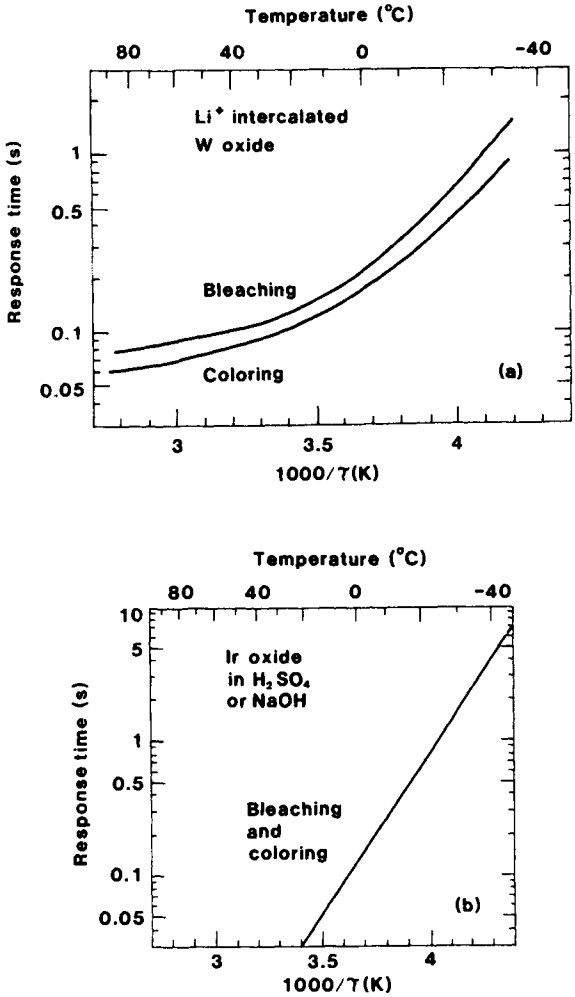

Fig. 31.6 Response times for coloring and bleaching of small W-oxide-based electrochromic devices (part a) and Ir-oxide-based films (part b) in different electrolytes. Data are shown as a function of inverse temperature τ. After Ando et al. *(106)* and Hackwood et al. *(1380)*.

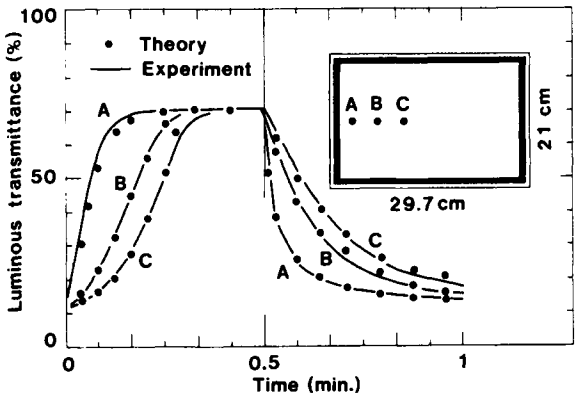

Fig. 31.7 Luminous transmittance during bleaching (left-hand part) and coloring (right-hand part) of a large electrochromic device with films of W oxide and Prussian Blue separated by an electrolyte of $LiClO_4$ + PC. Theoretical and experimental results are shown for three points on the device area, as represented in the inset. Here A, B, and C are at the same distance from either of the two long sides; the points lie 2, 6, and 10 cm, respectively, from one of the short sides. Fitted values of electrical resistivity and ion conductivity were used to obtain the *theoretical* data points. Curves indicate *measured* results (cf. Fig. 28.10). From Kase et al. *(1752)*.

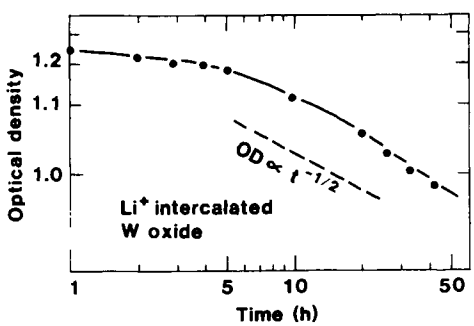

Fig. 31.8 Optical density OD vs. time t under open circuit conditions for an electrochromic device embodying a W oxide film in contact with a $LiClO_4$ + PC electrolyte. Dots denote experimental data, and the solid curve was drawn for convenience. The dashed line represents the slope predicted for diffusion of Li^+ from the film. From Morita *(2390)*.

31.4 Color/bleach Response Time: Effects of Geometric Area

The present section considers large electrochromic devices with electrical bus bars along the circumference or at opposite sides. At each area element, the optical properties are determined by the transported charge, and hence the voltage drop in the transparent electrically conducting film(s) as well as the ionic conductivity in the electrolyte govern the rate of optical modulation. Quantitative predictions of response dynamics involve continuum electrodynamics and are straight forward, at least in principle. The time dependent charge can be represented by a second-order two-dimensional differential equation, which should be solved with boundary conditions corresponding to the voltage applied to the bus bar *(1752)*. The situation is akin to the one represented by the telegraph equation for a leaky circuit.

Figure 31.7, from Kase et al. *(1752)*, shows luminous transmittance at three points on a 21 x 29.7 cm^2 electrochromic device of the indicated design (see also Fig. 28.9). Data based on experiments and on computations by use of the theory hinted at above are in good agreement and indicate the unevenness in the optical properties that occurs during coloring and bleaching of a large electrochromic device. Further data on size-dependent optical color/bleach dynamics can be found in *(1726, 1888, 2358, 2468, 2844, 3532)*. Variations in the response dynamics, analogous to those for size changes, have been observed in experiments on devices having different resistivities of the transparent electrical conductors *(1726, 1735, 2358, 2459)* or different ionic conductivities *(3314)*.

31.5 Non-volatility of the Optical Memory: Open Circuit Performance

One of the advantages of electrochromic devices is that the optical memory can be non-volatile, i.e., the optical properties can remain the same for extended periods of time without charge insertion from the drive circuit. A memory loss occurs when the inserted charge is removed from the electrochromic film through an electrical leakage current or ion diffusion. It is evident that the ion conductor plays a decisive role for the optical memory time, and it is natural to look at the performance of devices categorized according to the type of electrolyte or ion conductor.

Morita and Washida *(2390, 2396)* carried out a detailed study of the optical memory in devices with W oxide films in contact with liquid $LiClO_4$ + PC electrolytes. Figure 31.8 is a log-log plot of optical density as a function of time under open circuit conditions. Typically, OD dropped by ~15 % after 24 h. After some hours, the time-dependent decline approximately followed $OD \propto t^{-1/2}$, indicating that diffusion of Li^+ from the electrochromic film into the electrolyte is a likely cause for the memory loss. The memory is prolonged if the electrolyte is dehydrated and if the film density is high. Memory loss for films left in air was reported in *(2539)*, and some data on the bleaching of W oxide films in a H_2SO_4 electrolyte were given in *(2113)*.

Optical memory of an Ir oxide film in contact with 0.5 M H_2SO_4 was reported by Kang and Shay *(1744)*, whose results are indicated in Fig 31.9. The film was prepared by dc sputtering onto a cooled substrate, so that a highly porous hydrous deposit was obtained. The optical density of the colored material decreased marginally during the course of 100 h; for the bleached state, the change in optical density was more pronounced but still not severe during the first few hours. The shown time dependent change in coloration is comparable to the one found in anodized films *(339, 1266)*. On the other hand, films made by oxidation of evaporated Ir-C *(3023)*, as well as compact sputter-

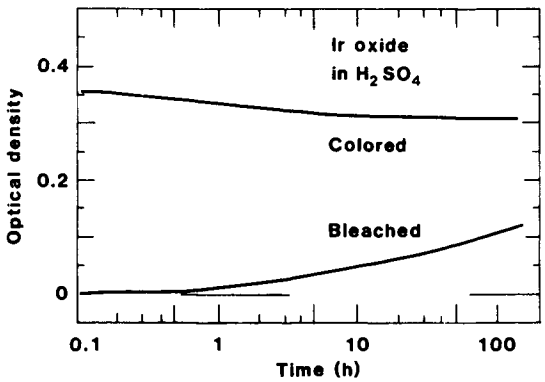

Fig. 31.9 Optical density vs. time under open circuit conditions for an electrochromic Ir oxide film left in colored and bleached state in contact with H_2SO_4. After Kang and Shay *(1744)*.

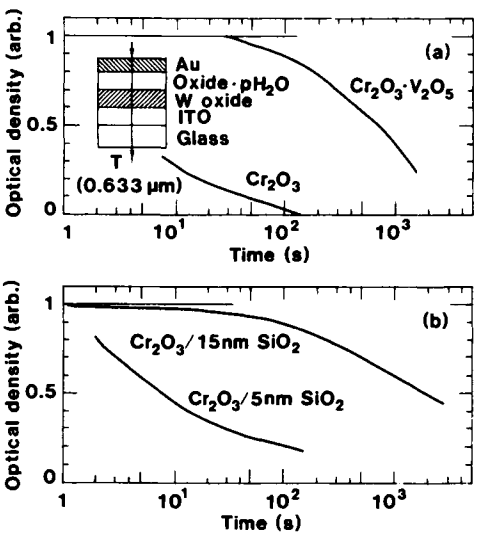

Fig. 31.10 Optical density vs. time under open circuit conditions for the Deb-type electrochromic device indicated in the inset. Parts (a) and (b) pertain to the shown compositions of the hydrated oxide(s). The data are based on measurements of transmittance *T*. After Sato et al. *(3020)* and Shizukuishi et al. *(3155)*.

deposited films *(1744)*, altered their properties rapidly under open circuit conditions.

Sato et al. *(3020)* and Shizukuishi et al. *(3155)* investigated the optical memory in Deb-type electrochromic devices, incorporating a hydrated Cr_2O_3-based layer between films of W oxide and Au. In Fig. 31.10(a), the lower curve indicates the short optical memory found if a 0.14-μm-thick Cr_2O_3 film was used as ion conductor. The memory was significantly improved if the Cr_2O_3 was mixed with 50 weight % V_2O_5 so that the total thickness was 0.28 μm; now the upper curve in Fig. 31.10(a) shows that a 15 % drop in OD takes ~2 minutes. Figure 31.10(b) reports data for devices with 0.3 μm of Cr_2O_3 and an electron blocking SiO_2 film in contact with the W oxide. The optical memory depended strongly on the thickness of the SiO_2, and 15 nm was sufficient to give only a 15 % drop of the OD during ~2 minutes. In devices with $Ta_2O_5 \cdot pH_2O$ layers between films of W oxide and Ir oxide, the resistivity of the Ta oxide was found to govern the optical memory *(3578)*. Tantalum oxide films have been used also for extending the open circuit memory in devices with polymer electrolytes (cf. Fig. 30.1) *(734)*.

A few results are available for devices with bulk-type electrolytes and ion conductors. Thus Kuwabara et al. *(1973, 1980)* found that the OD decreased from 0.76 to 0.63 during ~10 h under open circuit conditions if the ion conductor was ZP or SP. In devices with polymer electrolytes, the optical memory can last for weeks *(3314)*.

Short-circuit memory might be possible in electrochromic devices with a proper choice of electrolyte, as discussed by Beni *(331-2, 336)*. This would enable easy matrix addressing of electrochromic displays.

31.6 Non-volatility of the Optical Memory: Effect of Drive Circuitry

A practical electrochromic device must include drive circuitry connected to the transparent electrical conductor(s). The open circuit performance is hence not sufficient for assessing the device properties, but the influence of a load with a resistance R_L in the external circuit must be accounted for. Figure 31.11 shows data for a W film in contact with $LiClO_4$ + PC. Even if R_L was as large as 1 MΩ, there was a significant loss of memory and the OD typically was decreased by 15 % in ~2 h. A lower value of R_L yielded a shorter memory, and for R_L = 0.1 MΩ the memory loss was almost complete after ~5 minutes. The decline in OD can be understood from a model involving discharge of a capacitor. Unless R_L is very large, the internal resistance of the device must be taken as time-dependent. Additional data on optical memory for devices with $LiClO_4$ + PC electrolytes were given in *(1726, 2358, 3736)*.

Horio et al. *(1543)* found from studies of W oxide films in electrolytes based on H_2SO_4 that ion intercalation by a dc voltage with a superimposed ramped ac signal led to a prolonged optical memory. It was argued that the ac voltage yielded efficient and deep ion intercalation, but no detailed model was given to support this view.

31.7 Durability: Etching of Tungsten Oxide in Acid Electrolytes

There have been several studies on the etching of W oxide films in acids *(147, 1046, 2396, 2840, 2871, 3273)*. Photo-assisted etching was investigated in *(39)*. One could first observe that *crystalline* WO_3 dissolves in water to form WO_4^{2-} and $2H^+$, but the solubility is so small that only a

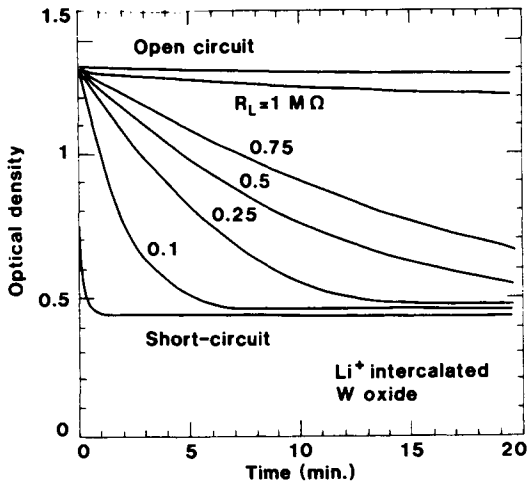

Fig. 31.11 Optical density vs. time for an electrochromic device embodying a W oxide film in contact with liquid $LiClO_4$ + PC. The external circuit was closed via a load resistor with the shown resistance R_L. Results are also shown for short-circuited and open conditions.

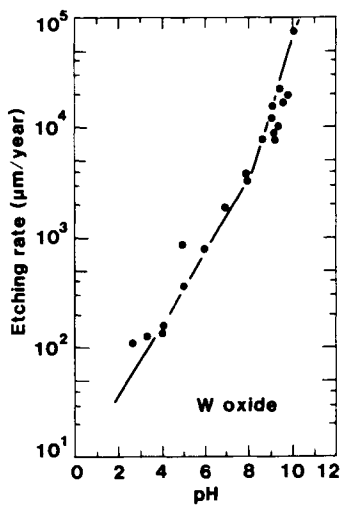

Fig. 31.12 Etching rate vs. pH for evaporated W oxide films. The various data points are based on optical interference measurements on films immersed in different buffered solutions under flowing-electrolyte conditions. The lines were drawn for convenience. From Faughnan and Crandall *(1046)*.

few nm are expected to be removed before saturation is reached in a 1 cm thick layer of a neutral solution at room temperature. Only about one molecule layer should be dissolved in an acidic environment with a pH of 1 to 2. Strongly *disordered* W oxide films, however, have etching rates that are many orders of magnitude higher, as illustrated in Fig. 31.12. The data were taken by Faughnan and Crandall *(1046)*, who studied evaporated films in flowing aqueous electrolytes bufferered with various substances so that the pH lay between 2 and 10. The etching rate r_e is seen to vary strongly with pH; at pH < 8 one finds $r_e \propto 10^{[pH]2/3}$. Even at pH = 0 the etching rate is expected to be ~10 μm/year, which is much too high for a practical device.

Randin *(2840)* investigated thickness decrements of W oxide films in stationary H_2SO_4/glycerin (1:10) electrolytes saturated with WO_3. The films were evaporated in 2 x 10^{-5} Torr of air onto substrates heated to 100°C. The amount of dissolved W oxide was inferred from spectrophotometric analysis of the electrolyte. The filled circles in Fig. 31.13 show data for films kept at 50°C in sealed ampoules. A steady thickness decrease is seen; it corresponds to ~2.5 nm/day--i.e., to ~1 μm/year--which is a much lower rate than the one encountered in a flowing unsaturated electrolyte but still too large for most applications. The open squares in Fig. 31.13 refer to measurements at room temperature under color/bleach cycling with 0.5 Hz. The etching rate is about the same as for films stored in electrolytes at 50°C. Extended cycling led to the development of a highly porous film structure and eventually to crumbling and complete disintegration after ~40 days.

The conspicuously high dissolution rate of disordered evaporated W oxide films was analyzed by Arnoldussen *(147)* and led him to propose the molecular configuration delineated in Fig. 3.10. Following work on the formation of polymeric anions in acidic solutions *(1779)*, it was argued that the directly dissolved species would be metatungstate ions ($H_2W_{12}O_{40}^{6-}$) or pseudo-metatungstate ions ($HW_6O_{20}^{3-}$), rather than the WO_4^{2-} ions dissolved from WO_3. Cathodic species such as WO_2^{2+} and WO_2OH^+ have been reported in acidic solutions with pH < 1 *(2506-7)*.

Realizing that the high dissolution rate is directly connected with the microstructure, it is a natural step to try to improve the durability of electrochromic W oxide films by modifications of the preparation and post-treatment conditions. A detailed study on the influence of evaporation in the presence of O_2 was reported by Sun and Holloway *(3273)*. Figure 31.14, taken from their work, shows data for films immersed in 3.6 N H_2SO_4. The amount of undissolved W oxide was determined by RBS. The etching rate decreased by one to two orders of magnitude when p_{O2} was increased from 10^{-5} to 10^{-3} Torr. The enhancement of p_{O2} also led to a compositional change from $WO_{2.7}$ to $WO_{2.9}$, a partial crystallization, and a decrease of the electrochromic coloration efficiency. The significance of the evaporation conditions was also stressed in *(2176, 3057)*. For sol-gel-produced films, the cycling durability was good only when the hydration was not too large, and films with a nominal composition $WO_3 \cdot 0.6H_2O$ could accept 2 x 10^6 color/bleach cycles *(1704)*.

Post-treatment offers possibilities of decreasing the etching rate of W oxide films, and beneficial effects have been found with UV irradiation *(1360)*, ion bombardment *(147)*, electron bombardment *(193-4, 1360)*, and pulsed laser irradiation *(513-4, 1916, 2767, 2932-3, 2947, 3522)*. The laser technique produced a four- to fivefold shortening of the color/bleach response times, which may be associated with roughening of the film surface. Improved durability of Mo oxide films has been obtained through exposure to UV light *(146)*, electron irradiation *(195, 1957, 2623)*, and hydrogen ion bombardment *(1359)*.

A straight-forward way of protecting W oxide films in H_2SO_4-based electrolytes is to cover the film surface with a durable proton-conducting film. Nafion can be used for this purpose, as

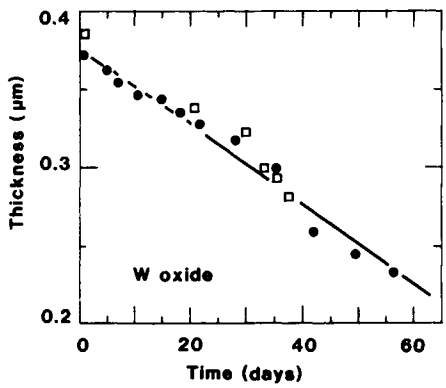

Fig. 31.13 Thickness vs. time for evaporated W oxide films in H_2SO_4 + glycerin. Filled circles refer to films stored at 50°C and open squares to films that have undergone color/bleach cycling at room temperature. The line represents an etching rate of 2.5 nm/day. After Randin *(2840)*.

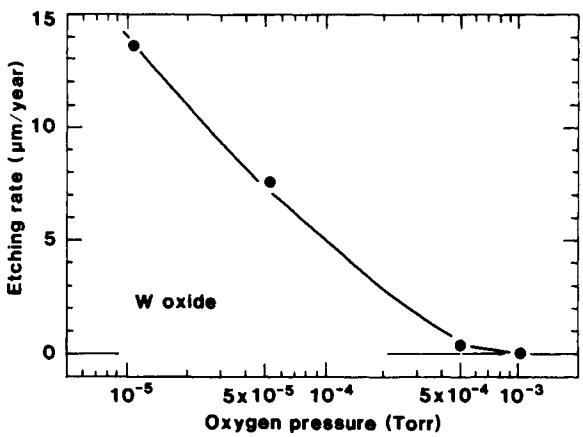

Fig. 31.14 Etching rate vs. oxygen pressure for reactively evaporated W oxide films. Data points are based on RBS measurements on films immersed in H_2SO_4. The curve was drawn for convenience. After Sun and Holloway *(3273)*.

shown recently by Shen et al. *(3122)*. It appears that the main function of the Nafion was to serve as a barrier preventing dissolved W-containing species from diffusing away from the film.

Even if there are some ways to diminish the etching of W oxide films in aqueous or glycerine solutions, it is of great importance to find better solvents. Much attention has been drawn to non-aqueous solvents, and Randin *(2840)* found no dissolution of films stored in sealed ampoules with PC, acetone, γ-butyrolactone, or methane sulfonic acid at 50°C for 90 days. The low dissolving power of propylene carbonate was corroborated in *(2396)*.

31.8 Durability: Non-reversible Ion Incorporation from the Electrolyte, and Cycling-induced Crystallization of Tungsten Oxide Films

An accumulation of non-mobile ions in the layers of an electrochromic device can give irreversible changes of the optical and electrical properties and may lead to degradation. The ions can come from different sources; the one closest at hand is is the electrolyte or ion conductor. These ions can be permanently incorporated in W oxide films as discussed in Sec. 7.1, where data based on SIMS, RBS, and NRA were presented. The buried ions lead to a downward shift of the EMF (cf. Fig. 6.4). Figure 31.15, from Nagai et al. *(2465, 2467)*, shows EMF data for 0.5-μm-thick W oxide films prepared by evaporation in the presence of some air so that a high porosity was achieved. Charge insertion from $LiClO_4$ + PC made the EMF go down, which is in good agreement with earlier results. Extended color/bleach cycling produced a cathodic shift of the EMF by about the same magnitude irrespective of the charge insertion. The shift was as large as ~0.5 V. The underlying cause is likely to be non-reversible ion exchange on internal surfaces of the W oxide film. The parallel displacement of the EMF curves is interesting from a device perspective, since it shows that an apparent degradation can be compensated by a voltage change in the drive circuit, or, in other words, the degradation would not be manifest in electrochromic devices with constant-current drive. EMF changes corresponding to those in Fig. 31.15 were also observed in *(2396, 3738)*. The shift could be halted in electrolytes containing $LiBF_4$ *(3741)*.

Apart from causing EMF shifts, ion accumulation can give structural changes. They are normally in the direction towards more crystalline modifications of the W oxides, with or without hydration *(860-2, 1030, 1143, 2227, 2747)*. Raman spectroscopy indicated that an initially strongly disordered W oxide film made by anodization could evolve towards a hexagonal crystalline configuration after many intercalation/deintercalation cycles in H_2SO_4.

The durability of electrochromic W oxide films with various oxidic or metallic additions has been investigated recently. The most comprehensive work is by Matsouka et al. *(2227)*, who considered the role of TiO_2, ZrO_2, Ta_2O_5, Nb_2O_5, SiO_2, Al_2O_3, MgO, Cr_2O_3, and NiO. Other studies regarded the specific influence of TiO_2 *(1270, 1437-8)*, of Ni and Co *(3124)*, and of (Ti,Nb)-doping *(1184-5)*. Figure 31.16, from Matsuoka et al. *(2227)*, indicates the number of cycles before breakdown when evaporated films of W oxide--with ~10 mol. % of either of nine different oxide additions--were cycled between +2.5 and 0 V in 1 M $LiClO_4$ + PC. It is striking that TiO_2 had a very beneficial effect and enhanced the number of allowed cycles by roughly an order of magnitude. All of the other oxides diminished the durability. Figure 31.17 reports the influence of different TiO_2 contents; it is seen that 10 to 15 mol. % TiO_2 gave the best results. The coloration efficiency was rather independent of the proportion of TiO_2. From measurements using SIMS and XRD, it was evident that the favorable effect of TiO_2 was associated with its ability to prevent

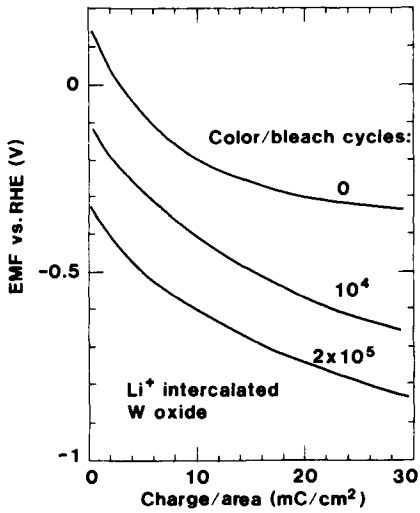

Fig. 31.15 Normalized EMF versus charge/area for Li^+ intercalated W oxide films. Data are shown for an evaporated film in as-deposited state and after extended color/bleach cycling. From Nagai et al. *(2465, 2467)*.

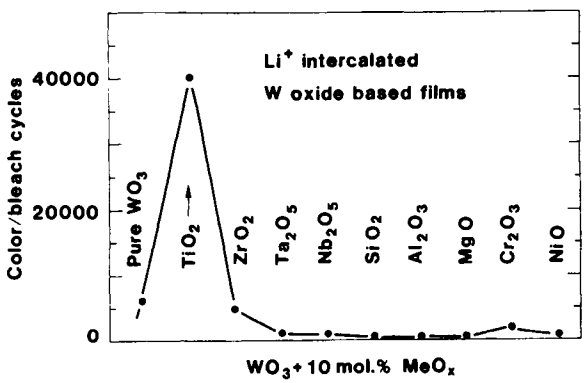

Fig. 31.16 Durability, i.e., the number of color/bleach cycles prior to breakdown, of electrochromic W-oxide-based films with the shown oxidic additions treated in Li^+ conducting electrolytes. Filled circles represent experimental data, and connecting lines were drawn for convenience. From Matsuoka et al. *(1438, 2227)*.

crystallization as well as permanent Li^+ incorporation during extended color/bleach cycling *(1438, 2227)*. Beneficial effects with regard to stability have been reported also for (Ti,Nb)-doping *(1184-5)* and for addition of Co, Cr, Fe, Mo, Ni, Ru, or Zn *(2384)*.

31.9 Durability: Effects of Ion Incorporation from the Substrate

The glass substrates used in most electrochromic devices are able to provide ions with harmful effects. The ions are particularly serious for devices that have undergone high-temperature treatment in order to produce crystalline films of W oxide or of a transparent conductor such as ITO. Mizuhashi et al. *(2357)* reported a detailed study on the migration of alkali ions from glass substrates. The out-diffusion was found to be proportional to the alkali content in the glass, and it could amount to as much as ~1 $\mu g/cm^2$ of Na_2O for a soda lime glass with an alkali content of 13 weight % annealed at 550°C for 1/2 to 1 hour. A silicon oxide coating on the glass could serve as a diffusion barrier and could diminish the out-migration by a factor that was strongly dependent on the method for coating fabrication. Thus coatings made by sol-gel technology or CVD were able to diminish the out-diffusion by a factor 10 to 20, whereas coatings made by evaporation or sputter-deposition were less efficient. The main role of the silicon oxide is to prevent moisture from penetrating into the glass. Ion permeation through silicon oxides was reported also in *(2355-6)*.

Alkali ions from glass substrates can have several unwanted effects on electrochromic devices. Their presence in transparent electrically conducting films of SnO_2:Sb--and almost certainly also in ITO, etc.--produces a structure with loosely connected grains and hence high resistivity *(2354)*. The net effect is to give slow color/bleach dynamics. Further diffusion of alkali ions into electrochromic W oxide films has been detected by XPS *(1762)* and SIMS *(3702)*. Figure 31.18 reports data by Yamanaka *(3702)* on devices with 0.3-μm-thick W oxide films on ITO-coated glass of three types: ordinary soda glass, Corning 7059 glass with low sodium content, and soda glass with a 0.15-μm-thick "spin-on glass" (SOG) coating. The latter coating comprises thermally decomposed SiO_2. The substrates were heat treated at 250°C for 1 h in vacuum before the W oxide film was deposited; this heating was done in order to augment the substrate influence. Color/bleach cycling with square wave (1.5 V, 1 Hz) drive was performed for devices with $LiClO_4$ + PC electrolytes. The charge insertion per cycle was low for soda glass, whereas it remained at ~5.5 mC/cm^2 up to ~3 x 10^5 cycles for Corning 7059 glass and for SOG-coated glass. The latter substrate seems to be superior beyond 3 x 10^5 cycles. Devices made with W oxide films evaporated onto unheated substrates had properties that were independent of the substrate type, at least for short-term color/bleach cycling. Sodium incorporation from impurities in a $LiClO_4$ + PC electrolyte was discussed in *(106)*.

31.10 Durability: Comments on Iridium Oxide Films

Iridium oxide films have been used in a number of electrochromic devices, and enough experience on durability has accumulated to warrant a unified discussion. Films of this material, if properly made, are able to show an excellent cycling durability. Thus sputter-deposited compact films could be run through 2 x 10^7 color/bleach cycles in 0.5 M H_2SO_4 with only a ~3% change in the exchanged charge density or of the optical density in the colored state *(819, 1380, 3042)*. Even at

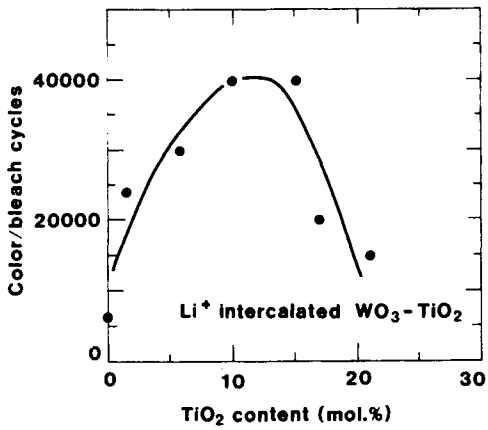

Fig. 31.17 Durability, i.e., the number of color/bleach cycles prior to breakdown, of electrochromic W-oxide-based films with different amounts of TiO_2 treated in Li^+ conducting electrolytes. Filled circles represent experimental data, and the curve was drawn for convenience. From Matsuoka et al. *(2227)*.

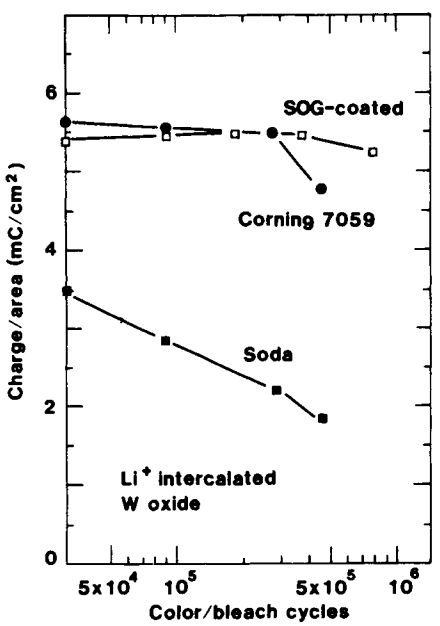

Fig. 31.18 Inserted charge per unit area and cycle during color/bleach cycling of electrochromic devices with evaporated W oxide films on the shown types of substrates in Li^+ containing electrolytes. SOG denotes "spin-on glass". Symbols indicate measured data, and lines were drawn for convenience. From Yamanaka *(3702)*.

73°C, 2.5 x 10^5 cycles could be accepted at a ~5% change in OD.

The durability of the Ir oxide films depends on the fabrication technique. This issue is illustrated in Fig. 31.19, from Sato *(3017)*, showing that films made by thermal oxidation of evaporated Ir-C could withstand more than 5 x 10^5 cycles without noticeable degradation, whereas anodized films lost part of their charge capacity already after ~10^4 cycles. The stability is likely to be coupled to the porosity, and sputter-deposited films can have a relative density of ~0.86, whereas anodic film may have a relative density of only ~0.17. Thermally oxidized evaporated Ir-C films are expected to have an intermediate porosity.

The limited durability of the anodic films is not necessarily a proof of a short device lifetime, since anodic films can be regrown on bulk Ir by expanding the voltage range of the cycling. This ability is obvious from the growth properties of anodic films; cf. Fig 14.4. Nevertheless, it may be desirable to improve the durability of the anodic films, which is feasible by treating them in hot H_2SO_4 for ~15 minutes *(339)* or by replacing the H_2SO_4 electrolyte by 0.5 M Na_2SO_4 (pH = 3.5) *(1265)*.

Yamanaka *(3705-6)* analyzed the influence of the electrolyte pH on the durability of anodically electrodeposited Ir oxide films. The electrolytes were buffered solutions of 1 M H_3PO_4+ NaOH. Figure 31.20 shows charge densities during electrochromic cycling with (0.6 V, 1 Hz) pulses. No deterioration was noticeable up to 7 x 10^6 color/bleach cycles for a pH of 3, 4, and 5. For larger or smaller pH, the films degraded significantly above 10^5 cycles.

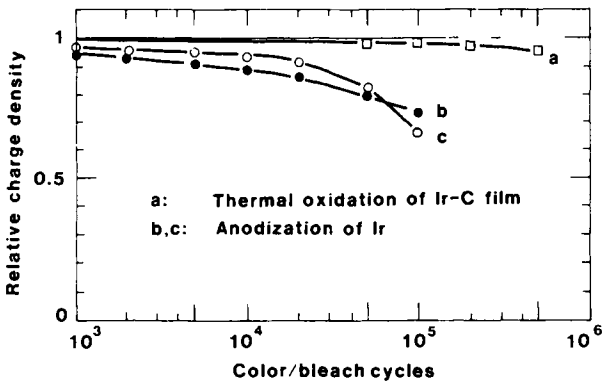

Fig. 31.19 Inserted relative charge density per cycle during long-term cycling of Ir oxide films in 0.5 M H_2SO_4. A square-wave voltage, switching from -0.2 to +1.0 vs. SCE at 1 Hz, was applied to films made by two techniques. Symbols denote measured data, and curves were drawn for convenience. From Sato *(3017)*.

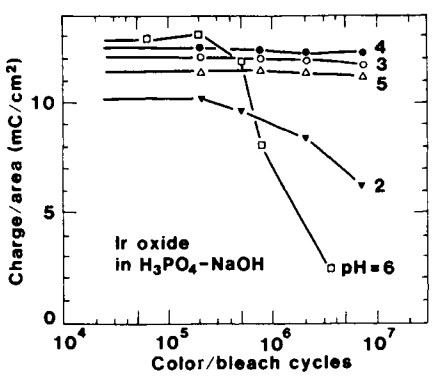

Fig. 31.20 Inserted charge density per cycle during long-term color/bleach cycling of anodically electrodeposited Ir oxide films in electrolytes of H_3PO_4 + NaOH with the shown pH values. Symbols denote measured data, and connecting straight lines were drawn for convenience. After Yamanaka *(3705)*.

Appendix

ABBREVIATIONS, ACRONYMS, AND SYMBOLS

A	Absorptance, or Area
a	Absorption coefficient
a_p	Absorption coefficient at the peak of the absorption band causing electrochromism (experimental)
a_{pol}	Absorption coefficient due to polaron absorption (theoretical)
Abs.	Absorption
ac	Alternating current
AES	Auger Electron Spectroscopy
AM	Air Mass
Am.	Amorphous
AMPS	Acrylamido-methyl-propane Sulfonic Acid
AN	Acetonitrile
Arb.	Arbitrary
ATR	Attenuated Total Reflectance
α	Angle
α_{CPE}	Angle for constant phase element
BAn	Benzyl Aniline
BL	Butyrolactone
BPEI	Branched Poly-ethylene Imine
Br	Bruggeman (effective medium theory)
β	Angle, or Bohr magneton
C	Capacitance
C_{ext}	Optical extinction cross-section (relative to surrounding material)
C_{DL}	Capacitance of double-layer
CE	Coloration Efficiency
CIE	Commission International d'Eclairage
CoE	Counter Electrode
Coeff.	Coefficient
CPE	Constant Phase Element
CR	Contrast Ratio
Cryst.	Crystalline
CVD	Chemical Vapor Deposition

d	Thickness of film
D_{e^-}	Diffusion constant for electrons
D_f	Fractal dimension
d_g	Thickness of glass substrate
D_{M+}	Diffusion constant for ionic species M+
D_{65}	Daylight illuminant
DC	Deeply Colored
dc	Direct current
Dep.	Deposition, or Deposited
DME	Dimethoxyethane
DMF	Dimethylformamide
DSC	Differential Scanning Calorimetry
DTA	Differential Thermal Analysis
DVB	Divinylbenzene
δ	Fractional water admixture
E	Emittance
e	Electronic charge
e^-	Electron
E_a	Activation energy for conduction
E_{el}	Electrostatic energy of solvation
E_F	Fermi energy
E_g	Semiconductor bandgap
E_p	Energy for the peak of the absorption band causing electrochromism
e-beam	Electron-beam (evaporation)
EELS	Electron Energy Loss Spectroscopy
EGA	Evolved Gas Analysis
EMT	Effective Medium Theory
EMF	Electromotive Force
EPR	Electron Paramagnetic Resonance
ESA	Ethylene Sulfonic Acid
eV	Electron volt
Evap.	Evaporation, or Evaporated
EW	Equivalent Weight
EXAFS	Extended X-ray Absorption Fine-structure Spectroscopy
ε	Dielectric function ($= \varepsilon_1 + i\,\varepsilon_2$)
$\bar{\varepsilon}$	Effective dielectric function ($= \bar{\varepsilon}_1 + i\,\bar{\varepsilon}_2$)
ε^{Drude}	Dielectric function for the Drude theory
ε^{eg}	Dielectric function for a free-electron gas
ε_0	Permittivity of free space
ε_∞	Dielectric function at high frequency
F	Electrical field
f	Filling factor (volume fraction)
F_c	Faraday's constant

f_s	Oscillator strength
FTIR	Fourier Transform Infrared (spectroscopy)
ϕ	Color stimulus
g	Landé factor
GF	Glass Former
Γ	Critical exponent
γ	Relaxation frequency ($= \gamma_1 + i\gamma_2$)
H	Hamiltonian
h	Planck's constant
$\hbar$	Planck's constant divided by 2π
h	Exponent in the electrical ac conductivity
H^o	Atomic hydrogen
HCF	Hexacyanoferrate
HEM	Hydroxy Ethyl Methacrylate
HUP	Hydrogen Uranyl Phosphate
I	Intensity
I_{UV}	Intensity of ultraviolet light
IR	Infrared
ITO	Indium Tin Oxide (In_2O_3:Sn)
J_d	Deintercalation current
J_i	Intercalation current
K	Normalization constant for tristimulus values
k	Wavevector
k	Extinction coefficient (optical constant)
k_B	Boltzmann's constant
k_F	Fermi wavevector
l	Mean free path
LAXRD	Low Angle X-ray Diffraction
LC	Lightly Colored
LO	Longitudinal Optical (phonon)
lum	Luminous
λ	Wavelength
M	Mole
m	Free-electron mass
M^+	Monovalent ion (H^+, Li^+,...)
m_c^*	Effective conduction-band mass for electrons
Me	Metal
MG	Maxwell Garnett (effective medium theory)

MMA	Methyl Methacrylate
N	Normal
N	Complex refractive index ($= n + ik$)
n	Refractive index (optical constant)
N_A	Avogadro's number
n_e	Free-electron density
n_i	Ion density
N_s	Number of color centers
Nafion	Poly-perfluoro sulfonic acid (tradename)
NASICON	$Na_{1+x}Zr_2Si_xP_{3-x}O_{12}$
NMR	Nuclear Magnetic Resonance
NRA	Nuclear Reaction Analysis
ν	Poisson's ratio
OMCTS	Octamethyl Cyclo Tetra Siloxane
Ox.	Oxide
ω	Angular frequency
ω_N	Plasma frequency (unscreened)
ω_{pl}	Plasma frequency (screened)
$\Omega_{1/2}$	Full width at half maximum for an absorption band (Gaussian)
P	Power
p	Degree of hydration
p	Gas pressure
p_s	Specularity parameter
PAA	Poly-acrylic Acid
PANI	Poly-aniline
PB	Prussian Blue (hexacyanoferrate)
PC	Propylene Carbonate
PECVD	Plasma Enhanced Chemical Vapor Deposition
PEG	Poly-ethylene Glycol
PEI	Poly-ethylene Imine
PEO	Poly-ethylene Oxide
PEOS	Poly-(ethylene oxide, siloxane)
PEOU	Poly-(ethylene oxide, urethane)
PMEO	Poly-*oligo*-oxyethylene Methacrylate
PMMA	Poly-methyl Methacrylate
PPG	Poly-propylene Glycol
PPO	Poly-propylene Oxide
PTFE	Poly-tetra Fluoro Ethylene
PVA	Poly-vinyl Alcohol
PVP	Poly-vinyl Pyrrolidone
PWA	Phosphotungstic Acid
Q	Electric charge density

q	Degree of hydroxylation
R	Reflectance
r_e	Etching rate
R_{EL}	Electrolyte resistance
R_g	Gas constant
R_I	Interfacial resistance
r_i	Ionic radius
R_L	Resistance of load resistor
R_{lum}	Reflectance of luminous radiation
R_{sol}	Reflectance of solar radiation
R_{sq}	Resistance per square
RBS	Rutherford Backscattering Spectroscopy
RDF	Radial Distribution Function
RE	Reference Electrode
rf	Radio frequency
RH	Relative Humidity
RHE	Reference Hydrogen Electrode
RHEED	Reflection High-energy Electron Diffraction
RPA	Random Phase Approximation
rpm	Revolutions per minute
RT	Room Temperature
RUC	Random Unit Cell
ρ	(Dynamical) electrical resistivity ($= \rho_1 + i\rho_2$)
ρ^{Drude}	(Dynamical) electrical resistivity for the Drude theory
S	Spin ($= S_x, S_y, S_z$)
S	Thermoelectric power
s	Exponent representing different scattering mechanisms
s	Sample length
$S(0)$	Scattering amplitude in the forward direction
SCE	Saturated Calomel Electrode
SEM	Scanning Electron Microscopy
SIMS	Secondary Ion Mass Spectroscopy
SOG	Spin-on Glass
sol	Solar
SP	Tin Phosphate
SSA	Styrene Sulfonic Acid
SSE	Saturated Sulfate Electrode
Σ	Irradiance function
σ	Conductivity
σ_s	Mechanical stress
T	Transmittance
t	Time

t_a	Annealing time
t_f	Time for complete deintercalation
T_{lum}	Transmittance of luminous radiation
T_{sol}	Transmittance of solar radiation
TEM	Transmission Electron Microscopy
TGA	Thermal Gravimetric Analysis
THF	Tetrahydrofuran
TO	Transverse Optical (phonon)
TSA	Toluene Sulfonic Acid
TSC	Thermally Stimulated Conductivity
τ	Temperature
τ_a	Annealing temperature
τ_g	Glass transition temperature
τ_s	Substrate temperature
θ	Angle (for diffraction or deflection)
U	Voltage
U_a	Anodization voltage
U_c	Starting voltage for cathodic reaction
U_d	Deintercalation voltage
U_i	Intercalation voltage
U_p	Polaron binding energy
UPS	Ultraviolet Photoelectron Spectroscopy
UV	Ultraviolet
v_F	Fermi velocity
VSA	Vinyl Sulfonic Acid
VTF	Vogel-Tamman-Fulcher (equation)
WE	Working Electrode
X	CIE tristimulus value
x	Ionic content (in electrochromic oxide)
x	CIE chromaticity coordinate
$\bar{x}$	Color matching function for ideal observer (red light)
x_c	"Critical" ion content for onset of metallic conduction
XANES	X-ray Absorption Near-edge Spectroscopy
XPS	X-ray Photoelectron Spectroscopy
XRD	X-ray Diffraction
XRF	X-ray Fluorescence
Y	CIE tristimulus value
Y	Young's modulus
y	Alloying fraction
y	CIE chromaticity coordinate

$\bar{y}$	Color matching function for ideal observer (green light), and photopic luminous efficiency
Z	CIE tristimulus value
Z	Impedance, and Ionic charge
z	Non-stoichiometry factor
z	CIE chromaticity coordinate
$\bar{z}$	Color matching function for ideal observer (blue light)
Z_{CPE}	Impedance of constant phase element
Z_W	Impedance of Warburg element
ZP	Zirconium Phosphate
ζ	Numerical value between zero and unity

This Page Intentionally Left Blank

References

A

1. (Anonymous), Electronics, (Jan. 18 1979), 67-68.
2. Aagard R.L., Appl. Phys. Lett. 27, 605-607 (1975).
3. Aal M.S.A. and A.H. Osman, Corrosion 36, 591-596 (1980).
4. Abbate M., H. Pen, M.T. Czyzyk, F.M.F. de Groot, J.C. Fuggle, Y.J. Ma, C.T. Chen, F. Sette, A. Fujimori, Y. Ueda and K. Kosuge, J. Electron Spectrosc. Related Phenomena 62, 185-195 (1993).
5. Abdellaoui A., L. Martin and A. Donnadieu, Phys. Stat. Sol. A 109, 455-462 (1988).
6. Abdullaev A.A. and L.D. Kislovskii, Kristallogr. 15, 988-991 (1970) [Soviet Phys. Crystallogr. 15, 860-862 (1971)].
7. Abdullaev A.A., L.D. Kislovskii and L. M. Belyaev, Opt. Spektrosk. 26, 1043-1044 (1969) [Opt. Spectrosc. 26, 256 (1969)].
8. Abe Y. and T. Fukuda, Japan. J. Appl. Phys. 32, L1167-L1168 (1993).
9. Abeles B., Appl. Solid State Sci. 6, 1-117 (1986).
10. Abeles B., Ping Sheng, M.D. Coutts and Y. Arie, Adv. Phys. 24, 407-461 (1975).
11. Abeles F., Y. Borensztein and T. Lopez-Rios, Festkörperprobleme 24, 93-117 (1984).
12. Abello L., E. Husson, Y. Repelin and G. Lucazeau, Spectrochim. Acta A 39, 641-651 (1983).
13. Abello L., E. Husson, Y. Repelin and G. Lucazeau, J. Solid State Chem. 56, 379-389 (1985).
14. Abello L. and G. Lucazeau, J. Chim. Phys. 81, 539-547 (1984).
15. Abello L. and C. Pommier, J. Chim. Phys. 80, 373-378 (1983).
16. Abraham K.M. and M. Alamgir, J. Electrochem. Soc. 137, 1657-1658 (1990).
17. Abraham K.M., J.L. Goldman and M.D. Dempsey, J. Electrochem. Soc. 128, 2493-2501 (1981).
18. Abram R.A., G.J. Rees and B.L.H. Wilson, Adv. Phys. 27, 799-892 (1978).
19. Abrantes L.M., L.M. Castillo, C. Norman and L.M. Peter, J. Electroanal. Chem. 163, 209-221 (1984).
20. Abuhadba N.M. and C.R. Aita, J. Appl. Phys. 71, 3045-3046 (1992).
21. Abu-Zeid M.E., A.E. Rakhshani, A.A. Al-Jassar and Y.A. Youssef, Phys. Stat. Sol. A 93, 613-620 (1986).
22. Ackermann R.J. and E.G. Rauh, J. Chem. Phys. 67, 2596-2601 (1963).
23. Adachi G., H. Sakaguchi, T. Shimogohri and J. Shiokawa, J. Less-Common Met. 116, L13-L14 (1986).
24. Adachi G., H. Sakaguchi, T. Shimogohri and J. Shiokawa, J. Less-Common Met. 133, 271-275 (1987).
25. Adachi S. and N. Susa, J. Electrochem. Soc. 132, 2980-2989 (1985).
26. Adams S., K.H. Ehses and G. Schwitzgebel, Synth. Met. 41-43, 3953-3956 (1991).
27. Adler D. and J. Feinleib, J. Appl. Phys. 40, 1586-1588 (1969).
28. Adler D. and J. Feinleib, Phys. Rev. B 2, 3112-3134 (1970).
29. Agashe C., B.R. Marathe, M.G. Takwale and V.G. Bhide, Thin Solid Films 164, 261-264 (1988).
30. Ageev V.N. and N.I. Ionov, Zh. Tekh. Fiz. 35, 2109-2116 (1965) [Soviet Phys. Tech. Phys. 10, 1614-1620 (1966)].
31. Agekyan V.T., Phys. Stat. Sol. A 43, 11-42 (1977).
32. Agnihotry S.A., S.S. Bawa, A.M. Biradar, C.P. Sharma and S. Chandra, Proc. Soc. Photo-Opt. Instrum. Engr. 428, 45-50 (1983).
33. Agnihotry S.A., K.K. Saini and S. Chandra, Indian J. Pure Appl. Phys. 24, 19-33 (1986).
34. Agnihotry S.A., K.K. Saini and S. Chandra, Indian J. Pure Appl. Phys. 24, 34-40 (1986).
35. Agnihotry S.A., K.K. Saini, T.K. Saxena and S. Chandra, Thin Solid Films 141, 183-192 (1986).

36. Agrawal A., J.P. Cronin and R. Zhang, Solar Energy Mater. Solar Cells 31, 9-21 (1993).
37. Agrawal A., H.R. Habibi, R.K. Agrawal, J.P. Cronin, D.M. Roberts, R'S. Caron-Popowich and C.M. Lampert, Thin Solid Films 221,239-253 (1992).
38. Agrawal A. and M. Habibi, Thin Solid Films 169, 257-270 (1989).
39. Aikawa Y., N. Nishimura and M. Sukigara, Denki Kagaki 52, 853-8543 (1984).
40. Aita C.R., Mater. Sci. Technol. 8, 666-672 (1992).
41. Aita C.R. and M.L. Kao, J. Vac. Sci. Technol. A 5, 2714-2717 (1987).
42. Aita C.R., C.-K. Kwok and M.L. Kao, Mater. Res. Soc. Symp. Proc. 82, 435-439 (1987).
43. Aita C.R., L.-J. Liou, C.-K. Kwok, R.C. Lee and E. Kolawa, Thin Solid Films 193-194, 18-26 (1990).
44. Aita C.R., Y.-L. Liu, M.L. Kao and S.D. Hansen, J. Appl. Phys. 60, 749-753 (1986).
45. Aka G., B. Dunn, J. Foreman and G.C. Farrington, Solid State Ionics 40-41, 83-86 (1990).
46. Akahane T., K.R. Hoffman, T. Chiba and S. Berko, Solid State Commun. 54, 823-826 (1985).
47. Akhtar M., R.M. Paiste and H.A. Weakliem, J. Electrochem. Soc. 135, 1597-1598 (1988).
48. Akhtar M. and H.A. Weakliem, in Electrochromic Materials, edited by M.K. Carpenter and D.A. Corrigan (The Electrochem. Soc., Pennington, USA, 1990), Proc. Vol. 90-2, pp. 232-236.
49. Akhtar M., H.A. Weakliem, R.M. Paiste and K. Gaughan, Synth. Metals 26, 203-208 (1988).
50. Akram H., M. Kitao and S. Yamada, J. Appl. Phys. 66, 4364-4367 (1989).
51. Akram H., H. Tatsuoka, M. Kitao and S. Yamada, J. Appl. Phys. 62, 2039-2043 (1987).
52. Aladjem A., D.G. Brandon, J. Yahalom and J. Zahavi, Electrochim. Acta 15, 663-671 (1970).
53. Alamgir M. and K.M. Abraham, J. Electrochem. Soc. 140, L96-L97 (1993).
54. Alamgir M., R.D. Moulton and K.M. Abraham, Electrochim. Acta 36, 773-782 (1991).
55. Albani O.A., J.O.Zerbino, J.R. Vilche and A.J. Arvia, Electrochim. Acta 31, 1403-1411 (1986).
56. Alberti G., Pontif. Acad. Sci. Scripta Varia 40, 629-669 (1976).
57. Alberti G., M. Casciola, U. Constantino and M. Leonardi, Solid State Ionics 14, 289-295 (1984).
58. Alberti G., M. Casciola, U. Constantino, G. Levi and G. Ricciardi, J. Inorg. Nucl. Chem. 40, 533-537 (1978).
59. Albinsson I., B.E. Mellander and J.R. Stevens, Polymer 32, 2712-2715 (1991).
60. Aldebert P., N. Baffier, N. Gharbi and J. Livage, Mater, Res. Bull. 16, 669-676 (1981).
61. Aldebert P., N. Baffier, N. Gharbi and J. Livage, Mater. Res. Bull. 16, 949-955 (1981).
62. Aldebert P., H.W. Haesslin, N. Baffier and J. Livage, J. Colloid Interface Sci. 98, 478-483 (1984).
63. Aldebert P., H.W. Haesslin, N. Baffier and J. Livage, J. Colloid Interface Sci. 98, 484-488 (1984).
64. Aldebert P. and V. Paul-Boncour, Mater. Res. Bull. 18, 1263-1274 (1983).
65. Al-Dhhan Z.T., C.A. Hogarth and N. Riddleston, Phys. Stat. Sol. B 145, 145-149 (1988).
66. Aleshina L.A., L.Ya. Berezin, S.V. Glazkova, V.P. Malinenko and A.D. Fofanov, Fiz. Tverd. Tela 32, 2111-2117 (1990) [Soviet Phys. Solid State 32, 1226-1229 (1990)].
67. Aleshina L.A., A.D. Fofanov and O.N. Shivrin, Dokl. Akad. Nauk. SSSR 267, 596-598 (1982) [Soviet Phys. Dokl. 27, 945-946 (1982)].
68. Aleshina L.A., V.P. Malinenko, G.B. Stefanovich and F.A. Chudnovskii, Fiz. Tverd. Tela 30, 914-916 (1988) [Soviet Phys. Solid State 30, 351-352 (1988)].
69. Alexander L.E., I.R. Beattie, A. Bukovszky, P.J. Jones, C.J. Marsden and G.J. Van Schalkwyk, J. Chem. Soc. Dalton Trans. (1974), 81-84.
70. Al-Ismail S.A.Y., K. Arshak and C.A. Hogarth, Phys. Stat. Sol. A 89, 363-374 (1985).
71. Al-Jumaily G.A. and S.M. Edlou, Thin Solid Films 209, 223-229 (1992).
72. Allara D.L., A.F. Hebard, F.J. Padden, R.G. Nuzzo and D.R. Falcone, J. Vac. Sci. Technol. A 1, 376-382 (1983).
73. Allen G.C. and J.M. Dyke, Chem. Phys. Lett. 37, 391-395 (1976).
74. Allen G.C. and N.S. Hush, in Progress in Inorganic Chemistry, edited by F.A. Cotton (Interscience, New York, 1967), Vol. 8, pp. 357-389.
75. Allersma T., R. Hakim, T.N. Kennedy and J.D. Mackenzie, J. Chem. Phys. 46, 154-160 (1967).
76. Alquié-Redon A.M., A. Aldaz and C. Lamy, Surf. Sci. 49, 627-644 (1975).
77. Al-Robaee M.S., M.G. Krishna, K.N. Rao and S. Mohan, J. Vac. Sci. Technol. A 9, 3048-3053 (1991).
78. Al-Robaee M.S., K.N. Rao and S. Mohan, J. Appl. Phys. 71, 2380-2386 (1992).

79. Amarilla J.M., B. Casal, J.C. Galvan and E. Ruiz-Hitsky, Chem. Mater. 4, 62-67 (1992).
80. Amarilla J.M., B. Casal and E. Ruiz-Hitsky, Mater. Lett (1989), 132-136.
81. Amarilla J.M., B. Casal and E. Ruiz-Hitsky, J. Solid State Chem. 99, 258-266 (1992).
82. Amatucci G.G., A. Safari, F.K. Shokoohi and B.J. Wilkens, Solid State Ionics 60, 357-365 (1993).
83. Ambegaokar V., S. Cochran and J. Kurkijärvi, Phys. Rev. B 8, 3682-3688 (1973).
84. Ambegaokar V., B.I. Halperin and J.S. Langer, Phys. Rev. B 4, 2612-2620 (1971).
85. Ambrose J., R.G. Barradas and D.W. Shoesmith, Electroanal. Chem. Interfacial Electrochem. 47, 47-64 (1973).
86. Ambrose J., R.G. Barradas and D.W. Shoesmith, Electroanal. Chem. Interfacial Electrochem. 47, 65-80 (1973).
87. Ampe B., J.M. Le Roy, D. Thomas and G. Tridot, Rev. Chim. Minérale 5, 801-812 (1968).
88. Ananth M.V. and K. Dakshinamurthi, J. Power Sources 40, 355-360 (1992).
89. Andersen E.K., I.G.K. Andersen, C.K. Møller, K.E. Simonsen and E. Skou, Solid State Ionics 7, 301-306 (1982).
90. Anderson J.S., J. Chem. Soc. Dalton Trans. (1973), 1107-1115.
91. Anderson J.S., J. Phys. (Paris) 38, C7 17-C7 27 (1977).
92. Anderson O., Vacuum 41, 1700-1702 (1990).
93. Anderson O. and K. Bange, Fresenius J. Anal. Chem. 341, 74-78 (1991).
94. Anderson P.W., Phys. Rev. 109, 1492-1505 (1958).
95. Andersson A.M., W. Estrada, C.G. Granqvist, A. Gorenstein and F. Decker, Proc. Soc. Photo-Opt. Instrum. Engr. 1272, 96-110 (1990).
96. Andersson A.M., C.G. Granqvist and J.R. Stevens, Proc. Soc. Photo-Opt. Instrum. Engr. 1016, 41-49 (1988).
97. Andersson A.M., C.G. Granqvist and J.R. Stevens, Appl. Opt. 28, 3295-3302 (1989).
98. Andersson A.M., C.G. Granqvist and J.R. Stevens, in Large-area Chromogenics: Materials and Devices for Transmittance Control, edited by C.M. Lampert and C.G. Granqvist (SPIE Opt. Engr. Press, Bellingham, 1990), Vol. IS4, pp. 471-481.
99. Andersson A.M., A. Talledo, C.G. Granqvist and J.R. Stevens, in Electrochromic Materials, edited by M.K. Carpenter and D.A. Corrigan (The Electrochem. Soc., Pennington, 1990), Vol. 90-2, pp. 261-273.
100. Andersson G. and A. Magnéli, Acta Chem. Scand. 4, 793-797 (1950).
101. Andersson K.E., M.K. Wahlström and A. Roos, Thin Solid Films 214, 213-218 (1992).
102. Andersson S., Acta Chem. Scand. 19, 1371-1375 (1965).
103. Andersson S., Z. Allg. Anorg. Chem. 351, 106-112 (1967).
104. Andersson S. and L. Jahnberg, Ark. Kemi 21, 413-426 (1963).
105. Andersson T.G., J. Phys. D 9, 973-985 (1976).
106. Ando E., K. Kawakami, K. Matsuhiro and Y. Masuda, Displays 6, 3-10 (1985).
107. Andrew P.L. and A.A. Haasz, J. Appl. Phys. 72, 2749-2757 (1992).
108. Andrukaitis E., E.A. Bishenden, P.W.M. Jacobs and J.W. Lorimer, J. Power Sources 26, 475-482 (1989).
109. Andrukaitis E., P.W.M. Jacobs and J.W. Lorimer, Solid State Ionics 27, 19-30 (1988).
110. Angardi M.A. and K. Nallamshetty, J. Mater. Sci. Lett. 8, 391-394 (1989).
111. Angelov S., C. Friebel, E. Zhecheva and R. Stoyanova, J. Phys. Chem. Solids 53, 443-448 (1992).
112. Ansermet J.-Ph., C.P. Slichter and J.H. Sinfelt, Progr. NMR Spectrosc. 22, 401-421 (1990).
113. Ansimov V.I., M.A. Korotin and I.V. Afanasyev, Physica (Utrecht) C 161, 59-65 (1989).
114. Antaya M., K. Cearns, J.S. Preston, J.M. Reimers and J.R. Dahn (1993), to be published.
115. Antaya M., J.R. Dahn, J.S. Preston, E. Rossen and J.N. Reimers, J. Electrochem. Soc. 140, 575-578 (1993).
116. Antonyuk A.D., E.Ya. Gol'dbberg, A.G. Dyachenko, N.P. Lavrishchev and A.D. Khromov, Fiz. Prot. Prib. Elektron. Tekh. (1980), 69-73.
117. Antropov A.E., O.F. Afonin, A.I. Gavrilyuk, B.P. Zakharchenya, F.A. Chudnovskii and N.Kh. Shaver, Pis'ma Zh. Tekh. Fiz. 4, 561-564 (1978) [Soviet Tech. Phys. Lett. 4, 224-225 (1978)].
118. Anwar M. and C.A. Hogarth, Phys. Stat. Sol. A 109, 469-478 (1988).
119. Anwar M. and C.A. Hogarth, Phys. Stat. Sol. A 114, 215-223 (1989).
120. Anwar M. and C.A. Hogarth, J. Mater. Sci. 25, 4918-4928 (1990).

121. Anwar M,, C.A. Hogarth and R. Bulpett, J. Mater. Sci. 24, 3087-3090 (1989).
122. Anwar M., C.A. Hogarth and R. Bulpett, J. Mater. Sci. 25, 1784-1788 (1990).
123. Anwar M., C.A. Hogarth and K.A.K. Lott, J. Mater. Sci. 24, 1660-1664 (1989).
124. Anwar M., C.A. Hogarth and C.R. Theocharis, J. Mater. Sci. 24, 2387-2390 (1989).
125. Anwar M., C.A. Hogarth and C.R. Theocharis, J. Mater. Sci. 25, 1108-1111 (1990).
126. Anwar M., G.A. Khan, C.A. Hogarth and C.R. Theocharis, J. Mater. Sci. 24, 4409-4413 (1989).
127. Aoki K., T. Miyamoto and Y. Ohsawa, Bull. Chem. Soc. Japan 62, 1658-1659 (1989).
128. Appel J., in Solid State Physics, edited by F. Seitz, D. Turnbull and H. Ehrenreich (Academic, New York, 1968), Vol. 21, pp. 193-391.
129. Apsley N.and P.H. Hughes, Philos. Mag. 30, 963-972 (1974).
130. Arai M., S. Hayashi, K. Yamamoto and S.S. Kim, Solid State Commun. 75, 613-616 (1990).
131. Araki B., C. Mailhé, N. Baffier, J. Livage and J. Vedel, Solid State Ionics 9-10, 439-444 (1983).
132. Arbaoui A., J. Dumas, E.B. Lopes and M. Almeida, Solid State Commun. 81, 567-570 (1992).
133. Arbizziani C., M. Mastragostino, S. Passerini, R. Pileggi and B. Scrosati, Electrochim. Acta 36, 837-840 (1991).
134. Ardizzone S., A. Carugati and S. Trasatti, J. Electroanal. Chem. 126, 287-292 (1981).
135. Arkhipenko D.K., Ya. S. Bobovich and M. Ya. Tsenter, Zh. Prikl. Spektrosk. 41, 304-307 (1984).
136. Armand M.B., Solid State Ionics 9-10, 745-754 (1983).
137. Armand M.B., Ann. Rev. Mater. Sci. 16, 245-261 (1986).
138. Armand M.B., in Polymer Electrolyte Reviews - 1, edited by J.R. MacCallum and C.A. Vincent (Elsevier Appl. Sci., London, 1987), pp. 1-22.
139. Armand M.B., J.M. Chabagno and M. Duclot, in Fast Ion Transport in Solids, edited by P. Vashishta, J.N. Mundy and G. Shenoy (North-Holland, Amsterdam, 1979), pp. 131-136.
140. Armand M.B., F. Dalard, D. Deroo and C. Mouliom, Solid State Ionics 15, 205-210 (1985).
141. Armand M.B., D. Deroo and D. Pedone, in Solid State Ionic Devices, edited by B.V.R. Chowdari and S. Radhakrishna (World Scientific, Singapore, 1988), pp. 515-520.
142. Armand M.B., W. Gorecki and A. Andréani, in Second International Symposium on Polymer Electrolytes, edited by B. Scrosati (Elsevier Appl. Sci., London, 1990), pp. 81-89.
143. Armstrong R.D. and E.A. Charles, J. Power Sources 25, 89-97 (1989).
144. Armstrong R.D. and M.D. Clarke, Electrochim. Acta 29, 1443-1446 (1984).
145. Armstrong R.D., A.K. Sood and M. Moore, J. Appl. Electrochem. 15, 603-607 (1985).
146. Arnoldussen T.C., J. Electrochem. Soc. 123, 527-531 (1976).
147. Arnoldussen T.C., J. Electrochem. Soc. 128, 117-123 (1981).
148. Arntz F.O., R.B. Goldner, B. Morel and T.E. Haas, Proc. Soc. Photo-Opt. Instrum. Engr. 1149, 40-45 (1989).
149. Arntz F.O., R.B. Goldner, B. Morel, T.E. Hass and K.K. Wong, J. Appl. Phys. 67, 3177-3179 (1990).
150. Arora M.R. and J. Childs, J. Electrochem. Soc. 123, 222-223 (1976).
151. Arora M.R. and R. Kelly, J. Electrochem. Soc. 119, 270-274 (1972).
152. Arora M.R. and R. Kelly, J. Electrochem. Soc. 120, 128-133 (1973).
153. Arora M.R. and R. Kelly, J. Electrochem. Soc. 124, 1493-1499 (1977).
154. Arora M.R. and R. Kelly, J. Mater. Sci. 12, 1673-1684 (1977).
155. Arsov Lj.D., C. Kormann and W. Plieth, J. Electrochem. Soc. 138, 2964-2970 (1991).
156. Arsov Lj.D., C. Kormann and W. Plieth, J. Raman Spectrosc. 22, 573-575 (1991).
157. Asai T., S. Sugimoto, S. Kawai, S. Okada and J.-I. Yamaki, Mater. Res. Bull. 24, 75-82 (1989).
158. Ashrit P.V., G. Bader, F.E. Girouard, T. Richard and V.-V. Truong, J. Appl. Phys. 70, 3797-3801 (1991).
159. Ashrit P.V., G. Bader, F.E. Girouard and V.-V. Truong, J. Appl. Phys. 65, 1356-1357 (1989).
160. Ashrit P.V., G. Bader, F.E. Girouard and V.-V. Truong, Proc. Soc. Photo-Opt. Instrum. Engr. 1149, 7-19 (1989).
161. Ashrit P.V., G. Bader, F.E. Girouard and V.-V. Truong, in Electrochromic Materials, edited by M.K. Carpenter and D.A. Corrigan (The Electrochem. Soc., Pennington, 1990), Proc. Vol. 90-2, pp. 45-53.
162. Ashrit P.V., G. Bader, F.E. Girouard and V.-V. Truong, Proc. Soc. Photo-Opt. Instrum. Engr. 1401, 119-129 (1990).

163. Ashrit P.V., G. Bader, F.E. Girouard, V.-V. Truong and T. Yamaguchi, Physica (Utrecht) A 157, 333-338 (1989).
164. Ashrit P.V., S. Badilescu, F.E. Girouard and V.-V. Truong, Appl. Opt. 28, 420-422 (1989).
165. Ashrit P.V., K. Benaissa, G. Bader, F.E. Girouard and V.-V. Truong, Proc. Soc. Photo-Opt. Instrum. Engr. 1728, 232-240 (1992).
166. Ashrit P.V., K. Benaissa, G. Bader, F.E. Girouard and V.-V. Truong, Solid State Ionics 59, 47-57 (1993).
167. Ashrit P.V., F.E. Girouard, V.-V. Truong and G. Bader, Proc. Soc. Photo-Opt. Instrum. Engr. 562, 53-60 (1985).
168. Ashrit P.V., D.J. Pelletier, F.E. Girouard and V.-V. Truong, J. Appl. Phys. 58, 564-567 (1985).
169. Aspnes D.E., Thin Solid Films 89, 249-262 (1982).
170. ASTM Standards, Annual Book, Vol. 15.03, pp. 316-320 (1991).
171. Ataka T., T. Sakuhara, M. Sigeno and K. Iwasa, Japan Display 1983, pp. 384-387.
172. Atanassov G., R. Thielsch and D. Popov, Thin Solid Films 223, 288-292 (1993).
173. Atlung S. and T. Jacobsen, Electrochim. Acta 26, 1447-1456 (1981).
174. Auborn J.J. and Y.L. Barberio, J. Electrochem. Soc. 134, 638-641 (1987).
175. Audiere J.P. and A. Madi, Thin Solid Films 101, L29-L31 (1983).
176. Audiere J.P., A. Madi and J.C. Grenet, J. Mater. Sci. 17, 2973-2978 (1982).
177. Augustynski J., M. Koudelka, J. Sanchez and B.E. Conway, J. Electroanal. Chem. 160, 233-248 (1984).
178. Aurian-Blajeni B., X. Beebe, R.D. Rauh and T.L. Rose, Electrochim. Acta 34, 795-802 (1989).
179. Austin I.G., B.D. Clay and C.E. Turner, J. Phys. C 1, 1418-1434 (1968).
180. Austin I.G., B.D. Clay, C.E. Turner and A.J. Springthorpe, Solid State Commun. 6, 53-56 (1968).
181. Austin I.G. and N.F. Mott, Adv. Phys. 18, 41-102 (1969).
182. Aveline A. and I.R. Bonilla, Solar Energy Mater. 5, 211-220 (1981).
183. Avena M.J., O.R. Camara and C.P. De Pauli, Colloids Surf. 69, 217-228 (1993).
184. Aveston J., E.W. Anacker and J.S. Johnson, Inorg. Chem. 3, 735-746 (1964).
185. Avramov L.K., Thermochim. Acta 10, 409-414 (1974).
186. Azarbayejani G.H. and A.L. Merlo, Phys. Rev. 137, A489-A490 (1965).
187. Azens A., A.A. Lavrentiev and U. Kanders, Surf. Sci. USSR (1990) (12), 74-78.
188. Azens A., G. Ramans, U. Kanders and A. Lavrentyev, Vacuum 43, 944-945 (1992).
189. Azens A., G. Romanovskis and U. Kanders, J. Phys. C 4, 5053-5060 (1992).
190. Azens A., A. Talledo, A.M. Andersson, G. A. Niklasson, B. Stjerna, C.G. Granqvist and J.R. Stevens, Proc. Soc. Photo-Opt. Instrum. Engr. 1728, 103-117 (1992).
191. Azumi K., T. Ohtsuka and N. Sato, Trans. Japan Inst. Met. 27, 382-392 (1986).
192. Azumi K., T. Ohtsuka and N. Sato, J. Electrochem. Soc. 134, 1352-1357 (1987).

B

193. Baba M. and T. Ikeda, Japan. J. Appl. Phys. 20, L149-L152 (1981).
194. Baba M., K. Ohta and T. Ikeda, Japan. J. Appl. Phys. 30, 2581-2584 (1991).
195. Baba M., M. Okamoto, K. Kumagai and T. Ikeda, Japan. J. Appl. Phys. 31, 947-948 (1992).
196. Baba N., Nihon Metal. Acad. 27, 443-451 (1988).
197. Baba N., S. Morisaki and N. Nishiyama, Japan. J. Appl. Phys. 23, L638-L639 (1984).
198. Baba N. and S. Watanabe, J. Metal Finishing Soc. Japan 35, 498-506 (1984).
199. Baba N. and T. Yoshino, J. Appl. Electrochem. 12, 607-612 (1982).
200. Baba N. and T. Yoshino, Rept. Asahi Glass Found. Ind. Technol. 40, 91-97 (1982).
201. Baba N., T. Yoshino and J. Fukawa, Japan Display 1986, pp. 380-382.
202. Baba N., T. Yoshino and M. Higashida, Memoirs Faculty Techn. Tokyo Metropolitan Univ. 42, 4641-4647 (1992).
203. Baba N., T. Yoshino and T. Kojima, Asahi Garasu Zaidan Kenkyuhokoku 60, 215-220 (1992).
204. Baba N., T. Yoshino, S. Morisaki and H. Masuda, Memoirs Faculty Techn. Tokyo Metropolitan Univ. 40, 4339-4347 (1990).

205. Baba N., T. Yoshino and K. Schwochau, Memoirs Faculty Techn. Tokyo Metropolitan Univ. 32, 3207-3220 (1982).
206. Babick L.V., Yu.V. Plyuto, E. Stoh, M.M. Aleksankina and A.A. Shuiko, Dokl. Akad. Nauk SSSR 319, 1155-1158 (1991).
207. Babinec S.J., Solar Energy Mater. Solar Cells 25, 269-291 (1992).
208. Babkin E.V., A.A. Charyev, A.P. Dolgarev and H.O. Urinov, Thin Solid Films 150, 11-14 (1987).
209. Babonneau F., P. Barboux, F.A. Josien and J. Livage, J. Chim. Phys. 82, 761-766 (1985).
210. Babulanam S.M., T.S. Eriksson, G.A. Niklasson and C.G. Granqvist, Solar Energy Mater. 16, 347-363 (1987).
211. Babulanam S.M., W. Estrada, M.O. Hakim, S. Yatsuya, A.M. Andersson, J.R. Stevens, J.S.E.M. Svensson and C.G. Granqvist, Proc. Soc. Photo-Opt. Instrum. Engr. 823, 64-71 (1987).
212. Bach S., M. Henry, N. Baffier and J. Livage, J. Solid State Chem. 88, 325-333 (1990).
213. Bach S., J.P. Pereira-Ramos, N. Baffier and R. Messina, J. Electrochem. Soc. 137, 1042-1048 (1990).
214. Bach S., J.P. Perreira-Ramos, N. Baffier and R. Messina, Electrochim. Acta 36, 1595-1603 (1991).
215. Bach S., J.P. Perreira-Ramos, N. Baffier and R. Messina, Electrochim. Acta 37, 1301-1305 (1992).
216. Bachmann H.G., F.R. Ahmed and W.H. Barnes, Z. Kristallogr. 115, 110-131 (1961).
217. Baddour R., J.P. Pereira-Ramos, R. Messina and J. Perichon, J. Electroanal. Chem. 277, 359-366 (1990).
218. Baddour R., J.P. Pereira-Ramos, R. Messina and J. Perichon, J. Electroanal. Chem. 314, 81-101 (1991).
219. Badilescu S., P.V. Ashrit, F.E. Girouard and V.-V. Truong, J. Electrochem. Soc. 136, 3599-3602 (1989).
220. Badilescu S., P.V. Ashrit and V.-V. Truong, Appl. Phys. Lett. 52, 1551-1553 (1988).
221. Badilescu S., K. Boufker, P.V. Ashrit, F.E. Girouard and V.-V. Truong, Appl. Spectrosc. 47, 749-752 (1993).
222. Badot J.C. and N. Baffier, Solid State Ionics 38, 143-148 (1990).
223. Badot J.C. and N. Baffier, J. Solid State Chem. 93, 53-62 (1991).
224. Badot J.C. and N. Baffier, J. Mater. Chem. 2, 1167-1174 (1992).
225. Badot J.C., A. Fourrier-Lamer and N. Baffier, J. Phys. (Paris) 46, 2107-2115 (1985).
226. Badot J.C., D. Gourier, B. Bourdeau, N. Baffier and A. Tabuteau, J. Solid State Chem. 92, 8-17 (1991).
227. Badyal J.P.S., X. Zhang and R. Lambert, Surf. Sci. Lett. 225, L15-L19 (1990).
228. Baez V.B., J.E. Graves and D. Pletcher, J. Electroanal. Chem. 340, 273-286 (1992).
229. Baffier N. and S. Bach, Ann. Chim. France 16, 467-471 (1991).
230. Baffier N., L. Znaidi and J.-C. Badot, J. Chem. Soc. Faraday Trans. 86, 2623-2628 (1990).
231. Baffier N., L. Znaidi and M. Huber, Mater. Res. Bull. 25, 705-713 (1990).
232. Bagouin M., D. Guérard and A. Hérold, Comptes Rendues Acad. Sci. Paris, Sér. C, 262, 557-559 (1966).
233. Bagus P.S., G. Pacchioni and F. Parmigiani, Chem. Phys. Lett. 207, 569-574 (1993).
234. Bai P., G.-R. Yang and T.-M. Lu, Appl. Phys. Lett. 56, 198-200 (1990).
235. Bailey G.C., Catalysis Rev. 3, 37-60 (1969).
236. Bailey J.K., T. Nagase, G.A. Pozarnsky and M.L. McCartney, Mater. Res. Soc. Symp. Proc. 180, 759-764 (1990).
237. Bailey J.K., G.A. Pozarnsky and M.L. McCartney, J. Mater. Res. 7, 2530-2537 (1992).
238. Bajars G., Ya. A. Pitkevich, A. Lusis, E.V. Pentyush, J. Benders and V. Bets, Electrokhim. 25, 336-342 (1989) [Soviet Electrochem. 25, 292-298 (1989)].
239. Bajars G., Ya. A. Pitkevich, J. Straumens and A. Lusis, Elektrokhim. 25, 833-836 (1989) [Soviet Electrochem. 25, 749-752 (1989)].
240. Balachandran U. and N.G. Eror, J. Less-Common Met. 84, 291-299 (1982).
241. Balachandran U. and N.G. Eror, Mater. Res. Bull. 17, 151-160 (1982).
242. Balberg I., B. Abeles and Y. Arie, Thin Solid Films 24, 307-310 (1974).
243. Balberg I. and S. Trokman, J. Appl. Phys. 46, 2111-2119 (1975).
244. Balerna A., E. Bernieri, E. Burattini, A. Kuzmin, A. Lusis, J. Purans and P. Cikmach, Nucl. Instr. Meth. Phys. Res. A 308, 234-239 (1991).
245. Balerna A., E. Bernieri, E. Burattini, A. Kuzmin, A. Lusis, J. Purans and P. Cikmach, Nucl. Instr. Meth. Phys. Res. A 308, 240-242 (1991).

246. Balerna A., E. Bernieri, A. Kuzmin and J. Purans, in Proc. Second European Conference on Progress in X-ray Synchrotron Radiation Research, edited by A. Balerna, E. Bernieri and S. Mobilio (SIF, Bologna, 1990), pp. 679-682.
247. Bali K., L.B. Kiss, T. Szörényi, M.I. Török and I. Hevesi, J. Phys. (Paris) 48, 431-434 (1987).
248. Bali K., L. Michailovits and I. Hevesi, Acta Phys. Chem. (Szeged) 25, 43-45 (1979).
249. Balkanski M., Phys. World (Nov. 1990), 29-33.
250. Ball R. and M. Blunt, J. Phys. A 21, 197-204 (1988).
251. Ballhausen C.J. and H.B. Gray, Inorg. Chem. 1, 111-122 (1962).
252. Banfield J.F., D.R. Veblen and D.J. Smith, Am. Mineralogist 76, 343-353 (1991).
253. Bange K., F.G.K. Baucke and B. Metz, Proc. Soc. Photo-Opt. Instrum. Engr. 1016, 170-175 (1988).
254. Bange K. and T. Gambke, Adv. Mater. 2, 10-16 (1990).
255. Bange K., R. Keller, W. Wagner and F. Rauch, Proc. Soc. Photo-Opt. Instrum. Engr. 1016, 50-56 (1988).
256. Bange K., U. Martens, A. Nemetz and A. Temmink, in Electrochromic Materials, edited by M.K. Carpenter and D.A. Corrigan (The Electrochem. Soc., Pennington, 1990), Proc. Vol. 90-2, pp. 334-348.
257. Bange K., C.R. Ottermann, O. Anderson, U. Jeschkowski, M. Laube and R. Feile, Thin Solid Films 197, 279-285 (1991).
258. Bange K., C. Ottermann, W. Wagner and F. Rauch, in Large-area Chromogenics: Materials and Devices for Transmittance Control, edited by C.M. Lampert and C.G. Granqvist (SPIE Opt. Engr. Press, Bellingham, 1990), Vol. 1S4, pp. 122-128.
259. Bannister D.J., G.R. Davies, I.M. Ward and J.E. McIntyre, Polymer 25, 1600-1602 (1984).
260. Baraldi P. and G. Davolio, Mater. Chem. Phys. 21, 143-154 (1989).
261. Barbero C., M.C. Miras and R. Kötz, Electrochim. Acta 37, 429-437 (1992).
262. Barboux P., N. Baffier, R. Morineau and J. Livage, Solid State Ionics 9-10, 1073-1080 (1983).
263. Barboux P., D. Gourier and J. Livage, Colloids Surf. 11, 119-128 (1984).
264. Barboux P., R. Morineau and J. Livage, Solid State Ionics 27, 221-225 (1988).
265. Barboux P., J.M. Tarascon and F.K. Shokoohi, J. Solid State Chem. 94, 185-196 (1991).
266. Barclay D.J., in Electrochromism and Electrochromic Displays, edited by B. Scrosati (Univ. Rome, 1982), pp. 63-73.
267. Bard A.J., editor, Encyclopedia of Electrochemistry of the Elements (Marcel Dekker, New York, 1975), Vol. 3, pp. 349-364.
268. Bard A.J. and L.R. Faulkner, Electrochemical Methods (Wiley, New York, 1980).
269. Bardwell J.A., B. MacDougall and M.J. Graham, J. Electrochem. Soc. 135, 413-418 (1988).
270. Barna G.G., J. Electronic Mater. 8, 153-173 (1979).
271. Barr T.L., J. Phys. Chem. 82, 1801-1810 (1978).
272. Barraclough C.-G., J. Lewis and R.S. Nyholm, J. Chem. Soc. (1959), 3552-3555.
273. Barral G., J.P. Diard and C. Montella, Electrochim. Acta 29, 239-246 (1984).
274. Bartl H., H. Bode, G. Sterr and J. Witte, Electrochem. Acta 16, 615-621 (1971).
275. Barton R.T., P.J. Mitchell and N.A. Hampson, Surf. Coatings Technol. 28, 1-9 (1986).
276. Bates J.B. and Y.T. Chu, Solid State Ionics 28-30, 1388-1395 (1988).
277. Bates J.B., Y.T. Chu and W.T. Stribling, Phys. Rev. Lett. 60, 627-630 (1988).
278. Bates J.B., N.J. Dudney, G.R. Gruzalski, R.A. Zuhr, A. Choudhury, C.F. Luck and J.D. Robertson, Solid State Ionics 53-56, 647-654 (1992).
279. Bates J.B., N.J. Dudney, C.F. Luck and L. Klatt, Ceram. Trans. 11, 35-45 (1990).
280. Bates J.B., N.J. Dudney, C.F. Luck, B.C. Sales, R.A. Zuhr and J.D. Robertson, J. Am. Ceram. Soc. 76, 929-943 (1993).
281. Battaglin G., A. De Battisti, A. Barbieri, A. Giatti and A. Marchi, Surf. Sci. 251/252, 73-77 (1991).
282. Baucke F.G.K., Schott Information (1983)(1), 11-17.
283. Baucke F.G.K., in Glass Current Issues, edited by A.F. Wright and J. Dupuy (Nijhoff, Dordrecht, 1985), pp. 506-518.
284. Baucke F.G.K., Dechema-Monogr. 102, 483-496 (1986).
285. Baucke F.G.K., Feinwerktechnik Messtechnik 94, 25-28 (1986).
286. Baucke F.G.K., Solar Energy Mater. 16, 67-77 (1987).

287. Baucke F.G.K., in Electrochromic Materials, edited by M.K. Carpenter and D.A. Corrigan (The Electrochem. Soc., Pennington, 1990), Proc. Vol. 90-2, pp. 298-311.
288. Baucke F.G.K., in Large-area Chromogenics: Materials and Devices for Transmittance Control, edited by C.M. Lampert and C.G. Granqvist (SPIE Opt. Engr. Press, Bellingham, 1990), Vol. IS4, pp. 518-538.
289. Baucke F.G.K., Mater. Sci. Engr. B 10, 285-292 (1991).
290. Baucke F.G.K., K. Bange and T. Gambke, Displays 9, 179-187 (1988).
291. Baucke F.G.K. and J.A. Duffy, Chem. Brittain (1985), 643-653.
292. Baucke F.G.K., J.A. Duffy and R.I. Smith, Thin Solid Films 186, 47-51 (1990).
293. Baucke F.G.K., J.A. Duffy and P.R. Woodruff, Thin Solid Films 148, L59-L61 (1987).
294. Baucke F.G.K., B. Metz and J. Zauner, Phys. unserer Zeit 18 (1), 21-28 (1987).
295. Baudry P., M.A. Aegerter, D. Deroo and B. Valla, in Electrochromic Materials, edited by M.K. Carpenter and D.A. Corrigan (The Electrochem. Soc., Pennington, 1990), Proc. Vol. 90-2, pp. 274-287.
296. Baudry P., M.A. Aegerter, D. Deroo and B. Valla, J. Electrochem. Soc. 138, 460-465 (1991).
297. Baudry P., A.C.M. Rodriguez, M.A. Aegerter and L.O. Bulhoes, J. Non-Cryst. Solids 121, 319-322 (1990).
298. Bauer J., D.M. Buss, H.-J. Harms and O. Glemser, J. Electrochem. Soc. 137, 173-178 (1990).
299. Baumeister P.W., Phys. Rev. 121, 359-362 (1961).
300. Bayard M.L. and G.C. Barna, J. Electroanal. Chem. 91, 201-209 (1978).
301. Bayard M., M. Pouchard, P. Hagenmuller and A. Wold, J. Solid State Chem. 12, 41-50 (1975).
302. Bayard M.L.F., T.G. Reynolds, M. Vlasse, H.L. McKinzie, A.J. Arnott and A. Wold, J. Solid State Chem. 3, 484-489 (1971).
303. Beard B.C. and P.N. Ross, Jr. J. Electrochem. Soc. 137, 3368-3374 (1990).
304. Beattie I.R. and T.R. Gilson, J. Chem. Soc. A (1969), 2322-2327.
305. Beattie I.R., K.M.S. Livingstone, D.J. Reynolds and G.A. Ozin, J. Chem. Soc. A (1970), 1210-1216.
306. Becker K.D. and T. He, Ber. Bunsenges. Phys. Chem. 96, 1886-1889 (1992).
307. Beckstead D.J., G.M. Pepin and J.L. Ord, J. Electrochem. Soc. 136, 362-368 (1989).
308. Bedeaux D. and J. Vlieger, Thin Solid Films 102, 265-281 (1983).
309. Beden B. and A. Bewick, Electrochim. Acta 33, 1695-1698 (1988).
310. Beden B. and C. Lamy, in Spectroelectrochemistry: Theory and Practice, edited by R.J. Gale (Plenum, New York, 1988), pp. 189-261.
311. Beebe X. and T.L. Rose, IEEE Trans. Biomed. Engr. BME-35, 494-495 (1988).
312. Beensh-Marchwicka G., L. Krol-Stepniewska and M. Slaby, Thin Solid Films 88, 33-39 (1982).
313. Begishev A.R., G.B. Galiev. A.S. Ignatev, V.G. Mokerov and V.G. Poshin, Fiz. Tverd. Tela 20, 1643-1650 (1978) [Soviet Phys. Solid State 20, 951-955 (1978)].
314. Behl W.K. and J.E. Toni, J. Electroanal. Chem. 31, 63-75 (1971).
315. Bélanger D. and G. Laperrière, Chem. Mater. 2, 484-486 (1990).
316. Bélanger D. and G. Laperrière, J. Electrochem. Soc. 137, 2355-2361 (1990).
317. Bélanger D., G. Laperrière and B. Marsan, J. Electroanal. Chem. 347, 165-183 (1993).
318. Belkind A., Z. Orban, J.L. Vossen and J.A. Woollam, Thin Solid Films 207, 242-247 (1992).
319. Bell J.M., D.C. Green, A. Patterson, G.B. Smith, K.A. MacDonald, K. Lee, L. Kirkup, J.D. Cullen, B.O. West, L. Spiccia, M.J. Kenny and L.S. Wielunski, Proc. Soc. Photo-Opt. Instrum. Engr. 1536, 29-36 (1991).
320. Bellingham J.R., A.P. Mackenzie and W.A. Phillips, Appl. Phys. Lett. 58, 2506-2508 (1991).
321. Bellingham J.R., W.A. Phillips and C.J. Adkins, Thin Solid Films 195, 23-31 (1991)
322. Bellingham J.R., W.A. Phillips and C. J. Adkins, J. Mater. Sci. Lett. 11, 263-265 (1992).
323. Belozerov V.V., Yu. I. Malyuk and L.I. Skatkov, Zh. Tekn. Fiz. 59, 172-176 (1989) [Soviet Phys. Tech. Phys. 34, 101-103 (1989)].
324. Benaissa K., P.V. Ashrit, G. Bader, F.E. Girouard and V.-V. Truong, Thin Solid Films 214, 219-222 (1992).
325. Benbow R.L. and Z. Hurdych, Phys. Rev. B 17, 4527-4536 (1978).
326. Benbow R.L., M.R. Thuler and Z. Hurdych, Phys. Rev. B 25, 7097-7101 (1982).
327. Benci S., M. Manfredi and G.C. Salviati, Solid State Commun. 33, 107-109 (1980).
328. Bendavid A., P.J. Martin, R.P. Netterfield, G.J. Sloggett, T.J. Kinder and C. Andrikidis, J. Mater. Sci. Lett. 12, 322-323 (1993).

329. Bendert R.M. and D.A. Corrigan, J. Electrochem. Soc. 136, 1369-1374 (1989).
330. Benhamza H., P. Barboux, A. Bouhaouss, F.-A. Josien and J. Livage, J. Mater. Chem. 1, 681-684 (1991).
331. Beni G., Appl. Phys. Lett. 37, 106-108 (1980).
332. Beni G., J. Electrochem. Soc. 127, 467C-477C (1980).
333. Beni G., Solid State Ionics 3-4, 157-163 (1981).
334. Beni G., in Electrochromism and Electrochromic Displays, edited by B. Scrosati (Univ. Rome, 1982), pp. 1-38.
335. Beni G., C.E. Rice and J.L. Shay, J. Electrochem. Soc. 127, 1342-1348 (1980).
336. Beni G. and L.M. Schiavone, Appl. Phys. Lett. 38, 593-595 (1981).
337. Beni G., L.M. Schiavone, J.L. Shay, W.C. Dautremont-Smith and B.S. Schneider, Nature 282, 281-283 (1979).
338. Beni G. and B. Scrosati, Chim. Ind. (Milan) 64, 487-491 (1982).
339. Beni G. and J.L. Shay, Appl. Phys. Lett. 33, 567-568 (1978).
340. Beni G. and J.L. Shay, in Fast Ion Transport in Solids, edited by P. Vashishta, J.N. Mundy and G.K. Shenoy (Elsevier, Amsterdam, 1979), pp. 75-78.
341. Beni G. and J.L. Shay, Phys. Rev. B 21, 364-367 (1980).
342. Beni G. and J.L. Shay, in Adv. Image Pickup and Display, edited by B. Kazan (Academic, New York, 1982), Vol. 5, pp. 83-136.
343. Benninghoven A., Appl. Phys. 1, 3-16 (1973).
344. Benninghoven A., C. Plog and N. Trieiz, Int. J. Mass Spectrosc. Ion Phys. 13, 415-424 (1972).
345. Benson D.K. and J.S.E.M. Svensson, in Large-area Chromogenics: Materials and Devices for Transmittance Control, edited by C.M. Lampert and C.G. Granqvist (SPIE Opt. Engr. Press, Bellingham, 1990), Vol. IS4, pp. 215-229.
346. Benson D.K. and C.E. Tracy, Proc. Soc. Photo-Opt. Instrum. Engr. 562, 46-52 (1985).
347. Benson D.K. and C.E. Tracy, Chemtech. (1991), 677-680.
348. Benson D.K., C.E. Tracy and M.R. Ruth, Proc. Soc. Photo-Opt. Instrum. Engr. 502, 46-53 (1984).
349. Benson D.K., C.E. Tracy, J.S.E.M. Svensson and B.E. Liebert, Proc. Soc. Photo-Opt. Instrum. Engr. 823, 72-80 (1987).
350. Benson J.E., H.W. Kohn and M. Boudart, J. Catalysis 5, 307-313 (1966).
351. Benson P., G.W.D. Briggs and W.F.K. Wynne-Jones, Electrochim. Acta 9, 275-280 (1964).
352. Benson P., G.W.D. Briggs and W.F.K. Wynne-Jones, Electrochim. Acta 9, 281-288 (1964).
353. Berak J.M. and M.J. Sienko, J. Solid State Chem. 2, 109-133 (1970).
354. Beraud J.-G. and D. Deroo, Proc. Soc. Photo-Opt. Instrum. Engr. 1728, 173-179 (1992).
355. Berera G., R.B. Goldner, F.O. Arntz, K.K. Wong, A. Ciaccia, M. Welch, T.E. Haas and L. Jauniskis, Mater. Res. Soc. Symp. Proc. 210, 69-74 (1991).
356. Berezin L.Ya. and V.P. Malinenko, Pis'ma Zh. Tekh. Fiz. 13, 401-404 (1987) [Soviet Tech. Phys. Lett. 13, 164-165 (1987)].
357. Berger J., I. Riess and D.S. Tannhauser, Solid State Ionics 15, 225-231 (1985).
358. Berggren K.-F. and B.E. Sernelius, Phys. Rev. B 24, 1971-1986 (1981).
359. Bergman D.J., Ann. Phys. (New York) 138, 78-114 (1982).
360. Bergman G.M., S.J. Ebel, E.S. Takeuchi and P. Keister, J. Power Sources 20, 179-185 (1987).
361. Berkowitz J., W.A. Chupka and M.G. Inghram, J. Chem. Phys. 27, 85-86 (1957).
362. Berkowitz J., W.A. Chupka and M.G. Inghram, J. Chem. Phys. 27, 87-90 (1957).
363. Berkowitz J., M.G. Inghram and W.A. Chupka, J. Chem. Phys. 26, 842-846 (1957).
364. Berkowitz-Mattuck J.B., A. Büchler, J.L. Engelke and S.N. Goldstein, J. Chem. Phys. 39, 2722-2730 (1963).
365. Bermudez de Zea V., D. Baril, J.-Y. Sanchez, M. Armand and C. Poinsignon, Proc. Soc. Photo-Opt. Instrum. Engr. 1728, 180-191 (1992).
366. Bernal J.D., Nature 183, 141-147 (1959).
367. Bernal J.D., Nature 185, 68-70 (1960).
368. Bernal J.D. and J. Mason, Nature 188, 910-911 (1960).
369. Bernard P., C. Gabrielli, M. Keddam, H. Takenouti, J. Leonardi and P. Blanchard, Electrochim. Acta 36, 743-746 (1991).

370. Bernasik A., M. Radecka, M. Rekas and M. Sloma, Appl. Surf. Sci. 65-66, 240-245 (1993).
371. Berning P.H., Appl. Opt. 22, 4127-4141 (1983).
372. Berthier C., W. Gorecki, M. Minier, M.B. Armand, J.M. Chabagno and P. Rigaud, Solid State Ionics 11, 91-95 (1983).
373. Berzelius J.J., Afhandlingar i fysik, kemi och mineralogie 4, 293-307 (1815).
374. Berzelius J.J., J. Chem. Phys. (Berlin) [also referred to as Schweigger's Journal] 16, 476-488 (1816).
375. Besenhard J.O., J. Heydecke and H.P. Fritz, Solid State Ionics 6, 215-224 (1982).
376. Besenhard J.O., J. Heydecke, E. Wudy, H.P. Fritz and W. Foag, Solid State Ionics 8, 61-71 (1983).
377. Besenhard J.O. and R. Schöllhorn, J. Electrochem. Soc. 124, 968-971 (1977).
378. Besenhard J.O., M. Schwake and N. Misailides, J. Power Sources 26, 409-414 (1989).
379. Bestwick T.D. and G.S. Oehrlein, J. Appl. Phys. 66, 5034-5038 (1989).
380. Bets V., A. Veispals, A. Lusis, J. Purans, G. Ramans, M. Sheromov, D. Kochubei and V. Fedorov, Nucl. Instr. Meth. Phys. Res. A 261, 175-177 (1987).
381. Bets V., T. Zamozdiks, A. Lusis, J. Purans, N. Bausk and M. Sheromov, Nucl. Instr. Meth. Phys. Res. A 261, 173-174 (1987).
382. Bewick A., C. Gutiérrez and G. Larramona, J. Electroanal. Chem. 332, 155-167 (1992).
383. Bhakta S.D., D.D. Macdonald, B.G. Pound and M. Urquidi-Macdonald, J. Electrochem. Soc. 138, 1353-1358 (1991).
384. Bhattacharya R.N., C.Y. Lee, F.H. Pollak and D.M. Schleich, J. Non-Cryst. Solids 91, 235-242 (1987).
385. Bianchi C.L., M.G. Cattania and P. Villa, Appl. Surf. Sci. 70-71, 211-216 (1993).
386. Bierstedt P.E., T.A. Bither and F.J. Darnell, Solid State Commun. 4, 25-26 (1966).
387. Bierwagen G.P., Electrochim. Acta 37, 1471-1478 (1992).
388. Biloen P. and G.T. Pott, J. Catal. 30, 169-174 (1973).
389. Bird R.E., R.L. Hulstrom and L.J. Lewis, Solar Energy 30, 563-573 (1983).
390. Birss V.I., H. Elzanowska and S. Gottesfeld, J. Electroanal. Chem. 318, 327-333 (1991).
391. Birss V.I., R. Myers, H. Angerstein-Kozlowska and B.E. Conway, J. Electrochem. Soc. 131, 1502-1510 (1984).
392. Bishop C.A., G. Edge, I. Sutherland and R.P. Howson, Vacuum 37, 279-282 (1987).
393. Bishop C.A., R.P. Howson and R.W. Lewin, Proc. Soc. Photo-Opt. Instrum. Engr. 653, 25-31 (1986).
394. Bissesseur R., D.C. de Groot, J.L. Schindler, C.R. Kannewurf and M.G. Kanatzidis, Chem. Commun. (1993), 687-689.
395. Blanc J. and D.L. Staebler, Phys. Rev. B 4, 3548-3557 (1971).
396. Blandenet G., M. Court and Y. Lagarde, Thin Solid Films 77, 81-90 (1981).
397. Blauner P.G., Y. Butt, J.S. Ro, C.V. Thompson and J. Melngailis, J. Vac. Sci. Technol. B 7, 1816-1818 (1989).
398. Blocher J.M., Jr., Thin Solid Films 77, 51-63 (1981).
399. Blondeau G., M. Froelicher, M. Froment and A. Hugot-Le Goff, Phys. Stat. Sol. A 26, 181-191 (1974).
400. Blondeau G., M. Froment and A. Hugot-Le Goff, Comptes Rendues Acad. Sci. Paris, Sér. C, 271, 795-298 (1970).
401. Blonsky P.M., D.F. Shriver, P. Austin and H.R. Allcock, J. Am. Chem. Soc. 106, 6854-6855 (1984).
402. Bludská and J. Vondrák, Chem. Listy 85, 776-784 (1991).
403. Blunt M., J. Phys. A 22, 1179-1192 (1989).
404. Bobbert P.A.and J. Vlieger, Physica (Utrecht) A 137, 209-242 (1986).
405. Bobbert P.A. and J. Vlieger, Physica (Utrecht) A 147, 115-141 (1987).
406. Bobbert P.A., J. Vlieger and R. Greef, Physica (Utrecht) A 137, 243-257 (1986).
407. Bobbert P.A., J. Vlieger and R. Greef, Thin Solid Films 164, 63-67 (1988).
408. Boccoli M., F. Bonino, M. Lazzari and B. Rivolta, Solid State Ionics 7, 65-74 (1982).
409. Bockris J.O'M., M.A. Genshaw, V. Brusic and H. Wroblowa, Electrochim. Acta 16, 1859-1894 (1971).
410. Bockris J. O'M. and A.K.N. Reddy, Modern Electrochemistry (Plenum, New York, 1973).
411. Bockris J. O'M., A.K.N. Reddy and B. Rao, J. Electrochem. Soc. 113, 1133-1144 (1966).
412. Bode H., K. Dehmelt and J. Witte, Electrochim. Acta 11, 1079-1087 (1966).
413. Bode H., K. Dehmelt and J. Witte, Z. Anorg. Allg. Chem. 366, 1-21 (1969).

414. Boggio R., A. Carugati and S. Trasatti, J. Appl. Electrochem. 17, 828-840 (1987).
415. Bogomolov V.G., E.K. Kudinov, D.N. Mirlin and Yu.A. Firsov, Fiz. Tverd. Tela 9, 2077-2090 (1968) [Soviet Phys. Solid State 9, 1630-1639 (1968)].
416. Bohé A.E., J.R. Vilche and A.J. Arvia, J. Appl. Electrochem. 14, 645-652 (1984).
417. Bohnke C., Solid State Ionics 9-10, 353-356 (1983).
418. Bohnke C. and O. Bohnke, J. Appl. Electrochem. 18, 715-723 (1988).
419. Bohnke C. and O. Bohnke, Solid State Ionics 39, 195-204 (1990).
420. Bohnke C. and M. Rezrazi, Mater. Sci. Engr. B 10, 313-320 (1991).
421. Bohnke O., Ph D Thesis, University of Besancon, France (1984), unpublished.
422. Bohnke O. and C. Bohnke, Displays 9, 199-206 (1988).
423. Bohnke O. and C. Bohnke, in Electrochromic Materials, edited by M.K. Carpenter and D.A. Corrigan (The Electrochem. Soc., Pennington, 1990), Proc. Vol. 90-2, pp. 312-321.
424. Bohnke O. and C. Bohnke, J. Electrochem. Soc. 138, 3612-3617 (1991).
425. Bohnke O., C. Bohnke and S. Amal, Mater. Sci. Engr. B 3, 197-202 (1989).
426. Bohnke O., C. Bohnke, A. Donnadieu and D. Davazoglou, J. Appl. Electrochem. 18, 447-453 (1988).
427. Bohnke O., C. Bohnke, G. Robert and B. Carquille, Solid State Ionics 6, 121-128 (1982).
428. Bohnke O., C. Bohnke, G. Robert and B. Carquille, Solid State Ionics 6, 267-273 (1982).
429. Bohnke O., C. Bohnke, G. Robert, B. Carquille and J.C. Vienot, L'Onde Electrique, October (1981), pp. 15-18.
430. Bohnke O. and M. Rezrazi, Mater. Sci. Engr. B 13, 323-326 (1992).
431. Bohnke O., M. Rezrazi, B. Vuillemin, C. Bohnke, P.A. Gillet and C. Rousselot, Solar Energy Mater. Solar Cells 25, 361-374 (1992).
432. Bohnke O. and G. Robert, Solid State Ionics 6, 115-120 (1982).
433. Bohnke O., C. Rousselot, P.A. Gillet and C. Truche, J. Electrochem. Soc. 139, 1862-1865 (1992).
434. Bohnke O. and B. Vuillemin, Mater. Sci. Engr. B 13, 243-246 (1992).
435. Bohren C.F. and D.P. Gilra, J. Colloid Interface Sci. 72, 215-221 (1979).
436. Boiko B.T., P.A. Panchekha, V.R. Kopach, Yu.L. Pozdeev, E. Turevskaya and M.I. Yanovskaya, Izv. Akad. Nauk SSSR Inorg. Mater. 21, 1905-1909 (1985) [Inorg. Mater. 21, 1659-1663 (1985)].
437. Boilot J.P., P. Colomban and N. Blanchard, Solid State Ionics 9-10, 639-644 (1983).
438. Boilot J.P., P. Colomban and G. Collin, Solid State Ionics 28-30, 403-410 (1988).
439. Bokii L.P., Yu. L. Danilyuk, M.N. D'yakonov, I.S. Kotousova, R.A. Mirzoev, V.M. Muzhdaba, L.A. Rozenberg and S.D. Khanin, Elektrokhim. 15, 1307-1312 (1979) [Soviet Electrochem. 15, 1132-1136 (1979)].
440. Bond G.C., P.A. Sermon and C.J. Wright, Mater. Res. Bull. 19, 701-704 (1984).
441. Bonino F., L. Busani, M. Lazzari, M. Manstretta, B. Rivolta and B. Scrosati, J. Power Sources 6, 261-270 (1981).
442. Bonino F., M. Ottaviani, B. Scrosati and G. Pistoria, J. Electrochem. Soc. 135, 12-15 (1988).
443. Bonino F., L. Peraldo Bicelli, B. Rivolta, M. Lazzari and F. Festorazzi, Solid State Ionics 17, 21-28 (1985).
444. Bonino F., B. Scrosati, A. Selvaggi, J. Evans and C.A. Vincent, J. Power Sources 18, 75-81 (1986).
445. Bonnet J.P., D. Benjelloun, C. Denage, J. Ravez and M. Onillon, J. Chim. Phys. 88, 2097-2103 (1991).
446. Bonnet J.P., E. Marquestaut and M. Onillon, Mater. Res. Bull. 12, 361-366 (1977).
447. Bonnet J.P., J.F. Marucco, M. Onillon and P. Hagenmuller, J. Solid State Chem. 40, 270-279 (1981).
448. Bonnet J.P. and M. Onillon, Solid State Ionics 12, 337-342 (1984).
449. Bootz B., H. Finkenrath, G. Franz and N. Uhle, Solid State Commun. 13, 1477-1479 (1973).
450. Born M. and E. Wolf, Principles of Optics, 6th edition (Pergamon, Oxford, 1980).
451. Borosy A.P., L. Nyikos and T. Pajkossy, Electrochim. Acta 36, 163-165 (1991).
452. Borovkov V.S., A.K. Ivanov-Shits and L.A. Tsvetnova, Elektrokhim. 10, 1000 (1974) [Soviet Electrochem. 10, 956 (1974)].
453. Borovkov V.S., A.K. Ivanov-Shits and L.A. Tsvetnova, Elektrokhim. 11, 664-666 (1975) [Soviet Electrochem. 11, 624-625 (1975)].
454. Bösch M.A., K.S. Kang, S. Hackwood, G. Beni and J.L. Shay, Appl. Phys. Lett. 41, 103-105 (1982).
455. Bosio L., R. Cortès, P. Delichère, M. Froment and S. Joiret, Surf. Interface Anal. 12, 380-384 (1988).

456. Bosman A.J. and Crevecoeur C., J. Phys. Chem. Solids 30, 1151-1160 (1969).
457. Bosman A.J and H.J. van Daal, Adv. Phys. 19, 1-117 (1970).
458. Böttger H. and V.V. Bryksin, Hopping Conduction in Solids (VCH Verlag, Weinheim, 1985), pp. 66-70.
459. Bouchard R.J. and J.L. Gillson, Inorg. Chem. 7, 969-972 (1968).
460. Boudart M., M.A. Vannice and J.E. Benson, Z. Phys. Chem. N.F. 64, 171-177 (1969).
461. Bouhaouss A. and P. Aldebert, Mater. Res. Bull 18, 1247-1256 (1983).
462. Bouhaouss A., P. Aldebert, N. Baffier and J. Livage, Rev. Chim. Minérale 22, 417-426 (1985).
463. Bouridah A., F. Dalard, D. Deroo and M.B. Armand, Solid State Ionics 18-19, 287-290 (1986).
464. Bouridah A., F. Dalard, D. Deroo, H. Cheradame and J.F. LeNest, Solid State Ionics 15, 233-240 (1985).
465. Bouyssoux G., M. Romand, H.D. Polaschegg and J.T. Calow, J. Electron Spectrosc. Related Phenomena 11, 185-196 (1977).
466. Bowen H.K., D. Adler and B.H. Auker, J. Solid State Chem. 12, 355-359 (1975).
467. Braconnier J.-J., C. Delmas, C. Fouassier, M. Figlarz, B. Beaudouin and P. Hagenmuller, Rev. Chim. Minérale 21, 496-508 (1984).
468. Braconnier J.-J., C. Delmas, C. Fouassier and P. Hagenmuller, Mater. Res. Bull. 15, 1797-1804 (1980).
469. Bradley A. and J. Illingworth, Proc. Roy. Soc. London A 157, 113-131 (1936).
470. Brahms S. and S. Nikitine, Solid State Commun. 3, 209-212 (1965).
471. Braig A. and T. Meisel, Dornier-Post (1992)(2), 29-30.
472. Brandow B.H., Adv. Phys. 26, 651-808 (1977).
473. Braunstein R., Solid State Commun. 28, 839-842 (1978).
474. Braunstein R. and I. Lefkowitz, Ferroelectrics 27, 225-230 (1980).
475. Bredesen R. and P. Kofstad, Solid State Ionics 27, 11-18 (1988).
476. Brett M.E., K.M. Parkin and M.J. Graham, J. Electrochem. Soc. 133, 2031-2035 (1986).
477. Brett M.J., J. Vac. Sci. Technol. A 6, 1749-1751 (1988).
478. Brett M.J., J. Mater. Sci. 24, 623-626 (1989).
479. Brett M.J., J. Mater. Sci. Lett. 8, 415-417 (1989).
480. Brett M.J., R.N. Tait, S.K. Dew, S. Kamasz, A.H. Labun and T. Smy, J. Mater. Sci. Mater. Electronics 3, 64-70 (1992).
481. Breusov O.M., A.N. Dremin, V.N. Drobyshev and S.V. Pershin, Zh. Neorg. Khim. 18, 295-300 (1973) [Russian J. Inorg. Chem. 18, 157-159 (1973)].
482. Briggs G.W.D., Chem. Soc. Special Periodic Rept. Electrochem. 4, 33-54 (1974).
483. Briggs G.W.D. and M. Fleichmann, Trans. Faraday Soc. 67, 2397-2407 (1971).
484. Briggs G.W.D., E. Jones and W.F.K. Wynne-Jones, Trans. Faraday Soc. 51, 1433-1442 (1955).
485. Briggs G.W.D., G.W. Stott and W.F.K. Wynne-Jones, Electrochim. Acta 7, 249-256 (1962).
486. Briggs G.W.D. and W.F.K. Wynne-Jones, Trans. Faraday Soc. 52, 1272-1281 (1956).
487. Briggs G.W.D. and W.F.K. Wynne-Jones, Electrochim. Acta 7, 241-248 (1962).
488. Brimm E.O., J.C. Brantley, J.H. Lorenz and M.H. Jellinek, J. Am. Chem. Soc. 73, 5427-5432 (1951).
489. Bringans R.D., H. Höchst and H.R. Shanks, Phys. Rev. B 24, 3481-3489 (1981).
490. Brinker C.J., G.C. Frye, A.J. Hurd and C.S. Ashley, Thin Solid Films 201, 97-108 (1991).
491. Brinker C.J., A.J. Hurd, G.C. Frye, K.J. Ward and C.S. Ashley, J. Non-Cryst. Solids 121, 294-302 (1990).
492. Brinker C.J., A. J. Hurd, P.R. Schunk, G.C. Frye and C.S. Ashley, J. Non-Cryst. Solids 147-148, 424-436 (1992).
493. Brinker C.J. and G.W. Scherer, Sol-Gel Science (Academic, San Diego, 1990).
494. Brishka A.A., T.V. Zamozdik, J.J. Kleperis, A.R. Lusis and O.A. Rode, Zh. Tekh. Fiz. 51, 976-980 (1981) [Soviet Phys. Tech. Phys. 26, 583-586 (1981)].
495. Brown B.W. and E. Banks, J. Am. Chem. Soc. 76, 963-966 (1954).
496. Brown J., Philos. Trans. 33, 17-24 (1724).
497. Brown O.R., in Physical Chemsitry of Organic Solvent Systems, edited by A.K. Covington and T. Dickinson (Plenum, New York, 1973), pp. 747-781.
498. Bruggeman D.A.G., Ann. Phys. (Leipzig) 24, 636-664 (1935).
499. Bruinink J., in Nonemissive Electrooptic Displays, edited by A.R. Kmetz and F.K. von Willisen (Plenum, New York, 1976), pp. 201-219.

500. Brundle C.R. and A.F. Carley, Chem. Phys. Lett. 31, 423-427 (1975).
501. Brus L.E., J. Chem. Phys. 80, 4403-4409 (1984).
502. Bryant A., M. Poirier, G. Riley, D.L. Lee and J.F. Vetelino, Sensors Actuators 4, 105-111 (1983).
503. Bryksin V.V., Fiz. Tverd. Tela 24, 1110-1117 (1982) [Soviet Phys. Solid State 24, 627-631 (1982)].
504. Bryksin V.V., A.V. Goltsev, S.D. Khanin, A.V. Novotelnova and A.N. Vasilev, Phys. Stat. Sol. B 161, 777-781 (1990).
505. Brytov I.A. and Yu.N. Romashchenko, Fiz. Tverd. Tela 20, 664-672 (1978) [Soviet Phys. Solid State 20, 384-389 (1978)].
506. Buckley D.N. and L.D. Burke, J. Chem. Soc. Faraday Trans. I 71, 1447-1459 (1975).
507. Buckley D.N. and L.D. Burke, J. Chem. Soc. Faraday Trans. I 72, 2431-2440 (1976).
508. Buckley D.N. and L.D. Burke, J. Electrochem. Soc. 126, 2171 (1979).
509. Buckley D.N., L.D. Burke and J.K. Mulcahy, J. Chem. Soc. Faraday. Trans. I 72, 1896-1902 (1976).
510. Budkevich B.A., I.A. Ges, V.A. Pilipovich, and I.M. Romanov, Dokl. Akad. Nauk BSSR 27, 602-605 (1983).
511. Budkevich B.A., I.A. Ges, V.A. Pilipovich, I.M. Romanov and L.I. Romanova, Dokl. Akad. Nauk BSSR 48, 988-991 (1984).
512. Budkevich B.A., I.A. Ges, E.I. Zhmaka, T.R. Katsubo, V.A. Pilipovich, A.M. Polikanin and I.M. Romanov, Dokl. Akad. Nauk BSSR 23, 425-427 (1979).
513. Budkevich B.A., I.A. Ges, S.P. Zhvavyi, G.D. Ivlev and V.A. Pilipovich, Phys. Stat. Sol. 110, 155-164 (1988).
514. Budkevich B.A., V.A. Pilipovich, I.A. Ges and I.M. Romanov, Dokl. Akad. Nauk BSSR 26, 310-313 (1982).
515. Buffat B. and F. Lerbet, Recherche 22, 434-442 (1991).
516. Bugayev A.A., F.A. Chudnovskii and B.P. Zakharchenya, in Semiconductor Physics, edited by V.M. Turkevich and V.Y. Frenkel (Consultants Bureau, New York, 1986), pp. 265-292.
517. Bukun N.G., I.A. Domashnev, E.I. Moskvina and E.A. Ukshe, Izv. Akad. Nauk SSSR Neorg. Mater. 24, 443-447 (1988) [Inorg. Mater. 24, 360-364 (1988)].
518. Bukun N.G., A.F. Gurov and V.V. Sinitsin, Elektrokhim. 26, 1513-1516 (1990) [Soviet Electrochem. 26, 1352-1355 (1990)].
519. Bullett D.W., J. Phys. C 13, L595-L599 (1980).
520. Bullett D.W., J. Phys. C 16, 2197-2207 (1983).
521. Bullett D.W., Solid State Commun. 46, 575-577 (1983).
522. Bullot J., P. Cordier, O. Gallais and M. Gauther, J. Non-Cryst. Solids 68, 135-146 (1984).
523. Bullot J., P. Cordier, O. Gallais, M. Gauthier and J. Livage, Phys. Stat. Sol. A 68, 357-361 (1981).
524. Bullot J., P. Cordier, O. Gallais, M. Gauthier and J. Livage, J. Non-cryst. Solids 68, 123-134 (1984).
525. Bullot J., O. Gallais, M. Gauthier and J. Livage, Appl. Phys. Lett. 36, 986-988 (1980).
526. Bullot J., O. Gallais, M. Gauthier and J. Livage, Phys. Stat. Sol. A71, K1-K4 (1982).
527. Bunkin F.V., N.A. Kirichenko, B.S. Lukyanchuk, A.V. Simakhin, G.A. Shafeev, L. Hanai and I. Hevesi, Acta Phys. Hung. 54, 111-118 (1983).
528. Burattini E., J. Purans and A. Kuzmin, Japan. J. Appl. Phys. 32, Pt. 1, Suppl. 32-1, 655-658 (1993).
529. Burba M.E., E. Degenkolb, S. Henck, M. Tabasky, E.D. Jungbluth and R. Wilson, J. Electrochem. Soc. 133, 2113-2118 (1986).
530. Burke L.D., in Electrodes of Conductive Metallic Oxides, Part A, edited by S. Trasatti (Elsevier, Amsterdam, 1980), pp. 141-181.
531. Burke L.D., M.J.G. Ahern and T.G. Ryan, J. Electrochem. Soc. 137, 553-561 (1990).
532. Burke L.D. and J.F. Healy, J. Electroanal. Chem. 124, 327-332 (1981).
533. Burke L.D., B.H. Lee and T.G. Ryan, J. Electrochem. Soc. 137, 2417-2422 (1990).
534. Burke L.D. and M.E.G. Lyons, in Modern Aspects of Electrochemistry, edited by R.E. White, J. O'M. Bockris and B.E. Conway (Plenum, New York, 1986), Vol. 18, pp. 169-248.
535. Burke L.D. and M.E.G. Lyons, J. Electroanal. Chem. 198, 347-368 (1986).
536. Burke L.D., M.E. Lyons and O.J. Murphy, J. Electroanal. Chem. 132, 247-261 (1982).
537. Burke L.D., M.E. Lyons, E.J.M. O'Sullivan and D.P. Whelan, J. Electroanal. Chem. 122, 403-407 (1981).

538. Burke L.D. and J.K. Mulcahy, J. Electroanal. Chem. 73, 207-218 (1976).
539. Burke L.D. and O.J. Murphy, J. Electroanal. Chem. 109, 199-212 (1980).
540. Burke L.D. and O.J. Murphy, J. Electroanal. Chem. 109, 373-377 (1980).
541. Burke L.D. and O.J. Murphy, J. Electroanal. Chem. 109, 379-383 (1980).
542. Burke L.D. and O.J. Murphy, J. Electroanal. Chem. 112, 379-382 (1980).
543. Burke L.D., O.J. Murphy, J.F. O'Neill and S. Venkatesan, J. Chem. Soc. Faraday Trans. I 73, 1659-1671 (1977).
544. Burke L.D. and K.J. O'Dwyer, Electrochim. Acta 34, 1659-1664 (1989).
545. Burke L.D. and K.J. O'Dwyer, Electrochim. Acta 35, 1821-1827 (1990).
546. Burke L.D. and K.J. O'Dwyer, Electrochim. Acta 35, 1829-1835 (1990).
547. Burke L.D. and E.J.M. O'Sullivan, J. Electroanal. Chem. 93, 11-18 (1978).
548. Burke L.D. and E.J.M. O'Sullivan, J. Electroanal. Chem. 97, 123-125 (1979).
549. Burke L.D. and E.J.M. O'Sullivan, J. Electroanal. Chem. 111, 383-384 (1980).
550. Burke L.D. and E.J.M. O'Sullivan, J. Electroanal. Chem. 112, 247-252 (1980).
551. Burke L.D. and E.J.M. O'Sullivan, J. Electroanal. Chem. 117, 155-160 (1981).
552. Burke L.D. and E.J.M. O'Sullivan, J. Electroanal. Chem. 129, 133-149 (1981).
553. Burke L.D. and R.A. Scannell, Platinum Metals Rev. 28, 56-61 (1984).
554. Burke L.D. and R.A. Scannell, J. Electroanal. Chem. 175, 119-141 (1984).
555. Burke L.D. and R.A. Scannell, J. Electroanal. Chem. 257, 101-121 (1988).
556. Burke L.D. and T.A.M. Twomey, in Proc. Symp. Nickel Electrode, edited by R.G. Gunter and S. Gross (The Electrochem. Soc., Pennington, 1982), pp. 75-96.
557. Burke L.D. and T.A.M. Twomey, J. Electroanal. Chem. 134, 353-362 (1982).
558. Burke L.D. and T.A.M. Twomey, J. Electroanal. Chem. 162, 101-119 (1984).
559. Burke L.D. and T.A.M. Twomey, J. Power Sources 12, 203-218 (1984).
560. Burke L.D., T.A.M. Twomey and D.P. Whelan, J. Electroanal. Chem. 107, 201-204 (1980).
561. Burke L.D. and D.P. Whelan, J. Electroanal. Chem. 103, 179-187 (1979).
562. Burke L.D. and D.P. Whelan, J. Electroanal. Chem. 109, 385-389 (1980).
563. Burke L.D. and D.P. Whelan, J. Electroanal. Chem. 124, 333-337 (1981).
564. Burke L.D. and D.P. Whelan, J. Electroanal. Chem. 135, 55-65 (1982).
565. Burke L.D. and D.P. Whelan, J. Electroanal. Chem. 162, 121-141 (1984).
566. Burrows B. and S. Kirkland, J. Electrochem. Soc. 115, 1164-1169 (1968).
567. Bursian E.V., Ya.G. Girshberg and E.N. Starov, Phys. Stat. Solidi B 46, 529-533 (1971).
568. Bursill L.A., J. Solid State Chem. 48, 256-271 (1983).
569. Burstein E., Phys. Rev. 93, 632-633 (1954).
570. Burstein G.T. and D.H. Davies, Corrosion Sci. 20, 989-995 (1980).
571. Buser H.J., D. Schwarzenbach, W. Petter and A. Ludi, Inorg. Chem. 16, 2704-2710 (1977).
572. Buss D.H., J. Bauer, W. Diembeck and O. Glemser, J. Chem. Soc. Chem. Commun. (1985), 81-82.
573. Butler M.A., J. Appl. Phys. 48, 1914-1920 (1977).
574. Butler M.A., Surf. Sci. 101, 155-161 (1980).
575. Butler M.A., R.D. Nasby and R.K. Quim, Solid State Commun. 19, 1011-1014 (1976).
576. Butler S.R. and J.L. Gillson, Mater. Res. Bull. 6, 81-90 (1971).
577. Button D.P., R.P. Tandon, H.L. Tuller and D.R. Uhlmann, J. Non-Cryst. Solids 42, 297-306 (1980).
578. Buttry D.A., in Electroanalytical Chemistry, edited by A.J. Bard (Marcel Dekker, New York, 1991), Vol. 17, pp. 1-85.
579. Buttry D.A., in Electrochemical Interfaces: Modern Techniques for In-situ Interface Characterization, edited by H.D. Abruna (VCH Publishers, New York, 1991), pp. 529-566.
580. Buttry D.A. and M.D. Ward, Chem. Rev. 92, 1355-1379 (1992).

C

581. Cabanel R., G. Barral, J.-P. Diard, B. Le Gorrec and C. Montella, J. Appl. Electrochem. 23, 93-97 (1993).

582. Cabanel R., J. Chaussy, J. Mazuer, G. Delabouglise, J.C. Joubert, G. Barral and C. Montella, J. Electrochem. Soc. 137, 1444-1451 (1990).
583. Cabannes-Ott C., Ann. Chim. (Paris) 5, 905-960 (1960).
584. Calecki D. and G. Fishman, Surf. Sci. 229, 110-112 (1990).
585. Calkin M.G. and P.J. Nicholson, Rev. Mod. Phys. 39, 361-372 (1967).
586. Camagni P., A. Manara, G. Campagnoli, A. Gustinetti and A. Stella, Phys. Rev. B 15, 4623-4630 (1977).
587. Campagna M., G.K. Wertheim, H.R. Shanks, F. Zumsteg and E. Banks, Phys. Rev. Lett. 34, 738-741 (1975).
588. Campet G., M.P. Dare-Edwards, A. Hamnett and J.B. Goodenough, Noveau J. Chim. 4, 501-507 (1980).
589. Campet G., C. Geoffroy, J.P. Manaud, J. Portier, Z.W. Sun, J. Salardenne and P. Keou, Mater. Sci. Engr. B 8, 45-52 (1991).
590. Campet G., B. Morel, M. Bourrel, J.M. Chabagno, D. Ferry, R. Garie, C. Quet, C. Geoffroy, J. Portier, C. Delmas and J. Salardenne, Mater. Sci. Engr. B 8, 303-308 (1991).
591. Campet G., S.J. Wen, S.D. Han, M.C.R. Shastry, J. Portier, C. Guizard, L. Cot, Y. Xu and J. Salardenne, Mater. Sci. Engr. B 18, 201-208 (1993).
592. Campet G., S.Z. Wen, C. Puprichitkun, J.P. Manaud and J. Claverie, Phys. Stat. Sol. A 103, 175-184 (1987).
593. Canaday J.D., S.F. Chehab, A.K. Kuriakose, A. Ahmad and T.A. Wheat, Solid State Ionics 48, 113-121 (1991).
594. Capehart T.W., D.A. Corrigan, R.S. Conell, K.I. Pandya and R.W. Hoffmann, Appl. Phys. Lett. 58, 865-867 (1991).
595. Caplan D. and M. Cohen, J. Electrochem. Soc. 108, 438-442 (1961).
596. Capon A. and R. Parsons, Electroanal. Chem. Interfacial Electrochem. 39, 275-286 (1972).
597. Carbonio R.E. and V.A. Macagno, An. Asoc. Quim. Argentina 73, 93-105 (1985).
598. Carbonio R.E., V.A. Macagno and A.J. Arvia, J. Electroanal. Chem. 147, 139-156 (1983).
599. Carbonio R.E., V.A. Macagno and A.J. Arvia, J. Electroanal. Chem. 177, 217-228 (1984).
600. Carbonio R.E., V.A. Macagno, M.C. Giordano, J.R. Vilche and A.J. Arvia, J. Appl. Electrochem. 12, 121-126 (1982).
601. Carbonio R.E., V.A. Macagno, M.C. Giordano, J.R. Vilche and A.J. Arvia, J. Electrochem. Soc. 129, 983-991 (1982).
602. Carcia P.F. and E.M. McCarron III, Thin Solid Films 155, 53-63 (1987).
603. Cardona M. and L. Ley, in Photoemission in Solids I, Topics in Applied Physics, edited by M. Cardona and L. Ley (Springer, Berlin, Heidelberg, 1978), Vol. 26, pp. 1-104.
604. Carey M.J., F.E. Spada, A.E. Berkowitz, W. Cao and G. Thomas, J. Mater. Res. 6, 2680-2687 (1991).
605. Carley A.F., P.R. Chalker and M.W. Roberts, Proc. Roy. Soc. London, A 399, 167-179 (1985).
606. Carpenter M.K. and R.S. Conell, Appl. Phys. Lett. 55, 2245-2247 (1989).
607. Carpenter M.K. and R.S. Conell, in Electrochromic Materials (The Electrochem. Soc., Pennington,1990), Proc. Vol. 90-2, pp. 322-333.
608. Carpenter M.K. and R.S. Conell, J. Electrochem. Soc. 137, 2464-2467 (1990).
609. Carpenter M.K., R.S. Conell and D.A. Corrigan, Solar Energy Mater. 16, 333-346 (1987).
610. Carpenter M.K., R.S. Conell and S.J. Simko, Inorg. Chem. 29, 845-850 (1990).
611. Carpenter M.K. and D.A. Corrigan, J. Electrochem. Soc. 136, 1022-1026 (1989).
612. Carpenter M.K. and D.A. Corrigan, editors, Electrochromic Materials (The Electrochem. Soc., Pennington, 1990), Proc. Vol. 90-2, pp. 1-370.
613. Cartier C., A. Tranchant, M. Verdaguer, R. Messina and H. Dexpert, Electrochim. Acta 35, 889-898 (1990).
614. Carver G.E., Thin Solid Films 63, 169-174 (1979).
615. Carver G.E., A. Divrechy, S. Karbal, J. Robin and A. Donnadieu, Thin Solid Films 94, 269-278 (1982).
616. Casal B., E. Ruiz-Hitzky, M. Crespin, D. Tinet and J.C. Galván, J. Chem. Soc. Faraday Trans. I 85, 4167-4177 (1989).
617. Casciola M. and D. Bianchi, Solid State Ionics 17, 287-293 (1985).
618. Case F.C., J. Vac. Sci. Technol. A 2, 1509-1512 (1984).
619. Case F.C., J. Vac. Sci. Technol. A 5, 1762-1766 (1987).
620. Case F.C., Appl. Opt. 26, 1550-1553 (1987).

621. Case F.C., J. Vac. Sci. Technol. A 6, 123-127 (1988).
622. Case F.C., Appl. Opt. 27, 1803-1806 (1988).
623. Case F.C., J. Vac. Sci. Technol. A 7, 1194-1198 (1989).
624. Case F.C., Appl. Opt. 28, 2731-2735 (1989).
625. Case F.C., J. Vac. Sci. Technol. A 8, 1395-1398 (1990).
626. Casey E.J., A.R. Dubois, P.E. Lake and W.J. Moroz, J. Electrochem. Soc. 112, 371-383 (1965).
627. Caskey G., B.P. Hichwa, H. Habibi and M. Ahern (1991), unpublished .
628. Cathro K.J., Solar Energy Mater. 9, 433-447 (1984).
629. Cava R.J., D.J. Kleinman and S.M. Zahurak, Mater. Res. Bull. 18, 869-873 (1983).
630. Cava R.J., D.W. Murphy and S.M. Zahurak, J. Electrochem. Soc. 130, 243-245 (1983).
631. Cava R.J., D.W. Murphy and S.M. Zahurak, J. Electrochem. Soc. 130, 2345-2351 (1983).
632. Cava R.J., A. Santoro, D.W. Murphy, S.M. Zahurak, R.M. Fleming, P. Marsh and R.S. Roth, J. Solid State Chem. 65, 63-71 (1986).
633. Cava R.J., A. Santoro, D.W. Murphy, S. Zahurak and R.S. Roth, Solid State Ionics 5, 323-326 (1981).
634. Cech R.E. and E.I. Alessandrini, Trans. ASM 51, 150-161 (1959).
635. Chain E.E., J. Vac. Sci. Technol. A 4, 432-435 (1986).
636. Chain E.E., J. Vac. Sci. Technol. A 5, 1836-1839 (1987).
636a. Chain E.E., Appl. Opt. 28, 713-716 (1989).
637. Chain E.E., K.A. Gesheva and B.O. Seraphin, Thin Solid Films 83, 387-392 (1981).
638. Chain E.E., K. Seshan and B.O. Seraphin, J. Appl. Phys. 52, 1356-1362 (1981).
639. Chaklanabish N.C. and H.S. Maiti, Solid State Ionics 21, 207-212 (1986).
640. Chamberland B.L., Mater. Res. Bull. 6, 425-432 (1971).
641. Chan S.S., I.E. Wachs, L.L. Murrell, L. Wang and W.K. Hall, J. Phys. Chem. 88, 5831-5835 (1984).
642. Chandra S., Superionic Solids (North-Holland, Amsterdam, 1981).
643. Chang H.L.M., Y. Gao, J. Guo, C.M. Foster, H. You, T.J. Zhang and D.J. Lam, J. Phys. IV (Paris) 1, C2 953-C2 960 (1991).
644. Chang H.L.M., Y. Gao, T.J. Zhang and D.J. Lam, Thin Solid Films 216, 4-7 (1992).
645. Chang H.L.M., Y. Gao, T.J. Zhang and D.J. Lam, Appl. Surf. Sci. 65-66, 220-226 (1993).
646. Chang H.L.M., H. You, Y. Gao, C.M. Foster, R.P. Chiarello, T.J. Zhang and D.J. Lam, J. Mater. Res. 7, 2495-2506 (1992).
647. Chang H.L.M., H. You, J. Guo, Y. Gao and D.J. Lam, in High Performance Ceramic Films and Coatings, edited by P. Vincenzini (Elsevier, Amsterdam, 1991), pp. 161-170.
648. Chang H.L.M., H. You, J. Guo and D.J. Lam, Appl. Surf. Sci. 48-49, 12-18 (1991).
649. Chang I.F., in Nonemissive Electrooptic Displays, edited by A.R. Kmetz and F.K. von Willisen (Plenum, New York, 1976), pp. 155-196.
650. Chang I.F., Displays (1981), 275-278.
651. Chang I.F., B.L. Gilbert and T.I. Sun, J. Electrochem. Soc. 122, 955-962 (1975).
652. Chang I.F. and W.E. Howard, IEEE Trans. Electron Devices ED-22, 749-758 (1975).
653. Chang M.R.-W., K. Shahi and J.B. Wagner, Jr., J. Electrochem. Soc. 131, 1213-1214 (1984).
654. Chang S.H., C. Delmas, J.P. Chaminade and P. Hagenmuller, Solid State Ionics 39, 305-310 (1990).
655. Chang S.H., M. Ménétrier, C. Delmas and J.P. Chaminade, J. Electrochem. Soc. 138, 1209-1211 (1991).
656. Changming F., G. Haichun, H. Yan, C. Zhengliang and Z. Yi, Solid State Ionics 48, 289-293 (1991).
657. Chao C.Y. and Z. Szklarska-Smialowska, Surf. Sci. 96, 426-442 (1980).
658. Chao C.Y., Z. Szklarska-Smialowska and D.D. MacDonald, J. Electroanal. Chem. 131, 279-287 (1982).
659. Chao C.Y., Z. Szklarska-Smialowska and D.D. MacDonald, J. Electroanal. Chem. 131, 289-297 (1982).
660. Chapman B.N., Glow Discharge Processes (Wiley, New York, 1980).
661. Chassaing E., B. Sapoval, G. Daccord and R. Lenormand, J. Electroanal. Chem. 279, 67-78 (1990).
662. Chattopadhyay D. and H.J. Queisser, Rev. Mod. Phys. 53, 745-768 (1981).
663. Chaurasia H.K. and W.A.G. Voss, Nature 249, 28-29 (1974).
664. Chazalviel J.-N., M. Campagna, G.K. Wertheim and H.R. Shanks, Phys. Rev. B 16, 697-705 (1977).
665. Chazalviel J.-N. and F. Ozanam, J. Electron Spectrosc. Related Phenomena 54-55, 1229-1238 (1990).
666. Chemseddine A., J. Non-Cryst. Solids 147-148, 313-319 (1992).

667. Chemseddine A., F. Babonneau and J. Livage, J. Non-Cryst. Solids 91, 271-278 (1987).
668. Chemseddine A., M. Henry and J. Livage, Rev. Chim. Minérale 21, 487-495 (1984).
669. Chemseddine A., R. Morineau and J. Livage, Solid State Ionics 9-10, 357-361 (1983).
670. Chemseddine A., R. Morineau and J. Livage, Vide Couches Minces 222, 239-241 (1984).
671. Chen C. and S. Trasatti, J. Appl. Electrochem. 23, 559-566 (1993).
672. Chen C.-T. and Cahan B.D., J. Electrochem. Soc. 129, 17-26 (1982).
673. Chen L. and J. Schoonman, Solid State Ionics 60, 227-231 (1993).
674. Chen L., C. Sheng, R. Xue, M. Dong and Y. Chen, Solid State Ionics 40-41, 495-498 (1990).
675. Chen L.-Q., M. Dong, L. Ding, M.-C. Zhang and L.-Z. Zhao, in Recent Advances in Fast Ion Conducting Materials and Devices, edited by B.V.R. Chowdari, Q.-G. Liu and L.-Q. Chen (World Scientific, Singapore, 1990),pp. 525-530.
676. Chen R., J. Appl. Phys. 40, 570-585 (1969).
677. Cheng K.H., A.J. Jacobson and M.S. Whittingham, Solid State Ionics 5, 355-358 (1981).
678. Cheng K.H. and M.S. Whittingham, Solid State Ionics 1, 151-161 (1980).
679. Cherkashin A.E. and F.I. Vilesov, Fiz. Tverd. Tela 11, 1319-1324 (1969) [Soviet Phys. Solid State 11, 1068-1072 (1969)].
680. Cherkashin A.E., F.I. Vilesov, G.L. Semin and L.G. Matvienko, Fiz. Tverd. Tela 11, 189-191 (1969) [Soviet Phys. Solid State 11, 142-143 (1969)].
681. Chernykh Yu.N. and A.A. Yakovleva, Elektrokhim. 7, 530-533 (1971) [Soviet Electrochem. 7, 510-512 (1971)].
682. Chernykh Yu.N. and A.A. Yakovleva, Elektrokhim. 7, 533-536 (1971) [Soviet Elektrochem. 7, 513-516 (1971)].
683. Cheung J.T. and M. Sankur, CRC Crit. Rev. Solid State Mater. Sci. 15, 63-109 (1988).
684. Chevalier J.-W., J.-Y. Bergeron and L.H. Dao, Polymer Commun. 30, 308-310 (1989).
685. Chevrier G., M. Touboul, A. Driouiche and M. Figlarz, J. Mater. Chem. 2, 639-640 (1992).
686. Chevrier J. and G. Siclet, Bull. Soc. Chim. France (1976), 1037-1042.
687. Chiang C.K., G.T. Davis, C.A. Harding and T. Takahashi, Macromol. 18, 825-827 (1985).
688. Chiba K. and K.Suzuki, Solar Energy Mater. Solar Cells 25, 113-123 (1992).
689. Chidambaram K., L.K. Malhotra and K.L. Chopra, Thin Solid Films 87, 365-371 (1982).
690. Chidsey C.E., B.J. Feldman, C. Lundgren and R.W. Murray, Anal. Chem. 58, 601-607 (1986).
691. Chigane M. and M. Ishikawa, J. Chem. Soc. Faraday Trans. 88, 2203-2205 (1992).
692. Childs G.N., Solar Energy Mater. 19, 403-408 (1989).
693. Chippindale A.M. and P.G. Dickens, J. Mater. Chem. 2, 601-608 (1992).
694. Chippindale A.M., P.G. Dickens and A.V. Powell, J. Solid State Chem. 93, 526-533 (1991).
695. Choi Y.-K., S.-S. Seo, K.-H. Chjo, Q.-W. Choi and S.-M. Park, J. Electrochem. Soc. 139, 1803-1807 (1992).
696. Chopra K.L., Thin Film Phenomena (McGraw-Hill, New York, 1969).
697. Chopra K.L, S. Major and K. Pandya, Thin Solid Films 102, 1-46 (1983).
698. Chowdhry U., J.R. Barkley, A.D. English and A.W. Sleight, Mater. Res. Bull. 17, 917-933 (1982).
699. Christensen N.E. and A.R. Mackintosh, Phys. Rev. B 35, 8246-8248 (1987).
700. Chu C.S. and R.S. Sorbello, Phys. Rev. B 38, 7260-7274 (1988).
701. Chu W.F., Solid State Ionics 52, 243-248 (1992).
702. Chu W.F., R. Hartmann, V. Leonhard and G. Ganson, Mater. Sci. Engr. B 13, 235-237 (1992)
703. Chu Y.T., Solid State Ionics 26, 299-302 (1988).
704. Chubachi Y. and K. Aoyama, Japan. J. Appl. Phys. 30, 1442-1446 (1991).
705. Chudnovskii F.A., Zh. Tekh. Fiz. 45, 1561-1583 (1975) [Soviet Phys. Tech. Phys. 20, 999-1012 (1976)].
706. Chudnovskii F.A., D.M. Schaefer, A.I. Gavrilyuk and R. Reifenberger, Appl. Surf. Sci. 62, 145-149 (1992).
707. Chudoba T., Thin Solid Films 131, 95-104 (1985).
708. Cikmach P.D., J.J. Kleperis, A.R. Lusis and G.M. Ramans, Phys. Stat. Sol. A 90, K1-K4 (1985).
709. Claesson Y., M. Georgson, A. Roos and C.-G. Ribbing, Solar Energy Mater. 20, 455-465 (1990).
710. Clark G.M.and W.P. Doyle, Spectrochim. Acta 22, 1441-1447 (1966).
711. Clark R.J.H., The Chemistry of Titanium and Vanadium (Elsevier, Amsterdam, 1968).

712. Clauws P., J. Broeckx and J. Vennik, Phys. Stat. Sol. B 131, 459-473 (1985).
713. Clauws P. and J. Vennik, Phys. Stat. Sol. B 66, 553-560 (1974).
714. Clauws P. and J. Vennik, Phys. Stat. Sol. B 69, 491-500 (1975).
715. Clauws P. and J. Vennik, Phys. Stat. Sol. B 76, 707-713 (1976).
716. Clayton J.C. and D.J. De Smet, J. Electrochem. Soc. 123, 174-179 (1976).
717. Clechet P., J.-R. Martin, R. Olier and C. Vallouy, Comptes Rendues Acad. Sci. Paris, Sér. C, 282, 887-890 (1976).
718. Cocciantelli J.M., J.P. Doumerc, M. Pouchard, M. Brouselly and J. Labat, J. Power Sources 34, 103-111 (1991).
719. Cocciantelli J.M., P. Gravereau, J.P. Doumerc, M. Pochard and P. Hagenmuller, J. Solid State Chem. 93, 497-502 (1991).
720. Cocciantelli J.M., M. Ménétrier, C. Delmas, J.P. Doumerc, M. Pouchard and P. Hagenmuller, Solid State Ionics 50, 99-105 (1992).
721. Cocciantelli J.M., K.S. Suh, J. Sénégas, J.P. Doumerc, J.L. Soubeyroux, M. Pouchard and P. Hagenmuller, J. Phys. Chem. Solids 53, 51-55 (1992).
722. Coey J.M.D. and P.J.K. Murphy, J. Non-Cryst. Solids 50, 125-129 (1982).
723. Cogan S.F., in Large-area Chromogenics: Materials and Devices for Transmittance Control, edited by C.M. Lampert and C.G. Granqvist (SPIE Opt. Engr. Press, Bellingham, 1990), Vol. IS4, pp. 313-325.
724. Cogan S.F., E.J. Anderson, T.D. Plante and R.D. Rauh, Appl. Opt. 24, 2282-2283 (1985).
725. Cogan S.F., E.J. Anderson, T.D. Plante and R.D. Rauh, Proc. Soc. Photo-Opt. Instrum. Engr. 562, 23-31 (1985).
726. Cogan S.F., N.M. Nguyen, S.J. Perrotti and R.D. Rauh, Proc. Soc. Photo-Opt. Instrum. Engr. 1016, 57-62 (1988).
727. Cogan S.F., N.M. Nguyen, S.J. Perrotti and R.D. Rauh, J. Appl. Phys. 66, 1333-1337 (1989).
728. Cogan S.F., T.D. Plante, R.S. McFadden and R.D. Rauh, Proc. Soc. Photo-Opt. Instrum. Engr. 692, 32-38 (1986).
729. Cogan S.F., T.D. Plante, R.S. McFadden and R.D. Rauh, Solar Energy Mater. 16, 371-382 (1987).
730. Cogan S.F., T.D. Plante, M.A. Parker and R.D. Rauh, J. Appl. Phys. 60, 2735-2738 (1986).
731. Cogan S.F., T.D. Plante, M.A. Parker and R.D. Rauh, Solar Energy Mater. 14, 185-193 (1986).
732. Cogan S.F. and R.D. Rauh, in Large-area Chromogenics: Materials and Devices for Transmittance Control, edited by C.M. Lampert and C.G. Granqvist (SPIE Opt. Engr. Press, Bellingham, 1990), Vol. IS4, pp. 482-493.
733. Cogan S.F., R.D. Rauh, N.M. Nguyen, T.D. Plante and J.D. Westwood, J. Electrochem. Soc. 140, 112-115 (1993).
734. Cogan S.F., R.D. Rauh, T.D. Plante, N.M. Nguyen and J.D. Westwood, in Electrochromic Materials, edited by M.K. Carpenter and D.A. Corrigan (The Electrochem. Soc., Pennington, 1990), Proc. Vol. 90-2, pp. 99-115.
735. Cogan S.F., R.D. Rauh, J.D. Westwood, D.I. Plotkin and R.B. Jones, Proc. Soc. Photo-Opt. Instrum. Engr. 1149, 2-6 (1989).
736. Cohan J.S., H. Yuan, R.S. Williams and J.I. Zink, Appl. Phys. Lett. 60, 1402-1403 (1992).
737. Cohen C., Electronics, (Aug. 11 1981), 65-66.
738. Cohen C., Electronics, (April 21 1982), 76-77.
739. Cohen M. and K. Hashimoto, J. Electrochem. Soc. 121, 42-45 (1974).
740. Colaitis D., Phys. Stat. Sol. B 165, 157-173 (1991).
741. Collin R.J., W.P. Griffith and D. Pawson, J. Mol. Struct. 19, 531-544 (1973).
742. Colomban P., M. Pham Thi and A. Novak, Solid State Commun. 53, 747-751 (1985).
743. Colpaert M.N., P. Clauws, L. Fiermans and J. Vennik, Surf. Sci. 36, 513-525 (1973).
744. Colson S., S.-P. Szu, L.C. Klein and J.M. Tarascon, Solid State Ionics 46, 283-289 (1991).
745. Colton R.J., A.M. Guzman and J.W. Rabalais, J. Appl. Phys. 49, 409-416 (1978).
746. Colton R.J., A.M. Guzman and J.W. Rabalais, Acc. Chem. Res. 11, 170-176 (1978).
747. Colton R.J. and J.W. Rabalais, Inorg. Chem. 15, 236-238 (1976).
748. Companion A.L. and M. Mackin, J. Chem. Phys. 42, 4219-4222 (1965).
749. Conell R.S., D.A. Corrigan and B.R. Powell, Solar Energy Mater. Solar Cells 25, 301-313 (1992).

750. Conlon D.C. and W.P. Doyle, J. Chem. Phys. 35, 752-753 (1961).
751. Conner W.T. and H.H. Sawin, Appl. Phys. Lett. 60, 557-559 (1992).
752. Consadori F. and A. Stella, Lett. Nuovo Cimento 3, 600-603 (1970).
753. Conway B.E. and J. Mozota, Electrochim. Acta 28, 9-16 (1983).
754. Cook J.G. and F.P. Koffyberg, Solar Energy Mater. 10, 55-67 (1984).
755. Cook J.G. and M.P. van der Meer, Thin Solid Films 144, 165-176 (1986).
756. Cordoba S.I., R.E. Carbonio, M.L. Teijelo and V.A. Macagno, Electrochim. Acta 31, 1321-1332 (1986).
757. Cordoba-Torresi S.I., C. Gabrielli, A. Hugot-LeGoff and R. Torresi, J. Electrochem. Soc. 138, 1548-1553 (1991).
758. Cordoba-Torresi S.I. and A. Gorenstein, Electrochim. Acta 37, 2015-2019 (1992).
759. Cordoba-Torresi S.I. and A. Gorenstein, Proc. Soc. Photo-Opt. Instrum. Engr. 1728, 92-102 (1992).
760. Cordoba-Torresi S.I., A. Gorenstein, R.M. Torresi and M.V. Vasquez, J. Electroanal. Chem. 318, 131-144 (1991).
761. Cordoba-Torresi S.I., A. Hugot-LeGoff and S. Joiret, J. Electrochem. Soc. 138, 1554-1559 (1991).
762. Cordoba-Torresi S.I., A. Hugot-LeGoff and H. Takenouti, Proc. Soc. Photo-Opt. Instrum. Engr. 1272, 152-161 (1990).
763. Cornilsen B.C., P.J. Karjala and P.L. Loyselle, J. Power Sources 22, 351-357 (1988).
764. Cornilsen B.C., X. Shan and P.L. Loyselle, in Proc. Symp. Nickel Hydroxide Electrodes (The Electrochem. Soc., Pennington, 1990), Proc. Vol. 90-4, pp. 82-96.
765. Cornilsen B.C., X. Shan and P.L. Loyselle, J. Power Sources 29, 453-466 (1990).
766. Cornish W.D. and L. Young L., Proc. Roy. Soc. London A 335, 39-50 (1973).
767. Corradini A., A.M. Marinangeli and M. Mastragostino, Electrochim. Acta 35, 1757-1760 (1990).
768. Corrigan D.A., J. Electrochem. Soc. 134, 377-384 (1987).
769. Corrigan D.A., Solar Energy Mater. Solar Cells 25, 293-300 (1992).
770. Corrigan D.A. and R.M. Bendert, J. Electrochem. Soc. 136, 723-728 (1989).
771. Corrigan D.A. and M.K. Carpenter, in Large-area Chromogenics: Materials and Devices for Transmittance Control, edited by C.M. Lampert and C.G. Granqvist (SPIE Opt. Engr. Press, Bellingham, USA, 1990), Vol. IS4, pp. 298-312.
772. Corrigan D.A. and S.L. Knight, J. Electrochem. Soc. 136, 613-619 (1989).
773. Corrigan D.A. and A.H. Zimmerman, editors, Proc. Symp. Nickel Hydroxide Electrodes (The Electrochem. Soc., Pennington, 1990), Proc. Vol. 90-4.
774. Coucou A., A. Driouiche, M. Figlarz, M. Touboul and G. Chevrier, J. Solid State Chem. 99, 283-289 (1992).
775. Coucou A. and M. Figlarz, Solid State Ionics 28-30, 1762-1765 (1988).
776. Cowen S., J.R. Sambles and A. Glidle, J. Electroanal. Chem. 261, 455-462 (1989).
777. Cowie J.M.G., in Polymer Electrolyte Reviews-1, edited by J.R. MacCallum and C.A. Vincent (Elsevier Appl. Sci., London, 1987), pp. 69-102.
778. Cowling R.D. and A.C. Riddiford, Electrochim. Acta 14, 981-989 (1969).
779. Cox P.A., Transition Metal Oxides (Clarendon, Oxford, 1992).
780. Craig J.B. and J.M. Grant, J. Mater. Chem. 2, 521-524 (1992).
781. Craigen D., A. Mackintosh, J. Hickman and K. Colbow, J. Electrochem. Soc. 133, 1529-1530 (1986).
782. Crandall R.S. and B.W. Faughnan, Appl. Phys. Lett. 26, 120-121 (1975).
783. Crandall R.S. and B.W. Faughnan, Appl. Phys. Lett. 28, 95-97 (1976).
784. Crandall R.S. and B.W. Faughnan, Phys. Rev. B 16, 1750-1752 (1977).
785. Crandall R.S. and B.W. Faughnan, Phys. Rev. Lett. 39, 232-235 (1977).
786. Crandall R.S., P.J. Wojtowicz and B.W. Faughnan, Solid State Commun. 18, 1409-1411 (1976).
787. Cronin J.P., D.J. Tarico, J.C.L. Tonazzi, A. Agrawal and S.R. Kennedy, Solar Energy Mater. Solar Cells 29, 371-386 (1993).
788. Crouch-Baker S. and P.G. Dickens, Mater. Res. Bull. 19, 1457-1462 (1984).
789. Crowley J.L., R.A. Wallace and R.H. Bube, J. Polymer Sci., Polymer Phys. Ed. 14, 1769-1787 (1976).
790. Crumbliss A.L., P.S. Lugg and N. Morosoff, Inorg. Chem. 23, 4701-4708 (1984).
791. Crumbliss A.L., P.S. Lugg, D.L. Patel and N. Morosoff, Inorg. Chem. 22, 3541-3548 (1983).

792. Cui Y., X. Xu, Z. Jin, C. Peng and S. Xie, Thin Solid Films 115, 195-201 (1984).
793. Cukman D. and M. Vukovic´, J. Electroanal. Chem. 279, 283-290 (1990).
794. Czanderna A.W. and C.M. Lampert, Solar Energy Research Institute Technical Report SERI/TP-255-3537 (July 1990), pp. 1-52, unpublished.
795. Czyzyk M.T., R. Potze and G.A. Sawatzky, Phys. Rev. B 46, 3729-3735 (1992).

D

796. D'Arco P., M. Causà, C. Roetti and B. Silvi, Phys. Rev. B 47, 3522-3529 (1993).
797. da Fonseca C.N.P., M.-A. De Paoli and A. Gorenstein, Adv. Mater. 3, 553-555 (1991).
798. Dahl J.P. and A.C. Switendick, J. Phys. Chem. Solids 27, 931-942 (1966).
799. Dahn J.R., U. von Sacken, M.W. Juzkov and H. Al-Janaby, J. Electrochem. Soc. 138, 2207-2211 (1991).
800. Dahn J.R., U. von Sacken and C.A. Michal, Solid State Ionics 44, 87-97 (1990).
801. Dallacasa V., M. Manfredi and G. Schianchi, Thin Solid Films 91, 1-8 (1982).
802. Dallacasa V., M. Manfredi and G. Schianchi, Solid State Commun. 46, 561-563 (1983).
803. Daly C.M. and R.G. Keil, J. Electrochem. Soc. 122, 350-353 (1975).
804. Daly C.M. and R.G. Keil, J. Electrochem. Soc. 122, 730-733 (1975).
805. Dance J.-M. and T. Oi, Thin Solid Films 104, L71-L73 (1983).
806. Daniel M.F., B. Desbat, J.C. Lassegues and R. Garie, J. Solid State Chem. 73, 127-139 (1988).
807. Daniel M.F., B. Desbat, J.C. Lassegues, B. Gerand and M. Figlarz, J. Solid State Chem. 67, 235-247 (1987).
808. Daniels R.R., G. Margaritondo, C.-A. Georg and F. Lévy, Phys. Rev. B 29, 1813-1818 (1984).
809. Dao L.H., J. Guay and M. Leclerc, Synth. Met. 29, E383-E388 (1989).
810. Dao L.H., A. Guerfi and M.T. Nguyen, in Electrochromic Materials, edited by M.K. Carpenter and D.A. Corrigan (The Electrochem. Soc., Pennington, 1990), Proc. Vol. 90-2, pp. 30-44.
811. Dao L.H., M. Leclerc, J. Guay and J.W. Chevalier, Synth. Met. 29, E377-E382 (1989).
812. Dao L.H. and M.T. Nguyen, in Proc. Intrasoc. Energy Conversion Engr. Conf., Washington, (IEEE, 1989), Vol. 4, pp. 1737-1741.
813. Dao L.H. and M.T. Nguyen, in Electrochromic Materials, edited by M.K. Carpenter and D.A. Corrigan (The Electrochem. Soc., Pennington, 1990), Proc. Vol. 90-2, pp. 246-260.
814. Dautremont-Smith W.C., Displays (January 1982), pp. 3-22.
815. Dautremont-Smith W.C., Displays (April 1982), pp. 67-80.
816. Dautremont-Smith W.C., G. Beni, L.M. Schiavone and J.L. Shay, Appl. Phys. Lett. 35, 565-567 (1979).
817. Dautremont-Smith W.C., M. Green and K.S. Kang, Electrochim. Acta 22, 751-759 (1977).
818. Dautremont-Smith W.C., L.M. Schiavone, G. Beni and J.L. Shay, SID Dig. (1980), 122-123.
819. Dautremont-Smith W.C., L.M. Sciavone, S. Hackwood, G. Beni and J.L. Shay, Solid State Ionics 2, 13-18 (1981).
820. Davazoglou D. and A. Donnadieu, Thin Solid Films 147, 131-142 (1987).
821. Davazoglou D. and A. Donnadieu, Thin Solid Films 164, 369-374 (1988).
822. Davazoglou D. and A. Donnadieu, J. Appl. Phys. 72, 1502-1511 (1992).
823. Davazoglou D., A. Donnadieu and O. Bohnke, Solar Energy Mater. 16, 55-65 (1987).
824. Davazoglou D., A. Donnadieu, R. Fourcade, A. Hugot-LeGoff, P. Delichere and A. Perez, Rev. Phys. Appl. 23, 265-272 (1988).
825. Davazoglou D., G. Leveque and A. Donnadieu, Solar Energy Materials 17, 379-390 (1988).
826. Davidson, M.R., G.B. Moflund, L. Niinistö and H.A. Laitinen, J. Electroanal. Chem. 228, 471-480 (1987).
827. Davies D.H. and G.T. Burstein, Corrosion Sci. 20, 973-987 (1980).
828. Davies J.H. and J.R. Franz, Phys. Rev. Lett. 57, 475-478 (1986).
829. Davies J.H., P.A. Lee and T.M. Rice, Phys. Rev. B 29, 4260-4271 (1984).
830. Davis C.A., D.R. McKenzie and R.C. McPhedran, Opt. Commun. 85, 70-82 (1991).
831. Day P., F. Herren, A. Ludi, H.U. Güdel, F. Hulliger and D. Givord, Helv. Chem. Acta 63, 148-153 (1980).
832. De Angelis B.A. and M. Schiavello, J. Solid State Chem. 21, 67-72 (1977).
833. De Angelis B.A. and M. Schiavello, Chem. Phys. Lett. 58, 249-251 (1978).

834. Deb S.K., Proc. Roy. Soc. London A 304, 211-231 (1968).
835. Deb S.K., Appl. Opt. Suppl. 3, 192-195 (1969).
836. Deb S.K., Philos. Mag. 27, 801-822 (1973).
837. Deb S.K., in Proc. 24th Electronic Components Conf. (IEEE, Washington, 1974), pp. 11-14.
838. Deb S.K., in Prog. 4 Int. Kongr. Reprographie und Information (1975), pp. 115-119.
839. Deb S.K., Phys. Rev. B 16, 1020-1024 (1977).
840. Deb S.K., Proc. Soc. Photo-Opt. Instrum. Engr. 692, 19-31 (1986).
841. Deb S.K., in Electrochromic Materials, edited by M.K. Carpenter and D.A. Corrigan (The Electrochemical Society, Pennington, 1990), Proc. Vol. 90-2, pp. 3-13.
842. Deb S.K., Solar Energy Mater. Solar Cells 25, 327-338 (1992).
843. Deb S.K. and J.A. Chopoorian, J. Appl. Phys. 37, 4818-4825 (1966).
844. Deb S.K. and H. Witzke, Proc. Electron Devices Meeting, Washington (IEEE, New York, 1975), pp. 393-397.
845. Deb S.K. and H. Witzke, Proc. Int. Microelectronics Conf., Orlando, Florida (1975), pp. 351-357.
846. De Battisti A., A. Barbieri, A. Giatti, G. Battaglin, S. Daolio and A.B. Boscoletto, J. Mater. Chem. 1, 191-195 (1991).
847. Decker F., S. Passerini, R. Pileggi and B. Scrosati, Electrochim. Acta 37, 1033-1038 (1992).
848. Decker F., R. Pileggi, S. Passerini and B. Scrosati, J. Electrochem. Soc. 138, 3182-3186 (1991).
849. de Faria I.C., R.M. Torresi and A. Gorenstein, Proc. Soc. Photo-Opt. Instrum. Engr. 1728, 54-65 (1992).
850. Degani Y., T.T. Sheng, A. Heller, D.E. Aspnes, A.A. Studna and J.D. Porter, J. Electroanal. Chem. 228, 167-178 (1987).
851. Degiorgi L., B. Alavi, G. Mihály and G. Grüner, Phys. Rev. B 44, 7808-7819 (1991).
852. Degiorgi L. and G. Grüner, Phys. Rev. B 44, 7820-7827 (1991).
853. Degiorgi L. and G. Grüner, Europhys. Lett. 16, 97-102 (1991).
854. Degiorgi L. and G. Grüner, J. Phys. I (Paris) 2, 523-528 (1992).
855. Degiorgi L., P. Wachter and D. Ihle, Phys.Rev. B 35, 9259-9264 (1987).
856. Delahaye-Vidal A., B. Beaudoin and M. Figlarz, Reactivity Solids 2, 223-233 (1986).
857. Delahaye-Vidal A. and M. Figlarz, J. Appl. Electrochem. 17, 589-599 (1987).
858. DeLand S.M., G. Mozurkewich and L.D. Chapman, Phys. Rev. Lett. 66, 2026-2029 (1991).
859. Delaplane R.G., J.A. Ibers, J.R. Ferraro and J.J. Rush, J. Chem. Phys. 50, 1920-1927 (1969).
860. Delichere P., P. Falaras, M. Froment, A. Hugot-Le Goff and B. Agius, Thin Solid Films 161, 35-46 (1988).
861. Delichere P., P. Falaras, and A. Hugot-Le Goff, Proc. Soc. Photo-Opt. Instrum. Engr. 1016, 12-18 (1988).
862. Delichere P., P. Falaras, and A. Hugot-Le Goff, Thin Solid Films 161, 47-58 (1988).
863. Delichere P., P. Falaras and A. Hugot-Le Goff, Solar Energy Mater. 19, 323-333 (1989).
864. Delichere P., A. Hugot-LeGoff and N. Yu, J. Electrochem. Soc. 133, 2106-2107 (1986).
865. Delichere P., S. Joiret, A. Hugot-Le Goff, K. Bange and B. Metz, Proc. Soc. Photo-Opt. Instrum. Engr. 1016, 165-169 (1988).
866. Delichere P., S. Joiret, A. Hugot-Le Goff, K. Bange and B. Metz, J. Electrochem. Soc. 135, 1856-1857 (1988).
867. Delmas C., Mater. Res. Soc. Symp. Proc. 293, 15-26 (1993).
868. Delmas C., J.J. Braconnier, Y. Borthomieu and P. Hagenmuller, Mater. Res. Bull. 22, 741-751 (1987).
869. Delmas C., J.J. Braconnier and P. Hagenmuller, Mater. Res. Bull. 17, 117-123 (1982).
870. Delmas C., S. Brèthes and M. Ménétrier, J. Power Sources 34, 113-118 (1991).
871. Delmas C., S.H. Chang, M. Menetrier, K.S. Suh, J. Senegas and J.P. Chaminade, Solid State Ionics 40-41, 560-562 (1990).
872. Delmas C., C. Fouassier, J.-M. Réau and P. Hagenmuller, Mater. Res. Bull. 11, 1081-1086 (1976).
873. Delmas C. and I. Saadoune, Solid State Ionics 53-56, 370-375 (1992).
874. Demiryont H., Proc. Soc. Photo-Opt. Instrum. Engr. 1323, 171-187 (1990).
875. Demiryont H., Proc. Soc. Photo-Opt. Instrum. Engr. 1536, 2-8 (1991).
876. Demiryont H., Appl. Opt. 31, 250-254 (1992).
877. Demiryont H. and K.E. Nietering, Appl. Opt. 28, 1494-1500 (1989).
878. Demiryont H. and S.C. Schulz, Proc. Soc. Photo-Opt. Instrum. Engr. 1149, 28-39 (1989).

879. Demiryont H. and J.R. Sites, J. Vac. Sci. Technol. A 2, 1457-1460 (1984).
880. Demiryont H., J.R. Sites and K. Geib, Appl. Opt. 24, 490-495 (1985).
881. De Mishima B.A.L., T. Ohtsuka, H. Konno and N. Sato, Electrochim. Acta 36, 1485-1489 (1991).
882. De Mishima B.A.L., T. Ohtsuka and N. Sato, J. Electroanal. Chem. 243, 219-223 (1988).
883. De Natale J.F., P.J. Hood and A.B. Harker, J. Appl. Phys. 66, 5844-5850 (1989).
884. Deneuville A. and P. Gérard, J. Electronic Mater. 7, 559-588 (1978).
885. Deneuville A., P. Gérard and R. Billat, Thin Solid Films 70, 203-223 (1980).
886. Denisov E.P., V.I. Kruglov, Yu. A. Salganik, N.A. Tikhonov and N.P. Sergushin, Izv. Akad. Nauk SSSR Neorg. Mater. 15, 171-172 (1979) [Inorg. Mater. 15, 134-136 (1979)].
887. Dennstedt W. and W. Löser, Electrochim. Acta. 16, 429-435 (1971).
888. De Pauli C.P., M.C. Giordano and J.O. Zerbino, Electrochim. Acta 28, 1781-1788 (1983).
889. de Picciotto L.A. and M.M. Thackeray, Solid State Ionics 18-19, 773-777 (1986).
890. de Picciotto L.A. and M.M. Tackeray, J. Power Sources 35, 323-331 (1991).
891. Deroo D., in Second International Symposium on Polymer Electrolytes, edited by B. Scrosati (Elsevier Appl. Sci., London, 1990), pp. 433-447.
892. De Rossi S., E. Iguchi, M. Schiavello and R.J.D. Tilley, Z. Phys. Chem. N.F. 103, 193-202 (1976).
893. Deschanvres A., G. Desgardin, B. Raveau and J.-C. Thomazeau, Bull. Soc. Chim. France (1967), 4537-4541.
894. Desikan A.N., L. Huang and S.T. Oyama, J. Phys. Chem. 95, 10050-10056 (1991).
895. Desilvestro J., D.A. Corrigan and M.J. Weaver, J. Phys. Chem. 90, 6408-6411 (1986).
896. Desilvestro J., D.A. Corrigan and M.J. Weaver, J. Electrochem. Soc. 135, 885-892 (1988).
897. De Smet D.J., Electrochim. Acta 21, 1137-1142 (1976).
898. De Smet D.J. and J.L. Ord, J. Electrochem. Soc. 130, 280-284 (1983).
899. De Smet D.J. and J.L. Ord, J. Electrochem. Soc. 134, 1734-1740 (1987).
900. De Smet D.J. and J.L. Ord, J. Electrochem. Soc. 136, 2841-2845 (1989).
901. Despotuli A.L., N.V. Lichkova, N.A. Minenkova and S.V. Nosenko, Elektrokhim. 26, 1524-1528 (1990) [Soviet Electrochem. 26, 1364-1367 (1990)].
902. Despotuli A.L., V.N. Zagorodnev, N.V. Lichkova and N.A. Minenkova, Fiz. Tverd. Tela 31, 242-244 (1989) [Soviet Phys. Solid State 31, 1613-1614 (1989)].
903. Deutschmann L., H. Suhr, W.A. Herrmann and P. Härter, Eur. J. Solid State Inorg. Chem. 28, 1161-1171 (1991).
904. Dexter D.L., in Solid State Physics, edited by F. Seitz and D. Turnbull (Academic, New York, 1958), Vol. 6, pp. 353-411.
905. Dey A.N., J. Electrochem. Soc. 114, 823-824 (1967).
906. Dey A.N. and B.P. Sullivan, J. Electrochem. Soc. 117, 222-224 (1970).
907. Dickens P.G. and J.J. Birtill, J. Electronic Mater. 7, 679-686 (1978).
908. Dickens P.G., J.J. Birtill and C.J. Wright, J. Solid State Chem. 28, 185-193 (1979).
909. Dickens P.G., A.M. Chippindale and S.J. Hibble, Solid State Ionics 34, 79-85 (1989).
910. Dickens P.G., A.M. Chippindale, S.J. Hibble and P. Lancaster, Mater. Res. Bull. 19, 319-324 (1984).
911. Dickens P.G., S. Crouch-Baker and M.T. Weller, Solid State Ionics 18-19, 89-97 (1986).
912. Dickens P.G., S.J. French, A.T. Hight and M.F. Pye, Mater. Res. Bull. 14, 1295-1299 (1979).
913. Dickens P.G., S.J. Hibble, S.A. Kay and M.A. Steers, Solid State Ionics 20, 209-212 (1986).
914. Dickens P.G. and R.J. Hurditch, Nature 215, 1266-1267 (1967).
915. Dickens P.G. and R.J. Hurditch, in The Chemistry of Extended Defects in Non-metallic Solids, edited by L. Eyring and M. O'Keefe (North-Holland, Amsterdam, 1970), pp. 555-560.
916. Dickens P.G. and R.H. Jarman, J. Electrochem. Soc. 128, 1390 (1981).
917. Dickens P.G. and S.A. Kay, Solid State Ionics 8, 291-295 (1983).
918. Dickens P.G., J.H. Moore and D.J. Neild, J. Solid State Chem. 7, 241-244 (1973).
919. Dickens P.G. and M.F. Pye, in Intercalation Chemistry, edited by M.S. Whittingham and A.J. Jacobson (Academic, New York, 1982), pp. 539-561.
920. Dickens P.G., R.M.P. Quilliam and M.S. Whittingham, Mater. Res. Bull. 3, 941-950 (1968).
921. Dickens P.G. and G.J. Reynolds, Solid State Ionics 5, 331-334 (1981).
922. Dickens P.G. and M.S. Whittingham, Quart. Rev. Chem. Soc. 22, 30-44 (1968).

923. Dietz R.E., M. Campagna, J.N. Chazalviel and H.R. Shanks, Phys. Rev. B 17, 3790-3800 (1978).
924. Dietz R.E., G.I. Parisot and A.E. Meixner, Phys. Rev. B 4, 2302-2310 (1971).
925. Dimitriev Y., V. Dimitrov, M. Arnaudov and D. Topalov, J. Non-Cryst. Solids 57, 147-156 (1983).
926. Ding J.R., X. Zhou, J.N. Bai and B.X. Liu, J. Vac. Sci. Technol. A 8, 3349-3351 (1990).
927. Dinh N.N., V.T. Bich, N.H. Hoang and L.Q. Minh, Phys. Stat. Sol. A 108, K157-K161 (1988).
928. Di Paola A., F. Di Quarto and G. Serravalle, J. Less-Common Met. 42, 315-324 (1975).
929. Di Paola A., F. Di Quarto and C. Sunseri, J. Electrochem. Soc. 125, 1344-1347 (1978).
930. Di Paola A., F. Di Quarto and C. Sunseri, Corrosion Sci. 20, 1067-1078 (1980).
931. Di Paola A., F. Di Quarto and C. Sunseri, Corrosion Sci. 20, 1079-1088 (1980).
932. Di Quarto F., V.O. Aimiuwu, S. Piazza and C. Sunseri, Electrochim. Acta 36, 1817-1822 (1991).
933. Di Quarto F., A. Di Paola, S. Piazza and C. Sunseri, Solar Energy Mater. 11, 419-433 (1985).
934. Di Quarto F., A. Di Paola and C. Sunseri, J. Electrochem. Soc. 127, 1016-1021 (1980).
935. Di Quarto F., A. Di Paola and C. Sunseri, Electrochim. Acta 26, 1177-1184 (1981).
936. Di Quarto F., S. Piazza, R. D'Agostino and C. Sunseri, J. Electroanal. Chem 228, 119-134 (1987).
937. Di Quarto F., S. Piazza and C. Sunseri, J. Electroanal. Chem. 248, 99-115 (1988).
938. Di Quarto F., S. Piazza and C. Sunseri, J. Electroanal. Chem. 248, 117-129 (1988).
939. Di Quarto F., S. Piazza and C. Sunseri, Electrochim. Acta 35, 99-107 (1990).
940. Di Quarto F., S. Piazza and C. Sunseri, Electrochim. Acta 38, 29-35 (1993).
941. Di Quarto F., G. Russo, C. Sunseri and A. Di Paola, J. Chem. Soc. Faraday Trans. I 78, 3433-3445 (1982).
942. Di Quarto F., C. Sunseri and S. Piazza, Ber. Bunsenges. Phys. Chem 90, 549-555 (1986).
943. Dirks A.G. and H.J. Leamy, Thin Solid Films 47, 219-233 (1977).
944. Dislich H. and P. Hinz, J. Non-Cryst. Solids 48, 11-16 (1982).
945. Dissado L.A. and R.M. Hill, J. Appl. Phys. 66, 2511-2524 (1989).
946. Ditchburn R.J. and G.B. Smith, J. Appl. Phys. 69, 3769-3771 (1991).
947. Dittmer G. and U. Niemann, Philips J. Res. 36, 89-113 (1981).
948. Divigalpitiya W.M.R., R.F. Frindt and S.R. Morrison, Thin Solid Films 188, 173-179 (1990).
949. Divigalpitiya W.M.R., S.R. Morrison and R.F. Frindt, Thin Solid Films 186, 177-192 (1990).
950. Dobrev D., V. Gadjokov, V. Velev and A. Gittis, Phys. Stat. Sol. A 95, 93-97 (1986).
951. Dobrowski S.A., G.R. Davies, J.E. McIntyre and I.M. Ward, Polymer 32, 2887-2891 (1991).
952. Doeff M.M., C.M. Lampert, S.J. Visco and Y.P. Ma, Proc. Soc. Photo-Opt. Instrum. Engr. 1728, 223-231 (1992).
953. Doeuff S., M. Henry, C. Sanchez and J. Livage, J. Non-Cryst. Solids 89, 84-97 (1987).
954. Doeuff S. and C. Sanchez, Comptes Rendues Acad. Sci. Paris, Sér. II, 309, 531-534 (1989).
955. Domengès B., N.K. McGuire and M. O'Keeffe, J. Solid State Chem. 56, 94-100 (1985).
956. Dong S. and Z. Jin, J. Electroanal. Chem. 256, 193-198 (1988).
956a. Donnadieu A., Mater. Sci. Engr. B 3, 185-195 (1989).
957. Donnadieu A., in Energy and Environment into the 1990s, edited by A.A.M. Sayigh (Pergamon, Oxford, 1990), Vol. 3, pp. 1424-1429.
958. Donnadieu A., in Large-area Chromogenics: Materials and Devices for Transmittance Control, edited by C.M. Lampert and C.G. Granqvist (SPIE Opt. Engr. Press, Bellingham, 1990), Vol. IS4, pp. 191-214.
959. Donnadieu A. and D. Davazoglou, Proc. Soc. Photo-Opt. Instrum. Engr. 653, 36-41 (1986).
960. Donnadieu A. and D. Davazoglou and A. Abdellaoui, Thin Solid Films 164, 333-338 (1988).
961. Donnadieu A. and D. Davazoglou and A. Abdellaoui, Proc. Soc. Photo-Opt. Instrum. Engr. 1016, 124-130 (1988).
962. Donnadieu A., M. Regragui, A. Abdellaoui and D. Davazoglou, Proc. Soc. Photo-Opt. Instrum. Engr. 1272, 197-206 (1990).
963. Donnadieu A., M. Regragui, B. Ducourant, R. Fourcade and O. Bohnke, Proc. Soc. Photo-Opt. Instrum. Engr. 1728, 2-12 (1992).
964. Döring H., K. Hashimoto and A. Fujishima, Ber. Bunsenges. Phys. Chem. 96, 620-622 (1992).
965. Douglass D.L. and R.B. Pettit, Solar Energy Mater. 4, 385-402 (1981).
966. Doumerc J.P., J.M. Cocciantelli, J.C. Grenier, M. Pouchard and P. Hagenmuller, Z. Anorg. Allg. Chem. 619, 748-752 (1993).

967. Dow J.D., Comments Solid State Phys. 4, 35-43 (1972).
968. Dow J.D. and D. Redfield, Phys. Rev. B 5, 594-610 (1971).
969. Doyle W.P. and G.A. Lonergan, Disc. Faraday Soc. 26, 27-33 (1958).
970. Driouiche A., F. Abraham, M. Touboul and M. Figlarz, Mater. Res. Bull. 26, 901-908 (1991).
971. Driouiche A., M. Figlarz and C. Delmas, Solid State Ionics 62, 113-117 (1993).
972. Driscoll T.J., L.D. McCormick and W.C. Lederer, Surf. Sci. 187, 539-558 (1987).
973. Drobny V.F. and D.L. Pulfrey, Thin Solid Films 61, 89-98 (1979).
974. Droog J.M.M., C.A. Alderliesten, P.T. Alderliesten and G.A. Bootsma, J. Electroanal. Chem. 111, 61-70 (1980).
975. Dudney N.J., J.B. Bates and J.D. Robertson, J. Vac. Sci. Technol. A11, 377-389 (1993).
976. Duek E.A.R., M.-A. De Paoli and M. Mastragostino, Adv. Mater. 4, 287-291 (1992).
977. Duffy J.A., M.D. Ingram and P.M.S. Monk, Solid State Ionics 58, 109-114 (1992).
978. Duffy M.T., C.C. Wang, A. Waxman and K.H. Zaininger, J. Electrochem. Soc. 116, 234-239 (1969).
979. Duggan M.J., T. Saito and T. Niwa, Solid State Ionics 62, 15-20 (1993).
980. Dumas J., A. Arbaoui, B. Daudin, M. Dubus, E.M. Lopes and M. Almeida, Synth. Met. 41-43, 3813-3820 (1991).
981. Dunstan D.J., J. Phys. C 15, L419-L424 (1982).
982. Dupon R., B.L. Papke, M.A. Ratner and D.F. Shriver, J. Electrochem. Soc. 131, 586-589 (1984).
983. Dyer C.K., J. Electrochem. Soc. 132, 13-18 (1985).
984. Dyer C.K. and J.S.L. Leach, Electrochim. Acta 20, 151-160 (1975).
985. Dyer C.K. and J.S.L. Leach, J. Electrochem. Soc. 125, 23-29 (1978).
986. Dyer C.K. and J.S.L. Leach, J. Electrochem. Soc. 125, 1032-1038 (1978).
987. Dzhanelidze R.B., I.M. Purtseladze, L.S. Khitarishvili, R.I. Chikovani and A.L. Shkol'nik, Fiz. Tverd. Tela 7, 2573-2575 (1965) [Soviet Phys. Solid State 7, 2082-2083 (1966)].
988. Dzimitrowicz D.J., J.B. Goodenough and P.J. Wiseman, Mater. Res. Bull. 17, 971-979 (1982).
989. Dzwonkowski P., C. Julien and M. Balkanski, Appl. Surf. Sci. 33-34, 838-843 (1988).

E

990. Echigoya J., S. Kato and H. Enoki, J. Mater. Sci. Mater. Electronics 3, 168-171 (1992).
991. Eckertova L., Physics of Thin Films, Second ed. (Plenum, New York, 1986).
992. Eckstein W. and J. László, J. Nucl. Mater. 183, 19-24 (1991).
993. Eckstein W. and J. Roth, Nucl. Instrum. Meth. Phys. Res. B 53, 279-284 (1991).
994. Eda K., J. Solid State Chem. 95, 64-75 (1991).
995. Eda K., J. Solid State Chem. 98, 350-357 (1992).
996. Edlinger J., J. Ramm and H.K. Pulker, Thin Solid Films 175, 207-212 (1989).
997. Edström K., J.O. Thomas and G.C. Farrington, Acta Cryst. B 47, 210-216 (1991).
998. Efros A.L. and A.L. Efros, Fiz. Tekh. Poluprovodn. 16, 1209-1214 (1982) [Soviet Phys. Semicond. 16, 772-775 (1982)].
999. Efros A.L. and M. Pollak, Electron-Electron Interactions in Disordered Systems (North-Holland, New York, 1985).
1000. Egdell R.G. and M.D. Hill, Chem. Phys. Lett. 85, 140-144 (1982).
1001. Egdell R.G. and M.D. Hill, Chem. Phys. Lett. 88, 503-507 (1982).
1002. Ekimov A.I. and A.A. Onuschenko, Pis'ma Zh. Eksp. Teor. Fiz. 40, 337-340 (1984) [JETP Lett. 40, 1136-1139 (1984)].
1003. Efremov B.N., M.R. Tarasevich, G.I. Zakharkin and S.R. Zhukov, Elektrokhim. 14, 1504-1509 (1978) [Soviet Electrochem. 14, 1303-1308 (1978)].
1004. El Ghandour M.F.M., Z. Phys. Chem. (Leipzig) 262, 514-524 (1981).
1005. Elich J.J.P., E.C. Boslooper and H. Haitjema, Thin Solid Films 177, 17-33 (1989).
1006. Elliot R.J., J.A. Krumhansl and P.L. Leath, Rev. Mod. Phys. 46, 465-543 (1974).
1007. Ellis B.H., M.A. Hopper and D.J. De Smet, J. Electrochem. Soc. 118, 860-864 (1971).

1008. Ellis D., M. Eckhoff and V.D. Neff, J. Phys. Chem. 85, 1225-1231 (1981).
1009. El Wakkad S.E.S. and A. Hickling, Trans. Faraday Soc. 46, 820-824 (1950).
1010. Emin D., Phys. Today (6), 34-40 (1982).
1011. Emin D., Phys. Rev. B 46, 9419-9427 (1992).
1012. Emrich R.J., L. Traynor, W. Gambogi and E. Buhks, J. Vac. Sci. Technol. A 5, 1307-1310 (1987).
1013. Engelmann C., M. Loeuillet and O. Bohnke, Trace Microprobe Tech. 4, 93-102 (1986).
1014. England W.A., M.G. Cross, A. Hamnett, P.J. Wiseman and J.B. Goodenough, Solid State Ionics 1, 231-249 (1980).
1015. Enjalbert R. and J. Galy, Acta Cryst. C 42, 1467-1469 (1986).
1016. Ensign T.C. and S.E. Stokowski, Phys. Rev. B 1, 2799-2810 (1970).
1017. Eremin A.I., I.D. Kovalev and A.M. Potapov, Zh. Neorg. Khim. 36, 1341-1348 (1992) [Russian J. Inorg. Chem. 37, 676-680 (1992)].
1018. Érlikh Yu.I., K.L. Anni and U.V. Palm, Elektrokhim. 14, 1066-1069 (1978) [Soviet Electrochem. 14, 925-927 (1978)].
1019. Erre R., H. Masbah, M. Crespin, H. Van Damme and D. Tinet, Solid State Ionics 37, 329-351 (1990).
1020. Estrada W., A.M. Andersson, F. Decker and A. Gorenstein, in Electrochromic Materials, edited by M.K. Carpenter and D.A. Corrigan (The Electrochem. Soc., Pennington, 1990), Proc. Vol. 90-2, pp. 54-69.
1021. Estrada W., A.M. Andersson and C.G. Granqvist, J. Appl. Phys. 64, 3678-3683 (1988).
1022. Estrada W., A.M. Andersson, C.G. Granqvist, A. Gorenstein and F. Decker, J. Mater. Res. 6, 1715-1719 (1991).
1023. Evans H.T., Jr. and M.E. Mrose, Acta Cryst. 11, 56-58 (1958).
1024. Evans R.G., L.A. Bursill and D.J. Smith, Optik 72, 137-142 (1986).
1025. Evdokimova T.F., S.L. Kraevskii, A.P. Prasolov, V.F. Solinov and E.V. Shishmentseva, Fiz. Khim. Stekla 4, 88-90 (1978).
1026. Ezhov B.B. and O.G. Malandin, J. Electrochem. Soc. 138, 885-889 (1991).
1027. Ezhov B.B., O.G. Malandin and S.N. Kudryashov, Elektrokhim. 25, 86-93 (1989) [Soviet Electrochem. 25, 70-77 (1989)].

F

1028. Faber M., O.M. Uy and R.D. Srivastava, J. Chem. Phys. 56, 5312-5315 (1972).
1029. Falaras P., M. Froelicher, M. Froment and A. Hugot-Le Goff, J. Microsc. Spectrosc. Electronics 9, 39-45 (1984).
1030. Falaras P., A. Hugot-Le Goff and S. Joiret, in Large-area Chromogenics: Materials and Devices for Transmittance Control, edited by C.M. Lampert and C.G. Granqvist (SPIE Opt. Engr. Press, Bellingham, 1990), Vol. IS4, pp. 447-470.
1031. Falcone G., Riv. Nuovo Cimento 13, 1-52 (1990).
1032. Falk U., in Electrochemical Power Sources, edited by M. Barak (Peregrinus, Stevenage, 1980), pp. 324-402.
1033. Falk U. and A.J. Salkind, Alkaline Storage Batteries (Wiley, New York, 1969).
1034. Fal'kengof A.T., E.V. Makhonina, B.M. Zhigarnovskii, V.S. Pervov and V.A. Bogdanovskaya, Izv. Akad. Nauk SSSR Neorg. Mater. 26, 2168-2171 (1990) [Inorg. Mater. 26, 1858-1861 (1990)].
1035. Fan J.C.C. and F.J. Bachner, Appl. Opt. 15, 1012-1017 (1976).
1036. Fan J.C.C. and W. Paul, Vide 150, 232-243 (1970).
1037. Fantini M.C.A., G.H. Bezerra, C.R.C. Carvalho and A. Gorenstein, Proc. Soc. Photo-Opt. Instrum. Engr. 1536, 81-92 (1991).
1038. Fantini M.C.A. and A. Gorenstein, Solar Energy Mater. 16, 487-500 (1987).
1039. Fantini M.C.A., A. Gorenstein, W.M. Chen and M. Tomkiewicz, Proc. Soc. Photo-Opt. Instrum. Engr. 1728, 42-53 (1992).
1040. Farcy J., R. Messina and J. Perichon, J. Electrochem. Soc. 137, 1337-1341 (1990).
1041. Farrington G.C. and J.L. Briant, Mater. Res. Bull. 13, 763-773 (1978).
1042. Farrington G.C. and W.L. Roth, Electrochim. Acta 22, 767-772 (1977).
1043. Faucheur C., R. Messina and J. Perichon, J. Electrochem. Soc. 135, 1871-1874 (1988).

1044. Faughnan B.W., Phys. Rev. B 4, 3623-3636 (1971).
1045. Faughnan B.W. and R.S. Crandall, Appl. Phys. Lett. 31, 834-836 (1977).
1046. Faughnan B.W. and R.S. Crandall, in Display Devices, edited by J.I. Pankove (Springer, Berlin, Heidelberg, 1980), Topics in Applied Physics, Vol. 40, pp. 181-211.
1047. Faughnan B.W., R.S. Crandall and P.M. Heyman, RCA Rev. 36, 177-197 (1975).
1048. Faughnan B.W., R.S. Crandall and M.A. Lampert, Appl. Phys. Lett. 27, 275-277 (1975).
1049. Faughnan B.W. and Z.J. Kiss, Phys. Rev. Lett. 21, 1331-1334 (1968).
1050. Faure C., Y. Borthomieu, C. Delmas and M. Fouassier, J. Power Sources 36, 113-125 (1991).
1051. Faure C., C. Delmas and M. Fouassier, J. Power Sources 35, 279-290 (1991).
1052. Faure C., C. Delmas, M. Fouassier and P. Willmann, J. Power Sources 35, 249-261 (1991).
1053. Faure C., C. Delmas, and P. Willmann, J. Power Sources 35, 263-277 (1991).
1054. Fauteux D., in Polymer Electrolyte Reviews - 2, edited by J.R. MacCallum and C.A. Vincent (Elsevier Appl. Sci., London, 1989), pp. 121-155.
1055. Fehlner F.P., G.H. Beall and W.J. Wein, Proc. Soc. Photo-Opt. Instrum. Engr. 1149, 72-77 (1989).
1056. Feinleib J., W.J. Scouler and A. Ferretti, Phys. Rev. 165, 765-774 (1968).
1057. Feist T.P. and P.K. Davies, J. Solid State Chem. 101, 275-295 (1992).
1058. Felderhof B.U., J. Phys. C 15, 3943-3951 (1982).
1059. Felderhof B.U., J. Phys. C 15, 3953-3966 (1982).
1060. Feldman B.J. and O.R. Melroy, J. Electroanal. Chem. 234, 213-227 (1987).
1061. Feldman B.J. and R.W. Murray, Inorg. Chem. 26, 1702-1708 (1987).
1062. Feng Q., Y. Miyai, H. Kanoh and K. Ooi, Langmuir (1992), 1861-1867.
1063. Fernández-Rodriquez J.M., L. Hernán, J. Morales and J.L. Tirado, Mater. Res. Bull. 23, 899-904 (1988).
1064. Fernández-Rodriquez J.M., J. Morales and J.L. Tirado, Reactivity Solids 4, 163-171 (1987).
1065. Ferretti A., D.B. Rogers and J.B. Goodenough, J. Phys. Chem. Solids 26, 2007-2011 (1965).
1066. Feuillade G. and R. Jacoud, Electrochim. Acta 14, 1297-1311 (1969).
1067. Fiermans L., P. Clauws, W. Lambrecht, L. Vandenbroucke and J. Vennik, Phys. Stat. Sol. A 59, 485-504 (1980).
1068. Figlarz M., Rev. Chim. Minérale 22, 177-194 (1985).
1069. Figlarz M., Chem. Scripta 28, 3-7 (1988).
1070. Figlarz M., Prog. Solid State Chem. 19, 1-46 (1989).
1071. Figlarz M., B. Gerand, A. Delahaye-Vidal, B. Dumont, F. Harb, A. Coucou and F. Fievet, Solid State Ionics 43, 143-170 (1990).
1072. Figlarz M., B. Gerand, B. Dumont, A. Delahaye-Vidal and F. Portemer, Phase Transitions 31, 167-179 (1991).
1073. Figlarz M., J. Guenot and J.-N. Tournemolle, J. Mater. Sci. 9, 772-776 (1974).
1074. Figlarz M. and S. Le Bihan, Comptes Rendues Acad. Sci. Paris, Sér. C, 272, 580-582 (1971).
1075. Finkenrath H., Z. Angew. Phys. 16, 503-510 (1964).
1076. Finkenrath H., Z. Naturforsch. 19a, 794-800 (1964).
1077. Finkenrath H., Infrared Phys. 28, 327-332 (1988).
1078. Finkenrath H., Infrared Phys. 28, 363-366 (1988).
1079. Finney J.L., Nature 266, 309-314 (1977).
1080. Finney J.L., in Amorphous Metallic Alloys, edited by F.E. Luborsky (Butterworths, London, 1983), pp. 42-57.
1081. Firsov Yu.A., Fiz. Tverd. Tela 10, 1950-1967 (1968) [Soviet Phys. Solid State 10, 1537-1548 (1969)].
1082. Fisher G.B. and J.L. Gland, Surf. Sci. 94, 446-455 (1980).
1083. Fishman G. and D. Calecki, Phys. Rev. Lett. 62, 1302-1305 (1989).
1084. Fitting H.J., J.J. Pinnis and A.R. Lusis, Phys. Stat. Sol. A 70, K185-K187 (1982).
1085. Fleich T.H. and G.J. Mains, J. Chem. Phys. 76, 780-786 (1982).
1086. Fleisch T.H., N. Winograd and W.N. Delgass, Surf. Sci. 78, 141-158 (1978).
1087. Fleich T.H., G.W. Zajac, J.O. Schreiner and G.J. Mains, Appl. Surf. Sci. 26, 488-497 (1986).
1088. Fletcher S., R.G. Barradas and J.D. Porter, J. Electrochem. Soc. 125, 1960-1968 (1978).
1089. Folquer, M.E., J.R. Vilche and A.J. Arvia, J. Electrochem. Soc. 127, 2634-2640 (1980).

1090. Fong R., U. von Sacken and J.R. Dahn, J. Electrochem. Soc. 137, 2009-2013 (1990).
1091. Fortin E. and D. Masson, Solid State Electronics 25, 281-283 (1982).
1092. Fortin E. and W.M. Sears, Can. J. Phys. 60, 901-908 (1982).
1093. Foster C.M., R.P. Chiarello, H.L.M. Chang, M. You, T.J. Zhang, H. Frase, J.C. Parker and D.J. Lam, J. Appl. Phys. 73, 2841-2847 (1993).
1094. Foster L.M. and J.E. Scardefield, J. Electrochem. Soc. 123, 141-142 (1976).
1095. Fouda A.S., J. Electroanal. Chem. 110, 357-360 (1980).
1096. Fracassi F. and J.W. Coburn, J. Appl. Phys. 63, 1758-1761 (1988).
1097. Franceschetti D.R., J. Electroanal. Chem. 178, 1-9 (1984).
1098. Franceschetti D.R., J. Chem. Phys. 86, 6495-6501 (1987).
1099. Franceschetti D.R. and J.R. Macdonald, J. Electrochem. Soc. 129, 1754-1756 (1982).
1100. Frand G., C. Rousselot and O. Bohnke, Proc. Soc. Photo-Opt. Instrum. Engr. 1728, 157-164 (1992).
1101. Frank G. and H. Köstlin, Appl. Phys. A 27, 197-206 (1982).
1102. Frankenthal R.P., Electrochim. Acta 16, 1845-1857 (1971).
1103. Fraser D.B. and H.D. Cook, J. Electrochem. Soc. 119, 1368-1374 (1972).
1104. Frechette V.D., J.C. Pulver and D.R. Rossington, J. Am. Ceram. Soc. 64, 463-468 (1981).
1105. Frederickson L.D., Jr. and D.M. Hausen, Anal. Chem. 35, 818-827 (1963).
1106. Friend R.H. and A.D. Yoffe, Adv. Phys. 36, 1-94 (1987).
1107. Fuchs J. and I. Brüdgam, Z. Naturforsch. B 32, 853-857 (1977).
1108. Fuchs K., Proc. Cambridge Philos. Soc. 34, 100-108 (1938).
1109. Fuchs R., J. Chem. Phys. 42, 3781-3789 (1965).
1110. Fujieda S., Sci. Light (Tokyo) 18, 1-32 (1969).
1111. Fujii M., T. Kawai, H. Nakamatsu and S. Kawai, J. Chem. Soc. Chem. Commun. (1983), 1428-1429.
1112. Fujikawa H., K. Yamashita and Y. Taga, Mater. Chem. Phys. 35, 11-14 (1993).
1113. Fujimori A., in Core-level Spectroscopy in Condensed Systems, edited by J. Kanamori and A. Kotani, (Springer, Berlin, Heidelberg, 1988), Springer Series in Solid State Sciences, Vol. 81, pp. 136-145.
1114. Fujimori A. and F. Minami, Phys. Rev. B 30, 957-971 (1984).
1115. Fujimori A., F. Minami and S. Sugano, Phys. Rev. B 29, 5225-5227 (1984).
1116. Fujinaka M. and A.A. Berezin, J. Appl. Phys. 54, 3582-3588 (1983).
1117. Fujino K., H. Tada and H. Kawahara, Proc. Soc. Photo-Opt. Instrum. Engr. 823, 124-129 (1987).
1118. Fujita Y., K. Miyazaki and C. Tatsuyama, Japan. J. Appl. Phys. 24, 1082-1086 (1985).
1119. Fujiwara H., K. Hara, M. Kamiya, T. Hashimoto and K. Okamoto, Thin Solid Films 163, 387-391 (1988).
1120. Fujiwara R., S.-I. Kawate and I. Shimizu, Japan Display 1983, pp. 50-52.
1121. Fukuma M., S. Zembutsu and S. Miyazawa, Appl. Opt. 22, 265-268 (1983).
1122. Furstenau R.P., G. McDougall and M.A. Langell, Surf. Sci. 150, 55-79 (1985).
1123. Furuta T., T. Shimomura, H. Mada and S. Kobayashi, Japan. J. Appl. Phys. 20, L768-L770 (1981).
1124. Fuschillo N., B. Lalevic and B. Leung, Thin Solid Films 24, 181-192 (1974).
1125. Fuyuki T. and H. Matsunami, Japan J. Appl. Phys. 25, 1288-1291 (1986).

G

1126. Gabrusenoks J.V., P.D. Cikmach, A.R. Lusis, J.J. Kleperis and G.M. Ramans, Solid State Ionics 14, 25-30 (1984).
1127. Gacoin T., J.C. Badot, N. Baffier and A. Fourrier-Lamer, Solid State Ionics 46, 147-150 (1991).
1128. Gadenne M., J. Lafait and P. Gadenne, Opt. Commun. 71, 273-278 (1989).
1129. Gadenne P., A. Beghdadi and J. Lafait, Opt. Commun. 65, 17-21 (1988).
1130. Gale R.J., editor, Spectroelectrochemistry: Theory and Practice (Plenum, New York, 1988).
1131. Gallego J.M. and C.B. Thomas, Thin Solid Films 98, 11-22 (1982).
1132. Galy J., J. Solid State Chem. 100, 229-245 (1992).
1133. Galyamov B.Sh., I.E. Obvintseva, Yu.E. Roginskaya and M.I. Yanovskaya, Pis'ma Zh. Tekh. Fiz. 15, 74-77 (1989) [Soviet Tech. Phys. Lett. 15, 69-71 (1989)].

1134. Galyamov B.Sh. and Yu.E. Roginskaya, Pis'ma Zh. Tekn. Fiz. 14, 280-283 (1988) [Soviet Tech. Phys. Lett. 14, 124-125 (1988)].
1135. Gambke T. and B. Metz, Glastechn. Ber. 62, 38-45 (1989).
1136. Garikepati P. and T. Xue, Solar Energy Mater. Solar Cells 25, 105-111 (1992).
1137. Garnett J.C.M., Philos. Trans. R. Soc. London 203, 385-420 (1904).
1138. Garnett J.C.M., Philos. Trans. R. Soc. London 205, 237-288 (1906).
1139. Garnich F., P.C. Yu and C.M. Lampert, Solar Energy Mater. 20, 265-275 (1990).
1140. Gassa L.M., J.R. Vilche and A.J. Arvia, J. Appl. Electrochem. 13, 135-145 (1983).
1141. Gatehouse B.M. and A.D. Wadsley, Acta Cryst. 17, 1545-1554 (1964).
1142. Gavrilko T.A., V.I. Stepkin and I.V. Shiyanovskaya, Zh. Tekn. Fiz. 60 (12), 135-138 (1990).
1143. Gavrilko T.A., V.I. Stepkin and I.V. Shiyanovskaya, J. Mol. Struct. 218, 411-416 (1990).
1144. Gavrilyuk A.I. and F.A. Chudnovskii, Pis'ma Zh. Tekh. Fiz. 3, 174-177 (1977) [Soviet Tech. Phys. Lett. 3, 69-70 (1977)].
1145. Gavrilyuk A.I., G.M. Gusinskii, A.A. Mansurov, L.A. Rassadin and F.A. Chudnovskii, Fiz. Tverd. Tela 28, 2053-2056 (1986) [Soviet Phys. Solid State 28, 1147-1149 (1986)].
1146. Gavrilyuk A.I., T.G. Lanskaya and F.A. Chudnovskii, Zh. Tekh. Fiz. 57, 1617-1622 (1987) [Soviet Phys. Tech. Phys. 32, 964-966 (1987)].
1147. Gavrilyuk A.I., T.G. Lanskaya, A.A. Mansurov and F.A. Chudnovskii, Fiz. Tverd. Tela 26, 200-206 (1984) [Soviet Phys. Solid State 26, 117-120 (1984)].
1148. Gavrilyuk A.I., A.A. Mansurov and F.A. Chudnovskii, Pis'ma Zh. Tekh. Fiz. 10, 693-697 (1984) [Soviet Tech. Phys. Lett. 10, 292-293 (1984)].
1149. Gavrilyuk A.I., A.A. Mansurov, A.Kh. Razikov, F.A. Chudnovskii and I.Kh. Shaver, Zh. Tekh. Fiz. 56, 958-960 (1986) [Soviet Phys. Tech. Phys. 31, 585-586 (1986)].
1150. Gavrilyuk A.I., V.G. Prokhvatilov and F.A. Chudnovskii, Fiz. Tverd. Tela 24, 982-992 (1982) [Soviet Phys. Solid State 24, 558-563 (1982)].
1151. Gavrilyuk A.I., N.M. Reinov and F.A. Chudnovskii, Pis'ma Zh. Tekh. Fiz. 5, 1227-1230 (1979) [Soviet Tech. Phys. Lett. 5, 514-515 (1979)].
1152. Gavrilyuk A.I., B.P. Zakharchenya and F.A. Chudnovskii, Pis'ma Zh. Tekh. Fiz. 6, 1196-1199 (1980) [Soviet Tech. Phys. Lett. 6, 512-513 (1980)].
1153. Gavrilyuk V.I. and I.M. Chernenko, Izv. Akad. Nauk SSSR Neorg. Mater. 18, 1176-1178 (1982) [Inorg. Mater. 18, 993-994 (1982)].
1154. Gavrilyuk V.I., I.M. Chernenko, A.I. Ivon and V.F. Katkov, Pis'ma Zh. Tekh. Fiz. 6, 1396-1400 (1980) [Soviet Tech. Phys. Lett. 6, 601-602 (1980)].
1155. Gavrilyuk V.I., A.I. Ivon and I.M. Chernenko, Pis'ma Zh. Tekh. Fiz. 6, 492-495 (1980) [Soviet Tech. Phys. Lett. 6, 211-212 (1980)].
1156. Gazzinelli R. and O.F. Schirmer, J. Phys. C 10, L145-L149 (1977).
1157. Geertsma W., J.E. Gols and L. Pietronero, Physica (Utrecht) A 158, 691-705 (1989).
1158. Gehlig R. and E. Salje, Philos. Mag. B 47, 229-245 (1983).
1159. Gehlig R., E. Salje, A.F. Carley and M.W. Roberts, J. Solid State Chem. 49, 318-324 (1983).
1160. Gehman B.L., S. Jonsson, T. Rudolph, S. Scherer, M. Weigert and R. Werner, Thin Solid Films 220, 333-336 (1992).
1161. Genin C., A. Delahaye-Vidal, F. Portemer, K. Tekaia-Elhsissen and M. Figlarz, Eur. J. Solid State Inorg. Chem. 28, 505-518 (1991).
1162. Genin C., A. Driouiche, B. Gerand and M. Figlarz, Solid State Ionics 53-56, 315-323 (1992).
1163. Gennero de Chialvo M.R. and A.C. Chialvo, Electrochim. Acta 33, 825-830 (1988).
1164. Gennero de Chialvo M.R. and A.C. Chialvo, Electrochim. Acta 35, 437-443 (1990).
1165. Gennero de Chialvo M.R., S.L. Marchiano and A.J. Arvia, J. Appl. Electrochem. 14, 165-175 (1984).
1166. Gerand B., G. Nowogrocki and M. Figlarz, J. Solid State Chem. 38, 312-320 (1981).
1167. Gerand B., G. Nowogrocki, J. Guenot and M. Figlarz, J. Solid State Chem. 29, 429-434 (1979).
1168. Gérard P., A. Deneuville and R. Courths, Thin Solid Films 71, 221-236 (1980).
1169. Gérard P., A. Deneuville, G. Hollinger and Tran Minh Duc, J. Appl. Phys. 48, 4252-4255 (1977).
1170. Gerlach E., J. Phys. C 19, 4585-4603 (1986).

1171. Gerlach E. and P. Grosse, Festkörperprobleme 17, 157-193 (1977).
1172. Gervasi C.A., S.R. Biaggio, J.R. Vilche and A.J. Arvia, Corrosion Sci. 29, 427-443 (1989).
1173. Gervasi C.A., S.R. Biaggio, J.R. Vilche and A.J. Arvia, Electrochim. Acta 36, 2147-2152 (1991).
1174. Gesheva K.A., E.E. Chain and B.O. Seraphin, Solar Energy Mater. 3, 415-424 (1980).
1175. Gesheva K.A., K. Seshan and B.O. Seraphin, Thin Solid Films 79, 39-49 (1981).
1176. Gesser H.D. and L. Kruczynski, J. Phys. Chem. 88, 2751-2753 (1984).
1177. Gharbi N., C. R'Kha, D. Ballutaud, M. Michaud, J. Livage, J.P. Audiere and G. Schiffmacher, J. Non-Cryst. Solids 46, 247-257 (1981).
1178. Gharbi N., C. Sanchez and J. Livage, J. Chim. Phys. 82, 755-759 (1985).
1179. Gharbi N., C. Sanchez, J. Livage, J. Lemerle, L. Nèjem and J. Lefebvre, J. Inorg. Chem. 21, 2758-2765 (1982).
1180. Gielisse P.J., J.N. Plendl, L.C. Mansur, R. Marshall, S.S. Mitra, R. Mykolajewycz and A. Smakula, J. Appl. Phys. 36, 2446-2450 (1965).
1181. Giglia R.D., SID Symp. Proc. (1975) (6), 52-53.
1182. Giglia R.D. and G. Haacke, SID Digest (1981) (4), 76-77.
1183. Giglia R.D. and G. Haacke, Proc. SID 23 (1), 41-45 (1982).
1184. Gillet P.A., J.L. Fourquet and O. Bohnke, Mater. Res. Bull. 27, 1145-1152 (1992).
1185. Gillet P.A., J.L. Fourquet and O. Bohnke, Proc. Soc. Photo-Opt. Instrum. Engr. 1728, 82-91 (1992).
1186. Gilson T.R., O.F. Bizri and N. Cheetham, J. Chem. Soc. Dalton Trans. (1973), 291-294.
1187. Giraudeau A., F.-R.F. Fan and A.J. Bard, J. Am. Chem. Soc. 102, 5137-5142 (1980).
1188. Giri A.P., Ph D. Thesis, The Pennsylvania State University (1984), unpublished.
1189. Giri A.P. and R. Messier, Mater. Res. Soc. Symp. Proc. 24, 221-227 (1984).
1190. Gissler W. and R. Memming, J. Electrochem. Soc. 124, 1710-1714 (1977).
1191. Giuliani G., A. Gustinetti and A. Stella, Phys. Lett. A 38, 515-516 (1972).
1192. Glarum S.H. and J.H. Marshall, J. Electrochem. Soc. 127, 1467-1474 (1980).
1193. Glarum S.H. and J.M. Marshall, J. Electrochem. Soc. 129, 535-542 (1982).
1194. Glass A.M., K. Nassau and T.J. Negran, J. Appl. Phys. 49, 4808-4811 (1978).
1195. Glassford K.M. and J.R. Chelikowsky, Phys. Rev. B 45, 3874-3876 (1992).
1196. Glassford K.M. and J.R. Chelikowsky, Phys. Rev. B 46, 1284-1298 (1992).
1197. Gledhill R.F., I.J. Hodgkinson and P.W. Wilson, J. Appl. Phys. 59, 1453-1455 (1986).
1198. Gleitzer C. and J.B. Goodenough, in Structure and Bonding (Springer, Berlin, Heidelberg, 1985), Vol. 61, pp. 1-76.
1199. Glemser O. and J. Einerhand, Z. Anorg. Allg. Chem. 261, 26-51 (1950).
1200. Glemser O. and C. Naumann, Z. Allg. Anorg. Chem. 265, 288-302 (1951).
1201. Glemser O. and H. Sauer, Z. Anorg. Chem. 252, 144-159 (1943).
1202. Glemser O. and R. v. Haeseler, Z. Allg. Anorg. Chem. 316, 168-181 (1962).
1203. Glezer V. and O. Lev, J. Am. Chem. Soc. 115, 2533-2534 (1993).
1204. Goda T., T. Yoshino and N. Baba, Denki Kagaku 51, 213-214 (1983).
1205. Godart C., M. Latroche, C. Fretigny and C. Levy-Clement, Phys. Stat. Sol. A 132, 253-268 (1992).
1206. Goel A.K., G. Skorinko and F.K. Pollak, Phys. Rev. B 24, 7342-7350 (1981).
1207. Goetz R., D.F. Mitchell, B. MacDougall and M.J. Graham, J. Electrochem. Soc. 134, 535-539 (1987).
1208. Gofuku E., Y. Toyoda, Y. Uehara, M. Kohara and M. Nunoshita, Appl. Surf. Sci. 48-49, 343-350 (1991).
1209. Göhr H., Electrochim. Acta 11, 827-834 (1966).
1210. Göhr H. and H. Krüger, Electrochim. Acta 11, 835-847 (1966).
1211. Gol'dshtein M.D., Ts.I. Zalkind and V.I. Veselovskii, Elektrokhim. 8, 606-609 (1972) [Soviet Electrochem. 8, 590-592 (1972)].
1212. Gol'dshtein M.D., Ts.I. Zalkind and V.I. Veselovskii, Elektrokhim. 9, 699-702 (1973) [Soviet Electrochem. 9, 673-675 (1973)].
1213. Gol'man E.K., A.G. Zaitsev, Yu.V. Likholetov, V.E. Loginov and B.T. Melekh, Pis'ma Zh. Tekh. Fiz. 18, 53-55 (1992) [Soviet Tech. Phys. Lett. 18, 783-784 (1992)].
1214. Golden S.J. and B.C.H. Steele, Solid State Ionics 28-30, 1733-1737 (1988).
1215. Golden S.J. and B.C.H. Steele, Mater. Res. Soc. Symp. Proc. 293, 395-400 (1993).

1216. Goldner R.B., in Solid State Ionic Devices, edited by B.V.R. Chowdari and S. Radhakrishna (World Scientific, Singapore, 1988), pp. 379-390.
1217. Goldner R.B., in Solid State Ionic Devices, edited by B.V.R. Chowdari and S. Radhakrishna (World Scientific, Singapore, 1988), pp. 351-358.
1218. Goldner R.B., F.O. Arntz, G. Berera, T.E. Haas, G. Wei, K.K. Wong and P.C. Yu, Proc. Soc. Photo-Opt. Instrum. Engr. 1536, 63-69 (1991).
1219. Goldner R.B., F.O. Arntz, G. Berera, T.E. Haas, G. Wei, K.K. Wong and P.C. Yu, Solid State Ionics 53-56, 616-627 (1992).
1220. Goldner R.B., G. Berrera, F.O. Arntz, T.E. Haas, B. Morel and K.K. Wong, in Electrochromic Materials, edited by M.K. Carpenter and D.A. Corrigan (The Electrochem. Soc., Pennington, 1990), Proc. Vol. 90-2, pp. 14-22.
1221. Goldner R.B., A. Brofos, G. Foley, E.L. Goldner T.E. Haas, W. Henderson, P. Norton, B.A. Ratnam, N. Weis and K.K. Wong, Proc. Soc. Photo-Opt. Instrum. Engr. 502, 54-58 (1984).
1222. Goldner R.B., A. Brofos, G. Foley, E.L. Goldner, T.E. Haas, W. Henderson, P. Norton, B.A. Ratnam, N. Weis and K.K. Wong, Solar Energy Mater. 12, 403-410 (1985).
1223. Goldner R.B., R.L. Chapman, G. Foley, E.L. Goldner, T. Haas, P. Norton, G. Seward and K.K. Wong, Proc. Soc. Photo-Opt. Instrum. Engr. 562, 32-38 (1985).
1224. Goldner R.B., R.L. Chapman, G. Foley, E.L. Goldner, T. Haas, P. Norton, G. Seward and K.K. Wong, Solar Energy Mater. 14, 195-203 (1986).
1225. Goldner R.B., G. Foley, E.L. Goldner, P. Norton, K. Wong, T. Haas, G. Seward and R. Chapman, Appl. Opt. 24, 2283-2284 (1985).
1226. Goldner R.B., T.E. Haas, F.O. Arntz, S. Slaven, K.K. Wong, B. Wilkens, C. Shepard and W. Lanford, Appl. Phys. Lett. 62, 1699-1701 (1993).
1227. Goldner R.B., T.E. Haas, G. Seward, K.K. Wong, P. Norton, G. Foley, G. Berera, G. Wei, S. Schulz and R. Chapman, Solid State Ionics 28-30, 1715-1721 (1988).
1228. Goldner R.B., D.H. Mendelsohn, J. Alexander, W.R. Henderson, D. Fitzpatrick, T.E. Haas, H.M. Sample, R.D. Rauh, M.A. Parker and T.L. Rose, Appl. Phys. Lett. 43, 1093-1095 (1983).
1229. Goldner R.B., P. Norton, K. Wong, G. Foley, E.L. Goldner, G. Seward and R. Chapman, Appl. Phys. Lett. 47, 536-538 (1985).
1230. Goldner R.B. and R.D. Rauh, Proc. Soc. Photo-Opt. Instrum. Engr. 428, 38-44 (1983).
1231. Goldner R.B. and R.D. Rauh, Solar Energy Mater. 11, 177-185 (1984).
1232. Goldner R.B., G. Seward, K. Wong, T. Haas, G.H. Foley, R. Chapman and S. Schulz, Solar Energy Mater. 19, 17-26 (1989).
1233. Goldner R.B., K. Wong, G. Foley, P. Norton, L. Wamboldt, G. Seward, T. Haas and R. Chapman, Proc. Soc. Photo-Opt. Instrum. Engr. 692, 39-42 (1986).
1234. Goldner R.B., K. Wong, G. Foley, P. Norton, L. Wamboldt, G. Seward, T. Haas and R. Chapman, Solar Energy Mater. 16, 365-370 (1987).
1235. Gols J.E. and W. Geertsma, J. Phys. Cond. Matter 1, 4469-4472 (1989).
1236. Gomes M.A.B. and L.O. de S. Bulhoes, Electrochim. Acta 35, 765-768 (1990).
1237. Gomes M.A.B., L.O. de S. Bulhoes, S.C. de Castro and A.J. Damiao, J. Electrochem. Soc. 137, 3067-3070 (1990).
1238. Gomes M.A.B., D. Goncalves, E.C. Pereira de Souza, B. Valla, M.A. Aegerter and L.O. de S. Bulhoes, Electrochim. Acta 37, 1653-1656 (1992).
1239. Gomez Meier H., J.R. Vilche and A.J. Arvia, J. Appl. Electrochem. 10, 611-621 (1980).
1240. Gomez Meier H., J.R. Vilche and A.J. Arvia, J. Electroanal. Chem. 134, 251-272 (1982)
1241. Gomez Meier H., J.R. Vilche and A.J. Arvia, J. Electroanal. Chem. 138, 367-379 (1982).
1242. Gonclaves R.M.C., H. Kellawi and D.R. Rosseinsky, J. Chem. Soc. Dalton Trans. (1983), 991-994.
1243. González-Elipe A.R., J.P. Hogado, R. Alvarez and G. Munuera, J. Phys. Chem. 96, 3080-3086 (1992).
1244. Goodenough J.B., Bull. Soc. Chim. France (1965) 1200-1207.
1245. Goodenough J.B., J. Appl. Phys. 37, 1415-1422 (1966).
1246. Goodenough J.B., in Progress in Solid State Chemistry, edited by H. Reiss (Pergamon, Oxford, 1971), Vol. 5, pp. 145-399.
1247. Goodenough J.B., Ann. Rev. Mater. Sci. 1, 101-138 (1971).

1248. Goodenough J.B., G. Dutta and A. Manthiram, Phys. Rev. B 43, 10170-10178 (1991).
1249. Goodenough J.B. and J.M. Longo, Landolt-Börnstein Tabellen, New Series (Springer, Berlin, 1970), Vol. III/4a, pp. 126-314.
1250. Goodenough J.B., A. Manthiram, A.C.W.P. James and P. Strobel, Mater. Res. Symp. Proc. Vol. 135, 391-415 (1989).
1251. Goodenough J.B., K. Mizushima and T. Takeda, Japan. J. Appl. Phys. 19, Suppl. 3, 305-313 (1980).
1252. Goodman L.A., IEEE Trans. Consumer Electronics CE-21, 247-259 (1975).
1253. Goodman L.A., Proc. SID 17 (1), 30-38 (1976).
1254. Goodman P., Acta Cryst. B 32, 3280-3285 (1976).
1255. Goodman P. and J.D. McLean, Acta Cryst. B 32, 3285-3286 (1976).
1256. Goossens A. and D.D. Macdonald, J. Electroanal. Chem. 352, 65-81 (1993).
1257. Gorenstein A., C.N.P. da Fonseca and R. Torresi, Proc. Soc. Photo-Opt. Instrum. Engr. 1536, 104-115 (1991).
1258. Gorenstein A., F. Decker, W. Estrada, C. Esteves, A.M. Andersson, S. Passerini, S. Pantaloni and B. Scrosati, J. Electroanal. Chem. 277, 277-290 (1990).
1259. Gorenstein A., F. Decker, M. Fantini and W. Estrada, in Large-area Chromogenics: Materials and Devices for Transmittance Control, edited by C.M. Lampert and C.G. Granqvist (SPIE Opt. Engr. Press, Bellingham, 1990), Vol. IS4, pp. 272-284.
1260. Goswami A. and A.P. Goswami, Indian J. Pure Appl. Phys. 13, 667-670 (1975).
1261. Goswami K.N. and R.W. Staehle, Electrochim. Acta 16, 1895-1907 (1971).
1262. Goto T., S. Saito and M. Tanaka, Solid State Commun. 80, 331-334 (1991).
1263. Gottesfeld S., J. Electrochem. Soc. 127, 272-277 (1980).
1264. Gottesfeld S., J. Electrochem. Soc. 127, 1922-1925 (1980).
1265. Gottesfeld S. and J.D.E. McIntyre, J. Electrochem. Soc. 126, 742-750 (1979).
1266. Gottesfeld S., J.D.E. McIntyre, G. Beni and J.L. Shay, Appl. Phys. Lett. 33, 208-210 (1978).
1267. Gottesfeld S., A. Redondo, I. Rubinstein and S.W. Feldberg, J. Electroanal. Chem. 265, 15-22 (1989).
1268. Gottesfeld S. and S. Srinivasan, J. Electroanal. Chem. 86, 89-104 (1978).
1269. Gottesfeld S., M. Yaniv, D. Laser and S. Srinivasan, J. Phys. (Paris) 38, C5 145 - C5 150 (1977).
1270. Götzsche J., A. Hinsch and V. Wittwer, Proc. Soc. Photo-Opt. Instrum. Engr. 1728, 13-25 (1992).
1271. Goulding M.R. and C.B. Thomas, Thin Solid Films 62, 175-188 (1979).
1272. Goulding M.R., C.B. Thomas and R.J. Hurditch, Solid State Commun. 46, 451-453 (1983).
1273. Gourier D., A. Tranchant, N. Baffier and R. Messina, Electrochim. Acta 37, 2755-2764 (1992).
1274. Graeffe R. and T. Wiik, J. Appl. Phys. 42, 2146-2147 (1971).
1275. Graham J. and A.D. Wadsley, Acta Cryst. 14, 379-383 (1961).
1276. Granqvist C.G., The Physics Teacher (1984), 372-383.
1277. Granqvist C.G., Physica Scripta 32, 401-407 (1985).
1278. Granqvist C.G., Window Industries (August 1987) (4 pages).
1279. Granqvist C.G., in Physics of Non-conventional Energy Sources and Material Science for Energy, edited by G. Furlan, N.A. Mancini, A.A.M. Sayigh and B.O. Seraphin (World Scientific, Singapore, 1987), pp. 217-302.
1280. Granqvist C.G., in Physics and Technology of Solar Energy, edited by H.P. Garg et al. (Reidel, Dordrecht, 1987), Vol. 2, pp. 191-276.
1281. Granqvist C.G., in Electricity: Efficient End Use and New Generation Technology and Their Implications for Electric Utility Planning and Policy, edited by T.B. Johansson, B. Bodlund and R.H. Williams (Lund University Press, Lund, 1989), pp. 89-123.
1282. Granqvist C.G., in Workshop on Materials Science and the Physics of Non-conventional Energy Sources, edited by G. Furlan, D. Nobili, A.A.M. Sayigh and B.O. Seraphin (World Scientific, Singapore, 1989), pp. 1-44.
1283. Granqvist C.G., Spectrally Selective Surfaces for Heating and Cooling Applications (SPIE Opt. Engr. Press, Bellingham, 1989), Vol. TT1.
1284. Granqvist C.G., Crit. Rev. Solid State Mater. Sci. 16, 291-308 (1990).
1285. Granqvist C.G., Appl. Phys. A 52, 83-93 (1991).

1286. Granqvist C.G., in Materials Science for Solar Energy Conversion Systems, edited by C.G. Granqvist (Pergamon, Oxford, 1991), pp. 106-167.
1287. Granqvist C.G., Solid State Ionics 53-56, 479-489 (1992).
1288. Granqvist C.G., Infrared Thin Films, edited by R.P. Shimshock (SPIE Opt. Engr. Press, Bellingham, 1992), Vol. CR39, pp. 156-178.
1289. Granqvist C.G., Appl. Phys. A 57, 3-12 (1993).
1290. Granqvist C.G., Appl. Phys. A 57, 19-24 (1993).
1291. Granqvist C.G., Mater. Sci. Engr. A 168, 209-215 (1993).
1292. Granqvist C.G., Proc. Soc. Photo-Opt. Instrum. Engr. 2017, 84-94 (1993).
1293. Granqvist C.G., in Physics of Thin Films, edited by M.H. Francombe and J.L. Vossen (Academic, San Diego, 1993), Vol. 17, pp. 301-370.
1294. Granqvist C.G., Solid State Ionics 60, 213-214 (1993).
1295. Granqvist C.G., Solar Energy Mater. Solar Cells (1994), to be published.
1296. Granqvist C.G., Solid State Ionics (1994), to be published.
1297. Granqvist C.G. and R.A. Buhrman, J. Appl. Phys. 47, 2200-2219 (1976).
1298. Granqvist C.G., I. Hamberg and J.S.E.M. Svensson, I & EC Product Res. & Dev. 24, 93-95 (1985).
1299. Granqvist C.G. and O. Hunderi, Phys. Rev. B 16, 3513-3534 (1977).
1300. Granqvist C.G. and O. Hunderi, Phys. Rev. B 18, 1554-1561 (1978).
1301. Gratzke U. and G. Simon, J. Phys. D: Appl. Phys. 24, 827-834 (1991).
1302. Greaves C., A.M. Malsbury and M.A. Thomas, Solid State Ionics 18-19, 763-767 (1986).
1303. Greaves C. and M.A. Thomas, Acta Cryst. B 42, 51-55 (1986).
1304. Greef R., R. Peat, L.M. Peter and J. Robinson, Instrumental Methods in Electrochemistry (Wiley, New York, 1985).
1305. Green D., Appl. Opt. 29, 4547-4549 (1990).
1306. Green D., Properties of Tungsten Oxide and Trigonally Bonded Compounds, Ph.D. Thesis, University of Sydney, Australia (1991), unpublished.
1307. Green D., J.M. Bell and G.B. Smith, Proc. Soc. Photo-Opt. Instrum. Engr. 1728, 26-30 (1992).
1308. Green D.W. and K.M. Ervin, J. Mol. Struct. 89, 145-158 (1981).
1309. Green M., Thin Solid Films 50, 145-150 (1978).
1310. Green M., J. Res. Inst. Catalysis Hokkaido Univ. 28, 163-168 (1980).
1311. Green M., in Electrochromism and Electrochromic Displays, edited by B. Scrosati (Univ. Rome, 1982), pp. 39-62.
1312. Green M., H.I. Evans and Z. Hussain, in Second Int. Symp. Polymer Electrolytes, edited by B. Scrosati (Elsevier Appl. Sci., London, 1990), pp. 449-459.
1313. Green M. and Z. Hussain, J. Appl. Phys. 69, 7788-7796 (1991).
1314. Green M. and K. Kang, Thin Solid Films 40, L19-L21 (1977).
1315. Green M. and K. Kang, Thin Solid Films 62, 385-387 (1979).
1316. Green M. and K. Kang, Solid State Ionics 3-4, 141-147 (1981).
1317. Green M. and K. Kang, Solid State Ionics 8, 281-289 (1983).
1318. Green M. and K. Kang, Displays (1988), 166-173.
1319. Green M. and D. Richman, Thin Solid Films 24, S45-S46 (1974).
1320. Green M., W.C. Smith and J.A. Weiner, Thin Solid Films 38, 89-100 (1976).
1321. Green M. and A. Travlos, Thin Solid Films 122, L101-L104 (1984).
1322. Green M. and A. Travlos, Philos. Mag. B 51, 501-520 (1985).
1323. Green M. and A. Travlos, Philos. Mag. B 51, 521-532 (1985).
1324. Green M.L., M.E. Gross, L.E. Papa, K.J. Schnoes and D. Brasen, J. Electrochem. Soc. 132, 2677-2685 (1985).
1325. Greenberg C.B., Thin Solid Films 110, 73-82 (1983).
1326. Greenberg C.B., Proc. 15th Conf. Aerospace Transparent Materials and Enclosures (Monterey, 1989), pp. 1126-1134.
1326a. Greenblatt M., Int. J. Mod. Phys. 7, 3937-3971 (1993).
1327. Grein C.H. and S. John, Phys. Rev. B 36, 7457-7468 (1987).
1328. Greneche J.M., J.M. Teillet and J.M.D. Coey, J. Non-Cryst. Solids 83, 27-34 (1986).

1329. Greneche J.M., J.M. Teillet and J.M.D. Coey, J. Phys. (Paris) 48, 1709-1714 (1987).
1330. Griesmar P., G. Papin, C. Sanchez and J. Livage, Chem. Mater. 3, 335-339 (1991).
1331. Griffith W.P. and P.J.B. Lesniak, J. Chem. Soc. A (1969), 1066-1071.
1332. Griffiths C.H. and H.K. Eastwood, J. Appl. Phys. 45, 2201-2206 (1974).
1333. Grimely R.T., R.P. Burns and M.G. Inghram, J. Chem. Phys. 34, 664-667 (1961).
1334. Gritsenko V.A., E.E. Meyerson, Ya.O. Royzin and K.K. Svitashev, Autometry (USSR) 2, 47-49 (1979).
1335. Gritsenko V.A., Ya.O. Roisin, L.E. Semenchuk and N.L. Schwarz, Solid State Commun. 38, 351-352 (1981).
1336. Griuliani G., A. Gustinetti and A. Stella, Phys. Lett. A 38, 515-516 (1972).
1337. Groenenboom C.J., G. Sawatzky, H.J. de L. Meijer and F. Jellinek, J. Organometall. Chem. 76, C4-C6 (1974).
1338. Grosse P., Freie Elektronen in Festkörpern (Springer, Berlin, 1979).
1339. Gruehn R., J. Less-Common Met. 11, 119-126 (1966).
1340. Gruehn R. and R. Norin, Z. Anorg. Allg. Chem. 355, 176-181 (1967).
1341. Gruehn R. and R. Norin, Z. Anorg. Allg. Chem. 367, 209-218 (1969).
1342. Grum F. and C.J. Bartleson, editors, Optical Radiation Measurements, Vol. 2, Color Measurement (Academic, New York, 1980).
1343. Grunin V.S., V.L. Makarov, I.B. Patrina and M.V. Razumeenko, Fiz. Tverd. Tela 30, 3091-3095 (1988) [Soviet Phys. Solid State 30, 1778-1780 (1988)].
1344. Grüner G., Rev. Mod. Phys. 60, 1127-1181 (1988).
1345. Guay D., G. Tourillon, E. Dartyge, A. Fontaine, J. McBreen, K.I. Pandya and W.E. O'Grady, J. Electroanal. Chem. 305, 83-95 (1991).
1346. Guay D., G. Tourillon, G. Laperrière and D. Belanger, J. Phys. Chem. 96, 7718-7724 (1992).
1347. Guérard D. and A. Hérold, Comptes Rendues Acad. Sci., Sér. C, 275, 571-572 (1972).
1348. Guérard D.and A. Hérold, Carbon 13, 337-345 (1975).
1349. Guerfi A.and L.H. Dao, J. Electrochem. Soc. 136, 2435-2436 (1989).
1350. Guignard M., B. Carquille, C. Bohnke and O. Bohnke, Displays (1982), 39-43.
1351. Gulliver E.A., J.W. Garvey, T.A. Wark, M.J. Hampden-Smith and A. Datye, J. Am. Ceram. Soc. 74, 1091-1094 (1991).
1352. Gummow R.J., D.C. Liles and M.M. Thackeray, Mater. Res. Bull. 28, 235-246 (1993).
1353. Gummow R.J. and M.M. Thackeray, Solid State Ionics 53-56, 681-687 (1992).
1354. Gummow R.J., M.M. Thackeray, W.I.F. David and S. Hull, Mater. Res. Bull. 27, 327-337 (1992).
1355. Gunter R.G. and S. Gross, editors, Proc. Symposium on the Nickel Electrode (The Electrochem. Soc., Pennington, 1982).
1356. Guo J.-D., K.P. Reis and M.S. Whittingham, Solid State Ionics 53-56, 305-314 (1992).
1357. Gupta H.M. and G.F.L. Ferreira, J. Appl. Phys. 50, 5036-5037 (1979).
1358. Gupta K., J.P. Marton and J. Shewchun, J. Electrochem. Soc. 121, 118-122 (1974).
1359. Gupta P.K. and K.L. Chopra, Appl. Phys. Lett. 51, 1527-1529 (1987).
1360. Gupta P.K. and K.L. Chopra, J. Appl. Phys. 62, 4273-4276 (1987).
1361. Gupta V.P. and N.M. Ravindra, Phys. Stat. Sol. B 100, 715-719 (1980).
1361a. Gutarra A., A. Azens, B. Stjerna and C.G. Granqvist, Appl. Phys. Lett. (1994), to be published.
1362. Gutiérrez C. and B. Beden, J. Electroanal. Chem. 293, 253-259 (1990).
1363. Gutiérrez C. and M.A. Martinez, J. Electrochem. Soc. 133, 1873-1874 (1986).
1364. Guyomard D. and J.M. Tarascon, J. Electrochem. Soc. 139, 937-948 (1992).
1365. Günter J.R., J. Solid State Chem. 5, 354 (1972).
1366. Günter J.R. and H.-R. Osswald, Bull. Inst. Chem. Kyoto Univ. 53, 249-255 (1975).

H

1367. Haacke G., Appl. Phys. Lett. 28, 622-623 (1976).
1368. Haacke G., Ann. Rev. Mater. Sci. 7, 73-93 (1977).

1369. Haas T.E. and R.B. Goldner, in Large-area Chromogenics: Materials and Devices for Transmittance Control, edited by C.M. Lampert and C.G. Granqvist (SPIE Opt. Engr. Press, Bellingham, 1990), Vol. IS4, pp. 170-180.
1370. Habib M.A., Proc. Soc. Photo-Opt. Instrum. Engr. 1149, 46-55 (1989).
1371. Habib M.A. and J.O'M. Bockris, J. Electroanal. Chem. 180, 287-306 (1984).
1372. Habib M.A. and D. Glueck, Solar Energy Mater. 18, 127-141 (1989).
1373. Habib M.A. and S.P. Maheswari, J. Electrochem. Soc. 138, 2029-2031 (1991).
1374. Habib M.A. and S.P. Maheswari, J. Electrochem. Soc. 139, 2155-2157 (1992).
1375. Habib M.A. and S.P. Masheswari, Solar Energy Mater. Solar Cells 25, 195-200 (1992).
1376. Habib M.A. and S.P. Maheswari, J. Appl. Electrochem. 23, 44-50 (1993).
1377. Habib M.A., S.P. Maheswari and M.K. Carpenter, J. Appl. Electrochem. 21, 203-207 (1991).
1378. Haber J., J. Stoch and L. Ungier, J. Solid State Chem. 19, 113-115 (1976).
1379. Hackwood S., G. Beni, M.A. Bösch, K. Kang, L.M. Schiavone and J.L. Shay, Phys. Rev. B 26, 7073-7075 (1982).
1380. Hackwood S., G. Beni, W.C. Dautremont-Smith, L.M. Schiavone and J.L. Shay, Appl. Phys. Lett. 37, 965-967 (1980).
1381. Hackwood S., G. Beni and P.K. Gallagher, Solid State Ionics 2, 297-299 (1981).
1382. Hackwood S., W.C. Dautremont-Smith, G. Beni, L.M. Schiavone and J.L. Shay, J. Electrochem. Soc. 128, 1212-1214 (1981).
1383. Hackwood S., A.H. Dayem and G. Beni, Phys. Rev. B 26, 471-478 (1982).
1384. Hackwood S., L.M. Schiavone, W.C. Dautremont-Smith and G. Beni, J. Electrochem. Soc. 128, 2569-2573 (1981).
1385. Hadzi-Jordanov S., H. Angerstein-Kozlowska, M. Vukovic and B.E. Conway, J. Electrochem. Soc. 125, 1471-1480 (1978).
1386. Hagenmuller P., in Progress in Solid State Chemistry, edited by H. Reiss (Pergamon, Oxford, 1971), Vol. 5, pp. 71-144.
1387. Hagenmuller P., in Comprehensive Inorganic Chemistry, edited by J.C. Bailar, H.J. Emeléus, R. Nyholm and A.F. Trotman-Dickenson (Pergamon, Oxford, 1973), Vol. 4, pp. 541-605.
1388. Hagenmuller P., in Solid State Ionic Devices, edited by B.V.R. Chowdari and S. Radhakrishna (World Scientific, Singapore, 1988), pp. 663-696.
1389. Hahn F., B. Beden, M.J. Croissant and C. Lamy, Electrochim. Acta 31, 335-342 (1986).
1390. Hahn F., D. Floner, B. Beden and C. Lamy, Electrochim. Acta 32, 1631-1636 (1987).
1391. Haitjema H., J.J.P. Elich and C.J. Hoogendoorn, Solar Energy Mater. 18, 283-297 (1989).
1392. Hajimoto Y. and T. Hara, Appl. Phys. Lett. 28, 228-229 (1976).
1393. Hajimoto Y., M. Matsushima and S. Ogura, J. Electronic Mater. 8, 301-310 (1979).
1394. Hall H.Y. and P.M.A. Sherwood, J. Chem. Soc. Faraday Trans. I 80, 135-152 (1984).
1395. Halley J.W., M.T. Michalewicz and N. Tit, Phys. Rev. B 41, 10165-10170 (1990).
1396. Halpert G., J. Power Sources 12, 177-192 (1984).
1397. Hamada H., K. Yano, H. Take, Y. Inami, M. Matsuura and T. Wada, Displays (1983), 221-225.
1398. Hamberg I. and C.G. Granqvist, J. Appl. Phys. 59, 2950-2952 (1986).
1399. Hamberg I. and C.G. Granqvist, J. Appl. Phys. 60, R123-R159 (1986).
1400. Hamberg I. and C.G. Granqvist, Solar Energy Mater. 14, 241-256 (1986).
1401. Hamberg I., C.G. Granqvist, K.-F. Berggren, B.E. Sernelius and L. Engström, Phys. Rev. B 30, 3240-3249 (1984).
1402. Hamilton J.C., J.C. Farmer and R.J. Anderson, J. Electrochem. Soc. 133, 739-745 (1986).
1403. Hammouche A. and A. Hammou, Electrochim. Acta 32, 1451-1452 (1987).
1404. Hamnett A., S. Higgins, R.S. Mortimer and D.R. Rosseinsky, J. Elcctroanal. Chem. 255, 315-324 (1988).
1405. Hampson N.A., S.A.G.R. Karunathilaka, R. Leek and T.J. Sinclair, Surf. Technol. 15, 101-112 (1982).
1406. Han S.H., H.S. Kim and K. Kim, Bull. Korean Chem. Soc. 12, 80-85 (1991).
1407. Hanafi Z.M. and M.A. Khilla, Z. Phys. Chem. N.F. 89, 230-236 (1974).
1408. Hanai T., Kolloid Z. 171, 23-31 (1960).
1409. Hanbold T., W. Krauss and H. Gleiter, Philos. Mag. 63, 245-247 (1991).
1410. Hansen M.A., I.A. McCabe, B.P. Hichwa and J.G.H. Mathew, Photonics Spectra (Jan. 1992), 102-103.

1411. Hansen S.D. and C.R. Aita, J. Vac. Sci. Technol. A 3, 660-663 (1985).
1412. Hansen S.G., G. Luckman, G.C. Nieman and S.D. Colson, J. Appl. Phys. 68, 2013-2021 (1990).
1413. Hara K., K. Kuboyama, H. Okabe, K. Matsushige and Y. Ishibashi, J. Phys. Soc. Japan 61, 2147-2153 (1992).
1414. Hara N. and K. Sugimoto, J. Electrochem. Soc. 126, 1328-1334 (1979).
1415. Hara N. and K. Sugimoto, J. Japan. Inst. Met. 44, 915-924 (1980).
1416. Hara N. and K. Sugimoto, Trans. Japan Inst. Met. 24, 236-245 (1983).
1417. Haranahalli A.R. and D.B. Dove, Appl. Phys. Lett. 36, 791-793 (1980).
1418. Haranahalli A.R. and P.M. Holloway, J. Electronic Mater. 10, 141-172 (1981).
1419. Harb F., B. Gérand and M. Figlarz, Comptes Rendues Acad Sci. Paris, Sér. II, 303, 445-447 (1986).
1420. Harb F., B. Gérand and M. Figlarz, Comptes Rendues Acad Sci. Paris, Sér. II, 303, 789-792 (1986).
1421. Harb F., B. Gérand, G. Nowogrocki and M. Figlarz, Comptes Rendues Acad. Sci. Paris, Sér. II, 303, 349-352 (1986).
1422. Harb F., B. Gérand, G. Nowogrocki and M. Figlarz, Solid State Ionics 32-33, 84-90 (1989).
1423. Hardcastle F.D. and I.E. Wachs, J. Raman Spectrosc. 21, 683-691 (1990).
1424. Hardcastle F.D. and I.E. Wachs, J. Phys. Chem. 95, 5031-5041 (1991).
1425. Hardee K.L. and A.J. Bard, J. Electrochem. Soc. 124, 215-224 (1977).
1426. Harding G.L., Thin Solid Films 138, 279-287 (1986).
1427. Hardy A., J. Galy, A. Casalot and M. Pouchard, Bull. Soc. Chim. France (1965), 1056-1065.
1428. Hardy A.C., Handbook of Colorimetry (Massachusetts Institute of Technology, Cambridge, 1963).
1429. Harshbarger W.R., R.A. Porter, T.A. Miller and P. Norton, Appl. Spectrosc. 31, 201-207 (1977).
1430. Hartmann M., E.W. Grabner and P. Bergveld, Anal. Chim. Acta 242, 249-257 (1991).
1431. Hartmann M., E.W. Grabner and P. Bergveld, Sensors Actuators B 4, 333-336 (1991).
1432. Hartstein A., J.R. Kirtley and J.C. Tsang, Phys. Rev. Lett. 45, 201-204 (1980).
1433. Hase Y., Spectrochim. Acta A 35, 377-378 (1979).
1434. Hashimoto H., T. Naiki, M. Mannami and K. Fujita, in Structure and Properties of Thin Films, edited by C.A. Neugebauer, J.B. Newkirk and D.A. Vermilyea (Wiley, New York, 1959), pp. 71-86.
1435. Hashimoto K. and M. Cohen, J. Electrochem.Soc. 121, 37-42 (1974).
1436. Hashimoto S. and H. Matsuoka, J. Appl. Phys. 69, 933-937 (1991).
1437. Hashimoto S. and H. Matsuoka, J. Electrochem. Soc. 138, 2403-2408 (1991).
1438. Hashimoto S. and H. Matsuoka, Surf. Interface Anal. 19, 464-468 (1992).
1439. Hashimoto S., H. Matsuoka, H. Kageshika, M. Susa and K.S. Goto, J. Electrochem. Soc. 137, 1300-1304 (1990).
1440. Hass G., J.B. Ramsey and R. Thun, J. Opt. Soc. Am. 48, 324-327 (1958).
1441. Hatta A., T. Ohshima and W. Suetaka, Appl. Phys. A 29, 71-75 (1982).
1442. Hatta A., Y. Suzuki and W. Suetaka, Appl. Phys. A 35, 135-140 (1984).
1443. Haubold T., W. Krauss and H. Gleiter, Philos. Mag. 63, 245-247 (1991).
1444. Haupt S. and H.-H. Strehblow, J. Electroanal. Chem. 228, 365-392 (1987).
1445. Haupt S. and H.-H. Strehblow, Langmuir 3, 873-885 (1987).
1446. Hauser M.R., B.B. Plapp and G. Mozurkewich, Phys. Rev. B 43, 8105-8112 (1991).
1447. Havlin S. and D. Ben-Avraham, Adv. Phys. 36, 695-798 (1987).
1448. Hayashi S., M. Fujii and K. Yamamoto, Japan. J. Appl. Phys. 28, L1464-L1466 (1989).
1449. Hayashi S., H. Sugano, H. Arai and K. Yamamoto, J. Phys. Soc. Japan 61, 916-923 (1992).
1450. Hayashi Y., T. Miyakoshi and M. Masuda, J. Less-Common Met. 172-174, 851-858 (1991).
1451. Heavens O.S., Optical Properties of Thin Solid Films (Butterworths, London, 1955).
1452. Hechtl E., J. Bohdansky and J. Roth, J. Nucl. Mater. 103-104, 333-338 (1981).
1453. Hecq M., A. Hecq and J. Van Cakenberghe, Thin Solid Films 42, 97-105 (1977).
1454. Hedge M.S., A. Srinivasan, D.D. Sarma and C.N.R. Rao, J. Electron Spectrosc. Related Phenomena 25, 231-236 (1982).
1455. Helder D.J., SAE Tech. Paper Series 870635 (1987), 9 pages.
1456. Heller A., D.E. Aspnes, J.D. Porter, T.T. Cheng and R.G. Vadimsky, J. Phys. Chem. 89, 4444-4452 (1985).

1457. Heller J., Thin Solid Films 17, 163-176 (1973).
1458. Henglein A., Topics in Current Chem. 143, 113-180 (1988).
1459. Hennion B., J.P. Pouget and M. Sato, Phys. Rev. Lett. 68, 2374-2377 (1992).
1460. Henri M., C. Sanchez, C. R'Kha and J. Livage, J. Phys. C 14, 829-837 (1981).
1461. Hensler D.H., J.D. Cuthbert, R.J. Martin and P.K. Tien, Appl. Opt. 10, 1037-1042 (1971).
1462. Hepel T., F.H. Pollak and W.E. O'Grady, J. Electrochem. Soc. 132, 2385-2390 (1985).
1463. Herion J., Appl. Phys. Lett. 34, 599-601 (1979).
1464. Hernán L., M. Macias, J. Morales, L. Sánchez and J.L. Tirado, Solid State Ionics 47, 75-79 (1991).
1465. Hernán L., M. Macias, J. Morales, L. Sánchez and J.L. Tirado, Solid State Ionics 48, 231-240 (1991).
1466. Hérold A., Bull. Soc. Chim. France (1955), 999-1012.
1467. Herren F., P. Fischer, A. Ludi and W. Hälg, Inorg. Chem. 19, 956-959 (1980).
1468. Herren G. and N.E. Walsöe de Reca, Mater. Sci. Engr. B 18, 72-77 (1993).
1469. Herrmann W.C., Jr., J. Vac. Sci. Technol. 18, 1303-1305 (1981).
1470. Hersh H.N., W.E. Kramer and J.H. McGee, Appl. Phys. Lett. 27, 646-648 (1975).
1471. Heurung G. and R. Gruehn, Z. Anorg. Allg. Chem. 491, 101-112 (1982).
1472. Heurung G. and R. Gruehn, Rev. Inorg. Chem. 5, 185-205 (1983).
1473. Heurung G. and R. Gruehn, J. Solid State Chem. 55, 337-343 (1984).
1474. Heurung G. and R. Gruehn, Z. Anorg. Allg. Chem. 513, 175-182 (1984).
1475. Heusler K.E. and O. Ohtsuka, Surf. Sci. 101, 194-204 (1980).
1476. Heusler K.E. and K. Schoner, Ber. Bunsenges. Phys. Chem. 77, 885-891 (1973).
1477. Hevesi I., Acta Phys. Acad. Sci. Hung. 23, 415-423 (1967).
1478. Hevesi I., A.A. Abdullaev and V.S. Lebedev, Kristallogr. 16, 334-338 (1971) [Soviet Crystallogr. 16, 275-278 (1971)].
1479. Hibble S.J., A.M. Chippindale and P.G. Dickens, J. Electrochem. Soc. 132, 2668-2669 (1985).
1480. Hibble S.J. and P.G. Dickens, Ber. Bunsenges. Phys. Chem. 90, 702-707 (1986).
1481. Hibble S.J. and P.G. Dickens, J. Solid State Chem. 61, 98-102 (1986).
1482. Hichman M.L. and S. Ramanathan, Electroanal. 4, 291-297 (1992).
1483. Hichwa B.P., G. Caskey, D.F. Betz and J.D. Harlow, J. Vac. Sci. Technol. A5, 1775-1777 (1987).
1484. Highfield J.G. and M. Grätzel, J. Phys. Chem. 92, 464-467 (1988).
1485. Hilbrig F., H.E. Göbel, H. Knözinger, H. Schmelz and B. Lengeler, J. Phys. Chem. 95, 6973-6978 (1991).
1486. Hill M.D. and R.G. Egdell, J. Phys. C 16, 6205-6220 (1983).
1487. Hill R.M. and L.A. Dissado, Solid State Ionics 26, 295-298 (1988).
1488. Hillman A.R., D.C. Loveday and S. Bruckenstein, Langmuir 7, 191-194 (1991).
1489. Hillman A.R., M.J. Swann and S. Bruckenstein, J. Phys. Chem. 95, 3271-3277 (1991).
1490. Hinokuma K., K. Ogasawara, A. Kishimoto, S. Takano and T. Kudo, Solid State Ionics 53-56, 507-512 (1992).
1491. Hirashima H. and S. Kamimura, Mater. Res. Soc. Symp. Proc. 121, 779-784 (1988).
1492. Hirashima H., S. Kamimura, R. Muratake and T. Yoshida, J. Non-Cryst. Solids 100, 394-398 (1988).
1493. Hirashima H. and K. Sudoh, J. Non-Cryst. Solids 121, 68-71 (1990).
1494. Hirashima H. and K. Sudoh, J. Non-Cryst. Solids 145, 51-54 (1992).
1495. Hirata T. and K. Yagisawa, J. Alloys Compounds 185, 177-182 (1992).
1496. Hiratsuka R.S., S.H. Pulcinelli and C.V. Santilli, J. Non-Cryst. Solids 121, 76-83 (1990).
1497. Hiratsuka R.S., C.V. Santilli, D.V. Silva and S.H. Pulcinelli, J. Non-Cryst. Solids 147-148, 67-73 (1992).
1498. Hiratta T. and Y. Fukuda, J. Mater. Sci. Lett. 9, 929-931 (1990).
1499. Hirochi K., M. Kitabatake and O. Yamazaki, J. Electrochem. Soc. 133, 1973-1974 (1986).
1500. Hirose T., J. Phys. Soc. Japan 49, 562-568 (1980).
1501. Hiruta Y., M. Kitao and S. Yamada, Japan. J. Appl. Phys. 23, 1624-1627 (1984).
1502. Hitchman M.L., J. Electroanal. Chem. 85, 135-144 (1977).
1503. Hitchman M.L., Thin Solid Films 61, 341-348 (1979).
1503a. Hitchman M.L. and S. Ramanathan, Anal. Chim. Acta 263, 53-61 (1992).
1504. Ho C., I.D. Raistrick and R.A. Huggins, J. Electrochem. Soc. 127, 343-350 (1980).
1505. Ho F.C. and J.L. Ord, J. Electrochem. Soc. 119, 139-145 (1972).

1506. Ho K.-C., J. Electrochem. Soc. 139, 1099-1104 (1992)
1507. Ho K.-C., D.E. Singleton and C.B. Greenberg, J. Electrochem. Soc. 137, 3858-3864 (1990).
1508. Ho K.-C., D.E. Singleton and C.B. Greenberg, in Electrochromic Materials, edited by M.K. Carpenter and D.A. Corrigan (The Electrochem. Soc., Pennington, 1990), Proc. Vol. 90-2, pp. 349-364.
1509. Hoare J.P., The Electrochemistry of Oxygen (Interscience, New York, 1968), pp. 271-306.
1510. Hobbs B.S. and A.C.C. Tseung, J. Electrochem. Soc. 119, 580-583 (1972).
1511. Höchst H. and R.D. Bringans, Appl. Surf. Sci. 11-12, 768-773 (1982).
1512. Höchst H., R.D. Bringans and H.R. Shanks, Phys. Rev. B 26, 1702-1712 (1982).
1513. Höchst H., R.D. Bringans, H.R. Shanks and P. Steiner, Solid State Commun. 37, 41-44 (1980).
1514. Hodes G., D. Cahen and J. Manassen, Nature 260, 312-313 (1976).
1515. Hodgkinson I.J. and P.W. Wilson, CRC Crit. Rev. Solid State Mater. Sci. 15, 27-61 (1988).
1516. Hoffmann H., Festkörperprobleme 22, 255-290 (1982).
1517. Hoffmann H. and J. Vancea, Thin Solid Films 85, 147-167 (1981).
1518. Hogarth C.A. and Z.T. Al-Dhhan, Phys. Stat. Sol. B 137, K157-K160 (1986).
1519. Hollinger G., T.M. Duc and A. Deneuville, Phys. Rev. Lett. 37, 1564-1567 (1976).
1520. Hollinger G., F.J. Himpsel, N. Mårtensson, B. Reihl, J.P. Doumerc and T. Akahane, Phys. Rev. B 27, 6370-6375 (1983).
1521. Hollinger G., F.J. Himpsel, B. Reihl, P. Pertosa and J.P. Doumerc, Solid State Commun. 44, 1221-1225 (1982).
1522. Hollinger G. and P. Pertosa, Chem. Phys. Lett. 74, 341-344 (1980).
1523. Hollinger G., P. Pertosa, J.P. Doumerc, F.J. Himpsel and B. Reihl, Phys. Rev. B 32, 1987-1991 (1985).
1524. Hollmann E.K., A.G. Zaitsev, V.E. Loginov and Y.V. Likholetov, J. Phys. D: Appl. Phys. 26, 504-505 (1993).
1525. Holm R., Angew. Chem. 83, 632-645 (1971).
1526. Holstein T., Ann. Phys. (NY) 8, 343-389 (1959).
1527. Honda K., M. Fujita, H. Ishida, R. Yamamoto and K. Ohgaki, J. Electrochem. Soc. 135, 3151-3154 (1988).
1528. Honda K. and H. Hayashi, J. Electrochem. Soc. 134, 1330-1334 (1987).
1529. Honda K. and H. Hayashi, Progr. Batteries Solar Cells 6, 255-256 (1987).
1530. Honda K. and A. Kuwano, J. Electrochem. Soc. 133, 853-854 (1986).
1531. Honda K., J. Ochiai and H. Hayashi, J. Chem. Soc. Chem. Commun. (1986), 168-170.
1532. Honders A. and G.H.J. Broers, Solid State Ionics 15, 173-183 (1985).
1533. Honders A., J.M. der Kinderen, A.H. van Heeren, J.H.W. de Wit and G.H.J. Broers, Solid State Ionics 15, 265-276 (1985).
1534. Honig J.M., in Electrodes of Conductive Metallic Oxides, Part A, edited by S. Trasatti (Elsevier, Amsterdam, 1980), pp. 1-96.
1535. Honig J.M., J.O. Dimmock and W.H. Kleiner, J. Chem. Phys. 50, 5232-5242 (1969).
1536. Hood P.J. and J.F. De Natale, J. Appl. Phys. 70, 376-381 (1991).
1537. Hooper A. and J.M. North, Solid State Ionics 9-10, 1161-1166 (1983).
1538. Hopfield J.J., Comments Solid State Phys. 1, 16-18 (1968).
1539. Hopper M.A. and J.L. Ord, J. Electrochem. Soc. 120, 183-187 (1973).
1540. Hoppmann G. and E. Salje, Phys. Stat. Sol. A 37, K187-K191 (1976).
1541. Horányi T.S., Thermochim. Acta 142, 143-150 (1989).
1542. Horie T., K. Kawabe and T. Iwai, Ann. Rep. Sci. Works Fac. Sci. Osaka Univ. 4, 45-78 (1956).
1543. Horio K., Y. Adachi and T. Ikoma, Japan. J. Appl. Phys. 19, L117-L118 (1980).
1544. Horio K., Y. Adachi and T. Ikoma, Denki Kagaku 51, 931-937 (1983).
1545. Horio K., Y. Adachi and T. Ikoma, Denki Kagaku 52, 169-173 (1984).
1546. Horkans J. and M.W. Shafer, J. Electrochem. Soc. 124, 1202-1207 (1977).
1547. Hörlin T., T. Niklewski and M. Nygren, Mater. Res. Bull. 7, 1515-1524 (1972).
1548. Hörlin T., T. Niklewski and M. Nygren, Mater. Res. Bull. 8, 179-190 (1973).
1549. Hornkjøl S., Electrochim. Acta 36, 1433-1446 (1991).
1550. Horsley J.A., I.E. Wachs, J.M. Brown, G.H. Via and F.D. Hardcastle, J. Phys. Chem. 91, 4014-4020 (1987).

1551. Houalla M., V. Perrichon and P. Turlier, Comptes Rendues Acad. Sci. Paris, Sér. C, 284, 1-4 (1977).
1552. Howe A.T., S.M. Sheffield, P.E. Childs and M.G. Shilton, Thin Solid Films 67, 365-370 (1980).
1553. Howe A.T. and M.G. Shilton, J. Solid State Chem. 34, 149-155 (1980).
1554. Howe R.F., J. Chem. Soc. Faraday Trans. I 71, 1689-1696 (1975).
1555. Howson R.P., in Large-area Chromogenics: Materials and Devices for Transmittance Control, edited by C.M. Lampert and C.G. Granqvist (SPIE Opt. Engr. Press, Bellingham, 1990), Vol. IS4, pp. 260-270.
1556. Howson R.P., K. Suzuki, C.A. Bishop and M.I. Ridge, Vacuum 34, 291-294 (1984).
1557. Hu X., X. Chen and M.G. Hutchins, Proc. Soc. Photo-Opt. Instrum. Engr. 1728, 73-79 (1992).
1558. Huang P.-N., X.-H. Huang and F.-X. Gan, Solid State Ionics 57, 169-172 (1992).
1559. Huang S., J. Zhou and J. Chang, Proc. Soc. Photo-Opt. Instrum. Engr. 823, 159-164 (1987).
1560. Huang Z.Q. and J.L. Ord, J. Electrochem. Soc. 132, 24-28 (1985).
1561. Hub S., A. Tranchant and R. Messina, Electrochim. Acta 33, 997-1002 (1988).
1562. Hubbard J., Proc. Roy. Soc. London A 240, 539-560 (1957).
1563. Hubbard J., Proc. Roy. Soc. London A 243, 336-352 (1957).
1564. Hubbard J., Proc. Roy. Soc. London A 276, 238-257 (1963).
1565. Hubbard J., Proc. Roy. Soc. London A 277, 237-259 (1963).
1566. Hudson A., in Electron Spin Resonance, edited by M.C.R. Symons (Roy. Soc. Chem., Letchworth, 1992), Vol. 13 A, pp. 187-201.
1567. Hüfner S., Z. Phys. B 58, 1-6 (1984).
1568. Hüfner S., Z. Phys. B 61, 135-138 (1985).
1569. Hüfner S., F. Hulliger, J. Osterwalder and T. Riesterer, Solid State Commun. 50, 83-86 (1984).
1570. Hüfner S., J. Osterwalder, T. Riesterer and F. Hulliger, Solid State Commun. 52, 793-796 (1984).
1571. Hüfner S., P. Steiner, I. Sander, M. Neumann and S. Witzel, Z. Phys. B 83, 185-192 (1991).
1572. Hüfner S., P. Steiner, I. Sander, F. Reinert and H. Schmitt, Z. Phys. B 86 207-215 (1992).
1573. Huggins R.A., Mater. Sci. Res. 9, 155-175 (1975).
1574. Huggins R.A., Electrochim. Acta 22, 773-781 (1977).
1575. Huggins R.A., M. Wohlfahrt-Mehrens and L. Jörissen, Mater. Res. Soc. Symp. Proc. 293, 57-62 (1993).
1576. Hughes A.J., P. Lloyd and R. Hurditch, J. Electronic Mater. 6, 752 (1977).
1577. Hugot-Le Goff A., S. Joiret and S. Cordoba-Torresi, in Electrochromic Materials, edited by M.K. Carpenter and D.A. Corrigan (The Electrochem. Soc., Pennington, 1990), Proc. Vol. 90-2, pp. 70-79.
1578. Hulstrom R., R. Bird and C. Riordan, Solar Cells 15, 365-391 (1985).
1579. Hunger M., D. Freude and H. Pfeifer, J. Chem. Soc. Faraday Trans. 87, 657-662 (1991).
1580. Hunter J.C., J. Solid State Chem. 39, 142-147 (1981).
1581. Hüppauff M. and B. Lengeler, J. Electrochem. Soc. 140, 598-602 (1993).
1582. Huq R., G.C. Farrington, R. Koksbang and P.E. Tonder, Solid State Ionics 57, 277-283 (1992).
1583. Hurditch R.J., Electronic Lett. 11, 142-144 (1975).
1584. Hurditch R., Electrocomponent Sci. Technol. 3, 247-251 (1977).
1585. Hush N.S., in Progress in Inorganic Chemistry, edited by F.A. Cotton (Interscience, New York, 1967), Vol. 8, pp. 391-444.
1586. Hussain A., Chem. Commun. Univ. Stockholm, No. 2 (1978), pp. 1-44.
1587. Hussain A., Acta. Chem. Scand. A 32, 479-484 (1978).
1588. Hussain A. and R. Gruehn, J. Crystal Growth 108, 831-833 (1991).
1589. Hussain A., B. Reitz and R. Gruehn, Z. Anorg. Allg. Chem. 535, 186-194 (1986).
1590. Hutchins M.G., G. McMeeking and Z.C. Orel, Proc. Soc. Photo-Opt. Instrum. Engr. 1728, 66-72 (1992).
1591. Hutchins M.G., G. McMeeking and H. Xingfan, Proc. Soc. Photo-Opt. Instr. Engr. 1272, 139-150 (1990).
1592. Hutchins M.G., P.J. Wright and P.D. Grebenik, Solar Energy Mater. 16, 113-131 (1987).
1593. Hwang J. and M.A. Dubson, J. Appl. Phys. 72, 1852-1857 (1992).
1594. Hyde B.G. and S. Andersson, Inorganic Crystal Structures (Wiley, New York, 1989).

I

1595. Igasaki Y., M. Ishikawa and G. Shimaoka, Appl. Surf. Sci. 33-34, 926-933 (1988).

1596. Igasaki Y. and H. Saito, J. Appl. Phys. 69, 2190-2195 (1991).
1597. Igasaki Y. and H. Saito, J. Appl. Phys. 70, 3613-3619 (1991).
1598. Iguchi E. and K. Akashi, J. Phys. Soc. Japan 61, 3385-3393 (1992).
1599. Iguchi E., K.J. Lee and A. Iguchi, J. Phys. Soc. Japan 62, 1135-1138 (1993).
1600. Iguchi E. and H. Miyagi, J. Phys. Chem. Solids 54, 403-409 (1993).
1601. Iijima K., T. Terashima, Y. Bando, K. Kamigaki and H. Terauchi, J. Appl. Phys. 72, 2840-2845 (1992).
1602. Iijima K., T. Terashima, K. Yamamoto, K. Hirata and Y. Bando, Appl. Phys. Lett. 56, 527-529 (1990).
1603. Iijima S. and J.G. Allpress, Acta Cryst. A 30, 22-29 (1974).
1604. Iijima S. and J.G. Allpress, Acta Cryst. A 30, 29-36 (1974).
1605. Iijima T., Y. Toyoguchi, J. Nishimura and H. Ogawa, J. Power Sources 5, 99-109 (1980).
1606. Ikeda H. and S. Narukawa, J. Power Sources 9, 329-334 (1983).
1607. Ikeda H., K. Tada and H. Hada, New Mater. New Processes 2, 413-419 (1983).
1608. Ikeshoji T., J. Electrochem. Soc. 133, 2108-2109 (1986).
1609. Il'yasova A.K., R.A. Geskina, G.K. Tarabrin, N.D. Omarova, A.V. Ekshtelis and A.S. Belkin, Zh. Neorg. Khim. 28, 279-282 (1983) [Russian J. Inorg. Chem. 28, 151-153 (1983)].
1610. Imai Y. and K. Nakamura, Japan. J. Appl. Phys. 16, 1471-1472 (1977).
1611. Inaba H., M. Iwaku, T. Tatsuma and N. Oyama, Denki Kagaku 61, 783-785 (1993).
1612. Inganäs O., in Large-area Chromogenics: Materials and Devices for Transmittance Control, edited by C.M. Lampert and C.G. Granqvist (SPIE Opt. Engr. Press, Bellingham, USA, 1990), Vol. IS4, pp. 328-334.
1613. Inoue E., K. Kawaziri and A. Izawa, Japan. J. Appl. Phys. 16, 2065-2066 (1977).
1614. Inoue E., H. Kokado and A. Izawa, Oyo Buturi 43, 54-55 (1974).
1615. Inoue T., M. Osone, H. Tohda, M. Hiramatsu, Y. Yamamoto, A. Yamanoka and T. Nakayama, J. Appl. Phys. 69, 8313-8315 (1991).
1616. Inumaru K., T. Okuhara and M. Misono, Chem. Lett. (1990) 1207-1210.
1617. Inumaru K., T. Okuhara and M. Misono, J. Phys. Chem. 95, 4826-4832 (1991).
1618. Inumaru K., T. Okuhara, M. Misono, N. Matsubayashi, H. Shimada and A. Nishijima, J. Chem. Soc. Faraday Trans. 87, 1807-1808 (1991).
1619. Inumaru K., T. Okuhara, M. Misono, N. Matsubayashi, H. Shimada and A. Nishijima, J. Chem. Soc. Faraday Trans. 88, 625-630 (1992).
1620. Ioffe V.A., I.B. Patrina, E.V. Zelenetskaya and V.P. Mikheeva, Phys. Stat. Sol. 35, 535-542 (1969).
1621. Ionov A.N. and I.S. Shlimak, in Hopping Transport in Solids, edited by M. Pollak and B. Shklovskii (Elsevier, Amsterdam, 1991), pp. 397-421.
1622. Iqbal M., An Introduction to Solar Radiation (Academic, New York, 1983).
1623. Ismail J., M.F. Ahmed and P.V. Kamath, J. Power Sources 41, 223-230 (1993).
1624. Israelsson M. and L. Kihlborg, Ark. Kemi 30, 129-140 (1968).
1625. Isutzu K., Denki Kagaku 48, 530-544 (1980).
1626. Itaya K., H. Akahoshi and S. Toshima, J. Appl. Phys. 53, 804-805 (1982).
1627. Itaya K., H. Akahoshi and S. Toshima, J. Electrochem. Soc. 129, 1498-1500 (1982).
1628. Itaya K., T. Ataka and S. Toshima, J. Am. Chem. Soc. 104, 3751-3752 (1982).
1629. Itaya K., T. Ataka and S. Toshima, J. Am. Chem. Soc. 104, 4767-4772 (1982).
1630. Itaya K., T. Ataka, S. Toshima and T. Shinohara, J. Phys. Chem. 86, 2415-2418 (1982).
1631. Itaya K., N. Shoji and I. Uchida, J. Am. Chem. Soc. 106, 3423-3429 (1984).
1632. Itaya K. and I. Uchida, Inorg. Chem. 25, 389-392 (1986).
1633. Itaya K., I. Uchida and V.D. Neff, Acc. Chem. Res. 19, 162-168 (1986).
1634. Itaya K., I. Uchida and S. Toshima, Denki Kagaku 50, 436-437 (1982).
1635. Itaya K., I. Uchida and S. Toshima, Denki Kagaku 51, 89-90 (1983).
1636. Itaya K., I. Uchida and S. Toshima, J. Phys. Chem. 87, 105-112 (1983).
1637. Itaya K., I. Uchida and S. Toshima, New Mater. New Processes 2, 508-512 (1983).
1638. Itaya K., I. Uchida and S. Toshima, Nippon Kagaku Kaishi (1984), 1849-1853.
1639. Itaya K., I. Uchida, S. Toshima and R.M. De La Rue, J. Electrochem. Soc. 131, 2086-2091 (1984).
1640. Ito K. and T. Kubo, Proc. 4th Sensor Symposium, edited by S. Kataoka (Inst. Electrical Engineers Japan, 1984), pp. 153-156.

1641. Ito K. and T. Ohgami, Appl. Phys. Lett. 60, 938-940 (1992).
1642. Ito Y., K. Kanehori, K. Miyauchi and T. Kudo, Solid State Ionics 23, 69-75 (1987).
1643. Ito Y., K. Miyauchi and T. Kudo, J. Phys. Chem. Solids 48, 161-169 (1987).
1644. Ito Y., K. Miyauchi and T. Oi, J. Non-Cryst. Solids 57, 389-400 (1983).
1645. Ito Y., K. Syakushiro, M. Hiratani, K. Miyauchi and T. Kudo, Solid State Ionics 18-19, 277-281 (1986).
1645a. Itoh K., T. Okamoto, S. Wakita, H. Niikura and M. Murabayashi, Appl. Organomet. Chem. 5, 295-301 (1991).
1646. Ivanov A.M., L.A. Sal'nikov, L.P. Timofeeva and L.O. Favorskaya, Elektrokhim. 21, 1287-1292 (1985) [Soviet Electrochem. 21, 1215-1219 (1985)].
1647. Ivanovskii A.L., V.A. Gubanov and F. Vergel, Zh. Strukt. Khim. 28 (4), 41-44 (1987) [J. Struct. Chem. 28, 495-497 (1987)].
1648. Iwai T., J. Phys. Soc. Japan 15, 1596-1600 (1960).
1649. Iwanowski R.J. and D. Trivich, Solar Cells 13, 253-264 (1984-1985).
1650. Iyengar R.D. and M. Codell, Adv. Colloid Interface Sci. 3, 365-388 (1972).
1651. Iyengar R.D., M. Codell, J. Karra and J. Turkevich, J. Am. Chem. Soc. 88, 5055-5060 (1966).
1652. Izumi F. and H. Kodama, J. Less-Common Met. 63, 305-307 (1979).

J

1653. Jackovitz J.F., in Proc. Symp. on the Nickel Electrode, edited by R.G. Gunther and S. Gross (The Electrochem. Soc., Pennington, 1982), pp. 48-68.
1654. Jacob U., J. Vancea and H. Hoffmann, Phys. Rev. B 41, 11852-11857 (1990).
1655. Jagadeesh M.S. and V. Damodara Das, J. Non-Cryst. Solids 28, 327-335 (1978).
1656. Jan S.-W. and S.-C. Lee, J. Electrochem. Soc. 134, 2056-2061 (1987).
1657. Jankowski A.F. and L.R. Schrawyer, Thin Solid Films 193-194, 61-71 (1990).
1658. Jankowski A.F., L.R. Schrawyer and P.L. Perry, J. Vac. Sci. Technol. A 9, 1184-1187 (1991).
1659. Jánossy A., T. Csiba and G. Kriza, Synth. Met. 41-43, 3821-3826 (1991).
1660. Jarman R.H. and P.G. Dickens, J. Electrochem. Soc. 129, 2276-2278 (1982).
1661. Jarzebski Z.M., Phys. Stat. Sol. A 71, 13-41 (1982).
1662. Jarzebski Z.M. and J.P. Marton, J. Electrochem. Soc. 123, 199c-205c (1976).
1663. Jarzebski Z.M. and J.P. Marton, J. Electrochem. Soc. 123, 299c-310c (1976).
1664. Jarzebski Z.M. and J.P. Marton, J. Electrochem. Soc. 123, 333c-346c (1976).
1665. Jayaraman T.R., V.K. Venkatesan and H.V.K. Udupa, Electrochim. Acta 20, 209-213 (1975).
1666. Jelle B.P., G. Hagen, S.M. Hesjevik and R. Ødegård, Mater. Sci. Engr. B 13, 239-241 (1992).
1666a. Jelle B.P., G. Hagen, S.M. Hesjevik and R. Ødegård, in Solid State Ionics, edited by M. Balkanski, T. Takahashi and H.L. Tuller (Elsevier Sci. Publ., Amsterdam, 1992), pp. 661-665.
1667. Jelle B.P., G. Hagen and S. Nødland, Electrochim. Acta 38, 1497-1500 (1993).
1668. Jelle B.P., G. Hagen and R. Ødegård, Electrochim. Acta 37, 1377-1380 (1992).
1669. Jelle B.P., G. Hagen, S. Sunde and R. Ødegård, Synth. Met. 54, 315-320 (1993).
1670. Jiang M. and Z. Zhao, J. Electroanal. Chem. 292, 281-287 (1990).
1671. Jiang M., X. Zhou and Z. Zhao, Ber. Bunsenges. Phys. Chem. 95, 720-727 (1991).
1672. Jiang S.-J., C.-B. Ye, M.S.R. Khan and C.G. Granqvist, Proc. Soc. Photo-Opt. Instrum. Engr. 1272, 185-196 (1990).
1673. Jiang S.-J., C.-B. Ye, M.S.R. Khan and C.G. Granqvist, Appl. Opt. 30, 847-851 (1991).
1674. Jiang Y., Z.-G. Liu, X.-X. Qu, X.J. Zhang and X.Y. Zhou, J. Phys. Cond. Matter. 3, 7129-7132 (1991).
1675. Jin Z.-C., I. Hamberg and C.G. Granqvist, J. Appl. Phys. 64, 5117-5131 (1988).
1676. Joensen P., R.F. Frindt and S.R. Morrison, Mater. Res. Bull. 21, 457-461 (1986).
1677. John S., Phys. Rev. B 35, 9291-9294 (1987).
1678. John S., C. Soukoulis, M.H. Cohen and E.N. Economou, Phys. Rev. Lett. 57, 1777-1780 (1986); 57, 2877 (1986).
1679. Johnston C. and P.R. Graves, Appl. Spectrosc. 44, 105-115 (1990).

1680. Johnson C.S. and J.T. Hupp, J. Electroanal. Chem. 345, 351-362 (1993).
1681. Johnston W.D., R.R. Heikes and D. Sestrich, J. Phys. Chem. Solids 7, 1-13 (1958).
1682. Jones E. and W.F.K. Wynne-Jones, Trans. Faraday Soc. 52, 1260-1272 (1956).
1683. Jonscher A.K., Dielectric Relaxation in Solids (Chelsea Dielectrics, London, 1983).
1684. Joo S.-K. and R.A. Huggins, Mater. Res. Bull. 20, 1265-1271 (1985).
1685. Joo S.-K., I.D. Raistrick and R.A. Huggins, Mater. Res. Bull. 20, 897-904 (1985).
1686. Joo S.-K., I.D. Raistrick and R.A. Huggins, Solid State Ionics 17, 313-318 (1985).
1687. Joo S.-K., I.D. Raistrick and R.A. Huggins, Solid State Ionics 18-19, 592-596 (1986).
1688. Jorgenson G.V. and J.C. Lee, Solar Energy Mater. 14, 205-214 (1986).
1689. Jorgenson G.V. and J.C. Lee, in Large-area Chromogenics: Materials and Devices for Transmittance Control, edited by C.M. Lampert and C.G. Granqvist (SPIE Opt. Engr. Press, Bellingham, 1990), Vol. IS4, pp. 142-159.
1690. Joseph J., H. Gomathi and G.P. Rao, Electrochim. Acta 36, 1537-1541 (1991).
1691. Joseph J., H. Gomathi and G.P. Rao, J. Electroanal. Chem. 304, 263-269 (1991).
1692. Joseph J., H. Gomathi and G.P. Rao, Solar Energy Mater. 23, 1-5 (1991).
1693. Jourdaine L., M. Bonnat and J.L. Souquet, Solid State Ionics 18-19, 461-466 (1986).
1694. Jouve G., Philos. Mag. B 64, 207-218 (1991).
1695. Jouve G. and Y. Belkacem, Comptes Rendues Acad. Sci. Paris 311, 929-934 (1990).
1696. Jovancicevic V., R.C. Kainthla, Z. Tang, B. Yang and J. O'M. Bockris, Langmuir 3, 388-395 (1987).
1697. Judd D.B. and G. Wyszecki, Color in Business, Science and Industry (Wiley, New York, 1975).
1698. Judeinstein P., A. Chemseddine and C. Sanchez, J. Chim. Phys. 89, 1469-1476 (1992).
1699. Judeinstein P. and J. Livage, Mater. Sci. Engr. B 3, 129-132 (1989).
1700. Judeinstein P. and J. Livage, Proc. Soc. Photo-Opt. Instrum. Engr. 1328, 344-351 (1990).
1701. Judeinstein P. and J. Livage, J. Mater. Chem. 1, 621-627 (1991).
1702. Judeinstein P. and J. Livage, J. Chim. Phys. 90, 1137-1147 (1993).
1703. Judeinstein P., J. Livage, A. Zarudiansky and R. Rose, Solid State Ionics 28-30, 1722-1725 (1988).
1704. Judeinstein P., R. Morineau and J. Livage, Solid State Ionics 51, 239-247 (1992).
1705. Juliao J.F., J.W.R. Chagas, H.L. Cesar, N.L. Dias, F. Decker and U.U. Gomes, Electrochim. Acta 36, 1297-1300 (1991).
1706. Julien C., Mater. Sci. Engr. B 6, 9-28 (1990).
1707. Julien C., Mater. Res. Soc. Symp. Proc. 293, 411-421 (1993).
1708. Julien C. and M. Balkanski, Mater. Res. Soc. Symp. Proc. 293, 27-37 (1993).
1709. Julien C., L. El-Farh, M. Balkanski, O.M. Hussain and G.A. Nazri, Appl. Surf. Sci. 65-66, 325-330 (1993).
1710. Julien C., O.M. Hussain, L. El-Farh and M. Balkanski, Solid State Ionics 53-56, 400-404 (1992).

K

1711. Kadono K., K. Mitani, K. Kinugawa and H. Tanaka, J. Non-Cryst. Solids 122, 214-215 (1990).
1712. Kadono K., K. Mitani, M. Yamashita and H. Tanaka, Solid State Ionics 47, 227-230 (1991).
1713. Kaga E. and H. Kokado, Denki Kagaku 48, 240-246 (1980).
1714. Kaganuma Y., Phys. Rev. B 38, 9797-9809 (1988).
1715. Kageyama Y. and Y. Taga, J. Vac. Sci. Technol. A 9, 604-608 (1991).
1716. Kahanda G.L.M.K.S. and M. Tomkiewicz, J. Electrochem. Soc. 137, 3223-3229 (1990).
1717. Kahn A., J. Livage and R. Collongues, Phys. Stat. Sol. A 26, 175-179 (1974).
1718. Kaito C., K. Fujita, H. Shibahara and M. Shiojiri, Japan. J. Appl. Phys. 16, 697- 704 (1977).
1719. Kaito C., T. Shimizu, Y. Nakata and Y. Saito, Japan. J. Appl. Phys. 24, 117-120 (1985).
1720. Kajiwara K., C. Isobe and M. Saitoh, Surf. Interface Anal. 19, 331-335 (1992).
1721. Kamath P.V. and M.F. Ahmed, J. Appl. Electrochem. 23, 225-230 (1993).
1722. Kamath P.V. and S. Ganguly, Mater. Lett. 10, 537-539 (1991).
1723. Kamath P.V. and P. Patrick, J. Phys. Chem. 96, 6829-6834 (1992).
1724. Kamath P.V. and G.N. Subbanna, J. Appl. Electrochem. 22, 478-482 (1992).

1725. Kamimori T., J. Nagai and M. Mizuhashi, Proc. Soc. Photo-Opt. Instrum. Engr. 428, 51-56 (1983).
1726. Kamimori T., J. Nagai and M. Mizuhashi, Solar Energy Mater. 16, 27-38 (1987).
1727. Kamiyama T., T. Itoh and K. Suzuki, J. Non-Cryst. Solids 100, 466-470 (1988).
1728. Kanai F., S. Kurita, S. Sugioka, M. Ii and Y. Mita, J. Electrochem. Soc. 129, 2633-2635 (1982).
1729. Kanai F., S. Sugioka, N. Ogawa, K. Taira and S. Kurita, Abstr. 27th Spring Meeting, Japan Soc. Appl. Phys. Related Soc. (Kofu, 1980), p. 129.
1730. Kanai T., M. Hara, H. Niiyama, T. Katsube and T. Ikoma, Shinkun (J. Vacuum Soc. Japan) 27, 143-149 (1984).
1731. Kanamura K., K. Yuasa and Z. Takehara, J. Power Sources 20, 127-134 (1987).
1732. Kanatzidis M.G. and C.-G. Wu, J. Am. Chem. Soc. 111, 4139-4141 (1989).
1732a. Kanatzidis M.G., C.-G. Wu, H.O. Marcy, D.C. DeGroot and C.R. Kannewurf, Chem. Mater. 2, 222-224 (1990).
1733. Kaneda K. and S. Suzuki, Japan. J. Appl. Phys. 30, 1841-1846 (1991).
1734. Kaneko H., T. Bessho and K. Miyake, in Electrochromic Materials, edited by M.K. Carpenter and D.A. Corrigan (The Electrochem. Soc., Pennington, 1990), Proc. Vol. 90-2, pp. 288-297.
1735. Kaneko H. and K. Miyake, Appl. Phys. Lett. 49, 112-114 (1986).
1736. Kaneko H. and K. Miyake, J. Appl. Phys. 66, 845-850 (1989).
1737. Kaneko H., K. Miyake and Y. Teramoto, J. Appl. Phys. 53, 3070-3075 (1982).
1738. Kaneko H., K. Miyake and Y. Teramoto, J. Appl. Phys. 53, 4416-4421 (1982).
1739. Kaneko H., F. Nagao and K. Miyake, J. Appl. Phys. 63, 510-517 (1988).
1740. Kaneko H., S. Nishimoto, K. Miyake and N. Suedomi, J. Appl. Phys. 59, 2526-2534 (1986).
1741. Kaneko M. and T. Okada, J. Electroanal. Chem. 255, 45-52 (1988).
1742. Kaneko M., S. Teratani and K. Harashima, J. Electroanal. Chem. 325, 325-332 (1992).
1743. Kang K.S. and M. Green, Thin Solid Films 113, L29-L32 (1984).
1744. Kang K.S. and J.L. Shay, J. Electrochem. Soc. 130, 766-769 (1983).
1745. Kang Y. and W.-K. Paik, Surf. Sci. 182, 257-268 (1987).
1746. Kanoh H., K. Ooi, Y. Miyai and S. Katoh, Langmuir 7, 1841-1842 (1991).
1747. Kanzaki Y., A. Taniguchi and M. Abe, J. Electrochem. Soc. 138, 333-334 (1991).
1748. Karprzak M.S., S.R. Crouch and G.E. Leroi, Appl. Specrosc. 32, 537-540 (1978).
1749. Karulkar P.C. and J.E. Nordman, J. Vac. Sci. Technol. 17, 462-465 (1980).
1750. Karunasiri R.P.U., R. Bruinsma and J. Rudnick, Phys. Rev. Lett. 62, 788-791 (1989).
1751. Kase T., M. Kawai and M. Ura, SAE Techn. Paper Series No. 861362 (1986) (6 pages).
1752. Kase T., T. Miyamoto, T. Yoshimoto, Y. Ohsawa, H. Inaba and K. Nakase, in Large-area Chromogenics: Materials and Devices for Transmittance Control, edited by C.M. Lampert and C.G. Granqvist (SPIE Opt. Engr. Press, Bellingham, 1990), Vol. IS4, pp. 504-517.
1753. Kashiwazaki N., Solar Energy Mater. Solar Cells 25, 349-359 (1992).
1754. Katada K., K. Nakahigashi and Y. Shimomura, Japan. J. Appl. Phys. 9, 1019-1028 (1970).
1755. Kato H., M. Hara and T. Katsube, Denki Kagaku 53, 634-635 (1985).
1756. Kato I., T. Nakato and K. Kuroda, Colloids Surf. 49, 241-245 (1990).
1757. Katsube T., J. Illumination Engr. Inst. Japan 70, 189-194 (1986).
1758. Katsube T., M. Hara, T. Yaji, S. Kobayashi, K. Suzuki and Y. Nakagawa, Japan Display 1986, pp. 376-379.
1759. Katsube T., M. Hara, T. Yaji, S. Kobayashi, K. Suzuki and Y. Nakagawa, Proc. SID 28, 233-237 (1987).
1760. Katsube T., I. Lauks and J.N. Zemel, Sensors Actuators 2, 399-410 (1982).
1761. Kaufman G.B., Inorganic Coordination Compounds: Nobel Prize Topics in Chemistry (Heyden, Philadelphia, 1981).
1762. Kawakami K., E. Ando, K. Matsuhiro, K. Matsumoto, M. Sugizaki, H. Nishimura and M. Noshiro, Rep. Res. Lab. Asahi Glass Co., Ltd. 33, 33-43 (1983).
1763. Kawaminami M. and T. Hirose, Sci. Rep. Kag. Univ. 27, 77-96 (1978).
1764. Kawate S.-I. , R. Fujiwara, S. Oda and I. Shimizu, Nippon Kagaku Kaishi (1986), 249-254.
1765. Keddam M. and H. Takenouti, Electrochim. Acta 33, 445 (1988).
1766. Keddam M., H. Takenouti and N. Yu, J. Electrochem. Soc. 132, 2561-2566 (1985).
1767. Keil R.G. and K. Ludwig, J. Electrochem. Soc. 118, 864-866 (1971)

1768. Keil R.G. and R.E. Salomon, J. Electrochem. Soc. 112, 643-644 (1965).
1769. Keil R.G. and R.E. Salomon, J. Electrochem. Soc. 115, 628-633 (1968).
1770. Kellawi H. and D.R. Rosseinsky, J. Electroanal. Chem. 131, 373-376 (1982).
1771. Kemp J.P. and P.A. Cox, J. Phys. C: Cond. Matter 2, 9653-9667 (1990).
1772. Kemp J.P. and P.A. Cox, J. Phys. Chem. Solids 51, 575-579 (1990).
1773. Kempf J.Y., B. Silvi, A. Dietrich, C.R.A. Catlow and B. Maigret, Chem. Mater. 5, 641-647 (1993).
1774. Kennedy J.H., Thin Solid Films 43, 41-92 (1977).
1775. Kennedy J.H., in Solid Electrolytes, edited by S. Geller (Springer, Berlin, 1977), pp. 105-141.
1776. Kennedy J.H., F. Chen and J. Hunter, J. Electrochem. Soc. 120, 454-458 (1973).
1777. Kennedy T.N., R. Hakim and J.D. Mackenzie, Mater. Res. Bull. 2, 193-201 (1967).
1778. Kenny N., C.R. Kannewurf and D.H. Whitmore, J. Phys. Chem. Solids 27, 1237-1246 (1966).
1779. Kepert D.L., in Comprehensive Inorganic Chemistry, edited by J.C. Bailar, Jr., M.J. Emeléus, R. Nyholm and A.F. Trotman-Dickenson (Pergamon, Oxford, 1973), Vol. 4, pp. 607-672.
1780. Kepert D.L. and J.M. Kyle, J. Chem. Soc. Dalton (1978), 133-137.
1781. Kera Y. and K. Hirota, J. Phys. Chem. 73, 3973-3981 (1969).
1782. Kera Y., H. Imori, S. Kida and K. Degawa, Bull. Chem. Soc. Japan 57, 2069-2074 (1984).
1783. Kera Y., T. Oonishi, H. Imori and S. Kida, Bull. Chem. Soc. Japan 58, 2263-2267 (1985).
1784. Kerker M., The Scattering of Light and Other Electromagnetic Radiation (Academic, New York, 1969).
1785. Kern W. and E. Tracy, RCA Rev. 41, 133-180 (1980).
1786. Kessler T., A. Visintin, M.R. de Chialvo, W.E. Triaca and A.J. Arvia, J. Electroanal. Chem. 261, 315-329 (1989).
1787. Kessler T., A. Visintin, W.E. Triaca, A.J. Arvia and M.R. Gennero de Chialvo, J. Appl. Electrochem. 21, 516-523 (1991).
1788. Kezuka H., R. Egerton, M. Masui, T. Wada, T. Ikehata, H. Mase and M. Takeuchi, Appl. Surf. Sci. 65-66, 293-297 (1993).
1789. Khabibullaev P.K. and B.G. Skorodumov, Determination of Hydrogen in Materials: Nuclear Physics Methods, Springer Tracts in Modern Physics (Springer, Berlin, Heidelberg, 1989), Vol. 117.
1790. Khamitov M.M., J.J. Kleperis and A.R. Lusis, Zh. Tekh. Fiz. SSSR 61, 191-192 (1991).
1791. Khan G.A. and C.A. Hogarth, J. Mater. Sci. 26, 597-600 (1991).
1792. Khan G.A. and C.A. Hogarth, J. Mater. Sci. 26, 1087-1092 (1991).
1793. Khan K.A. and C.G. Granqvist, Appl. Phys. Lett. 55, 4-6 (1989).
1794. Khan K.A., G.A. Niklasson and C.G. Granqvist, J. Appl. Phys. 64, 3327-3329 (1988).
1795. Khan M.S.R., K.A. Khan, W. Estrada and C.G. Granqvist, J. Appl. Phys. 69, 3231-3234 (1991).
1796. Kharitonov Yu.Ya., Yu.A. Busalev, A.A. Kuznetsova, Yu.G. Podzolko and L.V. Trofimova, Izv. Akad. Nauk SSSR Neorg. Mater. 2, 321-324 (1966) [Inorg. Mater. 2, 275-277 (1966)].
1797. Khawaja E.E., M.A. Kahn, F.F. Al-Adel and Z. Hussain, J. Appl. Phys. 68, 1205-1211 (1990).
1798. Khawaja E.E. and S.G. Tomlin, Thin Solid Films 30, 361-369 (1975).
1799. Khidekel M.L., A.D. Shebaldova and I.V. Kalechits, Russian Chem. Rev. 40, 669-678 (1971).
1800. Khodarev O.N., B.P. Filimonov, G.P. Ereiskaya and V.V. Ivanov, Elektrokhim. 27, 1046-1049 (1991) [Soviet Electrochem. 27, 922-925 (1991)].
1801. Kihlborg L., Ark. Kemi 21, 357-364 (1963).
1802. Kikuchi E., K. Iida and A. Fujishima, J. Electroanal. Chem. 351, 105-114 (1993).
1803. Killis A., J.-F. LeNest, H. Cheradame and A. Gandini, Macromol. Chem. 183, 2835-2845 (1982).
1804. Kim K.S., W.E. Baitinger, J.W. Amy and N. Winograd, J. Electron Spectrosc. Related Phenomena 5, 351-367 (1974).
1805. Kim K.S. and R.E. Davis, J. Electron Spectrosc. Related Phenomena 1, 251-258 (1972-1973).
1806. Kim K.S. and N. Winograd, Surf. Sci. 43, 625-643 (1974).
1807. Kim Y.-J. and L.F. Francis, J. Am. Ceram. Soc. 76, 737-742 (1993).
1808. Kinbara A., E. Kusano and S. Baba, J. Vac. Sci. Technol. A 10, 1483-1487 (1992).
1809. King D.A., T.E. Madey and J.T. Yates, Jr., J. Chem. Phys. 55, 3236-3246 (1971).
1810. King, D.A., T.E. Madey and J.T. Yates, Jr., J. Chem. Phys. 55, 3247-3253 (1971).
1811. Kinoshita K. and M. Nishibori, J. Vac. Sci. Technol. 6, 730-733 (1969).

1812. Kinsinger V., I. Sander, P. Steiner, R. Zimmermann and S. Hüfner, Solid State Commun. 73, 527-530 (1990).
1813. Kirino F., Y. Ito, K. Miyauchi and T. Kudo, Nippon Kagaku Kaishi (1986), 445-450.
1814. Kirkup L., J.M. Bell, D.C. Green, G.B. Smith and K.A. MacDonald, Rev. Sci. Instrum. 63, 2328-2329 (1992).
1815. Kishi K., J. Electron Spectrosc. Related Phenomena 46, 237-247 (1988).
1816. Kishimoto A., Denki Kagaku 61, 122-123 (1993).
1817. Kishimoto A., T. Kudo and T. Nanba, Solid State Ionics 53-56, 993-997 (1992).
1818. Kishimoto A., T. Nanba and T. Kudo, Solid State Ionics 40-41, 903-905 (1990).
1819. Kishimoto A., H. Sugimoto, T. Nanba and T. Kudo, J. Solid State Chem. 90, 102-108 (1991).
1820. Kishimoto A., H. Sugimoto, T. Nanba and T. Kudo, Thin Solid Films 204, L5-L8 (1991).
1821. Kislovskii L.D. and A.A. Abdullaev, Opt. Spektrosk. 29, 737-740 (1970) [Opt. Spectrosc. 29, 393-395 (1970)].
1822. Kiss A.B., Acta Chim. Acad. Sci. Hung. 84, 393-407 (1975).
1823. Kiss L.B., K. Bali, T. Szörényi and I. Hevesi, Solid State Commun. 58, 609-611 (1986).
1824. Kitabatake M., K. Hirochi and K. Wasa, J. Electrochem. Soc. 132, 433-435 (1985).
1825. Kitao M., H. Akram, H. Machida, K. Urabe and S. Yamada, Proc. Soc. Photo-Opt. Instrum. Engr. 1728, 165-172 (1992).
1826. Kitao M., H. Akram, K. Urabe and S. Yamada, J. Electronic Mater. 21, 419-422 (1992).
1827. Kitao M. and S. Yamada, in Solid State Ionic Devices, edited by B.V.R. Chowdari and S. Radhakrishna (World Scientific, Singapore, 1988), pp. 359-378.
1828. Kitao M., S. Yamada, Y. Hiruta, N. Suzuki and K. Urabe, Appl. Surf. Sci. 33-34, 812-817 (1988).
1829. Kitao M., S. Yamada, S. Yoshida, H. Akram and K. Urabe, Solar Energy Mater. Solar Cells 25, 241-255 (1992).
1830. Kittaka S., Y. Ayatsuka, K. Ohtani and N. Uchida, J. Chem. Soc. Faraday Trans. I 85, 3825-3832 (1989).
1831. Kittaka S., S. Sasaki, N. Ogawa and N. Uchida, J. Solid State Chem. 76, 40-51 (1988).
1832. Kittaka S., T. Suetsugi, R. Kuroki and M. Nagao, J. Colloid Interface Sci. 154, 216-224 (1992).
1833. Kittaka S., N. Uchida, T. Kihara, T. Suetsugi and T. Sasaki, Langmuir 8, 245-248 (1992).
1834. Kittaka S., N. Uchida, H. Miyahara and Y. Yokota, Mater. Res. Bull. 26, 391-398 (1991).
1835. Klein J.D., S.L. Clauson and S.F. Cogan, J. Mater. Res. 4, 1505-1510 (1989).
1836. Klein J.D., S.L. Clauson and S.F. Cogan, J. Vac. Sci. Technol. A 7, 3043-3047 (1989).
1837. Klein J.D. and A. Yen, Mater. Res. Soc. Symp. Proc. 293, 389-394 (1993).
1838. Klein J.D., A. Yen, R.D. Rauh and S.L. Clauson, Appl. Phys. Lett. 63, 599-601 (1993).
1839. Klemann L.P. and G.H. Newman, J. Electrochem. Soc. 128, 13-18 (1981).
1840. Kleperis J.J., G. Bajars, G. Vaivars, A. Kranevskis and A. Lusis, Elektrokhim. 28, 1444-1449 (1992) [Soviet Electrochem. 28, 1181-1185 (1992)].
1841. Kleperis J.J., A.A. Brishka, A.R. Lusis and O.A. Rode, Zh. Tekh. Fiz. 52, 709-714 (1982) [Soviet Phys. Tech. Phys. 27, 452-455 (1982)].
1842. Kleperis J.J., P.D. Cikmach and A.R. Lusis, Phys. Stat. Sol. A 83, 291-297 (1984).
1843. Kleperis J.J., J.V. Gabrusenoks, A.R. Lusis and G.M. Ramans, Izv. Akad. Nauk Latv. SSR, Ser. Fiz. Tekh. Nauk (1982) (5), 61-63.
1844. Kleperis J.J., A.M. Rodionov and A. Lusis, Elektrokhim. 28, 1450-1455 (1992) [Soviet Electrochem. 28, 1186-1190 (1992)].
1845. Kleperis J.J., S.J. Takeris and A.R. Lusis, Izv. Akad. Nauk Latv. SSR, Ser. Fiz. Tekh. Nauk (1983) (4), 122-126.
1846. Kleperis J.J., S.J. Takeris, A.R. Lusis and J.P. Stradins, Phys. Stat. Sol. A 81, K121-K125 (1984).
1847. Kleperis J.J., A. Veispals and A. Lusis, Izv. Akad. Nauk Latv. SSR, Ser. Fiz. Tekh. Nauk (1985) (3), 55-59.
1848. Klochikhin A.A. and S.G. Ogloblin, Phys. Stat. Sol. B 172, 371-385 (1992).
1849. Klug H.P. and L.E. Alexander, X-ray Diffraction Procedures for Polycrystalline and Amorphous Materials, Second edition (Wiley, New York, 1974).
1850. Klyavin Ya.K. and I.V. Milliere, Izv. Akad. Nauk. Latv. SSR, Ser. Khim. (1980) (4), 387-401.
1851. Knowles T.J., Appl. Phys. Lett. 31, 817-818 (1977).
1852. Kobayashi N., R. Hirohashi, H. Ohno and E. Tsuchida, Denki Kagaku 57, 1186-1189 (1989).

1853. Kobayashi N., R. Hirohashi, H. Ohno and E. Tsuchida, Solid State Ionics 40-41, 491-494 (1990).
1854. Kobayashi N., M. Nishikawa, H. Ohno, E. Tsuchida and R. Hirohashi, Nippon Shashin Gakukai-shi [J. Soc. Photo. Sci. Techn. Japan] 51, 375-380 (1988).
1855. Kobayashi N., H. Ohno, E. Tsuchida and R. Hirohashi, Kobunshi Ronbunshu 44, 317-322 (1987).
1856. Kobayashi N., S. Sunaga and R. Hirohashi, Polymer 33, 3044-3048 (1992).
1857. Kobayashi N., M. Uchiyama, K. Shigehara and E. Tsuchida, J. Phys. Chem. 89, 987-991 (1985).
1858. Kobayashi S., H. Sakamoto, F. Kaneko and N. Saito, Trans. Inst. Electronic Commun. Engr. Japan 67-C, 397-404 (1984).
1859. Kobayashi S., T. Takemura and F. Kaneko, Japan. J. Appl. Phys. 26, L1274-L1276 (1987).
1860. Kober F.P., J. Electrochem. Soc. 112, 1064-1067 (1965).
1861. Kober F.P., J. Electrochem. Soc. 114, 215-218 (1967).
1862. Kobosew N. and N.I. Nekrassow, Z. Elektrochem. 36, 529-544 (1930).
1863. Koch D.L. and A.S. Sangani, J. Electrochem. Soc. 138, 475-484 (1991).
1864. Kodintsev I.M., G.A. Kokarev and Yu. I. Kapustin, Elektrokhim. 21, 859-860 (1985) [Soviet Electrochem. 21, 800-801 (1985)].
1865. Kodintsev I.M., G.A. Kokarev, V.A. Kolesnikov and S.M. Sokolova, Elektrokhim. 19, 1137-1140 (1983) [Soviet Electrochem. 19, 1024-1027 (1983)].
1866. Kodintsev I.M., S. Trasatti, M. Rubel, A. Wieckowski and N. Kaufher, Langmuir 8, 283-290 (1992).
1867. Koffyberg F.P., Phys. Stat. Sol. B 80, 669-673 (1977).
1868. Koffyberg F.P. and F.A. Benko, Philos. Mag. B 38, 357-366 (1978).
1869. Koffyberg F.P. and F.A. Benko, J. Non-Cryst. Solids 40, 7-17 (1980).
1870. Koffyberg F.P. and F.A. Benko, J. Electrochem. Soc. 128, 2476-2479 (1981).
1871. Koffyberg F.P. and F.A. Benko, J. Appl. Phys. 53, 1173-1177 (1982).
1872. Koffyberg F.P., K. Dwight and A. Wold, Solid State Commun. 30, 433-437 (1979).
1873. Koffyberg F.P. and N.J. Koziol, J. Appl. Phys. 47, 4701-4702 (1976).
1874. Kofstad P., J. Electrochem. Soc. 109, 776-781 (1962).
1875. Kofstad P., High Temperature Oxidation of Metals: The Corrosion Monograph Series (Wiley, New York, 1966), pp. 251-263.
1876. Kofstad P. and K.P. Lillerud, J. Electrochem. Soc. 127, 2410-2419 (1980).
1877. Kohin M., S.J. Wein, J.D. Traylor, R.C. Chase and J.E. Chapman, Opt. Engr. 32, 911-925 (1993).
1878. Kohno K., J. Mater. Sci. 27, 658-660 (1992).
1879. Koksbang R., D. Fauteux, P. Norby and K.A. Nielsen, J. Electrochem. Soc. 136, 598-605 (1989).
1880. Koksbang R. and P. Norby, Electrochim. Acta 36, 127-133 (1991).
1881. Koksbang R., S. Yde-Andersen, K. West, B. Zachau-Christiansen and S. Skaarup, Solid State Ionics 28-30, 868-872 (1988).
1882. Kolawa E., F.C.T. So, W. Flick, X.-A. Zhao, E.T.-S. Pan and M.-A. Nicolet, Thin Solid Films 173, 217-224 (1989).
1883. Kolawa E., F.C.T. So, E.T.-S. Pan and M.-A. Nicolet, Appl. Phys. Lett. 50, 854-855 (1987).
1884. Kolb D.M., in Spectroelectrochemistry: Theory and Practice, edited by R.J. Gale (Plenum, New York, 1988), pp. 87-188.
1885. Kondo S., Electronics Mag. Japan 24, 1217-1222 (1979).
1886. Kondrat'ev V.V., I.A. Vinokurov, V.V. Bertsev, S.Ya. Khaikin and O.M. Zelenina, Elektrokhim. 28, 74-80 (1992) [Soviet Electrochem. 28, 58-63 (1992)].
1887. Konovalov I.A., Yu.A. Kulyupin, V.B. Nechitailo and V.I. Stepkin, Zh. Tekh. Fiz. 55, 1657-1661 (1985) [Soviet Phys. Tech. Phys. 30, 966-967 (1985)].
1888. Konovalov I.A., Yu.A. Kulyupin, V.B. Nechitalo, V.B. Stetsenko and A.S. Sukharier, Zh. Tekh. Fiz. 56, 1622-1625 (1986) [Soviet Phys. Tech. Phys. 31, 962-964 (1986)].
1889. Konovalov I.A., Yu.A. Kulyupin, V.B. Nechitailo and A.S. Sukharier, Zh. Tekh. Fiz. 56, 715-721 (1986) [Soviet Phys. Tech. Phys. 31, 431-434 (1986)].
1890. Kopp L., B.N. Harmon and S.H. Liu, Solid State Commun. 22, 677-679 (1977).
1891. Kosarev V.V., Fiz. Tekh. Poluprovodn. 8, 1378-1382 (1974) [Soviet Phys. Semicond. 8, 897-899 (1975)].
1892. Koshida N. and Y. Iketsu, Japan. J. Appl. Phys. 26, 1596-1597 (1987).

1893. Koshida N. and O. Tomita, J. Vac. Sci. Japan 27, 596-599 (1984).
1894. Koshida N. and O. Tomita, Japan. J. Appl. Phys. 24, 92-94 (1985).
1895. Koshida N. and O. Tomita, Japan. J. Appl. Phys. 25, 1932-1935 (1986).
1896. Koshida N., O. Tomita and Y. Iketsu, Proc. 17th Conf. on Solid State Devices and Materials, (Tokyo 1985), pp. 369-372.
1897. Koshida N., H. Wachi, K. Yoshida, M. Komuro and N. Atoda, Japan. J. Appl. Phys. 29, 2299-2302 (1990).
1898. Koslowski T. and W.von Niessen, Philos. Mag. 67, 317-329 (1993).
1899. Kosman M.S. and E.V. Bursian, Sovet Phys. Doklady 2, 354-356 (1957).
1900. Köstlin H., Festkörperprobleme 22, 229-254 (1982).
1901. Kötz R., C. Barbero and O. Haas, J. Electroanal. Chem. 296, 37-49 (1990).
1902. Kötz R., H.J. Lewerenz, P. Brüesch and S. Stucki, J. Electroanal. Chem. 150, 209-216 (1983).
1903. Kötz R., H.J. Lewerenz and S. Stucki, J. Electrochem. Soc. 130, 825-829 (1983).
1904. Kötz R. and H. Neff, Surf. Sci. 160, 517-530 (1985).
1905. Kötz R., H. Neff and S. Stucki, J. Electrochem. Soc. 131, 72-77 (1984).
1906. Kötz E.R. and S. Stucki, J. Appl. Electrochem. 17, 1190-1197 (1987).
1907. Kouda Y., T. Yoshino and N. Baba, Nippon Kagaku Kaishi (1985), 1050-1054.
1908. Kounavis P., A. Vomvas, E. Mitilineou, M. Roilos and L. Murawski, J. Phys. C: Solid State Phys. 21, 967-973 (1988).
1909. Koyama T., R. Hayashi, E. Masuda, A. Kurose, T. Hayakawa and N. Hojo, Polymer Commun. 29, 38-40 (1988).
1910. Kozlowski M.R., P.S. Tyler, W.H. Smyrl and R.T. Atanasoski, Surf. Sci. 194, 505-530 (1988).
1911. Kraevskii S.L., V.F. Solinov, E.V. Shishmentseva, T.F. Evdokimova and I. Yu. Martazova, Izv. Akad. Nauk SSSR Neorg. Mater. 15, 1897 (1979) [Inorg. Mater. 15, 1496 (1979)].
1912. Krasnov Yu.S., F.N. Patsyuk, A.K. Sandrovskii and A.T. Vas'ko, Elektrohim. 20, 1470-1475 (1984) [Soviet Electrochem. 20, 1359-1364 (1984)].
1913. Krasnov Yu.S., O.A. Sych, F.N. Patsyuk and A.T. Vas'ko, Elektrokhim. 24, 1468-1474 (1988) [Soviet Electrochem. 24, 1351-1357 (1988)].
1914. Krasnov Yu.S., O.A. Sych, F.N. Patsyuk and A.T. Vas'ko, Elektrokhim. 24, 1523-1526 (1988) [Soviet Electrochem. 24, 1405-1408 (1988)].
1915. Krasnov Yu.S., O.A. Sych, F.N. Patsyuk and A.T. Vas'ko, Ukr. Khim. Zh. 54, 1163-1165 (1988).
1916. Krasnov Yu.S., A.T. Vas'ko, F.N. Patsyuk and O.A. Sych, Ukr. Khim. Zh. 53, 951-956 (1987).
1917. Krasser W., Naturwissenschaften 56, 213-214 (1969).
1918. Kraus T., Laboratory Report at Balzers AG, Liechtenstein (entry made 30 July 1953), unpublished.
1919. Krause D. and V. Paquet, Electro-Opt. Systems Design 9 (11), 54-55 (1977).
1920. Krebs V.B., Acta Cryst. B 28, 2222-2231 (1972).
1921. Kreider K., J. Vac. Sci. Technol. A 4, 606-607 (1986).
1922. Kreuer K.-D., J. Mol. Struct. 177, 265-276 (1988).
1923. Kreuer K.-D., A. Rabenau and R. Messer, Appl. Phys. A 32, 45-53 (1983).
1924. Kreuer K.-D., A. Rabenau and R. Messer, Appl. Phys. A 32, 155-158 (1983).
1925. Krim J., Thin Solid Films 137, 297-303 (1986).
1926. Krishna M.G., K.N. Rao and S. Mohan, J. Appl. Phys. 73, 434-438 (1993).
1927. Krishna M.V.R. and R.A. Friesner, J. Chem. Phys. 95, 8309-8322 (1991).
1928. Krishna M.V.R. and R.A. Friesner, J. Chem. Phys. 96, 873-877 (1992).
1929. Krishnan N.G., W.N. Delgass and W.D. Robertson, Surf. Sci. 57, 1-11 (1976).
1930. Krug J. and P. Meakin, Phys. Rev. A 40, 2064-2077 (1989).
1931. Krug J. and P. Meakin, Phys. Rev. A 43, 900-919 (1991).
1932. Kruger J. and J.P. Calvert, J. Electrochem. Soc. 114, 43-49 (1967).
1933. Kruidhof W. and M. van der Leij, Solar Energy Mater. 2, 69-79 (1979).
1934. Krusin-Elbaum L., Thin Solid Films 169, 17-24 (1989).
1935. Krusin-Elbaum L. and M. Wittmer, J. Electrochem. Soc. 135, 2610-2614 (1988).
1936. Krusin-Elbaum L., M. Wittmer and D.S. Yee, Appl. Phys. Lett. 50, 1879-1881 (1987).
1937. Kruth R.F., in Handbook of X-rays, edited by E.F. Kaelble (McGraw-Hill, New York, 1967), Ch. 22.

1938. Kuboyama K., K. Hara and K. Matsushige, Japan. J. Appl. Phys. 31, L1609-L1610 (1992).
1939. Kucheiko S.I. and N.Ya. Turova, Koord. Khim. 13, 1057-1062 (1987) [Soviet J. Coord. Chem. 11, 590-595 (1988)].
1940. Kucheiko S.I., N.Ya. Turova, N.I. Kozlova and B.V. Zhadanov, Koord. Khim. 11, 1521-1528 (1985) [Soviet J. Coord. Chem. 11, 867-875 (1986)].
1941. Kudinov E.K., D.N. Mirlin and Yu.A. Firsov, Fiz. Tverd. Tela 11, 2789-2801 (1969) [Soviet Phys. Solid State 11, 2257-2266 (1969)].
1942. Kudo T., Nature 312, 537-538 (1984).
1943. Kudo T., Y. Aikawa, Y.M. Li and A. Kishimoto, Solid State Ionics 62, 99-104 (1993).
1944. Kudo T., A. Kishimoto, J. Oi and H. Inoue, Solid State Ionics 40-41, 567-571 (1990).
1945. Kudo T., J. Oi, A. Kishimoto and M. Hiratani, Mater. Res. Bull. 26, 779-787 (1991).
1946. Kudo T., H. Okamoto, K. Matsumoto and Y. Sasaki, Inorg. Chim. Acta 111, L27-L28 (1986).
1947. Kudo T., S. Takano, A. Kishimoto and Y. Aikawa, Denki Kagaku 59, 718-719 (1991).
1948. Kudo T., S. Takano, A. Kishimoto, T. Nanba and I. Yasui, in Recent Advances in Fast Ion Conducting Materials and Devices, edited by B.V.R. Chowdari, Q.-G. Liu and L.-Q. Chen (World Scientific, Singapore, 1990), pp. 191-199.
1949. Kudryavtseva, Z.I., V.A. Openkin, N.A. Zhuchkova, E.I. Khrushcheva and N.A. Shumilova, Elektrokhim. 11, 1488-1492 (1975) [Soviet Electrochem. 11, 1392-1395 (1975)].
1950. Kuhrt C. and M. Harsdorff, Philos. Mag. 63, 1247-1254 (1991).
1951. Kuklin R.N., Elektrokhim. 27, 1510-1515 (1991) [Soviet Electrochem. 27, 1335-1339 (1991)].
1952. Kukuyev V.I., L.F. Komolova, M.V. Lesovoy and Yu.Ya. Tomaspolsky, J. Microsc. Spectrosc. Electronics 14, 471-486 (1989).
1953. Kukuyev V.I., E.A. Tutov, E.P. Domashevskaya, M.I. Yanovskaya, I.E. Obvintseva and Yu.N. Venevtsev, Zh. Tekh. Fiz. 57, 1957-1961 (1987) [Soviet Phys. Tech. Phys. 32, 1176-1178 (1987)].
1954. Kulesza P.J. and L.R. Faulkner, J. Electroanal. Chem. 248, 305-320 (1988).
1955. Kulikov I.S., Z. Metallkunde 72, 525-529 (1981).
1956. Kulish N.R., V.P. Kunets and M.P. Lisitsa, Ukr. Fiz. Zh. 35, 1817-1821 (1990).
1957. Kumada F., M. Okamoto, M. Baba and T. Ikeda, Japan. J. Appl. Phys. 25, L574-L576 (1986).
1958. Kumagai N., Y. Matsuura, N. Kumagai and K. Tanno, J. Electrochem. Soc. 139, 3553-3558 (1992).
1959. Kumagai N., Y. Matsuura, Y. Umetzu and K. Tanno, Solid State Ionics 53-56, 324-332 (1992).
1960. Kumagai N., K. Tanno, T. Nakajima and N. Watanabe, Electrochim. Acta 28, 17-22 (1983).
1961. Kummer J.T., Progr. Solid State Chem. 7, 141-175 (1972).
1962. Kunitomo M., K. Eda, N. Sotani and M. Kaburagi, J. Solid State Chem. 99, 395-403 (1992).
1963. Kurik M.V., Phys. Stat. Sol. A 8, 9-45 (1971).
1964. Kurilenko L.N., Izv. Akad. Nauk SSSR, Ser. Khim. (1988), 966-972.
1965. Kurioka N., D. Watanabe, M. Haneda, T.Shimanouchi, T. Mizushima, N. Kakuta, A. Ueno, T. Hanaoka and Y. Sugi, Catal. Today 16, 495-501 (1993).
1966. Kuriyama H., M. Ii, T. Matsudo and S. Kurita, Japan Display 1983, pp. 370-371.
1967. Kurosawa S., H. Kitajima, Y. Ogawa, M. Muratsugu, E. Nemoto and N. Kamo, Anal. Chim. Acta 274, 209-217 (1993).
1968. Kurtz S.R. and R.G. Gordon, Thin Solid Films 147, 167-176 (1987).
1969. Kusano E., J.A. Theil and J.A. Thornton, J. Vac. Sci. Technol. A 6, 1663-1667 (1988).
1970. Kutznetsov V.A., Izv. Akad. Nauk SSSR Neorg. Mater. 28, 2432-2434 (1992) [Inorg. Mater. 28, 1986-1988 (1992)]
1971. Kuwabara K., Y. Gotoh and K. Sugiyama, Denki Kagaku 58, 868-870 (1990).
1972. Kuwabara K., S. Ichikawa and K. Sugiyama, Bull. Chem. Soc. Japan 60, 747-752 (1987).
1973. Kuwabara K., S. Ichikawa and K. Sugiyama, J. Mater. Sci. 22, 4499-4503 (1987).
1974. Kuwabara K., S. Ichikawa and K. Sugiyama, J. Electrochem. Soc. 135, 2432-2436 (1988).
1975. Kuwabara K., J. Itoh and K. Sugiyama, J. Mater. Sci. 27, 5315-5319 (1992).
1976. Kuwabara K., H. Nakamura and K. Sugiyama, Denki Kagaku 54, 66-70 (1986).
1977. Kuwabara K. and Y. Noda, Solid State Ionics 61, 303-308 (1993).
1978. Kuwabara K. and Y. Noda, J. Mater. Sci. (1993), to be published.

1979. Kuwabara K., M. Ohno and K. Sugiyama, Solid State Ionics 44, 319-323 (1991).
1980. Kuwabara K., A. Sakai and K. Sugiyama, Denki Kagaku 53, 243-247 (1985).
1981. Kuwabara K., K. Sugiyama and M. Ohno, Solid State Ionics 44, 313-318 (1991).
1982. Kuwabara K., K. Sugiyama and A. Sakai, Denki Kagaku 52, 536-537 (1984).
1983. Kuwabara K. and M. Yamada, Solid State Ionics 59, 25-31 (1993).
1984. Kuwabata S., S. Hirao and H. Yoneyama, Denki Kagaku 60, 1097-1100 (1992).
1985. Kuwano J., M. Asano, K. Shigehara and M. Kato, Solid State Ionics 40-41, 472-475 (1990).
1986. Kuzmin A. and J. Purans, J. Phys. Cond. Matter 5, 267-282 (1993).
1987. Kuzmin A. and J. Purans, J. Phys. Cond. Matter 5, 2333-2340 (1993).

L

1988. Labat J., J. Chim. Phys. 60, 1253-1263 (1963).
1989. Labbé P., M. Goreaud, B. Raveau and J.C. Monier, Acta Cryst. B 34, 1433-1438 (1978).
1990. Labbé P., M. Goreaud, B. Raveau and J.C. Monier, Acta Cryst. B 35, 1557-1564 (1979).
1991. Labunov V. and V. Parkin, Thin Solid Films 63, 162 (1979).
1992. Lado F. and S. Torquato, Phys. Rev. B 33, 3370-3378 (1986).
1993. Ladouceur M., J.P. Dodelet, L. Parent and S. Dallaire, Thin Solid Films 166, 249-254 (1988).
1994. Lagzdons J.L., G.E. Bajars and A.R. Lusis, Phys. Stat. Sol. A 84, K197-K200 (1984).
1995. Lake M.R., G.B. Smith, D.R. McKenzie and A.S. Dzurak, J. Non-Cryst. Solids 109, 318-326 (1989).
1996. Lam N.Q. and R. Kelly, Can. J. Phys. 50, 1887-1895 (1972).
1997. Lambrecht W., B. Djafari-Rouhani, M. Lannoo, P. Clauws, L. Fiermans and J. Vennik, J. Phys. C 13, 2503-2517 (1980).
1998. Lambrecht W., B. Djafari-Rouhani, M. Lannoo and J. Vennik, J. Phys. C. 13, 2485-2501 (1980).
1999. Lambrecht W., B. Djafari-Rouhani and J. Vennik, J. Phys. C 14, 4785-4795 (1981).
2000. Lambrecht W., B. Djafari-Bouhani and J. Vennik, Surf. Sci. 126, 558-564 (1983).
2001. Lampe-Önnerud C., T. Gustafsson and J.O. Thomas, Mater. Res. Soc. Symp. Proc. 293, 49-56 (1993).
2002. Lampert C.M., Solar Energy Mater. 11, 1-27 (1984).
2003. Lampert C.M., Proc. Soc. Photo-Opt. Instrum. Engr. 1272, 174-184 (1990).
2004. Lampert C.M., in Large-area Chromogenics: Materials and Devices for Transmittance Control, edited by C.M. Lampert and C.G. Granqvist (SPIE Opt. Engr. Press, Bellingham, 1990), Vol. IS4, pp. 414-446.
2005. Lampert C.M. and R'S. Caron-Popowich, Proc. Soc. Photo-Opt. Instrum. Engr. 1149, 56-71 (1989).
2006. Lampert C.M. and C.G. Granqvist, editors, Large-area Chromogenics: Materials and Devices for Transmittance Control (SPIE Opt. Engr. Press, Bellingham, 1990), Vol. IS4, pp. 1-606.
2007. Lampert C.M., T.R. Omstead and P.C. Yu, Proc. Soc. Photo-Opt. Instrum. Engr. 562, 15-22 (1985).
2008. Lampert C.M., T.R. Omstead and P.C. Yu, Solar Energy Mater. 14, 161-174 (1986).
2009. Landolt-Börnstein, Numerical Data and Functional Relationships in Science and Technology, New Series (Springer, Berlin, Heidelberg, 1975), Vol. III/7b1, pp. 596-605.
2010. Landolt-Börnstein, Numerical Data and Functional Relationships in Science and Technology, New Series (Springer, Berlin, Heidelberg, 1984), Vol. III/17g, pp. 282-291, 581-595.
2011. Langell M.A. and S.L. Bernasek, Phys. Rev. B 23, 1584-1593 (1981).
2012. Laperrière G., B. Marsan and D. Bélanger, Synth. Met. 29, F201-F206 (1989).
2013. Larramona G. and C. Gutiérrez, J. Electrochem. Soc. 136, 2171-2178 (1989).
2014. Larsson R., B. Folkesson and G. Schön, Chem. Scripta 3, 88-90 (1973).
2015. Laser D., M. Yaniv and S. Gottesfeld, J. Electrochem. Soc. 125, 358-365 (1978).
2016. Lassègues J.-C. and D. Rodriguez, Proc. Soc. Photo-Opt. Instrum. Engr. 1728, 241-249 (1992).
2017. Lauks I., M.F. Yuen and T. Dietz, Sensors Actuators 4, 375-379 (1983).
2018. Laves F., W. Petter and H. Wulf, Naturwissenschaften 51, 633-634 (1964).
2019. Lawrence S.A., S. Stevenson, K. Mavadia and P.A. Sermon, Proc. Roy. Soc. London A 411, 95-121 (1987).
2020. Lazukova N.I., V.A. Gubanov and V.G. Mokerov, Int. J. Quantum Chem. 12, 915-929 (1977).

2021. Leamy H.J., G.H. Gilmer and A.G. Dirks, in Current Topics in Materials Science, edited by E. Kaldis (North-Holland, Amsterdam, 1980), Vol. 6, pp. 309-340.
2022. LeBihan S. and M. Figlarz, J. Crystal Growth 13-14, 458-461 (1972).
2023. LeBihan S. and M. Figlarz, Electrochim. Acta 18, 123-124 (1973).
2024. LeBihan S. and G. Grandet, Vide 222, 213-217 (1984).
2025. LeBihan S., J. Guenot and M. Figlarz, Comptes Rendues Acad. Sci. Paris, Sér. C, 270, 2131-2133 (1970).
2026. Lee C.-H., B. Cahan and E. Yeager, J. Electrochem. Soc. 120, 1689-1692 (1973).
2027. Lee G. and S.-J. Oh, Phys. Rev. B 43, 14674-14682 (1991).
2028. Lee G.R. and J.A. Crayston, J. Mater. Chem. 1, 381-386 (1991).
2029. Lee M.H., P.J. Dobson and B. Cantor, Thin Solid Films 219, 199-205 (1992).
2030. Lee R.C. and C.R. Aita, J. Appl. Phys. 70, 2094-2103 (1991).
2031. Lee R.C. and C.R. Aita, J. Vac. Sci. Technol. A 10, 1777-1783 (1992).
2032. Lefkowitz I. and G.W. Taylor, Opt. Commun. 15, 340-342 (1975).
2033. Legendre J.-J., P. Aldebert, N. Baffier and J. Livage, J. Colloid Interface Sci. 94, 84-89 (1983).
2034. Legendre J.-J. and J. Livage, J. Colloid Interface Sci. 94, 75-83 (1983).
2035. Leising R.A. and E.S. Takeuchi, Chem. Mater. 5, 738-742 (1993).
2036. Leitner K., J.W. Schultze and U. Stimmung, J. Electrochem. Soc. 133, 1561-1568 (1986).
2037. Leja E., K. Marszalek and T. Stapinski, Acta Phys. Polonica A 67, 467-470 (1985).
2038. Leland J.K. and A.J. Bard, J. Phys. Chem. 91, 5083-5087 (1987).
2039. Le Mehaute A., in The Fractal Approach to Heterogeneous Chemistry, edited by D. Avnir (Wiley, New York, 1989), pp. 311-328.
2040. Lemerle J., L. Nejem and J. Lefebvre, J. Chem. Res. Miniprint (1978), 5301-5309.
2041. Lemerle J., L. Nejem and J. Lefebvre, J. Inorg. Nucl. Chem. 42, 17-20 (1980).
2042. Lemons R.A., G.D. Boyd, J.C. Phillips, J.P. Remeika and E.G. Spencer, Solid State Commun. 30, 73-76 (1979).
2043. Lemordant D., A. Bouhaouss, P. Aldebert and N. Baffier, J. Chim. Phys. 83, 105-113 (1986).
2044. Lenhart S.J., D.D. Macdonald and B.G. Pound, J. Electrochem. Soc. 135, 1063-1071 (1988).
2045. Leonova L.S., A.I. Korosteleva and E.A. Ukshe, Elektrokhim. 27, 1547-1549 (1991) [Soviet Electrochem. 27, 1371-1374 (1991)].
2046. Lepage J., A. Mezin and D. Paulmier, J. Micros. Spectrosc. Electronics 9, 365-388 (1984).
2047. Le Page Y. and P. Strobel, J. Solid State Chem. 43, 314-319 (1982).
2048. Le Page Y. and P. Strobel, J. Solid State Chem. 44, 273-281 (1982).
2049. Le Page Y. and P. Strobel, J. Solid State Chem. 47, 6-15 (1983).
2050. Levasseur A., B. Cales, J.-M. Reau and P. Hagenmuller, Mater. Res. Bull. 13, 205-209 (1978).
2051. Levasseur A., M. Kbala, J.C. Brethous, J.M. Réau, P. Hagenmuller and M. Couzi, Solid State Commun. 32, 839-844 (1979).
2052. Levasseur A., M. Kbala, P. Hagenmuller, G. Couturier and Y. Danto, Solid State Ionics 9-10, 1439-1444 (1983).
2053. Leventis N. and Y.C. Chung, J. Electrochem. Soc. 137, 3321-3322 (1990).
2054. Leventis N. and Y.C. Chung, J. Electrochem. Soc. 138, L21-L23 (1991).
2055. Leventis N. and Y.C. Chung, Chem. Mater. 4, 1415-1422 (1992).
2056. Leventis N. and Y.C. Chung, J. Mater. Chem. 2, 289-293 (1992).
2057. Levine J.R., J.B. Cohen and Y.W. Chung, Surf. Sci. 248, 215-224 (1991).
2058. Levy M., J.J. Falco and R.B. Herring, J. Less-Common Met. 34, 321-343 (1974).
2059. Lewis K.B., S.T. Oyama and G.A. Somorjai, Appl. Surf. Sci. 52, 241-248 (1991).
2060. Lewis M.B. and R.A. Perkins, J. Electrochem. Soc. 126, 544-547 (1979).
2061. Lezna R.O., K. Kunimatsu, T. Ohtsuka and N. Sato, J. Electrochem. Soc. 134, 3090-3094 (1987).
2062. Li F. and S. Dong, Electrochim. Acta 32, 1511-1513 (1987).
2063. Li J., A.E. Mintz and I.M. Khan, Chem. Mater. 4, 1131-1134 (1992).
2064. Li L. and G. Pistoia, Solid State Ionics 47, 231-240 (1991).
2065. Li L. and G. Pistoia, Solid State Ionics 47, 241-249 (1991).

2066. Li M., Q. Li, D. Guan, L. Li, G. Wang and C. Wang, in Solid State Ionic Devices, edited by B.V.R. Chowdari and S. Radhakrishna (World Scientific, Singapore, 1988), pp. 421-424.
2067. Li W., J.N. Reimers and J.R. Dahn, Phys. Rev. B46, 3236-3246 (1992).
2068. Lian K.K. and V.I. Birss, J. Electrochem. Soc. 138, 2877-2884 (1991).
2069. Lian K.K. and V.I. Birss, J. Electrochem. Soc. 138, 2885-2890 (1991).
2070. Liang C.C., in Fast Ion Transport in Solids, edited by W. van Gool (North-Holland, Amsterdam, 1973), pp. 19-31.
2071. Liang C.C., J. Electrochem. Soc. 120, 1289-1292 (1973).
2072. Liaw B.Y., I.D. Raistrick and R.A. Huggins, Solid State Ionics 18-19, 828-832 (1986).
2073. Liaw B.Y., I.D. Raistrick and R.A. Huggins, Solid State Ionics 45, 323-328 (1991).
2074. Lichter S. and J. Chen, Phys. Rev. Lett. 56, 1396-1399 (1986).
2075. Lieberman D., Electronic Prod. 28 (10), 19-21 (1985).
2076. Lieberman M.L. and R.C. Medrud, J. Electrochem. Soc. 116, 242-247 (1969).
2077. Lightsey P.A., Phys. Rev. B 8, 3586-3589 (1973).
2078. Lightsey P.A., D.A. Lilienfeld and D.F. Holcomb, Phys. Rev. B 14, 4730-4732 (1976).
2079. Lillerud K.P. and P. Kofstad, J. Electrochem. Soc. 127, 2397-2410 (1980).
2080. Lin J.K., J.M. Sivertsen and J.H. Judy, J. Appl. Phys. 57, 4000-4002 (1985).
2081. Lin R.-J. and N. Toshima, Bull. Chem. Soc. Japan 64, 136-148 (1991).
2082. Lin T.T. and D. Lichtman, J. Appl. Phys. 50, 1298-1303 (1979).
2083. Lindhard J., K. Dan. Vidensk. Selsk. Mat.-Fys. Medd. 28 (8), (1954).
2084. Lines M.E., Phys. Rev. B 21, 5793-5801 (1980).
2085. Lines M.E., J. Non-Cryst. Solids 46, 1-12 (1981).
2086. Lipscomb W.N. and R.A. Jacobson, in Physical Methods of Chemistry, Second edition, edited by B.W. Rossiter and J.F. Hamilton (Wiley, New York, 1990), Vol. 5, pp. 1-121.
2087. Liu Y.-J., D.C. de Groot, J.L. Schindler, C.R. Kannewurf and M.G. Kanatzidis, Adv. Mater. 5, 369-372 (1993).
2088. Liu Y.-J., D.C. de Groot, J.L. Schindler, C.R. Kannewurf and M.G. Kanatzidis, J. Chem. Soc. Chem. Commun. (1993), 593-596.
2089. Livage J., J. Phys. (Paris) 42, C4 981-C4 992 (1981).
2090. Livage J., Mater. Res. Soc. Symp. Proc. 32, 125-134 (1984).
2091. Livage J., J. Solid State Chem. 64, 322-330 (1986).
2092. Livage J., Chem. Mater. 3, 578-593 (1991).
2093. Livage J., Mater. Res. Bull. 26, 1173-1180 (1991).
2094. Livage J., Mater. Res. Soc. Symp. Proc. 293, 261-271 (1993).
2095. Livage J. and R. Collongues, Mater. Sci. Engr. 23, 297-299 (1976).
2096. Livage J., N. Gharbi, M.C. Leroy and M. Michaud, Mater. Res. Bull. 13, 1117-1124 (1978).
2097. Livage J., M. Henry and C. Sanchez, Prog. Solid State Chem. 18, 259-341 (1988).
2098. Livage J. and J. Lemerle, Ann. Rev. Mater. Sci. 12, 103-122 (1982).
2099. Lobitz P., H. Füllbier, A. Reiche, J.C. Illner, H. Reuter and S. Höring, Solid State Ionics 58, 41-48 (1992).
2100. Lodi G., A. De Battisti, G. Bordin, C. De Asmundis and A. Benedetti, J. Electroanal. Chem. 277, 139-150 (1990).
2101. Lodi G., G.L. Zucchini, A. De Battisti, A. Giatti, G. Battaglin and G. Della Mea, Surf. Sci. 251-252, 836-840 (1991).
2102. Lorteije J.H.J., Nachrichtentech. Z. 28, 196-200 (1975).
2103. Lottici P.P., D. Bersani, M. Braghini and A. Montenero, J. Mater. Sci. 28, 177-183 (1993).
2104. Lu P.W.T. and S. Srinivasan, J. Electrochem. Soc. 125, 1416-1422 (1978).
2105. Lu S., L. Hou and F. Gan, J. Mater. Sci. 28, 2169-2177 (1993).
2106. Lubin F., A. Lecerf, M. Broussely and J. Labat, J. Power Sources 34, 161-173 (1991).
2107. Ludi A. and W. Feitknecht, Helv. Chem. Acta 46, 2226-2238 (1963).
2108. Ludi A. and H.U. Güdel, Structure Bonding (Berlin) 14, 1-21 (1973).
2109. Lukovtsev P.D. and G. Ya. Slaidin', Elektrokhim. 6, 996-998 (1970) [Soviet Electrochem. 6, 963-964 (1970)].

2110. Luksich J. and C.R. Aita, J. Vac. Sci Technol. A 9, 542-546 (1991).
2111. Lundgren C.A. and R.W. Murray, Inorg. Chem. 27, 933-939 (1988).
2112. Lunkenheimer P., A. Loidl, C.R. Ottermann and K. Bange, Phys. Rev. B 44, 5927-5930 (1991).
2113. Luo Z., Proc. Soc. Photo-Opt. Instrum. Engr. 1728, 31-37 (1992).
2114. Luo Z., Z. Ding and Z. Jiang, J. Non-Cryst. Solids 112, 309-313 (1989).
2115. Lusis A.R., Proc. Soc. Photo-Opt. Instrum. Engr. 1536, 116-124 (1991).
2116. Lusis A.R., J.K. Klavins and V.A. Mikolaitis, in Physics and Chemistry of Glass-forming Systems (LSU, Riga, 1974).
2117. Lusis A.R., J.J. Kleperis, A.A. Brishka and E.V. Pentyush, Solid State Ionics 13, 319-324 (1984).
2118. Lusis A.R., Ya.L. Klyavin', Ya.Ya. Kleperis, Ya.Ya. Pinnis and O.A. Rode, Elektrokhim. 18, 1538-1542 (1982) [Soviet Electrochem. 18, 1372-1376 (1982)].
2119. Lyham L., S.J. Cyvin, B.N. Cyvin and J. Brunvoll, Spectrosc. Lett. 9, 859-864 (1976).
2120. Lynam N.R., SAE Tech. Paper Series 870636 (1987), 9 pages .
2121. Lynam N.R., in Electrochromic Materials, edited by M.K. Carpenter and D.A. Corrigan (The Electrochem. Soc., Pennington, 1990), Proc. Vol. 90-2, pp. 201-231.
2122. Lynam N.R. and A. Agrawal, in Large-area Chromogenics: Materials and Devices for Transmittance Control, edited by C.M. Lampert and C.G. Granqvist (SPIE Opt. Engr. Press, Bellingham, 1990), Vol. IS4, pp. 46-84.
2123. Lynam N.R. and H.R. Habibi, Proc. Soc. Photo-Opt. Instrum. Engr. 1016, 63-75 (1988).
2124. Lynam N.R., F.H. Moser and B.P. Hichwa, Proc. Soc. Photo-Opt. Instrum. Engr. 823, 130-137 (1987).
2125. Lynch D.W., R. Rosei, J.H. Weaver and C.G. Olson, J. Solid State Chem. 8, 242-252 (1973).
2126. Lyon S.B. and D.J. Fray, Solid State Ionics 15, 21-31 (1985).

M

2127. Ma Y.-P., P.C. Yu and C.M. Lampert, Proc. Soc. Photo-Opt. Instrum. Engr. 1536, 93-103 (1991).
2128. MacAdam D.L., Color Measurement: Theme and Variations, Springer Series in Optical Sciences (Springer, Berlin, Heidelberg, 1981), Vol. 27.
2129. Macagno V.A., J.R.Vilche and A.J. Arvia, J. Electrochem. Soc. 129, 301-310 (1982).
2130. MacArthur D.M., J. Electrochem. Soc. 117, 422-426 (1970).
2131. MacArthur D.M., J. Electrochem. Soc. 117, 729-733 (1970).
2132. MacCallum J.R., M.J. Smith and C.A. Vincent, Solid State Ionics 11, 307-312 (1984).
2133. MacCallum J.R. and C.A. Vincent, editors, Polymer Electrolyte Reviews - 1 (Elsevier Appl. Sci., London, 1987).
2134. MacCallum J.R. and C.A. Vincent, editors, Polymer Electrolyte Reviews - 2 (Elsevier Appl. Sci., London, 1989).
2135. MacChesney J.B. and H.J. Guggenheim, J. Phys. Chem. Solids 30, 225-234 (1969).
2136. Macdonald D.D., in Techniques for Characterization of Electrodes and Electrochemical Processes, edited by R. Varma and J.R. Selman (Wiley, New York, 1991), pp. 515-580.
2137. Macdonald D.D., M. Urquidi-Macdonald, S.D. Bhakta and B.G. Pound, J. Electrochem. Soc. 138, 1359-1363 (1991).
2138. Macdonald J.R., editor, Impedance Spectroscopy (Wiley, New York, 1987).
2139. MacDougall B. and J.A. Bardwell, J. Electrochem. Soc. 135, 2437-2441 (1988).
2140. MacDougall B. and M.J. Graham, J. Electrochem. Soc. 128, 2321-2325 (1981).
2141. MacDougall B., D.F. Mitchell and M.J. Graham, J. Electrochem. Soc. 127, 1248-1252 (1980).
2142. Macedo M.A., L.H. Dall'Antonia, B. Valla and M.A. Aegerter, in Proc. Sixth Int. Workshop on Glasses and Ceramics from Gels, Sevilla, Spain, Oct. 1991.
2143. Macedo M.A., L.H. Dall'Antonia, B. Valla and M.A. Aegerter, J. Non-Cryst. Solids 147-148, 792-798 (1992).
2144. Machida K. and M. Enyo, J. Electrochem. Soc. 137, 1169-1175 (1990).
2145. Machida N., R. Fuchida and T. Minami, J. Electrochem. Soc. 136, 2133-2136 (1989).
2146. Machida N., R. Fuchida and T. Minami, Solid State Ionics 35, 295-298 (1989).

2147. Machida N., I. Sakono, M. Tatsumisago and T. Minami, Chem. Lett. (1985), 1501-1502.
2148. Machida N., M. Tatsumisago and T. Minami, J. Electrochem. Soc. 133, 1963-1966 (1986).
2149. Mackintosh W.D. and H.H. Plattner, J. Electrochem. Soc. 123, 523-527 (1976).
2150. Macklin W.J. and R.J. Neat, Solid State Ionics 53-56, 694-700 (1992).
2151. Macklin W.J., R.J. Neat and R.J. Powell, J. Power Sources 34, 39-49 (1991).
2152. Macklin W.J., R.J. Neat and S.S. Sandhu, Electrochim. Acta 37, 1715-1720 (1992).
2153. MacLeod H.A., J. Vac. Sci. Technol. A 4, 418-422 (1986).
2154. Maddalena A.R., R. Dal Maschio, S. Diri and A. Raccanelli, J. Non-Cryst. Solids 121, 365-369 (1990).
2155. Madou M.J. and M.C.H. McKubre, J. Electrochem. Soc. 130, 1056-1061 (1983).
2156. Madou M.J. and S.R. Morrison, Chemical Sensing with Solid State Devices (Academic, San Diego, 1989).
2157. Maekawa T., J. Tamaki, N. Miura and N. Yamazoe, Chem. Lett. (1992), 639-642.
2158. Magnéli A., Ark. Kemi 1, 513-523 (1949-50).
2159. Magnéli A., Acta Chem. Scand. 7, 315-324 (1953).
2160. Magnéli A., G. Andersson and G. Sundkvist, Acta Chem. Scand. 9, 1402 (1955).
2161. Mahan G., Many Particle Physics (Plenum, New York, 1981).
2162. Maheswari S.P. and M.A. Habib, Solar Energy Mater. 18, 75-82 (1988).
2163. Maheswari S.P. and M.A. Habib, Proc. Soc. Photo-Opt. Instrum. Engr. 1149, 20-27 (1989).
2164. Maier J., J. Electrochem. Soc. 134, 1524-1535 (1987).
2165. Maleknia S., J. Brodbelt and K. Pope, J. Am. Soc. Mass Spectrometry 2, 212-219 (1991).
2166. Malinenko V.P., G.B. Stefanovich and F.A. Chudnovskii, Pis'ma Zh. Tekh. Fiz. 9, 754-757 (1983) [Soviet Tech. Phys. Lett. 9, 325-326 (1983)].
2167. Malpas R.E. and A.J. Bard, Anal. Chem. 52, 109-112 (1980).
2168. Malyuk Yu.I., Pis'ma Zh. Tekh. Fiz. 14, 1479-1482 (1988) [Soviet Tech. Phys. Lett. 14, 643-644 (1988)].
2169. Malyuk Yu.I. and L.I. Skatkov, Pis'ma Zh. Tekh. Fiz. 13, 504-507 (1987) [Soviet Tech. Phys. Lett. 13, 209-210 (1987)].
2170. Mance A.M., M.A. Habib, S.P. Maheswari and S.J. Simko, J. Appl. Electrochem. 22, 501-505 (1992).
2171. Mandelcorn L., Chem. Rev. 59, 827-839 (1959).
2172. Mandelcorn L., editor, Non-stoichiometric Compounds (Academic, New York, 1964).
2173. Manev V., A. Momchilov, A. Nassalevska and A. Kozawa, J. Power Sources 43-44, 551-559 (1993).
2174. Manev V., A. Momchilov, A. Nassalevska, G. Pistoia and M. Pasquali, J. Power Sources 43-44, 561-568 (1993).
2175. Manfredi M., C. Paracchini, G.C. Salviati and G. Schianchi, Thin Solid Films 79, 161-166 (1981).
2176. Manfredi M. and G.C. Salviati, Thin Solid Films 75, 133-137 (1981).
2177. Mani T., R. Mani and J.R. Stevens, Solid State Ionics 60, 113-117 (1993).
2178. Mani T. and J.R. Stevens, Polymer 33, 834-837 (1992).
2179. Manifacier J.C., Thin Solid Films 90, 297-308 (1982).
2180. Maniv S., W. Low and A. Gabay, J. Phys. Chem. Solids 32, 815-817 (1971).
2181. Maniv S., C.J. Miner and W.D. Westwood, J. Vac. Sci. Technol. A 1, 1370-1375 (1983).
2182. Maniv S. and W.D. Westwood, J. Vac. Sci. Technol. 17, 403-406 (1980).
2183. Mann C.K., in Electroanalytical Chemistry, edited by A.J. Bard (Marcel Dekker, New York, 1969), Vol. 3, pp. 57-134.
2184. Mann R.S. and K.C. Khulbe, Bull. Chem. Soc. Japan 48, 1021-1023 (1975).
2185. Mansfeld F. and W.J. Lorenz, in Techniques for Characterization of Electrodes and Electrochemical Processes, edited by R. Varma and J.R. Selman (Wiley, New York, 1991), pp. 581-647.
2186. Mansingh A., M. Sayer and J.B. Webb, J. Non-Cryst. Solids 28, 123-137 (1978).
2187. Marchiano S.L., C.I. Elsner and A.J. Arvia, J. Appl. Electrochem. 10, 365-377 (1980).
2188. Marszalek K., Thin Solid Films 175, 227-233 (1989).
2189. Marszalek K., E. Leja and T. Stapinski, Proc. Soc. Photo-Opt. Instrum. Engr. 653, 42-46 (1986).
2190. Marszalek K., E. Leja and T. Stapinski, Solar Energy Mater. 16, 47-53 (1987).
2191. Marszalek K.W., M.J. Marszalek, T. Stapinski and E. Leja, in Large-area Chromogenics: Materials and Devices for Transmittance Control, edited by C.M. Lampert and C.G. Granqvist (SPIE Opt. Engr. Press, Belingham, 1990), Vol. IS4, pp. 181-190.

2192. Martin P.J., J. Mater. Sci. 21, 1-25 (1986).
2193. Martin P.J. and R.P. Netterfield, in Progress in Optics, edited by E. Wolf (Elsevier, Amsterdam, 1986), Vol. XXIII, pp. 113-182.
2194. Martin P.J. and R.P. Netterfield, Thin Solid Films 199, 351-358 (1991).
2195. Martin P.J., R.P. Netterfield and T.J. Kinder, Thin Solid Films 193-194, 77-83 (1990).
2196. Martin P.J., R.P. Netterfield, T.J. Kinder and V. Stambouli, Appl. Phys. Lett. 58, 2497-2499 (1991).
2197. Martin P.J., W.G. Sainty and R.P. Netterfield, Appl. Opt. 23, 2668-2669 (1984).
2198. Martin S.W., J. Am. Ceram. Soc. 74, 1767-1783 (1991).
2199. Martinez M.A., J. Herrero and M.T. Gutierrez, Solar Energy Mater. Solar Cells 26, 309-321 (1992).
2200. Maruyama T. and S. Arai, Solar Energy Mater. Solar Cells 30, 257-262 (1993).
2201. Maruyama T. and S. Arai, Appl. Phys. Lett. 63, 869-870 (1993).
2202. Maruyama T. and K. Fukui, J. Appl. Phys. 70, 3848-3851 (1991).
2203. Maruyama T. and T. Nakai, Solar Energy Mater. 23, 25-29 (1991).
2204. Marvin A.M., F. Toigo and A. Martian, Surf. Sci. 211-212, 422-431 (1989).
2205. Masbah H., D. Tinet, M. Crespin, R. Erre, R. Setton and H. Van Damme, J. Chem. Soc. Chem. Commun. (1985), 935-936.
2206. Mashimoto S., H. Matsuoka, H. Kageshika, M. Susa and K.S. Goto, J. Electrochem. Soc. 137, 1300-1304 (1990).
2207. Masing L., J.E. Orme and L. Young, J. Electrochem. Soc. 108, 428-438 (1961).
2208. Masson J. and J. Nechtschein, Bull. Soc. Chim. France (1968), 3933-3938.
2209. Masuda H. and N. Baba, Chem. Lett. (1987), 1877-1890.
2210. Masuda H., K. Nishio and N. Baba, Japan. J. Appl. Phys. 31, L1775-L1777 (1992).
2211. Masuda H., K. Nishio and N. Baba, Thin Solid Films 223, 1-3 (1993).
2212. Masuda H., H. Tanaka and N. Baba, Bull. Chem. Soc. Japan 66, 305-311 (1993).
2213. Masuda H., T. Yoshino, K. Arai and N. Baba, Chem. Lett. (1988), 1337-1338.
2214. Masuda H., T. Yoshino, K. Arai and N. Baba, Hyomen Kagaku (J. Surf. Sci. Soc. Japan) 12, 641-643 (1991).
2215. Matienzo L.J., L.I. Yin, S.O. Grim and W.E. Swartz, Jr., Inorg. Chem. 12, 2762-2769 (1973).
2216. Matsuda S., K. Hosoya and K. Sugimoto, J. Japan Inst. Met. 50, 999-1008 (1986).
2217. Matsuda S. and K. Sugimoto, J. Japan Inst. Metals 49, 224-230 (1985).
2218. Matsudaira N., K. Fukuyoshi, Y. Yorimoto, Y. Ikeda and K. Yoshida, Japan Display 1983, pp. 54-56.
2219. Matsueda H., Thin Solid Films 52, 373-378 (1978).
2220. Matsueda H. and B.L. Averbach, Mater. Sci. Engr. 23, 131-134 (1976).
2221. Matsueda H. and B.L. Averbach, Surf. Sci. 86, 542-548 (1979).
2222. Matsuhiro K., E. Ando, K. Kawakami and Y. Masuda, Japan Display 1983, pp. 62-65.
2223. Matsuhiro K. and Y. Masuda, SID Symp. Dig. (1979) (10), 78-79.
2224. Matsuhiro K. and Y. Masuda, Proc. SID 21, 101-106 (1980).
2225. Matsuhiro K. and Y. Masuda, Shinkuu (J. Vacuum Soc. Japan) 23, 503-514 (1980).
2226. Matsumoto Y. and J. Hombo, J. Electroanal. Chem. 348, 441-445 (1993).
2227. Matsuoka H., S. Hashimoto and H. Kageshika, Surf. Techn. (Japan) 42(2), 104-110 (1991).
2228. Matsuoka T., J. Kuwata, Y. Fujita, and A. Abe, Japan. J. Appl. Phys. 27, L1199-L1200 (1988).
2229. Matsuoka T., J. Kuwata, M. Nishikawa, Y. Fujita, T.Tohda and A. Abe, Japan. J. Appl. Phys. 27, 1088-1091 (1988).
2230. Mattes R., H. Bierbüsse and J. Fuchs, Z. Anorg. Allg. Chem. 385, 230-242 (1971).
2231. Mattes R. and F. Schröder, Z. Naturforsch. 24b, 1095-1100 (1969).
2232. Mattheiss L.F., Phys. Rev. 181, 987-1000 (1969).
2233. Mattheiss L.F., Phys. Rev. B 2, 3918-3935 (1970).
2234. Mattheiss L.F., Phys. Rev. B 5, 290-306 (1972).
2235. Mattheiss L.F., Phys. Rev. B 5, 306-315 (1972).
2236. Mattheiss L.F., Phys. Rev. B 6, 4718-4740 (1972).
2237. Mattheiss L.F., Phys. Rev. B 13, 2433-2450 (1976).
2238. Matthews C.G., J.L. Ord and W.P. Wang, J. Electrochem. Soc. 130, 285-290 (1983).

2239. Mattox D.M., J. Vac. Sci. Technol. A 7, 1105-1114 (1989).
2240. Maurer S.M., D. Ng and E.I. Ko, Catal. Today 16, 319-331 (1993).
2241. Mayadas A.F. and M. Shatzkes, Phys. Rev. B 1, 1382-1389 (1970).
2242. Mazor A., D.J. Srolovitz, P.S. Hogan and B.G. Bukiet, Phys. Rev. Lett. 60, 424-427 (1988).
2243. Mbise G., G.B. Smith and C.G. Granqvist, Thin Solid Films 174, L123-L127 (1989).
2244. Mbise G., G.B. Smith, G.A. Niklasson and C.G. Granqvist, Appl. Phys. Lett. 54, 987-989 (1989).
2245. Mbise G., G.B. Smith, G.A. Niklasson and C.G. Granqvist, Proc. Soc. Photo-Opt. Instrum. Engr. 1149, 179-199 (1989).
2246. McBreen J., in Modern Aspects of Electrochemistry, edited by R.E. White, J.O'M. Bockris and B.E. Conway (Plenum, New York, 1990), pp. 29-63.
2247. McBreen J., W.E. O'Grady, K.I. Pandya, R.W. Hoffman and D.E. Sayers, Langmuir 3, 428-433 (1987).
2248. McBreen J., W.F. O'Grady, G. Tourillon, E. Dartyge, A. Fontaine and K.I. Pandya, J. Phys. Chem. 93, 6308-6311 (1989).
2249. McCargar J.W. and V.D. Neff, J. Phys. Chem. 92, 3598-3604 (1988).
2250. McCarley R.E., H.-H. Lii, P.A. Edwards and L.F. Brough, J. Solid State Chem. 57, 17-24 (1985).
2251. McCarroll B., J. Chem. Phys. 46, 863-869 (1967).
2252. McCarron III E.M., J. Chem. Soc. Chem. Commun. (1986), 336-338.
2253. McCarron III E.M. and J.C. Calabrese, J. Solid State Chem. 91, 121-125 (1991).
2254. McConnell A.A., J.S. Anderson and C.N.R. Rao, Spectrochim. Acta A 32, 1067-1076 (1976).
2255. McDevit N.T. and W.Z. Baun, Spectrochim. Acta 20, 799-808 (1964).
2256. McEwen R.S., J. Phys. Chem. 75, 1782-1789 (1971).
2257. McGee J.H., W.E. Kramer and H.N. Hersh, SID Symp. Proc. (1975) (6), 50-51.
2258. McGuire G.E., G.K. Schweitzer and T.A. Carlsson, Inorg. Chem. 12, 2450-2453 (1973).
2259. McHardy J. and J.O'M. Bockris, J. Electrochem. Soc. 120, 53-60 (1973).
2260. McIntyre J.D.E., J. Electrochem. Soc. 126, 2171-2172 (1979).
2261. McIntyre J.D.E., J. Electrochem. Soc. 126, 338c (1979).
2262. McIntyre J.D.E., J. Electrochem. Soc. 129, 1268-1269 (1982).
2263. McIntyre J.D.E. and D.E. Aspnes, Surf. Sci. 24, 417-434 (1971).
2264. McIntyre J.D.E., S. Basu, W.F. Peck, Jr., W.L. Brown and W.M. Augustyniak, Solid State Ionics 5, 359-362 (1981).
2265. McIntyre J.D.E., S. Basu, W.F. Peck, Jr., W.L. Brown and W.M. Augustyniak, Phys. Rev. B 25, 7242-7254 (1982).
2266. McIntyre J.D.E. and D.M. Kolb, Proc. Symp. Faraday Soc. (1970) (4), 99-112.
2267. McIntyre J.D.E. and W.F. Peck, Jr., J. Electrochem. Soc. 126, 338c (1979).
2268. McIntyre J.D.E., W.F. Peck, Jr., and S. Nakahara, J. Electrochem. Soc. 127, 1264-1268 (1980).
2269. McIntyre J.D.E., W.F. Peck , Jr., and G.P. Schwartz, J. Electronic Mater. 8, 707 (1979).
2270. McIntyre J.D.E., W.F. Peck, Jr., and V. Tierney, J. Electrochem. Soc. 129, 98c (1982).
2271. McIntyre N.S., T.E. Rummery, M.G. Cook and D. Owen, J. Electrochem. Soc. 123, 1164-1170 (1976).
2272. McKay J.M. and V.E. Henrich, Phys. Rev. Lett. 53, 2343-2346 (1984).
2273. McKay J.M. and V.E. Henrich, Phys. Rev. B 32, 6764-6772 (1985).
2274. McNally J.J., G.A. Al-Jumaily and J.R. McNeil, J. Vac. Sci. Technol. A 4, 437-439 (1986).
2275. McNatt J.L., Phys. Rev. Lett. 23, 915-918 (1969).
2276. McPhedran R.C. and D. Maystre, Appl. Phys. 14, 1-20 (1977).
2277. McPhedran R.C. and G.W. Milton, Appl. Phys. A 26, 207-220 (1981).
2278. Meakin P., CRC Crit. Rev. Solid State Mater. Sci. 13, 143-189 (1987).
2279. Meakin P. and J. Krug, Europhys. Lett. 11, 7-12 (1990).
2280. Meakin P. and J. Krug, Phys. Rev. A 46, 3390-3399 (1992).
2281. Meakin P. and B. Sapoval, Phys. Rev. A 43, 2993-3004 (1991).
2282. Meisel A., K.H. Hallmeier, R. Szargan, J. Müller and W. Schneider, Phys. Scripta 41, 513-516 (1990).
2283. Meisel T. and R. Braun, Proc. Soc. Photo-Opt. Instrum. Engr. 1728, 200-210 (1992).
2284. Melendres C.A., W. Paden, B. Tani and W. Walczak, J. Electrochem. Soc. 134, 762-763 (1987).
2285. Melendres C.A. and B.S. Tani, J. Electrochem. Soc. 133, 1059-1060 (1986).

2286. Melendres C.A. and S. Xu, J. Electrochem. Soc. 131, 2239-2243 (1984).
2287. Melville H.W. and J.C. Robb, Proc. Roy. Soc. London, Ser. A., 196, 445-465 (1949).
2288. Melville H.W. and J.C. Robb, Proc. Roy. Soc. London, Ser. A., 196, 466-478 (1949).
2289. Melville H.W. and J.C. Robb, Proc. Roy. Soc. London, Ser. A., 196, 479-493 (1949).
2290. Melville H.W. and J.C. Robb, Proc. Roy. Soc. London, Ser. A., 196, 494-509 (1949).
2291. Mendelsohn D.H. and R.B. Goldner, J. Electrochem. Soc. 131, 857-860 (1984).
2292. Méndez-Vivar J., Inorg. Chim. Acta 179, 77-82 (1991).
2293. Mendiboure A., C. Delmas and P. Hagenmuller, Mater. Res. Bull. 19, 1383-1392 (1984).
2294. Meng L.-J., M. Andritschky and M.P. dos Santos, Thin Solid Films 223, 242-247 (1993).
2295. Meng L.-J. M. Andritschky and M.P. dos Santos, Appl. Surf. Sci. 65-6, 235-239 (1993).
2296. Meng L.-J. and M.P. dos Santos, Appl. Surf. Sci. 68, 319-325 (1993).
2297. Meng L.-J. and M.P. dos Santos, Thin Solid Films 226, 22-29 (1993).
2298. Mercier R., O. Bohnke, C. Bohnke, G. Robert, B. Carquille and M.-F. Mercier, Mater. Res. Bull. 18, 1-7 (1983).
2299. Mertin W., S. Andersson and R. Gruehn, J. Solid State Chem. 1, 419-424 (1970).
2300. Messelhäuser J., E.B. Flint and H. Suhr, Appl. Phys. A 55, 196-202 (1992).
2301. Messier R., J. Vac. Sci. Technol. A 4, 490-495 (1986).
2302. Messier R., A.P. Giri and R.A. Roy, J. Vac. Sci. Technol. A 2, 500-503 (1984).
2303. Messier R. and J.E. Yehoda, J. Appl. Phys. 58, 3739-3746 (1985).
2304. Metikos-Hukovic M. and M. Ceraj-Ceric, J. Electrochem. Soc. 134, 2193-2197 (1987).
2305. Michailovits L., K. Bali, T. Szörényi and I. Hevesi, Acta Phys. Acad. Sci. Hung. 49, 217-221 (1980).
2306. Michailovits L., I. Hevesi, L. Phan and Zs. Varga, Thin Solid Films 102, 71-76 (1983).
2307. Michalak F., L. Rault and P. Aldebert, Proc. Soc. Photo-Opt. Instrum. Engr. 1728, 278-288 (1992).
2308. Michaud M., M.C. Leroy and J. Livage, Mater. Res. Bull. 11, 1425-1431 (1976).
2309. Michel C., M. Hervieu, R.J.D. Tilley and B. Raveau, J. Solid State Chem. 52, 281-291 (1984).
2310. Miedzinska K.M.E., B.R. Hollebone and J.G. Cook, J. Phys. Chem. Solids 49, 1355-1362 (1988).
2311. Mikula M., J. Blecha and M. Ceppan, J. Electrochem. Soc. 139, 3470-3474 (1992).
2312. Miles M.H., D.A. Fine and D.E. Stilwell, Proc. Soc. Photo-Opt. Instrum. Engr. 1323, 200-209 (1990).
2313. Miles M.H., D.E. Stilwell, R.A. Hollins and R.A. Henry, in Electrochromic Materials, edited by M.K. Carpenter and D.A. Corrigan (The Electrochem. Soc., Pennington, 1990), Proc. Vol. 90-2, pp. 137-156.
2314. Miller A. and E. Abrahams, Phys. Rev. 120, 745-755 (1960).
2315. Milner P.C. and U.B. Thomas, in Advances in Electrochemistry and Electrochemical Engineering, edited by C.W. Tobias (Interscience, New York, 1967), Vol. 5, pp. 1-86.
2316. Milton G.W., J. Appl. Phys. 52, 5286-5293 (1981).
2317. Milton G.W., J. Appl. Phys. 52, 5294-5304 (1981).
2318. Minami T., H. Nanto, S. Shooji and S. Takata, Thin Solid Films 111, 167-174 (1984).
2319. Minami T., H. Nanto and S. Takata, Japan. J. Appl. Phys. 23, L280-L282 (1984).
2320. Minami T., H. Nanto and S. Takata, Thin Solid Films 124, 43-47 (1985).
2321. Minami T., H. Sato, H. Nanto and S. Takata, Japan. J. Appl. Phys. 24, L781-L784 (1985).
2322. Minami T., H. Sato, H. Nanto and S. Takata, Thin Solid Films 176, 277-282 (1989).
2323. Minett M.G. and J.R. Owen, J. Power Sources 28, 397-408 (1989).
2324. Minett M.G. and J.R. Owen, J. Power Sources 32, 81-97 (1990).
2325. Minkova N., M. Krusteva and G. Nikolov, J. Mol. Struct. 115, 23-26 (1984).
2326. Misho R.H., W.A. Murad, G.H. Fatahalah, I.M. Abdul Aziz and H.M. Al-Doori, Phys. Stat. Sol. A 109, K101-K104 (1988).
2327. Misiano C. and E. Simonetti, Vacuum 27, 403-406 (1977).
2328. Misonou M. and H. Kawahara, in Large-area Chromogenics: Materials and Devices for Transmittance Control, edited by C.M. Lampert and C.G. Granqvist (SPIE Opt. Engr. Press, Bellingham, USA, 1990), Vol. IS4, pp. 402-412.
2329. Mitchell D., D.A.J. Rand and R. Woods. J. Electroanal. Chem. 84, 117-126 (1977).
2330. Mitchell D.F. and M.J. Graham, J. Electrochem. Soc. 133, 936-938 (1986).
2331. Miura T., K.-I. Aoki and T. Kishi, Denki Kagaku 59, 157-160 (1991).

2332. Miura T., T. Hijikata, Y. Muranushi and T. Kishi, Denki Kagaku 57, 740-741 (1989).
2333. Miura T., T. Hijikata, Y. Muranushi and T. Kishi, Denki Kagaku 58, 755-756 (1990).
2334. Miura T., N. Kanamori, Y. Muranushi and T. Kishi, Denki Kagaku 57, 29-32 (1989).
2335. Miura T., N. Kanamori, Y. Muranushi and T. Kishi, Denki Kagaku 57, 33-36 (1989).
2336. Miura T., S. Kunihiro, Y. Muranushi and T. Kishi, Denki Kagaku 57, 393-396 (1989).
2337. Miura T., Y. Maeda and T. Kishi, Denki Kagaku 59, 252-253 (1991).
2338. Miura T., E. Sugiura, T. Kishi and T. Nagai, Denki Kagaku 56, 413-418 (1988).
2339. Miura T., C. Takehara and T. Kishi, Denki Kagaku 59, 149-151 (1991).
2340. Miyake K., H. Kaneko, M. Sano and N. Suedomi, J. Appl. Phys. 55, 2747-2753 (1984).
2341. Miyake K., H. Kaneko, N. Suedomi and S. Nishimoto, J. Appl. Phys. 54, 5256-5261 (1983).
2342. Miyake K., H. Kaneko and Y. Teramoto, J. Appl. Phys. 53, 1511-1515 (1982).
2343. Miyake S., K. Honda, T. Kohno, Y. Setsuhara, M. Satou and A. Chayahara, J. Vac. Sci. Technol. A 10, 3253-3259 (1992).
2344. Miyake S., T. Kobayashi, M. Satou and F. Fujimoto, J. Vac. Sci. Technol. A 9, 3036-3040 (1991).
2345. Miyamura M., S. Tomura, A. Imai and S. Inomata, Solid State Ionics 3-4, 149-152 (1981).
2346. Miyano T., M. Iwanishi, C. Kaito and M. Shiojiri, Japan. J. Appl. Phys. 22, 863-868 (1983).
2347. Miyata N. and S. Akioshi, J. Appl. Phys. 58, 1651-1655 (1985).
2348. Miyata N., K. Miyake and Y. Yamaguchi, Appl. Phys. Lett. 37, 180-182 (1980).
2349. Miyauchi K., T. Kudo and T. Suganuma, Appl. Phys. Lett. 37, 799-800 (1980).
2350. Miyauchi K., K. Matsumoto, K. Kanehori and T. Kudo, Solid State Ionics 9-10, 1469-1472 (1983).
2351. Miyazaki S., S. Kikkawa and M. Koizumi, Synth. Met. 6, 211-217 (1983).
2352. Miyoshi T. and K. Iwasa, SID Symp. Dig. (1980) (11), 126-127.
2353. Mizuhashi M., Thin Solid Films 70, 91-100 (1980).
2354. Mizuhashi M., J. Non-Cryst. Solids 38-39, 329-334 (1980).
2355. Mizuhashi M., Glastechn. Ber. 56K, 1040-1045 (1983).
2356. Mizuhashi M. and Y. Gotoh, Repts. Res. Lab. Asahi Glass Co., Ltd. 32(2), 79-86 (1982).
2357. Mizuhashi M., Y. Gotoh, K. Matsumoto and K. Adachi, Repts. Res. Lab. Asahi Glass Co. Ltd. 36(1), 1-14 (1986).
2358. Mizuhashi M., J. Nagai and T. Kamimori, in Large-area Chromogenics: Materials and Devices for Transmittance Control, edited by C.M. Lampert and C.G. Granqvist (SPIE Opt. Engr. Press, Bellingham, 1990), Vol. IS4, pp. 494-503.
2359. Mizuhashi M., K. Suzuki and S. Takagi, Japan. Patent Appl. 63-199862 (1988).
2360. Mizuno M., T. Niwa and T. Endo, Japan Display 1989, pp. 111-113.
2361. Mizushima K., P.C. Jones, P.J. Wiseman and J.B. Goodenough, Mater. Res. Bull. 15, 783-789 (1980).
2362. Mizushima K., P.C. Jones, P.J. Wiseman and J.B. Goodenough, Solid State Ionics 3-4, 171-174 (1981).
2363. Mochizuki S., Phys. Stat. Sol. B 110, 219-225 (1982).
2364. Mochizuki S., Phys. Stat. Sol. B 126, 105-114 (1984).
2365. Mochizuki S. and M. Satoh, Phys. Stat. Sol. B 106, 665-674 (1981).
2366. Modinos A. and N. Stefanou, Acta Phys. Pol. A 81, 91-99 (1992).
2367. Mogab C.J., A.C. Adams and D.L. Flamm, J. Appl. Phys. 49, 3796-3803 (1978).
2368. Mohapatra S.K., J. Electrochem. Soc. 125, 284-288 (1978).
2369. Mohapatra S.K., G.D. Boyd, F.G. Storz, S. Wagner and F. Wudl, J. Electrochem. Soc. 126, 805-808 (1979).
2370. Mohapatra S.K. and S. Wagner, J. Electrochem. Soc. 125, 1603-1604 (1978).
2371. Mohapatra S.K. and S. Wagner, J. Appl. Phys. 50, 5001-5006 (1979).
2372. Mokerov V.G., L.V. Makarov, V.B. Tulvinskii and A.R. Begishev, Opt. Spektrosk. 40, 104-110 (1976) [Opt. Spectrosc. 40, 58-61 (1976)].
2373. Mokerov V.G. and B.L. Sigalov, Fiz. Tverd. Tela 14, 3405-3412 (1972) [Soviet Phys. Solid State 14, 2875-2879 (1973)].
2374. Molenda J., Phys. Stat. Sol. B 122, 591-598 (1984).
2375. Molenda J., Reactivity Solids 5, 305-314 (1988).
2376. Molenda J., C. Delmas and P. Hagenmuller, Solid State Ionics 9-10, 431-436 (1983).
2377. Molenda J. and A. Stoklosa, Solid State Ionics 36, 43-52 (1989).

2378. Molenda J. and A. Stoklosa, Solid State Ionics 38, 1-4 (1990).
2379. Molenda J. and A. Stoklosa, Solid State Ionics 53-56, 370-375 (1992).
2380. Molinié P. and S. Paoli, Comptes Rendues Acad. Sci. Paris, Sér. II, 299, 1243-1246 (1984).
2381. Mollet H.F. and B.C. Gerstein, J. Chem. Phys. 60, 1440-1446 (1974).
2382. Molnar B.J., A.R. Haranahalli and D.B. Dove, J. Vac. Sci. Technol. 15, 261-263 (1978).
2383. Momchilov A., V. Manev, A. Nassalevska and A. Kozawa, J. Power Sources 41, 305-314 (1993).
2384. Monk P.M.S. and S.L. Chester, Electrochim. Acta 38, 1521-1526 (1993).
2385. Morales J., An. Quim. 87, 691-702 (1991).
2386. Mori Y., J. Electronic Engn. (Aug. 1985), 53-59.
2387. Morin F.J., Phys. Rev. Lett. 3, 34-36 (1959).
2388. Morisaki H. and K. Yazawa, Appl. Surf. Sci. 33-34, 818-825 (1988).
2389. Morisaki S., K. Kawakami and N. Baba, Japan. J. Appl. Phys. 27, 314-318 (1988).
2390. Morita H., Japan. J. Appl. Phys. 21, 655-658 (1982).
2391. Morita H., Japan. J. Appl. Phys. 24, 723-727 (1985).
2392. Morita H., Japan. J. Appl. Phys. 24, 744-749 (1985).
2393. Morita H., Japan. J. Appl. Phys. 24, 750-754 (1985).
2394. Morita H., T. Miura and H. Washida, Japan. J. Appl. Phys. 20, L323-L325 (1981).
2395. Morita H. and H. Washida, Japan. J. Appl. Phys. 19, L228-L230 (1980).
2396. Morita H. and H. Washida, Oyo Buturi 51, 488-494 (1982).
2397. Morita H. and H. Washida, Japan. J. Appl. Phys. 23, 754-759 (1984).
2398. Moroney L.M., R. St. C. Smart and M.W. Roberts, J. Chem. Soc. Faraday Trans. I 79, 1769-1778 (1983).
2399. Mortimer R.J. and D.R. Rosseinsky, J. Electroanal. Chem. 151, 133-147 (1983).
2400. Mortimer R.J. and D.R. Rosseinsky, J. Chem. Soc. Dalton Trans. (1984), 2059-2061.
2401. Mortimer R.J., D.R. Rosseinsky and A. Glidle, Solar Energy Mater. Solar Cells 25, 211-223 (1992).
2402. Mosfegh A.Z. and A. Ignatiev, Thin Solid Films 198, 251-268 (1991).
2403. Moss T.S., Proc. Phys. Soc. London B 63, 167-174 (1950).
2404. Moss T.S., Photoconductivity in the Elements (Butterworths, London, 1952).
2405. Moss T.S., Proc. Phys. Soc. London B 67, 775-782 (1954).
2406. Moss T.S., Optical Properties of Semi-Conductors (Butterworths, London, 1961).
2407. Moss T.S., Phys. Stat. Sol. B 131, 415-427 (1985).
2408. Mosset A., P. Lecante, J. Galy and J. Livage, Philos. Mag. 46, 137-149 (1982).
2409. Motohiro T., S. Noda, A. Isogai and O. Kamigaito, Mater. Res. Soc. Symp. Proc. 159, 419-424 (1990).
2410. Motohiro T. and Y. Taga, Appl. Opt. 28, 2466-2482 (1989).
2411. Motohiro T. and Y. Taga, Thin Solid Films 172, L71-L74 (1989).
2412. Mott N.F., Adv. Phys. 16, 49-144 (1967).
2413. Mott N.F., J. Non-Cryst. Solids 1, 1-17 (1968).
2414. Mott N.F., Philos. Mag. 19, 835-852 (1969).
2415. Mott N.F., Festkörperprobleme 9, 22-45 (1969).
2416. Mott N.F., Adv. Phys. 21, 785-823 (1972).
2417. Mott N.F., Philos. Mag. 35, 111-128 (1977).
2418. Mott N.F., Metal-Insulator Transitions, Second edition (Taylor and Francis, London, 1990).
2419. Mott N.F. and E.A. Davis, Electronic Processes in Non-crystalline Materials, Second edition (Oxford University Press, Oxford, 1979).
2420. Moudden A.H., M. Elmiger, S.M. Shapiro, B.T. Collins and M. Greenblatt, Phys. Rev. B 44, 3324-3327 (1991).
2421. Moutou J.M., M. Vlasse, M. Cervera-Marzal, J.P. Chaminade and M. Pouchard, J. Solid State Chem. 51, 190-195 (1984).
2422. Movchan B.A. and A.V. Demchishin, Fiz. Metal. Metalloved. 28, 653-660 (1969) [Phys. Met. Metallogr. 28, 83-90 (1969)].
2423. Mozota J. and B.E. Conway, J. Electrochem. Soc. 128, 2142-2149 (1981).
2424. Mozota J. and B.E. Conway, Electrochim. Acta 28, 1-8 (1983).
2425. Muhlestein L.D. and G.C. Danielson, Phys. Rev. 158, 825-832 (1967).

2426. Mulder W.H. and J.H. Sluyters, Elektrochim. Acta 33, 303-310 (1988).
2427. Mulder W.H., J.H. Sluyters, T. Pajkóssy and L. Nyikos, J. Electroanal. Chem. 285, 103-115 (1990).
2428. Muller O. and R. Roy, J. Less-Common Met. 16, 129-146 (1968).
2429. Munshi M.Z.A. and B.B. Owens, Solid State Ionics 26, 41-46 (1988).
2430. Munshi M.Z.A. and W.M. Smyrl, Solid State Ionics 45, 183-189 (1991).
2431. Munshi M.Z.A., W.H. Smyrl and C. Schmidtke, Chem. Mater. 2, 530-534 (1990).
2432. Muramatsu H., T. Itoh, A. Watanabe and K. Hara, Japan. J. Appl. Phys. 21, L73-L74 (1982).
2433. Muranuchi Y., T. Miura and T. Kishi, Denki Kagaku 55, 756-761 (1987).
2434. Muranuchi Y., T. Miura, T. Kishi and T. Nagai, Denki Kagaku 54, 691-695 (1986).
2435. Murawala P.A., M. Sawai, T. Tatsuta, O. Tsuji, S. Fujita and S. Fujita, Japan. J. Appl. Phys. 32, 368-375 (1993).
2436. Murawski L., C. Gledel, C. Sanchez, J. Livage and J.P. Audiere, J. Non-Cryst. Solids 89, 98-106 (1987).
2437. Murawski L., C. Sanchez, J. Livage and J.P. Audiere, J. Non-Cryst. Solids 124, 71-75 (1990).
2438. Murphy D.W., R.J. Cava, S.M. Zahurak and A. Santoro, Solid State Ionics 9-10, 413-418 (1983).
2439. Murphy D.W., P.A. Christian, F.J. Di Salvo, J.N. Carides and J.V. Waszczak, J. Electrochem. Soc. 128, 2053-2060 (1981).
2440. Murphy D.W., P.A. Christian, F.J. Di Salvo and J.V. Waszczak, Inorg. Chem. 18, 2800-2803 (1979).
2441. Murphy D.W., F.J. Di Salvo, J.N. Carides and J.V. Waszczak, Mater. Res. Bull. 13, 1395-1402 (1978).
2442. Murphy D.W., M. Greenblatt, R.J. Cava and S.M. Zahurak, Solid State Ionics 5, 327-330 (1981).
2443. Murphy D.W., M. Greenblatt, S.M. Zahurak, R.J. Cava, J.V. Waszczak, G.W. Hull, Jr. and R.S. Hutton, Rev. Chim. Minérale 19, 441-449 (1982).
2444. Murphy O.J., T.E. Pou, J. O'M. Bockris and L.L. Tongson, J. Electrochem. Soc. 131, 2785-2790 (1984).
2445. Mücke K., F. Böhm, T. Gambke, C. Ottermann and K. Bange, Proc. Soc. Photo-Opt. Instrum. Engr. 1323, 188-199 (1990).
2446. Myland J.C. and K.B. Oldham, J. Electroanal. Chem. 347, 49-91 (1993).
2447. Müller A., G.S. Popkirov and R.N. Schindler, Ber. Bunsenges. Phys. Chem. 96, 1432-1437 (1992).
2448. Müller K.A., W. Berlinger and R.S. Rubins, Phys. Rev. 186, 361-371 (1969).
2449. Müller K.A., Th. von Waldkirch, W. Berlinger and B.W. Faughnan, Solid State Commun. 9, 1097-1101 (1971).
2450. Müller K.-H., J. Appl. Phys. 58, 2573-2576 (1985).
2451. Müller-Pfeiffer S., H.-J. Anklam and W. Haubenreisser, Phys. Stat. Sol. B 160, 491-504 (1990).
2452. Müller-Pfeiffer S., H. van Kranenburg and J.C. Loder, Thin Solid Films 213, 143-153 (1992).

N

2453. Nabavi M., S. Doeuff, C. Sanchez and J. Livage, Mater. Sci. Engr. B 3, 203-207 (1989).
2454. Nabavi M. and C. Sanchez, Comptes Rendues Acad. Sci. Paris, Sér. II, 310, 117-121 (1990).
2455. Nabavi M., C. Sanchez and J. Livage, Philos. Mag. B 63, 941-953 (1991).
2456. Nabavi M., C. Sanchez and J. Livage, Eur. J. Solid State Inorg. Chem. 28, 1173-1192 (1991).
2457. Nabavi M., C. Sanchez, F. Taulelle, J. Livage and A. de Guibert, Solid State Ionics 28-30, 1183-1186 (1988).
2458. Nag B.R., Electron Transport in Compound Semiconductors, Springer Series in Solid-State Sciences (Springer, Berlin, Heidelberg, 1980), Vol. 11.
2459. Nagai J., Proc. Soc. Photo-Opt. Instrum. Engr. 1016, 28-33 (1988).
2460. Nagai J., Japan. J. Opt. 17(4), 164-165 (1988).
2461. Nagai J., Solid State Ionics 40-41, 383-387 (1990).
2462. Nagai J., Proc. Soc. Photo-Opt. Instrum. Engr. 1728, 194-199 (1992).
2463. Nagai J. and T. Kamimori, Japan. J. Appl. Phys. 22, 681-687 (1983).
2464. Nagai J., T. Kamimori and M. Mizuhashi, Rept. Res. Lab. Asahi Glass Co., Ltd., 33, 99-116 (1983).
2465. Nagai J., T. Kamimori and M. Mizuhashi, Proc. Soc. Photo-Opt. Instrum. Engr. 502, 59-66 (1984).
2466. Nagai J., T. Kamimori and M. Mizuhashi, Proc. Soc. Photo-Opt. Instrum. Engr. 562, 39-45 (1985).

2467. Nagai J., T. Kamimori and M. Mizuhashi, Solar Energy Mater. 13, 279-295 (1986).
2468. Nagai J., T. Kamimori and M. Mizuhashi, Solar Energy Mater. 14, 175-184 (1986).
2469. Nagai J., M. Mizuhashi and T. Kamimori, in Large-area Chromogenics: Materials and Devices for Transmittance Control, edited by C.M. Lampert and C.G. Granqvist (SPIE Opt. Engr. Press, Bellingham, 1990), Vol. IS4, pp. 368-377.
2470. Nagai J., M. Mizuhashi and T. Kamimori, in Large-area Chromogenics: Materials and Devices for Transmittance Control, edited by C.M. Lampert and C.G. Granqvist (SPIE Opt. Engr. Press, Bellingham, USA, 1990), Vol. IS4, pp. 378-385.
2471. Nagai J., T. Seike, J. Shigesato and T. Kamimori, Japan. Patent No. 88, 106, 731 (1988).
2472. Nagamachi S., Y. Yamakage, H. Maruno, M. Ueda, S. Sugimoto, M. Asari and J. Ishikawa, Appl. Phys. Lett. 62, 2143-2145 (1993).
2473. Nagaoka K., H. Naruse, I. Shinohara and M. Watanabe, J. Polymer Sci. Polymer Lett. Ed. 22, 659-663 (1984).
2474. Nagase K., Y. Shimizu, N. Miura and N. Yamazoe, Appl. Phys. Lett. 60, 802-804 (1992).
2475. Nagase K., Y. Shimizu, N. Miura and N. Yamazoe, Appl. Phys. Lett. 61, 243-245 (1992).
2476. Nagasu M. and N. Koshida, Appl. Phys. Lett. 57, 1324-1325 (1990).
2477. Nagasu M. and N. Koshida, J. Appl. Phys. 71, 398-402 (1992).
2478. Nagiev V.M., Zh. Strukt. Khim. 16, 998-1001 (1975) [J. Struct. Chem. 16, 917-920 (1975)].
2479. Naguib H.M. and R. Kelly, J. Phys. Chem. Solids 33, 1751-1759 (1972).
2480. Nakamura A., T. Kawauchi, K. Urabe, M. Kitao and S. Yamada, J. Vac. Soc. Japan 24, 471-475 (1981).
2481. Nakamura A. and S. Yamada, Appl. Phys. 24, 55-59 (1981).
2482. Nakamura K., M. Kitajima and T. Hirata, J. Mater. Sci. Lett. 11, 805-806 (1992).
2483. Nakamura O. and J.B. Goodenough, Solid State Ionics 7, 119-123 (1982).
2484. Nakamura O., T. Kodama, I. Ogino and Y. Miyake, Chem. Lett. (1979), 17-18.
2485. Nakao Y. and H. Yamada, Surf. Sci. 176, 578-592 (1986).
2486. Nakato T., T. Ise, Y. Sugahara, K. Kuroda and C. Kato, Mater. Res. Bull. 26, 309-315 (1991).
2487. Nakato T., I. Kato, K. Kuroda and C. Kato, J. Colloid Interface Sci. 133, 447-451 (1989).
2488. Nakhodkin N.G. and A.I. Shaldervan, Thin Solid Films 10, 109-122 (1972).
2489. Namba Y., Japan. J. Appl. Phys. 9, 1326-1329 (1970).
2490. Nan C.-W. and D.M. Smith, Mater. Lett. 10, 109-111 (1990).
2491. Nan C.-W. and D.M. Smith, Mater. Sci. Engr. B 10, 99-106 (1991).
2492. Nanba T., Y. Nishiyama and I. Yasui, J. Mater. Res. 6, 1324-1333 (1991).
2493. Nanba T., S. Takano, I. Yasui and T. Kudo, J. Solid State Chem. 90, 47-53 (1991).
2494. Nanba T. and I. Yasui, J. Solid State Chem. 83, 304-315 (1989).
2495. Nandra S.S., J. Vac. Sci. Technol. A 8, 3179-3185 (1990).
2496. Nandra S.S., F.G. Wilson and C.D. DesForges, Thin Solid Films 107, 335-344 (1983).
2497. Nanto H., T. Minami, S. Orito and S. Takata, J. Appl. Phys. 63, 2711-2716 (1988).
2498. Nanto H., T. Minami, S. Shooji and S. Takata, J. Appl. Phys. 55, 1029-1034 (1984).
2499. Natan M.J., D. Bélanger, M.K. Carpenter and M.S. Wrighton, J. Phys. Chem. 91, 1834-1842 (1987).
2500. Natan M.J., T.E. Mallouk and M.S. Wrighton, J. Phys. Chem. 91, 648-654 (1987).
2501. Nath P. and R.F. Bunshah, Thin Solid Films 69, 63-68 (1980).
2502. Nath P., R.F. Bunshah, B.M. Basol and O.M. Staffsud, Thin Solid Films 72, 463-468 (1980).
2503. Nazar F.M. and M.T. Atiq, Int. J. Electronics 50, 493-498 (1981).
2504. Nazar F.M. and M.T. Atiq, Int. J. Electronics 51, 165-171 (1981).
2505. Nazar F.M. and F. Mahmood, Int. J. Electronics 56, 57-62 (1984).
2506. Nazarenko V.A. and E.N. Poluektova, Z. Neorg. Khim. 14, 204-211 (1969) [Russian J. Inorg. Chem. 14, 105-109 (1969)].
2507. Nazarenko V.A., E.N. Poluektova and G.G. Shitareva, Z. Neorg. Khim. 22, 998-1001 (1977) [Russian J. Inorg. Chem. 22, 551-553 (1977)].
2508. Nazri G., D.A. Corrigan and S.P. Maheswari, Langmuir 5, 17-22 (1989).
2509. Nazri G. and C. Julien, Solid State Ionics 53-56, 376-382 (1992).
2510. Nedjar R., M.M. Borel, M. Hervieu and B. Raveau, Mater. Res. Bull. 23, 91-97 (1988).

2511. Nefedkin S.I., N.V. Korovin, I.P. Gladkikh, G.N. Mansurov and O.A. Petrii, Elektrokhim. 24, 397-400 (1988) [Soviet Electrochem. 24, 371-374 (1988)].
2512. Nefedov V.I., D. Gati, B.F. Dzhurinskii, N.P. Sergushin and Ya.V. Salyn, Zh. Neorg. Khim. 20, 2307-2314 (1975) [Russian J. Inorg. Chem. 20, 1279-1283 (1975)].
2513. Nefedov V.I., Ya.V. Salyn, A.A. Chertkov and L.N. Padurets, Zh. Neorg. Chem. 19, 1443-1445 (1974) [Russian J. Inorg. Chem. 19, 785-787 (1974)].
2514. Nefedov V.I., Ya.V. Salyn, G. Leonhardt and R. Scheibe, J. Electron Spectrosc. 10, 121-124 (1977).
2515. Neff V.D., J. Electrochem. Soc. 125, 886-887 (1978).
2516. Neff V.D., J. Electrochem. Soc. 132, 1382-1384 (1985).
2517. Neikirk D.L., J.C. Fagerli, M.L. Smith, D. Mosman and T.C. DeVore, J. Mol. Struct. 244, 165-181 (1991).
2518. Nemetz A., A. Temmink, K. Bange, S. Cordoba-Torresi, C. Gabrielli, R. Torresi and H. Hugot-Le Goff, Solar Energy Mater. Solar Cells 25, 93-103 (1992).
2519. Netterfield R.P., W.G. Sainty, P.J. Martin and S.H. Sie, Appl. Opt. 24, 2267-2272 (1985).
2520. Neugebauer E. and C. von Fragstein, Optik 29, 150-161 (1968).
2521. Newman R. and R.M. Chrenko, Phys. Rev. 114, 1507-1513 (1959).
2522. Ng K.T. and D.M. Hercules, J. Phys. Chem. 80, 2094-2102 (1976).
2523. Nguyen M.T. and L.H. Dao, J. Electrochem. Soc. 136, 2131-2132 (1989).
2524. Nichols G.W., Trans. Electrochem. Soc. 62, 393-403 (1932).
2525. Niehus H., Surf. Sci. 78, 667-680 (1978).
2526. Nieuwenhuizen J.M. and H.B. Haanstra, Philips Techn. Rev. 27, 87-91 (1966).
2527. Niklasson G.A., J. Appl. Phys. 57, 157-158 (1985).
2528. Niklasson G.A., J. Appl. Phys. 62, 258-265 (1987).
2529. Niklasson G.A., J. Appl. Phys. 62, R1-R14 (1987).
2530. Niklasson G.A., Physica (Utrecht) D 38, 260-265 (1989).
2531. Niklasson G.A., in Materials Science for Solar Energy Conversion Systems, edited by C.G. Granqvist (Pergamon, Oxford, 1991), pp. 7-43.
2532. Niklasson G.A. and H.G. Craighead, Thin Solid Films 125, 165-170 (1985).
2533. Niklasson G.A. and C.G. Granqvist, J. Appl. Phys. 55, 3382-3410 (1984).
2534. Nikolaichik V.I. and A.L. Despotuli, Philos. Mag. Lett. 67, 19-24 (1993).
2535. Nilsson T.M.J. and G.A. Niklasson, Proc. Soc. Photo-Opt. Instrum. Engr. 1272, 129-138 (1990).
2536. Nimmo K.M. and J.S. Andersson, J. Chem. Soc. Dalton Trans. (1972), 2328-2337.
2537. Nishikawa M., H. Ohno, N. Kobayashi, E. Tsuchida and R. Hirohashi, Nippon Shashin Gakukai-shi [J. Soc. Photo. Sci. Tech. Japan] 51, 184-190 (1988).
2538. Nishimura K., Solid State Commun. 20, 523-524 (1976).
2539. Nishimura N., Y. Aikawa and M. Sukigara, Nippon Shashin Gakukai-shi [J. Photo. Sci. Techn. Japan] 48, 421-423 (1985).
2540. Nishimura R., K. Kudo and N. Sato, Surf. Sci. 96, 413-425 (1980).
2541. Nishimura T., K. Taira and S. Kurita, Appl. Phys. Lett. 36, 585-587 (1980).
2542. Nishioka Y., S. Kimura, H. Shinriki and K. Mukai, J. Electrochem. Soc. 134, 410-415 (1987).
2543. Nishiyama N., S. Morisaki and N. Baba, Denki Kagaku 56, 985-989 (1988).
2544. Nishiyama N., S. Morisaki and N. Baba, Denki Kagaku 58, 852-855 (1990).
2545. Niwa T., K. Uchikawa and T. Endo, Japan Display 1986, pp. 372-375.
2546. Noda H., K. Oikawa, T. Ogata, K. Matsuki and H. Kamada, Nippon Kagaku Kaishi (1986), 1084-1090.
2547. Noda T., K. Kudo and N. Sato, J. Japan Inst. Met. 37, 1088-1093 (1973).
2548. Nohma T., Y. Yamamoto, I. Nakane and N. Furukawa, J. Power Sources 39, 51-57 (1992).
2549. Nomura K., K. Hirayama, T. Ohsaka, M. Nakanishi, O. Hatozaki and N. Oyama, J. Macromol. Sci. Chem. A 26, 593-608 (1989).
2550. Nomura T., F. Tanaka, T. Yamada and H. Itoh, Anal. Chim. Acta 243, 273-278 (1991).
2551. Nonaka K., A. Takase and K. Miyakawa, J. Mater. Sci. Lett. 12, 274-277 (1993).
2552. Norby P., A. Nørlund Christensen, H. Fjellvåg and M. Nielsen, J. Solid State Chem. 94, 281-293 (1991).
2553. Norin R., Acta Chem. Scand. 17, 1391-1404 (1963).

2554. Norin R., Naturwissenschaften 52, 300 (1965).
2555. Norin R., Acta Chem. Scand. 29, 871-880 (1966).
2556. Norin R., M. Carlsson and B. Elgqvist, Acta Chem. Scand. 20, 2892-2893 (1966).
2557. Norin R. and A. Magnéli, Naturwissenschaften 47, 354-355 (1960).
2558. Norman M.R., Phys. Rev. B 44, 1364-1367 (1991).
2559. Norrman S., T. Andersson, C.G. Granqvist and O. Hunderi, Phys. Rev. B 18, 674-695 (1978)
2560. Novák P. and P. Podhájecky, J. Power Sources 35, 235-247 (1991).
2561. Novoselsky I.M. and N.R. Menglisheva, Electrochim. Acta 29, 21-27 (1984).
2562. Nozue Y., Z.K. Tang and T. Goto, Solid State Commun. 73, 531-534 (1990).
2563. Nyberg G.A. and R.A. Buhrman, J. Vac. Sci. Technol. A 2, 301-302 (1984).
2564. Nyikos L. and T. Pajkossy, Electrochim. Acta 35, 1567-1572 (1990).

O

2565. Obara K., S.-I. Saito and T. Ogushi, Nucl. Instrum. Meth. Phys. Res. B 39, 652-656 (1989).
2566. Obvintseva I.E., M.I. Yanovskaya, S.I. Kucheiko, N.Ya. Turova, R.R. Shifrina, V.I. Kukuev, E.N. Lubnin and Yu.N. Venevtsev, Izv. Akad. Nauk SSSR Neorg. Mater. 24, 790-794 (1988) [Inorganic Mater. 24, 661-665 (1988)].
2567. Ogawa H., T. Iijima, A. Morita and J. Nishimura, Prog. Batteries Solar Cells 3, 93-95 (1980).
2568. Ogumi Z., Y. Uchimoto, E. Endo and Z. Takehara, Electrochim. Acta 37, 1483-1986 (1992).
2569. Ogumi Z., Y. Uchimoto, E. Endo, K. Yasuda and Z. Takehara, to be published (1992).
2570. Ogumi Z., Y. Uchimoto and Z.I. Takehara, Chem. Lett. (1988), 1811-1814.
2571. Ogumi Z., Y. Uchimoto and Z.I. Takehara, J. Electrochem. Soc. 136, 625-630 (1989).
2572. Ogumi Z., Y. Uchimoto, Z. Takehara and F.R. Foulkes, J. Electrochem. Soc. 137, 29-34 (1990).
2573. Ogumi Z., Y. Uchimoto, Z.I. Takehara and Y. Kanamori, J. Electrochem. Soc. 135, 2649-2650 (1988).
2574. Ogura S. and H.A. MacLeod, Thin Solid Films 34, 371-375 (1976).
2575. Ohfuji S.-I., Thin Solid Films 115, 299-307 (1984).
2576. Ohlidal I. and K. Navarátil, Thin Solid Films 74, 51-58 (1980).
2577. Ohlsen W.D., Phys. Rev. B 7, 4058-4060 (1973).
2578. Ohmori A., K.-C. Park, M. Inuzuka, Y. Arata, K. Inoue and N. Iwamoto, Thin Solid Films 201, 1-8 (1991).
2579. Ohno H., Electrochim. Acta 37, 1649-1651 (1992).
2580. Ohno H. and H. Yamazaki, Solid State Ionics 59, 217-222 (1993).
2581. Ohsaka T., F. Izumi and Y. Fujiki, J. Raman Spectrosc. 7, 321-324 (1978).
2582. Ohtani B., T. Atsumi, S.-I. Nishimoto and T. Kagiya, Chem. Lett. (1988), 295-298.
2583. Ohtsuka H., S. Okada and J.-I. Yamaki, Solid State Ionics 40-41, 964-966 (1990).
2584. Ohtsuka T., N. Goto and N. Sato, J. Electroanal. Chem. 287, 249-264 (1990).
2585. Ohtsuka T., N. Goto, N. Sato and K. Kunimatsu, Ber. Bunsenges. Phys. Chem. 91, 313-316 (1987).
2586. Ohtsuka T., J. Guo and N. Sato, J. Electrochem. Soc. 133, 2473-2476 (1986).
2587. Ohtsuka T., M. Masuda and N. Sato, J. Electrochem. Soc. 132, 787-792 (1985).
2588. Ohtsuka T., M. Masuda and N. Sato, J. Electrochem. Soc. 134, 2406-2410 (1987).
2589. Ohtsuka T. and N. Sato, J. Electrochem. Soc. 128, 2522-2528 (1981).
2590. Ohtsuka T. and N. Sato, J. Electroanal. Chem. 147, 167-179 (1983).
2591. Ohtsuka T., K. Schoner and K.E. Heusler, J. Electroanal. Chem. 93, 171-182 (1978).
2592. Ohwada K., Spectrochim. Acta A 26, 1035-1044 (1970).
2593. Ohzuku T. and T. Hirai, Electrochim. Acta 27, 1263-1266 (1982).
2594. Ohzuku T. and T. Hirai, in Proc. Symp. on Manganese Dioxide Electrode Theory for Electrochemical Applications, edited by B. Schumm, Jr., R.L. Middaugh, M.P. Grotheer and J.C. Hunter (The Electrochem. Soc., Pennington, 1985), Proc. Vol. 85-4, pp. 141-157.
2595. Ohzuku T., Y. Iwakoshi and K. Sawai, J. Electrochem. Soc. 140, 2490-2498 (1993).
2596. Ohzuku T., J. Kato, K. Sawai and T. Hirai, J. Electrochem. Soc. 138, 2556-2560 (1991).
2597. Ohzuku T., M. Kitagawa and T. Hirai, J. Electrochem. Soc. 136, 3169-3174 (1989).

2598. Ohzuku T., M. Kitagawa and T. Hirai, J. Electrochem. Soc. 137, 40-46 (1990).
2599. Ohzuku T., M. Kitagawa and T. Hirai, J. Electrochem. Soc. 137, 769-775 (1990).
2600. Ohzuku T., T. Kodama and T. Hirai, J. Power Sources 14, 153-166 (1985).
2601. Ohzuku T., K. Sawai and T. Hirai, J. Electrochem. Soc. 132, 2828-2834 (1985).
2602. Ohzuku T., Z. Takehara and S. Yoshihawa, Electrochim. Acta 24, 219-222 (1979).
2603. Ohzuku T., A. Ueda and M. Nagayama, J. Electrochem. Soc. 140, 1862-1870 (1993).
2604. Ohzuku T., A. Ueda, M. Nagayama, Y. Iwakoshi and H. Komori, Electrochim. Acta 38, 1159-1167 (1993).
2605. Oi J., A. Kishimoto and T. Kudo, Nippon Kagaku Kaishi (1991), 1296-1300.
2606. Oi J., A. Kishimoto and T. Kudo, J. Solid State Chem. 96, 13-19 (1992).
2607. Oi J., A. Kishimoto and T. Kudo, J. Solid State Chem. 103, 176-185 (1993).
2608. Oi T., Appl. Phys. Lett. 37, 244-245 (1980).
2609. Oi T., Mater. Res. Bull. 19, 451-457 (1984).
2610. Oi T., Mater. Res. Bull. 19, 1077-1082 (1984).
2611. Oi T., Mater. Res. Bull. 19, 1343-1348 (1984).
2612. Oi T., Ann. Rev. Mater. Sci. 16, 185-201 (1986).
2613. Oi T. and K. Miyauchi, Mater. Res. Bull. 16, 1281-1289 (1981).
2614. Oi T., K. Miyauchi and J.-M. Dance, in Inorganic Solid Fluorides: Chemistry and Physics, edited by P. Hagenmuller (Academic, Orlando, 1985), pp. 489-492.
2615. Oi T., K. Miyauchi and K. Uehara, J. Appl. Phys. 53, 1823 (1982).
2616. Oka Y., N. Yamamoto, T. Ohtani and T. Takada, Nippon Seramikkusu Kyokai Gakujutsu Ronbunshi [J. Ceram. Soc. Japan] 97, 1441-1445 (1989).
2617. Oka Y., N. Yamamoto and T. Yao, Solid State Ionics 57, 103-107 (1992).
2618. Oka Y., T. Yao and N. Yamamoto, Nippon Seramikkusu Kyokai Gakujutsu Ronbunshi [J. Ceram. Soc. Japan] 98, 1365-1367 (1990).
2619. Oka Y., T. Yao and N. Yamamoto, J. Solid State Chem. 86, 116-124 (1990).
2620. Oka Y., T. Yao and N. Yamamoto, J. Mater. Chem. 1, 815-818 (1991).
2621. Okada M., H. Fukaya and T. Ido, Denki Kagaku 53, 109-113 (1985).
2622. Okamoto H., K. Yamanaka and T. Kudo, Mater. Res. Bull. 21, 551-557 (1986).
2623. Okamoto M., M. Baba and T. Ikeda, Japan. J. Appl. Phys. 29, L518-L520 (1990).
2624. Okamoto M. and M. Sakamoto, Seramikkusu (Japan) 18, 862-867 (1983).
2625. Oku M. and K. Hirokawa, J. Electron Spectrosc. Related Phenomena 10, 103-110 (1977).
2626. Oku M., H. Tokuda and K. Hirokawa, J. Electron Spectrosc. Related Phenomena 53, 201-211 (1991).
2627. Okuno S. and G.E. Matsubayashi, Bull. Chem. Soc. Japan 66, 459-463 (1993).
2628. Okuno S. and G.E. Matsubayashi, Chem. Lett. (1993), 799-802.
2629. Okuyama M. and S. Haruyama, Corrosion Sci. 14, 1-14 (1974).
2630. Olevskii S.S., M.S. Sergeev, A.L. Tolstikhina, A.S. Avilov, S.M. Shkornyakov and S.A. Semiletov, Dokl. Akad. Nauk SSSR 275, 1415-1419 (1984) [Soviet Phys. Dokl. 29 (4), 260-262 (1984)].
2631. Oliva P., J. Leonardi, J.F. Laurent, C. Delmas, J.J. Braconnier, M. Figlarz, F. Fievet and A. de Guibert, J. Power Sources 8, 229-225 (1982).
2632. Olivi P., E.C. Pereira, E. Longo, J.A. Varella and L.O. de S. Bulhoes, J. Electrochem. Soc. 140, L81-L82 (1993).
2633. Olsen L.C., F.W. Addis and W. Miller, Solar Cells 7, 247-279 (1982-1983).
2634. Olthuis W., M.A.M. Robben, P. Bergveld, M. Bos and W.A. van der Linden, Sensors Actuators B 2, 247-256 (1990).
2635. Ooi K., Y. Miyai and J. Sakakihara, Langmuir 7, 1167-1171 (1991).
2636. Ord J.L., Surf. Sci. 56, 413-424 (1976).
2637. Ord J.L., J. Electrochem. Soc. 127, 2682-2687 (1980).
2638. Ord J.L., J. Electrochem. Soc. 129, 335-339 (1982).
2639. Ord J.L., J. Electrochem. Soc. 129, 767-771 (1982).
2640. Ord J.L., S.D. Bishop and D.J. De Smet, in Electrochromic Materials, edited by M.K. Carpenter and D.A. Corrigan (The Electrochem. Soc., Pennington, 1990), Proc. Vol. 90-2, pp. 116-124.
2641. Ord J.L., S.D. Bishop and D.J. De Smet, J. Electrochem. Soc. 138, 208-214 (1991).

2642. Ord J.L., J.C. Clayton and K. Brudzewski, J. Electrochem. Soc. 125, 908-914 (1978).
2643. Ord J.L., J.C. Clayton and D.J. De Smet, J. Electrochem. Soc. 124, 1714-1719 (1977).
2644. Ord J.L., J.C. Clayton and W.P. Wang, J. Electrochem. Soc. 124, 1671-1677 (1977).
2645. Ord J.L. and D.J. De Smet, J. Electrochem. Soc. 113, 1258-1262 (1966).
2646. Ord J.L. and D.J. De Smet, J. Electrochem. Soc. 116, 762-767 (1969).
2647. Ord J.L. and D.J. De Smet, J. Electrochem. Soc. 118, 206-209 (1971).
2648. Ord J.L. and D.J. De Smet, J. Electrochem. Soc. 123, 1876-1882 (1976).
2649. Ord J.L. and D.J. De Smet, J. Electrochem. Soc. 139, 359-363 (1992).
2650. Ord J.L. and D.J. De Smet, J Electrochem. Soc. 139, 728-732 (1992).
2651. Ord J.L., D.J. De Smet and D.J. Beckstead, J. Electrochem. Soc. 136, 2178-2184 (1989).
2652. Ord J.L., D.J. De Smet and Z.Q. Huang, J. Electrochem. Soc. 134, 826-832 (1987).
2653. Ord J.L., M.A. Hopper and W.P. Wang, J. Electrochem. Soc. 119, 439-445 (1972).
2654. Ord J.L. and Z.Q. Huang, in Proc. Symp. on Manganese Dioxide Electrode Theory for Electrochemical Applications, edited by B. Schumm, Jr., R.L. Middaugh, M.P. Grotheer and J.C. Hunter (The Electrochem. Soc., Pennington, 1985), Proc. Vol. 85-4, pp. 541-555.
2655. Ord J.L. and E.M. Lushiku, J. Electrochem. Soc. 126, 1374-1380 (1979).
2656. Ord J.L. and W.P. Wang, J. Electrochem. Soc. 130, 1809-1814 (1983).
2657. Orel Z.C., M.G. Hutchins and G. McMeeking, Solar Energy Mater. Solar Cells 30, 327-337 (1993).
2658. Orman H.J. and P.J. Wiseman, Acta Cryst. C 40, 12-14 (1984).
2659. Ortiz P.I., M. López Teijelo and M.C. Giordano, An. Asoc. Quim. Argentina 74, 539-553 (1986).
2660. Ortiz P.I., M. López Teijelo and M.C. Giordano, J. Electroanal. Chem. 243, 379-391 (1988).
2661. Osborn D.E., editor, Selected Papers on Solar Radiation and Solar Thermal Systems (SPIE Opt. Engr. Press, Bellingham, 1993), Vol. MS-54.
2662. Oshitani M., Y. Sasaki and K. Takashima, J. Power Sources 12, 219-231 (1984).
2663. Osteryoung J., Acc. Chem. Res. 26, 77-83 (1993).
2664. Ottaviani M., S. Panero, S. Morzilli, B. Scrosati and M. Lazzari, Solid State Ionics 20, 197-202 (1986).
2665. Otten J.M. and W. Visscher, Electroanal. Chem. Interfacial Electrochem. 55, 1-11 (1974).
2666. Otten J.M. and W. Visscher, Electroanal. Chem. Interfacial Electrochem. 55, 13-21 (1974).
2667. Ottermann C., K. Bange, W. Wagner, M. Laube and F. Rauch, Surf. Interface Anal. 19, 435-438 (1992).
2668. Otterman C., J. Segner and K. Bange, Proc. Soc. Photo-Opt. Instrum. Engr. 1728, 211-222 (1992).
2669. Ottermann C., A. Temmink and K. Bange, Thin Solid Films 193-194, 409-417 (1990).
2670. Ottermann C., A. Temmink and K. Bange, Proc. Soc. Photo-Opt. Instrum. Engr. 1272, 111-121 (1990).
2671. Otto K., Phys. Chem. Glasses 7, 29-37 (1966).
2672. Ovadyahu Z., B. Ovryn and H.W. Kraner, J. Electrochem. Soc. 130, 917-921 (1983).
2673. Overhof H., Phys. Stat. Sol. B 67, 709-714 (1975).
2674. Owen J.F., K.J. Teegarden and H.R. Shanks, Phys. Rev. B 18, 3827-3837 (1978).
2675. Owens B.B., in Advances in Electrochemistry and Electrochemical Engineering, edited by C.W. Tobias (Wiley, New York, 1971), Vol. 8, pp. 1-62.
2676. Owens B.B. and G.R. Argue, J. Electrochem. Soc. 117, 898-900 (1970).
2676a. Oyama T., N. Hashimoto, J. Shimizu, Y. Akao, H. Kojima, K. Aikawa and K. Suzuki, J. Vac. Sci. Technol. A 10, 1682-1686 (1992).
2677. Oyama N., T. Ohsaka, M. Menda and H. Ohno, Denki Kagaku 57, 1172-1177 (1989).
2678. Ozanam F. and J.-N. Chazalviel, J. Electron Spectrosc. Related Phenomena 54-55, 1219-1228 (1990).
2679. Özer N., Thin Solid Films 214, 17-24 (1992).
2680. Özer N., H. Demiryont and J.H. Simmons, Appl. Opt. 30, 3661-3666 (1991).
2681. Özer N. and F. Tepehan, Solar Energy Mater. Solar Cells 30, 13-26 (1993).
2682. Özer N., F. Tepehan and N. Bozkurt, Thin Solid Films 219, 193-198 (1992).
2683. Ozin G.A., S. Öskar and R.A. Prokopowicz, Acc. Chem. Res. 25, 553-560 (1992).

P

2684. Paatsch W., Surf. Sci. 37, 59-66 (1973).
2685. Paatsch W., J. Phys. (Paris) 38, C5 151-C5 155 (1977).
2686. Paik S.M., S. Kim, I.K. Schuller and R. Ramirez, Phys. Rev. B 43, 1843-1846 (1991).
2687. Paik W.-K. and J. O'M. Bockris, Surf. Sci. 28, 61-68 (1971).
2688. Paik W.-K. and Z. Szklarska-Smialowska, Surf. Sci. 96, 401-412 (1980).
2689. Pajkossy T., J. Electroanal. Chem. 300, 1-11 (1991).
2690. Pajkossy T. and L. Nyikos, Electrochim Acta 34, 171-179 (1989).
2691. Palatnik L.S., Yu.I. Malyuk and V.V. Belozerov, Doklady Akad. Nauk SSSR 215, 1182-1185 (1974) [Doklady Chem. Technol. 215 (5), 68-71 (1974)].
2692. Palik E.D., editor, Handbook of Optical Constants of Solids (Academic, New York, 1985).
2693. Palik E.D., editor, Handbook of Optical Constants of Solids II (Academic, New York, 1991).
2694. Palombari R. and B. Sebastiani, J. Electroanal. Chem. 336, 349-355 (1992).
2695. Pan C.A. and T.P. Ma, Appl. Phys. Lett. 37, 163-165 (1980).
2696. Pan C.A. and T.P. Ma, J. Electrochem. Soc. 128, 1953-1957 (1981).
2697. Pan C.A. and T.P. Ma, J. Electronic Mater. 10, 43-57 (1981).
2698. Pandya K.I., W.E. O'Grady, D.A. Corrigan, J. McBreen and R.W. Hoffman, J. Phys. Chem. 94, 21-26 (1990).
2699. Panero S., M. Pasquali and G. Pistoia, J. Electrochem. Soc. 130, 1225-1227 (1983).
2700. Panicker M.P.R. and W.F. Essinger, J. Electrochem. Soc. 128, 1943-1947 (1981).
2701. Pankajakshan V.S., K. Neelakandan and C.S. Menon, Thin Solid Films 215, 196-199 (1992).
2702. Pantaloni S., S. Passerini and B. Scrosati, J. Electrochem. Soc. 134, 753-755 (1987).
2703. Parent P., H. Dexpert, G. Tourillon and J.-M. Grimal, J. Electrochem. Soc. 139, 276-281 (1992).
2704. Parent P., H. Dexpert, G. Tourillon and J.-M. Grimal, J. Electrochem. Soc. 139, 282-285 (1992).
2705. Park H.-K., K. Podolske, Z. Munshi, W.H. Smyrl and B.B. Owens, J. Electrochem. Soc. 138, 627-628 (1991).
2706. Park H.L., C.H. Chung, C.H. Kim and H.S. Kim, J. Mater. Sci. Lett. 6, 1093-1095 (1987).
2707. Parker A.J., Electrochim. Acta 21, 671-679 (1976).
2708. Parker J.C., D.J. Lam, Y.-N. Xu and W.Y. Ching, Phys. Rev. B 42, 5289-5293 (1990).
2709. Parlebas J.C., Phys. Stat. Sol. B 178, 9-35 (1993).
2710. Paroli P., L. Ryabova, V. Salun and A. Tucciarone, Phys. Stat. Sol. A 75, K209-K210 (1983).
2711. Partlow D.P., S.R. Gurkovich, K.C. Radford and L.J. Denes, J. Appl. Phys. 70, 443-452 (1991).
2712. Pasquali M. and G. Pistoia, Electrochim. Acta 36, 1549-1553 (1991).
2713. Passerini S., R. Pileggi and B. Scrosati, Electrochim. Acta 37, 1703-1706 (1992).
2714. Passerini S. and B. Scrosati, Solid State Ionics 53-56, 520-524 (1992).
2715. Passerini S., B. Scrosati and A. Gorenstein, J. Electrochem. Soc. 137, 3297-3300 (1990).
2716. Passerini S., B. Scrosati, A. Gorenstein, A.M. Andersson and C.G. Granqvist, J. Electrochem. Soc. 136, 3394-3395 (1989).
2717. Passerini S., B. Scrosati, A. Gorenstein, A.M. Andersson and C.G. Granqvist, in Electrochromic Materials, edited by M.K. Carpenter and D.A. Corrigan (The Electrochem. Soc., Pennington, 1990), Proc. Vol. 90-2, pp. 237-245.
2718. Patrina I.B. and V.A. Ioffe, Fiz. Tverd. Tela 6, 3227-3234 (1964) [Soviet Phys. Solid State 6, 2581-2585 (1965)].
2719. Paulson G.G. and A.I.. Friedberg, Thin Solid Films 5, 47-52 (1970).
2720. Paulson W.M., F.S. Hickernell and R.L. Davis, J. Vac. Sci. Technol. 16, 307-310 (1979).
2721. Pawlewicz W.T. and R. Busch, Thin Solid Films 63, 251-256 (1979).
2722. Pawlewicz W.T., P.M. Martin, D.D. Hays and I.B. Mann, Proc. Soc. Photo-Opt. Instrum. Engr. 325, 105-116 (1982).
2723. Pedone D., M. Armand and D. Deroo, Solid State Ionics 28-30, 1729-1732 (1988).
2724. Peignon M.C., C. Cardinaud and G. Turban, J. Appl. Phys. 70, 3314-3323 (1991).
2725. Peignon M.C., C. Cardinaud and G. Turban, J. Electrochem. Soc. 140, 505-512 (1993).

2726. Pelleg J., J. Less-Common Met. 35, 299-304 (1974).
2727. Pennisi A. and C.M. Lampert, Proc. Soc. Photo-Opt. Instrum. Engr. 1016, 131-144 (1988).
2728. Pennisi A. and F. Simone, Proc. Soc. Photo-Opt. Instrum. Engr. 1016, 176-181 (1988).
2729. Pennisi A. and F. Simone, Appl. Phys. A 57, 13-17 (1993).
2730. Pennisi A., F. Simone and C.M. Lampert, Solar Energy Mater. Solar Cells 28, 233-247 (1992).
2731. Pereira-Ramos J.P., R. Baddour, S. Bach and N. Baffier, Solid State Ionics 53-56, 701-709 (1992).
2732. Pereira-Ramos J.P., R. Baddour-Hadjean, N. Kumagai and K. Tanno, Electrochim. Acta 38, 431-436 (1993).
2733. Pereira-Ramos J.P., R. Messina and J. Perichon, J. Power Sources 16, 193-204 (1985).
2734. Pereira-Ramos J.P., R. Messina, C. Piolet and J. Devynck, Electrochim. Acta 33, 1003-1008 (1988).
2735. Pereira-Ramos J.P., R. Messina, L. Znaidi and N. Baffier, Solid State Ionics 28-30, 886-894 (1988).
2736. Perthuis H., Ph. Colomban, J.P. Boilot and G. Velasco, in Ceramic Powders, edited by P. Vincenzini (Elsevier, Amsterdam, 1983), pp. 575-582.
2737. Pertosa P., G. Hollinger and F.M. Michel-Calendini, Phys. Rev. B 18, 5177-5183 (1978).
2738. Peterson C.W., J. Parlett and R.S. Crandall, Am. J. Phys. 47, 772-775 (1979).
2739. Peuckert, M. Surf. Sci. 141, 500-514 (1984).
2740. Peuckert, M., J. Electroanal. Chem. 185, 379-391 (1985).
2741. Peuckert, M. and P.H. Bonzel, Surf. Sci. 145, 239-259 (1984).
2742. Pfluger P., H.U. Künzi and H.-J. Güntherodt, Appl. Phys. Lett. 35, 771-772 (1979).
2743. Pham Thi M., Chem. Phys. Lett. 115, 130-133 (1985).
2744. Pham Thi M. and P. Colomban, Solid State Ionics 17, 295-306 (1985).
2745. Pham Thi M., P. Colomban and A. Novak, J. Phys. Chem. Solids 46, 565-578 (1985).
2746. Pham Thi M. and G. Velasco, Solid State Ionics 14, 217-220 (1984).
2747. Pham Thi M. and G. Velasco, Rev. Chim. Minérale 22, 195-208 (1985).
2748. Phan L., L. Michailovits and I. Hevesi, Acta. Phys. Hung. 54, 119-124 (1983).
2749. Picard A. and G. Turban, Plasma Chem. Plasma Processes 5, 333-351 (1985).
2750. Pichat P., M.-N. Mozzanega and C. Hoang-Van, J. Phys. Chem. 92, 467-470 (1988).
2751. Pickelmann L. and P. Schlotter, in Proc. First European Display Research Conf., Eurodisplay '81 (München, Sept. 1981).
2752. Pickett D.F. and J.T. Maloy, J. Electrochem. Soc. 125, 1026-1032 (1978).
2753. Pickup P.G. and V.I. Birss, J. Electroanal. Chem. 220, 83-100 (1987).
2754. Pickup P.G. and V.I. Birss, J. Electroanal. Chem. 240, 171-183 (1988).
2755. Pickup P.G. and V.I. Birss, J. Electroanal. Chem. 240, 185-199 (1988).
2756. Pickup P.G. and V.I. Birss, J. Electrochem. Soc. 135, 41-45 (1988).
2757. Pickup P.G. and V.I. Birss, J. Electrochem. Soc. 135, 126-133 (1988).
2758. Pifer J.H. and E.K. Sichel, J. Electronic Mater. 9, 129-140 (1980).
2759. Pifer J.H., S. Ziemski, M. Greenblatt and B.M. Wanklyn, J. Solid State Chem. 45, 93-98 (1982).
2760. Pigeat P., N. Pacia and B. Weber, Thin Solid Films 201, 217-230 (1991).
2761. Pigeat P., N. Pacia and B. Weber, Surf. Sci. 251-252, 180-184 (1991).
2762. Pigeat P., N. Pacia and B. Weber, Surf. Sci. 269-270, 538-544 (1992).
2763. Pigeat P., N. Pacia and B. Weber, Surf. Interface Anal. 18, 571-575 (1992).
2764. Pigeat P., D. Paulmier, N. Pacia and B. Weber, Thin Solid Films 145, 185-196 (1986).
2765. Pigorsch E. and W.E. Steger, Phys. Stat. Sol. A 117, K189-K191 (1990).
2766. Pijolat M., M. Soustelle, A. Coucou, F. Portemer and M. Figlarz, J. Chim. Phys. Phys.-Chim. Biol. 87, 1223-1232 (1990).
2766a. Pilipovich V.A., B.A. Budkevich, V.L. Malevich, I.M. Romanov, and I.A. Ges, Dokl. Akad. Nauk BSSR 27, 20-22 (1983).
2767. Pilipovich V.A., B.A. Budkevich, I.M. Romanov, G.D. Ivlev, I.A. Ges and S.P. Zhvavyi, Phys. Stat. Sol. A 89, 709-717 (1985).
2768. Pilipovich V.A., K.A. Kaliev, G.V. Kuz'mich and I.M. Romanov, Pis'ma Zh. Tekh. Fiz. 18, 4-7 (1992) [Soviet Tech. Phys. Lett. 18, 585-586 (1992)].
2769. Pistoia G., M.L. Di Vona and P. Tagliatesta, Solid State Ionics 24, 103-109 (1987).
2770. Pistoia G., S. Panero, M. Tocci, R.V. Moshtev and V. Manev, Solid State Ionics 13, 311-318 (1984).

2771. Pistoia G., M. Pasquali, M. Tocci, R.V. Moshtev and V. Manev, J. Electrochem. Soc. 132, 281-284 (1985).
2772. Pistoia G., M. Pasquali, G. Wang and L. Li, J. Electrochem. Soc. 137, 2365-2370 (1990).
2773. Pistoia G., F. Rodante and M. Tocci, Solid State Ionics 20, 25-30 (1986).
2774. Pistoia G., G. Wang and C. Wang, Solid State Ionics 58, 285-292 (1992).
2775. Platt J.R., J. Chem. Phys. 34, 862-863 (1961).
2776. Plichon V., M. Bardin M., J.P. Delboulbe, C. Galland and B. Zaid, Proc. Soc. Photo-Opt. Instrum. Engr. 1728, 149-156 (1992).
2777. Plichon V. and S. Besbes, J. Electroanal. Chem. 284, 141-153 (1990).
2778. Plichon V. and S. Besbes, Electrochim. Acta 37, 501-506 (1992).
2779. Plichon V., J.C. Giron, J.P. Delboulbe and F. Lerbet, Proc. Soc. Photo-Opt. Instrum. Engr. 1563, 37-47 (1991).
2780. Plichta E., W.K. Behl, D. Vujic, W.H.S. Chang and D.M. Schleich, J. Electrochem. Soc. 139, 1509-1513 (1992).
2781. Plichta E., M. Salomon, S. Slane, M. Uchiyama, D. Chua, W.B. Ebner and H.W. Lin, J. Power Sources 21, 25 (1987).
2782. Plichta E., S. Slane, M. Uchiyama, M. Salomon, D. Chua, W.B. Ebner and H.W. Lin, J. Electrochem. Soc. 136, 1865-1869 (1989).
2783. Plumb I.C. and K.R. Ryan, Plasma Chem. Plasma Processes 6, 205-230 (1986).
2784. Poelman H., L. Fiermans, J. Vennik and G. Dalmai, Solid State Commun. 84, 811-814 (1992).
2785. Poelman H., J. Vennik and G. Dalmai, Phys. Stat. Sol. A 107, 731-737 (1988).
2786. Polak A.J., S. Petty-Weeks and A.J. Buehler, Sensors Actuators 9, 1-7 (1986).
2787. Polevoi P.G., N.N. Nastenko and E.I. Burmakin, Elektrokhim. 28, 1540-1545 (1992) [Soviet Electrochem. 28, 1261-1265 (1992)].
2788. Pollak M., J. Non-Cryst. Solids 11, 1-24 (1972).
2789. Pollak M., Philos. Mag. 65, 756-667 (1992).
2790. Popov A.V., Yu.G. Metelin and Yu.D. Tretyakov, J. Solid State Chem. 32, 343-350 (1980).
2791. Popov D.N. and P.I. Docheva, Vacuum 42, 53-55 (1991).
2792. Portemer F., M. Sundberg, L. Kihlborg and M. Figlarz, J. Solid State Chem. 103, 403-414 (1993).
2793. Porter J.D., A. Heller and D.E. Aspnes, Nature 313, 664-666 (1985).
2794. Porter V.R., W.B. White and R. Roy, J. Solid State Chem. 4, 250-254 (1972).
2795. Porto S.P.S., P.A. Fleury and T.C. Damen, Phys. Rev. 154, 522-526 (1967).
2796. Potdar H.S., N. Pavaskar, A. Mitra and A.P.B. Sinha, Solar Energy Mater. 4, 291-299 (1981).
2797. Pouget J.P., B. Hennion, C. Escribe-Filippini and M. Sato, Phys. Rev. B 43, 8421-8430 (1991).
2798. Poumellec B., P.J. Durham and G.Y. Guo, J. Phys. Condens. Matter 3, 8195-8204 (1991).
2799. Pourbaix M., Atlas of Electrochemical Equilibrium in Aqueous Solutions (Pergamon, Oxford, 1969).
2800. Powell R.J. and W.E. Spicer, Phys. Rev. B 2, 2182-2193 (1970).
2801. Pradel A. and M. Ribes, Mater. Sci. Engr. B 3, 45-56 (1989).
2802. Pramanik D., A.J. Sievers and R.H. Silsbee, Solar Energy Mater. 2, 81-91 (1979).
2803. Pramanik P. and S. Bhattacharya, J. Electrochem. Soc. 137, 3869-3870 (1990).
2804. Pratt G.W., Jr. and R. Coelho, Phys. Rev. 116, 281-286 (1959).
2805. Presecatan R.T., S.H. Pulcinelli and C.V. Santilli, J. Non-Cryst. Solids 147-148, 340-345 (1992).
2806. Preudhomme J. and P. Tarte, Spectrochim. Acta A 27, 1817-1835 (1971).
2807. Prinz H., U. Müller and M.-L. Ha-Eierdanz, Z. Anorg. Allg. Chem. 609, 95-98 (1992).
2808. Przyluski J. and W. Wieczorek, Solid State Ionics 36, 165-169 (1989).
2809. Przyluski J. and W. Wieczorek, Synth. Met. 45, 323-333 (1991).
2810. Ptitsyn M.V., Ya.R. Rakhmilevich, K.I. Tikhonov and A.L. Rotinyan, Elektrokhim. 16, 740-742 (1980) [Soviet Electrochem. 16, 640-642 (1980)].
2811. Ptitsyn M.V., K.I. Tikhonov and A.L. Rotinyan, Elektrokhim. 17, 1558-1562 (1981) [Soviet Electrochem. 17, 1297-1299 (1981)].
2812. Ptushinskii Yu.G. and B.A. Chuikov, Surf. Sci. 6, 42-56 (1967).
2813. Pulker H.K., M. Bühler and R. Hora, Proc. Soc. Photo-Opt. Instrum. Engr. 678, 110-114 (1986).
2814. Pulker H.K. and E. Jung, Thin Solid Films 9, 57-66 (1971).

2815. Pulker H.K., G. Paesold and E. Ritter, Appl. Opt. 15, 2986-2991 (1976).
2816. Pundur P.A., V.D. Daugul and A.R. Lusis, Zh. Tekh. Fiz. 55, 964-967 (1985) [Soviet Phys. Tech. Phys. 30, 580-581 (1985)].
2817. Purdes A.J., B.F.T. Bolker, J.D. Bucci and T.C. Tisone, J. Vac. Sci. Technol. 14, 98-101 (1977).
2818. Pye M.F. and P.G. Dickens, Mater. Res. Bull. 14, 1397-1402 (1979).

R

2819. Rabalais J.W., R.J. Colton and A.M. Guzman, Chem. Phys. Lett. 29, 131-133 (1974).
2820. Radecka M., K. Zakrzewska, H. Czternastek, T. Stapinski and S. Debrus, Appl. Surf. Sci. 65-66, 227-234 (1993).
2821. Radhakrishnan K. and B.V.R. Chowdari, Mater. Sci. Engr. B 14, 17-22 (1992).
2822. Raistrick I.D., Solid State Ionics 9-10, 425-430 (1983).
2823. Raistrick I.D., Ann. Rev. Mater. Sci. 16, 343-370 (1986).
2824. Raistrick I.D., Solid State Ionics 18-19, 40-49 (1986).
2825. Raistrick I.D., Electrochim. Acta 35, 1579-1586 (1990).
2826. Raistrick I.D., A.J. Mark and R.A. Huggins, Solid State Ionics 5, 351-354 (1981).
2827. Rajan K.P. and V.D. Neff, J. Phys. Chem. 86, 4361-4368 (1982).
2828. Rakhovskaya S.M., S.A. Egorova, N.E. Bolotina and R.E. Tugushev, Kolloid. Zh. 47, 195-198 (1985) [Colloid J. USSR 47, 168-170 (1985)].
2829. Rakhshani A.E., Solid-State Electronics 29, 7-17 (1986).
2830. Rakotoniaina J.C., R. Mokrani-Tamellin, J.R. Gavarri, G. Vacquier, A. Casalot and G. Calvarin, J. Solid State Chem. 103, 81-94 (1993).
2831. Ramans G.M., J.V. Gabrusenoks, A.R. Lusis and A.A. Patmalnieks, J. Non-Cryst. Solids 90, 637-640 (1987).
2832. Ramans G.M., J.V. Gabrusenoks and A.A. Veispals, Phys. Stat. Sol. A 74, K41-K44 (1982).
2833. Ramesham R., S. Thakoor, T. Daud and A.P. Thakoor, J. Electrochem. Soc. 137, 1935-1939 (1990).
2834. Ramirez R., B. Casal, L. Utrera and E. Ruiz-Hitzky, J. Phys. Chem. 94, 8960-8965 (1990).
2835. Ramsier R.D. and J.T. Yates, Jr., Surf. Sci. Rept. 12, 243-378 (1991).
2836. Rand D.A.J. and R. Woods, Electroanal. Chem. Interfacial Electrochem. 55, 375-381 (1974).
2837. Rand D.A.J., R. Woods and D. Mitchell, in Proc. Symp. Electrode Materials and Processes for Energy Conversion and Storage, edited by J.D.E. McIntyre, S. Srinivasan and F.G. Will (The Electrochem. Soc., Princeton, 1977), Proc. Vol. 77-6, pp. 217-233.
2838. Randall J.N. and J.C. Wolfe, Appl. Phys. Lett. 39, 742-743 (1981).
2839. Randhawa H.S., M.D. Matthews and R.F. Bunshah, Thin Solid Films 83, 267-271 (1981).
2840. Randin J.-P., J. Electronic Mater. 7, 47-63 (1978).
2841. Randin J.-P., in Proc. First European Display Research Conf.: Eurodisplay '81 (VDE-Verlag, Berlin, 1981), pp. 94-98.
2842. Randin J.-P., Electronics (Dec. 29 1981), 89-91.
2843. Randin J.-P., J. Electrochem. Soc. 129, 1215-1220 (1982).
2844. Randin J.-P., in Large-area Chromogenics: Materials and Devices for Transmittance Control, edited by C.M. Lampert and C.G. Granqvist (SPIE Opt. Engr. Press, Bellingham, 1990), Vol. IS4, pp. 539-547.
2845. Randin J.-P. and R. Viennet, J. Electrochem. Soc. 129, 2349-2354 (1982).
2846. Randin J.-P., A.K. Vijh and A.B. Chughtai, J. Electrochem. Soc. 120, 1174-1184 (1973).
2847. Randles J.E.B., Disc. Faraday Soc. 1, 11-19 (1947).
2848. Range K.-J. and R. Zintl, Mater. Res. Bull. 18, 411-419 (1983).
2849. Ratner M.A., in Polymer Electrolyte Reviews - 1, edited by J.R. MacCallum and C.A. Vincent (Elsevier Appl. Sci., London, 1987), pp. 173-236.
2850. Ratner M.A. and D.F. Shriver, Chem. Rev. 88, 109-124 (1988).
2851. Rauch F., D. Kuhn and W. Wagner, Nucl. Tracks Radiation Measurement 19, 939-942 (1991).
2852. Rauch F., W. Wagner and K. Bange, Nucl. Instrum. Meth. Phys. Res. B 42, 264-267 (1989).

2853. Rauh R.D., Electrochem. Soc. Extended Abstracts 88-2, 1054-1055 (1988).
2854. Rauh R.D. and S.F. Cogan, Solid State Ionics 28-30, 1707-1714 (1988).
2855. Rauh R.D. and S.F. Cogan, J. Electrochem. Soc. 140, 378-386 (1993).
2856. Rauh R.D., S.F. Cogan and M.A. Parker, Proc. Soc. Photo-Opt. Instrum. Engr. 502, 38-45 (1984).
2857. Rauh R.D., T.L. Rose and S.N. Benoit, Appl. Phys. Lett. 48, 362-364 (1986).
2858. Ravindra N.M., S. Auluck and V.K. Srivastava, Phys. Stat. Sol. 93, K155-K159 (1979).
2859. Ray S., R. Banerjee, N. Basu, A.K. Batabyal and A.K. Barua, J. Appl. Phys. 54, 3497-3501 (1983).
2860. Ray S., J. Dutta, A.K. Barua and S.K. Deb, Thin Solid Films 199, 201-207 (1991).
2861. Razavi A., L. Bobyak and P. Fallon, J. Vac. Sci. Technol. A 8, 1391-1394 (1990).
2862. Real S.G., J.R. Vilche and A.J. Arvia, Corrosion Sci. 20, 563-586 (1980).
2863. Reau J.-M., J. Calverie, G. Campet, C. Desportes, D. Ravaine, J.L. Souquet and A. Hammou, Comptes Rendues Acad. Sci. Paris, Sér. C, 280, 325-327 (1975).
2864. Reau J.-M., C. Fourassier, G. Le Flem, J.-Y. Barraud, J.-P. Doumerc and P. Hagenmuller, Rev. Chim. Minérale 7, 975-988 (1970).
2865. Reau J.-M. and J. Grannec, in Inorganic Solid Fluorides: Chemistry and Physics, edited by P. Hagenmuller (Academic, Orlando, 1985), pp. 423-467.
2866. Reau J.-M., C. Lucat, J. Portier, P. Hagenmuller, L. Cot and S. Vilminot, Mater. Res. Bull. 13, 877-882 (1978).
2867. Rechtin M.D. and B.L. Averbach, J. Phys. Chem. Solids 36, 893-897 (1975).
2868. Reddy A.K.N. and B. Rao, Can. J. Chem. 47, 2687-2692 (1969).
2869. Reddy A.K.N. and B. Rao, Can. J. Chem. 47, 2693-2698 (1969).
2870. Reddy A.K.N., M.G.B. Rao and J.O'M. Bockris, J. Chem. Phys. 42, 2246-2248 (1965).
2871. Reddy T.B. and E.A. Battistelli, in Proc. 19th Electronic Materials Conf. of AIME (Cornell University, Ithaca, New York, 1977), p. 35.
2872. Redfield D., Phys. Rev. 130, 914-915 (1963).
2873. Redfield D., Phys. Rev. 130, 916-918 (1963).
2874. Regragui M. and A. Donnadieu, J. Phys. III (Paris) 2, 383-394 (1992).
2875. Reichman B. and A.J. Bard, J. Electrochem. Soc. 126, 583-591 (1979).
2876. Reichman B. and A.J. Bard, J. Electrochem. Soc. 126, 2133-2139 (1979).
2877. Reichman B. and A.J. Bard, J. Electrochem. Soc. 127, 241-242 (1980).
2878. Reichman B. and A.J. Bard, J. Electrochem. Soc. 128, 344-346 (1981).
2879. Reichman B., A.J. Bard and D. Laser, J. Electrochem. Soc. 127, 647-654 (1980).
2880. Reik H.G., Z. Phys. 203, 346-361 (1967).
2881. Reilly S., D. Arasteh and S. Selkowitz, Solar Energy Mater. 22, 1-14 (1991).
2882. Reimers J.N. and J.R. Dahn, J. Electrochem. Soc. 139, 2091-2097 (1992).
2883. Reimers J.N., W. Li and J.R. Dahn, Phys. Rev. B 47, 8486-8493 (1993).
2884. Reimers J.N., W. Li, E. Rossen and J.R. Dahn, Mater. Res. Soc. Symp. Proc. 293, 3-13 (1993).
2885. Reis K.P., E. Prince and M.S. Whittingham, Chem. Mater. 4, 307-312 (1992).
2886. Reis K.P., A. Ramanan and S.M. Whittingham, J. Solid State Chem. 96, 31-47 (1992).
2887. Reiss G., E. Hastreiter, H. Brückl and J. Vancea, Phys. Rev. B 43, 5176-5179 (1991).
2888. Reiss G., J. Vancea and H. Hoffmann, Phys. Rev. Lett. 56, 2100-2103 (1986).
2889. Reith T.M. and P.J. Ficalora, J. Vac. Sci. Technol. A1, 1362-1369 (1983).
2890. Repelin Y., E. Husson, L. Abello and G. Lucazeau, Spectrochim. Acta A 41, 993-1003 (1985).
2891. Repoux M., Surf. Interface Anal. 18, 567-570 (1992).
2892. Reshina I.I., Fiz. Tverd. Tela 14, 345-349 (1972) [Soviet Phys. Solid State 14, 287-290 (1972)].
2893. Reyes J.M., M. Sayer and R. Chen, Can. J. Phys. 54, 408-412 (1976).
2894. Reynolds T.G. and A. Wold, J. Solid State Chem. 6, 565-568 (1973).
2895. Rezrazi M., O. Bohnke and J. Pagetti, Displays 8, 119-126 (1987).
2896. Rezrazi M., B. Vuillemin and O. Bohnke, J. Electrochem. Soc. 138, 2770-2774 (1991).
2897. Ribbing C.-G. and E. Valkonen, Proc. Soc. Photo-Opt. Instrum. Engr. 652, 166-178 (1986).
2898. Rice C.E., Appl. Phys. Lett. 35, 563-565 (1979).
2899. Rice C.E. and P.M. Bridenbaugh, Appl. Phys. Lett. 38, 59-61 (1981).

2900. Rietman E.A., J. Mater. Sci. Lett. 5, 231-239 (1986).
2901. Rietveld H.M., Acta Crystallogr. 22, 151-152 (1967).
2902. Rietveld H.M., J. Appl. Crystallogr. 2, 65-71 (1969).
2903. Rifflet J.C. and A.M. Anthony, Rev. Int. Hautes Tempéartures Réfractaires 20, 37-44 (1983).
2904. Rifflet J.C., A.M. Anthony and J.P. Coutures, Mater. Res. Bull. 13, 55-60 (1978).
2905. Riga J., C. Trenet-Noël, J.S. Pireaux, R. Caudano, J.J. Verbist and Y. Gobillon, Phys. Scripta 16, 351-354 (1977).
2906. Riou A., A. Leclerf, Y. Gerault and Y. Cudennec, Mater. Res. Bull. 27, 269-275 (1992).
2907. Ripert M., C. Poinsignon, Y. Chabre and J. Pannetier, Phase Transitions 32, 205-209 (1991).
2908. Rishpon J. and S. Gottesfeld, J. Electrochem. Soc. 131, 1960-1968 (1984).
2909. Ritala M., M. Leskelä, L.-S. Johansson and L. Niinistö, Thin Solid Films 228, 32-35 (1993).
2910. Ritala M., M. Leskelä, E. Nykänen, P. Soininen and L. Niinistö, Thin Solid Films 225, 288-295 (1993).
2911. Ritschel M., N. Mattern, W. Brückner, H. Opperman, G. Stöver, W. Modenhauer, J. Henke and E. Wold, Kristall Technik 12, 1221-1232 (1977).
2912. Ritsko J.J., H. Witzke and S.K. Deb, Solid State Commun. 22, 455-458 (1977).
2913. Ritter C., W. Müller-Warmuth and R. Schöllhorn, J. Chem. Phys. 83, 6130-6138 (1985).
2914. Rivoalen L., A. Revcolevschi, J. Livage and R. Collongues, J. Non-Cryst. Solids 21, 171-179 (1976).
2915. Robblee L.S., J.L. Lefko and S.B. Brummer, J. Electrochem. Soc. 130, 731-733 (1983).
2916. Robblee L.S., M.J. Mangaudis, E.D. Lasinsky, A.G. Kimball and S.B. Brummer, Mater. Res. Soc. Symp. Proc. 55, 303-310 (1986).
2917. Roberts M.W., Pure Appl. Chem. 53, 2269-2281 (1981).
2918. Roberts M.W. and R. St. C. Smart, Surf. Sci. 100, 590-604 (1980).
2919. Roberts M.W. and R. St. C. Smart, Surf. Sci. 108, 271 (1981).
2920. Robertson J.D., J.B. Bates, N.J. Dudney and R.A. Zuhr, Nucl. Instrum. Meth. Phys. Res. B 56-57, 722-725 (1991).
2921. Robin M.B. and P. Day, Adv. Inorg. Chem. Radiochem. 10, 247-422 (1967).
2922. Robitaille C.D. and D. Fauteux, J. Electrochem. Soc. 133, 315-325 (1986).
2923. Rocchiccioli-Deltcheff C., Comptes Rendues Acad. Sci. Paris, Ser. B, 268, 45-47 (1969).
2924. Rocchiccioli-Deltcheff C., R. Thouvenot and R. Frank, Spectrochim. Acta A 32, 587-597 (1976).
2925. Rodante F. and M. Tocci, Thermochim. Acta 94, 249-256 (1985).
2926. Rogers D.B., R.D. Shannon, A.W. Sleight and J.L. Gillson, Inorg. Chem. 8, 841-849 (1969).
2927. Rogers K.D., J.A. Coath and M.C. Lovell, J. Appl. Phys. 70, 1412-1415 (1991).
2928. Roginskaya Yu.E., T.V. Varlamova, M.D. Goldstein, I.D. Belova, B.Sh. Galyamov, R.R. Shifrina, V.A. Shepelin and V.N. Fateev, Mater. Chem. Phys. 30, 101-113 (1991).
2929. Roland J.-F. and F.C. Anson, J. Electroanal. Chem. 336, 245-261 (1992).
2930. Roman H.E., J. Phys. Condens. Matter 2, 3909-3917 (1990).
2931. Roman H.E., A. Bunde and W. Dieterich, Phys. Rev. B 34, 3439-3445 (1986).
2932. Romanov I.M., G.D. Ivlev, B.A. Budkevich, V.A. Pilipovich, I.A. Ges and S.P. Zhvavyi, Izv. Akad. Nauk SSSR Ser. Fiz. 49, 1157-1161 (1985) [Bull. Acad. Sci. USSR Phys. Ser. 49, 110-114 (1985)].
2933. Romanov I.M., G.D. Ivlev, B.A. Budkevich, V.A. Pilipovich, I.A. Ges and S.P. Zhvavyi, Zh. Tekh. Fiz. 54, 2366-2368 (1984) [Soviet Phys. Tech. Phys. 29, 1395-1396 (1984)].
2934. Roos A., T. Chibuye and B. Karlsson, Solar Energy Mater. 7, 453-465 (1983).
2935. Roos A. and B. Karlsson, Solar Energy Mater. 7, 467-480 (1983).
2936. Rosolen J.M., F. Decker, M. Fracastoro-Decker, A. Gorenstein, R.M. Torresi and S.I. Cordoba-Torresi, J. Electroanal. Chem. 354, 273-279 (1993).
2937. Rosolen J.M., M. Fracastoro-Decker and F. Decker, J. Electroanal. Chem. 346, 119-133 (1993).
2938. Ross R.C., J. Vac. Sci. Technol. A 8, 3175-3178 (1990).
2939. Rossen E., D.C.W. Jones and J.R. Dahn, Solid State Ionics 57, 311-318 (1992).
2940. Rossen E., J.N. Reimers and J.R. Dahn, Solid State Ionics 62, 53-60 (1993).
2941. Rossi C.E. and W. Paul, J. Phys. Chem. Solids 30, 2295-2305 (1969).
2942. Rossouw M.H., A. de Kock, D.C. Liles, R.J. Gummow and M.M. Thackeray, J. Mater. Chem. 2, 1211 (1992).

2943. Rossouw M.H., D.C. Liles, M.M. Thackeray, W.I.F. David and S. Hull, Mater. Res. Bull. 27, 221-230 (1992).
2944. Rossouw M.H. and M.M. Thackeray, Mater. Res. Bull. 26, 463-473 (1991).
2945. Roth R.S., Progr. Solid State Chem. 13, 159-192 (1980).
2946. Roth W.L. and G.C. Farrington, Science 196, 1332-1334 (1977).
2947. Rothschild M. and A.R. Forte, Appl. Phys. Lett. 59, 1790-1792 (1991).
2948. Rousselot C., P.A. Gillet and O. Bohnke, Thin Solid Films 204, 123-131 (1991).
2949. Rubin M., J. Vac. Sci. Technol. A 10, 1905-1907 (1992).
2950. Rubio F., J.M. Abella, J. Denis and J.M. Martinez-Duart, J. Vac. Sci. Technol. 21, 1043-1045 (1982).
2951. Rubio F, J. Denis, J.M. Albella and J.M. Martinez-Duart, Thin Solid Films 90, 405-408 (1982).
2952. Ruf C., K. Bärner and R. Braunstein, Solid State Commun. 54, 111-114 (1985).
2953. Ruiz-Hitzky E. and B. Casal, J. Chem. Soc. Faraday Trans. I 82, 1597-1604 (1986).
2954. Ryabova L.A., V.S. Salun and I.A. Serbinov, Thin Solid Films 92, 327-332 (1982).
2955. Ryan K.R. and I.C. Plumb, Plasma Chem. Plasma Processes 4, 271-283 (1984).
2956. Ryden W.D., A.W. Lawson and C.C. Sartain, Phys. Lett. A 26, 209-210 (1968).
2957. Ryden W.D., A.W. Lawson and C.C. Sartain, Phys. Rev. B 1, 1494-1500 (1970).
2958. Rüscher C.H., Physica (Utrecht) C 200, 129-139 (1992).
2959. Rüscher C.H. and M. Nygren, J. Phys. C: Cond. Matter 3, 3997-4003 (1991).
2960. Rüscher C., E. Salje and A. Hussain, J. Phys. C: Solid State Phys. 21, 3737-3749 (1988).

S

2961. Sabbatini L., P.M.A. Sherwood and P.G. Zambonin, J. Electrochem. Soc. 130, 2199-2205 (1983).
2962. Sacré S. and L.K. Thomas, Thin Solid Films 203, 221-226 (1991).
2963. Safonova T.Ya., O.A. Petrii and T.N. Khvostova, Elektrokhim. 26, 471-475 (1990) [Soviet Electrochem. 26, 421-425 (1990)].
2964. Sagnes I., A. Halimaouli, G. Vincent and P.A. Badoz, Appl. Phys. Lett. 62, 1155-1157 (1993).
2965. Sahle W., J. Solid State Chem. 45, 324-342 (1982).
2966. Sahle W. and M. Nygren, J. Solid State Chem. 48, 154-160 (1983).
2967. Sahle W. and M. Sundberg, Chem. Scripta 16, 163-168 (1980).
2968. Sahu S.N., J. Scarminio and F. Decker, J. Electrochem. Soc. 137, 1150-1154 (1990).
2969. Sainz M.A., A. Durán and J.M.F. Navarro, J. Non-Cryst. Solids 121, 315-318 (1990).
2970. Saito M., T. Kishi and T. Nagai, Denki Kagaku 47, 298-302 (1979).
2971. Saito T., Y. Ushio, M. Yamada and T. Niwa, Solid State Ionics 40-41, 499-501 (1990).
2972. Saito Y., C. Kaito and T. Naiki, J. Crystal Growth 79, 436-442 (1986).
2973. Saito Y. and T. Shiosaki, Japan. J. Appl. Phys. 31, 3164-3169 (1992).
2974. Sakurai Y., S. Okada, J. Yamaki and T. Okada, J. Power Sources 20, 173-177 (1987).
2975. Sakurai Y. and Y. Yamaki, J. Electrochem. Soc. 132, 512-513 (1985).
2976. Salje E., J. Appl. Cryst. 7, 615-617 (1974).
2977. Salje E., Acta Cryst. A 31, 360-363 (1975).
2978. Salje E., Opt. Commun. 24, 231-232 (1978).
2979. Salje E., A.F. Carley and M.W. Roberts, J. Solid State Chem. 29, 237-251 (1979).
2980. Salje E., R. Gehlig and K. Viwanathan, J. Solid State Chem. 25, 239-250 (1978).
2981. Salje E. and B. Güttler, Philos. Mag. 50, 607-620 (1984).
2982. Salje E. and G. Hoppmann, Philos. Mag. B 43, 105-114 (1981).
2983. Salje E. and K. Viswanathan, Acta Cryst. A 31, 356-359 (1975).
2984. Salomon R.E., G.B. Adams and W.M. Graven, J. Electrochem. Soc. 110, 1163-1165 (1963).
2985. Salomonsen G., N. Norman, O. Lønsjø and T.G. Finstad, J. Less-Common Met. 158, 251-265 (1990).
2986. Salvati L., Jr., L.E. Makovsky, J.M. Stencel, F.R. Brown and D.M. Hercules, J. Phys. Chem. 85, 3700-3707 (1981).

2987. Samant M.S., A.S. Kerkar, S.R. Bharadwaj and S.R. Dharwadkar, J. Alloys Compounds 187, 373-379 (1992).
2988. Sambles J.R., K.C. Elsom and D.J. Jarvis, Philos. Trans. Roy. Soc. London A 304, 365-396 (1982).
2989. Sanchez C., F. Barbonneau, R. Morineau, J. Livage and J. Bullot, Philos. Mag. B 47, 279-290 (1983).
2990. Sanchez C., M. Henry, J.C. Grenet and J. Livage, J. Phys. C: Solid State 15, 7133-7141 (1982).
2991. Sanchez C., J. Livage, J.P. Audiere and A. Madi, J. Non-Cryst. Solids 65, 285-300 (1984).
2992. Sanchez C., J. Livage, M. Henry and F. Babonneau, J. Non-Cryst. Solids 100, 65-76 (1988).
2993. Sanchez C., J. Livage and G. Lucazeau, J. Raman Spectrosc. 12, 68-72 (1982).
2994. Sanchez C., R. Morineau and J. Livage, Phys. Stat. Sol. A 76, 661-666 (1983).
2995. Sanchez C., M. Nabavi, P. Judeinstein and S. Doeuff, J. Chim. Phys. 86, 1593-1606 (1989).
2996. Sanchez C., M. Nabavi and F. Taurelle, Mater. Res. Soc. Symp. Proc. 121, 93-104 (1988).
2997. Sánchez F., M. Varela, C. Ferrater, M.V. Garcia-Cuenca, R. Aguiar and J.L. Morenza, Appl. Surf. Sci. 70-71, 94-98 (1993).
2998. Sander U., H.-H. Strehblow and J.K. Dohrmann, J. Phys. Chem. 85, 447-450 (1981).
2999. Sanjinés R., A. Aruchamy and F. Lévy, Solid State Commun. 64, 645-650 (1987).
3000. Sanjinés R., A. Aruchamy and F. Lévy, J. Electrochem. Soc. 136, 1740-1743 (1989).
3001. Sanjinés R., M. Heintze, A. Grisel and F. Lévy, Helv. Phys. Acta 59, 160-163 (1986).
3002. Sapoval B., J.-N. Chazalviel and J. Peyrière, Phys. Rev. A 38, 5867-5887 (1988).
3003. Sarasola C., T. Fernández and Y. Jiménez, Electrochim. Acta 33, 1295-1301 (1988).
3004. Sarma D.D. and C.N.R. Rao, J. Electron Spectrosc. Related Phenomena 20, 25-45 (1980).
3005. Sasaki T., Y. Komatsu and Y. Fujiki, Chem. Commun. (1991), 817-818.
3006. Sasaki T.A., Y. Baba, H. Yamamoto, M. Sasase and S. Isobe, Surf. Interface Anal. 20, 682-686 (1993).
3007. Sato H., T. Minami, S. Takata, T. Mouri and N. Ogawa, Thin Solid Films 220, 327-332 (1992).
3008. Sato N. and K. Kudo, Electrochim. Acta 19, 461-470 (1974).
3009. Sato N., K. Kudo and T. Noda, Corrosion Sci. 10, 785-794 (1970).
3010. Sato N., K. Kudo and T. Noda, Electrochim. Acta 16, 1909-1921 (1971).
3011. Sato N., T. Noda and K. Kudo, Electrochim. Acta 19, 471-475 (1974).
3012. Sato N. and T. Ohtsuka, J. Electrochem. Soc. 125, 1735-1740 (1978).
3013. Sato S., Oyu Buturi 47, 656-657 (1978).
3014. Sato S. and Y. Seino, Shinkuu (J. Vacuum Soc. Japan) 24, 568-570 (1981).
3015. Sato S. and Y. Seino, Trans. Inst. Electronic Commun. Engr. Japan 65-C, 629-636 (1982).
3016. Sato Y., Japan. J. Appl. Phys. 25, 189-193 (1986).
3017. Sato Y., J. Appl. Phys. 66, 1810-1815 (1989).
3018. Sato Y., Japan. J. Appl. Phys. 28, 1290-1291 (1989).
3019. Sato Y., Vacuum 41, 1198-1200 (1990).
3020. Sato Y., R. Fujiwara, I. Shimizu and E. Inoue, Japan. J. Appl. Phys. 21, 1642-1646 (1982).
3021. Sato Y., N. Matsueda, H. Tokugawa and K.Kobayakawa, Chem. Lett. (1993), 901-904.
3022. Sato Y., T. Nomura, H. Tanaka and K. Kobayakawa, J. Electrochem. Soc. 138, L37-L39 (1991).
3023. Sato Y., K. Ono, T. Kobayashi, H. Wakabayashi and H. Yamanaka, J. Electrochem. Soc. 134, 570-575 (1987).
3024. Sato Y. and I. Shimizu, Japan Display 1983, pp. 376-378.
3025. Sato Y., M. Yanagida, H. Yamanaka and H. Tanigawa, J. Electrochem. Soc. 136, 863-866 (1989).
3026. Savariault J.-M., D. Lafargue, J.-L. Parize and J. Galy, J. Solid State Chem. 97, 169-178 (1992).
3027. Sävborg Ö. and M. Nygren, Phys. Stat. sol. A 43, 645-652 (1977).
3028. Savvides N., Thin Solid Films 163, 13-32 (1988).
3029. Sawada S. and G.C. Danielson, Phys. Rev. 113, 1008-1013 (1959).
3030. Sawatzky G.A., in Core-level Spectroscopy in Condensed Systems, edited by J. Kanamori and A. Kotani, Springer Series in Solid State Sciences (Springer, Berlin, Heidelberg, 1988), Vol. 81, pp. 99-124.
3031. Sawatzky G.A. and J.W. Allen, Phys. Rev. Lett. 53, 2339-2342 (1984).
3032. Sawatzky G.A. and A. Antonides, J. Phys. (Paris), Colloq. 37, C4 117-C4 123 (1976).
3033. Scarminio J., W. Estrada, A. Andersson, A. Gorenstein and F. Decker, J. Electrochem. Soc. 139, 1236-1239 (1992).

3034. Scarminio J., A. Gorenstein, F. Decker, S. Paserini, R. Pileggi and B. Scrosati, Proc. Soc. Photo-Opt. Instrum. Engr. 1536, 70-80 (1991).
3035. Scarminio J., S.N. Sahu and F. Decker, J. Phys. E 22, 755-757 (1989).
3036. Scarminio J., A. Talledo, A.M. Andersson, S. Passerini and F. Decker, Electrochim. Acta 38, 1637-1642 (1993).
3037. Scarminio J., A. Urbano, B.J. Gardes and A. Gorenstein, J. Mater. Sci. Lett. 11, 562-563 (1992).
3038. Scherer A., O.T. Inal and A.J. Singh, Solar Energy Mater. 9, 139-158 (1983).
3039. Schiavello M., F. Pepe, M. Cannizzaro, S. De Rossi and R.J.D. Tilley, Z. Phys. Chem. N.F. 106, 45-56 (1977).
3040. Schiavello M., R.J.D. Tilley, S. De Rossi and E. Iguchi, Z. Phys. Chem. N.F. 104, 165-176 (1977).
3041. Schiavone L.M., W.C. Dautremont-Smith, G. Beni and J.L. Shay, Appl. Phys. Lett. 35, 823-825 (1979).
3042. Schiavone L.M., W.C. Dautremont-Smith, G. Beni and J.L. Shay, J. Electrochem. Soc. 128, 1339-1342 (1981).
3043. Schiller S., G. Beister, S. Schneider and W. Sieber, Thin Solid Films 72, 475-483 (1980).
3044. Schiller S., G. Beister, W. Sieber, G. Schirmer and E. Hacker, Thin Solid Films 83, 239-245 (1981).
3045. Schirmer O.F., Z. Phys. B 24, 235-244 (1976).
3046. Schirmer O.F., J. Phys. (Paris), Colloque 6, 479-484 (1980).
3047. Schirmer O.F., K.W. Blazey, W. Berlinger and R. Diehl, Phys. Rev. B 11, 4201-4211 (1975).
3048. Schirmer O.F. and E. Salje, J. Phys. C 13, L1067-L1072 (1980).
3049. Schirmer O.F. and E. Salje, Solid State Commun. 33, 333-336 (1980).
3050. Schirmer O.F., V. Wittwer, G. Baur and G. Brandt, J. Electrochem. Soc. 124, 749-753 (1977).
3051. Schissel P.O. and O.C. Trulson, J. Chem. Phys. 43, 737-743 (1965).
3052. Schlaikjer C.R. and C.C. Liang, in Fast Ion Transport in Solids, edited by W. van Gool (North-Holland, Amsterdam, 1973), pp. 685-694.
3053. Schlaschke B. and R. Schöllhorn, Rev. Chim. Minérale 19, 534-544 (1982).
3054. Schlemminger W. and D. Stark, Thin Solid Films 137, 49-57 (1986).
3055. Schlenker C., in Physics of Disordered Materials: Mott Festschrift, edited by D. Adler, H. Fritzsche and S.R. Ovshinsky (Plenum, New York, 1985), Vol. 3, pp. 369-389.
3056. Schlotter P., Proc. Soc. Photo-Opt. Instrum. Engr. 653, 32-35 (1986).
3057. Schlotter P., Solar Energy Mater. 16, 39-46 (1987).
3058. Schlotter P. and L. Pickelmann, J. Electronic Mater. 11, 207-236 (1982).
3059. Schlotter P. and L. Pickelmann, J. Electrochem. Soc. 130, C114 (1983).
3060. Schmid S., R.L. Withers and J.G. Thompson, J. Solid State Chem. 99, 226-242 (1992).
3061. Schöllhorn R., Angew. Chem. Int. Ed. 19, 983-1003 (1980).
3062. Schönberg N., Acta Chem. Scand. 8, 240-245 (1954).
3063. Schoolmann D., O. Trinquet and J.-C. Lassègues, Electrochim. Acta 37, 1619-1621 (1992).
3064. Schreiber M. and Y. Toyosawa, J. Phys. Soc. Japan 51, 1544-1550 (1982).
3065. Schreibler Guzmán R.S., J.R. Vilche and A.J. Arvia, Corrosion Sci. 18, 765-778 (1978).
3066. Schreibler Guzmán R.S., J.R. Vilche and A.J. Arvia, J. Appl. Electrochem. 8, 67-70 (1978).
3067. Schreibler Guzmán R.S., J.R. Vilche and A.J. Arvia, J. Electrochem. Soc. 125, 1578-1587 (1978).
3068. Schreibler Guzmán R.S., J.R. Vilche and A.J. Arvia, J. Appl. Electrochem. 9, 183-189 (1979).
3069. Schreibler Guzmán R.S., J.R. Vilche and A.J. Arvia, J. Appl. Electrochem. 9, 321-327 (1979).
3070. Schröder F.A. and H. Felser, Z. Kristallogr. 135, 391-398 (1972).
3071. Schultze J.W., S. Mohr and M.M. Lohrengel, J. Electroanal. Chem. 154, 57-68 (1983).
3072. Schumm B., Jr., R.L. Middaugh, M.P. Grotheer and J.C. Hunter, editors, Manganese Dioxide Electrode Theory and Practice for Electrochemical Applications (The Electrochemical Society, Pennington, USA, 1984).
3073. Schuster A.P., D. Nguyen and O. Caporaletti, Solar Energy Mater. 13, 153-160 (1986).
3074. Schwab R.G., R.A. Steiner, G. Mages and H.-J. Beie, Thin Solid Films 207, 283-287 (1992).
3075. Schwab R.G., R.A. Steiner, G. Mages and H.-J. Beie, Thin Solid Films 207, 288-293 (1992).
3076. Scott J.F., R.F. Reheny, J.P. Remeika and A.R. Sweedler, Phys. Rev. B 2, 3883-3887 (1970).

3077. Scriven L.E., in Better Ceramics Through Chemistry III, edited by C.J. Brinker, D.E. Clark and D.R. Ulrich (Mater. Res. Soc., Pittsburgh, 1988), pp. 717-729.
3078. Scrosati B., Brit. Polymer J. 20, 219-226 (1988).
3079. Scrosati B., in Solid State Ionic Devices, edited by B.V.R. Chowdari and S. Radhakrishna (World Scientific, Singapore, 1988), pp. 341-349.
3080. Scrosati B., Philos. Mag. B 59, 151-160 (1989).
3081. Scrosati B., Chimicaoggi, (June 1989), pp. 41-45.
3081a. Scrosati B., in Solid State Ionics: Materials and Applications, edited by B.V.R. Chowdari (World Scientific, Singapore, 1992)), pp. 321-336.
3082. Scrosati B., A. Selvaggi, F. Croce and W. Gang, J. Power Sources 24, 287-294 (1988).
3083. Sears W.M. and E. Fortin, Solar Energy Mater. 10, 93-103 (1984).
3084. Sears W.M. and M.A. Gee, Thin Solid Films 165, 265-277 (1988).
3085. Searson P.C. and R.M. Latanision, Electrochim. Acta 35, 445-450 (1990).
3086. Searson P.C., R.M. Latanision and U. Stimming, J. Electrochem. Soc. 135, 1358-1363 (1988).
3087. Seike T. and J. Nagai, Hyomen Kagaku (J. Surf. Sci. Soc. Japan) 10, 314-319 (1989).
3088. Seike T. and J. Nagai, Solar Energy Mater. 22, 107-117 (1991).
3089. Sekai K., H. Azuma, A. Omaru, S. Fujita, H. Imoto, T. Endo, K. Yamaura, Y. Nishi, S. Mashiko and M. Yokogawa, J. Power Sources 43-44, 241-244 (1993).
3090. Seki M. and K. Sato, Macromol. Chem. 193, 2971-2978 (1992).
3091. Sekushin N.A. and A.A. Tsyganenko, Zh. Fiz. Khim. 61, 159-164 (1987) [Russian J. Phys. Chem. 61, 82-85 (1987)].
3092. Selkowitz S., Glass Mag. (Aug. 1986), 86-91.
3093. Sella C., L. Tertian and J. Deschamps, Rev. Phys. Appl. 5, 415-422 (1970).
3094. Semiletov S.A. and S.M. Shkornyakov, Mikroelektronika (USSR) 11, 470-473 (1982).
3095. Senoh T., S. Ueno, T. Miura and T. Kishi, Denki Kagaku 61, 561-564 (1993).
3096. Seo M., R. Saito and N. Sato, J. Electrochem. Soc. 127, 1909-1912 (1980).
3097. Serbinov I.A., S.M. Babulanam, G.A. Niklasson and C.G. Granqvist, J. Mater. Sci. 23, 2076-2078 (1988).
3098. Serbinov I.A., L.A. Ryabova and Ya.S. Savitskaya, Thin Solid Films 27, 171-176 (1975).
3099. Sermon P.A. and G.C. Bond, J. Chem. Soc. Faraday Trans. I 72, 730-744 (1976).
3099a. Sernelius B.E., Phys. Rev. B 36, 4878-4887 (1987).
3100. Sernelius B.E., Thin Solid Films 208, 96-99 (1992).
3101. Sernelius B.E., K.-F. Berggren, Z.-C. Jin, I. Hamberg and C.G. Granqvist, Phys. Rev. B 37, 10244-10248 (1988).
3102. Serruys Y., T. Sakout and D. Gorse, Surf. Sci. 282, 279-287 (1993).
3103. Serwicka E.M., J. Solid State Chem. 51, 300-306 (1984).
3104. Serwicka E.M., Z. Phys. Chem. N.F. 167, 87-92 (1990).
3105. Seshan K., P.D. Hillman, K.A. Gesheva, E.E. Chain and B.O. Seraphin, Mater. Res. Bull. 16, 1345-1359 (1981).
3106. Severdenko V.P., V.A. Labunov, E.M. Kosarevish, L.V. Kogietov and V.M. Parkun, Thin Solid Films 41, 243-246 (1977).
3107. Seward G., R.B. Goldner, K. Wong, T. Haas, G.H. Foley, R. Chapman and S. Schulz, Proc. Soc. Photo-Opt. Instrum. Engr. 823, 90-93 (1987).
3108. Shahi K.and S. Chandra, Phys. Stat. Sol. A 28, 653-661 (1975).
3109. Shahi K. and J.B. Wagner, Jr., J. Electrochem. Soc. 128, 6-13 (1981).
3110. Shalaginov V.V., I.D. Belova, Yu.E. Roginskaya and D.M. Shub, Elektrokhim. 14, 1708-1712 (1978) [Soviet Electrochem. 14, 1485-1488 (1978)].
3111. Shalaginov V.V., D.M. Shub, N.V. Kozlova and V.N. Lomova, Elektrokhim. 19, 537-541 (1983) [Soviet Electrochem. 19, 479-483 (1983)].
3112. Shamina I.S., O.G. Malandin, S.M. Rakhovskaya and L.A. Vereshchagina, Electrokhim. 10, 1571-1574 (1974) [Soviet Electrochem. 10, 1494-1496 (1974)].
3113. Shanks H.R., P.H. Sidles and G.C. Danielson, Adv. Chem. Ser. 39, 237-245 (1963).
3114. Shaojun D. and L. Fengbin, J. Electroanal. Chem. 210, 31-44 (1986).

3115. Shaojun D. and L. Fengbin, J. Electroanal. Chem. 217, 49-63 (1987).
3116. Sharon M., M.K. Sharan and S.R. Jawalekar, Solar Energy Mater. 10, 329-334 (1984).
3117. Shaver P.J., Appl. Phys. Lett. 11, 255-257 (1967).
3118. Shay J.L. and G. Beni, Proc. SID 20, 213-218 (1979).
3119. Shay J.L. and G. Beni, IEEE Trans. Electronic Devices ED-26, 1138-1143 (1979).
3120. Shay J.L., G. Beni and L.M. Schiavone, Appl. Phys. Lett. 33, 942-944 (1978).
3121. Shay J.L., L.M. Schiavone, R.W. Epworth and D.W. Taylor, J. Appl. Phys. 53, 6004-6006 (1982).
3122. Shen P.K., H.T. Huang and A.C.C. Tseung, J. Mater. Chem. 2, 497-499 (1992).
3123. Shen P.K., H.T. Huang and A.C.C. Tseung, J. Electrochem. Soc. 139, 1840-1845 (1992).
3124. Shen P.K., J. Syed-Bokhari and A.C.C. Tseung, J. Electrochem. Soc. 138, 2778-2783 (1991).
3125. Shen P.K. and A.C.C. Tseung, J. Mater. Chem. 2, 1141-1147 (1992).
3126. Shen X.-M. and A. Clearfield, J. Solid State Chem. 64, 270-282 (1986).
3127. Sheng P., Phys. Rev. Lett. 45, 60-63 (1980).
3128. Sheng P., Philos. Mag. B 65, 357-384 (1992).
3129. Shi Y., Y. Yang and Z. Yin, Proc. Soc. Photo-Opt. Instrum. Engr. 1728, 40-41 (1992).
3130. Shibata A., Japan. J. Appl. Phys. 30, L650-L652 (1991).
3131. Shibata T. and Y.-C. Zhu, Denki Kagaku 61, 853-856 (1993).
3132. Shigesato Y., Japan. J. Appl. Phys. 30, 1457-1462 (1991).
3133. Shigesato Y., Y. Hayashi and T. Haranoh, Appl. Phys. Lett. 61, 73-75 (1992).
3134. Shigesato Y., Y. Hayashi, A. Masui and T. Haranou, Japan. J. Appl. Phys. 30, 814-819 (1991).
3135. Shigesato Y., A. Murayama, T. Kamimori and K. Matsuhiro, Rept. Res. Lab. Asahi Glass Co., Ltd., 38(1), 39-55 (1988).
3136. Shigesato Y., A. Murayama, T. Kamimori and K. Matsuhiro, Appl. Surf. Sci. 33-34, 804-811 (1988).
3137. Shigesato Y. and D.C. Paine, Thin Solid Films, to be published (1993).
3138. Shigesato Y., S. Takaki and T. Haranoh, Appl. Surf. Sci. 48-49, 269-275 (1991).
3139. Shigesato Y., S. Takaki and T. Haranoh, Proc. MRS Fall Meeting, (Boston 1991).
3140. Shigesato Y., S. Takaki and T. Haranoh, J. Appl. Phys. 71, 3356-3364 (1992).
3141. Shilton M.G. and A.T. Howe, Mater. Res. Bull. 12, 701-706 (1977).
3142. Shilton M.G. and A.T. Howe, in Fast Ion Transport in Solids, edited by P. Vashishta, J.N. Mundy and G.K. Shenoy (North-Holland, Amsterdam, 1979), pp. 727-730.
3143. Shilton M.G. and A.T. Howe, J. Solid State Chem. 34, 137-147 (1980).
3144. Shimizu I., M. Shizukuishi and E. Inoue, J. Appl. Phys. 50, 4027-4032 (1979).
3145. Shimizu Y., K. Nagase, N. Miura and N. Yamazoe, Japan. J. Appl. Phys. 29, L1708-L1711 (1990).
3146. Shimizu Y., K. Nagase, N. Miura and N. Yamazoe, Solid State Ionics 53-56, 490-495 (1992).
3147. Shimomura T., T. Furuta and T. Maki, Japan. J. Appl. Phys. 26, L299-L301 (1987).
3148. Shinar R. and J.H. Kennedy, Solar Energy Mater. 6, 323-335 (1982).
3149. Shiojiri M., T. Miyano and C. Kaito, Japan. J. Appl. Phys. 17, 567-568 (1978).
3150. Shiojiri M., T. Miyano and C. Kaito, Japan. J. Appl. Phys. 18, 1937-1945 (1979).
3151. Shirai H., H. Sakaguchi and G. Adachi, J. Less-Common Met. 159, L17-L19 (1990).
3152. Shirley D.A., Phys. Rev. B 5, 4709-4714 (1972).
3153. Shiyanovskaya I.V., T.A. Gavrilko and E.V. Gabrusenoks, J. Mol. Struct. 293, 295-298 (1993).
3154. Shizukuishi M., E. Kaga, I. Shimizu, H. Kokado and E. Inoue, Japan. J. Appl. Phys. 20, 581-586 (1981).
3155. Shizukuishi M., I. Shimizu and E. Inoue, Japan. J. Appl. Phys. 19, 2121-2126 (1980).
3156. Shizukuishi M., I. Shimizu and E. Inoue, Japan. J. Appl. Phys. 20, 575-579 (1981).
3157. Shizukuishi M., I. Shimizu and E. Inoue, Japan. J. Appl. Phys. 20, 2359-2363 (1981).
3158. Shklovskii B.I., Fiz. Tekh. Poluprovodn. 6, 2335-2340 (1972) [Soviet Phys. Semicond. 6, 1964-1967 (1973)].
3159. Shklovskii B.I. and A.L. Efros, Usp. Fiz. Nauk 117, 401-435 (1975) [Soviet Phys. Usp. 18, 845-862 (1976)].
3160. Shklovskii B.I. and A.L. Efros, Fiz. Tekh. Poluprovodn. 14, 825-858 (1980) [Soviet Phys. Semicond. 14, 487-506 (1980)].
3161. Shlesinger M.F., Ann. Rev. Phys. Chem. 39, 269-290 (1988).

3162. Shluger A.L. and A.M. Stoneham, J. Phys. Cond. Matter 5, 3049-3086 (1993).
3163. Shoesmith D.W., S. Sunder, M.G. Bailey, G.J. Wallace and F.W. Stanchell, J. Electroanal. Chem. 143, 153-165 (1983).
3164. Shokoohi F.K., J.M. Tarascon and B.J. Wilkens, Appl. Phys. Lett. 59, 1260-1262 (1991).
3165. Shokoohi F.K., J.M. Tarascon, B.J. Wilkens, D. Guyomard and C.C. Chang, J. Electrochem. Soc. 139, 1845-1849 (1992).
3166. Shu Z.X., R.S. McMillan and J.J. Murray, J. Electrochem. Soc. 140, 922-927 (1993).
3167. Shumilova N.A. and V.S. Bagotzky, Electrochim. Acta 13, 285-293 (1968).
3168. Sichel E.K. and J.I. Gittleman, Appl. Phys. Lett. 33, 564-566 (1978).
3169. Sichel E.K. and J.I. Gittleman, J. Electronic Mater. 8, 1-9 (1979).
3170. Sichel E.K., J.I. Gittleman and J. Zelez, Appl. Phys. Lett. 31, 109-111 (1977).
3171. Sienko M.J., Adv. Chem. Ser. 39, 224-236 (1963).
3172. Sienko M.J. and J.M. Berak, in The Chemistry of Extended Defects in Non-metallic Solids, edited by L. Eyring and M. O'Keefe (North-Holland, Amsterdam, 1970), pp. 541-554.
3173. Sikkens M., I. J. Hodkinson, F. Horowitz, H.A. Macleod and J.J. Wharton, Proc. Soc. Photo-Opt. Instrum. Engr. 505, 236-246 (1984).
3174. Simmons G.W. and B.C. Beard, J. Chem. Phys. 91, 1143-1148 (1987).
3175. Simmons G.W., E. Kellerman and H. Leidheiser, Jr., J. Electrochem. Soc. 123, 1276-1284 (1976).
3176. Simmons G.W., A. Vértes, M.L. Varsányi and H. Leidheiser, Jr., J. Electrochem. Soc. 126, 187-189 (1979).
3177. Simpraga R.P., J. Electroanal. Chem. 355, 79-96 (1993).
3178. Singer J., W.L. Fielder, H.E. Kautz and J.S. Fordyca, J. Electrochem. Soc. 123, 614-617 (1976).
3179. Singwi K.S., M.P. Tosi, R.H. Land and A. Sjölander, Phys. Rev. 176, 589-599 (1968).
3180. Siperko L.M. and T. Kuwana, J. Electrochem. Soc. 130, 396-402 (1983).
3181. Siperko L.M. and T. Kuwana, J. Electrochem. Soc. 133, 2439-2440 (1986).
3182. Siperko L.M. and T. Kuwana, J. Vac. Sci. Technol. A 5, 1303-1306 (1987).
3183. Siperko L.M. and T. Kuwana, Electrochim. Acta 32, 765-771 (1987).
3184. Skerlavaj A., Y. Claesson and C.-G. Ribbing, Thin Solid Films 186, 15-26 (1990).
3185. Skettrup T., Phys. Rev. B 18, 2622-2631 (1978).
3186. Slade R.C.T., J. Barker and T.K. Halstead, Solid State Ionics 24, 147-153 (1987).
3187. Slade R.C.T., P.R. Hirst and B.C. West, J. Mater. Chem. 1, 281-288 (1991).
3188. Slade R.C.T., P.R. Hirst, B.C. West, R.C. Ward and A. Magerl, Chem. Phys. Lett. 155, 305-312 (1989).
3189. Slade R.C.T., A. Ramanan, P.R. Hirst and H.A. Pressman, Mater. Res. Bull. 23, 793-798 (1988).
3190. Slade R.C.T., B.C. West and G.P. Hall, Solid State Ionics 32-33, 154-161 (1989).
3191. Slade R.C.T., B.C. West, A. Ramanan, W.I.F. David and W.T.A. Harrison, Eur. J. Solid State Inorg. Chem. 26, 15-22 (1989).
3192. Slade R.C.T., K.E. Young and N. Bonanos, Solid State Ionics 46, 83-88 (1991).
3193. Slaidins, G.J., Elektrokhim. 8, 1840-1842 (1972) [Soviet Electrochem. 8, 1783-1785 (1972)].
3194. Slaidins, G.J., A.R. Lusis, J.J. Kleperis, Z.V. Purvina and S.J. Takeris, Izv. Akad. Nauk Latv. SSR, Ser. Obs. (1983) (8), 94-96.
3195. Slaidins, G.J. and A. Spricis, Latvijas PSR Zinatnu Akad. Vestis, Kim. Sér. (1979) (2) 201-205.
3196. Sleigh A.K., J.J. Murray and W.R. McKinnon, Electrochim. Acta 36, 1469-1474 (1991).
3197. Sleight A.W., Inorg. Chem. 8, 1764-1769 (1969).
3198. Smakula A., Z. Physik 59, 603-614 (1930).
3199. Smith G.B., Opt. Commun. 71, 279-284 (1989).
3200. Smith G.B., Appl. Opt. 29, 3685-3693 (1990).
3201. Smith G.B., A. Ignatiev and G. Zajac, J. Appl. Phys. 51, 4186-4196 (1980).
3202. Smith G.B., G.A. Niklasson, J.S.E.M. Svensson and C.G. Granqvist, J. Appl. Phys. 59, 571-581 (1986).
3203. Smith R.A., Semiconductors, Second edition (Cambridge University Press, Cambridge, 1978).
3204. Sobhan M.A., R.T. Kivaisi, B. Stjerna and C.G. Granqvist (1994), to be published.
3205. Solodukha A.M. and O.K. Zhukov, Fiz. Tverd. Tela 28, 579-580 (1986) [Soviet Phys. Solid State 28, 323-324 (1986)].

3206. Solodukha A.M. and O.K. Zhukov, Izv. Akad. Nauk. SSSR Neorg. Mater. 26, 2335-2337 (1990) [Inorg. Mater. 26, 2002-2004 (1990)].
3207. Solodukha A.M., O.K. Zhukov and M.V. Lesovoi, Izv. Akad. Nauk SSSR Neorg. Mater. 19, 2053-2055 (1983) [Inorg. Mater. 19, 1805-1807 (1983)].
3208. Solodukha A.M., O.K. Zhukov, M.V. Lesovoi and N.N. Makeeva, Izv. Akad. Nauk SSSR Neorg. Mater. 25, 777-779 (1989) [Inorg. Mater. 25, 662-664 (1989)].
3209. Soltan A.S., R. Vassen and P. Jung, J. Appl. Phys. 70, 793-797 (1991).
3210. Sondheimer E.H., Adv. Phys. 1, 1-42 (1952).
3211. Sood A.K., J. Appl. Electrochem. 16, 274-280 (1986).
3212. Soppe W., F. Aldencamp and H.W. den Hartog, J. Non-Cryst. Solids 91, 351-374 (1987).
3213. Soriano L., M. Abbate, J. Vogel, J.C. Fuggle, A. Fernández, A.R. González-Elipe, M. Sacchi and J.M. Sanz, Chem. Phys. Lett. 208, 460-464 (1993).
3214. Sotani N., Rev. Phys. Chem. Japan 46, 1-8 (1976).
3215. Sotto M., J. Electroanal. Chem. 69, 229-237 (1976).
3216. Sotto M., J. Electroanal. Chem. 70, 291-315 (1976).
3217. Sotto M., J. Electroanal. Chem. 72, 287-306 (1976).
3218. Spalvins T. and W.A. Brainard, J. Vac. Sci. Technol. 11, 1186-1192 (1974).
3219. Speck K.R., H.S.-W. Hu, M.E. Sherwin and R.S. Potember, Thin Solid Films 165, 317-322 (1988).
3220. Spencer A.G., M. Georgson, C.A. Bishop, E. Stenberg and R.P. Howson, Solar Energy Mater. 18, 87-95 (1988).
3221. Sperlich G., P. Urban and G. Frank, Z. Physik 263, 315-328 (1973).
3222. Spevack P.A. and N.S. McIntyre, J. Phys. Chem. 96, 9029-9035 (1992).
3223. Spichiger-Ulmann M. and J. Augustynski, J. Appl. Phys. 54, 6061-6064 (1983).
3224. Spindler R. and D.F. Shriver, in Conducting Polymers: Special Applications, edited by L. Alcácer (Reidel, Dordrecht, 1987), pp. 151-160.
3225. Sprenger D. and O. Anderson, Fresenius J. Anal. Chem. 341, 116-120 (1991).
3226. Spricis A.A., G.J. Slaidins, J.J. Abele and J.R. Dzelme, Elektrokhim 18, 339-343 (1982) [Soviet Electrochem. 18, 301-305 (1982)].
3227. Spurdens P.C., J. Drennan, J.R. Owen, B.C.H. Steele, J.M. Gonzales-Calbet and D.A. Jefferson, Solid State Ionics 5, 335-338 (1981).
3228. Srivastava V.C., S. Gupta, K.N. Rai and J. Kumar, Mater. Res. Bull. 23, 341-348 (1988).
3229. Srolovitz D.J., A. Mazor and B.G. Bukiet, J. Vac. Sci. Technol. A6, 2371-2380 (1988).
3230. Stangar U.L., B. Orel, I. Grabec and B. Ogorvec, Proc. Soc. Photo-Opt. Instrum. Engr. 1728, 118-129 (1992).
3231. Stapinski T. and E. Leja, Proc. Soc. Photo-Opt. Instrum. Engr. 1016, 162-164 (1988).
3232. Starnberg H.I., M.T. Johnson and H.P. Hughes, J. Phys. C 19, 2689-2700 (1986).
3233. Steele B.C.H. and S.J. Golden, Appl. Phys. Lett. 59, 2357-2359 (1991).
3234. Stefanou N. and A. Modinos, J. Phys. Cond. Matter 3, 8135-8148 (1991).
3235. Stefanou N. and A. Modinos, J. Phys. Cond. Matter 3, 8149-8157 (1991).
3236. Stencel J.M., L.E. Makovsky, J.R. Diehl and T.A. Sarkus, J. Raman Spectrosc. 15, 282-287 (1984).
3237. Stephan K., H. Deutsch and T.D. Märk, J. Chem. Phys. 83, 5712-5720 (1985).
3238. Stephens J.S. and D.W.J. Cruickshank, Acta Cryst. B 26, 222-226 (1970).
3239. Stephenson N.C. and R.S. Roth, Acta Cryst. B 27, 1010-1017 (1971).
3240. Stephenson N.C. and R.S. Roth, Acta Cryst. B 27, 1018-1024 (1971).
3241. Stephenson N.C. and R.S. Roth, Acta Cryst. B 27, 1025-1031 (1971).
3242. Stephenson N.C. and R.S. Roth, Acta Cryst. B 27, 1031-1036 (1971).
3243. Stephenson N.C. and R.S. Roth, Acta Cryst. B 27, 1037-1044 (1971).
3244. Stevens J.R., J.S.E.M. Svensson, C.G. Granqvist and R. Spindler, Appl. Opt. 26, 3489-3490 (1987).
3245. Stevens R. and J.P.G. Binner, J. Mater. Sci. 19, 695-715 (1984).
3246. Stikans M.P., Yu.Ya. Kleperis and Ya.K. Klyavin, Izv. Akad. Nauk Latvian SSR, Fiz. Tekh. Nauk 4, 43-47 (1988).

3247. Stikans M.P., Yu.Ya. Purans and Ya.K. Klyavin, Zh. Tekn. Fiz. 61, 91-96 (1991) [Soviet Tech. Phys. 36, 53-56 (1991)].
3248. Stilwell D.E., K.H. Park and M.H. Miles, J. Appl. Electrochem. 22, 325-331 (1992).
3249. Stizza S., M. Benfatto, A. Bianconi, J. Garcia, G. Mancini and C.R. Natoli, J. Phys. (Paris) 47, C8 691-C8 696 (1986).
3250. Stizza S., I. Davoli and M. Benfatto, J. Non-Cryst. Solids 95-96, 327-334 (1987).
3251. Stizza S., G. Mancini, M. Benfatto, C.R. Natoli, J. Garcia and A. Bianconi, Phys. Rev. B 40, 12229-12236 (1989).
3252. Stjerna B. and C.G. Granqvist, Proc. Soc. Photo-Opt. Instrum. Engr. 1272, 12-25 (1990).
3253. Stjerna B. and C.G. Granqvist, Thin Solid Films 193-194, 704-711 (1990).
3254. Stjerna B. and C.G. Granqvist, Appl. Phys. Lett. 57, 1989-1991 (1991).
3255. Stjerna B., C.G. Granqvist, A. Seidel and L. Häggström, J. Appl. Phys. 68, 6241-6245 (1990).
3256. Stocker H.J., S. Singh, L.G. VanUitert and G.J. Zydzik, J. Appl. Phys. 50, 2993-2994 (1979).
3257. Stoklosa A., J. Molenda and Do Than, Solid State Ionics 15, 211-216 (1985).
3258. Stoneham M.A., Phys. Today (1980) (1), 34-42.
3259. Stonehart P., J.G. Koren and J.S. Brinen, Anal. Chim. Acta 40, 65-75 (1968).
3260. Stonehart P., H.A. Kozlowska and B.E. Conway, Proc. Roy. Soc. London A 310, 541-563 (1969).
3261. Stoyanova R., E. Zhecheva and S. Angelov, Mater. Chem. Phys. 26, 239-244 (1990).
3262. Strehblow H.-H. and B. Titze, Electrochim. Acta 25, 839-850 (1980).
3263. Strobel P. and C. Mouget, Mater. Res. Bull. 28, 93-100 (1993).
3264. Stroud D. and F.P. Pan, Phys. Rev. B 17, 1602-1610 (1978).
3265. Stroud J.E., W.C. Tripp and J.M. Wimmer, J. Am. Ceram. Soc. 57, 172-175 (1974).
3266. Studer F., A. Lebail and B. Raveau, J. Solid State Chem. 63, 414-423 (1986).
3267. Sudoh K. and H. Hiratshima, J. Non-Cryst. Solids 147-148, 386-388 (1992).
3268. Sugimoto K. and S. Matsuda, Mater. Sci. Engr. 42, 181-189 (1980).
3269. Suhail M.H., G.M. Rao and S. Mohan, J. Appl. Phys. 71, 1421-1427 (1992).
3270. Suiyang H., C. Fenbo and Z. Jicai, in Solid State Ionic Devices, edited by B.V.R. Chowdari and S. Radhakrishna (World Scientific, Singapore, 1988), pp. 521-526.
3271. Sukhotin A.M., M.N. Shlepakov and V.I. Popov, Elektrokhim. 21, 1673-1675 (1985) [Soviet Electrochem. 21, 1582-1584 (1985)].
3272. Sumi H. and Y. Toyosawa, J. Phys. Soc. Japan 31, 342-358 (1971).
3273. Sun S.-S. and P.H. Holloway, J. Vac. Sci. Technol. A 1, 529-533 (1983).
3274. Sun S.-S. and P.H. Holloway, J. Vac. Sci. Technol. A 2, 336-340 (1984).
3275. Sun Z.W. and G. Campet, Mater. Sci. Engr. B 5, 455-464 (1990).
3276. Sundaram K.B. and P. Wahid, Phys. Stat. Sol. B 161, K63-K66 (1990).
3277. Sundaram K.B., P.F. Wahid and P.J. Sisk, Thin Solid Films 221, 13-16 (1992).
3278. Sunseri C., F. Di Quarto and A. Di Paola, J. Appl. Electrochem. 10, 669-675 (1980).
3279. Sunseri C., S. Piazza, A. Di Paola and F. Di Quarto, J. Electrochem. Soc. 134, 2410-2416 (1987).
3280. Susa N., J. Electrochem. Soc. 132, 2762-2767 (1985).
3281. Suzuki K., N. Hashimoto, T. Oyama, J. Shimizu, Y. Akao and H. Kojima, Thin Solid Films 226, 104-109 (1993).
3282. Suzuki M. and Y. Taga, J. Appl. Phys. 71, 2848-2854 (1992).
3283. Svensson J.S.E.M., D.K. Benson and C.E. Tracy, Proc. Soc. Photo-Opt. Instrum. Engr. 1016, 19-27 (1988).
3284. Svensson J.S.E.M. and C.G. Granqvist, Appl. Phys. Lett. 45, 828-830 (1984).
3285. Svensson J.S.E.M. and C.G. Granqvist, Proc. Soc. Photo-Opt. Instrum. Engr. 502, 30-37 (1984).
3286. Svensson J.S.E.M. and C.G. Granqvist, Solar Energy Mater. 11, 29-34 (1984).
3287. Svensson J.S.E.M. and C.G. Granqvist, Thin Solid Films 126, 31-36 (1985).
3288. Svensson J.S.E.M. and C.G. Granqvist, Solar Energy Mater. 12, 391-402 (1985).
3289. Svensson J.S.E.M. and C.G. Granqvist, Appl. Opt. 24, 2284-2285 (1985).
3290. Svensson J.S.E.M. and C.G. Granqvist, Appl. Phys. Lett. 49, 1566-1568 (1986).
3291. Svensson J.S.E.M. and C.G. Granqvist, Proc. Soc. Photo-Opt. Instrum. Engr. 653, 10-15 (1986).

3292. Svensson J.S.E.M. and C.G. Granqvist, Solar Energy Mater. 16, 19-26 (1987).
3293. Svensson J.S.E.M. and C.G. Granqvist, Appl. Opt. 26, 1554-1556 (1987).
3294. Svensson J.S.E.M. and C.G. Granqvist, in Large-area Chromogenics: Materials and Devices for Transmittance Control, edited by C.M. Lampert and C.G. Granqvist (SPIE Opt. Engr. Press, Bellingham, 1990), Vol. IS4, pp. 285-297.
3295. Sviridov D.V. and A.I. Kulak, Elektrokhim 22, 83-89 (1986) [Soviet Electrochem. 22, 70-76 (1986)].
3296. Sviridov D.V. and A.I. Kulak, Thin Solid Films 198, 191-198 (1991).
3297. Swann J.T. and D.J. De Smet, J. Appl. Phys. 58, 1335-1338 (1985).
3298. Swanson A.B. and J.S. Anderson, Mater. Res. Bull. 3, 149-152 (1968).
3299. Swanson J.G., Glass Digest, (July 15 1987), 56-62.
3300. Sweitzer G., Energy 18, 107-114 (1993).
3301. Sych O.A., Y.S. Krasnov, A.T. Vasko, F.N. Patsyuk and I.E. Lastochkina, Ukr. Khim. Zh. SSSR 57, 628-632 (1991).
3302. Syono Y., M. Kikuchi, T. Goto and K. Fukuoka, J. Solid State Chem. 50, 133-137 (1983).
3303. Szczyrbowski J. and A. Czapla, J. Phys. D 12, 1737-1751 (1979).
3304. Szklarska-Smialowska Z. and W. Kozlowski, J. Electrochem. Soc. 131, 234-241 (1984).
3305. Szklarska-Smialowska Z. and H. Oranowska, Surf. Sci. 16, 355-362 (1976).
3306. Szörényi T., K. Bali and I. Hevesi, J. Non-Cryst. Solids 35-36, 1245-1248 (1980).
3307. Szörényi T., K. Bali and I. Hevesi, J. Phys. (Paris) 46, 473-477 (1985).
3308. Szörényi T., K. Bali, M.I. Török and I. Hevesi, Thin Solid Films 121, 29-34 (1984).
3309. Szörényi T., L. Baufay, M.C. Joliet, F. Hanus, R. Andrew and I. Hevesi, Rev. Roum. Phys. 31, 1043-1046 (1986).
3310. Szörényi T., L. Baufay, M.C. Joliet, F. Hanus, R. Andrew and I. Hevesi, Appl. Phys. A 39, 251-255 (1986).
3311. Szücs B., J. Adam and P. Jakob, Acta Phys. Acad. Sci. Hung. 49, 159-166 (1980).
3312. Szymanski J.T. and A.C. Roberts, Can. Mineral. 22, 681-688 (1984).

T

3313. Tada H., in Large-area Chromogenics: Materials and Devices for Transmittance Control, edited by C.M. Lampert and C.G. Granqvist (SPIE Opt. Engr. Press, Bellingham, 1990), Vol. IS4, pp. 230-245.
3314. Tada H., Y. Bito, K. Fujino and H. Kawahara, Solar Energy Mater. 16, 509-516 (1987).
3315. Tada H., K. Fujino and H. Kawahara, J. Polymer Sci. A, Polymer Lett. Ed. 22, 659-663 (1984).
3316. Tada H., K. Fujino and H. Kawahara, J. Polymer Sci. A, Polymer Chem. 25, 3015-3024 (1987).
3317. Tada H., K. Fujino, H. Kawahara and N. Baba, Denki Kagaku 54, 584-589 (1986).
3318. Tada H., Y. Saito and H. Kawahara, J. Electrochem. Soc. 138, 140-144 (1991).
3319. Tada H., Y.-I. Yano, K. Fujino and H. Kawahara, J. Polymer Sci. A, Polymer Chem. 25, 1745-1753 (1987).
3320. Taga Y. and T. Motohiro, J. Cryst. Growth 99, 638-642 (1990).
3321. Taimni I.K. and S.N. Tandon, Anal. Chim. Acta 22, 34-37 (1960).
3322. Tait R.N., S.K. Dew, T. Smy and M.J. Brett, J. Appl. Phys. 70, 4295-4300 (1991).
3323. Tait R.N., T. Smy and M.J. Brett, J. Vac. Sci. Technol. A 10, 1518-1521 (1992).
3324. Tait R.T., T. Smy and M.J. Brett, Thin Solid Films 226, 196-201 (1993).
3325. Takada K., T. Kanbara, Y. Yamamura and S. Kondo, Eur. J. Solid State Inorg. Chem. 28, 533-545 (1991).
3326. Takahashi T., J. Appl. Electrochem. 3, 79-90 (1973).
3327. Takahashi T., in Superionic Conductors, edited by G.D. Mahan and W.L. Roth, (Plenum, New York, 1976), pp. 379-394.
3328. Takahashi T., editor, High Conductivity Solid Ionic Conductors: Recent Trends and Applications (World Scientific, Singapore, 1989).
3329. Takahashi T., S. Ikeda and O. Yamamoto, J. Electrochem. Soc. 119, 477-482 (1972).
3330. Takahashi T., S. Ikeda and O. Yamamoto, J. Electrochem. Soc. 120, 647-651 (1973).
3331. Takahashi T., S. Tanase and O. Yamamoto, J. Appl. Electrochem. 10, 415-416 (1980).

3332. Takahashi T., O. Yamamoto and S. Ikeda, Denki Kagaku 37, 796-799 (1969).
3333. Takahashi Y., Kagaku [Japan. J. Opt.] (1982), 365-371.
3334. Takahashi Y., M. Kanamori, H. Hashimoto, Y. Moritani and Y. Masuda, J. Mater. Sci. 24, 192-198 (1989).
3335. Takahashi Y. and T. Niwa, Kogyo Zairyo 31, 48-51 (1983).
3336. Takai O., Japan Display 1983, pp. 58-61.
3337. Takai O., Proc. SID 25, 305-309 (1984).
3338. Takai O., Proc. SID 28, 243-246 (1987).
3339. Takaki S., K. Matsumoto and K. Suzuki, Appl. Surf. Sci. 33-34, 919-925 (1988).
3340. Takase A. and K. Miyakawa, Japan. J. Appl. Phys. 30, L1508-L1511 (1991).
3341. Takata S., T. Minami and H. Nanto, Thin Solid Films 135, 183-187 (1986).
3342. Take H., H. Hamada, K. Yano, Y. Inami, M. Matsuura and T. Wada, Japan Display 1983, pp. 380-383.
3343. Takeda Y., R. Kanno, Y. Oyabe, O. Yamamoto, K. Nobugaya and F. Kanamaru, J. Power Sources 14, 215-221 (1985).
3344. Takeda Y., R. Kanno, Y.Tsuji and O. Yamamoto, J. Electrochem. Soc. 131, 2006-2010 (1984).
3345. Takeda Y., R. Kanno, Y.Tsuji, O. Yamamoto and H. Taguch, J. Power Sources 9, 325-328 (1983).
3346. Takei H., Japan. J. Appl. Phys. 7, 827-836 (1968).
3347. Takei H. and S. Koide, J. Phys. Soc. Japan 21, 1010 (1966).
3348. Takei K., K. Kumai, T. Iwahori, T.Uwai and F. Furusyo, Denki Kagaku 61, 421-430 (1993).
3349. Takeuchi E.S. and P. Piliero, J. Power Sources, 21, 133-141 (1987).
3350. Takeuchi E.S. and W.C. Thiebolt, J. Electrochem. Soc. 135, 2691-2694 (1988).
3351. Takeuchi E.S. and W.C. Thiebolt, J. Electrochem. Soc. 138, L44-L45 (1991).
3352. Talledo A., Vanadium Pentoxide-based Thin Films: Optical, Structural and Electrophysical Characterization, Ph. D. Thesis (UNI, Lima, Peru, 1992), unpublished.
3353. Talledo A., A.M. Andersson and C.G. Granqvist, J. Mater. Res. 5, 1253-1256 (1990).
3354. Talledo A., A.M. Andersson and C.G. Granqvist, J. Appl. Phys. 69, 3261-3265 (1991).
3355. Talledo A., A.M. Andersson and C.G. Granqvist, in Surface Science: Lectures on Basic Concepts and Applictions, Springer Proceedings in Physics, edited by F.A. Ponce and M. Cardona (Springer, Berlin, Heidelberg, 1992), Vol. 62, pp. 315-316.
3356. Talmey P., U.S. Patent 2,281,013 (1942)
3357. Talmey P., U.S. Patent 2,319,765 (1943).
3358. Tanahashi I., A. Tsujimura, T. Mitsuyu and A. Nishino, Japan. J. Appl. Phys. 29, 2111-2115 (1990).
3359. Tanahashi I., M. Yoshida and T. Mitsuyu, Bull. Chem. Soc. Japan 64, 2281-2283 (1991).
3360. Tang C., S. Alexander and R. Bruinsma, Phys. Rev. Lett. 64, 772-775 (1990).
3361. Tang C., P. Georgopoulos, M.E. Fine, J.B. Cohen, M. Nygren, G. S. Knapp and A. Aldred, Phys. Rev. B 31, 1000-1011 (1985).
3362. Tang Z.K., Y. Nozue and T. Goto, J. Phys. Soc. Japan 60, 2090-2094 (1991).
3363. Tanimoto S., M. Matsui, M. Aoyagi, K. Kamisaki, K. Kuroiwa and Y. Tarui, Japan. J. Appl. Phys. 30, L330-L333 (1991).
3364. Tarascon J.M., J. Electrochem. Soc. 134, 1345-1351 (1987).
3365. Tarascon J.M. and D. Guyomard, J. Electrochem. Soc. 138, 2864-2868 (1991).
3366. Tarascon J.M. and G.W. Hull, Solid State Ionics 22, 85-96 (1986).
3367. Tarascon J.M., E. Wang, F.K. Shokoohi, W.R. KcKinnon and S. Colson, J. Electrochem. Soc. 138, 2859-2864 (1991).
3368. Tarte P., Spectrochim. Acta 20, 238-240 (1964).
3369. Tarte P., Spectrochim. Acta 21, 313-319 (1965).
3370. Tate T.J., M. Garcia-Parajo and M. Green, J. Appl. Phys. 70, 3509-3511 (1991).
3371. Tatsumisago M., I. Sakono, T. Minami and M. Tanaka, J. Non-Cryst. Solids 46, 119-123 (1981).
3372. Tatsumisago M., I. Sakono, T. Minami and M. Tanaka, J. Mater. Sci. 17, 3593-3597 (1982).
3373. Tatsumisago M., K. Yoneda, N. Machida and T. Minami, J. Non-Cryst. Solids 95-96, 857-864 (1987).
3374. Tauc J., in Amorphous and Liquid Semiconductors, edited by J. Tauc (Plenum, London, 1974), pp. 159-220.
3375. Tauc J., R. Grigorovici and A. Vancu, Phys. Stat. Sol. 15, 627-637 (1966).
3376. Tauster S.J. and J.H. Sinfelt, J. Phys. Chem. 74, 3831-3832 (1970).

3377. Taylor G.H., J. Solid State Chem. 1, 359-367 (1969).
3378. Tedjar F. and J. Guitton, Thermochim. Acta 181, 13-22 (1991).
3379. Tell B., J. Electrochem. Soc. 127, 2451-2554 (1980).
3380. Tell B. and S. Wagner, Appl. Phys. Lett. 33, 837-838 (1978).
3381. Tell B. and F. Wudl, J. Appl. Phys. 50, 5944-5946 (1979).
3382. Temmink A., O. Anderson, K. Bange, H. Hantsche and X. Yu, Thin Solid Films 192, 211-218 (1990).
3383. Temmink A., O. Anderson, K. Bange, H. Hantsche and X. Yu, Vacuum 41, 1144-1146 (1990).
3384. Tench D. and L.F. Warren, J. Electrochem. Soc. 130, 869-872 (1983).
3385. Terabe K., S. Yamaguchi and Y. Iguchi, Solid State Ionics 40-41, 111-114 (1990).
3386. Terakura K., T. Oguchi, A.R. Williams and J. Kübler, Phys. Rev. B 30, 4734-4747 (1984).
3387. Terakura K., A.R. Williams, T. Oguchi and J. Kübler, Phys. Rev. Lett. 52, 1830-1833 (1984).
3388. Terao N., Japan. J. Appl. Phys. 4, 8-15 (1965).
3389. Terao N., Japan. J. Appl. Phys. 6, 21-34 (1967).
3390. Terashima T. and Y. Bando, J. Appl. Phys. 56, 3445-3450 (1984).
3391. Terui H. and M. Kobayashi, Appl. Phys. Lett. 32, 666-668 (1978).
3392. Terukov E.I., K.-D. Ufert and F.A. Chudnovskii, Fiz. Tverd. Tela 18, 2479-2482 (1976) [Soviet Phys. Solid State 18, 1450-1451 (1976)].
3393. Tesanovic' Z., J. Phys. C 20, L829-L834 (1987).
3394. Tesanovic' Z., M.V. Jaric' and S. Maekawa, Phys. Rev. Lett. 57, 2760-2763 (1986).
3395. Thackeray M.M., S.D. Baker, K.T. Adendorff and J.B. Goodenough, Solid State Ionics 17, 175-181 (1985).
3396. Thackeray M.M., W.I.F. David, P.G. Bruce and J.B. Goodenough, Mater. Res. Bull. 18, 461-472 (1983).
3397. Thackeray M.M., M.H. Rossouw, A. de Kock, A.P. de la Harpe, R.J. Gummow, K. Pearce and D.C. Liles, J. Power Sources 43-44, 289-300 (1993).
3398. Thackeray M.M., M.H. Rossouw, R.J. Gummow, D.C. Liles, K. Pearce, A. De Kock, W.I.F. David and S. Hull, Electrochim. Acta 38, 1259-1267 (1993).
3399. Thakoor A.P., A. Moopenn, T. Daud and A.P. Thakoor, J. Appl. Phys. 67, 3132-3135 (1990).
3400. Thakoor A.P., A. Moopenn, J. Lambe and S.K. Khanna, Appl. Opt. 26, 5085-5092 (1987).
3401. Théobald F., J. Less-Common Met. 53, 55-71 (1977).
3402. Théobald F., R. Cabala and J. Bernard, J. Solid State Chem. 17, 431-438 (1976).
3403. Thiel P.A. and T.E. Madey, Surf. Sci. Rept. 7, 211-385 (1987).
3404. Thomas C.B. and M.R. Goulding, Philos. Mag. 49, 219-230 (1984).
3405. Thomas C.B. and P. Lloyd, Microelectronics 7 (3), 29-34 (1976).
3406. Thomas G.R. and J.R. Owen, Solid State Ionics 53-56, 513-519 (1992).
3407. Thomas M.G.S.R., P.G. Bruce and J.B. Goodenough, J. Electrochem. Soc. 132, 1521-1528 (1985).
3408. Thomas M.G.S.R., P.G. Bruce and J.B. Goodenough, Solid State Ionics 17, 13-19 (1985).
3409. Thomas M.G.S.R., P.G. Bruce and J.B. Goodenough, Solid State Ionics 18-19, 794-798 (1986).
3410. Thomas M.G.S.R., W.I.F. David, J.B. Goodenough and P. Groves, Mater. Res. Bull. 20, 1137-1146 (1985).
3411. Thomas R., F.P.J.M. Kerkhof, J.A. Moulijn, J. Medema and V.H.J. de Beer, J. Catalysis 61, 559-561 (1980).
3412. Thomas R., J.A. Moulijn, F.P.J.M. Kerkhof, Rech. Trav. Chim. Pays-Bas 96, M134-M135 (1977).
3413. Thornton J.A., Ann. Rev. Mater. Sci. 7, 239-260 (1977).
3414. Tillement O., J. Angenault, J.C. Couturier and M. Quarton, Solid State Ionics 53-56, 391-399 (1992).
3415. Tinet D. and J.J. Fripiat, Rev. Chim. Minérale 19, 612-632 (1982).
3416. Tinet D., M.H. Legay, L. Gatineau and J.J. Fripiat, J. Chem. Phys. 90, 948-950 (1986).
3417. Tinnemans A.H.A., T.P.M. Koster, D.H.M.W. Thewissen, A. Mackor and J. Schoonman, Ber. Bunsenges. Phys. Chem. 90, 383-390 (1986).
3418. Tokutaka H., N. Ishihara, K. Nishimori, S. Kishida and K. Isomoto, Surf. Interface Anal. 18, 697-704 (1992).
3419. Tölgyesi M. and M. Novák, Japan. J. Appl. Phys. 32, 93-96 (1993).
3420. Tolstikhina A.K., V.N. Petrov, S.S. Olevskii, A.V. Koschchienko, S.A. Semiletov and B.I. Kozyrkin, Izv. Akad. Nauk. SSSR Neorg. Mater. 23, 968-972 (1987) [Inorg. Mater. 23, 863-867 (1987)].

3421. Tolstikhina A.I., V.N. Petrov, A.B. Vasil'ev, S.A. Semiletov and B.I. Kozyrkin, Izv. Akad. Nauk SSSR Neorg. Mater. 24, 1840-1844 (1988) [Inorg. Mater. 24, 1571-1575 (1988)].
3422. Tomellini M., J. Chem. Soc. Farady Trans. I 84, 3501-3510 (1988).
3423. Tomellini M., J. Electron Spectrosc. Related Phenomena 58, 75-78 (1992).
3424. Tominaga K., R. Muhammet, I. Kobayashi and M. Okada, Japan. J. Appl. Phys. 31, L585-L587 (1992).
3425. Tomita K., Nippon Kagaku Kaishi (1993), 69-78.
3426. Tonazzi J.C.L., B. Valla, M.A. Macedo, P. Baudry, M.A. Aegerter, A.C.M. Rodrigues and L.O. Bulhoes, Proc. Soc. Photo-Opt. Instrum. Engr. 1328, 375-390 (1990).
3427. Torresi R.M., O.R. Camara, C.P. de Pauli and M.C. Giordano, An. Asoc. Quim. Argentina 74, 361-372 (1986).
3428. Torresi R.M., M.V. Vásquez, A. Gorenstein and S.I. Córdoba-Torresi, Thin Solid Films 229, 180-186 (1993).
3429. Toshima N., R.-J. Lin and M. Kaneko, Chem. Lett. (1989), 1099-1102.
3430. Toshima N., R.-J. Lin and M. Kaneko, Chem. Lett. (1990), 485-488.
3431. Tossici R., R. Marassi, M. Berrettoni, S. Stizza and G. Pistoia, Solid State Ionics 57, 227-234 (1992).
3432. Tougaard S., Surf. Interface Anal. 11, 453-472 (1988).
3433. Tourillon G., M. Ladouceur and J.P. Dodelet, Physica (Utrecht) B 158, 251-252 (1989).
3434. Toyoda T., J. Appl. Phys. 63, 5166-5168 (1988).
3435. Tracy C.E. and D.K. Benson, J. Vac. Sci. Technol. 4, 2377-2383 (1986).
3436. Tranchant A., J.M. Blegino, J. Farcy and R. Messina, J. Electrochem. Soc. 139, 1243-1248 (1992).
3437. Tranchant A. and R. Messina, J. Power Sources 24, 85-93 (1988).
3438. Tranchant A., R. Messina and J. Perichon, J. Electroanal. Chem. 113, 225-232 (1980).
3439. Trasatti S. and G. Lodi, in Electrodes of Conductive Metallic Oxides, Part A, edited by S. Trasatti (Elsevier, Amsterdam, 1980), pp. 301-358.
3440. Treitinger L. and H. Voit, Nachr. Tech. Gesell. (NTG Fachber.) 79, 324-335 (1982).
3441. Tretyakov Yu.D., A.V. Popov and Yu.G. Metlin, Solid State Ionics 17, 265-272 (1985).
3442. Triberis G.P., J. Non-Cryst. Solids 74, 1-10 (1985).
3443. Triberis G.P., Phys. Stat. Sol. B 132, 641-652 (1985).
3444. Triberis G.P., Phys. Stat. Sol. B 136, 393-398 (1986).
3445. Triberis G.P., J. Phys. C 20, 3707-3718 (1987).
3446. Triberis G.P., J. Phys. C 21, L821-L825 (1988).
3447. Triberis G.P., J. Non-Cryst. Solids 104, 135-138 (1988).
3448. Triberis G.P., Phys. Stat. Sol. B 158, K149-K153 (1990).
3449. Triberis G.P. and L.R. Friedman, J. Phys. C 14, 4631-4639 (1981).
3450. Triberis G.P. and L.R. Friedman, J. Phys. C 18, 2281-2286 (1985).
3451. Triberis G.P., X. Zianni, A.N. Yannacopoulos and V.C. Karavolas, J. Phys. Cond. Matter 3, 337-346 (1991).
3452. Trichet L. and J. Rouxel, Mater. Res. Bull. 12, 345-354 (1977).
3453. Trivedi N. and N.W. Ashcroft, Phys. Rev. B 38, 12298-12309 (1988).
3454. Tronstad L., Trans. Faraday Soc. 29, 502-514 (1933).
3455. Trost J., P. Fröbel and K. Bärner, Solid State Commun. 81, 201-205 (1992).
3456. Truong V.-V., Interface (May-June 1986), 15-20.
3457. Truong V.-V., F.G. Girouard and P.V. Ashrit, in Large-area Chromogenics: Materials and Devices for Transmittance Control, edited by C.M. Lampert and C.G. Granqvist (SPIE Opt. Engr. Press, Bellingham, USA, 1990), Vol. IS4, pp. 386-401.
3458. Tsai P.P. and M. Greenblatt, J. Non-Cryst. Solids 103, 101-107 (1988).
3459. Tsang C.C. and D.W. Hess, J. Electrochem. Soc. 131, 115-120 (1984).
3460. Tsikmach P.D., Yu.A. Benders, Ya.Ya. Kleperis and A.R. Lusis, Zh. Tekh. Fiz. 60, 171-175 (1990) [Soviet Phys. Tech. Phys. 35, 852-854 (1990)].
3461. Tsikmach P.D. and A.R. Lusis, Izv. Akad. Nauk Latv. SSR Ser. Fiz. Tekh. Nauk (1985), 61-65.
3462. Tsu R., L. Esaki and R. Ludeke, Phys. Rev. Lett. 23, 977-979 (1969).
3463. Tsuchida E., H. Ohno, K. Tsunemi and N. Kobayashi, Solid State Ionics 11, 227-233 (1983).

3464. Tsuru T. and S. Haruyama, J. Japan. Inst. Met. 40, 1172-1177 (1976).
3465. Tsutsumi H., M. Yamamoto, M. Morita, Y. Matsuda, T. Nakamura and H. Asai, Electrochim. Acta 37, 1183-1186 (1992).
3466. Tsutsumi H., M. Yamamoto, M. Morita, Y. Matsuda, T. Nakamura and H. Asai, J. Power Sources 41, 291-298 (1993).
3467. Tsuyumoto I., A. Kishimoto and T. Kudo, Solid State Ionics 59, 211-216 (1993).
3468. Tsuzuki A., S. Kawakami, M. Awano, T. Sekiya and Y. Torii, Mater. Res. Bull. 23, 327-332 (1988).
3469. Tsygarenko A.A. and V.N. Filimonov, Spectrosc. Lett. 5, 477-487 (1972).
3470. Tubbs M.R., Phys. Stat. Sol. A 21, 253-260 (1974).
3471. Tubbs M.R. and H. Booth, in Proc. Roy. Phys. Soc. Conf. on Non-silver Photographic Processes (Oxford, England, 1973), pp. 181-199.
3472. Tuller H.L., D.P. Button adn D.R. Uhlmann, J. Non-Cryst. Solids 40, 93-118 (1980).
3473. Tunstall D.P., Phys. Rev. B 14, 4735-4736 (1976).
3474. Tuomi D., J. Electrochem. Soc. 112, 1-12 (1965).
3475. Turkovic' A., M. Ivanda, A. Drasner, V. Vranesa and M. Persin, Thin Solid Films 198, 199-205 (1991).
3476. Turkovic' A., M. Ivanda, V. Vranesa and A. Drasner, Vacuum 43, 471-473 (1992).
3477. Turkovic' A. and D. Sokcevic', Appl. Surf. Sci. 68, 477-479 (1993).
3478. Tysyachnyi V.P. and O.S. Ksenzhek, Elektrokhim. 9, 901-904 (1973) [Soviet Electrochem. 9, 864-866 (1973)].
3479. Tysyachnyi V.P., O.S. Ksenzhek and L.M. Pototskaya, Elektrokhim. 8, 1692-1696 (1972) [Soviet Electrochem. 8, 1630-1654 (1972)].
3480. Tytko K.-H. and O. Glemser, in Advances in Inorganic Chemistry and Radiochemistry, edited by H.J. Emeléus and A.G. Sharpe (Academic, New York, 1976), Vol. 19, pp. 239-315.
3481. Tyuliev G. and M. Sokolova, Appl. Surf. Sci. 52, 343-349 (1991).

U

3482. Uchimoto Y., Z. Ogumi and Z. Takehara, Solid State Ionics 40-41, 624-627 (1990).
3483. Uchimoto Y., Z. Ogumi, Z. Takehara and F.R. Foulkes, J. Electrochem. Soc. 137, 35-40 (1990).
3484. Ufert K.-D., Phys. Stat. Solidi A 42, 187-190 (1977).
3485. Ufert K.-D., K. Steenbeck and E. Steinbeiss, Kristall Technik 12, 603-608 (1977).
3486. Uhle N. and J. Windscheif, Phys. Stat. Sol. B 74, K15-K18 (1976).
3487. Uhlenbrock S., C. Scharfschwerdt, M. Neumann, G. Illing and H.-J. Freund, J. Phys. Cond. Matter 4, 7973-7978 (1992).
3488. Unates M.E., M.E. Folquer, J.R. Vilche and A.J. Arvia, J. Electrochem. Soc. 135, 25-31 (1988).
3489. Unates M.E., M.E. Folquer, J.R. Vilche and A.J. Arvia, J. Electrochem. Soc. 139, 2697-2704 (1992).
3490. Unuma H., K. Tonooka, Y. Suzuki, T. Furusaki, K. Kodaira and T. Matsushita, J. Mater. Sci. Lett. 5, 1248-1250 (1986).
3491. Urbach F., Phys. Rev. 92, 1324-1325 (1953).
3492. Ursu I., L. Nanu, M. Dinescu, A. Hening, I.N. Mikhailescu, L.C. Nistor, V.S. Teodorescu, E. Szil, I. Hevesi, J. Kovacs and L. Nanai, Appl. Phys. A 35, 103-108 (1984).

V

3493. Vaivars G., J. Kleperis and A. Lusis, Elektrokhim. 28, 1438-1443 (1992) [Soviet Electrochem. 28, 1176-1180 (1992)].
3494. Vaivars G., J. Kleperis and A. Lusis, Solid State Ionics 61, 317-321 (1993).
3495. Valentini C.R., C.A. Moina, J.R. Vilche and A.J. Arvia, Corrosion Sci. 25, 985-997 (1985).
3496. Valkonen E. and B. Karlsson, Energy Res. 11, 397-403 (1987).
3497. Valkonen E., B. Karlsson and C.-G. Ribbing, Solar Energy 32, 211-222 (1984).
3498. Valkonen E. and C.-G. Ribbing, Mater. Lett. 3, 29-32 (1984).

3499. Valkonen E., C.-G. Ribbing and J.-E. Sundgren, Proc. Soc. Photo-Opt. Instrum. Engr. 652, 235-242 (1986).
3500. Valla B., M.A. Macedo, L.H. Dall'Antonia, J.C.L. Tonazzi, M.A. Aegerter and L.O. Bulhoes, in Proc. III Congresso Internacional Iberoamericano de Ceramica, Vidro e Refratário, Belo Horizonte, Brazil (Associacao Brasileira de Ceramica, 1991), pp. 457-464.
3501. Valla B., J.C.L. Tonazzi, M.A. Macedo, L.H. Dall'Antonia, M.A. Aegerter, M.A.B. Gomez and L.O. Bulhoes, Proc. Soc. Photo-Opt. Instrum. Engr. 1536, 48-62 (1991).
3502. Valletta R.M. and W.A. Pliskin, J. Electrochem. Soc. 114, 944-947 (1967).
3503. van Attekum P.M.T.M., P.H. Woerlee, G.C. Verkade and A.A.M. Hoeben, Phys. Rev. B 29, 645-650 (1984).
3504. Vancea J., Int. J. Mod. Phys. B 3, 1455-1501 (1989).
3505. Vancea J. and H. Hoffmann, Thin Solid Films 92, 219-225 (1982).
3506. Vancea J., H. Hoffmann and K. Kastner, Thin Solid Films 121, 201-216 (1984).
3507. Vancea J., G. Reiss and H. Hoffmann, J. Mater. Sci. Lett. 6, 985-986 (1987).
3508. Van Damme H., M. Letellier, D. Tinet, B. Kihal and R. Erre, Mater. Res. Bull. 19, 1635-1642 (1984).
3509. van de Hulst H.C., Light Scattering by Small Particles (Dover, New York, 1981).
3510. Vandenborre M.T., R. Prost, E. Huard and J. Livage, Mater. Res. Bull. 18, 1133-1142 (1983).
3511. van der Veen J.F., F.J. Himpsel and D.E. Eastman, Phys. Rev. B 22, 4226-4233 (1980).
3512. Vandyshev Yu.V., V.S. Dneprovskii and V.I. Klimov, Pis'ma Zh. Eksp. Teor. Fiz. 53, 301-306 (1991) [JETP Lett. 53, 314-318 (1991)].
3513. van Elp J., H. Eskes, P. Kuiper and G.A. Sawatzky, Phys. Rev. B 45, 1612-1622 (1992).
3514. van Elp J., J.L. Wieland, H. Eskes, P. Kuiper, G.A. Sawatzky, F.M.F. de Groot and T.S. Turner, Phys. Rev. B 44, 6090-6103 (1991).
3515. van Glabbeek J.J. and R.E. van de Leest, Thin Solid Films 201, 137-145 (1991).
3516. Vangrunderbeek J., C. Van Haesendonck, Y. Bruynseraede, P. Vermeiren, C. Winckelmans and R. Leysen, Mater. Res. Bull. 23, 923-930 (1988).
3517. Vanhaelst M. and P. Clauws, Phys. Stat. Sol. B 87, 719-723 (1978).
3518. van Kerkhof J.C., W. Olthuis, P. Bergveld and M. Bos, Sensors Actuators B 3, 129-138 (1991).
3519. Van Mieghem P., Rev. Mod. Phys. 64, 755-793 (1992).
3520. Vashishta P. and K.S. Singwi, Phys. Rev. B 6, 875-887 (1972).
3522. Vas'ko A.T., Yu.S. Krasnov, F.N. Patsyuk and S.M. Chumak, Ukr. Khim. Zh. 51, 152-157 (1985).
3523. Vas'ko N.P., Yu.G. Ptushinskii and B.A. Chuikov, Surf. Sci. 14, 448-456 (1969).
3524. Vasyutinskii N.A., Izv. Akad. Nauk SSSR Neorg. Mater. 22, 2005-2008 (1986) [Inorg. Mater. 22, 1755-1758 (1986)].
3525. Vazquez M.V., R.E. Carbonio and V.A. Macagno, J. Electrochem. Soc. 138, 1874-1876 (1991).
3526. Vazquez M.V., G.F. Darbyshire, R.E. Carbonio and V.A. Macagno, J. Power Sources 25, 75-86 (1989).
3527. Veggetti E., I.M. Kodintsev and S. Trasatti, J. Electroanal. Chem. 339, 255-268 (1992).
3528. Verleur H.W., A.S. Barker, Jr., and C.N. Berglund, Phys. Rev. 172, 788-798 (1968).
3529. Vermilyea D.A., J. Phys. Chem. Solids 26, 133-141 (1965).
3530. Vértes A. and R. Schiller, J. Appl. Phys. 54, 199-203 (1983).
3531. Vetelino J., R.K. Lade and R.S. Falconer, IEE Trans. UFFC 34, 156-161 (1987).
3532. Viennet R., J.-P. Randin and I.D. Raistrick, J. Electrochem. Soc. 129, 2451-2453 (1982).
3533. Viguié J.C. and J. Spitz, J. Electrochem. Soc. 122, 585-588 (1975).
3534. Vilche J.R. and A.J. Arvia, in Passivity of Metals, edited by R.P. Frankenthal and J. Kruger (The Electrochem. Soc., Princeton, 1978), pp. 861-877.
3535. Vilche J.R. and A.J. Arvia, in The Nickel Electrode, edited by R.G. Gunther and S. Gross (The Electrochem. Soc., Pennington, 1982), pp. 17-47.
3536. Villachon-Renard Y., G. Leveque, A. Abdellaoui and A. Donnadieu, Thin Solid Films 203, 33-39 (1991).
3537. Vincent C.A., in Electrochemical Science and Technology of Polymers - 2, edited by R.G. Linford (Elsevier Appl. Sci., London, 1990), pp. 47-96.
3538. Visco S.J., M. Liu, M.M. Doeff, Y.P. Ma, C. Lampert and L.C. De Jonghe, Solid State Ionics 60, 175-187 (1993).
3539. Visintin A., A.C. Chialvo, W.E. Triaca and A.J. Arvia, J. Electroanal. Chem. 225, 227-239 (1987).

3540. Visscher W. and E. Barendrecht, Electrochim. Acta 25, 651-655 (1980).
3541. Visscher W. and E. Barendrecht, J. Electroanal. Chem. 154, 69-80 (1983).
3542. Visscher W. and E. Barendrecht, Surf. Sci. 135, 436-452 (1983).
3543. Viswanathan K., K. Brandt and E. Salje, J. Solid State Chem. 36, 45-51 (1981).
3544. Vitin'sh A., T.Ya. Safonova and O.A. Petrii, Elektrokhim. 26, 614-623 (1990) [Soviet Electrochem. 26, 548-556 (1990)].
3545. Vlieger J. and D. Bedeaux, Thin Solid Films 69, 107-130 (1980).
3546. Volynskii V.A. and Yu.N. Chernykh, Elektrokhim. 13, 1070-1074 (1977) [Soviet Electrochem. 13, 909-912 (1977)].
3547. Volynskii V.A. and Yu.N. Chernykh, Elektrokhim. 13, 1874-1877 (1977) [Soviet Electrochem. 13, 1619-1621 (1977)].
3548. von Alpen U., A. Rabenau and G.H. Talat, Appl. Phys. Lett. 30, 621-623 (1977).
3549. Vondrák J., I. Jukubec and J. Bludská, J. Power Sources 43-44, 547-550 (1993).
3550. Vondrák J., J. Bludská and I. Jakubec, Electrochim. Acta 37, 603-606 (1992).
3551. Vossen J.L., in Physics of Thin Films, edited by G. Hass, M.H. Francombe and R.W. Hoffman (Academic, New York, 1977), Vol. 9, pp. 1-71.
3552. Vukovic' M., J. Appl. Electrochem. 17, 737-745 (1987).
3553. Vukovic' M., J. Appl. Electrochem. 20, 969-973 (1990).
3554. Vukovic' M. and D. Cukman, J. Electroanal. Chem. 333, 195-203 (1992).
3555. Vukovic' M., D. Cukman, M. Milun, L.D. Atanasoska and R.T. Atanasoski, J. Electroanal. Chem. 330, 663-673 (1992).

W

3556. Wagner C.D., J. Vac. Sci. Technol. 15, 518-523 (1978).
3557. Wagner C.D., W.M. Riggs, L.E. Davis, J.F. Moulder and G.E. Muilenberg, Handbook of X-ray Photoelectron Spectroscopy (Perkin-Elmer Corp., Eden Prairie, 1979).
3558. Wagner H. and W. Beyer, Solid State Commun. 48, 585-587 (1983).
3559. Wagner H.J., P. Driessen and C.F. Schwerdtfeger, J. Non-Cryst. Solids 34, 335-338 (1979).
3560. Wagner W., F. Rauch and K. Bange, Fresenius Z. Anal. Chem. 333, 478-480 (1989).
3561. Wagner W., F. Rauch and K. Bange, Proc. 63. Glastechn. Tagung, Stuttgart, May 1989 (Deutsche Glastechn. Gesell.), pp. 206-209.
3562. Wagner W., F. Rauch, C. Ottermann and K. Bange, Nucl. Instrum. Meth. Phys. Res. B 50, 27-30 (1990).
3563. Wagner W., F. Rauch, C. Ottermann and K. Bange, Surf. Interface Anal. 16, 331-334 (1990).
3564. Wagner W., F. Rauch, C. Ottermann and K. Bange, Nucl. Instrum. Meth. Phys. Res. B 68, 262-265 (1992).
3565. Wahid P.F., K.B. Sundaram and P.J. Sisk, Opt. Laser Technol. 24, 263-266 (1992).
3566. Walck S. and A.D. Buonaquisti, J. Vac. Sci. Technol. A 3, 2214-2215 (1985).
3567. Walk C.R., in Lithium Batteries, edited by J.P. Gabano (Academic, New York, 1983), pp. 265-280.
3568. Walter U., R.E. Thomson, B. Burk, M.F. Crommie, A. Zettl and J. Clarke, Phys. Rev. B 45, 11474-11480 (1992).
3569. Wang B., S.P. Szu and M. Greenblatt, J. Non-Cryst. Solids 134, 249-258 (1991).
3570. Wang B., S. Szu, M. Greenblatt and L.C. Klein, Chem. Mater. (1992), 191-197.
3571. Wang J.C., Solid State Ionics 28-30, 1436-1440 (1988).
3572. Wang J.-S., Proc. Cambridge Philos. Soc. 32, 657-662 (1936).
3573. Wang Y. and N. Herron, Phys. Rev. B 42, 7253-7255 (1990).
3574. Wang Y. and N. Herron, J. Chem. Phys. 95, 525-532 (1991).
3575. Wang Y., A. Suna, W. Mahler and R. Kasowski, J. Chem. Phys. 87, 7315-7322 (1987).
3576. Warburg E., Ann. Phys. Chem. 67, 493-499 (1899).
3577. Ward L., The Optical Constants of Bulk Materials and Films (Hilger, Bristol, 1988).
3578. Watanabe M., Y. Koike, T. Yoshimura and K. Kiyota, Japan Display 1983, pp. 372-375.
3579. Watanabe M. and N. Ogata, in Polymer Electrolyte Reviews - 1, edited by J.R. MacCallum and C.A. Vincent (Elsevier Appl. Sci., London, 1987), pp. 39-68.

3580. Watanabe M., M. Rikukawa, K. Sanui, N. Ogata, H. Kato, T. Kobayashi and Z. Ohtaki, Macromol. 17, 2902-2908 (1984).
3581. Watanabe M., M. Togo, K. Sanui, N. Ogata, T. Kobayashi and Z. Ohtaki, Macromol. 17, 2908-2912 (1984).
3582. Watson J., K. Ihokura and G.S.V. Coles, Measurement Sci. Technol. 4, 711-719 (1993).
3583. Weaver J.H. and D.W. Lynch, Phys. Rev. B 6, 3620-3623 (1972).
3584. Weber M.F., L.C. Schumacher and M.J. Dignam, J. Electrochem. Soc. 129, 2022-2028 (1982).
3585. Webman I., J. Jortner and M.H. Cohen, Phys. Rev. B 11, 2885-2892 (1975).
3586. Webman I., J. Jortner and M.H. Cohen, Phys. Rev. B 13, 713-724 (1976).
3587. Wechter M.A., H.R. Shanks and A.F. Voigt, Inorg. Chem. 7, 845-846 (1968).
3588. Wei G., T.E. Haas and R.B. Goldner, in Electrochromic Materials, edited by M.K. Carpenter and D.A. Corrigan (The Electrochem. Soc., Pennington, 1990), Proc. Vol. 90-2, pp. 80-88.
3589. Wei G., T.E. Haas and R.B. Goldner, Solid State Ionics 58, 115-122 (1992).
3590. Weibel G.E., in Nonemissive Electrooptic Displays, edited by A.R. Kmetz and F.K. von Willisen (Plenum, New York, 1976), pp. 196-200.
3591. Weininger J.L. and M.W. Breiter, J. Electrochem. Soc. 110, 484-450 (1963).
3592. Weininger J.L. and M.W. Breiter, J. Electrochem. Soc. 111, 707-712 (1964).
3593. Weller H., Ber. Bunsenges. Phys. Chem. 95, 1361-1365 (1991).
3594. Weller H., Adv. Mater. 5, 88-95 (1993).
3595. Weller H., Angew. Chem. Int. Ed. 32, 41-53 (1993).
3596. Weller H., Ber. Bunsenges. Phys. Chem. 97, 630-635 (1993).
3597. Weller M.T. and P.G. Dickens, Solid State Ionics 18-19, 1081-1086 (1983).
3598. Wells A.F., Structural Inorganic Chemistry, 5th ed. (Clarendon Press, Oxford, 1984).
3599. Weltner W., Jr., and D. McLeod, Jr., J. Mol. Struct. 17, 276-299 (1965).
3600. Wemple S.H., J. Chem. Phys. 67, 2151-2168 (1977).
3601. Wemple S.H. and M. Di Domenico, Jr., Phys. Rev. B 3, 1338-1351 (1971).
3602. Wen S.J., G. Campet, J. Portier, G. Couturier and J.B. Goodenough, Mater. Sci. Engr. B 14, 115-119 (1992).
3603. Wen T.-C. and C.-C. Hu, J. Electrochem. Soc. 139, 2158-2163 (1992).
3604. Weppner W. and R.A. Huggins, J. Electrochem. Soc. 124, 35-38 (1977).
3605. Wernick S. and R. Pinner, The Surface Treatment and Finishing of Aluminium and Its Alloys, 4th edition (Robert Draper, Teddington, 1972).
3606. Wertheim G.K., M. Campagna, J.-N. Chazalviel, D.N.E. Buchanan and H.R. Shanks, Appl. Phys. 13, 225-230 (1977).
3607. Wertheim G.K. and H. J. Guggenheim, Phys. Rev. B 22, 4680-4683 (1980).
3608. West A.R., J. Mater. Chem. 1, 157-162 (1991).
3609. West K., B. Zachau-Christiansen, T. Jacobsen and S. Atlung, J. Power Sources 14, 235-245 (1985).
3610. West K., B. Zachau-Christiansen, T. Jacobsen and S. Skaarup, Solid State Ionics 28-30, 1128-1131 (1988).
3611. West K., B. Zachau-Christiansen, T. Jacobsen and S. Skaarup, Electrochim. Acta 38, 1215-1220 (1993).
3612. West K., B. Zachau-Christiansen, T. Jacobsen and S. Skaarup, J. Power Sources 43-44, 127-134 (1993).
3613. West K., B. Zachau-Christiansen, T. Jacobsen and S. Skaarup, Mater. Res. Soc. Symp. Proc. 293, 39-47 (1993).
3614. West K., B. Zachau-Christiansen, M.J.L Østergård and T. Jacobsen, J. Power Sources 20, 165-172 (1987).
3615. West K., B. Zachau-Christiansen, S. Skaarup and T. Jacobsen, Solid State Ionics 53-56, 356-363 (1992).
3616. West K., B. Zachau-Christiansen, S.V. Skaarup and F.W. Poulsen, Solid State Ionics 57, 41-47 (1992).
3617. Westwood W.D., in Physics of Thin Films, edited by M.H. Francombe and J.L. Vossen (Academic, New York, 1989), Vol. 14, pp. 1-79.
3618. Westwood W.D., R.J. Boynton and S.J. Ingrey, J. Vac. Sci. Technol. 11, 381-384 (1974).
3619. White W.B. and V.G. Keramidas, Spectrochim. Acta A 28, 501-509 (1972).
3620. Whittingham M.S., J. Electrochem. Soc. 122, 713-714 (1978).
3621. Whittingham M.S., in Solid State Ionic Devices, edited by B.V.R. Chowdari and S. Radhakrishna (World Scientific, Singapore, 1988), pp. 325-340.

3622. Whittingham M.S. and M.B. Dines, J. Electrochem. Soc. 124, 1387-1388 (1977).
3622a. Whittingham M.S. and A.J. Jacobson, editors, Intercalation Chemistry (Academic, New York, 1982).
3623. Wicaksana D., A. Kobayashi and A. Kinbara, J. Vac. Sci. Technol. A 10, 1479-1482 (1992).
3624. Wieczorek W., K. Such, H. Wycislik and J. Plocharski, Solid State Ionics 36, 255-257 (1989).
3625. Wiesener K., W. Schneider, D. Ilic, E. Steger, K.H. Hallmeier and E. Brackmann, J. Power Sources 20, 157-164 (1987).
3626. Wilcox P.S. and W.D. Westwood, Can. J. Phys. 49, 1543-1548 (1971).
3627. Wiles D.B. and R.A. Young, J. Appl. Crystallogr. 14, 149-151 (1981).
3628. Wilhelm S.M. and N. Hackerman, J. Electrochem. Soc. 128, 1668-1674 (1981).
3629. Wilhelmi K.-A., Acta Chem. Scand. 12, 1965-1976 (1958).
3630. Wilhelmi K.-A., Chem. Commun. (1966), 437-439.
3631. Wilhelmi K.-A., Ark. Kemi 26, 131-139 (1966).
3632. Wilhelmi K.-A., Ark. Kemi 26, 141-147 (1966).
3633. Wilhelmi K.-A., Acta Chem. Scand. 22, 2565-2573 (1968).
3634. Wilhelmi K.-A., K. Waltersson and L. Kihlborg, Acta Chem. Scand. 25, 2675-2687 (1971).
3635. Willems H., A.G.C. Kobussen, J.H.W. de Wit and G.H.J. Broers, J. Electroanal. Chem. 170, 227-242 (1984).
3636. Willems H., A.G.C. Kobussen, I.C. Vinke, J.H.W. de Wit and G.H.J. Broers, J. Electroanal. Chem. 194, 287-303 (1985).
3637. Williams C.C., J.G. Ekerdt, J.-M. Jehng, F.D. Hardcastle, A.M. Turek and I.E. Wachs, J. Phys. Chem. 95, 8781-8791 (1991).
3638. Williams C.C., J.G. Ekerdt, J.-M. Jehng, F.D. Hardcastle and I.E. Wachs, J. Phys. Chem. 95, 8791-8797 (1991).
3639. Wilson J.A. and A.D. Yoffe, Adv. Phys. 18, 193-335 (1969).
3640. Wind M.M., P.A. Bobbert, J. Vlieger and D. Bedeaux, Physica (Utrecht) A 143, 164-182 (1987).
3641. Wind M.M., P.A. Bobbert, J. Vlieger and D. Bedeaux, Thin Solid Films 164, 57-62 (1988).
3642. Wind M.M., J. Vlieger and D. Bedeaux, Physica (Utrecht) A 141, 33-57 (1987).
3643. Wiseman P.J. and P.G. Dickens, J. Solid State Chem. 6, 374-377 (1973).
3644. Wittrig T.W., D.E. Ibbotson and W. M. Weinberg, Surf. Sci. 102, 506-517 (1981).
3645. Wittwer V., O.F. Schirmer and P. Schlotter, Solid State Commun. 25, 977-980 (1978).
3646. Witzke H. and S.K. Deb, J. Electronic Mater. 6, 748-749 (1977).
3647. Wixwat W., J.R. Stevens, A.M. Andersson and C.G. Granqvist, in Second International Symposium on Polymer Electrolytes (Elsevier Appl. Sci., London, 1990), pp. 461-465.
3648. Wöhler F., Ann. Phys. 2, 350-358 (1824).
3649. Wold A. and K. Dwight, in Adv. Synthesis and Reactivity of Solids (JAI Press, 1991), pp. 133-171.
3650. Wolf J.F., L.-S.R. Yeh and A. Damjanovic, Electrochim. Acta 26, 409-416 (1981).
3651. Wolf J.F., L.-S.R. Yeh and A. Damjanovic, Electrochim. Acta 26, 811-817 (1981).
3652. Wolfram T., Phys. Rev. Lett. 29, 1383-1387 (1972).
3653. Wolfram T. and S. Ellialtioglu, Phys. Rev. B 19, 43-46 (1979).
3654. Wolfram T. and S. Ellialtioglu, Phys. Rev. B 25, 2697-2714 (1981).
3655. Wolfram T., E.A. Kraut and F.J. Morin, Phys. Rev. B 7, 1677-1694 (1973).
3656. Wolfram T. and L. Sutcu, Phys. Rev. B 31, 7680-7687 (1985).
3657. Wood D.L. and J. Tauc, Phys. Rev. B 5, 3144-3151 (1972).
3658. Wooten F., Optical Properties of Solids (Academic, New York, 1972).
3659. Wright A.C., Philos. Mag. B 50, L23-L28 (1984).
3660. Wright P.V., J. Macromol. Sci. Chem. A 26, 519-550 (1989).
3661. Wronkowska A.A., Surf. Sci. 214, 507-522 (1989).
3662. Wruck D.A., Electrochromism in Nickel Oxide Films, Ph.D. Thesis (University of California, Berkeley, 1991), unpublished.
3663. Wruck D.A., M.A. Dixon, M. Rubin and S.N. Bogy, J. Vac. Sci. Technol. A9, 2170-2173 (1991).
3664. Wruck D.A., S. Ramamurthi and M. Rubin, Thin Solid Films 182, 79-85 (1989).
3665. Wruck D.A. and M. Rubin, J. Electrochem. Soc. 140, 1097-1104 (1993).

3666. Wu C.G., M.G. Kanatzidis, H.O. Marcy, D.C. DeGroot and C.R. Kannewurf, Polymer Mater. Sci. Engr. 61, 969-973 (1989).
3667. Wu L.C. and J.E. Greene, J. Appl. Phys. 50, 4966-4971 (1979).
3668. Wycoff R.W.G., Crystal Structures, Second edition (Wiley, New York, 1964).
3669. Wyss H.R. and M. Falk, Can. J. Chem. 48, 607-614 (1970).
3670. Wyszecki G., in Handbook of Optics, edited by W.G. Driscoll and W. Vaughan (McGraw-Hill, New York, 1978), Sec. 9.
3671. Wyszecki G. and W.S. Stiles, Color Science, Second edition (Wiley, New York, 1982).

X

3672. Xia D.W., D. Soltz and J. Smid, Solid State Ionics 14, 221-224 (1984).
3673. Xidis A. and V.D. Neff, J. Electrochem. Soc. 138, 3637-3642 (1991).
3674. Xu G. and L. Chen, Solid State Ionics 28-30, 1726-1728 (1988).
3675. Xu Q. and G. Wan, J. Power Sources 41, 315-320 (1993).
3676. Xu W.W., R. Kershaw, K. Dwight and A. Wold, Mater. Res. Bull. 25, 1384-1392 (1990).
3677. Xu Y., J. Salardenne, S. Wen, G. Campet, T. Buffeteau and B. Desbat, ISSI Lett. 3, 7-8 (1992).
3678. Xu Z., J.F. Vetelino and D.C. Parker, J. Vac. Sci. Technol. A 8, 3634-3638 (1990).

Y

3679. Yafaev N.R., N.S. Garif'yanov and Yu.V. Yablokov, Fiz. Tverd. Tela 5, 1673-1677 (1963) [Soviet Phys. Solid State 5, 1216-1219 (1963)].
3680. Yagil Y. and G. Deutscher, Appl. Phys. Lett. 52, 373-374 (1988).
3681. Yagil Y., P. Gadenne, C. Julien and G. Deutscher, Phys. Rev. B 46, 2503-2511 (1992).
3682. Yagil Y., M. Yosefin, D.J. Bergman, G. Deutscher and P. Gadenne, Phys. Rev. B 43, 11342-11352 (1991).
3683. Yagoubi B. and C.A. Hogarth, J. Mater. Sci. 28, 239-242 (1993).
3684. Yahalom J. and J. Zahavi, Electrochim. Acta 15, 1429-1435 (1970).
3685. Yamada S., Y. Hiruta, N. Suzuki, K. Urabe, M. Kitao and K. Toyoda, Japan. J. Appl. Phys. Suppl. 24-3, 142-144 (1985).
3686. Yamada S. and M. Kitao, in Large-area Chromogenics: Materials and Devices for Transmittance Control, edited by C.M. Lampert and C.G. Granqvist (SPIE Opt. Engr. Press, Bellingham, 1990), Vol. IS4, pp. 246-259.
3687. Yamada S., T. Nakamura, Y. Hiruta, K. Urabe and M. Kitao, Japan. J. Appl. Phys. 22, 789-793 (1983).
3688. Yamada S., S. Yoshida and M. Kitao, Solid State Ionics 40-41, 487-490 (1990).
3689. Yamada S., T. Yoshioka, M. Miyashita, K. Urabe and M. Kitao, J. Appl. Phys. 63, 2116-2119 (1988).
3690. Yamada S., T. Yoshioka, M. Miyashita, K. Urabe and M. Kitao, Proc. Soc. Photo-Opt. Instrum. Engr. 1016, 34-40 (1988).
3691. Yamagishi K. and Y. Tarui, Japan. J. Appl. Phys. 25, L306-L308 (1986).
3692. Yamaguchi O., D. Tomihisa, H. Kawabata and K. Shimizu, J. Am. Ceram. Soc. 70, C94-C96 (1987).
3693. Yamaguchi S., K. Terabe, Y. Iguchi and A. Imai, Solid State Ionics 25, 171-176 (1987).
3694. Yamamoto N., T. Ohsaka, T. Terashima and N. Oyama, J. Electroanal. Chem. Interfacial Electrochem. 296, 463-472 (1990).
3695. Yamamoto O., Y. Takeda, R. Kanno, Y. Oyabe and Y. Shinya, J. Power Sources 20, 151-156 (1987).
3696. Yamamoto O., Y. Takeda, R. Kanno and K. Tone, in Materials for Solid State Batteries, edited by B.V.R. Chowdari and S. Radhakrishna (World Scientific, Singapore, 1986), pp. 475-479.
3697. Yamamoto S., T. Yamanaka and Z. Ueda, J. Vac. Sci. Technol. A 5, 1952-1955 (1987).
3698. Yamanaka K., Japan. J. Appl. Phys. 19, L517-L518 (1980).
3699. Yamanaka K., Japan. J. Appl. Phys. 20, L307-L308 (1981).
3700. Yamanaka K., Japan. J. Appl. Phys. 21, 926-929 (1982).
3701. Yamanaka K., Japan. J. Appl. Phys. 21, 1108 (1982).

3702. Yamanaka K., J. Appl. Phys. 54, 1128-1132 (1983).
3703. Yamanaka K., Japan. J. Appl. Phys. 25, 1073-1077 (1986).
3704. Yamanaka K., Japan. J. Appl. Phys. 26, 1884-1890 (1987).
3705. Yamanaka K., Japan. J. Appl. Phys. 28, 632-637 (1989).
3706. Yamanaka K., Japan. J. Appl. Phys. 30, 1285-1289 (1991).
3707. Yamanaka K., H. Oakamoto, H. Kidou and T. Kudo, Japan. J. Appl. Phys. 25, 1420-1426 (1986).
3708. Yamanaka S., M. Ohashi, M. Sumihara and M. Hattori, Chem. Lett. (1984), 1403-1406.
3709. Yamase T., M. Matsuzawa and Y. Sasaki, Inorg. Chim. Acta 127, L9-L12 (1987).
3710. Yamase T., Y. Sasaki and T. Motowaki, Inorg. Chim. Acta 121, L19-L22 (1986).
3711. Yampol'skii V.I. and A.A. Mal'tsev, Zh. Neorg. Khim. 15, 1998-1999 (1970) [Russian J. Inorg. Chem. 15, 1029-1030 (1970)].
3712. Yang H.-X., X.-P. Ai, M. Lei and S.-X. Li, J. Power Sources 43-44, 399-403 (1993).
3713. Yang S.C., in Large-area Chromogenics: Materials and Devices for Transmittance Control, edited by C.M. Lampert and C.G. Granqvist (SPIE Opt. Engr. Press, Bellingham, 1990), Vol. IS4, pp. 335-365.
3714. Yano Y., N. Kinugasa, H. Yoshida, K. Fujino and H. Kawahara, in Electrochromic Materials, edited by M.K. Carpenter and D.A. Corrigan (The Electrochem. Soc., Pennington, 1990), Proc. Vol. 90-2, pp. 125-136.
3715. Yanovskaya M.I., I.E. Obvintseva, V.G. Kessler, B.Sh. Galyamov, S.I. Kucheiko, R.R. Shifrina and N.Ya. Turova, J. Non-Cryst. Solids 124, 155-166 (1990).
3716. Yao J.N., K. Hashimoto and A. Fujishima, Nature 355, 624-626 (1992).
3717. Yao J.N., B.H. Loo and A. Fujishima, Ber. Bunsenges. Phys. Chem. 94, 13-17 (1990).
3718. Yao J.N., B.H. Loo, K. Hashimoto and A. Fujishima, J. Electroanal. Chem. 290, 263-267 (1990).
3719. Yao J.N., B.H. Loo, K. Hashimoto and A. Fujishima, Ber. Bunsenges. Phys. Chem. 95, 554-556 (1991).
3720. Yao J.N., B.H. Loo, K. Hashimoto and A. Fujishima, Ber. Bunsenges. Phys. Chem. 95, 557-559 (1991).
3721. Yao J.N., B.H. Loo, K. Hashimoto and A. Fujishima, Ber. Bunsenges. Phys. Chem. 96, 699-701 (1992).
3722. Yao T., Y. Oka and N. Yamamoto, J. Mater. Chem. 2, 331-336 (1992).
3723. Yao T., Y. Oka and N. Yamamoto, J. Mater. Chem. 2, 337-340 (1992).
3724. Yao T., Y. Oka and N. Yamamoto, Mater. Res. Bull. 27, 669-675 (1992).
3725. Yao Y.F. and J.T. Kummer, J. Inorg. Nucl. Chem. 29, 2453-2474 (1967).
3726. Yataev N.R., N.S. Garif'yanov and Yu.V. Yablokov, Fiz. Tverd. Tela 5, 1673-1677 (1963) [Soviet Phys. Solid State 5, 1216-1219 (1963)].
3727. Yazami R. and T. Nakajima, Synth. Met. 40, 387-392 (1991).
3728. Yazami R., T. Nakajima, J.L. Hodeau and T. Fournier, Mater. Sci. Forum 91-93, 29-34 (1992).
3729. Yee K.K. and L. Young, Appl. Opt. 14, 1316-1321 (1975).
3730. Yoldas B.E. and I.K. Lloyd, Mater. Res. Bull. 18, 1171-1177 (1983).
3731. Yoldas B.E. and D.P. Partlow, Bull. Am. Ceram. Soc. 59, 640-642 (1980).
3732. Yoldas B.E. and D.P. Partlow, Appl. Opt. 23, 1418-1424 (1984).
3733. Yoneyama H. and Y. Shoji, J. Electrochem. Soc. 137, 3826-3830 (1990).
3734. Yoneyama H., N. Takahashi and S. Kuwabata, J. Chem. Soc. Chem. Commun. (1992), 716-717.
3735. Yoshida S., Appl. Opt. 17, 145-150 (1978).
3736. Yoshida T., K. Okabayashi, T. Asaoka and K. Abe, J. Electrochem. Soc. 135, C370 (1988).
3737. Yoshiike N., M. Ayusawa and S. Kondo, J. Electrochem. Soc. 131, 2600-2605 (1984).
3738. Yoshiike N. and S. Kondo, J. Electrochem. Soc. 130, 2283-2287 (1983).
3739. Yoshiike N. and S. Kondo, J. Electrochem. Soc. 131, 809-812 (1984).
3740. Yoshiike N. and S. Kondo, Denki Kagaku 54, 423-430 (1986).
3741. Yoshiike N., Y. Mizuno and S. Kondo, J. Electrochem. Soc. 131, 2634-2641 (1984).
3741a. Yoshimura K., M. Tazawa and S. Tanemura, in Proc. ISES Congr. on Passive Strategies and Materials (Pergamon, New York, 1991), pp. 2859-2863.
3742. Yoshimura T., J. Appl. Phys. 57, 911-919 (1985).
3743. Yoshimura T., M. Watanabe, K. Kiyota and M. Tanaka, Japan. J. Appl. Phys. 21, 128-132 (1982).
3744. Yoshimura T., M. Watanabe, Y. Koike, K. Kiyota and M. Tanaka, J. Appl. Phys. 53, 7314-7320 (1982).
3745. Yoshimura T., M. Watanabe, Y. Koike, K. Kiyota and M. Tanaka, Japan. J. Appl. Phys. 22, 152-156 (1983).

3746. Yoshimura T., M. Watanabe, Y. Koike, K. Kiyota and M. Tanaka, Japan. J. Appl. Phys. 22, 157-160 (1983).
3747. Yoshimura T., M. Watanabe, Y. Koike, K. Kiyota and M. Tanaka, Thin Solid Films 101, 141-151 (1983).
3748. Yoshino T. and N. Baba, Nippon Kagaku Kaishi (1983), 955-957.
3749. Yoshino T., N. Baba and K. Arai, Japan. J. Appl. Phys. 26, 1547-1549 (1987).
3750. Yoshino T., N. Baba and Y. Kouda, Hyomen Kagaku [J. Surf. Sci. Soc. Japan] 6, 198-205 (1985).
3751. Yoshino T., N. Baba and Y. Kouda, Japan. J. Appl. Phys. 26, 782-783 (1987).
3752. Yoshino T., N. Baba, H. Masuda and K. Arai, in Electrochromic Materials, edited by M.K. Carpenter and D.A. Corrigan (The Electrochem. Soc., Pennington, 1990), Proc. Vol. 90-2, pp. 89-98.
3753. Yoshino T., N. Baba and S. Watanabe, Hyomen Gijutsu 40, 840-844 (1989).
3754. Yoshino T., N. Baba and K. Yasuda, Nippon Kagaku Kaishi (1988), 1525-1529.
3755. Yoshino T., J.-I. Fukawa and N. Baba, Hyomen Kagaku [J. Surf. Sci. Soc. Japan] 7, 480-486 (1986).
3756. Yoshio M., H. Tanaka, K. Tominaga and H. Noguchi, J. Power Sources 40, 347-353 (1992).
3757. Young E.W.A., J.H. Gerretsen and J.H.W. de Wit, J. Electrochem. Soc. 134, 2257-2260 (1987).
3758. Young L. and F.G.R. Zobel, J. Electrochem. Soc. 113, 277-284 (1966).
3759. Yous B., S. Robin, A. Donnadieu, G. Dufour, C. Maillot, M. Roulet and C. Senemaud, Mater. Res. Bull. 19, 1349-1354 (1984).
3760. Yu P.C., Characterization of Indium Sesquioxide and Niobium Pentoxide for the Application as Counter-electrode in an Electrochromic Window, Ph. D. Thesis, (Tufts University, USA, 1991), unpublished.
3761. Yu P.C., T.E. Haas, R.B. Goldner and S.F. Cogan, Mater. Res. Soc. Symp. Proc. 210, 63-68 (1991).
3762. Yu P.C. and C.M. Lampert, Proc. Soc. Photo-Opt. Instrum. Engr. 823, 113-123 (1987).
3763. Yu P.C. and C.M. Lampert, Solar Energy Mater. 19, 1-16 (1989).
3764. Yu P.C., G. Nazri and C.M. Lampert, Proc. Soc. Photo-Opt. Instrum. Engr. 653, 16-24 (1986).
3765. Yu P.C., G. Nazri and C.M. Lampert, Solar Energy Mater. 16, 1-17 (1987).
3766. Yu S.-Q., Chinese Sci. Bull. 35, 627-631 (1990).
3767. Yuan Y.F. and O.S. Heavens, Thin Solid Films 217, 138-145 (1992).
3768. Yuan Y.F. and O.S. Heavens, Appl. Surf. Sci. 65-66, 252-256 (1993).
3769. Yuan Z., R.J. Phuddephatt and M. Sayer, Chem. Mater. 5, 908-910 (1993).
3770. Yuancheng L., P. Xiaoren, X. Sujiang, Z. Dechun and L. Yongmei, Vacuum 43, 1075-1077 (1992).
3771. Yuancheng L., P. Xiaoren, Z. Yihua, Y. Xuemei and W. Quansheng, Vacuum 43, 1071-1073 (1992).
3772. Yuen M.F., I. Lauks and W.C. Dautremont-Smith, Solid State Ionics 11, 19-29 (1983).
3773. Yurkinskii V.P., E.G. Firsova and A.G. Morachevskii, Zh. Prikl. Khim. 57, 1380-1382 (1984) [J. Appl. Chem. USSR 57, 1281-1282 (1984)].
3774. Yurkinskii V.P., E.G. Firsova and A.G. Morachevskii, Elektrokhim. 22, 370-373 (1986) [Soviet Electrochem. 22, 339-342 (1986)].
3775. Yurkinskii V.P., E.G. Firsova and A.G. Morachevskii, Zh. Prikl. Khim. 60, 2103-2105 (1987) [J. Appl. Chem. USSR 60, 1944-1946 (1987)].
3776. Yurkinskii V.P., E.G. Firsova, A.G. Morachevskii and I.N. Galitskii, Zh. Prikl. Khim. 57, 518-522 (1984) [J. Appl. Chem. USSR 57, 476-479 (1984)].
3777. Yurkinskii V.P., E.G. Firsova, A.G. Morachevskii and A.A. Maiorov, Zh. Prikl. Khim. 57, 695-698 (1984) [J. Appl. Chem. USSR 57, 642-645 (1984)].
3778. Yurkinskii V.P., V.M. Muzdhab, M.A. Sidorova and A.G. Morachevskii, Elektrokhim. 23, 298-301 (1987) [Soviet Electrochem. 23, 276-279 (1987)].

Z

3779. Zaanen J. and G.A. Sawatzky, J. Solid State Chem. 88, 2-27 (1990).
3780. Zachau-Christiansen B., K. West and T. Jacobsen, Solid State Ionics 9-10, 399-404 (1983).
3781. Zachau-Christiansen B., K. West and T. Jacobsen, Mater. Res. Bull. 20, 485-492 (1985).
3782. Zaki M.I. and C. Kappenstein, Z. Phys. Chem. 176, 97-116 (1992).
3783. Zakis Y.R., A.R. Lusis and Y.L. Lagzdons, J. Non-Cryst. Solids 47, 267-269 (1982).

3784. Zakroczymski T., C.-J. Fan and Z. Szklarska-Smialowska, J. Electrochem. Soc. 132, 2862-2867 (1985).
3785. Zakroczymski T., C.-J. Fan and Z. Szklarska-Smialowska, J. Electrochem. Soc. 132, 2868-2871 (1985).
3786. Zallen R., The Physics of Amorphous Solids (Wiley, New York, 1983).
3787. Zamin M. and M.B. Ives, J. Electrochem. Soc. 126, 470-474 (1979).
3788. Zane D., F. Decker and G. Razzini, Electrochim. Acta 38, 37-42 (1993).
3789. Zelaya-Angel O., C. Menezes, F. Sánchez-Sinencio and G.F.L. Ferreira, J. Appl. Phys. 51, 6022-6026 (1980).
3790. Zeller H.R., in Nonemissive Electrooptic Displays, edited by A.R. Kmetz and F.K. von Willisen (Plenum, New York, 1976), pp. 149-154.
3791. Zeller H.R. and H.U. Beyeler, Appl. Phys. 13, 231-237 (1977).
3792. Zerbino J.O., M.R. de Tacconi and A.J. Arvia, J.Electrochem. Soc. 125, 1266-1276 (1978).
3793. Zhang J. and K. Colbow, Appl. Phys. Lett. 58, 1013-1014 (1991).
3794. Zhang J., J.F. Ma, S.E. Nagler and S.E. Brown, Phys. Rev. Lett. 70, 3095-3098 (1993).
3795. Zhang J., S.A. Wessel and K. Colbow, Thin Solid Films 185, 265-277 (1990).
3796. Zhang J.G. and P.C. Eklund, J. Appl. Phys. 64, 729-733 (1988).
3797. Zhang J.G. and P.C. Eklund, J. Mater. Res. 8, 558-564 (1993).
3798. Zhang L. and K.S. Goto, Thin Solid Films 161, 67-75 (1988).
3799. Zhang L. and K.S. Goto, in Electrochromic Materials, edited by M.K. Carpenter and D.A. Corrigan (The Electrochem. Soc., Pennington, 1990), Proc. Vol. 90-2, pp. 23-29.
3800. Zhang S., Y.F. Zhu and D.E. Brodie, Thin Solid Films 213, 265-270 (1992).
3801. Zhang Y., J.K. Bailey, C.J. Brinker, N. Raman, R.M. Crooks and C.S. Ashley, Proc. Soc. Photo-Opt. Instrum. Engr. 1758, 596-603 (1992).
3802. Zhang Y., N. Raman, J.K. Bailey, C.J. Brinker and R.M. Crooks, J. Phys. Chem. 96, 9098-9100 (1992).
3803. Zhecheva E., R. Stoyanova and S. Angelov, Mater. Chem. Phys. 25, 351-360 (1990).
3804. Zhecheva E., R. Stoyanova and S. Angelov, Mater. Chem. Phys. 25, 361-373 (1990).
3805. Zheng S.-Y. (1991), unpublished.
3806. Zheng S.-Y., A.M. Andersson, B. Stjerna and C.G. Granqvist, Appl. Opt. 32, 6303-6309 (1993).
3807. Zhong Q. and K. Colbow, Thin Solid Films 196, 305-313 (1991).
3808. Zhong Q. and K. Colbow, Thin Solid Films 205, 85-88 (1991).
3809. Zhong Q., J.R. Dahn and K. Colbow, J. Electrochem. Soc. 139, 2406-2409 (1992).
3810. Zhong Q., J.R. Dahn and K. Colbow, Phys. Rev. B 46, 2554-2560 (1992).
3811. Zhong Q., S.A. Wessel, B. Heinrich and K. Colbow, Solar Energy Mater. 20, 289-296 (1990).
3812. Zhou G., S.A. Wessel and K. Colbow, J. Phys. D 21, 1802-1806 (1988).
3813. Zhou H.S., I. Honma, H. Komiyama and J.W. Haus, J. Phys. Chem. 97, 895-901 (1993).
3814. Zhou M., P. Sheng, L. Chen and B. Abeles, Philos. Mag. B 65, 867-871 (1992).
3815. Zhou Z.-J. and J.-J. Yan, J. Magn. Magn. Mater. 115, 87-98 (1992).
3816. Ziegler J.P. and J.C. Hemminger, J. Electrochem. Soc. 134, 358-363 (1987).
3817. Ziegler J.P., E.K. Lesniewski and J.C. Hemminger, J. Appl. Phys. 61, 3099-3104 (1987).
3818. Zimmermann A.H., J. Power Sources 12, 233-245 (1984).
3819. Zimmermann A.H., M.R. Martinelli, M.C. Janecki and C.C. Badcock, J. Electrochem. Soc. 129, 289-293 (1982).
3820. Znaidi L., N. Baffier and M. Huber, Mater. Res. Bull. 24, 1501-1514 (1989).
3821. Znaidi L., N. Baffier and D. Lemordant, Solid State Ionics 28-30, 1750-1755 (1988).
3822. Zvyagin I.P., Phys. Stat. Sol. B 58, 443-449 (1973).
3823. Zvyagin I.P., in Hopping Transport in Solids, edited by M. Pollak and B. Shklovskii (Elsevier, Amsterdam, 1991), pp. 143-174.
3824. Zylberstein A. and N.F. Mott, Phys. Rev. B 11, 4383-4395 (1975).

Index

A

B

D

E

N

O

P

Q

R

S

T

W

X

Y

Z

This Page Intentionally Left Blank